

جامعة بجاية
Tasdawit n Bgayet
Université de Béjaïa

Faculty of Technology
Department of Electrical Engineering

2nd Electrical Engineering International Conference

EEIC'23

Conference Proceedings

University of Bejaia
December 05-06, 2023

ISBN : 978-9969-9732-0-4

Laboratoire de Maitrise des Energies Renouvelables



The 2nd Electrical Engineering International Conference EEIC'23

The 2nd Electrical Engineering International Conference
Bejaia, December 05-06, 2023

Editor : Electrical Engineering Department, Faculty of Technology
Adress : University A. Mira of Bejaia, Road of Targa Ouzemmour, 06000, Bejaia, Algeria
Tel/Fax : +213 34 81 37 13
E-Mails : eeic23@univ-bejaia.dz / dept.ge@tech.univ-bejaia.dz

© Publication of the Electrical Engineering Department, 2023
All rights of translation, reproduction and adaptation are reserved

ISBN : 978-9969-9732-0-4

Topics

The 121 communications selected by the Scientific Committee will be presented in twenty oral sessions and three poster sessions. The selected communications cover the following topics:

T1. Control System and Applications
T2. Electrical Machines and Drives
T3. Electric Power Systems
T4. Electromagnetic Field and Compatibility
T5. Electrostatics and High Voltage Engineering
T6. Power Electronics and Applications
T7. Renewable and Sustainable Energy
T8. Robotics and Artificial Intelligence
T9. Signal and Image Processing
T10. Telecommunication Systems and Networks

Committees

Honorary chairs

Pr. Abedelkrim Beniaïche, Rector of Bejaia University, Algeria
Pr. Mohand Amokrane Bradai, Dean of Technology Faculty, Bejaia University, Algeria

Conference General Chair

Pr. Sofia Lalouni Belaid

Conference Co-Chair

Dr. Ahmed Kasdi

Organizing Committee

Dr. Abdelli	Radia	Dr. Chekkal	Samira	Pr. Taib	Nabil
Dr. Ait Mokhtar	El Hassene	Dr. Djermouni	Kamal	Pr. Boualem	Mohamed
Dr. Amrouche	Bessam	Dr. Idjdarene	Souad	Dr. Tamalouzt	Salah
Dr. Aouzellag	Haroune	Dr. Laifaoui	Abdelkrim	Dr. Tazerart	Farid
Dr. Atroune	Salah	Dr. Mekhmoukh	Abdenour	Dr. Lehouche	Hocine

Scientific Committee

Dr. Abdelli Radia, Univ. of Bejaia, Algeria
Pr. Abudura Salam, Univ. of Medea, Algeria
Pr. Achour Abdelyazid, Univ. of Bejaia, Algeria
Dr. Aissou Massinissa, Univ. Ain Temouchent, Algeria
Dr. Ait Mokhtar El Hassene, Univ. of Bejaia, Algeria
Dr. Ait Said Hakim, Univ. of Relizane, Algeria
Dr. Amimeur Hocine, Univ. of Bejaia, Algeria
Pr. Aouzellag Djamal, Univ. of Bejaia, Algeria
Dr. Aouzellag Haroune, Univ. of Bejaia, Algeria
Dr. Aouzellag Lahacani Narimen, Univ. Bejaia, Algeria
Dr. Azib Ahmed, Univ. of Bejaia, Algeria
Dr. Azni Mohamed, Univ. of Bejaia, Algeria
Pr. Bacha Seddik, Univ. of Grenoble, France
Dr. Bajaj Mohit, G. E, Dehradun, India
Pr. Bechouche Ali, Univ. of Tizi Ouzou, Algeria
Pr. Belaid Lalouni Sofia, Univ. of Bejaia, Algeria
Pr. Belkaid Abdelhakim, Univ. of Bejaia, Algeria
Dr. Bellahsene Hocine, Univ. of Bejaia, Algeria
Pr. Bendahmane Boukhalfa, Univ. of Bejaia, Algeria
Dr. Bendahmane Akila, Univ. of Bejaia, Algeria
Dr. Bensafia Yassine, Univ. of Bouira, Algeria
Pr. Berkouk El Madjid, ENP Algiers, Algeria
Pr. Berrah Smail, Univ. of Bejaia, Algeria
Pr. Boualem Mohammed, Univ. of Bejaia, Algeria
Pr. Boualem Bareche Aicha, Univ. of Bejaia, Algeria
Pr. Boubakeur Ahmed, ENP Algiers, Algeria
Pr. Boubertakh Hamid, Univ. of Jijel, Algeria
Dr. Bouddou Riyadh, Univ. center of Naama, Algeria
Pr. Bouden Sofiane, Univ. of Khenchela, Algeria
Pr. Boudries Zoubir, Univ. of Bejaia, Algeria
Pr. Bouhali Omar, Univ. of Jijel, Algeria
Pr. Boukhezzar Boubeker, Univ. Constantine, Algeria
Pr. Boulouh Messaoud, Univ. of Guelma, Algeria
Dr. Bouzida Ahcene, Univ. of Bouira, Algeria
Dr. Bouzidi Athmane, Univ. of Bejaia, Algeria
Dr. Chabour Ferhat, Univ. of Le Havre, France
Pr. Chaiba Azeddine, Univ. of Khenchela, Algeria
Pr. Chemori Ahmed, Univ. of Montpellier, France
Pr. Chouder Aissa, Univ. of M'sila, Algeria
Pr. Dascalescu Lucien, Univ. of Poitiers, France
Pr. Ghedamsi Kaci, Univ. of Bejaia, Algeria
Pr. Ghoneim Sherif S.M., Taif Univ., Saudi Arabia
Pr. Guegyen Hervé, Centrale Supélec, Rennes, France
Pr. Haddad Salah, Univ. of Tizi Ouzou, Algeria
Pr. Hamoudi Farid, Univ. of Bejaia, Algeria
Dr. Houari Azeddine, Univ. of Nantes, France
Pr. Idjdarene Kassa, Univ. of Bejaia, Algeria
Dr. Iffouzar Koussaila, ESSA Alger, Algeria
Dr. Kasdi Ahmed, Univ. of Bejaia, Algeria
Dr. Kasmi Reda, Univ. of Bejaia, Algeria
Dr. Kermadi Mostefa, Univ. of Malaya, Malaysia
Pr. Khireddine Abdelkrim, Univ. of Bejaia, Algeria
Pr. Kouzou Abdellah, Univ. of Djelfa, Algeria
Pr. Krim Fateh, Univ. of Setif1, Algeria
Pr. Laggoune Radouane, Univ. of Bejaia, Algeria
Dr. Lehouche Hocine, Univ. of Bejaia, Algeria
Pr. Maouche Bachir, Univ. of Bejaia, Algeria
Pr. Medjdoub Abdallah, Univ. of Bejaia, Algeria
Pr. Mekhaldi Abdelouahab, ENP Algiers, Algeria
Pr. Mekhilef Saad, Univ. of Malaya, Malaysia
Dr. Mekhmoukh Abdenour, Univ. of Bejaia, Algeria
Pr. Mendil Boubekeur, Univ. of Bejaia, Algeria
Pr. Merabet Adel, Saint Mary's Univ., Canada
Dr. Mohammedi Ahmed, Univ. of Bejaia, Algeria
Dr. Mohit Bajaj, Graphic Era, Dehradun, India
Dr. Mokrani Zahra, Univ. of Bejaia, Algeria
Pr. Naimi Djemai, Univ. of Biskra, Algeria
Pr. Nichita Cristian, Univ. Le Havre, France
Pr. Nouri Hamou, Univ. of Setif1, Algeria
Pr. Onishchenko Oleg, National Univ. OMA, Odessa, Ukraine
Dr. Ouari Kamel, Univ. of Bejaia, Algeria
Dr. Ouatah Elhanafi, Univ. of Bejaia, Algeria
Pr. Petrushin Viktor, Odessa National Polytechnic Univ., Ukraine
Dr. Rahmani Allaoua, Univ. of Bejaia, Algeria
Dr. Reboul Jean-Michel, Univ. of Caen, France
Pr. Rekioua Toufik, Univ. of Bejaia, Algeria
Pr. Rekioua Ziani Djamila, Univ. of Bejaia, Algeria
Dr. Rouha Nacéra, Univ. of Bejaia, Algeria
Pr. Saou Rachid, Univ. of Bejaia, Algeria
Pr. Slimani Linda, Univ. of Setif1, Algeria
Pr. Soufi Youcef, Univ. of Tebessa, Algeria
Dr. Tafinine Farid, Univ. of Bejaia, Algeria
Pr. Taib Nabil, Univ. of Bejaia, Algeria
Pr. Takorabet Noureddine, Univ. of Nancy, France
Dr. Tamalouzt Salah, Univ. of Bejaia, Algeria
Dr. Tazerart Farid, Univ. of Bejaia, Algeria
Pr. Tounzi Abdelmounaïm, Univ. of Lille, France
Pr. Zougab Nabil, Univ. of Bejaia, Algeria

Preface

The second Electrical Engineering International conference (EEIC'23) will be hosted at the University Abderrahmane Mira of Bejaia, Algeria, organized by the department of Electrical Engineering, Faculty of Technology with the consortium of three research laboratories (LT2I, LGEB, LMER).

Our main aim is to provide an attractive forum for PhD students and researchers to present, share and discuss novel ideas in the field of Electrical Engineering and related topics.

The conference is held over two days, during 05 and 06 December 2023. We received about 160 submissions and after review process, 121 papers were selected for presentation (68 in oral form and 53 in poster) and were included in this EEIC'23 proceeding.

The conference EEIC'23 includes altogether four Keynote sessions and twenty parallel sessions which will be presented by national and international communicants.

We would like to extend our warmest thanks to all who contributed to the success of the conference, namely: organizing committee, scientific committee, session chairs, keynote speakers, PhD students and our partners.

Pr BELAID LALOUNI Sofia

On behalf of the EEIC'23

Organizing Committee

Table of Contents

Preface v

I PLENARY CONFERENCES 1

I.1 The Electrical Vehicle in the point of view of the sources, storages and converters 2
Becherif Mohamed

I.2 The flexibility and its frameworkat the service of massive and harmonious grid integration of renewables 3
Bacha Seddik

I.3 Artificial intelligence in the heart of electrical engineering 4
Soufi Youcef

I.4 Advanced power electronics for future energy systems: challenges and opportunities 5
Ghedamsi Kaci

II CONTROL SYSTEM AND APPLICATIONS (CSA) 6

II.1 Delayed sliding mode control design for chaotic systems 7
Baghdadi Hamidouche, Guesmi Kamel, Essounbouli Najib

II.2 DTC using self-tuning fuzzy speed controller design for fuel cell electric vehicle 13
Tazerart Farid, Kerrouche Farid, Rekioua Toufik, Taib Nabil

II.3 Development of antilock braking system based fuzzy logic controller for diverse road conditions 19
Kedjouti Seddik, Bouchareb Ilhem

II.4 Neuro-fuzzy controller of a dual star induction motor supplied with renewable power based on multi-level converters 23
Zaidi Elyazid, Layachi Djedoui, Bentouhami Larafi, Zouache Rafik, Rreffas Abderrahim

II.5 Speed and flux estimation of an asymmetrical six-phase induction machine using machine learning 30
Hamoudi Yanis, Amimeur Hocine, Benamara Katia, Hassaini Faycal

II.6 Enhancing wind turbine efficiency: a comparative study of two innovative MPPT control algorithms 36
Larabi Zina, Ghedamsi Kaci, Aouzellag Djamal, Nafa Fares

II.7 Application of a fractional-order synergetic controller for active power filter to enhance power quality 42
Deffaf Brahim, Sayeh Karim Fathi, Hamoudi Farid, Tamalouzt Salah

II.8 Novel six switch nine level inverter designed for electric traction . 47
Kerrouche Farid, Tazerart Farid, Taib Nabil

II.9 Single-objective optimization of Fuzzy MPPT using GWO algorithm 53
Belhaddad Abdelah, Bouchabane Abdeslem, Kacimi Mohand Akli

III ELECTRICAL MACHINES AND DRIVES (EMD) 59

III.1 Improvement of steady-state performance of direct torque control for dual star induction motor drives 60
Guedida Sifelislam, Tabbache Bekheira, Nounou Kamal, Idir Abdelhakim, Mohamed Benbouzid

III.2 Performances and lifetime improvement of hybrid electric vehicles by using NPC five-level inverter 66
Abdellaoui Hassina, Ghedamsi Kaci, Bechouche Ali

III.3 Electrical and mechanical parameters identification of a double stator induction machine 73
Lounnas Fatma, Haddad Salah, Habchi Lynda, Benouarab Saliha

III.4 Study of the parameters influencing the performance of a self-excited induction generator 79
Fares Belynda, Abdelli Radia, Bouzida Ahcene

III.5 Open phase fault tolerance solution for dual star induction machine 85
Hassaini Faycal, Chekkal Samira, Aouzellag Djamal, Hamoudi Yanis

III.6 Detection of rotor bar breakages in a dual-star induction machine . 91
Chekkal Samira, Imaouchen Yacine, Aouzellag Djamal, Hassaini Faycal

III.7 Transient thermal model analysis of three phase induction motor using both lumped parameter thermal network and finite element method 96
Bouheraoua Mustapha, Khaldi Rabah

III.8 Hybrid model for modeling air gap in electrical machines 102
Mousli Wafia

III.9 Enhancing wind power conversion efficiency with vernier dspm generator and sliding mode control 108
Redouane Abderrahmane, Saou Rachid, Guerroudj Cherif, Oukaour Amrane

III.10 Nonlinear predictive control for an asynchronous machine 115
Brahami Sofiane, Ghedamsi Kaci, Achour Abdelyazid

III.11 Behavior analysis of double star induction motor under open phase fault 119
Abbas S., Iffouzar K., Amrouche B., Ghedamsi K., Houari A., Benkhoris M. F.

III.12 Levitation force electromagnetic calculations for medium-speed trains 123
Ferroudj Yanis, Bouzidi Athmane, Takorabet Nourddine

IV ELECTRIC POWER SYSTEMS (EPS) 127

IV.1 A new efficient meta-heuristic method for solving the optimal power flow problem in power system 128
Aroua Fatima, Salhi Ahmed, Salhi Souheil, Naimi Djemai

IV.2 Multi-objective optimal power flow solution using bonobo optimizer algorithm 134
Benhabsa Imadeddine, Kouadri Ramzi, Slimani Linda

IV.3 Application of new metaheuristic algorithm for optimal placement and sizing of STATCOM device 140
Kouadri Ramzi, Benhabsa Imadeddine, Souici Oussama, Mouassa Souhil

IV.4 Deep reinforcement learning based virtual inertia control for islanded microgrids with high sharing of renewable energy sources . 146
Deboucha Houssam, Mekhilef Saad

IV.5 Bald eagle search-based optimization algorithm for optimal power flow solution in power systems 152
Ferroudj Nour el islem, Amroune Mohammed, Slimani Linda

IV.6 Enhancing power distributed generation with storage systems for sustainable energy integration 156
Rahman Md Jahidur, Tafticht Tahar, Tchakala Mouctar, Doumbia Mamadou Lamine

IV.7 Use of the dual stator induction machine in a hybrid renewable energy pumping system 162
Adjati Arezki, Rekioua Toufik, Rekioua Djamila

IV.8 Transient stability analysis of a multimachine power system . . . 168
Idirene Dimya, Medjdoub Abdellah

IV.9 Impact of TCSC on energy performance in electrical networks . . 174
Ouali Fateh, Lahacani Narimen

IV.10 Economic load dispatch with saving environment by greenhouse gas emission reduction using genetic algorithms 179
Bouzidi Athmane, Hidra Lahlou, Kenza Ydjedd, Mohand Akli Ouakli

IV.11 Analysis of space vector identification method in series active filters for electrical power quality improvement 185
Asnoun Mustapha, Kachenoura Rahma, Rahoui Adel, Brahimi Brahim

IV.12 Investigation about ferranti effect and challenge to harmonics suppression in a specific long power transmission line 191
Ainouche Toufik, Belkhiri Yamina, Moulai Hocine, Yousfi Nabil

IV.13 Estimation of the schavemaker arc model parameters for high-voltage circuit breakers 196
Latri Fatiha, Gherbi Ahmed, Nabab Alam Mahamad

IV.14 Planning study for electrical substations in Algeria 202
Laib Farah, Bouzidi Athmane

IV.15 Impact of the fault location and machine damping on the transient stability of an electrical power network 207
Idri Souad, Abdelli Radia, Hamoudi Farid

IV.16 Optimal placement of TCSC for optimizing active and reactive power using AAC PSO algorithm 213
Labed Mohamed Amir, Benidir Mohamed, Sekhane Hocine

V ELECTROMAGNETIC FIELD AND COMPATIBILITY (EMC) 217

V.1 The effect of horizontally stratified ground on the Lightning electromagnetic field calculated by the 3D-FDTD method 218
Ziane Ahmed, Arzag Kaddour, Azzouz Zin-eddine

V.2 Design of three permanent magnets drum separator for the extraction of fine iron particles 226
Belounis Abdallah, Mehasni Rabia, Belguet Oussama

V.3 Dynamic hysteresis loops using the Jiles Atherton Model based on Loss-surface formulation 230
Aidel Sofiane, Hamimid Mourad

V.4 Semi-analytical model of an electromagnetic energy harvester . . 234
Idir Badea, Maouche Bachir, Zerguini Sakina

V.5 Simulation of a non-destructive testing process equipped with a ferromagnetic core probe 239
Medjahed Sakina, Kasdi Ahmed, Maouche Bachir

V.6 Extracting of ultrasonic pulse generated by piezoelectric material using machine learning 243
Mechnane Amel, Hafdaoui Hichem, Benatia Djamel

V.7 Recovery of electromechanical vibratory energy from electromagnetic shock absorbers of vehicles 248
Bouchebbah Badis, Maouche Bachir

VI ELECTROSTATICS AND HIGH VOLTAGE ENGINEERING (EHVE) 253

VI.1 Light emission calibration technique for high voltage discharge currents measurement in liquid dielectrics 254
Moulai Hocine, Beroual Abderrahman, Nacer Azzeddine

VI.2 Comparative analysis of defect detection in electric cables by analyzing potential and electric field distribution on the outer cable surface 258
Meziani Madjid, Teguar Madjid, Mekhaldi Abdelouahab

VI.3 Influence of geometric parameters on the K factor of the current-voltage characteristic of DC corona discharge. 264
Chouali Sabrina, Kasdi Ahmed, Atroune Salah, Dascalescu Lucian

VI.4 Evaluating the lifetime of polyvinyl chloride insulation under sinusoidal voltage stress 270
Laifaoui Abdelkrim, Ait Said Hakim, Reboul Jean-Michel, Herzine Mohand Seghir

VI.5 Controlled discharge of filters media surface 278
Messaoudène Akila, Bendahmane Boukhalfa, Rahmani Allaoua, Dascalescu Lucian

VI.6 Physical study of an electrically aged silicone insulator under pollution 283
Rouha Nacera, Bouchelga Fatma, Ouchenir Nouredine, Remache Saadi

VI.7 Experimental study of a vibratory-type triboelectric charging device 289
Atroune Salah, Taib Nabil

VI.8 Study of space charge current in power cables using the alternating thermal wave method 294
Brakna Ikram, Reboul Jean-Michel, Aissou Massinissa, Laifaoui Abdelkrim

VI.9 A graphical tool for the tracking of a single particle in an electric field 298
Kachi Miloud, Bechkoura Hana, Mouhoub Sarra, Bouchelkha Abdelhafid

VI.10 Simulation of lightning strikes on photovoltaic farms 302
Nacereddine Kamal, Boubakeur Ahmed, Mekhaldi Abdelouahab, Teguar Madjid, Moulai Hocine

VI.11 Electric field behavior of a water droplet on the surface of polymer insulators under ac stress using finite element method 308
Aouabed Fatiha, Bayadi Abdelhafid, Boudissa Rabah

VI.12 Influence of the number of superhydrophobic coating layers on their electrical performance 314
Alouache Sara, Medjdoub Abdellah

VI.13 Electric field and potential quantification on a deposit of drops covering a superhydrophobic surface under AC voltage 318
Bouchelga Fatma, Rouha Nacera, Hamour Khaled, Kornhuber Stefan

VI.14 Optimizing the two-plane electrostatic precipitator with a small blade for airborne particulate matter filtration 325

Hebbar Nihed, Aissou Massinissa, Ait Said Hakim

VI.15 Aging of composite insulators under desert conditions 330
Sahli Zahir

VII POWER ELECTRONICS AND APPLICATIONS (PEA) 336

VII.1 Effect of bandwidth of spiral micro coil on electrical parameters . 337
Benazzouz Younes, Guendouz Djilalia

VII.2 Intelligent and robust control for direct gridconnected pv system powered arc welding machine 343
Halledj Salah Eddine, Bouafassa Amar

VII.3 Flyback DC-DC micro-converter with integrated octagonal monolithic planar micro-transformer 349
Derkaoui Mokhtaria, Benhadda Yamina

VII.4 Integrated square on-chip inductor for photovoltaic converter applications 355
Derkaoui Mokhtaria, Benhadda Yamina

VII.5 Modeling of octagonal planar microtransformer for DC-DC converter applications 361
Derkaoui Mokhtaria, Benhadda Yamina

VIII RENEWABLE AND SUSTAINABLE ENERGY (RSE) 367

VIII.1 Direct vector control and particle swarm optimisation in dual star induction generator 369
Benamara Katia, Amimeur Hocine, Hamoudi Yanis

VIII.2 Energy management of a non-autonomous photovoltaic station for hybrid vehicle loading 375
Djermouni Kamel, Berboucha Ali, Ghedamsi Kaci, Aouzellag Djamal, Tamalouzt Salah

VIII.3 Management of a hybrid system of renewable energies in pumping 381
Adjati Arezki, Rekioua Toufik, Rekioua Djamila

VIII.4 A control strategy of dual stars induction generator with power limitation 387
Hamitouche Kamel, Chekkal Samira, Aouzellag Djamal

VIII.5 A finite state machine based energy management for fuel-cell hybrid vehicle 393
Aouzellag Haroune, Amrouche Bessam, Iffouzar Koussaila

VIII.6 Robust control of dfig wind turbines in sub/super-synchronous operation using integral backstepping controller 399
Itouchene Hichem, Amrane Fayssal, Boudries Zoubir

VIII.7 Control of a wind turbine based on dfig by improved direct torque control using fuzzy logic 404
Sayeh Karim Fathi, Tamalouzt Salah, Zaine Djamel, Sahri Younes, Deffaf Brahim, Lalouni Belaid Sofia

VIII.8 Enhancing photovoltaic array performance through optimizing power during mismatch conditions under Series-parallel (SP) and Total Cross-Tied (TCT) configurations 408
Abad Lahlou, Tamalouzt Salah, Djermouni Kamel, Sayeh Karim Fathi

VIII.9 Sizing and energy management of a multi-source pumping system 413
Amrouche Karim, Abdelli Radia, Benhacine Nasr-Eddine

VIII.10 Characterization and mitigation of multipeak phenomena in photovoltaic systems under environmental conditions and electrical fault 419
Abad Lahlou, Tamalouzt Salah, Djermouni Kamel, Sayeh Karim Fathi

VIII.11 Power management strategy for stand-alone DFIG-based wind turbine with battery storage 423
Djoudi Oualid, Lalouni Belaid Sofia, Tamalouzt Salah

VIII.12 Enhancing wind energy conversion system efficiency with fuzzy logic controllers for doubly fed induction generators 429
Abdelli Radia, Bouzida Ahcene

VIII.13 Enhancement DTC control for SEIG in variable-speed wind turbines, associated with a energy storage system 435
Berabez Kahina, Hacini Ismail, Hamoudi Farid, Idjdarene Kassa

VIII.14 Fuzzy logic MPPT algorithm for standalone photovoltaic water pumping system using separately excited DC motor 441
Zoughab Samir, Belhaouchet Nouri, Sayah Samir

VIII.15 Artificial intelligence technique to compare between the performance of different technologies of PV Modules in the photovoltaic systems 447
Hafdaoui H., Belhaouas N., Boudjelthia E. K., Assem H., Hadjrioua F., Madjoudj N.

VIII.16 Wind energy conversion system based on dual stator windings permanent magnet synchronous generator fed by multilevel converter 451
Madi Yazid, Dendouga Abdelhakim, Aouzellag Djamal

VIII.17 Grid-connected multi-source energy systems: control and management 458
Chenna Amina, Aouzellag Djamal, Ghedamsi Kaci

VIII.18 Comparative analysis of P&O, PSO, and ANN methods for MPPT in photovoltaic systems 464
Lagoune Meryem, Latreche Samia, Babes Badreddine, Khemliche Mabrouk

VIII.19 Energy management strategy of PV system with battery supercapacitor hybrid energy storage for stand-alone applications 469
Hacini Ismail, Lalouni Belaid Sofia, Idjdarene Kassa, Berabez Kahina

VIII.20 Energy management for renewable electricity production system including hybrid hydrogen sub-system 474
Zidane Nourredine, Lalouni Belaid Sofia

VIII.21 Model predictive for enhancing resistive droop control stability in isolated AC microgrid 480
Bousbia Larbi, Toufouti Riad

VIII.22 Study and manufacture of a parabolic solar concentrator with automatic tracking - Experimental tests 484
Mebarki Youcef

VIII.23 Robust input-output linearizing and decoupling control of wind turbine based on DFIG under variable wind speed 490
Itouchene Hichem, Boudries Zoubir, Amrane Fayssal, Issaadi Idris

VIII.24 Optimal location and sizing of DG using fuzzy logic for improving voltage profile and reducing power losses 496
Kennouche Samir, Aouzellag Narimen, Chekkal Samira

VIII.25 Enhancement of fuzzy direct torque control performances for doubly fed induction generator wind turbines 501
Sayeh Karim Fathi, Tamalouzt Salah, Zaine Djamel, Djermouni Kamel, Deffaf Brahim, Lalouni Belaid Sofia

VIII.26 Power management for Hybrid Electric Vehicles (HEVs) based on Permanent Magnet Synchronous Motors (PMSMs) using passivity control 506
Amrouche B., Aouzellag H., Iffouzar K., Nacef S., Cherif T. O., Ghedamsi K.

IX ROBOTICS AND ARTIFICIAL INTELLIGENCE (RAI) 512

IX.1 A sampling-based approach for path planning of unmanned aerial manipulators 513
Zamoum Housseyn, Bouzid Yasser, Guiatni Mohamed

IX.2 Multispectral stereo-vision for outdoor localization 519
Benyounes Fahima, Nemra Abdelkrim

IX.3 Robust PUMA560 control with backstepping-ADRC 525
Ben Messaoud Safinaz, Belkhiri Mohammed

IX.4 Optimal trajectory planning with obstacle avoidance based on water cycle algorithm for a flying robot 531
Tenniche Nesrine, Mendil Boubekeur, Tighzert Lyes

IX.5 Remote control of mentor robot via Bluetooth 537
Sait Oussama, Latréche Samia, Khemliche Mabrouk, Sait Belkacem

IX.6 Comparative study between two parametric identification methods used to identify the building heating system 543
Ouaret Ahmed, Lehouche Hocine, Mendil Boubekeur, Gueguen Hervé, Fredj Siham

IX.7 Asymptotic stabilization of a morphing drone using interconnection and damping assignment-passivity based control 549
Belmouhoub Amina, Bouzid Yasser, Medjmadj Slimane, Derrouaoui Saddam Hocine, Guiatni Mohamed

IX.8 A comparison of fuzzy logic and adaptative backstepping in diabetics controler 556
Touitou Ikram, Ziani Salim

IX.9 Model-based states estimation approach applied to a reconfigurable quadrotor for position and attitude tracking control 561
Salmi Abdenour, Guiatni Mohamed, Bouzid Yasser, Derrouaoui Saddam Hocine, Boudjema Fares

X SIGNAL AND IMAGE PROCESSING (SIP) 567

X.1 A new algorithm for extracting fetal (fECG) signal from abdominal (aECG) using wavelet transform 568
Radjef Lilia, Omari Tahar, Benlatreche Mohamed Salah, Cherif Ahmed El-amine Tayeb, Ladgi Khaoula

X.2 A comparative study of local binary pattern and local ternary pattern for fault detection in induction motors 577
Behloul Fatiha, Tafinine Farid

X.3 Speech denoising based on empirical wavelet transform and adaptive threshold 581
Kemiha Mina, Kacha Abdellah, Chouikhi Lotfi

X.4 Efficient ECG signal denoising technique based on the empirical mode decomposition method and the discrete wavelet transform . 586
Kahlessenane Yaaqoub, Bouaziz Fatiha, Siarry Patrick, Hamouche Oulhadj

X.5 Efficient gear fault detection in rotating machines through envelope-derivative operator analysis 591
Bouhafs Lina, Tamalouzt Salah, Bouzida Ahcene

X.6 Comparative evaluation of YOLOv5 and YOLOv8 across diverse datasets 595
Sid Ahmed Soumia, Belaalia Asma, Namoune Khaoula

XI TELECOMMUNICATION SYSTEMS AND NETWORKS (TSN) 601

XI.1 Analytical study on energy optimization via dynamic transmission power adjustment for task offloading in edge computing . . . 602
Babaghayou Messaoud, Chaib Noureddine, Labraoui Nabila

XI.2 Performance analysis of spatially modulated MIMO systems . . . 608

Beknadj Dalil, Tounsi Mohamed, Tayakout Hakim, Hamadi Yasmine

XI.3 Inter-numerology interference analysis and mitigation techniques for 5G networks 614
Ouazziz Yacine, Azni Mohamed, Tounsi Mohamed

XI.4 Enhacing the performances of 5G communication systems with rate splitting multiple access. 620
Bellahsene Hocine, Kharouni Sounia

XI.5 Enhancing the performance of wireless communication systems through the use of beamforming antenna and massive MIMO technology 626
Zareb Nour El Houda, Bellahsene Hocine, Merabet Nesrine

XI.6 Terahertz for wireless communication and radio frequency 632
Latreche Sofiane, Bellahsene Hocine, Taleb-Ahmed Abdelmalik

XI.7 Cellular-connected UAVs : coverage analysis using SWIPT and up-tilted antenna 638
Alkama Dina, Ouamri Mohamed Amine, Alkama Lynda, Azni Mohamed

XI.8 Improved gain for T-Shaped slot antenna using new EBG/AMC reflector for IOT applications 643
Merabet Imen, Rouabah Khaled, Belazzoug Massinissa

XI.9 Design and simulation of rectangular microstrip patch antenna for WLAN applications 649
Degachi Riadh, Ghendir Said

XII Author Index **653**



Conference Program

EEIC'23 Program

Tuesday 05 December 2023

08:00 - 09:00	**Registration**			
09:00 - 09:30	**Opening Ceremony**			
09:30 - 10:15	**Plenary 1: Pr Mohamed BECHERIF -The Electrical Vehicle in the Point of View of the Sources, Storages and Converters (Chairs : Pr SOUFI, Pr TAIB)**			
10:15 - 10:45	**Poster Session 1 & Coffee Break**			
	Chairs : Dr AMIMEUR, Dr RAHMANI, Dr ROUHA, Dr BOUZIDI, Dr BOUZIDA			
	PEA : 02 - 03	*EMC : 01 - 06 - 07*	*EHVE : 08 - 09 - 10 - 11*	*CSA : 08-09 | RSE-18*
	EMD : 09 - 10 - 11		*EPS : 07 - 13 - 14 - 15*	
10:45 - 11:30	**Plenary 2 : Pr Seddik BACHA -The Flexibility and its Frameworkat the Service of Massive and Harmonious Grid Integration of Renewables (Chairs : Pr KRIM, Pr GHEDAMSI)**			
	Oral Communications - Session 1 -			
	Room A	***Room B***	***Room C***	***Room D***
	Chairs: Pr IDJDARENE Pr BELAID	**Chairs: Pr CHAIBA Pr D. AOUZELLAG**	**Chairs: Pr MEDJDOUB Dr N. AOUZELLAG**	**Chairs: Pr KHIREDDINE Dr MEKHMOUKH**
	T7 (RSE)	**T2 (EMD)**	**T3 (EPS)**	**T9 (SIP)**
11:30 - 11:45	*RSE-01 (K. Benamara)*	*EMD-01 (S. Guedida)*	*EPS-01 (F. Aroua)*	*SIP-01 (L. Radjef)*
11:45 - 12:00	*RSE-02 (K. Djermouni)*	*EMD-02 (H. Abdellaoui)*	*EPS-02 (I. Benhabsa)*	*SIP-02 (F. Behloul)*
12:00 - 12:15	*RSE-03 (A. Adjati)*	*EMD-03 (K. Benzaoui)*	*EPS-03 (R. Kouadri)*	*SIP-03 (M. Kemiha)*
12:15 - 12:30	*RSE-04 (K. Hamitouche)*	*EMD-04 (F. Lounnas)*	*EPS-04 (S. Boudab)*	*SIP-04 (Y. Kahlessenane)*
12:30 - 14:00	**Lunch**			
14:00 – 14:45	**Plenary 3: Pr Youcef SOUFI – Artificial Intelligence in the Heart of Electrical Engineering (Chairs : Pr D. REKIOUA, Dr HADJ ARAB)**			
	Oral Communications - Session 2 -			
	Room A	***Room B***	***Room C***	***Room D***
	Chairs: Dr KASDI Dr LAIFAOUI	**Chairs: Dr ABDELLI Dr TAMALOUZT**	**Chairs: Pr MAOUCHE Dr A. BENDAHMANE**	**Chairs: Pr KRIM Pr BOUDRIES**
	T5 (EHVE)	**T1 (CSA)**	***T4 (EMC)***	**T7 (RSE)**
14:45 - 15:00	*EHVE-01 (H. Moulai)*	*CSA-01 (H. Baghdadi)*	*EMC-04 (B. Idir)*	*RSE-05 (H. Aouzellag)*
15:00 - 15:15	*EHVE-02 (M. Meziani)*	*CSA-02 (F. Tazerart)*	*EMC-2 (A. Belounis)*	*RSE-06 (H. Itouchene)*
15:15 - 15:30	*EHVE-03 (S. Chouali)*	*CSA-03 (S. Kedjouti)*	*EMC-3 (S. Aidel)*	*RSE-07 (K. Sayeh)*
15:30 – 16:00	**Poster Session 2 & Coffee Break**			
	Chairs : Pr MOHAMMEDI, Dr MEZZAI, Dr TAFININE, Dr KASMI			
	PEA-04	*RAI : 08 - 09*	*SIP : 05 - 06*	*TSN : 08 - 09*
	RSE : 10 - 14 - 16 - 17 - 19 - 20 - 21 - 22 - 25			
	Oral Communications - Session 3 -			
	Room A	***Room B***	***Room C***	***Room D***
	Chairs: Pr BERRAH Dr BELLAHSENE	**Chairs: Pr D. REKIOUA Pr CHAIBA**	**Chairs: Pr ACHOUR Pr MENDIL**	**Chairs: Dr BOUZIDI Pr B. BENDAHMANE**
	T10 (TSN)	**T7 (RSE)**	**T8 (RAI)**	***T4 (EMC)***
16:00 - 16:15	*TSN-01 (M. Babaghayou)*	*RSE-08 (L. Abad)*	*RAI-01 (H. Zamoum)*	*EHVE-04 (A. Laifaoui)*
16:15 - 16:30	*TSN-02 (D. Beknadj)*	*RSE-09 (K. Amrouche)*	*RAI-02 (A. Nemra)*	*EHVE-16 (A. Laifaoui)*
16:30 - 16:45	*TSN-03 (Y. Ouazziz)*	*PEA-01 (Y. Benazzouz)*	*RAI-03 (S. Ben Messaoud)*	*EMC-5 (S. Medjahed)*
19:00	**Dinner**			

EEIC'23 Program

Wednesday 06 December 2023				
08:00 - 09:00	**Registration**			
09:00 – 09:45	**Plenary 4: Pr. Kaci GHEDAMSI - Advanced Power Electronics for Future Energy Systems: Challenges and Opportunities (Chairs : Pr KRIM, Pr TAIB)**			
Oral Communications - Session 4 -				
	Room A	***Room B***	***Room C***	***Room D***
	Chairs: Pr HAMOUDI Dr BOUZIDI	**Chairs: Pr BERRAH Pr KHIREDDINE**	**Chairs: Pr BELKAID Dr TAZERART**	**Chairs: Pr BOUKHEZZAR Dr LEHOUCHE**
	T3 (EPS)	***T10 (TSN)***	**T7 (RSE)**	**T8 (RAI)**
09:45 - 10:00	*EPS-05 (H. Deboucha)*	*TSN-04 (H. Bellahsene)*	*RSE-11 (O. Djoudi)*	*RAI-04 (N. Tenniche)*
10:00 - 10:15	*EPS-06 (N. Ferroudj)*	*TSN-05 (N. Zareb)*	*RSE-12 (R. Abdelli)*	*RAI-05 (O. Sait)*
10:15 - 10:30	*EPS-08 (H. Terbah)*	*TSN-06 (S. Latreche)*	*RSE-13 (K. Berabez)*	*RAI-06 (A. Ouaret)*
10:30 - 10:45		*TSN-07 (D. Alkama)*		*RAI-07 (Y. Bouzid)*
10:45 – 11:15	**Poster Session 3 & Coffee Break**			
	Chairs : Dr N. AOUZELLAG, Dr RAHMANI, Dr H. AOUZELLAG, Dr AZIB, Dr MOKRANI			
	PEA-05	*EPS : 16 - 17 - 18 - 19*	*EMD : 12 - 13 - 14*	*TSN-10*
	EHVE : 12 - 13 - 14 - 15		*RSE : 15 - 23 - 24 - 26*	
Oral Communications - Session 5 -				
	Room A	***Room B***	***Room C***	***Room D***
	Chairs: Pr SAOU Pr CHAIBA	**Chairs: Dr LAIFAOUI Dr OUATAH**	**Chairs: Pr HAMOUDI Pr MEDJDOUB**	**Chairs: Pr BOUDRIES Pr OUARI**
	T2 (EMD)	***T5 (EHVE)***	***T3 (EPS)***	***T1(CSA)***
11:15 - 11:30	*EMD-05 (F. Belynda)*	*EHVE-05 (A. Messaoudene)*	*EPS-09 (A. Adjati)*	*CSA-04 (E. Zaidi)*
11:30 - 11:45	*EMD-06 (A. Chahmi)*	*EHVE-06 (N. Rouha)*	*EPS-10 (D. Idirene)*	*CSA-05 (Y. Hamoudi)*
11:45 - 12:00	*EMD-07 (F. Hassaini)*	*EHVE-07 (S. Atroune)*	*EPS-11 (F. Ouali)*	*CSA-06 (Z. Larabi)*
12:00 -12:15	*EMD-08 (S. Chekkal)*		*EPS-12 (A. Bouzidi)*	*CSA-07 (B. Deffaf)*
12:15 - 12:45	**Closing ceremony**			
12:45 -13:00	**Photo participants EEIC'23**			
13:00	**Lunch**			

Laboratoire de Maitrise des Energies Renouvelables

UPI
The best solution with the right partner

Force

Star ستار

ASUS
IN SEARCH OF INCREDIBLE

ceVital

REBOBINAGE INDUSTRIEL
Etablissement BOUKARI Boualem
Adresse:TIZI VLG IGHIL OUAZZOUG BEJAIA
TEL/FAX:034 11 61 64 Mob: 0550 90 88 25
e-mail: boukari.rebobinage@yahoo.fr

HB HOTEL BRAHMI

I

PLENARY CONFERENCES

Sommaire

I.1 The Electrical Vehicle in the point of view of the sources, storages and converters **2**

I.2 The flexibility and its frameworkat the service of massive and harmonious grid integration of renewables **3**

I.3 Artificial intelligence in the heart of electrical engineering **4**

I.4 Advanced power electronics for future energy systems: challenges and opportunities **5**

The Electrical Vehicle in the Point of View of the Sources, Storages and Converters

Pr. Mohamed BECHERIF

(University of Technology of Belfort-Montbéliard, France)

***Abstract*— The Electrical vehicle (EV) is more and more sold and used in modern countries. For example, the Tesla model Y was the world's Best-Selling car in Q1 2023. This electrical vehicle is challenging many issues in the point of view of the Electrical Engineering engineers and researchers in terms of the embedded sources, storages and converters. This talk will present some of the issues and technological aspects. Different EV topologies is presented and discussed.**

Biography:



Mohamed Becherif obtained his Engineer in Automatic Control from Polytechnical School of Algeria 99, DEA and PhD in Automatic Control from University of Paris Sud/Supélec in 2001 and 2004 respectively and joined UTBM since 2004. He is the Head of the Smart Building and Energy Efficiency, Energy Department and member of Femto-ST CNRS Lab. He is/was a scientific co-responsible or Principal Investigator in three European Projects FP7, French and international projects, and several industrial projects. He is co-author of more than 125 journal papers and more than 300 conference papers. He was/is the Manager Editor and Guest Editor of different Special Issue in different Elsevier Journals.

He was the General Chair of the following conferences: ICEREGA'16 + 17 +18+20, EMF'17, cochair of ICEE'17, International Examinator on Energies for Czech Republic, Estonia, EAU, Egypt. He was/is the supervisor of 20 PhD and jury member in 21. He was invited professor in China, Canada, Egypt and Algeria. In 2020, 2021, 2022 and 2023, he was/is listed by Stanford University as one of the World's top 2% Scientists (most cited scientists in various disciplines).

The Flexibility and its Framework at the Service of Massive and Harmonious Grid Integration of Renewables

Pr. Seddik BACHA

(University of Grenoble Alpes, France)

Biography:



Seddik Bacha (Senior Member, IEEE) was born in Ighram, Algeria in 1958. He received the engineering and magister degrees from the National Polytechnic School of Algiers, El Harrach, Algeria, in 1982 and 1990, and the Ph.D. and H.D.R. degrees from Grenoble Electrical Engineering Laboratory, Grenoble, France, in 1993 and 1998, respectively. He was an Assistant Professor during six years in Algeria with the National Polytechnic School of Algiers and University of Bejaïa, Algeria. In 1993 he has been appointed as an Assistant Professor with Grenoble University, Grenoble, and got Full Professor position in 1998. He has been leading the Power System Group inside G2Elab during more than ten years. He was the Deputy Director of the GDR SEEDS. He is currently Program Scientific Director and Scientific Council Chairman with the SuperGrid Institute of Energy Transition, France. His research interests include based on the modelling and control of electrical energy processes: Renewable energy systems, intelligent buildings, V2G, microgrids and HVDC super grids.

EEIC'23

Artificial Intelligence in the Heart of Electrical Engineering

Pr. Youcef SOUFI

(University of Tebessa, Algeria)

***Abstract*— Artificial intelligence is revolutionizing industries and transforming the way we live and work. One area where AI is particularly impactful is electrical engineering, where it is being used to create smarter, more efficient systems. The combination of electrical engineering and artificial intelligence is driving the future of innovation and efficiency in various industries, including energy, transportation, and manufacturing. As artificial intelligence continues to evolve, we can expect to see even more exciting applications of this technology in the field of electrical engineering. Artificial intelligence has provided a great potential and space for optimization in the field of electrical engineering. This can not only bring about a significant improvement not only with regards to the economic aspects but also in the safety and the actual control of the operation where, the world economy is undergoing transformations associated with the transition to innovative and digital technologies due to the need to reduce production costs, save resources, improve environmental safety, reduce industrial and man-made disasters, etc. Digitalization and artificial intelligence penetrate into most sectors of the economy, including the electrical engineering which requires the development and widespread use of end-to-end technologies based on the introduction of industrial Internet, components of robotics, wireless communications, artificial intelligence.**

The application of Artificial Intelligence technologies in electrical engineering has been an active area of research for about a decade and significant successes have been achieved and the rapid development and advancement of artificial intelligence can provide powerful tools in many aspects of the electrical system, including power system planning and design, coordinated control, simulation, prediction, estimation, diagnosis and identification.

This presentation addresses critical issues on the introduction of the artificial intelligence technology in electrical engineering where the main objective of this presentation is to provide a contemporary look at the current state of the art on the application of the artificial intelligence in electrical systems as well as to provide a better understanding of the technologies, potential advantages and research challenges of this approach and provoke interest among the research community to further explore this promising research area.

Biography:



Youcef SOUFI received the B.Eng. (1991) and PhD degree (2012) from the Universit of Annaba, Algeria in Electrical Engineering. Since 2000 he has been with the Department of Electrical Engineering, Laboratory of Electrical Engineering at the University Echahid Larbi Tebessi, Tebessa, Algeria where: He is currently a Professor in electrical engineering. His main and current major research interests include application of Artificial intelligence in electrical engineering, Renewable energy, electrical machines control, power electronics and drives. He has published and co-authored more than 200 technical papers in scientific journals and conference proceedings since 2000. He is the member of editorial board of many journals, and the member of technical program committee / international advisory board/ international steering committee of many international conferences. His email address is: youcef.soufi@univ-tebessa.dz or y_soufi@yahoo.fr

Advanced Power Electronics for Future Energy Systems: Challenges and Opportunities

Pr. Kaci GHEDAMSI

(University of Bejaia, Algeria)

***Abstract*— The global energy landscape is undergoing a profound change, driven by the urgent need for sustainability and efficiency. As we navigate this transition, the role of power electronics is becoming increasingly important. Power electronics, which encompasses a wide range of technologies that facilitate the conversion and control of electrical energy, is at the forefront of innovation. Its development is critical to meeting the challenges of future energy systems, while opening up exciting prospects for a more sustainable and adaptable energy future.**

The keynote will focus on current energy systems, the challenges and perspectives of advanced power electronics in the context of emerging energy systems.

Biography:



Professor GHEDAMSI Kaci received the B. Eng. degree in Electrical Engineering from the University of Tizi-0uzou in 1999, and his Magister of Electrical Engineering from Military School Polytechnic of Algiers in 2002, and his Ph.D of Sciences from National School Polytechnic of Algiers in 2008. He is currently a research professor in the Electrical Engineering Department, he is also Director of the LMER Laboratory at the University of Bejaia. His research interests include the power electronics, electrical drives, and renewable energy. His email address is: kaci.ghedamsi@univ-bejaia.dz.

II

CONTROL SYSTEM AND APPLICATIONS (CSA)

Sommaire

II.1 Delayed sliding mode control design for chaotic systems 7
II.2 DTC using self-tuning fuzzy speed controller design for fuel cell electric vehicle 13
II.3 Development of antilock braking system based fuzzy logic controller for diverse road conditions 19
II.4 Neuro-fuzzy controller of a dual star induction motor supplied with renewable power based on multi-level converters 23
II.5 Speed and flux estimation of an asymmetrical six-phase induction machine using machine learning 30
II.6 Enhancing wind turbine efficiency: a comparative study of two innovative MPPT control algorithms 36
II.7 Application of a fractional-order synergetic controller for active power filter to enhance power quality 42
II.8 Novel six switch nine level inverter designed for electric traction 47
II.9 Single-objective optimization of Fuzzy MPPT using GWO algorithm 53

Delayed Sliding Mode Control Design for Chaotic Systems

Baghdadi HAMIDOUCHE[1], Kamel GUESMI[2], Najib ESSOUNBOULI[2]
[1]LAADI, Djelfa University, Djelfa, Algeria
E-mail: b.hamidouche@univ-djelfa.dz
[2]SCReSTIC, Reims University, Reims, France
E-mail: guesmi01@univ-reims.fr
[3]SCReSTIC, Reims University, Reims, France
E-mail: essounbouli01@univ-reims.fr

Abstract—
This paper presents a novel approach for controlling and stabilizing chaotic systems. The proposed approach combines the widely used sliding mode control with the time-delayed synchronization technique. By using both of them in one control law, the synchronization error between the system's current state and its delayed state by one period should be eliminated. Indeed, this error is utilized to define the sliding surfaces with the objective to force the synchronization error as well as the sliding surface to attain the origin. The effectiveness of the proposed approach is demonstrated using the Lyapunov stability theory with an analytical analysis and verification of the system's stability under the proposed control approach. Furthermore, numerical simulations are conducted to show the simplicity, stability, efficiency, and robustness of the proposed approach.

Chaotic systems, Sliding mode control, Synchronization techniques, Time-delayed system, Unstable periodic orbits, Rossler system.

I. Introduction

Chaos theory is a subdivision within the broader framework of nonlinear systems theory. Edward Lorenz made the initial observation of the chaos phenomenon in 1963 during his examination of a model representing the convective processes in Earth's atmosphere [1], Lorenz's notable contribution was a third-order autonomous system that had only two quadratic terms involving multiplication. Surprisingly, despite its simplicity, this system exhibited highly intricate and complex dynamical behaviors. Many systems were developed, after that, such as the Rossler system [2], Henon system [3], Chen's system [4], and Lü system [5].
Chaos refers to the unpredictable, non-repetitive long-term behavior observed in deterministic systems. It is characterized by its aperiodic nature and its high sensitivity to initial conditions. This last indicates that the system has a positive Lyapunov exponent.
At first, it was believed to be impossible to control the chaotic system until the 1990s, when Ott, Grebogi, and Yorke developed the OGY method to control chaos [6]. In the same year, Pecora and Carroll demonstrated that two identical chaotic systems, despite having different initial conditions, can be synchronized when they are coupled in a configuration where one system acts as a master and the other as a slave. This arrangement enables the master system to impose synchronization on the slave system [7].

Following the works of Ott et al., Pecora, and Carroll, many control techniques for stabilizing and synchronizing chaotic systems have been extensively studied in the past decades such as the delayed feedback control (DFC) technique proposed in 1992 by Pyragas for the control and suppression of chaos [8], the stabilization through synchronization with a stable system [9], the generalized predictive control (GPC) [10], the optimal control [11], the adaptive backstepping control [12], the impulsive approach [13], the adaptive control [14], the proportional-integral (PI) technique [15], and the sliding mode control (SMC) [16]–[18].

The sliding mode control design is indeed recognized as one of the most powerful control techniques extensively investigated for the stabilization and control of chaotic systems. This method offers robustness against uncertainties and disturbances, making it particularly suitable for dealing with the inherent complexity and unpredictability of chaotic dynamics. The SMC effectively stabilizes and controls chaotic systems by defining a sliding surface and implementing a control law that ensures the system's trajectory convergence to and stays on this surface. It uses the control action's discontinuous nature to precisely and swiftly move the system's state onto a desired sliding surface, ensuring hence adaptability and robustness against disturbances and unpredictability.

The SMC is a popular choice and a useful tool for solving the challenges posed by chaotic dynamics. Numerous algorithms and strategies have been developed as a consequence of the extensive research on

SMC to stabilize diverse chaotic systems. Indeed, within this research direction, a notable approach involving the combination of DFC and SMC was proposed in [19]. This hybrid approach combines the advantages of both methods to effectively control chaotic systems. This combination has been explored in various studies such as the control of chaos in an Atomic Force Microscope (AFM) system where the control objective was to ensure the system's asymptotic stability [20]. We can also find the same idea of hybridization used to eliminate chattering in the control of an autonomous underwater vehicle based on the state feedback approach and the sliding mode control [21]. The synchronization of time delayed chaotic system via robust adaptive sliding mode control can be found in [22], [23], and the control and stabilization of chaos in the Rossler chaotic system by three control laws formulated by the combination of the SMC and time-delayed synchronization were discussed in [24]. These studies demonstrate promising results in the use of hybrid control laws to stabilize chaotic systems and enhance controller performance and capabilities.

In this context, we present in this paper a new hybrid strategy that combines, in one control law, the SMC with synchronization techniques to effectively control and stabilize unstable periodic orbits (UPOs) of chaotic systems. Indeed, the synchronization's goal is to align or synchronize the behavior of the current state of the system with its state delayed by exactly one period of UPOs. With the incorporation of the SMC, known for its robustness and ability to handle uncertainties, with the synchronization technique, we aim to achieve stabilization of UPOs. The synchronization technique facilitates the coordination and alignment of the system's trajectories, ensuring that the unstable periodic orbits are controlled and stabilized. The combined approach presented in this paper offers a promising method to manipulate and stabilize UPOs in chaotic systems. By leveraging the strengths of both SMC and synchronization techniques, we demonstrate the potential to effectively control and stabilize these critical trajectories in chaotic dynamics through a numerical example.

The remainder of this paper is structured as follows: Section II, presents and analyzes the benchmark Rossler system as an example of chaotic systems. It serves as a representative case study to illustrate the concepts and techniques that will be discussed in this paper. Section III includes the formulation of the stabilization problem, which aims to provide a theoretical foundation for the proposed approach. Additionally, the Lyapunov function is presented to validate the theoretical results and show its effectiveness. The last section IV illustrates the simulation results of the Rossler benchmark controlled by the proposed approach.

II. Problem statement

In the literature, numerous benchmarks of chaotic systems are available for researchers to use as standardized models for testing and validation purposes. In our case, we have chosen the Rossler system given by (1), to demonstrate the effectiveness of the proposed approach.

$$\begin{cases} \dot{x}(t) = -y(t) - z(t) \\ \dot{y}(t) = x(t) + ay(t) \\ \dot{z}(t) = b + z(t)(x(t) - c) \end{cases} \tag{1}$$

where x, y and z are the state variables, a, b and c are the system parameters. When they are chosen as $a = 0.2, b = 0.2$, $c = 5.7$, and for initial conditions $[x(0), y(0), z(0)] = [1, 2, 5]$ the system attractor is represented by figure 1. On the other hand, figure 2 illustrates the system states time evolution.

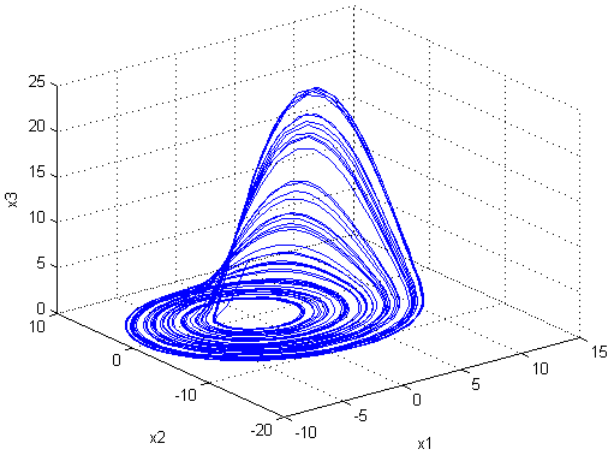


Figure 1. Rossler system behavior without control

By examining figures 1 and 2, it is obvious to say that the Rossler system exhibits chaotic behavior. To accurately assess and quantify this behavior, the Lyapunov exponent is utilized as the most reliable qualitative measure for characterizing the system's dynamics. In order to calculate the Lyapunov exponent, we employ Wolf's algorithm [25] built into the Matlab environment. By using this algorithm, we can accurately determine the Lyapunov exponent as:
$\lambda_1 = 0.0738$, $\lambda_2 = 0.0005$ and $\lambda_3 = -2.3069$.
Given that the Rossler system exhibits chaotic behavior with a positive Lyapunov exponent, the objective is, now, to find a control law that can structurally stabilize the system and guide system towards a more regular

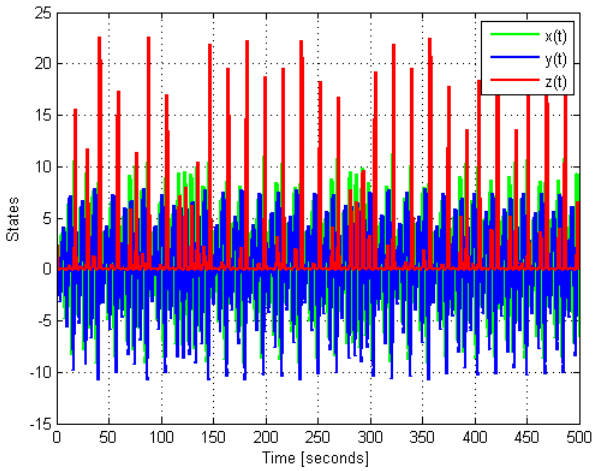


Figure 2. Time behavior of $x(t)$, $y(t)$ and $z(t)$ states without control

and predictable state.
To achieve this objective, we propose to use a hybrid strategy that integrates sliding mode control with synchronization technique into one single control law. The objective of this approach is to achieve synchronization between the current state of the system and its delayed state by exactly one period of UPOs. By doing so, the aim is to stabilize the system at the desired unstable periodic orbit (UPO).

III. Main results

In this section, the SMC control law is employed to accomplish the state synchronization of the Rossler system's present state with its delayed state by one period. The objective is to address synchronization challenges for stabilizing chaotic systems by using the synchronization error to define the switching surface-based approach, for which a sliding mode control (SMC) is developed. This SMC design ensures the achievement of synchronization between the master and slave systems.
To achieve the desired synchronization, the master and slave Rossler systems are described by the differential equations (2) and (3), respectively.
Master system:

$$\begin{cases} \dot{x}(t-\tau) = -y(t-\tau) - z(t-\tau) \\ \dot{y}(t-\tau) = x(t-\tau) + ay(t-\tau) \\ \dot{z}(t-\tau) = b + z(t-\tau)(x(t-\tau) - c) \end{cases} \tag{2}$$

Slave system:

$$\begin{cases} \dot{x}(t) = -y(t) - z(t) \\ \dot{y}(t) = x(t) + ay(t) \\ \dot{z}(t) = b + z(t)(x(t) - c) + u(t) \end{cases} \tag{3}$$

where $(x(t-\tau), y(t-\tau), z(t-\tau)), (x(t), y(t), z(t))$ are the states of the systems (2), (3) respectively, τ is the delay time equal to the period of the target UPO and $u(t)$ is the controller to be designed.

The behavior of the synchronization error between the master (2) and the slave (3) is expressed as:

$$\begin{cases} e_1(t) = x(t) - x(t-\tau) \\ e_2(t) = y(t) - y(t-\tau) \\ e_3(t) = z(t) - z(t-\tau) \end{cases} \tag{4}$$

The objective of synchronization is to find a suitable controller $u(t)$ that minimizes the synchronization error, denoted by (4) until it reaches zero. This implies that:

$$\begin{cases} \dot{e_1}(t) = \dot{x}(t) - \dot{x}(t-\tau) \\ \dot{e_2}(t) = \dot{y}(t) - \dot{y}(t-\tau) \\ \dot{e_3}(t) = \dot{z}(t) - \dot{z}(t-\tau) \end{cases} \tag{5}$$

and

$$\begin{cases} \dot{e_1}(t) = -e_2(t) - e_3(t) \\ \dot{e_2}(t) = e_1(t) + ae_2(t) \\ \dot{e_3}(t) = e_1(t)e_3(t) + z(t-\tau)e_1(t) + x(t-\tau)e_3(t) \\ \qquad -ce_3(t) + u(t) \end{cases} \tag{6}$$

Now, the controller $u(t)$ is defined as follows:

$$u(t) = u_{eq}(t) + u_{sw}(t) \tag{7}$$

and the switching surface is defined as:

$$s = k_1 e_1(t) + k_2 e_2(t) + k_3 e_3(t) \tag{8}$$

where k_1, k_2, and k_3 are constant parameters.
In the sliding manifold, the equivalent control (u_{eq}) is obtained when the derivative of the switching surface $(\dot{s})$ is equal to zero. However, it is important to note that the equivalent control (u_{eq}) alone cannot achieve sliding motion if the initial state of the system does not lie on the switching surface. Sliding motion occurs when the system's state trajectory remains on the switching surface during operation.
The control input (u_{sw}) is designed for the error dynamics in a way that satisfies the reaching condition $s(t)\dot{s}(t) < 0$, which ensures the sliding motion onto the sliding surface $(s(t) = 0)$. The derivation of the control input (u_{sw}) is presented below.
When the system operates in sliding mode, it satisfies the following conditions [26]:

$$\begin{cases} s(t) = 0 \\ \dot{s}(t) = 0 \end{cases} \tag{9}$$

By deriving equation (8) with respect to time and replacing the $\dot{e_1}, \dot{e_2}$ and $\dot{e_3}$ values from equation (6) we

get:

$$\begin{aligned}\dot{s}(t) =& k_1\dot{e_1}(t) + k_2\dot{e_2}(t) + k_3\dot{e_3}(t)\\ =& k_1(-e_2(t) - e_3(t)) + k_2(e_1(t) + ae_2(t))\\ &+ k_3(e_1(t)e_3(t) + z(t-\tau)e_1(t) + x(t-\tau)e_3(t)\\ &- ce_3(t) + u_{eq}(t))\end{aligned} \tag{10}$$

Consequently, when the system operates in the sliding manifold and the derivative of the switching surface $(\dot{s}(t))$ is equal to zero, the equivalent control (u_{eq}) in the sliding mode is given by:

$$\begin{aligned}u_{eq}(t) = 1/k_3[&-k_1(-e_2(t) - e_3(t)) - k_2(e_1(t) + ae_2(t))(t)e_3(t)\\ &- k_3(e_1(t)e_3(t) + z(t-\tau)e_1(t) + x(t-\tau)e_3(t) - ce_3(t)]\end{aligned} \tag{11}$$

Next, the control action (u_{sw}) is designed as follows:

$$u_{sw}(t) = -\delta.sign(s) \tag{12}$$

where δ is a positive constant and $sign(.)$ is the signum function.
Therefore, the overall design of the controller $u(t)$ can be described by the following equation:

$$\begin{aligned}u(t) =& u_{eq}(t) + u_{sw}(t)\\ =& 1/k_3[-k_1(-e_2(t) - e_3(t)) - k_2(e_1(t) + ae_2(t))(t)e_3(t\\ &- k_3(e_1(t)e_3(t) + z(t-\tau)e_1(t) + x(t-\tau)e_3(t)\\ &- ce_3(t)] - \delta.sign(s)\end{aligned} \tag{13}$$

Now, we aim to solve for the switching surface such that the equivalent sliding mode dynamics (equation (8)) become asymptotically stable. To achieve this, we define a Lyapunov function.

$$V = \frac{1}{2}s^2 \tag{14}$$

By evaluating its time derivative along the trajectory described by (6), we obtain:

$$\begin{aligned}\dot{V} =& s\dot{s}\\ =& s[k_1\dot{e_1}(t) + k_2\dot{e_2}(t) + k_3\dot{e_3}(t)]\\ =& s[k_1(-e_2(t) - e_3(t)) + k_2(e_1(t) + ae_2(t))\\ &+ k_3(e_1(t)e_3(t) + z(t-\tau)e_1(t) + x(t-\tau)e_3(t)\\ &- ce_3(t) + u(t))]\\ =& s\{k_1[-e_2(t) - e_3(t)] + k_2[e_1(t) + ae_2(t)]\\ &+ k_3[e_1(t)e_3(t) + z(t-\tau)e_1(t) + x(t-\tau)e_3(t)\\ &- ce_3(t) + (1/k_3[-k_1(-e_2(t) - e_3(t)) - k_2(e_1(t)\\ &+ ae_2(t))(t)e_3(t) - k_3(e_1(t)e_3(t) + z(t-\tau)e_1(t)\\ &+ x(t-\tau)e_3(t) - ce_3(t)] - \delta.sign(s))]\}\\ =& s[-\delta.sign(s)]\\ =& -\delta.\mid s \mid\end{aligned} \tag{15}$$

As $\delta > 0$, so $V < 0$. Then, based on Lyapunov stability theory, it can be concluded that the error dynamics system (4) under the controller $u(t)$ given by (13) is asymptotically stable.

IV. Simulation results

To illustrate the proposed approach, we maintain the benchmark Rossler system (1) with the same initial conditions $[1, 2, 5]$, the parameters' values $a = 0.2$, $b = 0.2$, $c = 5.7$, the time delay τ equal to the first period of UPO ($\tau = T_1 = 5,88105$). The controller $u(t)$ (13) parameters k_1, k_2, k_3, and δ are equal to $3, 3, 0.08$ and 0.1 respectively.
The resulting time evolution of the system is depicted in figure 3 and the time response of $x(t), y(t)$ and $z(t)$ states are shown in figure 4 and the controller $u(t)$ is represented in figure 5.

Figure 3 shows that the behavior of the system

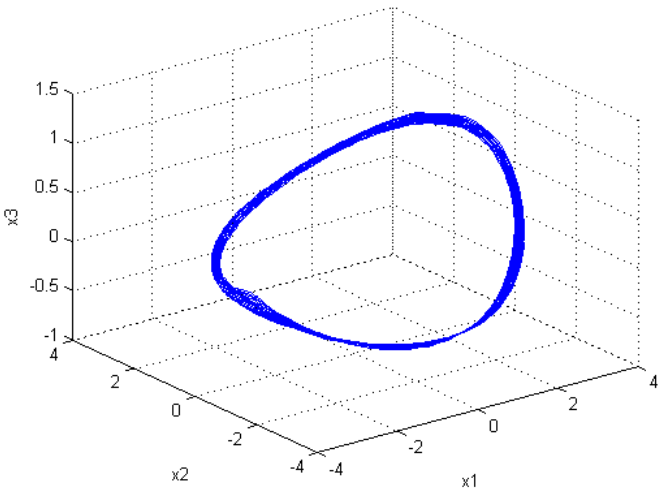


Figure 3. Rossler System behavior under control

follows a single and periodic pattern, which is the simplest and the most predictable behavior exhibited by a dynamic system. To provide a more comprehensive understanding, figure 4 illustrates the time behavior of the system. This figure presents a visual representation of how the system evolves and behaves over time.
Once the stabilization process is guaranteed, as depicted in Figure 5, it can be observed that the control signal converges to zero, indicating a successful stabilization of the Rossler system. Additionally, the system exhibits a stable period-one behavior, maintaining a consistent and predictable pattern over time. This outcome demonstrates the efficiency of the proposed approach in achieving stable and controlled dynamics of the Rossler system.

Figure 6 demonstrates that the sliding surface $s(t)$

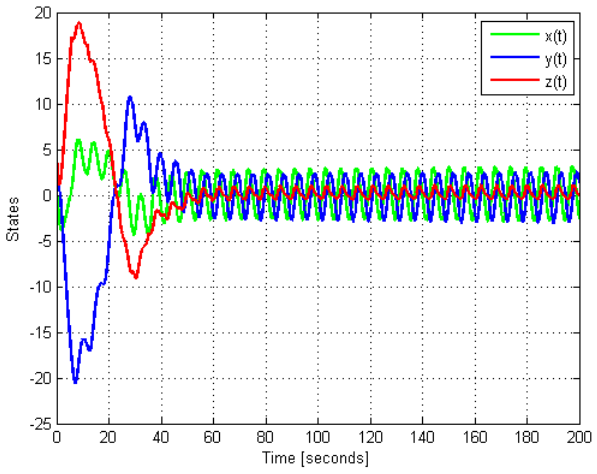


Figure 4. Time response $x(t), y(t)$ and $z(t)$ under control

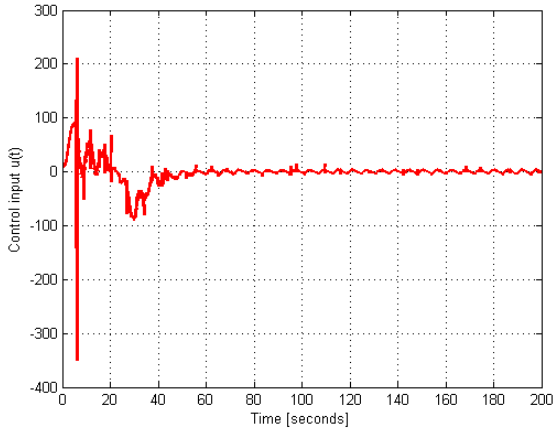


Figure 5. Control action $u(t)$

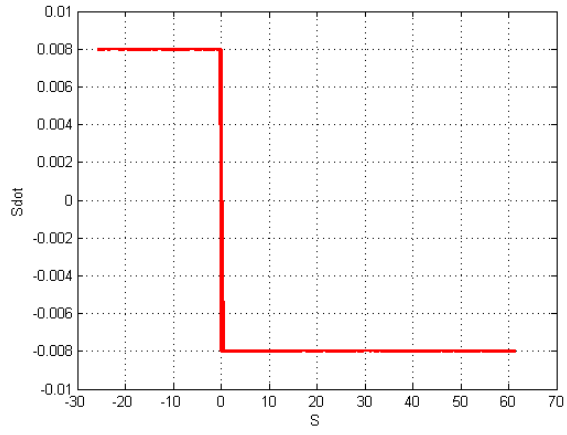


Figure 6. Switching phase plane

converges to zero under the influence of the proposed control. This observation indicates that the control strategy effectively drives the system towards the desired sliding surface, achieving stability and ensuring accurate tracking of the reference trajectory.

V. Conclusion

This paper introduced a novel sliding mode control technique specifically designed for stabilizing chaotic systems. The key novelty of this technique lies in the selection of the tracking error used as an argument in the sliding surface. The delayed state by one value of the period of UPOs is chosen as a reference, resulting, hence, in a modified tracking error. The proposed approach offers several advantages, including its simplicity, fast convergence, robustness, and accuracy in ensuring the structural stability of chaotic systems. The numerical simulations conducted successfully validated the proposed approach and highlighted its simplicity and efficiency in stabilizing chaotic systems in the sense of structural stability. These results reinforce the effectiveness and practicality of the proposed approach to manage and control chaotic dynamics.

References

[1] E. N. Lorenz, "Deterministic nonperiodic flow," *Journal of the atmospheric sciences*, vol. 20, no. 2, pp. 130–141, 1963.

[2] O. E. Rössler, "An equation for continuous chaos," *Physics Letters A*, vol. 57, no. 5, pp. 397–398, 1976.

[3] M. Hénon, "A two-dimensional mapping with a strange attractor," *The theory of chaotic attractors*, pp. 94–102, 2004.

[4] C. Guanrong and U. Tetsushi, "Yet another chaotic attractor," *International Journal of Bifurcation and Chaos*, vol. 9, no. 07, pp. 1465–1466, 1999.

[5] J. Lü and G. Chen, "A new chaotic attractor coined," *International Journal of Bifurcation and chaos*, vol. 12, no. 03, pp. 659–661, 2002.

[6] E. Ott, C. Grebogi, and J. A. Yorke, "Controlling chaos," *Physical review letters*, vol. 64, no. 11, p. 1196, 1990.

[7] L. M. Pecora and T. L. Carroll, "Synchronization in chaotic systems," *Physical review letters*, vol. 64, no. 8, p. 821, 1990.

[8] K. Pyragas, "Continuous control of chaos by self-controlling feedback," *Physics letters A*, vol. 170, no. 6, pp. 421–428, 1992.

[9] B. Hamidouche, K. Guesmi, and N. Essounbouli, "Control and stabilization of dynamical chaotic systems," in *2021 International Conference on Engineering and Emerging Technologies (ICEET)*. IEEE, 2021, pp. 1–6.

[10] L. Zhang and Y. Yan, "Discrete active model predictive control of continuous unified chaotic system," in *2019 Chinese Control And Decision Conference (CCDC)*. IEEE, 2019, pp. 3390–3394.

[11] S. Luo, F. L. Lewis, Y. Song, and H. Ouakad, "Accelerated adaptive fuzzy optimal control of three coupled fractional-order chaotic electromechanical transducers," *IEEE Transactions on Fuzzy Systems*, vol. 29, no. 7, pp. 1701–1714, 2020.

[12] A. Yingdong and W. Huanqing, "Fixed-time anti-synchronization of unified chaotic systems via adaptive backstepping approach," *IEEE Transactions on Circuits and Systems II: Express Briefs*, vol. 70, no. 2, pp. 626–630, 2022.

[13] X. Li and C. Zhu, "Saturated impulsive control of nonlinear systems with applications," *Automatica*, vol. 142, p. 110375, 2022.

[14] M. M. Aziz and S. A.-U. Mohammed, "Analysis of stability and chaos of discrete time system with local bifurcation," in *2022 8th International Conference on Contemporary Information Technology and Mathematics (ICCITM)*. IEEE, 2022, pp. 425–429.

[15] B. Hamidouche, K. Guesmi, and N. Essounbouli, "Lyapunov exponent-based pi optimization for the delayed feedback control of chaos," in *2022 International Conference of Advanced Technology in Electronic and Electrical Engineering (ICATEEE)*. IEEE, 2022, pp. 1–5.

[16] Q. Cao and D. Q. Wei, "Dynamic surface sliding mode control of chaos in the fourth-order power system," *Chaos, Solitons & Fractals*, vol. 170, p. 113420, 2023.

[17] N. Wongvanich, N. Roongmuanpha, and W. Tangsrirat, "Finite-time integral backstepping nonsingular terminal sliding mode control to synchronize a new six-term chaotic system and its circuit implementation," *IEEE Access*, vol. 11, pp. 22 233–22 249, 2023.

[18] S. Vaidyanathan and C. Lien, *Applications of sliding mode control in science and engineering*. Springer, 2017, vol. 709.

[19] J.-J. Yan, Y.-S. Yang, T.-Y. Chiang, and C.-Y. Chen, "Robust synchronization of unified chaotic systems via sliding mode control," *Chaos, Solitons & Fractals*, vol. 34, no. 3, pp. 947–954, 2007.

[20] M. T. Arjmand, H. Sadeghian, H. Salarieh, and A. Alasty, "Chaos control in afm systems using nonlinear delayed feedback via sliding mode control," *Nonlinear Analysis: Hybrid Systems*, vol. 2, no. 3, pp. 993–1001, 2008.

[21] H.-Y. Zhou, K.-Z. Liu, and X.-S. Feng, "State feedback sliding mode control without chattering by constructing hurwitz matrix for auv movement," *International Journal of Automation and Computing*, vol. 8, no. 2, pp. 262–268, 2011.

[22] A. Khan and Shikha, "Combination synchronization of time-delay chaotic system via robust adaptive sliding mode control," *Pramana*, vol. 88, pp. 1–10, 2017.

[23] A. Khan and D. Shikha, "Combination synchronization of genesio time delay chaotic system via robust adaptive sliding mode control," *International Journal of Dynamics and Control*, vol. 6, pp. 758–767, 2018.

[24] B. Hamidouche, K. Guesmi, and N. Essounbouli, "Sliding mode control and structural stabilization of the Rossler system," in *International Conference on Electrical Engineering*. Ecole Militaire Polytechnique d'Alger, 2023.

[25] A. Wolf, J. B. Swift, H. L. Swinney, and J. A. Vastano, "Determining lyapunov exponents from a time series," *Physica D: nonlinear phenomena*, vol. 16, no. 3, pp. 285–317, 1985.

[26] S. Vaidyanathan and C.-H. Lien, *Applications of sliding mode control in science and engineering*. Springer, 2017, vol. 709.

EEIC'23

DTC Using Self-Tuning Fuzzy Speed Controller Design For Fuel Cell Electric Vehicle

Farid TAZERART, Farid KERROUCHE, Toufik REKIOUA, Nabil TAIB

Laboratoire de Technologie Industrielle et de l'Information (LTII), Faculté de Technologie, Université de Bejaia, 06000 Bejaia, Algérie.

Corresponding Author Email: farid.tazerart@univ-bejaia.dz

***Abstract*— Electric vehicles (EVs) speed and torque control undergo different road constraints is very difficult using classical control methods.This paper, introduces a new approach to the direct torque control (DTC) with using self-tuning fuzzy speed controller, which is proposed for EV applications. A self-tuning fuzzy proportional-integral-derivative (PID) controller is designed through continuous updating of its output scaling factor.DTC describes the way in which the control of torque and speed are directly based on the electromagnetic state of the motor. There is no need for a modulator and DTC works correctly during at high speeds and without a speed sensor. However, DTC uses in electric vehicle propulsion in medium and low speed regions. The purpose and the main idea of this article are to design a structure DTC using self-tuning fuzzy speed controller for driving a fuel cell electric vehicle for low speed urban use. Furthermore, good control performance is simulated and proved that the adaptive fuzzy PI control method assure efficiency comportment compared to the classical PI controller.**

***Keywords:* DTC, Self-Tuning Fuzzy Controller, Fuel Cell, Electric Vehicle**.

I. INTRODUCTION

In recent years, electric vehicles (EVs) have been typically proposed to replace conventional vehicles. Since 1970s, people have begun to focus on hybrid electric vehicles (HEVs), who integrate power devices such as engine, motor, battery, which allow its both strong points of pure electric and traditional automobile. There are several configurations of electric and hybrid vehicles [1,2]: 1. Electric vehicles equipped with electric batteries and/or supercapacitors. 2. Hybrid electric vehicles which combine conventional propulsion and electric motor powered by batteries or supercapacitors. 3. Electric vehicles equipped with fuel cells batteries [2].

Electric Vehicle with fuel cell battery and hybrid vehicle takes a considerable interest of industrial and is considered very rapidly as a solution to energy and ecological problems. Fuel cell electric vehicles (FCEVs) produce electricity using a fuel cell battery powered by hydrogen to power an electric motor. FCEVs use the battery for recapturing braking energy, providing extra power during short acceleration events, and to smooth out the power delivered from the fuel cell with the option to idle or turn off the fuel cell during low power needs.

Using electric motors efficient, electric vehicles provide the means to achieve a clean and efficient urban transport system and a friendly environment [3]. Different control techniques that use power electronics devices have evolved in the works looking for improving the performance of electric motors [2]. DTC is an approach employed to regulate electric motors. This technique selects an appropriate voltage vector to regulate torque and flow in electric motors. DTC has many advantages, such as less machine parameter dependence, and any current regulator, simpler implementation and quicker torque response [4]. However, DTC presents some drawbacks: difficulty to control torque and flux at very low speeds, high current ripple causing high torque ripple and variable switching frequency behavior [5]. EV commanded with DTC control require regulation of speed variables with PID type. The major problems in applying a conventional control algorithm PI in a speed controller for DTC are the effects Ohmic voltage drop. The estimate of the flux is generally calculated by integrating the voltage supplying the motor. Because of errors in the measurement of the voltage and in the knowledge of the stator resistance and domination of Ohmic voltage drop, this integral tends to become erroneous at low speed. PID controller response can be tuned for obtaining better oscillations, steady state response and reduced error by changing the PID parameters. Fuzzy logic controller gives a promising result when PID parameters are controlled using fuzzy rules. Different types of adaptive FLC's such as self-tuning and self-organizing controllers have been developed and implemented for various practical processes. In the first part of this paper direct torque controlis described. The second part described the structure of the PI type self-tuning fuzzy logic controller. In the third part of this paper, a PID parameters self-tuning fuzzy controller is proposed for DTC control loop applied for the traction of a hybrid electric vehicle with fuel cell battery, in which the rules and membership functions of controller are adjusted. The principal components of the electric vehicle loads with their equations model is set in part 4.In the last part simulation results are presented. Furthermore, good control performance is simulated and a PID parameters self-tuning fuzzy controller provide robust and reliable performance for most systems.

II. DIRECT TORQUE CONTROL STRATEGY

The algorithm of DTC is shown in the Figure 1.

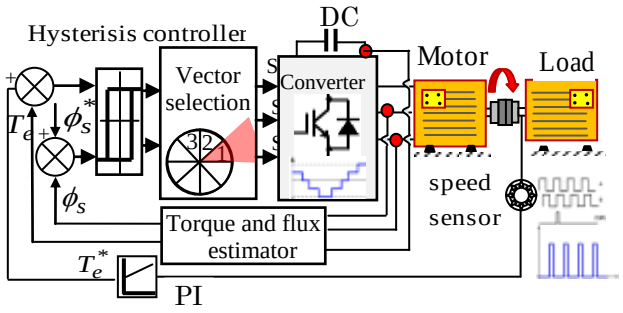


Figure 1.Simplified basic scheme of theDTC technique

DTC method uses a simple switching table to identify the most suitable inverter state to achieve a desired output torque [6-9]. Based on the flux and torque hysteresis controllers, determines the voltage needed to drive the flux and torque to the desired values. The stator flux components $\phi_{s\alpha}$ and $\phi_{s\beta}$ can be estimated by equation (1) as:

$$\begin{cases} \phi_{s\alpha}(t) = \int (V_{s\alpha}(t) - R_s.i_{s\alpha}(t))dt \\ \phi_{s\beta}(t) = \int (V_{s\beta}(t) - R_s.i_{s\beta}(t))dt \end{cases} \quad (1)$$

Where: $V_{s\alpha}$, $V_{s\beta}$, $i_{s\alpha}$and $i_{s\beta}$ are stator voltages and currents along $\alpha$and β stator axes respectively. The magnitude of the stator flux can then be estimated by equation (2)as:

$$\phi_s = \sqrt{{\phi_{s\alpha}}^2 + {\phi_{s\beta}}^2} \quad (2)$$

The phase angle of the stator flux can be calculated as:

$$\theta_s = \tan^{-1}\frac{\phi_{s\beta}}{\phi_{s\alpha}} \quad (3)$$

And the electromagnetic torque can be calculated as :

$$T_e = \frac{3}{2}.p.(\phi_{s\alpha} i_{s\beta} - \phi_{s\beta} i_{s\alpha}) \quad (4)$$

A. Stator flux control

Figure 2 shows the voltage vectors which are usually used in DTC scheme with, as example, the stator flux located in sector 1, the stator flux vector is varied in the same direction as the applied stator voltage vector thus in each sector four of the six non zero voltage vectors along with zero vectors may be used.

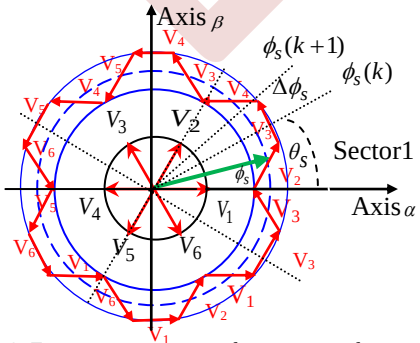


Figure 2. Forming appropriate voltage vector selection.

B. Switching Table For Controlling Flux And Torque

According to the signal generated by the hysteresis controller of stator flux and electromagnetic torque, just one voltage vector can be selected to adjust the torque and flux. The choice of this vector depends on the outputs of the torque and flux controller and the position of the stator flux vector, as shown in Table 1 [9].

TABLE I. Switching table

H_ϕ	H_{Te}	S(1)	S(2)	S(3)	S(4)	S(5)	S(6)
	1	V_2	V_3	V_4	V_5	V_6	V_1
1	**0**	V_0	V_7	V_0	V_7	V_0	V_7
	-1	V_6	V_1	V_2	V_3	V_4	V_5
	1	V_3	V_4	V_5	V_6	V_1	V_2
-1	**0**	V_7	V_0	V_7	V_0	V_7	V_0
	-1	V_5	V_6	V_1	V_2	V_3	V_4

III. FUZZY CONTROL REGULATOR STRUCTURE

Fuzzy control is basically an adaptive and nonlinear control, which gives robust performance for a linear or nonlinear plant with parameter variation [10]. Using linguistic variables in place of numerical variables, that approach represents a substantive departure from the conventional quantitative techniques of system analysis and control. The basic configuration of a FLC (fuzzy logic controller) with five linguistic variables (two inputs and three output) is shown in Figure 3.The fuzzy controller is a system with 2-input, 3-output, $e(k)$ and $\Delta e(k)$ are input variables, K_P, K_I and k_D are output variables. The error and the change in error is modelled using equations (4) and (5) as:

$$e(k) = \omega_{ref} - \omega_r \quad (5)$$

$$\Delta e(k) = e(k) - e(k-1) \quad (6)$$

Where ω_{ref} is the reference speed, ω_r is the actual rotor speed, e(k) is the error and Δe(k) is the change in error.
Figure 3 shows the value of parameter Kp, Ki and Kd are tuned by using signals from fuzzy logic block based on the changes in the error between reference signals and output signals. Here r(t) is the control signal, y(t) is the output response, e(t) is the error and (De) is the derivete of error.

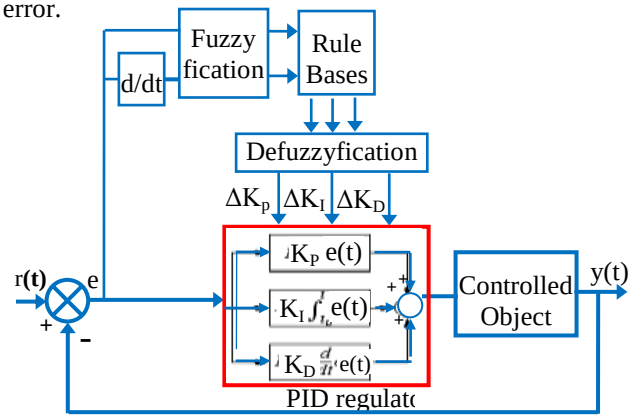


Figure 3. Basic block diagram of a fuzzy controller

IV. PROPOSED DTC USING SELF-TUNING FUZZY SPEED CONTROLLER

A simplified block diagram of the DTC strategy with speed control loop [11] using self tuned Fuzzy PID controller for electric vehicle , is shown in Figure 4.

The output of the "fuzzy logic controller" system is the torque, which is used as reference input for the DTC drive, in difference to the classic DTC that operates with PI regulator. Electric traction motor use powers from the fuel cell and the traction battery pack, this motor drives the vehicle's wheels.

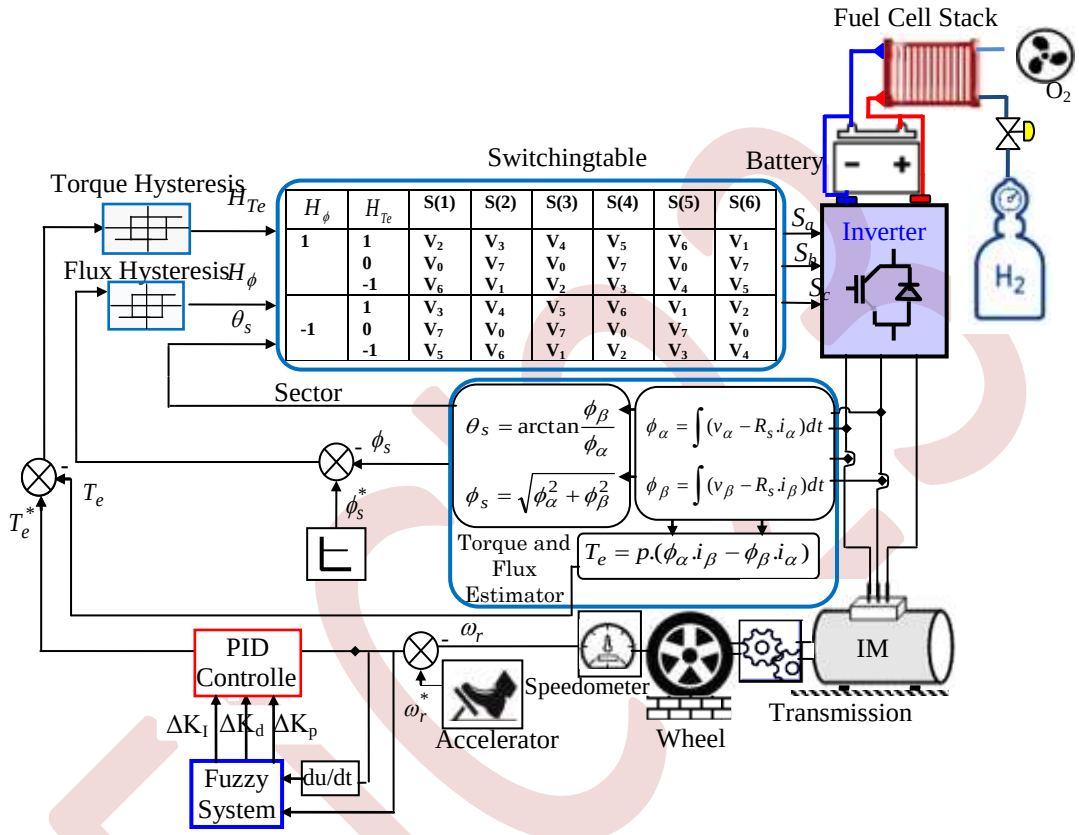
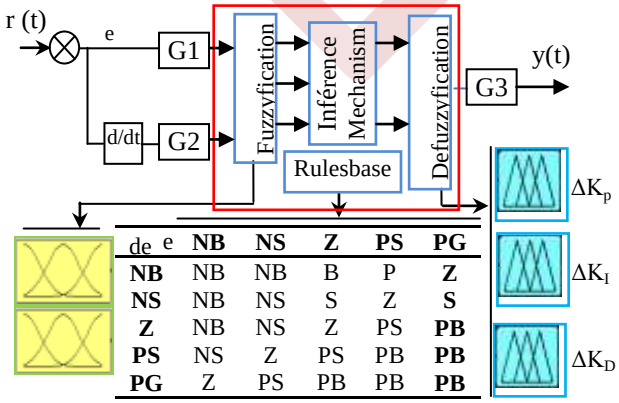


Figure 4.DTC with a speed control loop using self tuning Fuzzy PID controllerfor electric vehicle

A. SELF TUNED FUZZY PID FOR DTC

Self-tuning fuzzy PID controller means that the three parameters Kp, Ki and Kd of PID controller are tuned by using fuzzy tuner [12]. The proportional, integral and derivative terms are summed to calculate the output of the PID controller. Hence, it is necessary to automatically tune the PID parameters. The structure of the self-tuning fuzzy PID controller is shown in Figure 5.



de / e	NB	NS	Z	PS	PG
NB	NB	NB	B	P	Z
NS	NB	NS	S	Z	S
Z	NB	NS	Z	PS	PB
PS	NS	Z	PS	PB	PB
PG	Z	PS	PB	PB	PB

Figure 5. Structure of fuzzy self-tuning PID controller

PID parameters fuzzy self-tuning is to find the fuzzy relationship between the three parameters of PID and "e" and "de", and according to the principle of fuzzy control, to modify the three parameters in order to meet different requirements for control parameters when "e" and "de" are different, and to make the control object a good dynamic and static performance. The meaning of the linguistic variables used for the computation of K_p and K_I regulators are explained in Table 2 and Table3.

TABLE II. Fuzzy rules for computation of Kp

Kp	*De*			
	NB	***Z***	***PB***	
	NB	***Z***	***PB***	***Z***
e	***Z***	***Z***	***PS***	***PM***
	PB	***Z***	***PB***	***Z***

TABLE III. Fuzzy rules for computation of K_I

Ki	*De*			
	NB	***Z***	***PB***	
	NB	***P***	***Z***	***P***
e	***Z***	***P***	***P***	***P***
	PB	***P***	***Z***	***P***

V. FUEL CELL ELECTRIC VEHICLE ARCHITECTURE

The chain of electric traction [13] is shown in Figure 6. It consists of 4 components: Control strategy, DC/DC converter [14,15], inverter, induction motor. In Figure 7 the power of the electric motor operate the drive train by the mechanical transmission [16,17,18]. Fuel tank stores hydrogen gas on board the vehicle until it's needed by the fuel cell.

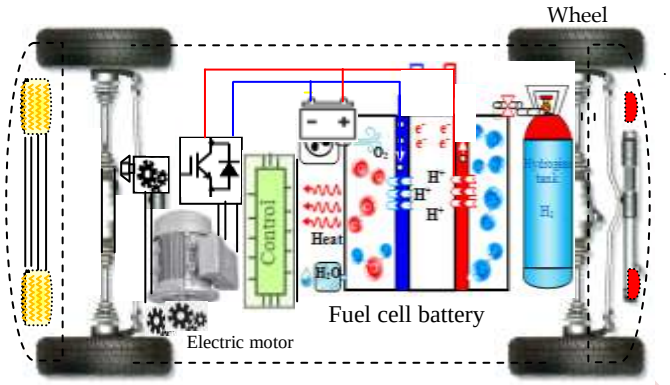


Figure 6.Electric drive powered by the fuel cell battery

A. FUEL CELL BATTERY

The simulink and functional diagram of the fuel cell batterysubsystem block as shown in Figure 7.

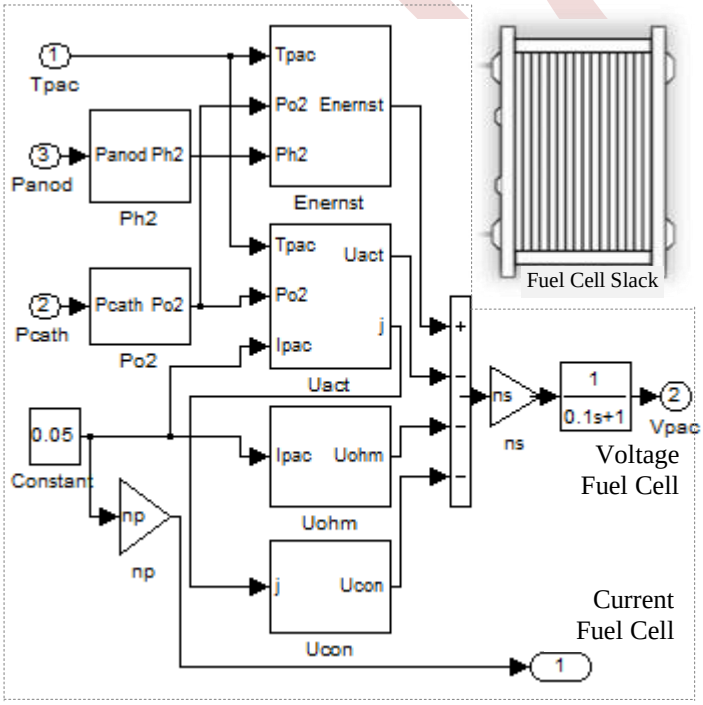


Figure 7.Functional diagram of the fuel cell battery

The transient and steady state operating of IM (parameters are given in Table 4), fed by an inverter and controlled under direct torque control has been simulated using (MATLAB/Simulink) software. Electrical vehicle mechanical and aerodynamic characteristics are also given in the Table 5. Simulation results are given in Figures 8-13.

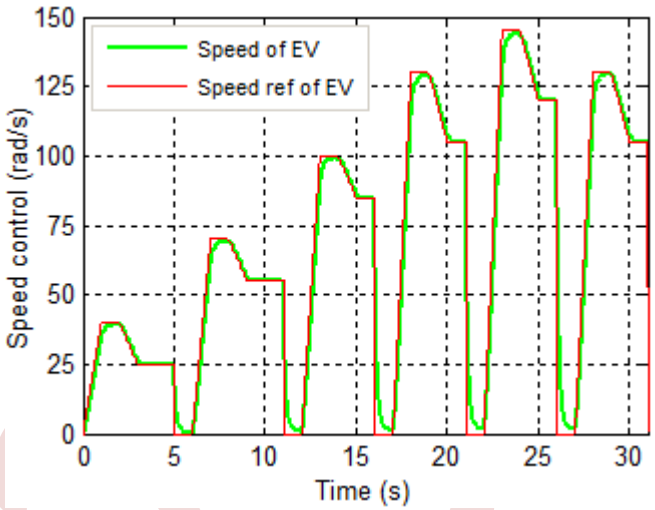


Figure 8.Vehicle wheels speed with test urban cycle

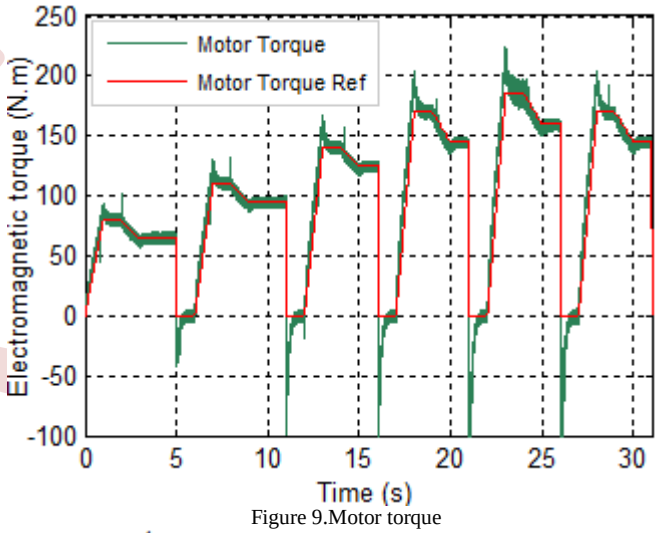


Figure 9.Motor torque

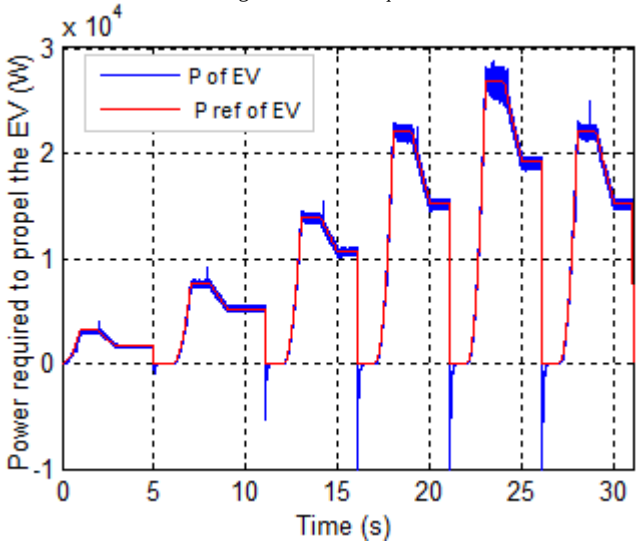


Figure 10.Power required to propel the EV

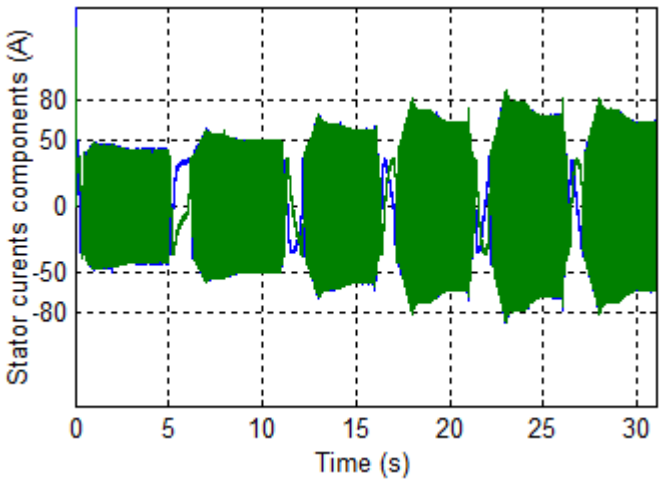


Figure 11. Instantaneous statorcurrents

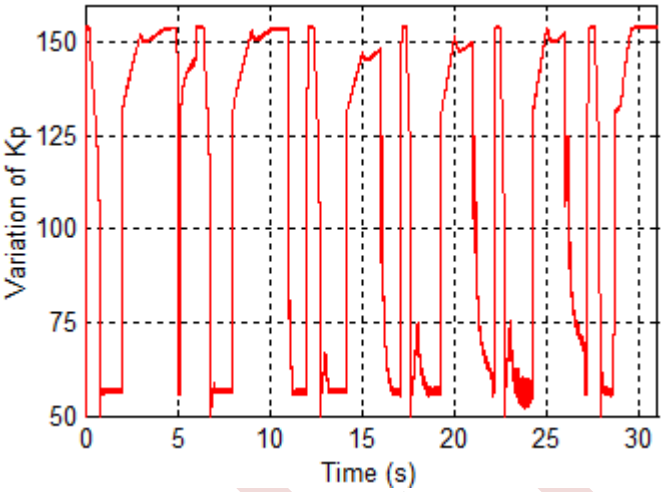


Figure 12. Kp with self-adaptive

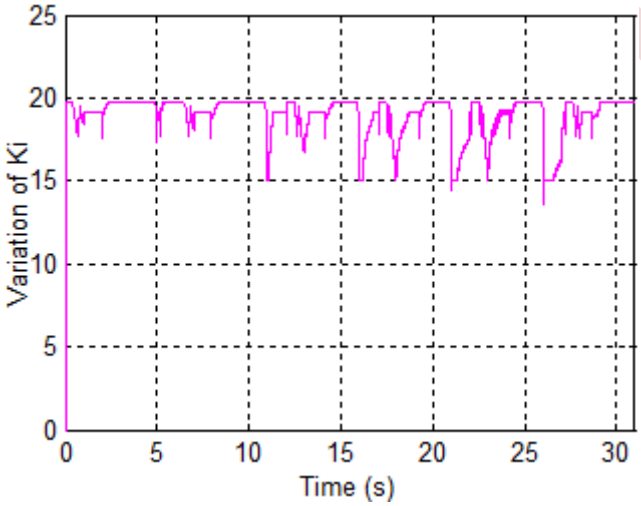


Figure 13. Ki with self-adaptive

VI. DISCUSSIONS OF RESULTS

Figure 8 shows the test cycle and urban sequence, is a series of data points representing the vehicle speed versus time. It is characterized by low vehicle speed (maximum 80 km/h) and is useful for testing EV performances in urban areas. Figure 9 illustrates the EV dynamics, the developed torque in induction motor on, with changes in the acceleration and the electromagnetic torque compensates the resisting torque.These figures showsthat, the torque and the speed reaches its reference values, and reveal that the system using Fuzzy self-adaptation speed regulator improves the precision of speed and torque control.

Figure 10 illustrate the power required to move the EV. To find the power taken from the battery to provide the tractive effort, we have to be able to find various efficiencies at all operating points. Figure 11 illustrate the stator currents robustness and shows that the stator current absorbed by the induction machine is almost sinusoidal. Figures 12 and 13 specify the variation of K_P and K_I respectively, with error (e) and change of error (Δe).

VII. CONCLUSIONS

The paper, proposed a simple but robust self-tuning scheme for direct torque control induction motor, dedicated to the traction of an urban fuel cell vehicle at low speed. This is performed by incorporating a self adjusting regulator block into a classical direct torque control system.Self-tuning fuzzy controller was applied to tune the value of Kp and Ki of the PI controller.

The fuzzy regulator has a very interesting dynamic performance compared with the conventional PI-regulator.

In fact, the fuzzy regulator synthesis is realized without take in account the machine model. Simulation results show the effectiveness of the proposed method DTC withself-tuning speed controller and results demonstrate that the designed self-tuned PID controller realize a good dynamic behavior of the DTC, a perfect low speed tracking with minimum overshoot and give better performance compared to the conventional PID controller.

Finally the proposed approach it appears to be very convenient for EV applications.

REFERENCES

[1] G. Eason, B. Noble, and I. N. Sneddon, "On certain integrals of Lipschitz-Hankel type involving products of Bessel functions," Phil. Trans. Roy. Soc. London, vol. A247, pp. 529–551, April 1955. *(references)*

[2] Jia-Sheng Hu, Dejun Yin, Feng-Rung Hu. (2011). A robust traction control for electric vehicles without chassis velocity. In S. Soylu (Ed.), Electric Vehicles - Modelling and Simulations, (1 ed., pp. 107-126). Chapter 5.Croatia. https://doi.org/10.5772/16942

[3] Bayindir , K. C, Gozukucuk, M.A, Teke, A.(2011). Acomprehensiveoverwiew of hybrid electric vehicle: Powertrain configurations, powertrain control techniques and electronic control units. Energy Conversion and Management, Elsevie, nr. 52, 13051313.https://doi.org/10.1016/j.enconman.2010.09.028

[4] Tazerart F, Mokrani Z, Rekioua D, Rekioua T. (2015). Direct torque control implementation with losses minimization of induction motor for electric vehicle applications with high operating life of the battery. Int J Hydrogen Energy, Vol. 40, No. 39, pp. 13827-13838. https://doi.org/10.1016/j.ijhydene.2015.04.052

[5] Abdelli R,Rekioua D, Rekioua T. (2011).Performances improvements and torque ripple minimization for VSI fed induction machine with DTC, ISA Transactions, 50(2) : 213-219.DOI: 10.1016/j.isatra.2010.11.008

[6] Taïb N, MetidjiB, RekiouaT. (2010). A Fixed Switching Frequency Direct Torque Control Strategy for Induction Motor Drives Using Indirect Matrix Converter. Arabian Journal for Science and Engineering (AJSE). Publisher Springer Berlin Heidelberg 2013: 2191-4281. DOI 10.1007/s13369-013-0731-x

[7] Ziane D, Aissou S, Azib A, Rekioua T.(2014). Performance test of the control strategy applied to the electric vehicle, in the case of FWD and 4WD. Int J Hydrogen Energy; 39: 21259-21264.https://doi.org/10.1016/j.ijhydene.2014.10.065

[8] Metidji B, Taib N, Baghli L, Rekioua T, Bacha S. (2012).Low-cost direct torque control algorithm for induction motor without AC phase current sensors. IEEE Transactions on Power Electronics, 27(9):4133-4135.DOI: 10.1109/TPEL.2012.2190101

[9] Metidji B, Azib A, Tazerart F, Taib N, Rekioua T.(2011). Fuzzy direct torque control with torque ripple reduction for induction motor drives fed by matrix converters. International Journal of Research and Reviews in Computing Engineering, Vol. 1, No. 1.

[10] M Depenbrock. (1988).Direct self-control of inverter-fed induction machine. IEEE Transactions on Power Electronics. 1988; 3(4): 420-429. DOI: 10.1109/63.17963.

[11] Veeraiah M. P, ChitralekhaMahanta S. M. (2004). Fuzzy proportional Integral–proportional derivative (PI-PD) controller. Proceeding of the 2004 American control conferences, pp. 4028–4033, Boston Massachusetts . DOI: 10.23919/ACC.2004.1383938

[12] Tazerart F, Taïb N, Rekioua T, Rekioua D, Tounzi A. (2014).Direct torque control optimization with loss minimization of induction motor. Conférence Internationale en Sciences Technologies Electriques au Maghreb-CISTEM, Tunis. Publisher: IEEE.DOI: 10.1109/CISTEM.2014.7077002

[13] Visioli A. (2001).Tuning of PID controllers with fuzzy logic. IEE Proc.-Control Theory Appl., Vol. 148, No. I.DOI**:** 10.1049/ip-cta:20010232

[14] Xingzhi H.(2017). Analysis of Traction Control System in Hybrid Electric Vehicle based on Engine-Motor Coordinated Control Strategy. in Electrotehnica, Electronica, Automatica (EEA),vol. 65, no. 3, pp. 42-48, ISSN 1582-5175. DOI: 10.3390/wevj5020460

[15] Mihăescu M, Popescu. (2018)Simulink modelling of transient operating regimes of a four-port DC-DC converter used in hybrid vehicles. in Electrotehnica, Electronica, Automatica (EEA), vol. 66, no. 3, pp. 26-34, ISSN 1582-5175.

[16] Baodong Huang, Lijie Su, Yabo Ren. (2017). DC/DC Converter Common Mode EMI in Parallel-Series PHEV. in Electrotehnica, Electronica, Automatica (EEA), 2017, vol. 66, no. 1, pp. 41-46, ISSN 1582-5175.

[17] MAnsour K, Reza K.(2011).A new strategy for traction control in turning via engine modelling.in IEEE Transactions on Vehicular Technology, vol.60(6),pp. 1540-1548. DOI: 10.1109/25.966584

[18] LiJ, Zhu Y, Xu Y. (2014). Research on control strategy optimization in power transmission system of hybrid electric vehicle.in Machinery Design & Manufacture, vol.67(3), pp.138-141.

NOMENCLATURE

C_1	Constant1
C_2	Constant2
e	Error
Δe	Change of error
K_p	Proportional sensitivity
K_I	Integralsensitivity
V_s	Stator voltage vector
$V_{s\alpha}$	Componentstator voltage along α axis,V
$V_{s\beta}$	Componentstator voltage along βaxis,V
$i_{s\alpha}$	Componentstator current along αaxis, A
$i_{s\beta}$	Componentstator current along βaxis, A
R_s	Stator resistance, Ω
L	Inductance, mH
T_e	Electromagnetic torque, Nm
p	Pair-pole number of the induction machine
g	Gravitational acceleration constant
R	Wheel radius
P_{drive}	Vehicle driving power, W
Out	Output
Inp	Input

Greek symbols

α	Nomination for axis
β	Nomination for axis
ϕ	Stator flux, Wb
θ_s	Angular position of flux, deg
v	Vehicle speed
ω_r	Rotor mechanical speed, rad/s
ω_{ref}	Reference rotor mechanical speed, rad/s

Abbreviations

AC	Alternating Current
DC	Direct Current
D	Diode
DTC	Direct Torque Control
EV	Electric Vehicle
FC	Fuel Cell
FLC	Fuzzy Logic Controller
IM	Induction Motors
NB	Negative big
NS	Negative small
PB	Positive big
PI	Proportional Integral controller
PD	proportional derivative controller
PID	Proportional-Integral-Derivative controller
PS	Positive small
REF	Reference
T	Transistor
Z	Zero

Appendix

TABLE 4. Parameters of the induction machine

Parameter	Value
Rated power	37kW
Speed	1420 rpm
Voltage	230V
Stator current	I_s=64 A
Stator resistance	R_s=0.0851 Ω
Rotor resistance	R_r =0.0658 Ω
Stator inductance	L_s=0.0314 H
Rotor inductance	L_r=0.0291 H
Mutual inductance	M=0.0291 H
Number of pole pairs	P=2

TABLE 5. Parameters of the EV and the traction system

Parameter	Value
Vehicle Mass	1540 Kg
Vehicle frontal area	1.8 m^2
Tire rolling resistance coeffi	0.015
Aerodynamic drag coefficient	0.25
Stokes coefficient	0.22
Air density	0.23 Kg/m^2
Wheel radius.	0.3 m
Transmission ratio.	2

Development of Antilock Braking System Based Fuzzy Logic Controller for Diverse Road Conditions

Seddik Kedjouti [1], Ilhem Bouchareb [2]

[1] *Laboratory of Electrical Engineering Polytechnic of Constantine (LGEPC), Constantine, Algeria*

kedjoutiseddik@yahoo.fr

[2] *Laboratory of Electrical Engineering Polytechnic of Constantine (LGEPC), Constantine, Algeria*

bouchareb.ilhem@gmail.com

***Abstract*— Antilock braking system (ABS) is able to stop a vehicle wheel without locking, in addition it decreases the stopping distance. ABS provide safe driving for many different road conditions. This paper is about the development of an Antilock braking system complemented by a fuzzy logic controller for automatic braking dedicated to Advanced Driver Assistance Systems (ADAS). This controller used to improve the braking performance of the vehicle particularly the stopping distance, for different environmental road conditions (two scenarios of vehicle speed), without forgetting to maintain the optimum value of the slip ratio of the wheel.**

***Keywords:* Antilock Braking System (ABS), Fuzzy Logic, Stopping Distance, MATLAB/Simulink.**

I. INTRODUCTION

In recent years, antilock braking system (ABS) is an important development for vehicle safety [1]. All modern vehicles are equipped with an ABS system that prevents wheel locking up. It reduces the vehicle's stopping distance and improves vehicle control compared to other braking systems [2] [3].

Designing an ABS system is a very difficult task considering the fact of non-linearity of the system due to variation in parameters such as road condition, vehicle conditions and uncertainty in sensor signals. Many control strategies are involved. In this study, the Fuzzy Logic controller is used because it is very effective in dealing with model uncertainty and complexity in order to enhance vehicle performance [4] [5]. This controller is designed for the ABS system, where the variables obtained by wheel speed sensors and vehicle acceleration sensors are the input of the controller [6].

The organization of the paper is as follows: In session 2 we describe the anti-lock braking system, and the mathematical model of the non-linear tire. Session 3 will introduce Fuzzy Logic and a discussion on its application for the ABS system. Detailed analyses and the numerical results will be provided in session 4. Finally, conclusions.

II. ANTILOCK BRAKING SYSTEM (ABS)

ABS is a safety system that prevents the vehicle's wheels from locking up and sliding during braking. It focuses on reducing stopping distance while maintaining control of the vehicle [7] [8]. It worked when the driver hit the brakes hard, suddenly or in slippery conditions. The performance of the anti-lock braking system depends on the type of road surface [4]. ABS systems use a combination of electronic and hydraulic systems to modulate the brakes [9].

The components of ABS are:

1. Wheel-Speed Sensors: used to calculate the acceleration and deceleration of the wheel.
2. Electronic Control Unit (ECU): shortly known as ECU is the controller that receives information from each individual speed senor, and activates the ABS modulator.
3. Hydraulic Pressure Modulator: is an electro-hydraulic device for pressure modulation i.e. reducing, holding and building pressure.
4. Solenoid Valve: The ECU output signal actuates the solenoid valves and motor in order to achieve targeted pressure as the pressure sensor measures a pressure inside calipers.

The main goal of the ABS system is to reduce the vehicle's stopping distance during braking using the fuzzy logic based antilock braking system in order to avoid skidding and improve the vehicle's steering ability during emergency or hard braking [9].

A. Mathematical Model

ABS can be described mathematically as a model to be tested and developed [3], for Matlab/Simulink Newton's Second Law of motion is used:

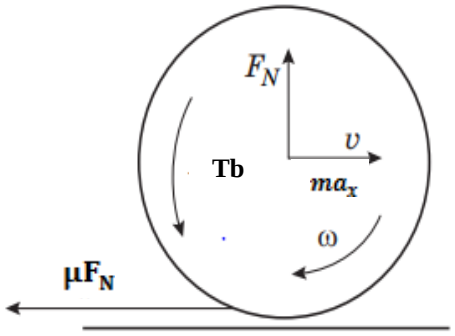


Figure 1. Single wheel model.

At the wheel center, the torque is:

$$J_w\dot{\omega} = \mu R F_N - Tb \quad (1)$$

$$ma_x = -\mu F_N = m\frac{dV_x}{dt} \quad (2)$$

$$\lambda = \frac{V_x - \omega R}{V_x} \quad (3)$$

a_x **:** the linear acceleration, F_N : vertical force, V_x : vehicle speed, **ω :** angular speed, **R** : radius of tire, **λ** : slip ratio of the wheel, m : mass, **Tb** :braking torque, J_w : moment of inertia and μ : coefficient of friction between the wheel and the road.

The goal of ABS control is to regulate wheel slip to increase the coefficient of friction between the wheel and the road for diverse road surface. Generally, the relationship between the coefficient of friction μ during the braking process, the slip ratio of the wheel, and vehicle speed as a function used in [10] are given:

$$\mu(\lambda, V_x) = [c_1(1 - e^{-c_2\lambda}) - c_3\lambda]e^{-c_4 V_x} \quad (4)$$

Where,
C_1, C_2, C_3, and C_4: constants for different road conditions, which are as follows:

TABLE I. VALUES OF CONSTANTS FOR DIFFERENT ROAD [9] [11].

Surface Condition	C_1	C_2	C_3	C_4
Dry asphalt	1.2801	23.99	0.52	0.02 ~ 0.04
Wet asphalt	0.857	33.822	0.347	
Concrete	1.1973	25.168	0.5373	
Cobblestone	1.37	6.46	0.67	

III. FUZZY LOGIC CONTROLLER.

Fuzzy logic controller is an intelligent, knowledge based control methodology that works well in nonlinear and complex systems and without mathematical description [6]. It consists of three main processes, Fuzzification, Inference (inference deals with rules into which human experience can easily be injected through linguistic rules), and Defuzzification.

The Mamdani Fuzzy Logic Controller (FLC) have two inputs (slip error (E) and rate of change of slip error (CE)) and single output (Brake (Tb). Both of inputs and output are having three Gaussian memberships functions. Nomenclature used for the rule base is as follows: N-Negative, Z- Zero, P-Positive.

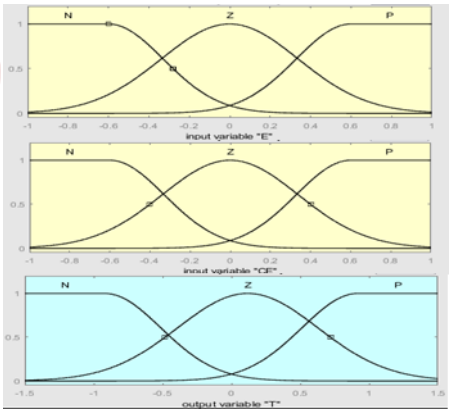


Figure 2. Memberships functions of inputs and output

According to [4], the best performance of ABS occurs when 3x3 fuzzy rules is implemented (to keep the value of λ near to 0.2). The rules are developed in the form of :

IF (E) IS.... AND (CE) IS.... THEN (T) IS....

TABLE II. RULE BASE FOR THE TWO INPUTS.

Slip Error \ Change of Error	N	Z	P
N	Z	N	N
Z	P	Z	N
P	P	P	Z

The Fig. 3, describes the relation of pressure as output and the two input data.

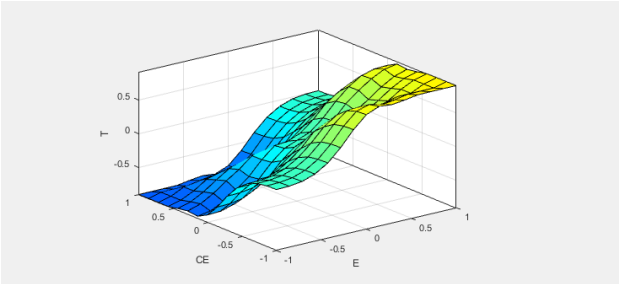


Figure 3. Surface viewer for the fuzzy inference system.

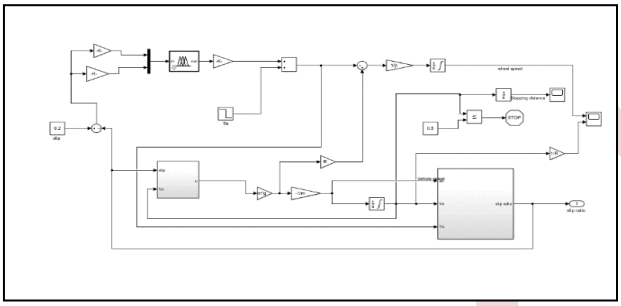


Figure 4. Simulink vehicle model.

Technical specifications of the vehicle model are listed in the following table [10]:

TABLE III. TECHNICAL SPECIFICATIONS

Symbol	Value
m	342 Kg
g	9.81 m/s2
R	0.33
J_w	1.13 Kgm^2
Tb Max	1200 Nm

IV. SIMULATION RESULTS

After implementation of the model system in Matlab Simulink,

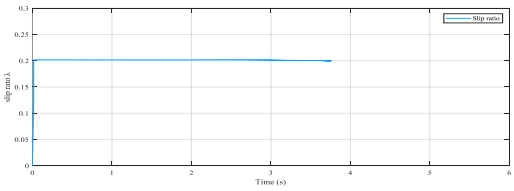


Figure 5. Slip ratio.

A. For speed of 50 Km/h

The vehicle speed and wheel speed has a zero value at 1.47 s. This indicates that the wheel is not locked befor the vehicle stopping.

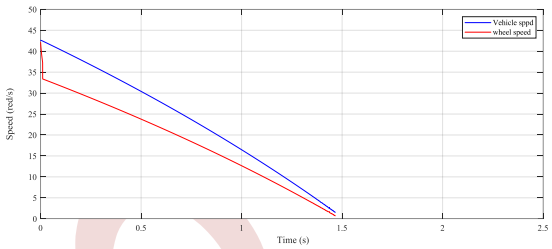


Figure 6. Vehicle speed vs Wheel speed.

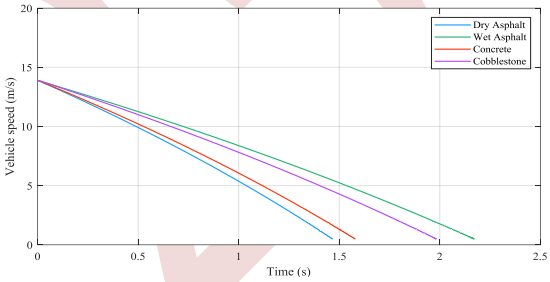


Figure 7. Comparison vehicle speed for different road conditions.

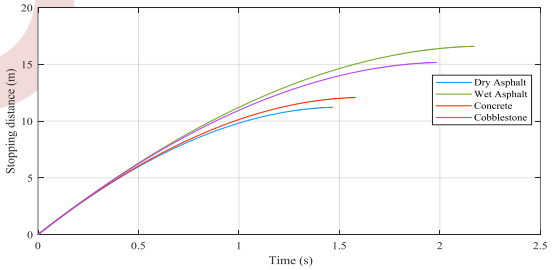


Figure 8. Comparison stopping distance for different road conditions.

B. For speed of 100 Km/h

The vehicle speed and wheel speed has a zero value at 3.75 s. This indicates that the wheel is not locked befor the vehicle stopping.

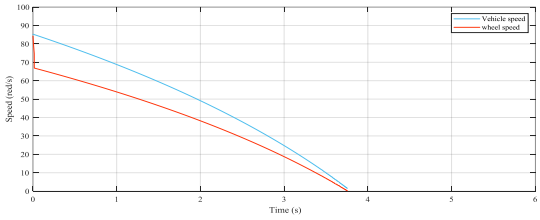


Figure 9. Vehicle speed vs Wheel speed.

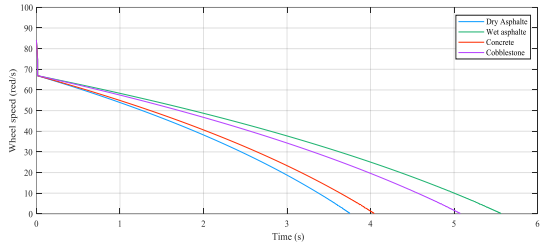


Figure 10. Comparison vehicle speed for different road conditions.

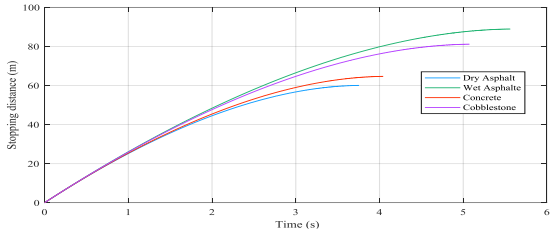


Figure 11. Comparison stopping distance for different road conditions.

V. CONCLUSIONS

In this work, Antilock Braking system for vehicle is modeled and implemented in Matlab/Simulink. Main focus is to showed the effect of road condition and speed to the stopping distance of vehicle while braking using fuzzy logic controller.

For comparison, we used different road conditions (Tab. 1) at different vehicle speeds (50 km/h, 100Km/h). The results showed that when the vehicle speed was low and the condition of road was dry road, the time to stopping and the stopping distance are shorter , and vice versa.

A fuzzy controller is modeled by defining input outputs, then fuzzy rules. Based on fuzzy control, ABS can effectively prevent the wheels from locking, braking more efficiently by reaching the optimum value of slip ratio.

REFERENCES

[1] Q. Gengxin, F.Xiaobin, Z. Shuaiwei, C. Xinbo, W. Pan, and L.Hao 'Research on Robust Control of Automobile Anti-lock Braking System Based on Road Recognition', Jordan Journal of Mechanical and Industrial Engineering, vol. 16, pp. 343-352, 2022

[2] R. Keshmiri, and A. M. Shahri 'Intelligent ABS Fuzzy Controller for Diverse Road Surfaces', International Journal of Mechanical and Mechatronics Engineering, vol. 1, pp. 257-262, 2007.

[3] K. M. Algadah, and A. S. Alaboodi 'Anti-Lock Braking System Components Modelling', International Journal of Innovative Technology and Exploring Engineering (IJITEE), vol. 9, pp. 3969-3975, 2019.

[4] F. N. Zohedi, M.A. Rahmat, and H. A. Kasdirin 'A Critical Analysis of Fuzzy Logic Controller for Slip Control in Antilock Braking System (ABS)', International Journal of Engineering & Technology, vol. 7, pp. 116-123, 2018.

[5] I. Shinko, E. Shurdha, B. Kamo, E. Agastra, and K. Dhoska 'A fuzzy logic-based Anti-Lock Braking Systems', INTERNATIONAL SCIENTIFIC JOURNAL "MACHINES. TECHNOLOGIES. MATERIALS", vol. 2, pp. 58-60, 2020.

[6] P. Ujwal, and S. Krishna 'Fuzzy based Adaptive Control of Antilock Braking System', International Journal of Engineering Research & Technology (IJERT), vol. 5, pp. 139-143, 2016.

[7] Ayush, A. Kumar, A. Kumar, S. Sridevi, and K. Venkateswaran 'ABS using Fuzzy Logic in MATLAB and Its Hardware Implementation', International Journal of Recent Technology and Engineering (IJRTE), vol. 8, pp. 1007-1010, 2019.

[8] D. K. Yadav, 'Modeling An Intelligent Controller For Anti-Lock Braking System', International Journal of Technical Research and Applications, vol. 3, pp. 122-126, 2015.

[9] M. N. Mane, and N. V. Vivekanandan 'Design and Analysis of Antilock Braking System with Fuzzy Controller for Motorcycle', International Research Journal of Engineering and Technology (IRJET), vol. 6, pp. 2211-2217, 2019

[10] A. B. Sharkawy, 'Genetic fuzzy self-tuning PID controllers for antilock braking systems', Engineering Applications of Artificial Intelligence, vol. 23, pp. 1041–1052, 2010.

[11] M. Dousti, S.Ç. Başlamışl, T. Onder, and S. Solmaz 'Design of a Multiple Model Switching Controller for ABS braking dynamics', Transactions of the Institute of Measurement and Control, vol. 37, pp. 582-595, 2015.

Neuro-fuzzy controller of a dual star induction motor supplied with renewable power based on multi-level converters

Elyazid Zaidi [1], Layachi Djedoui[2], Larafi Bentouhami [3], Rafik Zouache [3], Abderrahim Rreffas[3]

[1] *Hydraulics Department National School of Hydraulics 29 route de soumaa, Blida, Algiers, Algeria* e.zaidi@ensh.dz

[2] *Electronics Department, Université de Blida1 29 route de soumaa, Blida, Algeria.* djedoui1@)yahoo.fr

[3] *Electronics Department, Université de Bordj Bou Arreridj Bord Bou Arreridj 34000, Algeria.* bentouhamilarafi@univ-bba.dz

[3] *Electronics Department, Université de Bordj Bou Arreridj Bord Bou Arreridj 34000, Algeria.* rafik.zouache@)univ-bba.dz

[3] *Electronic Department, Université de Bordj Bou Arreridj Bord Bou Arreridj 34000, Algeria.* abderrahim.rreffas@)univ-bba.dz

***Abstract**-The main objective of this paper is the study a new approach for the speed regulator of dual star induction motor drives (DSIM) performances, this drive system is supplied by multi-level converters (MLC). The new approach uses a Neuro-Fuzzy controller (NFC) with an indirect field oriented (IFOC) technique. To realize a control of this machine, two voltage source multi-level converters of the pulse width modulation (PWM) methods are applied. So, a four-layer artificial neural network (ANN) structure is utilized to train the parameters of the fuzzy logic control (FLC) based on the minimization of the square of the error. Simulation results obtained are very satisfactory and showed that neuro-fuzzy control performance is enhanced using two MLC with introduces load disturbances and the parameter variation.*

Keywords-- Dual star induction motor, indirect field oriented control, multi-level converters, Neuro-fuzzy controller, fuzzy logic control.

I. INTRODUCTION

The DSIM powered by voltage source MLC offers numerous benefits compared to conventional three-phase electrical motors. These advantages include decreased harmonic currents in the rotor and reduced current per phase without the need for increased voltage per phase, resulting in improved reliability and diminished torque pulsations (as depicted in Fig. 1 [1-2-3]). The DSIM is designed with two windings that are spatially displaced by $\alpha = 30°$ electrical degrees, each with isolated neutrals, as shown in Fig. 1 [4-8].

Coupling between the field and the torque. To address this issue, vector control techniques have been developed, enabling decoupling between the field and the torque, similar to the control principles used in DC machines [9]. Specifically, the indirect vector control scheme for the dual stator winding induction machine assumes that the machine can be treated as two independent induction machines that are coupled through the same rotor shaft [10-11]. This approach has proven to be effective in achieving precise control over these powerful machines, expanding their versatility across a diverse range of industrial applications.

Conventional control algorithms, such as PI and PID controllers, have significant room for improvement due to their drawbacks. They are highly sensitive to variations in system parameters, struggle to effectively handle internal disturbances and load fluctuations, and heavily rely on precise machine models with specific parameters [8-12]. In contrast, intelligent controller designs present a promising alternative by not relying on the exact mathematical model of the drive systems. As a result, there is a growing need to focus on intelligent controllers when seeking to control the speed of high-performance induction machine drive systems.

Numerous innovative approaches have emerged as potential replacements for the PI and PID techniques. Among these alternatives are the fuzzy logic controller [5-6-8] and artificial neural networks (ANNs) [9-10-12]. Nevertheless, when implementing a simple fuzzy controller for machine drive speed control, its effectiveness is constrained within a narrow operational range, demanding substantial manual fine-tuning through trial and error to achieve optimal performance [8]. Consequently, the creation of a comprehensive training dataset capable of handling all modes of operation for the ANN becomes an exceptionally formidable endeavor [9].

The NFC controller has been specifically tailored for induction machine drives [11], capitalizing on the strengths of both FLC and ANN to enhance performance and efficiency. To validate its effectiveness in practical applications, a comprehensive simulation model has been developed in *MATLAB/SOFTWARE*.

This model encompasses the indirect field-oriented control of the DSIM powered by two multi-level converters, fully incorporating the proposed NFC. The simulation results demonstrate the NFC's efficacy in real-world scenarios, showcasing its potential to revolutionize the field of intelligent control systems for machine drives.

II. DSIM MODELING

The DSIM is designed with two sets of three-phase windings spatially phase shifted by 30 electrical degrees [9-10], sharing a common stator magnetic core, as illustrated in Fig. 2 [15]. Nevertheless, modeling and controlling the DSIM in its original reference frame present significant challenges. To overcome these challenges, it becomes imperative to obtain a simplified model. Consequently, the mathematical modeling approach for the DSIM closely resembles that of standard induction machines, often employing similar simplifying assumptions [1-16]:

- Motor windings undergo sinusoidal distribution;
- Both sets of windings have identical parameters;
- The flux path within the motor is linear;
- The model incorporates mutual leakage inductances.

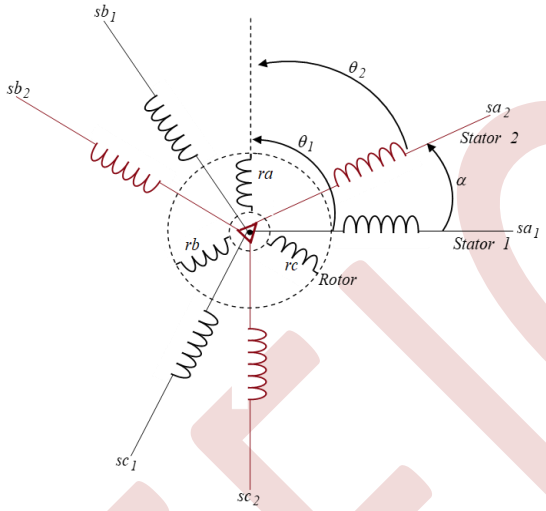


Fig. 1. Windings of the dual stator induction motor.

We can express the equation for the stator voltages as:

$$\begin{cases} v_{ds1} = R_s i_{ds1} + \frac{d\lambda_{ds1}}{dt} - \omega_s \lambda_{qs1} \\ v_{qs1} = R_s i_{qs1} + \frac{d\lambda_{qs1}}{dt} + \omega_s \lambda_{ds1} \end{cases} \quad (1)$$

$$\begin{cases} v_{ds2} = R_s i_{ds2} + \frac{d\lambda_{ds2}}{dt} - \omega_s \lambda_{qs2} \\ v_{qs2} = R_s i_{qs2} + \frac{d\lambda_{qs2}}{dt} + \omega_s \lambda_{ds2} \end{cases} \quad (2)$$

The equation for the rotor voltages is given by:

$$\begin{cases} 0 = R_r i_{dr} + \frac{d\lambda_{dr}}{dt} - (\omega_s - \omega_r)\lambda_{qr} \\ 0 = R_r i_{qr} + \frac{d\lambda_{qr}}{dt} + (\omega_s - \omega_r)\lambda_{dr} \end{cases} \quad (3)$$

The equation for the rotor and the stator flux linkages are:

$$\begin{cases} \lambda_{ds1} = l_s i_{ds1} + L_m(i_{ds1} + i_{ds2} + i_{dr}) \\ \lambda_{qs1} = l_s i_{qs1} + L_m(i_{qs1} + i_{qs2} + i_{qr}) \end{cases} \quad (4)$$

$$\begin{cases} \lambda_{ds2} = l_s i_{ds2} + L_m(i_{ds1} + i_{ds2} + i_{dr}) \\ \lambda_{qs2} = l_s i_{qs2} + L_m(i_{qs1} + i_{qs2} + i_{qr}) \end{cases} \quad (5)$$

$$\begin{cases} \lambda_{dr} = l_r i_{dr} + L_m(i_{ds1} + i_{ds2} + i_{dr}) \\ \lambda_{qr} = l_r i_{qr} + L_m(i_{qs1} + i_{qs2} + i_{qr}) \end{cases} \quad (6)$$

A. Mechanical Equation

The rotor speed can be expressed as:

$$J\frac{d\omega_r}{dt} = C_{em} - Cr - f\omega_r \quad (7)$$

The electromagnetic torque of the DSIM are given as:

$$C_{em} = P\frac{L_m}{L_m + L_r}\left(\lambda_{dr}(i_{qs1} + i_{qs2}) - \lambda_{qr}(i_{qs1} + i_{qs2})\right) \quad (8)$$

Where: ω_s, ω_r : speed of synchronous reference frame and rotor electrical angular; L_s and L_r stator and rotor inductances; L_m : resultant magnetizing inductance; P :number of pole pairs; J : moment of inertia; C_r : load torque; f : total viscous friction coefficient, λ : flux.

III. CONTROLE TEHENIQUE (IFOC)

The indirect field-oriented control (IFOC) serves as the main objective to enable autonomous manipulation of the rotor flux and electromagnetic torque of a machine, akin to the approach employed in DC machines [9-10-16]. By implementing the IFOC technique in the DSIM drive system, the control strategy streamlines the model.

$$\lambda_{dr} = \lambda_r^* \quad (9)$$

$$\lambda_{qr} = 0 \quad (10)$$

The rotor currents in terms of the stator currents are derived from (11) and (12) as:

$$i_{dr} = \frac{1}{L_m}(\lambda^* - L_m(i_{ds1} + i_{ds2})) \quad (11)$$

$$i_{qr} = \frac{-L_m}{L_r}(i_{qs1} + i_{qs2}) \quad (12)$$

Substituting both quadrature and direct rotor currents from (11) and (12) into (3) can be written as follows:

$$i_{ds}^* = \frac{1}{L_m}\lambda_r^* + \frac{T_r}{L_m}\frac{d\lambda_r^*}{dt} \quad (13)$$

$$i_{qs}^* = \frac{L_r}{PL_m\lambda_r^*}C_{em}^* \quad (14)$$

$$\omega_{sl} = \frac{L_m}{T_r\lambda_r^*}i_{qs} \quad (15)$$

where :

$$T_r = \frac{L_r}{R_r}$$

Furthermore, the same substitution of the rotor currents from (11) and (12) the electromagnetic torque is given by:

$$C_{em}^{*} = P\frac{L_m}{L_r}\lambda_r^{*} i_{qs}^{*} \quad (16)$$

where : the stator current components can be calculated as following:

$$i_{ds}^{*} = i_{ds1}^{*} + i_{ds2}^{*} \quad (17)$$

$$i_{qs}^{*} = i_{qs1}^{*} + i_{qs2}^{*} \quad (18)$$

The commands/references voltages are derived by substituting the (9) and (10) in (1) and (2) the following are obtained:

$$\begin{cases} v_{ds1}^{*} = R_s i_{ds1} + l_s p i_{ds1} - \omega_s^{*}\left(l_s i_{qs1} + T_r \lambda_r^{*} \omega_{sl}^{*}\right) \\ v_{qs1}^{*} = R_s i_{qs1} + l_s p i_{qs1} + \omega_s^{*}(l_s i_{ds1} + \lambda_r^{*}) \end{cases} \quad (19)$$

$$\begin{cases} v_{ds2}^{*} = R_s i_{ds2} + l_s p i_{ds2} - \omega_s^{*}\left(l_s i_{qs2} + T_r \lambda_r^{*} \omega_{sl}^{*}\right) \\ v_{qs2}^{*} = R_s i_{qs2} + l_s p i_{qs2} + \omega_s^{*}(l_s i_{ds2} + \lambda_r^{*}) \end{cases} \quad (20)$$

The block diagram NFC with IFOC the proposed control process, the IFOC of the DSIM drive fed by two MLC is shown in Fig. 2**.**

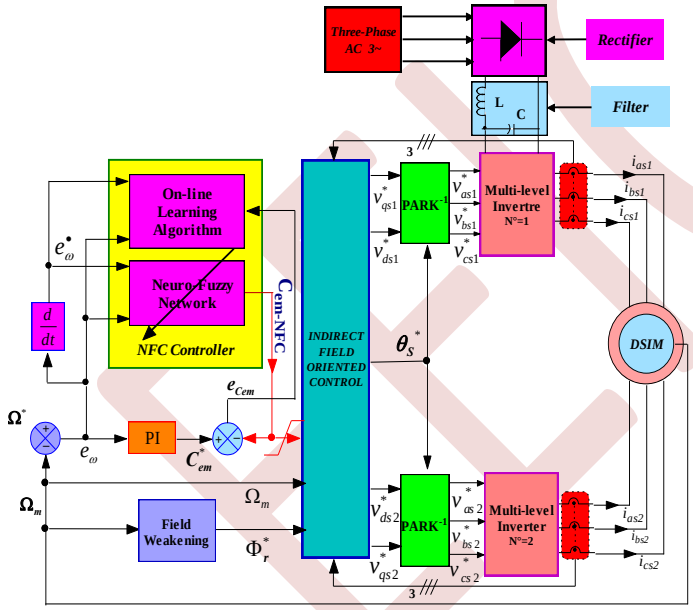


Fig. 2. Block diagram of neuro-fuzzy for speed control of IFOC-DSIM.

VI. Multi-level Converters Model

The bridge multi-level converters (CHMLC) present a multitude of advantages compared to conventional bipolar inverters, especially in industrial drives systems. Among these benefits are enhanced electromagnetic compatibility, decreased voltage stress on the switches, and reduced harmonics content at higher levels, thereby lowering the reliance on filters and resulting in a more refined output voltage waveform with minimal total Harmonic distortion (THD) [17-18]. As for the various topologies of multi-level converters, the diode-clamped, flying capacitor, and cascade H-bridge structures (illustrated in Fig .4) stand out as the most popular choices [19]. These advancements in converter technology offer significant improvements in efficiency and performance for industrial drive applications.

The proposed multi-level three-phase cascaded H-bridge converters, for example, the topology of a seven-level includes a standard three-leg converters (one leg for each phase) and H-bridge in series with each converters leg as shown in fig. 4 [17-18]. All signals for controlling the cascade H-bridge MLC are created by a PWM signal modulated technique, for controlling the active devices, the most popular and easiest technique to implement uses several triangle carrier signals and one reference is shown in Fig. 3.

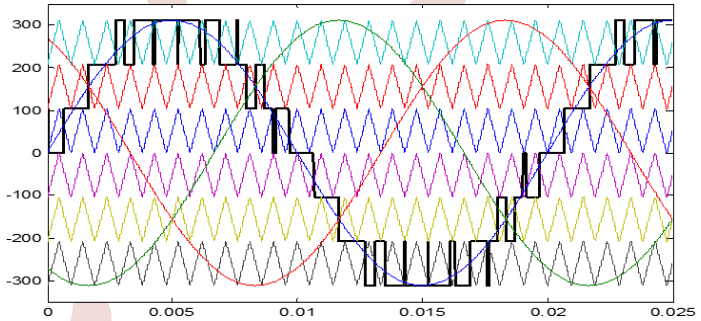


Fig. 3. A principle of multi-carrier PWM strategy for MLC with seven levels.

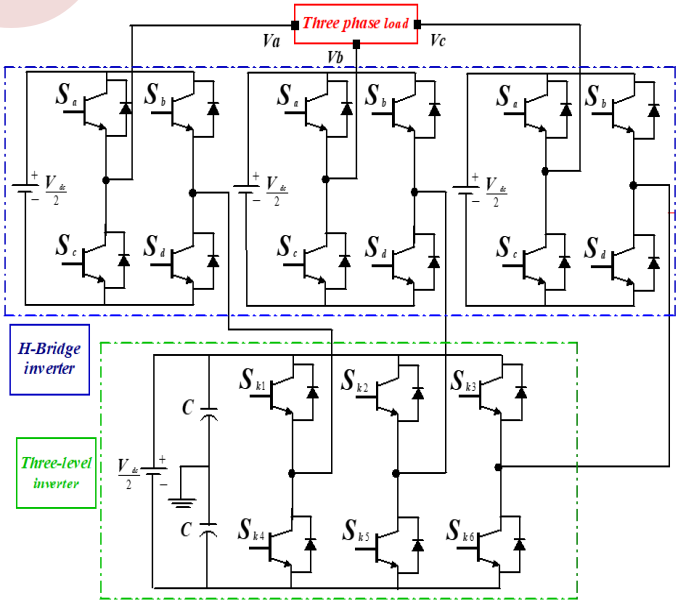


Fig. 4. The topology of the seven level three-phase cascaded H-bridge Multi-level converters.

IV. DSIM NEURO-FUZZY CONTROLLER

The NFC system is a sophisticated combination of an on-line learning algorithm and a neuro-fuzzy network, as visually presented in Fig. 2. The neuro-fuzzy network undergoes rigorous training using the on-line learning algorithm. To facilitate the fuzzy inference process, the system is equipped with two inputs: 'speed error' and its changing, identified as 'input 1' and 'input 2,' respectively [20]. The desired outcome, known as the 'torque command,' is produced as the output [20-21]. The structure of the artificial neural network (ANN) can be visualized in Fig. 5, consisting of four distinct layers. The first layer is responsible for handling inputs, the second layer handles Fuzzufication, the third layer performs crucial fuzzy rule evaluation, and the fourth layer takes charge of the Defuzzification process [21-22].

The desired electromagnetic torque C_{em}^{*} is achieved through the implementation of a PI controller. In this context, the term 'error' refers to the disparity between the desired torque C_{em}^{*} and the control torque C_{em-NFC}, which is currently being generated by the neuro-fuzzy controller.

A. *Back propagation algorithm*

The detailed discussions on different layers of the neuro-fuzzy network are given below.

First layer: Each input node in this layer corresponds to the specific input variable, the inputs of this layer are given by $net_1^I = e_\omega$ and $net_1^I = e_\omega^*$.

The outputs of this layer are given by:

$$y_1^I = f_1^I(net_1^I) = e_\omega \text{ and } y_2^I = f_2^I(net_2^I) = e_\omega^*.$$

The weights of this layer are unity and fixed.

Second layer: Each node performs a membership function that can be referred to as the Fuzzufication procedure, each input has seven Gaussian membership functions (MFs) as shown in Fig. 5.

$$\text{net}_{1,j}^{II} = -\left(\frac{x_{1,j}^{II} - m_{1,j}^{II}}{\sigma_{1,j}^{II}}\right)^2 \quad (21)$$

$$\text{net}_{2,k}^{II} = -\left(\frac{x_{2,k}^{II} - m_{2,k}^{II}}{\sigma_{2,k}^{II}}\right)^2 \quad (23)$$

$$\begin{cases} y_{1,j}^{II} = f_{1,j}^{II}\left(\text{net}_{1,j}^{II}\right) = e^{\text{net}_{1,j}^{II}} \\ y_{2,k}^{II} = f_{2,k}^{II}\left(\text{net}_{2,k}^{II}\right) = e^{\text{net}_{2,k}^{II}} \end{cases} \quad (24)$$

where : $m_{1,j}^{II}$, $m_{2,k}^{II}$: represents the Gaussian MFs centers and $\sigma_{1,j}^{II}$, $\sigma_{2,k}^{II}$: determines the MFs widths.

Third layer: Is called inference and decision layer, the output of every node is the product of all input signals. Based on 49 rules in the rule-base of fuzzy inference system the rule base of the neuro-fuzzy controller is given in Table. 1, there are 49 nodes in this layer with function as:

Table. 1. Rules base for FLC controller.

e \ de	NB	NM	NS	ZE	PS	PM	PB
PB	ZE	NS	NM	NB	NB	NB	NB
PM	PS	ZE	NS	NM	NB	NB	NB
PS	PM	PS	ZE	NS	NM	NB	NB
ZE	PB	PM	PS	ZE	NS	NM	NB
NS	PB	PB	PM	PS	ZE	NS	NM
NM	PB	PB	PB	PM	PS	ZE	NS
NB	PB	PB	PB	PB	PM	PS	ZE

The values of weights between second layer and third layer are unity.

Fourth layer: is called defuzzifier layer, the center of gravity method is used to determine the output of NFC each node equation is specified as flowing:

$$a = \sum_j \sum_k \left(\omega_{jk}^{IV}\, y_{jk}^{III}\right), b = \sum_j \sum_k \left(y_{jk}^{III}\right) \quad (26)$$

$$\text{net}_0^{IV} = \frac{a}{b}\ , y_0^{IV} = f_0^{IV} = \frac{a}{b} \quad (27)$$

ω_{jk}^{IV} : specify the values of the output membership functions used in the FLC, ω_0^{IV} y_0^{IV} is an output of the defuzzification layer ***a*** and ***b*** are the numerator and the denominator of the function used in the center of area technique, respectively. In the NFC, the object of the learning algorithm is correction the weights ω_{jk}^{IV}, the $m_{1,j}^{II}$, $m_{2,k}^{II}$ and $\sigma_{1,j}^{II}$, $\sigma_{2,k}^{II}$. For the learning algorithm, we use the supervised gradient descent method. Therefore, the error ***E*** we take for describe the back propagation algorithm.

$$E(l) = \frac{1}{2} e_{C_{em}}^2 \quad (28)$$

$$e_{C_{em}} = d - y \quad (29)$$

where: d : Desired torque controller G_{em}^{*} (Output of classical PI controller) and y: Actual output (y is equal to output of NFC (G_{em-NFC}).

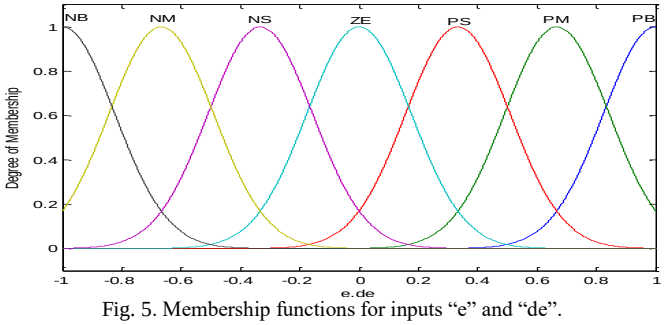


Fig. 5. Membership functions for inputs "e" and "de".

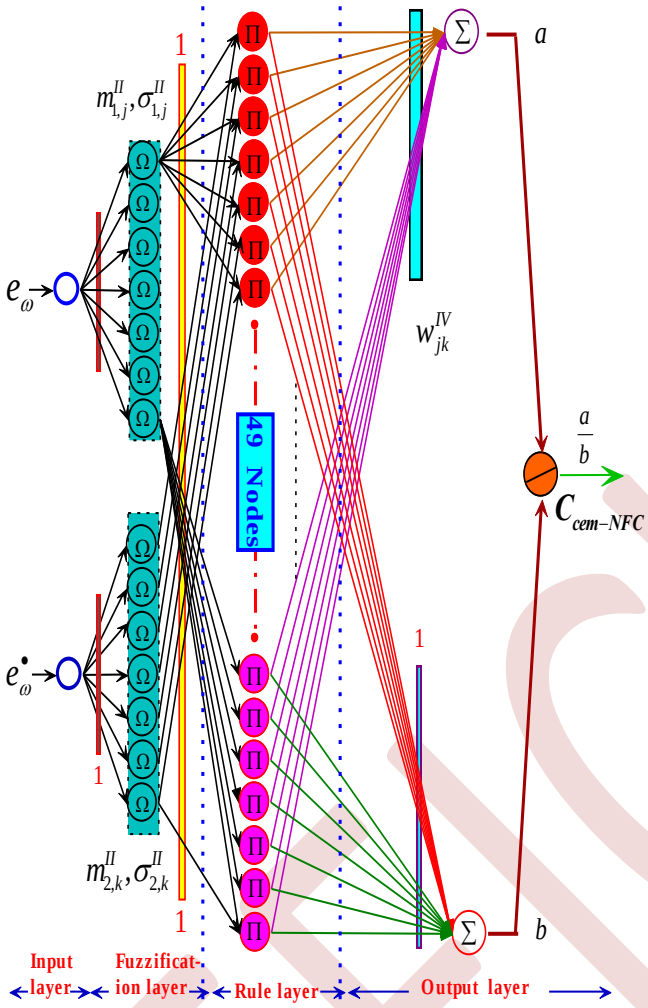


Fig. 6. NFC network building.

V. SIMULATION RESULTS

The proposed controller NFC underwent rigorous simulation using *MATLAB/SIMULINK*. A series of tests were performed to thoroughly evaluate the performance and robustness of the IFOC-DSIM when driven by the CHMLC and to compare its effectiveness against the classical PI controller. To achieve the supply voltage, two CHMLCs, employing a suitable PWM control technique, enforced voltage commands. Throughout the simulations, the drive was subjected to a step reference speed control set at approximately 2500 rpm. Additionally, the drive's performance and robustness were further assessed through the introduction of step changes in load torque and speed inversion. For detailed simulation parameters for the DSIM, please refer to Table 2.

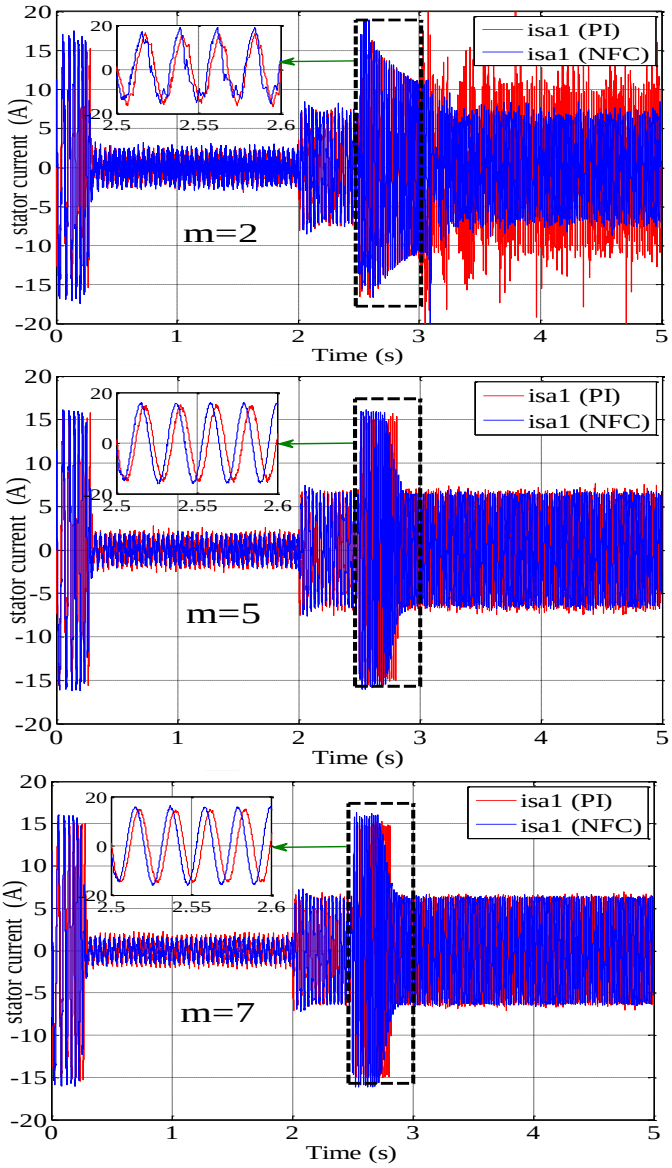
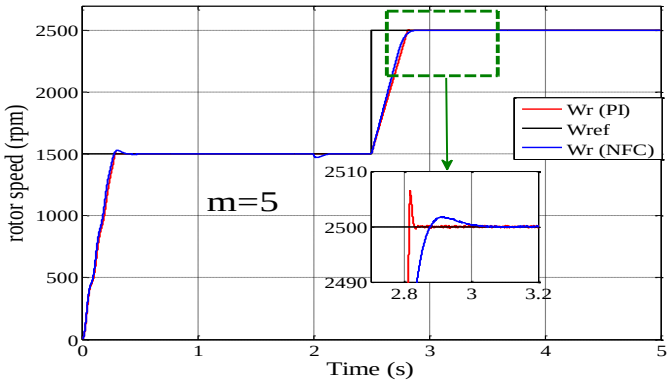


Fig.7. Simulated responses of outputs current for different number of levels m, with increased rotor resistance (ΔRr% = +50%) followed by applying load torque (14N.m).



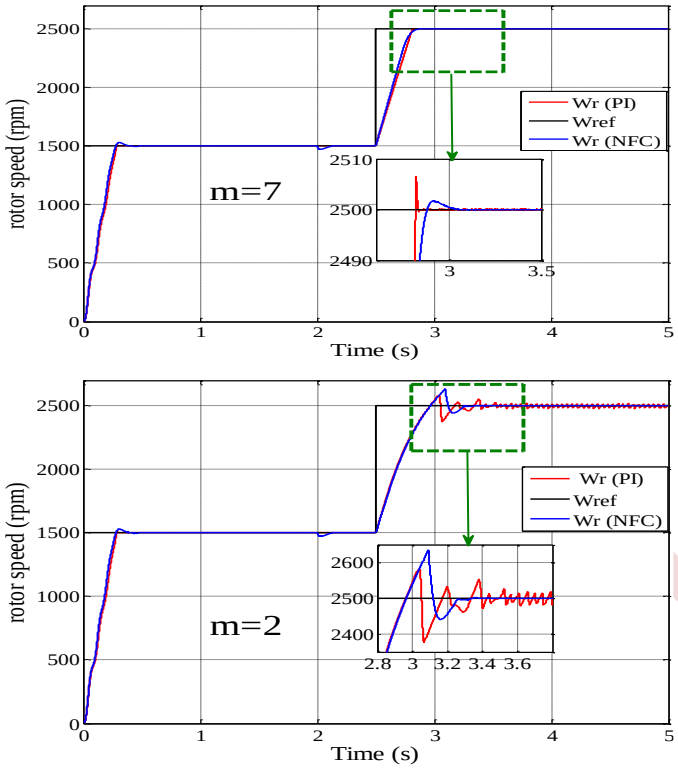
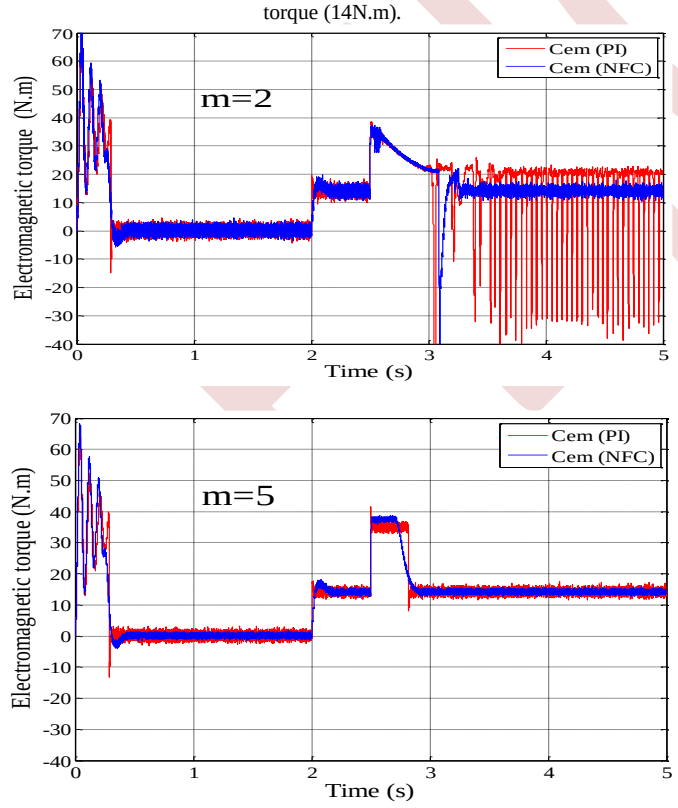


Fig. 8. Simulated responses of the rotor speed for different number of levels m with increased rotor resistance (ΔRr% = +50%) followed by applying load torque (14N.m).



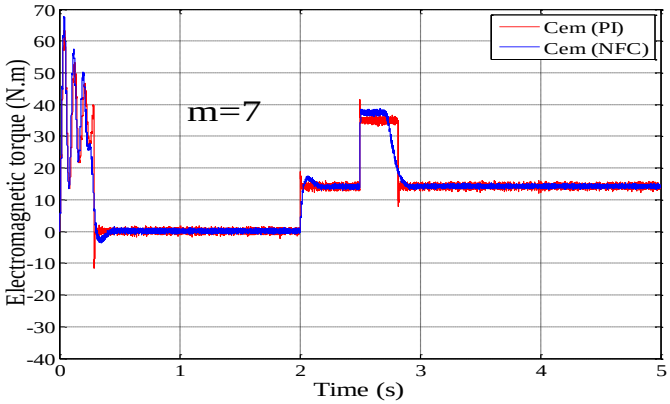


Fig. 9. Simulated responses of the electromagnetic torque for different number of levels m, with increased rotor resistance (ΔRr% = +50%) followed by applying load torque (14N.m).

Fig. 7 presents the stator current per phase for converters with varying levels from m = 2 to m = 7. At t = 2s, a load of Cr = 14 N.m is applied. To assess robustness, we conducted tests using both the NFC and PI controller, with the rotor resistance (Rr) undergoing a variation of Rn + 50% after t = 1s. The findings reveal a noteworthy trend: as the number of levels decreases, the output voltage progressively approaches a more ideal sinusoidal waveform. This suggests that reducing the number of levels in the converter has a positive impact on achieving a better sinusoidal output.

The proposed controller demonstrates numerous advantages compared to conventional converters, as evidenced in Fig. 8. It showcases the remarkable robustness of NFC and PI speed control, even when faced with changes in rotor resistance and an increase in reference speed. Moreover, Fig. 8 presents the DSIM response to varying reference speeds, ranging from 1500 rpm to 2500 rpm. Surprisingly, despite an increase in rotor resistance (ΔRr% = +50%) at t=1s, followed by the application of load torque (Cr = 14 N.m) at t=2s, no change in speed is observed.

One notable finding is the insensitivity of the NFC to constant time variation, in contrast to the different response exhibited by the PI controller. These results emphasize the superior performance and robustness of the proposed controller in diverse operating conditions.

The results presented in Fig. 9 reveal a continuous and gradual decrease in electromagnetic torque ripple in steady state as the number of levels in the converters increases, coupled with variations in the rotor resistance. Notably, as the inverter voltage level rises from m=2 to m=7, the electromagnetic torque ripple experiences a significant reduction. This suggests a positive correlation between the

number of levels in the converters and the mitigation of electromagnetic torque ripple.

Together simulation results indicate that the proposed NFC controller gives better performances and robustness than the classical PI controller. It is observed a substantial reduction in the magnitude of pulsations in the electromagnetic torque and stator currents with a multi-level inverter compared to a conventional inverter.

VI. CONCLUSION

The present paper introduces a novel design that utilizes NFC for speed regulation of DSIM fed by MLC. The NFC control offers several advantages, including high performance, simplicity in composition, robustness against disturbances, and improved tracking performance of speed. The simulations conducted on DSIM fed by MLC, with the latter solely providing power to the AC and maintaining the output voltage at a predefined level, yielded satisfactory results. The fuzzy system control, implemented with a four-layer NN architecture and utilizing error speed and its derivative as inputs, was successfully employed. The NFC's learning process relied on the gradient descent technique. The simulation results unambiguously demonstrate NFC's superiority over the classical PI controller in terms of robustness. Furthermore, the proposed controller showcased high reliability and efficiency in regulating the speed of the DSIM across various operating conditions and increasing levels.

APPENDIX 1

Table.2: Dual star induction machine parameters for simulation.

Quantity	**Symbol and magnitude**
Rated power Pn	4.5 kW
Rated voltage Vn	220/380 V
Rated current In	6 A
Rated speed Nn	2753 rpm
Number of poles P	2
Rated frequency f	50 Hz
Stator resistance R_S	3.72 Ω
Rotor resistance Rr	2.12 Ω
Stator inductance L_S	0.022 H
Rotor inductance Lr	0.006 H
Mutual inductance L_m	0.3672 H
Moment of inertia J	0.0662 kg.m2
Coefficient of viscous friction f	0.006 N.m.s/rad

REFERENCES

[1] S. Lekhchine, T. Bahib, and Y. Soufi," Indirect rotor field oriented control based on fuzzy logic controlled double star induction machine," In: Electrical Power and Energy Systems, vol. 57, pp. 206-211, 2014

[2] E. Zaidi, K. Marouani, and H. Bouadi, ''Speed Control for Multi-phase Induction Machine Fed by Multi-level Converters Using New Neuro-Fuzzy'', Chapter books, Springer Nature Switzerland AG 2019, ICAIRES 2018, vol. 62, pp. 457-468, 2019.

[3] E. Levi," Recent developments in high performance variable-speed multi-phase induction motor drives," sixth international symposium nikola tesla, Belgrade, SASA, Serbia, Oct 18-20, 2006.

[4] E. Levi," Multi-phase electric machines for variable-speed applications," In: IEEE transactions industrial electronics, vol. 55, no. 5, May 2008.

[5] S. Y. Yi, and M. J. Chung," Robustness of fuzzy logic control for an uncertain dynamic system," In: IEEE Trans. Fuzzy Syst, vol. 6, pp. 216–224, 1998.

[6] E. Merabet, H. Amimeur, F. Hamoudi and R. Abdessemed, "Self–Tuning Fuzzy Logic Controller for a Dual Star Induction Machine," In: Journal of Electrical Engineering & Technology, vol. 6, no. 1, pp. 133-138, 2011.

[7] E. Zaidi, K. Marouani, H. Bouadi, L. Bentouhami, and E. Merabet, ''Fuzzy Sliding Mode Method for Speed regulation of a Dual Star Induction Machine Drive fed by Multi-level Inverters'', In IEEE 2018 International Conference on Applied Smart Systems (ICASS2018), 24-25 November 2018, Médéa, Algiers, Algeria, 2018.

[8] U. Michael, T. Wishart, and R. G. Harley," Identification and Control of Induction Machines Using Artificial Neural Networks, In: IEEE Transactions on Industry Applications, vol. 31, no. 3, 1995.

[9] S. Lekhchine, T. Bahi, Y. Soufi, and H. Merabet, "Neural Fuzzy Speed Control for Six Phase Induction Machines," In: International conference of control, engineering & information technology (CEIT'13) Algeria, vol. 3, pp. 123-127, 2013.

[10] M. N. Uddin, M. A. Abido, and M. A. Rahman, "Development and implementation of a hybrid intelligent controller for interior permanent magnet synchronous motor drive," In: IEEE Trans. Ind. Appl, vol. 40, no. 1, pp. 68-76, 2004.

[11] J-S. R. Jang," ANFIS: Adaptive-Network-Based Fuzzy Inference Systems," In: IEEE Trans. System, Man, and Cybernetics, vol. 23, no. 3, pp. 665-684 ,1993.

[12] E. Zaidi, K. Marouani, A. E Mabrek, E. Merabet and L. Bentouhami, ''Fuzzy Logic Control of Multi-Phase Induction Machine Drives Based on Cascaded Hybrid Multi-level Inverters,'' In IEEE the International Conference on Electrical Sciences and Technologies in Maghreb CISTEM 2018, USTHB-Algiers, Algeria, 29-31 October 2018.

Speed and Flux Estimation of an Asymmetrical Six-Phase Induction Machine Using Machine Learning

Yanis Hamoudi [1], Hocine Amimeur [1], Katia Benamara [1], Faycal Hassaini [1]

[1] *Laboratoire de Maitrise des Energies Renouvelables(LMER), Faculté de Technologie, Université de Bejaia, 06000 Bejaia, Algeria.*

yanis.hamoudi@univ-bejaia.dz

***Abstract*— This paper investigates the estimation of the speed and flux of an asymmetric six-phase induction machine (ASIM) using machine learning (ML) algorithms. For well-exp0loiting the characteristics of ML, two concepts are introduced: a) the grey box principle, by using our knowledge of the ASIM to provide more simple and effective estimator inputs; B) hyperparameter optimization using the Bayesian optimization (BO) algorithm. Intensive simulations are done under MATLAB/Simulink, using different ML algorithms to select the optimal algorithm for this application. The performance comparison reveals that the Gaussian Process regression presents the highest accuracy in the test, making it more suitable for speed and flux estimation.**

***Keywords:* Asymmetric Six-Phase Induction Machine, Supervised Machine Learning Algorithms, Hyperparameter Optimization.**

I. INTRODUCTION

Nowadays the exponential development of artificial intelligence and its success in a wide range of areas motivate researchers to explore more applications [1], [2]. In renewable energy systems, like solar and wind turbines, machine learning is used to estimate some nonlinear quantities used to diagnose and control these systems.

The speed and flux are essential parameters used to control the machine. Where the supervised ML can be used as an estimator. There are many ML algorithms that have been used in the literature. Such as in [3], [4] where the problem is considered like a black box, so the training step can take more time and provide poor results. Moreover, the hyperparameters are set manually such as in [5], [6]. This strategy not only imposes a significant amount of human work adjusting the model's correctness but also severely restricts its performance.

A bad choice of the estimator input and the hyperparameter of these algorithms can provide poor results and can decrease ML performances. To outrun these two problems and provide high-accuracy estimation using ML two improvements are presented in this paper: a) the best choice of the estimator inputs is insured using the grey box principle, this principle consists to exploit our previous knowledge of the machine to provide more simple and effective inputs; b) the hyperparameter is optimized using Bayesian Optimization (BO) algorithm. The proposed estimator is represented in Fig. 1.

The contributions of this article are classed in the following points:

- High precision of estimation.
- Adaptation to the parametric variation.
- Avoid wasting time by manually searching.

This article is ordered as follows: section 2 is devoted to the ASIM modelling with the magnetic circuit saturation; Section 3 shows the Gaussian process regression theory amyloid with the grey-box principle and the Bayesian hyperparameter optimization; Section 4 presents the training and the test result of GPR.

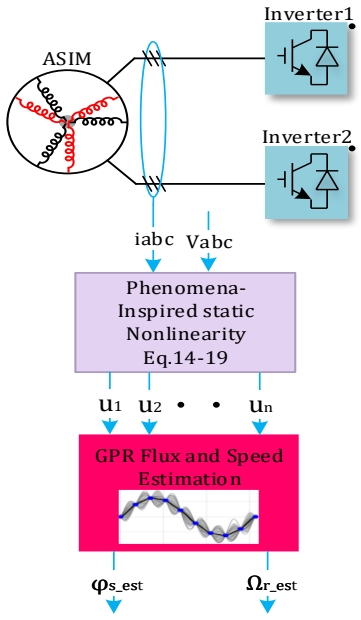


Figure 1. Proposed GPR flux and speed estimator.

II. MODELLING OF ASIG

The machine used in this article is an asymmetric six-phase induction machine. This machine's stator is constituted by two identical stars shifted by 30 degrees. Electrical equations are expressed as flow [7]:

$$\begin{cases} \bar{v}_{s1} = r_{s1}\bar{\imath}_{s1} + \dfrac{d}{dt}\bar{\varphi}_{s1} \\ \bar{v}_{s2} = r_{s2}\bar{\imath}_{s2} + \dfrac{d}{dt}\bar{\varphi}_{s2} \\ \bar{v}_r = r_r\bar{\imath}_r + \dfrac{d}{dt}\bar{\varphi}_r - j\omega_r\bar{\varphi}_r = 0 \end{cases} \quad (1)$$

Where: $r_{sx}(x = 1,2)$; r_r: is the stator, rotor resistance; ω_r: the rotor electrical angular speed. All of the other symbols represent their usual significance. The formulas of the stator and rotor flux linkages are as follows [8]:

$$\begin{cases} \bar{\varphi}_{s1} = L_{ls1}\bar{\imath}_{s1} + L_m(\bar{\imath}_{s1} + \bar{\imath}_{s2} + \bar{\imath}_r) \\ \bar{\varphi}_{s1} = L_{ls2}\bar{\imath}_{s2} + L_m(\bar{\imath}_{s1} + \bar{\imath}_{s2} + \bar{\imath}_r) \\ \bar{\varphi}_r = L_{lr}\bar{\imath}_r + L_m(\bar{\imath}_{s1} + \bar{\imath}_{s2} + \bar{\imath}_r) \end{cases} \quad (2)$$

Where: L_{lx} $(x = s1, s2, r)$: is the leakage inductance of the stator (or rotor), and L_m: The magnetizing inductance, expressed by [9], [10] :

$$L_m = 0.1406 + 0.0014\,\imath_m - 0.0012\,{\imath_m}^2 + 0.00005\,{\imath_m}^3 \quad (3)$$

The magnetizing current is expressed as follows [9]:

$$\imath_m = \sqrt{[Re(\bar{\imath}_s + \bar{\imath}_r)]^2 + [Im(\bar{\imath}_s + \bar{\imath}_r)]^2} \quad (4)$$

With

$$\bar{\imath}_s = \bar{\imath}_{s1} + \bar{\imath}_{s2} \quad (5)$$

The electromagnetic torque is determined as follows:

$$\begin{cases} T_{em1} = P\ Im\{\bar{\varphi}_{s1}^{\circledast}\,\bar{\imath}_{s1}\} \\ T_{em2} = P\ Im\{\bar{\varphi}_{s2}^{\circledast}\,\bar{\imath}_{s2}\} \\ T_{em} = T_{em1} + T_{em2} \end{cases} \quad (6)$$

The mechanical equation of the machine is defined as follows:

$$T_{em} - T_g = J\frac{d\Omega}{dt} + f\Omega \quad (7)$$

III. GAUSSIAN PROCESS REGRESSION

The Gaussian process regression kernel model is a sophisticated probabilistic algorithm.

The GPR is a generalization of the relevant probability distribution. The Gaussian distribution takes an input vector and computes its probability, which has the features of a mean and variance equation (8) [11]. A mean function (the prediction) $\mu(x)$ Equation (9) and a covariance function $k(x, x')$ Equation (10) specify the GPR.

$$g(x) \sim gp\big(\mu(x), k(x, x')\big) \quad (8)$$

$$\mu(x) = E[g(x)] \quad (9)$$

$$k(x, x') = E\big[\big(g(x) - \mu(x)\big)\big(g(x') - \mu(x')\big)\big] \quad (10)$$

The mean function is initialized to zero to simplify and prevent complicated calculations, as shown in Fig. 2-a.

For this application, the kernel function is the Rational Quadratic for the speed estimator Equation.11 and the Matern for the flux estimator Equation (12) [12].

$$K_{RQ}(x_i, x_j) = \sigma_f^2\left(1 + \frac{r^2}{2\alpha{\sigma_l}^2}\right)^{-\alpha} \quad (11)$$

$$K_{Mat}(x_i, x_j) = \sigma_f^2\left(1 + \frac{\sqrt{5}r}{\sigma_l} + \frac{5r^2}{3\sigma_l^2}\right)exp\left(-\frac{\sqrt{5}r}{\sigma_l}\right) \quad (12)$$

The GPR inputs are chosen using the grey box approach to improve the estimator's efficacy, and the Hyperparameters are optimized using Bayesian optimization, as discussed in these subsequent:

A. Hyperparameter Optimization

Bayesian optimization is a method of finding the best values of some parameters that affect the performance of a system or a function. It works by the construction a probabilistic model of the function, called the surrogate function, then searched efficiently with an acquisition function, in our situation, we used the predicted improvement per second plus as indicated in equation (13).

$$\alpha_t(x) = \frac{\big(g(X_{best}) - \mu(X)\big)\,\mathcal{C}\big(g(X_{best}); \mu(X)\big) + \sigma_f(X)\,\mathcal{N}\left(g(X_{best}); \mu(X); \sigma_f(X)\right)}{\mu(X)} \quad (13)$$

The surrogate function is updated with the new observations, and the process is repeated until a satisfactory

solution is found. These phases are organized in pseudocode (see algorithm 1).

Fig. 2 shows the first four iterations for a better understanding.

B. Grey-Box Concept

A black box model is a model that does not assume any prior knowledge about the internal structure or logic of the system. This method can be complex to construct an effective estimator.

A grey box principle is a model that associate a theoretical knowledge with data to complete the model. A grey box model is useful when some information about the system is known, but not enough to create a fully deterministic or analytical model. A grey box model can also incorporate physical constraints and prior information into the model. The grey box model can provide better performance if some information about the system is known, but not enough to create a fully deterministic or analytical model. To acquire more meaningful estimator inputs, we employ the grey box concept in our case.

Equations (14)-(19) show the transformations we utilized in this paper [13]. The new inputs are derived from complex conversions from the voltages and currents of the ASIM. These nonlinear transformations help to improve the performance and efficiency of the system.

Algorithm 1. Bayesian optimization pseudo-code with the surrogate model GP

1: Input dataset $\mathcal{D} = \{X, Y\}$

2: Initial random part of dataset $\mathcal{D}_0 = \{X_0, Y_0\}$

3: Calculate a **Surrogate Function** (GP) g to find $Y_0 = g(X_0)$

4: for $t = 1, 2, \ldots$ do

5: Chose another part of dataset $\mathcal{D}_t = \{X_t, Y_t\}$ by minimizing the **Acquisition Function** α (expected improvement per second plus. Eq.13)**:**

$$X_t = \arg\max_x \alpha(X; \mathcal{D}_t)$$

6: Increase the dataset $\mathcal{D}_t = \mathcal{D}_{t-1} \cup \{(X_t, Y_t)\}$

7: Examine the **Surrogate Function** g to find

$$Y_t = g(X_t)$$

8: end

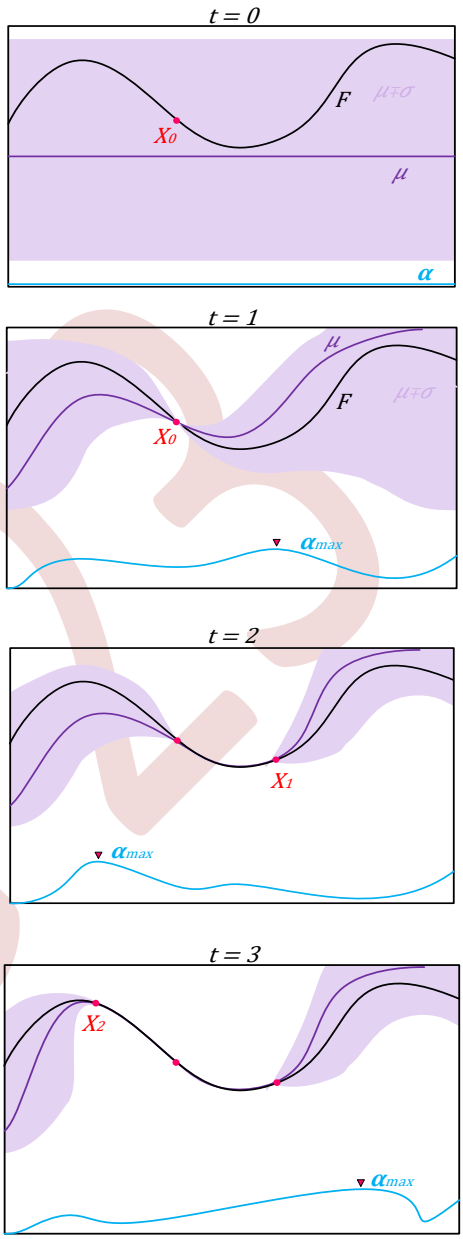


Figure 2. Visualization of a few Algorithm 1 iterations.

$$u_{1x} = |\bar{v}_{s1}| \tag{14}$$

$$u_{2x} = |\bar{\imath}_{s1}| \tag{15}$$

$$u_{3x} = Re\{\bar{v}_{s1}\, \bar{\imath}_{s1}{}^{\circledast}\} \tag{16}$$

$$u_{4x} = Im\{\bar{v}_{s1}\, \bar{\imath}_{s1}{}^{\circledast}\} \tag{17}$$

$$u_{5x} = Re\left\{\frac{\bar{v}_{s1}}{\bar{\imath}_{s1}}\right\} \tag{18}$$

$$u_{6x} = Im\left\{\frac{\bar{v}_{s1}}{\bar{\imath}_{s1}}\right\} \tag{19}$$

IV. TRAINING RESULTS

The GPR-supervised learning approach is used to estimate the flux and the rotation speed of an ASIM. During the training phase, three separate databases are employed. The initial dataset contains 7876 samples that were utilized for training. Another dataset has 1688 samples, and the holdout validation approach was used to test the correctness of the trained model and protect it from overfitting. The final dataset contains 1688 samples used to assess the model's efficiency.

The signal standard deviation is fixed to 0.1088. The GPR estimator's hyperparameters are adjusted using BO. The training results of the GPR are compared with other ML. These algorithms are: Artificial Neural Network (ANN); Support Vector Machine (SVM); Ensemble Learning (EL); and Decision Tree (DT). Four indicators are utilized: The Root Mean Square Error (RMSE); coefficient of determination (R^2); Mean Square Error (MSE); and Mean Absolute Error (MAE), Equations (20)-(23), respectively.

$$RMSE = \frac{\sqrt{\sum_{i=1}^{n}(\hat{y}_i - y_i)^2}}{n} \quad (20)$$

$$R^2 = 1 - \frac{\sum_{i=1}^{n}(\hat{y}_i - y_i)^2}{\sum_{i=1}^{n}(\check{y}_i - y_i)^2} \quad (21)$$

$$MSE = \frac{1}{n}\sum_{i=1}^{n}(\hat{y}_i - y_i)^2 \quad (22)$$

$$MAE = \frac{1}{n}\sum_{i=1}^{n}|\hat{y}_i - y_i| \quad (23)$$

With: n: the size of the training data, y_i: the actual (observed) answer, and $\hat{y}_i$: the value estimated.

Tables 1 and 2 illustrate the training achievements for speed and flux estimators, respectively.

The GPR presents the best estimation performance in the test with an RMSE of 0.27412 for the speed estimation and 0.005042 for the flux estimation.

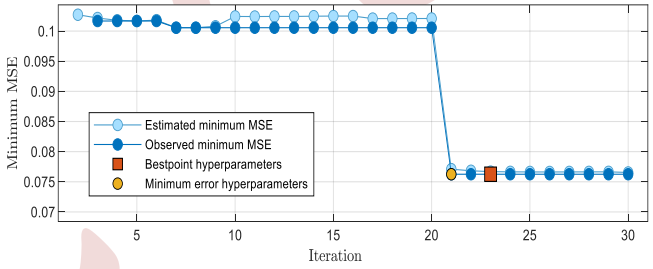
TABLE I. PERFORMANCE OF SPEED ESTIMATOR

Speed	ANN	SVM	EL	DT	GPR
RMSE(validation)	0.99045	3.6243	3.3403	3.3611	**0.27658**
(test)	1.3321	2.786	3.1116	2.9657	**0.27412**
R^2 (validation)	**1.00**	0.99	**1.00**	**1.00**	**1.00**
(test)	1.00	1.00	1.00	1.00	1.00
MSE (validation)	0.98099	13.136	11.158	11.297	**0.076498**
(test)	1.7745	7.7621	9.6818	8.7956	**0.07514**
MAE (validation)	0.71611	2.143	2.4024	2.0371	**0.21719**
(test)	0.97354	1.8061	2.3535	1.8879	**0.21417**
Prediction speed (~obs/sec)	**160000**	100000	47000	130000	3300
Training time (sec)	140.82	223.7	40.253	**18.676**	2427.5

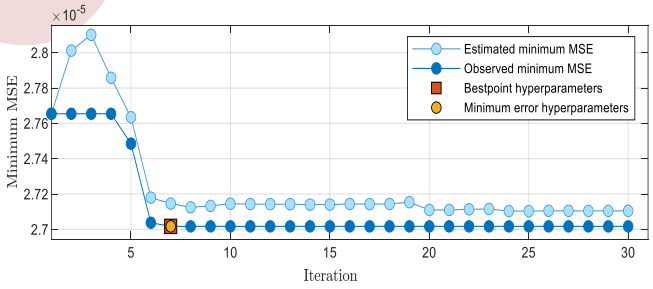
TABLE II. PERFORMANCES FLUX ESTIMATOR

Flux	ANN	SVM	EL	DT	GPR
RMSE(valid)	0.015035	0.017103	0.016529	0.021983	**0.0052222**
(test)	0.012887	0.016238	0.014499	0.020285	**0.0050421**
R^2 (valid)	0.99	0.99	0.99	0.98	**1.00**
(test)	0.99	0.99	0.99	0.98	**1.00**
MSE (valid)	0.00022604	0.00029252	0.0002732	0.0004832	**2.7271e-5**
(test)	0.00016609	0.00026366	0.0002102	0.0004114	**2.5423e-5**
MAE (valid)	0.010463	0.012947	0.0094641	0.010803	**0.0035783**
(test)	0.0093419	0.012361	0.0083299	0.010395	**0.0033773**
Prediction speed (~obs/sec)	95000	**110000**	42000	47000	5700
Training time (sec)	338.4	2385.5	63.999	**36.918**	1022.6

Fig. 3 depicts the performance optimization of the (a) speed and (b) flux estimation. At iteration number 23, the speed estimator achieved the optimal point hyperparameter. The flux estimator, on the other hand, reached the optimum point hyperparameter after seven iterations. Table 3 displays the optimum hyperparameters determined for the GPR method.



(a) speed estimator



(b) Flux estimator

Figure 3. The MSE of the GPR hyperparameters.

TABLE III. OPTIMIZED GPR HYPERPARAMETERS

	Speed	**Flux**
Sigma	493.9326	0.043146
Basis function	Constant	Linear
Kernel function	Nonisotropic Rational Quadratic	Nonisotropic Matern 5/2
Standardize	False	False

Fig. 4 depicts the speed and flux estimators' training outcomes. The estimated values are adequately adjusted on the diagonal, which represents the line of ideal predictions. As a

consequence, the model is not overfitted (validation result) and is well generalized (test result).

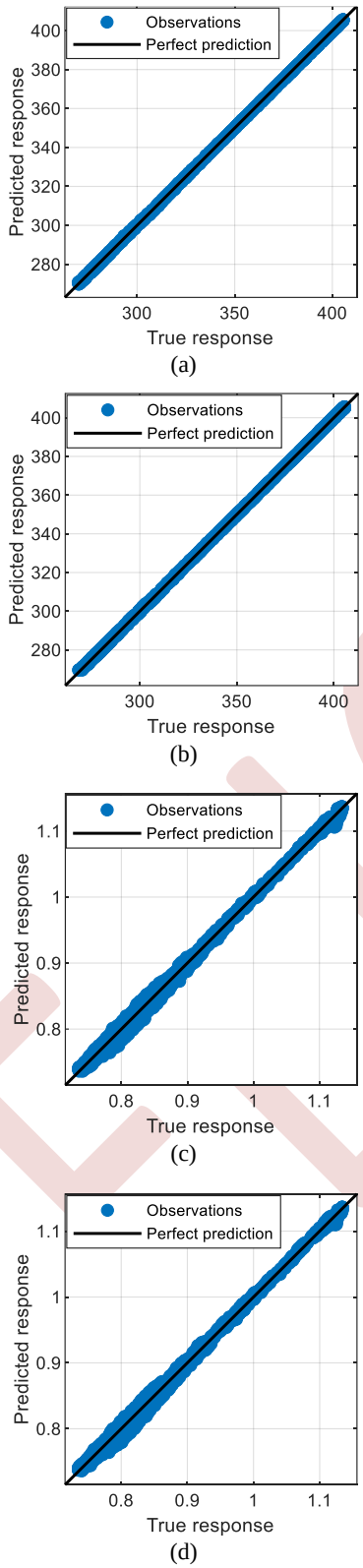


Figure 4. Validation and testing of the GPR with the optimal hyperparameters for the speed estimation (a), (b), and the flux estimation (c), (d).

V. CONCLUSION

Using supervised machine learning methods, this article presents an estimator of the speed and flux of an ASIM. To maximize the capabilities of ML, we employed two enhancements: a) the gray box concept, which we used to give more simple and effective estimator inputs using our understanding of the ASIG model; and B) hyperparameter optimization utilizing the Bayesian optimization technique. A comparison of the top ML algorithms for flux and speed estimates is performed in MATLAB/Simulink under the same conditions. According to the results of the comparison, Gaussian process regression presents the best approach, with an MSE of 0.07514 for speed estimation and 2.5423e-5 for flux estimation.

In future work, we can estimate other ASIM parameters like voltage and current using machine learning algorithms.

ACKNOWLEDGEMENT

We are grateful to Algeria's DGRSDT for supplying our laboratory with the required subventions.

REFERENCES

[1] Y. Hamoudi, H. Amimeur, D. Aouzellag, M. G. M. Abdolrasol, and T. S. Ustun, "Hyperparameter Bayesian Optimization of Gaussian Process Regression Applied in Speed-Sensorless Predictive Torque Control of an Autonomous Wind Energy Conversion System," *Energies 2023, Vol. 16, Page 4738*, vol. 16, no. 12, p. 4738, Jun. 2023, doi: 10.3390/EN16124738.

[2] A. L. Oliveira, "Biotechnology, Big Data and Artificial Intelligence," *Biotechnol. J.*, vol. 14, no. 8, p. 1800613, Aug. 2019, doi: 10.1002/biot.201800613.

[3] A. I. Ridhatullah, A. Joret, I. D. P. Karyatanti, and A. Ponniran, "Three-Phase Induction Motor Speed Estimation Using Recurrent Neural Network Structure," *J. Electron. Volt. Appl.*, vol. 2, no. 2, pp. 23–35, 2021, doi: 10.30880/jeva.2021.02.02.003.

[4] E. Pintelas, I. E. Livieris, and P. Pintelas, "A Grey-Box Ensemble Model Exploiting Black-Box Accuracy and White-Box Intrinsic Interpretability," *Algorithms*, vol. 13, no. 1, p. 17, Jan. 2020, doi: 10.3390/a13010017.

[5] X. Sun, L. Chen, Z. Yang, and H. Zhu, "Speed-Sensorless Vector Control of a Bearingless Induction Motor With Artificial Neural Network Inverse Speed Observer," *IEEE/ASME Trans. Mechatronics*, vol. 18, no. 4, pp. 1357–1366, Aug. 2013, doi: 10.1109/TMECH.2012.2202123.

[6] Seong-Hwan Kim, Tae-Sik Park, Ji-Yoon Yoo, and Gwi-Tae Park, "Speed-sensorless vector control of an induction motor using neural network speed estimation," *IEEE Trans. Ind. Electron.*, vol. 48, no. 3, pp. 609–614, Jun. 2001, doi: 10.1109/41.925588.

[7] M. Benakcha, L. Benalia, D. E. Tourqui, and A. Benakcha, "Backstepping control of dual stator induction generator used in wind energy conversion system," *Int. J. Renew. Energy Res.*, vol. 8, no. 1, pp. 384–395, 2018, doi: 10.20508/ijrer.v8i1.7025.g7313.

[8] M. Benakcha, L. Benalia, F. Ameur, and D. E. Tourqui, "Control of dual stator induction generator integrated in wind energy conversion system," *J. Energy Syst.*, vol. 1, no. 1, pp. 21–31, 2017, doi: 10.30521/jes.351269.

[9] H. Amimeur, R. Abdessemed, D. Aouzellag, E. Merabet, and F. Hamoudi, "Modeling and Analysis of Dual-Stator Windings Self-Excited Induction Generator," *J. Electr. Eng.*, pp. 1–6.

[10] Y. Bendjeddou, R. Abdessemed, and E. Merabet, "Improved field oriented control for stand alone dual star induction generator used in

wind energy conversion," *Eng. Rev.*, vol. 40, no. 2, pp. 34–46, 2020, doi: 10.30765/er.40.2.05.

[11] J. Kocijan, K. Ažman, and A. Grancharova, "The concept for Gaussian process model based system identification toolbox," in *Proceedings of the 2007 international conference on Computer systems and technologies - CompSysTech '07*, New York, New York, USA: ACM Press, 2007, p. 1. doi: 10.1145/1330598.1330647.

[12] C. E. Rasmussen, "Gaussian Processes in machine learning," *Lect. Notes Comput. Sci. (including Subser. Lect. Notes Artif. Intell. Lect. Notes Bioinformatics)*, vol. 3176, pp. 63–71, 2004, doi: 10.1007/978-3-540-28650-9_4.

[13] B. Ufnalski and L. M. Grzesiak, "Selected methods in angular rotor speed estimation for induction motor drives," *EUROCON 2007 - Int. Conf. Comput. as a Tool*, pp. 1764–1771, 2007, doi: 10.1109/EURCON.2007.4400678.

EEIC'23

Enhancing Wind Turbine Efficiency: A Comparative Study of Two Innovative MPPT Control Algorithms

Zina Larabi[1,2], Kaci Ghedamsi[3], Djamal Aouzelag[3], Fares Nafa[4]

[1] *Departement of Electrical Engineering, University of Tizi-Ouzou, Algeria*

[2]*Departement of Electrical Systems Engineering, University of Boumerdes, Algeria*

z.larabi@univ-boumerdes.dz

[3]*Laboratoire de Maitrise des Energies Renouvelables, University of Bejaia, Algeria*

kaci.ghedamsi@univ-bejaia.dz djamal.aouzellag@univ-bejaia.dz

[4]*Laboratoire d'Ingénierie des Systèmes et des Telecommunications, University of Boumerdes, Algeria*

f.nafa@univ-boumerdes.dz

***Abstract*— This paper presents two novel maximum power point tracking (MPPT) control strategies utilizing the gradient optimization algorithm to maximize the wind turbine's output power while minimizing the chattering effect resulting from intermittent control switching. In the first method, the gradient algorithm is integrated with sliding mode control (GSMC), and in the second technique, it is combined with adaptive fuzzy sliding mode control (GAFSMC). To assess the robustness and tracking capabilities of these techniques, numerical simulations were conducted under varying wind speed profiles. The results obtained demonstrate superior performance of the two newly developed methods when compared to classical SMC and fuzzy logic approaches.**

***Keywords:* Gradient Algorithm, MPPT, Sliding Mode Control.**

I. INTRODUCTION

Given environmental issues and the shortage of fossil energy sources in the near future, the use of "green" energy is becoming increasingly important for a much more sustainable world [1], [2]. Among these resources, Wind power is one of the world's most interesting, it is inexhaustible, unlimited, and abundantly available everywhere [3]. However, wind power is principally dependent on the geographical and seasonal climate conditions. Therefore, it is necessary to design a system capable of generating maximum power under these conditions [4], [5]. This is known as maximum power point tracking (MPPT).

Extensive research has been conducted into various approaches for tracking wind energy systems' maximum power point [6], [7]. To date, numerous MPPT control techniques have been investigated, such as conventional Tip speed ratio (TSR) and optimal torque control (OTC) [8], [9], intelligent fuzzy logic (FL) [10], [11], nonlinear sliding mode control (SMC) [12], [13], and other hybrid techniques like FLSMC and adaptive fuzzy sliding mode control (AFSMC) [14 – 16]. These techniques are distinguished by their simplicity, speed, price, and convergence efficiency [15].

As a non-linear control technique, sliding mode control is widely appreciated for its outstanding properties, such as high accuracy, fast dynamic response, stability, and ease of conception and implementation [17]. Nevertheless, a significant shortcoming of the SMC is the chattering effect created by the intermittent switching of the control [16], [17]. To remedy this problem, various solutions have been proposed in the literature [15-19], either by modifying the classical SMC or associating it with other control methods.

In this paper, the gradient optimization algorithm is suggested as a solution to minimize the chattering effect and enhance the robustness of the MPPT control methods of the wind turbine, specifically SMC and AFSMC. For this purpose, the remainder of the paper is structured as follows: Section 2 is reserved for describing and modeling the wind turbine considered in this study. Section 3 introduces two innovative methods, GSMC and GAFSMC, developed to track the maximum power point of wind power. Simulation results and discussion are presented in section 4. Finally, the main findings of this work are presented in section 5.

II. MODELING OF THE WIND TURBINE

The wind turbine is designed to convert a part of the wind's kinetic energy into mechanical power and then, via a generator, into electrical power [20].

The output power of the wind turbine can be calculated using the following formula [21]:

$$P_t = \frac{1}{2}\pi\rho C_P R^2 V_w^3 \quad (1)$$

Where: V_w : The wind speed; ρ: The air density; R: The turbine radius.

The power coefficient C_P is a non-linear function of the blade pitch angle β and the tip speed ratio (TSR) λ. The considered model in this paper is described by [22]:

$$C_p = 0.5\left(\frac{116}{\lambda'} - 0.43\beta - 5\right)e^{-\frac{21}{\lambda'}} \quad (2)$$

With: $$\lambda' = \frac{1}{\lambda + 0.008\beta} - \frac{0.035}{1+\beta^3} \quad (3)$$

and: $$\lambda = \frac{\Omega_t R}{V_w} \quad (4)$$

Where: Ω_t: The angular speed of the wind turbine.

In this study, we consider a low-speed generator driven directly by the mechanical torque developed on the rotor shaft of the turbine as presented in Fig. 1. This torque is described by [20]:

$$T_m = \frac{P_t}{\Omega_t} \quad (5)$$

The dynamics of the angular velocity of the turbine is given by (6).

$$\dot{\Omega}_t = \frac{1}{J_t}\left(T_m - T_g - f_v\,\Omega_t\right) \quad (6)$$

Where: J_t: The total moment of inertia; T_g: The generator torque; f_v: The viscous friction coefficient.

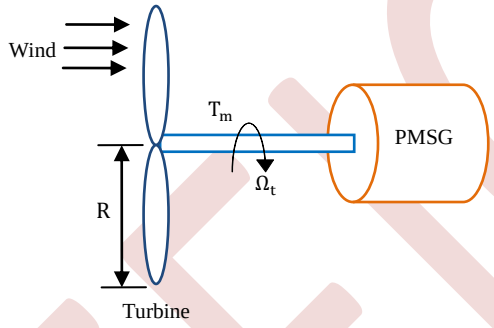


Figure 1. Diagram of a studied part of the wind turbine conversion system

III. Design of the Proposed Methods

In wind turbines, the MPPT control algorithm is utilized to achieve the maximum output power value during fluctuations in wind speed. This section introduces two novel MPPT control strategies based on the gradient algorithm, which aim to improve the wind turbine's efficiency.

A. Gradient Sliding Mode Control

The gradient sliding mode control principle is based on optimizing the turbine's power coefficient by the gradient ascent algorithm to get the optimum speed corresponding to the maximum power extracted from the wind. However, sliding mode control adjusts the turbine's angular speed to its optimum reference, allowing it to adapt to wind fluctuations while maintaining its optimum operation.

To maximize the energy extracted from wind power, it's important to maximize the power coefficient C_P with respect to λ and β. To achieve this goal, the gradient ascent algorithm is used. In the remainder of this work, we consider β=0°.

By minimizing the criterion: $J = \frac{1}{2}c_p^2$ the dynamics of λ_{opt} can be given by:

$$\dot{\lambda}_{opt} = \eta.\nabla_\lambda c_p.c_p = \eta\frac{\partial c_p}{\partial \lambda}c_p \quad (7)$$

Where: $\eta > 0$

A discrete expression of (7) can be given by:

$$\lambda_{t+1} = \lambda_t + \eta\frac{\partial c_p}{\partial \lambda}c_p\,\Delta t \quad (8)$$

Thus, the optimal speed of the wind turbine can be deduced by:

$$\Omega_{opt} = \lambda_{opt}\frac{V_w}{R} \quad (9)$$

The SMC control is defined as the sum of the equivalent control T_{geq} and the switching control T_{gs} .

$$T_g^* = T_{geq} + T_{gs} \quad (10)$$

And the sliding surface (S) is chosen to be equal to the turbine speed error $\tilde{\Omega}$ defined by:

$$S = \tilde{\Omega} = \Omega_t - \Omega_{opt} \quad (11)$$

Recalling (6) and (9), the dynamics of S is given by :

$$\dot{S} = \dot{\tilde{\Omega}} = \dot{\Omega}_t - \dot{\Omega}_{opt} \quad (12)$$

Or:

$$\dot{S} = \frac{1}{J_t}\left(T_m - T_g - f_v\,\Omega_t\right) - \dot{\Omega}_{opt} \quad (13)$$

With:

$$\dot{\Omega}_{opt} = \dot{\lambda}_{opt}\frac{V_w}{R} + \lambda_{opt}\frac{\dot{V}_w}{R} \quad (14)$$

By definition, the equivalent control is deduced for $\dot{S} = 0$, and accordingly, (13) gives:

$$T_{geq} = -J_t\dot{\Omega}_{opt} + T_e - f_v\,\Omega_t \quad (15)$$

Let define now the following Lyapunov function candidate V as:

$$V = \frac{1}{2}S^2 \quad (16)$$

The times derivative of (16) yields to:

$$\dot{V} = \dot{S}S \quad (17)$$

Using (10), (13), (14) and (15) and choosing the switching control T_{gs} as:

$$T_{gs} = (-k_1 \text{sign}(S) + Q_1 S)\, J_t \tag{18}$$

where $k_1 > 0$ and $Q_1 > 0$, the dynamics (13) becomes such as:

$$\dot{S} = -k_1 \text{sign}(S) - Q_1 S \tag{19}$$

Clearly, by replacing (19) in (17), one has:

$$\dot{V} = -k_1 |S| - Q_1 S^2 < 0, \quad \forall S \neq 0 \tag{20}$$

According to Lyapunov theory, the system is globally asymptotically stable and converges to 0 in a finite time. That is $\Omega \to \Omega_{opt}$ as $t \to \infty$.

Consider the angular dynamics (6) and its optimal value (9). The control law given by (10), (15) and (18) ensures all signals in the closed-loop system will be bounded and the sliding surface (11) converges to zero asymptotically.

B. Gradient Adaptative Fuzzy Logic Sliding Mode Control

In this case, the control of the wind turbine speed is ensured by the AFSMC and the optimal referential speed is obtained by the gradient ascent algorithm.

We suppose that the control input meet the condition of the universal approximation, and it can be approximated via the following fuzzy system so that:

$$T_g = \xi_z^T \theta \tag{21}$$

We suppose that there exists a fuzzy system in the form of (21) with some optimal parameters θ^* such that:

$$\sup_{T_g \epsilon \Omega_z} \left| T_g - \xi_z^T \theta^* \right| \leq \epsilon; \quad \epsilon > 0 \tag{22}$$

Then T_g^* can be expressed as:

$$T_g^* = \xi_z^T \theta^* + \varepsilon(z) \tag{23}$$

Where: ξ_z^T: is a set of fuzzy basis functions; $\varepsilon(z)$: is the fuzzy approximation error.

Let's define the error between the T_g^* and T_g as:

$$e_T = T_g - T_g^* \tag{24}$$

Using (21) and (23), (24) gives:

$$e_T = \xi_z^T \tilde{\theta} - \varepsilon(z) \text{ , with } \tilde{\theta} = \theta - \theta^* \tag{25}$$

Recalling that: $T_g = T_g - T_g^* + T_g^*$ and combining it with (6), (12) and (14), gives:

$$\dot{\tilde{\Omega}} = \frac{1}{J_t} \left(T_e - T_g^* - e_T - f_v \Omega \right) - \dot{\lambda}_{opt} \frac{V_w}{R} + \lambda_{opt} \frac{\dot{V}_w}{R} \tag{26}$$

Using (15) and (18), we get:

$$\dot{\tilde{\Omega}} = -k_1 \text{sign}(\tilde{\Omega}) - Q_1 \tilde{\Omega} - \frac{e_T}{J_t} \tag{27}$$

Consider now a quadratique cost function that measures the difference between the controller (10) and the fuzzy controller defined by:

$$J(\theta) = \frac{1}{2J_t} e_T^2 = \frac{1}{2J_t} \left(T_g^* - \xi_z^T \theta \right)^2 \tag{28}$$

Using gradient descent method to minimize (28) with respect to θ yields to:

$$\dot{\theta} = -\eta_\theta . \nabla_\theta J(\theta), \text{ with } \eta_\theta > 0 \tag{29}$$

From formulae (27) and (29), we find:

$$\dot{\theta} = -\eta_\theta \xi_z^T \left[\dot{\tilde{\Omega}} + k_1 \text{sign}(\tilde{\Omega}) + Q_1 \tilde{\Omega} \right] \tag{30}$$

A discrete expression of (30) can be given by:

$$\theta_{t+1} = \theta_t - \Delta t\, \eta_\theta \xi_z^T \left[\dot{\tilde{\Omega}} + k_1 \text{sign}(\tilde{\Omega}) + Q_1 \tilde{\Omega} \right] \tag{31}$$

IV. RESULTS AND DESCUSSION

The simulation of the modeling turbine with the suggested MPPT control methods is performed using a Matlab script. The developed methods are analyzed under two different wind speed profiles to evaluate their robustness and tracking capabilities. The results are then compared with the SMC and Fuzzy logic methods. The simulation parameters of the considered turbine are [23-25]: $R = 23.5$ m, $J_t = 222\,963$ kg.m^2, $f_v = 743.21$ N.m.s/rad.

A. Robustness Test

The robustness of the two developed methods is investigated under the rapid changing of the wind speed as illustrated in Fig. 2. The characteristics of the power coefficient (Cp), the output power and the angular velocity are presented in Fig. 3, Fig. 4 and Fig. 5, respectively. These figures demonstrate that the wind turbine operates at the optimal speed for each wind speed variation and achieves the maximum power point efficiently. The comparative study with the traditional SMC and fuzzy logic methods shows that the two proposed methods perform better. Indeed, we note the absence of the chattering effect in the GSMC method and the non-sensitivity of the GAFSMC method to sudden variations in wind speed.

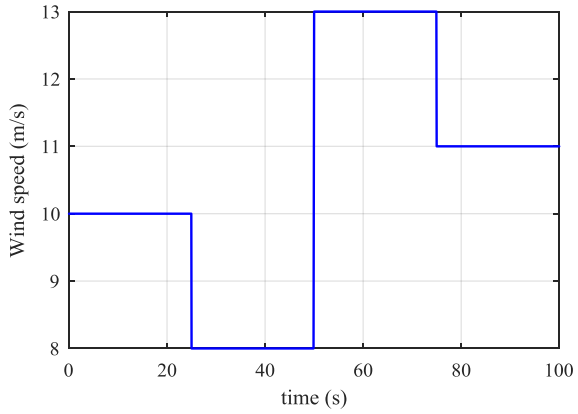


Figure 2. Wind speed profile

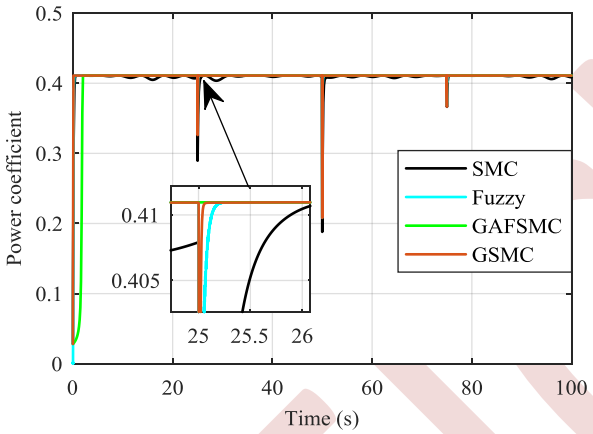


Figure 3. *Power coefficient caracteristic's*

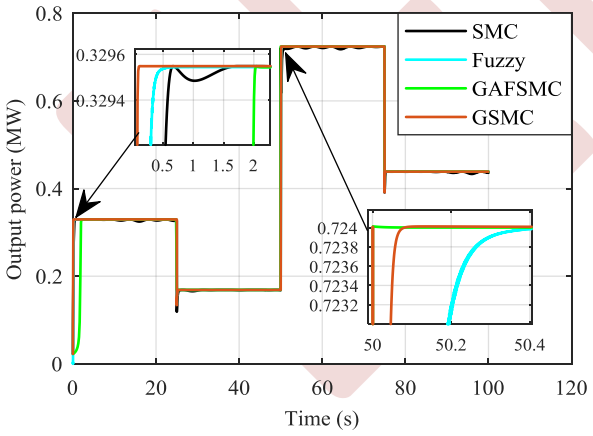


Figure 4. *Output power of the wind turbine*

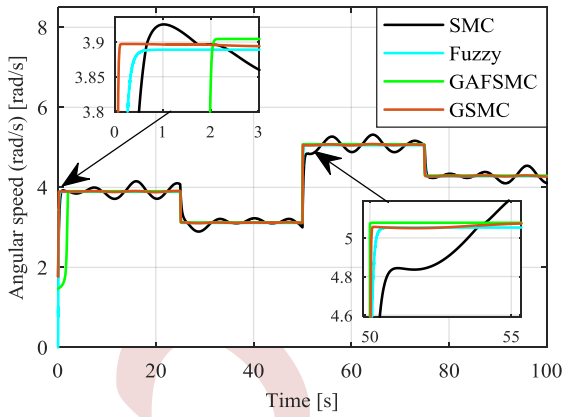


Figure 5. *Angular speed of the wind tuebine*

B. *Tracking Test*

The tracking test of the two proposed strategies is analyzed under the intermittent wind speed profile which is illustrated in Fig. 6. The different characteristics of the wind turbine are presented in Fig. 7 to Fig. 10. These results show good tracking capabilities of the proposed methods and well-ensured MPPT control. Also, it reveals an excellent dynamic response of the GSMC compared to the other methods.

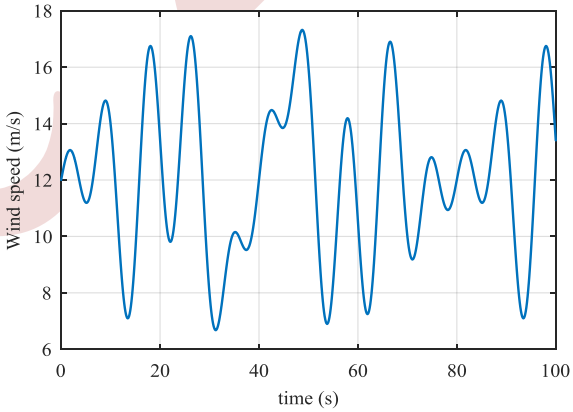


Figure 6. *Intermittent wind profile*

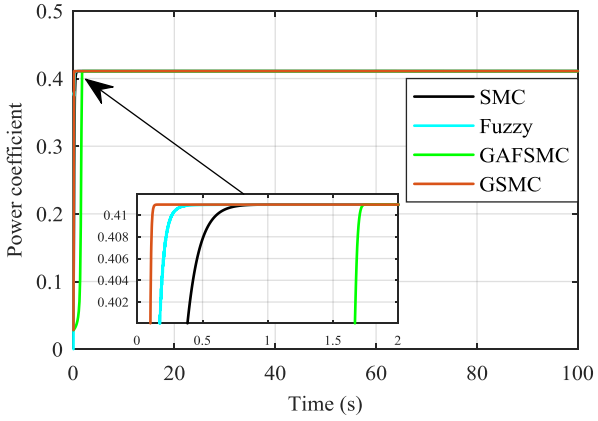


Figure 7. *Power coeffcient caracteristic's*

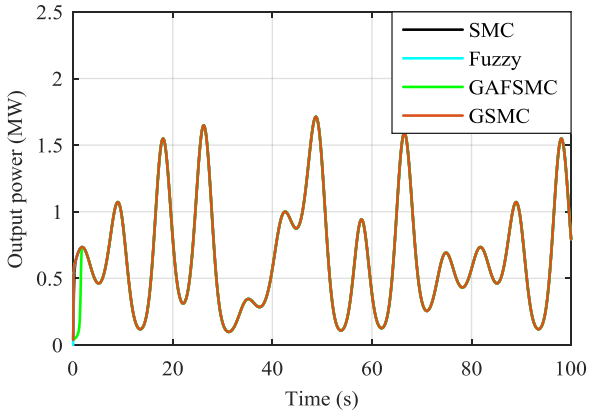


Figure 8. *Output power of the turbine*

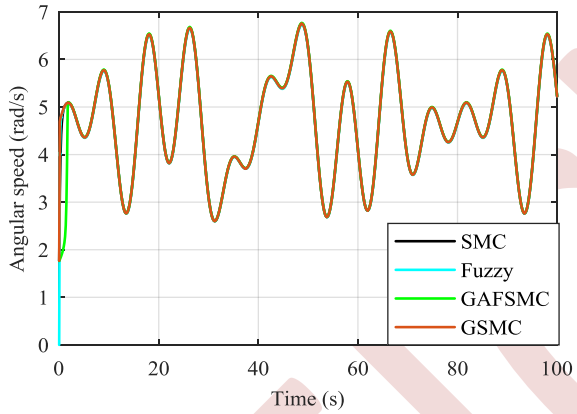


Figure 9. *Angulare speed of the wind turbine*

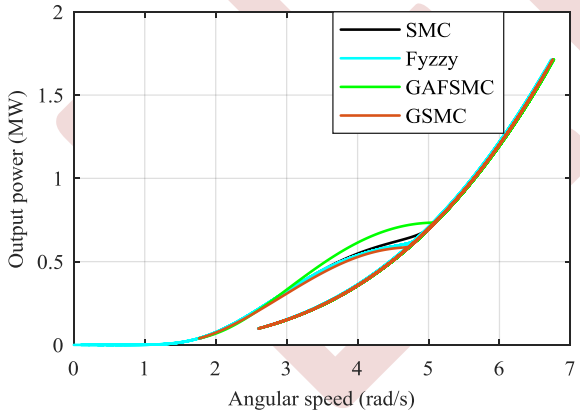


Figure 10. *Output power versus angular speed*

V. CONCLUSION

Two innovative methods, GSMC and GASMC, have been developed to maximize power extraction from wind sources. Their performance is thoroughly analyzed and compared against two traditional methods, SMC and Fuzzy Logic. The incorporation of the gradient ascent algorithm enhances the performance of these newly proposed methods by minimizing the chattering effect associated with SMC and improving its dynamic response. Additionally, it enhances their reliability and tracking capabilities, ensuring effective MPPT control. This study establishes the consistency and effectiveness of these methods beyond doubt.

REFERENCES

[1] J.G., Ndirangu, N.Nderuj, C.M. Maina, A. M. Muhia, "power output maximization of a pmsg based standalone wind energy conversion system using fuzzy logic", IOSR Journal of Electrical and Electronics Engineering (IOSR-JEEE) e-issn: 2278-1676, p-issn: 2320-3331, vol. 11, issue 1 ver. ii (Jan. – Feb. 2016), pp 58-66. http://www.iosrjournals.org/iosr-jeee/Papers/V0l11%20Issue%201/Version-2/I011125866.pdf

[2] T., George, P., Jayapraksh, T., Francis, C. Ezhil, "Wind energy conversion system-based PMSG for maximum power tracking and grid synchronization using adaptive fuzzy logic control", J. Appl. Res. Technol [online]. 2022, vol.20, n.6, pp.703-717. epub 08-mayo-2023. issn 2448-6736. https://doi.org/10.22201/icat.24486736e.2022.20.6.12566

[3] R., Tiwari,N.R., Babu, "Fuzzy logic based MPPT for permanent magnet synchronous generator in wind energy conversion system", IFAC-Papers Online, vol.49, pp.462-467. https://doi.org/10.1016/j.ifacol.2016.03.097

[4] H.Q., Minh, N., Frédéric, E., Najib, H., abdelaziz, "Fuzzy control of variable speed wind turbine using permanent magnet synchronous machine for stand-alone system", In: N.,M'sirdi, A., Namaane, R., J., Howlett, L., C., Jain, Eds. Sustainability in energy and buildings. smart innovation, systems and technologies, vol 12. springer, berlin, heidelberg. 2012. https://doi.org/10.1007/978-3-642-27509-8_3

[5] F., Tahiri, K.,Chikh M., khafallah, "MPPT strategy using fuzzy-pi controller applied to a standalone wind energy conversion system", paper presented at the SCA 2018: proceedings of the 3rd international conference on smart city applications, Tetouan. https://doi.org/10.1145/3286606.3286847

[6] Y., Zhu, M.; Cheng, W.; Hua, W.; Wang, "A novel maximum power point tracking control for permanent magnet direct drive wind energy conversion systems", Energies 2012, vol. *5*, pp. 1398-1412. https://doi.org/10.3390/en5051398

[7] A. Kadri, H. Marzougui and F. Bacha, "MPPT control methods in wind energy conversion system using DFIG", 4th International Conference on Control Engineering & Information Technology (CEIT), Hammamet, Tunisia, 2016, pp. 1-6. https://doi.org/10.1109/CEIT.2016.7929115

[8] M., Hannachi O, Elbeji M., Benhamed L., Sbita, "Comparative study of four MPPT for a wind power system", Wind engineering. 2021, 45(6), pp. 1613-1622. https://doi.org/10.1177/0309524X21995946

[9] X., Zhang, J., Jia, L., Zheng, W., Yi, Z., Zhang, "Maximum power point tracking algorithms for wind power generation system: Review, comparison and analysis". Energy Science & Engineering, 2022, 11(1), pp. 430-444. https://doi.org/10.1002/ese3.1313

[10] H., Gaied M., Naoui H., Kraiem B.S., Goud, A., Flah, M.L.,Alghaythi, H., Kotb, S.G., Ali, K., Aboras, "Comparative analysis of MPPT techniques for enhancing a wind energy conversion system", Front. Energy Res. 2022, 10:975134. https://doi.org/10.3389/fenrg.2022.975134

[11] O., Zebraoui, M., Bouzi, "Improved MPPT controls for a standalone PV/wind/battery hybrid energy system", International Journal of Power Electronics and Drive Systems, 2020, vol. 11, pp. 988-1001. http://doi.org/10.11591/ijpeds.v11.i2.pp988-1001

[12] S., Kahla, Y., Soufi, M., Sedraoui, M., Bechouat, "Maximum power point tracking of wind energy conversion system using multi-objective grey wolf optimization of fuzzy-sliding mode controller", International Journal of Renewable Energy Research-IJRER, 7(2), 2017, pp. 926-936. https://doi.org/10.20508/ijrer.v7i2.6125.q7073

[13] N.K., Agarwal, P.K., Sadhu, S., Chakraborty, "MPPT based PMSG wind turbine system using sliding model control (smc) and artificial Neural Network (ANN) Based Regression Analysis", IETE Journal of research, 68(3), 2022, pp. 1652-1660, https://doi.org/10.1080/03772063.2019.1662336

[14] M. B., Toriki, M. K., Asy'ari, A., Musyafa, "Enhanced performance of PMSG in WECS using MPPT – Fuzzy sliding mode control", Journal Europeen des Systemes Automatisés, 2021, *54*(1), 85-96. https://doi.org/10.18280/jesa.540110

[15] P.A., Malobe, P., Djondiné, P.N., Eloundou, H.A., Ndongo, "A Novel hybrid mppt for wind energy conversion systems operating under low variations in wind speed". Energy and Power Engineering, 12(12), *2020*, pp.716-728. https://doi.org/10.4236/eps.2020.1212042

[16] D., Cherifi, Y., Miloud, "Hybrid control using adaptive fuzzy sliding mode control of doubly fed induction generator for wind energy conversion system", Periodica Polytechnica Electrical Engineering and Computer Science, 64(4), 2020, pp. 374–381. https://doi.org/10.3311/ppee.15508

[17] Y., Mousavi, G., Bevan, I.B., Kucukdemiral, A. Fekih, "Sliding mode control of wind energy conversion systems: Trends and applications", Renewable and Sustainable Energy Reviews, vol. 167, 112734, 2022. https://doi.org/10.1016/j.rser.2022.112734

[18] M., Benkahla, R., Taleb, Z., Boudjema, "A new robust control using adaptive fuzzy sliding mode control for a DFIG supplied by a 19-level inverter with less number of switches", Electrical Engineering & electromechanics, 2018, (4), pp. 11–19. https://doi.org/10.20998/2074-272x.2018.4.02

[19] O., Bellounis, H., Labar, "Fuzzy sliding control of DFIG for wind energy conversion", International Journal of Intelligent enginneering and systems, 10(2), 2017. https://doi.org/10.22266/ijies2017.0430.18

[20] M., Atallah, A., Mezouar, K., Belgacem, Y., Saidi, M. A., Benmahdjoub, "Modeling and control strategy for a wind turbine by an AG-SMC without wind speed sensor", J. Ren. Energies, 1(1), 2022, pp. 9-19. https://doi.org/10.54966/jreen.vlil.1034

[21] M., Hannachi, O., Elbeji, M., Benhamed, L., Sbita, "Comparative study of four MPPT for a wind power system", Wind Engineering, 45(6), 2021, pp. 1613-1622. https://doi.org/10.1177/0309524X21995946

[22] A.E., Yaakoubi, L., Amhaimar, K., Attari, M.H., Harrak, M.E., Halaoui, A., Asselman, "Non-linear and intelligent maximum power point tracking strategies for small size wind turbines: Performance analysis and comparison", Energy Reports, vol. 5, 2019, pp. 545-554. https://doi.org/10.1016/j.egyr.2019.03.001

[23] N., Laverdure, "On the integration of wind turbine generators into weak or insular grids" (Sur l'intégration des générateurs éoliens dans les réseaux faibles ou insulaires), Phd Thesis, Polytecnic National Institute of Grenoble, France, 2005. (in French). [online] Available at : https://theses.hal.science/tel-00170128 [Accessed: 02 September 2023]

[24] H., Bekka, S., Taraft, D., Rekioua, S., Bacha, "Power control of a wind generator connected to the grid in front of srrong winds", Journal of Electrical Systems, 09(03), 2013, pp. 267-278.

[25] A., Teninge, C., Jecu, D., Roye, S., Bacha, J., Duval, R., Belhomme, "Contribution to frequency control through wind turbine inertial energy storage", IET renewable power generation, 11(1), 2008, pp. 358-370. http://doi.org/10.1049/iet-rpg.2008.0078

EEIC'23

Application of a fractional-order synergetic controller for active power filter to enhance power quality

Brahim Deffaf [1], Karim Fathi Sayeh [2], Farid Hamoudi [1] , Salah Tamalouzt [2]

[1] *Laboratoire de Maitrise des Energies Renouvelables (LMER), Bejaia, Algeria*

brahim.deffaf@univ-bejaia.dz ; farid.hamoudi@univ-bejaia.dz

[2] *Laboratoire de Technologie Industrielle et de l'Information (LTII), Bejaia, Algeria*

karimfathi.sayeh@univ-bejaia.dz; salah.tamalouzt@univ-bejaia.dz

***Abstract*— This paper introduces a fractional-order synergetic controller (FOSC) applied to a shunt active power filter (SAPF). The SAPF is specifically designed to address issues related to reactive power compensation and the elimination of current harmonics caused by non-linear loads and unbalanced source voltages. The proposed FOSC serves as a robust control method capable of ensuring rapid convergence and stable closed-loop system performance, both in transient and steady-state conditions. Extensive simulation tests were carried out to validate the efficacy of this control approach, considering unbalanced source voltages as well. The results unequivocally demonstrate that the FOSC outperforms the conventional proportional-integral (PI) control method.**

***Keywords:* Shunt active power filter, fractional-order, synergetic control, Power Quality.**

I. INTRODUCTION

Harmonics refer to electrical waveform alterations characterized by frequencies that are multiples of the primary power system frequency [1]. These distortions can originate from nonlinear loads and have diverse detrimental impacts on the power system, including reduced effectiveness, heightened energy losses, diminished power factor, and potential equipment harm [2].

Numerous solutions have been proposed to mitigate the negative impact of harmonics on an electrical grid. One widely adopted method involves the use of harmonic filters, designed to lower harmonic levels within the system [3]. These filters can be placed at the Point of common coupling (PCC), where the harmonic-generating loads connect to the system, or directly at the source of harmonics. Passive harmonic filters, utilizing passive components, are commonly employed to reduce harmonics in electrical networks [4]. Nevertheless, they have limitations, such as reduced effectiveness in certain scenarios and the potential to create adverse environmental conditions that can damage equipment [5].

Active filters employ power electronics to inject current into the system, effectively mitigating harmonics. This approach brings advantages such as enhanced flexibility, improved power factor, greater efficiency, and reduced equipment damage risk. Nonetheless, active filters require a reliable power supply and, if not constructed and controlled correctly, may generate harmonics [6, 7].

When dealing with nonlinear systems that require high precision and dynamic characteristics, conventional control methods such as the proportional-integral (PI) controller may not always be the optimal choice for power electronics applications [8]. Instead, nonlinear and intelligent approaches like sliding mode control (SMC) [9], backstepping control (BC) [10], and high-order SMC techniques have demonstrated success in reducing current fluctuations and improving power quality. However, implementing these methods can be intricate and challenging.

As an alternative, fractional-order synergetic control (FOSC) has gained traction due to its added design flexibility and relative simplicity [11]. Synergetic control (SC) [12] has also garnered attention from researchers in various studies for its ability to effectively regulate nonlinear and uncertain systems, even in chaotic conditions.

This paper proposes utilizing Fractional-Order Synergetic Control (FOSC) as the preferred method for managing a three-phase three-level T-type inverter-based SAPF. When source voltages are uneven, this control strategy is favored due to its simplicity, resilience, and straightforward implementation. Its primary objective is to improve current quality and reduce overall system expenses. Additionally, the fractional synergetic control technique is employed to oversee DC voltage regulation and Compensation reactive power in grid.

The primary advancements include:

- Reducing the (THD) in the current.
- Enhancing the filtering system's dynamic responsiveness.
- Enhancing power quality in situations with unbalanced source voltage.

This article is organized as follows: In the following section (Section 2), we elaborate on the 3-level T-type inverter-based SAPF, including its control principle. Moving on to Section 3,

we provide a theoretical review of fractional-order synergetic control and its implementation in active filter control. The significant outcomes, including those for scenarios with unbalanced source voltages, are presented in Section 4 and compared to traditional PI control methods. Finally, in Section 5, we wrap up the paper by summarizing the key discoveries and outlining future research directions.

II. DESIGN AND CONTROL OF SAPF

A. Design of system

Broadly, the system investigated in this study comprises two components: power and control. These components are linked to a PCC. The first part involves a three-phase grid connected to a non-linear load, depicted as a three-phase diode rectifier. Meanwhile, the second part involves a 3-level T-type inverter with a specific control approach. As shown in the Fig. 1.

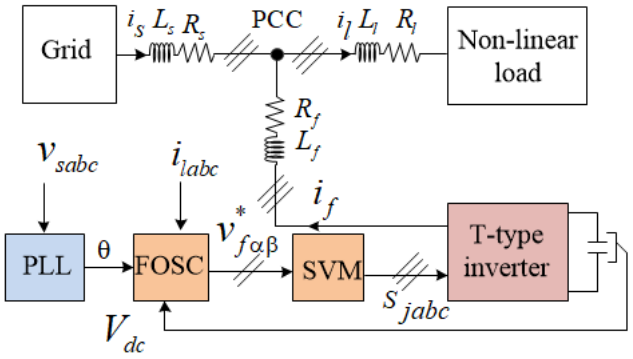


Figure 1. Schematic block of SAPF.

The dynamic model in αβ axes for the SAPF as follows:

$$\begin{cases} \frac{di_{f\alpha}}{dt} = -\frac{R_f}{L_f} i_{f\alpha} - \frac{1}{L_f} v_{s\alpha} + \frac{1}{L_f} v_{f\alpha} \\ \frac{di_{f\beta}}{dt} = -\frac{R_f}{L_f} i_{f\beta} - \frac{1}{L_f} v_{s\beta} + \frac{1}{L_f} v_{f\beta} \end{cases} \quad (1)$$

The formula representing the connection between current and voltage in the dc-link is as follows:

$$C_{dc} \frac{dV_{dc}}{dt} = i_{dc} \quad (2)$$

The active filter controller must generate reference currents to remove unwanted elements. This is achieved by estimating the reference source current and then subtracting the load current to determine the inverter reference current, to achieve this, we follow the method mentioned in [13] as follows:

$$\begin{aligned} I_{u1} &= \sin(\theta) \\ I_{u2} &= \sin\left(\theta + \tfrac{2\pi}{3}\right) \\ I_{u3} &= \sin\left(\theta - \tfrac{2\pi}{3}\right) \end{aligned} \quad (3)$$

By employing a PLL, the angle θ is derived from the primary voltage waveform to uphold a unity power factor, leading to a balanced current devoid of harmonics and reactive power [13]. The reference source currents are outlined as follows:

$$\begin{cases} i^*_{sa} = I^*_{max} \sin(\theta) \\ i^*_{sb} = I^*_{max} \sin\left(\theta + \frac{2\pi}{3}\right) \\ i^*_{sa} = I^*_{max} \sin\left(\theta - \frac{2\pi}{3}\right) \end{cases} \quad (4)$$

Hence, the active filter reference currents can be formulated as follows:

$$\begin{cases} i^*_{fa} = i^*_{la} - i^*_{sa} \\ i^*_{fb} = i^*_{lb} - i^*_{sb} \\ i^*_{fc} = i^*_{lc} - i^*_{sc} \end{cases} \quad (5)$$

B. T-type inverter

Research has indicated that the T-type inverter serves as an active power converter in shunt active filter systems. In comparison to the typical NPC inverter, the T-type inverter necessitates a lower number of clamping diodes per phase leg. This is achieved by connecting the DC-link voltage neutral point using two active bidirectional switches [14, 15]. Fig 3 depicts the power circuit diagram of a 3-level T-type converter, which consists of four IGBT active switches denoted as T1 to T4, arranged in the shape of a T. On the DC side, two capacitors, C1 and C2, are employed to split the DC input into two voltages and generate the neutral point. The combinations of switch states required to achieve each of the three potential states [P], [O], or [N] for each leg of a T-type inverter are outlined in Table 1.

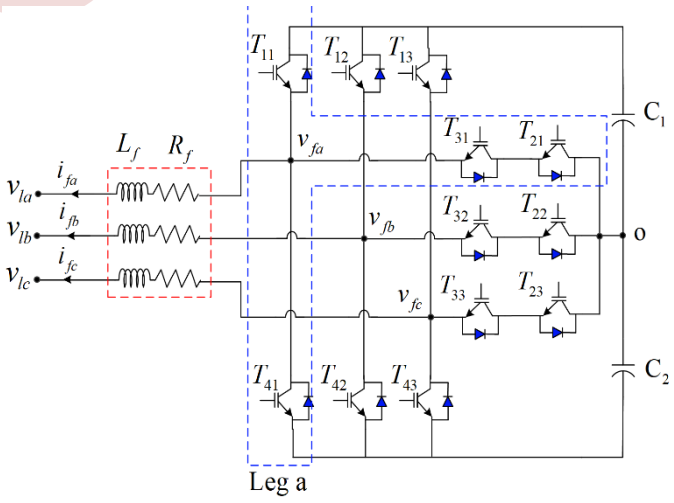


Figure 2. Diagram of a 3-level T-type inverter.

TABLE I. SWITCHING STATE FOR INVERTER.

States	Status of switching devices (x=1,2,3)				Voltage
	Tx1	*Tx2*	*Tx3*	*Tx4*	
P	1	1	0	0	Vdc/2
O	0	1	1	0	0
N	0	0	1	1	-Vdc/2

III. DESIGN OF CONTROL FOR SAPF

In this research, we integrated both the SC outlined in [11] and the FO [12] into the SAPF system. This combination aims to reduce harmonic disturbances and manage reactive power within the grid, ensuring a reliable closed-loop system and achieving efficient tracking control. To expand the controller's flexibility, we define the macro-variable using the equation provided below.

$$\psi_{\omega fr} = K_p(x^* - x) + K_i I_a^{\mu}(x^* - x) \tag{6}$$

K_p and K_i are coefficients associated with macro-variable, whereas x^* and x denote the real controlled and reference values, and μ indicates the fractional integral order.

The objective of the SC is to direct the system to an MV where to zero. by the following equation:

$$T\dot{\psi} + \psi = 0; \quad T > 0 \tag{7}$$

The examination of system stability can be carried out through the utilization of the Lyapunov function, which functions as follows according to reference [16]:

$$V = \frac{1}{2}\psi(x,t)^2 \tag{8}$$

A. Control of DC bus voltage

The primary objective of the voltage FOSC is to effectively control the DC-link voltage and adhere to a predefined reference profile. In particular, the DC-link controller aims to mirror the DC voltage reference, which is outlined as follows:

$$e_{vdc} = V_{dc}^* - V_{dc} \tag{9}$$

The MV is expressed as:

$$\psi_{dcfr} = K_{p_{vdc}} e_{vdc} + K_{ivdc} I^{\mu_{vdc}} e_{vdc} \tag{10}$$

By replacing equation (9) and (10) with equation (7), the dynamics can be represented as follows:

$$T\left(K_{p_{vdc}}(\dot{V}_{dc}^* - \dot{V}_{dc}) + K_{i_{vdc}} I^{\mu_{vdc}-1}(V_{dc}^* - V_{dc})\right) + K_{p_{vdc}} e_{vdc} + K_{i_{vdc}} I^{\mu_{vdc}} e_{vdc} = 0 \tag{11}$$

Upon inserting equation (2) into equation (11) and reorganizing the FOSC, we obtain the following result:

$$i_{dc} = \frac{C_{dc}}{TK_{p_{vdc}}}\left(TK_{p_{vdc}}\dot{V}_{dc}^* + TK_{i_{vdc}} I^{\mu_{vdc}-1} e_{vdc} + \psi_{vdc}\right) \tag{12}$$

B. Design of current control

The goal of the current controller is to produce the input for Space Vector Modulation (SVM) to control the inverter switching signals. The variance in currents can be depicted in the following manner:

$$\begin{cases} e_{if\alpha} = i_{f\alpha}^* - i_{f\alpha} \\ e_{if\beta} = i_{f\beta}^* - i_{f\beta} \end{cases} \tag{13}$$

Therefore, two micro variables are selected in the following manner:

$$\begin{cases} \psi_{i_{f\alpha}fr} = K_{p\alpha} e_{if\alpha} + K_{i\alpha} I^{\mu_\alpha} e_{if\alpha} \\ \psi_{i_{f\beta}fr} = K_{p\beta} e_{if\beta} + K_{i\beta} I^{\mu_\beta} e_{if\beta} \end{cases} \tag{14}$$

When the equations are replaced and simplified, it becomes possible to illustrate the control inputs to an SVM as follows:

$$\begin{cases} v_{f\alpha}^* = \frac{L_f\left(A + T_\alpha K_{i\alpha} I^{\mu_\alpha - 1} e_{if\alpha} + \psi_{if\alpha}\right)}{T_\alpha K_{p_\alpha}} \\ v_{f\beta}^* = \frac{L_f\left(B + T_\beta K_{i\beta} I^{\mu_\beta - 1} e_{if\beta} + \psi_{if\beta}\right)}{T_\beta K_{p_\beta}} \end{cases} \tag{15}$$

Were

$$A = T_\alpha K_{p_\alpha} \dot{i}_{f\alpha}^* + T_\alpha K_{p_\alpha}\left(\frac{R_f}{L_f} i_{f\alpha} + \frac{1}{L_f} v_{s\alpha}\right)$$

$$B = T_\beta K_{p_\beta} \dot{i}_{f\beta}^* + T_\beta K_{p_\beta}\left(\frac{R_f}{L_f} i_{f\beta} + \frac{1}{L_f} v_{s\beta}\right)$$

C. Space Vector Modulation

The SVM approach stands out as a promising modulation technique for running multi-level inverters. It extends the modulation range by 15%, enhances flexibility in gate signal control by the same margin, and reduces current harmonic distortion when compared to the traditional sinusoidal PWM method, as indicated in [17]. Within this research, the SVM method assumes a critical role in choosing switching states and sequences, as well as determining dwell periods. Although the primary emphasis is not on the algorithm itself, readers can refer to the provided overview for a basic grasp of this approach, with additional algorithm specifics available in [18].

IV. RESULTS AND DISCUSSION

This section discusses the results obtained from the utilization of a 3-level T-type inverter-based SAPF with a FOSC in MATLAB software. Fig. 1 illustrates the filter, and its essential characteristics are outlined in reference [11]. Simulation results are performed under two scenarios to assess the FOSC effectiveness: one with a balanced source voltage and the other with an unbalanced source voltage. In both cases, a load change is introduced at t=0.3 sec. The simulation results are then compared to those obtained using the conventional PI control method.

Fig. 3 showcases the findings of SAPF performance using FOSC and PI methodologies, displaying waveforms for source voltage, load current, source current, and voltage and current in Phase (a) across various voltage scenarios, encompassing both balanced and unbalanced conditions. Importantly, when the active filter is connected at the PCC, both control strategies yield sinusoidal source currents. Nonetheless, the differentiation between the two controls become evident when observing the variation in current ripples, with the PI control exhibiting more pronounced ripples. This highlights the effectiveness of the proposed control approach in mitigating ripples and minimizing current harmonics compared to the PI control. Furthermore, Fig. 4 reveals the response of the DC-bus voltage for both the proposed control and the traditional PI control. It becomes clear that the designed control quickly attains the desired voltage level without any overshoot right after connecting the active filter to the grid. Moreover, it demonstrates a rapid response following a load alteration. In contrast, the PI control exhibits a slow response, overshooting the reference value when filter connection and responding slowly to load fluctuations. These findings emphasize that the designed control betters the conventional PI control in terms of response time and stability. Comprehensive comparative results between the proposed FOSC and the PI control are presented in Tables 2 and 3.

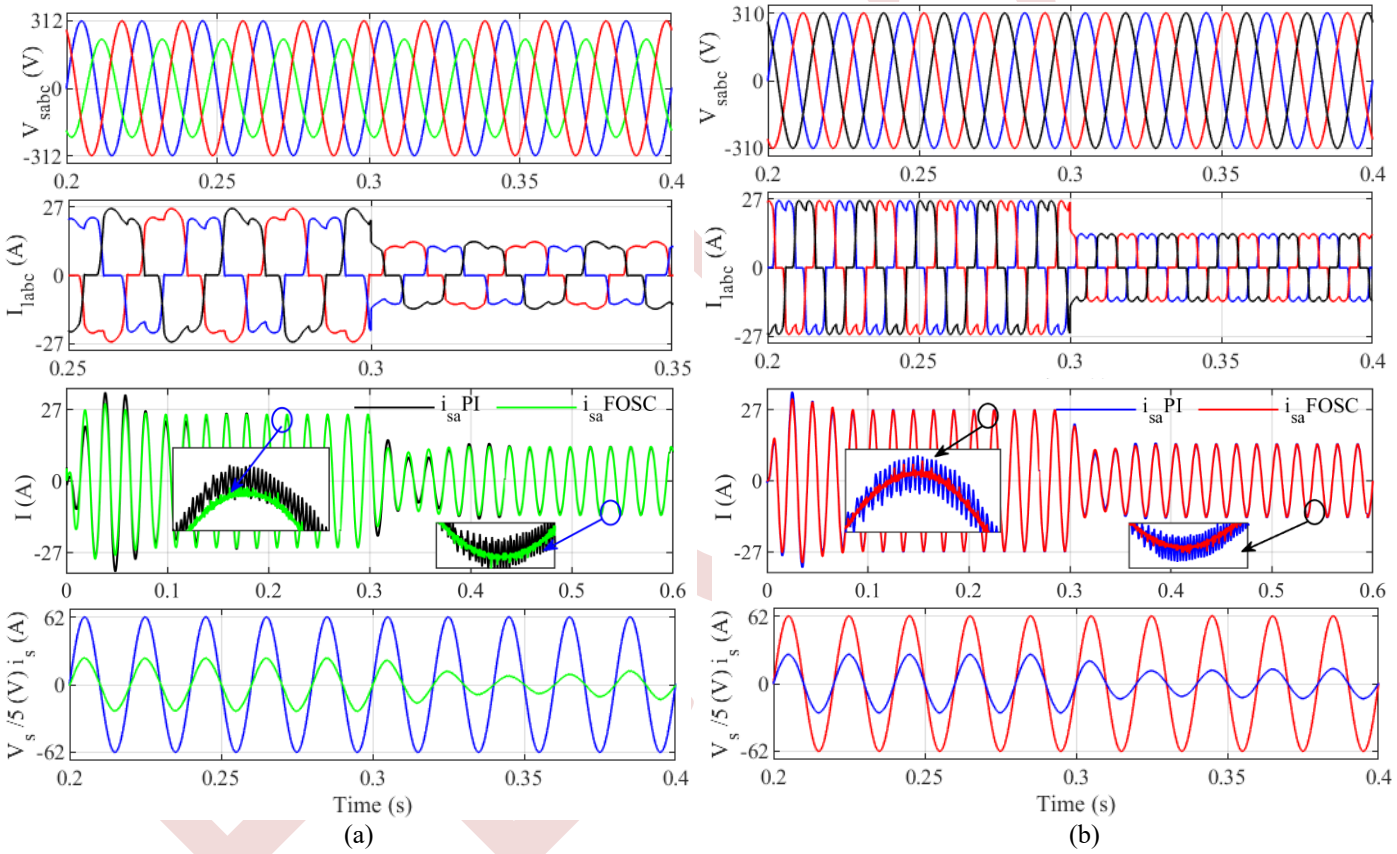


Figure 3. Performance of SAPF using FOSC and PI; (a) Source voltage unbalanced, (b) Source voltage balanced.

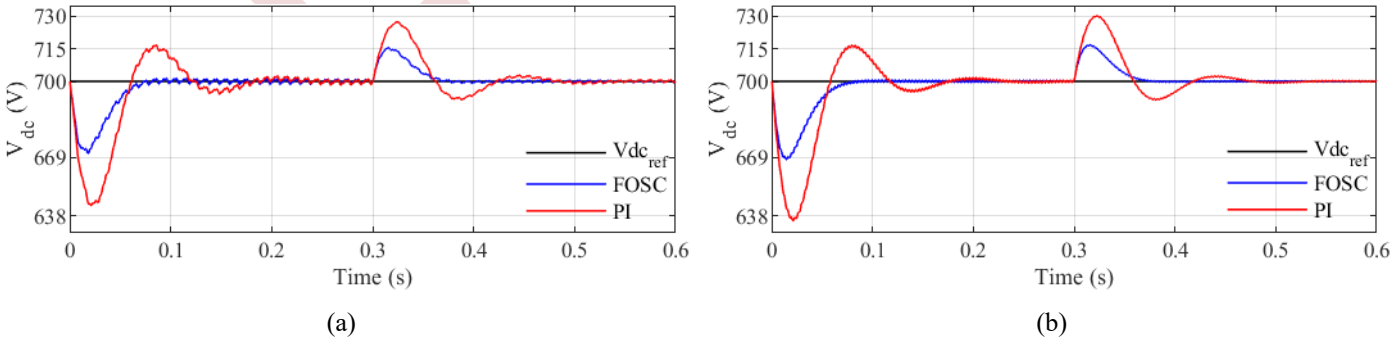


Figure 4. DC-bus voltage using FOSC and PI; (a) source voltage unbalanced, (b) source voltage balanced.

TABLE II. QUANTITATIVE ANALYSIS FOR DC BUS VOLTAGE.

Transient Time (s)	Settling Time (s)		Overshoot (%)	
	FOSC	***PI***	***FOSC***	***PI***
0	0.08	0.22	4.4	8.85
0.3	0.07	0.18	2.14	4.28

TABLE III. COMPARATIVE OF THD SOURCE CURRENT .

THD (%)	FOSC		PI	
	t < 0.3s	***t > 0.3s***	***t < 0.3s***	***t > 0.3s***
Source current before filtering	25.11	26.67	25.11	26.67
Source voltages Balanced	0.85	0.77	1.32	2.12
Source voltages unbalanced	2.17	2.23	3.02	3.49

V. CONCLUSION

This article introduces an approach for enhancing the performance of a 3-level T-type inverter-based SAPF. The approach utilizes a FOSC along with a PLL technique to address issues related to harmonics and DC bus voltage tracking. The control strategy is designed to effectively handle various voltage conditions in the grid, such as balanced and unbalanced voltages, while ensuring a low THD in the source current to meet IEEE-519 requirements. Simulation results confirm the effectiveness of this strategy, showcasing its ability to achieve its intended objectives. Furthermore, the article compares the proposed control strategy with traditional PI control, highlighting its superior performance. The use of FOSC is validated as a robust and well-established method. Future research directions include exploring innovative approaches that combine different nonlinear strategies, as fractional-order backstepping control to enhance energy quality and SAPF durability.

ACKNOWLEDGMENT

We would like to thank all the participants who generously devoted their time and effort to providing the necessary data and information for this study.

REFERENCES

[1] Michalec, Ł.; Jasiński, M.; Sikorski, T.; Leonowicz, Z.; Jasiński, Ł.; Suresh, V. Impact of Harmonic Currents of Nonlinear Loads on Power Quality of a Low Voltage Network–Review and Case Study. Energies 2021, 14, p. 3665.

[2] P. Kuwałek and G. Wiczyński, "Problem of total harmonic distortion measurement performed by Smart Energy Meters," Measurement Science Review, vol. 22, no. 1, pp. 1–10, 2022.

[3] D. Li, T. Wang, W. Pan, X. Ding, and J. Gong, "A comprehensive review of improving power quality using active power filters," Electric Power Systems Research, vol. 199, p. 107389, 2021.

[4] G. Varshney, U. Mittal, and A. Pawar, "Power quality enhancement using passive power filters," Macromolecular Symposia, vol. 407, no. 1, p. 2100442, 2023.

[5] Massavie, V.; Despesse, G.; Carcouet, S.; Maynard, X. Comparison between Piezoelectric Filter and Passive LC Filter in a Class L−Piezo Inverter. Electronics 2022, 11, p. 3983.

[6] Cao, X.; Dong, K.; Wei, X. An Improved Control Method Based on Source Current Sampled for Shunt Active Power Filters. Energies 2020, 13, 1405.

[7] Y. Yorozu, M. Hirano, K. Oka, and Y. Tagawa, "Electron spectroscopy studies on magneto-optical media and plastic substrate interface," IEEE Transl. J. Magn. Japan, vol. 2, pp. 740–741, August 1987 [Digests 9th Annual Conf. Magnetics Japan, p. 301, 1982.

[8] B. Deffaf, F. Hamoudi, N. Debdouche and A. Chebabhi, "Comparative analysis between Backstepping, Sliding mode and PI control applied to Shunt Active Filter," 2022 2nd International Conference on Advanced Electrical Engineering (ICAEE), Constantine, Algeria, 2022, pp. 1-6

[9] B. Deffaf, F. Hamoudi and N. Debdouche, "Sliding Mode Control of a Shunt Active Filter-Comparative analysis with conventional PI control," 2022 19th International Multi-Conference on Systems, Signals & Devices (SSD), Sétif, Algeria, 2022, pp. 1422-1427

[10] B. Deffaf, F. Hamoudi, N. Debdouche, Y. A. Amor, and S. Medjmadj, "Super-twisting sliding mode control for a multifunctional double stage grid-connected photovoltaic system," Advances in Electrical and Electronic Engineering, vol. 20, no. 3, pp. 240–249, 2022.

[11] N. Debdouche, L. Zarour, A. Chebabhi, B. Deffaf and S. Ouchen, "Super Twisting Sliding Mode Direct Power Control of SAPF with Space Vector Modulation for Power Quality improvement," 2022 2nd International Conference on Advanced Electrical Engineering (ICAEE), Constantine, Algeria, 2022, pp. 1-6

[12] Deffaf, B.; Debdouche, N Benbouhenni, H.;Hamoudi, F.; Bizon, N. A New Control for Improving the Power Quality Generated by a Three-Level T-Type Inverter. Electronics 2023, 12, 2117.

[13] Deffaf, B., Farid, H., Benbouhenni, H., Medjmadj, S., & Debdouche, N. (2023). Synergetic control for three-level voltage source inverter-based shunt active power filter to improve power quality. Energy Reports, 10, 1013-1027.

[14] Chedjara, Z., Massoum, A., Massoum, S., Wira, P., Safa, A., &Gouichiche, A. A novel robust PLL algorithm applied to the control of a shunt active power filter using a self-tuning filter concept. In 2018 IEEE International Conference on Industrial Technology (ICIT), Lyon, France, 20-22 February 2018.

[15] Benbouhenni, H.; Bizon, N. A Synergetic Sliding Mode Controller Applied to Direct Field-Oriented Control of Induction Generator-Based Variable Speed Dual-Rotor Wind Turbines. Energies 2021, 14, 4437.

[16] Chao, K.-H.; Chang, L.-Y.; Hung, C.-C. Fault Diagnosis and Tolerant Control for Three-Level T-Type Inverters. Electronics 2022, 11, 2496.

[17] Ayachi Amor, Y., Hamoudi, F., Kheldoun, A., Didier, G., &Rabiai, Z. Fuzzy logic enhanced control for a single-stage grid-tied photovoltaic system with shunt active filtering capability. International Transactions on Electrical Energy Systems2021, 10, e13008.

[18] Debdouche, N., Deffaf, B., Benbouhenni, H., Laid, Z., & Mosaad, M. I. (2023). Direct Power Control for Three-Level Multifunctional Voltage Source Inverter of PV Systems Using a Simplified Super-Twisting Algorithm. Energies, 16(10), 4103.

Novel Six Switch Nine Level Inverter designed for Electric Traction

Farid KERROUCHE, Farid TAZERART, Nabil TAIB

Laboratoire de Technologie Industrielle et de l'Information (LTII), Faculté de Technologie, Université de Bejaia, 06000 Bejaia, Algérie.

Corresponding Author Email: farid.kerrouche@univ-bejaia.dz

***Abstract*— In recent times, there has been significant attention directed towards Multilevel inverters within the research community. This article introduces an original configuration for a nine level inverter that utilizes just six adjustable switches. The novel architecture showcased in this study holds considerable advantages, particularly within the realm of embedded systems like electric propulsion systems. This specific configuration stands out due to its ability to generate a nine level output voltage while employing a reduced number of switches. It is derived from a three-level nine-switch inverter, resulting in a combination that offers exceptional flexibility and control capabilities. To validate the effectiveness of the proposed nine level inverter, a series of simulations were conducted, initially involving an inductive load and subsequently powering a controlled PMSM (Permanent Magnet Synchronous Motor) electric propulsion mechanism. The simulation results unequivocally demonstrate the efficiency and performance of the newly suggested topology. These outcomes underline the significance of this research, as it makes a substantial contribution towards the development of innovative nine level inverter configurations that hold practical utility for electric propulsion systems and various other embedded applications.**

Keywords— electric traction drive, nine level inverter, field-oriented control, pulse width modulation PWM, PMSM, total harmonic distortion

I. INTRODUCTION

The demand for power converters is on the rise, particularly for high-performance industrial applications, so does the importance of multilevel inverters. Multilevel inverters have numerous important advantages. One of the primary advantages is the ability to generate larger output voltage while using lower device voltage ratings. This allows for decreased harmonic content, higher output fundamental voltage, lower dv/dt, and increased overall efficiency. Furthermore, Multilevel inverters are critical in smoothly integrating renewable energy sources with the utility grid, hence improving overall system performance.

Multilevel inverters have a wide range of applications, including unified power flow controllers, motor drives, HVDC systems, and electric vehicles. Multilevel inverters efficiently reduce distortion in the output voltage waveform by employing a systematic way of producing output voltage in a staircase pattern. This staircase output voltage is achieved via intelligent manipulation of dc-link voltages and semiconductor switches [1–4].

Three prominent topologies have taken lead position in the field of Multilevel inverters: Cascaded H-bridge (CHB), flying capacitors (FC), and neutral point clamped (NPC). These well-established topologies have been widely adopted and deployed in a wide range of applications. Despite their various advantages over standard two-level inverters, these topologies do have certain drawbacks, notably in terms of higher-level voltage production.

The amplitudes of the input source can be used to classify multilevel inverters. This difference creates symmetrical and asymmetrical topologies. Symmetrical arrangements keep consistent voltage ratings for input sources, keeping the topology's flexibility. Asymmetrical arrangements, on the other hand, allow for a higher number of levels while using the same number of devices. Nonetheless, the disparity in voltage ratings across devices in these asymmetrical topologies jeopardizes their flexibility and usefulness [5-6].

The reduction of component count is an important part of multilevel topology design. Furthermore, reducing isolated dc voltage sources is an important consideration. In this context, the use of capacitors instead of dc voltage sources has gained traction. These capacitors are charged and discharged to provide different quantities of input power. Notably, due to their practicality, multiple inverter topologies with a single dc voltage source are gaining appeal [7].

In the proposed topology [8-15], its primary drawback lies in the elevated number of controllable switches, which contributes to increased conduction losses. The topologies mentioned in [16-18] involve polarity-changing cells that switch at the output voltage frequency, leading to heightened switching demands. Certain configurations necessitate the utilization of multiple floating capacitors. Across all these topologies, a common limitation is the substantial number of additional controllable switches, intensifying control complexity and losses.

This study delves into the examination of a novel traction power supply system founded on a nine-level asymmetrical voltage source inverter. The inventive single-phase inverter topology, characterized by a minimized switch count, relies on four unidirectional controllable IGBT switches and two IGBT cell pairs integrated within a diode bridge to ensure bidirectional control. The interconnection of four unbalanced voltage sources results in a 9-level output voltage.

The paper is structured into four sections. Section 2 provides a detailed account of the proposed topology, encompassing its operational modes and potential for generalization to different levels. Section 3 is bifurcated into two segments. The initial part focuses on the control strategy for the nine-level single-phase inverter of the proposed topology, while the subsequent part elaborates on the derived three-phase structure. Section 4 demonstrates the application of the nine-level structure within a PMSM-based electrical training setup, presenting results and corresponding analysis. The concluding observations of the findings are encapsulated in Section 5.

II. PROPOSED TOPOLOGY DESCRIPTION AND OPERATION

The single-phase topology configuration of the nine-level inverter is shown in Figure 1. It's constituted of four unidirectional controllable switches of type IGBT (K1, K2, K3 and K4) and two cells of IGBTs embedded in diode bridge to provide a bidirectional controllability of both current and voltage. The series connection of four asymmetric voltage sources allows to obtain an output stair voltage waveform with nine level.

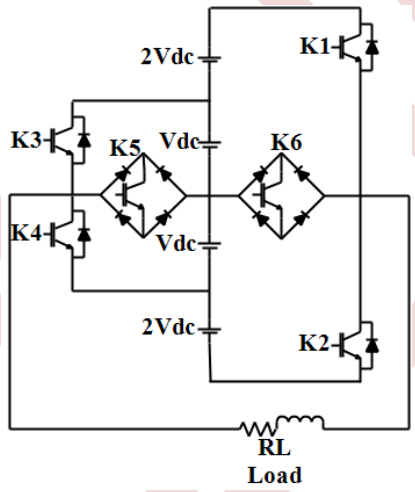


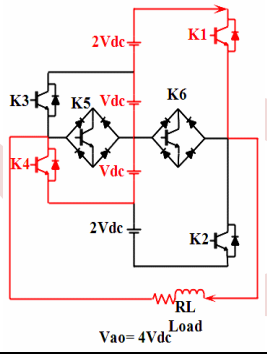
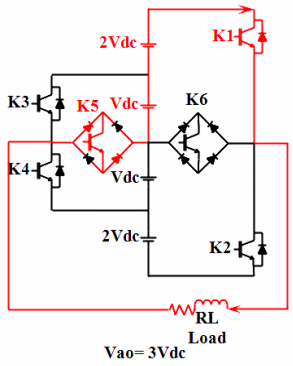
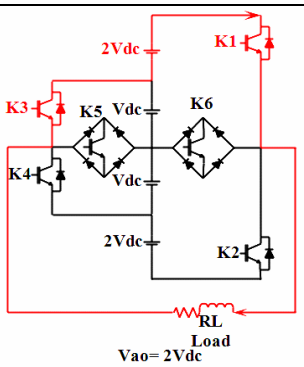
Figure 1. Proposed topology of nine level inverter

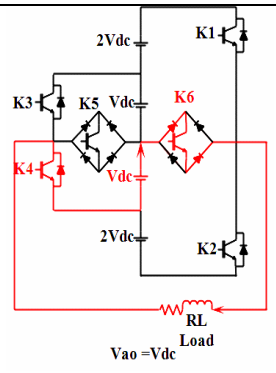
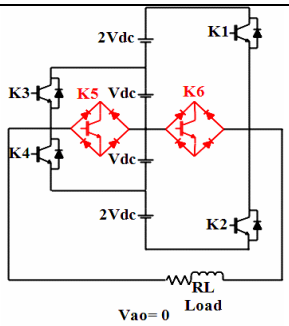
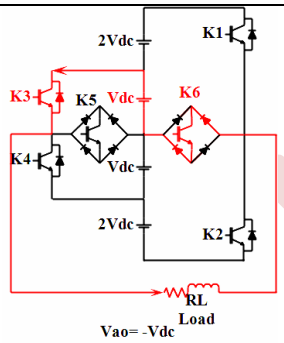
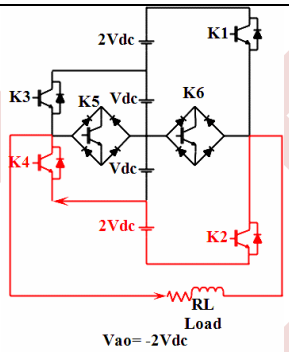
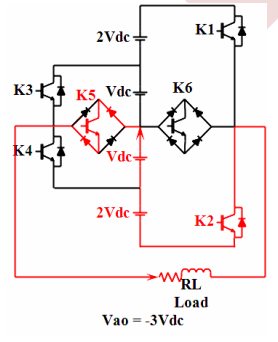
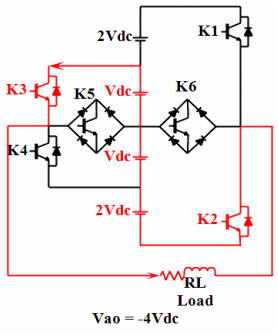
TABLE I. SWITCHING TABLE OF SWITCHES FOR A PHASE OF THEPROPOSED TOPOLOGY

K1	K2	K3	K4	K5	K6	Van	Mode	IGBTs actifs
1	0	0	1	0	0	4Vdc	1	2
1	0	0	0	1	0	3Vdc	2	2
1	0	1	0	0	0	2Vdc	3	2
0	0	0	1	0	1	Vdc	4	2
0	0	0	0	1	1	0	5	2
0	0	1	0	0	1	-Vdc	6	2
0	1	0	1	0	0	-2Vdc	7	2
0	1	0	0	1	0	-3Vdc	8	2
0	1	1	0	0	0	-4Vdc	9	2

The different operation modes of the proposed topology are highlighted in Table II shown below where the red lines highlight the current flow in each operation mode. It is worth noticing that at least two IGBTs have to ON in order to have an output voltage level as it can be seen from Table I. Using only two IGBTs for providing an output voltage level will improve the efficiency of this topology since the conductive losses will be reduced. In order to avoid short circuiting the four series asymmetric voltage sources.

TABLE II. DIFFERENT OPERATING MODE

Mode	figure	Description
1		**By setting:** $\begin{pmatrix} K_1 \\ K_2 \\ K_3 \\ K_4 \\ K_5 \\ K_6 \end{pmatrix} = \begin{pmatrix} 1 \\ 0 \\ 0 \\ 1 \\ 0 \\ 0 \end{pmatrix}$ **the total voltage applied to the load is equal to 4Vdc**
2		**By setting:** $\begin{pmatrix} K_1 \\ K_2 \\ K_3 \\ K_4 \\ K_5 \\ K_6 \end{pmatrix} = \begin{pmatrix} 1 \\ 0 \\ 0 \\ 0 \\ 1 \\ 0 \end{pmatrix}$ **the total voltage applied to the load is equal to 3Vdc**
3		**By setting:** $\begin{pmatrix} K_1 \\ K_2 \\ K_3 \\ K_4 \\ K_5 \\ K_6 \end{pmatrix} = \begin{pmatrix} 1 \\ 0 \\ 1 \\ 0 \\ 0 \\ 0 \end{pmatrix}$ **the total voltage applied to the load is equal to 2Vdc**

4		**By setting:** $\begin{pmatrix}K_1\\K_2\\K_3\\K_4\\K_5\\K_6\end{pmatrix}=\begin{pmatrix}0\\0\\0\\1\\0\\1\end{pmatrix}$ **the total voltage applied to the load is equal to 4Vdc**
5		**By setting:** $\begin{pmatrix}K_1\\K_2\\K_3\\K_4\\K_5\\K_6\end{pmatrix}=\begin{pmatrix}0\\0\\0\\0\\1\\1\end{pmatrix}$ **the total voltage applied to the load is equal to 0 V**
6		**By setting:** $\begin{pmatrix}K_1\\K_2\\K_3\\K_4\\K_5\\K_6\end{pmatrix}=\begin{pmatrix}0\\0\\1\\0\\0\\1\end{pmatrix}$ **the total voltage applied to the load is equal to -Vdc**
7		**By setting:** $\begin{pmatrix}K_1\\K_2\\K_3\\K_4\\K_5\\K_6\end{pmatrix}=\begin{pmatrix}0\\1\\0\\1\\0\\0\end{pmatrix}$ **the total voltage applied to the load is equal to -2Vdc**
8		**By setting:** $\begin{pmatrix}K_1\\K_2\\K_3\\K_4\\K_5\\K_6\end{pmatrix}=\begin{pmatrix}0\\1\\0\\0\\1\\0\end{pmatrix}$ **the total voltage applied to the load is equal to -3Vdc**
9		**By setting:** $\begin{pmatrix}K_1\\K_2\\K_3\\K_4\\K_5\\K_6\end{pmatrix}=\begin{pmatrix}0\\1\\1\\0\\0\\0\end{pmatrix}$ **the total voltage applied to the load is equal to -4Vdc**

III. COMPARISON

The proposed topology is compared to the most relevant ones as summarized in Table III. It could be concluded that the proposed topology requires has optimized the number of controllable switches which will reduce the commutation losses and enhance system efficiency. In addition to that, the control of the proposed topology will be easier. The proposed new nine-level inverter topology retains all the advantages of the conventional multilevel inverter and eliminates their disadvantages.

TABLE III. COMPARISON WITH RECENT DIFFERENT NINE LEVEL INVERTERS

Topologies	IGBTs	Diodes	Voltage sources	Nbr of optimized IGBTs
Topology [7]	10	12	3	4
Topology [8]	8	10	4	2
Topology [9]	8	11	3	2
Topology [10]	9	10	3	3
Topology [11]	8	10	4	2
Topology [12]	8	7	3	2
Topology [13]	10	10	4	4
Topology [14]	8	12	4	2
Topology [15]	7	10	4	1
Topology [16]	10	16	4	4
Topology [17]	9	11	3	3
Topology [18]	12	12	3	6
Proposed topology	6	12	4	~~0~~

IV. SIMULATION OF PROPOSED TOPOLOGY

This section presents the different simulation results performed under Matlab-Simulink. First, single phase of the proposed topology is simulated along with an RL load that emulates the required traction power. After that, three phase nine level inverter Figure 2 of the proposed topology is simulated under the same conditions. Finally, the three phase nine level inverter was integrated in a field-oriented control strategy to control the speed of the PMSM that ensures the traction of an electric vehicle. In order to test the proposed topology, nine level topology was used with a single-phase inductive load. POD-PWM control strategy is used for the control of the proposed strategy. Further details about the last-mentioned control strategy are provided in [19]. The following parameters are used for the simulation of the single phase proposed topology: Vdc = 25V, for inductive loads, R = 0.5Ω, L = 10 mH.

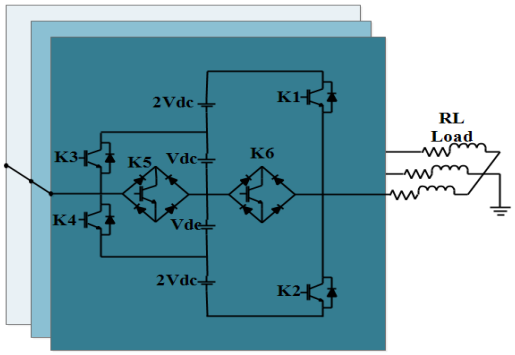


Figure 2. Proposed three phase nine level inverter

V. INVERTER PROPOSED FOR ELECTRIC TRACTION APPLICATIONS

Nowadays, PMSMs are the most widely used in industrial applications in the field of motion control. The main reasons for their popularity are high power density and high efficiency. However, the PMSM is multivariable, non-linear, highly coupled and very sensitive to external perturbations and parameter variation, which makes it difficult for conventional linear control technologies applied to achieve perfect PMSM control performance [4][20]. PMSM vector control has become a mature technology. A position sensor fixed on the rotor shaft is required to obtain an accurate control of the rotor position/speed. This control is based on an independent control of the flux/current and torque/current components. The objective of the PMSM Vector Control is to improve the dynamic behavior of the PMSM Vector Control [20][21]. The proposed nine level inverter is used to power PMSM. The vector control technique is applied in the motor controller. The motor-topology-motor assembly is shown in Figure 3. The performance of the nine level inverter proposed for the motor drive presented above has been verified by simulation. Simulation results were performed with MATLAB Simulink. for machine parameters see Table IV.

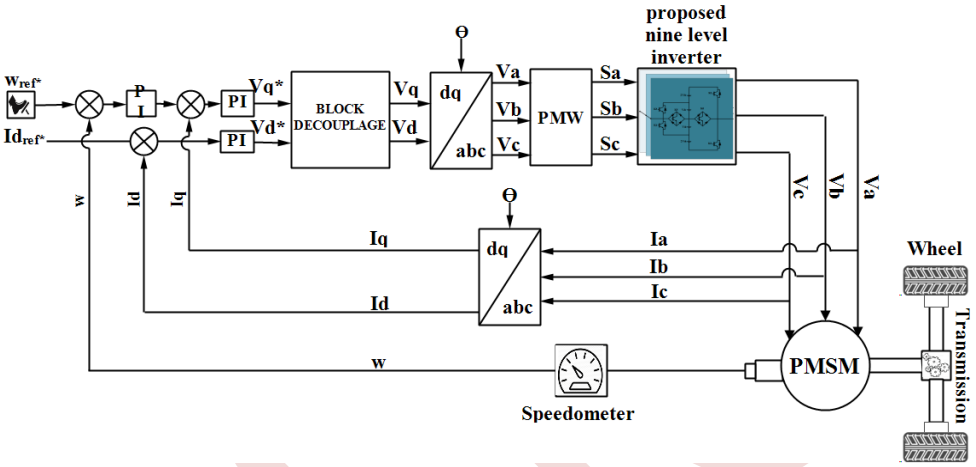


Figure 3. The control-topology-motor system

TABLE IV. Parameters of the permanent magnet synchronous machine

Parameters	Specification
Switching Frequency	10 kHz
Rated Speed	3000 RPM
Rated Torque	111 N.m
Rated Voltage	560 V
Number of Poles	4
Lq	0,000635 H
Ld	0,000635 H
rs	0,05 Ω
Flux(φ)	0,192 Wb
Inertia (J)	0,011 kg.m^2
Friction	0,001889 N.m.s

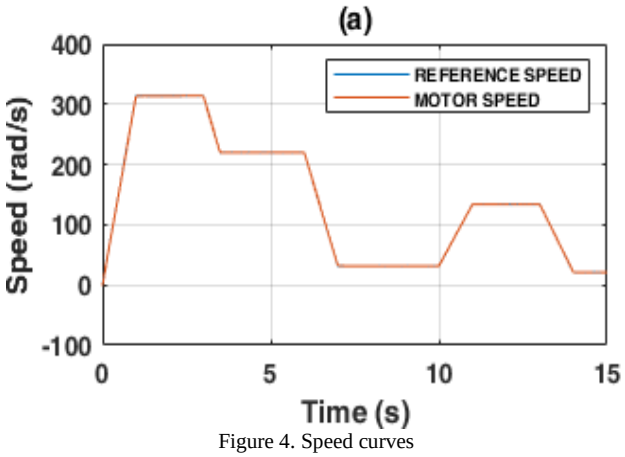


Figure 4. Speed curves

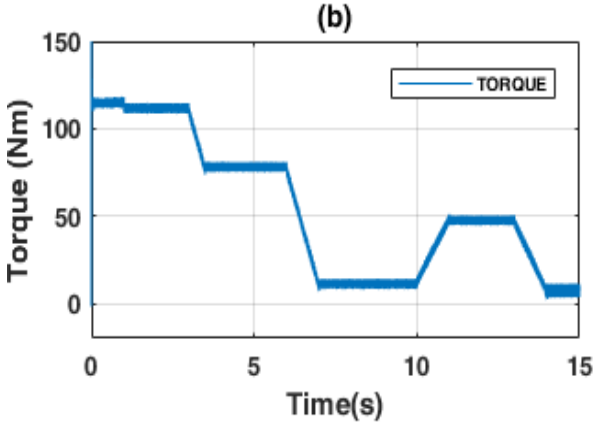


Figure 6. Torque curves

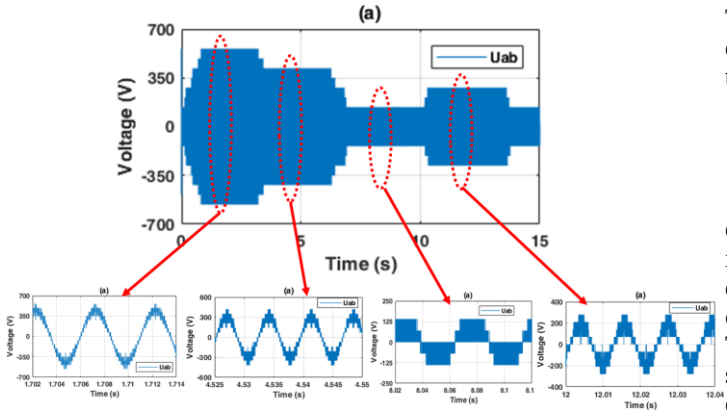


Figure 5. Phase to phase voltage waveform

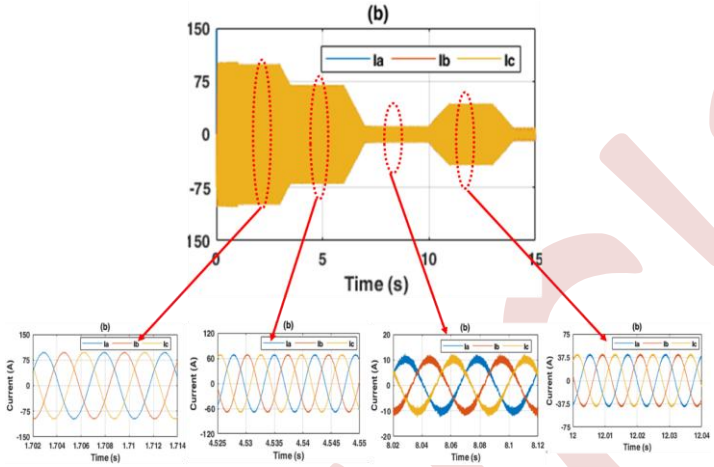


Figure 7. Output Phase Currents Iabc

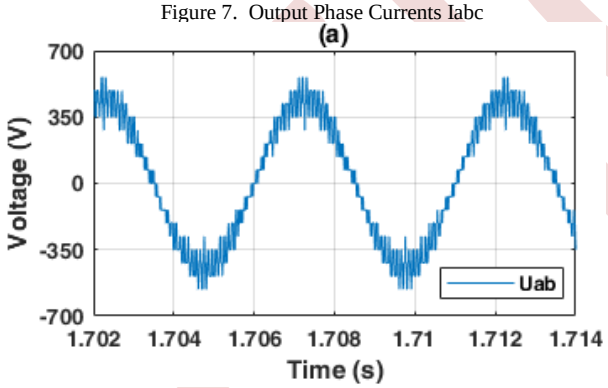


Figure 8. The voltage waveform at maximum speed

COMMENTARY

The vehicle's velocity tracks the specified reference speed pattern, as depicted in Figure 4. Over the initial 0 to 1-second interval, the machine's speed transitions from 0 rad/s to the synchronous speed of 314 rad/s, accompanied by a nominal torque of 111 Nm. At the 3-second mark, the machine commences deceleration, ultimately stabilizing at 21 rad/s by 4 seconds, with a torque of 7.5 Nm. The speed subsequently recommences, reaching and maintaining its nominal value at 8 seconds. Then, it decreases to 146.5 rad/s, accompanied by a torque of 51.8 Nm. The voltage profiles corresponding to different speeds are depicted in Figure 5. Notably, the voltage exhibits variation in correspondence with speed changes, revealing a distinct nine-level pattern at synchronization speed. The current waveforms, as represented in Figure 7, portray diverse patterns in response to torque alterations. Additionally, the frequency exhibits changes in line with speed fluctuations.

CONCLUSION

In this study, a novel three-phase nine level inverter designed specifically for electric traction drive applications is introduced. This inverter topology is capable of producing nine distinct voltage levels while minimizing the number of controllable switches and voltage sources required. The reduction in the quantity of switches not only leads to cost savings but also enhances system reliability and simplifies the control scheme. The proposed 9-level inverter demonstrates a commendable ability to deliver high-quality voltage waveforms. The outcomes presented strongly indicate the suitability of the proposed topology for effectively addressing the requirements of electric traction applications.

REFERENCES

[1] N. Prabaharan, K. Palanisamy, A comprehensive review on reduced switch multilevel inverter topologies, modulation techniques and applications, Renew. Sustain. Energy Rev. 76 (February) (2017) 1248–1282, https://doi.org/:10.1016/j.rser.2017.03.121

[2] A. Nabae, I. Takahashi, H. Akagi, A New Neutral-Point-Clamped PWM Inverter, IEEE Trans. Ind. Appl. IA-17 (5) (1981) 518–523, https://doi.org/10.1109/TIA.1981.4503992

[3] M. Vijeh, M. Rezanejad, E. Samadaei, K. Bertilsson, A General Review of Multilevel Inverters Based on Main Submodules: structural Point of View, IEEE Trans. Power Electron. 34 (10) (Oct. 2019) 9479–9502, https://doi.org/10.1109/TPEL.2018.2890649

[4] P.R. Bana, K.P. Panda, R.T. Naayagi, P. Siano, G. Panda, Recently Developed Reduced Switch Multilevel Inverter for Renewable Energy Integration and Drives Application: topologies, Comprehensive Analysis and Comparative Evaluation, IEEE Access 7 (2019) 54888–54909, https://doi.org/10.1109/ACCESS.2019.2913447

[5] A. Salem, H. Van Khang, K.G. Robbersmyr, M. Norambuena, J. Rodriguez, Voltage Source Multilevel Inverters with Reduced Device Count: topological Review and Novel Comparative Factors, IEEE Trans. Power Electron. 36 (3) (Mar. 2021) 2720–2747, https://doi.org/10.1109/TPEL.2020.3011908

[6] A. Iqbal, M.D. Siddique, B. Prathap Reddy, P.K. Maroti, R. Alammari, A New Family of Step-up Hybrid Switched-Capacitor Integrated Multilevel Inverter Topologies with Dual Input Voltage Sources, IEEE Access (2020), https://doi.org/10.1109/ACCESS.2020.3046192.

[7] SIDDIQUE, Marif Daula et MEKHILEF, Saad. A new configuration of nine-level boost inverter with reduced component count. e-Prime-Advances in Electrical Engineering, Electronics and Energy, 2021, vol. 1, p. 100010. https://doi.org/10.1016/j.prime.2021.100010

[8] Siddique, M. D., Iqbal, A., Memon, M. A., & Mekhilef, S. (2020). A new configurable topology for multilevel inverter with reduced switching components. IEEE Access, 8, 188726-188741 https://doi.org/10.1109/ACCESS.2020.3030951

[9] Liu, J., Lin, W., Wu, J., & Zeng, J. (2018). A novel nine-level quadruple boost inverter with inductive-load ability. IEEE Transactions on Power Electronics, 34(5), 4014-4018. https://doi.org/10.1109/TPEL.2018.2873188

[10] Siddique, M. D., Mekhilef, S., Shah, N. M., Sandeep, N., Ali, J. S. M., Iqbal, A., ... & Orabi, M. (2019). A single DC source nine-level switched-capacitor boost inverter topology with reduced switch count. IEEE Access, 8, 5840-5851. https://doi.org/10.1109/ACCESS.2019.2962706

[11] Lin, W., Zeng, J., Hu, J., & Junfeng, L. (2020). Hybrid nine-level boost inverter with simplified control and reduced active devices. IEEE Journal of Emerging and Selected Topics in Power Electronics. https://doi.org/10.1109/JESTPE.2020.2983205

[12] Naik, B. S., Suresh, Y., Venkataramanaiah, J., & Panda, A. K. (2020). A hybrid nine-level inverter topology with boosting capability and reduced

component count. IEEE Transactions on Circuits and Systems II: Express Briefs, 68(1), 316-320. https://doi.org/10.1109/TCSII.2020.2998496

[13] Ali, J. S. M., Almakhles, D. J., Ibrahim, S. A., Alyami, S., Selvam, S., & Bhaskar, M. S. (2020). A Generalized Multilevel Inverter Topology With Reduction of Total Standing Voltage. IEEE Access, 8, 168941-168950.https://doi.org/10.1109/ACCESS.2020.3022040

[14] Wang, Y., Yuan, Y., Li, G., Chen, T., Wang, K., & Liang, J. (2020). A Generalized Multilevel Inverter Based on T-Type Switched Capacitor Module with Reduced Devices. Energies, 13(17), 4406. https://doi.org/10.3390/en13174406

[15] Ye, Y., Hua, T., & Wang, X. (2021). Nine-Level Inverter Based on Resonant Switched-Capacitor and NPP/NPC Unit. IEEE Access, 9, 60328-60339 https://doi.org/10.1109/ACCESS.2021.3074141

[16] Said, N. A. M., Saleh, W. A. A., & Abd Halim, W. (2020). Voltage harmonics reduction in single phase 9-level transistor clamped H-bridge inverter using nearest level control method. Indonesian Journal of Electrical Engineering and Computer Science, 20(3), 1725-1732. http://dx.doi.org/10.11591/ijeecs.v20.i3.pp1725-1732

[17] Liu, J., Wu, J., Zeng, J., & Guo, H. (2016). A novel nine-level inverter employing one voltage source and reduced components as high-frequency AC power source. IEEE Transactions on Power Electronics, 32(4), 2939-2947. https://doi.org/10.1109/TPEL.2016.2582206

[18] Sandeep, N., & Yaragatti, U. R. (2017). Operation and control of an improved hybrid nine-level inverter. IEEE Transactions on industry applications, 53(6), 5676-5686. https://doi.org/10.1109/TIA.2017.2737406

[19] McGrath, B. P., & Holmes, D. G. (2002). Multicarrier PWM strategies for multilevel inverters. IEEE Transactions on industrial electronics, 49(4), 858-867. https://doi.org/10.1109/TIE.2002.801073

[20] Walid, H., Djamel, R., Sami, M., Elbaki, D.A. (2019). Fractional order direct torque control of permanent magnet synchronous machine. European Journal of Electrical Engineering, Vol. 21, No. 5, pp. 431-438. https://doi.org/10.18280/ejee.210505

[21] Medjmadj, S. (2019). Fault tolerant control of pmsm drive using luenberger and adaptive Back-EMF observers. European Journal of Electrical Engineering, Vol. 21, No. 3, pp. 333-339. https://doi.org/10.18280/ejee.210311.

EEIC'23

Single-objective optimization of Fuzzy MPPT using GWO Algorithm

Abdelah BELHADDAD [1], Abdeslem BOUCHABANE [2], Mohand Akli KACIMI [3]

[1,2] *Faculté de Technologie, Université de Bejaia,06000 Bejaia, Algérie*

abdellah.belhaddad@tech.univ-bejaia.dz

abdeslem.bouchabane@tech.univ-bejaia.dz

[3] *Laboratoire de Technologie Industrielle et de l'Information (LTII), Faculté de Technologie, Université de Bejaia,06000 Bejaia, Algérie*

mohandakli.kacimi@univ-bejaia.dz

***Abstract*— The main aim of the introduced work is to enhance the efficiency of photovoltaic panels using intelligent control strategy. The proposed strategy is based on fuzzy logic control tuned with Grey Wolf Optimization Algorithm. The findings achieved by this strategy has been compared with classical method P&O where they show very promising potentials in dealing with sudden changes in climatic conditions in terms of rapidity and accuracy. The proposed technique is implemented using Matlab/Simulink software**.

Keywords— PV system; DC-DC converter; Optimization; Grey Wolf algorithm; Mamdani fuzzy controller

I. INTRODUCTION

Due to population growth and advances in technology and industry, the demand for energy is increasing every year [1]. Growing concern over global warming, mainly attributed to carbon dioxide emissions (CO_2) [2] led the global community to establish the Kyoto Protocol in 1997 [3], an agreement which aim to promote sustainable development [4].

One of the main challenges in PV systems is dealing with the nonlinear nature of output, since it affected by meteorological conditions. Therefore, it results in power loss according to the principle of maximum power transfer [5]. Which leads us to ask this thorny question: "*how to adjust the load characteristics so that the system can deliver the maximum power in real time as much as possible?"*

Under uniform conditions, photovoltaic (PV) systems exhibit only one peak, called the maximum power point (MPP), on its P-V (power-voltage) curve. Maximum Power Point Tracking (MPPT) are required in order to maximize the extracted power from photovoltaic generator [6].

In the literature several different MPPT control methods are introduces. Traditional methods mainly including: hill climbing [7], perturb and observe [8-9] and incremental conductance method [10] are widely used for their simplicity of use and implementation [11]. However, these classical algorithms have many weaknesses that lead to loss of efficiency in extracting energy and tracking the MPP. Advanced control methods like: adaptative control [12-13] and predictive control [14] based on mathematical model are also used in MPPT control. Thanks to their ability to deal with the non-linearities and changing process dynamics associated with the BOOST converter, they offer more efficiency in comparison to the classical algorithms.

Recently, artificial intelligence techniques including fuzzy logic method (FLC) [15-16], artificial neural network (ANN)[17-18], and metaheuristic algorithms [19] are largelly used in MPPT problem thanks to their learning ability. Despite the difficult nature of the problem, these techniques have been successfully used for efficient maximum power point tracking. Among the intelligent techniques, fuzzy logic seems really interesting, this approach combines learning ability and similarity to the human reasoning. In [20], authors show that the fuzzy controller can track the system MPP very fast with less fluctuations in steady state compared with conventional controllers.

In this paper an optimized fuzzy controller with Grey Wolf Optimization algorithm (GWO) is used to track the MPP of a photovoltaic panel. To validate the robustness of its control, the obtained FLC will be compared with the conventional perturb and observe method (P&O). The rest of the paper is organized as follow: in section 2 the mathematical model of solar cell is presented, as well as system containing the PV panel (Kyocera KC200GT), the DC-DC converter and the load. The structure of the optimized fuzzy controller is described in section 3. Section 4 presents the simulation results and discussion. Finally, the paper will be fenced with general conclusion in section 5.

II. STUDIED PV SYSTEM

This work is dedicated to the study of a standalone PV system described in Fig. 1. The studied system consists of three parts: the PV panel, the DC-DC converter and a resistive load. For the first part, Kyocera KC200GT is used to generate the electrical currant from the photovoltaic effect [21]. Theoretically, each photovoltaic cell is modeled by a single-diode circuit model [22-23] as shown in Fig. 2. From this model, the current and voltage behavior can be given as function as the irradiance and ambiante temperature [24]:

$$I_{pv} = I_{ph} - I_s.\left(e^{\frac{q.(V_{pv}+I_{pv}.R_S)}{A.K.T}} - 1\right) - \frac{R_S.I_{pv}+V_{pv}}{R_{sh}} \quad (1)$$

$$I_{ph} = [I_{sc} + K_i.(T - T_{STC})].\frac{G}{G_{STC}} \quad (2)$$

$$I_s = I_{rs}\left(\frac{T}{T_{STC}}\right)^3.e^{\frac{e.g.q}{A.K}\left(\frac{1}{T_{STC}}-\frac{1}{T}\right)} \quad (3)$$

These equations can be extended for the whole panel containing *Ns* cells connected in series and *Np* in parallel [25]:

$$I_{pv} = N_p I_{ph} - N_p I_s\left(e^{\frac{q(V_{pv}+I_{pv}R_S)}{N_S AKT}} - 1\right) - \frac{R_S I_{pv}+V_{pv}\left(\frac{N_p}{N_S}\right)}{R_{sh}} \quad (4)$$

Table. I present the specifications of the Kyocera KC200GT panel. By using these specifications, the behavior of supplied current and power as function as voltage are drawn, it is illustrated in Fig. 3.

The employed DC-DC converter is a BOOST type that increases the load voltage, according to the duty-cycle control signal. The dynamic of this converter is expressed in equation (5) [11], and Table. II presents its component value.

$$\begin{cases} V_o = \frac{V_{pv}}{1-\alpha} \\ I_o = (1-\alpha)I_{pv} \end{cases} \quad (5)$$

Where V_o and I_o are respectively the voltage and the current output and α is the duty ratio of the converter.

TABLE I. KYOCERA KC200GT PARAMETERS

Maximum Power Pmax	*200.143 (W)*
Open Circuit Voltage Voc	*32.9 (V)*
Short-Circuit Isc	*8.21 (A)*
Voltage at Maximum Power Vmpp	*26.3(V)*
Current at Maximum Power Impp	*7.61 (A)*
Temperature Coefficient of Voc	*-0.35502%/C°*
Temperature Coefficient of Isc	*0.06/C°*

TABLE II. BOOST CONVERTER COMPONENT VALUE

Parameter	Label	Value
Switching frequency	*f*	*25 KHZ*
BOOST inductor	*L*	*1.5mH*
Input capacitor	C_1	*330 µF*
Output capacitor	C_2	*157µF*
Load	*R*	*30Ω*

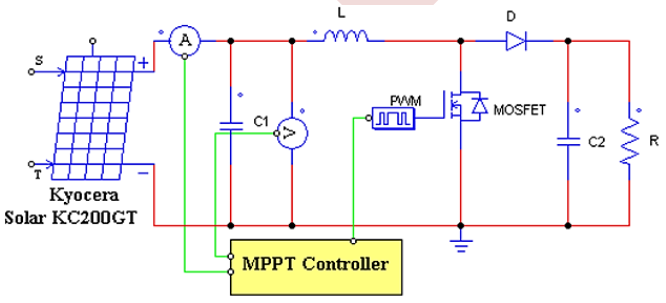


Figure 1. Electrical circuit of the studied PV system

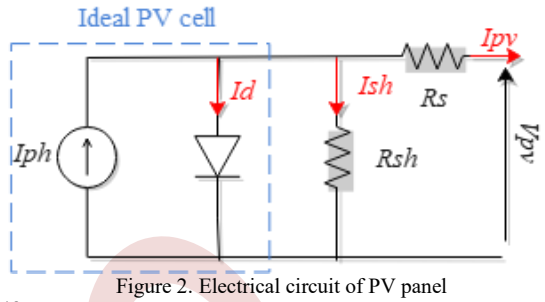


Figure 2. Electrical circuit of PV panel

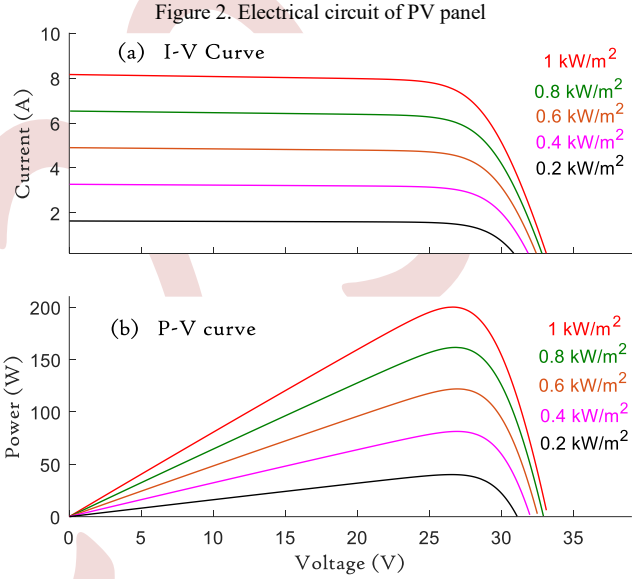


Figure 3. KC200GT module characteristics under different Irradiance for fixed temperature 25°C. (a) P-I curves, (b) V-I curves

III. PROPOSED OPTIMIZED CONTROLLER FUZZY SYSTEM

The proposed MPPT strategy is based on the use of a linguistic fuzzy controller (Mamdani type) [26] tuned by an optimization algorithm (Grey Wolf optimizer) [27] to search for optimal parameters achieving high performances formulated as a good tradeoff between rapidity and accuracy. Fig. 4 gives a synoptic diagram of the introduced strategy.

The fuzzy controller uses two inputs expressing the error $E(k)$ and its variation $\Delta E(k)$, as expressed in equation (6), to calculate the control signal $u(k)$. The inputs and the output are associated to the scaling factors $G_{E(k)}$, $G_{\Delta E(k)}$, $G_{u(k)}$ respectively.

$$\begin{cases} E(k) = \frac{P_{pv}(k)-P_{pv}(k-1)}{V_{pv}(k)-V_{pv}(K-1)} \\ \Delta E(k) = E(k) - E(k-1) \end{cases} \quad (6)$$

The use of these scaling factors simplifies the tuning of the fuzzy logic controller since the universe of discourse is normalized in the interval [-1, 1].

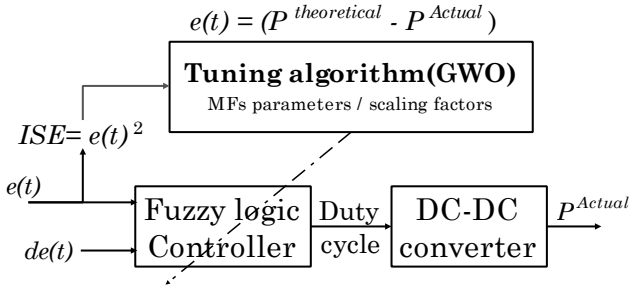


Figure 4. The introduced strategy of tuning the fuzzy controller with GWO algorithm

a. Fuzzy logic controller

The general structure of the fuzzy controller consists of four incorporated blocks: Fuzzification, defuzzification, rule base, and the inference engine as illustrated in Fig. 5.

The fuzzification interface converts the real input values variables of $e(k)$ and $\Delta e(k)$ into fuzzy linguistic terms represented by five triangular membership functions (MFs) denoted as: NB (*Negative Big*), NM (*Negative Medium*), ZR (*Zero*), PM (*Positive Medium*) and PB (*Positive Big*). These terms are used to describe each variable as illustrated in Fig. 6. The linguistic terms obtained from fuzzification are used by the inference engine to determine the appropriate rules first before calculating the output fuzzy set corresponding to the final decision. When the final fuzzy set is calculated, the defuzzification interface converts the latter into crisp value [28].

The rule base constitutes the whole possible decisions that can be taken by the fuzzy controller. According to the observed inputs, the inference engine determines the individual decision from the list of available rules. Here, as illustrated in Table. III, the rule base is presented in form of table where colons and lines form the antecedents and the intersection cell corresponds to the associated decision. For example, the colored cell corresponds to the following rule [11]

If (e(k) is PB) and (Δe(k) is ZR) then (u(k) is NB)

In this work, the fuzzy logic controller needs to be tuned in order to achieve a good performance [11]. According to the proposal, the MFs parameters in addition to the scaling factors need to be fixed. This task is very hard to do manually. Therefore, an optimization algorithm is used to search their optimal values. The mentioned parameters form the decision variables of the optimization algorithm structured in vector as illustrated in Fig. 6 varying in intervals defined by tests as shown in Table. IV. Meanwhile, the pseudo-random behavior of the optimization algorithm makes this technique operating on off-line.

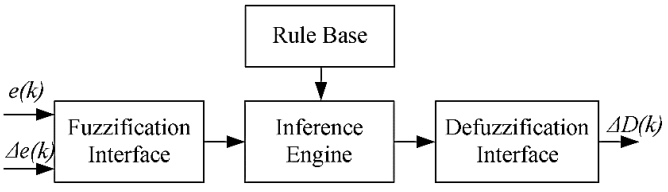


Figure 5. General structure of the Fuzzy Logic Controller

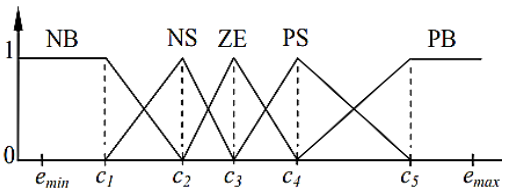


Figure 6. Triangular fuzzy sets of the error input e(t)

TABLE III. FUZZY RULE BASE

e(k) \ Δe(k)	NB	NM	ZR	PM	PB
NB	ZR	ZR	PB	PB	PB
NM	ZR	ZR	PM	PM	PM
ZR	PM	ZR	ZR	ZR	NM
PM	NM	NM	NM	ZR	ZR
PB	NB	NB	NB	ZR	ZR

TABLE IV. VARYING INTERVALS FOR OPTIMIZED PARAMETERS

	C1	C2	C3	C4	C5	$G_{E(k)}$	$G_{\Delta E(k)}$	$G_{u(k}$
Min	-1	-0.35	-0.1	0.1	0.35	0	0	0
Max	-0.35	-0.1	0.1	0.35	1	2	2	10

The coding of MFs exploit the idea of sharing parameters between two adjacent functions in order to reduce the total number of variables to tune by the Grey Wolf Optimizer (GWO) [29]. The intervals defined in table IV are used to guaranty readability and semantic interpretability of the final fuzzy controller.

b. GWO Algorithm

The GWO algorithm uses the leadership pyramid and the hunting behavior of grey wolves in the wild as the basis for its mathematical formula presented in equation (7), (8), (9) and (10) which is introduced to iteratively adjust the positions of the wolves during the optimization process.

$$\begin{cases} \overrightarrow{D_\alpha} = |\overrightarrow{C_1}.\overrightarrow{X_\alpha}(t) - \overrightarrow{X_\iota}(t)| \\ \overrightarrow{D_\beta} = |\overrightarrow{C_2}.\overrightarrow{X_\beta}(t) - \overrightarrow{X_\iota}(t)| \\ \overrightarrow{D_\delta} = |\overrightarrow{C_3}.\overrightarrow{X_\delta}(t) - \overrightarrow{X_\iota}(t)| \end{cases} \quad (7)$$

$$\begin{cases} \overrightarrow{X_1(t)} = |\overrightarrow{X_\alpha}(t) - \overrightarrow{A_1}.\overrightarrow{D_\alpha}| \\ \overrightarrow{X_2(t)} = |\overrightarrow{X_\beta}(t) - \overrightarrow{A_2}.\overrightarrow{D_\beta}| \\ \overrightarrow{X_3(t)} = |\overrightarrow{X_\delta}(t) - \overrightarrow{A_3}.\overrightarrow{D_\delta}| \end{cases} \quad (8)$$

$$\overrightarrow{X_\iota(t+1)} = \frac{\overrightarrow{X_1(t)} + \overrightarrow{X_2(t)} + \overrightarrow{X_3(t)}}{3} \quad (9)$$

$$\begin{cases} \overrightarrow{A_k} = 2.\vec{a}.\overrightarrow{r_1} - \vec{a} \\ \overrightarrow{C_k} = 2.\overrightarrow{r_2} \end{cases} \text{ ; given that: k=1,2,3} \quad (10)$$

Where t, $\vec{D}$: represents respectively the current iteration, the distance between the omega grey wolves and the searching agents: α, β, δ. $\overrightarrow{A_1}$ and $\overrightarrow{C_1}$ are the coefficient vectors of exploration and exploitation features. $\overrightarrow{X_\alpha}$, $\overrightarrow{X_\beta}$, $\overrightarrow{X_\delta}$ are the searching agents position vectors and $\overrightarrow{X_\iota}$ indicates the grey wolf position vector. The components $\overrightarrow{r_1}$, $\overrightarrow{r_2}$ are randomly generated vectors between 0 and 1 and the $\vec{a}$ component decreasing

linearly from 0 to 2. Table. V gives a simplified pseudo code of the GWO algorithm and Table. VI shows the GWO parameters. For this work, 12 individual form the main population, each individual is defined by 18 values corresponding to the parameters of the fuzzy controller.

TABLE V. PSEUDO-CODE OF THE GWO ALGORITHM

	Standard GWO Algorithm
01:	*Objective function: ISE, X_i(i = 1, 2, …, n), a, Search area limits, Search space dimensions, Max iterations and set t=0;*
02:	*Evaluate all search agents and grade them (Xα, X β, Xδ);*
03:	***do***
04:	*Update position for current individual X_i ;*
05:	*Update a, A, and C;*
06:	*Evaluate all search agents and grade them (Xα, X β, Xδ);*
07:	*Update the positions of Xα, Xβ, and Xδ and increment t;*
08:	***While** (t<Max iterations);*

TABLE VI. GREY WOLF ALGORITHM PAREMETERS

Value	Parameter
Population size	12
Maximum number of iterations	200
Search area limits	[0, 1]
Search space dimensions	18

IV. SIMULATION, RESULTS AND DISCUSSION

During the learning process, the Standalone PV system is submitted to the irradiance (G) and temperature (T) illustrated in Fig. 7. The theoretical power values associated to these irradiance and temperature are determined from the P-V characteristic curves of Fig. 3. They are respectively: 200.1(W), 121.8(W) and 161.5(W).

An objective function to minimize is also defined in order to determine the score of each wolve and determine the best one to guide the search process. This function estimates the difference between the actual power generated by the system and the theoretical value estimated from the P-V curve. Named Integral Square Error (ISE), it is expressed by equation (9).

$$ISE = \sum_{k=1}^{N}(P_{theoretical}(k) - P_{actual}(k))^2 \qquad (9)$$

Fig. 8 shows the evolution of the best score per iteration. We can notice a rapid decrease in the first fifty iterations corresponding to a global search and a slower decrease corresponding to a local search phase. The last value at 200th iteration corresponds to the best score of the best solution X_α representing the optimal fuzzy MFs of inputs-output shown in Fig. 9 and the optimal scaling factors $G_{E(k)}$ =5; $G_{\Delta E(k)}$=1; $G_{u(k)}$=0.1

The simulation of these optimal fuzzy parameters is illustrated in Fig. 10. It underlines the performance of the fuzzy controller to extract the maximum power from the PV panel with respect to irradiance and temperature scenario of Fig. 7. We can easily notice the efficiency of the fuzzy controller since the actual power is closer to the theoretical power estimated from the P-V curve. To confirm this observation, a numerical criterion is used to estimate this performance. It is expressed in equation (10), and its evolution per simulation time is illustrated in Fig. 11. More this ratio (E_{index}) is closer to 1 more the harvesting performance is better. The proposed approach has an E_{index} = 0.9980, thing which confirms that the fuzzy model has successfully learned the system dynamic thanks to the proposed GWO algorithm.

$$E_{index} = \sum_{k=1}^{N} P_{actual(K)} \Big/ \sum_{k=1}^{N} P_{theoretical(K)} \qquad (10)$$

To validate the efficiency of the introduced approach, it is compared to the P&O technique where we perform a test under a scenario that was not encountered during the learning phase. Both techniques are exposed to the same irradiance and temperature conditions as illustrated in Fig. 12. The associated theoretical powers are: 180.9(W), 81.2(W), and 141.8(W). The results of the comparative study are shown in (Fig. 13- Fig. 14).

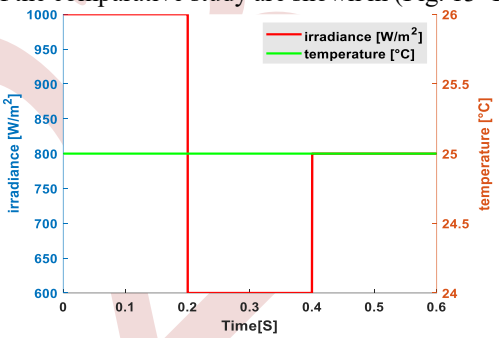


Figure 7. Learning profile

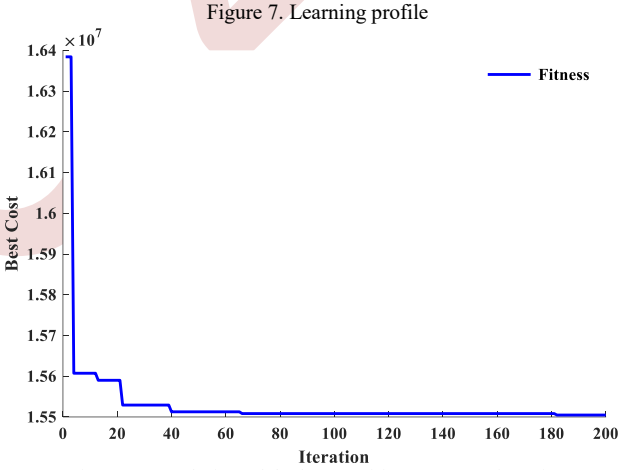


Figure 8. Evolution of the best position score per iteration

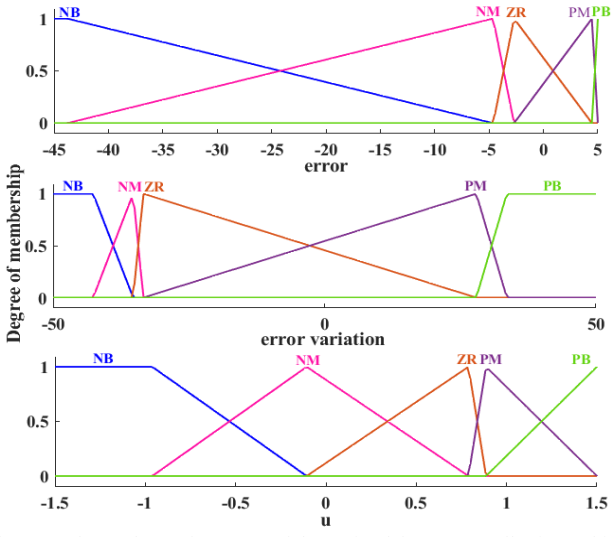


Figure 9. shows the performance of the optimal fuzzy controller in tracking the maximum power point (MPP)

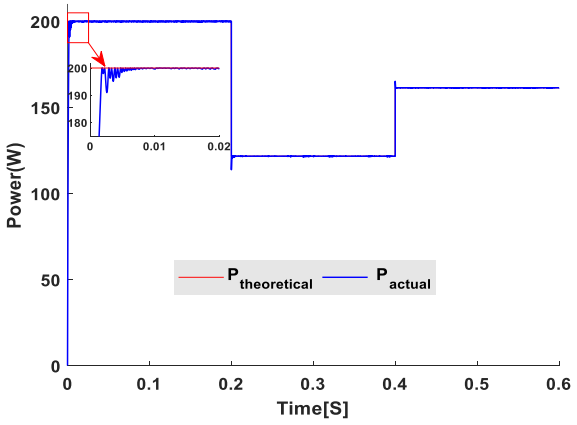


Figure 10. MPPT under learning profile

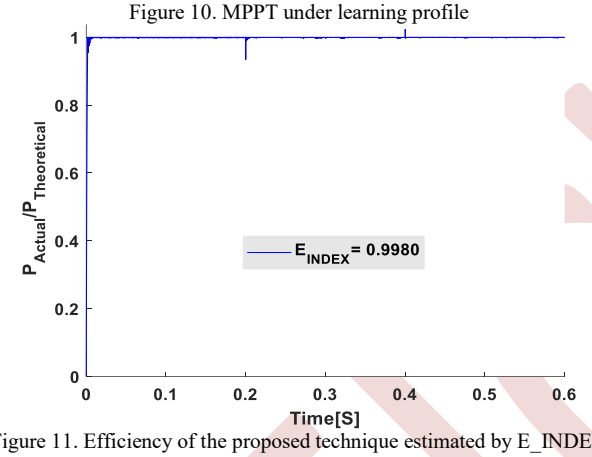


Figure 11. Efficiency of the proposed technique estimated by E_INDEX

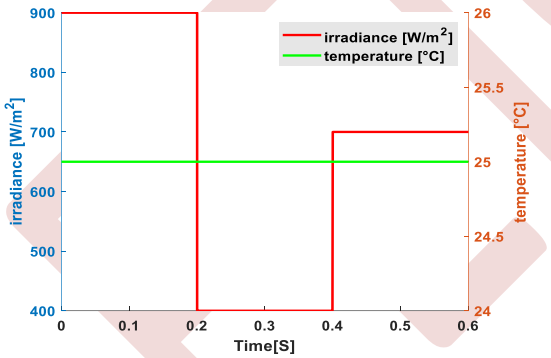


Figure 12. Irradiance and temperature profile

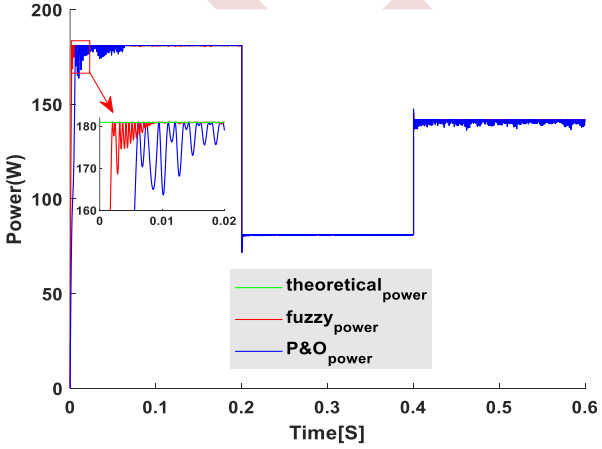


Figure 13. Efficiency of the proposed technique and conventional P&O

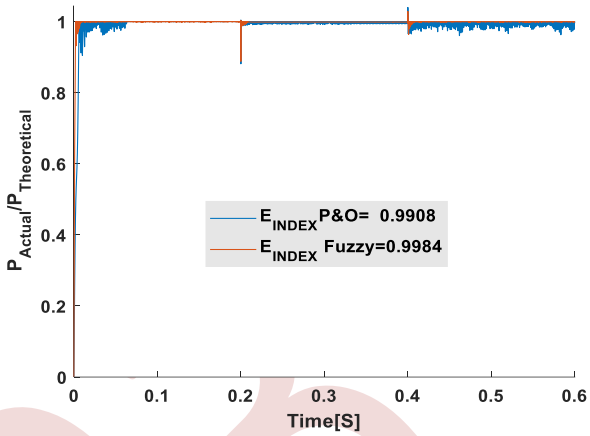


Figure 14. Efficiency of the proposed technique and the conventional P&O estimated by E_INDEX

From Fig. 13 we can see the effectiveness of the proposed approach that outperforms the P&O control in terms of system's response (see Table. VII), which are clearly visible at start-up. It also proves the ability of the proposed approach to track the MPP into different irradiance conditions, while stabilizing the operating point without oscillation in steady-state. This observation is also confirmed numerically (Fig. 14) since the proposed approach has an E_{index}=0.9984, while the conventional P&O has an E_{index}=0.9908.

The following table summarizes all results obtained under conditions illustrated in Fig. 12:

TABLE VII. COMPARISON TABLE OF STUDIED MPPT METHODS

	P&O	**Optimized FLC**
P_{MPP}	*198.25908 (W)*	*199.77984 (W)*
Transient time	*64 (ms)*	*8 (ms)*

V. CONCLUSION

This paper introduces a new approach to deal with the MPPT problems based on the use of an optimized fuzzy logic controller. The introduced strategy was compared with the conventional P&O control technique and the obtained results (Fig.13) highlights the superiority of the proposed approach in dealing with rapid change of climatic conditions and oscillation at steady-state. By optimizing the parameters of membership functions, we achieved significant improvement in response speed and accuracy.

Meanwhile, these results will be verified latter on the partial shading PV problems and by experimental validation.

REFERENCES

[1] N. KANNAN et D. VAKEESAN, "Solar energy for future world," *Renewable and sustainable energy reviews,* vol. 62, pp. 1092-1105, 2016. https://doi.org/10.1016/j.rser.2016.05.022

[2] M. LACHEHEB, A. ABDUL RAHIM et A. SIRAG, "Economic Growth and Dioxide Emissions: Investigating the Environmental Kuznets Curve Hypothesis in Algeria," *International Journal of Energy Economics and Policy,* vol. 5, n° 4, pp. 1125-1132, 2015.

[3] S. BARRETT, "Political Economy of the Kyoto Protocol," *Oxford review of economic policy,* vol. 14, n° 4, pp. 20-39, 1998. https://doi.org/10.1093/oxrep/14.4.20

[4] A. M. OMER, "Energy, environment and sustainable development," *Renewable and sustainable energy reviews,* vol. 12, n° 9, pp. 2265-2300, 2008. https://doi.org/10.1016/j.rser.2007.05.001

[5] C. KONG, "A General Maximum Power Transfer Theorem," *IEEE Transactions on Education,* vol. 38, n° 3, pp. 296-298, 1995. https://doi.org/10.1109/13.406510

[6] X. LI, Q. WANG, H. WEN et W. XIAO, "Comprehensive studies on operational principles for maximum power point tracking in photovoltaic systems," *IEEE Access,* vol. 7, pp. 121407-121420, 2019. https://doi.org/10.1109/ACCESS.2019.2937100

[7] W. ZHU, L. SHANG, P. LI et H. GUO, "Modified hill climbing MPPT algorithme with reduced steady-state oscillation and improved tracking efficiency," *The journal of Engineering,* vol. 2018, n° 17, pp. 1878-1883, 2018. https://doi.org/10.1049/joe.2018.8337

[8] J. J. NEDUMGATT, K. JAYAKRISHNAN, S. UMASHANKAR, D. VIJAYAKUMAR et D. KOTHARI, "Perturb and observe MPPT algorithm for solar PV systems-modeling and simulation," *Annual IEEE India Conference,* pp. 1-6, 2011. https://doi.org/10.1109/INDCON.2011.6139513

[9] J. RIBY, Z. RICHU et M. S SHEIK, "Variable step size Perturb and observe MPPT algorithm for stadalone solar photovoltaic system," *IEEE International Conference on Intelligent Techniques in Control, Optimization and Signal Processing(INCOS),* pp. 1-6, 2017. https://doi.org/10.1109/ITCOSP.2017.8303163

[10] A. ILYAS, M. AYYUB, M. R. KHAN, A. JAIN et M. A. HUSAIN, "Realization of Incremental Conductance MPPT Algorithm for Solar Photovoltaic System," *International Journal of Ambient Energy,* vol. 39, n° 8, pp. 873-884, 2018. https://doi.org/10.1080/01430750.2017.1354322

[11] O. GUENOUNOU, B. DAHHOU et F. CHABOUR, "Adaptive fuzzy controller based MPPT for photovoltaic systems," *Energy Conversion and Management,* vol. 78, pp. 843-850, 2014. https://doi.org/10.1016/j.enconman.2013.07.093

[12] A. V. SANT, V. KHADKIKAR, W. XIAO, H. ZEINELDIN et A. AL-HINAI, "Adaptative control of grid connected photovoltaic inverter for maximum VA utilization," *IECON 2013- 39th Annual Conference of the IEEE Industrial Electronics Society,* pp. 388-393, 2013. https://doi.org/10.1109/EICON.2013.6699167

[13] S. MANNA, D. K. SINGH, A. K. AKELLA, H. KOTB, K. M. ABORAS, H. M. ZAWBAA et S. KAMEL, "Design and implementation of a new adptative MPPT controller for solar PV systems," *Energy Reports,* vol. 9, pp. 1818-1829, 2023. https://doi.org/10.1016/j.egyr.2022.12.152

[14] O. ABDEL-RAHIM et H. WANG, "A New High Gain DC-DC Converter With Model-Predictive-Control Based MPPT Technique for Photovoltaic Systems," *CPSS Teansaction on power Electronics and Applications,* vol. 5, n° 2, pp. 191-200, 2020. https://doi.org/10.24295/CPSSTPEA.2020.00016

[15] R. B. ROY, E. BASHER, R. YASMIN et M. ROKONUZZAMAN, "Fuzzy Logic Based MPPT Approach In A Grid Connected Photovoltaic System," *The 8th International Conference On Software, Knowledge, Information Management and Applications (SKIMA 2014),* pp. 1-6, 2014. https://doi.org/10.1109/SKIMA.2014.7083525

[16] C. R. ALGARIN, J. T. GIRALDO et O. R. ALVAREZ, "Fuzzy Logic Based MPPT Controller for a PV System," *Energies,* vol. 10, n° 12, p. 2036, 2017. https://doi.org/10.3390/en10122036

[17] R. SRINIVASAN et C. R. BALAMURUGAN, "Deep neural network based MPPT algorithm and PR controller based SMO for grid connected PV system," *International Journal of Electronics,* vol. 109, n° 14, pp. 576-595, 2022. https://doi.org/10.1080/00207217.2021.1914192

[18] R. DIVYASHARON, R. BANU et D. DEVARAJ, "Artificial Neural Netwerk based MPPT with CUK Converter Topology for PV Systems Under Varying Climatic Conditions," *IEEE International Conference on Intelligent Techniques in Control, Optimization and Signal Processing (INCOS),* pp. 1-6, 2019. https://doi.org/10.1109/INCOS45849.2019.8951321

[19] A. MOHAMED, A. Z. DIAB et H. REZK, "Partial Shading Mitigation of PV Systems Via different meta-heuristic techniques," *Renewable energy,* vol. 130, pp. 1159-1175, 2019. https://doi.org/10.1016/j.renene.2018.08.077

[20] M. ARGYROU, P. CHRISTODOULIDES et S. KALOGIROU, "Modeling of photovoltaic system with different MPPT techniques using MATLAB/Simulink," *IEEE International energy conference (ENERGYCON),* vol. 6, pp. 1-6, 2018. https://doi.org/10.1109/ENERGYCON.2018.8398734

[21] A. E. BECQUEREL, "Research into the effects of chemical radiation from sunlight using elecric currents," "Recherches sur les effets de la radiation chimique de la lumiere solaire au moyen des courants electriques," *Report from the French Academy of Sciences,* vol. 9, n° 1, pp. 145-149, 1839.

[22] C. AOUGHLIS, A. BELKAID, M. A. KACIMI, I. COLAK et O. GUENOUNOU, "New Dynamic and Self-Adaptative Incremental Conductance Algorithm for Standalone PV System," *11th IEEE International Conference on Renewable Energy Research and Applications (ICRERA),* pp. 268-273, 2022. https://doi.org/10.1109/ICRERA55966.2022.9922758

[23] H. RAUSCHENBACH, "Solar cell array design handbook: the principles and technology of photovoltaic energy conversion," Springer Science & Business Media, United States of America, 2012. https://doi.org/10.1007/978-94-011-7915-7

[24] M. G. VILLALVA, J. R. GAZOLI et E. R. FILHO, "Comprehensive Approach to Modeling and," *IEEE TRANSACTIONS ON POWER ELECTRONICS,* vol. 24, n° 5, pp. 1198 - 1208, 2009. https://doi.org/10.1109/TPEL.2009.2013862

[25] S. CHANDER, A. PUROHIT, . A. SHARMA, S. NEHRA et M. DHAKA, "Impact of temperature on performance of series and parallel connected mono-crystalline silicon solar cells," *Energy Reports,* vol. 1, pp. 175-180, 2015. https://doi.org/10.1016/j.egyr.2015.09.001

[26] E. MAMDANI et S. ASSILIAN, "An experiment in linguistic synthesis with a fuzzy logic controller," *International Journal of Man-Machine Studies,* vol. 7, n° 1, pp. 1-13, 1975. https://doi.org/10.1016/S0020-7373(75)80002-2

[27] S. MIRJALILI, S. M. MIRJALILI et A. LEWIS, "Grey Wolf Optimizer," *Advanced in engineering software,* vol. 69, pp. 46-61, 2014. https://doi.org/10.1016/j.advengsoft.2013.12.007

[28] M. A. KACIMI, O. GUENOUNOU, L. BRIKH, F. YAHIAOUI et N. HADID, "New mixed-coding PSO algorithm for a self-adaptive and automatic learning," *Engineering Applications of Artificial Intelligence,* vol. 89, p. 103417, 2020. https://doi.org/10.1016/j.engappai.2019.103417

[29] N. YUBAZAKI, M. OTANI, T. ASHIDA et K. HIROTA, "Dynamic fuzzy control method and its application to positioning of induction motor," *Proceedings of 1995 IEEE International Conference on Fuzzy Systems.,* vol. 3, pp. 1095-1102, 1995. https://doi.org/10.1109/FUZZY.1995.409820

III

ELECTRICAL MACHINES AND DRIVES (EMD)

Sommaire

III.1 Improvement of steady-state performance of direct torque control for dual star induction motor drives 60
III.2 Performances and lifetime improvement of hybrid electric vehicles by using NPC five-level inverter 66
III.3 Electrical and mechanical parameters identification of a double stator induction machine 73
III.4 Study of the parameters influencing the performance of a self-excited induction generator 79
III.5 Open phase fault tolerance solution for dual star induction machine 85
III.6 Detection of rotor bar breakages in a dual-star induction machine 91
III.7 Transient thermal model analysis of three phase induction motor using both lumped parameter thermal network and finite element method 96
III.8 Hybrid model for modeling air gap in electrical machines 102
III.9 Enhancing wind power conversion efficiency with vernier dspm generator and sliding mode control 108
III.10 Nonlinear predictive control for an asynchronous machine 115
III.11 Behavior analysis of double star induction motor under open phase fault 119
III.12 Levitation force electromagnetic calculations for medium-speed trains 123

Improvement of Steady-State Performance of Direct Torque Control for Dual Star Induction Motor Drives

Sifelislam Guedida [1], Bekheira Tabbache [2], Kamal Nounou [3], Abdelhakim Idir [4], Mohamed Benbouzid [5]

[1,2,3] *UER ELT, Ecole Militaire Polytechnique, 16111 Algiers, Algeria*

d_guedida.sifelislam@emp.mdn.dz, bekheira.tabbache@emp.mdn.dz, kamel.nounou@emp.mdn.dz

[4]*DEE, University Mohamed Boudiaf of M'sila, M'sila 28000, Algeria*

abdelhakim.idir@univ-msila.dz

[5]*UMR CNRS 6027 IRDL, University of Brest, 29238 Brest, France*

Mohamed.Benbouzid@univ-brest.fr

***Abstract*—In this paper, a new method for the reduction of steady-state torque error and compensation of harmonic current components is presented for the direct torque control (DTC) of the dual star induction motor (DSIM). The main problem encountered in classical direct torque control (DTC-THR) of multiphase machines is harmonic current distortion, often due to lack of control in (x-y) subspace. Therefore, this paper presents MDTC-THR based on a two-step process that allows the selection of an appropriate voltage vector to control the stator flux in the (x-y) subspace. This significantly reduces harmonic currents and generates a purely sinusoidal phase current form. The classical three-level torque hysteresis regulator (THR) causes a large steady-state torque error due to zero voltage vectors. An MDTC-THRM based on a modification of the torque regulator, which can effectively reduce the steady-state torque error. Simulation results validate the effectiveness of MDTC-THR and MDTC-THRM.**

***Keywords:* Direct Torque Control (DTC), Dual Star Induction Motors (DSIM), Current Harmonics, Steady State Torque Error.**

I. INTRODUCTION

Recently, multiphase machines have become more widely used in industry due to their improved reliability, greater fault tolerance, higher power capacity and reduced torque ripple [1-2]. The dual star induction motor (DSIM) has a stator with two identical three-phase windings shifted by an electrical angle of 30 degrees, while the rotor is identical to that of a three-phase induction machine [3]. Fig. 1 shows the DSIM supplied by a six-leg inverter, which causes large current harmonics of 5th, 7th, 17th and 19th order [4]. These harmonics increase losses and risk deterioration of semiconductor components.

The dual star induction motor has become more popular in various control strategies in recent years. Direct torque control (DTC) is one of these most widely used strategies in the literature, due to its simple structure and good dynamic response in electric drive systems [5]. In addition, DTC uses a single voltage vector in a sampling period which is selected from a switching table based on the output of both stator flux and torque hysteresis regulators. This generates significant current harmonics, a critical challenge for driving DSIM [6].

In order to minimize circulating currents and improve the form of phase currents, several techniques based on modification of the DTC by introduction of space vector modulation (SVM) have been developed. Although these techniques are effective in reducing current harmonics, they require higher computing power [7]. In contrast, classical direct torque control, based on the torque hysteresis regulator (DTC-THR), no higher controls the circulating current in (x-y) subspace, resulting in a non-sinusoidal form of the phase currents. This paper is presented a modified direct torque control (MDTC-THR) similar to the technique [8-9], which controls the stator flux in the (x-y) subspace in two steps, thus minimizing harmonic current components and obtaining a purely sinusoidal phase current form.

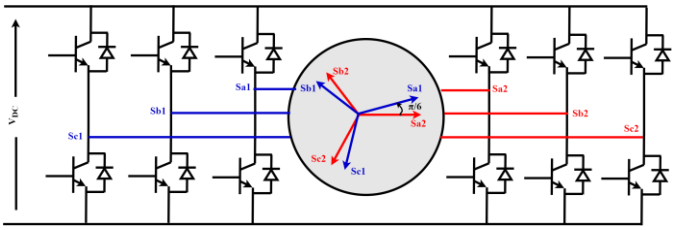


Figure 1. DSIM supplied by six-leg inverter.

Several control strategies are based on modifying the DTC to deal with torque and stator flux ripples, but they have not been analyzed or studied with regard to steady-state torque error, i.e., the average torque value that does not follow its reference [10]. The classical DTC-THR and MDTC-THR are not capable of reducing steady-state torque error. In this paper, a direct torque control is proposed, based on the modification of the three-level torque hysteresis regulator (MDTC-THRM),

in order to minimize the steady-state torque error. Simulation results will validate the effectiveness of the MDTC-THR and MDTC-THRM.

II. MODELING DSIM AND STRUCTURE OF DTC-THR

A. *Mathematical Model of DSIM*

Fig. 1 shows the drive system of a dual star induction motor fed by a six-leg inverter. To simplify the model, a decoupling method based on the vector space decomposition (VSD) approach must be used to enable observation and control of the harmonic components of the current. According to the transformation matrix in [4], the DSIM mathematical model can be decomposed into three subspaces (α-β), (x-y) and (o1-o2), and can be written as follows:

$$V_{s(\alpha-\beta)} = Rs\ I_{s(\alpha-\beta)} + d\Psi_{s(\alpha-\beta)}/dt \quad (1)$$

$$V_{s(x-y)} = R_s\ I_{s(x-y)} + d\Psi_{s(x-y)}/dt \quad (2)$$

$$\Psi_{s(\alpha-\beta)} = L_s\ I_{s(\alpha-\beta)} + \Psi_{r(\alpha-\beta)} \quad (3)$$

$$\Psi_{s(x-y)} = L_{ls}\ I_{s(x-y)} \quad (4)$$

The torque can be expressed as follows:

$$T_e = p\ (\Psi_{s\alpha}\ I_{s\beta} - \Psi_{s\beta}\ I_{s\alpha}) \quad (5)$$

Where:

$V_{s(\alpha-\beta)}$, $I_{s(\alpha-\beta)}$, $\Psi_{s(\alpha-\beta)}$: stator voltage, current and flux vectors in α-β subspace.

$V_{s(x-y)}$, $I_{s(x-y)}$, $\Psi_{s(x-y)}$: stator voltage, current and flux vectors in x-y subspace.

L_{ls} : stator leakage inductance.

p: number of pole pairs.

According to equations (1-5), the machine model after the transformation shows that electromagnetic torque conservation depends on subspace (α-β), which simply corresponds to torque control in the three-phase motor. It can be seen that the circulating current depends on the flux in subspace (x-y).

B. *Classical DTC-THR Principle*

Based on the combination of a six-leg inverter with a dual star induction motor (DSIM), a total of 64 switching states are possible. Each of these states is defined by six binary states (Sa1 Sb1 Sc1 Sa2 Sb2 Sc2), where the value "1" indicates a closed switching state and the value "0" indicates an open switching state. These 64 switching states thus generate 64 voltage vectors, which are grouped into four distinct groups (G1, G2, G3 and G4). These groups of voltage vectors are represented in the (α-β) and (x-y) subspaces respectively, as illustrated in Fig. 2.

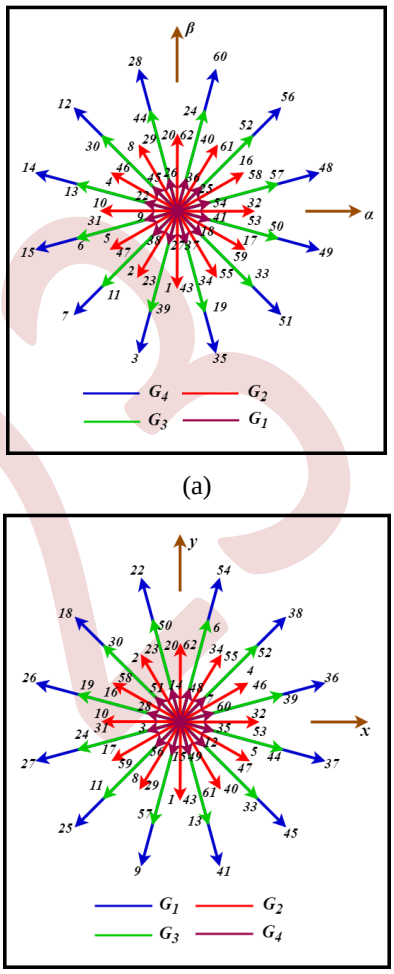


Figure 2. Representation of voltage vectors in two subspaces: (a) α-β subspace; (b) x-y subspace.

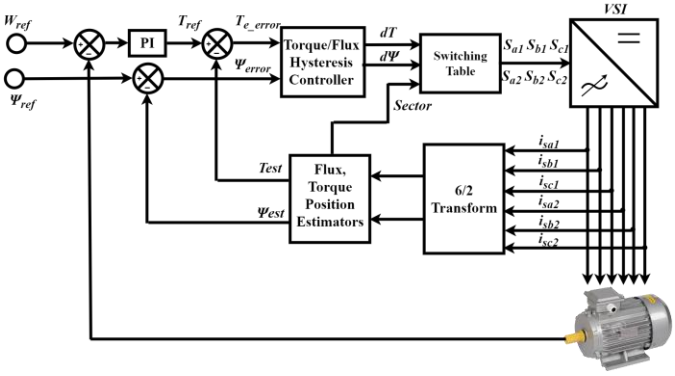


Figure 3. Classical direct torque control (DTC-THR) for DSIM drives.

Fig. 3 shows a slight modification of the switching table of the three-phase induction motor, obtaining a new switching table for the classical DTC-THR of the dual star induction

motor (DSIM). This modification is based on the use of 12 large voltage vectors of group 4 (G4) of subspace (α-β) and allows this subspace (α-β) to be divided into 12 sectors, as illustrated in Fig. 4.

For one sampling period, a voltage vector selected from Table I is to be applied based on the outputs of two hysteresis regulators of stator flux, torque and estimated stator flux position. However, the large voltage vectors selected in the α-β subspace generate small voltages of group 1 (G1) in the (x-y) subspace that are not controlled by the classical DTC-THR. Consequently, this results in the excitation of significant circulating currents and a non-sinusoidal phase current form.

TABLE I. CLASSICAL SWITCHING TABLE

Flux Stator in Sector k		Torque Error		
		-1	*0*	*1*
Flux Error	*-1*	V_{k-4}	V_0	V_{k+3}
	1	V_{k-3}	V0	V_{k+2}

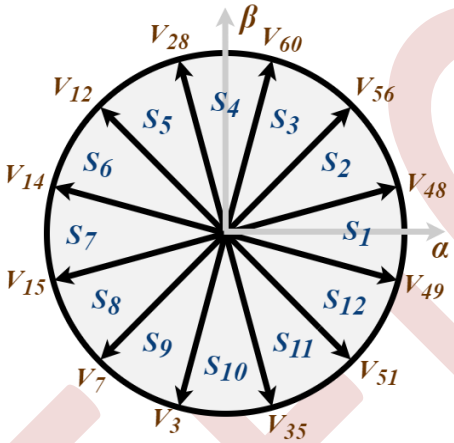


Figure 4. The 12 sectors and large voltage vectors applied in DTC-THR.

III. ENHANCEMENT OF PERFORMANCE FOR CLASSICAL DTC-THR

A. Minimization of Harmonic Currents in Subspace (x-y)

In order to minimize harmonic currents in subspace (x-y), it is remarkable from equation (4) that stator flux is proportional to current in subspace (x-y). Therefore, reducing stator flux in subspace (x-y) can significantly reduce circulating currents. Fig. 2.a shows that the voltage vectors of the groups (G1, G3 and G4) are in the same direction in subspace (α-β), and have a similar effect on the control of flux and torque in the DTC strategy, in particular the vectors of group (G4) produce a dynamic torque response and generate fewer harmonic currents compared to the other groups. It is clear that in subspace (x-y), group (G3) has an opposite effect to groups (G4 and G1) on the influence of stator flux variation (see Fig. 2.b).

Fig. 5 shows the MDTC-THR, whose principle is similar to that proposed in [8-9] for minimizing the harmonic currents of a five-phase induction motor in two steps. To clarify the method, step 1 is based on the outputs of the stator flux, torque and flux position regulators in subspace (α-β), using a modified switching table to select the group (Gi: from i =1 to 12) rather than the voltage vector. The goal of step 1 is to maintain the dynamic response of the system similar to that of classic DTC-THR.

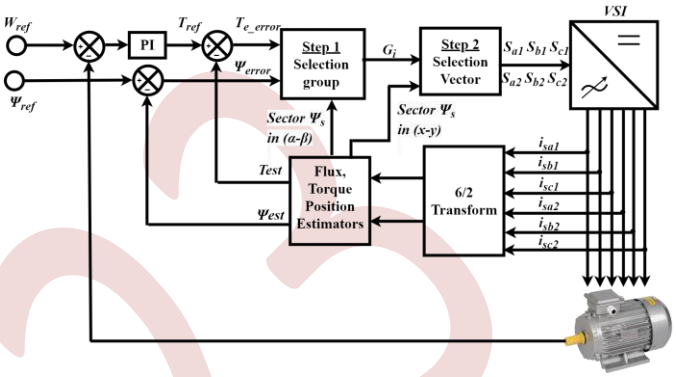


Figure 5. MDTC-THR principle.

Clearly, the voltage vectors divide the (x-y) subspace into semicircles with orthogonal diameters. Furthermore, Step 2 is an extension of Step 1, but it is more dependent on the position of the stator flux in the (x-y) subspace. Fig. 6 illustrates that when the flux is in sector 2 and the selected group includes vectors (V6 and V15), for example, the application of the V15 vector minimizes the amplitude of the stator flux, resulting in a reduction in harmonic currents. Table II provides a summary of the voltage vectors applied for each sector in which the magnetic flux is located in the (x-y) subspace.

TABLE II. MODIFIED SWITCHING TABLE FOR STEP 2

Set group	Sector of flux in subspace (x-y)	Selected appropriate vector
Group 1	7, 8, 9, 10, 11, 12	V48
	1, 2, 3, 4, 5, 6	V57
Group 2	12, 1, 2, 3, 4, 5	V56
	6, 7, 8, 9, 10, 11	V52
Group 3	5, 6, 7, 8, 9, 10	V60
	11, 12, 1, 2, 3, 4	V24
Group 4	10, 11, 12, 1, 2, 3	V28
	4, 5, 6, 7, 8, 9	V44
Group 5	3, 4, 5, 6, 7, 8	V12
	9, 10, 11, 12, 1, 2	V30
Group 6	8, 9, 10, 11, 12, 1	V14
	2, 3, 4, 5, 6, 7	V13
Group 7	1, 2, 3, 4, 5, 6	V15
	7, 8, 9, 10, 11, 12	V6
Group 8	6, 7, 8, 9, 10, 11	V7
	12, 1, 2, 3, 4, 5	V11
Group 9	11, 12, 1, 2, 3, 4	V3
	5, 6, 7, 8, 9, 10	V39
Group 10	4, 5, 6, 7, 8, 9	V35
	10, 11, 12, 1, 2, 3	V19
Group 11	9, 10, 11, 12, 1, 2	V51
	3, 4, 5, 6, 7, 8	V33
Group 12	2, 3, 4, 5, 6, 7	V49
	8, 9, 10, 11, 12, 1	V50

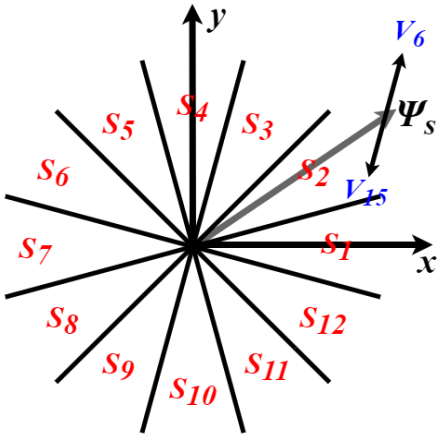


Figure 6. influence of voltage vectors (G3 and G4) on stator flux in step 2.

B. MDTC-THRM Principle

Minimizing torque ripple and steady-state error in DTC control is a key area of research for improving the performance of electric motor control systems. Several papers, in particular in [10], have found that decreasing and increasing torque variations need to be treated differently, especially at medium and high speeds. In this paper, a modified three-level hysteresis torque regulator to significantly reduce the steady-state torque error named (MDTC-THRM).

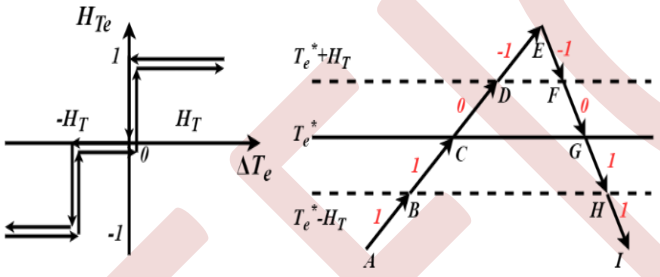


Figure 7. Modified torque hysteresis regulator.

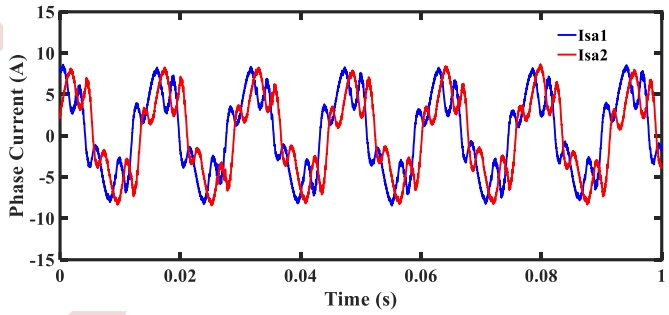
Fig. 7 shows the modifications to the classical three-level torque hysteresis regulator (THR). An applied voltage vector is clearly indicated for each segment. The investigation presented is based on the application of a zero vector in the FG segment to reduce torque with low variation, and an active vector in the GH segment to increase torque with high variation. However, MDTC-THRM, applied to the Dual Star Induction Motor (DSIM), reduces the steady-state torque error, i.e., the average torque value follows its reference under different speed conditions, due to the effect of the active vectors.

IV. Simulation Results

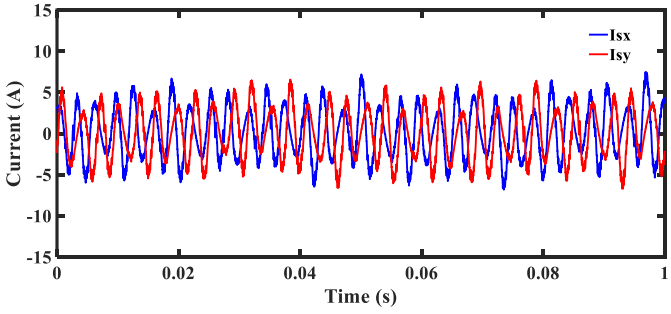
To verify the efficiency of the MDTC-THRM and the MDTC-THR compared with the classical DTC-THR, a simulation using MATLAB/Simulink software was carried out with a sampling time of 5 µs. The parameters of the dual star induction motor (DSIM) are given in Table 3. The torque hysteresis regulator band was set to 10% of nominal torque, i.e., ΔTe = 0.3 Nm, while the stator flux band was $\Delta\Psi_s$ = 0.0125 Wb. Simulation results are presented for machine operating conditions with a speed of 100 rad/s and a load torque of 20 Nm.

Figs. 8-10 present the simulation results of the classical DTC-THR, MDTC-THR, and MDTC-THRM methods for the drive of the dual star induction motor (DSIM) in steady state. It is evident that DTC-THR allows harmonic currents in subspace (x-y) to flow freely through the machine, generating a non-sinusoidal phase current form and resulting in severe 5th-, 7th-, 17th-, and 19th-order current harmonics, as shown in Fig. 8.a, Fig. 8.b, and Fig. 8.e.

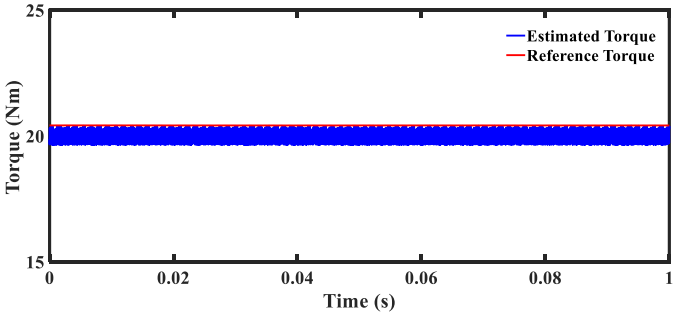
Using the MDTC-THR, harmonic currents are minimized in the (x-y) subspace with total THD reduced from 40.39% to 12.94%, as well as the 5th and 7th harmonic components which are minimized from 37.02%, 13.08% to 4.99%, 1.63%, respectively, thus generating a purely sinusoidal phase current form. In addition, the MDTC-THRM slightly minimizes the total THD from 12.94% to 12.34% compared to the MDTC-THR (see Figs. 8-10.a, Figs. 8-10.b, Figs. 8-10.e).



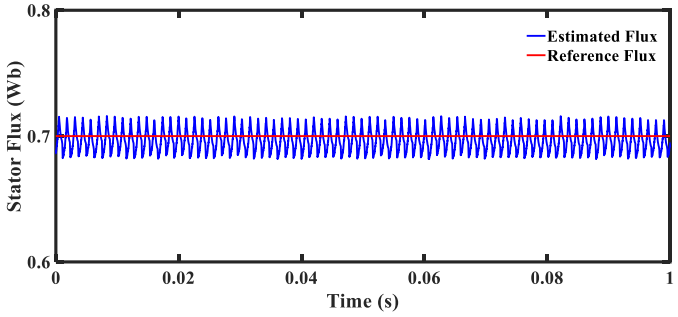
(a)



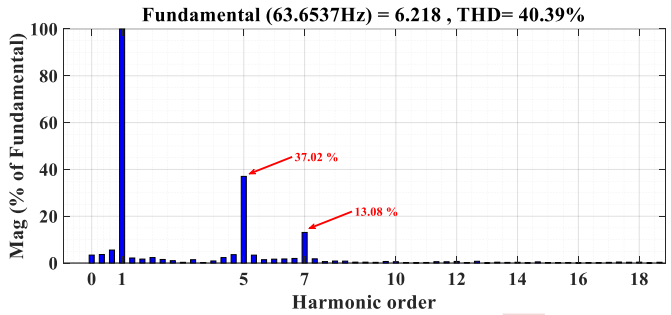
(b)



(c)

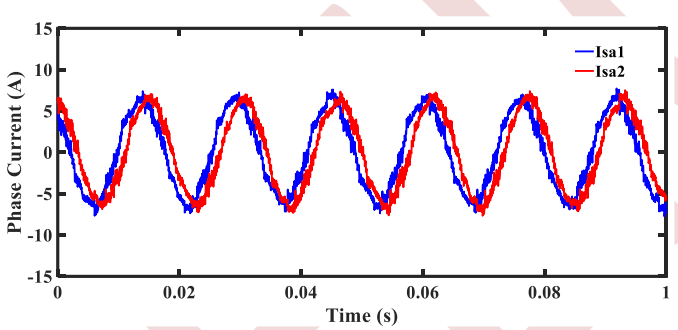


(d)

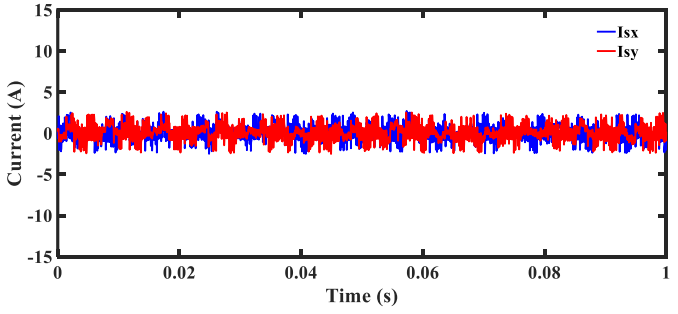


(e)

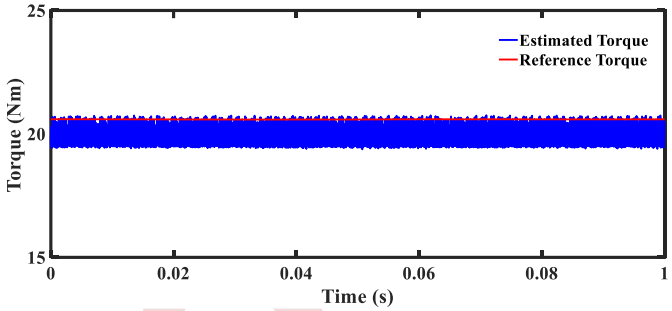
Figure 8. Steady-state performance of classical DTC-THR.



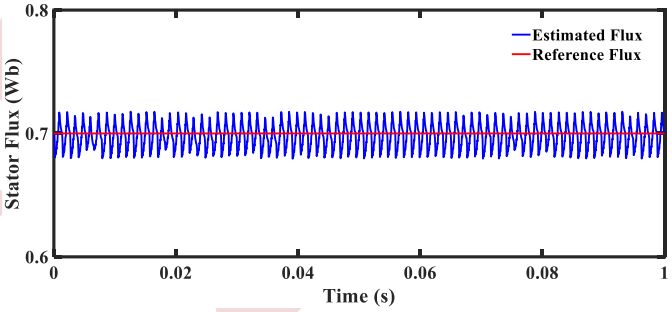
(a)



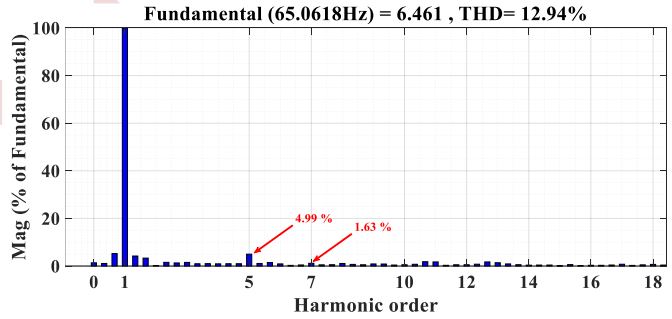
(b)



(c)

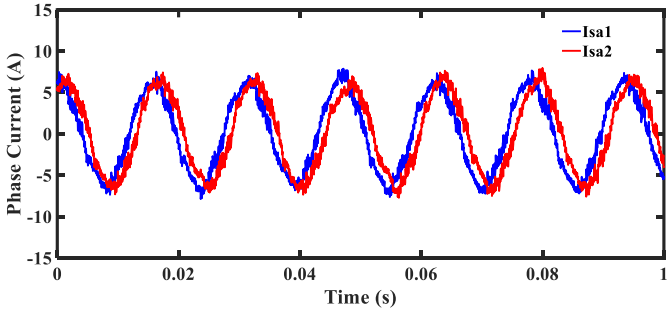


(d)

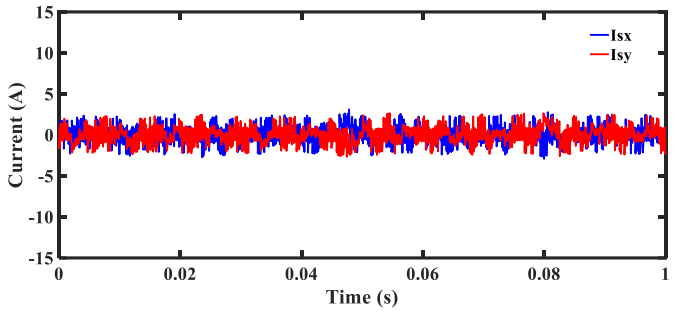


(e)

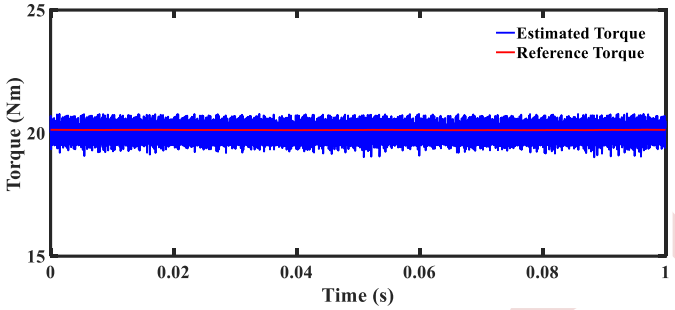
Figure 9. Steady-state performance of MDTC-THR.



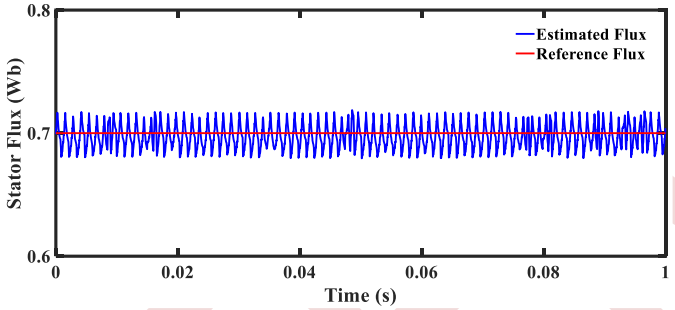
(a)



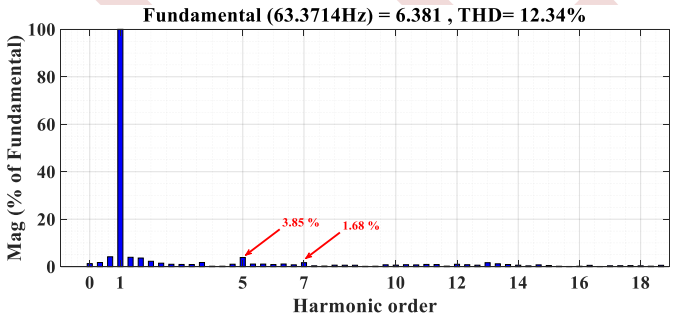
(b)



(c)



(d)



(e)

Figure 10. Steady-state performance of MDTC-THRM.

Figs. 8-10.d show the mean value of stator flux following its reference in the DTC-THR, MDTC-THR and MDTC-THRM methods. However, in DTC-THR and MDTC-THR, a considerable steady-state torque error is observed, as shown in Figs. 8-9.c. In contrast, the MDTC-THRM can reduce the steady-state torque error, and the mean torque value follows its reference (see fig. 10.c).

TABLE III. DUAL STAR INDUCTION MACHINE (DSIM) PARAMETERS

Quantity	magnitude
Rated power	5.5 kW
Rated voltage	220 V
Rated current	6 A
Rated speed	950 rpm
Number of poles	3
Stator and Rotor resistance	2.03 Ω, 3 Ω
Stator and Rotor inductance	0.215 H

V. CONCLUSION

This paper presents the application of direct torque control (DTC) to the drive of the dual star induction motor (DSIM). In order to minimize harmonic current components in the (x-y) subspace, the MDTC-THR based on stator flux control in the (x-y) subspace using two steps significantly reduces circulating currents, which results in a purely sinusoidal current form. Simulation results confirmed that MDTC-THRM based on the modification of the three-level torque hysteresis regulator can significantly reduce the steady-state torque error.

REFERENCES

[1] E. Levi, "Multiphase electric machines for variable-speed applications," IEEE Transactions on industrial electronics, vol. 55, pp. 1893–1909, May 2008.

[2] E. Levi, R. Bojoi, F. Profumo, A. H. Toliyat, S. Williamson, "Multiphase induction motor drives–a technology status review," IET electric power applications, vol. 1, pp. 489–516, Jul 2007.

[3] M. Nesri, K. Nounou, K. Marouani, A. Haouari, M. Benkhoris, "Efficiency improvement of a vector-controlled dual star induction machine drive system," Electrical Engineering, vol. 102, pp. 939–952, Jan 2020.

[4] Y. Zhao, A. Lipo, "Space vector PWM control of dual three-phase induction machine using vector space decomposition," IEEE Transactions on industry applications, vol. 31, pp. 1100–1109, Oct 1995.

[5] J. Xu, M. Odavic, Q. Z. Zhu, Z. Wu, N. Freire, "Switching-table-based direct torque control of dual three-phase PMSMs with closed-loop current harmonics compensation," IEEE Transactions on Power Electronics, vol. 36, pp. 10645–10659, Sep 2021.

[6] J. K. Pandit, M. Aware, R. V. Nemade, E. Levi, "Direct torque control scheme for a six-phase induction motor with reduced torque ripple," IEEE Transactions on Power Electronics, vol. 32, pp. 7118–7129, Sep 2016.

[7] E. Benyoussef, S. Barkat, "Direct torque control based on space vector modulation with balancing strategy of dual star induction motor," Rev. Roum. Sci. Techn. - Sér. Électrotech. Énerg, vol. 67, pp. 15–20, 2022.

[8] Y. Gao, L. Parsa, "Modified direct torque control of five-phase permanent magnet synchronous motor drives," February 2007, Twenty-Second Annual IEEE Applied Power Electronics Conf. APEC, p. 1428-1433.

[9] K. Hoang, Y. Ren, Q. Z. Zho, M. Foster, "Modified switching-table strategy for reduction of current harmonics in direct torque controlled dual-three-phase permanent magnet synchronous machine drives," IET Electric Power Applications, vol. 9, pp. 10–19, 2015.

[10] Q. Z. Zhu, Y. Ren, J. Liu, "Improved torque regulator to reduce steady-state error of torque response for direct torque control of permanent magnet synchronous machine drives," IET Electric Power Applications, vol. 8, pp. 108–116, 2014.

Performances and Lifetime Improvement of Hybrid Electric Vehicles by Using NPC Five-Level Inverter

Hassina Abdellaoui[1], Kaci Ghedamsi[2], Ali Bechouche[3]

[1]*Departement of Electrical Engineering, Mouloud MAMMERI University, Tizi-Ouzou, Algeria*

hassina.abdellaoui@ummto.dz

[2] *LMER Laboratory, University of Bejaia , Bejaia, Algeria*

kaci.ghedamsi@univ-bejaia.dz

[3]*L2CSP Laboratory, Mouloud MAMMERI University, Tizi- Ouzou, Algeria*

ali.bechouche@ummto.dz

Abstract—**Power electronic converters are the main devices in electric vehicle systems. In order to ensure proper operation with high performances during normal and/or faulted operation conditions, multilevel inverters are being preferred over conventional two-level voltage source inverters to feed hybrid electric vehicles (HEV).This paper focuses on performances improvement of HEV by using neutral point clamped (NPC) multilevel inverters.The used traction motor which is the permanent magnet synchronous motor (PMSM) is fed through multilevel inverters (three levels and five levels).Performances of HEV and the total harmonic distortion (THD) are compared. From this comparison, it is possible to show the advantage of using multilevel inverters for increasing the lifetime of HEV. Moreover, its confirmed that the five NPC multilevel inverter present interesting capabilities for improving the lifetime of the system.**

Keywords: NPC multilevel inverter, PMSM, FLC, hybrid source FC/UC.

I. INTRODUCTION

Hybrid Electric Vehicles (HEVs) have been proven to be a promising solution to environmental pollution and fuel savings. The benefit of the solution is generally realized as the amount of fuel consumption saved [1].

Due to their high power density and high efficiency, permanent-magnet synchronous machines (PMSM) are gradually considered as the better choice for traction motors [2, 3].These machines must be designed for high torque/power densities, wide speed range, over load capability, high efficiency at all speeds, low cost and weight, fast acceleration and deceleration, while meeting performance and reliability expectations [4].If an error occurs, the system will be able to repair itself and to continue its job without any interruption. The main point in these systems is reliability feature which is so important. There are many solutions that can increase reliability in these systems [5].In order to obtain a proper operation in faulted mode, and to maintain high performances in normal operation conditions, a multiphase fault tolerant converter should be used to supply the motor.

For power converters, many configurations and topologies have been proposed by researchers to address the inclusion of the most proper converter configuration into the EV drivetrain [5, 6].Nowadays, the neutral point clamped (NPC) inverter is the most commonly used for application in high-power high-voltage (or medium-voltage) drives, because the imposed voltage across each switching power devices is half of the conventional two-level inverter with the same device ratings [7].

In recent years, a great deal of research has been carried out on the development of fault-tolerant AC motor electric drives. For instance, in [6], a reconfiguration system based on bidirectional electronic valves has been designed for three-phase cascaded H-bridge inverters, but the need to have as many sources of voltages of the H-bridge makes of this a bulky and expensive topology. It's his only drawback in applications like EV and HEV.

In [8], theIGBT based cascaded multilevel inverter has been developed and it is interfaced with 20kW 3-phase induction motors that proved to be suitable for HEVs. It is found that the cascaded multilevel inverter reduces harmonics and produces sinusoidal voltages. Cascade inverters are proper converters for medium-voltage high-power applications. However, based on their configurations, they are more complicated than other types of converters and more expensive. Therefore, in diode-clamped converters, there is simplicity in extending the voltage to higher levels. In addition, diode clamped converters are widely used in medium- and low-power applications [9].

The three–level NPC inverter presented in [11] was changed comparing with the original NPC topology by adding active switches to the inverters clamping diodes applied to a three-phase induction motor. However, the proposed solution has some disadvantages, such as additional redundant power devices and increased stress in all devices. Also, power

devices have to withstand higher voltages under a fault-tolerant operation mode.

In this paper a comparison between 3-level, 5-level NPC inverters in HEV will be presented. No additional devices are necessary. Several simulation results of HEV (speed, power, torque, current and THD) will be presented in order to compare between these two levels of inverter and choose the appropriate inverter for HEV.

II. SYSTEM DESCRIPTION

The global system is detailed in Fig. 1. It is composed of two sources: the fuel cell (FC) and the ultracapacitor (UC), which are connected to the DC link via a unidirectional DC/DC converter and a current bidirectional DC/DC converter respectively.

The FC/UC currents are controlled using a PI regulator and the DC link voltage is chosen to be maintained to 500V to supply the traction motor (PMSM) with employing of an NPC multilevel inverter to convert the DC voltage on AC voltage. The energy management of hybrid source based on fuzzy logic is used in the whole vehicle cycle. Simulations are obtained using MATLAB/Simulink under various operating conditions to show the effectiveness of the proposed method. Simulation results show the effectiveness of the proposed scheme in different operating conditions (steady and dynamic states).

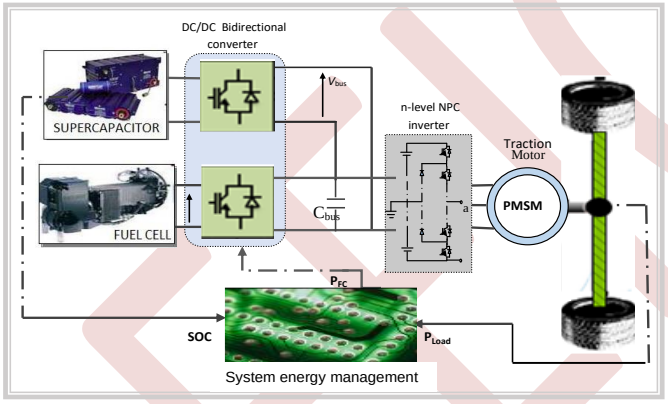


Figure 1.FC/UC hybrid electric vehicle.

III. NPC MULTILEVEL INVERTER MODELING

One of the widely used multilevel structures that have gained a lot of attention is the multilevel diode inverter also known as a neutral-point multilevel inverter [11], which was first introduced by (Nabae, Takahashi et Akagi, 1981) [12].

capacitors in series on the DC bus u_{s1}. The voltage across each capacitor is $v_{ci}=v_{dc}=us_1/n-1$.

As shown in Fig.2, the three-phase NPC n-levels inverter consists of three switching cells, supplied with (n-1) The three commutation circuits of 2(n-1) transistors enable the modulated voltages u_{m1} and u_{m2} to be reversible. As the load current is alternative, the required switches are made of 2(*n-1*) transistors with anti-parallel diodes for each phase.

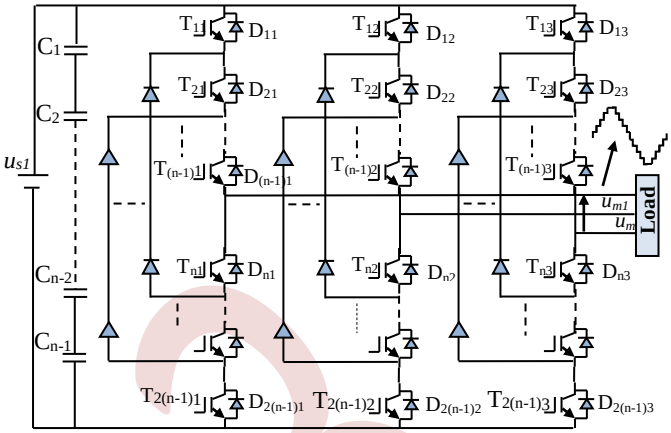


Figure 2.Schematic diagram of the three-phase NPC n-level inverter.

To produce n voltage levels, we need (n-1) capacitors (C_1, C_2, C_3,... C_{n-1}) connected to the DC voltage source u_{s1}. The voltage at the terminals of each capacitor is equal to $u_{s1}/n-1$. Consider the switching circuit c (Fig. 3), the output voltage v_{c0} is equal to [13, 14]:

- full level (u_{s1}), closing the sets {T_{1c}, D_{1c}}, {T_{2c}, D_{2c}}, ... and {$T_{(n-1)c}$, $D_{(n-1)c}$}.
- level (u_{s1}/n-1), closing the sets {T_{2c}, D_{2c}}, {T_{3c}, D_{3c}}, ..., {$T_{(n-1)c}$, $D_{(n-1)c}$}.
- …..
- Level zero, closing the sets {T_{nc}, D_{nc}},{ $T_{(n+1)c}$, $D_{(n+1)c}$},... {$T_{2(n-1)c}$, $D_{2(n-1)c}$}.

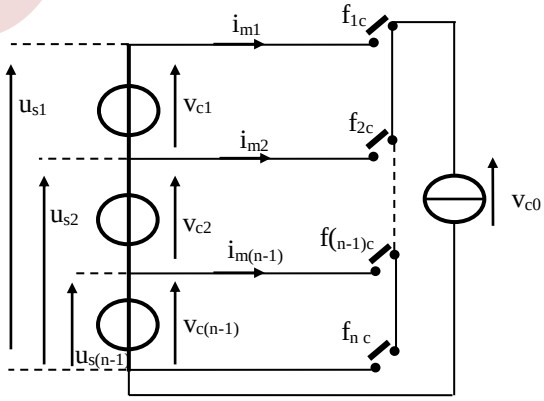


Figure 3. Equivalent diagram of the arm c using the connection functions, $c\epsilon(1,2,3)$.

TABLE I. EQUIVALENT SWITCHING CELL

Control Signals										Connection Functions					V_{c0}
Upper arm					Lower arm										
T_{1c}	T_{2c}	…	$T_{(n-2)c}$	$T_{(n-1)c}$	T_{nc}	$T_{(n+1)c}$	…	$T_{(2(n-1)-1)c}$	$T_{(2(n-1))c}$	f_{1c}	f_{2c}	…	$f_{(n-1)c}$	f_{nc}	
1	1	…	1	1	0	0	…	0	0	1	0	…	0	0	u_{s1}
0	1		1	1	1	0	…	0	0	0	1	…	0	0	$\frac{(n-1)}{n}u_{s1}$
:	:	:	:	:	:	:	:					:			
0	0	…	1	1	1	1	…	0	0	0	0	…	0	0	$\frac{2}{n}u_{s1}$
0	0	…	0	1	1	1	…	1	0	0	0	…	1	0	$\frac{1}{n}u_{s1}$
0	0	…		0	1	1	…	1	1	0	0	…	0	1	0

Therefore, this switching cell is equivalent to a switching cell with ideal switches (f_{rc}), illustrated in Fig. 4. If f_{rc} = 1, the corresponding ideal switch is closed, otherwise (f_{rc} = 0) it is open. r is the line number and c is the column number of the ideal conversion matrix,$r\epsilon\{1\dots,n-1,n\}$ and$c\epsilon\{1,2,3\}$. The last connection function is deduced by:

$$f_{nc} = \overline{f}_{1c}.\overline{f}_{2c}\dots.\overline{f}_{(n-1)c} \quad (1)$$

There are (n) configurations in each arm (c) (Table 1). Considering a continuous conduction mode, the converter equivalent to ideal switches is used to facilitate the modeling and design of the control (Fig. 4). The connection functions $f_{rc}$are defined as follows (Table I):

$$f_{rc} = T_{(r-1)c}T_{rc}\dots.T_{(r+n-2)c} \quad (2)$$

with: $r\epsilon\{1,\dots\dots,n\}$

for: $r\epsilon\{1,\dots\dots,n-1\}$ and$c = \{1,2,3\}$

In order to apply the reference connection functions ($f_{rc\text{-}ref}$), the control transistors signals are calculated by:

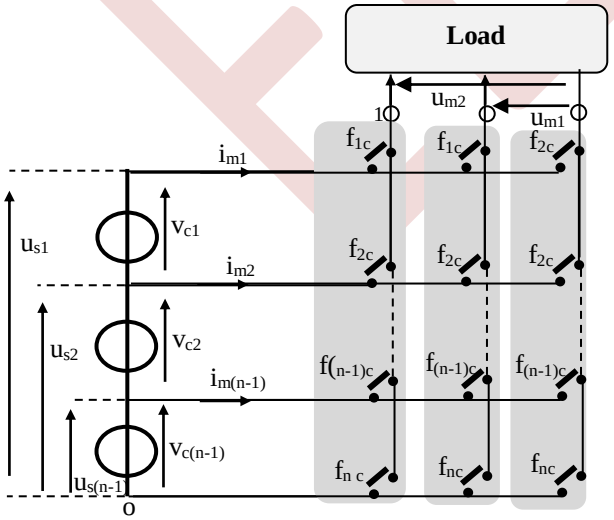


Figure 4.Matrix structure of a three-phase n-level inverter.

$$T_{1c}=f_{1c-ref} \quad (3)$$

$$T_{2c}=f_{1c-ref}+f_{2c-ref}$$

:

$$T_{(n-1)c}=f_{1c-ref}+f_{2c-ref}+\dots+f_{(n-1)c-ref} \quad (4)$$

The general expression can be:

$$T_{(r-1)c} = \sum_{j=1}^{r-1} f_{jc-ref} \quad (5)$$

$$T_{(n+r)c} = \overline{T}_{rc} \quad (6)$$

For an easier analysis of the operation and to establish the mathematical description of the voltage conversion, the equivalent matrix structure shown in Fig.4 is used.

The simple modulated voltages are expressed by:

$$V_{c0} = (V_c - V_0) = \sum_{r=1}^{n} f_{rc}\,.u_{sr} \quad (7)$$

And the compound modulated voltages are:

$$u_{m1} = v_{10} - v_{30} = \sum_{r=1}^{n} (f_{r1} - f_{r3})u_{sr} \quad (8)$$

$$u_{m2} = v_{20} - v_{30} = \sum_{r=1}^{n} (f_{r2} - f_{r3})u_{sr} \quad (9)$$

Each compound modulated voltage is formed by n modulated elementary voltages as follows:

$$u_{mc} = \sum_{r=1}^{n} v_{mrc},\ c\ \epsilon\{1,2\} \quad (10)$$

Elementary modulated voltages are expressed by:

$$u_{mrc} = m_{rc}u_{sr}\ ,\ r\ \epsilon\{1,\dots,n\} \quad (11)$$

with: $m_{rc} = f_{rc} - f_{r3}$

Multilevel voltage results from the combination of n voltages across capacitors (u_{sn}).

By additional switching devices, the number of levels can be increased to a higher level and with these additions the inverter can achieve the sinusoidal voltage with a low harmonic distortion [15].

IV. CONTROL SYSTEM AND REGULATION

A. Control Algorithm PWM N-Level

To generate the control pulses PWM of an N-level converter voltages, N-1 triangular carriers are needed. These carriers have the same frequency (f_c =15 kHz) and the same amplitude.

As shown in Fig.5, the carrier signals ($C_{1,2...n}$) are compared with modulating signal (U_{ref}) to produce the desired output. Each comparison gives 1 if a carrier is greater than or equal to the reference, and 0 otherwise. At the output of the modulator, the sum of results from the comparison is then decoded, and gives the value corresponding to each voltage level.

For an N-level inverter, the amplitude modulation index m_a and the frequency modulation index m_f are defined as follows [16], [17]:

$$m_a = \frac{A_m}{(N-1)A_c}\ ,\ m_f = \frac{f_c}{f_m} \qquad (12)$$

where$A_m$is the amplitude of the modulating signal, $A_c$is the peak-to-peak amplitude of the carrier signal, f_c is the frequency of the carrier signal and $f_m$is the frequency of the modulating signal.

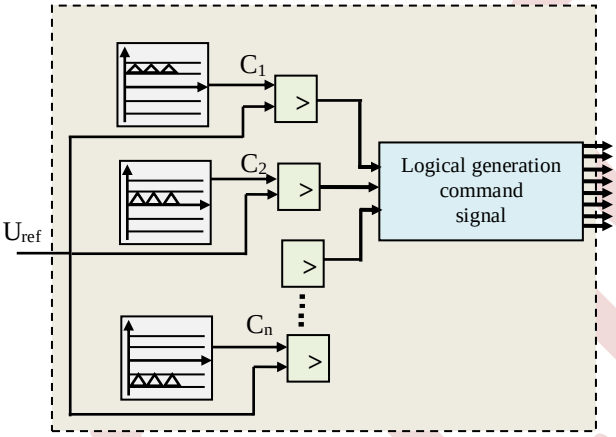


Figure5. Principle of Sine Pulse Width Modulation (SPWM) in multilevel inverters.

B. Speed Regulation of PMSM

For nonlinear systems that have performance limitations with a conventional linear controller, fuzzy logic control is the most commonly used among many types of control systems [18].

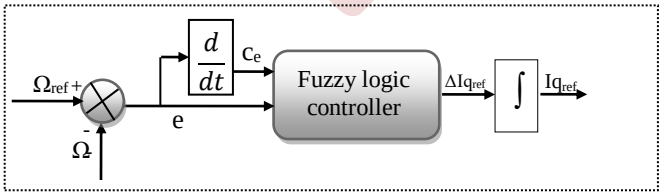


Figure 6.Structure of fuzzy speed controller.

As illustrated in Fig.6, the FLC is a standard structure with inputs of speed error e and change in speed error c_e, and output is changed in q-axis reference current Δiq_{ref}. The membership function is used and the input and output scaling factors are determined. The FLC executes the rule base taking the fuzzy variables e and c_e as the inputs and quantity of Δiq_{ref} as the output which are processed in the defuzzification unit.

In this article, the functions of belonging triangular and trapezoidal type, method of max- min reasoning, defuzzificationmethod are used as they are frequently cited in the literature [18, 20].

The Fig.7 shows the vector control of the traction motor (PMSM).

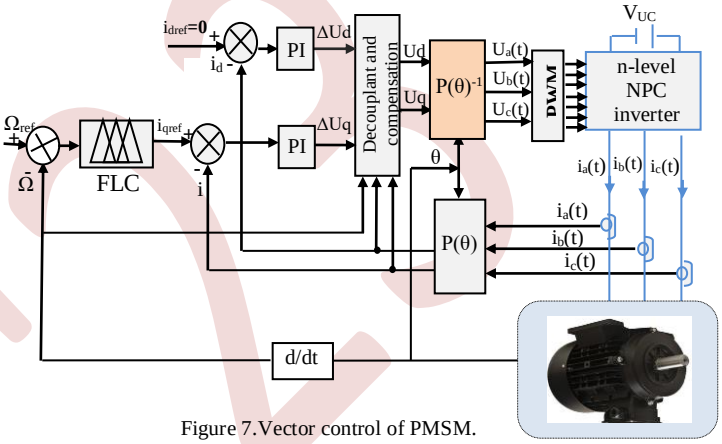


Figure 7.Vector control of PMSM.

TABLE II. PMSM PARAMETERS

Sizes	Values
Power	50 KW
Stator resistance	0.05 Ω
d-axis inductance	0.00065 H
q-axis inductance	0.00065 H
Induced flux magnets	0.2 Wb
Inertia	0.1 kg.m²
Friction	0.005 Nm.s
Number of pairs of poles	03

C. Control of FC/UC hybrid source

In this work, the control of the currents of hybrid source and the DC bus voltage is realized by using PI regulators. As shown in fig.8, the FC power reference P_{FCref} is divided by the FC voltage to obtain the current reference value I_{FCref}.

The FC current I_{FC} is measured and compared with a reference value, and the error signal is processed through a simple proportional integral (PI) controller. On the other hand, the bidirectional buck-boost converter transforms unregulated DC power to a regulated DC bus power in the hybrid configuration. We should control PWM (Pulse Width Modulation) of T_{12} and T_{22} to make DC bus voltage V_{bus}stable and to limit the UC current I_{sc}[19].

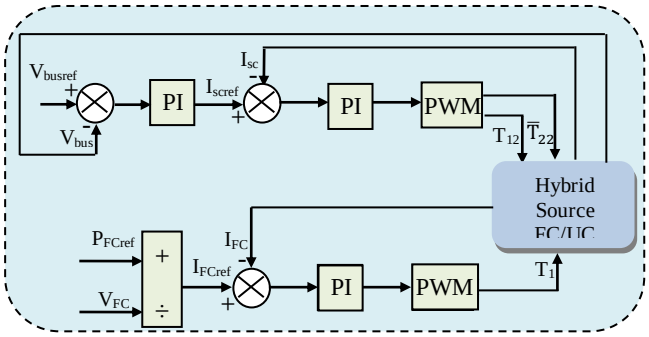


Figure 8. Hybrid source control.

D. Energy management using fuzzy logic

In HEV, the energy management becomes crucial and many works have adopted intelligent techniques, to manage the multiple electrical power sources in hybrid systems. Principally, fuzzy logic is widely employed in many applications [19]. Fuzzy control system is a control method which is applied with great success in various control applications. It is used fornonlinear systems that represent a difficulty in the deriving of its mathematical model.The energy management strategy using fuzzy logic (Fig.9) coordinates all the elements in the system to continuously provide the necessary traction, to keep constant the DC bus voltage (V_{bus}) and maintain the UC SOC (state-of-charge).

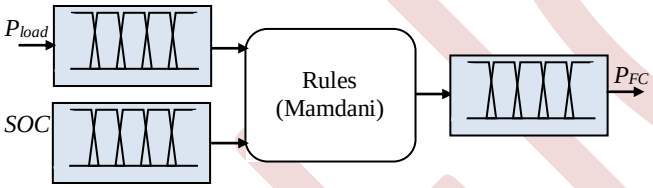


Figure 9.Energy management using fuzzy logic.

The inputs of FLC (Fuzzy logic control) are: The load power (P_{load}) and ultracapacitor SOC, and the output of the FLC is the fuel cell power (P_{FC}).

V. SIMULATION RESULTS AND DISCUSSIONS

To validate the proposed work, simulation studies have been realized by using MATLAB/SIMULINK. The multilevel inverters are loaded with 3-phase 50kW permanent magnet synchronous motor to drive HEV powertrains. The results have been done using the New European Driving Cycle (NDEC), with 120 km/h maximum speed as shown in Fig.10.

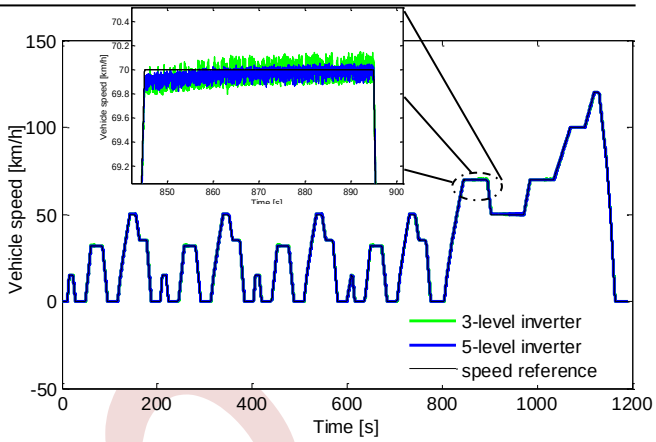


Figure 10.NDEC Drive cycle and speed vehicle.

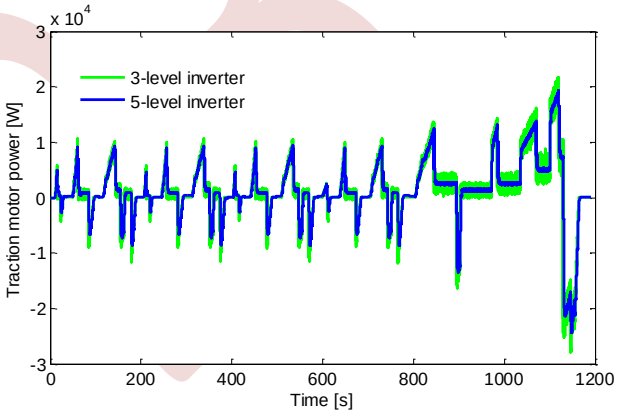


Figure 11.Traction motor power.

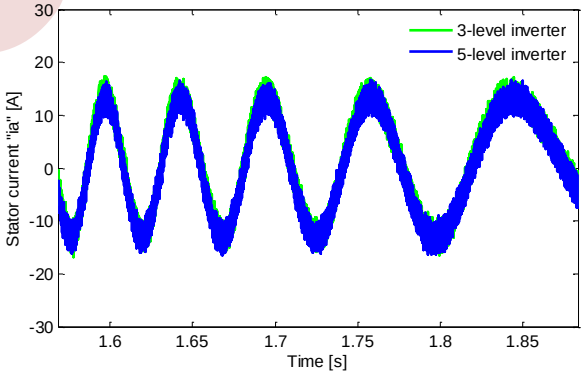


Figure 12.Comparison of stator current "ia".

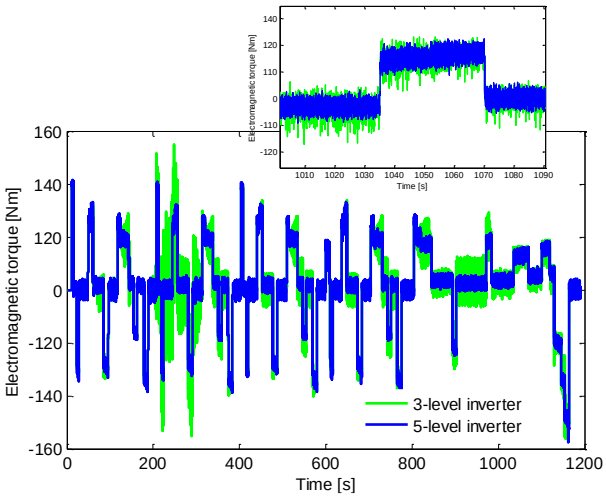


Figure 13.Electromagnetic torque.

The speed of the vehicle follows the reference speed as shown in Fig.10, but with the use of a five-level inverter, the speed is smoother compared to that obtained with the three-level inverter.

The current, the power and the electromagnetic torque of the traction motor are shown respectively in Figs. 11-13. It can be observed that power and electromagnetic torque are more distorted with three-level inverter. But, with five-level inverter, the electrical and mechanical performances of traction motor are significantly improved.

TABLE III. TOTAL HARMONIC DISTORTION (THD) COMPARISON FOR THREE AND FIVE LEVELS.

N-level	**3**	**5**
V_{THD} (%)	59.16	36.05
I_{THD} (%)	17.33	16.73

It is seen that the voltage waveform on result from the fundamental components while other harmonics components prove to be negligible.

The results obtained in Table II show that by increasing the number of levels inverter, the current and voltage harmonic distortion decreases and the lowest THD value is obtained by using the NPC five-level inverter.

VI. CONCLUSION

In this paper, two different levels (3and 5) of NPC inverter to supplythe traction motor (PMSM) in the HEV have been presented. No additional devices have been necessary. The different characteristics of the vehicle waveforms are plotted.

Simulation results show that by increasing the number of levels, the inverter is able to achieve higher AC voltage, producing more voltage steps that will be approaching sinusoidal with minimum harmonic distortion and improve the characteristic of the HEV.

The comparison between 3-level and 5-level NPC inverters in HEV presented in this work shows that the five-level inverter is accurate and effective for improving the performance and the lifetime of the HEV. It is highly useful to get the lowest THD value and able to sustain the operating performance of HEV in fault-tolerant mode.

REFERENCES

[1] F.Zhang, L.Wang and all, "Energy management strategies for hybrid electric vehicles: review, classification, comparison, and outlook", Energies , Vol.*13*, issue 13, June 2020.

[2] H. Wang, Ji Leng, "Summary on development of permanent magnet synchronous motor", The 30th Chinese Control and Decision Conference (2018 CCDC), 2018.

[3] F. J. Anayi and M. M. A. Al Ibraheemi, "Estimation of Rotor Position for Permanent Magnet Synchronous Motor at Standstill Using Sensorless Voltage Control Scheme",in *IEEE/ASME Transactions on Mechatronics*, vol. 25, no. 3, pp. 1612-1621, June 2020.

[4] S. Thangavel, D. Mohanraj and all, "A Comprehensive Review on Electric Vehicle: Battery Management System, Charging Station, Traction Motors," in IEEE Access, vol. 11, pp. 20994-21019, 2023.

[5] M. Fatemeh and K. Abbas, "A preliminary study for improving reliability in hybrid vehicles", Procedia Computer Science, Vol. 42, pp. 308–312, 2014.

[6] B. Pablo and D. Juan, "Fault tolerant reconfiguration system for asymmetric multilevel converters using bi-directional power switches", Industrial Electronics, IEEE Transactions, Vol. 56. pp.1300 – 1306,2008.

[7] P. Je-Jong, K. Tae-Jin and H. Dong-Seok, "Study of neutral point potential variation for three-level NPC inverter under fault condition", Industrial Electronics (IECON). 34th Annual Conference of IEEE, pp. 983 – 988, 2008.

[8] A.K. Verma, P.R. Thakura, K.C. Jana and G. Buja, "Cascaded multilevel inverter for hybrid electric vehicles", India International Conference on Power Electronics (IICPE), pp. 1 – 6, 28-30 Jan 2011.

[9] S. Mahdi, M. Sangdehi, S. Hamidifar and C.Kar. Narayan, "A novel bidirectional DC/AC stacked matrix converter design for electrified vehicle applications", IEEE Transactions on Vehicular Technology, vol. 63, no. 7, September 2014.

[10] T.D. Mai, CH. Yonghua and D.Y. Johan, "Fault-tolerant operation of power converters in phevs coupled by a scott transformer": 38th Annual Conference of the IEEE Industrial Electronics Society (IECON). Montréal, Canada, pp. 4258-4263, 2012.

[11] H.Vahedi, "Modeling, Development and Control of Multilevel Converters for Power System Application". Ph.D thesis, école de technologie supérieure université du Québec, November 11th, 2016.

[12] S.Rezini, Z.E. Azzouz "Contribution of multilevel inverters in improving electrical energy quality : study and analysis". European Journal of Electrical Engineering, Vol 23, no 3, pp. 255-263, 2021.

[13] S. Alepuz, S. BusquetsMonge and all "A Survey on Capacitor Voltage Control in Neutral-Point-Clamped Multilevel Converters". Electronics 2022, 11, 527.

[14] M. Mohammed Haleth, R. Prakash Kumar and J Josaline Priska."Cascaded Multilevel Inverter for Hybrid Electric Vehicles". International Journal of Advanced Research in Electrical, Electronics and Instrumentation Engineering 2016. 5(issue7), pp.116-124**.**

[15] B.Ch. Hina and K.M. Meeta."A Review of Modulation Techniques for Hybrid Multilevel Inverter, Emerging Technology Trends in Electronics", Communication and Networking (ET2ECN), December 2012: 1-7.

[16] A. Mohamed andI. Kenji."Modulation Index Variation Effect on Harmonic Behavior of Fifteen Multilevel Inverter Neutral-Point-Clamped Topology", International Journal of Electrical and Computer Engineering (IJECE) Vol.7, No.4, August 2017: IJECE ,7 (No. 4), August 2017: 1892 –1898.

[17] A. Abdelsalam and C. Shumei. "A fuzzy logic global power management strategy for hybrid electric vehicles based on a permanent magnet electric variable transmission", Energies 2012, 5, 1175-1198.

[18] H.Abdellaoui, "Amélioration des performances des convertisseurs électromécaniques basés sur la machine synchrone à aimants

permanents " . Ph.D. thesis, Université Mouloud Mammeri de Tizi-Ouzou,Algerie, 2020.

[19] T. Iancu . "Mamdani FLC with various implications", 11th International Symposium on Symbolic and Numeric Algorithms for Scientific Computing - SYNASC 09, IEEE Computer Society, Los. 2009.

EEIC'23

Electrical and Mechanical Parameters Identification of a Double Stator Induction Machine

Fatma Lounnas [1], Salah Haddad [2], Lynda Habchi [3], Saliha Benouarab [4]

[1] *Mouloud Mammeri University of Tizi-Ouzou 1st author, Tizi-Ouzou, Algeria*
fat_lounas@yahoo.fr

[2] *Mouloud Mammeri University of Tizi-Ouzou 2nd author, Tizi-Ouzou, Algeria*
hddsalah@yahoo.fr

[3] *Mouloud Mammeri University of Tizi-Ouzou 3rd author, Tizi-Ouzou*, Algeria
lyndahabchi9@gmail.com

[4] *Mouloud Mammeri University of Tizi-Ouzou 4th author, Tizi-Ouzou*, Algeria
benouarabsaliha756gmail.com

***Abstract*— This paper deals with the determination of the electrical and mechanical parameters of a double stator induction machine. The concerned machine is manufactured by the "ELECTRO-INDUSTRIES" company located in Azazga (Tizi-Ouzou). The stator of this machine is composed by two windings which are shifted by an electrical angle α which is equal in our case to (π/3), and a common squirrel cage rotor, the rated power of each stator is 1, 1Kw.To be able to exploit the developed model of this machine we need to identify its parameters. In this work we have used classic identification methods. An experimental test bench has been realized in the laboratory to carry out the different tests related to the identification of the different parameters of this machine.**

Keywords: Double stator induction machine, identification, electrical parameters, mechanical parameters.

NOMENCLATURE

R_{s1}	stator 1 resistance
R_{s2}	stator 2 resistance
R_r	rotor resistance
L_{s1}	stator 1 leakage inductance
L_{s2}	stator 2 leakage inductance
L_r	rotor leakage inductance
L_m	magnetizing inductance
p	pole pairs number
C_{em}	electromagnetic torque
ω_s	angular rotation speed
(v_{ds1}, v_{qs1})	stator 1 voltage (d, q) components
(v_{ds2}, v_{qs2})	stator 2 voltage (d, q)components
(v_{dr}, v_{qr})	rotor voltage (d, q) components
(i_{ds1}, i_{qs1})	stator 1 current (d, q) components
(i_{ds2}, i_{qs2})	stator 2 current (d, q) components
(i_{dr}, i_{qr})	rotor current (d, q) components
$(\varphi_{ds1}, \varphi_{qs1})$	stator 1 flux (d, q) components
$(\varphi_{ds2}, \varphi_{qs2})$	stator 2 flux (d, q) components
$(\varphi_{dr}, \varphi_{qr})$	rotor flux (d, q) components
$\overline{V_S}$	Stator single phase voltage
R_S	per phase stator resistance
X_S	per phase stator leakage reactance
$R_r^{'}$	rotor resistance brought to the stator
X_r	rotor leakage reactance brought to the stator
$\overline{E_1}$	stator magnetizing electromotive force
R_m	resistance representing iron losses
X_m	magnetizing reactance

I. INTRODUCTION

Doubly fed induction generator (DFIG) based wind turbine system has become the most popular configuration for wind energy applications [1]. These have decisive advantages for electricity generation in the market for high-power wind turbines operating at variable speed [2], [3]. The presence of the slip rings and brushes system in the doubly fed induction machine reduces its reliability, its robustness and requires periodic maintenance [4], [5], [6].

To develop a machine capable of surpassing these disadvantages, several studies have been carried out since the beginning of the 20th century. These studies led to the development of a Brushless Doubly fed Induction Machine (BDFIM)) [7], [8], [9].

Brushless doubly fed induction generator (BDFIG), which derives from cascade induction machine technology, has grown in popularity as a wind electric generator due to its advantages over the doubly fed induction generator (DFIG) and the permanent magnet synchronous generator (PMSG), such as the absence of slip rings and brushes and high-cost permanent magnets. Wind energy research is critical for any country's economic development and long-term sustainability [10] [11]. The double stator induction generator is a type of the Brushless doubly fed induction generator (BDFIG), it is composed by two sets of winding in the same stator and a common squirrel cage rotor [12].

Several studies have been realized in order to identify dual stator induction machine parameters. Genetic algorithm is proposed in [13] to identify the induction machine parameter from no load start transients. Standstill, rotating machine and time domain parameter identification methods are presented in comparison [14] for multiphase induction machines parameters identification with reasonable good agreement. A new optimal method to identify the parameters of the two stator winding induction machines [15] using only industrial measurement equipment (Voltmeter, Ampere-meter, Power – meter) from standard tests (no load and two phase short circuit) is proposed in [16].

Many works have been developed to control this type of machine. Active and Reactive Power Control of a Dual Stator Induction Machine (DSIM) using PI Controllers for wind energy conversion is presented in [17], [18]. Sensorless Control with Adaptive Speed Observer Using Power Winding Information for Dual-Stator Winding Induction Starter/Generator is studied in [19].

In this paper we propose to use theoretical and experimental tests to identify electrical and mechanical parameters of a double stator induction generator.

The paper is organized as follows: Section 2: description of the double stator induction generator, Section 3: Modeling of the dual stator induction generator, Section 4: identification of the parameters of double stator induction machines, Section 5: conclusions.

II. DESCRIPTION OF THE DOUBLE STATOR INDUCTION GENERATOR

The name double stator induction machine is due to the fact that the stator contains two windings. It's also called a double-star induction machine when the windings or the two stators are both star connected. The rotor is a squirrel cage one, identical to that of a conventional induction machine. The angular displacement between the two stators is equal to (π/3) and the rated power for each stator is equal to 1,1 kW.

Fig 1. shows a photo representing the double-stator asynchronous machine manufactured by the Algerian company '' ELECTRO-INDUSTRIES'' located in Azazga. This type of machine is not commercialized by this company but it is especially realized for research needs.



Figure 1. Photo of a Double Stator Induction Machine

IV. MODELING OF THE DOUBLE STATOR INDUCTION GENERATOR

The dual stator induction machine "DSIM" is composed of two fixed three-phase stator windings denoted as stator 1 and stator 2 shifted by an electrical angle α, and a common squirrel cage mobile rotor [17], [7], [12], as shown in Fig 2.

The mathematical model of the DSIM derives from PARK's theory in order to simplify the differential equations [17], [7], [12].

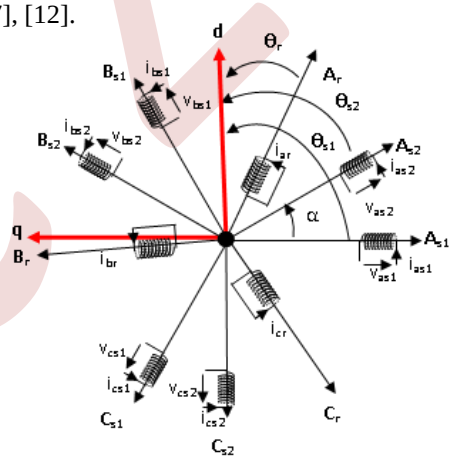


Figure 2. Electrical diagram of the windings of a Double Stator Induction Machine

Voltage and flux equations characterizing the double stator induction generator model in an arbitrary reference frame are given by:

A. *Stator 1*

$$\begin{cases} v_{ds1} = R_{s1}.i_{ds1} + \dfrac{d\varphi_{ds1}}{dt} - \dfrac{d\theta_{s1}}{dt}.\varphi_{qs1} \\ v_{qs1} = R_{s1}.i_{qs1} + \dfrac{d\varphi_{qs1}}{dt} + \dfrac{d\theta_{s1}}{dt}.\varphi_{ds1} \end{cases} \quad (1)$$

$$\begin{cases} \varphi_{ds1} = (L_{s1} + L_m) i_{ds1} + L_m (i_{ds2} + i_{dr}) \\ \varphi_{qs1} = (L_{s1} + L_m) i_{qs1} + L_m (i_{qs2} + i_{qr}) \end{cases} \quad (2)$$

B. Stator 2

$$\begin{cases} v_{ds2}=R_{s2}.i_{ds2}+\dfrac{d\varphi_{ds2}}{dt}-\dfrac{d\theta_{s2}}{dt}.\varphi_{qs2} \\ v_{qs2}=R_{s2}.i_{qs2}+\dfrac{d\varphi_{qs2}}{dt}+\dfrac{d\theta_{s2}}{dt}.\varphi_{ds2} \end{cases} \quad (3)$$

$$\begin{cases} \varphi_{ds2}=(L_{s2}+L_m)i_{ds2}+L_m(i_{ds1}+i_{dr}) \\ \varphi_{qs2}=(L_{s2}+L_m)i_{qs2}+L_m(i_{qs1}+i_{qr}) \end{cases} \quad (4)$$

C. Rotor

$$\begin{cases} v_{dr}=R_r.i_{dr}+\dfrac{d\varphi_{dr}}{dt}-\dfrac{d\theta_r}{dt}\varphi_{qr}=0 \\ v_{qr}=R_r.i_{qr}+\dfrac{d\varphi_{qr}}{dt}+\dfrac{d\theta_r}{dt}.\varphi_{dr}=0 \end{cases} \quad (5)$$

$$\begin{cases} \varphi_{dr}=(L_r+L_m)i_{dr}+L_m(i_{ds1}+i_{ds2}) \\ \varphi_{qr}=(L_r+L_m)i_{qr}+L_m(i_{qs1}+i_{qs2}) \end{cases} \quad (6)$$

The electromagnetic torque equation is given by:

$$C_{em}=p\frac{L_m}{L_r+L_m}\left[(i_{qs1}+i_{qs2})\,j_{dr}-(i_{ds1}+i_{ds2})\,j_{qr}\right] \quad (7)$$

V. Identification of the Double Stator Induction Machine Parameters

The exploitation of the developed model of the machine requires the knowledge of its electrical and mechanical parameters. In the following we will identify these parameters using an analytical method based on general mechanical and electrical equations and standard tests.

This identification method is based on the equivalent diagram given in Fig 3 and uses two tests: a no-load test and a locked-rotor or short-circuit test.

The results of these experimental tests require the realization of an experimental test bench which is represented by Fig. 4.

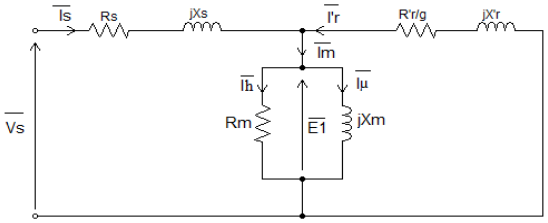


Figure 3. Equivalent phase circuit of DSIM

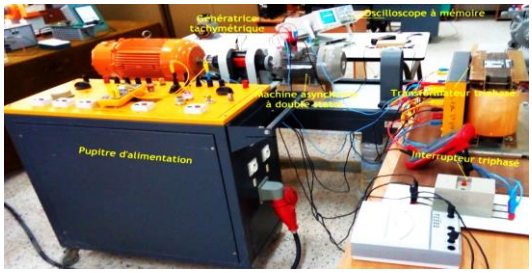


Figure 4. Experimental test bench

A. Electrical parameters identification

1) Stator resistance measurement

The Stator resistance is measured using a method, in which one phase of the stator winding is supplied by a DC voltage source, as illustrated in Fig 5.

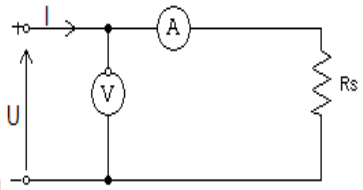


Figure 5. Stator resistance measurement scheme

This test requires a voltmeter and an amperemeter to record the various voltage and current measurements that characterize resistance using Ohm's law:

$$R_S=\frac{V}{I} \quad (8)$$

The results of this test are given in Table 1.

TABLE I. Stator Resistance Measurement Result

V (V)	57,5	40,5	21
I (A)	2,5	1,74	0,9
R_s [Ω]	7.73		

The stator resistance is the mean of these measured resistances.

2) Locked rotor experiment

In this test, the rotor is mechanically locked to prevent it rotating (g=1). The stator is supplied by a reduced AC voltage so as not to exceed the rated current, and the following measurements are taken:

- Supply voltage.
- Stator current.
- Absorbed power.

The locked rotor test gave the results shown in Table 2:

TABLE II. Locked Rotor Test Result

Vcc (V)	40
Icc (A)	2,65
Pcc (W)	247,5

The elimination of the magnetizing branch is due to the fact that the impedance of the rotor branch is very low compared to the magnetizing impedance (g=1). As a result, the current flowing through the magnetizing branch is negligible compared with the rotor current, and the magnetizing branch can be considered as an open circuit (Fig 6).

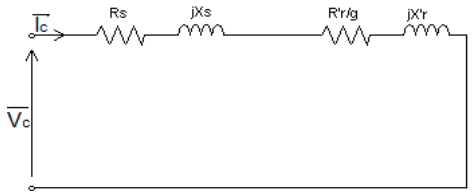


Figure 6. Equivalent locked-rotor scheme

a) Calculation of rotor resistance

The locked rotor electrical power absorbed P_{CC} represents the sum of the stator Joule losses P_{Js} and the rotor Joule losses

$$P_{cc} = 3R_s.I_{cc}^2 + 3R_r^{'}.I_{cc}^2$$
$$P_{cc} = 3I_{cc}^2.\left(R_s + R_r^{'}\right) \quad (9)$$

Then

$$R_r^{'} = \frac{P_{cc}}{3I_{cc}^2} - R_s \quad (10)$$

b) Calculation of stator and rotor inductances

The equivalent impedance is:

$$Z_{cc} = \frac{\overline{V_{cc}}}{\overline{I_{cc}}} \quad (11)$$

With

$$Z_{cc} = \left(R_s + R_r^{'}\right) + j\left(X_s + X_r^{'}\right) \quad (12)$$

We note

$$R_{cc} = R_s + R_r^{'} \quad (13)$$
$$R_{cc} = R_s + R_r^{'} \quad (14)$$
$$X_{cc} = X_s + X_r^{'} \quad (15)$$
$$V_{cc} = \sqrt{\left(R_s + R_r^{'}\right)^2 + \left(X_s + X_r^{'}\right)^2}.I_{cc} \quad (16)$$

Then

$$X_{cc} = \sqrt{\left(\frac{V_{cc}}{I_{cc}}\right)^2 - R_{cc}^{\ 2}} \quad (17)$$

For small motors, it is assumed that:

$$X_s = X_r^{'} = \frac{1}{2}.X_{cc} \quad (18)$$

$$X_s = L_s.\omega$$
$$X_r^{'} = L_r^{'}.\omega \quad (19)$$

We determine the leakage inductances as follows:

$$L_s = \frac{X_s}{\omega}$$
$$L_r^{'} = \frac{X_r^{'}}{\omega} \quad (20)$$

3) No load experiment

This test is performed when the load is equal to zero, so the machine rotates at a constant speed approaching the synchronous speed.

This test allows us to measure the machine's no-load losses. To do this, we need to measure:

- No load supply voltage V_0.
- No load absorbed current I_0.
- No load absorbed power P_0 .

The results of the no load experiment are shown in Table 3.

TABLE III. NO LOAD TEST RESULT

I_0(A)	0,4	0,5	0,6	0,9	1,2	1,65
P_0(w)	30	36	45	75	120	174
V_0(V)	60	80	100	140	180	220

The slip g_0 obtained at no load condition is usually very low. However, the fictive resistance $\frac{R_r^{'}}{g}$ is very high compared to the other impedances and therefore the current $I_r^{'}$ is insignificant compared to the current I_0. The rotor branch can be considered as an open circuit, resulting in the diagram shown in Fig 7

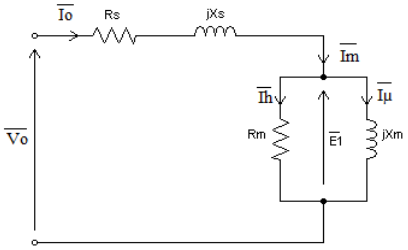


Figure 7. No load equivalent scheme

a) Determination of iron and mechanical losses

The electrical power absorbed at no load condition is the sum of stator Joule and iron losses and mechanical losses, as follows:

$$P_0 = 3R_s.I_0^2 + P_{fs} + P_{méc} \quad (21)$$

In this test, we start the motor by increasing the voltage from 0 to its rated value (220 V) and note the value of the speed of rotation.

We decrease the voltage and read the voltage, current and power each time, while checking the speed and ensuring that it has not decreased.

We continue to reduce the voltage until the rotation speed drops significantly.

Then we plot $P_0 - 3R_s.I_0^2$ as a function of V_0^2 which should be a straight line. Extrapolating this straight line to the

origin gives the value of the mechanical losses, which are assumed to be constant when the speed is kept constant.

The iron losses are deduced at the rated point as follows:

$P_{fs}=P_0-3R_sI_0^2-P_{méc}$ at the rated point (V_0 =220V).

These losses are considered constant for nominal operating condition. The iron losses are the difference at the nominal point between $P_0-3R_sI_{S0}^2$ and the mechanical losses (Fig 8).

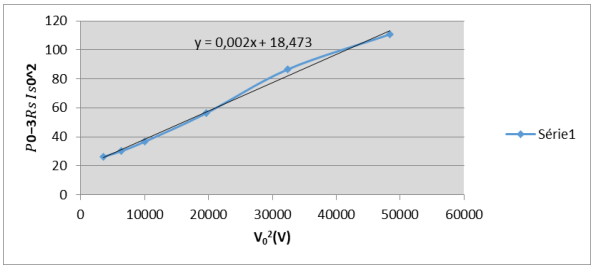


Figure 8. Characteristic of the sum of iron and mechanical losses as a function of V_0^2

After extrapolation to the origin, we find the value of the mechanical losses (18,47W), the iron losses are deduced by subtraction, at point V=220V, so P_{fer}=61,65W.

b) Determination of R_m *and* L_m

The following electrical equation can be derived from the equivalent no load scheme:

$$\overline{V_0}=(R_s+jX_s)\overline{I_0}+\overline{E_1} \quad (22)$$

Then

$$\overline{E_1}=\overline{V_0}-(R_s+jX_s)\overline{I_0} \quad (23)$$

With

$$\overline{E_1}=R_m\overline{I_h}=X_m\overline{I_\mu} \quad (24)$$

$$P_0=3.V_0.I_0.\cos(\varphi_0) \quad (25)$$

$$\cos(\varphi_0)=\frac{P_0}{3V_0I_0} \quad (26)$$

$$\sin(j_0)=\sqrt{1-\cos(\varphi_0)^2} \quad (27)$$

$$\overline{I_h}=\overline{I_0}.\cos(\varphi_0) \quad (28)$$

$$\overline{I_\mu}=\overline{I_0}.\sin(\varphi_0) \quad (29)$$

- *Magnetizing resistance* R_m

$$R_m=\frac{\overline{E_1}}{\overline{I_h}} \quad (30)$$

- *Magnetizing inductance* L_m

$$X_m=\frac{\overline{E_1}}{\overline{I_m}} \quad (31)$$

$$X_m=L_m.\omega \quad (32)$$

Then

$$L_m=\frac{X_m}{\omega} \quad (33)$$

B. Mechanical parameters identification

The identification of the electrical parameters only is not sufficient to make a correct study for the electrical machine, for this reason, an identification of the mechanical parameters is necessary.

Knowing the mechanical parameters enables us to determine the dynamics of the rotating speed according to the following equation of motion:

$$C_e-C_r=J\frac{d\Omega}{dt}+K_f\Omega \quad (34)$$

The mechanical time constant is identified using the deceleration test method.

3) Deceleration method experiment

The deceleration method experiment consists of supplying the machine at no load with the rated voltage and suddenly switching off the supply and recording the rotation speed transient using a memory oscilloscope (Fig 9.).

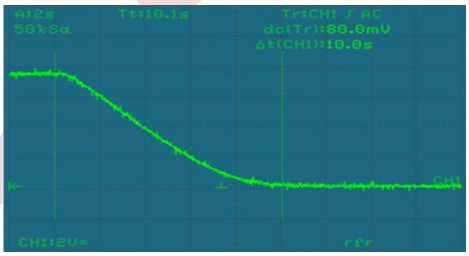


Figure 9. Characteristic of the sum of iron and mechanical losses as a function of V_{02}

a) Measurement of the coefficient of friction

From $P_0=3.R_SI_0^2+P_{fs}+P_{méc}$, we can deduce the mechanical losses.

$$P_{méc}=P_{abs}-P_{js}-P_f \quad (35)$$

$$K_f=\frac{P_{méc}}{\Omega^2} \quad (36)$$

b) Moment of inertia measurement

The solution of the equation of motion is:

$$\Omega(t)=\Omega_{r0}.\exp\left(-\frac{t}{\tau_m}\right) \quad (37)$$

With

$$\tau_m=\frac{J}{K_f} \quad (38)$$

Where τ_m is mechanical time constant

Then

$$J=K_f.\tau_m \quad (39)$$

The two stators of the machine are identical then the identification tests were carried out on a single stator.

The results of the identification of the double stator induction machine parameters are summarized in following table.

TABLE IV. RESULTS OF PARAMETERS IDENTIFICATION

$R_{s1}= R_{s2}$	7,73 [Ω]
R'_r	R'_r= 4,01 [Ω]
$L_{s1}= L_{s2}$	0,015[H]
L_m	0,4 [H]
R_m	777,76 [Ω]
L'_r	0,015[H]
K_f	0,00075 [Nm.s/rad]
J	0,0075 [Kg.m^2]

VI. CONCLUSION

In this paper parameters estimation of a dual stator induction machine has been presented. In order to study this type of machine using its mathematical model, it is necessary to identify its parameters. An experimental test bench has been built for this purpose and experimental tests have been realized. The results obtained from these experimental tests and the equivalent diagram of this machine have been used to determine its electrical and mechanical parameters.

As a future work, other methods of identification could be used in order to confirm the results obtained in this present paper.

ACKNOWLEDGMENT

I would like to thank my colleagues Madjid Si Brahim and Rabah Rouas for their contributions during the experimental tests.

REFERENCES

[1] M. Cheng, Y. Z. S. Du, and T. A. Lipo, "Fault tolerant control for power side current sensor in wind energy conversion system with cascaded brushless DFIG," National Natural Science Foundation of China, 978-1-5090-4281-4/17/$31.00 ©2017 IEEE.

[2] I. A. Gowaid, A. S. Abdel-Khalik, A. M. Massoud and S. Ahmed "Ride-Through Capability of Grid-Connected Brushless Cascade DFIG Wind Turbines in Faulty Grid Conditions-A Comparative Study," IEEE Transactions on Sustainable Energy, vol. 4, no. 4, Octobre 2013.

[3] T. Ghennam, "Supervision d'une ferme éolienne pour son integration dans la gestion d'un réseau électrique, Apports des onvertisseurs multi niveaux au réglage des éoliennes à base de machine asynchrone à double alimentation,'' Thèse de doctorat de l'École Centrale de Lille et l'École Militaire Polytechnique d'Alger, Septembre 2011.

[4] R. Cardenas, R. Pena, P. Wheeler, J. Clare, A. Munoz, and A. Sureda, *"*Control of a wind generation system based on a Brushless Doubly-Fed Induction generator fed by a matrix converter,*''* Electric Power Systems Research "ELSEVIER'', June 2013.

[5] Z. Tir, H. Rajeai, and R. Abdessemed, "Analysis and Vector Control of a Cascaded Doubly Fed Induction Generator in Wind Energy Applications,'' The International Conference on Electrical Engineering, Electronic and Automatic :(ICEEA10), November 2010, Abderrahmane Mira University, Bejaia.

[6] A.Maafa, D.Aouzellag, K.Ghedamsi, S. Chekkal and R.Abdessemed, "Influence du décalage des stators sur les harmoniques dans une cascade de deux machines asynchrones,'' The International Conference on Electronics & Oil: From Theory to Applications, March 05-06, 2013, Ouargla, Algeria.

[7] **F. Lounas,** R. Kachenoura, M. Si Brahim, S. Haddad and N. Benamrouche, "Electrical and Mechanical Behavior Study of a Cascaded Doubly Fed Induction Machine,'' in the International Conference on Electronics and Electrical Engineering (IC3E'18), November 12-13, 2018, University of Bouira, Algeria.

[8] C. Henrique, S. Vasconcelos, A. C. Ferreira and R. M. Stephan, "Stator Flux Orientation Control of the Cascaded Doubly Fed Induction Machine,'' IEEE, 24th International Symposium on Industrial Electronics (ISIE), 3-5 June 2015.

[9] D. B. Lima, F. Lessa, A. C. Ferreira and R. M. Stephan, "Steady State Analysis of the Doubly Fed Cascaded Induction Machine," 'INDUSCON 2010', 9th IEEE/IAS International Conference on Industry Applications.

[10] A Mesbahi, M Khafallah, A Saad, and A Nouaiti, "Emulator design for a small wind turbine driving a self-excited induction generator," 2017 international Conference on Electrical and Information Technologies (ICEIT). IEEE, 2017.

[11] H. Polinder, J.A Ferreira, B.B Jensen, A.B Abrahamsen, K. Atallah, R.A McMahon, "Trends in wind turbine generator systems," EEE Journal of emerging and selected topics in power electronics, 2013, vol. 1, no. 3, pp. 174–185.

[12] F. Lounas, S. Haddad and N. Benamrouche, "Active and Reactive Power Control of a Dual Stator Induction Machine (DSIM) using PI Controllers," Indonesian Journal of Electrical Engineering and Informatics (IJEEI), vol. 7 (2019), no. 4, pp. 664 – 676; DOI: 10.11591/ijeei. v7i4.1424.

[13] A. Raie, V. Raschtchi, "Accurate identification of parameters, in winding function model of induction motor, using genetic algorithm", SICE Proc. 2002 Aug. 5-7, Osaka, pp. 2430-2434.

[14] J. A. Riveros Yepes, A. G. Barrero, F. Doval-Gandoy, J. Bogado, B. Lopez, O. Jones, M. and E. Levi, "Parameter Identification of Multiphase Induction Machines with Distributed Windings - Part 2," Time-Domain Techniques, IEEE Trans. on Energy Conversion, Vol. 27, N4. 4, December 2012, pp. 1067-1077.

[15] L.N Tutelea, S.I. Deaconu, I. Boldea,and N. Budișan, "Design, control and 2D-FEM validation for an double stator winding induction generator," *IECON 2013-39th Annual Conference of the IEEE Industrial Electronics Society*. IEEE, 2013.

[16] L.N Tutelea, I. Boldea, S.I. Deaconu, "Parameter optimal identification of dual three phase stator winding induction machine," 2014 International Conference on Optimization of Electrical and Electronic Equipment (OPTIM). IEEE, 2014.

[17] F. Lounnas, "Contribution à la modélisation et à la commande d'un système de conversion de l'énergie éolienne à base d'une machine asynchrone à double stator," Thèse de doctorat en Sciences, Université Mouloud Mammeri de Tizi Ouzou, 2021.

[18] Lounas, Fatma, Salah Haddad, and Nacereddine Benamrouche. "Active and reactive power control of a dual stator induction generator for wind energy conversion." *International Journal of Modelling, Identification and Control* 34.3 (2020): 235-244.

[19] Liu, Haozhe, et al. "Sensorless Control With Adaptive Speed Observer Using Power Winding Information for Dual-Stator Winding Induction Starter/Generator." *IEEE ransactions on Industrial Electronics* (2023).

Study of the parameters influencing the performance of a self-excited induction generator

Belynda Fares [1], Radia Abdelli [2], Ahcene Bouzida [3]

[1] *Department of Electrical Engineering* University of Bejaia, Bejaia, Algeria
belynda.fares@univ-bejaia.dz
[2] *Department of Electrical Engineering* University of Bejaia, Bejaia, Algeria
radia.abdelli@univ-bejaia.dz
[3] *Department of Electrical Engineering* University of Bouira, Bouira, Algeria
a.bouzida@univ-bouira.dz

***Abstract*— Generating electricity is a challenge for future generations, and the focus is presently on renewable energy, particularly wind power. Wind power systems in remote regions employ self-excited induction generators, which are an excellent choice for this type of application. Many criteria impact the performance of self-excited induction generators, including rotor speed, capacitance value, and driven load value. In this paper, we will look at how changing these parameters affects the output quantities of the self-excited generator.**

***Keywords:* self-excitation, finite elements, induction generator.**

I. INTRODUCTION

Demand for electrical energy is rising steadily, and to date, energy production relies mainly on traditional sources, with 86% of the energy produced from fossil fuels [1,2]. The indiscriminate use of fossil fuels has increased global greenhouse gas emissions by three-quarters. These greenhouse gas emissions contribute to global warming and are the primary barrier for future generations [3] not to mention additional detrimental impacts like acid rain and smog. The adverse consequences and depletion of traditional resources have led to a growing interest in renewable energy resources such as wind, solar, tidal, and micro-hydro power [4]. The main factors driving the use of this type of energy are the many advantages they offer: inexhaustible, clean and environmentally friendly, sustainable over time, and reliable [5]. Among renewable energy sources, wind power is the most promising because of its clean nature, wide availability, and ease of procurement [6,7]. In a wind energy conversion chain, the wind turbine converts the kinetic energy captured in the wind into electrical energy using a generator [8]. The three-phase induction generator is one of the best types of generator to use with wind turbines for autonomous power generation; it is a relatively inexpensive, robust, simple construction; with good reliability; and high efficiency [9,10]. The induction generators used in isolated wind energy systems are called self-excited induction generators (SEIGs) [11]. The operation of a self-excited induction generator requires the presence of reactive power. Which, in the case of stand-alone applications is provided by a capacitor bank. The self-excitation phenomenon occurs when we connect a capacitor bank between the machine terminals to produce the required reactive power. Combined with the presence of a residual field in the rotor, we'll see the birth of a small voltage across the stator terminals, which will increase the magnetism of the rotor due to the capacitive current flow that will increase the voltage again. The process of buildup continues until saturation. The capacitance value determines the voltage generated for a certain rotor speed [11,12, 13]. The value of the voltage produced by a self-excited generator is affected by several quantities. In this work, we propose to study the influence of the parameters affecting the output voltage of a self-excited induction generator. For this fact, a model of the induction machine was carried out using the finite element technique with time step, then the phenomenon of self-excitation is studied by varying several parameters such as the value of the excitation capacity, the speed of rotation of the rotor and also the load value. All results are presented and validated by simulation.

II. SELF -EXCITATION PHENOMENON AND MAGNETIZATION CURVE

If the induction motor rotor rotates faster than the synchronous speed, it can operate in generator mode and create energy. Equation (1) expresses the synchronous speed:

$$n_s = \frac{120\,f}{P} \tag{1}$$

f is the frequency Hz.
p is the number of poles.
The slip of a machine is the difference between the synchronous speed and the rotor speed, expressed by the following equation :

$$s = \frac{n_s - n}{n_s} \quad (2)$$

n is the mechanical speed of the rotor.

As the rotor speed exceeds the synchronous speed, this causes a negative slip, which means that the induction machine will produce a negative conjugate, thus operating as a generator [14]. In the case of stand-alone operation, the connection of a capacitor bank to the terminals of the induction generator is necessary, as shown in Figure 1, to meet its reactive power requirement. Note that in practical diagrams, it is advisable to connect each excitation capacitor to each phase of the motor winding, either Δ-Δ or Y-Y [15].

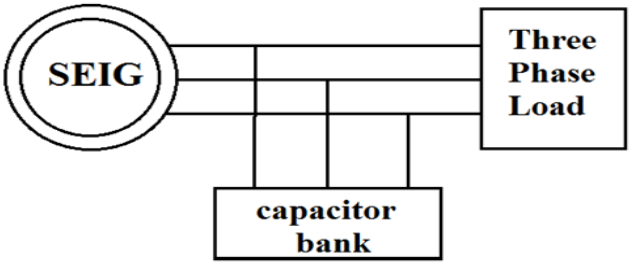


Figure 1. Capacitor self-excited induction generator.

Induction generators used in isolated wind energy systems are called self-excited induction generators (SEIGs). The self-excitation phenomenon occurs on the one hand if we ensure the presence of reactive power, which is supplied by the capacitor bank, and on the other if the machine has a so-called residual magnetic field. If there is no appropriate value of residual magnetism, the self-excitation process will not take place [16][17]. When the rotor of an induction machine rotates at the required speed, the residual magnetism present in the rotor iron generates a small voltage across the stator. This voltage produces a capacitor current. This current generates a flux that assists the residual flux, resulting in a greater one and, as a result, higher voltage created across the stator. This voltage causes a current to flow through the capacitor bank, resulting in the generation of a voltage. This cumulative process of voltage growth continues until the induction generator's saturation curve crosses the capacitor's charging line, as shown at point A in Figure 2, creating a no-load electromotive force [18].

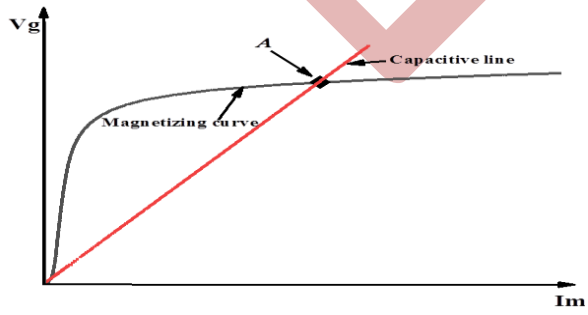


Figure 2. Induction generator magnetization curve.

III. DETERMINING THE VALUE OF SELF-EXCITATION CAPACITY

Several approaches to determining the capacitance required to excite a self-excited induction generator have been reported [19, 18]. According to [19], equation (3) is used to calculate the capacitance of the capacitor bank (in the delta link) to be connected in parallel with the induction generator. Several approaches to determining the capacitance required to excite a self-excited induction generator have been reported [19, 18]. According to [19], equation (3) is used to calculate the capacitance of the capacitor bank (in the delta link) to be connected in parallel with the induction generator.

$$C_\Delta = \frac{Q_g}{3V^2 2\pi f} \quad (3)$$

Qg is the reactive power absorbed as a generator;

V is the phase voltage.

To find the value of C_Δ it is necessary to determine the value of the reactive power absorbed as a generator. For this reason, several equations are beneficial to find this value [20]. In motor mode, the active and reactive power is calculated from the following equations:

$$P_n = S\cos\varphi_m \ \eta_m \quad (4)$$

$$Q_m = S\sin\varphi_m \quad (5)$$

With apparent power

$$S = \sqrt{3}U_{line}I_{line} \quad (6)$$

while in generator mode the electrical power is :

$$P_{elg} = S\cos\varphi_g \quad (7)$$

Given that the following condition must be guaranteed: S_motor = S_generator the electrical power in generator operation is equal to:

$$P_{elg} = \frac{P_n}{\eta_m}\frac{\sin\varphi_g}{\sin\varphi_m} \quad (8)$$

using equations (4) and (5) we find the reactive energy consumed as a motor

$$Q_m = \frac{P_n}{\eta_m} tag\varphi_m \quad (9)$$

The reactive power of the generator is estimated as a function of the rated power of the machine operating as a motor using equation (4) and Figure 3. It is given by [20] :

$$Q_g = \frac{\sin \varphi_g}{\sin \varphi_m} Q_m \quad (10)$$

Where

Pn is the rated mechanical power;

ηm is the efficiency as a driving action;

φm is the power factor angle as a motor.

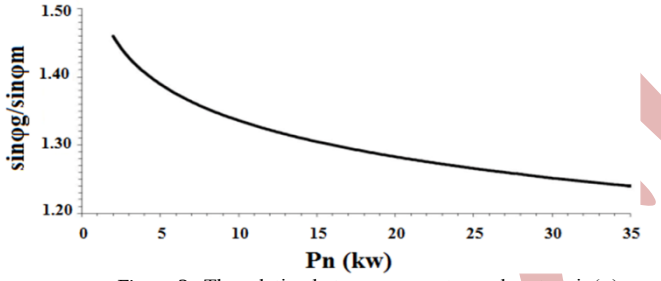


Figure 3. The relation between generator and motor sin(φ).

For our study, we have chosen a squirrel-cage asynchronous machine whose characteristics are shown in the table below:

TABLE I. SEIG PARAMETERS

Parameter	***Value***
Rated power	*400 KW*
Rated Voltage	*400 V*
Coupling	*Delta*
Poles Number	*4*
Motoring rated speed	*1491 (rmp)*
Rated frequency	*50 (Hz)*
Working temperature	*75(°)*

After performing the necessary calculations to determine the value of the self-excitation capacity, we modeled the induction generator and the self-excitation phenomenon using the time-stepped finite element method (TSFEM). The figure below illustrates the induction generator model and its field distribution.

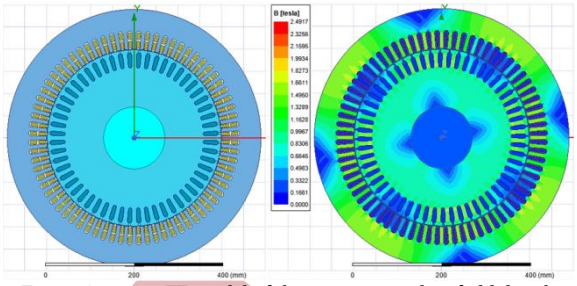


Figure 4. FE model of the generator and its field distribution.

IV. INFLUANCING OF DIFFERENT PARAMETERS

The output voltage of a self-excited induction generator is affected by several parameters: the rotor speed, the associated load, and the capacitance value. In this section, we'll take a closer look at the influence of these parameters on the output values of a self-excited induction generator.

A. Influence of capacity value

After selecting the minimum value for the self-excitation capacitance, we obtained the results shown in Figures 5, 6, and 7 for the value CΔ=500µF. We then varied this value by increasing it to 600µF, then to 700µF, 800µF and finally to 900µF.

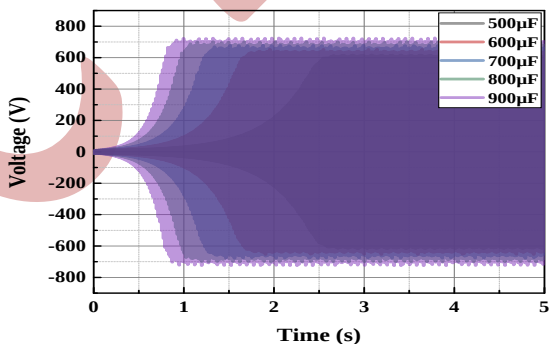


Figure 5. Voltage evolution for different capacitance values

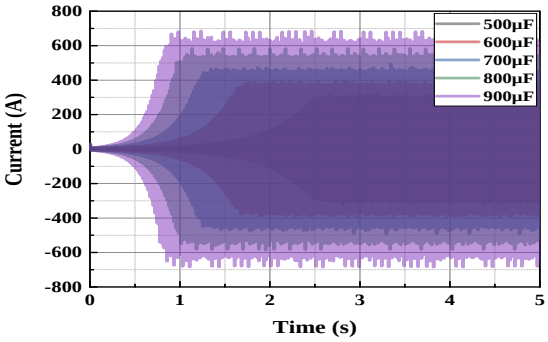


Figure 6. Current evolution for different capacitance values

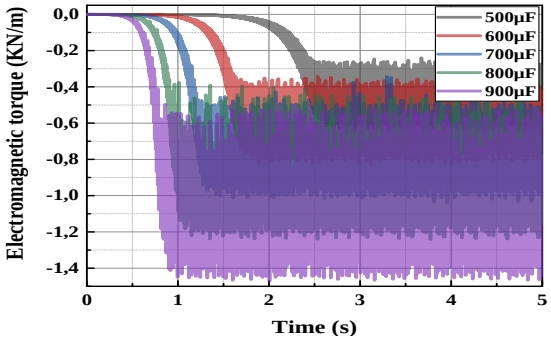


Figure 7. Electromagnetic torque evolution for different capacitance values

From Figures 5, 6, and, 7. We can see that the value of the capacitance has a significant influence on the generator's electrical quantities, whether current, voltage, or electromagnetic torque, all of which increase as the value of the capacitance increases. The voltage value increases less than the current value because the saturation of the magnetic circuit is almost reached (figure 3). Figure 8 shows the evolution of RMS voltage versus RMS current. The increase in capacitance value also influences the generator's self-excitation time, with the higher the value of C, the shorter the self-excitation time.

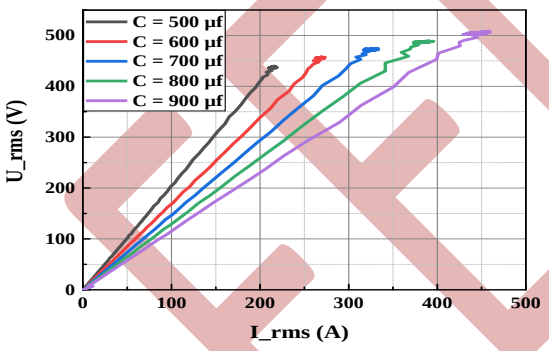


Figure 8. Voltage vs. current curves

B. Influence of speed

The second parameter that influences the generator's electrical parameters is the rotor speed, for which we set the capacitance value at CΔ = 700µF and then created a variable speed profile, as shown in Figure 9.

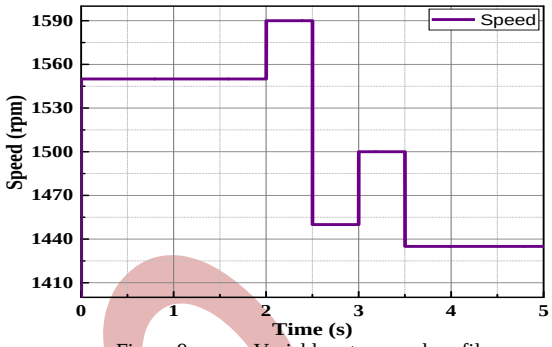


Figure 9. Variable rotor speed profile

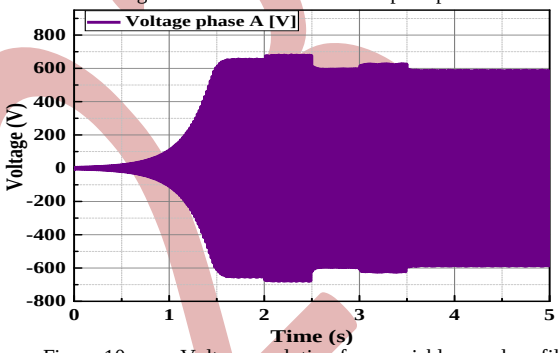


Figure 10. Voltage evolution for a variable speed profile

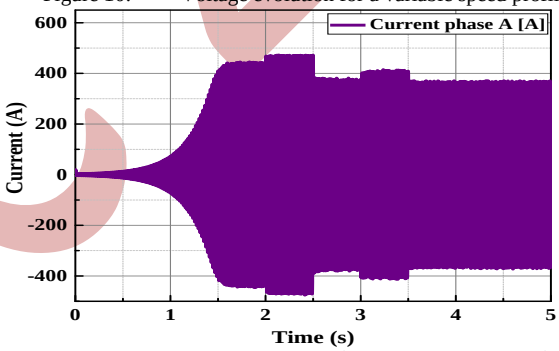


Figure 11. Current evolution for a variable speed profile

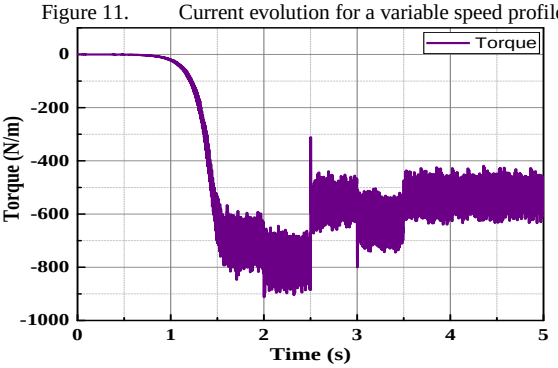


Figure 12. Electromagnetic torque evolution for a variable speed profile

The variation in rotor speed influences the electrical quantities of the induction generator. We note that if speed increases, current, voltage, and torque increase, whereas if speed decreases, these quantities decrease. We also note that

once the generator reaches a steady state, the rotor speed can drop below synchronous speed without causing the voltage to collapse.

C. Influence of load

In this last section, we'll look at the impact of load on generator operation. Once a steady state has been reached, we'll apply a balanced three-phase load of 1 ohm at time t=2s, then repeat this scenario with a 5-ohm load, followed by a 10-ohm load.

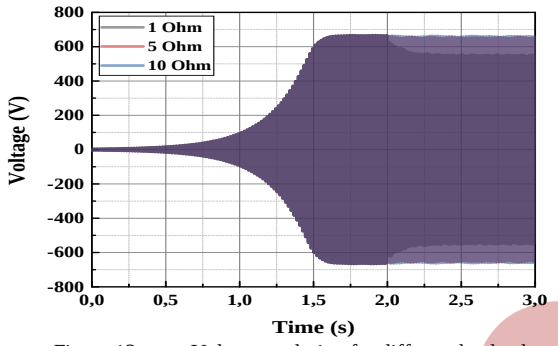


Figure 13. Voltage evolution for different load values

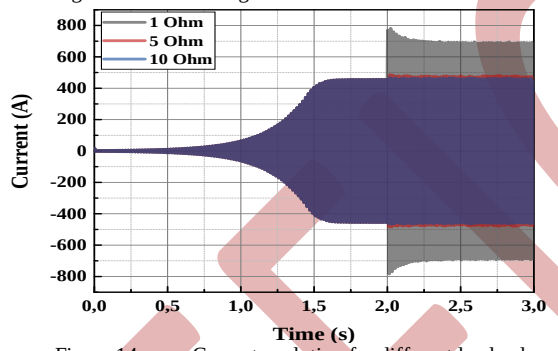


Figure 14. Current evolution for different load values

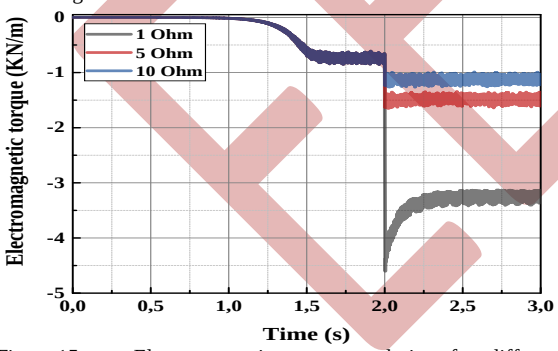


Figure 15. Electromagnetic torque evolution for different load values

Different load values influence the operation of the generator: once the load is applied, the output voltage decreases by a certain amount, and as the load increases, so does the value of the decrease, while the current and torque increase as the load is applied, and as the load increases, so does the increase.

V. CONCLUSION

Wind power generation presents a solution to the world's energy challenges. The utilization of a self-excited induction generator (SEIG) in wind energy production stands as a favorable choice due to its numerous advantages: robustness, minimal maintenance requirements, economical construction, and suitability for isolated operation. In this study, an examination of various parameters influencing SEIG performance was conducted, underscoring the significance of determining accurate capacitance values to ensure effective SEIG start-up.

Under constant rotor speed conditions, altering the capacitance value impacts the generator's output parameters: a higher capacitance value corresponds to elevated electrical parameter values such as voltage, current, and torque. Conversely, variations in rotor speed alter the generator's output characteristics for a fixed capacitance value; reduced rotor speed leads to declines in voltage, current, and torque, whereas heightened speed results in increased voltage, current, and torque.

Once the self-excited induction generator achieves steady-state operation, connecting a balanced three-phase load influences the levels of current, voltage, and torque. This connection causes a reduction in voltage and simultaneous increases in current and torque. This variation diminishes as the load value escalates. Selecting the appropriate parameters for the operating conditions of the self-excited induction generator is of paramount importance to ensure its optimal performance.

REFERENCES

[1] L. E. Chaar, L. A. Lamont and N. Elzein, "Wind energy technology — Industrial update," 2011 IEEE Power and Energy Society General Meeting, Detroit, MI, USA, 2011, pp. 1-5, doi: 10.1109/PES.2011.6039575.

[2] K. B. Porate, Nandkishor Urkude and R. Gathe. "PERFORMANCE ANALYSIS OF SQUIRREL CAGE INDUCTION GENERATOR USING STATCOM." (2013).

[3] A. SHARMA, and G. KAUR, "Assessment of capacitance for self-excited induction generator in sustaining constant air-gap voltage under variable speed and load". Energies, 2018, vol. 11, no 10, p. 2509

[4] H. P. TIWARI, and J. K. DIWEDI, "Minimum capacitance requirement for self-excited induction generator". In : Proc. 12th Nat. Power System Conf. 2002. p. 5-10.

[5] NETO, Cleto de Oliveira Fernandes and BARROS, Luciano Sales, "Maximum Power Point Tracking of Squirrel-Cage Induction Generator-based Wind Energy Conversion Systems". In : 2020 IEEE Power & Energy Society General Meeting (PESGM). IEEE, 2020. p. 1-5.

[6] KHADTARE, Sarang A., SAI, Boni Satya Varun, and CHATTERJEE, Debashis. A Model Based Control Strategy for Variable Speed Operation of Three Phase Induction Generator. In : 2020 International Conference on Computational Intelligence for Smart Power System and Sustainable Energy (CISPSSE). IEEE, 2020. p. 1-5.

[7] LIU, Yu, YANG, Jian, JIANG, Changming, et al. Review on met mast site selection methods in grid-connected wind farm. In : 2019 IEEE 3rd International Electrical and Energy Conference (CIEEC). IEEE, 2019. p. 1134-1137.

[8] GOUDARZI, Navid et ZHU, W. D. A review of the development of wind turbine generators across the world. In : ASME International Mechanical Engineering Congress and Exposition. American Society of Mechanical Engineers, 2012. p. 1257-1265.

[9] ALKHAMİS, Omran ALABED et ABUSAFE, Abdulmotaleb. STUDY OF INDUCTION GENERATORS PERFORMANCE OF TWO-SPEED USED IN STANDALONE WIND TURBINES. International Journal of Energy and Smart Grid, vol. 1, no 2, p. 37-57.

[10] KARAKASIS, N., MESEMANOLIS, A., et MADEMLIS, C. Performance study of start-up control techniques in a Wind Energy Conversion System with induction generator. In : International Symposium on Power Electronics Power Electronics, Electrical Drives, Automation and Motion. IEEE, 2012. p. 547-552.

[11] TUDORACHE, T., MELCESCU, L., et PATURCA, S. V. Finite element analysis of self-excited induction generator for isolated small power wind turbines. In : 2007 International Conference on Clean Electrical Power. IEEE, 2007. p. 656-661.

[12] TAHIR, Ahmed, RAJAB, Zakariya, KHALIL, Ashraf, et al. Evaluating the value of the excitation capacitance of a wind turbine/induction generator system using genetic algorithms. In : 2017 8th international renewable energy congress (IREC). IEEE, 2017. p. 1-6.

[13] KHAMIS, Abdussalam AH et AHMED-ZAID, Said. Computer simulation of a series-connected induction generator and determination of minimum required capacitance for self-excitation for wind energy applications. In : 2020 11th International Renewable Energy Congress (IREC). IEEE, 2020. p. 1-6.

[14] VANCO, Wagner E., SILVA, Fernando B., GONCALVES, Felipe AS, et al. Evaluation of the capacitor bank design for self-excitation in induction generators. IEEE Latin America Transactions, 2018, vol. 16, no 2, p. 482-488.

[15] Godoy Simões and Felix A. Farret, " Modeling and Analysis with Induction Generators". Third Edition. POWER ELECTRONICS AND APPLICATIONS SERIES. Taylor & Francis Group, 2015.

[16] OFUALAGBA, G., UBEKU, E. U., et al. The analysis and modelling of a self-excited induction generator driven by a variable speed wind turbine. Fundamental and Advanced Topics in Wind Power, 2011, p. 5-9.

[17] TUDORACHE, T., MELCESCU, L., et PATURCA, S. V. Finite element analysis of self-excited induction generator for isolated small power wind turbines. In : 2007 International Conference on Clean Electrical Power. IEEE, 2007. p. 656-661.

[18] Anamika Kumari1 , A. G. Thosar , S. S. Mopari, " Determination of Excitation Capacitance of a Three Phase Self Excited Induction Generator". International Journal of Advanced Research in Electrical, Electronics and Instrumentation Engineering, Vol. 4, Issue 5, May 2015

[19] SANDEEP, V., et al. Experimental study on different modes of self excited induction generator operation. In : 2020 2nd PhD Colloquium on Ethically Driven Innovation and Technology for Society (PhD EDITS). IEEE, 2020. p. 1-2.

[20] J.M Chapallaz, J. Dos Ghali, P Eichenberger, G. Fischer, "Manuel on induction motors used as generator", GATA,vol 10,1992.

Open Phase Fault Tolerance Solution for Dual Star Induction Machine

Faycal Hassaini [1], Samira Chekkal [1], Djamal Aouzellag [1], Yanis Hamoudi [1]

[1] *Laboratoire de Maitrise des Energies Renouvelables, Faculté de Technologie, Université de Bejaia, 06000 Bejaia, Algeria*

faycal.hassaini@univ-bejaia.dz

samirachekkal@yahoo.fr

aouzellag@hotmail.com

yanis.hamoudi@univ-bejaia.dz

***Abstract*— This article aims to restore the balance of the Dual Star Induction Machine (DSIM) in the presence of an open phase fault (OPF). This method involves creating a second phase opening and forming an angle (θ = 90°) with the faulty phase. To improve this approach, the neutrals of the two stars are connected, exploiting the DSIM model in natural landmarks. Following simulations carried out in MATLAB, it has been shown that this method is effective in reducing disturbances and fault effects. In addition, reducing amplitudes brings them back to their usual stable levels (healthy state).**

Keywords- DSIM with wound rotor; modeling and simulation; healthy and degraded regimes; OPF; comparison of results for cases connected and not connected to neutral.

I. INTRODUCTION

Variable-speed electric drive systems are used to precisely and efficiently control the rotational speed of an electric machine, usually a motor. These systems are generally implemented on three-phase electrical machines, such as a double-star DSIM with a caged rotor or a wound rotor.

The squirrel cage induction motor is characterized by its low maintenance requirements, due to the absence of slip rings and brushes. In contrast, A wound induction motor requires regular maintenance to replace the brushes, which wear out over time. Unlike the accessible wound rotor, the wound rotor motor has higher maintenance costs than a squirrel cage rotor, mainly due to the replacement of the supply brushes. It is not possible to add an external resistor to the rotor of a squirrel cage motor. This adjustable resistor is used to regulate the torque/speed characteristic of the motor. In particular, squirrel cage motors have a high starting current, whereas wound induction motors have a low starting current. Although wound rotor motors have a much higher starting electromagnetic torque, they offer the possibility of connecting a neutral. [1][2].

This type of machine can be subject to a number of electrical faults [3], which can be grouped into two categories: stator and rotor faults. As far as the stator is concerned, failures are mainly due to thermal (overheating), electrical (dielectric) and mechanical (winding) problems [4]. As far as the rotor is concerned, if it is a wound rotor, it can be affected by the same faults as the stator[5]. On the other hand, faults can manifest themselves in the form of bar or ring breakage in the case of a squirrel-cage rotor.

One of the most frequently encountered faults in electrical machines is the phase opening fault.

This type of fault can have catastrophic consequences, particularly for three-phase machines. This leads to reduced torque, unbalanced currents, motor overheating, winding and rotor damage and reduced energy efficiency.

The increase in the number of phases is found in one of the most common configurations, namely the double-star machine. This machine has two three-phase stars in the stator, which gives it more degrees of freedom than the conventional three-phase machine. We aim to exploit the advantages of the double-star machine to tolerate the phase opening fault.

Several studies have addressed the problem of continuity of operation in the event of a phase opening fault. These include [3], [6]-[11], where this problem is addressed by complex modifications to the control algorithms. However, some research neglects to take into account whether the various

neutrals are connected or not, unlike the study in this paper where the connection of the neutral is taken into account to prove its influence on the correct operation of the machine in the event of a fault. In addition, the modeling carried out in the reference frame (d-q-0) becomes invalid in the event of a phase opening fault. We addressed two problems in this study. Firstly, we looked for a more straightforward solution without having to modify the control algorithms. Secondly, we dealt directly with the Natural domain, which is valid in healthy operation as well as in the event of a fault. In our work, we aim to create another phase opening to restore equilibrium. This second phase opening forms an angle of (θ =90°) with the faulty phase. We examined the behavior of the machine in two cases: Neutral connected and not connected. In addition, we modeled it in the natural reference, Frame. Our work is organized according to the following elements: modeling of the DSIM with a stator and rotor phase opening fault. Study DSIM in case of faults (OPF) and use the method of opening the second phase with an angle of (θ) with the faulty phase in the natural reference frame (abc). Examine in both cases of opening stator and rotor.

II. MODELLING OF THE DSIM WITH A STATOR AND ROTOR PHASE OPENING FAULT

"Fig. 1" and "Fig. 2" shows the multiphase drive under consideration. It consists of a double-star induction machine with two electrically offset independent three-phase windings. An electrical angle of π/6 rad offsets these independent three-phase bearings. The modelling approach introduces a high resistance in series with the faulty phase, which cancels the current and allows faults to be simulated. This gives both the connected and unconnected neutral cases. It is important to note that to simplify the modelling, common assumptions are used (the machine is not saturated, the no-load back EMF waveform is sinusoidal, the rotor is not dirty, the harmonics of the winding space are minimal and the effects of hysteresis and eddy currents are minimal)[11].

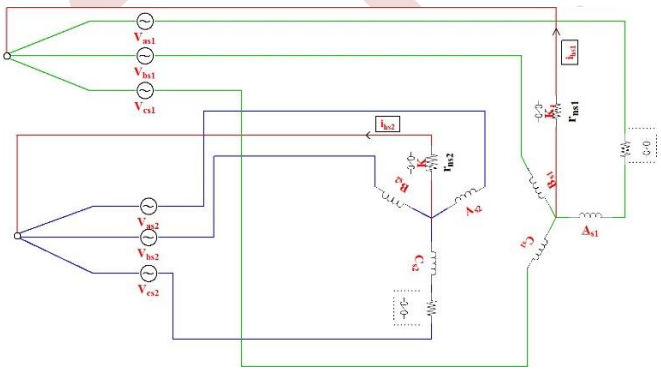


Figure 1. Phase opening fault diagram stator phases

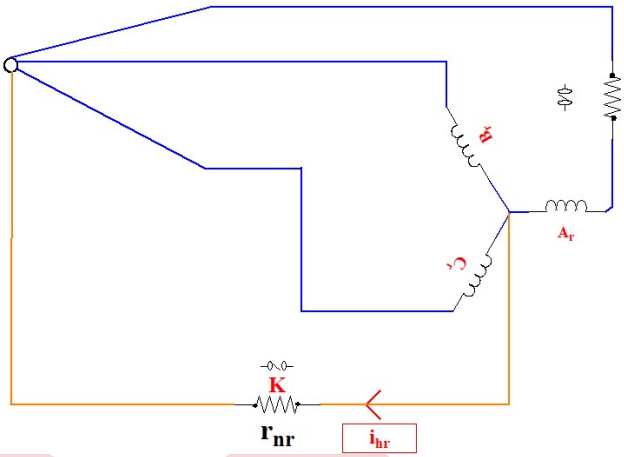


Figure 2. Phase opening fault diagram rotor phases

A. DSIM electrical equations

The DSIM voltages represent ohmic and inductive windings driven by the flux.

1) Stator star 1

$$\begin{cases} v_{as1} - v_{ns1} = r_{as1} i_{as1} + \dfrac{d\varphi_{as1}}{dt} - v_{nc1} \\ v_{bs1} - v_{ns1} = r_{bs1} i_{bs1} + \dfrac{d\varphi_{bs1}}{dt} - v_{nc1} \\ v_{cs1} - v_{ns1} = r_{cs1} i_{cs1} + \dfrac{d\varphi_{cs1}}{dt} - v_{nc1} \end{cases} \quad (1)$$

SYSTEM (1) IS REWRITTEN AS :

$$\begin{cases} v_{as1} = r_{as1} i_{as1} + \dfrac{d\varphi_{as1}}{dt} + \Delta v_{ns1} \\ v_{bs1} = r_{bs1} i_{bs1} + \dfrac{d\varphi_{bs1}}{dt} + \Delta v_{ns1} \\ v_{cs1} = r_{cs1} i_{cs1} + \dfrac{d\phi_{cs1}}{dt} + \Delta v_{ns1} \end{cases} \quad (2)$$

With: $\Delta v_{ns1} = v_{ns1} - v_{nc} = r_{ns1}\left(\underbrace{i_{as1} + i_{bs1} + i_{cs1}}_{i_{hs1}}\right)$:

The different potential between source and neutral, respectively; $r_{ns1}$and i_{hs1}Resistance and zero sequence current between two neutrals in the stator1.

2) Stator star 2

$$\begin{cases} v_{as2} - v_{ns2} = r_{as2} i_{as2} + \dfrac{d\varphi_{as2}}{dt} - v_{nc2} \\ v_{bs2} - v_{ns2} = r_{bs2} i_{bs2} + \dfrac{d\varphi_{bs2}}{dt} - v_{nc2} \\ v_{cs2} - v_{ns2} = r_{cs2} i_{cs2} + \dfrac{d\varphi_{cs2}}{dt} - v_{nc2} \end{cases} \quad (3)$$

SYSTEM (3) IS REWRITTEN AS :

$$\begin{cases} v_{as2} = r_{as2}i_{as2} + \dfrac{d\varphi_{as2}}{dt} + \Delta v_{ns2} \\ v_{bs2} = r_{bs2}i_{bs2} + \dfrac{d\varphi_{bs2}}{dt} + \Delta v_{ns2} \\ v_{cs2} = r_{cs2}i_{cs2} + \dfrac{d\varphi_{cs2}}{dt} + \Delta v_{ns2} \end{cases} \quad (4)$$

With: $\Delta v_{ns2} = v_{ns2} - v_{nc} = r_{ns2}\left(\underbrace{i_{as2} + i_{bs2} + i_{cs2}}_{i_{hs2}}\right)$:

The different potential between source and neutral, respectively; r_{ns2} and i_{hs2}: Resistance and zero sequence current between two neutrals at the stator2.

3) For the rotor

$$\begin{cases} v_{ar} - v_{nr} = r_{ar}i_{ar} + \dfrac{d\varphi_{ar}}{dt} - v_{nc} \\ v_{br} - v_{nr} = r_{br}i_{br} + \dfrac{d\varphi_{br}}{dt} - v_{nc} \\ v_{cr} - v_{nr} = r_{cr}i_{cr} + \dfrac{d\varphi_{cr}}{dt} - v_{nc} \end{cases} \quad (5)$$

SYSTEM (5) IS REWRITTEN AS :

$$\begin{cases} v_{ar} = r_{ar}i_{ar} + \dfrac{d\varphi_{ar}}{dt} + \Delta v_{nr} \\ v_{br} = r_{br}i_{br} + \dfrac{d\varphi_{br}}{dt} + \Delta v_{nr} \\ v_{cr} = r_{cr}i_{cr} + \dfrac{d\varphi_{cr}}{dt} + \Delta v_{nr} \end{cases} \quad (6)$$

With: $\Delta v_{nr} = v_{nr} - v_{nc} = r_{nr}\left(\underbrace{i_{ar} + i_{br} + i_{cr}}_{i_{hr}}\right)$:

The different potential between source and neutral, respectively; r_{nr} and i_{hr} : Resistance and zero sequence current between two neutrals at the rotor.

B. DSIM stator and rotor voltage equations

$$\begin{cases} [v_{s1}] = [r_{s1}][i_{s1}] + \dfrac{d[\varphi_{s1}]}{dt} + [\Delta v_{ns1}]I_3 \\ [v_{s2}] = [r_{s2}][i_{s2}] + \dfrac{d[\varphi_{s2}]}{dt} + [\Delta v_{ns2}]I_3 \\ [v_r] = [r_r][i_r] + \dfrac{d[\varphi_r]}{dt} + [\Delta v_{nr}]I_3 \end{cases} \quad (7)$$

With: I_3 Identity matrix (3 X 3).

Magnetic equations in the abc reference frame [12]

$$\begin{cases} [\varphi_{s1}] = [L_{s1,s1}][i_{s1}] + [M_{s1,s2}][i_{s2}] + [M_{s1,r}][i_r] \\ [\varphi_{s2}] = [L_{s2,s2}][i_{s2}] + [M_{s2,s1}][i_{s1}] + [M_{s2,r}][i_r] \\ [\varphi_r] = [M_{r,s1}][i_{s1}] + [M_{r,s2}][i_{s2}] + [L_{r,r}][i_r] \end{cases} \quad (8)$$

a) The sub-matrices of the star's natural inductances (1 and 2)

$$[L_{s1,s1}] = [L_{s2,s2}] = \begin{bmatrix} L_s + L_{ms} & \frac{-L_{ms}}{2} & \frac{-L_{ms}}{2} \\ \frac{-L_{ms}}{2} & L_s + L_{ms} & \frac{-L_{ms}}{2} \\ \frac{-L_{ms}}{2} & \frac{-L_{ms}}{2} & L_s + L_{ms} \end{bmatrix} \quad (9)$$

b) The rotor self-inductance sub-matrix

$$[L_{r,r}] = \begin{bmatrix} L_r + L_{mr} & \frac{-L_{mr}}{2} & \frac{-L_{mr}}{2} \\ \frac{-L_{mr}}{2} & L_r + L_{mr} & \frac{-L_{mr}}{2} \\ \frac{-L_{mr}}{2} & \frac{-L_{mr}}{2} & L_s + L_{mr} \end{bmatrix} \quad (10)$$

c) The mutual inductance sub-matrix coupled between the two stator stars is written as

$$[M_{s1,s2}] = L_{ms}\begin{bmatrix} \cos(\alpha) & \cos(\alpha + \frac{2\pi}{3}) & \cos(\alpha - \frac{2\pi}{3}) \\ \cos(\alpha - \frac{2\pi}{3}) & \cos(\alpha) & \cos(\alpha + \frac{2\pi}{3}) \\ \cos(\alpha + \frac{2\pi}{3}) & \cos(\alpha - \frac{2\pi}{3}) & \cos(\alpha) \end{bmatrix} \quad (11)$$

d) The mutual inductance sub-matrix coupled between stator star (1) and rotor is written as[13]

$$[M_{s1,r}] = L_{ms}\begin{bmatrix} \cos(\theta_r) & \cos(\theta_r + \frac{2\pi}{3}) & \cos(\theta_r - \frac{2\pi}{3}) \\ \cos(\theta_r - \frac{2\pi}{3}) & \cos(\theta_r) & \cos(\theta_r + \frac{2\pi}{3}) \\ \cos(\theta_r + \frac{2\pi}{3}) & \cos(\theta_r - \frac{2\pi}{3}) & \cos(\theta_r) \end{bmatrix} \quad (12)$$

e) The mutual inductance sub-matrix coupled between stator star (2) and rotor is written as

$$[M_{s2,r}] = L_{ms}\begin{bmatrix} \cos(\theta_r - \alpha) & \cos(\theta_r - \alpha + \frac{2\pi}{3}) & \cos(\theta_r - \alpha - \frac{2\pi}{3}) \\ \cos(\theta_r - \alpha - \frac{2\pi}{3}) & \cos(\theta_r - \alpha) & \cos(\theta_r - \alpha + \frac{2\pi}{3}) \\ \cos(\theta_r - \alpha + \frac{2\pi}{3}) & \cos(\theta_r - \alpha - \frac{2\pi}{3}) & \cos(\theta_r - \alpha) \end{bmatrix} \quad (13)$$

Or: $[M_{s2,s1}] = [M_{s1,s2}]^t$, $[L_{r,s1}] = [M_{s1,r}]^t$ and $[M_{r,s2}] = [M_{s2,r}]^t$

By inserting expressions (8) - (13) into expression (7):

$$\begin{cases} [v_{s1}] = [r_{s1}][i_{s1}] + \frac{d}{dt}\left([L_{s1,s1}][i_{s1}] + [M_{s1,s2}][i_{s2}] + [M_{s1,r}][i_r]\right) \\ \quad + r_{ns1}(i_{as1} + i_{bs1} + i_{cs1})I_3 \\ [v_{s2}] = [r_{s2}][i_{s2}] + \frac{d}{dt}\left([L_{s2,s2}][i_{s2}] + [M_{s2,s1}][i_{s1}] + [M_{s2,r}][i_r]\right) \\ \quad + r_{ns2}(i_{as2} + i_{bs2} + i_{cs2})I_3 \\ [v_r] = [r_r][i_r] + \frac{d}{dt}\left([M_{r,s1}][i_{s1}] + [M_{r,s2}][i_{s2}] + [L_{r,r}][i_r]\right) \\ \quad + r_{nr}(i_{ar} + i_{br} + i_{cr})I_3 \end{cases} \quad (14)$$

As the mutual stator/rotor, inductances do not depend on time but on θ_r, the system of equations (14) becomes:

$$\begin{cases} \frac{d}{dt}([i_{s1}]) = [L_{s1,s1}]^{-1}\begin{pmatrix}[v_{s1}]-[r_{s1}][i_{s1}]-[M_{s1,s2}]\frac{d}{dt}([i_{s2}])-\omega_r\frac{d}{d\theta_r}([M_{s1,r}])[i_r] \\ -[M_{s1,r}]\frac{d}{dt}([i_r])-r_{ns1}(i_{as1}+i_{bs1}+i_{cs1})I_3\end{pmatrix} \\ \frac{d}{dt}([i_{s2}]) = [L_{s2,s2}]^{-1}\begin{pmatrix}[v_{s2}]-[r_{s2}][i_{s2}]-[M_{s2,s1}]\frac{d}{dt}([i_{s1}])-\omega_r\frac{d}{d\theta_r}([M_{s2,r}])[i_r] \\ -[M_{s2,r}]\frac{d}{dt}([i_r])-r_{ns2}(i_{as2}+i_{bs2}+i_{cs2})I_3\end{pmatrix} \\ \frac{d}{dt}([i_r]) = [L_{r,r}]^{-1}\begin{pmatrix}[v_r]-[r_r][i_r]-\omega_r\frac{d}{d\theta_r}([M_{r,s1}])[i_{s1}]-[M_{r,s1}]\frac{d}{dt}([i_{s1}])-\omega_r\frac{d}{d\theta_r}([M_{r,s2}])[i_{s2}] \\ -[M_{r,s2}]\frac{d}{dt}([i_{s2}])-r_{nr}(i_{ar}+i_{br}+i_{cr})I_3\end{pmatrix} \end{cases} \quad (15)$$

C. *Electromagnetic torque equation*

$$T_{em} = p\left([i_{s1}]^t\frac{d}{d\theta_r}[M_{s1,r}][i_r]+[i_{s2}]^t\frac{d}{d\theta_r}[M_{s2,r}][i_r]\right) \quad (16)$$

D. *Mechanical equation*

$$J\frac{d\Omega_r}{dt} = T_{em} - T_r - f\Omega_r \quad (17)$$

With: $\Omega_r = \frac{\omega_r}{p}$: Mechanical and electrical rotation speeds, respectively

III. RESULTS AND DISCUSSION

A. *Stator opening*

"Fig. 3" to "Fig. 7" illustrate the simulation results of the DSIM in the presence of open faults of two stator phases in the two cases of connected and unconnected neutral giving the natural reference. Initially, we start it at no load (the healthy state) and then add a load at time t=1 s we are going to apply the load to the machine. Then at t=2 s, we introduce a phase opening fault in the stator phase of the first stator phase of the star (1) in the case of connected neutral, At t=4 s the second phase opening fault is introduced in the third phase of the star (2) in the case of connected neutral, then at t=6 s to t=10s we repeat the same simulation but with an unconnected neutral. The following changes can be observed:

- "Fig. 3" shows the trend of the stator currents of Star '1', after the transient period caused by the application of the two faults, which leads to an increase in amplitude giving the two phases i_{sb1} and i_{sc1} its maximum value and {12.1 and 11.65 (A)} done the case OPF (1) and {15.2 A} done the case phase opening 2 (OP (2)) and for the unconnected neutral we notice the decrease in the amplitude of the currents i_{sb1} and i_{sc1} it is approximately the same value as its healthy state in the case OPF (1) and for the case OP (2) we will have {18.16 and 15.74 (A)} if we take the sum of the currents we notice that it cancels out. For i_{sa} it cancels the 2 cases of opening neutral handles (connected and not connected).
- "Fig. 4" shows the trend in the stator currents of Star '2', after application of the fault. OPF (1) Shows an increase in amplitude compared to their healthy state. In addition, an imbalance between the three phases, especially when the neutral is disconnected a (t=6s), their frequency is 50 Hz, its oscillations take the same sinusoidal form when the phase is opened OP (2) (t=4s) with an rms value of 15.2A with a period of 0.02s (50 Hz frequency), and their amplitudes are superimposed. Their sums are not equal to 0A. On the other hand, when the neutral is not connected (t=8), the currents are symmetrical and their sums are equal to zero.
- "Fig. 5", "Fig. 6" and "Fig. 7" illustrate the rotor currents, the electromagnetic torque and the rotor speed respectively. These three will experience a period of oscillations at their level, especially if the neutral is not connected, the frequency of the torque and speed is 100 Hz whether the neutral is connected or not, but when the second phase is opened the curves return to their usual stable form for the torque and speed with the mains frequency and sinusoidal for the currents

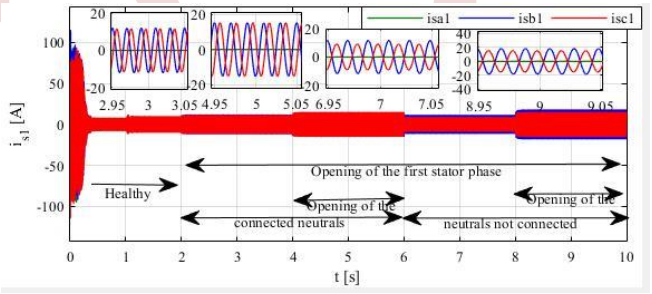


Figure 3. Stator currents 1 when OPF (1) and OP (2) in stator with neutral connected and not connected

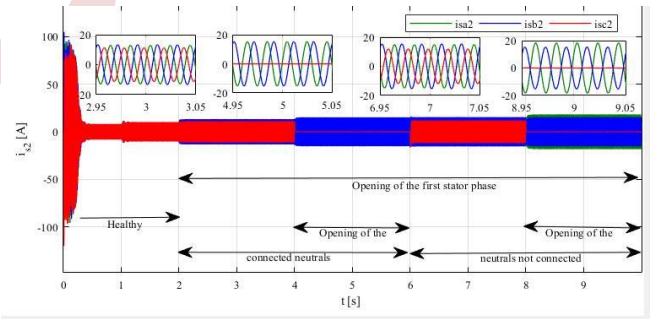


Figure 4. stator currents 2 when OPF (1) and OP (2) in the stator with neutral connected and not connected

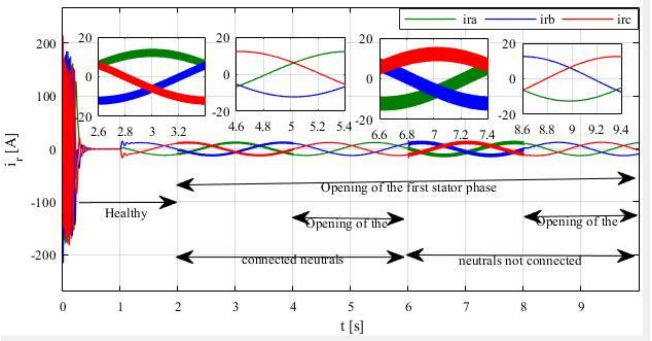


Figure 5. Courants du rotor lorsque l'OPF (1) et l'OP (2) dans le stator avec le neutre connecté et non connecté

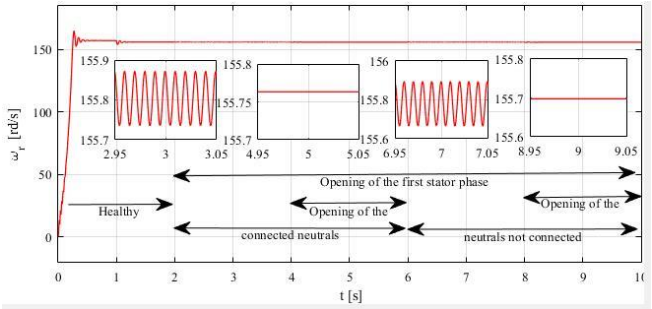


Figure 6. Speed when OPF (1) and OP (2) in the stator with neutral connected and not connected

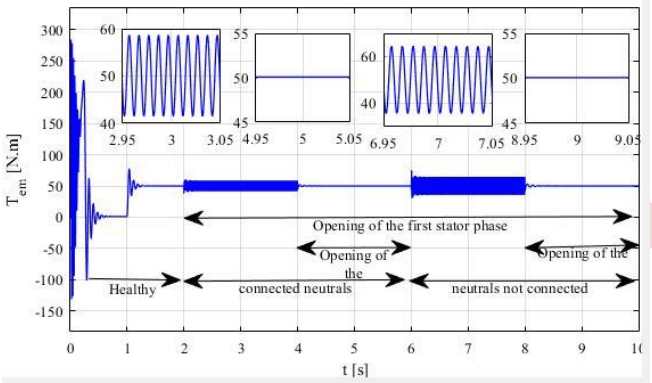


Figure 7. Electromagnetic torque when OPF (1) and OP (2) in stator with neutral connected and not connected

B. *Rotor opening*

- "Fig. 8" and "Fig. 9" show stator currents 1 and 2 respectively when the rotor phase is open. OPF rotor The rotor phase is open, the currents of two stars are influenced and disturbances are observed at their levels, The fault accumulates when the value of the unconnected neutral exceeds 33A
- "Fig. 10" illustrates the rotor currents which become completely random and non-periodic when the rotor phase opens. In contrast, in the case of an unconnected neutral, the currents become organised and periodic again but their sums equal to 0 A unlike the connected neutral.
- "Fig. 11" and "Fig. 12" illustrate the changes in torque and speed when rotor phases open, both showing a disturbed response for a connected neutral and a very disturbed response for a neutral that is not connected.

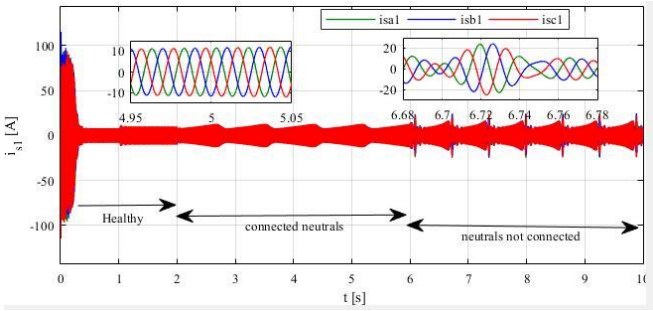


Figure 8. Stator currents 1 when OPF rotoric with neutral connected and not connected

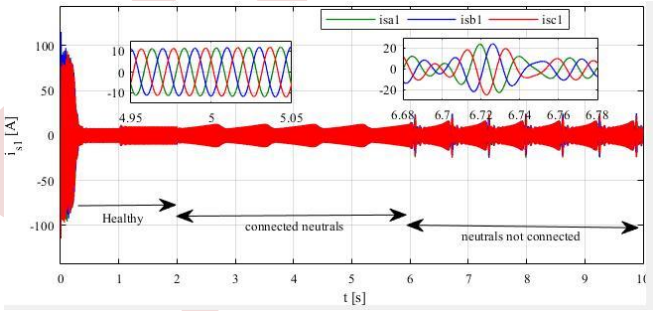


Figure 9. Stator currents 2 when OPF rotoric with neutral connected and not connected

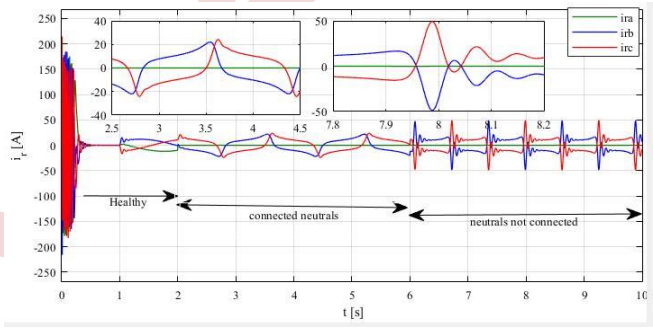


Figure 10. Rotor currents when OPF rotoric with neutral connected and not connected

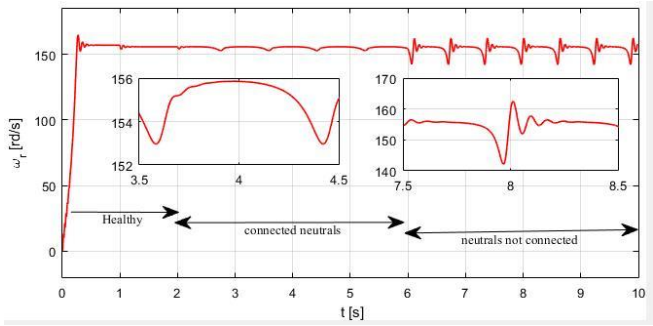


Figure 11. Speed when OPF rotor with neutral connected and not connected

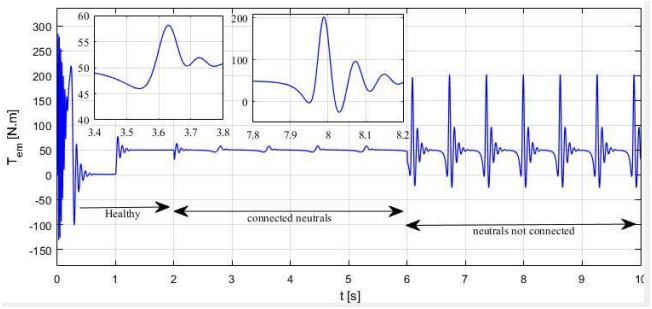


Figure 12. Electromagnetic torque when OPF rotor with neutral connected and not connected

IV. CONCLUSION

We have carried out an in-depth analysis of the operation of the double star asynchronous machine in the presence of faults such as phase openings (stator or rotor) in both the neutral connected and unconnected cases. We sought to understand the progressive impact of these faults on the machine's behavior.

This approach has enabled us to obtain significant results on the impact of stator and rotor faults on the overall behavior of the DSIM.

These results have contributed to a better understanding of the variations observed in the machine's quantities in the presence of these faults, offering prospects for more detection that is accurate and diagnostic measurements. These observations provide in-depth information that lays the foundations for future studies on the DSIM, in particular on fault detection and monitoring.

REFERENCES

[1] Y. Hamoudi, H. Amimeur, D. Aouzellag, M. G. M. Abdolrasol, and T. S. Ustun, "Hyperparameter Bayesian Optimization of Gaussian Process Regression Applied in Speed-Sensorless Predictive Torque Control of an Autonomous Wind Energy Conversion System," *Energies*, vol. 16, no. 12, p. 4738, Jun. 2023.

[2] Z. Yang, Q. Ding, X. Sun, J. Ji, and Q. Zhao, "Design and analysis of a novel wound rotor for a bearingless induction motor," *Int. J. Electron.*, vol. 106, no. 12, pp. 1829–1844, 2019.

[3] L. Khaldi, S. Chekkal, K. Ghedamsi, and D. Aouzellag, "Performance Analysis of Dual Star Induction Generator Under Open Phase Fault," no. August, 2022.

[4] E. Amirouche, K. GHEDAMSI, K. IFFOUZAR "Modélisation dynamique et commande d'une génératrice hydrolienne polyphasée en fonctionnement non conventionnel," 2022.

[5] J.-C. Trigeassou,"*Electrical Machines Diagnosis*," Wiley, 2011.

[6] X. Wang, Z. Wang, and Z. Xu, "A hybrid direct torque control scheme for dual three-phase PMSM drives with improved operation performance," *IEEE Trans. Power Electron.*, vol. 34, no. 2, pp. 1622–1634, 2019.

[7] L. Liu and Q. Zhang, "Open-Circuit Fault-Tolerant Control of a Six-Phase Asymmetric Permanent Magnet Synchronous Motor Drive System," *Electronics.*, vol. 12, no. 5, pp. 1–15, 2023.

[8] W. Huang, W. Hua, F. Chen, and J. Zhu, "Enhanced Model Predictive Torque Control of Fault-Tolerant Five-Phase Permanent Magnet Synchronous Motor with Harmonic Restraint and Voltage Preselection," *IEEE Trans. Ind. Electron.*, vol. 67, no. 8, pp. 6259–6269, 2020.

[9] M. Salehifar, R. S. Arashloo, M. Moreno-Eguilaz, V. Sala, and L. Romeral, "Observer-based open transistor fault diagnosis and fault-tolerant control of five-phase permanent magnet motor drive for application in electric vehicles," *IET Power Electron.*, vol. 8, no. 1, pp. 76–87, 2015.

[10] Z. Zhang, Y. Wu, H. Su, and Q. Sun, "Research on Open-circuit Fault Tolerant Control of Six-phase Permanent Magnet Synchronous Machine Based on Fifth Harmonic Current Injection," *CES Trans. Electr. Mach. Syst.*, vol. 6, no. 3, pp. 306–314, 2022.

[11] K. Iffouzar, M.-F.Benkhoris, B. Amirouche, A. Houari, K. Ghedamsi, and A. Djerioui,"A New Post-Fault Reconfiguration Strategy under Open-Phase Operation Conditions of Asymmetrical Double-Star Induction Machines," Energies, vol. 16, no. 15, p.5740, Aug 2023.

[12] X. Zheng, X. Wu, X. Yi, H. Liu, and R. Ni, "Fault-tolerant Control of a 15-phase Induction Machine with Non-sinusoidal Supply under Open-circuited Fault Conditions," *2019 22nd Int. Conf. Electr. Mach. Syst. ICEMS 2019*, pp. 1–4, 2019.

[13] Z. Bo, Z. Jimin, H. Guiqing, Z. Jibin, and X. Yongxiang, "Asymmetry of inductance and torque ripple of multi-unit permanent magnet synchronous motor," *2011 Int. Conf. Electr. Mach. Syst. ICEMS 2011*, no. 1, pp. 1–4, 2011.

Detection of rotor bar breakages in a dual-star induction machine

Samira Chekkal epouse Ait ouaret[1], Yacine Imaouchen[2], Djamal Aouzellag [1], Faycal Hassaini[1]

1 Laboratoire de Maitrise des Energies Renouvelables, Faculté de Technologie, Université de Bejaia, 06000 Bejaia, Algeria
samira.chekkal@univ-bejaia.dz djamal.aouzellag @univ-bejaia.dz faycal.hassaini@univ-bejaia.dz
2 Laboratoire de Genie Electrique Bejaia, Faculté de Technologie, Université de Bejaia, 06000 Bejaia, Algeria
yacine.imaouchen@univ-bejaia.dz

***Abstract*— Asynchronous motors, widely used in the commercial sector, are exposed to faults caused by a variety of electrical, thermal, mechanical, magnetic and environmental constraints during operation. This study focuses on the control of these engines, with the aim of assessing their overall consistency, reliability and stability. Particular emphasis is placed on broken rotor bars, a potentially critical problem, especially in high-power machines. Damaged rotor bars can lead to major failures, sometimes resulting from manufacturing faults, frequent start-ups, or mechanical and thermal constraints. Fault analysis is performed as a function of the number of broken rotor bars, providing an accurate overview of the severity of potential problems. For this study, we carried out a fault detection analysis of broken bars on a double-star cage induction machine. Modelling was carried out in the ABC reference frame, adapting the machine model to take into account only rotor bar resistances, and also including short-circuit ring resistances.**

***Keywords:* DSIM, Broken bars, squirrel-cage, fault detection. modeling in the abc natural reference frame.**

I. INTRODUCTION

In spite of their vital significance in the industrial sector, asynchronous machines raise significant concerns because they often lead to production disruptions resulting from mechanical or electrical issues. These unplanned stoppages generate significant costs and are often caused by malfunctions affecting various components such as the rotor, stator, their misalignment, or bearing problems. These challenges represent significant stakes for industrial operations. To address these issues, the literature proposes several control approaches. According to [1], [2] the degradation of the bars of an asynchronous motor can result from several major factors. These include direct starting, which imposes excessively severe thermal and mechanical constraints on the rotor, which was not initially designed to withstand them. In addition, other factors, such as unexpected mechanical variations in load or faults resulting from faulty design, insufficient manufacturing or incorrect assembly, can also contribute to these failures. To evaluate the efficiency of an induction motor, maintenance technicians examine different signals emitted by the device. The time and frequency variations of these signals, in fact, can yield vital insights into the motor's state. Specialized literature mentions that the most commonly used signals for diagnostic purposes include stator current [3], Park vector [4], instantaneous power, torque, mechanical vibration and axial leakage magnetic flux [5]. The authors of reference [6] have described a new method for detecting broken rotor bars in polyphase induction motors. This approach is based on in-phase analysis of the Fourier Transform of the stator current, offering effective detection even at low load. What's more, by integrating the Hilbert Transform, it also identifies partially broken bars when the load reaches 25% or more. The major advantage of this method is that it does not require a motor in good condition as a reference for assessing the state of the rotor cage. The study by Jose Rangel-Magdaleno and all [7] presents a real-time pre-processing method that uses motor current analysis and mathematical morphology, integrated in a low-cost FPGA, to improve the detection of broken bars. The results of a statistical analysis corroborate the effectiveness of this approach. The authors of this paper [8] review condition monitoring techniques for detecting broken rotor bar (BRB) faults in asynchronous motors, based on the fault signature. The authors explore different approaches to signal processing and diagnostics at different load levels. They propose classification criteria based on load level, number of broken bars, validation methodology and signal processing technique, analyzing each fault signature according to these criteria. Article [9] presents a novel technique for detecting damaged rotor bars by employing statistical analysis of the stator inrush current envelope, employing the Hilbert Transform. This method guarantees precise, swift, and non-invasive fault diagnosis. In a different investigation, Ridha Kechida and al. [10] introduced a technique to identify flaws in damaged rotor bars by analyzing the stable spectral components of the stator, notably employing the Fast Fourier Transform (FFT). While this approach yielded anticipated outcomes, it does exhibit certain constraints. The precision of the method is influenced

by alterations in load and constant motor speed. Enhancing this technique would require addressing these dependencies and devising compensation strategies for variable conditions. Our study focuses on rotor fault detection in a dual-star induction machine with a squirrel-cage rotor. The windings of this machine are favored due to their ability to improve energy efficiency, reduce line currents, balance phases, and ensure continuity of service, as will be explained in our paper using our approach. This approach will be detailed further in the paper. The system under study is linear, which means the saturation effect of the magnetic material is not considered. It consists of a stator equipped with two identical windings phased at 30 electrical degrees, as well as a squirrel-cage rotor

II. MODEL OF THE ASYNCHRONOUS MACHINE

A. *The modified squirrel cage*

This template has been tailored for output on US letter-sized paper.

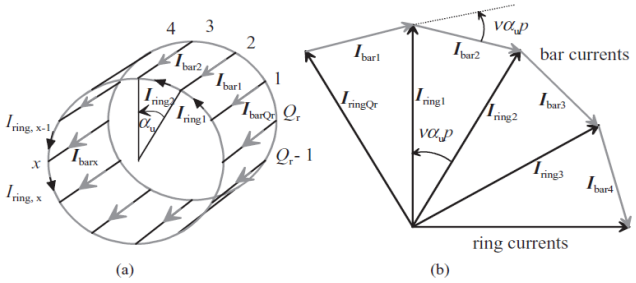


Figure1. (a): Diagram for a cage winding; (b) a sector of a polygon of the phasors of the bar currents and a section of the current phasor diagram [11].

Here $\alpha_u$is given in mechanical degrees, and the corresponding electrical degrees are given as $p\alpha_u$. Note that in reality the currents in the opposite sides of the cage have different signs.

Fig.1 illustrates a simplified cage winding (a) and phasors (b) of the bar and ring currents for the cage winding. The bars are numbered from 1 to Q_r. The bar and ring currents are denoted respectively, the arrows indicating the positive directions. If the resistance of a single bar is R_{bar} and the inductance is L_{bar} , and finally R_{ring} and L_{ring} are the respective values of the ring section between two bars, then the resultant impedance of the complete winding can be calculated as follows.

A current phasor diagram for the rotor bars is constructed for the harmonic v in such a way that the angular phase shift of the bar currents is $v\alpha_u p$. As a squirrel cage rotor can operate with different stator pole pair numbers , we use $\alpha_u$here as a mechanical angle, so then the corresponding electrical angle is $p\alpha_u$ (cf. Fig.1). Next, a polygon is constructed for the bar currents [11].

They follow Kirchhoff's first law at each connection point of the bar and the ring-see Fig.1 (a):

$$\underline{I}_{ring,x} = \underline{I}_{bar,x} + \underline{I}_{ring,x-1} \quad (1)$$

The mutual phase angle between the ring currents is also $v\alpha_u p$.

The phase shift between the currents of the two ring segments is equal to αp.The bar consists of a single winding in a rotor phase, where the number of turns $N_r = \frac{1}{2}$.The current flowing in a bar is the current of a rotor phase. Now, the RMS value of the induced current in one bar is I_{bar} as seen in figure 1 (b), we get the current in the ring as follows:

$$I_{ring} = \frac{I_{barv}}{2.\sin\left(\frac{p\pi}{Qr}\right)} \quad (2)$$

The expressions for the rotor resistance and leakage inductance of one rotor bar with the addition of the proportion of short-circuit rings are written as follows:

$$R_r = R_{bar} + \frac{R_{ring}}{2.\sin^2\left(\frac{p\pi}{Qr}\right)} \quad (3)$$

$$L_r = L_{bar} + \frac{L_{ring}}{2.\sin^2\left(\frac{p\pi}{Qr}\right)} \quad (4)$$

Where:

R_r and L_r: Resistance and leakage inductance of a one-bar (with the addition of the proportion of short-circuit rings), respectively.

R_{ring} and L_{ring}: Resistance and leakage inductance of short-circuit ring , respectively.

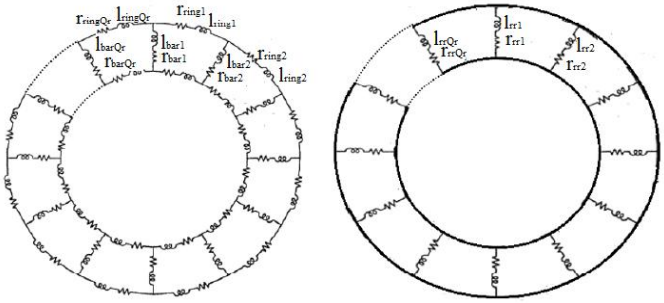


Figure.2 Squirrel cage before and after adding the ring proportions to the rotor bars.

B. *Mathematical model of the Dual star induction machine*

In this section, we present the mathematical model of the machine under study in the natural system of coordinates (ABC), neglecting spatial harmonics.

1) *Electrical equations*

The double-star asynchronous machine under study consists of two stars, each with three stator phases and 38 rotor phases (rotor bars). The electrical equations of the machine, expressed in the natural coordinate system (ABC), are as follows:

$$\begin{cases} [v_{s1}] = [R_{s1}][i_{s1}] + \frac{[d\psi_{s1}]}{dt} \\ [v_{s2}] = [R_{s2}][i_{s2}] + \frac{[d\psi_{s2}]}{dt} \\ [v_r] = [R_r][i_r] + \frac{[d\psi_r]}{dt} \end{cases} \quad (5)$$

With:

$$[v_{s1}]=\begin{bmatrix}v_{as1}\\v_{bs1}\\v_{cs1}\end{bmatrix};\ [i_{s1}]=\begin{bmatrix}i_{as1}\\i_{bs1}\\i_{cs1}\end{bmatrix};\ [\psi_{s1}]=\begin{bmatrix}\psi_{as1}\\\psi_{bs1}\\\psi_{cs1}\end{bmatrix};$$

$$[R_{s1}]=\begin{bmatrix}R_{as1}&0&0\\0&R_{bs1}&0\\0&0&R_{cs1}\end{bmatrix}$$

$$[v_{s2}]=\begin{bmatrix}v_{as2}\\v_{bs2}\\v_{cs2}\end{bmatrix};\ [i_{s2}]=\begin{bmatrix}i_{as2}\\i_{bs2}\\i_{cs2}\end{bmatrix};\ [\psi_{s2}]=\begin{bmatrix}\psi_{as2}\\\psi_{bs2}\\\psi_{cs2}\end{bmatrix};$$

$$[R_{s2}]=\begin{bmatrix}R_{as2}&0&0\\0&R_{bs2}&0\\0&0&R_{cs2}\end{bmatrix};\quad [v_r]=\begin{bmatrix}v_{ar}\\v_{br}\\\vdots\\v_{Qrr}\end{bmatrix};$$

$$[i_r]=\begin{bmatrix}i_{ar}\\i_{br}\\\vdots\\i_{Qrr}\end{bmatrix};\ [\psi_r]=\begin{bmatrix}\psi_{ar}\\\psi_{br}\\\vdots\\\psi_{Qrr}\end{bmatrix};$$

$$[R_r]=\begin{bmatrix}R_{ar}&0&\cdots&0\\0&R_{br}&\ddots&\vdots\\\vdots&\ddots&\ddots&0\\0&\cdots&0&R_{Qrr}\end{bmatrix}$$

2) Magnetic equations

The expressions of the statoric and rotor flows are given by the following matrix form:

$$\begin{cases}[\psi_{s1}]=[L_{s1,s1}][i_{s1}]+[M_{s1,s2}][i_{s2}]+[M_{s1,r}][i_r]\\[\psi_{s2}]=[L_{s2,s2}][i_{s2}]+[M_{s2,s1}][i_{s1}]+[M_{s2,r}][i_r]\\[\psi_r]=[L_{r,r}][i_r]+[M_{r,s1}][i_{s1}]+[M_{r,s2}][i_{s2}]\end{cases}\quad(6)$$

With:

$$[L_{s1,s1}]=[L_{s2,s2}]=\begin{bmatrix}l_{fs}+l_{ms}&\frac{-l_{ms}}{2}&\frac{-l_{ms}}{2}\\\frac{-l_{ms}}{2}&l_{fs}+l_{ms}&\frac{-l_{ms}}{2}\\\frac{-l_{ms}}{2}&\frac{-l_{ms}}{2}&l_{fs}+l_{ms}\end{bmatrix}(7)$$

$$[L_{r,r}]=\begin{bmatrix}l_{rr}+l_{mb}&l_{mb}\cos\left(\frac{2\pi}{Q_r}\right)&l_{mb}\cos\left(\frac{2.2\pi}{Q_r}\right)&l_{mb}\cos\left(\frac{3.2\pi}{Q_r}\right)&\cdots&l_{mb}\cos\left(\frac{(Q_r-1)2\pi}{Q_r}\right)\\l_{mb}\cos\left(\frac{2\pi}{Q_r}\right)&l_{rr}+l_{mb}&l_{mb}\cos\left(\frac{2\pi}{Q_r}\right)&l_{mb}\cos\left(\frac{2.2\pi}{Q_r}\right)&\cdots&l_{mb}\cos\left(\frac{(Q_r-2)2\pi}{Q_r}\right)\\l_{mb}\cos\left(\frac{2.2\pi}{Q_r}\right)&l_{mb}\cos\left(\frac{2\pi}{Q_r}\right)&l_{rr}+l_{mb}&l_{mb}\cos\left(\frac{2\pi}{Q_r}\right)&\cdots&l_{mb}\cos\left(\frac{(Q_r-3)2\pi}{Q_r}\right)\\l_{mb}\cos\left(\frac{3.2\pi}{Q_r}\right)&l_{mb}\cos\left(\frac{2.2\pi}{Q_r}\right)&l_{mb}\cos\left(\frac{2\pi}{Q_r}\right)&\ddots&\cdots&l_{mb}\cos\left(\frac{(Q_r-4)2\pi}{Q_r}\right)\\\vdots&\vdots&\vdots&\cdots&\ddots&\vdots\\l_{mb}\cos\left(\frac{(Q_r-1)2\pi}{Q_r}\right)&l_{mb}\cos\left(\frac{(Q_r-2)2\pi}{Q_r}\right)&l_{mb}\cos\left(\frac{(Q_r-3)2\pi}{Q_r}\right)&l_{mb}\cos\left(\frac{(Q_r-4)2\pi}{Q_r}\right)&\cdots&l_{rr}+l_{mb}\end{bmatrix}(8)$$

Matrices of stator and rotor inductors respectively; l_{fs}And l_{rr}: Stator and rotor leakage inductors, respectively; l_{ms} and l_{mb}: Maximum stator and rotor magnetization inductors, respectively;

$$[M_{s1,r}]=[M_{r,s1}]^t=\begin{bmatrix}\cos\left(\theta_r+\frac{\pi}{Q_r}\right)&\cos\left(\theta_r+\frac{3\pi}{Q_r}\right)&\cos\left(\theta_r+\frac{5\pi}{Q_r}\right)&\cdots&\cos\left(\theta_r+\frac{(2Q_r-1)\pi}{Q_r}\right)\\\cos\left(\theta_r+\frac{\pi}{Q_r}-\frac{2\pi}{3}\right)&\cos\left(\theta_r+\frac{3\pi}{Q_r}-\frac{2\pi}{3}\right)&\cos\left(\theta_r+\frac{5\pi}{Q_r}-\frac{2\pi}{3}\right)&\ldots&\cos\left(\theta_r+\frac{(2Q_r-1)\pi}{Q_r}-\frac{2\pi}{3}\right)\\\cos\left(\theta_r+\frac{\pi}{Q_r}+\frac{2\pi}{3}\right)&\cos\left(\theta_r+\frac{3\pi}{Q_r}+\frac{2\pi}{3}\right)&\cos\left(\theta_r+\frac{5\pi}{Q_r}+\frac{2\pi}{3}\right)&\cdots&\cos\left(\theta_r+\frac{(2Q_r-1)\pi}{Q_r}+\frac{2\pi}{3}\right)\end{bmatrix}(9)$$

$$[M_{s2,r}]=[M_{r,s2}]^t=\begin{bmatrix}\cos\left(\theta_r-\alpha+\frac{\pi}{Q_r}\right)&\cos\left(\theta_r-\alpha+\frac{3\pi}{Q_r}\right)&\cos\left(\theta_r-\alpha+\frac{5\pi}{Q_r}\right)&\cdots&\cos\left(\theta_r-\alpha+\frac{(2Q_r-1)\pi}{Q_r}\right)\\\cos\left(\theta_r-\alpha+\frac{\pi}{Q_r}-\frac{2\pi}{3}\right)&\cos\left(\theta_r-\alpha+\frac{3\pi}{Q_r}-\frac{2\pi}{3}\right)&\cos\left(\theta_r-\alpha+\frac{5\pi}{Q_r}-\frac{2\pi}{3}\right)&\ldots&\cos\left(\theta_r-\alpha+\frac{(2Q_r-1)\pi}{Q_r}-\frac{2\pi}{3}\right)\\\cos\left(\theta_r-\alpha+\frac{\pi}{Q_r}+\frac{2\pi}{3}\right)&\cos\left(\theta_r-\alpha+\frac{3\pi}{Q_r}+\frac{2\pi}{3}\right)&\cos\left(\theta_r-\alpha+\frac{5\pi}{Q_r}+\frac{2\pi}{3}\right)&\cdots&\cos\left(\theta_r-\alpha+\frac{(2Q_r-1)\pi}{Q_r}+\frac{2\pi}{3}\right)\end{bmatrix}(10)$$

$$m_{sr}=\sqrt{l_{ms}.l_{mb}}$$

After the development of the two equations (5) and (6) we obtain the following system of equation:

$$\begin{cases}\frac{d}{dt}[i_{s1}]=[L_{s1,s1}]^{-1}\left\{[v_{s1}]-[R_{s1}][i_{s1}]-[M_{s1r}]\frac{d}{dt}[i_r]-\omega_r\frac{d}{d\theta_r}[M_{s1r}][i_r]\right\}\\\frac{d}{dt}[i_{s2}]=[L_{s2,s2}]^{-1}\left\{[v_{s2}]-[R_{s2}][i_{s2}]-[M_{s2r}]\frac{d}{dt}[i_r]-\omega_r[i_r]\frac{d}{d\theta_r}[M_{s2r}]\right\}\\\frac{d}{dt}[i_r]=[L_{r,r}]^{-1}\begin{Bmatrix}[v_r]-[R_r][i_r]-[M_{rs1}]\frac{d}{dt}[i_{s1}]-[M_{rs2}]\frac{d}{dt}[i_{s2}]\\-\omega_r[i_{s1}]\frac{d}{d\theta_r}[M_{rs1}]-\omega_r[i_{s2}]\frac{d}{d\theta_r}[M_{rs2}]\end{Bmatrix}\end{cases}\quad(11)$$

The derivatives of the mutual inductance between the stator and the rotor are:

$$\frac{d}{d\theta_r}[M_{s1,r}]=\frac{d}{d\theta_r}[M_{r,s1}]^t-m_{s1,r}$$

$$=\begin{bmatrix}\sin\left(\theta_r+\frac{\pi}{Q_r}\right)&\sin\left(\theta_r+\frac{3\pi}{Q_r}\right)&\sin\left(\theta_r+\frac{5\pi}{Q_r}\right)&\cdots&\sin\left(\theta_r+\frac{(2Q_r-1)\pi}{Q_r}\right)\\\sin\left(\theta_r+\frac{\pi}{Q_r}-\frac{2\pi}{3}\right)&\sin\left(\theta_r+\frac{3\pi}{Q_r}-\frac{2\pi}{3}\right)&\sin\left(\theta_r+\frac{5\pi}{Q_r}-\frac{2\pi}{3}\right)&\ldots&\sin\left(\theta_r+\frac{(2Q_r-1)\pi}{Q_r}-\frac{2\pi}{3}\right)\\\sin\left(\theta_r+\frac{\pi}{Q_r}+\frac{2\pi}{3}\right)&\sin\left(\theta_r+\frac{3\pi}{Q_r}+\frac{2\pi}{3}\right)&\sin\left(\theta_r+\frac{5\pi}{Q_r}+\frac{2\pi}{3}\right)&\cdots&\sin\left(\theta_r+\frac{(2Q_r-1)\pi}{Q_r}+\frac{2\pi}{3}\right)\end{bmatrix}(12)$$

$$\frac{d}{d\theta_r}[M_{s2,r}]=\frac{d}{d\theta_r}[M_{r,s2}]^t-m_{s2,r}$$

$$=\begin{bmatrix}\sin\left(\theta_r-\alpha+\frac{\pi}{Q_r}\right)&\sin\left(\theta_r-\alpha+\frac{3\pi}{Q_r}\right)&\sin\left(\theta_r-\alpha+\frac{5\pi}{Q_r}\right)&\cdots&\sin\left(\theta_r-\alpha+\frac{(2Q_r-1)\pi}{Q_r}\right)\\\sin\left(\theta_r+-\alpha\frac{\pi}{Q_r}-\frac{2\pi}{3}\right)&\sin\left(\theta_r-\alpha+\frac{3\pi}{Q_r}-\frac{2\pi}{3}\right)&\sin\left(\theta_r-\alpha+\frac{5\pi}{Q_r}-\frac{2\pi}{3}\right)&\ldots&\sin\left(\theta_r-\alpha+\frac{(2Q_r-1)\pi}{Q_r}-\frac{2\pi}{3}\right)\\\sin\left(\theta_r-\alpha+\frac{\pi}{Q_r}+\frac{2\pi}{3}\right)&\sin\left(\theta_r-\alpha+\frac{3\pi}{Q_r}+\frac{2\pi}{3}\right)&\sin\left(\theta_r-\alpha+\frac{5\pi}{Q_r}+\frac{2\pi}{3}\right)&\cdots&\sin\left(\theta_r-\alpha+\frac{(2Q_r-1)\pi}{Q_r}+\frac{2\pi}{3}\right)\end{bmatrix}(13)$$

3) Electromagnetic torque equation

In general, the equation of the electromagnetic torque is written:

Where p is the number of pair poles. Knowing that matrices L_{ss} and L_{rr} are independent of the position, the expression of the electromagnetic torque is reduced to:

$$T_{em}=p\left([i_{s1}]^t\frac{d}{d\theta_r}[M_{s1,r}][i_r]+[i_{s2}]^t\frac{d}{d\theta_r}[M_{s2,r}][i_r]\right)\quad(14)$$

4) Mechanical equation

The general equation of the speed rotation of the machine is written:

$$J\frac{d\Omega_r}{dt}=T_{em}-T_r-K_f\Omega_r\quad(15)$$

III. SIMULATION RESULTS

In order to create a diagnostic procedure, a simulation is carried out in the MATLAB/Simulink environment. The aim of this simulation is to observe how the differential variables behave both under normal operating conditions and in the event of a fault. The object of study concerns faults linked to the breakage of bars in the cage of the double-star asynchronous machine. The simulation of this specific fault involves an artificial manipulation consisting in significantly increasing the resistance of the broken bar (incriminated by a

sufficient factor), so as to reduce the current flowing through it as much as possible (as close as possible to zero) in steady state. In this modeling approach, it should be noted that breaking a bar does not alter the rotor cage's self and mutual inductances. We have opted for a specific simulation configuration, choosing a simulation time of t=6 seconds, a sampling step of te=0.0001 seconds, and using the 'Runge Kutta 4' method to solve the differential equations. In this simulation, we considered several scenarios: Initially, we assumed that the machine was operating normally without any problems. At time t = 1.5 seconds, we introduced a load torque of 100 N.m, simulating a disturbance in the system. At time t = 3 s, we modeled the breakage of a rotor bar, which had a significant impact on the machine's behavior. Finally, at time t = 4.5s, we simulated the breakage of a second rotor bar, which further altered the machine's operating conditions. These parameters and specific events enable us to analyze the machine's behavior in a variety of situations and to understand how it reacts to these disturbances. From the results obtained, it is clear that the presence of two adjacent broken bars has a significant impact on various aspects of machine performance. Figs. 3 and 4 illustrate the evolution of speed and torque as a function of time. The transition from no-load to loaded operation at time t=1.5 seconds is almost instantaneous, with no significant oscillations and a slight overshoot. A slight fluctuation is observed when the first rotor bar breaks (at time t=3 s). This fluctuation, which intensifies when the second fault occurs (at time t=4.5 s), oscillates at a frequency of 2gfs. This speed variation is very small, as it depends mainly on the inertia of the machine-load assembly. The greater the inertia of this assembly, the less significant the speed variation. Analysis of the electromagnetic torque reveals a noticeable change in its shape when rotor faults occur. A slight modulation disturbs the evolution of torque when the first bar breaks. Moreover, this modulation becomes more pronounced with the appearance of the second fault.

When analyzing stator current responses before and after bar breakage, stator current modulation increases significantly with the number of broken bars (Figs. 5 and 6). Fig. 7 shows the rotor currents in the first three rotor bars. It can be seen that the current in the first bar cancels out at t=3 s. Similarly, the second bar current cancels out at t=4.5 s. Figs. 10 to 12 show the distribution of currents through the rotor bars at time t for the three operating modes studied: healthy rotor, one broken bar and two broken bars. We can see that breaking the first bar induces a very slight increase in the current flowing through it. At the moment of the first fault, the current flowing through the broken bar is shared by the adjacent rotor bars. When the second bar is broken, the current in bar n°3 increases significantly.

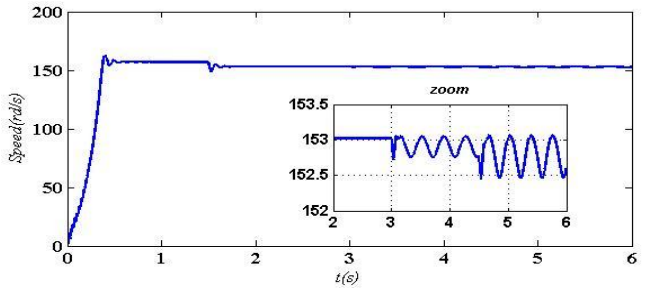


Figure3. Speed of machine

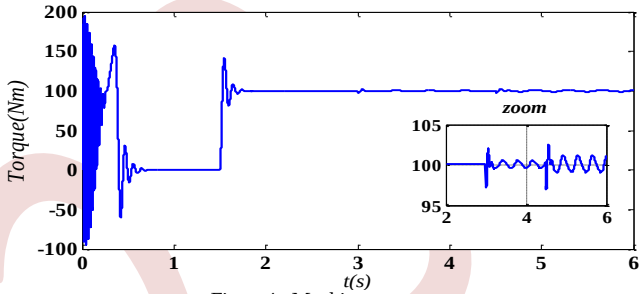


Figure4. Machine torque

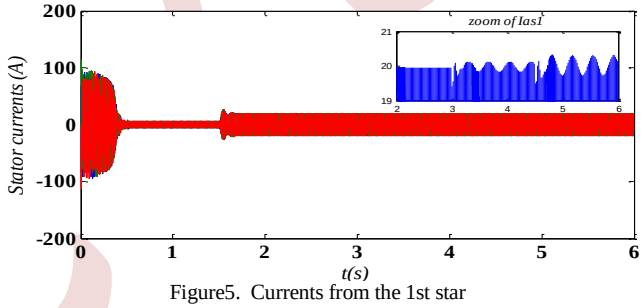


Figure5. Currents from the 1st star

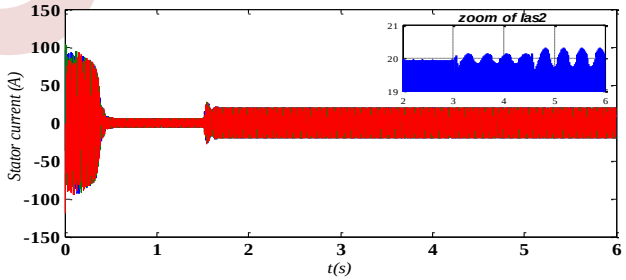


Figure 6. Currents from the 2nd star

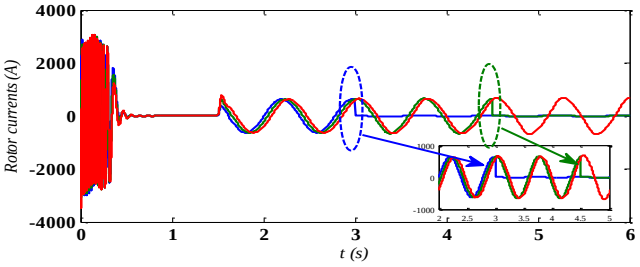


Figure7. Rotor-bar currents 1, 2 and 3

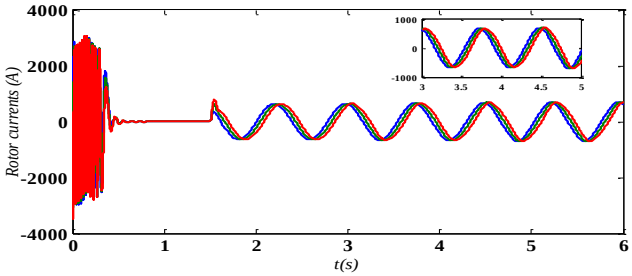


Figure8. Rotor-bar currents 20, 21 and 22

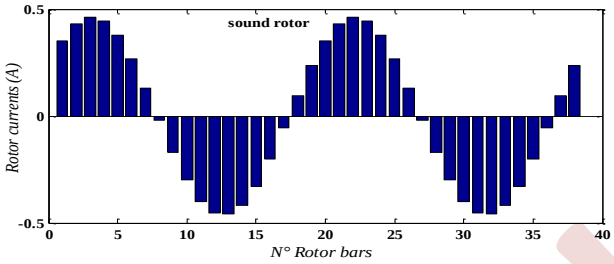


Figure9a. Sound rotor

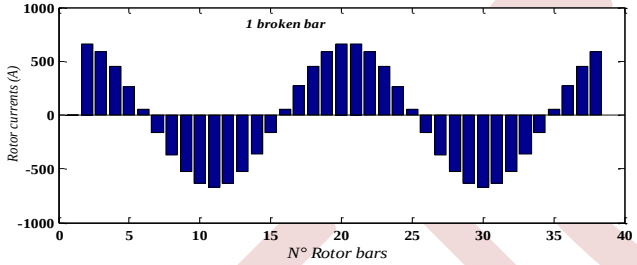


Figure 9b. First broken bar

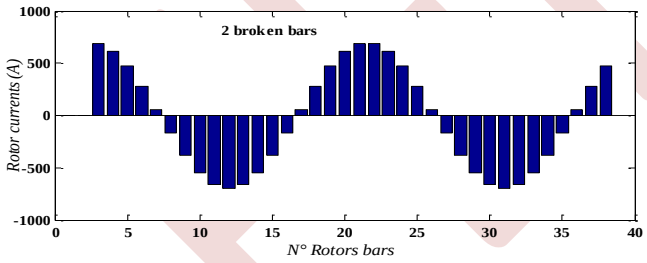


Figure 9c. Second broken bar

Figure9. Current repartition in the rotor bars at time t

IV. CONCLUSION

The work presented here is part of a study of faults in double-star cage induction machine. In this study, we focused on the rotor bar breakage fault. We calculated the mathematical equations in the natural reference frame (ABC) that describes the machine. It should be noted that this methodology is used in the context of fault diagnosis. We then plotted the characteristics of the machine in the absence and presence of faults, highlighting the impact of rotor bar breakage, while neglecting spatial harmonics. The results obtained revealed that bar breaks lead to oscillations in the machine's torque and speed, a slight increase in the amplitude of rotor bar currents, and the appearance of harmonics in stator currents. It is important to note that the detection of broken-bar faults in no-load mode proves complex. A comparison of our results with other studies leads us to conclude that the modeling method we have employed is proving effective.

REFERENCES

[1] AH. Bonnett, GC.Soukup, "Cause and analysis of stator and rotor failures in three-phase squirrel-cage induction motors," IEEE Transactions on Industry Applications 28, pp.921-937, 1992.

[2] M. Ojaghi, M. Sabouri and J. Faiz, "Diagnosis methods for stator winding faults in three-phase squirrel-cage induction motors," International Transactions on Electrical Energy Systems. vol. 24, pp 891-912, 2013.

[3] R.R. Schoen, B.k.Lin, T.G. Habetler, J.H.Schlagand s.Farag, "An unsupervised, on line system for induction motor fault detection using stator current monitoring,"Conference, Rec,IEEE Transactions on Industry Applications, vol.13,pp.1280-1286,1995

[4] M. Benouzza, M. Drif, A.J. Marques Cardos and J.A. Dente, "Emploi de l'approche des vecteurs de Park pour la détection des défauts de barres dans les moteurs asynchrones à cage d'ecureuil," Rev. Energ. Ren, pp.71-76,1999.

[5] P. J. Tavner, J. Penman, "Condition monitoring of electrical machines, " Wiley and sons, New-York, 1987.

[6] G. Didier, E. Ternisien,O. Caspary and H. Razik, "A new approach to detect broken rotor bars in induction machines by current spectrum analysis, " Mechanical Systems and Signal Processing 21, pp.1127-1142, 2007.

[7] J.Rangel-Magdaleno,J.Ramirez-Cortes and H.Peregrina-Barreto, " Broken Bars Detection on Induction Motor Using MCSA and Mathematical Morphology: An Experimental Study, " IEEE Instrumentation and Measurement Technology Conference,2013.

[8] H. Ola , A. Motaz , A. Ahmed, W. Barry ," Induction motor broken rotor bar fault detection techniques based on fault signature analysis-a review, " IET Electr. Power Appl.,vol. 12 , pp. 895-907,2018.

[9] M.Abd-el-Malek, K. Abdelsalam, O.Hassan ,"Induction motor broken rotor bar fault location detection through envelope analysis of start-up current using Hilbert Transform, ", Mechanical Systems and Signal Processing, 93, pp332–350,2017.

[10] R.Kechida, A.Menacer, H.Cherif, "Broken rotor bars fault detection in induction motors using FFT: simulation and experimentally study,", Algerian Journal of Engineering and Technology, 01,pp.019–024,2019.

[11] J.Pyrhönen, T.Jokinen, V.Hrabovcová, "Design of Rotating Electrical Machines," UK, J.Wiley & Sons. Ltd, 2008.

Transient Thermal model analysis of Three phase Induction motor using both Lumped paramter Thermal network and Finite element method

M.Bouheraoua ,R.Khaldi

Mouloud Mammeri university,Tizi ouzou ,Algeria

bouheraoua@hotmail.com

Mouloud Mammeri university,Tizi ouzou ,Algeria

Khaldi_rabah@yahoo.fr

***Abstract*—Paper's authors use lumped parameter thermal network technique and 2D finite element method to predict the machine temperature distribution in transient state at different operating conditions. The application has been done for a totally enclosed fan cooled (TEFC) induction motor 2.2 kW, 3 phases, 4 poles, 380 V delta connection manufactured in Algeria by Electro-Industries [1]. Areas including the notion of thermal contact resistance have been introduced. It is observed that the computed transient temperatures of the machine parts at various modes of operations compare satisfactorily well with the measured transient temperature.**

***Keywords:* Thermal model, Finite element, Lumped parameter.**

I. INTRODUCTION

The induction motor is a robust, economical industrial machine which requires little maintenance, but which is subject to stresses which may be harmful to the machine. Among these constraints, we distinguish the thermal effect on the electrical and magnetic performance of the motor on which the torque and the efficiency depend.

In order to ensure a good design of electric machines, it is necessary to predict with accuracy the temperature distribution in the different sensitive parts of the machine to prevent faults that may occur during the rotation of the motor by breakdown of the stator winding insulation or by mechanical distortion and fatigue of the rotor structure. The prediction of the temperature distribution also allows tracking its influence on the machine performances [2-4].

Two main methods are usually used to model the thermal behavior of electrical machines: lumped parameter thermal network (LPTN) method [5],13] and finite element analysis (FEA) [12],[13],[14]. In this paper, lumped parameter thermal network and finite element model suitable for 2.2 kW totally enclosed fan-cooled (TEFC) induction motors, is used to predict machines temperatures in transient state and obtained results are compared to measured one given by sensors placed in the test motor. The heat generated within a machine (losses) is computed by using 2D non linear coupled Electric-magnetic complex finite element method [12],[13],[14]. Some parameters of the thermal model, such as the contact resistance and the convection heat transfer coefficient of the environment are taken into account and calculated accurately as possible [8],[10],[11].

II. ELECTROMAGNETIC- THERMAL COUPLED FORMULATION

A. electromagnetic field analysis

The machine analyzed in this study, designed for use in machine industrial applications is the kind of three phase induction motor manufactured by Electro-Industrie Algeria [1]. The geometry and flux density distribution of the studied TEFC motor is represented in Fig.5 and its Motor Characteristics is depicted in table II.

The vector potential formulation of electromagnetic equation in the stator winding and rotor bars of the machine is written respectively as follows

$$\nabla \times (\nu \nabla \times \bar{A}_z) = J = \frac{N_C}{S_{cu}} \cdot \vec{n} \qquad (1)$$

$$\nabla \times (\nu \nabla \times \bar{A}_z) + js\sigma\omega_s \bar{A} = \sigma \frac{U_r}{L} \cdot \vec{n} \qquad (2)$$

In which ν is the complex reluctivity, σ the electrical conductivity,ω_s the angular frequency of the time variation, and U_r the electric scalar potential, s the slip, N_c is the number conductor in the slot , S_{cu} the cooper cross sectional area in the slot, I_s the phase current, L the length of the core region and $\bar{A}_z$ being the z component of magnetic vector potential. The underscore means that the quantities are complex variables. In practice, the electromagnetic devices are usually driven by external circuits, as shown in Fig. 1.

The finite formulation of (1) leads to the following matrix system.

$$[S^s][A] - [B_s][I_s] = [0] \quad (3)$$

Equation (1) shows that I_s is an unknown when the induction motor is supplied by a voltage source. In this case, an extra equation can be formulated using the connection between the supply and terminals of the induction motor. This can be expressed for star connection using Kirchoff current Law.

$$\bar{U}_i = R_{ph}\bar{I}_i + jL_{endw}\omega\bar{I}_i + \bar{E}_i \quad (4)$$

In witch $\bar{E}_i = \frac{L}{S_{cu}}\iint_{S_{cu}} \beta_s\, j\omega \cdot \bar{A}_z \cdot d\Omega$ is back electromotive force in each coil.$\bar{U}_i$ Being the voltage source, and L_{endw} , R_{ph} takes into account the end effects of the 2D magneto dynamic model. The per phase circuit corresponding to (4) is shown in Fig. 1.

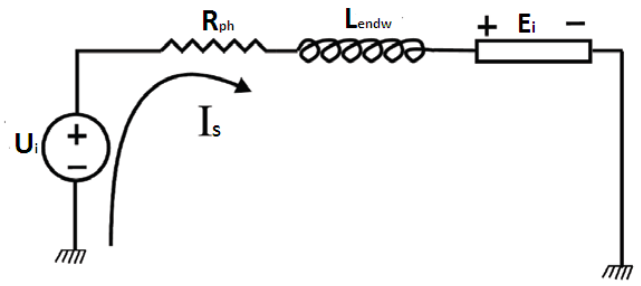


Fig. 1. Coupling between external voltage supplies and FEM 2D model. This loop represents one phase of the stator.

The stator phase equations are expressed in following matrix form.

$$[\bar{U}_i] = [R_{ph}][I_{d3}][\bar{I}_i] + jL_{endw}[I_{d3}][\bar{I}_i] + [\bar{E}_i] \quad (5)$$

With I_{d3} being the (3×3) identity matrix, and $i = 1,2,3$ being the phase location index.

In the rotor bars domain, the equation (2) is valid. The finite element formulation of this equation leads to the following matrix system as follows.

$$[S]^r \cdot [A] + js\omega_s[M] \cdot [A] - [B_r][U_r] = 0 \quad (6)$$

The term appearing in (2) takes into account the eddy currents induced in solid conductors. Last term in (2) takes into account the end effect of the rotor cage, represents the voltage difference between consecutive bars in the rotor. Thus, the term appearing in (2), is also another unknown variable that can be solved according to the circuit topology of the squirrel cage. By Kirchhoff's current law, rotor bar current and endring current are coupled as follows.

$$I_r = -[M]^t \cdot [I] \quad (7)$$

Where $[M]$ is the matrix which determines the relation between bars current $[I_r]$ and end ring$[I]$.
From Kirchhoff's voltage law,

$$2[U] = [M][U_r] = [R_{sc}][I] + [L_{sc}]js\omega_s[I] = [Z_{cc}][I] \quad (8)$$

With $[R_{sc}] = 2R_{sc} \cdot [I_{nb\times nb}]$, $[L_{sc}] = 2 \cdot L_{sc} \cdot [I_{nb\times nb}]$ are the end ring impedance of rotor cage.

$[I_{nb\times nb}]$ is the unit matrix having the number of rotor bars as a dimension. U_r is the potential difference between both ends of rotor bar and U is .the voltage across a portion of endring. The potential difference is

$$U_r = L\frac{\partial\varphi}{\partial z} \quad (9)$$

Where L is core lamination length. The bar current is

$$I_r = \iint_{S_b} \sigma\left(-\frac{d\vec{A}}{dt} - \frac{\partial\varphi}{\partial z}\right)d\Omega \quad (10)$$

Where S_b is the cross sectional area of rotor bar .from (5) to (8), rotor circuit equation is.

$$-\frac{[M]^t[M]}{[Z_{cc}]} + \sigma\iint_{S_b}\sigma\frac{\partial\bar{A}_z}{\partial t}d\Omega + \sigma\iint_{S_b}\frac{\partial\varphi}{\partial t}d\Omega = 0 \quad (11)$$

All the systems of matrix equations (3),(5),(6) and (11) are grouped together to form an equation which describes the entire behavior of the machine with A, U_r ,Is are the unknowns of the problem to be determined. . More details about this study can be found in [8- 13].

$$\begin{bmatrix} [S(A)] & [B_r] & [B_s] \\ [B_r]^t & [C_r] & [\text{zero}] \\ [B_s]^t & [\text{zero}] & [C_s] \end{bmatrix}\begin{bmatrix} [A] \\ [U_r] \\ [I_s] \end{bmatrix} = \begin{bmatrix} [0] \\ [0] \\ [U_s] \end{bmatrix} \quad (12)$$

The matrices$[S(A)]$,$[B_r]$,$[B_s]$ and $[C_r]$ are defined in reference [13].

B. Transient thermal field analysis

The merit of thermal models of electric machines is the ability to predict the temperature distribution during the design stages. Several approaches are used such as lumped parameter thermal network (LPTN), finite element analysis (FEA), and computational fluid dynamics (CFD)[10],[11],[14],[18]. A 2D lumped parameter thermal network (LPTN) is used in order to compute the motor temperature in transient state. The choice of this method lies for its ease of execution and its low calculation time. This method exploiting the analogy between electric and thermal phenomena, the networks include resistances, capacities for the transient analysis, and current sources that represent the internal losses of the motor. Many

researchers have used this method for solving heat transfer problems in electrical machines [3],[6] and [8],[9],[11],[12],[19]. The machine structure can be compared to a set of isothermal volume of coaxial cylinders whose center is represented by nodes as stator cooper, yoke, stator teeth, rotor core, rotor teeth, air gap and the environment. Each node of the 2D lumped parameter thermal network is then associated to a volume V_i, temperature θ_i, heat capacity C_i , and a heat source P_i as shown by the figure.2 and since the machine has symmetry; it is possible to divide the machine into elements that are concentric around the shaft. If the asymmetrical axial distribution of the temperature due to the presence of the external fan is neglected, then only half the machine needs to be considered [10].In developing a thermal model for heat transfer in a machine, it is assumed that heat flows in the axial and radial directions are independent, The heat generation is uniformly distributed, a single mean temperature defines the heat flow in the three directions, Only the axial heat transfer in the winding is considered and that flow in the circumferential direction is negligible [8],[10][15],16]. Based on the assumptions, the T-network [10] is adopted in this paper to represent the thermal resistance distribution in a certain direction. To consider the temperatures of six surfaces for a component, a 3-D T-network of an arc-segment [19] is illustrated in Figure.2. There are three 1-D T-networks corresponding to radial, circumferential and axial directions respectively, and they are combined by connecting the points of mean temperature θ_m , where internal heat P is introduced. The formulas of thermal resistances in 3-D T-network are summarized in Table I , where λa, λc and λr are the corresponding thermal conductivities. Based on the above assumptions, the lumped parameter thermal networkt (LPTN) developed is shown in Fig.3.

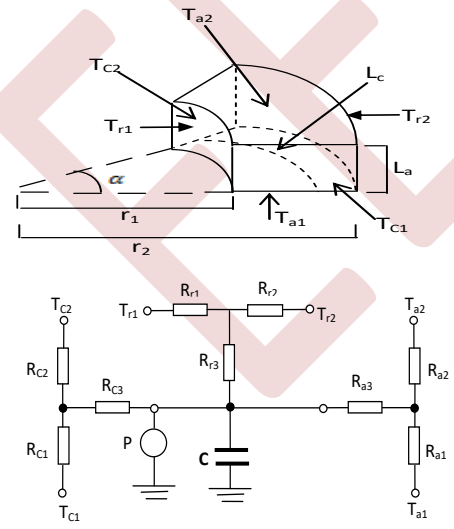


Fig.2 . Geometric and T-network representation of an arc-segment

Table I. Thermal resistances in 3-D T-network of an arc-segment [19].

R	Radial direction (subscript r)	Axial direction (subscript a)	Circumferential direction (subscript c)
R_1	$\frac{90}{\alpha\pi\lambda_r}\left[\frac{2r_2^2 Ln\left(\frac{r_2}{r_1}\right)}{r_2^2-r_1^2}-1\right]$	$\frac{180L_a}{\alpha\pi\lambda_a(r_2^2-r_1^2)}$	$\frac{L_c}{2\pi\lambda_c L_a(r_2-r_1)}$
R_2	$\frac{90}{\alpha\pi\lambda_r}\left[1-\frac{2r_2^2 Ln\left(\frac{r_2}{r_1}\right)}{r_2^2-r_1^2}\right]$	$\frac{180L_a}{\alpha\pi\lambda_a(r_2^2-r_1^2)}$	$\frac{L_c}{2\pi\lambda_c L_a(r_2-r_1)}$
R_3	$\frac{-45}{\alpha\pi\lambda_r L_a(r_2^2-r_1^2)}\left[r_2^2+r_1^2-\frac{4r_1^2r_2^2 Ln\left(\frac{r_2}{r_1}\right)}{r_2^2-r_1^2}\right]$	$\frac{-60L_a}{\alpha\pi\lambda_a(r_2^2-r_1^2)}$	$\frac{-L_C}{6\lambda_C L_a(r_2-r_1)}$

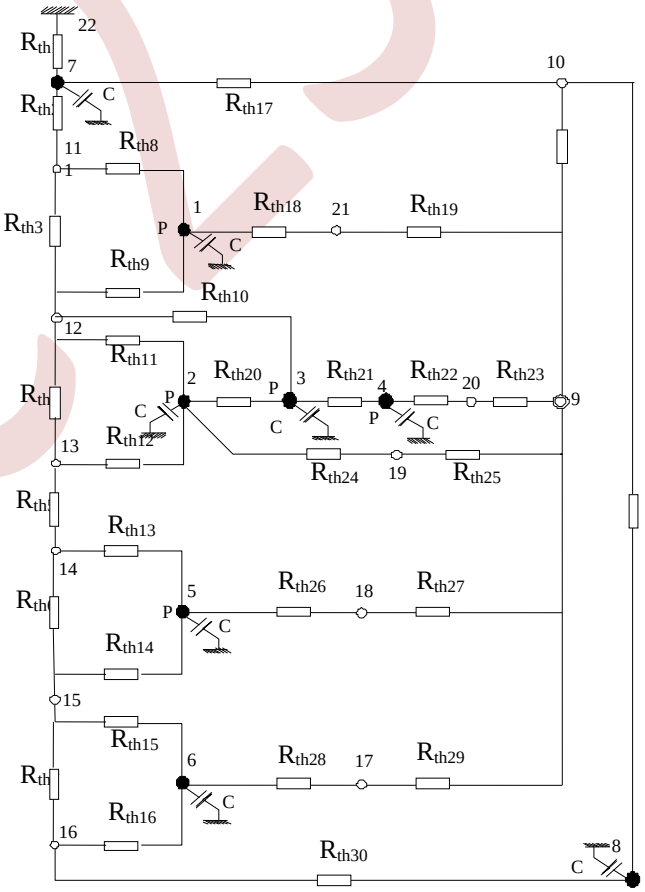


Fig.3. Lumped parameter transient thermal network of induction motor

Connections nodes ; solid elements nodes

P heat sources ; **C** thermal capacitances ; $\mathbf{R_{th}}$ thermal resistances.

1) Stator yoke ; 2) stator teeth ; 3) stator cooper 4) End windings; 5) rotor bars; 6) rotor core;7) Frame; 8) shaft.

III. FORMULATION OF THE THERMAL MODEL EQUATION

The transient lumped parameter thermal network developed shown in the Fig.3 contains (17) nodes. The numbered nodes from 1 to 9 correspond to the conductive elements (solid elements of the machine) and comprise heat capacities. Whilst nodes 9 and 10 represent respectively a convective element (end cap air) of which we neglected his heat capacity.The remaining (06) nodes represent the connections nodes. These equations are then rearranged and grouped to form the following system [3].

$$[\boldsymbol{C}]\{\dot{\boldsymbol{\theta}}_{\boldsymbol{\iota}}\} + [\boldsymbol{G_{11}}]\{\boldsymbol{\theta_i}\} + [\boldsymbol{G_{12}}]\{\boldsymbol{\theta_2}\} = \{\boldsymbol{P_i}\} \quad (13)$$

$$[\boldsymbol{G_{21}}]\{\dot{\boldsymbol{\theta}}_{\boldsymbol{i}}\} + [\boldsymbol{G_{22}}]\{\boldsymbol{\theta_2}\} = \{\boldsymbol{0}\} \quad (14)$$

Where: [C] Is the diagonal matrix of the capacitances and $[G_{11}]$,$[G_{12}]$,$[G_{21}]$,$[G_{22}]$ are the matrices of the thermal conductance's. $\{\dot{\theta}_i\}$And $\{\theta_2\}$ are the vector of the unknown temperatures and $\{P_i\}$ the column vector of power losses. The system (13) and (14) lead to the following differential system.

$$\{\dot{\theta}_i\} + [G_{eq}]\{\theta_i\} = \{P_i\} \quad (15)$$

With$\{F_i\} = \frac{1}{[C]}[P_i]and[G_{eq}] = \frac{1}{[C]}\left([G_{11}] - [G_{12}]\frac{1}{[G_{22}]}[G_{21}]\right)$

From (13) we calculate the vector of temperature $\{\theta_i\}$ and after substitution in (14) we obtain the vector of temperature $\{\theta_2\}$ .A computer program written in Matlab software was developed in which these systems are solve using Range-Kutta method. In order to predict dynamic temperature distribution of the induction motor, an analysis procedure is developed and shown in Fig. 4.

TableII. Motor characteristics

Parameters	Values
Rated output power,kW	2.2
Frequency, Hz	50 z
Rated speed, Rpm	1416
Cos φ	0.87
Rated line voltage, V	380
Rated line current, A	5.2
Rated Torque, N.m	15 Nm
Stator winding connection	Δ
Insulation class	F
Protection	IP 55
Number of poles	4
Number of stator slots	36
Number of rotor slots	28
Frame external diameter, mm	153
Frame axial length, mm	192
Stator back iron external diameter, mm	145
Stator back iron internal diameter, mm	119.53
Stator internal diameter, mm	88.5
Air gap length, mm	0.25
Rotor external diameter, mm	88
Rotor back iron external diameter, mm	57.75
Shaft diameter ,mm	37

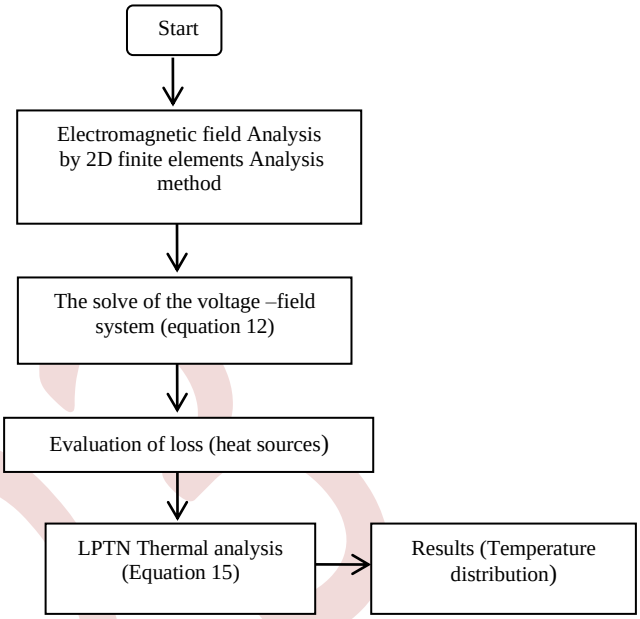


Fig.4. Diagram of computation procedure

IV. EXPERIMENTAL WORK

The test rig consists of a 2.2 KW, 3 phase, 4 pole, 380V, squirrel cage induction motor mechanically coupled to a separately excited DC machine which represents the load. The temperature measurements at different points within the motor were obtained using thermocouples placed at strategic locations of the motor. The thermocouples outputs were monitoring using a 12 channels microprocessor based data logger unit. More details about the experimental procedure can be found in [8].

V. RESULTS AND DISCUSSSION

The electromagnetic model computes the flux density and the different losses inside the machine, which are the thermal sources in the thermal model. Stator and rotor currents computation is based on 2-D coupled nonlinear complex finite element method [8]. Figure.5 and figure.6 shows the distribution of magnetic flux density and losses densities distribution in the different parts of the analyzed motor respectively In order to validate the results obtained by the model, the experimental tests are carried out on the studied machine. We carried out a test with variable load. The comparison of the experimental results under various modes of operation ($\boldsymbol{100\%I_n}$, $\boldsymbol{90\%I_n}$, $\boldsymbol{80\%I_n}$, $\boldsymbol{100\%I_n}$), where $\boldsymbol{I_n}$ is the rated current, with those obtained by the thermal model developed in the various parts of the machine is illustrated by figure.7. We compared for three different modes, the simulated and measured temperatures. The simulation results obtained compared with the experimental results are with a good agreemt.

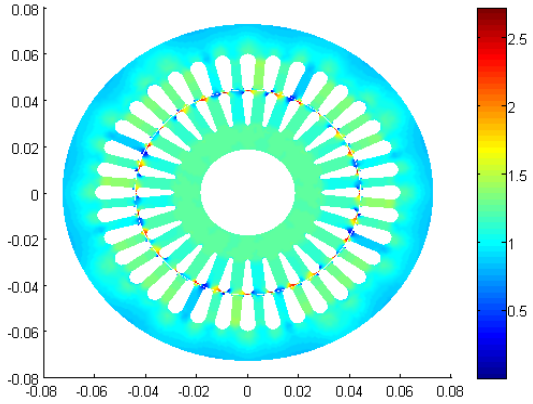


Fig.5. Magnetic flux density (Tesla) at rated load (s=0.05)

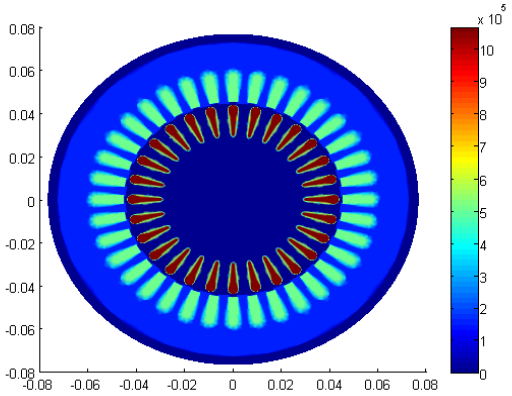
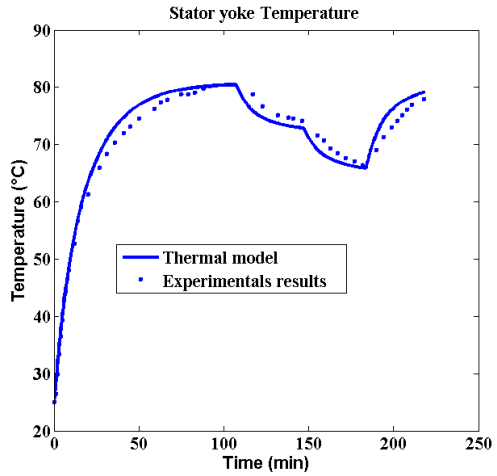
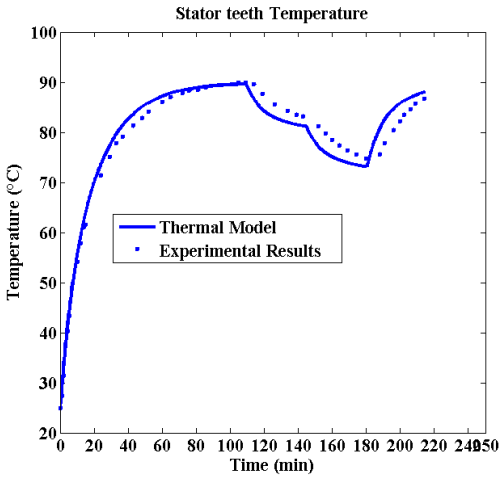
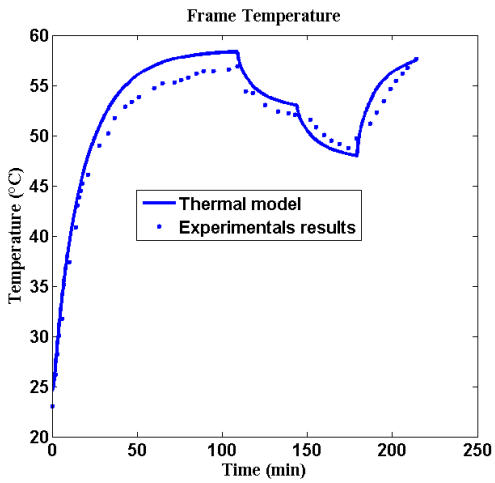
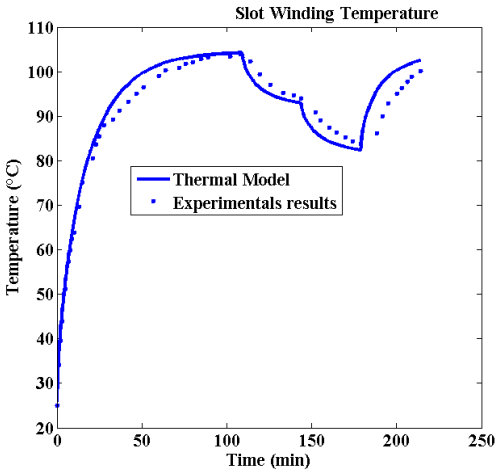


Fig.6. Losses densities distribution in the induction motor at rated load (s=0.05).









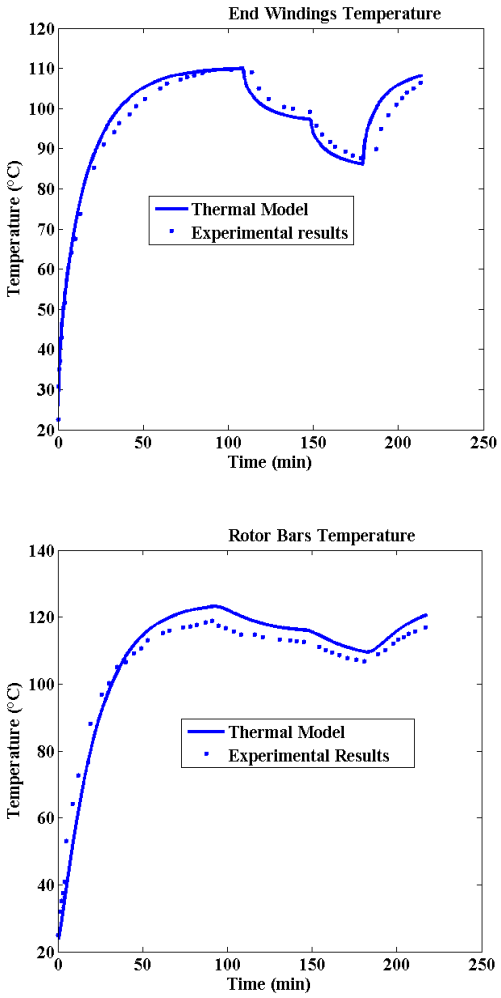


Fig.7.Evolution of temperature distribution in different parts of the machine at several load conditions ($100\%\mathbf{I_n}$, $90\%\boldsymbol{I_n}$, $80\%\boldsymbol{I_n}$, $100\%\boldsymbol{I_n}$).

VI. CONCLUSION

In this paper, a lumped parameter thermal network of an induction motor of 2.2 kW is developed. The validity of the cylindrical lumped components approach has been tested through the comparaison between the experimental data and the simulation results. The transient thermal measurements carried out on the test machine show that the proposed thermal network model is able to predict the mean temperature in the test machine with reasonable accuracy during various modes of operations. The errors observed between the measured and calculated may be due to the fact that the developed thermal model calculates the average temperatures inside the stator , whereas the installed thermoelements mesure only the outside temperature of the stator. Probable error may be due to the errors emanating from the calculation of the model's thermal resistances and capacitances which are dependent on the material properties of the machine which accurate information from the manufacturer on same is highly necessary. These errors are, however, within acceptable limits for practical purposes.

REFERENCES

[1] Electro-Industries,'' Company specialized in manufacturing and marketing motors'', Azazga,Algeria

[2] J. M. KaufFmann, B. Laporte, "Analyse des performances des machines dlectriques" RGE, No 8, Sept. 1994, pp. 36-40.

[3] D. Roye, Modélisation thermique des machines électriques tournantes. Application a la machine a induction, Thèse de doctorat, I.N.P. Grenoble (France), Nov. 1983.

[4] Sciascera, C., and Giangrande, Paolo., and Papini, Luca., and Gerada, C., and Galea, Michael., ''Analytical thermal model for fast stator winding temperature prediction,'' IEEE Transactions on Industrial Electronics,64 (8). pp. 6116-6126. ISSN 0278-0046, 2017

[5] Qixu Chen., Zhongyue Zou., and Binggang Cao., "Lumped-Parameter Thermal Network Model and Experimental Research of Interior PMSM for Electric Vehicle," CES Transactions on electrical machines and systems, vo. 1, no. 3. December, 2017.

[6] Payam Shams Ghahfarokhia.,Ants Kallastea.,,Anouar Belahcenb.,Toomas Vaimanna.,Anton Rassõlkina.,''Hybrid thermal model of a synchronous reluctance machine,'' Case Studies in Thermal Engineering 12 (2018) pp.381–389. Ed. Elsevier, 2018. *DOI:*10.1016/j.csite.2018.05.00.

[7] Galea, Michael., and Gerada, C., and Raminosa, Tsarafidy., and Wheeler, Patrick.,''A thermal improvement technique for phase windings of electrical machines,'' IEEE Transactions on Industry Applications, 48 (1). pp. 79-87. ISSN 1939-9367.

[8] M.bouheraoua,N.benamrouche, A.Bousbaine.;'' A More Refined Thermal Model for a Totally Enclosed Fan-cooled Induction Motor''Electric Power Components And Systems,Vol.40,Issue 2,2011;

[9] Amel Adouni., ., Antonio J. Marques Cardoso.,'' Thermal Analysis of Synchronous Reluctance Machines-A Review,''Electric Power component and systems.pp.1-15,2019.

[10] P. H. Mellor., D. Roberts., and D. R. Turner., "Lumped parameter thermal model for electrical machines of TEFC design," IEE Proceedings B-Electric Power Applications, vol. 138, no. 5, pp. 205–218, 1991.VolNo. Sept. DOI: 10.1049/ip-b.1991.0025.

[11] A. Boglietti et al., "Evolution and modern approaches for thermal analysis of electrical machines," IEEE Trans. Ind. Electron, vol. 56, no. 3, pp. 871–882, 2009, MarDOI: 10.1109/TIE.2008.2011622.

[12] Y. Lee and H.-b. Lee, "Temperature analysis of induction motor with distributed heat sources by finite element method," *IEEE Trans. Magn.*,vol. 33, no. 2, pp. 1718–1721, 1997.

[13] Arkkio, A., Analysis of Induction Motors Based on the Numerical Solution of the Magnetic Field and Circuit Equations, Thesis of Acta Polytechnica Scandinavia, Electrical Engineering Series No. 59, Helsinki, Finland,1987.

[14] S. Mezani, R. Ibtiouen, R. Kechroud, O. Touhami, B. Laporte, "Finite element thermal modeling of an induction motor", *Electric Power Components and Systems*, No. 29, 2001, pp. 821-834.

[15] J. Driesen, R.J.M. Belmans, K. Hameyer, Methodologies for coupled transient electromagnetic-thermal Finite-Element modeling of electrical energy transducers, IEEE Transactions on Industry Applications 38 (5) (2002) 1244-1250.

[16] F.P. Incropera and D.P. De Witt, *Fundamental of Heat and Mass Transfer*: Wiley, 1990.

[17] Ying, X.; Jinpeng, G.; Peng, C.; Zhiwei, L. Coupled Fluid-Thermal Analysis for Induction Motors with Broken Bars Operating under the Rated Load. Energies **2018**, doi.org/10.3390/en11082024

[18] Wang, S.W.; Zhang, Y.; Hu, J. Thermal Analysis of Water-Cooled Permanent Magnet Synchronous Motor for Electric Vehicles. Appl. Mech. Mater. **2014**, 610, 129–135.

[19] Simpson, N., Wrobel, R., Mellor, P. H., " A general arc-segment element for three-dimensional thermal modeling. ", IEEE Transactions on Magnetics, 50(2): 265-268 (2014) . http://dx.doi.org/10.1109 TMAG.2013.2278866.

Hybrid Model for Modeling Air gap in Electrical Machines

Wafia Mousli

University of Jijel, L2EI Laboratory, Algeria

wafia.mousli91@gmail.com

***Abstract*—The aim of this study is to describe a mathematical approach allowing a direct coupling between analytical solution by separation of variables method and the method of permeance network. This hybrid analytical modeling will allow the resolution of the problem of modeling air gap in electrical machines. First step, we calculated the magnetic potential in each node of the network of a permanent magnet synchronous motor by applying Kirchhoff's law in this network of permeances. Once the matrix system is defined, we move on to algebraic resolution to calculate the flux crossing each branch. The analytical resolution of Laplace equation in a ring by separation of variables method makes it possible to obtain the analytical expression of the vector potential at the air gap, and from the conditions of passage between two locations, we calculate the expression of the current at the edge of the stator which then makes it possible to obtain the electromagnetic torque of the motor from Maxwell tensor. The results obtained by previous experiments are adopted to verify the accuracy of this study. The goal of this work is to optimize the power and speed by changing turns number in the machine and find precise results in a short calculation time.**

Keywords: **Permeance Network Method, Outer Rotor Permanent Magnet Synchronous Motor, Separation of Variables Method, Air Gap, Hybrid Model.**

I. INTRODUCTION

In this paper, we are interested in the development of hybrid model based on permeance network method (PNM) and an analytical one. The model was applied to an outer-rotor permanent magnet synchronous motor (OR-PMSM) which is one of the machines adopted by the automotive industry of its high mass performance and good efficiency. This development is mainly due to determinate the magnetic field and also due to find the main electromagnetic parameters at the air gap.

The permeance network method is very interesting, in particular, in the dynamic simulations of an electrical machine. In order to increase the accuracy of the equivalent permeance network modeling of studied motor, the separation of variables method is used to calculate the current at the edge of the stator, power and speed with good accuracy.

The prototype of the parametric analysis tool is developed entirely on Matlab, it offers a high-level programming environment oriented towards the development of mathematical algorithms and offers very powerful capacities for the treatment of matrices, which represents a whole major for the rapid development of algorithms specific to electrical networks often represented in matrix form as in [1]. In the end, some simulation results are shown to validate the proposed model.

II. STUDIED MACHINE

The studied machine is a permanent magnet synchronous motor as in [2]. It is an outer-rotor motor with 6 poles, 36 teeth and 3 phases full bridge circuit. This machine is available at the L2ES-UTBM laboratory and it is integrated in a bicycle wheel. For reasons of symmetry and by neglecting the extremity effects, one pole pair of the geometry is sufficient to model the entire machine. "Fig. 1" shows the considered machine.

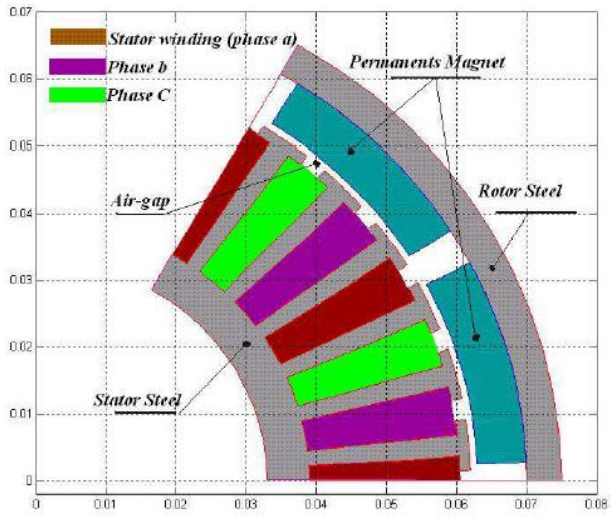


Figure 1. Two dimentional transverse cross section of the studied motor.

III. PERMEANCE NETWORK MODELING

The values of the permeances have been calculated from simple mathematical formulations for every leakage flux path which are taken into account as separate and independent flux path. Two categories of permeances exist depending on the fact that they are constant or variable with respect to the rotor position as in [3]. Table 1 shows the constant permeances values in the studied OR-PMSM. Only the air gap permeances depend on the rotor angle position.

The equations of the stator permeances and the rotor ones $(P_{r,s})$ and the permanent magnet permeances (P_{pm}) are expressed as follows:

$$P_{r,s} = \mu_0 \mu_{r,s} \frac{l.\ln\left(\frac{r_{ext}}{r_{int}}\right)}{\alpha} \quad (1)$$

$$P_{pm} = \mu_0 \mu_{pm} \frac{\alpha}{\ln\left(\frac{r_{ext}}{r_{int}}\right)} \quad (2)$$

TABLE I. CONSTANT PERMEANCES OF THE STUDIED MACHINE.

Permeance index	Location in the motor	Value (H)
P_r	Rotor steel permeance	4.3286×10^{-6}
P_{pm}	Permanent magnet (PM) permeance	2.8611×10^{-7}
P_{pm-pm}	Leakage permeance between PM pole	8.26×10^{-9}
P_{st-st}	Leakage permeance between stator teeth	3.6391×10^{-8}
P_{st}	Permeance of one stator teeth	1.659×10^{-4}
P_s	Stator steel permeance	1.1205×10^{-4}

A. Air Gap Permeance Calculation

The air-gap region is subdivided of air-gap elements each of them is modeled by a permeance which depend on the rotor position. Ostovic method gives a possible air gap element permeance expression relating "the stator tooth, i" to "the rotor pole, j" versus "the rotor relative position, γ" as in [4]. So, the permeances of the air gap region have been defined as a function of the angular position of the rotor, see "Fig. 2".

$$P_{i,j} = \begin{cases} P_{max} & \text{For } 0 \le \gamma \le \gamma_t' \text{ and } 2\pi-\gamma_t' \le \gamma \le 2\pi \\ P_{max}\dfrac{1+\cos\pi\dfrac{\gamma-\gamma_t'}{\gamma_t-\gamma_t'}}{2} & \text{For } \gamma_t' \le \gamma \le \gamma_t \\ P_{max}\dfrac{1+\cos\pi\dfrac{\gamma-2\pi+\gamma_t'}{\gamma_t-\gamma_t'}}{2} & \text{For } 2\pi-\gamma_t \le \gamma \le 2\pi-\gamma_t' \\ 0 & \text{For } \gamma_t \le \gamma \le 2\pi-\gamma_t \end{cases} \quad (3)$$

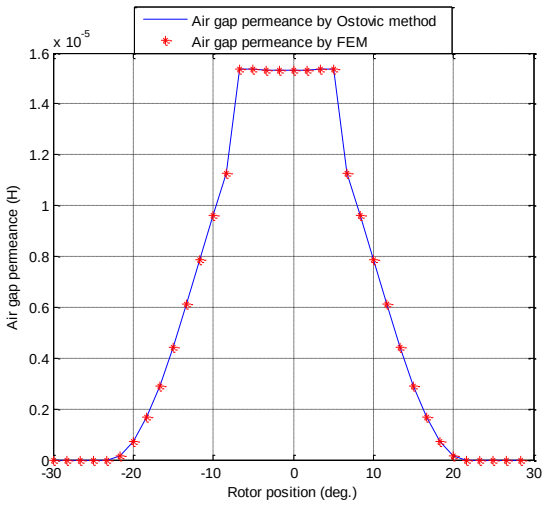


Figure 2. Aair gap permeance variation with the rotor position.

B. Method of Solving Permeance Network

In order to solve the problem which aims to calculate the flux crossing in each branch of the machine we use the law of nodes which can be automated in order to obtain the matrix system to be solved. From an elementary system, see "Fig. 3" the equation of the first node can be established.

Node one is connected with three nodes and a node exceptionally introduced for a first iteration which plays the role of the reference potential in order to be able to solve this system. Between two consecutive nodes, we admit the existence of a "magnetomotive force, F" and having for each node a "magnetic potential, U" as in [5,6].

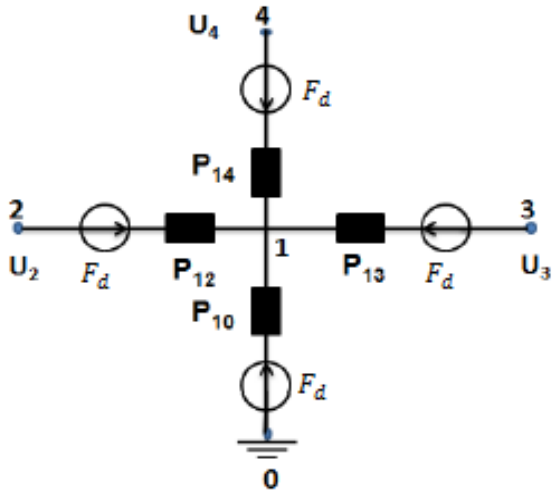


Figure 3. Elementary permeance network.

By applying the law of Kirchhoff in this case, we obtain the equation

$$(U_1 - U_4 - F_d)P_{14} + (U_1 - U_3 - F_d)P_{13} + (U_1 - U_2 - F_d)P_{12} + (U_1 - 0 - F_d)P_{10} = 0 \quad (4)$$

Wich give

$$U_1(P_{10} + P_{12} + P_{13} + P_{14}) - U_4P_{14} - U_3P_{13} - U_2P_{12} = -F_dP_{10} - F_dP_{12} - F_dP_{13} - F_dP_{14} \quad (5)$$

The generalization of the equation for a network comprising "n" nodes leads to

$$U_i\left(P_{i0} + \sum_{j=1, j\neq i}^{n} P_{i,j}\right) - \sum_{j=1, j\neq i}^{n} U_iP_{i,j} = -\sum_{j=0, j\neq i}^{n} F_{i,j}P_{i,j} = -\sum_{j=0, j\neq i}^{n} \varphi_{S_{i,j}} \quad (6)$$

By applying the law of Kirchhoff in the equivalent permeance network given in "Fig. 4" as in [2], we notice that the studied magnetic circuit has 16 nodes and 34 branches. Thus, the dimension of the matrix is equal to 16×16.

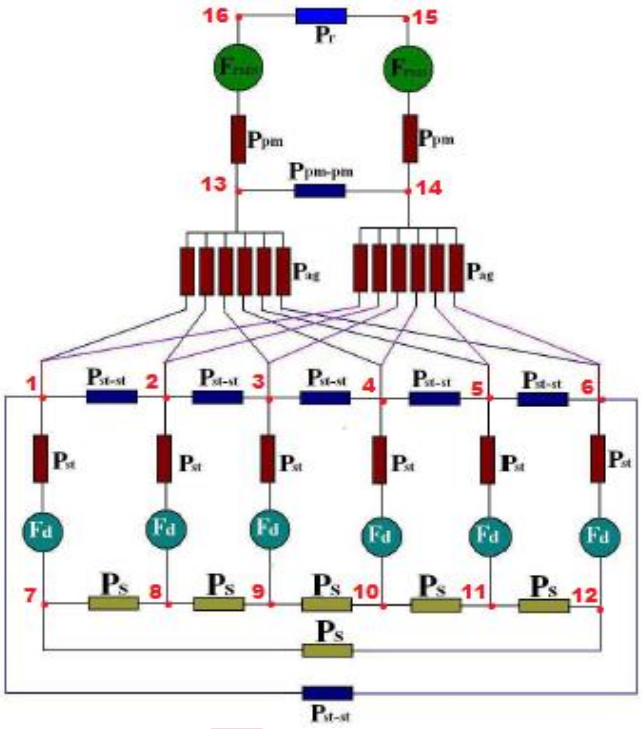


Figure 4. Equivalent permeance network to an OR-PMSM.

So, the matrix system is defined by

$$\begin{bmatrix} A & B & 0 & 0 & 0 & B & C & 0 & 0 & 0 & 0 & 0 & D & D & 0 & 0 \\ B & A & B & 0 & 0 & 0 & 0 & C & 0 & 0 & 0 & 0 & D & D & 0 & 0 \\ 0 & B & A & B & 0 & 0 & 0 & 0 & C & 0 & 0 & 0 & D & D & 0 & 0 \\ 0 & 0 & B & A & B & 0 & 0 & 0 & 0 & C & 0 & 0 & D & D & 0 & 0 \\ 0 & 0 & 0 & B & A & B & 0 & 0 & 0 & 0 & C & 0 & D & D & 0 & 0 \\ B & 0 & 0 & 0 & B & A & 0 & 0 & 0 & 0 & 0 & C & D & D & 0 & 0 \\ C & 0 & 0 & 0 & 0 & 0 & J & R & 0 & 0 & 0 & 0 & 0 & 0 & 0 & 0 \\ 0 & C & 0 & 0 & 0 & 0 & R & J & R & 0 & 0 & 0 & 0 & 0 & 0 & 0 \\ 0 & 0 & C & 0 & 0 & 0 & 0 & R & J & R & 0 & 0 & 0 & 0 & 0 & 0 \\ 0 & 0 & 0 & C & 0 & 0 & 0 & 0 & R & J & R & 0 & 0 & 0 & 0 & 0 \\ 0 & 0 & 0 & 0 & C & 0 & 0 & 0 & 0 & R & J & R & 0 & 0 & 0 & 0 \\ 0 & 0 & 0 & 0 & 0 & C & 0 & 0 & 0 & 0 & R & J & 0 & 0 & 0 & 0 \\ D & D & D & D & D & D & 0 & 0 & 0 & 0 & 0 & 0 & T & K & 0 & M \\ D & D & D & D & D & D & 0 & 0 & 0 & 0 & 0 & 0 & K & T & M & 0 \\ 0 & 0 & 0 & 0 & 0 & 0 & 0 & 0 & 0 & 0 & 0 & 0 & 0 & M & Y & X \\ 0 & 0 & 0 & 0 & 0 & 0 & 0 & 0 & 0 & 0 & 0 & 0 & M & 0 & X & Y \end{bmatrix} \times \begin{bmatrix} U_1 \\ U_2 \\ U_3 \\ U_4 \\ U_5 \\ U_6 \\ U_7 \\ U_8 \\ U_9 \\ U_{10} \\ U_{11} \\ U_{12} \\ U_{13} \\ U_{14} \\ U_{15} \\ U_{16} \end{bmatrix} = \begin{bmatrix} -F_dP_{st} \\ -F_dP_{st} \\ -F_dP_{st} \\ F_dP_{st} \\ F_dP_{st} \\ F_dP_{st} \\ F_dP_{st} \\ F_dP_{st} \\ F_dP_{st} \\ -F_dP_{st} \\ -F_dP_{st} \\ -F_dP_{st} \\ -F_{pm-N}P_{pm} \\ F_{pm-S}P_{pm} \\ -F_{pm-S}P_{pm} \\ F_{pm-N}P_{pm} \end{bmatrix} \quad (7)$$

While the elements of the matrix are equal to:

$A = P_{st} + 2P_{ag} + 2P_{st-st}$, $B = -P_{st-st}$, $C = -P_{st}$, $D = -P_{ag}$
$J = P_{st} + 2 \times P_s$, $R = -P_s$, $T = P_{pm} + P_{pm-pm} + 6P_{ag}$, $K = -P_{pm-pm}$
$M = -P_{pm}$, $X = -P_r$, $Y = P_{pm} + P_r$.

Once the matrix system is defined, we pass to the algebraic solution in order to calculate the flux crossing each branch based on the equation

$$[U] = [P]^{-1}[\varphi_S] \quad (8)$$

Therefore, the flux is expressed in the form

$$\varphi(i,j) = P(i,j).\big(U(i) - U(j)\big) + \varphi_S(i,j) \quad (9)$$

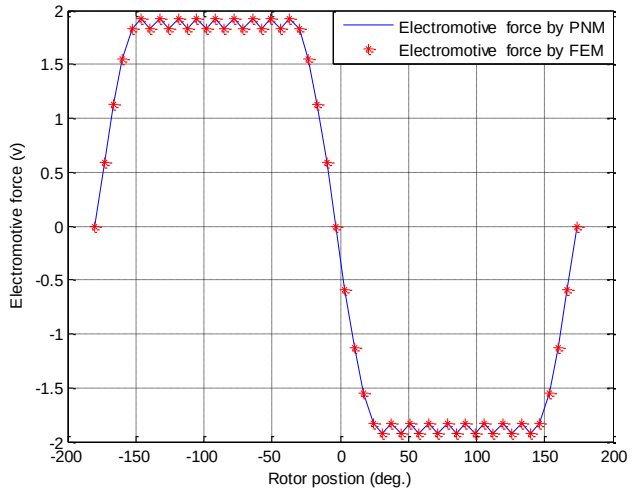


Figure 5. Electromotive force waveform according to the rotor position.

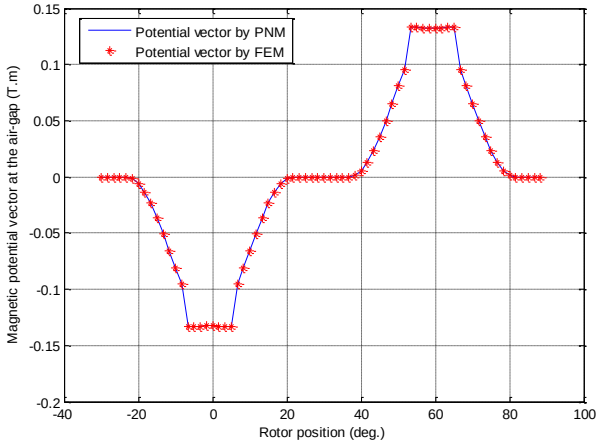


Figure 6. Magnetic potential vector at the air gap.

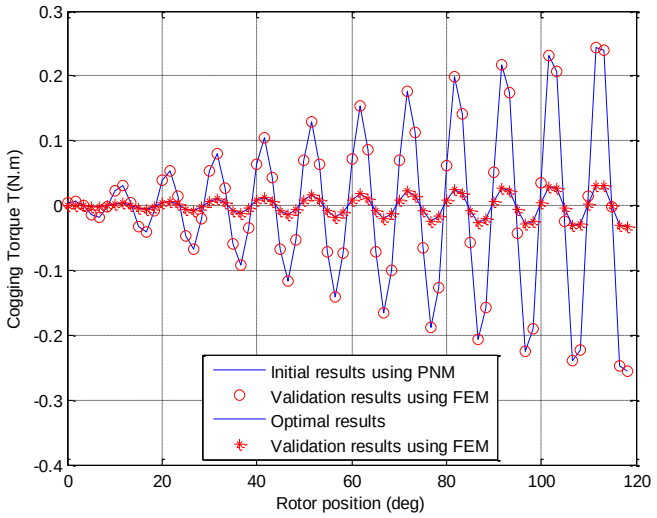


Figure 7. Initial model and optimal model comparison of the cogging torque.

IV. HYBRID MODEL

The hybrid model is obtained by the direct coupling of the permeance network method and the analytical model in what follows the flowchart allowing this coupling in figure below.

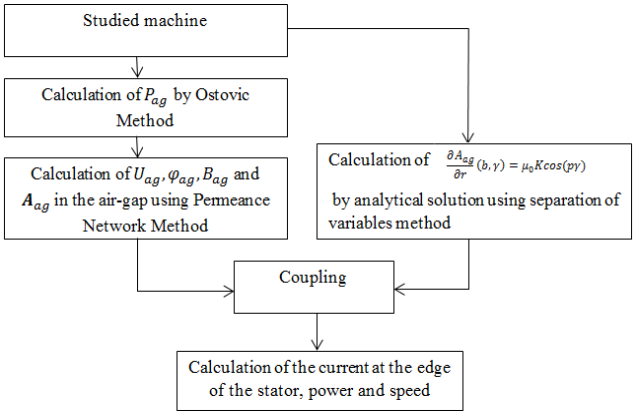


Figure 8. Flowchart of hybrid model of the analytical solution with the permeance network method.

It is shown that the stator windings placed in the slots can be represented by an equivalent linear current density placed on the bore of the stator $(r = b)$ as shown in the following figure. If we consider only the "fundamental of the current sheet, K", its equation as in [7]:

$$k(\gamma) = K\cos(p\gamma) \tag{10}$$

Where p is the number of pole pairs and the external radius is $(r = a)$.

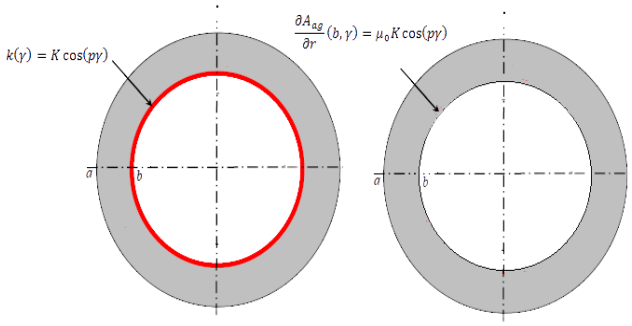


Figure 9. Simplified representation of the stator winding by a current sheet.

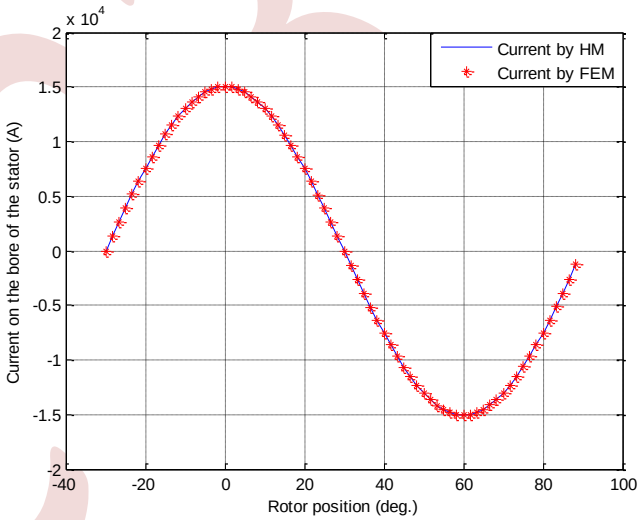


Figure 10. Simplified representation of the stator winding by a current at the edge of the stator.

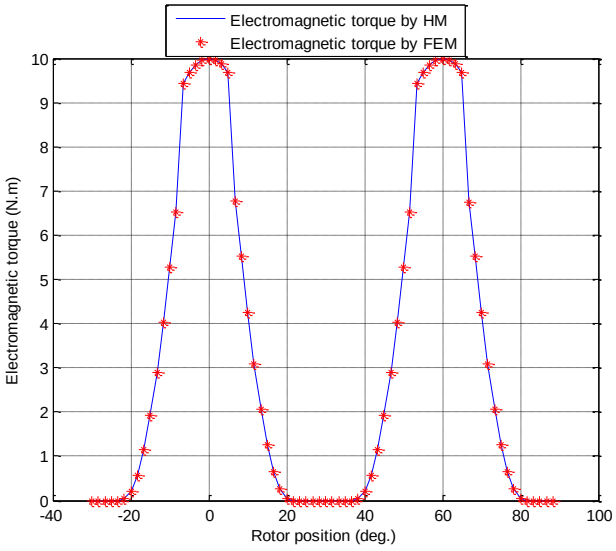


Figure 11. Electromagnetic torque result using hybrid model.

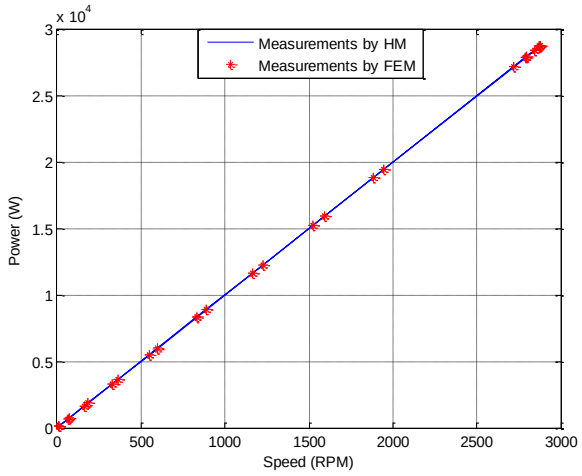


Figure 12. Continuous straight line variation between power and speed.

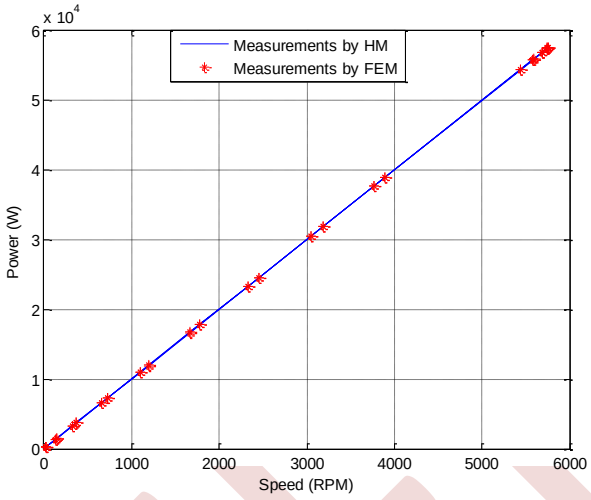


Figure 13. The linear function for doubling speed and power by doubling the turns number.

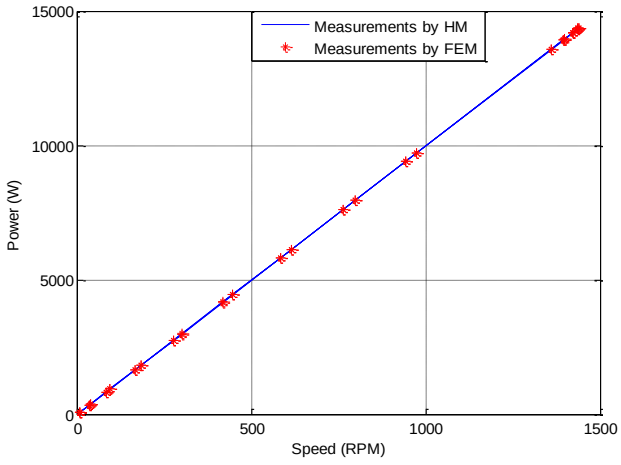


Figure14. The linear function for speed and power by calculating half of number of turns.

V. SIMULATION RESULTS AND DISCUSSION

In order to validate the proposed approach, the air gap permeance is modeled using the Ostovic method and the finite element method (FEM). These two techniques are generally adopted to achieve the calculation of the air gap permeance. The "Fig. 2" shows an acceptable concordance between the two methods. Due to the matrix system we obtain the results of the magnetic potential in all the nodes of permeance network.

The "Fig. 5" represents the result of the electromotive force (EMF) of the studied motor. The permeance network method gives acceptable values and we validate this agreement with finite element method.

By a simple inversion in the magnetic branch equation we can compute the magnetic flux then also makes it possible to obtain the distribution of radial flux density at the air gap. It is therefore the possibility of calculating the magnetic potential vector in "Fig. (6)".

A general analytical expression for cogging torque is derived by the energy method and the Fourier series analysis as in [8], the goal of this calculation is to obtain the optimal values for minimum cogging torque in order to minimize audible noises, vibration and speed ripples in permanent magnet machines. Cogging torque waveform in "Fig. 7" has confirmed the correctness of the results obtained by permeance network method by previous results in [2], and for the minimization of the cogging torque we take the half of the least common multiple of the number of permanent magnet poles and the number of stator slots.

By using the separation of variables method and by applying the boundary conditions, the current at the edge of the stator in the machine is defined in "Fig. (10)".

The electromagnetic torque obtained by hybrid model in "Fig. 11" is compared by the experimental results in [2]. We can remark that the maximal value of the electromagnetic torque in the machine is $T = 10\ N.m$, so, we have improved the correctness of this study.

Regarding "Fig. 12", "Fig. 13" and "Fig. 14", these results confirmed the linear function between power and speed in studied motor. So the base of this hybrid model is to increase the performance analysis of the electrical machines.

VI. CONCLUSION

In this paper a permeance network method of an outer rotor permanent magnet synchronous motor has been developed to compute the magnetic potential in all the nodes and flux values in all the branch of the machine. The modeling of air gap is the most delicate part, it can be calculated by finite element method with good precision results but it has a drawback which is significant time,

contrary to analytical calculation which is described using a well-known mathematical function, and it specifies a low calculation time. In general, for solving Laplace equation in the air gap by separation of variables method, it is necessary to define the boundary conditions using permeance network method, with this hybridization we calculate the expression of the potential vector in the air gap which then makes it possible to compute the current density at the edge of the stator, Laplace force and electromagnetic torque to achieve a desired power or speed in the studied motor. These values have illustrated the advantage of the proposed model and give acceptable results to describe a main of electromagnetic parameters with good accuracy and make it possible for solving the demagnetization problem and eddy current losses in electrical machines.

ACKNOWLEDGMENT

I would like to acknowledge and give my warmest thanks to all who made this work possible.

REFERENCES

[1] Philippe Junior ossoucah, "Analyse paramétrique des réseaux électriques sur Matlab, Departement de génie électrique," école polythechnique de Montréal, Decembre 2010.

[2] S. Touati, R. Ibtiouen, O. Touhami, A. Djerdir, "Experimental investigation and obtimization of permanent magnet motor based on coupling boundary element method with permeance network," Progress in electromagnetics reaserch, vol.111, pp.71.90, 2011.

[3] J. Farouq, S. Srairi, A. Djerdir, A. Miraoui, "Use of permeance network method in the demagnetization phenomenon modeling in a permanent magnet motor," IEEE transactions on magnetics, vol.42, n.04, April 2006.

[4] V. Ostovic, "Dynamics of saturated Electric Machines," New York: Spring-verlag, 1989.

[5] Dan llea, "Conception optimale des moteurs à reluctance variable à commutation électrique pour la traction des véhicules électriques légers," Thèse prepare dans le laboratoire L2EP Ecole Doctorale SPI 072, Université Lille Nord-de-France, Octobre 2011.

[6] Hibatallah Bouker, "Conception et optimization des machines synchrones à aimants permanents à haute vitesse dédiées aux véhicules électriques hybrides," thèse de doctorat de l'université Paris-Saclay, préparée à l'école normale supérieur de Cachan, Ecole Doctorale N°575, novembre 2016.

[7] Thierry Lubin, "Equations aux dérivées partielles (EDP), Méthode de resolution des EDP par separation de variables ; Applications," Master, Université de Lorraine, Faculté des sciences et Technologies, Nancy France, 2017.

[8] Li Zhu, S. Z. Jiang, Z.Q. Zhu, C. C. Chan, "Analytical Methods for Minimizing Cogging Torque in Permanent Magnet Machines," IEEE Transactions on magnetics, vol.45, no. 4, April 2009.

Enhancing Wind Power Conversion Efficiency with Vernier DSPM Generator and Sliding Mode Control

Abderrahmane Redouane [1], Rachid Saou [1], Cherif Guerroudj [2,3], Amrane Oukaour [4]

[1] *Laboratoire de Génie Électrique, Faculté de Technologie, Université de Bejaia, 06000 Bejaia, Algeria*

abderrahmane.redouane@univ-bejaia.dz , rachid.saou@univ-bejaia.dz

[2] *Laboratoire des systèmes électriques industriels (LSEI), BP N◦32 El Alia, Bab Ezzouar 1611, Alger, Algérie*

[3]*Université de Lorraine - GREEN, 54000 Nancy, France.*

cherif.guerroudj@univ-lorraine.fr

[4] *Laboratoire de Recherche en Sciences du Numérique GREYC, Université de Caen Normandie, 6 Boulevard du Maréchal Juin, 14032 Caen, France*

amrane.oukaour@unicaen.fr

***Abstract*—In order to enhance the efficiency of wind power conversion systems, a DC conversion system that combines a wind turbine with a battery is introduced in this paper. The Vernier Doubly Salient Permanent Magnet (V-DSPM) generator at the center of this system, designed for low speeds and high torque, eliminates the need for troublesome gearboxes. The proposed control employs MPPT based on tip speed ratio with output as reference current of boost converter and a sliding mode control-based Gao's constant plus proportional rate reaching law to track the reference current. Three tests were performed to determine the efficiency of the proposed strategy. Moreover, a comparison with a conventional PI controller was carried out. The simulations were performed using MATLAB and Simulink. The obtained results show that the system with SMC has better performance than the system with PI.**

***Keywords:* Direct driven, Low speed, DSPM, Wind turbine, Sliding mode control.**

I. INTRODUCTION

In recent years, wind power turbines have gained increasing popularity as an alternative to fossil fuels. Additionally, the growing demand for generators tailored to wind energy conversion, featuring higher power and torque densities has gradually increased [1]. Conventional wind turbine generators are often equipped with gearboxes to achieve the required speed. However, these gearbox systems have many drawbacks, including being large, expensive, and requiring regular maintenance [2, 3]. To overcome these problems, a special structure machine that operates at low speed, known as slow machine or direct attack machine is proposed in [4]. This innovative structure is called a Doubly Salient Permanent Magnet Machine (DSPM). Unlike traditional designs, its stator has a large number of teeth, and the rotor also has a large number of teeth and it doesn't contain windings or permanent magnets (PMs). The statoric tooth step, τ_s, is identical to that of the rotor, τ_r. Instead, it is excited by non-rotating PMs, inset in the stator yoke [4]. Nevertheless, the primary disadvantage of this machine is its tendency to produce a non-sinusoidal electromotive force (e.m.f.) and high electromagnetic torque ripples, leading to generation of vibrations, noise [4-5]. To mitigate the electromagnetic torque ripples and enhance performance of the DSPM the paper [6] proposes a Vernier Doubly Salient Permanent Magnet machine (V-DSPM). The Vernier effect in this new machine, as employed in the present study, is achieved by setting the statoric tooth step, τ_s, to be different from that of the rotor, τ_r.

Furthermore, maximizing the output power of wind turbines presents a significant challenge in wind power control. Various methods have been presented in the literature. In [7] a sensorless maximum power point tracking discrete-time integral terminal sliding mode controller (DITSMC) is developed to increase the energy efficiency of a WECS by reducing convergence-time and error-bounds. An integral sliding mode voltage regulator-based tip speed ratio (TSR) is proposed in [8] to maximize turbine output power. The suggested method provides robust tracking capabilities. Paper [9] presents a comparative study between tip speed ratio-based PI (TSR-PI) MPPT and perturbation & observation (P&O) MPPT. A Novel Hybrid MPPT is proposed in [10]. The suggested strategy uses a fuzzy controller to optimize the sliding mode controller. The main objective of the hybrid MPPT is to overcome certain problems of sliding mode control, such as the chattering phenomenon. A new maximum power point tracking controller based on voltage-mode Second-Order Fast Terminal Sliding Mode Control (SO-FTSMC) is proposed in [11]. The main purpose of the proposed control is to ensure that the system operates at the maximum power reference with enhanced effectiveness.

In this paper, a DC conversion system based on wind power turbine and a battery is proposed. Our system utilizes a Vernier Doubly Salient Permanent Magnet generator, a non-conventional direct-drive machine. To extract the maximum

power from wind turbine, a proposed tip speed ratio based sliding mode control is employed to regulate the inner loop of the DC-DC boost converter. To assess the efficiency of the proposed control, three tests were conducted. The first test is performed with a constant load and constant wind speed, the second one involved varying the wind speed while maintaining a constant load, and the last one is carried out with variation in both parameters wind speed and load. Additionally, we provide a comparative analysis of our suggested technique with the conventional PI control method.

II. ENERGY CONVERSION SYSTEM CONFIGURATION

The system contains a wind turbine to capture wind power, a three-phase V-DSPM generator, a three-phase uncontrolled rectifier, a DC/DC boost converter to extract maximum power from wind turbine, a battery with bidirectional DC/DC converter to regulate the DC bus, and variable load. The global scheme is presented in Fig. 1.

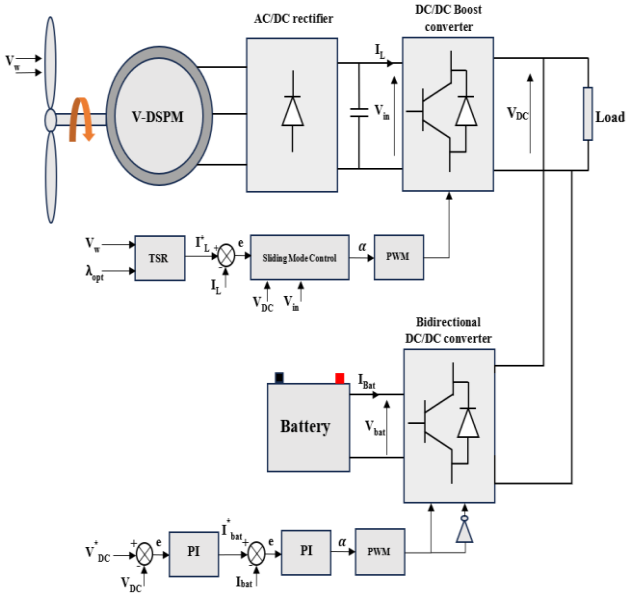


Figure 1: Proposed DC hybrid system

A. *Wind turbine modeling*

The following is an expression for aerodynamic power derived from wind kinetic energy:

$$P_t = 0.5\,\rho\,\pi\,R^2\,C_P(\lambda)\,V_w^3 \quad (1)$$

The power coefficient C_p depends on tip speed ratio, tip speed ratio λ is given by:

$$\lambda = \frac{\Omega_t\,R}{V_w} \quad (2)$$

Where ρ, R, C_p, V_w and Ω_t are, respectively, the air density, turbine radius, power coefficient, wind speed, and mechanical shaft speed.

B. *V-DSPM modeling*

The machine used in this study is a V-DSPM, a three-phase double-salient toothed-slot machine with a large number of rotor teeth and permanent magnets housed in the stator yoke (see Fig. 2). The stator slots carry the windings of the three phases, while the rotor is passive, without any electrical windings.

In the stator of the V-DSPM machine, there are N_s = 48 teeth distributed across the 12 slots. We have maintained N_{ps}=12 slots and N_{dp}=4 teeth per slot. The number of teeth on the rotor, N_r = 64, is fixed in order to achieve a typical electrical frequency of 50 Hz at the nominal speed of 50 rpm [6]. The rotation speed of the DSPM is inversely proportional to the number of rotor teeth.

The V-DSPM is a conventional DSPM [4] that exploits the Vernier effect, achieved by having a rotor tooth pitch τ_r different from the stator tooth pitch τ_s.

$$\begin{cases} \tau_s = \frac{2\pi}{N_{seq}} \\ \tau_r = \frac{2\pi}{N_r} \end{cases} \quad (3)$$

N_{seq}, different from N_s, represents the number of stator teeth the machine would have if the stator armature were distributed-toothed and not slotted.

To ensure energy conversion and torque production, the studied structure must satisfy the following conditions [6]:

$$\begin{cases} \pm N_{seq} \pm N_r = \pm P \pm P_e \\ N_{seq} \neq 2P \neq 2P_e \\ N_r \neq 2P \neq 2P_e \end{cases} \quad (4)$$

P_e and P denote the number of magnet pairs and slot pairs per phase, respectively.

These conditions are met, for machine, when considering N_{seq}=68 and N_{seq}=60. The machine with N_{seq}=68 demonstrates better performances according to [6], which is why it was chosen for this study.

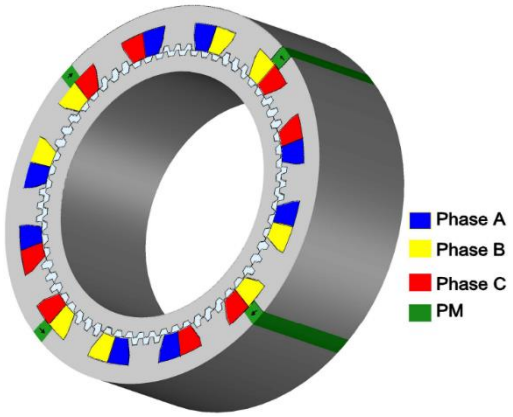


Figure 2: Cross- section of the studied Vernier Doubly Salient Permanent Magnet machine

The dynamic model of the V-DSPM is simplified using the Fourier transform. Terms of harmonics of order greater than 1 have been ignored. As a result, the V-DSPM's self-inductances, mutual inductances, and magnetic phase flux linkage with

respect to rotor position, obtained through the finite element method (FEM), can be respectively expressed as:

$$\begin{cases} L_a = L_0 + L_1 \cos\theta_e \\ L_b = L_0 + L_1 \cos\left(\theta_e - \frac{2}{3}\pi\right) \\ L_c = L_0 + L_1 \cos\left(\theta_e - \frac{4}{3}\pi\right) \end{cases} \quad (5)$$

$$\begin{cases} M_{ab} = M_{ba} = M_0 + M_1 \cos\left(\theta_e - \frac{4}{3}\pi\right) \\ M_{ac} = M_{ca} = M_0 + M_1 \cos\left(\theta_e - \frac{2}{3}\pi\right) \\ M_{bc} = M_{cb} = M_0 + M_1 \cos\theta_e \end{cases} \quad (6)$$

$$\begin{cases} \varphi_{ma} = \varphi_0 + \varphi_1 \cos\theta_e \\ \varphi_{mb} = \varphi_0 + \varphi_1 \cos\left(\theta_e - \frac{2}{3}\pi\right) \\ \varphi_{mc} = \varphi_0 + \varphi_1 \cos\left(\theta_e - \frac{4}{3}\pi\right) \end{cases} \quad (7)$$

Park transformation is applied for generator equations in stator reference frame and the direct and quadrature voltages expressions of the V-DSPM in the d-q reference frame are given by:

$$\begin{cases} V_d = -\left(R_s + 2w_e M_{dq}\right) i_d + \frac{w_e}{2}\left(3L_d - L_q\right) i_q \\ \qquad -L_d \frac{di_d}{dt} - M_{dq} \frac{di_q}{dt} \\ V_q = -\left(R_s - 2w_e M_{dq}\right) i_q + \frac{w_e}{2}\left(3L_d - L_q\right) i_d \\ \qquad -L_q \frac{di_q}{dt} - M_{dq} \frac{di_d}{dt} - \sqrt{\frac{3}{2}}\varphi_1 w_e \end{cases} \quad (8)$$

R_s represents the stator resistance, i_d and i_q denote the direct and quadrature currents, L_d and L_q signify the direct and quadrature inductances, M_{dq} stands for mutual inductance, w_e represents the electrical velocity and φ_1 represents the first harmonic of permanent magnet flux.

With:

$$\begin{cases} L_{dq} = L_0 - M_0 \pm \frac{1}{2}(L_1 + 2M_1)\cos(3\theta_e) \\ M_{dq} = -\frac{1}{2}(L_1 + 2M_1)\sin(3\theta_e) \\ \theta_e = \int w_e \, dt \end{cases} \quad (9)$$

θ_e represents the electrical position.

The direct and quadratic magnetic flux equations are:

$$\begin{cases} \varphi_d = L_d i_d + M_{dq} i_q + \sqrt{\frac{3}{2}}\varphi_1 \\ \varphi_q = L_q i_q + M_{dq} i_d \end{cases} \quad (10)$$

The electromagnetic torque T_{em} is written in Equation (11):

$$\begin{cases} \mathrm{T_{em}} = -\sqrt{\frac{3}{2}}\mathrm{N_r}\varphi_1 \mathrm{i_q} + \frac{1}{2}\mathrm{N_r}\left(\mathrm{L_d}\text{-}\mathrm{L_q}\right)\mathrm{i_d}\mathrm{i_q} \\ \qquad -\frac{1}{2}\mathrm{N_r}\mathrm{M_{dq}}\left(\mathrm{i_d^2}\text{-}\mathrm{i_q^2}\right) \end{cases} \quad (11)$$

Mechanical equation is expressed as:

$$J\frac{d\Omega_t}{dt} = T_{em} - T_m - f\Omega_t \quad (12)$$

Active and reactive machine powers are expressed by the following equations:

$$\begin{cases} P = v_d i_d + v_q i_q \\ Q = v_d i_q - v_q i_d \end{cases} \quad (13)$$

On the other hand, Joule and iron losses are given by the following formulas:

$$\begin{cases} P_{cu} = R_s i_d^2 + R_s i_q^2 \\ P_{ir} = \frac{3}{2} N_r \Omega_t \left[M_{dq}\left(i_d^2 - i_q^2\right) - \left(L_d - L_q\right) i_d i_q\right] + \\ \qquad \frac{1}{2}\left(L_d \frac{di_d^2}{dt} + L_q \frac{di_q^2}{dt}\right) + M_{dq} \frac{d(i_d i_q)}{dt} \end{cases} \quad (14)$$

The power factor can be evaluated with the help of the mean values of active and reactive powers as:

$$\cos\psi = \left| \frac{P_{mean}}{\sqrt{P_{mean}^2 + Q_{mean}^2}} \right| \quad (15)$$

III. CONTROLLER DESIGN

A. *MPPT based Tip speed ration*

The MPPT strategy is used to determinate the optimal operating point of the wind turbine. Several algorithms have been presented in literature, such as Optimal Torque (OT) control, Tip Speed Ratio (TSR) control, Power Signal Feedback (PSF) control, and Perturbation and Observation (P&O) control.

In this paper, TSR control is chosen due its several advantages, including simplicity of implementation, fast convergence speed, and high performance under varying wind speeds. Fig. 3 illustrates the TSR based MPPT algorithm.

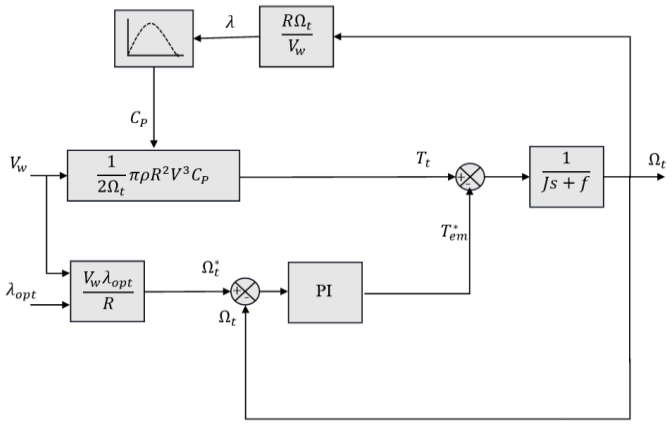


Figure 3: TSR based MPPT algorithm

The wind turbine's C_p (λ) curve is presented in Fig. 4. The angle γ is set to zero due to the assumption of a fixed pitch rotor. It can be observed that the C_p has single maximum point, $C_{pmax} = 0.428$ at $\lambda_{opt} = 2.25$.

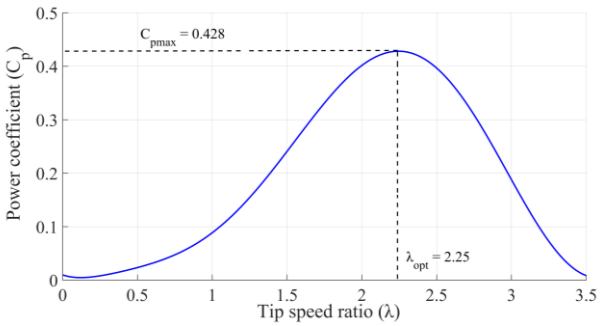


Figure 4: Wind turbine power coefficient C_p

B. *Proposed silidng mode control current*

Sliding mode control is a nonlinear control technique that can be applied to both linear and nonlinear systems. It is a robust control technique known for its excellent disturbance resistance and rapid dynamics response [12].

The first step involves defining the sliding surface. In this study the sliding surface is defined as follows:

$$S = i_L^* - i_L \tag{16}$$

The sliding mode control signal is the sum of the equivalent and discontinuous control signals, and is given as follow:

$$u = u_{eq} + u_{dis} \tag{17}$$

The equation of the current inductor is given as follow:

$$\frac{di_L}{dt} = \frac{v_{in}}{L} - (1-u)\frac{v_{DC}}{L} \tag{18}$$

The Gao's low is given as follow [13]:

$$\dot{S} = -\alpha\, S - \beta\, sign(S) \tag{19}$$

From equations (16), (18), and (19), the sliding mode control signal-based Goa's law is obtained in (20):

$$u = \frac{v_{DC}-v_{in}}{v_{DC}} + \frac{L(\alpha S + \beta\, \mathrm{sign}(S))}{v_{DC}} \tag{20}$$

Where, α, $\beta > 0$ are parameters to be tuned.

The control signal block diagram is shown in Fig. 5.

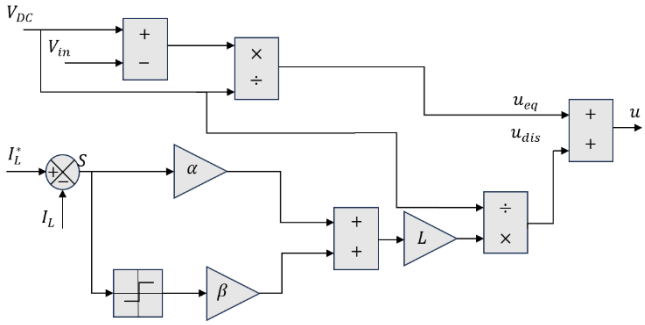


Figure 5: The proposed control method diagram

IV. SIMULATION RESULTS

To verify robustness of the proposed control method, three tests were carried out. Test (1) was performed with a constant load and constant wind speed, test (2) consisted of varying the wind speed while maintaining a constant load, and test (3) was carried out with variations in both wind speed and load.

Fig. 6, shows wind speed profile, with speed variations ranging from 5.5 m/s to 9.2 m/s. From 0 s to 5s the speed remains constant at 8m/s. From 5 s to 15 s, the speed varies. Fig. 7a presents the V-DSPM speed, demonstrating that the generator speed follows the variation of the wind speed. Fig. 7b shows the generator's high electromagnetic torque which is a result of the low rotation speed of this generator. Fig. 8 displays the phase voltage and phase current of the V-DSPM. Fig. 9 presents the direct and the quadratic current of the V-DSPM generator.

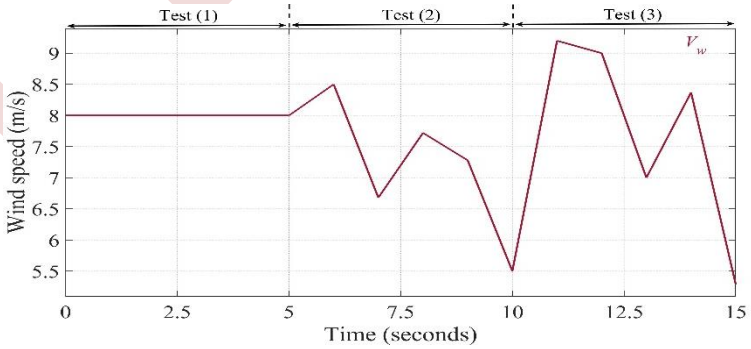
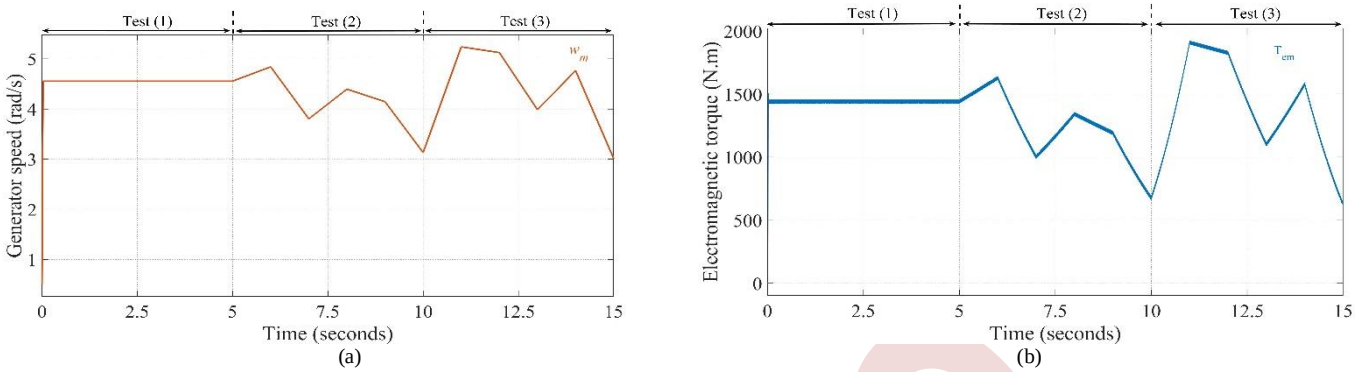


Figure 6: Wind speed profile V_w



(a) (b)

Figure 7: Simulation results of (a) Generator speed Ω_m, (b) Electromagnetic torque generator T_{em}

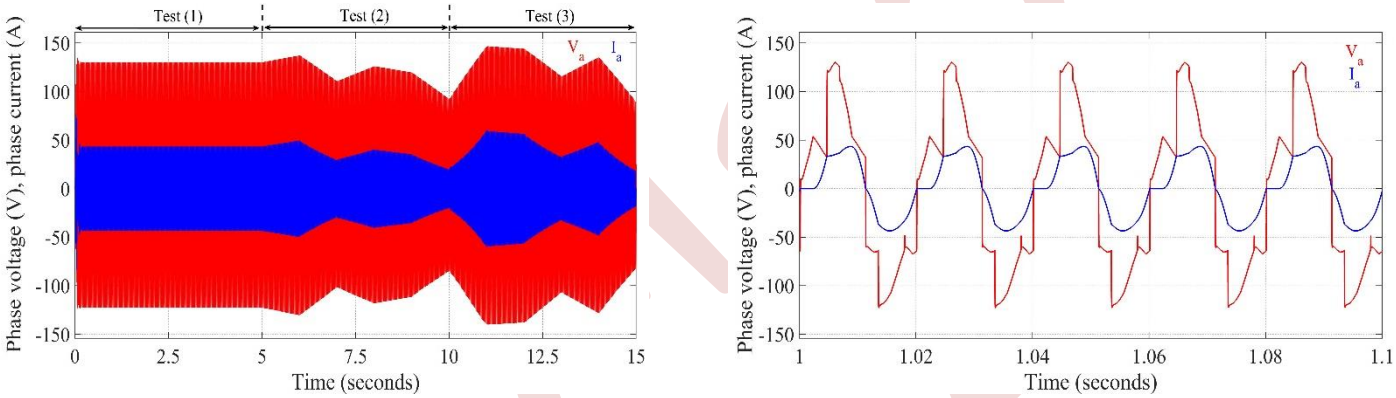


Figure 8: Generator phase voltage and phase current V_a & I_a.

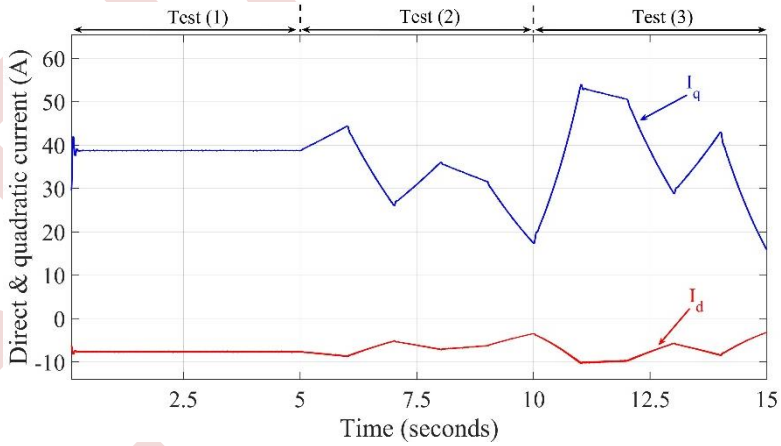


Figure 9: V-DSPM direct I_d and quadratic I_q current.

Fig. 10, Fig. 11 and Fig. 12 display the simulation results of DC/DC booster inductor current and wind turbine output power, and battery power under three different tests using the proposed control and conventional PI control. During the three tests the proposed sliding mode control (SMC) converges to the maximum power point with a fast response compared to PI control. It can be observed that the SMC control exhibits higher efficiency in extracting the maximum power from wind turbine under varying wind conditions and load fluctuations. Table 1 summarizes the performance of the different techniques.

From Fig. 13, it is evident that the DC-bus voltage remains balanced even during disturbances and is maintained at the desired operating value of 500 V.

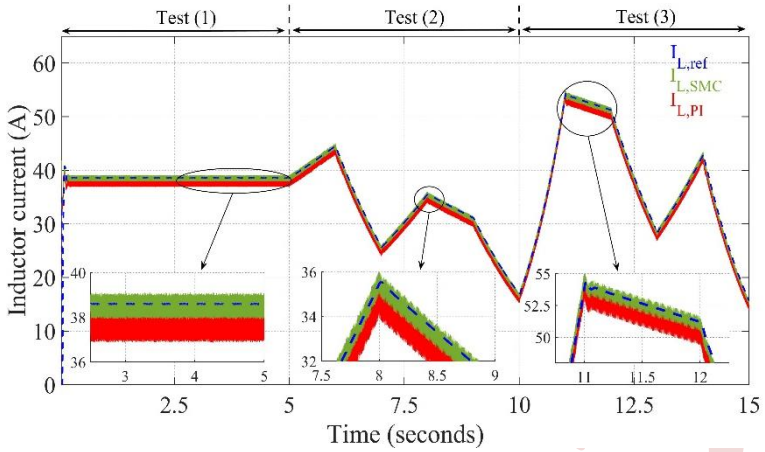


Figure 10: Inductor current I_L

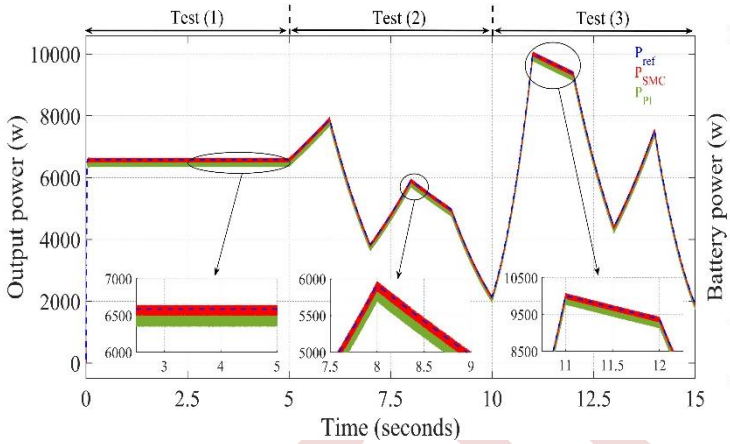


Figure 11: Wind turbine output power P_{wind}

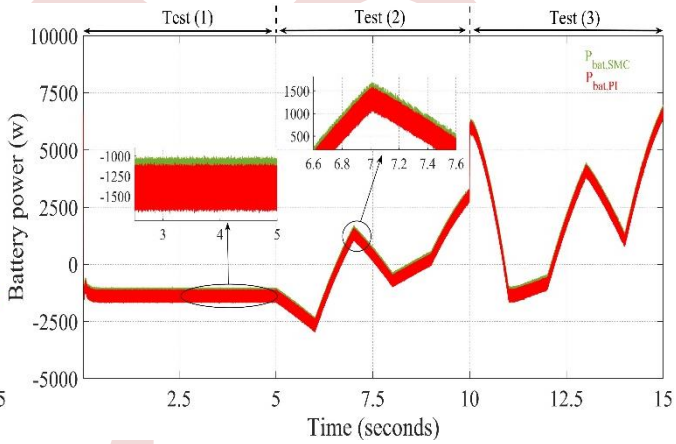


Figure 12: Battery power P_{bat}

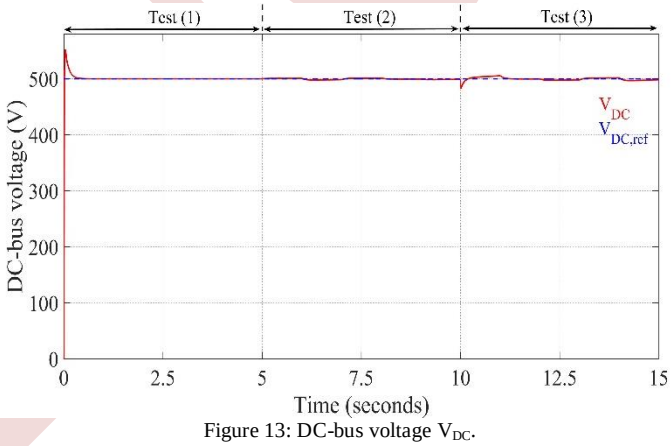


Figure 13: DC-bus voltage V_{DC}.

TABLE I. PERFORMANCE OF THE DIFFERENT TECHNI QUES

	Test (1)		**Test (2)**		**Test (3)**	
Mean	***PI***	***SMC***	***PI***	***SMC***	***PI***	***SMC***
P_{wind} (w)	6486.4	6586.6	5395.8	5403.8	6675.1	6756.83
$I_{indcutor}$ (A)	37.87	38.52	32.28	32.83	37.78	38.46

V. CONCLUSION

To enhance the efficiency of wind power system, this paper proposes a non-conventional generator with low rotation speed and high electromagnetic torque. The purpose of using this type of generator is to eliminate the gearbox from the conversion system and address the associated issues such as large size, coast, power losses, and maintenance. Furthermore, a sliding mode control is suggested to optimize the output power of the wind turbine under different scenarios, including wind speed variations and load fluctuations. The simulation results demonstrate that the proposed control enhances the performance of the wind power system by maximizing power extraction.

APPENDIX

TABLE A1. V-DSPM parameters

Parameters
R_s: Stator resistance (87.37 mΩ)
L_0: Continuous self-inductance (30.5 mH)
L_1: First harmonic self-inductance (1.4 mH)
M_0: Continuous mutual-inductance (-15.5 mH)
M_1: First harmonic mutual-inductance (6.7 mH)
φ_1: First harmonic permanent magnet flux (0.4147 Wb)
N_r: Number of teeth in the rotor (64)
N_s: Number of teeth in the stator (48)
N_{seq}: Number of equivalent teeth in the stator (68)
N_{ps}: Stator pole (12)
P: Number of magnet pairs (2)
P_e: Number of slot pairs per phase (4)
τ_r, τ_s: Rotor and stator tooth pitch
J: Rotor inertia (Nm s^{-1})
f: Viscous friction coefficient
P_n: Rated power (10 kW)
Ω_n: Rated rotor speed (50 rpm)

TABLE A2. Wind turbine parameters

Parameters
V_w: Wind speed (9.2 m/s)
C_{pmax}: maximum power coefficient (0.428)
λ_{opt}: Optimal tip speed ratio (2.25)
ρ: Air density (1.225 Kg/m^3)
R: Wind turbine radius (3.951 m)
P_n: Rated wind turbine power (10 kW)
Number of blade: 3

TABLE A3. Variables

Variables
v_d, v_q: Direct and quadratic voltages (V)
i_d, i_q: Direct and quadratic currents (A)
φ_d, φ_q: Direct and quadratic flux (Wb)
w_e: Electrical velocity (rad/s)
θ_e: Electrical position (rad)
L_d, L_q: Direct and quadratic inductance (H)
M_{dq}: Mutual inductance (H)
T_m: Mechanical torque (Nm)
T_{em}: Electromagnetic Torque (Nm)
P: Active power (W)
Q: Reactive power (VAR)
P_{cu}: Joule losses (W)
P_{ir}: Iron losses (W)
P_{mean}: Mean active power (W)
Q_{mean}: Mean reactive power (W)
$Cos\ \psi$: Power factor
i_L: Inductance current of the DC/DC converter (A)
v_{in}: Input voltage (V)
v_{DC}: DC bus voltage (V)
u_{eq}, u_{dis}: Equivalent and discontinuous control signals
S: Sliding surface
α, β: Sliding mode control parameters

REFERENCES

[1] H. Kim, S. Kang, S. Jung, *et al*, ''Design and Analysis of Permanent-Magnet Vernier Machine for Direct-Driven Wind Power Generator Considering Pole-Slot Combinations,'' J. Electr. Eng. Technol. Vol 18, pp. 319–327, 2023.

[2] A. Remli, C. Guerroudj, *et al*, ''Control of an Outer Rotor Doubly Salient Permanent Magnet Generator for Fixed Pitch kW Range Wind Turbine Using Overspeed Flux Weakening Operations,'' Actuators , vol 12, pp. 168, 2023.

[3] A. Rezzoug, M. E. Zaïm (ed.), "Non-conventional electrical machines," John Wiley & Sons, 2013.

[4] R. Saou, M. E. Zaïm, and K. Alitouche, "Optimal designs and comparison of the doubly salient permanent magnet machine and flux-reversal machine in low-speed applications," Power Components Syst., Vol. 36, No. 9, pp. 914–931, 2008.

[5] L. Bekhouche, R. Saou, C. Guerroudj, A. Kouzou, M.E.Zaïm , ''Electromagnetic Torque Ripple Minimization of Slotted Doubly-Salient-Permanent-Magnet Generator for Wind Turbine Applications,'' Progress In Electromagnetics Research M, Vol. 83, pp.181-190, 2019.

[6] C. Guerroudj, R. Saou, A. Boulayoune, M. E. Zaïm, L. Moreau, ''Performance analysis of Vernier slotted doubly salient permanent magnet generator for wind power,'' International Journal of Hydrogen Energy, Vol 42, pp 8744-8755, 2017.

[7] I. Yazıcı, E. K. Yaylacı, ''Discrete-time integral terminal sliding mode based maximum power point controller for the PMSG-based wind energy system,'' IET Power Electronics, vol 12, pp. 3688-3696, 2019.

[8] I. Yazici, E. K. Yaylaci, "Improving Efficiency of the Tip Speed Ratio-MPPT Method for Wind Energy Systems by Using an Integral Sliding Mode Voltage Regulator," J. Energy Resour. Technol., vol.140, pp. 051203, Nov. 2017.

[9] E. H. Dursun, A. A. Kulaksiz, ''MPPT Control of PMSG Based Small-Scale Wind Energy Conversion System Connected to DC-Bus,'' International Journal of Emerging Electric Power Systems, vol. 21, pp. 20190188, 2020.

[10] P. Malobe, P. Djondine, P. Eloundou, H. Ndongo, ''A Novel Hybrid MPPT for Wind Energy Conversion Systems Operating under Low Variations in Wind Speed,'' Energy and Power Engineering, vol 12, pp. 716-728, 2020.

[11] E. H. Dursun, A. A. KULAKSIZ, ''Second-order fast terminal sliding mode control for MPPT of PMSG-based wind energy conversion system,'' Elektronika ir Elektrotechnika, vol 26, 2020.

[12] I. Sami, S. Ullah, A. Basit, N. Ullah, J. -S. Ro, ''Integral Super Twisting Sliding Mode Based Sensorless Predictive Torque Control of Induction Motor,'' in IEEE Access, vol. 8, pp. 186740-186755, 2020.

[13] A. Bartoszewicz, ''A new reaching law for sliding mode control of continuous time systems with constraints,'' Transactions of the Institute of Measurement and Control, vol 37,pp. 515-521, 2015.

Nonlinear predictive control for an asynchronous machine

Brahami Sofiane [1] , Ghedamsi Kaci[1], Achour Abdelyazid[2]

[1] *Laboratoire de Maitrise des Energies Renouvelables, LMER, Faculté de Technologie, Université de Bejaia, Algérie*

sofiane.brahami@univ-bejaia.dz

[2] *Laboratoire de Technologie Industrielle et de l'Information, LTII, Faculté de Technologie, Université de Bejaia, Algérie*

abdelyazid.achour@univ-bejaia.dz

***Abstract*— Induction machines are widely used in industry because they are more rugged, reliable, compact, efficient and less expensive compared to other machines used in similar applications. They however, represent highly nonlinear, coupled, multivariable, complex control plant with unknown disturbances and time varying parameters requiring complex control algorithms. This paper deals with the development of a high performance nonlinear predictive control induction motor drive. The research work is directed towards improving trajectory tracking capability, stability guarantee, robustness to parameters variations and disturbance rejection. The main part of nonlinear predictive control is the system behavior prediction model.A multivariable controller is used for the system control, with the rotor speed and the rotor flux norm as outputs. Simulation studies show the performance of the proposed control algorithm.**

***Keywords:* model predictive control, asynchronous machine, optimal control.**

I. INTRODUCTION

Asynchronous motors, also known as induction motors, are widely used in various industrial applications. These motors exhibit nonlinear characteristics and complex dynamic behaviors, the control of this process is complicated due to its nonlinear nature, its dynamics, and the variation of its parameters during operation [1,2]. The development of different asynchronous motor control methods is justified by the need to take into account its nonlinear structure. Different controls have been developed to vary the speed of the asynchronous machine, namely vector control by flow orientation, direct torque control and nonlinear predictive control [3,4]. Predictive control is among the most used advanced controls in the industrial environment, so demanding in terms of performance and simplicity of implementation. Many industrial applications exist, especially for systems for which the trajectory to follow is known in advance, such as robots, machine tools, applications in the petroleum, biochemical or chemical industry, aeronautics and thermal [5].

In this article, nonlinear predictive control is applied for an asynchronous machine for speed variation, disturbance rejection and robustness to parametric variations.

The research work is directed towards improving the trajectory tracking capability, stability guarantee, robustness to parameter variations, and disturbance rejection. Simulation results and the concluding remarks on the advantages and perspectives are also presented.

II. INDUCTION MOTOR MODEL

The analysis of the operation of the induction motor associated with an inverter with a view to its control is not simple because of the non-linear behavior of these two elements. Starting from the induction motor equations written in a frame linked to the rotating field, we obtain the following equations [6,7]:

A. *Electrical equations*

$$\begin{cases} V_{ds} = R_s i_{ds} + \frac{d\Phi_{ds}}{dt} - \frac{d\theta_s}{dt}\Phi_{qs} \\ V_{qs} = R_s i_{qs} + \frac{d\Phi_{qs}}{dt} + \frac{d\theta_s}{dt}\Phi_{ds} \\ 0 = R_r i_{dr} + \frac{d\Phi_{dr}}{dt} - \left(\frac{d\theta_s}{dt} - P\Omega\right)\Phi_{qr} \\ 0 = R_r i_{qr} + \frac{d\Phi_{qr}}{dt} + \left(\frac{d\theta_s}{dt} - P\Omega\right)\Phi_{dr} \end{cases} \quad (1)$$

B. *Magnetic equations*

$$\begin{cases} \Phi_{ds} = L_{ss}\ i_{ds} + M\ i_{dr} \\ \Phi_{qs} = L_{ss}\ i_{qs} + M\ i_{qr} \\ \Phi_{dr} = L_{rr}\ i_{dr} + M\ i_{ds} \\ \Phi_{qr} = L_{rr}\ i_{qr} + M\ i_{qs} \end{cases} \quad (2)$$

C. *The expression of the electromagnetic torque*

$$C_{em} = P\frac{L_m}{L_r}\left(\emptyset_{dr} I_{qs} - \emptyset_{qr} I_{ds}\right) \quad (3)$$

Therefore, the model of an asynchronous motor is defined in the following form [1,2]:

$$\dot{x} = f(x) + g(x).V(t) \quad (4)$$

Where $\dot{x} = [I_{ds}\ I_{qs}\ \emptyset_{dr}\emptyset_{qr}\Omega]^T$; $V(t)=[V_{ds}\ \ V_{qs}]^T$

The state **x** belongs to the set $\Omega = \{x \in R^5 : \emptyset_{dr}^2 + \emptyset_{qr}^2 \neq 0\}$

Vector function f and matrix g are defined as follows

$$f(x)=\begin{bmatrix} -\gamma I_{ds} & +\omega_s I_{qs} & +\frac{K}{T_r}\emptyset_{dr} \quad +PK\Omega\emptyset_{qr} \\ -\omega_s I_{ds} & -\gamma I_{qs} & -PK\Omega\emptyset_{dr} \quad +\frac{K}{T_r}\emptyset_{qr} \\ \frac{L_m}{T_r} I_{ds} & -\frac{1}{T_r}\emptyset_{dr} & +(\omega_s - P\Omega)\emptyset_{qr} \\ \frac{L_m}{T_r} I_{qs} & -(\omega_s - P\Omega)\emptyset_{dr} & -\frac{1}{T_r}\emptyset_{qr} \\ \frac{pL_m}{JL_r}(\emptyset_{dr} I_{qs} - \emptyset_{qr} I_{ds}) & -\frac{f_r}{J} & -\frac{C_r}{J} \end{bmatrix}$$

$$g(x)=\begin{bmatrix} \frac{1}{\delta L_s} & 0 \\ 0 & \frac{1}{\delta L_s} \\ 0 & 0 \\ 0 & 0 \\ 0 & 0 \end{bmatrix}$$

$$\sigma = 1 - \frac{L_m^2}{L_s L_r}; K = \frac{L_m}{\sigma L_s L_r}\ ;\ \gamma = \frac{1}{\sigma L_s}\left(R_s + R_r \frac{L_m^2}{L_r^2}\right).$$

I_{ds} , I_{qs} denote the stator currents , $\emptyset_{dr}, \emptyset_{qr}$ the rotor fluxes, Ω the rotor speed, V_{ds} , V_{qs} the stator voltages and C_r the resistant torque, J moment of inertia of the rotating masses, L_s, L_r stator inductance and rotor inductance, L_m inductance mutual , P the number of rotor pole pairs, R_S, R_r stator and rotor resistances.

III. NONLINEAR MODEL PREDICTIVE CONTROL

To solve the problem of tracking trajectories, in what follows we present the nonlinear predictive control (NPC) strategy, the prediction model is carried out using starting from a mathematical development on the machine model. The variable to be controlled in the motor are the motor speed and the squared rotor flux amplitude[8,9].

$$\begin{cases} y_1 = h_1(x) = \Omega \\ y_2 = h_1(x) = \emptyset_{dr}^2 + \emptyset_{qr}^2 \end{cases} \quad (5)$$

Nonlinear model predictive control (NMPC) algorithm belongs to the family of optimal control strategies, where the cost function is defined over a future horizon [3]

$$\Im(x,u) = \frac{1}{2}\int_0^{T_p} [y(t+\tau) - y_r(t+\tau)]^T [y(t+\tau) - y_r(t+\tau)] d\tau \quad (6)$$

Where τ_r is the prediction time, y(t+τ) a step ahead prediction of the system output and y_1(t+τ) the future reference trajectory. The control weighting term is not included in the cost function [10]. However, the control effort can be achieved by adjusting prediction time. The objective of model predictive control is to compute the control u(t) in such a way the future plant output y(t+τ) is driven close to y_1(t+τ).This is accomplished by minimizing $\Im$.

The relative degree of the output, defined to be the number of times of output differentiation until the control input appears, is r1=2 for speed output and r2=2 for flux output. Taylor series expansion [4] can be used for the prediction of the machine outputs in the moving time frame. The differentiation of the outputs according to time is repeated r times.[5]

$$y_i(t+\tau) = h_i(x) + \tau L_f h_i(x) + \cdots + \frac{\tau^2}{2!} L_f^2 h_i(x) + \frac{\tau^{r_i}}{r_i!} L_g L_f^{(r_i-1)} h_i(x) u(t) \quad (7)$$

The predicted output y (t+τ) is carried out from

$$y(t+\tau) = \overline{T}(\tau).Y(t) \quad (8)$$

Where $\overline{T}(\tau) = \left[I_{2*2} \quad \tau I_{2*2} \ \frac{\tau 2}{2} \ I_{2*2}\right]$, I_{2*2} : Identity matrix

The outputs differentiations are given in matrix form as

$$Y(t)=\begin{bmatrix} y(t) \\ \dot{y}(t) \\ \ddot{y}(t) \end{bmatrix} = \begin{bmatrix} h(x) \\ L_f h(x) \\ L^2{}_f h(x) \end{bmatrix} + \begin{bmatrix} 0 \\ 0 \\ G(x)u(t) \end{bmatrix} \quad (9)$$

Where $L_f^i h(x)=[L_f^i h_1(x) \ L_f^i h_2(x)]^T$, (i=0 ,1 ,2)

$$G_1(x)=\begin{bmatrix} L_{g11} L_f h_1(x) & L_{g12} L_f h_1(x) \\ L_{g11} L_f h_2(x) & L_{g12} L_f h_2(x) \end{bmatrix} \quad (10)$$

A similar computation is used to find the predicted reference y_1(t+τ) [2,8].

$$y_r(t+\tau) = \overline{T}(\tau).Y_r(t) \quad (11)$$

Where $Y_r(t) = [y_r(t) \ \dot{y_r}(t) \ \ddot{y_r}(t)]T$

$y_r(t) = [\omega_{ref} \Phi_{ref}^2]T$

Using (10) and (11), the cost function (6) can be simplified as

$$\Im(x,u) = \frac{1}{2}[Y(t) - Y_r(t)]^T \overline{\Pi} \ [Y(t) - Y_r(t)] \quad (12)$$

Where [2]:

$$\overline{\Pi}(\tau) = \int_0^{\tau_r} T(\tau)^T T(\tau) d\tau = \begin{bmatrix} \tau_r I_{2*2} & \frac{\tau_r^2}{2} I_{2*2} & \frac{\tau_r^3}{6} I_{2*2} \\ \frac{\tau_r^2}{2} I_{2*2} & \frac{\tau_r^3}{3} I_{2*2} & \frac{\tau_r^4}{8} I_{2*2} \\ \frac{\tau_r^3}{6} I_{2*2} & \frac{\tau_r^4}{8} I_{2*2} & \frac{\tau_r^5}{20} I_{2*2} \end{bmatrix}$$

The optimal control is carried out by making $\frac{\partial \Im}{\partial u}$=0

$$u(t)=-G_1(x)^{-1}\left[\overline{\Pi}_3^{-1}\overline{\Pi}_2^T \quad I_{2*2}\right]M \quad (13)$$

Where $$M = \begin{bmatrix} h(x) \\ L_f h(x) \\ L^2{}_f h(x) \end{bmatrix} - \begin{bmatrix} y_r(t) \\ \dot{y_r}(t) \\ \ddot{y_r}(t) \end{bmatrix}$$

$\det [G_1(x)]$= - $2pL_m^2/J\sigma L_s^2 L_r^2 T_r (\Phi_{dr}^2 + \Phi_{qs}^2)$

The conditions $\{\emptyset_{dr}(0)\ ,\ \emptyset_{qr}(0)\} \neq 0$ and the set $\Omega\{\emptyset_{dr}^2 + \emptyset_{qr}^2 \neq 0\}$ allow G_1 to be invertible. The optimal control is developed as

$$u(t) = -G(x)\left[k_0\left(h(x) - y_r(t)\right) + k_1\left(L_f h(x) - \dot{y}_r(t)\right) + k_2\left(L_f^2 h(x) - \ddot{y}_r(t)\right)\right] \quad (14)$$

Where $k_0 = \frac{10}{3T_r^2}, k_1 = \frac{5}{2T_r}, k_2 = 1$

The general structure of generalized predictive nonlinear control for induction motor is shown by figure.1[11.12].

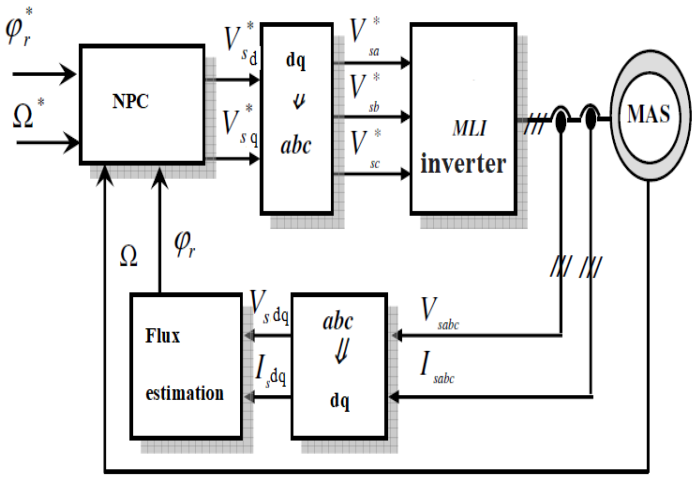


Figure.1. The general structure of generalized predictive nonlinear control NPC for induction motor.

IV. RESULTS OF SIMULATION

The simulation have been carried out in Simulink/Matlab to verify the performance of the proposed controller which is nonlinear predictive for induction motor.The details about the motor are given in appendix. The performance of our command was tested based on the simulation for a variation of load torque and rotor resistance 15Nm at time (3 seconds).

These figures shows the results of simulation of nonlinear predictive control for induction motor.

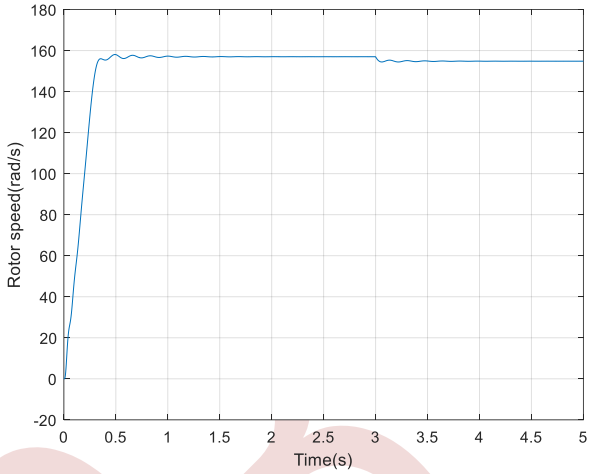


Figure. 2. Rotor speed.

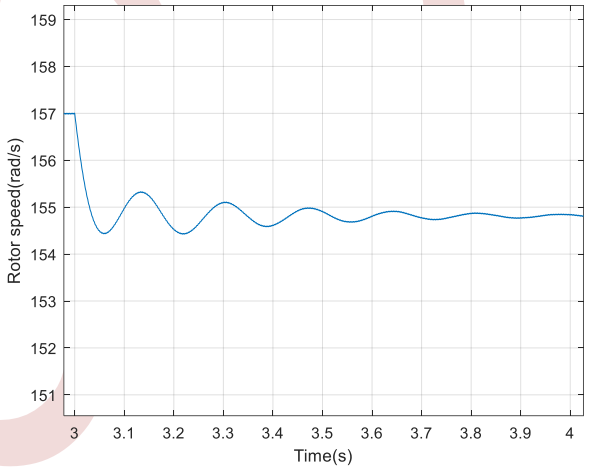


Figure.3. Zoom of rotor speed.

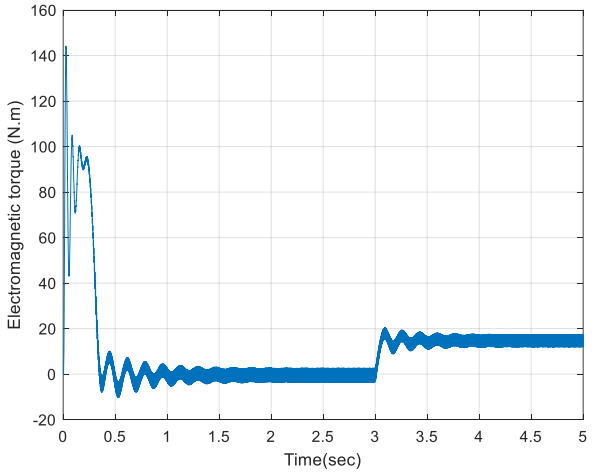


Figure. 4. Electromagnetic torque of the three-phase induction motor with a full-load torque step change at t=3 sec.

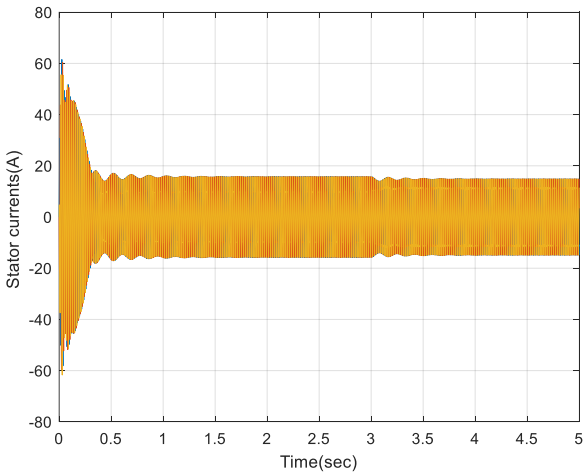


Figure.5. Stator currents.

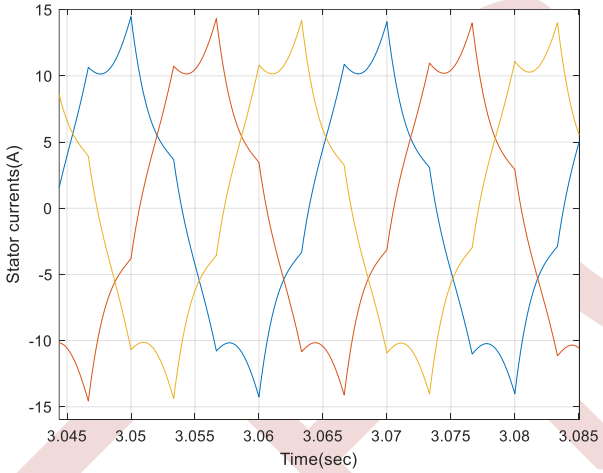


Figure.6. Zoom stator currents.

We notice in figure 2 that the speed is established at its value without static errors, at the instant t=3 where the load torque is applied, the speed reduces slightly but it restores again with a little error.

The figure 4 represents the torque at transient regime, we note that it reaches 144 N.m (starting torque) then it starts to go down, at t=3s we have applied a resisting torque, the electromagnetic torque tends towards 15 (N.m).

The figure 5 shows the evolution of the stator current as a function of time. When we apply a load torque at the instant (t=3 seconds), we notice more current consumption.

The simulation results show that the performance of the nonlinear predictive controller is satisfactory and strategy regarding trajectory tracking, sensitivity to the induction motor parameters variations and disturbance rejection.

V. CONCLUSION

Nonlinear predictive controller is a powerful control strategy that offers several advantages for induction motors. It can provide precise control, adaptability to nonlinearities, robustness to disturbances, and the ability to handle various control objectives. However, its implementation complexity and computational demands should be carefully considered in practical applications. Additionally, selecting an appropriate predictive model and tuning the cost function and constraints are crucial for achieving the desired control performance.

VI. APPENDIX

The process to control is an induction machine used by whose parameters are R_r =1.8 Ω; J=0.07kgm^2; f=0; p=2 R_s=1.8 Ω; Lm=0.15H; Ls=0.1554H; Lr=0.1568H.

REFERENCES

[1] Merabet A, Nonlinear Control with Predictive Model for an Asynchronous Machine", University of Quebec Research Seminar, Canada, January 27, 2006

[2] Merabet. A, Nonlinear control with a predictive model for an asynchronous machine, doctoral thesis University of Quebec, May 2007.speed and flux tracking in induction motor drives.

[3] W. Feng, J. O'Reilly and D.J. Balance, "MIMO Nonlinear PID Predictive Controller," IEE Proceedings Control Theory application, vol. 149, no. 3, pp. 203-208, 2002.

[4] M.K. Maaziz. P. Boucher and D. Dumur, "A New Control Strategy for Induction Motor Based on Non-linear Predictive Control and Feedback Linearization, International Journal of adaptive Control and Signal Processing, 14. pp. 313-329, 2000.

[5] Hedjar, R. Toumi, P. Boucher and D. Dumur. Two Cascaded Nonlinear Predictive Controls of Induction Motor, IEEE Conference on Control Applications. vol. 1, Istanbul, Turkey, pp. 458-463, 2003.

[6] Cho Y., Bak Y., Lee K.B., Torque-Ripple Reduction and Fast Torque Response Strategy for Predictive Torque Control of Induction Motors, IEEE Transactions on Power Electronics, vol. 33, no. 3, pp.2458 2470,2017.

[7] Zhang Y., Yang H., Model predictive torque control of induction motor drives with optimal duty cycle control, IEEE Trans. Power. Electron., vol. 29, no. 12, pp. 6593–6603 (2014).

[8] W. Xie, X. Wang, F. Wang, W. Xu, R. Kennel, and D. Gerling, "Dynamic Loss Minimization of Finite Control Set-Model Predictive Torque Control for Electric Drive System," IEEE Transactions on Power Electronics, vol. 31, no. 1, pp. 849–860, jan 2016.

[9] P. A Egiguren ,O. B Caramazana and J.A Cortajarena Etxeberria "Linear Generalized Predictive Speed Control of Induction Motor Drives ". University of the Basque Country (UPV/EHU) Spain. IEEE 2011

[10] Ahmed A. Zaki Diab , Denis A. Kotin, Vladimir V. Pankratov "Speed Control of Sensorless Induction Motor Drive Based On Model Predictive Control" XIV International Conference On Micro/Nanotechnologies And Electron Devices EDM. IEEE 2013.

[11] W. Xie, X. Wang, F. Wang, W. Xu, R. Kennel, and D. Gerling,"Dynamic Loss Minimization of Finite Control Set-Model Predictive Torque Control for Electric Drive System," IEEE Transactions on Power *Electronics,* vol. 31, no. 1, pp. 849–860, jan 2016.

[12] E. Fuentes, D. Kalise, J. Rodriguez, and R. M. Kennel, "Cascade-Free Predictive Speed Control for Electrical Drives," *IEEE Transactions on Industrial Electronics*, vol. 61, no. 5, pp. 2176–2184, May 2014.

Behavior analysis of double star induction motor under open phase fault

Abbas sadia [1], Iffouzar Koussaila [2], Amrouche Bessam[3] , Ghedamsi Kaci [3], Houari Azeddine [4], Benkhoris Mohamed-Fouad [4].

[1] *Laboratoire de Technologies Industrielle et de l'Information, LTII Faculté de Technologies, Université de Béjaia, Bejaia 06000.*
E_mail: sadia.abbas@univ-bejaia.dz

[2] *Laboratoire des Sciences Appliquées, Ecole Nationale Supérieure des Technologies Avancées ENSTA, Alger, 16000.*

[3] *Laboratoire de Maitrise des Energies Renouvelables, LMER Faculté de Technologie, Université de Béjaia, Béjaia 06000.*

[4] *Institut de Recherche en Energie Electrique de Nantes Atlantique, IREENA, France 44000*.

***Abstract*—The fault tolerance of multiphase induction machines makes them increasingly used in the field of traction and electric propulsion. The use of polyphase drives is mainly justified on their fault-tolerant abilities; the most common failure in the polyphase induction machine is the Open Phase Fault (OPF). However, machine performance deteriorates during OPF. This work concerns the study of behavior of DSIM under stator open phase fault, the model of the DSIM is proposed, and simulation results are analyzed and discussed.*)**

Keywords: **Double Stator, Induction Motor, Open Phase Fault.**

I. INTRODUCTION

The electrification of the traction and propulsion actuators is made possible thanks to technological advances in the field of semiconductors and power electronics topologies; this has allowed the use of these machines at variable speeds. After the study of the three-phase machine, scientific research focuses on machines with a phase number greater than three, such as polyphase machines and/or multi-star machines. The quality of energy delivered by these machines and their tolerance to defects make them more interesting than their three-phase counterparts in applications or comfort and discretion and mandatory [1-4]. Fault tolerance of the multiphase machine was first undertaken in [5]. In recent research, DSIM is one of the most widely used multi-phase machines due to their ability to reuse conventional three-phase converters [3, 4]. They ensure degraded operation without additional external equipment after one or more failures (as long as the number of healthy phases remains greater than or equal to three), also improve the reliability of the system at the expense of a reduction in power supplied after a fault. Several control strategies have been studied when a fault appears at the power converter or machine level, including the control [4-6], to build a robust control of the DSIM in degraded mode it necessary to study this last.

II. ASYMMETRICAL DUAL STAR INDUCTION MOTOR MODELING

The analyzed multiphase drive is shown in Fig.1. It is composed by a dual three-phase voltage source and a dual star induction machine, with two independent three-phase windings shifted an electrical angle of π/6 rad.

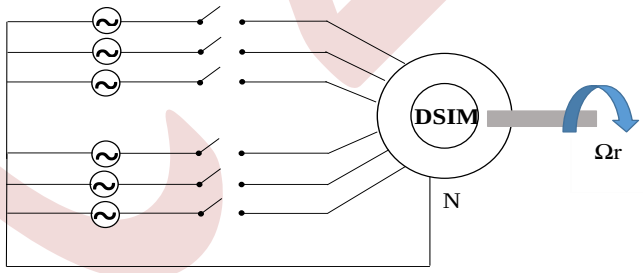


Figure1. Diagram of the DSIM drive.

The modeling approach introduces a high resistance in series with the faulty phase, which cancels the current and allows the simulation of faults. Note that, in order to simplify the modeling, usual as assumptions are made (the machine is not saturated, the non-load back electromotive force waveform is sinusoidal, the rotor is non-salient, the winding space harmonics are negligible and hysteresis and eddy current effects are negligible). Considering the distribution of the phases, the general expression of the stator voltages is:

$$\begin{pmatrix}[v_{s1}]\\[v_{s2}]\\[v_r]\end{pmatrix}=\begin{pmatrix}[R_{s1}]\\[R_{s2}]\\[R_r]\end{pmatrix}\begin{pmatrix}[i_{s1}]\\[i_{s2}]\\[i_r]\end{pmatrix}+\frac{d}{dt}\begin{pmatrix}[\psi_{s1}]\\[\psi_{s2}]\\[\psi_r]\end{pmatrix} \quad (1)$$

By introducing magnetic flux equations becomes

$$\begin{cases}[v_{s1}] = [R_{s1}][i_{s1}] + \frac{d}{dt}\left([L_{1,1}][i_{s1}] + [L_{1,2}][i_{s2}] + [L_{1,r}][i_r]\right) \\ [v_{s2}] = [R_{s2}][i_{s2}] + \frac{d}{dt}\left([L_{2,2}][i_{s2}] + [L_{2,1}][i_{s1}] + [L_{2,r}][i_r]\right) \\ [v_r] = [R_r][i_r] + \frac{d}{dt}\left([L_r][i_r] + [L_{r,1}][i_{s1}] + [L_{r,2}][i_{s2}]\right)\end{cases} \quad (2)$$

being the different inductance matrixes:

$$[L_{1,1}] = [L_{2,2}] = \begin{bmatrix} L_s & L_m cos\left(\frac{2\pi}{3}\right) & L_m cos\left(\frac{4\pi}{3}\right) \\ L_m cos\left(\frac{4\pi}{3}\right) & L_s & L_m cos\left(\frac{2\pi}{3}\right) \\ L_m cos\left(\frac{2\pi}{3}\right) & L_m cos\left(\frac{4\pi}{3}\right) & L_s \end{bmatrix} \quad (3)$$

$$[L_r] = \begin{bmatrix} L_r & L_m cos\left(\frac{2\pi}{3}\right) & L_m cos\left(\frac{4\pi}{3}\right) \\ L_m cos\left(\frac{4\pi}{3}\right) & L_r & L_m cos\left(\frac{2\pi}{3}\right) \\ L_m cos\left(\frac{2\pi}{3}\right) & L_m cos\left(\frac{4\pi}{3}\right) & L_r \end{bmatrix} \quad (4)$$

$$[L_{1,2}] = [L_{2,1}]^t = L_m \begin{bmatrix} cos(\alpha) & cos\left(\alpha + \frac{2\pi}{3}\right) & cos\left(\alpha + \frac{4\pi}{3}\right) \\ cos\left(\alpha - \frac{2\pi}{3}\right) & cos(\alpha) & cos\left(\alpha + \frac{2\pi}{3}\right) \\ cos\left(\alpha - \frac{4\pi}{3}\right) & cos\left(\alpha - \frac{2\pi}{3}\right) & cos(\alpha) \end{bmatrix} \quad (5)$$

$$[L_{1,r}] = [L_{r,1}]^t = L_m \begin{bmatrix} cos(\theta_r) & cos\left(\theta_r + \frac{2\pi}{3}\right) & cos\left(\theta_r + \frac{4\pi}{3}\right) \\ cos\left(\theta_r - \frac{2\pi}{3}\right) & cos(\theta_r) & cos\left(\theta_r + \frac{2\pi}{3}\right) \\ cos\left(\theta_r - \frac{4\pi}{3}\right) & cos\left(\theta_r - \frac{2\pi}{3}\right) & cos(\theta_r) \end{bmatrix} \quad (6)$$

$$[L_{2,r}] = [L_{r,2}]^t = L_m \begin{bmatrix} cos(\theta_r - \alpha) & cos\left(\theta_r - \alpha + \frac{2\pi}{3}\right) & cos\left(\theta_r - \alpha + \frac{4\pi}{3}\right) \\ cos\left(\theta_r - \alpha + \frac{2\pi}{3}\right) & cos(\theta_r - \alpha) & cos\left(\theta_r - \alpha + \frac{2\pi}{3}\right) \\ cos\left(\theta_r - \alpha + \frac{4\pi}{3}\right) & cos\left(\theta_r - \alpha + \frac{2\pi}{3}\right) & cos(\theta_r - \alpha) \end{bmatrix} \quad (7)$$

$$\frac{d}{dt}[i_{s1}] = [L_{1,1}]^{-1}([v_{s1}] - [R_{s1}][i_{s1}] - [L_{1,2}]\frac{d}{dt}([i_{s2}]) - [L_{1,r}]\frac{d}{dt}([i_r]) - \omega r\frac{d}{d\theta_r}([L_{1,r}])[i_r])$$

$$\frac{d}{dt}[i_{s2}] = [L_{2,2}]^{-1}([v_{s2}] - [R_{s2}][i_{s2}] - [L_{21}]\frac{d}{dt}([i_{s1}]) - [L_{2,r}]\frac{d}{dt}([i_r]) - \omega r\frac{d}{d\theta_r}([L_{2,r}])[i_r]) \quad (8)$$

$$\frac{d}{dt}[i_r] = [L_r]^{-1}(-[R_r][i_r] - [L_{r1}]\frac{d}{dt}([i_{s1}]) - [L_{r,2}]\frac{d}{dt}([i_{s2}]) - \omega r\frac{d}{d\theta_r}([L_{r,1}])[i_{s1}] - \omega r\frac{d}{d\theta_r}([L_{r,2}])[i_{s2}])$$

The electromagnetic torque and mechanic expression complete the system:

$$c_{em} = p\left\{[i_{s1}]^t\frac{d}{d\theta_r}[L_{1,r}][i_r] + [i_{s2}]^t\frac{d}{d\theta_r}[L_{2,r}][i_r]\right\} \quad (9)$$

$$c_{em} - c_r = J\frac{d\Omega r}{dt} + f_r\Omega_r \quad (10)$$

With:

p number of pairs of poles;

$\Omega_r = \frac{\omega_r}{p}$ is the rotating speed;

J total inertia of mechanical movement;

f_r machine's viscous friction coefficient;

c_r is the load torque;

c_{em} electromagnetic torque developed by machine.

The joule losses of the machine are expressed by the following formula:

$$pjs = Rs1(is1a^2 + is1b^2 + is1c^2) + Rs2(is2a^2 + is2b^2 + is2c^2) \quad (11)$$

III. RESULTS ANALYSIS AND DISCUSSION

To show the validity of the proposed theory, some simulations were done for stator open phase fault with MATLAB/Simulink.

The 4.5 kW DSIM is supplied by two symmetrical three-phase voltage sources which are offset by 30°.

After the machine is started under normal operating conditions, a nominal load with a torque Cr = 15 N.m is applied. At t = 1.9 s a stator phase open fault is caused after this time.

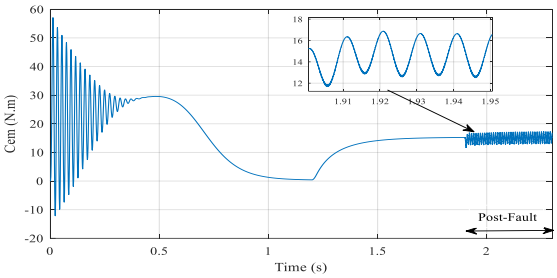


Figure 2. Electromagnetic Torque before and during the fault

Figure 2 shows the behavior of the electromagnetic torque before and during the fault. The introduced fault generates exaggerated ripples, which exceed 13% of the nominal torque.

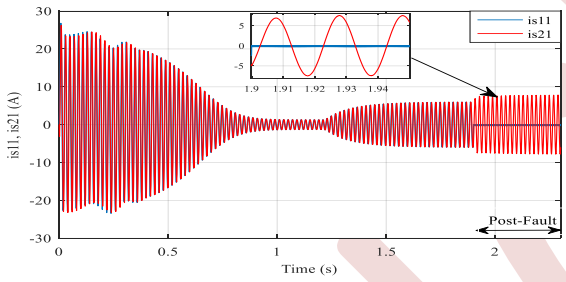


Figure 3. stator currents of the first phase of the two stars before and during the fault

The stator currents follow a symmetrical path from start-up at time t= 0 s until t=1.9 s, when the fault is introduced; consequently, the current of one star becomes zero.

In order to maintain the electromagnetic torque developed, the machine draws a larger current from the second star.

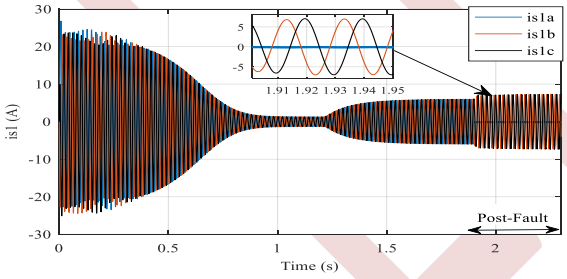


Figure 4. stator currents of the first star before and during the fault

Figure 4 shows that the current in one phase of a star is cancelled as soon as the fault is applied. As a result, the currents in the other two phases increase to make up the shortfall caused by the lack of current in the third phase.

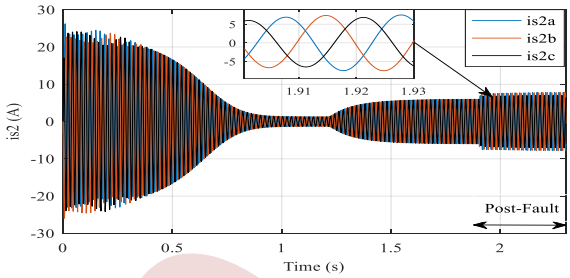


Figure 5. stator currents of the second star before and during the fault

The stator currents of the second star become more significant from the moment the fault is introduced at t=1.9 s. This is justified by the disturbance and non-equilibrium of the currents in the first star due to the absence of current in one phase.

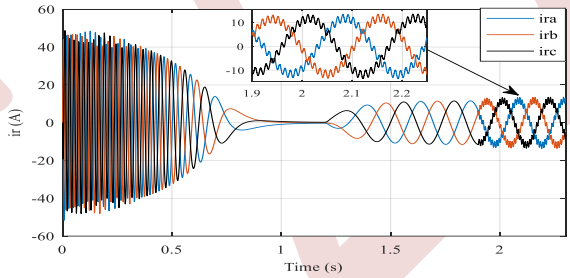


Figure 6. Rotor currents before and during the fault

Figure 6 shows the time evolution of the rotor currents from start-up in the transient regime and the subsequent application of the load, which causes an increase in these currents in the steady state. After the fault has been introduced, a chattering effect has been view in the currents rotor witch is cosed by the methode of introdussing the fault of open phase.

i.e: inserting of the serial higher value resistance with fault phase.

Table : FFT analysis.

	Machine in healthy mode		Machine in fault mode	
	Amp fund (A)	THD(%)	Amp fund (A)	THD(%)
i_{ra}	11,39	1,30	11,25	20
i_{rb}	11,39	1,30	11,84	15,9
i_{rc}	11,39	1,30	11,72	16,59

The table above shows the amplitudes of the fundamental wave of the three rotor phases of the machine in healthy and fault modes.

These currents remain in equilibrium and are almost equal in amplitude in healthy and faulted modes. However, the harmonic distortion rates increase considerably with the application of phase opening faults.

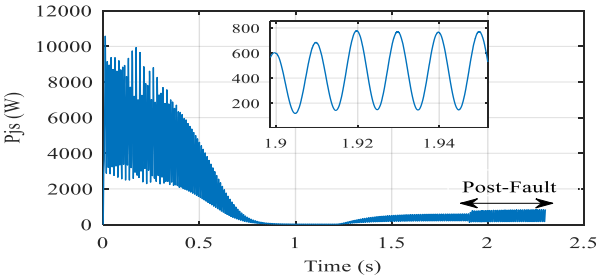


Figure 7. Stator joules losses before and during the fault

In the steady state of the machine, the stator joule losses are constant. As soon as the Open Phase Fault (OPF) is applied, these losses increase significantly, leading to a reduction in the machine's useful power and, consequently, its useful torque.

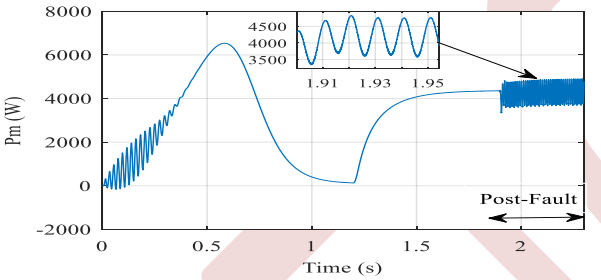


Figure 8. Mechanical power before and during the fault

Figure 8 shows the evolution of the mechanical power as a function of time from start-up at time t = 0 s to t = 1.9 s, when the steady state operation of the machine is disturbed by the application of the fault. The OPF has caused ripples in the mechanical power, which is directly related to the machine torque.

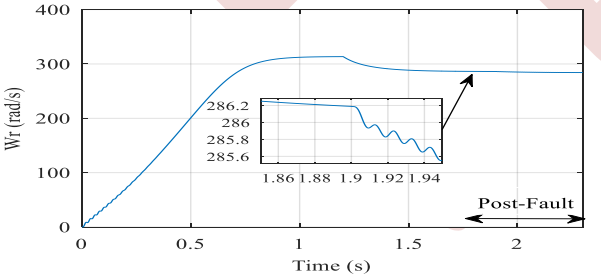


Figure 9. Electrical speed before and during the fault

The speed of the machine increases progressively from the start until it reaches almost synchronous speed. As soon as a resisting torque cr=15 N.m is applied to the machine, the speed decreases and reaches a steady-state speed wr=286 rad /s. After the moment t=1.9s when the fault is applied, the speed drops sharply and ripples are generated.

IV. CONCLUSION

AC induction machines, like all electrical machines, are subject to a very complex phenomenon: the open phase fault. This paper presents MATLAB/Simulink simulation results of a DSIM subjected to an open phase fault. After the instantaneous fault is applied, the currents in the two stator stars increase and become unbalanced due to the cancellation of a current in one phase (the faulted phase). This inrush current causes an increase in Joule losses, which are directly linked to the stator current, leading to overheating of the machine and even loss of the rated load. The electromagnetic torque reached by the OPF in turn justifies the appearance of ripples on the latter, which is directly linked to the speed of the machine, which in turn undergoes a sudden drop and the appearance of ripples. The chattering effect is visible in the rotor currents and is due to the way of opening phase. In fact, the open phase fault leads to deterioration in all the characteristics of the DSIM and a reduction in its service life.

APPENDIX

$$R_s = 3.72\ \Omega, R_r = 2.12\Omega, L_m = 0.2448\ H, J = 0.0625\ \frac{N.m}{Kg}, l_s = 0.022H,$$

$$l_r = 0.006\ H, f = 0.001\ N.\frac{m}{rd}, p = 1$$

REFERENCES

[1] K. Matsuse, D. Matsuhashi, "New Technical Trends on Adjustable SpeedAC Motor Drives. Chinese Journal of Electrical Engineering," vol. 3, no. 1, pp. 1-9, 2017.

[2] L. Khaldi, "Etude et Commande des Architectures de Convertisseurs Statiques AC/AC Tolérantes aux Défauts Associés à une Génératrice Polyphasée," thèse de doctorat.

[3] F Barrero, M. Duran, "Recent advances in the design, modeling and control of multiphase machines-Part I," IEEE Trans. Ind. Electron, vol. 63, no. 1, pp. 449-458, 2016.

[4] M. Duran, F. Barrero, "Recent advances in the design, modeling and control of multiphase machines-Part II," IEEE Trans. Ind. Electron, vol. 63, no. 1, pp. 459-468, 2016.

[5] T. M. Jahns, "Improved reliability in solid-state AC drives by means of multiple independent phase drive units," IEEE Transactions on Industry Applications, IA-16, pp. 321-331, 1980.

[6] P. Gonçalves, S. Cruz, A. Mendes, "Finite Control Set Model Predictive Control of Six-Phase Asymmetrical Machines-An Overview," Energies, vol. 12, no.24, 2019.

[7] K. Iffouzar, M. F. Benkhoris, B. Amrouche, A. Houari, K. Ghedamsi, A. Djérioui, "A New Post-Fault Reconfiguration Strategy under Open-Phase Operation Conditions of Asymmetrical Double-Star Induction Machines,"Energies 2023,16, 5740. https://doi.org/10.3390/en16155740.

[8] K. Iffouzar, L. Khaldi, A. Djérioui, A. Houari, K. Ghedamsi, M. F. Benkhoris, "New Analysis Model of Stator Open Phase Faults in a Five-Phase Induction Motor," http://iieta.org/journals/jesa, vol. 53, No. 2, April, 2020, pp. 213-218.

levitation force electromagnetic calculations for medium-speed trains

Yanis FERROUDJ [1], Athmane BOUZIDI [1], Nourreddine TAKORABET [2]

[1] *Laboratoire de Génie Electrique de Bejaia, Faculté de Technologie, Université de Bejaia, 06000 Bejaia, Algeria*

[2] Université de Lorraine – GREEN Nancy, France

yanis.ferroudj@univ-bejaia.dz

athmane.bouzidi@univ-bejaia.dz

noureddine.takorabet@univ-lorraine.fr

***Abstract*— This paper suggests a 200 km/h semi-high-speed Maglev train that is under development in Korea. For translation thrust and electromagnetic sustentation, it makes use of a linear induction motor (LIM) [1]. This system's levitation force characteristic is examined through the use of two-dimensional (2D) numerical electromagnetic field emission microscopy calculations. The Maxwell stress tensor and Lorenz, block integral which based on the deference of the co energy, and, finally, the analytical method as a function of levitation coil currents and air gap distance can all be used to calculate the attractive levitation force. The study presents a comparison of the levitation force calculations made using various finite elements method formulations on a studied geometric model.**

***Keywords:* semi-high-speed Maglev, Finite element method, Levitation force, field flux, Maxwell stress tensor.co-energy**

I. INTRODUCTION

While the quality and speed of practical transportation have evolved over time, the wheel-rail system has till now satisfied today's standards. The latter necessitates a sturdy, dependable, and long-lasting structure, but it suffers mechanical issues owing to friction and irregular collisions between wheel and rail, as well as irritating vibrations and noise. The magnetic levitation vehicle enables contactless, wheel less mobility, which overcomes all of these issues simultaneously; it therefore provides an excellent quality of travel without the negative, disruptive consequences of wheels. Like conventional rail uses, maglev vehicles are vulnerable to air resistance and lateral disturbance. The latter, on the other hand, may be adjusted by the control system, resulting in a smoother ride [1]. Maglev trains excel at hill climbing Smaller radius for curved lane performance and requirements. This results in more flexibility in route selection criteria, lowering construction costs. For starters, it is less susceptible to weather conditions. Second, due to their construction, maglev trains have minimal risk of derailment and demonstrate great stability even when the levitation system fails, as emergency wheels may be deployed.

There are high-speed and medium-speed trains, depending on their operating speed. The former is similar to Germany's trains fast, while the latter, like Korea's Urban Maglev, is driven by a linear induction motor (LIM) and levitates by an electromagnet. This paper is concerned with electromagnetic formulation and finite element modeling of the latter, followed by a parametric examination and analysis of the magnetic levitation phenomena. The force of levitation is estimated using all three methods (block integral, Maxwell tensor, and analytic form). The parametric finite element research and analytical findings indicate levitation force behavior [3] [1].

The first section is devoted to the mathematical model of levitation, the second to the technique of calculating this force, and the third to the geometric description of the model utilized, taking into consideration its geometrical dimensions and the interpretation of the results produced. Finally, a resolution is reached.

II. LEVITATION MODELING

The electromagnetic phenomenon governing translation and levitation is driven by Maxwell's four equations, the laws of medium behavior and the conditions of passage between two media of different properties. Using simplifying assumptions and considering linear and isotropic media, we obtain the following formulation in terms of the vector magnetic potential $\vec{A}$:

$$\vec{\nabla}\Lambda\left(\frac{1}{\mu}\,\vec{\nabla}\Lambda\vec{A}\right)=\vec{J} \qquad (1)$$

Where *J* is the electric current density.

Various methods can be used to solve the partial derivation equation system (1); analytical [7] digital [7] or semi-analytical methods are recommended.

For the study of magnetic levitation, we have chosen the finite element method in matlab, which allows us to calculate the magnetic vector potential *A* at all location points of the mesh studied after discretizing the domain. Furthermore, derived quantities such as magnetic induction *(B)* and magnetic field *(H)* are obtained from the magnetic vector potential *(A).*

$$\vec{B} = R\vec{O}TA \tag{2}$$

$$\vec{B} = \mu\vec{H} \tag{3}$$

The components B_x and B_y are calculated as follows:

$$B_x = \frac{\partial A}{\partial y} \tag{4}$$

$$B_y = -\frac{\partial \mathrm{A}}{\partial \mathrm{X}} \tag{5}$$

Where $\vec{B}$ stands for magnetic induction, A is the magnetic potential and $\vec{H}$ represents the magnetic field, B_x and B_y are the induction along the x and y axis.

III. LEVITATION FORCE

Levitation forces are calculated using various methods such as Lorenz method, which is based on induced currents and the magnetic field created by another current source, Maxwell's tensor, co- energy and the analytical form. Lorenz method can't be used in our study because of the in magneto static regime.

Maxwell's tensor method

Calculation of the levitation force was carried out using Maxwell tensor subroutine in Matlab. The Maxwell tensor components are defined by:

$$\tau_{ij} = \mu_0(H_i H_j - \frac{1}{2}\,\delta_{ij} H^2) \tag{6}$$

where τ_{ij} is the maxwell tensor H_i is the field along x and H_j is the field along y s is the chronekerx function and H is the magnetic field modulus

The overall force acting on the material of volume $d\Omega$ is given by:

$$F = \int_\Omega F\, d\Omega = \int_\Omega div\, T\, d\Omega \tag{7}$$

The force in a direction i is written as follow:

$$F_i = \oint T_i\, n\, ds \tag{8}$$

T_i stands for Maxwell tensor and n for surface norm vector and ds for surface element

$$Fx = T_x\, dl \tag{9}$$

$$Fy = T_y\, dl \tag{10}$$

Where dl is the element length.

Analytic form

the analytical form used to calculate the levitating force is given by the following relationship:

$$F = \frac{L\,\mu_0\,L_X\,(2\,I)^2}{(2\,e)^2} \tag{11}$$

L is the length of the part to be lifted and L_X is the magnetic circuit thickness μ_0 is vacuum permeability and I is the value of the current injected into the coils and e is the air gap

block integral form (weighted stress tensor):

Stress weighted by the tensorial integral requires that the areas over which the force is calculated be completely surrounded by air and/or contiguous to a boundary. When the target region adjoins an air-free zone, force results can be calculated using co-energetic differentiation:

$$F = \frac{W_c\,(p+\delta) - W_c(p)}{\delta} \tag{12}$$

where p represents the starting position, $p+\delta$ represents the disturbed location, and is the magnitude of the perturbation. The force component calculated in this way acts in the direction of the disturbance, two such processes are required to obtain the horizontal and vertical force components [8].

Lorenz method

Lorentz's electromagnetic force results from the coexistence of a magnetic induction resulting from an excitation source and an induced current density in a

conducting medium. The expression of this force is given by:

$$F = \iiint_{\Omega} \vec{J} X \vec{B} \; d\Omega \qquad (13)$$

$\vec{J}$: Current density [A/m2].

The term $(\vec{J}X\vec{B})$ represents magnetic force density.

IV. RESULTS AND DISCUSSION

Structure of the levitation electromagnet

The device configurations system of electromagnet medium speed maglev is used as shown in Figures 1 and 2. The first (Fig. 1) is composed of air, the levitation part and electromagnets of an iron core and 4 coils.

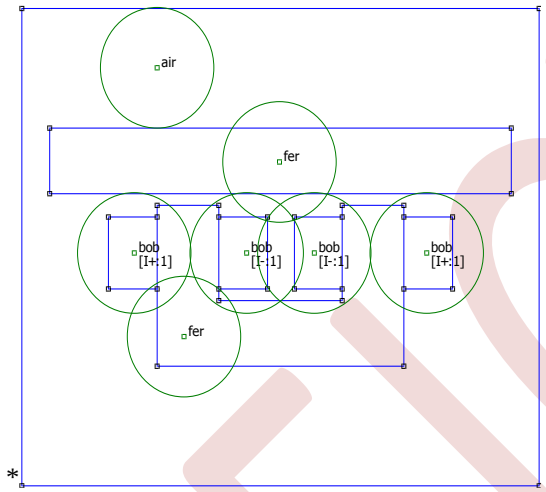


Figure 1. Geometry of levitation model

The DC excitation current feeds two levitation coils on the two lateral bares of the iron core Perpendicular to the rail in the first device configuration and only one levitation coil on the central bares of the iron core parallel to the rail in the second configuration.

The coils were made of copper sheet material to save weight and improve heat dissipation sheet coil outperforms circular coils. Insulation materials are not suited for heat release in the case of circular coils, and heat will quickly build [1].

TABLE 1. GEOMETRIC DEMENSIONS OF THE LEVITATION MODEL

Item	value
magnetic circuit width	220 mm
magnetic circuit height	134mm
coil width	42.9mm
coil height	59.9mm
width of part to be lifted	410mm
lifting part height	55mm
air gap	4mm

The field flux produced by coils used to achieve levitation by contact with the core pure iron material put along the guide path [6].

Discuss result

To examine the field flux and levitation force, the modeling FEM analysis is shown in "Fig 2". Assessments of levitation electromagnets with one or two coils are conducted for comparison [5].

Field Flux Analysis

The field flux for a two-coil levitating electromagnet is shown in "Fig. 2," the flux is well channeled, the end effect is reduced in the iron of the input and output cores, and the magnetic field lines are ordered in the pure iron of the core for current values ranging from *0(A)* to *42(A)* and a permeability of the ferromagnetic material fixed equal *Ur =1000*, and the air gap is constant
e =4 (mm) [3].

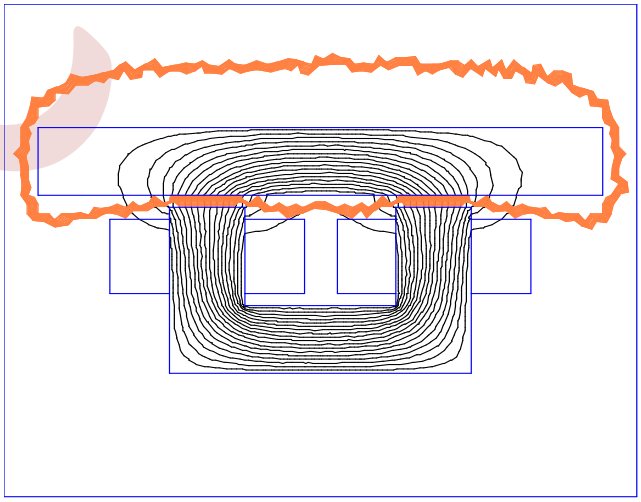


Figure 2. distribution of field lines.

TABLE 2. SPECIFICATION OF STATIC LEVITATION FORCE FOR MEDIUN SPEED-TRAIN

Item	value
Levitation force	31.17N (e = 4mm)
Indicator coil resistance	10 mΩ
Indicator coil inductance	0.065 mH
Number of turns	50 turns

Core material	Pure iron
core magnetic permeability	1000

Lifting force along the air gap for a constant height

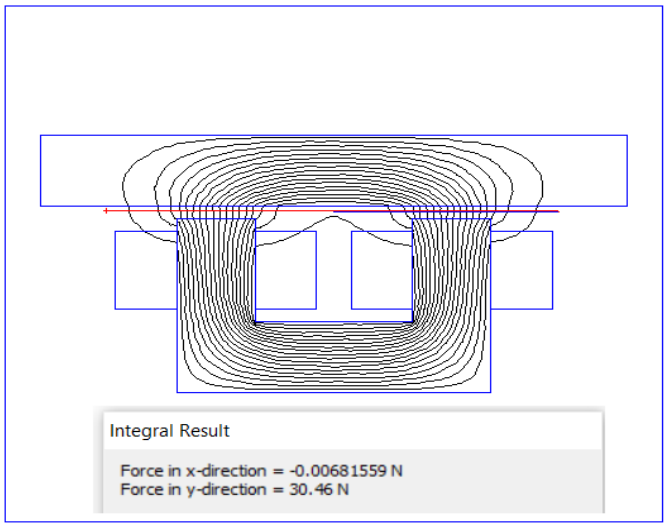


Figure 3. uniformity of lifting force.

The lifting force created by the interaction between the indicator's magnetic field and the ferromagnetic part to be raised is constant at *F=30.46 (kN)* for a constant air gap height along the air gap *d=2 (mm)*, demonstrating the lifting force's uniformity.

Forces levitation analysis

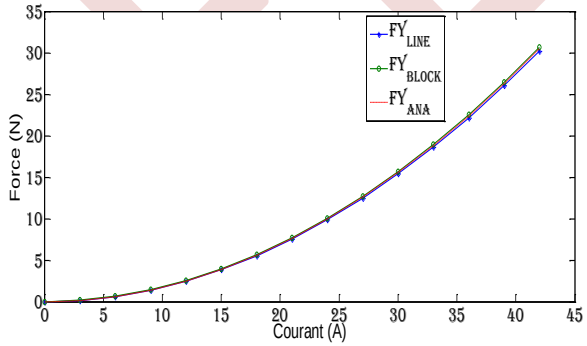


Figure 4. Levitation force.

The bulk of electromagnetic levitation systems rely on an attractive normal force between the motor and the guideway's iron core [2].

"Fig. 3" of the picture depicts an examination of the levitation force as a function of current input to levitation coils with a constant air gap of *4 (mm)*. All three approaches compute the levitation forces. The levitation forces have the same values and behavior for varied DC excitation current values ranging from *0 (A)* to *42 (A)*, attaining high values as the current value in the levitation coils increases, and the maximum levitation force value is *F=31.17 (kN)* for *I = 42 (A)*.

V. Conclusion

Several methods are used to calculate force. Using the finite element approach to calculate magnetic potential in the train's geometrical model allowed us to demonstrate that the force's behavior is identical. The geometrical dimensions of the levitation device, the length of the air gap, and the variation of the current injected into the coils all play an important role in achieving high values, reducing the final effect, and channeling the magnetic field throughout the magnetic circuit and orderly field lines. Because it lowers vibrations and interruptions, force is a crucial element for train control.

References

[1] J. Lim, C.-H. Kim, J.-M. Lee et al., "Design of magnetic levitation electromagnet for High Speed Maglev train," in 2013 International Conference on Electrical Machines and Systems (ICEMS), IEEE, 2013, pp. 1975-1977.

[2] H.-W. Cho, C.-H. Kim, H.-S. Han et al., "Levitation and thrust forces analysis of hybrid-excited linear synchronous motor for magnetically levitated vehicle," in Journal of Electrical Engineering & Technology, vol. 7, no. 4, pp. 564-569, 2012.

[3] H.-W. Cho, C.-H. Kim, J.-M. Lee et al., "3-Dimensional finite element analysis of linear synchronous motor for magnetically levitated vehicle," in 2010 International Conference on Electrical Machines and Systems, IEEE, 2010, pp. 1555-1558.

[4] J. Jeong, C.-W. Ha, J. Lim et al., "Analysis and control of electromagnetic coupling effect of levitation and guidance systems for semi-high-speed maglev train considering current direction," in IEEE Transactions on Magnetics, vol. 53, no. 6, pp. 1-4, 2017.

[5] J. Jeong, C.-W. Ha, M. Kim et al., "Experimental verification and electromagnetic analysis for force performance of levitation and guidance electromagnet in semi-high-speed Maglev train," in 2016 IEEE Conference on Electromagnetic Field Computation (CEFC), IEEE, 2016, pp. 1-1.

[6] J. Jeong, C. Ha, J. Lim, et al., "Analysis and control of the electromagnetic coupling effect of the levitation and guidance systems for a semi-high-speed MAGLEV using a magnetic equivalent circuit," IEEE Transactions on Magnetics, vol. 52, no. 7, pp. 1-4, 2015.

[7] M. E. H. Latreche et O. Nehal, "Etude et modélisation des paliers planaires," 2009.

[8] D. Meeker, "Finite Element Method Magnetics," 2006.

IV

ELECTRIC POWER SYSTEMS (EPS)

Sommaire

IV.1 A new efficient meta-heuristic method for solving the optimal power flow problem in power system 128
IV.2 Multi-objective optimal power flow solution using bonobo optimizer algorithm 134
IV.3 Application of new metaheuristic algorithm for optimal placement and sizing of STATCOM device 140
IV.4 Deep reinforcement learning based virtual inertia control for islanded microgrids with high sharing of renewable energy sources 146
IV.5 Bald eagle search-based optimization algorithm for optimal power flow solution in power systems 152
IV.6 Enhancing power distributed generation with storage systems for sustainable energy integration 156
IV.7 Use of the dual stator induction machine in a hybrid renewable energy pumping system 162
IV.8 Transient stability analysis of a multimachine power system 168
IV.9 Impact of TCSC on energy performance in electrical networks 174
IV.10 Economic load dispatch with saving environment by greenhouse gas emission reduction using genetic algorithms 179
IV.11 Analysis of space vector identification method in series active filters for electrical power quality improvement 185
IV.12 Investigation about ferranti effect and challenge to harmonics suppression in a specific long power transmission line 191
IV.13 Estimation of the schavemaker arc model parameters for high-voltage circuit breakers 196
IV.14 Planning study for electrical substations in Algeria 202
IV.15 Impact of the fault location and machine damping on the transient stability of an electrical power network 207
IV.16 Optimal placement of TCSC for optimizing active and reactive power using AAC PSO algorithm 213

A New Efficient Meta-heuristic Method for Solving the Optimal Power Flow Problem in Power System

Fatima Zohra Aroua [1], Ahmed Salhi [1], Souheil Salhi [1] Djemai Naimi [1]

[1] *Electrical department LGEB Laboratory, University of Biskra, BP 145, Biskra 07000, Algeria*

zohra.aroua@univ-biskra.dz

a_salhi_m@yahoo.fr

s.souheil@univ-biskra.dz

d.naimi@univ-biskra.dz

***Abstract*— In this paper, a new nature-based meta-heuristic technique, named cheetah optimizer (CO) algorithm is suggested to solve six well-known Optimal Power Flow (OPF) problem in electric power system. The optimization method is inspired from the hunting behavior of cheetahs in the wild. The investigation process for optimal global solution is based on three principal prey-hunting strategies, namely search, sit-and-wait, and attack. The presented technique is applied to minimise the objective functions, such as total fuel cost, total gas emission, total active power losses, voltage stability index and voltage deviation. The proposed approach has been employed for the IEEE 30-bus test system. The effectiveness of CO method is justified based a comparison report of its simulation results with those of other optimization algorithms recently developed in the literature.**

Keywords— **Cheetah optimizer algorithm, Fuel cost, Valve-point effects, Gas emission, Active losses, Voltage deviation, Electric power system, Optimal power flow.**

I. INTRODUCTION

The optimal power flow (OPF) is considered the most important problem for energy system managers. This is used in many applications as an indispensable and efficient tool for optimal network planning and operation by tuning certain control parameters. The principal objective of solving the OPF problem is satisfying at the same time all the network constraints (equality and inequality)[1], with the reduction in a specified non-linear objective function, such as the total cost of electricity generation, the total emission of pollutant gases by the thermal power plant ,total active power losses, voltage deviation and voltage stability index[2, 3] .The OPF problem was first proposed by Carpentier in 1962 and further elaborated by Dommel and Tinny[4, 5] .

Several classical methods have been applied to solve the OPF problem, such as Nonlinear and Quadratic Programming (NLP, QP)[6], Newton, Linear Programming and Interior Point Methods (NM, LP, IPM)[7] . However, most of these methods cannot guarantee convergence towards the global optimum and are often blocked at the local optimum. To avoid the disadvantages of traditional techniques, several meta-heuristic optimization algorithms have been effectively used to solve the OPF problem in recent years, such as Dragonfly Algorithm (DA)[8], Grasshopper Optimization Algorithm (GOA)[9] , Slap Swarm Optimization (SSO)[10], Harris Hawks Optimization (HHO)[11] , Teaching Learning Based Optimization (TLBO)[12], Slime Mould Algorithm(SMA) [13] , and so on. In this paper, we present a new population-based meta-heuristic algorithm for solving OPF problems, called the Cheetah Optimizer (CO) algorithm, proposed in 2022 by Mohammad Amin Akbari et al[14], inspired by the hunting behavior of cheetahs in nature. This algorithm (CO) is based on three principal prey- hunting strategies, searching, sitting-and-waiting, and attacking. The possibility of leaving the prey and returning home during the chase is included in the hunting process. The performance of the CO algorithm avoids any local optima in the OPF solution and ensures a balance between the exploration and exploitation phases. Based on the results obtained from simulations using the IEEE 30-bus test system, demonstrate the efficiency of the CO algorithm compared to other optimization techniques described in the literature. The rest of this work is arranged as follows: Section II describes the mathematical formulation of the OPFproblem, while Section III explains the CO method. In Section IV, the simulation results are discussed and compared with other existing techniques in the literature. Finally, Section V ends with a conclusion.

II. OPTIMAL POWER FLOW PROBLEM

A. Formulation Problem

The goal of solving the OPF problem is to obtain the optimal values of decision parameters that provide the minimum value objective function while satisfying all operating constraints. The basic formulation of the OPF problem is given as follows[2, 12]:

$$\begin{cases} \text{Minimise}: & \boldsymbol{f}(x,u) & & (1) \\ \text{Subject to}: & \boldsymbol{g_j}(x,u) = \mathbf{0} & j = 1,2,\dots,r & (2) \\ & \boldsymbol{h_j}(x,u) \le \mathbf{0} & j = 1,2,\dots,z & (3) \end{cases}$$

B. State and Control Variables

The vectors of the state and control variables (***x, u***) of the electrical system can be defined as follows[1, 11]:

$$\boldsymbol{x} = \left[P_{G_1}, V_{L_1}, \dots, V_{L_{N_L}}, Q_{G_1}, \dots, Q_{G_{N_G}}, S_{l_1}, \dots, S_{l_{nl}}\right]' \quad (4)$$

$$\boldsymbol{u} = \left[P_{G_2} \dots P_{G_{N_G}}, V_{G_1} \dots V_{G_{N_G}}, Q_{C_1}, \dots Q_{C_{Nc}}, T_1, \dots T_{N_T}\right]' \quad (5)$$

C. Optimal power flow constraints

1) Equality Constraints*:* represent the balance between generation and load powers as given belo[8]:

$$P_{Gi} - P_{Di} - V_i \sum_{j=1}^{N_B} V_j \left[G_{ij} \cos \delta_{ij} + B_{ij} \sin \delta_{ij}\right] = 0 \quad (6)$$

$$Q_{Gi} - Q_{Di} - V_i \sum_{j=1}^{N_B} V_j \left[G_{ij} \sin \delta_{ij} + B_{ij} \cos \delta_{ij}\right] = 0 \quad (7)$$

2) Inequality Constraints: these are the operating limits of power system equipment, such as generators, transformers, VAR sources, and security, as shown below respectively [11]:

$$\begin{cases} V_{i,min} \le V_i \le V_{i,max}\ , & i = 1,2,\dots,N_G \quad (8) \\ P_{Gi,min} \le P_{Gi} \le P_{Gi,max}\ , & i = 1,2,\dots,N_G \quad (9) \\ Q_{Gi,min} \le Q_{Gi} \le Q_{Gi,max}\ , & i = 1,2,\dots,N_G \quad (10) \\ T_{i,min} \le T_i \le T_{i,max}\ , & i = 1,2,\dots,N_T \quad (11) \\ Q_{Ci,min} \le Q_{Ci} \le Q_{Ci,max}\ , & i = 1,2,\dots,N_C \quad (12) \\ V_{Li,min} \le V_{Li} \le V_{Li,max}\ , & i = 1,2,\dots,N_L \quad (13) \\ S_{li,min} \le S_{li} \le S_{li,max}\ , & i = 1,2,\dots,n_l \quad (14) \end{cases}$$

D. Objective Function

1) Quadratic total fuel cost function*:** The total fuel cost (Fc***) for each power plan can be expressed as follows[1, 3]:

$$\boldsymbol{F_C} = \sum_{i=1}^{N_G} a_i + b_i P_{Gi} + c_i P_{Gi}^2 \quad (15)$$

2) Total fuel cost function with valve point effects: Valve point load effects (VPLE) can be taken into account by adding a sinusoidal term to the fuel cost function (***Fcval***), as shown below[9]:

$$\boldsymbol{F_{Cval}} = \sum_{i=1}^{N_G} a_i + b_i P_{Gi} + c_i P_{Gi}^2 + \left|d_i \sin\left(e_i (P_{Gi}^{min} - P_{Gi})\right)\right| \quad (16)$$

3) Total gas emission function*:* The greenhouse gas emission reduction function ***(Em)*** is given as follows[2, 9] :

$$\boldsymbol{E_m} = \sum_{i=1}^{N_G} \alpha_i + \beta_i P_{Gi} + \lambda_i P_{Gi}^2 + \xi_i e^{(\theta_i P_{Gi})} \quad (17)$$

4) Total Active power losses function: Active power losses on transmission lines(***TPL***) are expressed by the following formula[8, 12]:

$$\boldsymbol{TPL} = \sum_{b=1}^{n_l} \left(G_{b(ij)} (V_i^2 + V_j^2 - 2V_i V_j \cos \delta_{ij})\right) \quad (18)$$

5) Voltage deviation function: The reduction of all load bus voltage deviations (***VD***) from a specified value of 1.0 pu , is defined by the following function[10, 13]:

$$\boldsymbol{VD} = \left(\sum_{i=1}^{NL} |V_{Li} - 1.0|\right) \quad (19)$$

6) Voltage stability index function : The decrease in the maximum value of the system voltage stability indicator (***VSI***) is given as follows [10, 13]:

$$\boldsymbol{L_j} = \left|1 - \sum_{i=1}^{N_G} F_{ji} \frac{V_i}{V_j}\right| ; \quad \text{where,} \quad \boldsymbol{F_{ji}} = -[Y_1]^{-1}[Y_2] \quad (20)$$

$$\boldsymbol{VSI} = \max(L_j); \quad \text{where,} \quad j = 1,2,\dots\dots,N_L \quad (21)$$

III. CHEETAH OPTIMIZER ALGORITHM

This section presents the principles of the CO optimization technique for solving complex optimization problems, described in the following subsections:

A. Source of inspiration

The cheetah is one of the most recognizable cats in the world. It is known for its speed (120 km per hour). It starts its hunt from a high place , it moves slowly towards its prey (gazelles, zebras, impalas, etc.). The hunt takes about half a minute with an average distance of 173 m. The cheetah stumbles its prey and bites it in the throat. But if the hunt takes too long, it gives up. Thus, biological studies show that the cheetah's flexibility allows it to turn immediately from one side to the other, its long tail serves as a balance and the flexibility of its spine allows it to "fly" between two jumps during the pursuit of a prey [14] .The Cheetah hunting behavior is shown in Fig.1.



Figure 1.Cheetah hunting behavior.

B. Mathematical model of CO

The CO algorithm is based on an intelligent exploitation of hunting strategies, as shown in Fig.2, during the hunting phases (iterations). Each prey is a place of a decision variable corresponding to the best solution, and the cheetah situations constitute a population. The pseudo-code[14] of the CO algorithm for solving the OPF problem is given in Fig.3.

In this section, we present the mathematical model for each hunting strategy as below:

1) Search strategy*:* The cheetah must scan its territory to find its prey; one of two modes: scanning (sitting or standing) or active mode. This strategy is illustrated in Fig.2a, and expressed by the following search equation:

$$\boldsymbol{X_{i,j}^{t+1}} = X_{i,j}^t + \hat{r}_{i,j}^{-1} . \alpha_{i,j}^t , \ \text{Where,} \ \boldsymbol{\alpha_{i,j}^t} = 0.001 \times t/T \quad (22)$$

2) Waiting strategy *(sit and wait):* After detecting a prey in an unsuitable situation, the cheetah sits and waits for the prey to approach its side; if not, it will choose a better situation. This strategy is illustrated in Fig. 2b. This is expressed mathematically as follows:

$$X_{i,j}^{t+1} = X_{i,j}^{t} \tag{23}$$

3) Attack strategy*:* The two fundamental steps of this strategy, and its mathematical equations are described below:

a) *Rushing:* The cheetah, which decided to attack, accelerates its speed to catch its prey, as shown in Fig. 2c.

b) *Capturing:* The Cheetah attack and capture their prey quickly using both their speed and agility, as shown in Fig.2d.

$$X_{i,j}^{t+1} = X_{B,j}^{t} + \check{r}_{i,j} \cdot \beta_{i,j}^{t} \tag{24}$$

$$\text{where,} \quad \check{r}_{i,j} = |r_{i,j}|^{exp\left(r_{i,j}/2\right)} \sin(2\pi\, r_{i,j}) \tag{25}$$

4) Abandoning the prey and returning home*:* This strategy comprises the following two stages:

a) *Impossibility of hunting prey :*If the cheetah is unable to hunt its prey for a certain period of time, it will move on to the last available prey.

b) *Unsuccessful hunt for prey:* If the hunt for prey is unsuccessful, the cheetah must change location or return home.

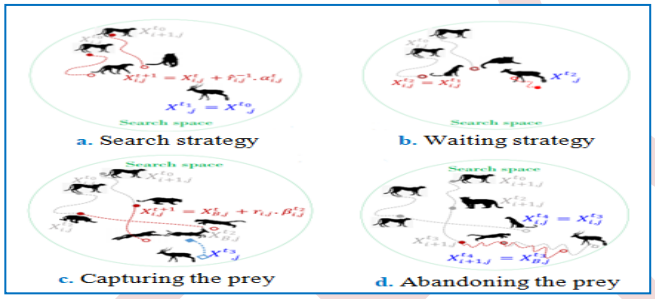


Figure 2.Schematic representation of CO hunting strategies.

IV. RESULTS AND SIMULATION

In this study, the novel CO algorithm is implemented in power system optimization. Six different cases of OPF problems are solved and tested on the standard IEEE 30 bus power system as shown in Fig. 4. The bus and line data are given in [15] with a total power demand of 2834 MW + j 1262 MVAR. Table 1 describes the parameters of the CO algorithm, while the gas emission coefficients for each generator and the quadratic fuel cost coefficients are taken as in [9] and[1] respectively. The convergence curves of the CO algorithm are shown in Figure 5, while the voltage levels for each bus are shown in Figure 6. Table 2 shows the simulation results for the six objective functions with the optimal control values obtained by the CO method. The superiority and robustness of the proposed CO technique is shown in Table 3, which provides a better solution than the other techniques reported in the literature, as detailed below:

TABLE I. CHARACTERISTICS OF CO ALGORITHM

Algorithms	IEEE 30-Bus Power Systems
Population Size (n)	n = 180
Number of search agents in a group(N)	N = 60
Optimization problem dimension(D)	D=25
Number of iterations(MaxIt)	MaxIt = 200
Random numbers $\mathbf{r_1}$; $\mathbf{r_2}$ and $\mathbf{r_3}$	[0 1]
Random number $\mathbf{r_4}$	[0 3]
Random value **H**	$H = e^{2(1-t/T)}(2_{r1} - 1)$

A. Case 1: Fuel cost reduction

The first case aims to reduce the total cost of the quadratic fuel function for power generation, expressed by equation (15). The CO method in Table 2 has the lowest fuel cost (**799.25** $/hr) compared to the other approaches in Table 3.

B. Case 2: Fuel cost with VPLE reduction

The objective function in equation (16) is used for reducing the total fuel cost with VPLE. The CO algorithm had the best total fuel cost of **809.29** ($/h) as compared to other techniques (see Table 3).

C. Case 3: Gas emission level reduction

In this case, the objective function defined by equation (17) is used to reduce the gas emission level. The use of CO algorithm led to a reduction in gas emissions (**0.204** Ton/h) in Table 2 compared to other methods, as shown in Table 3.

D.Case 4: Active power losses reduction

According to the simulation results in Table 2 based on the CO method, the optimal values of active power losses defined by equation (18), equal to **2.956** MW, are smaller than those obtained by other approaches in Table 3.

E.Case 5: Fuel cost with Voltage deviation reduction

The goal of this case is to minimize both fuel cost and voltage deviation using equations (15) and (19). The CO method yields lower optimum values of **815.10** ($/h) and **0.105** (p.u.) compared to other techniques in Table 3.

F.Case 6: Fuel cost with voltage stability index reduction

Equations (15) and (21) simultaneously reduce the fuel cost and improve the voltage stability index. According to Table 3, the CO method proves to be superior to other approaches, with simulation results of **810.82** ($/h) and **0.115.**

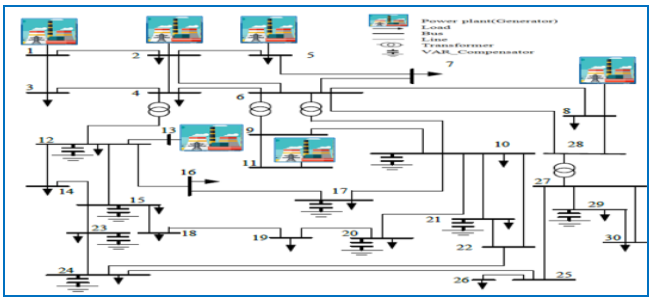
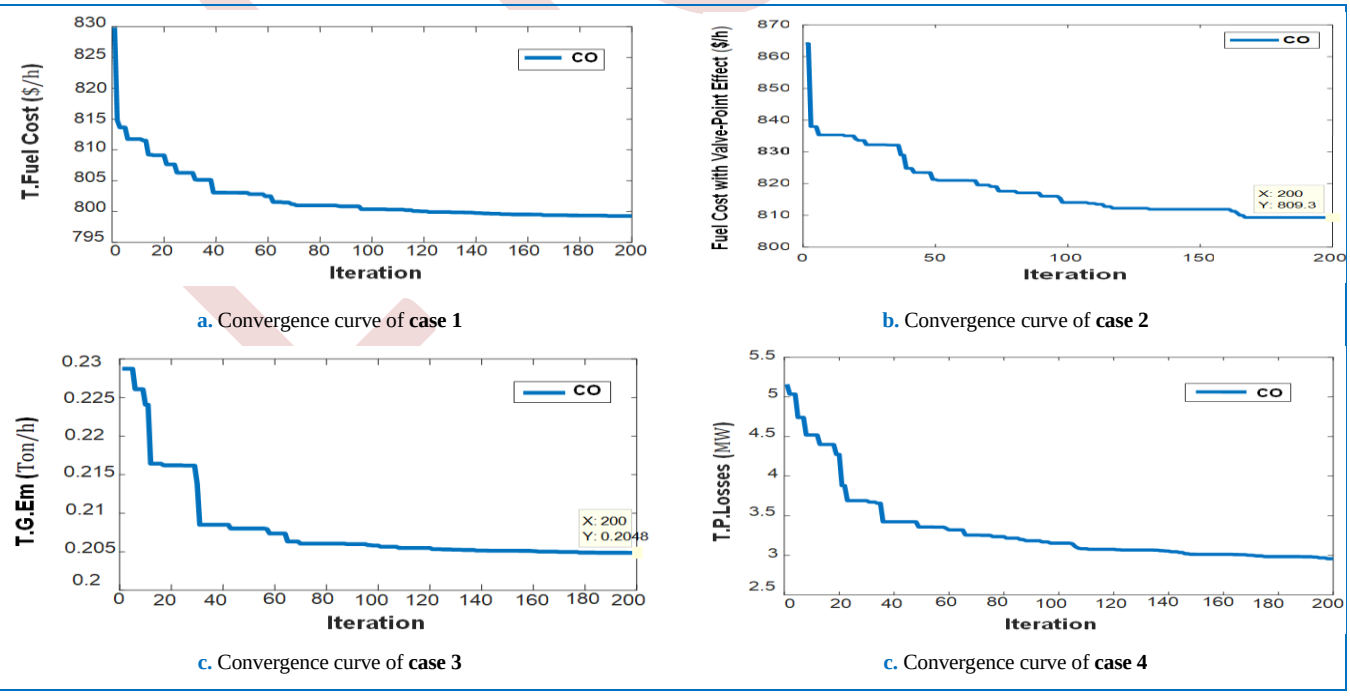


Figure 4. Single-line diagram of the IEEE 30-bus system

Define the problem data, dimension (D),and the initial population size(n)
Generate the initial population of cheetahs X_i (i =1,2,…,n) and evaluate the fitness of each cheetah
Initialize the population's home, leader, and prey solutions
$t \leftarrow 0$
$it \leftarrow 1$
$MaxIter \leftarrow$desired maximum number of iterations
T$\leftarrow$ 60 x [D/10]
while $it \leq MaxIter$ **do**
  Select m ($2 \leq m \leq n$)members of cheetahs randomly
  for each member $i \in m$ **do**
  Define the neighbor agent of member i
    for each arbitrary arrangement $j \in \{1,2,\ldots, D\}$ **do**
    Calculate $\hat{r}, \check{r}, \alpha, \beta$, and H
    $r_2, r_3 \leftarrow$ random number is chosen uniformly from 0 to 1
    if $r_2 \leq r_3$ **then**
      $r_4 \leftarrow$ a random number is chosen uniformly from 0 to 3
      if $H \geq r_4$ **then**
        Calculate the new position of member i in arrangement j using Equation (22) **// Search**
      Else
        Calculate the new position of member i in arrangement j using Equation (24) **// Attack**
      End
    Else
      Calculate the new position of member i in arrangement using Equation (23) **// Sit-and-wait**
    End
  End
  Update the solutions of member and the leader
 End
 $t \leftarrow t+1$
 if $t > rand$ x T and the leader position doesn't change for a time, **then // Leave the prey and go back home**
  Implement the leave the prey and go back home strategy and change the leader position
  Substitute the position of member by the prey position
  $t \leftarrow 0$
 End
 $it \leftarrow it+1$
 Update the prey (global best) solution
End

Figure 3. Pseudo-code of CO algorithm



a. Convergence curve of **case 1**

b. Convergence curve of **case 2**

c. Convergence curve of **case 3**

c. Convergence curve of **case 4**

Figure 5. Convergence curves for the objective function optimal power flow **(**IEEE 30-bus power system)

TABLE II: RESULTS OF OPF PROBLEM USING **CO** ALGORITHM FOR IEEE 30-BUS POWER SYSTEM

Variables	Min	Case 1	Case 2	Case 3	Case 4	Case 5	Case 6	Max
P_{G1} (MW)	50	178.0793	149.7507	63.7276	52.2776	174.2740	177.3620	200
P_{G2} (MW)	20	48.3974	51.9888	67.9677	79.4892	48.5704	49.2206	200
P_{G5} (MW)	15	21.2856	23.3656	49.9815	49.9444	22.4919	20.9048	80
P_{G8} (MW)	10	20.0822	30.2051	34.9897	34.9390	20.4547	21.2306	35
P_{G11} (MW)	10	12.2660	19.0750	29.9852	29.9797	13.9446	11.1129	35
P_{G13} (MW)	12	12.0264	16.8154	39.9661	39.7262	13.5086	12.2985	40
V_{G1} (p.u)	0.95	1.0996	1.0509	1.0717	1.0897	1.0383	1.0996	1.1
V_{G2} (p.u)	0.95	1.0859	1.0289	1.0650	1.0841	1.0244	1.0857	1.1
V_{G5} (p.u)	0.95	1.0604	1.0010	1.0427	1.0640	1.0202	1.0560	1.1
V_{G8} (p.u)	0.95	1.0685	0.9998	1.0547	1.0706	1.0068	1.0627	1.1
V_{G11} (p.u)	0.95	1.0985	1.0412	1.0679	1.0967	1.0202	1.0987	1.1
V_{G13} (p.u)	0.95	1.0977	1.0586	1.0936	1.0990	0.9986	1.0992	1.1
$T_{11\ (6\text{-}9)}$	0.90	0.9983	1.0178	1.0513	1.0021	1.0227	1.0448	1.1
$T_{12\ (6\text{-}10)}$	0.90	1.0065	0.9870	0.9229	0.9414	0.9002	0.9188	1.1
$T_{15\ (4\text{-}12)}$	0.90	1.0361	1.0260	1.0034	0.9889	0.9590	0.9939	1.1
$T_{36\ (28\text{-}27)}$	0.90	0.9810	0.9837	0.9919	0.9691	0.9623	0.9506	1.1
Q_{C10} (Mvar)	0	2.8030	4.2491	3.7358	4.4691	3.4524	4.9408	5
Q_{C12} (Mvar)	0	3.6956	3.1405	0.4191	4.5957	2.7200	4.9198	5
Q_{C15} (Mvar)	0	4.3801	3.1065	1.1912	4.3531	4.4617	4.7867	5
Q_{C17} (Mvar)	0	4.6096	2.1573	3.9948	4.0590	0.2268	3.8658	5
Q_{C20} (Mvar)	0	3.0708	2.3468	3.0672	4.7039	4.2538	4.8061	5
Q_{C21}(Mvar)	0	4.6254	4.0631	3.9376	4.7850	4.3933	4.3449	5
Q_{C23}(Mvar)	0	2.0134	2.6013	3.0393	3.7095	4.5662	3.5754	5
Q_{C24}(Mvar)	0	4.7441	4.6717	4.8298	4.5367	4.5584	4.7766	5
Q_{C29}(Mvar)	0	3.4895	2.4736	4.9514	3.3497	2.4291	4.4795	5
F_C ($/h)	-	**799.2530**	**809.2989**	944.7781	965.1057	**815.1045**	**810.8296**	-
F_E (Ton/h)	-	0.3687	0.3002	**0.2048**	0.2071	0.3572	0.3672	-
TPL(MW)	-	8.7368	7.8005	3.2177	**2.9561**	9.8442	8.7294	-
VD (p.u)	-	1.3935	0.2322	1.0774	1.7735	**0.1052**	1.7397	-
VSI	-	0.1217	0.1405	0.1259	0.1177	0.1371	**0.1153**	-

TABLE III. COMPARING **CO** WITH OTHER METHODS FOR SIX CASES

Cases	Methods	F_C ($/h)	E_m (Ton/h)	TPL (MW)	VD (p.u)	VSI
Case 1	DA [8]	802.12	0.364	9.427	-	-
	HHO[11]	801.82	1.263	9.387	-	-
	PSO [10]	801.23	0.369	9.260	1.060	0.156
	GOA [9]	800.97	0.361	9.014	0.887	-
	TLBO[12]	800.67	0.366	9.019	0.912	-
	SSO [10]	799.41	0.368	8.776	0.910	0.139
	CO	**799.25**	0.368	8.736	1.393	0.121
Case 2	GOA[9]	836.21	0.419	10.602	0.457	-
	TLBO[12]	832.53	0.438	10.687	0.865	-
	CO	**809.29**	0.300	7.800	0.232	0.140
Case 3	HHO [11]	950.98	0.285	3.570	-	-
	SMA [13]	936.11	0.217	3.593	0.475	0.148
	SSO [10]	944.72	0.205	3.220	1.340	0.135
	PSO [10]	948.47	0.205	4.530	0.890	0.129
	CO	944.77	**0.204**	3.217	1.077	0.125
Case 4	HHO [11]	966.12	0.296	3.490	-	-
	PSO [10]	968.08	0.207	3.278	0.800	0.141
	DA [8]	967.89	0.207	3.198	-	-
	TLBO[12]	967.71	0.207	3.110	0.882	-
	SMA [13]	964.57	0.221	2.993	1.467	0.122
	CO	965.10	0.207	**2.956**	1.773	0.117
Case 5	SSO [10]	830.33	0.442	10.260	1.540	0.131
	PSO [10]	830.37	0.443	10.410	1.610	0.130
	SMA [13]	868.05	0.256	6.209	0.109	0.137
	CO	**815.10**	0.357	9.844	**0.105**	0.137
Case 6	PSO [10]	859.71	0.310	10.620	1.780	0.125
	SSO [10]	818.83	0.340	8.300	1.910	0.124
	CO	**810.82**	0.367	8.729	1.739	**0.115**

Main advantages of CO method

- The strategies of the hunting process create a good balance between the exploration and exploitation phases and prevent premature convergence or avoidance of local solutions in the different optimization problems.
- The control and state variables of the CO method have been verified and constrained by equality and inequality bounds, including safety constraints, within their acceptable range, as shown in Table 2.
- The comparison report presented in Tables 3, confirms the CO algorithm's ability to reach the best possible solutions through its smooth convergence curves, as illustrated in Fig. 5.

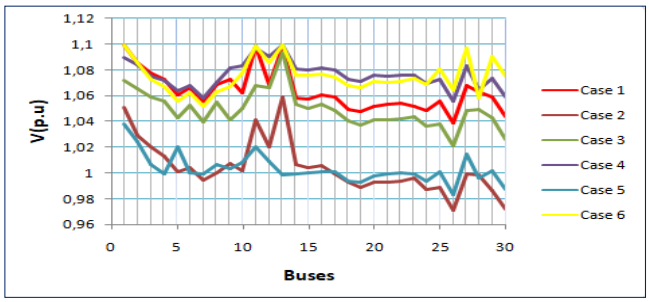


Figure 6. Voltage profile values of the IEEE30-bus test system

The voltage profile of six OPF optimization cases in the 30-bus system is presented in Figure 6. The voltage amplitudes for the load buses are within permissible ranges.

CONCLUSION

This paper proposes a new nature-inspired optimization algorithm, Cheetah Optimizer (CO), to solve the OPF problem, considering different cases of OPF objective function. The performance of the CO algorithm is verified via the IEEE30-bus test system. The simulation results under the MATLAB environment prove the robustness and effectiveness of the proposed CO method in solving the OPF problem more than other well-known meta-heuristic techniques mentioned in the recent literature. It can be clearly stated that the new CO method reduces in six cases the objective function more efficiently than the other methods used in the comparison.

ABBREVIATION AND ACRONYMS

P_{G1}	Generated active power of slack bus (MW)
P_{Di}	Active power of load demand at bus i (MW)
Q_{Di}	Reactive power of load demand at bus i (MVar)
P_i	Active power injection at bus (MW)
Q_{Gi}	Reactive power output of generator i (MVar)
P_{Gi}	Active power output of generator i (MW)
Q_{Ci}	Injected reactive power of shunt VAR compensator i
Q_i	Reactive power injection at bus i (MVar)
V_{Li}	Voltage magnitude of load bus i (kV)
S_{li}	Apparent power flow in transmission line i (kVA)
V_{Gi}	Voltage magnitude of generator connected to bus i
T_i	Regulating of transformer i
N_G	Number of generator buses (PV buses)
N_C	Number of shunt compensator
n_l	Number of the transmission lines
N_T	Number of transformer
r,z	Number of equality and inequality constraints.
N_B	Number of buses
V_i, V_j	Voltage magnitudes at node i and node j, respectively.
N_T	Number of regulating transformers
N_{PQ}	Number of load buses
Max	Denotes the maximum value
Min	Denotes minimum value
$f(x,u)$	Objective function to be minimized
$g_j(x,u)$	Equality constraints
$h_j(x,u)$	Inequality constraints
B_{ij}	Susceptance of transmission line between buses i and j (imaginary part of admittance)
G_{ij} / G_b	Conductance of transmission line between buses i and j (real part of admittance)
δ_{ij}	Difference angle between voltage angles and δ_j of buses i and j, respectively (rad).
a_i, b_i, c_i	Cost coefficients of i-th power plant respectively ($/hr),
d_i, e_i	($/MW.hr) and ($/MW².hr), ($/hr) and (rad/ MW)
α_i, β_i,	Emission coefficients of i-th power plant respectively
λ_i,θ_i, ξ_i	(ton/h), (ton/MW.hr) , (ton/MW².hr), (ton/h) and (rad/MW)
Y_1	Admittance sub-matrix (vector of injected currents and load bus voltages).
Y_2	Admittance sub-matrix (vector of injected load bus currents and PV bus voltages).
D	Dimension of the optimization problem
t	Actual hunting time
T	Maximum period of hunting time.
X	Current position of the prey in arrangement j
$\acute{r}^1_{i,j}$	Random number used for each cheetah during different hunting periods
$\alpha^t_{i,j}$	Step length of cheetah i in layout j
$\check{r}_{i,j}$	Random number used in the rotation factors of cheetah i in arrangement j
H	Random value chosen for one of the two strategies (search or attack).
$\beta^t_{i,j}$	Random number used in the interaction factors of cheetah i in arrangement j
$X^t_{i,j}$	Present positions of cheetah i in arrangement j
$X^{t+1}_{i,j}$	Next positions of cheetah i in arrangement j
n	Number of cheetahs i in the population(i =1.2…n)

REFERENCES

[1] A. Salhi, D. Naimi, and T. Bouktir, "Optimal power flow resolution using artificial bee colony algorithm based grenade explosion method," Journal of Electrical Systems, vol. 12, pp. 734-756, 2016.

[2] H. Ouafa, S. Linda, and B. Tarek, "Multi-objective optimal power flow considering the fuel cost, emission, voltage deviation and power losses using Multi-Objective Dragonfly algorithm," in Proceedings of the International Conference on Recent Advances in Electrical Systems, Hammamet, Tunusia, 2017, pp. 22-24.

[3] A. Salhi, D. Naimi, and T. Bouktir, "Fuzzy multi-objective optimal power flow using genetic algorithms applied to algerian electrical network," Advances in Electrical and Electronic Engineering, vol. 11, pp. 443-454, 2013.

[4] J. Carpentier, "Optimal power flows: uses, methods and developments," IFAC Proceedings Volumes, vol. 18, pp. 11-21, 1985.

[5] H. W. Dommel and W. F. Tinney, "Optimal power flow solutions," IEEE Transactions on power apparatus and systems, pp. 1866-1876, 1968.

[6] J. A. Momoh, R. Adapa, and M. El-Hawary, "A review of selected optimal power flow literature to 1993. I. Nonlinear and quadratic programming approaches," IEEE transactions on power systems, vol. 14, pp. 96-104, 1999.

[7] J. A. Momoh, M. El-Hawary, and R. Adapa, "A review of selected optimal power flow literature to 1993. II. Newton, linear programming and interior point methods," IEEE transactions on power systems, vol. 14, pp. 105-111, 1999.

[8] S. Khunkitti, A. Siritaratiwat, S. Premrudeepreechacharn, R. Chatthaworn, and N. R. Watson, "A hybrid DA-PSO optimization algorithm for multiobjective optimal power flow problems," Energies, vol. 11, p. 2270, 2018.

[9] A. Alhejji, M. E. Hussein, S. Kamel, and S. Alyami, "Optimal power flow solution with an embedded center-node unified power flow controller using an adaptive grasshopper optimization algorithm," IEEE Access, vol. 8, pp. 119020-119037, 2020.

[10] R. A. El Sehiemy, F. Selim, B. Bentouati, and M. Abido, "A novel multi-objective hybrid particle swarm and salp optimization algorithm for technical-economical-environmental operation in power systems," Energy, vol. 193, p. 116817, 2020.

[11] M. Z. Islam, N. I. A. Wahab, V. Veerasamy, H. Hizam, N. F. Mailah, J. M. Guerrero, and M. N. Mohd Nasir, "A Harris Hawks optimization based single-and multi-objective optimal power flow considering environmental emission," Sustainability, vol. 12, p. 5248, 2020.

[12] A. Alanazi, M. Alanazi, Z. A. Memon, and A. Mosavi, "Determining Optimal Power Flow Solutions Using New Adaptive Gaussian TLBO Method," Applied Sciences, vol. 12, p. 7959, 2022.

[13] M. Al-Kaabi, V. Dumbrava, and M. Eremia, "A slime mould algorithm programming for solving single and multi-objective optimal power flow problems with pareto front approach: A case study of the iraqi super grid high voltage," Energies, vol. 15, p. 7473, 2022.

[14] M. A. Akbari, M. Zare, R. Azizipanah-Abarghooee, S. Mirjalili, and M. Deriche, "The cheetah optimizer: A nature-inspired metaheuristic algorithm for large-scale optimization problems," Scientific reports, vol. 12, p. 10953, 2022.

[15] R. Christie, "Power Systems Test Case Archive: 30 Bus Power Flow Test Case," ed, 1993.

Multi-Objective Optimal Power Flow Solution Using Bonobo Optimizer Algorithm

Imadeddine Benhabsa [1], Ramzi Kouadri [2], Linda Slimani [3]

[1] *Department of Electrical Engineering, University of Ferhat Abbas Setif-1 Setif, Algeria.*
benhabsa.imadeddine@univ-setif.dz

[2] *Department of Electrical Engineering, University of Ferhat Abbas Setif-1 Setif, Algeria.*
ramzikouadri@univ-setif.dz

[3] *Department of Electrical Engineering, University of Ferhat Abbas Setif-1 Setif, Algeria.*
slimaniblinda@gmail.com

***Abstract*— This paper presents a new metaheuristic algorithm used to solve the optimal power flow (OPF) problem, called Bonobo optimizer (BO). The proposed algorithm is evaluated and tested on the standard IEEE 30-bus system to solve single – and multi-objective OPF problems. The selected objectives to be improved are fuel cost, active power loss and voltage deviation. The results obtained are compared with another method called jellyfish (JS) and other methods in the literature are presented to establish the validity and efficiency of the proposed algorithm. The results of this study demonstrate the superior performance of the BO technique to solve the OPF problem in comparison to these recent metaheuristic methods.**

***Keywords*: Optimal power flow, optimization, metaheuristic algorithm, Bonobo optimizer (BO), jellyfish (JS).**

I. INTRODUCTION

OPF is the primary tool for providing high-quality electric power at the lowest cost to achieve secure, efficient, and economical operation of the power grid [1], [2]. It was first proposed in the early 1960s by French scholar Carpentier[2]. Its main aim is to optimize a specified objective function while satisfying a set of equality and inequality constraints[3] among which the production limits of the generating stations, transmission capacities of power lines, Shunt VAR compensator limits of Transformer tap settings and other boundaries. Recently, a multi-objective OPF (MOOPF) was developed to address multiple objective functions, namely the fuel cost, emissions, voltage deviation and active power loss, In essence, the MOOPF problem is a minimum optimization with multiple contradictory objectives and strict [4],[5].

The OPF problem has been extensively studied in the past decades, and many optimization methods have been utilized to solve this problem. In this context, several mathematical optimization techniques have been adopted to find the solution to the OPF problem. These techniques are based on conventional and advanced intelligence optimization methods. Among the most common and widely used traditional optimization techniques are: gradient-based methods, Newton-based methods, Linear programming (LP), quadratic programming (QP), and interior point (IP) [6]. The last method is the most effective, it gives very good performance in terms of convergence speed for large-scale problems. The disadvantage of conventional methods is the lack of flexibility to integrate various constraints specific [7]. According to the latest research, advanced artificial intelligence optimization methods have advantages over conventional methods to solve the OPF problem.

Research result in recent years, which is based on advanced intelligence optimization methods we found have advantages compared to traditional methods of solving OPF problem [4]. With the significant development of computers in the modern era in terms of speed, improved characteristics and performance[8], we find that many researchers have used metaheuristic algorithms to solve the OPF problem. Generally, metaheuristics algorithms are inspired by physics (simulated recruitment), biology (evolutionary algorithms) or even ethology (colonies of ants, special tests) [7], where it was tested on IEEE 30-bus systems e.g. In [6] a black-hole-based optimization approach was proposed to solve the optimal power flow problem in a power system, the AMTPG-Jaya algorithm [9], Honey Badger Algorithm [10], backtracking search optimization algorithm[11]. equilibrium optimization algorithm[3], the Salp swarm algorithm [12], and the Beetle Swarm Method [13]. Hybridization is a trend observed in many works carried out on metaheuristics over the last ten years e.g. in [7] the combined optimization exploitation based on BBO biogeography to the exploration of differential evolution DE was proposed to solve the optimal power flow problem.

In this paper, the BO algorithm has been used to solve OPF problems. The proposed algorithm is evaluated on the standard IEEE 30-bus system, to minimize single and multi-objective functions based on fuel cost, active power loss and voltage deviation. Based on the quality of the solutions, a comparison of

the proposed algorithm with the jellyfish algorithm and other methods in the literature has been presented in this study.

The main contributions of this work can be summarized below:

- Used the new algorithm BO to solve the OPF problem.
- Comparison of the BO algorithm with a modern algorithm JS for three cases studied based on single objective and multi-objective functions.

II. FORMULATION OF THE OPTIMAL POWER FLOW

A. Problem formulation

The main goal of OPF is to optimize selected objective functions while satisfying both equality and inequality constraints of the electrical network. The mathematical expression can be represented as shown in Eq.(1) and Eq.(2) [14].

$$Minimize \quad F(x,u) \tag{1}$$

$$Subject\,to \begin{cases} g(x,u)=0 \\ h(x,u)\le 0 \end{cases} \tag{2}$$

where $F(x,u)$ is an objective function to be optimized, $g(x,u)$ is the set of equality constraints, $h(x,u)$ is the set of inequality constraints, *x* and *u* are the vector of control (independent) and state (dependent) variables. These vectors can be represented in Eq.(3) and Eq.(4), respectively:

$$x=\left[P_{G_2}...P_{G_{NG}},V_{G_1}...V_{G_{NG}},Q_{c_1}...Q_{c_{NC}},T_1...T_{NT}\right] \tag{3}$$

where NG, NT and NC are the number of generators, the number of regulating transformers and the number of VAR compensators, respectively. P_{Gi} is the i-th generator active power at the PV buses excluding the slack bus,V_G is the i-th generator voltage magnitude at PV buses, T is tap setting of transformer and Q_c is injected reactive power of *i-th* shunt VAR compensation.

$$u=\left[P_{G_1},V_{L_1}...V_{L_{NL}},Q_{G_1}...Q_{G_{NC}},S_l...S_{l_{nl}}\right] \tag{4}$$

where, *NL* and *nl* are the numbers of load buses and transmission lines, respectively. P_{G_1} is the active power output at slack bus V_{L_i} voltage magnitude of *i-th* load buses, Q_{Gi} is the reactive power generation of all generator units, indices S_l is the apparent power flow.

B. Objective function

The objective functions of the OPF problem are composed generally of:

- ***Total fuel cost (FC)***

The equation represents the objective function of the total production fuel cost [15].

$$F_{Cost}(x,u)=\left(\sum_{i=1}^{NG}\left(a_i+b_iP_{G_i}+c_iP_{G_i}^2\right)\right) \quad \$/h \tag{5}$$

where a_i, b_i and c_i are the cost coefficients of *i-th* thermal generators, *NG* is the number of generators and represents the active power output of the generator.

- ***Active power loss (Ploss)***

Active power transmission lines play a very important role in transmitting energy to the loads. Transmission of energy causes loss of energy. Eq. (6) represents the objective function of the active power loss [15].

$$P_{loss}(x,u)=\sum_{i=1}^{NB}P_{G_i}-\sum_{i=1}^{NB}P_{D_i} \quad MW \tag{6}$$

Where P_{D_i} is active power load demand and NB denotes the total number of buses.

- ***Voltage Deviation (DV)***

Voltage deviation is a measure of voltage quality in the network. The voltage deviation indicator is formulated as the cumulative deviation of voltages of all PQ buses in the network from the nominal value of 1.0 p.u. This objective function can be formulated as shown in Eq. (7) [15].

$$VD(x,u)=\sum_{i=1}^{NL}\left|V_i-1.0\right| \quad p.u \tag{7}$$

Where NL is the number of load buses.

C. Equality constraint

Equation (8) and (9) represents equality constraints in OPF problem [14] :

$$P_{G_i}-P_{D_i}=V_i\sum_{i=1}^{NB}V_j\left[G_{ij}\cos\left(\delta_i-\delta_j\right)+B_{ij}\sin\left(\delta_i-\delta_j\right)\right]=0 \quad \forall\in NB \tag{8}$$

$$Q_{G_i}-Q_{D_i}=V_i\sum_{i=1}^{NB}V_j\left[G_{ij}\sin\left(\delta_i-\delta_j\right)-B_{ij}\cos\left(\delta_i-\delta_j\right)\right]=0 \quad \forall\in NB \tag{9}$$

where $P_{D_i}$and Q_{D_i} are active power and reactive power demand at i -th bus, V_i is voltage magnitude at i-th bus, NB is a number of buses, G_{ij} and B_{ij} are transfer conductance and transfer susceptance between *i* and *j*, respectively.

D. Inequality constraint

These inequality constraints can be classified as follows [14]

- Generator constraints:

$$\begin{aligned} V_{G_i}^{min} &\le V_{G_i} \le V_{G_i}^{max}...\forall i\in NG \\ P_{G_i}^{min} &\le P_{G_i} \le P_{G_i}^{max}...\forall i\in NG \\ Q_{G_i}^{min} &\le Q_{G_i} \le Q_{G_i}^{max}...\forall i\in NG \end{aligned} \tag{10}$$

- Shunt VAR compensator constraints:

$$Q_{c_i}^{min} \le Q_{c_i} \le Q_{c_i}^{max}...\forall i\in NC \tag{11}$$

- Transformer tap settings constraints:

$$T_{NTi}^{min} \le T_{NTi} \le T_{NTi}^{max} ... \forall i \in NT \quad (12)$$

- Voltage magnitude of load buses:

$$V_{L_i}^{min} \le V_{L_i} \le V_{L_i}^{max} ... \forall i \in NL \quad (13)$$

- Apparent power flow in transmission lines:

$$|S_{li}| \le S_{li}^{\max} ... \forall i \in nl \quad (14)$$

To maintain the state variables, under constraints (inequalities), we can add the penalty function which is found at [13]

III. BONOBO OPTIMIZER ALGORITHM

Amit Kumar Das and Dilip Kumar Pratihar proposed a new algorithm in 2022, that first simulates the social behavior and reproductive strategy of bonobos, called bonobo optimizer (BO) [16]. The best solution is the alpha bonobo (α_{bonobo}), he is considered the most rank in his super hierarchy in a class of bonobos. The mathematical model for the BO technique is discussed in detail in the following section:

A. Initialization

We can express the non-user-defined parameters of BO as follows:

$$ppc = 0, npc = 0, P_{xgm} = P_{xgm_initial}, tsgs_{factor} = tsgs_{factor_initial}$$
$$P_p = 0.5, P_d = 0.5$$

Where, ppc is positive phase count, P_{xgm} and $tsgs_{factor}$ are the probability of extra group mating and temporary sub-group size factor, respectively. P_p and P_d are probability of phase and directional probability, finally npc represent negative phase count, N is the total population size. In the first phase PP (positive phase), which expresses calm and good living conditions i.e. access in the best-obtained solution, is alpha bonobo, And contrary to the aforementioned circumstances the phase called negative phase NP [16].

B. Selection of a bonobo using fission-fusion social strategy

Depending upon the phase (PP or NP), different updating mechanisms are used, At first [16]

$$tsgs_{\max} = \max imum\left(2, \left(tsgs_{factor} \times N\right)\right) \quad (15)$$

Where $\left(tsgs_{factor} \times N\right)$ is not obtained as an integer value, then the next integer is to be taken.

We can see that the minimum value of $tsgs_{factor}$ could be equal to 2.

C. Creation of new bonobo using different mating strategies

- *Promiscuous and restrictive mating strategies*

If a random number (r) in the range [0.0, 1.0]≤Pp , a new bonobo is generated by either promiscuous mating or restrictive mating depending on [16]:

$$\begin{aligned} &new_bonobo = bonobo_j^i + \\ &r_1 \times scab \times \left(\alpha_{bonobo}^j - bonobo_j^i\right) + \\ &(1-r) \times scsb \times flag \\ &\times \left(bonobo_j^i - bonobo_j^p\right) \end{aligned} \quad (16)$$

Where α_{bonobo}^j and new_bonobo_j are $j^{th} - \text{var}iables$ of the alpha bonobo and offspring, respectively. j varies from 1 to L (where L is the total number of variables of a given optimization problem). $bonobo_j^i$ And $bonobo_j^p$ are the $j^{th} - \text{var}iables$ of the i^{th} ,respectively. r_1 is a random number created in the range of [0.0 1.0], scab and scsb are the other two parameters denoted as sharing coefficient for α_{bonobo} and $P^{th} - bonobo$, respectively. The flag only gets a value of either 1 or -1.

- *Consortship and extra-group mating strategies*

$$\beta_1 = e^{\left(r_4^2 + r_4 - 2/r_4\right)} \quad (17)$$

$$\beta_2 = e^{\left(-r_4^2 + 2 \times r_4 - 2/r_4\right)} \quad (18)$$

$$new_bonobo_j = bonobo_j^i + \beta_1 \times \left(Var_\max_j - bonobo_j^i\right), \quad if\left(\alpha_{bonobo}^j \ge bonobo_j^i, r_3 \le P_L\right) \quad (19)$$

$$new_bonobo_j = bonobo_j^i - \beta_2 \times \left(-Var_\min_j + bonobo_j^i\right), \quad if\left(\alpha_{bonobo}^j \ge bonobo_j^i, r_3 \succ P_L\right) \quad (20)$$

$$new_bonobo_j = bonobo_j^i - \beta_1 \times \left(-Var_\min_j + bonobo_j^i\right), \quad if\left(\alpha_{bonobo}^j \prec bonobo_j^i, r_3 \le P_L\right) \quad (21)$$

$$new_bonobo_j = bonobo_j^i + \beta_2 \times \left(Var_\max_j - bonobo_j^i\right), \quad if\left(\alpha_{bonobo}^j \prec bonobo_j^i, r_3 \succ P_L\right) \quad (22)$$

Where, β_1 *and* β_2 are two intermediate measured values utilized to determine the value new_bonobo_j . r_4 is a random number generated [0.0,1.0] and $r_4 \neq 0$.

$Var_\min_j$ *and* $Var_\max_j$ are the lower and upper boundary values corresponding to the $j^{th} - \text{var}iables$, respectively.

If $r_2 > P_{xgm}$, a new bonobo is generated by applying the consortship mating strategy and it is given as follows [16]:

$$new_bonobo_j = \begin{cases} bonobo_j^i + flag \times e^{(-r_5)} \times \left(bonobo_j^i - bonobo_j^p\right), \\ if\left(flag = 1 \| r_6 \le P_L\right), bonobo_j^p, \\ otherwise \end{cases} \quad (23)$$

Figure 1. The pseudo-code of the proposed BO algorithm

Provide user defined parameters values and initialize other parameters
Initialize of population size N
Evaluate the best objective values and identify α_{bonobo} *among N*
$iter = 1$
While stopping criterion is not met
From $Eq(1)$, *obtain* $tsgs_{\max}$
For $i = 1$ *to N*
Select tsgs
Choose using fission – fusion strategy
Determine flag
if $r \le p_p$
  for $j = 1$ *to L*
    create new $_bonobo_j, using\ Eq(2)$
    Apply variable boundary limiting condition
  end
else
  for $j = 1$ *to L*
    if $r_2 \le P_{xgm}$
      if $\alpha^j_{bonobo} \ge bonobo^i_j$
        if $r_3 \le p_L$
          create new $_bonobo_j, using\ Eq(3)\ and\ (5)$
        else
          create new $_bonobo_j, using\ Eq(4)\ and\ (6)$
        end
      else
        if $r_3 \le p_L$
          create new $_bonobo_j, using\ Eq(3)\ and\ (7)$
        else
          create new $_bonobo_j, using\ Eq(4)\ and\ (8)$
        end
      end
    else
      create new $_bonobo_j, using\ Eq(9)$
    end
    Apply variable boundary limiting condition
  end
end
Apply acceptance criteria for new_{bonobo} *and identify the alpha bonobo*
end
update the parameters
$iter = iter + 1$
end
display α_{bonobo}

IV. RESULTS AND DISCUSSION

The proposed BO algorithm was applied to the IEEE 30 bus test system, and different cases were studied to evaluate the performance and efficiency of the algorithm. The main characteristics of the IEEE 30-bus test system are given in TABLE I**.** Whereas the limits of control variables are shown in Table II. The fuel cost coefficients used in this paper are given in [3].

TABLE I. THE MAIN CHARACTERISTICS OF THE STUDIED SYSTEM

IEEE 30		
Characteristics	**Value**	**details**
Buses	30	[17]
Branches	41	[17]
Generators	6	Buses:1,2,5,8,11 and 13
Load voltage limits	24	[0.95, 1.05]
Shunt compensators	9	Buses: 10, 12, 15, 17, 20, 21, 23, 24 and 29.
Tap setting	4	Branches:11,12,15and 36
Control variable	24	-

I used it for this work MATLAB software, and simulations were carried out on a computer with an Intel Core i5 CPU @ 1.6 GHz, and 8 GB of RAM, under the Windows 10 64-bit operating system. The load flow is obtained using MATPOWER software. The population size and the iteration number of the BO and JS algorithms are 50 and 500, respectively. The results are obtained after 20 times run for better validation.

In this study, three different cases have been considered, including both single-objective and multi-objective functions, as detailed below:

1) ***Case 1****: Minimization of fuel cost (single objective)*

In the first case, the single objective based on the fuel cost is selected to be optimized:

$$F_1 = F_{\cos t}(x,u) + penality \tag{24}$$

2) ***Case 2****: Minimization of fuel cost and active power loss*

Both the fuel cost and the active power loss are optimized simultaneously in the second case. This objective function is expressed as follows:

$$F_2 = F_{\cos t}(x,u) + \left(\lambda_{loss} \times P_{loss}(x,u)\right) + penality \tag{25}$$

where λ_{loss} is a weight factor selected to balance between the two fitness functions. we take $\lambda_{loss} = 40$ [1].

3) ***Case 3***: *Minimization of fuel cost and deviation voltage*

In the last case, both the fuel cost and the voltage deviation are optimized simultaneously as expressed in the following equation:

$$F_3 = F_{\text{Cost}} + \left(\lambda_{DV} \times DV(x,u)\right) + penality \tag{26}$$

where $\lambda_{VD} = 100$ [1]

The optimal control variables obtained by BO are displayed in TABLE II. From this table, it can be seen that all optimal values of control variables are within their acceptable limits.

TABLE II. THE BEST SOLUTION FOR THREE CASES

Control variables	Min	Max	Case1	Case2	Case3
$P_1(MW)$	50	200	*177.1003*	*102.5126*	*176.3554*
$P_2(MW)$	20	80	*48.7168*	*55.6165*	*48.7706*
$P_5(MW)$	15	50	*21.3778*	*38.1210*	21.6199
$P_8(MW)$	10	30	*21.2857*	*35.0000*	22.3141
$P_{11}(MW)$	10	30	*11.9185*	*30.0000*	12.1620
$P_{13}(MW)$	12	40	*12.0000*	*26.6751*	12.0000
$V_1(p.u)$	0.95	1.1	*1.0834*	*1.0682*	1.0412
$V_2(p.u)$	0.95	1.1	*1.0644*	*1.0575*	1.0235
$V_5(p.u)$	0.95	1.1	*1.0333*	*1.0341*	1.0129
$V_8(p.u)$	0.95	1.1	*1.0380*	*1.0424*	1.0047
$V_{11}(p.u)$	0.95	1.1	*1.0839*	*1.0629*	1.0556
$V_{13}(p.u)$	0.95	1.1	*1.0452*	*1.0557*	0.9875
$T_{11}(p.u)$	0.9	1.1	*1.0749*	*1.0669*	1.0780
$T_{12}(p.u)$	0.9	1.1	*0.9000*	*0.9002*	0.9000
$T_{15}(p.u)$	0.9	1.1	*0.9638*	*0.9866*	0.9379
$T_{36}(p.u)$	0.9	1.1	*0.9732*	*0.9732*	0.9706
$Q_{c10}(MVAR)$	0	5	*2.1432*	*4.9139*	5.0000
$Q_{c12}(MVAR)$	0	5	*0.0000*	*0.0623*	0.0011
$Q_{c15}(MVAR)$	0	5	*4.1826*	*3.8960*	5.0000
$Q_{c17}(MVAR)$	0	5	*5.0000*	*5.0000*	0.0000
$Q_{c20}(MVAR)$	0	5	*3.9357*	*3.8758*	5.0000
$Q_{c21}(MVAR)$	0	5	*5.0000*	*5.0000*	4.9995
$Q_{c23}(MVAR)$	0	5	*2.8812*	*2.8604*	4.9959
$Q_{c24}(MVAR)$	0	5	*5.0000*	*5.0000*	5.0000
$Q_{c29}(MVAR)$	0	5	*2.3478*	*2.2770*	2.6316
Fuel cost ($/h)	–	–	*800.3925*	*859.0717*	803.5853
Power loss(MW)	–	–	*8.9991*	*4.5252*	9.8221
Deviation voltage (p.u)	–	–	*0.9072*	*0.9217*	0.0952

In the first case, the fuel cost is 800.3925 $/h. In the second case, the fuel cost and active power loss are 859.0717 $/h and 4.5252 MW, respectively. In the last case, the fuel cost value is 803.5853$/h and the value of voltage deviation is 0.0952 p.u. From these values, it can be seen that the total cost is higher in the 2nd case, also that we have a greater loss of active power in the 1st and 3rd cases compared to the 2nd case. Moreover, it can be seen in the last case that the value of the voltage deviation is reduced compared to that obtained in cases 1 and 2.

Table III summarizes the comparative results of BO with JS and other algorithms in the literature for three cases studied. The results in the first case indicate that the fuel cost applying BO led to 800.3925 $/h which is less compared to the JS algorithm. In case 2, the combination of fuel cost and the active power losses applying BO led to 859.0717 $/h and 4.5252 MW, respectively, which is less for fuel cost and superior for active power loss compared to the JS algorithm. In the last case, the fuel cost and voltage deviation obtained by the proposed algorithm are 803.5853 $/h and 0.0952 p.u, which is less than the JS algorithm for both values. In addition, it can be seen that the JS gives the best results for active power losses compared to the BO in case 2, whereas the BO is still more effective for OPF solution compared to JS and other existing techniques mentioned in the literature in Table III.

TABLE III. COMPARISON OF THE RESULTS FOR CASES 1-3 IN THE IEEE 30 BUS SYSTEM

Case	Algorithm	fitness	FC($/h)	Ploss(MW)	VD(p.u)
Case1	BO	800.3925	**800.3925**	8.9991	0.9072
	JS	800.4128	800.4128	8.9968	0.9086
	EO[3]	800.4235	800.4235	8.9871	0.9245
	MPA[3]	800.4273	800.4273	9.0000	0.9103
	MSA [18]	800.5099	800.5099	9.0345	0.9036
	TLBO[9]	800.4604	800.4604	9.0723	-
	SP-DE[19]	800.4293	800.4293	9.0583	0.9101
Case2	BO	1040.0825	**859.0717**	**4.5252**	0.9217
	JS	1040.1793	859.5742	4.5151	0.9112
	EO[3]	1040.168	859.5815	4.5139	0.9321
	MPA[3]	1040.222	859.0757	4.5287	0.9251
	MSA [18]	1040.808	859.1915	4.5404	0.9285
Case 3	BO	**813.1044**	**803.5853**	9.8221	**0.0952**
	JS	814.2645	804.4542	9.8476	0.1081
	BSOA[13]	813.9984	803.1457	9.8493	0.1045
	EO [3]	813.1898	803.5848	9.8237	0.0960
	AEO[3]	813.8005	804.0766	9.9557	0.0972
	BSA[11]	-	803.4294	9.3751	0.1147
	MSA[1]	814.1545	803.3125	9.7206	0.1084

As shown in Fig 2, the optimal solutions are obtained without any violation of the bus voltage amplitude limit.

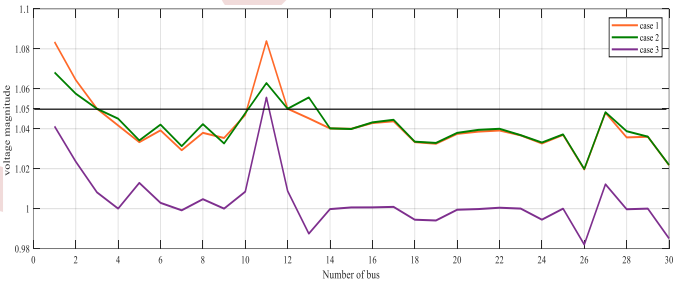


Figure 2. PV and PQ buses voltage profiles using BO algorithm *(cases 1,2 and 3)*

Fig.3, Fig.4 and Fig.5 show the convergence speed of the two algorithms for the three cases, the BO algorithm outperforms the JS algorithm in terms of speed and results for the three cases. Therefore, the result obtained by the BO algorithm is more robust compared to the JS to obtain the best solution to solve the OPF problem.

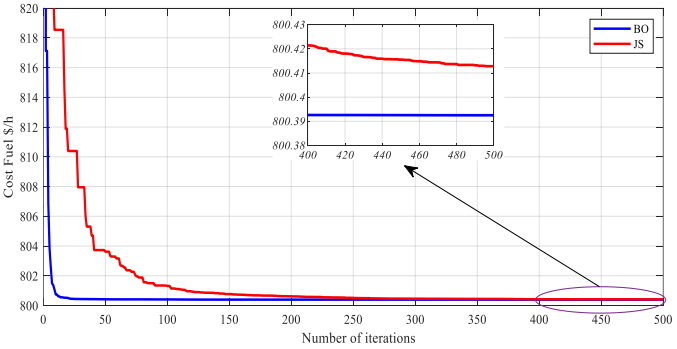


Figure 3. Convergence characteristics of BO and JS for the IEEE 30-bus system: Case 1

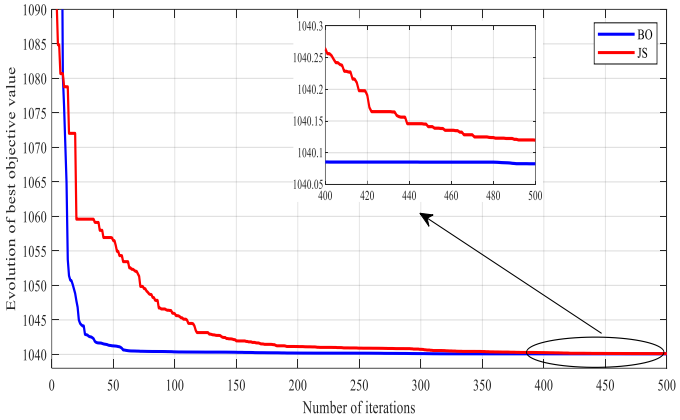


Figure 4. Convergence characteristics of BO and JS for the IEEE 30-bus system: Case 2

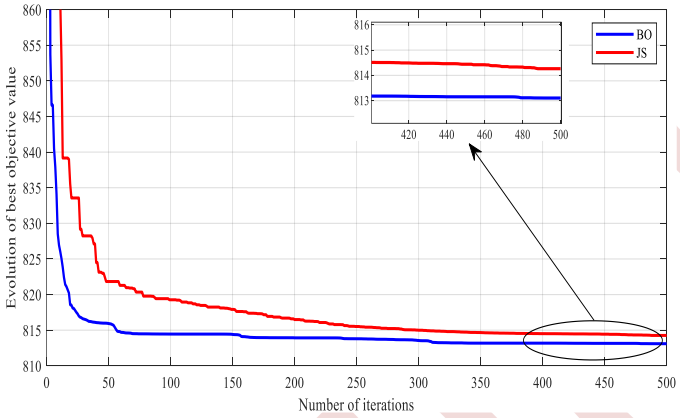


Figure 5. Convergence characteristics of BO and JS for the IEEE 30-bus system: Case 3

V. CONCLUSION

In this paper, the OPF problem has been solved using a new metaheuristic optimization technique, called bonobo optimizer (BO) algorithm. The efficiency and performance of the proposed algorithm have been tested on the standard IEEE 30-bus test system with different cases based on both single and multi-objective functions. These functions include the fuel cost, active power loss as well and voltage deviation. According to the results shown above, we find that the proposed algorithm significantly outperformed JS and other existing optimization techniques in the literature to solve the OPF problem considering single and multi-objective functions for the IEEE 30-bus system.

REFERENCES

[1] A.-A. A. Mohamed, Y. S. Mohamed, A. A. M. El-Gaafary, and A. M. Hemeida, "Optimal power flow using moth swarm algorithm," *Electr. Power Syst. Res.*, vol. 142, pp. 190–206, Jan. 2017, doi: 10.1016/j.epsr.2016.09.025.

[2] G. Chen, X. Yi, Z. Zhang, and H. Lei, "Solving the Multi-Objective Optimal Power Flow Problem Using the Multi-Objective Firefly Algorithm with a Constraints-Prior Pareto-Domination Approach," *Energies*, vol. 11, no. 12, p. 3438, Dec. 2018, doi: 10.3390/en11123438.

[3] M. Amroune, "Wind integrated optimal power flow considering power losses, voltage deviation, and emission using an equilibrium optimization algorithm," *Energy Ecol. Environ.*, vol. 7, no. 4, pp. 369–392, Aug. 2022, doi: 10.1007/s40974-022-00249-2.

[4] T. H. B. Huy, D. Kim, and D. N. Vo, "Multiobjective Optimal Power Flow Using Multiobjective Search Group Algorithm," *IEEE Access*, vol. 10, pp. 77837–77856, 2022, doi: 10.1109/ACCESS.2022.3193371.

[5] G. Chen, J. Qian, Z. Zhang, and Z. Sun, "Multi-Objective Optimal Power Flow Based on Hybrid Firefly-Bat Algorithm and Constraints- Prior Object-Fuzzy Sorting Strategy," *IEEE Access*, vol. 7, pp. 139726–139745, 2019, doi: 10.1109/ACCESS.2019.2943480.

[6] H. R. E. H. Bouchekara, "Optimal power flow using black-hole-based optimization approach," *Appl. Soft Comput.*, vol. 24, pp. 879–888, Nov. 2014, doi: 10.1016/j.asoc.2014.08.056.

[7] O. Herbadji, L. Slimani, and T. Bouktir, "Optimal Power Flow With Four Conflicting Objective Functions Using Multiobjective Ant Lion Algorithm: A Case Study of the Algerian Electrical Network," *Iran. J. Electr. Electron. Eng.*, vol. 15, no. 1, Mar. 2019, doi: 10.22068/IJEEE.15.1.94.

[8] H. R. E. H. Bouchekara, A. E. Chaib, and M. A. Abido, "Optimal power flow using GA with a new multi-parent crossover considering: prohibited zones, valve-point effect, multi-fuels and emission," *Electr. Eng.*, vol. 100, no. 1, pp. 151–165, Mar. 2018, doi: 10.1007/s00202-016-0488-9.

[9] W. Warid, "Optimal power flow using the AMTPG-Jaya algorithm," *Appl. Soft Comput.*, vol. 91, p. 106252, Jun. 2020, doi: 10.1016/j.asoc.2020.106252.

[10] "A Modified Honey Badger Algorithm for Solving Optimal Power Flow Optimization Problem," *Int. J. Intell. Eng. Syst.*, vol. 15, no. 4, Aug. 2022, doi: 10.22266/ijies2022.0831.14.

[11] A. E. Chaib, H. R. E. H. Bouchekara, R. Mehasni, and M. A. Abido, "Optimal power flow with emission and non-smooth cost functions using backtracking search optimization algorithm," *Int. J. Electr. Power Energy Syst.*, vol. 81, pp. 64–77, Oct. 2016, doi: 10.1016/j.ijepes.2016.02.004.

[12] M. H. Sulaiman and Z. Mustaffa, "An application of improved salp swarm algorithm for optimal power flow solution considering stochastic solar power generation," *E-Prime - Adv. Electr. Eng. Electron. Energy*, vol. 5, p. 100195, Sep. 2023, doi: 10.1016/j.prime.2023.100195.

[13] K. Sriram, S. P. Mangaiyarkarasi, S. Sakthivel, and L. Jebaraj, "An Extensive Study Using the Beetle Swarm Method to Optimize Single and Multiple Objectives of Various Optimal Power Flow Problems," *Int. Trans. Electr. Energy Syst.*, vol. 2023, pp. 1–33, Mar. 2023, doi: 10.1155/2023/5779700.

[14] H. Su, Q. Niu, and Z. Yang, "Optimal Power Flow Using Improved Cross-Entropy Method," *Energies*, vol. 16, no. 14, p. 5466, Jul. 2023, doi: 10.3390/en16145466.

[15] R. Kouadri, I. Musirin, L. Slimani, T. Bouktir, and Othman,M M, "Optimal Power Flow Control Variables using Slime Mould Algorithm for Generator Fuel Cost and Loss Minimization with Voltage Profile Enhancement Solution," *Int. J. Emerg. Trends Eng. Res.*, vol. 8, no. 1.1, pp. 36–44, Sep. 2020, doi: 10.30534/ijeter/2020/0681.12020.

[16] A. K. Das and D. K. Pratihar, "Bonobo optimizer (BO): an intelligent heuristic with self-adjusting parameters over continuous spaces and its applications to engineering problems," *Appl. Intell.*, vol. 52, no. 3, pp. 2942–2974, Feb. 2022, doi: 10.1007/s10489-021-02444-w.

[17] O. Alsac and B. Stott, "Optimal Load Flow with Steady-State Security," *IEEE Trans. Power Appar. Syst.*, vol. PAS-93, no. 3, pp. 745–751, May 1974, doi: 10.1109/TPAS.1974.293972.

[18] A.-A. A. Mohamed, Y. S. Mohamed, A. A. M. El-Gaafary, and A. M. Hemeida, "Optimal power flow using moth swarm algorithm," *Electr. Power Syst. Res.*, vol. 142, pp. 190–206, Jan. 2017, doi: 10.1016/j.epsr.2016.09.025.

[19] P. P. Biswas, P. N. Suganthan, and G. A. J. Amaratunga, "Optimal power flow solutions incorporating stochastic wind and solar power," *Energy Convers. Manag.*, vol. 148, pp. 1194–1207, Sep. 2017, doi: 10.1016/j.enconman.2017.06.071.

Application of New Metaheuristic Algorithm for Optimal Placement and Sizing of STATCOM Device

Ramzi Kouadri [1], Imad eddine Benhabsa [2], Oussama Souici [3], Souhil Mouassa [4]

[1,2,3] *Department of Electrical Engineering, University of Ferhat Abbas Setif-1, Setif, Algeria.*

[1] ramzikouadri@univ-setif.dz, [2] imadeddinebenhabsa@gmail.com, [3] Oussamasouici507@gmail.com

[4] *Department of Electrical Engineering, University of Akli Mohand Oulhadj, Bouira, Algeria.*

souhil.mouassa@univ-bouira.dz

***Abstract*— The main contribution of this work is the application of the new metaheuristic optimization algorithm called Self-adaptive Bonobo Optimizer (SaBO) to solve the optimal power flow (OPF) problem incorporating the static synchronous compensator (STATCOM) device. In this context, the objective function is to find the optimal placements and sizing of STATCOM in the power system based on the minimum value of the total generation fuel cost (TGFC). The proposed algorithm has been tested on the IEEE 30-bus and the IEEE 57-bus systems with different cases based on the number of STATCOMs. The results obtained by the proposed algorithm demonstrate a significant enhancement in the voltage profile through the optimal integration of the STATCOM devices. Moreover, this integration has led to a notable reduction in generation fuel cost and active power loss.**

***Keywords*: Metaheuristic optimization algorithm, Optimal power flow, Self-adaptive Bonobo Optimizer, static synchronous compensator.**

I. INTRODUCTION

Nowadays, the modern power network confronts numerous daily challenges. These challenges include ensuring a high-quality electricity supply, enhancing the operation of a transmission system, improving the voltage profile, as well as guaranteeing continuity of customer service. To achieve these objectives, one promising option is the incorporation of Flexible AC Transmission System (FACTS) devices in the power system. FACTS devices are based on power electronics, and capable of controlling the voltage, current, impedance and phase angle in order to regulate the most critical applications related to the power system network such as voltage stability improvement, increased transmission line capacity, improved power flow control, as well as enhanced renewable energy integration [1]. The classification of FACTS devices involves three primary types: series controllers, shunt controllers, and combined series-shunt controllers. Shunt FACTS controllers such as static synchronous compensators (STATCOM) can provide or absorb reactive current in power systems to improve voltage profile and increase power transfer capability [2].

As FACTS devices continue to gain traction in power systems, the implementation of Optimal Power Flow (OPF) becomes essential to ensure the economic integration of STATCOM devices and enhance the overall system performance. The OPF poses a significant challenge as a large-scale, nonlinear, and non-convex optimization problem with numerous constraints. Since its introduction by Carpentier in 1962 [3], the OPF has been extensively studied and is now regarded as a pivotal tool in the operation and planning of power systems. The OPF aims to determine optimal values for the system's control variables to minimize or maximize the desired objective function [4]. This process must be achieved while adhering to a set of physical and operational constraints, which include both equality and inequality constraints.

In the literature, numerous mathematical optimization methods have been proposed and applied to solve the OPF problem. These techniques can be categorized into conventional and advanced intelligence optimization methods. Ref [5] classifies intelligence optimization methods into several categories, including evolutionary methods, metaheuristic methods, artificial neural networks, fuzzy logic approaches, and combinations of these methods. Among the different techniques that are employed to solve OPF, we are interested in this study using the metaheuristic-based advanced intelligence optimization methods, which were introduced by Glover in 1986 [6]. Metaheuristic optimization methods have the advantage of rapid convergence to the optimal solution, finding one or many solutions to complicated optimization problems, as well as being applicable in small and large-scale systems.

In recent years, there has been a growing interest among researchers in exploring the OPF problem to determine where STATCOM devices should be placed in the power networks. Different metaheuristic methods have been employed within this context to address and solve this issue. For instance, the authors in [7] have applied the particle swarm optimization (PSO) and firefly algorithm (FA) to find the optimal sizing and placement of STATCOM in the IEEE 14-bus system. In this work, two single objective functions have been considered to minimize, which are the active power losses and voltage

deviations. In attempting the same problem, the particle swarm optimization (PSO) technique is suggested in [2] to identify the location of STATCOM based on the minimum active power losses, all while ensuring that the voltage remains within acceptable limits. Reference [8] used an improved Harmony Search Algorithm (IHAS) to minimize multi-objective OPF in order to locate the STATCOMs devices in the IEEE 30-bus power system. The numerical results demonstrate the superior performance of the proposed algorithm in comparison to the standard harmony search algorithm (HAS) when addressing this specific problem. TAO ZHANG et al. in [9] introduced an enhanced algorithm called the improved differential evolution harmony search (DEHS) to determine the optimal placement and sizing of multiple STATCOMs in the IEEE 30-bus power system. Furthermore, various interesting applications of diverse metaheuristic methods to determine the best placement of STATCOM devices include the Gravitational search algorithm (GSA) [10], Particles Swarm Optimization (PSO) [11], and Whale Optimization Algorithm (WOA) [12].

This paper aims to optimize the capacity and placement of the STATCOMs within the IEEE 30-bus and IEEE 57-bus power systems. In this context, a new flexible and efficient optimization algorithm called Self-adaptive Bonobo Optimizer (SaBO) has been proposed to address this issue with the objective function is to minimize the total generation cost.

This paper is organized as follows: Section 2 presents the structure and mathematical model of STATCOM followed by the formulation of the OPF problem incorporating STATCOMs in Section 3. The implementation of the proposed algorithm SaBO is explained in section 4. Section 5 presents the numerical results and explanations. Finally, section 6 presents the conclusion of this study.

II. STATCOM MODELLING

A. *The STATCOM structure*

The STATCOM is a power electronics device that is used to improve power factor stability and power quality in power networks by adjusting the reactive power in the lines [13]. The STATCOM is mainly composed of a voltage source converter (VSC) which employs high-speed thyristors like GTOs and IGBTs, a controller to control the (VSC) with reference inputs like voltage, active and reactive power, a coupling transformer, and finally an energy storage system which mainly composes of batteries, capacitors and inductances as seen in the following figure:

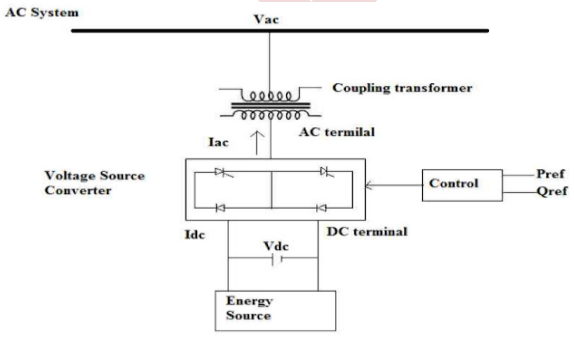


Figure 1. Circuit diagram of a STATCOM

B. *STATCOM mathematical model*

The mathematical model of the STATCOM can be derived from Fig. 2, which shows a single-line model with a synchronous voltage source representing the STATCOM voltage source which has maximum and minimum boundaries.

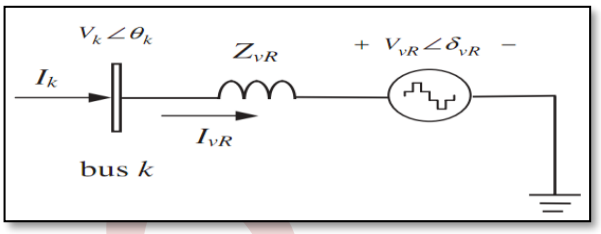


Figure 2. STATCOM model [14]

1) ***STATCOM power flow equation****:* From Fig. 2, we can assume the voltage source and the current absorbed by the STATCOM. Thus, the STATCOM power flow equation is given as follows:

$$E_{VR} = V_{VR}\left(\cos\left(\delta_{VR}\right) + j\sin\left(\delta_{VR}\right)\right) \quad (1)$$

$$I_{VR} = Y_{VR}\left(V_{VR} - V_K\right) \quad (2)$$

$$S_{VR} = E_{VR}I_{VR}^{*} = V_{VR}Y_{VR}^{*}\left(V_{VR}^{*} - V_{VR}^{*}\right) \quad (3)$$

where S_{VR} is the apparent power of STATCOM, $I_{VR\,is}$ the branch current and E_{VR} is the STATCOM AC voltage.

Using (1), (2) and (3) we can obtain the following power equations:

$$\begin{cases} P_{VR} = V_{VR}^2 G_{VR} + V_k V_{VR}\left[G_{VR}\cos\left(\delta_{VR} - \theta_k\right) + B_{VR}\sin\left(\delta_{VR} - \theta_k\right)\right] \\ Q_{VR} = -V_{VR}^2 B_{VR} + V_k V_{VR}\left[G_{VR}\sin\left(\delta_{VR} - \theta_k\right) - B_{VR}\cos\left(\delta_{VR} - \theta_k\right)\right] \end{cases} \quad (4)$$

$$\begin{cases} P_k = V_k^2 G_{VR} + V_k V_{VR}\left[G_{VR}\cos\left(\theta_k - \delta_{VR}\right) + B_{VR}\sin\left(\theta_k - \delta_{VR}\right)\right] \\ Q_k = -V_k^2 B_{VR} + V_k V_{VR}\left[G_{VR}\sin\left(\theta_k - \delta_{VR}\right) - B_{VR}\cos\left(\theta_k - \delta_{VR}\right)\right] \end{cases} \quad (5)$$

Where P_{VR}, Pk and $Q_{VR,}$ Q_k are the STATCOM active and reactive powers and the bus k active and reactive powers respectively.

2) ***Implementation of STATCOM into the Newton-Raphson PF****:* The original load flow Jacobian matrix dubbed as J of the NR power flow contains four essential elements the partial derivation of active power over the angle and the voltage and the partial derivation of reactive power over the angle and voltage of the bus k as shown in (6):

$$[J] = \begin{pmatrix} \frac{\partial P}{\partial \delta} & \cdots & \frac{\partial P}{\partial V} \\ \vdots & \ddots & \vdots \\ \frac{\partial Q}{\partial \delta} & \cdots & \frac{\partial Q}{\partial v} \end{pmatrix} \quad (6)$$

After using (4) & (5) and the implantation the equation of load flow for *NR* becomes as follows:

$$\begin{pmatrix} \Delta P_k \\ \Delta Q_k \\ \Delta P_{VR} \\ \Delta Q_{VR} \end{pmatrix} = \begin{pmatrix} \frac{\partial P_k}{\partial \theta_k} & \frac{\partial P_k}{\partial V_k} V_k & \frac{\partial P_k}{\partial \delta_{VR}} & \frac{\partial P_k}{\partial V_{VR}} V_{VR} \\ \frac{\partial Q_k}{\partial \theta_k} & \frac{\partial Q_k}{\partial V_k} V_k & \frac{\partial Q_k}{\partial \delta_{VR}} & \frac{\partial Q_k}{\partial V_{VR}} V_{VR} \\ \frac{\partial P_{VR}}{\partial \theta_k} & \frac{\partial P_{VR}}{\partial V_k} V_k & \frac{\partial P_{VR}}{\partial \delta_{VR}} & \frac{\partial P_{VR}}{\partial V_{VR}} V_{VR} \\ \frac{\partial Q_{VR}}{\partial \theta_k} & \frac{\partial Q_{VR}}{\partial V_k} V_k & \frac{\partial Q_{VR}}{\partial \delta_{VR}} & \frac{\partial Q_{VR}}{\partial V_{VR}} V_{VR} \end{pmatrix} \begin{pmatrix} \Delta \theta_k \\ \frac{\Delta V_k}{V_k} \\ \Delta \delta_{VR} \\ \frac{\Delta V_{VR}}{V_{VR}} \end{pmatrix} \quad (7)$$

where ΔP_k, ΔQ_k, ΔP_{VR} *and* ΔQ_{VR} are the active and reactive powers mismatch for both the bus *k* and the *VSC* respectively [14]. The elements in the first two rows of the system Jacobian matrix relate to the power mismatch equations, while the latter two rows belong to the STATCOM control.

III. FORMULATION OF THE OPF PROBLEM

A. Objective function

The objective function is minimizing the total generation fuel cost which is given by:

$$F_i(P_i) = \left(\sum_{i=1}^{N} a_i + b_i P_{G_i} + c_i P_{G_i}^2 \right) \quad (8)$$

where P_{Gi} represents the active power generated by the generators, *and a*, *b* and *c* are the cost coefficients of the generator. The function is subjected to equality and inequality constraints which are demonstrated in the following points.

B. Constraints OPF

a) ***Equality constraints****: The following are the equality constraints that reflect the load balance equation for active and reactive powers.*

$$P_{G_i} - P_{d_i} = V_i \sum_{j=1}^{N} V_j \left(g_{ij} \cos \delta_{ij} + z_{ij} \sin \delta_{ij} \right) \quad (9)$$

$$Q_{G_i} - Q_{d_i} = V_i \sum_{j=1}^{N} V_j \left(g_{ij} \sin \delta_{ij} + z_{ij} \cos \delta_{ij} \right) \quad (10)$$

b) ***Inequality constraints****: When it comes to incorporating FACTS devices, the inequality constraints that indicate the limitations of power system operation while incorporating STATCOM are as follows:*

$$\begin{cases} P_{Gi}^{min} \le P_{Gi} \le P_{Gi}^{max} \\ Q_{Gi}^{min} \le Q_{Gi} \le Q_{Gi}^{max} \\ V_{Gi}^{min} \le V_{Gi} \le V_{Gi}^{max} \\ T_{nTi}^{min} \le T_{nTi} \le T_{nTi}^{max} \\ Q_{Ci}^{min} \le Q_{Ci} \le Q_{Ci}^{max} \\ V_{STATCOMi}^{min} \le V_{STATCOMi} \le V_{STATCOMi}^{max} \\ Q_{STATCOMi}^{min} \le Q_{STATCOMi} \le Q_{STATCOMi}^{max} \end{cases} \quad (11)$$

C. Control variables

The vector of OPF control variables incorporating STATCOM in the power system can be expressed by (12):

$$u = \left[P_{G2} \dots P_{GnG}, N_{STATCOM1} \dots N_{nSTATCOM}, Q_{STATCOM1} \dots Q_{nSTATCOM} \right] \quad (12)$$

where P_G is the generated active power of the n^{th} generator and $Q_{STATCOM}$ is the reactive power injected by the STATCOM. *nG* is the number of generators, *nC* is the number of shunt capacitors, *nT* is the number of tap-change transformers and $n_{STATCOM}$ is the number of STATCOM devices.

D. State variables

This vector represents the set of state variables of the power system and it's represented as follows:

$$x = \left[P_{G_{slack}}, Q_{G_1} \dots Q_{G_{NG}}, V_{STATCOM1} \dots V_{nSTATCOM}, V_{L_1} \dots V_{L_{NL}}, S_{l_1} \dots S_{l_{nl}} \right] \quad (13)$$

where P_{Gslack} is the active power generated by the slack bus, Q_G is the reactive power of the generators, V_L is the voltage of load buses or *PQ* buses, S_l represents the apparent power of the transmission lines, *nG* is the number of generators, *NL* is the number of load buses and *nl* is the number of transmission lines, and $V_{STATCOM}$ is the voltage of the STATCOM devices.

IV. SELF-ADAPTIVE BONOBO OPTIMIZER (SABO)

Self-adaptive bonobo optimizer (SaBO) is a new improvement of the original metaheuristic optimization technique the bonobo optimizer (BO) proposed by Amit Kumar Das *et al.* in 2023 [15], which was inspired by the mating strategies and social behavior of the bonobo community [15]. Bonobos, unlike their cousins the chimpanzees, bonobos tend to be more social and peaceful, and more cooperative, and establish strong family bonds. Bonobos live in groups, and the leader of this group is an alpha bonobo. The alpha bonobo is the best bonobo in the group, it coordinates the group's movements, and directs the group towards food sources, and protects the group from aggressors and predators insuring well-being. Bonobos adopt the fission-fusion technique to perform their daily activities where they split into several groups during the day to look for food and safe places this phase is called fission and the regroup to sleep together or fight this is called fusion.

The details of the different steps of the SaBO optimization strategies are explained below:

A. Memory and its updating

The SaBO has a memory of three populations called *oldpop*, *worsepop* and *badpop*. These are the initial population of the SaBO, afterwards they are updated in each iteration. These populations are comparable in size to the current population. The updating procedures are detailed here.

- *Oldpop:* when the fitness value of the i^{th} new bonobo is observed to be better than the i^{th} parent bonobo then the new bonobo is accepted in the current population. The parent bonobo is then moved to *oldpop* in the i^{th} position.
- *Worsepop:* when the new i^{th} bonobo is found to be worse than the parent i^{th} bonobo in the fitness value then the new bonobo is unaccepted into the current population and instead it is sent to the *worsepop* in the i^{th} position.

Identify the applicable funding agency here. If none, delete this text box.

- *Badpop:* this population is of *N* size, and it is picked from a mixture of both *worsepop* & *badpop* of the size *2N*. The selection procedure is as follows. The unique solutions based on their fitness value in the mixed population are identified and are called *l.*
  - **Case 1: if *l*<N:** Then (N-*l*) the number of solutions are randomly chosen and copied to *badpop.*
  - **Case 2: if *l*>N:** Then a number l_1 is randomly selected where l_1 >N this number is the minimum between l , N_2 , where N_2 is calculated as follows:

$$N_2 = ceil(df \times N) \quad (14)$$

Where *df* is the diversity factor. It initially varies from $[df_{\min}, df_{\max}] = [1.2, 1.8]$, and during the iteration is varies according to the MATLAB function *ceil.*

B. Repulsion-based learning

In the SaBO, the controlling parameters P_P & S_C (sharing parameter) are updated during each iteration through repulsion-based learning thus they become self-adaptive. This learning process is dependent on the input collected from the search process. Both these numbers vary in the range from [0, 1] and are expected to be different, the number *N* of P_P or S_C is chosen at the start. *N* number of these parameters is generated from the normal distribution of mean and standard deviation equal to 0.5 and σ, respectively [15]. Initially, we create N number of these parameters each from the normal distribution of mean and standard deviation equal to 0.5 and σ, respectively. the normal distribution [15]. At the start, the parameter σ starts at its maximum value and then it varies in the range $[\sigma_{\min}, \sigma_{\max}]$ in accordance with the search process. The process to update P_P is as follows.

Firstly, we identify the solutions which are modified according to the controlling parameters. For P_P all the solutions of the population are considered [15]. However, only solutions that would partake in either promiscuous or restrictive mating processes are selected for S_C updating. Among these solutions, we select the ones whose fitness values are improved. Furthermore, the controlling variables and the changes in fitness values are identified and if the number of such good solutions is seen to be greater than the pre-determined number *N*, then N_1 is a number of solutions with higher fitness values are selected and N_1 is calculated using (15).

$$N_1 = \max of\,(5, ceil(N \times 0.08)) \quad (15)$$

Then a $P_{Pbetter}$ is the best P_P is obtained as follows, all of the individual changes in fitness values are divided by the sum of the changes in fitness values of these selected good solutions. Assume that the matrix holding the associated controlling parameter values and containing these adjusted changes in fitness values is termed as $[F]_{m\times1}$ & $[P]_{m\times1}$ where $0<m\leq N_1$ then we transpose [F] and multiply it by $[P]_{m\times1}$. Following this procedure, we obtain a single worst phase probability $P_{Pworst.}$
Now the repulsion effects between P_{Pworse} & $P_{Pbetter,}$ we observe that $P_{Pbetter}$ changes in the different direction of P_{Pworse} and the modified values are calculated using (16).

$$P_{Pbetter}^{modified} = P_{Pbetter} \pm \frac{\sigma \times P_{Pbetter} \times P_{Pworse}}{e^{(P_{Pbetter} - P_{Pworse})^2}} \quad (16)$$

C. Mating strategies

Similar to the BO, the SaBO has PP and NP to create a new bonobo. The solutions are updated with a phase probability P_P at each iteration via *PP* or *NP*. Moreover, with a probability of 0.5, new bonobos are formed in *PP* by using either a promiscuous or restrictive mating strategy presented in (17) and (18). During *NP*, however, either an extra-group mating strategy ((19) and (20)) or a consortship strategy ((21), (22) and (23)) is used to generate a new bonobo. P_{xgm} is the probability of extra-group mating occurrence, where the values of this parameter are variable and range from $[P_{xgm}^{\min}, P_{xgm}^{\max}]$.

$$new_bonobo_i = bonobo_i + Sc_i \times \left[\left(bonobo_p - bonobo_i\right) + \left(bonobo_{k1} - oldpop_{k2}\right) + \left(oldpop_{k3} - badpop_{k4}\right)\right] \quad (17)$$

$$new_bonobo_i = bonobo_i + Sc_i \times \left[\left(bonobo_p - bonobo_i\right) + \left(bonobo_{k1} - oldpop_{k2}\right) + \left(bonobo_{k3} - badpop_{k4}\right)\right] \quad (18)$$

$$new_bonobo_j^i = bonobo_j^i + I_2 \times (\text{var_max}_j - bonobo_j^i), \ if \ \ r_2 \leq 0.5 \quad (19)$$

$$new_bonobo_j^i = bonobo_j^i - I_2 \times (bonobo_j^i - V_\min_j), \ if \ \ r_2 > 0.5 \quad (20)$$

$$new_bonobo_j^i = bonobo_j^i + I_3 \times (bonobo_j^i - badpop_j^i) \quad (21)$$

$$new_bonobo_j^i = bonobo_j^i + I_2 \times (bonobo_j^i - badpop_j^i) \quad (22)$$

$$new_bonobo_j^i = bonobo_p^j + I_5 \times (bonobo_p^j - badpop_j^i) \quad (23)$$

where I_2, I_3 and I_5 are intermediates. Where $I_2 = e^{\left(r_1 - \frac{1}{r_1}\right)}$, $I_3 = e^{\left(r_1 - \frac{2}{r_1}\right)}$, and $I_5 = e^{\left(r_1 - \frac{I_4}{r_1}\right)}$, respectively.

V. Results and Discussions

This part of the study aims to use the proposed algorithm to find the optimal placement and sizing of the STATCOM device on the standard IEEE 30-Bus and IEEE 57-Bus power systems based on the determination of the lowest voltage in the load buses (PQ). The STATCOM has a capacity of ±50 MVar. In this test, three different cases are considered based on the number of STATCOM devices installed as follows.

- **Case 01:** OPF without the incorporation of STATCOM;
- **Case 02:** OPF with the incorporation of one STATCOM;
- **Case 03:** OPF with the incorporation of two STATCOMs;

A. Application on the standard IEEE 30-Bus system

This part aims to solve the OPF problem to find the optimal placement of STATCOM devices on the standard IEEE 30-bus system under contingency conditions. In this context, the loads are increased by 45% from the base case. The test is run several times for better validation of the results obtained by the SaBO. The simulation results obtained by the proposed algorithm are presented in the following table.

TABLE I. COMPARISON OF THE RESULTS IN THE IEEE 30-BUS SYSTEM

Control Variables	Limits		Active power loading 410.93 MW		
	Min	*Max*	*Case 1*	*Case 2*	*Case 3*
P_{G1}	50	200	200.0000	200.0000	200.0000
P_{G2}	20	80	80.0000	80.0000	80.0000
P_{G5}	15	50	41.1902	40.7778	40.7048
P_{G8}	10	35	35.0000	35.0000	35.0000
P_{G11}	10	30	30.0000	30.0000	30.0000
P_{G13}	12	40	40.0000	40.0000	40.0000
$OP_{STATCOM\text{-}1}$	1	30	-	**24**	**24**
$OP_{STATCOM\text{-}2}$	1	29	-	-	**30**
$V_{STATCOM}$ 1	0.9	1.1	-	1.0207	1.0171
$V_{STATCOM}$ 2	0.9	1.1	-	-	1.0072
$Q_{STATCOM}$ 1	-50	50	-	-20.70	-17.08
$Q_{STATCOM}$ 2	-50	50	-	-	-7.20
V_{min} (p.u)	0.9	1.1	0.9249	0.9541	0.9786
Total generation cost ($/h)			**1345.6474**	**1343.1219**	**1342.6772**
Power losses (MW)			15.2602	14.8478	14.7748
Voltage deviation (p.u.)			0.6411	0.3477	0.2858

From Table I, the optimal location to install one STATCOM in the Case 02 is determined at bus 24. However, for the installation of two STATCOMs in the Case 03, the proposed algorithm selected buses 24 and 30 as optimal locations within the IEEE 30-bus system. These optimal selections were made by considering the dual criteria of minimizing fuel cost and improving the voltage profile. Furthermore, the result obtained from Case 3 has the lowest fuel cost at 1342.6772 $/h, minimal power losses of 14.7748 MW, and the lowest TVD value of 0.2858. The results are superior to Case 02's, which achieved values for fuel cost, power losses, and TVD of 1343.1219 $/h, 14.8478 MW, and 0.3477, respectively. Additionally, compared to Case 01, which has no STATCOM, the incorporation of STATCOMs in Cases 02 and 03 gives significant advantages to the power system by reducing fuel costs and improving the voltage profile. Therefore, the SaBO has been successful in solving OPF for the IEEE 30-Bus considering STATCOMs.

Fig. 3 shows the TGC convergence curves for all the cases in IEEE 30-bus. This figure demonstrates that Case 03 converges with greater speed and at an optimal TGC value than Cases 01 and 02.

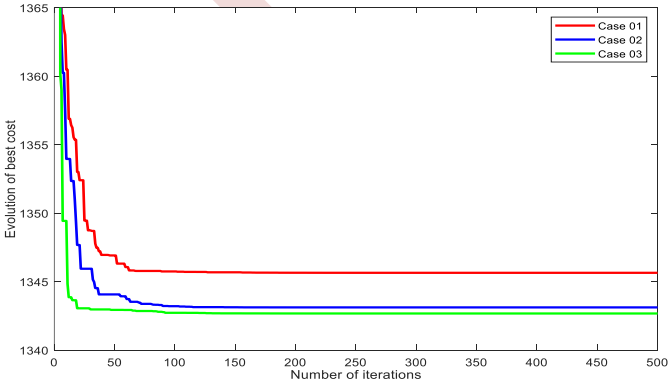


Figure 3. Convergence curves of TGC in IEEE 30-bus system for all the cases

The voltage profiles of the three cases are shown in Fig. 4. The voltage profile for Case 03 is better compared to Cases 01 and 02 where there is a lot of buses experiencing voltage drop. Moreover, it can be seen that the buses where the STATCOMs are placed, bus 24 for Case 02 and buses 24 & 30 for Case 03 the voltages are 1 p.u and the buses closer to the STATCOM are improved as well.

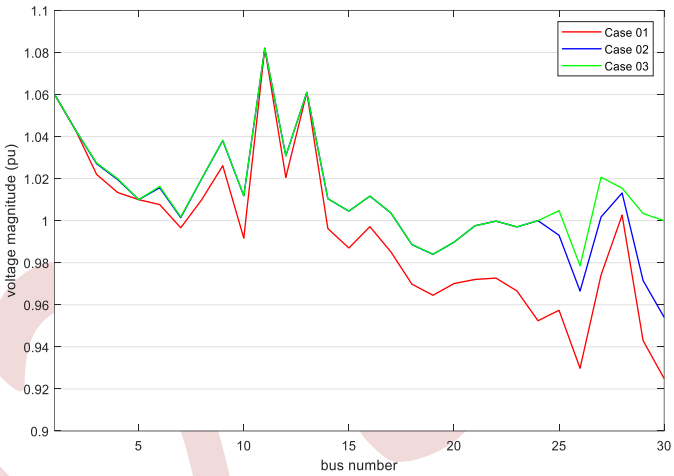


Figure 4. Voltage profile comparison of IEEE 30-bus system

B. Application on the IEEE 57-Bus system

In the second test, the OPF problem with incorporate the STATCOM devices in the IEEE 57-bus system has been proposed. This test system involves the following characteristics, 7 generators, 80 transmission lines, 15 branches under load tap setting transformer branches and 3 reactive compensators. The total load demand of this system is 1250.8 MW + j 336.4 MVAR. Table II shows the detail results of the simulation obtained by the proposed algorithm.

TABLE II. COMPARISON OF THE RESULTS IN THE IEEE 57-BUS SYSTEM

Control Variables	Limits		Active power loading 1250.8 MW		
	Min	*Max*	*Case 1*	*Case 2*	*Case 3*
P_{G1}	100	575.9	143.8387	143.9189	143.9131
P_{G2}	10	100	100.0000	97.9060	97.8668
P_{G5}	14	140	45.4802	45.3854	45.3845
P_{G8}	10	100	70.2099	69.1651	69.0547
P_{G11}	200	550	455.7460	456.0782	456.0894
P_{G13}	10	100	92.6872	94.8848	94.8339
$OP_{STATCOM\text{-}1}$	1	57	-	**31**	**31**
$OP_{STATCOM\text{-}2}$	1	56	-	-	**53**
$V_{STATCOM}$ 1	0.9	1.1	-	1.0069	1.0067
$V_{STATCOM}$ 2	0.9	1.1	-	-	1.0078
$Q_{STATCOM}$ 1	-50	50	-	-6.88	-6.69
$Q_{STATCOM}$ 2	-50	50	-	-	-7.97
V_{min} (p.u)	0.9	1.1	0.9373	0.9809	0.9786
Total generation cost ($/h)			41805.749	41776.265	41767.589
Power losses (MW)			17.9681	17.2734	17.0659
Voltage deviation (p.u.)			1.3498	1.1252	1.1417

Table II shows a comparison of the results obtained for the IEEE 57-Bus for the three cases studied. From the results, it can be seen that the total fuel cost with two STATCOMs installed on buses 31 and 53 is lower than Case 02 (one STATCOM at bus 31) and Case 01 (Without STATCOMs), where the costs are 41767.5899 $/h, 41776.2653 $/h and 41805.74914 $/h, respectively. Moreover, the active power loss is also lower in Case 03 compared to Case 02 and Case 01 where the results are 17.0659 MW, 17.2734 MW and 17.9681 MW, respectively. As for the TVD, it appears that Case 02 yielded a better result than Case 03 and Case 01 where the results are 1.1252, 1.1417 and 1.3498. This indicated that SaBO proved its performance in order to solve OPF with incorporating of STATCOM devices in the mid-scale power system.

Fig. 5 shows a comparison of the TGC convergence curves obtained by the proposed algorithm for all cases. From this figure, it can be seen that the convergence curve of Case 03, which incorporates the presence of two STATCOMs, is better than both cases 01 and 02, where it converges faster towards the lowest generation fuel cost.

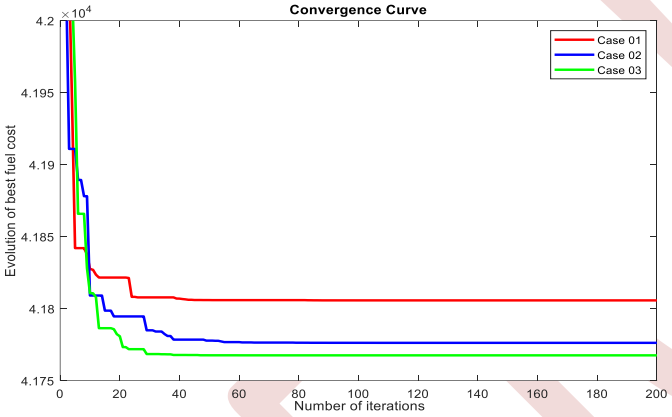


Figure 5. Convergence curves of TGC in IEEE 30-bus system for all the cases

The comparison of voltage profile with and without STATCOMs devices is shown in Fig. 6. From this Figure, it can be seen that after installing the STATCOMs in the optimal locations for cases 02 and 03, the voltage profile improved greatly. As a result, the STATCOM can improve the bus voltage where it's connected as well as the voltages of nearby buses.

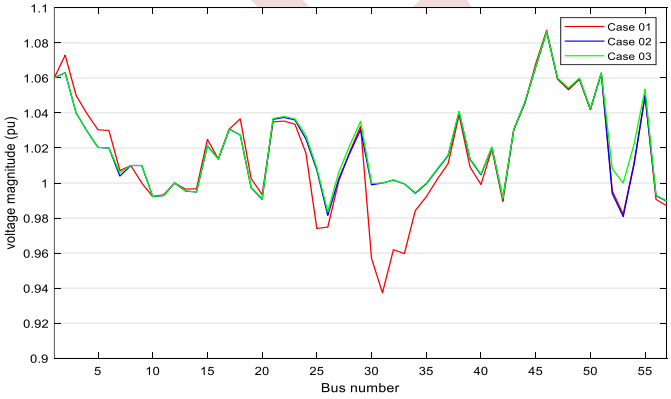


Figure 6. Voltage profile comparison of IEEE 57-bus system

CONCLUSION

In this paper, the application of the proposed algorithm SaBO for solving the OPF problem with the integration of STATCOM devices has been addressed. The objective function was to minimize the generation of fuel cost according to the optimal power dispatch. The proposed algorithm has been tested on the standard IEEE 30-bus and IEEE 57-bus systems. Three different cases were studied depending on the number of integrated STATCOM devices. The results obtained through the simulation indicate that the optimal location of the STATCOM device lowers the overall generation fuel cost and reduces the active power losses as well as improves the voltage profile. Furthermore, the proposed algorithm has successfully solved the OPF problem considering STATCOM devices.

REFERENCES

[1] A. AL Ahmad and R. Sirjani, "Optimal placement and sizing of multi-type FACTS devices in power systems using metaheuristic optimisation techniques: An updated review," *Ain Shams Eng. J.*, vol. 63, 2019.

[2] M. O. Okelola, S. O. Ayanlade, and E. I. Ogunwole, "Particle Swarm Optimization for Optimal Allocation of STATCOM on Transmission Network," *J. Phys. Conf. Ser.*, vol. 1880, no. 1, 2021.

[3] Carpentier, "Contribution to the economic dispatch problem," *Bull Soc Fmnc Efeci*, vol. 3, pp. 431–447, 1962.

[4] R. Kouadri, I. Musirin, L. Slimani, T. Bouktir, and M. M. Othman, "Optimal power flow control variables using slime mould algorithm for generator fuel cost and loss minimization with voltage profile enhancement solution," *Int. J. Emerg. Trends Eng. Res.*, vol. 8, no. 1, 2020.

[5] M. Ebeed, S. Kamel, and F. Jurado, "Optimal power flow using recent optimization techniques," in *Classical and Recent Aspects of Power System Optimization*, Elsevier Inc., 2018, pp. 157–183.

[6] F. Glover, "Future paths for integer programming and links to artificial intelligence," *Comput. Oper. Res.*, vol. 13, no. 5, pp. 533–549, 1986.

[7] A. Jimoh, S. O. Ayanlade, E. I. Ogunwole, D. E. Owolabi, A. B. Jimoh, and F. M. Aremu, "Metaheuristic Optimization Algorithm Performance Comparison for Optimal Allocation of Static Synchronous Compensator," *Adv. Sci. Technol. Eng. Syst. J.*, vol. 8, no. 1, pp. 116–124, 2023.

[8] R. Kouadri, L. Slimani, and T. Bouktir, "Slime Mould Algorithm for Practical Optimal Power Flow Solutions Incorporating Stochastic Wind Power and Static Var Compensator Device," *Electr. Eng. Electromechanics*, vol. 0, no. 6, pp. 45–54, 2020.

[9] T. Zhang, X. Xu, Z. Li, A. Abu-Siada, and Y. Guo, "Optimum Location and Parameter Setting of STATCOM Based on Improved Differential Evolution Harmony Search Algorithm," *IEEE Access*, vol. 8, pp. 87810–87819, 2020.

[10] P. R. Reddy and A. L. Devi, "Optimal sizing and placement of statcom in transmission systems using gravitational search algorithm," *IJARIIE*, vol. 4, no. 2, pp. 3027–3034, 2018.

[11] A. S. Emam, A. M. R. Azmy, and E. E. M. Rashad, "Egyptian Power System Optimal Allocation of STATCOM Devices based on Particles Swarm optimization Technique," *2019 21st Int. Middle East Power Syst. Conf. MEPCON 2019 - Proc.*, pp. 125–130, 2019.

[12] M. A. Taher, S. Kamel, F. Jurado, and A. Ahmed, "Optimal Allocation of STATCOM for Voltage Stability and System Loadability," *2018 20th Int. Middle East Power Syst. Conf. MEPCON 2018 - Proc.*, pp. 632–637, 2019.

[13] G. Choudhary, N. Singhal, and K. S. Sajan, "Optimal placement of STATCOM for improving voltage profile and reducing losses using crow search algorithm," *ICCCCM 2016 - 2nd IEEE Int. Conf. Control Comput. Commun. Mater.*, pp. 2–7, 2017.

[14] R. Al-Rubayi and M. Eesee, "Optimal Location and Parameter Setting of STATCOM Device Based PSO for Iraqi Grid Voltage Profile Enhancement and Power Losses Minimizing," *Eng. Technol. J.*, vol. 37, no. 2A, pp. 60–69, 2019.

[15] A. K. Das, S. Sahoo, and D. K. Pratihar, "An Improved Design of Knee Orthosis Using Self-Adaptive Bonobo Optimizer (SaBO)," *J. Intell. Robot. Syst. Theory Appl.*, vol. 107, no. 1, Jan. 2023.

Deep Reinforcement Learning based Virtual Inertia Control for Islanded Microgrids with High sharing of Renewable Energy sources

Houssam Deboucha [1], Saad Mekhilef [2,3], (IEEE fellow)

[1]Laboratoire de Technologie Industrielle et de l'Information (LTII),
Faculté de Technologie,
Université de Bejaia, Algérie
houssam.deboucha@univ-bejaia.dz

[2]School of Science, Computing and Engineering Technologies, Swinburne University of Technology, Hawthorn, VIC 3122, Australia
[3]Electrical Engineering Department, College of Engineering, University of Ha'il, Ha'il 81481, Saudi Arabia
smekhilef@swin.edu.au

***Abstract*—The rapid integration of renewable distributed generation (DGs) units led to a major reduction of inertia of power system, which resulted in serious challenges of system stability, rapid rate of change of frequency (RoCoF) and large frequency nadir/overshoot. Hence, a virtual inertia control loop comes as an effective solution. This paper proposes a deep reinforcement learning with Soft Actor-Critic (SAC) optimization algorithm based on virtual inertia control. The performance of the proposed method is verified under different disturbances, which show a robust frequency support in low inertia system and high renewable energy sources (RESs).**

***Index Terms:* virtual inertia control (VIC), deep reinforcement learning (DRL), microgrids (MGs), renewable energy sources (RESs).**

I. INTRODUCTION

The traditional power system has been gradually transforming from a conventional structure, where the synchronous machines have been mainly used as power sources and provide natural inertia for the power system, to microgrids (MGs) with high level sharing of renewable energy sources (RESs) such as photovoltaic (PV) and wind turbine (WT) interfaced through power electronic converters [1]. Consequently, numerous challenges have emerged in terms of frequency and voltage stability due to the lack of the inertia support and damping of the power system. The low inertia of the power system may lead to a rapid rate of change of frequency (RoCoF) and large frequency deviation (nadir frequency) results in, triggering the under-frequency load shedding relays (UFLS) and may lead to cascading outages [2].

In order to stabilize the power system and achieve high reliability and resiliency, a virtual inertia (VIC) control loop is incorporated to mimic the synchronous machine behavior virtually [3], [4]. So far, numerous approaches to virtual inertia control have been proposed in the literature [5-12]. In [5], a proportional integral PI controller is proposed for VIC. In [6], Fuzzy-logic method-based VIC is proposed to enhance the frequency deviation in islanded MG with high penetration of RESs under different scenarios. In [7], model predictive control is proposed and compared with the Fuzzy-logic approach, it shows improving performance of the RoCoF during sudden load change. proportional-integral (PI) is proposed for virtual inertia control [8], In [9] VIC based on PI is proposed for wind power to regulate the frequency stability. In [10], the robust H□ controller-based VIC is designed for frequency stability for interconnected microgrids, the proposed method outperforms the conventional VIC and optimal tuned PI controller under different scenarios of inertia system values. In [11] the derivative control-based VIC is proposed to support the frequency deviation in multi-area interconnected. Deep reinforcement learning (DRL) methods are successfulin solving complex nonlinear dynamics systems. In [12] proposed reinforcement learning approach for VIC, the proposed method has shown advantages over the H□ and PI controller under disturbances/uncertainties of load and RESs. In [13] Reinforcement Learning based MIMO Controller for Virtual Inertia Control in Isolated Microgrids is proposed. In this paper, Soft Actor-Critic (SAC), an off-policy maximum entropy DRL algorithm, is developed for virtual inertia control. The SAC algorithm provides sample efficient learning and stability. The remainder of this paper is organized as follow: Section II discusses the dynamic model of the

microgrid regarding for frequency supporting, and the proposed DRL-based VIC design is discussed. In Section III, the frequency response of islanded microgrid is investigated under challenging cases. Finally, the conclusion is outlined in Section VI.

II. DYNAMIC MODELLING OF THE STUDIED MICROGRID

A. Frequency control model

The dynamic model of the studied islanded microgrid shown in Fig. 1 is Kerdpol's real AC-DC system with high RESs which has been adopted in several studies [10]. The studied microgrid contains different sources of power generation (thermal power plant, PV plant, wind farm, and energy storage system). In order to obtain a precise dynamic model, physical constraints have been considered in the linearized model of the thermal power plant. The governor is characterized by the generation rate constraint (GRC) and turbine with frequency limiter of opening/closing the valve (V_U, V_L) and time delay for the secondary control. The renewable energy sources and load demand are considered as random signals with first-order holders, which represent the disturbances/uncertainties to the islanded microgrid, the power converters are modeled as low-pass filters which is sufficient for frequency control. The hierarchical architecture control loops contain three main states: the first state is inertia control loop-based ESS, the second state is the primary control loop with droop coefficient (1/R), the third state is the secondary control loop has an area.

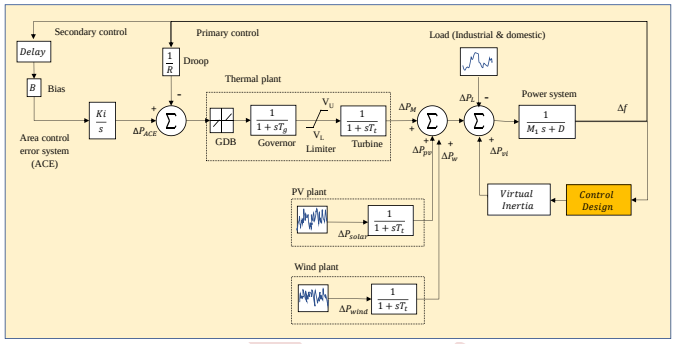


Figure. 1 Dynamic model of the studied microgrid with virtual inertia control for frequency response analysis

control error (ACE) with the bias factor B, frequency controller Ki and first-order integrator. The microgrid dynamic system is modeled as a transfer function with damping factor D and inertia system H. The frequency deviation of the studied islanded microgrid, including the hierarchical control loops, can be developed as:

$$\Delta f = \frac{1}{2H+D}\left(\Delta P_M + \Delta P_{wind} + \Delta P_{PV} + \Delta P_{inertia} - \Delta P_L\right) \quad (1)$$

where,

$$\Delta P_M = \frac{1}{1+sT_r}\Delta P_g \quad (2)$$

$$\Delta P_g = \frac{1}{1+sT_g}\left(\Delta P_{ACE} - \frac{1}{R}\Delta f\right) \quad (3)$$

$$\Delta P_{wind} = \frac{1}{1+sT_{WT}}\Delta P_{wind} \quad (4)$$

$$\Delta P_{PV} = \frac{1}{1+sT_{PV}}\Delta P_{solar} \quad (5)$$

$$\Delta P_{Tie} = \frac{2\Pi}{s}\left(\Delta f_1 - \Delta f_2\right) \quad (6)$$

$$\Delta P_{vi} = \frac{K_{vi}}{1+sT_{vi}}\frac{d}{dt}(\Delta f) \quad (7)$$

TABLE I. PARAMETERS OF ISLANDED MICROGRID.

Variable	Variable Physical meaning	Nominal Value	Unit
ΔP_m	power changes of the thermal plant	-	p.u.
T_t	time constant of the turbine	0.4	s
ΔP_g	governor valve-position change	-	p.u.
T_g	time constant of the governor	0.1	s
ΔP_{ACE}	control signal for secondary control	-	-
K_I	integral control variable gain	0.05	s
R	Droop coefficient	2.4	Hz/p.u.MW
H	System inertia	0.083	p.u. s
D	Damping coefficient	0.015	p.u./Hz
ΔP_W	Wind power change	0.1-0.125	p.u.
T_{WT}	time constant of wind turbines	1.85	s
ΔP_{PV}	PV power change	0.08-0.13	p.u.
T_{PV}	time constant of the solar system	1.5	s
V_U	Maximum governor valve limit	0.5	-
V_L	Minimum governor valve limit	0	-
GRC	Generated rate constraint	±12%	p.u. Mw/min
ΔP_{L1}	Industrial load change	0.22-0.3	p.u.
ΔP_{L2}	Domestic load change	0.15-0.24	p.u.

B. The proposed virtual inertia control design

Primarily, virtual inertia (VI) based inverters are part of the virtual synchronous machine (VSM) or synchronous generator (VSG). Which designed to reduce the frequency fluctuation and frequency nadir driven by the lack of inertia system.

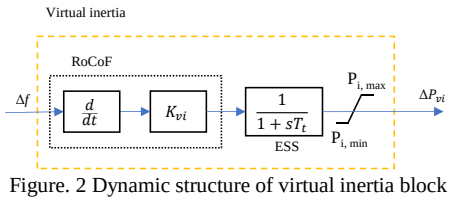


Figure. 2 Dynamic structure of virtual inertia block

Fig. 2 presents the dynamic structure of virtual inertia, which consists of the derivative part to determine the rate of change of frequency (RoCoF), which is used to determine the power added to the set point (equation (7)). The inertia power in this work is emulated through ESS.

1) Soft Actor-Critic Algorithm:

Generally, in deep reinforcement Learning (DRL), the agent interacts with the environment as described in Fig.3 by making an observation of the current state of the environment (MG) s_t (i.e., Δf_t, d(Δf)/dt, f/s, ΔP_e, ΔP_{vi}) then take action a_t

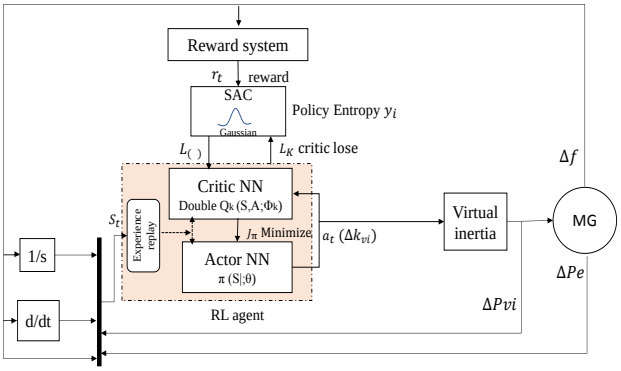


Figure. 3 scheme of the proposed DRL control structure-based VIC

(K_{vi}) the action is selected based on the policy π, the agent receives a reward r_t (s_t, a_t) when the right action is taken otherwise, a punishment - r_t will be received. The Soft Actor-Critic (SAC) is an off-policy DRL algorithm that aims to optimize the stochastic policy that maximizes the long-term expected reward and the entropy term; unlike the deep deterministic policy gradient DDPG, the SAC algorithm adds the entropy term in the optimal policy resulted in better exploration. The architecture of the agent is a combination of two artificial neural networks: the critic network Q_k ($S,A;\Phi_k$) that estimates the expected cumulative long-term reward, which is modeled as a feed-forward Deep Neural Network (DNN) with parameter vector k to increase the learning stability. The stochastic critic network π ($S|;\theta$) that selects an action a_t stochastically based on a given observation state s_t. The policy π is perceived as an m-dimensional multivariate Gaussian distribution featuring a diagonal covariance matrix. Its actions undergo processing through a *tanh* squashing function to guarantee their definition within finite boundaries. The pseudo-code of the SAC algorithm, is summarized in Algorithm 1 [14].

2) RL rewarding system

The RL rewarding/punishment mechanism proposed in [12] is adjusted in order to establish a more precise reward/punishment system for DRL agent-based virtual inertia control as follows:

$$\begin{cases} \frac{1}{0.5+|\Delta f|}, & \text{if } |\Delta f| < 0.05, \\ -2|\Delta f|, & \text{if } |\Delta f| > 0.05, \\ 1|\Delta P_{vi}|, & \text{if } |\Delta P_{vi}| > 0.075, \\ -0.5|\Delta P_{vi}|, & \text{if } |\Delta P_{vi}| > 0.075, \end{cases} \quad (8)$$

The regulation system can be outlined as follow: the initial signal undergoes a transformation into it absolute value, denoted as {$|\Delta f|$, $|\Delta P_{vi}|$, $|\Delta P_e|$}. If Δf is less than 0.05, ΔP_{vi} is less than 0.075, and ΔP_e is less than 0.01, the DRL agent receives a reward $\pm r$. To ensure the equitable allocation of rewards for each action, the reward is bounded within the range of $\Delta f \in [0.05, 2]$. However, the punishment action remains unrestricted and is magnified by a constant factor of 2. For the inertia control, the reward control is magnified by constant 0.1 and punishment action by 0.5.

Algorithm 1: SAC Algorithm [14]

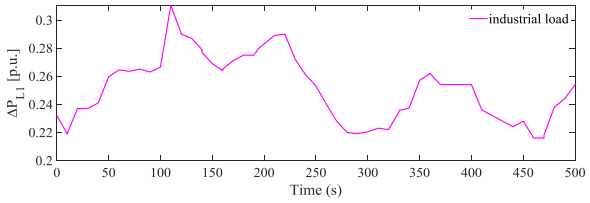
1: Initialize $\boldsymbol{\theta}$, k1, k2 parameters for policy $\pi\boldsymbol{\theta}$ and double Q-function Qk1,2;
2: Set target parameters k`$_1 \leftarrow$ k1 and k`$_2 \leftarrow$ k2;
3: Initialize empty memory buffer D, minibatch β, learning rate λ and smoothing factor τ;
4: Observe initial state s_0;
5: **for** each time step t do
6: Sample action $a_t \sim \pi_{\boldsymbol{\theta}}$ ($\cdot \mid s_t$);
7: Observe next state and reward $s_{t+1} = f$ (s_t, a_t), $r\tilde{}$(s_t, a_t);
8: Store transition sample (s_t, a_t, $r\tilde{}$(s_t, a_t), s_{t+1}) in D ;
9: Sample a minibatch of transition samples β ={(s_t, a_t, $r\tilde{}$(s_t, a_t), s_{t+1})} from D;
11: Update Q-function parameters: k$_i \leftarrow$ k$_i$ -$\lambda\nabla_{ki}$ (1/β) Σ L_Q(k$_i$, β) for i = 1, 2;
13: Update policy parameter: $\boldsymbol{\theta} \leftarrow \boldsymbol{\theta}$, $\lambda\nabla_{\boldsymbol{\theta}}$ (1/β) Σ J_π ($\boldsymbol{\theta}$, β)
14: Update the temperature hyperparameter: $\eta \leftarrow \eta$ - $\lambda\nabla_\eta L$ (η)
15: Update target Q-function parameters: k`$_i \leftarrow$ (1 – $\tau$) k$_i$ + $\tau$k`$_i$ for i = 1, 2;
end

III. SIMULATION AND RESULTS

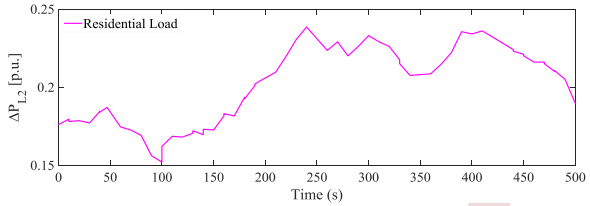
In this section, we investigate the performance of the proposed DRL based virtual inertia control. The simulations were conducted in MATLAB/Simulink environment. The details of the studied islanded MG parameters are given in Table I. Simulations were carried out under the comprehensive operation of both primary and secondary controls within the system. The performance of the proposed control architecture is tested under varying inertia system and uncertainties/disturbances, connection of variable load and (dis)connection of renewable energy sources. Two different scenarios are considered in this study with different system inertia values High (100%, H=0.083) , Low (30%, H=0.0249).

Scenario 1 (Nominal case): in this scenario, the operation system is performed without any change (dis)connection during the time (T=500). Fig. 5 and 6 show the performance

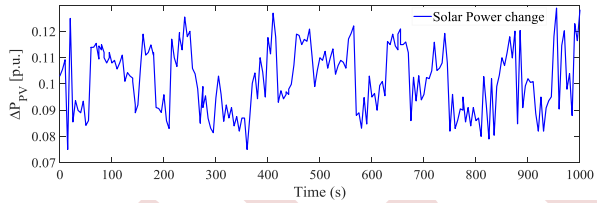
results without and with the proposed DRL-based VIC with high system inertia (i.e., H=100%). It can be seen from Fig. 5(a) that the proposed DRL control structure improves the frequency performance by reducing the frequency excursion and frequency nadir compared to the results without the virtual inertia control. Where the proposed DRL control maintained the frequency deviation within ±0.05 Hz. In the opposite,



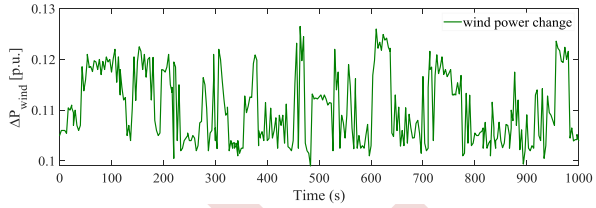
(a)



(b)

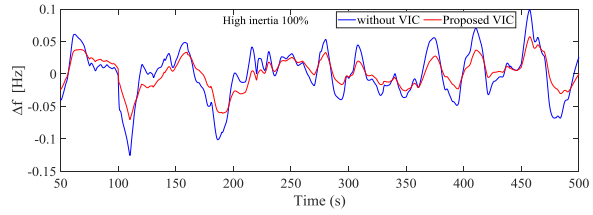


(c)

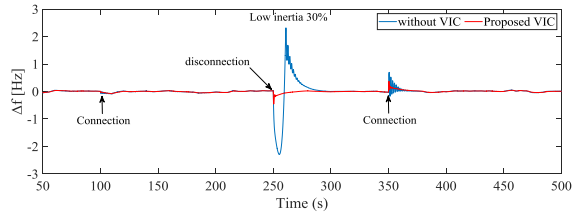


(d)

Fig. 4 Simulated dynamics (a) industrial load, (b) residential load, (c) solar energy, (d) wind energy.

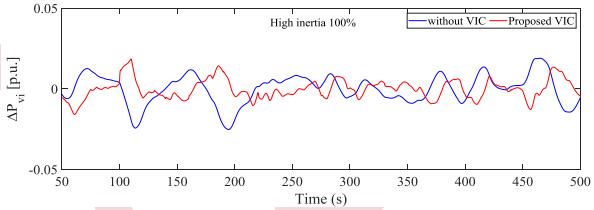


(a)

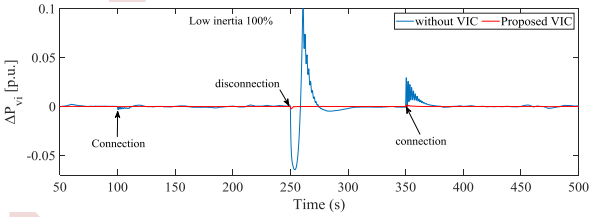


(b)

Fig. 5 Frequency deviation with different inertia system, (a) scenario 1 with normal operation, (b) scenario 2 with disturbances.



(a)



(b)

Fig. 6 power flow in ESS with different inertia system, (a) scenario 1 normal operation, (b) scenario 2 with disturbances.

higher frequency oscillation ±0.12 Hz has been shown in the case without virtual control.

Scenario 2 (Load and RES (dis)connection): In this challenging scenario, multiple disturbances have been conducted through the period time (T=500 s) to test the robustness of the proposed DRL-based VIC, where industrial load connection at time step 70 s followed by a disconnection of PV power plant at time step 250 s and a connection of wind power plant at time step 350 s. Furthermore, the critical condition of the reduced inertia system (i.e., H=30%) is performed. It is clear from Fig. 5(b) that the proposed DRL control structure outperforms the case without virtual inertia control which maintained the frequency deviation within the acceptable range ±0.45 Hz and showed better damping of frequency oscillation in the steady state. The results see Fig. 5(b) demonstrate the effectiveness of the proposed virtual inertia control, where in the case of disconnection of PV power plant at time step 250s led to high frequency oscillation ±2 Hz in the absence of virtual inertia control.

Fig. 6(a) and Fig. 6 (b) illustrate the power flow through the energy storage system (ESS) in scenario 1 and scenario 2, respectively. It can be seen that the proposed DRL virtual inertia control influence at the usage of energy accumulated in ESS by minimizing the power flow through ESS to balance the power of the system compared to the system without virtual inertia control. Consequently, reducing the ESS capacity installed. It's clear from the results of Fig. 6(a, b) that the level of the inertia system affects the power flow through ESS, where a lower inertia system leads to lower energy stored.

To verify the system performance with and without DRL based VIC in both scenarios 1 and 2, two metrics have been used. The integral absolute error (IAE) and root mean square error (RMSE) defined as:

$$IAE = \int_{50}^{T} |\Delta f| dt \quad (9)$$

$$RMSE = \sqrt{\frac{1}{N} \sum_{i=0}^{N} (\Delta f_i)^2} \quad (10)$$

TABLE II. PARAMPERFORMANCE COMPARISON USING IAE METRIC

Approach	Proposed DRL	Without VIC
Scenario 1	9.75	10.97
Scenario 2	10.34	39.9

TABLE III. PARAMPERFORMANCE COMPARISON USING RMSE METRIC

Approach	Proposed DRL	Without VIC
Scenario 1	0.00942	0.01047
Scenario 2	0.00975	0.01052

where,

T is the simulation time period and N is the number of samples. The transient response (i.e., T= [0-50] s) of the system is eliminated to avoid the high oscillations. The metrics results are summarized in Tables I and II. The results confirm the superiority of the proposed DRL-based VIC against the system without VIC.

IV. CONCLUSION

This paper proposes the deep reinforcement learning with Soft Actor-Critic (SAC) optimization algorithm based on virtual inertia control to support the frequency stability of the islanding microgrid with high penetration of RESs. The proposed DRL-based VIC is evaluated under different disturbances of (dis)connection of load and RESs considering the reduction of the inertia system. The results confirm the superiority of the proposed DRL against the system without VIC to suppress the frequency deviation during the uncertainties/disturbances of the isolated MG. In addition, reducing the ESS capacity installed resulted in minimizing the installation cost. In conclusion, the proposed DRL DRL-based VIC could be generalized for more complex systems with multi-area interconnected MGs for future work.

REFERENCES

[1] V. Skiparev, R. Machlev, N. R. Chowdhury, Y. Levron, E. Petlenkov, and J. Belikov, "Virtual inertia control methods in islanded microgrids," *Energies*, vol. 14, no. 6. MDPI AG, Mar. 02, 2021. doi: 10.3390/en14061562.J. Clerk Maxwell, A Treatise on Electricity and Magnetism, 3rd ed., vol. 2. Oxford: Clarendon, 1892, pp.68–73.

[2] F. Gonzalez-Longatt, J. M. Roldan-Fernandez, H. R. Chamorro, S. Arnaltes, and J. L. Rodriguez-Amenedo, "Investigation of Inertia Response and Rate of Change of Frequency in Low Rotational Inertial Scenario of Synchronous Dominated System," *Electronics 2021, Vol. 10, Page 2288*, vol. 10, no. 18, p. 2288, Sep. 2021, doi: 10.3390/ELECTRONICS10182288.

[3] U. Tamrakar, D. Shrestha, M. Maharjan, B. P. Bhattarai, T. M. Hansen, and R. Tonkoski, "Virtual inertia: Current trends and future directions," *Applied Sciences (Switzerland)*, vol. 7, no. 7. MDPI AG, Jun. 26, 2017. doi: 10.3390/app7070654.

[4] D. Alonso Sørensen, D. Vázquez Pombo, and E. Torres Iglesias, "Energy storage sizing for virtual inertia contribution based on ROCOF and local frequency dynamics," *Energy Strategy Reviews*, vol. 47. Elsevier Ltd, May 01, 2023. doi: 10.1016/j.esr.2023.101094.

[5] P. F. Frack, P. E. Mercado, and M. G. Molina, "Extending the VISMA concept to improve the frequency stability in Microgrids," *2015 18th International Conference on Intelligent System Application to Power Systems, ISAP 2015*, Nov. 2015, doi: 10.1109/ISAP.2015.7325530.

[6] Kerdphol, M. Watanabe, K. Hongesombut, and Y. Mitani, "Self-Adaptive Virtual Inertia Control-Based Fuzzy Logic to Improve Frequency Stability of Microgrid with High Renewable Penetration," *IEEE Access*, vol. 7, pp. 76071–76083, 2019, doi: 10.1109/ACCESS.2019.2920886.

[7] T. Kerdphol, F. S. Rahman, Y. Mitani, K. Hongesombut, and S. Küfeoğlu, "Virtual Inertia Control-Based Model Predictive Control for Microgrid Frequency Stabilization Considering High Renewable Energy Integration," *Sustainability 2017, Vol. 9, Page 773*, vol. 9, no. 5, p. 773, May 2017, doi: 10.3390/SU9050773.

[8] F. M. Gonzalez-Longatt, "Effects of the synthetic inertia from wind power on the total system inertia: Simulation study," in *2nd International Symposium on Environment Friendly Energies and Applications, EFEA 2012*, 2012, pp. 389–395. doi: 10.1109/EFEA.2012.6294049.

[9] A. Mohamed, H. Elzoghby, M. Bahgat, and A. G. Mohamed, "Enhanced Non-linear PID-Based on Virtual Inertia Control to Enhance the Frequency Stability of a Hybrid Power System," *International Journal of Advanced Engineering and Business Sciences*, vol. 0, no. 0, pp. 1–18, Aug. 2022, doi: 10.21608/ijaebs.2022.155614.1029.

[10] T. Kerdphol, F. S. Rahman, Y. Mitani, M. Watanabe, and S. Kufeoglu, "Robust Virtual Inertia Control of an Islanded Microgrid Considering High Penetration of Renewable Energy," *IEEE Access*, vol. 6, pp. 625–636, 2018, doi: 10.1109/ACCESS.2017.2773486.

[11] T. Kerdphol, F. S. Rahman, M. Watanabe, Y. Mitani, D. Turschner, and H. P. Beck, "Enhanced Virtual Inertia Control Based on Derivative Technique to Emulate Simultaneous Inertia and Damping Properties for Microgrid Frequency Regulation," *IEEE Access*, vol. 7, pp. 14422–14433, 2019, doi: 10.1109/ACCESS.2019.2892747.

[12] V. Skiparev, J. Belikov, and E. Petlenkov, "Reinforcement learning basedapproach for virtual inertia control in microgrids with renewable energysources," inProc. IEEE PES Innov. Smart Grid Technol. Eur., The Hague,Netherlands, 2020, pp. 1020–1024.

[13] V. Skiparev, J. Belikov, and E. Petlenkov, "MIMO reinforcement learningbased approach for frequency support in microgrids with high renewableenergy penetration," inProc. IEEE Power Energy Soc. Gen. Meeting, 2021,pp. 1–5.

[14] K. Dally and E.-J. van Kampen, "Soft Actor-Critic Deep Reinforcement Learning for Fault Tolerant Flight Control," Feb. 2022, AIAA SCITECH 2022 Forum. 2022, doi: 10.2514/6.2022-2078.

EEIC'23

Bald eagle search-based optimization algorithm for optimal power flow solution in power systems

N. Ferroudj [1], M. Amroune [2], L. Slimani [3]

[1] *Department of Electrical Engineering, University of Ferhat Abbas Setif 1, Setif 19000, Algeria*
islemferroudj@gmail.com

[2] *Department of Electrical Engineering, University of Ferhat Abbas Setif 1, Setif 19000, Algeria*
mohammed.amroune@yahoo.fr

[3] *Department of Electrical Engineering, University of Ferhat Abbas Setif 1, Setif 19000, Algeria*
slimani_b_linda@yahoo.fr

***Abstract*— In the present paper, a recently developed optimization algorithm called bald eagle search (BES) will be used to solve the optimal power flow (OPF) problem. The main goal is to minimize the active power generation cost of thermal generators. To evaluate the efficiency of the BES algorithm in the OPF problem, the IEEE 30-bus test system will be used. A comparative study will be done to show the efficiency of the BES algorithm compared to other recently developed metaheuristic algorithms such as equilibrium optimization algorithm (EO), marine predator algorithm (MPA), optimization algorithm based on artificial ecosystem (AEO), and slime mold algorithm (SMA), as well as with other well-known algorithms. Based on the results obtained, the BES algorithm gives the best results.**

Keywords: **Power Systems, BES Algorithm, Economic Dispatch.**

I. INTRODUCTION

Optimal power flow (OPF) has remained a widely debated topic in the power systems research community since its inception about half a century ago. The main objective of OPF is to minimize the cost of power generation by optimally setting some control variables. While optimizing power generation costs, system constraints on generator capacity, line capacity, bus voltage, and power flow balance must be satisfied. OPF with thermoelectric generator has been widely studied by researchers around the world.

In recent years, many metaheuristic optimization algorithms such as Genetic Algorithms (GA) [1], Evolutionary Programming (EP) [2], Differential Evolution (DE) [3], Particle Swarm Optimization (PSO) [4], biogeography-based optimization (BBO) [5], gravity search algorithm (GSA) [6], etc. were proposed to solve the OPF problem. The results reported are promising and encouraging for future research in this direction. Most recent literature [7] applied equilibrium optimization algorithm (EO), marine predator algorithm (MPA), artificial ecosystem optimizer (AEO), and slime mold algorithm (SMA) on numerous objectives of OPF for various test systems to show the effectiveness of the algorithms in terms of quality solution. The comparison results proved the superiority of the EO algorithm.

The bald eagle search (BES) algorithm is one of the powerful nature-inspired meta-heuristic optimization algorithms. The main idea of this algorithm is mimicry of the hunting strategy or intelligent social behavior of bald eagles, in nature, as they search for fish [8]. In this paper, the BES algorithm is proposed to solve the OPF problem. The main goal is to optimize the active power generation cost of thermal generators in the power system. To evaluate the effectiveness of the BES algorithm in the OPF problem, the standard IEEE 30-bus network is used as a test system.

II. PROBLEM FORMULATION

A. Objective function

The fuel cost of a thermal generating unit is typically expressed as a quadratic function as shown in Equation (1).

$$f_1 = \sum_{i=1}^{N_G} (a_i + b_i P_i + c_i P_i^2) \quad (\$/\text{h}) . \tag{1}$$

where a_i, b_i, and c_i represent the quadratic cost coefficients of the ith thermal generator, P_i represents the thermal generator's power output, and N_G represents the number of thermal generators.

B. Constraints

To solve the OPF problem, a set of equality and inequality constraints must be satisfied.

Equality constraints are power balance equations designed to maintain an equal power balance between active and reactive powers.

$$P_{gi} - P_{di} - V_i \sum_{j=1}^{NB} V_j \left[G_{ij} \cos(\delta_{ij}) + \mathrm{B}_{ij} \sin(\delta_{ij}) \right] = 0 . \quad (2)$$

$$Q_{gi} - Q_{di} - V_i \sum_{j=1}^{NB} V_j \left[G_{ij} \sin(\delta_{ij}) + \mathrm{B}_{ij} \cos(\delta_{ij}) \right] = 0 . \quad (3)$$

where P_{gi} and Q_{gi} represent the active and reactive powers of the *i*th generator, while P_{di} and Q_{di} represent the active and reactive loads of the *i*th bus.

Inequality constraints represent both the limitations on the physical devices in the power system and the security constraints imposed on the system. Following is a summary of these inequality constraints.

- Voltage magnitude of the thermal generators

$$V_{gi}^{\min} \le V_{gi} \le V_{gi}^{\max} \quad i = 1, 2, ..., N_G . \quad (4)$$

where V_{gi} represents the voltage magnitude of *i*th generator bus, N_G is the number of thermal generators.

- Active and reactive power of the thermal generators

$$P_{gi}^{\min} \le P_{gi} \le P_{gi}^{\max} \quad i = 1, 2, ..., N_{TG} . \quad (5)$$

$$Q_{gi}^{\min} \le Q_{gi} \le Q_{gi}^{\max} \quad i = 1, 2, ..., N_{TG} . \quad (6)$$

Transformers tap

$$T_i^{\min} \le T_i \le T_i^{\max} \quad i = 1, 2, ..., N_{Tap} . \quad (7)$$

where T^{min} and T^{max} are the limits of *i*th tap changer transformer T_i, N_{Tap} is the number of transformers.

- Shunt compensators

$$Q_{Ci}^{\min} \le Q_{Ci} \le Q_{Ci}^{\max} \quad i = 1, 2, ..., N_{Cap} . \quad (8)$$

where N_{Cap} represents the number of shunt compensators.

III. BALD EAGLE SEARCH ALGORITHM

The bald eagle is considered one of the smartest birds in the process of searching for food. These eagles are carnivorous and primarily feed on fish. They are skilled hunters and are known for their impressive fishing abilities. However, they also eat other birds, small mammals, and carrion.

The main key for Bald Eagle Search (BES) optimization algorithm inspiration is its strategy for searching for prey which can be summarized as follows [8]:

A. Select space

In this stage, the eagles begin to take their initial positions/food positions. A suitable space can be determined using the following equation.

$$P_{new,i} = P_{best} + \alpha \times r \left(P_{mean} - P_i \right) . \quad (9)$$

where P_{best} is the search space chosen by bald eagles; α is the control parameter in the interval [1.5 2]; r is a random number in the range [0 1]; P_{mean} designates that these eagles have used up all of the information from the preceding points; P_i is the current position of the eagle.

B. Search in space

In this stage, the eagle updates its position based on equation (10).

$$P_{new,i} = P_i + y(i) \times \left(P_i - P_{i+1} \right) + x(i) \times \left(P_i - P_{mean} \right) . \quad (10)$$

C. Swooping

The swooping strategy of eagles can be described by:

$$P_{new,i} = rand \times P_{best} + x_1(i) \times \left(P_i - c_1 \times P_{mean} \right) + y_1(i) \times \left(P_i - c_2 \times P_{best} \right) . \quad (11)$$

where $c_1, c_2 \in [1, 2]$.

After the aforementioned stages, an initial set of randomly generated candidate solutions is enhanced through several iterations until the global optimum has been achieved. The pseudo-code of the complete algorithm is provided in Algorithm 1.

Algorithm 1: BES algorithm

Start
Generate initial population of BES P_i (i = 1, 2, 3, …, n)
Calculate the fitness values of the initial population: $f(P_i)$
Iteration t =1
while t < Max iteration
Select space
for (each point i in the population)
$P_{new} = P_{best} + \alpha \times r \left(P_{mean} - P_i \right)$. (9)
if $f(P_{new}) < f(P_i)$
$P_i = P_{new}$
end if
if $f(P_{new}) < f(P_{best})$
$P_{best} = P_{new}$
end if
end for
Search in space
for (each point i in the population)
$P_{new} = P_i + y(i) \times \left(P_i - P_{i+1} \right) + x(i) \times \left(P_i - P_{mean} \right)$. (10)
if $f(P_{new}) < f(P_i)$
$P_i = P_{new}$
end if
if $f(P_{new}) < f(P_{best})$
$P_{best} = P_{new}$
end if
end for
Swoop
for (each point i in the population)

$$P_{new} = rand \times P_{best} + x_1(i) \times \left(P_i - c_1 \times P_{mean}\right) + y_1(i) \times \left(P_i - c_2 \times P_{best}\right) \quad (11)$$

if $f(P_{new}) < f(P_i)$
$P_i = P_{new}$
end if
if $f(P_{new}) < f(P_{best})$
$P_{best} = P_{new}$
end if
end for
$t = t+1$
end while
end

IV. SIMULATION RESULTS

In this section, the BES algorithm is applied to solve the OPF problem on the standard IEEE 30-bus test system [9]. Figure 2 shows the single-line diagram of this system which consists of six thermal generators at buses 1, 2, 5, 8, 11, and 13, 41 branches, four tap changer transformers, and nine shunt capacitors at buses 10, 12, 15, 17, 20, 21, 23, 24 and 29. The base real power of this test system is 283.4 MW and the reactive power demand is 126.2 MVAr. The minimum and maximum bus voltage limits of generating units are considered between [0.95, 1.1] p.u., while these limits are taken between [0.95, 1.05] p.u. for the remaining buses. The tap tuning for tap changing transformers varies between [0, 0.05] p.u. The limits of VAR sources are assumed to vary between [0, 5] MVAr. The cost coefficients of the thermal generating units are stated in Table I.

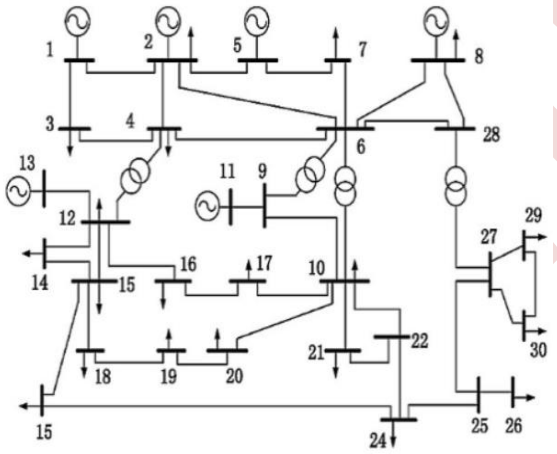


Figure 1. Single line diagram of the IEEE 30-bus test system.

TABLE I. SETTINGS OF THE PARAMETERS OF THE ALGORITHM

Algorithm	Parameters settings	Value
BES	Pupulation size	150
	Maximum number of iterations	500
	Position control parameter (α)	2
	The corner between point search in the central point (α)	10
	Number of search cycles (R)	1.5

TABLE II. COST COEFFICIENTS OF THE THERMAL GENERATING UNITS.

Generator no.	Generator bus	Fuel cost coefficients			P_{min} (MW)	P_{max} (MW)
		a	*b*	*c*		
1	1	0	2	0.00375	50	200
2	2	0	1.75	0.0175	20	80
3	5	0	1	0.0625	15	50
4	8	0	3.25	0.00834	10	35
5	11	0	3	0.025	10	30
6	13	0	3	0.025	12	40

A simulation is performed to check the effectiveness of the BES algorithm for solving the OPF problem. The convergence curve of the BES algorithm is shown in Figure 2. From this figure, it is seen that the value of the fuel cost function converges smoothly at a small number of iterations (about 50 iterations), which indicates the ability to quickly reach the optimal global solution. The optimal solutions obtained by the BES algorithm are reported in detail in Table II. The fuel cost for the BES algorithm is found to be 800.4112 $/h.

Table III shows the comparison of BES with other existing methods in the literature. According to these results, the BES algorithm outperforms the Equilibrium Optimizer (EO) [7], Marine Predators Algorithm (MPA) [7], Artificial Ecosystem Optimizer (AEO) [7], Slime Mold Algorithm (SMA) [7], and other algorithms.

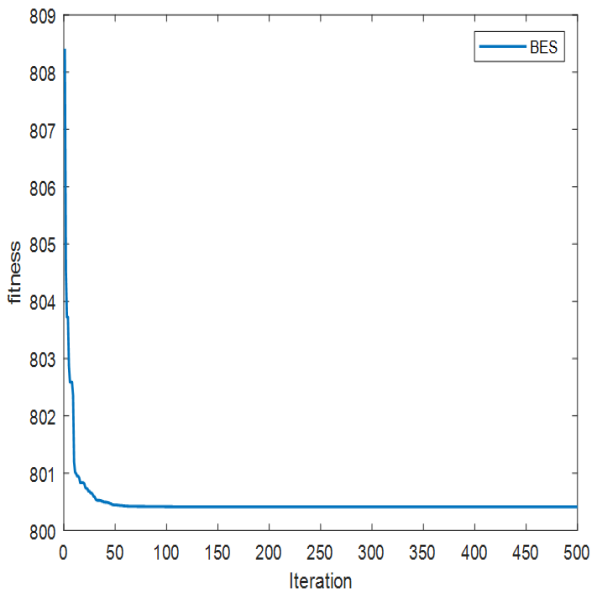


Figure 2. Comparison of the BES algorithm with other algorithms

TABLE III. OPTIMAL SOLUTION OBTAINED USING BES ALGORITHM

Control variables	Min	Max	Optimal values
P_1 (MW)	50	200	177.105
P_2 (MW)	20	80	48.7157
P_5 (MW)	15	50	21.3953
P_8 (MW)	10	30	21.1779
P_{11} (MW)	10	30	11.9381
P_{13} (MW)	12	40	12.0006
V_1 (p.u.)	0.95	1.1	1.0834
V_2 (p.u.)	0.95	1.1	1.0644
V_5 (p.u.)	0.95	1.1	1.0332
V_8 (p.u.)	0.95	1.1	1.0379
V_{11} (p.u.)	0.95	1.1	1.0948
V_{13} (p.u.)	0.95	1.1	1.0447
T_{11} (p.u.)	0.9	1.1	1.0340
T_{12} (p.u.)	0.9	1.1	0.9411
T_{15} (p.u.)	0.9	1.1	0.9641
T_{36} (p.u.)	0.9	1.1	0.9727
Q_{C10} (MVAR)	0	5	0.0030
Q_{C12} (MVAR)	0	5	0.4371
Q_{C15} (MVAR)	0	5	4.0380
Q_{C17} (MVAR)	0	5	5.0000
Q_{C20} (MVAR)	0	5	3.9206
Q_{C21} (MVAR)	0	5	4.9996
Q_{C23} (MVAR)	0	5	2.9404
Q_{C24} (MVAR)	0	5	4.9991
Q_{C29} (MVAR)	0	5	2.3309
Total cost ($/h)	-	-	**800.4112**
CPU Time (s)	-	-	**927.9258**

TABLE IV. COMPARISON OF THE BES ALGORITHM WITH OTHER ALGORITHMS

Algorithm	Fuel cost ($/h)
BES	**800.4112**
EO [7]	800.4235
MPA [7]	800.4262
AEO [7]	800.4836
SMA [7]	800.5683
SP-DE [10]	800.4293
ABCGLN [11]	800.4464
TLBO [12]	800.4604
Jaya [13]	800.4794
PSOGSA [14]	800.4985
MSA [15]	800.5099
SKH [16]	800.5141
ARCBBO [17]	800.5159
GPU-PSO [18]	800.53
ABC [19]	800.6600
MFA [15]	800.6863

V. CONCLUSION

In this paper, a new algorithm called the Bald Eagle Search (BES) algorithm is proposed to solve the OPF problem of power systems with the objective function of minimizing fuel cost. The effectiveness of the proposed BES method to solve the OPF problem is verified by a standard 30-bus test system. The results obtained are compared with other well-established algorithms and it is revealed that the BES algorithm gives better results.

REFERENCES

[1] M.S. Osman, M.A. Abo-Sinna, A.A. Mousa, "A solution to the optimal power flow using genetic algorithm," *Applied Mathematics and Computation*, vol. 155, p. 391-405, 2004.

[2] H.T. Yang, P.C Yang, C.L Huang, "Evolutionary programming based economic dispatch for units with non-smooth fuel cost functions," *IEEE Transactions on Power Systems*, vol. 11, p. 112-118, 1996.

[3] A.A. Abou El Ela, M.A. Abido, S.R. Spea, "Optimal power flow using differential evolution algorithm," *Electr Eng*, vol. 91, p. 69-78, 2009.

[4] M.A. Abido, "Optimal power flow using particle swarm optimization », *J Electr Power Energy Syst*," vol. 24, nº 7, p. 563-571, 2002.

[5] A. Bhattacharya, PK. Chattopadhyay, "Application of biogeography-based optimisation to solve different optimal power flow problems," *IET Gener Transm Distrib*, vol. 5, nº 1, p. 70-80, 2011.

[6] S. Duman, U. Guvenc, Y. Sonmez, N. Yorukeren, Chattopadhyay, "Optimal power flow using gravitational search algorithm," *Energy Convers Manag*, vol. 59, p. 86-95, 2012.

[7] A. Mohamed, "Wind integrated optimal power flow considering power losses, voltage deviation, and emission using equilibrium optimization algorithm," *Energ. Ecol. Environ*, vol. 7, p. 369–392, 2022.

[8] H. A. Alsattar, A. A. Zaidan, B. B. Zaidan, "Novel meta-heuristic bald eagle search optimisation algorithm," *Artif. Intell. Rev*. vol. 53, nº 3, p. 2237–2264, 2020.

[9] D. Zimmerman, E. Murillo-Sanchez, J. Thomas, MATPOWER, "steady-state operations, planning and analysis tools for power systems research and education," *IEEE Trans Power Syst*, vol. 26, nº 1, p. 12–19, 2011.

[10] P. Biswas, N. Suganthan, R. Mallipeddi, G. Amaratunga, "Optimal power flow solutions using differential evolution algorithm integrated with effective constraint handling techniques," *Eng Appl Artif Intell*, vol. 68, p. 81–100, 2018.

[11] C. Bansal, S. Jadon, "Optimal power flow using artificial bee colony algorithm with global and local neighbourhoods *Int J Syst Assur Eng Manag*," vol. 8, p. 2158, 2017.

[12] W. Warid, "Optimal power flow using the AMTPG-Jaya algorithm," *Appl Soft Comput J*, vol. 91, p. 106252, 2020.

[13] W. Warid, H. Hizam, N. Mariun, I. Abdul-Wahab, "Optimal power flow using the Jaya algorithm," *Energies*, vol. 9, nº 9, p. 678, 2016.

[14] J. Radosavljevic, D. Klimenta, M. Jevtic, N. Arsic, J. Thomas, "Optimal power flow using a hybrid optimization algorithm of Particle swarm optimization and gravitational search algorithm," *Electric Power Compon Syst*, vol. 43, p. 1958–1970, 2015.

[15] A. Mohamed, S. Yahia, S. Mohamed, A. El-Gaafary, A. Hemeida, "Optimal power flow using moth swarm algorithm," *Electric Power Syst Res*, vol. 142, p. 190-206, 2017.

[16] H. Pulluri, R. Naresh, V. Sharma, "Application of stud krill algorithm for solution of optimal power problems," *Int Trans Electr Energy Syst*, vol. 27, p. 2316, 2017.

[17] R. Kumar, L. Premalatha, "Optimal power flow for a deregulated power system using adaptive real coded biogeography-based optimization," *Int J Electr Power Energy Syst*, vol. 73, p. 393–354, 2015.

[18] V. Roberge, M. Tarbouchi, F. Okou, "Optimal power flow based on parallel metaheuristics for graphics processing units," *Electric Power Syst Res*, vol. 140, p. 344–353, 2016.

[19] R. Adaryani, A. Karami, "Artificial bee colony algorithm for solving multi-objective optimal power flow problem," *Electr Power Energy Syst*, vol. 53, p. 219–230, 2013.

Enhancing Power Distributed Generation with Storage Systems for Sustainable Energy Integration

Md Jahidur Rahman [1], Tahar Tafticht [1], Mouctar Tchakala [1], Mamadou Lamine Doumbia [2]

[1] *Université du Québec en Abitibi-Témiscaminguer, Rouyn-Noranda, Canada*

mdjahidur.rahman@uqat.ca

tahar.tafticht@uqat.ca

mouctar.tchakala@uqat.ca

[2] *Université du Québec à Trois-Rivières, Trois-Rivières, Canada*

mamadou.doumbia@uqtr.ca

***Abstract*— Distributed Generation (DG) introduces innovative concepts aimed at enhancing the efficiency of power networks and mitigating environmental pollution. However, managing the fluctuations inherent to Renewable Energy Sources (RESs) poses a significant challenge. The natural variability of RESs makes it undesirable to maintain constant power generation. Consequently, the dynamic stability of network frequency becomes increasingly complex, particularly with the substantial integration of RESs. This paper presents a control algorithm designed for a wind-based energy storage system, aiming to enhance the dynamic stability of the overall power grid. The outcomes of this research demonstrate a notable reduction in both the transient time of wind power flow and the frequency fluctuation rate, compared to previous studies. To enhance network stability, a storage system (battery) is employed to store surplus energy, thereby minimizing wastage from wind turbine power generation.**

Keywords: **Distributed Generation, Wind Energy, Storage System, Power Stability, Frequency Control.**

I. INTRODUCTION

In recent years, substantial transformations have taken place in power generation and consumption technologies, primarily driven by growing concerns about rapid climate change. Numerous countries have set ambitious goals to reduce greenhouse gas emissions by 20% by 2020 and have sought solutions through the incorporation of RESs like wind, solar, and hydro energy, particularly through the adoption of DG systems. Presently, DG is at the forefront of developing innovative concepts to enhance the efficiency of power networks while minimizing environmental air pollution [1] [2]. The increasing global demand for electricity, driven by factors such as population growth, urbanization, and industrialization, has placed unprecedented strain on existing power generation and distribution infrastructure. Conventional centralized power generation systems, heavily reliant on fossil fuels, not only struggle to meet this surging demand but also give rise to significant environmental issues, including greenhouse gas emissions and resource depletion. In response to these challenges, DG, when coupled with Energy Storage Systems (ESS), has emerged as a promising paradigm shift in the energy sector [3]. DG, characterized by small-scale, decentralized power generation units located proximate to the point of consumption, offers a viable alternative to traditional centralized power plants. These Distributed Energy Resources (DERs) encompass a diverse array of technologies, including solar photovoltaics, wind turbines, microturbines, and fuel cells, enabling flexibility and adaptability within local power grids. However, the intermittent nature of many renewable energy sources, especially solar and wind, underscores the necessity of integrating energy storage systems [4]. These systems are essential to ensure a dependable and uninterrupted power supply while enhancing grid stability in the face of fluctuating energy generation. Various control algorithms, including proportional-integral-derivative (PID) controllers and advanced control strategies, are used to manage the frequency of power systems by adjusting energy storage and generation [5]. Predictive control methods, such as model predictive control (MPC), have been studied to improve the performance of energy storage systems by predicting future energy demand and adjusting storage accordingly [6]. This conference paper explores the critical synergy between distributed generation and energy storage systems, addressing their role in achieving sustainability, grid resilience, and energy independence [7] [8]. To enhance energy efficiency and avoid excessive energy wastage in a high-penetration DG network system, we have proposed an innovative control technique. This approach is designed to optimize the regulation of wind power distribution and frequency while seamlessly integrating a storage system into the network. Consequently, this development aims to effectively manage various parameters, ensuring the sustained and optimal flow of wind power frequency within the power grid, while also facilitating the increased integration of DG. The simulation was performed using the MATLAB Simulink software.

The rest of this paper can be highlighted as follows: Section II describes distributed generation power networks.

Section III presents the control techniques of distributed generation power networks. Section IV presents the control method implemented within the network. Section V presents the simulation results and discussions, and finally, Section VI concludes the paper.

II. Distributed Generation Power Networks

A. Wind Turbine

The wind DG system is outfitted with an Asynchronous Machine (ASM) boasting a power rating of 480 kVA and an inertia of 2 seconds. The primary purpose of the wind DG is to generate Pwind, which is wind power used to control the rotational speed of the ASM shaft and, consequently, determine its mechanical torque. In this context, the DG is regarded as a power generator operating at a constant velocity, and as such, it does not allow for control over its pitch angle [7] [9].

B. Energy Storage System

The Energy Storage System (ESS) comprises a battery bank. The bidirectional IGBT bridge transistor, with a power rating of 150 kW (PS_NAME = 150 kW), is controlled in current mode. The primary function of the IGBT transistor is to convert DC sources into AC sources at the interface of the ESS, which connects to an isolated power network. The ESS has a rated capacity of 390 Ah at a voltage of 240 V, enabling it to charge and discharge according to the load demands of the power network. Fig. 1 illustrates the control scheme for the Current Controlled Inverter (CCI). The control methodology for the CCI involves a structure based on rotating dq-coordination. To synchronize with the grid voltage waveform, a phase-locked loop (PLL) is employed to provide the reference for the dq-abc and abc-dq transformations. The CCI's output current is computed and transformed within the rotating frame, with both active and reactive currents being regulated in all four quadrants to generate a Pulse Width Modulation (PWM) signal. This control process is executed using a PID controller. Additionally, an LC filter is integrated into the CCI to minimize current ripples. To connect the ESS to an isolated network, a step-down transformer rated at 120 kV / 480V and 150 kVA is utilized [4] [7].

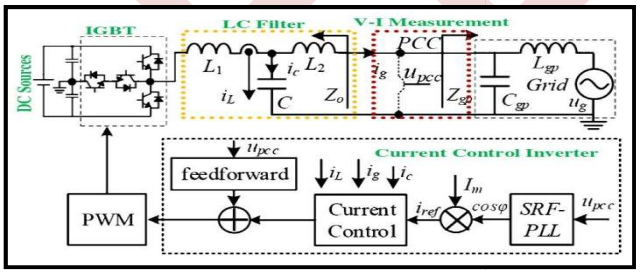


Figure 1. Block diagram of ESS and power converter.

C. Secondary Load System

The secondary load system, named Dump Load (DL) plays a crucial role in regulating the system frequency by absorbing surplus wind energy corresponding to consumer demand. It is composed of eight sets of three-phase resistors connected in series with Gate turn-off thyristor switches. The nominal power of all these resistors is adjustable in a binary (8-bit) fashion, enabling them to absorb wind power as needed by the DL. The load can be modified within a range of 0 to 446.25 kW, with increments of 1.75 kW. The primary purpose of the DL is to manage fluctuations in the power grid's frequency by consuming excess power generated by the wind turbine, ensuring that the battery remains unchanged [4] [8] [10].

D. Synchronous Condenser

The Synchronous Condenser, rated at a nominal power of 300 kVA, produces a voltage signal to manage network voltage when the diesel engine is inactive. Its voltage regulator is responsible for modulating the condenser's excitation to deliver reactive power at a consistent voltage level across various buses. In this context, the primary role of the synchronous condenser is to provide reactive power within the DG network [7].

III. Control Techniques of Distributed Generation Power Networks

In order to control the network frequency, it's essential to produce and utilize an immediate amount of active power through the loads. To sustain the target level of wind power injection, the DL absorbs the active power that the Energy Storage System (ESS) cannot store due to its capacity constraints [4] [7] [11]. In this scenario, P_T (Wind turbine generated power) exceeds P_L (Load consumed power) when P_S (ESS supplied power) is greater than 0. The ESS contributes energy to the Wind-Disel Hybrid Power System (WDHPS). Conversely, when P_S is less than 0, P_T falls short of P_L, resulting in the ESS drawing power from the WDHPS.

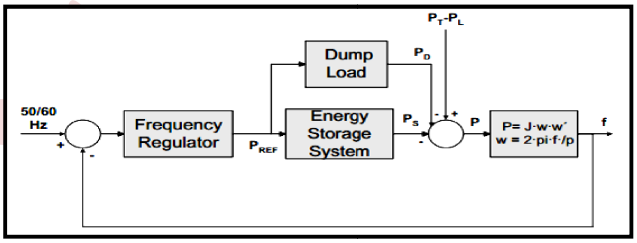


Figure 2. The control scheme of the WDHPS system.

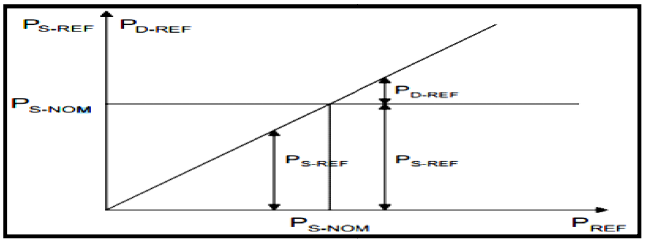


Figure 3. Power sharing strategy between the ESS and DL.

Fig. 2 and 3 illustrate the underlying concept of the frequency control scheme for a WDHPS and the approach to power distribution between ESS and DL, respectively [3, 10]. In this context, a three-phase-locked loop (PLL) is employed to monitor the frequency error, which represents the deviation between the reference frequency (60 Hz) and the actual network frequency. The PLL generates P_{REF} (Power-Sharing Priority Reference) to establish the priority of power allocation between the ESS and DL through a logical algorithm shown in

Fig. 4. Under normal operating conditions, the power level at the ESS node remains at its nominal value.

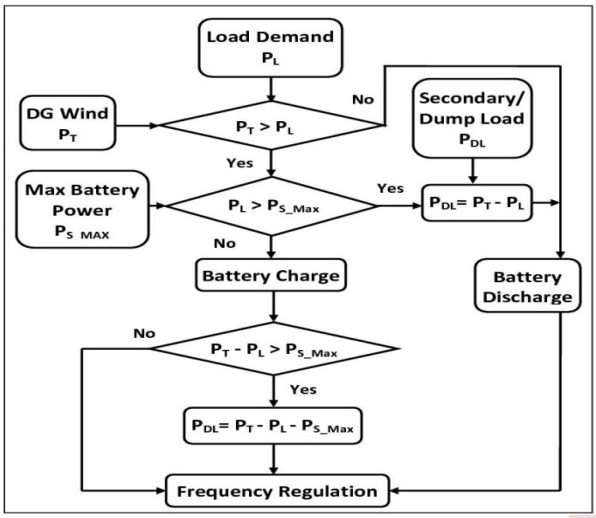


Figure 4. Power sharing strategy between the ESS and DL.

The control strategies for both the ESS and DL systems need to be synchronized. The DL's role is to absorb any excess wind power that the ESS is unable to store. Hence, we can express this as follows:

$$P_T - P_L = P_D + P_S \quad (1)$$

$$P_{REF} = P_{S_REF} + P_{D_REF} \quad (2)$$

$$P_{D_REF} = 0 \ when \ P_{REF} < P_{S_NOM} \quad (3)$$

When the ESS reaches its maximum capacity (PS-REF), equation 2 simplifies to $P_{D\text{-}REF} = P_{REF}$. In cases where the P_{REF} exceeds the ESS's nominal power, the DL plays a crucial role in absorbing the excess wind power. The $P_{S\text{-}MAX}$ is adjusted within the range of 0 and $P_{S\text{-}NOM}$ through the utilization of a PLL signal. The distribution of power between the ESS and DL is determined by a priority-based consumption algorithm. In other words, the DL exclusively utilizes surplus power that cannot be stored by the ESS.

However:

$$P_{S_REF} = P_{REF} \ when \ P_{REF} \leq 0 \quad (4)$$

$$P_{S_REF} = P_{S_MAX} \ when \ P_{RFE} > 0 \quad (5)$$

In:

$$P_{D_REF} = P_{REF} - P_{S_MAX} \ when \ P_{RFE} > 0 \quad (6)$$

$$P_{D_REF} = 0 \ when \ P_{RFE} \leq 0 \quad (7)$$

The ESS and DL must jointly acknowledge the P_{REF} and ensure precise synchronization during their operation. Consequently, three distinct control techniques can be employed:

- Utilizing the DL exclusively when the ESS is fully charged, with the condition $P_{S\text{-}MAX} < P_T - P_L$, resulting in $P_S = 0$.
- Relying solely on the ESS (PD = 0) when $|P_T - P_L|$ is less than or equal to P_{S_NOM}.
- Engaging both the ESS and DL when $P_{REF} > 0$ and $P_T - P_L > 0$.

IV. CONTROL METHODS IMPLEMENTED WITHIN THE NETWORK.

The analysis of wind power flow and network frequency stability was conducted using a PID controller. Fig. 5 displays the operational block diagrams for the PID controllers.

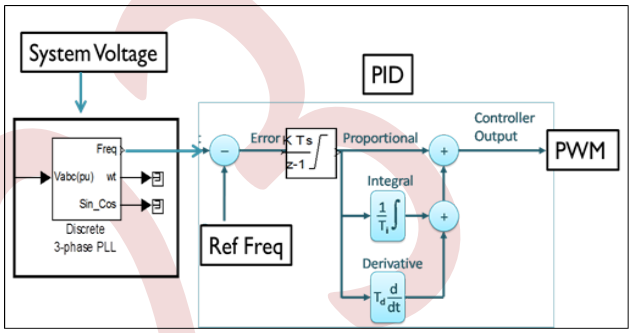


Figure 5. Operational scheme of distributed generation network.

A three-phase PLL was employed to enhance the amplification of the network frequency. The network voltage serves as the input for the PLL. In the process of generating a frequency error, a reference frequency of 60 Hz is generated and compared to the network frequency. Subsequently, the frequency error is integrated to obtain a phase error. Finally, this phase error is processed by a PID controller to generate an output signal that achieves the desired level of load power.

In this paper, we investigated the frequency dynamics within a power network while incorporating a storage system in various scenarios. The study was based on a model developed for the WDHPS. This approach, initially promoted by Hydro-Quebec for remote areas, aimed to minimize electricity costs by harnessing wind power. The maximum wind power capacity within the network is contingent upon accessible wind resources and fuel costs [4]. To conduct this study, we utilized specific components, including a 480 V, 275 kVA wind turbine with an induction generator, a 480 V, 300 kVA synchronous generator, a variable secondary load ranging from 0 to 446.25 kW, a 240 V, 390Ah battery, and a 230 kW consumer load, as per the different scenarios examined.

In this particular case study, we examined two distinct modes of power system operation and control:

- Case 1: Occurring when wind power (P_T) surpasses the total load (P_L). In this scenario, the battery (P_S) is charged.
- Case 2: This takes place when wind power (P_T) falls below the total load (P_L). Here, the battery (P_S) is discharged.

Table 1 highlights data from the tested system.

TABLE I. DATA OF TESTED SYSTEM

Sources	Symbols/Parameters
Synchronous Generator	Synchronous Generator: 480 V, 300 kVA
Wind Turbine	480 V, 275 kVA, Pnom= 200 kW Vwind_nom= 10 m/s Pitch angle 0^0 , P=Pnom & V=Vnom
Load Buses	Synchronous Condenser Bus (SC) Main Load Bus (Load) Secondary/Dump Load Bus (DL) Storage System (SS) Wind Turbine Bus (WT)
Loads	Main Load 100 kW Extra Load 50 kW + 30 kW + 45kW Dump Load vary 0 to 446.25 kW by step of 1.75 kW
Transformer	150 kVA, 120 kV/ 480 V
Energy Storage	240V, 390 Ah, SOC 50%

V. SIMULATION RESULTS AND DISCUSSIONS

A. When Wind Power P_T > Total Load P_L

To generate a sufficient power supply, the wind turbine needs to maintain a wind velocity of 10 m/s. In this configuration, the diesel generator remains inactive, while the synchronous machine operates as a synchronous condenser by setting the mechanical power input (Pm) to zero. At a wind turbine operating velocity of 10 m/s, we achieve an output power of 206 kW. However, it's worth noting that 200 kW is effectively produced by the wind turbine after accounting for losses in the Asynchronous Machine (ASM).

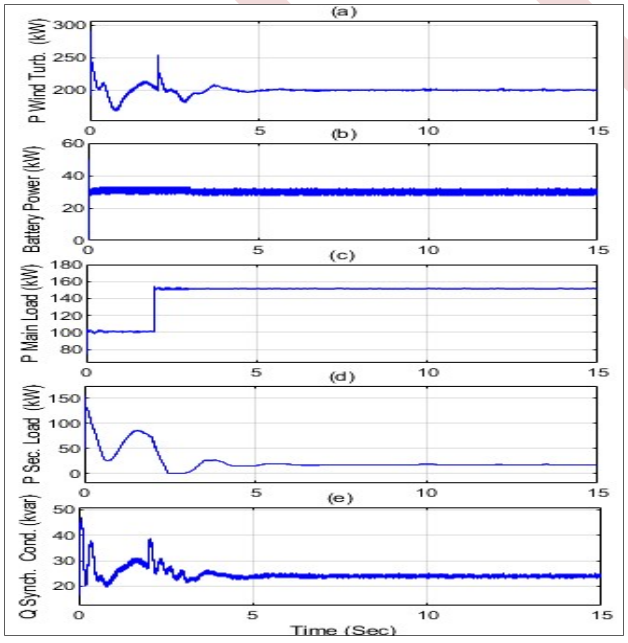


Figure 6. (a) Wind turbine power output, (b) Battery power output, (c) Main load power consumption, (d) Secondary load power consumption, (e) Reactive power from condenser when wind power P_T > total load P_L.

Due to some asynchronous machine losses, the wind turbine generates 200 kW shown in Fig. 6 (a). Fig 6 (b) shows the battery is charging (rate of 30 kW) at 3s. Fig. 6 (c) shows the consumer (main) load is 100 kW. At 2s, an extra 50kW has been added. So the secondary/dump load absorbs 20 kW to regulate a 60 Hz frequency shown in Fig. 6(d). To maintain an acceptable voltage level within the power network, the synchronous condenser supplies reactive power at a rate of 24 kVA, as shown in Fig. 6 (e).

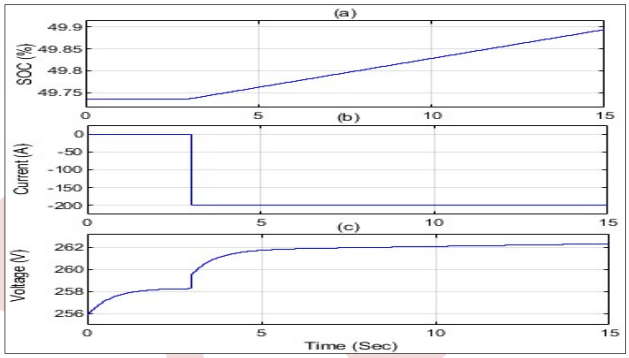


Figure 7. (a) Battery state of charge (SOC), (b) Battery current, and (c) Battery voltage during charging when wind power P_T > total load P_L.

Fig. 7 (a) shows the state of charge (SOC) of the battery is depicted at 50%, and it begins charging at 3s. Throughout the simulation, the battery charge increases from 49.75% to 49.9%. Fig. 6 (b) illustrates the battery's current status. Prior to 3s, the battery current was at zero. However, after 3s, the battery registers a current of -200 a as it charges itself at a rate of 30 kW. In Fig. 6 (c), the voltage is shown to increase at 3s and remains stable at 262 v until the conclusion of the simulation.

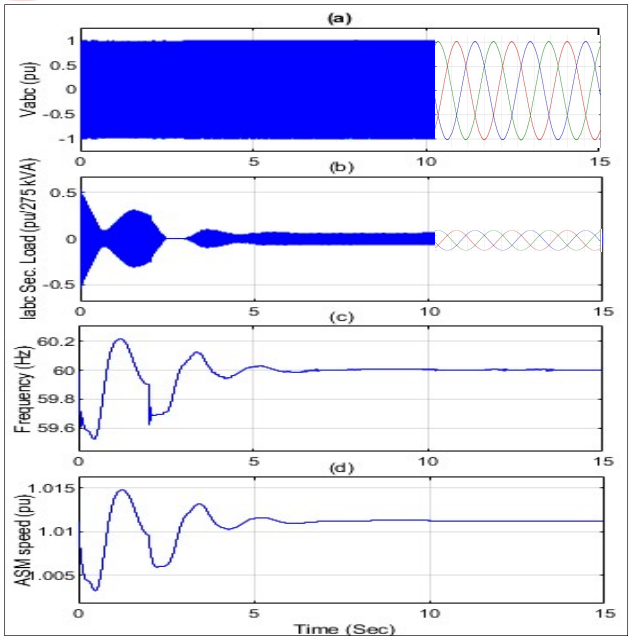


Figure 8. (a) Load bus voltage (b) Secondary load current (c) Load bus frequency (d) Asynchronous generator speed when wind power P_T > total load P_L.

Fig. 8 (a) depicts a constant load voltage of 1 (per unit) within the observation window of 10s to 15s. In Fig. 8 (b), the secondary load current exhibits a decrease at 2.5s, attributed to an additional 50 kW load, and at 3s, as the battery begins charging at a rate of 30 kW. Fig. 8 (c) shows that after 15s of simulation, the frequency initially drops to 59.62 Hz at 2.5s, which is due to the introduction of an extra 50 kW load. Subsequently, at 3s, the battery starts charging at a rate of 30 kW. Fig. 8 (d) shows that the asynchronous machine's speed remains above 1.011 per unit, indicating it operates in generator mode.

B. When Wind Power P_T < Total Load P_L

To generate a sufficient power supply, the wind turbine needs to maintain a wind velocity of 10 m/s. In this configuration, the diesel generator remains inactive, while the synchronous machine operates as a synchronous condenser by setting the mechanical power input (Pm) to zero. At a wind turbine operating velocity of 10 m/s, we achieve an output power of 206 kW. However, it's worth noting that 200 kW is effectively produced by the wind turbine after accounting for losses in the Asynchronous Machine (ASM).

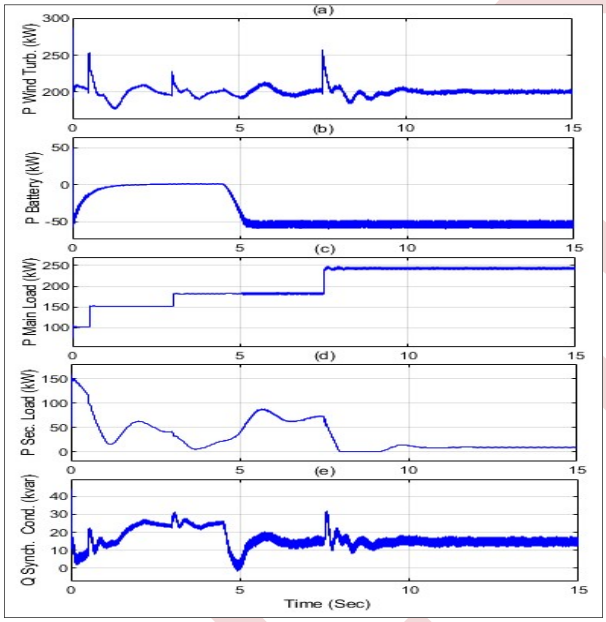


Figure 9. (a) Wind turbine power output, (b) Battery power output, (c) Main load power consumption, (d) Secondary load power consumption, (e) Reactive power from condenser when wind power P_T < total load P_L.

Fig. 9 (a) illustrates the wind turbine generating 200 kW of power. In Fig. 9 (b), the battery is discharging at 4.5s, at a rate of 50 kW. Fig. 9 (c) depicts the primary consumer load consistently at 100 kW. However, additional loads of 50 kW at 0.5s, 30 kW at 3s, and 45 kW at 7.5s are introduced, resulting in a total system load of 230 kW. Consequently, the secondary load absorbs 20 kW to maintain a 60 Hz frequency in the network, as shown in Fig. 9 (d). To maintain an acceptable voltage level within the power network, the synchronous condenser supplies reactive power at a rate of 15 kVA, as shown in Fig. 9 (e).

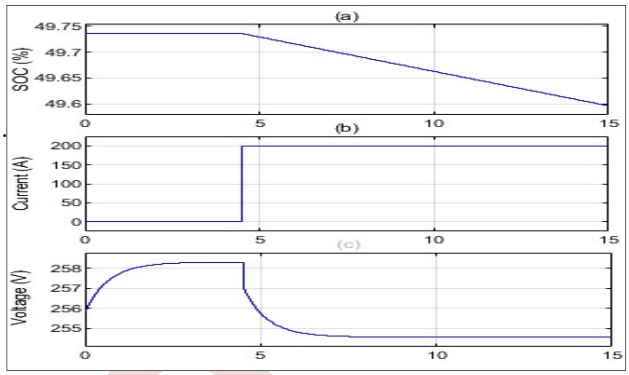


Figure 10. (a) Battery state of charge (SOC), (b) Battery current, and (c) Battery voltage during charging when wind power P_T < total load P_L.

Fig. 10 (a) displays the State of Charge (SOC) of the battery, initially at 50%, and discharging at 4.5s. By the end of the simulation, the battery's charge had reduced from 49.73% to 49.60%. In Fig. 10 (b), the battery's current status is presented. Prior to 4.5s, the battery's current was at zero. However, starting from 4.5s, the battery exhibits a current of 200 A as it discharges at a rate of 50 kW to maintain network loads. Fig. 10 (c) illustrates the voltage, which drops at 4.5s and then remains constant at 254 V until the end of the simulation.

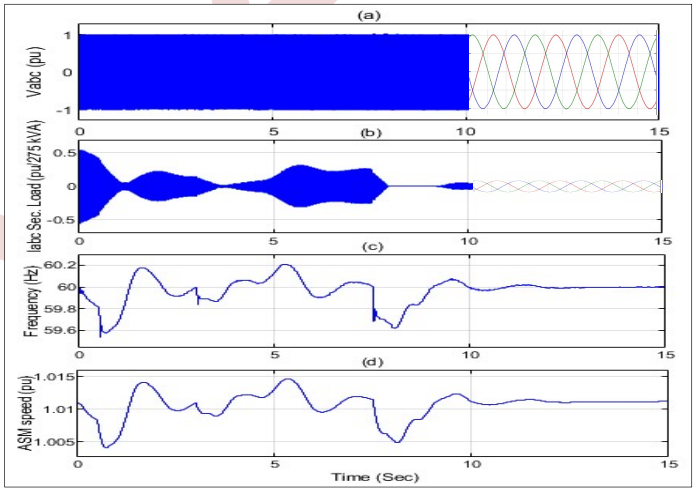


Figure 11. (a) Load bus voltage (b) Secondary load current (c) Load bus frequency (d) Asynchronous generator speed when wind power P_T < total load P_L.

Figure 11 (a) shows that the load voltage remains at 1 (per unit) throughout the observation period, which spans from 10s to 15s. In Figure 11 (b), the secondary load current decreases at 0.5s, 3s, and 7.5s, due to additional loads of 50kW, 30kW, and 45kW, respectively. At 4.5s, the current decreases further due to the battery discharging at a rate of 50kW. Subsequently, the load current remains steady at 0.1 (per unit) until the end of the simulation. Figure 11 (c) demonstrates that after 15 seconds of simulation, the frequency drops to 59.58 Hz, 59.82 Hz, and 59.60 Hz at 0.5s, 3s, and 7.5s, respectively, due to the extra loads of 50kW, 30kW, and 45kW. At 4.5s, the battery begins discharging at a rate of 50kW to meet the high load demand. Figure 11 (d) shows that the asynchronous machine's speed

remains above 1.011 per unit, indicating it operates in generator mode.

From the simulation results, it is evident that a storage system (battery) is effectively utilized to balance power generation and load demand, avoiding the need to dissipate excess power into a secondary/dump load in order to maintain an acceptable frequency level within the system.

VI. CONCLUSION

This paper explores the technology related to Distributed Generation (DG) wind power flow and frequency fluctuation behavior associated with wind turbines, offering simulations to better understand these aspects. It also briefly outlines methods for frequency control and discusses how energy storage can effectively address the challenges posed by the high penetration of wind turbines. The study investigates frequency fluctuations in the load bus using a PID controller and highlights the potential of using a storage system to store excess energy for subsequent supply during periods of high load demand relative to wind turbine power generation. However, it's important to note that the response of the battery, contingent on its specific dynamics, may be slow, depending on the technology employed, and could introduce significant frequency variations. The simulation introduces varying levels of additional load at different times to assess the system's frequency stability under the influence of the PID controller. For future work, advancements in DG wind power technology can be analyzed to improve frequency control mechanisms and energy storage solutions to address the challenges posed by high wind turbine penetration. Research can explore more sophisticated control strategies and technologies to ensure an efficient and reliable energy supply during varying load demands.

REFERENCES

[1] D. Lai, C. Chen, S. Tang, Z. Bie and J. Wang, "Analytical Derivation of Frequency Response Rate Constraint in Distribution System Restoration With Single Master Diesel-Based DG," in *IEEE Transactions on Smart Grid*, vol. 14, no. 2, pp. 1341-1344, March 2023, doi: 10.1109/TSG.2022.3227752.

[2] M. Dashtdar *et al*., "Improving the Power Quality of Island Microgrid With Voltage and Frequency Control Based on a Hybrid Genetic Algorithm and PSO," in *IEEE Access*, vol. 10, pp. 105352-105365, 2022, doi: 10.1109/ACCESS.2022.3201819.

[3] M. H. Nazari, M. Ilić and J. P. Lopes, "Dynamic stability and control design of modern electric energy systems with large penetration of distributed generators, "*2010 IREP Symposium Bulk Power System Dynamics and Control - VIII (IREP)*, Rio de Janeiro, 2010, pp. 1-7, doi: 10.1109/IREP.2010.5563270.

[4] Mott, L., B. Saulnier. 2014. "Commercial Wind-Diesel Project, St. Paul Island, Alaska," *14th Prime Power Diesel Inter-Utility Conference*, May 28-June 2, Winnipeg, Manitoba, Canada.

[5] Elkasem, A. H., Khamies, M., Hassan, M. H., Nasrat, L., & Kamel, S. (2023). Utilizing controlled plug-in electric vehicles to improve hybrid power grid frequency regulation considering high renewable energy penetration. *International Journal of Electrical Power & Energy Systems*, 152, 109251.

[6] Zhu, J., Cui, X., & Ni, W. (2022). Model predictive control based control strategy for battery energy storage system integrated power plant meeting deep load peak shaving demand. *Journal of Energy Storage*, 46, 103811.

[7] Sebastián, R. & Quesada, J., 2006. "Distributed control system for frequency control in a isolated wind system," *Renewable Energy, Elsevier,* vol. 31(3), pages 285-305.

[8] N. E. L. Yakine Kouba, M. Menaa, M. Hasni and M. Boudour, "Load Frequency Control in multi-area power system based on Fuzzy Logic-PID Controller," *2015 IEEE International Conference on Smart Energy Grid Engineering (SEGE)*, Oshawa, ON, 2015, pp. 1-6, doi: 10.1109/SEGE.2015.7324614.

[9] J. Choi, S. I. Habibi and A. Bidram, "Distributed Finite-Time Event-Triggered Frequency and Voltage Control of AC Microgrids," in *IEEE Transactions on Power Systems*, vol. 37, no. 3, pp. 1979-1994, May 2022, doi: 10.1109/TPWRS.2021.3110263.

[10] Sockeel, N.; Gafford, J.; Papari, B.; Mazzola, M. Virtual Inertia Emulator-Based Model Predictive Control for Grid Frequency Regulation Considering High Penetration of Inverter-Based Energy Storage System. *IEEE Trans. Sustain. Energy* 2020.

[11] Ahshan, R.; Saleh, S.; Al-Badi, A. Performance Analysis of a Dq Power Flow-Based Energy Storage Control System for Microgrid Applications. *IEEE Access* 2020, *8*, 178706–178721.

Use of the dual stator induction machine in a hybrid renewable energy pumping system.

1st Arezki Adjati [1], 2nd Toufik Rekioua [2], 3rd Djamila Rekioua [3]

[1] *Industrial and Information Technology Laboratory, Faculty of Technology, A.Mira University, Bejaia, Algeria*
arezki.adjati@univ-bejaia.dz

[2] *Industrial and Information Technology Laboratory, Faculty of Technology, A. Mira University, Bejaia, Algeria*
to_reki@yahoo.fr

[3]*Industrial and Information Technology Laboratory, Faculty of Technology, A. Mira University, Bejaia, Algeria*
dja_rekioua@yahoo.fr

***Abstract*— In this article, we propose a hybrid power supply of a water pumping station. The combination of photovoltaic, wind turbine and fuel cell (FC) powers the dual stator inductor motor (DSIM) that drives the centrifugal pump. The novelty of this contribution is to replace the usual actuators used for pumping by a DSIM motor that offers power segmentation and a possibility to operate in degraded mode. Adoption of FC helps get rid of carbon dioxide to migrate to hydrogen.**

I. INTRODUCTION

Bernal-Agustin & al [1] insist on the need for the adoption of hybridization in remote, off-grid areas. Bajpai and Dash [2] offer hybridization to any stand-alone application in order to provide uninterrupted power without greenhouse gas emissions. Zarour [3] ensured through his study, the complementarity between solar and wind energy. Bouzidi [4], through his efforts, has summarized by a comparative study, the advantages and disadvantages of photovoltaic and wind systems.

Hajdidj et al [5] had introduced a battery storage system in the PV-wind hybrid system and stated that the failure of one of the sources is the main obstacle to energy production for hybrid systems. Ipsakis and his team [6] proposed management strategies for a hybrid system with hydrogen storage. Dufo-Lapez [7] drew the intention on the additional cost of hydrogen storage compared to conventional systems.

In this contribution, it is wise to study the behavior of the sources involved in order to ensure continuity of service despite the random characteristics of renewable energies. The adoption of the DSIM must ensure the continuity of pumping even if half of the power phases are out of service.

II. COMPONENTS OF HYBRID PUMPING SYSTEM

In order to ensure the continuous supply of water to a locality we proposed a combination illustrated in Figure 1.

The system contains a photovoltaic power generator (GPV), a wind turbine which drives a double star asynchronous generator (DSIG) and a fuel cell (FC) as energy sources used to power a double star asynchronous motor (DSIM) used to drive a centrifugal pump and power an electrolyzer to produce hydrogen.

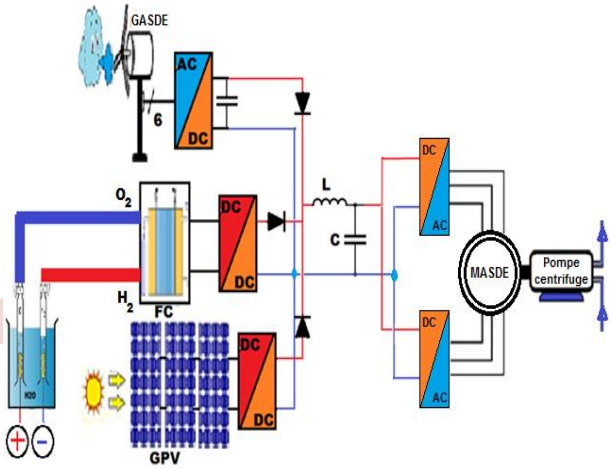


Figure 1. Hybrid photovoltaic-wind-FC installation [8]

III. MODELLING OF THE PHOTOVOLTAIC GENERATOR

In order to improve the efficiency of the GPV, mathematical models developed to identify the multiple parameters having non-linear behavior in order to be able to control them [9, 10].

In the case where all the cells used are identical and operate under the same conditions, figure (2) represents the equivalent electrical diagram of the GPV [8].

Each group of panels requires an «np» number of branches in parallel consisting of a number of cells «ns» in series.

$$\begin{vmatrix} V_G = n_s.V \\ I_G = n_p.I \\ I_{rp} = n_p.i_{rp} \\ R_p = \frac{n_s}{n_p}.r_p \end{vmatrix} \quad and \quad \begin{vmatrix} V_d = n_s.v_d \\ I_d = n_p.i_d \\ I_{ph} = n_p.i_{ph} \\ R_s = \frac{n_s}{n_p}.r_s \end{vmatrix} \quad (1)$$

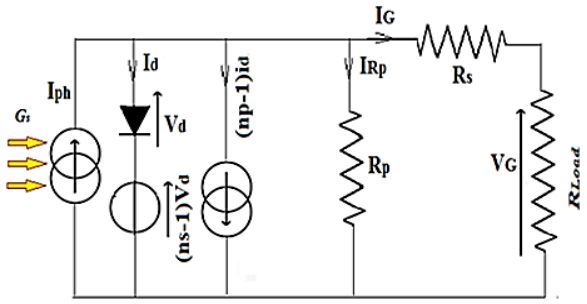


Figure 2. Electrical diagram of a group of panels "single diode model" [8].

The following relation gives the current delivered by the photovoltaic panel [8]:

$$I_G = P_1 G_s + P_1 P_2 G_s (G_s - G_{sref}) + P_1 P_3 G_s (T_j - T_{jref}) - \frac{V_G + R_s I_G}{R_p} - P_4 T_j^3 exp\left(\frac{-E_g}{K.T_j}\right)\left[exp\left(\frac{e(V_G + R_s I_G)}{A.K.T_j}\right) - 1\right] \quad (2)$$

The coefficients A, P1, P2, P3, and P4 are:

$$P_1 = 0.00345\ ;\ P_2 = \frac{P_4}{V_{co}}\ ;\ P_3 = ln\left(\frac{I_{cc}(1+P_1) - I_m}{P_1 I_{cc}}\right)$$

$$P_4 = ln\left(\frac{1+P_1}{P_1}\right);\ A = ln\left(\frac{P_3}{P_4}\right)/ln\left(\frac{V_m}{V_{co}}\right)$$

IV. MODELING THE WIND TURBINE

The wind turns the turbine, which picks up some of the energy swept by the blades and transfers it to the hub attached to the turbine shaft, which then transmits the mechanical energy to the DSIG via a speed multiplier.

A. Theoretically recoverable available wind energy

The kinetic energy as a function of mass and wind speed is [11]:

$$E_c = \frac{1}{2}mv^2 \quad (3)$$

The average available power contained in the form of kinetic energy associated with a displacement of an available air mass on a surface S [m²] of a wind turbine is [8, 12]:

$$P = \frac{1}{2}\rho_{air} S v^3 \quad (4)$$

B. Really recoverable wind energy

Wind energy truly recoverable is;

$$P_{recup} = \frac{1}{2}.\frac{16}{27}\rho S v_1^3 = \frac{1}{2}C_p \rho S v_1^3 \quad (5)$$

C. Power coefficient Cp

For a small wind turbine, the analytical equation of the power coefficient Cp as a function of λ is [8, 13]:

$$C_p(\lambda) = 7{,}9563.10^{-5}\lambda^5 - 17{,}375.10^{-4}\lambda^4 - 9{,}86.10^{-3}\lambda^3 - 9{,}41.10^{-3}\lambda^2 + 6{,}38.10^{-2}\lambda + 0.001 \quad (6)$$

D. Aerodynamic power

With R[m] the length of a blade, the aerodynamic power is [8, 14]:

$$P_{wind} = \frac{1}{2}\rho\pi R^2 C_p(\lambda) v^3 \quad (7)$$

E. Turbine torque

The turbine toque is [8, 14]:

$$C_T = \frac{P_T}{\Omega_T} = \frac{1}{2}\rho\pi R^3 C_p(\lambda) v^2 \quad (8)$$

V. STUDY OF THE DSIG

The capacitors used for self-priming of the GASDE, represented by figure 3 have a value of 40µF. The rectifier is a double parallel PD3. Two rectifiers used for the two stars of the DSIG [8, 15].

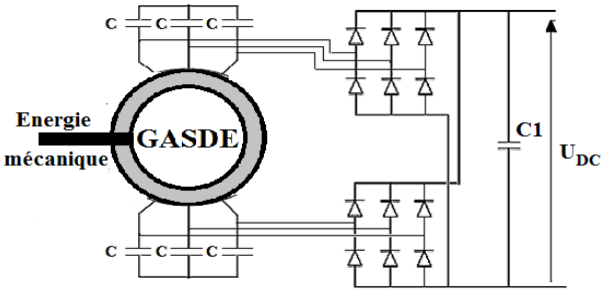


Figure 3. Dual PD3 rectifier of the voltage generated by the DSIG [8]

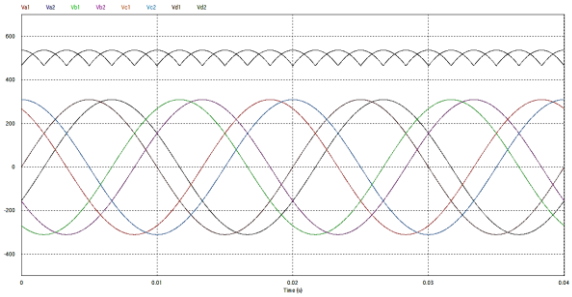


Figure 4. Voltage at Rectifier Inlet and Outlet (PSIM)

The average value of the rectified voltage is [8]:

$$U_{dc} = \sqrt{3}\, V_m \frac{sin\frac{\pi}{6}}{\frac{\pi}{6}} \quad (9)$$

In addition, the effective value of the straightened tension is:

$$U_{eff} = V_m \times \sqrt{\frac{3\times\left(1+sin\frac{2\pi}{6}\right)}{2\times\frac{2\pi}{6}}} \quad (10)$$

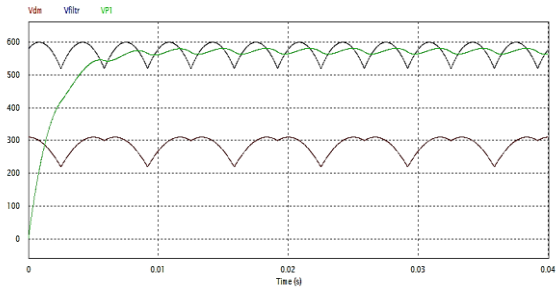


Figure 5. Shape of rectified voltages (PSIM)

Figures 4 and 5 shows that the output voltage of the rectifier is composed of the sum of the two rectified voltages with a frequency equal to 6 times the frequency of the source.

In order to be able to power the DSIM inverters, the voltages generated by the GSID are converted.

VI. MODELING OF THE PEMFC

PEMFC technology allows a low operating temperature not exceeding 100°C and has a rapid start-up and easy heat dissipation [16].

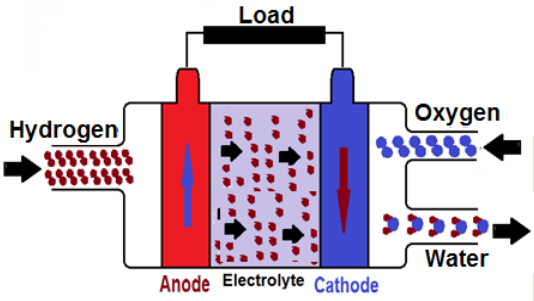


Figure 6. Proton exchange membrane Fuel Cell "PEMFC" [8, 17].

The hydrogen cell uses hydrogen as a fuel, and oxygen as an oxidizer, usually taken from ambient air. The hydrogen used is either stored in compressed gas cylinders or in metal hydrides or produced by water reforming of different fuels [17].

To describe the chemical reactions at the anode and cathode levels of the FC, several models exist in the literature, including that of the evolution of the voltage, which combines empirical models with elementary laws [8, 16].

Indeed, Maxwell's equations model the transport of matter, Nernst's equations, the thermodynamic equilibrium potentials and Tafel's equations take care of activation overvoltage. Nernst-Planck equations determine internal resistance [16, 23].

This equation give the global real potential of the Proton Exchange Membrane Fuel Cells (PEMFC):

$$U_{FC} = E_{Nernst} - V_{act} - V_{ohm} - V_{conc} \quad (11)$$

Equivalent electrical circuit represent the dynamic behavior of the fuel cell [8, 16]:

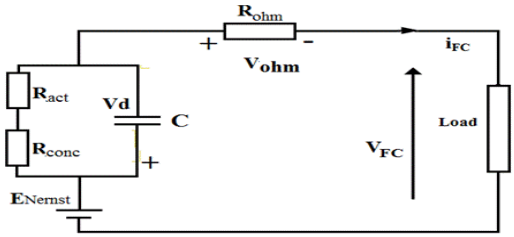


Figure 7. Equivalent dynamic electrical diagram of a FC [16].

TAFEL equation give the activation losses:

$$V_{act} = A \times \ln\left(\frac{I_{FC}+I_n}{i_0}\right) \quad (12)$$

The ohmic losses with Rm total resistance of the FC:

$$V_{ohm} = R_m \times (I_{FC} + I_n) \quad (13)$$

The Concentrations losses:

$$V_{conc} = -B \times \ln\left(1 - \frac{I_{FC}+I_n}{I_L}\right) \quad (14)$$

Nernst voltage is the thermodynamic equilibrium potential defined for standard temperature and pressure values and is write as follows [16]:

$$E_{nernst} = 1.229 - 0.85.10^{-3}(T - 298.15) + 4.31.10^{-5}T\left[\ln(PH_2) + \tfrac{1}{2}\ln(PO_2)\right] \quad (15)$$

The temperature of the membrane and the partial pressures of the gas vary proportionally as a function of the current, on the other hand the pressures of hydrogen and oxygen vary inversely with variations in the current [16].

VII. PUMP MODELLING

The pumping rate "Q" is the amount of water that a pump can move during a given time interval. The static level is the distance from the ground to the surface of the water before pumping and named dynamic level for pumping at an average flow. The difference between these two levels called drawdown.

A. *Total dynamic head (TDH)*

To convey a liquid, the pump should provide some pressure called TDH. This is the pressure difference in meters of water gauge (mwg) between the aspiration and discharge orifices [8].

The expression of TDH is [8]:

$$TDH = H_g + (J_a + J_r) + P_r \quad (16)$$

The TDH is the sum of the residual pressure at the outlet of the delivery tube and the geometric height also known as the total delivery height and the pressure losses "Jc" in the suction tube, the strainer, the valve, the or valves, etc.

The geometric height "Hg" is only the sum of the suction height "Ha" and that of the discharge "Hr". "Jc" represents the overall pressure losses at suction and discharge.

$$TDH = (H_a + H_r) + J_c + P_r \quad (17)$$

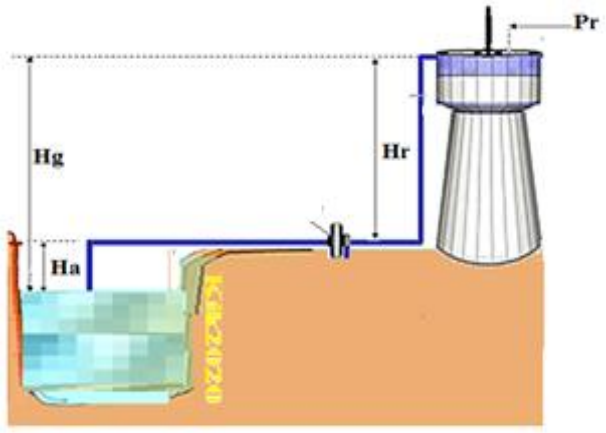


Figure 8. Surface Pump [8]..

There are standardized values of pressure losses expressed as a percentage of the geometric height depending on the flow rate and the section of the pipes provided by the manufacturer in the form of tables.

Practically, to calculate pressure losses 10% to 15% of the geometric height are used [8].

B. Pump power

According to Bernoulli's theorem, the hydraulic power supplied by the pump is:

$$P_h = \rho_{water} \times g_t \times Q \times HMT \quad (18)$$

BRAUNSTEIN and KORNFELD introduced in 1981 the expression of mechanical power [8].

$$P_{mec} = K_r \times \omega_r^3 \quad (19)$$

The centrifugal pump opposes a resistant torque from which its expression is:

$$T_r = K_r \times \omega_r^2 + T_s \quad (20)$$

PELEIDER PETERMAN gives the model identified by the expression of the TDH [9]:

$$TDH = K_0 \times \omega_r^2 + K_1 \omega_r Q - K_2 Q^2 \quad (21)$$

VIII. DUAL STATOR INDUCTION MACHINE MODELING

A. Magnetic power

The expression of magnetic energy is:

$$w_{mag} = \left[[i_{s1}]^t[\varphi_{s1}] + [i_{s2}]^t[\varphi_{s2}] + [i_r]^t[\varphi_r]\right]/2 \quad (22)$$

B. Electromagnetic torque

The partial derivative of the energy with respect to the mechanical angle θm give the electromagnetic torque [8, 9].

$$C_{em} = \frac{dw_{mag}}{d\theta_m} = p \times \frac{dw_{mag}}{d\theta_e} \quad (23)$$

p represents the number of pole pairs and θe= θr the electrical angle, the torque expression becomes [8, 9]:

C. Mechanical equation

The movement of the rotor is:

$$J \times \frac{d\Omega}{dt} = C_{em} - C_r - f_r \times \Omega \quad (24)$$

D. Inverter Modeling

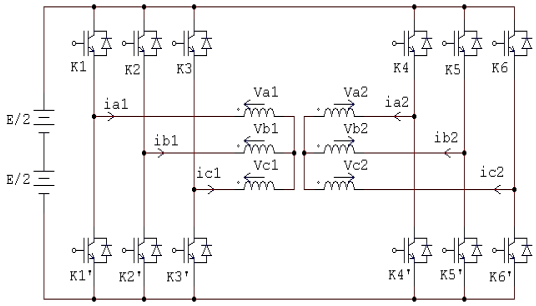


Figure 9. Power supply of the stator by voltage inverters [8]

Two three-phase inverters, with controlled switches used to power the two stars of the machine.

Control by sine-triangle pulse width modulation 'PWM' consists of comparing a low-frequency modulating wave called 'reference voltage' to a high-frequency triangular-shaped carrier wave [8, 9, 18].

IX. PUMPING STATION SIZING

The actual water needs of this locality during the year must be determined, in order to predict the capacity of the reservoir and the pumping time [8].

TABLE I. PUMPING DATA

Pumping time	9 hours	Inverter efficiency	0.95
Tank volume	150 m^3	DSIM efficiency	0.85
Flow	17 m^3/h	Pump efficiency	0.55
TDH	30 m	Total efficiency	0.444

Under an expected nominal flow rate of Q_n=17 m^3/h and a total dynamic head TDH=30, the pumping time is approximately 9 hours. The table 1 groups the results found after a rigorous design basis [8].

TABLE II. DIMENSIONS OF THE RENEWABLES SOURCES [8].

Photovoltaic generator			
Normalized power	3960 W	Number of panels	36
Number of serial panels	18	Number of parallel panels	2
Wind turbine		Mechanic power	5000 W
DSIG efficiency		Multiplier gain	0.9
Multiplier	30.5	Blade radius	5 m
Fuel Cell		Number of cells	1000
Electric current	6.29 A	Surface	4.83 cm^2
Fuel	Hydrogen	Oxidizer	Oxygen

X. RESULTS AND COMMENTS

The points of intersection between the carrier and the modulator determine the switching times. The carrier sets the switching frequency of the switches.

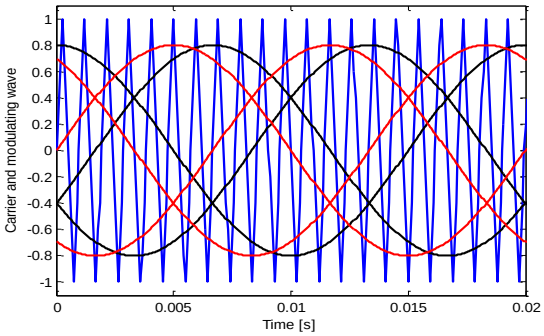


Figure 10. PWM working principal

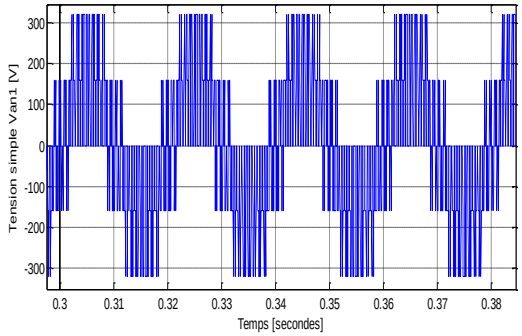


Figure 11. Voltage from the inverter Va1

At start-up, the torque of the machine oscillates, reaching 26 Nm (Fig. 12), before stabilizing, with some ripples, around a value of 12.5 Nm. The pump, in turn, opposes a resistant torque, which increases rapidly, for a period of 0.8 s, before following the evolution of the engine torque. Figure 13 confirms the quadratic relationship between TDH and rotation speed.

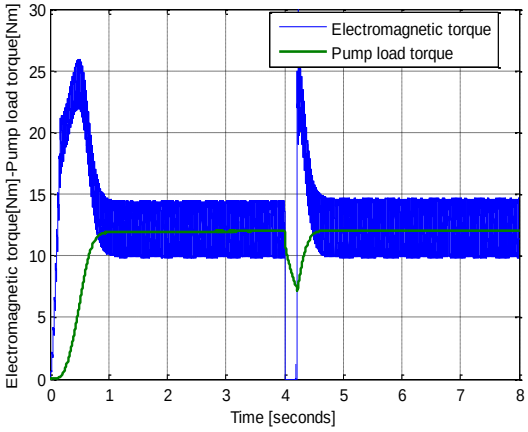


Figure 12. Electromagnetic torque – Resistive torque

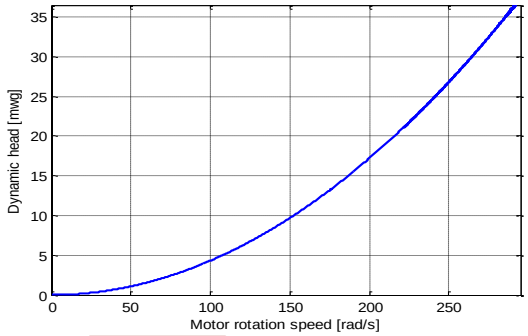


Figure 13. Dynamic head vs Motor rotation speed

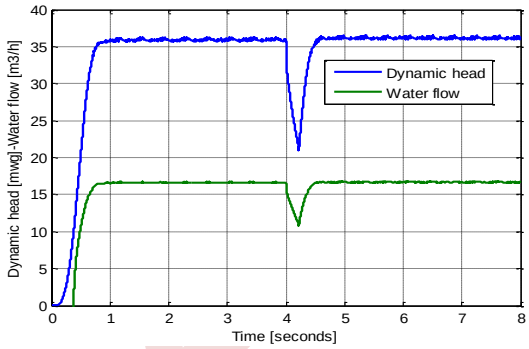


Figure 14. TDH and water flow versus time

Figure 14 shows the evolution of the water flow and the TDH. To have a flow in the pipes, it would be necessary that the pump reach a certain speed of rotation obtained after a few moments.

From Figure 15, the pump will start pumping water if and only if the rotation speed is at beyond the threshold speed, which is equal to 151 rad/sec. It is also interesting to note that the speed of rotation of the engine and the water flow are directly proportional.

The pump torque, rotation speed, pumped flow and HMT depend on the variation of the sunshine. However, the use of the maximum power search technique can overcome the handicap of low lighting.

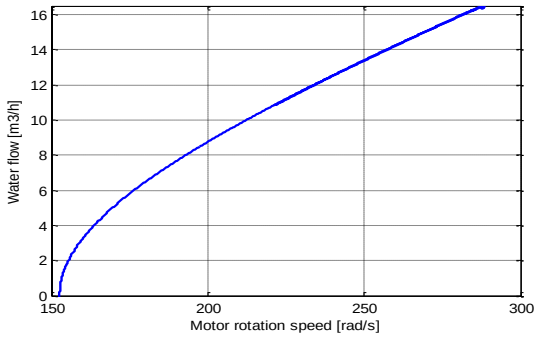


Figure 15. Water Flow vs Motor rotation speed

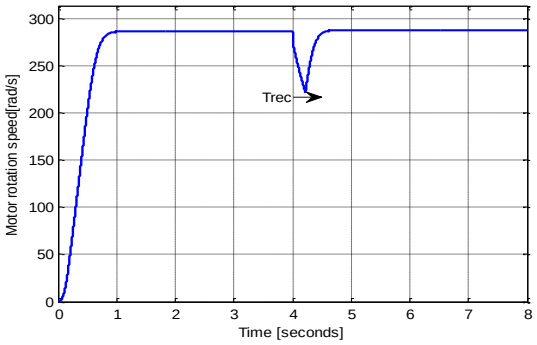


Figure 16. Motor rotation speed

In the case of absence of the sun and a solicitation of a pumping after decrease of the level of the tank, the fuel cell will ensure the relay. The FC offer a continuous voltage to the two inverters use to power the asynchronous motor with dual star, thus training the pump.

XI. CONCLUSION

We proposed a hybrid power supply composed of a photovoltaic generator, a wind turbine and a fuel cell using hydrogen obtained by an electrolyzer to power the pumping station isolated from the conventional power grid.

With this hybridization, renewable sources are complementary instead of being competitive, a way to counteract the intermittent natures of these sources.

We chose the DSIM to run a centrifugal pump and the DSIG as the wind turbine generator. This choice is justified by the segmentation of power and the increase of the service life of the installation or by the possibility of operation in degraded mode, offering an additional degree of freedom.

The flow rates pumped during a day are increased compared to single source systems and the operating strategy directly influences the performance, efficiency and service life of the installation.

REFERENCES

[1] L. Bemal-Agustin, R. Dufo-Lapez, "Simulation and optimization of standalone hybrid renewable energy systems", Renew. Sustain. Energy Rev., vol. 13, pp. 2111 - 2118,. doi: 10.1016/j.rser.2009.01.010

[2] P. Bajpai and V. Dash, "Hybrid renewable energy systems for power generation in stand-alone applications: A review," Rene w. Sustain. Energy Rev., vol. 16, no. 5, pp. 2926-2939,2012 . doi: 1O.1016/j .rser.2012 .02.009

[3] L. Zarour. « Etude technique d'un système d'énergie hybride photovoltaique-eolien hors réseau ». Doctorat en électrotechnique, Mentouri University Constantine. 2010.

[4] B. Bouzidi, "Viability of solar or wind for water pumping systems in the Algerian Sahara regions case study Adrar," Renewable and Sustainable Energy Reviews. 15:4436-42. 2011.

[5] Hajdidj, M.S., Bibi-Triki, N., Didi, F. "Study and optimization of a renewable system of small power generation". European Journal of Electrical Engineering, 19(3-4): 133-154. 2017. https://doi.org/10.3166/EJEE.19.133-154.

[6] D. Ipsakis, S. Voutetakis, P. Seferlis, F. Stergiopoulos, and C. Elmasides. Power management strategies for a stand-alone power system using renewable energy sources and hydrogen storage. Int. 1. Hydrogen Energy, vol. 34, no. 16, pp. 7081- 7095. 2009.

[7] R. Dufo-Lapez and J. L. Bemal-Agustin. "Simulation and optimization of standalone hybrid renewable energy systems," Renew. Sustain. Energy Rev., vol. 13, pp. 2111 - 2118. 2009.
doi: 10.1016/j.rser.2009.01.010.

[8] A. Adjati, "Etude des machines asynchrones à double étoile en pompage hybride à énergies renouvelables", Doctoral thesis in science, University A. Mira Bejaia, Algeria, 2022.

[9] A. Adjati, "Etude des machines asynchrones à double étoile en pompage", Thèse de Magister de l'université A. Mira Bejaia, systèmes électro-énergétique.2012.

[10] A. Adjati, A. Azib et T. Rekioua, "Etude d'une machine asynchrone à double alimentation en pompage photovoltaïque", Revue des Energies Renouvelables, Vol. 17 N°3 411 – 418. 2014.

[11] A. Adjati, T. Rekioua, D. Rekioua, "Use of the Dual Stator Induction Machine in Photovoltaic - Wind Hybrid Pumping", Journal Européen des Systèmes Automatisés, Vol.54, N°.1, pp. 115-124, February 2021.

[12] Nachida KASBADJI MERZOUK,. "Evaluation du gisement énergétique éolien, contribution à la détermination du profil vertical de la vitesse du vent en Algérie". Université abou bekr belkaid de Tlemcen, 2006 .

[13] Kasbadji Merzouk N. , M. Merzouk, N.Messen et B. Benyoucef, . Profil Vertical de la Vitesse du Vent en milieu semiaride.Test des modèles d'Extrapolation. International congress on Photovoltaic and wind energy, Tlemcen.2003.

[14] A.Guettaf; "Direct field oriented control of induction motor fed by wind turbine generator under saturation effect". Mediterranean Journal of Measurement and Control, Vol 7, N°1, pp 190-196, 2011.

[15] G.Seguier, F.Notelet, «Electrotechnique industrielle, technique et documentation», page 484, édition Lavoisier, Paris, 1994,.

[16] Adjati, A., Rekioua, T., Rekioua, D. "Study of dual stator induction motor in photovoltaic-fuel cell hybrid pumping Application". Journal Européen des Systèmes Automatisés, 53(5): 601-608. 2020.
http://doi.org/10.18280/jesa.530502

[17] M. A. J. Cropper, S. Geiger et D. M. Jollie, "Fuel cells: a survey of current developments," Journal of Power Sources, vol. 131, n° 1-2, pp. 57-61, mai 2004.

[18] K. Hamitouche, S. Chekkal, H. Amimeur, D. Aouzellag " A new control strategy of dual stator induction generator with power regulation" Journal Européen des Systèmes Automatisés:53:469-478, 2020

Transient Stability Analysis of a multimachine power system

Dimya Idirene , Abdallah Medjdoub

Laboratoire de Génie Électrique Bejaia (LGEB)

Faculté de Technologie, Université de Bejaia 06000, Algérie

dimya.idirene@univ-bejaia.dz ; abdellah.medjdoub@univ-bejaia.dz

***Abstract*— Improving the reliability of power systems is one of the most challenging research areas in electrical engineering. For this purpose, the determination of the transient stability is a crucial step in power system analysis. This paper is a contribution to the study of the transient stability of a multimachine system. The classical model is applied to a 3-Machine, 6-bus system. A three-phase fault is introduced on two different segments of the line to analyze the effect of the fault location and critical clearing time on the system stability. The fault is cleared by opening breakers at both ends of the line to increase stability margin hence decrease damages. In order to answer the question of stability, it is necessary to plot and inspect the swing curves. A program that displays the machine phase angles is developed using MATLAB. It is also preceded by a power flow program using the Newton's Raphson method.**

Keywords: **Transient Stability, Power system, Multimachine System, Classical Model, Critical Clearing Time, Fault Location.**

I. INTRODUCTION

Operational requirements for electrical utilities are extremely high because of their size and complexity due to the elevated demand for electricity. Thus, power systems must continually maintain their reliability and security. Among the various analyses of dynamic security, the transient stability is one of the most essential and important assessments [1],[2]. In fact, when the disturbances occur on an interconnected power system, a detailed study of the transient stability must be carried out to ensure its safety.

Multimachine systems are the most affected by disturbances. These disturbances can be fault such as a short circuit on a transmission line, a loss of load or of a generator…etc. A stable multimachine system is one in which the synchronous machines, when perturbed, will either return to their original state or will acquire a new state without losing synchronism [3].

The time domain simulation method, the direct method and artificial intelligence method are commonly used in the literature for transient stability analysis [4].

The time domain simulation methods consist of solving the differential equations which describe the transient process of the system using various numerical integration method [5]. The stability is judged according to the change of the rotor angle of the synchronous generators [6], [7], [8]. One of the first studies concerning this method is that of Rovnyak, Liu, Ma & Throp (1995). Their work uses the swing equation in a simplified two machine system to predict the stability condition [9]. Kaur & Kumar (2016) presented a study that deals with the transient stability analysis and its improvement using Power Word Simulator. They demonstrated the effectiveness of shunt FACTS devices for improving the system stability [10]. Iyambo & Tzoneva (2007) analyzed the transient stability of the IEEE 14-bus electric power system and the many factors affecting the CCT (Critical clearing time). They conclude that it is recommended that the designers of electrical systems carry out appropriate inspections on the design regarding transient stability [11].

The direct method is basically based on Lyapunov stability criterion. It consists of constructing a function directly in order to quantitatively measure the power system transient stability [4]. This method shows merits in performing fast contingency screening and providing quantitative information for the degree of stability [12].

Artificial intelligence method can be applied to on line transient stability analysis. It consists to establish the relationship of the input characteristics and the stable state of transient stability characteristics [4],[12].

The present paper deals with the transient stability analysis of a multimachine power system composed of 3 machines, 6 buses using the classical model. This system, while small, is large enough to be significant and permits the illustration of several stability concepts and results. The study consists of analyzing the effect of the fault location in conjunction with the fault clearing time. The simulation is performed using MATLAB. The paper is organized in IV sections. The power system studied is described in the first one. Section II focuses on multimachine transient stability including the preliminary calculations and the model used for this purpose. In section III, the detailed simulation procedure and the results are presented. Finally, a conclusion is given in the last section.

ILLUSTRATIVE SYSTEM EXAMPLE

The system taken as an example of application in this article is the 3-machine, 6-bus system. Its single line diagram is shown in "Fig. 1".

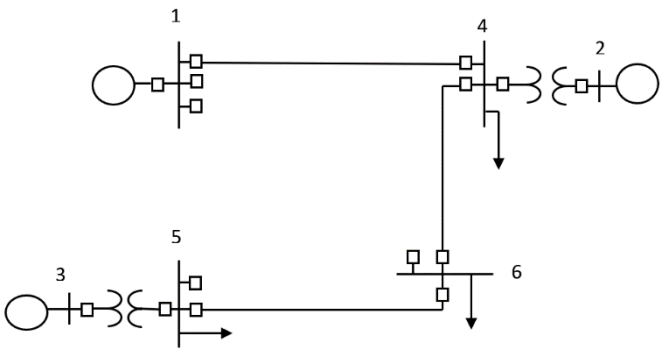


Figure 1. One line diagram of the 3-Machine, 6-bus system

The load data and generation schedule are respectively tabulated on "Table. 1" and "Table. 2".

Table 1. Load data

		Bus No.					
		1	2	3	4	5	6
Load data	MW	0	0	0	100	90	160
	Mvar	0	0	0	70	30	110

Table 2. Generation schedule

Bus No.	Voltage Mag.	Generation MW	Mvar Limits Min	Max
1	1.06			
2	1.04	150	0	140
3	1.03	100	0	90

On a 100 MVA base, lines and generators data in per unit are also illustrated on "Table. 3" and "Table. 4".

Table 3. Line data

Bus No.	Bus No.	R PU	X PU	½ B PU
1	4	0.035	0.225	0.0065
1	5	0.025	0.105	0.0045
1	6	0.040	0.215	0.0055
2	4	0.000	0.035	0.000
3	5	0.000	0.042	0.000
4	6	0.028	0.125	0.0035
5	6	0.026	0.175	0.0300

Table 4. Machine data

Gen	R_a	X_d'	H
1	0	0.20	20
2	0	0.15	4
3	0	0.25	5

The disturbances causing the transient are three-phase faults. The first occurs on line 5-6 near to the bus 5. The second on the same line but close to the bus 6. Although the system is small, it remains representative of a certain number of transient stability concepts of a multimachine system.

II. MULTIMACHINE TRANSIENT STABILITY

Several assumptions are considered in multimachine systems to reduce the complexity of the transient stability analysis. They can be quoted as follows [13]:

-The input powers remain constant during the study period.

-The effect of saliency is neglected, and the flux linkages are assumed to be constant. Thus, each synchronous machine is represented by a constant reactance in series with a constant voltage source.

-The loads are converted to shunt admittances which are assumed to remain constant.

-The mechanical angle of each machine rotor coincides with the electrical phase of the internal voltage.

-Damping and synchronous powers are neglected.

Three states are considered for the system [11]:

-The pre-fault state determines the initial condition for angles.

-The fault state which is starting at $t = 0$ until the fault is cleared at $t = t_c$.

-The post fault state at $t_c < t < CCT$. Where CCT is the critical clearing time.

A. Preliminary calculations

To carry out the analysis of the transient stability of a multimachine system, preliminary calculations are required [3],[11]:

-Convert to a common base all system data.

-Solve the initial load flow and determine the generator voltages and their initial angles. The machine currents before the fault can be deduced using the relation "(1)":

$$I_i = \frac{S_i^*}{V_i^*} = \frac{P_i - jQ_i}{V_i^*} \qquad i = 1,2,\dots,m \qquad (1)$$

Where:

m : The number of generators.

V_i : The terminal voltage of the i^{th} generator.

P_i and Q_i : The generator active and reactive powers.

Thus, the voltages behind the transient reactance are then obtained:

$$E_i' = V_i + jX_d' I_i \qquad (2)$$

-Loads are represented by equivalent shunt admittances as bellow:

$$y_{i0} = \frac{S_i^*}{|V_i|^2} = \frac{P_i - jQ_i}{|V_i|^2} \qquad (3)$$

-Calculate the admittance bus matrix Y_{bus}.

-The node voltage equation with node 0 as reference is given by:

$$I_{bus} = Y_{bus} V_{bus} \qquad (4)$$

Where:

I_{bus} : The injected bus currents.

V_{bus} : The vector of bus voltages measured from the reference node.

Elements of the Y_{bus} matrix are:
Y_{ii} : The sum of admittances connected to node *i.*
Y_{ij} : The negative of admittances between node *i* and node *j*.
-In order to simplify the analysis, all the nodes except the generator internal nodes are eliminated by using the Kron reduction formula. The reduced admittance matrix is then obtained, and it has *(m*m)* dimensions:

$$Y_{bus}^{red} = Y_{mm} - Y_{nm}^{t} Y_{nn}^{-1} Y_{nm} \quad (5)$$

Where:
m : The number of generators.
-Finally, the electrical power output of each machine is expressed by the relation bellow:

$$P_{ei} = R[E_i' I_i] \quad (6)$$

The polar form is given by the relation "(7)":

$$P_{ei} = \sum_{j=1}^{m} |E_i'| |E_j'| |Y_{ij}| \cos(\theta_{ij} - \delta_i + \delta_j) \quad (7)$$

Before the fault, there is equilibrium between the mechanical power input and the electric power.

B. Classical transient stability model

The classical transient stability model is the simplest one that can be used to study the power system dynamics. The studies using this model can be conducted in a short time and at minimum cost. Despite its simplicity, it can provide useful and significant information. They can be used as preliminary study to identify the parts of power system that involve more detailed model [3], [14].
The classical transient stability study consists of applying a three-phase fault at bus *k* implying then $V_k=0$ which is simulated by removing the k^{th} row and column from the pre-fault bus admittance matrix. Considering that the generator excitation voltages during the faulted and post-fault states remains constant and eliminating all nodes except the internal generator nodes, the new bus admittance matrix is then reduced [15]. Knowing the electrical power of the i^{th} generator in terms of the new reduced bus admittance matrices and neglecting the damping, the swing equation for machine *i* is given by the relation "(8)":

$$\frac{H_i}{\pi f_0} \frac{d^2\delta_i}{dt^2} = P_{mi} - \sum_{j=1}^{m} |E_i'| |E_j'| |Y_{ij}| \cos(\theta_{ij} - \delta_i + \delta_j) \quad (8)$$

Where:
Y_{ij}: The elements of the faulted reduced bus admittance matrix.
H_i: The inertia constant of machine expressed on the common MVA base.
The equation "(8)" can be transformed into state variable model yields as bellow:

$$\begin{cases} \frac{d\delta_i}{dt} = \Delta\omega_i \quad i = 1,2,\dots,m \\ \frac{d\Delta\omega_i}{dt} = \frac{\pi f_0}{H_i}\left(P_m - P_e^f\right) \end{cases} \quad (9)$$

Where:
P_e^f : The electrical power of the i^{th} generator.

III. SIMULATION AND RESULTS

The current section deals with the transient stability of the system shown in "Fig. 1" when it's subjected to a three-phase fault in two different locations. The effect of clearing time of fault is also analyzed.

A. Simulation procedure

The steps illustrated in "Fig. 2" are followed to conduct the analysis of the transient stability of the multimachine system. For this purpose, the MATLAB environment is used.

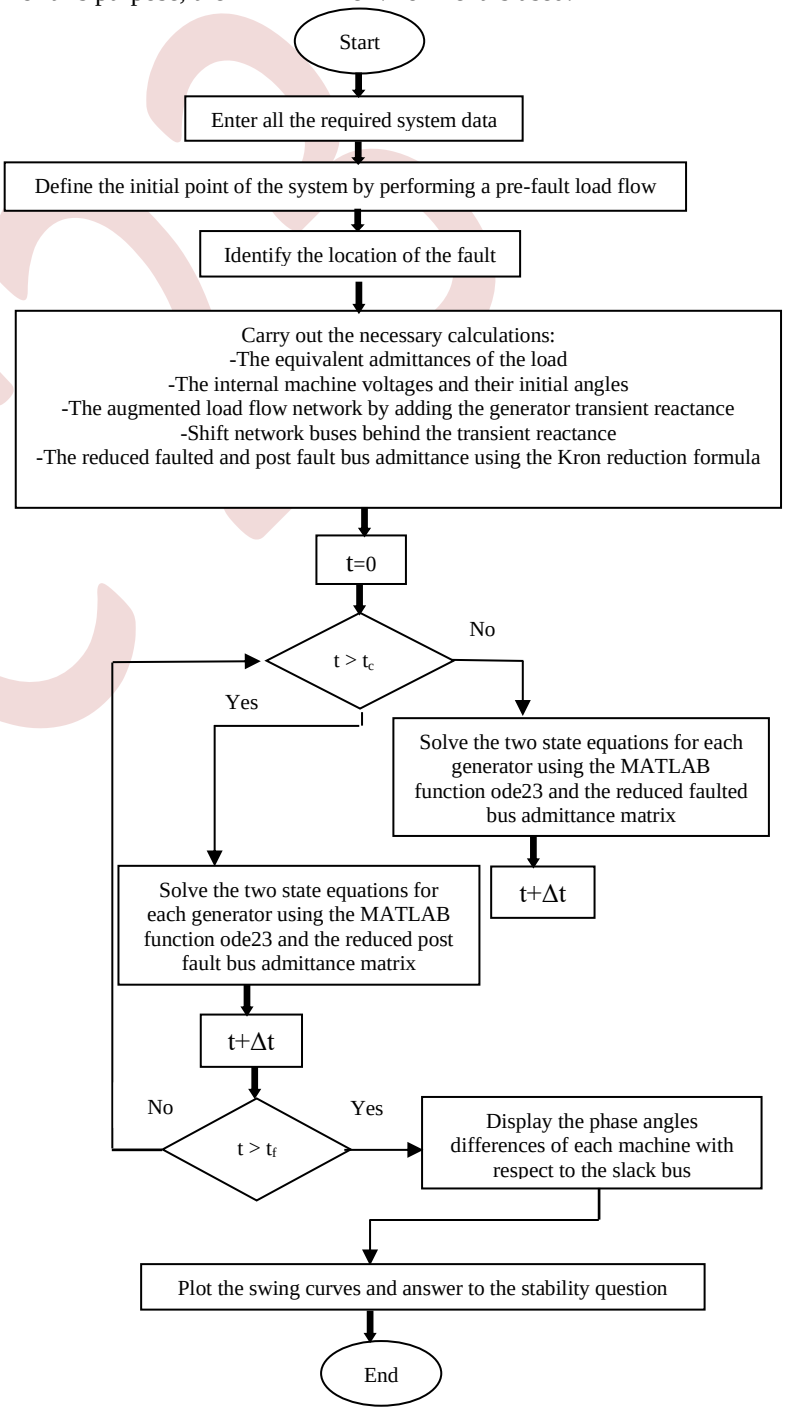


Figure 2. Flow diagram of the simulation procedure

B. Results

As mentioned previously, the analysis of transient stability analysis of the 3-machine, 6-bus system requires preliminary calculations including the initial power flow. The Newton's Raphson method is used, it converges after 4 iterations as follows:

Table 5. Power flow solution by Newton's Raphson method

Bus	Voltage	Angle	Load		Generation		Injected
No.	Mag	Degree	MW	Mvar	MW	Mvar	Mvar
1	1.060	0.000	0.000	0.00	105.287	107.335	0.000
2	1.040	1.470	0.000	0.00	150.000	99.771	0.000
3	1.030	0.800	0.000	0.00	100.000	35.670	0.000
4	1.008	-1.401	100.0	70.00	0.000	0.000	0.000
5	1.016	-1.499	90.00	30.00	0.000	0.000	0.000
6	0.941	-5.607	160.0	110.00	0.000	0.000	0.000

The reduced pre-fault bus admittance matrix obtained is:

$$Y_{bf} = \begin{bmatrix} 0.3517 - 2.8875i & 0.2542 + 1.1491i & 0.1925 + 0.9856i \\ 0.2542 + 1.1491i & 0.5435 - 2.8639i & 0.1847 + 0.6904i \\ 0.1925 + 0.9856i & 0.1847 + 0.6904i & 0.2617 - 2.2835i \end{bmatrix}$$

The equilibrium point for the three generators is given on "Table. 6":

Table 6. The generator interne voltages, their initial angles, and mechanical powers

G(i)	E´(i)	δ_0(i)	P_m(i)
1	1.2781	8.9421	1.0529
2	1.2035	11.8260	1.5000
3	1.1427	13.0644	1.000

This study is achieved to analyze the effect of fault location in conjunction with its clearing time.

Two three-phase fault occurs on line 5-6, they are cleared by simultaneous opening of breakers at both ends of line. The first is close to the bus 5 and the second is far from this bus.

- ***Three phase-fault on line 5-6 close to bus 5***

The reduced faulted bus admittance matrix in this case is:

$$Y_{df} = \begin{bmatrix} 0.2142 - 3.7380i & 0.1152 + 0.5521i & 0 \\ 0.1152 + 0.5521i & 0.4156 - 3.2810i & 0 \\ 0 & 0 & 0 - 3.4247i \end{bmatrix}$$

Considering that the faulted bus is the 6th and the fault is clearing by isolating the line 5-6, the reduced postfault admittance matrix is:

$$Y_{af} = \begin{bmatrix} 0.3392 - 2.8879i & 0.2622 + 1.1127i & 0.1637 + 1.0251i \\ 0.2622 + 1.1127i & 0.6020 - 2.7813i & 0.1267 + 0.5401i \\ 0.1637 + 1.0251i & 0.1267 + 0.5401i & 0.2859 - 2.0544i \end{bmatrix}$$

Fault clearness before critical clearing time:

Firstly, we consider the clearing time of fault $t_c = 0.3\ sec$. The phase angle differences of each machine with respect to the slack bus is presented in "Fig. 3".

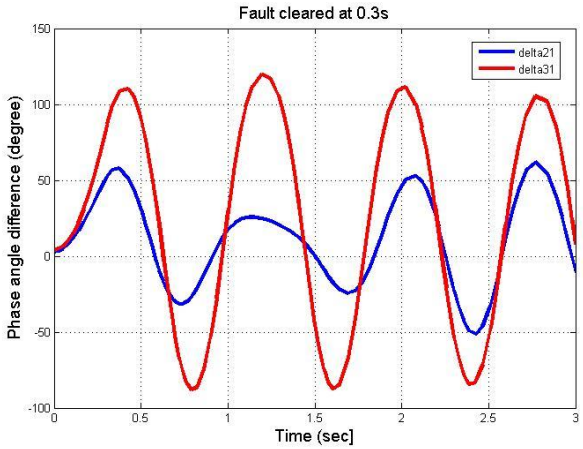


Figure 3. Swing curves for machines 2 & 3, fault on bus 5 cleared at 0.3 seconds

Fault clearness after critical clearing time:

For $t_c = 0.4\ sec$, the swing curves are illustrated in "Fig. 4".

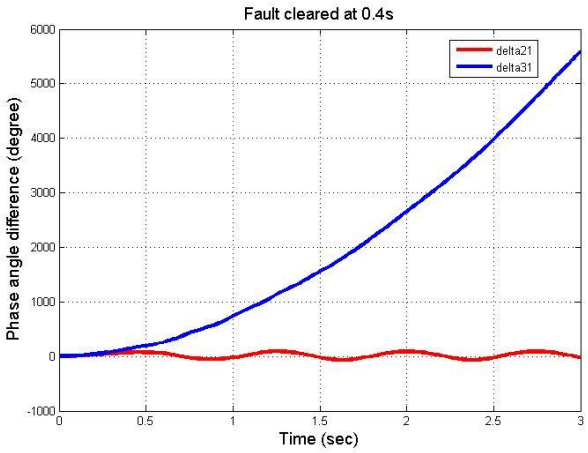


Figure 4. Swing curves for machines 2 & 3, fault on bus 5 cleared at 0.4 seconds

The results show that the system is stable when the fault is cleared in 0,3 seconds and the machines swing together. However, it quickly loses its stability when the fault is cleared after 0,4 seconds.

- ***Three phase-fault on line 5-6 close to bus 6***

The reduced faulted bus admittance matrix:

$$Y_{df} = \begin{bmatrix} 0.1913 - 3.5849i & 0.0605 + 0.3644i & 0.0523 + 0.4821i \\ 0.0605 + 0.3644i & 0.3105 - 3.7467i & 0.0173 + 0.1243i \\ 0.0523 + 0.4821i & 0.0173 + 0.1243i & 0.1427 - 2.6463 \end{bmatrix}$$

The reduced postfault admittance matrix:

$$Y_{af} = \begin{bmatrix} 0.3392 - 2.8879i & 0.2622 + 1.1127i & 0.1637 + 1.0251i \\ 0.2622 + 1.1127i & 0.6020 - 2.7813i & 0.1267 + 0.5401i \\ 0.1637 + 1.0251i & 0.1267 + 0.5401i & 0.2859 - 2.0544i \end{bmatrix}$$

Fault clearness before critical clearing time:

For *tc=0.4 sec*, the swing curves are given in "Fig. 5".

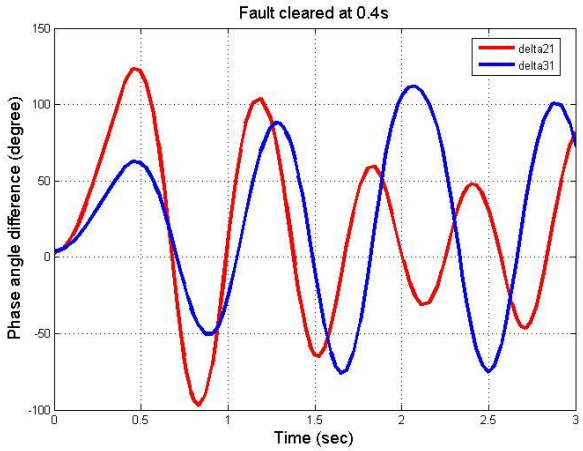


Figure 5. Swing curves for machines 2 & 3, fault on bus 6 cleared at 0.4 seconds

Fault clearness after critical clearing time:

The results continue for t_c=*0,5 sec*.

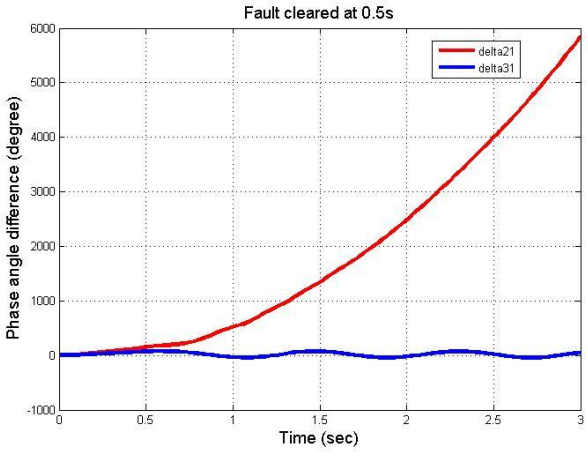


Figure 6. Swing curves for machines 2 & 3, fault on bus 6 cleared at 0.5 seconds

The results show that the phase angles differences, after reaching a maximum decrease and the machines swing together. Hence, the system is stable when the fault is cleared in 0,4 seconds.

When the fault is cleared in 0,5 seconds, the phase angles differences increase without limits, the system is than unstable. After several simulations, the *CCT* found for each of the two previous cases is given in the "Table. 7":

Table 7. The CCT corresponding to each case of fault

Localisation of the three-phase fault	CCT (sec)
Line 5-6 close to bus 5	0,35
Line 5-6 close to bus 6	0,46

The *CCT* found when the three-phase fault occurs far from the generating station is higher than that found when the disturbance is close to the generator.

IV. CONCLUSION

Several parameters affect the transient stability of the multimachine systems. The location of the disturbance is one of them. In fact, the fault which is closer to the generating station must be cleared rapidly than the fault on the line far from the generation station. Quick clearance of faults is essential to maintain the stability of the power system and avoid damages to lines and insulators. Additionally, the study shows that fault clearness after the *CCT* makes the system unstable while fault clearness before the *CCT* keeps the system in synchronism. Particular attention must be paid to the analysis of transient stability to ensure reliable and continuous operation of electrical networks.

the analysis of the transient stability of power systems in the time domain is the oldest, most accurate and time-consuming method. This method requires the whole system detailed model and accurate information about the nature and the location of the disturbances to solve the non-linear differential equations. Thus, the study becomes difficult for a larger and more complex system. The approach used in this paper can be applied to a real network and under multiple contingences. Each of the methods cited in the literature review has certain advantages and disadvantages. Considering the importance of transient stability phenomena, it seems that combining these methods could be more effective solution.

REFERENCES

[1] A. Shrivastava, H. M. Siddiqui, "A simulation analysis of optimal power flow using differential evolution algorithm for IEEE-30 bus system", 2014, International Journal of Recent Development in Engineering and Technology, 2(3), 50-57.

[2] W. Rahmouni, L. Benasla, "Analyse de la stabilité transitoire du réseau IEEE-5 nœuds par le critère des aires égales et la méthode du plan de phase,",2017.

[3] V. Vittal, J.D. McCalley, P.M. Anderson, A.A. Fouad, "Power system control and stability,", 2019, John Wiley & Sons.

[4] H. Wang, Z. Li, "A Review of Power System Transient Stability Analysis and Assessment,", 2019, Prognostics & System Health Management Conference .

[5] M. L. Crow, " Computational methods for electric power systems", 2015,Crc Press.

[6] L. Zhu, D.J. Hill, C. Lu, "Hierarchical deep learning machine for power system online transient stability prediction",2020, IEEE Trans. Power Syst.

[7] Y. Li, Z. Yang, "Application of EOS-ELM with binary jaya-based feature selection to real-time transient stability assessment using PMU data, ", 2017, IEEE Access 5, 23092–23101.

[8] M. Li, A. Pal, A.G. Phadke, J.S. Thorp, "Transient stability prediction based on apparent impedance trajectory recorded by PMUs, ",2014, Int. J. Electr. Power Energy Syst. 54 (2014) 498–504.

[9] S. Rovnyak, C.W. Liu, J. Lu, W. Ma, J. Thorp, " Predicting future behavior of transient events rapidly enough to evaluate remedial control options in real-time, ", 1995, IEEE Trans. Power Syst. 10 (3) (1995) 1195–1203. Aug.

[10] R. Kaur, D. Kumar, "Transient stability improvement of IEEE 9 bus system using power world simulator,", 2016, In MATEC Web of Conferences (Vol. 57, p. 01026). EDP Sciences.

[11] P.K. Iyambo, R. Tzoneva, "Transient stability analysis of the IEEE 14-bus electric power system,", 2007, In AFRICON 2007 (pp. 1-9). IEEE.

[12] Qiu, Z., Duan, C., Yao, W., Zeng, P., & Jiang, L, "Adaptive Lyapunov Function Method for Power System Transient Stability Analysis,", 2022, IEEE Transactions on Power Systems.

[13] H. Saadat, "Power system analysis,", 1999, Vol. 2, McGraw-hill.

[14] N. Anwar, A. Hanif, H.F. Khan, M.F. Ullah, "Transient stability analysis of the IEEE-9 bus system under multiple contingencies,", 2020, Engineering, Technology & Applied Science Research, 10(4), 5925-5932.

[15] R. Kamdar, M.Kumar, G. Agnihotri, "Transient stability analysis and enhancement of IEEE-9 bus system. Electrical & Computer Engineering,", 2014, An International Journal (ECIJ), 3(2), 41-51.

EEIC'23

Impact of TCSC on Energy Performance in Electrical Networks

1st Fateh Ouali [1], 2nd Narimen A. Lahaçani [2],

[1] *Laboratoire de Maitrise des Energies Renouvelables, Faculté de Technologie, Université de Bejaia, 06000 Bejaia*
fateh.ouali@univ-bejaia.dz

[2] *Laboratoire de Maitrise des Energies Renouvelables, Faculté de Technologie, Université de Bejaia, 06000 Bejaia*
narimen.lahacani@univ-bejaia.dz

***Abstract*— The evolution of electrical networks in response to the increasing demand for energy and the integration of renewable energy sources requires a thorough analysis of technologies that enhance network performance. Among these, Thyristor-Controlled Series Compensators (TCSC) play a crucial role. The dynamic transformation of networks, characterized by the growing integration of renewable energies and rising energy demand, calls for advanced solutions to ensure the efficiency, stability, and reliability of electrical systems. Flexible AC Transmission Systems (FACTS) devices, including TCSC, are vital for regulating the series reactance of transmission lines. This study aims to analyze the impact of TCSC on the performance of electrical networks, contributing to existing research through a critical evaluation of previous work, with the IEEE 57 model as a realistic case study.**

Keywords: TCSC; FACTS; Electrical Networks; Energy Performance; Comparative Analysis

I. INTRODUCTION

At the heart of one of the most complex technological challenges of our time lies the electrical grids. This is due to the current era of energy transformation, characterized by the increasing power of renewable energies, the growth in energy demand, and the constant pursuit of efficiency [1], [2]. In this context, FACTS (Flexible Alternating Current Transmission Systems) devices emerge as essential components in the quest for optimal energy performance [3]. Among them, Thyristor-Controlled Series Compensators (TCSCs) stand out due to their ability to modify the equivalent reactance of electric transmission lines [4], [5]. They can fundamentally transform the dynamics of electrical networks by enabling precise power flow regulation, enhancing stability, and strengthening transfer capacity.

The significance of this technology lies in its ability to address the challenges posed by load variations, network disturbances, and the growing need for integrating renewable energies. A review of prior work on TCSCs provides valuable insights into the progress made thus far while encouraging further exploration into real-time control to enhance network stability and power flow optimization by adjusting this equivalent reactance. It also delves into how these devices can be optimized to meet the complex requirements of modern electrical grids.

The IEEE 57-node model was selected as a case study due to its realistic complexity. This model is considered to provide the ideal environment for evaluating the efficiency and impact of TCSCs, thus bringing it closer to reality. We will explore how this model can be used as a crucial testing platform for comparative analysis, thereby enhancing our understanding of how TCSCs can be integrated into diverse and complex electrical grids.

However, amidst these promising advancements, areas of uncertainty persist in the literature. Despite significant progress, some fundamental questions remain unanswered, such as integration with variable energy sources, cybersecurity considerations, and overall energy performance optimization. The importance of conducting a comparative analysis of TCSCs is highlighted by this introduction. Our research is positioned within the current context of energy transformation, to contribute to enhancing grid stability, thereby reducing the risks of outages and failures while increasing power transmission capacity. This is crucial to meet the growing energy demand, ensuring a sustainable future for electrical grids.

II. METHODOLOGY FOR COMPARATIVE ANALYSIS

To conduct a comprehensive comparative analysis of the influence of TCSC devices on the energy performance of electrical networks, a rigorous methodology has been employed in this section.

This approach has been meticulously developed to ensure an accurate and reliable assessment of the impacts of FACTS

devices. Detailed simulations are carried out to evaluate these effects, using a 57-node IEEE electrical network.

A. Modelling of the 'TCSC' Device

The significance of TCSC modelling becomes evident through its role in understanding their impact on electrical networks and their efficient integration into power transmission systems, which includes enhancing transfer capacity and controlling power flow within a transmission line. The integration of TCSC devices into the network is carried out using a precise mathematical model, where the firing angle of the thyristors is considered a state variable. The parameters of the TCSC, including their capacity, series resistance, and location, have been configured based on theoretical calculations. These TCSC models have been strategically placed within the network to assess their impact on voltage stability and power flow.

1) Thyristor-Controlled Series Compensator (TCSC) Model

The basic circuit structure of the TCSC is presented in Figure 1. It consists of a capacitor in series with a fixed reactance 'X_C' in parallel with a thyristor-controlled variable reactance 'X_L'. The condition $X_C < X_L$ is maintained so that the TCSC can operate as a variable capacitive reactance.

The thyristor firing angle "α" is adjusted to modify the inductive reactance, allowing for the attainment of minimal equivalent capacitive reactance when the inductive reactance is maximal (or when the inductive branch is open).

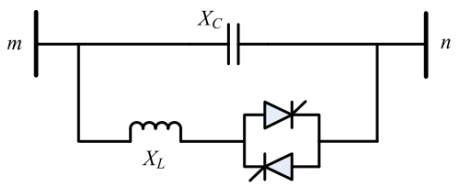


Figure 1. The basic circuit structure of the TCSC

As a result, the equivalent reactance of the TCSC, with a fixed capacitive reactance Xc and a variable inductive reactance and $X_L(\alpha)$ can be expressed as follows:

$$X_{TCSC}(\alpha) = \frac{Xc.X_L(\alpha)}{X_L(\alpha) - Xc} \quad (1)$$

The expression for reactance X_L is directly related to the thyristor firing angle 'α', which can vary in the range of 90° to 180° according to the relationship above:

$$X_L(\alpha) = x_L\left[\frac{\pi}{2\pi - 2\alpha - \sin(2\alpha)}\right] \quad (2)$$

$$\begin{cases} x_L = L\omega \\ X_C = \dfrac{1}{LC\omega} \end{cases} \quad (3)$$

ω: Angular frequency, defined as ω = 2πf, where f represents the frequency of the grid (50 Hz).

C: Capacitance of the capacitor bank.

L: Inductance of the parallel inductive reactance.

α: Thyristor firing angle.

The voltage controlled by the TCSC is:

$$V_{TCSC} = I_L * X_{TCSC}(\alpha) \quad (4)$$

The reactive power controlled by the TCSC is:

$$Q_{TCSC}(\alpha) = \frac{{V_{TCSC}}^2}{X_{TCSC}(\alpha)} \quad (5)$$

With, I_L representing the line current, V_{TCSC} and Q_{TCSC} being the controlled maximum voltage and reactive power by the TCSC, respectively.

2) Evaluation of Electrical Line Capacity

The evaluation of the power transfer capability of a line safely and without overloading fundamentally relies on power calculations. Equation (6) expresses the maximum amount of power that can be transferred safely by each line, taking into account the voltages at the ends, the phase angle, and the equivalent reactance of the line. This approach aims to ensure that the line operates within acceptable ranges, thereby minimizing the risks of overloading and preserving the overall stability of the electrical network.

$$P = \frac{V_1 V_2 \sin\delta}{X} \quad (6)$$

Pmax: represents the maximum power transfer.

V_1 is the voltage at the starting node

V_2 is the voltage at the receiving node.

X: is the reactance of the line.

δ: is the phase angle between the starting and receiving voltages.

III. CALCULATION OF STABILITY INDICES

This section focuses on calculating voltage stability indices, specifically the Voltage Stability Index (FVSI) and Lmn [7], [8], for each node in the electrical network. We will explore the methodology for computing these indices, emphasizing their significance in assessing the overall energy performance of the network.

A. Fast voltage stability index (FVSI)

The Voltage Stability Index (FVSI), as proposed by Musirin and colleagues, is based on a specific approach where it is maintained at a value greater than or equal to zero [9][10].

Regarding a standard transmission line, the FVSI is calculated using the following formula:

$$FVSI = \frac{4Z^2 Q_{eq}}{V_s^2 X} \quad (7)$$

The FVSI must remain below 1 to ensure the stability of the transmission line. When the FVSI exceeds 1, it indicates that at

least one of the nodes connected to the line is at risk of experiencing a sudden voltage drop, which can lead to a system collapse.

B. Line Stability Index (Lmn)

The "Line Stability Index" (Lmn), as proposed by Moghavemmi et al., is based on the same concept as FVSI, in which the discriminant of the quadratic equation of voltage is adjusted to be greater than or equal to zero [11]. For a typical transmission line, Lmn is calculated as follows:

$$Lmn = \frac{4XQ_r}{(V_s \sin(\theta - \delta))^2} \quad (8)$$

In the context of these indices, 'FVSI' and 'Lmn,' the influences of active power on voltage stability and the shunt admittance of the line are neglected. System stability is maintained as long as the value of the Lmn index remains below 1. However, if this index exceeds 1, the system loses its stability, and voltage collapses. To evaluate these situations, power flow simulations under various operating conditions may be required to identify critical nodes.

IV. Topology and System Configuration

The IEEE 57-node test network, as illustrated in Figure 2, consists of 7 generators. This test system is equipped with 79 transmission lines. The total load demanded by the system amounts to 1195.8 MW in active power and 318.9 MVAR in reactive power. Data related to this test system were extracted from references

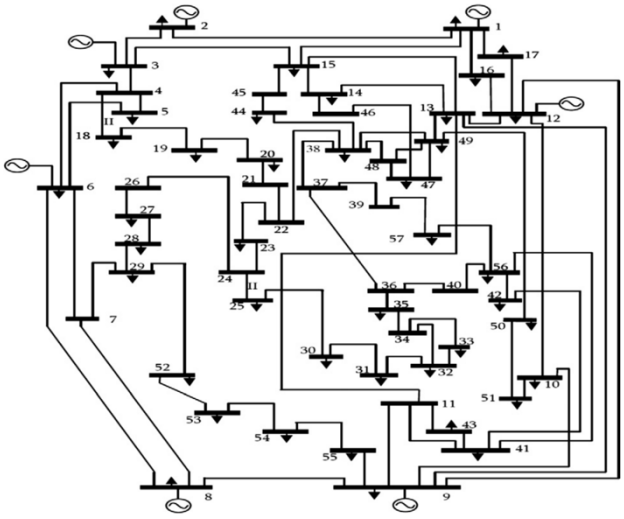


Figure 2.Single-line diagram of an IEEE 57-node test system

V. STRATEGIES FOR OPTIMIZING TCSC SITING

In this section, the focus will be on the strategy and approach adopted to optimize the placement of TCSC within electrical networks, using the "Lmn" and "FVSI" stability indices as references. Figure 3, highlighting the voltage stability indices "Lmn" and "FVSI", holds vital significance by providing the essential foundation for result analysis, particularly regarding the selection of optimal locations of TCSCs.

In this figure, the results are presented with each line of the network being represented along with their respective 'Lmn' and 'FVSI' values. Five distinct lines of the network are highlighted, and those for which the indices exceed a value of 1 are considered critical. For instance, a value of 1.0850 is observed for line 16, connecting nodes 1 to 16, and a value of 2.9163 is noted for line 35, connecting nodes 24 and 25, in relation to these indices. Similarly, each of the other lines has its own set of values. These pieces of information are crucial for evaluating the stability and voltage levels of the electrical network. These results will serve as the basis for determining the optimal placement of TCSC devices in the network to enhance overall system performance.

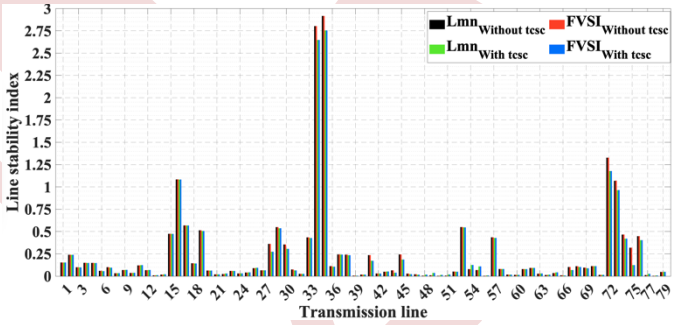


Figure 3. Lmn and FVSI values for each transmission line

VI. Simulation Results and Observation

In this section, simulation results and insightful observations are presented.

Figure 4 presents a comparison of voltage profiles before and after the insertion of the TCSC. Following TCSC insertion, a noticeable change in the voltage profile with just one TCSC device is observed: an increase from 0.8228 pu to 0.9636 pu at bus 25. This change highlights the impact of TCSC on voltage regulation and stability within the electrical network. TCSC's effectiveness in enhancing voltage control and optimizing network performance is demonstrated, which is essential for ensuring a reliable power supply to consumers.

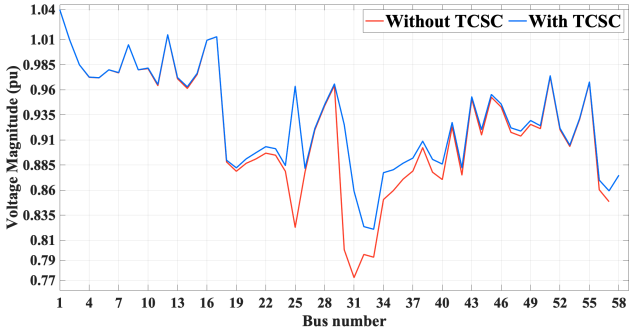


Figure 4 . Voltage profiles before and after TCSC device insertion

Figure 5 compares transmission line performance in the IEEE 57-node network with and without TCSC insertion. The

primary goal of this comparison is to determine the extent to which the lines' maximum transport capacity has been exceeded, highlighting critical areas within the network. The most significant result is that 40% of the lines exceeded their maximum transport capacity, underscoring the importance of effectively managing thermal constraints in these vulnerable regions. Additionally, a single TCSC plays a vital role in significantly reducing overall network losses by 2.63%. Furthermore, the installation of a TCSC has resulted in a significant increase in transmitted power within the equipped zone. This increase in transmission capacity demonstrates the effectiveness of TCSC in enhancing the electrical network's performance.

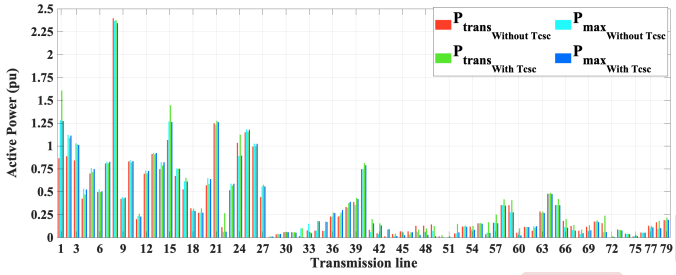


Figure 5. Impact of TCSC on Transmission Line Performance

Figure 6 portrays the influence of TCSC insertion on active and reactive power losses in the electrical network. The figure offers a thorough comparison of power losses for individual lines both before and after TCSC deployment. A substantial reduction of 3.7622 kVAR in reactive power losses is evident, highlighting the effectiveness of TCSC in regulating series reactance and elevating voltage levels.

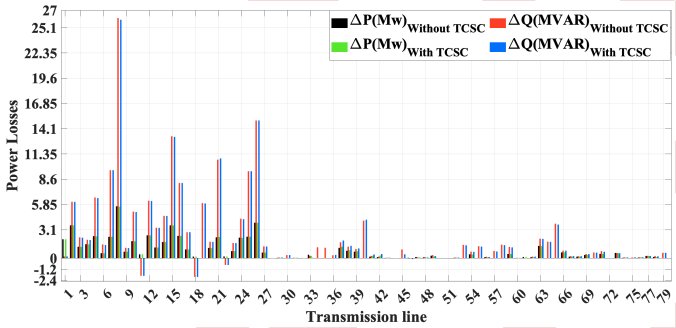


Figure 6. TCSC insertion effect on active and reactive power losses

DISCUSSION

In this study, the integration of a single TCSC and the subsequent comparison of results with and without its insertion have provided significant insights into its impact on the electrical network. The carefully chosen location of the TCSC, guided by the transmission line stability indices 'Lmn' and 'FVSI,' played a crucial role in the observed outcomes.

The findings highlight that TCSC deployment at strategically selected locations can lead to substantial improvements in voltage stability and control. The increase in voltage profile signifies a more stable and reliable electrical network, which is essential for ensuring a consistent and efficient power supply to consumers.

Furthermore, the effectiveness of TCSC in reducing reactive power losses, optimizing the network's performance, and enhancing voltage regulation was demonstrated. While active power losses remained relatively unchanged, the focus on mitigating reactive power losses underscores the TCSC's role in voltage stability and reactive power management. These results underscore the potential of TCSC as a targeted and effective means to enhance the energy performance of electrical networks while emphasizing the importance of thoughtful placement guided by stability indices. However, in this study, the optimization of the number of TCSCs to be installed is necessary.

CONCLUSION

In conclusion, our investigation into the impact of TCSC technology on energy performance within electrical networks has provided valuable insights into the strategic placement of TCSCs. The analysis has focused on optimizing TCSC locations based on stability indices such as 'Lmn' and 'FVSI'. While the optimization of the number of TCSC installations was not addressed in this study, we have contributed to an understanding of how the precise placement of TCSCs can significantly enhance grid stability and transmission capacity.

The potential to address voltage stability concerns and mitigate the risk of sudden voltage drops has been demonstrated through the strategic positioning of TCSCs in the network. This research underscores the importance of considering stability indices in the placement of TCSCs to ensure grid reliability and performance optimization. Further research in this area is necessitated to ensure grid reliability and performance optimization. This article highlights the continuing evolution of power grid management, accentuating the need for continued exploration and innovation to strengthen grid stability, minimize outages, and improve electricity transmission capacity, thereby contributing to a resilient and sustainable energy landscape.

ACKNOWLEDGEMENT

We would like to thank the DGRSDT of Algeria for providing the necessary subsidies for the research laboratory and Laboratoire de Maitrise des Energies Renouvelables, Faculty of Technology, University of Bejaia,

REFERENCES

[1] Ninla Elmawati Falabiba, 'A New Voltage Stability Index For Predicting Voltage Collapse In Electrical Power System Networks', pp. 27–30, 2019.

[2] M. Mathew, S. B. D, V. P.S., and N. M.S., 'Effect of TCSC on Line Voltage Stability Indices under Single Line Outage Condition', *IJIREEICE*, vol. 3, no. 8, pp. 101–105, Aug. 2015, doi: 10.17148/IJIREEICE.2015.3822.

[3] L. G. Narain G. Hingorani, *Understanding FACTS: Concepts and Technology of Flexible AC Transmission Systems*. 2008.

[4] M. T. Mouwafi, R. A. El-Sehiemy, and A. A. A. El-Ela, 'A two-stage method for optimal placement of distributed generation units and capacitors in distribution systems', *Appl. Energy*, vol. 307, no. September 2021, p. 118188, Feb. 2022, doi: 10.1016/j.apenergy.2021.118188.

[5] K. K. Sen and M. L. Sen, *Introduction to Facts Controllers*. Wiley, 2009.

[6] M. Kamel, A. A. Karrar, and A. H. Eltom, 'Development and Application of a New Voltage Stability Index for On-Line Monitoring and Shedding', *IEEE Trans. Power Syst.*, vol. 33, no. 2, pp. 1231–1241, 2018, doi: 10.1109/TPWRS.2017.2722984.

[7] A. Selim, S. Kamel, and F. Jurado, 'Voltage stability analysis based on optimal placement of multiple DG types using hybrid optimization technique', *Int. Trans. Electr. Energy Syst.*, vol. 30, no. 10, pp. 1–20, Oct. 2020, doi: 10.1002/2050-7038.12551.

[8] P. Molekar and V. N. Pande, 'Voltage Stability Assessment and Loss Minimisation by Power System Reconfiguration', *Int. J. Res. Rev. Vol*, vol. 6, no. 8, pp. 468–477, 2019, [Online]. Available: www.ijrrjournal.com.

[9] J. Yang *et al.*, 'Identification and Stabilization of Constant Power Loads in AC Microgrids', *IEEE Trans. Ind. Electron.*, vol. PP, pp. 1–10, 2023, doi: 10.1109/TIE.2023.3257386.

[10] J. Modarresi, E. Gholipour, and A. Khodabakhshian, 'A comprehensive review of the voltage stability indices', *Renew. Sustain. Energy Rev.*, vol. 63, pp. 1–12, Sep. 2016, doi: 10.1016/j.rser.2016.05.010.

[11] K. Sandhya and K. Chatterjee, 'Two-stage ANN based intelligent technique for optimal positioning and sizing of DERs in distribution system', *Eng. Appl. Artif. Intell.*, vol. 121, no. July 2022, p. 105932, May 2023, doi: 10.1016/j.engappai.2023.105932.

[12] M. R. Narimani, R. Azizipanah-Abarghooee, B. Zoghdar-Moghadam-Shahrekohne, and K. Gholami, 'A novel approach to multi-objective optimal power flow by a new hybrid optimization algorithm considering generator constraints and multi-fuel type', *Energy*, vol. 49, no. 1, pp. 119–136, Jan. 2013, doi: 10.1016/j.energy.2012.09.031.

[13] A. Vinkovic, M. Suhadolc, and R. Mihalic, 'Current-based models of FACTS devices for three-phase load-flow calculations using the Newton-Raphson method', *Int. J. Electr. Power Energy Syst.*, vol. 45, no. 1, pp. 117–128, Feb. 2013, doi: 10.1016/j.ijepes.2012.08.070.

Economic load Dispatch Saving Environment by Greenhouse Gas Emission Reduction Using Genetic Algorithms

1st Bouzidi Athmane [1], 2nd Hidra Lahlou [2], 3rd Ydjedd Kenza [2,], , 4th Ouakli Mohand Akli [1,],

[1] *Laboratoire de Génie Electrique de Bejaia, Faculté de Technologie, Université de Bejaia, 06000 Bejaia, Algeria*
athmane.bouzidi@univ-bejaia.dz*, mohandakli.ouakli@univ-bejaia.dz
[2] *Département de génie électrique,Faculté de Technologie, Université de Bejaia, 06000 Bejaia, Algeria*
hidralahlou@gmail.com , idjedk@gmail.com

***Abstract*— The current policy of continuously reducing fossil fuels to protect the environment and reduce global warming concerns polluting industries and activities, as well as consumers. Electricity companies are directly concerned and must take this issue into account. Firstly, through awareness-raising campaigns to encourage their customers to consume less; secondly, in their planning, by investing in less polluting energies (renewable energies); and thirdly, in the day-to-day management of electrical energy production, by protecting the environment through the reduction of greenhouse gas emissions. The aim of our work is to manage production economically while protecting the environment by reducing greenhouse gas emissions, in addition to the traditional objectives of satisfying demand, ensuring service quality and continuity, and minimizing production costs. The multi-objective genetic algorithm method makes it possible to reduce costs, minimize losses, and, above all, reduce greenhouse gas emissions while satisfying demand and the technical constraints of the network.**

***Keywords:* Economic dispatch, OPF, Greenhouse gas emission, sustainable environment.**

I. INTRODUCTION

The central mission of any company tasked with electrical energy production is to ensure the continuous and reliable supply of both active and reactive power, meeting the needs of users in every location and at all times. Moreover, it is imperious that the company maintains an acceptable power quality while keeping operational costs minimized. Indeed, managing a power grid involves both technical and economic challenges. A crucial issue is often the economic allocation of energy resources. In the first instance, the solution is often to push the most efficient units to the limit. However, this approach is not cost-effective in the long term, as it accelerates equipment wear, this led researchers to explore innovative methodologies aimed at alleviating these concerns [1, 2].

A comprehensive survey of the literature reveals that a plethora of classical and modern techniques have been employed to tackle the ED problem in electrical energy management. In the contemporary landscape, there is increasing interest in exploiting artificial intelligence, with genetic algorithm (GA) at the forefront. This development of the DE problem introduces two critical elements for the calculation and allocation of transmission losses: the first involves meticulous modeling of the power network, often referred to the optimal network power flow model, and the second encompasses the development of a formula [2]. The Newton-Raphson OPF method provides not only voltage information but also valuable data on branch flows, active and reactive losses in transmission lines, and overall network losses.

For network dispatchers, managers and power system planning experts, the main objectives are double: to orchestrate network operations in such a way as to minimize production costs, and to give priority to quality and continuity of service. To achieve these aims, multi-objective optimization methods are often used, generally in the field of meta-heuristics [3-5]. Given their remarkable effectiveness, this study adopts the methodology of genetic algorithms (GA), focusing on an IEEE-30 bus network as a case study. The inclusion of active losses (PL) can be achieved either by Kron's approximate formula [6], or by determining losses through optimal power calculation (OPF) [6, 7].

The emission of greenhouse gases, notably sulfur dioxide (SO2), nitrogen oxide (NOx) and carbon dioxide (CO2), poses environmental problems by contributing to air pollution, health risks and ozone depletion. In light of these concerns, this study incorporates a multi-objective function into the ED problem, aimed at minimizing total production cost, losses and greenhouse gas emissions [8].

II. PROBLEM FORMULATION

The ED problem consists in minimizing the objective or multi-objective function given by the following equation:

$$fobj = w_1 f_1 + w_2 f_2 + w_3 f_3 + \cdots \quad (1)$$

The objectives functions ($f_1, f_2, f_3, \ldots, f_n$) can be normalized by dividing them by their maximum values as follows :

$$fobj = w_1 f_1/\bar{f}_1 + w_2 f_2/\bar{f}_2 + w_3 f_3/\bar{f}_3 + \cdots \quad (2)$$

where

$\bar{f}_1, \bar{f}_2, \bar{f}_3 \ldots \bar{f}_n$ are the maximums of the objectives functions ($f_1, f_2, f_3, \ldots, f_n$) respectivelly,

As they can be reduced to the magnitude order of one of the objective functions like f_1 using conversion factors H_i such as

$$H_i = \frac{f_i}{\bar{f}_i}, \quad i = 1, 2, 3, \ldots n \quad (3)$$

If the chosen objective magnitude order is f_1 in ED case which represents the total production cost Ct, the two other objective functions f_2 and f_3 denote the P_L losses and $EGAS$ greenhouse gases emission respectively. They are represented in the multi-objective function by the following equation:

$$fobj(P_{gi}) = Ct + H_{gaz} EGAS + H_{PL} P_L \quad (4)$$

$$Ct = \sum_{i=1}^{ng} C_i(P_{gi}) \quad (5)$$

The objective function to minimize is subject to the following equality and inequality constraints:

- Equality constraint;

$$\sum_{i=1}^{nd} P_{gi} = P_D + P_L \quad (6)$$

$$P_D = \sum_{i=1}^{nd} P_{Di} \quad (7)$$

where :

P_D : is the total active power consumed by the entire load.

P_{Di}: is the active power consumed by the ith load.

P_L : is the transmission lines active losses.

nd : Load busbar number.

- Inequality constraint :

$$P_{gi} - P_{gi}^{max} \leq 0 \quad (8)$$

$$P_{gi}^{min} - P_{gi} \leq 0 \quad (9)$$

$$P_{gi}^{min} \leq P_{gi} \leq P_{gi}^{max}, \quad i = 1, 2, \ldots ng \quad (10)$$

where

P_{gi}^{max} : Maximum active power of the ith generator,

P_{gi}^{min} : Minimal active power of the ith generator.

ng : generation busbar number.

- Other inequality constraints include:

Generated reactive power (Q_{gi}) :

$$Q_{gi}^{min} \leq Q_{gi} \leq Q_{gi}^{max}, \quad i = 1, 2, \ldots n \quad (11)$$

To maintain electrical service quality and system safety, busbar voltage levels must always be between their limits.

$$V_i^{min} \leq V_i \leq V_i^{max}, \quad i = 1, 2, \ldots n \quad (12)$$

The electrical currents flowing through the lines (I_{ij}) must be in the limits:

$$I_{ij}^{min} \leq I_{ij} \leq I_{ij}^{max} \quad (13)$$

A. Total production costs

The total production cost is given by the following equation:

$$C_t(P_{gi}) = \sum_{i=1}^{ng} (a_i + b_i P_{gi} + c_i P_{gi}^2) \quad (14)$$

a_i, b_i, c_i : are coefficients of the cost function specific to each ith generator.

B. Greenhouse gas emissions (NOx, SO2, CO2 and CO)

The function used to calculate gas emissions in (kg/h) is given by the following equation [9] :

$$EGAS(P_{gi}) = \sum_{i=1}^{ng} (\alpha_i + \beta_i P_{gi} + \gamma_i P_{gi}^2 + d_i \, exp(e_i P_{gi})) \quad (15)$$

α_i, β_i, γ_i, d_i et e_i : are the emission function coefficients attached to each production group.

C. Active power losses (P_L)

The active power losses (P_L) to minimize in IEEE-30 bus network lines is given by approximate or precise methods as follows:

C.1) Kron's approximate formula

Using a mathematical expression based on the power output of each production unit, with the corresponding loss coefficients, given by Kron's equation (16) [10].

$$P_L = \sum_{i=1}^{n} \sum_{i=1}^{n} P_{gi} B_{ij} P_{gi} + \sum_{i=1}^{n} P_{gi} B_{0i} + B_{00} \quad (16)$$

C.2) Precise methods (Newton Raphson)

After using the Newton Raphson OPF, the following formula is used to calculate active power losses [11]:

$$P_L = \sum P_{ij} \quad (17)$$

where P_{ij} represents the active power transiting the ijth line.

III. GENETIC ALGORITHM OPTIMIZATION (GA)

To use the Matlab GA optimization, run the genetic algorithm function 'ga' with the syntax :

[X, FVAL] = ga(fitnessfun,nvars, A, B ,A_{eq}, B_{eq}, L_B, U_B, nonlcon ,Options)

The "ga" function solves problems of the form :

Min F (X) subject to constraints :

- Equality constraint : $A_{eq} \times X = B_{eq}$

- Inequality constraint A*X ≤ B and $L_B \leq X \leq U_B$

X represents the vector of control variables to be optimized.

The 'ga' algorithm is called with the following fields:

fitnessfun: < Fitnessfunction (or objective function)>

nvars: < Number of design variables >

A: <Equality constraint matrix>

B : < Inequality constraint vector B >

$\boldsymbol{A_{eq}}$: <Equality constraint Matrix A_{eq} >

$\boldsymbol{B_{eq}}$: < Equality constraint vector B_{eq} >

LB: <Lower limit of X>

UB: <Upper limit of X>

nonlcon: < non-linear constraints>

Options : < Option structure created with gaoptimset >

IV. GENETIC ALGORITHM ED RESULTS AND DISCUSSION

The multi-objective fitness function is optimized to obtain the optimum value of total production cost (*Ct*), losses (P_L) and greenhouse gases (*EGAS*), subject to equality and inequality constraints. The fitness function is given by equation (4).

The ED applied to the IEEE-30 bus network will be performed for different cases:

Case 1: By minimizing only the total cost of production (*Ct*), without and with taking account losses (P_L).

Case 2: Minimizing the total cost of production (*Ct*) and losses (PL) calculated by the Kron and OPF formulas [5, 6].

Case 3: Minimizing total production cost (Ct) and greenhouse gas emissions (*EGAS*).

Case 4: Minimizing total production cost (*Ct*), losses (P_L) and greenhouse gas emissions (*EGAS*).

A. IEEE-30 bus test network characteristics

The IEEE-30 bus bar network was chosen to solve the ED problem. The electrical network is made up of six production units (at buses n° 2, 5, 8, 11, 13) and equilibrium bus (slack bus) located at busbar n° 1, The network feeds 24 loads through 41 electrical lines as shown in figure 1, the total power demand is 283.4 MW. The voltage of the equilibrium bus (n°1) is forced to 1.060∠0 [12].

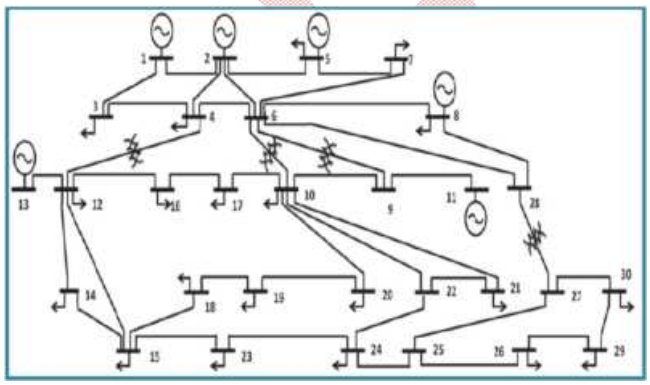


Figure 1. Single-line diagram of the IEEE 30 bus bar test network.

B. ED minimiizing production cost without taking in acount the losses

In this part we neglect the losses ($P_L = 0$), the multi-objective function to optimize is the total production cost Ct formulated by equation 14 is as follows:

$$f_{eval} = C_t \qquad (18)$$

Subject to the equality (6) and inequality (10-12) constraints.

The GA simulation results give the generator output, the total production cost (Ct) and the execution time (t) shown in table 1. The iterative process and unit's production are sown in figure (2).

TABLE 1. OPTIMAL POWER DISPATCH WITH ONLY MINIMIZING TOTAL COST.

Minimisation Sans pertes du Ct : $f_{eval} = C_t$	
Pg1(MW)	11.17
Pg_2 (MW)	24.85
Pg_5 (MW)	50.63
Pg_8 (MW)	99.62
Pg_{11} (MW)	60.97
Pg_{13} (MW)	36.07
feval ($/h)	600.6392
PG (MW)	283.32
Ct(MW)	**600.5675**
PL (MW)	0
t(s)	**60.7842**
EGAS (Kg/hr)	-------

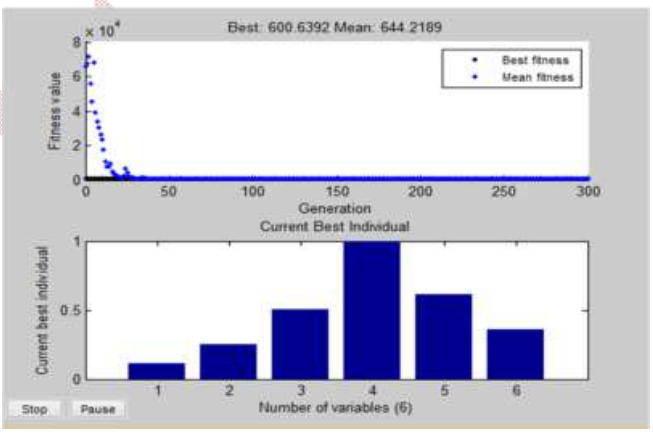


Figure 2. Result and convergence process of Economical dispatching without losses.

C. ED minimiizing production cost taking account active losses

In this section, the ED minimizing only total cost, is performed by GA. The fitness function is then given by equation (18): $f_{eval} = C_t$

Subject to equality (6) and inequality (10-12) constraints

a) Losses calculated using Kron's approximate formula

A mathematical expression based on the powers generated by each production unit, with the corresponding loss coefficients, given by equation (16) is used.

b) OPF losses calculation

The simulation uses the GA with the same fitness function (18), where the P_L losses are determined through Newton-Raphson OPF calculation by using equation 17. The generator outputs (Pgi) of each production unit, the total production cost (Ct) and the execution time (t) obtained by the GA in the two cases a and b are shown in table 2.

TABLE 2. ED WITH TOTAL COST MINIMIZATION WITH TAKING ACCOUNT LOSSES (P_L).

Total cost minimization Ct : $f_{eval} = C_t$		
Losses calculation	*Kron formula*	*OPF*
Pg_1(MW)	*11.96*	*14.64*
Pg_2 (MW)	*26.93*	*27.71*
Pg_5 (MW)	*59.71*	*52.43*
Pg_8 (MW)	*95.29*	*94.26*
Pg_{11} (MW)	*57.73*	*63.47*
Pg_{13} (MW)	*34.02*	*34.42*
feval ($/h)	*605.9493*	*609.1299*
PG (MW)	*285.65*	*286.93*
Ct ($/h)	***605.8228***	***608.9807***
P_L (MW)	***2.3596***	***3.6528***
EGAS (Kg/h)	*----*	*----*
t (s)	***88.6551***	***351.0081***

The production cost shown in table 2 are obtained by the ED using the Kron and OPF formulas are similarly close to 605.8228, 608.9807 $/h respect ctively with an error of 0.52%.

The calculation time obtained using Kron's approximate formula is very interesting, it is almost four times less than that obtained using the OPF 88.7s and 351s respectively. The Kron formula, on the other hand, gives a less precise estimate of losses less than a third of that obtained by OPF 2.3596 and 3.6528 MW respectively. When we need approximate results, Kron's formula gives an acceptable total cost ED in a short time.

Newton Raphson's power flow calculation for the GA optimal productions gives the voltages (module and phase) shown in table 3. The table parameters are:

Type : 1 : slack bus, 2 production bus, 0 : load bus

$|V|$ (pu) : Voltage magnitude

Teta (°) : phase angle voltage

Pl (MW) : Active load power

Ql (MVar) : Reactive load power

Pg (MW) : Active production power

Qg (MVar) : Reactive production power

Qinj (Mvar) : Reactive power compensation

We note that all bus-bars voltages are close to 1pu, with a minimum voltage value of 0.9829 pu, corresponding to a very low voltage drop of 0.0171 pu. The ED makes it possible to distribute power appropriately, with voltages within the admissible limits and reducing total production costs (Ct=608.98$/h).

TABLE 3. VOLTAGE MAGNITUDES AND PHASES AFTER THE ED OF NORMAL LOAD IEEE-30 BUS NETWORK.

Bus	Type	$\|V\|$ (pu)	Teta (°)	Pl (MW)	Ql (MVar)	Pg (MW)	Qg (Mvar)	Qinj Mvar
1	1	1.0600	0	0	0	1.5000	0	0
2	2	1.0430	-0.0147	21.70	12.7	31.4815	33.98	0
3	0	1.0295	0.0738	2.4	1.2	0.0011	0	0
4	0	1.0220	0.2026	7.6	1.6	-0.0014	0	0
5	2	1.0100	-1.8080	94.2	19.0	63.4954	29.57	0
6	0	1.0171	0.6633	0	0	0.0212	0	0
7	0	1.0073	-0.8952	22.8	10.9	0.0024	0	0
8	2	1.0100	2.1924	30.0	30.0	98.5762	12.69	0
9	0	1.0189	1.3162	0.0	0	0.2076	0	0
10	0	1.0118	-1.0942	5.8	2.0	-0.0077	0	3
11	2	1.0172	6.4995	0.0	0	45.0164	15.15	0
12	0	1.0513	-1.0901	11.2	7.5	0.0131	0	3
13	2	1.0710	1.3809	0	0.0	34.6721	5.25	0
14	0	1.0327	-1.9622	6.2	1.6	0.0017	0	0
15	0	1.0248	-1.9440	8.2	2.5	0.0026	0	3
16	0	1.0274	-1.3594	3.5	1.8	0.0067	0	0
17	0	1.0111	-1.3870	9.0	5.8	0.0084	0	3
18	0	1.0079	-2.3690	3.2	0.9	0.0026	0	0
19	0	1.0010	-2.4231	9.5	3.4	0.0053	0	0
20	0	1.0029	-2.1484	2.2	0.7	0.0029	0	3
21	0	1.0002	-1.6372	17.5	11.2	0.0105	0	3
22	0	1.0011	-1.6454	0	0	0.0006	0	0
23	0	1.0076	-2.2810	3.2	1.6	0.0015	0	3
24	0	0.9932	-2.3776	8.7	6.7	0.0077	0	4.3
25	0	1.0009	-2.8557	0	0	0.0013	0	0
26	0	0.9829	-3.2893	3.5	2.3	0.0006	0	0
27	0	1.0147	-2.8647	0	0	0.0017	0	0
28	0	1.0167	0.5405	0	0	-0.0024	0	0
29	0	0.9947	-4.1155	2.4	0.9	0.0003	0	3
30	0	0.9831	-5.0139	10.6	1.9	0.0014	0	0

D. ED optimizing total cost, losses and/or greenhouse gases emission of normal loaded network

In this part, the ED is realized with the total costs production (Ct), losses (P_L) and/or greenhouse gases emission ($EGAS$) minimization of normal loaded network. The multi-objective fitness function are given by different combinations of the terms in equation 4, resulting in the following cases:

$$fobj = Ct \quad (19)$$

$$fobj = Ct + H_{PL}P_L \quad (20)$$

$$fobj = Ct + H_{gas}EGAS \quad (21)$$

$$fobj = Ct + H_{PL}P_L + H_{gas}EGAS \quad (22)$$

Subject to equality (6) and inequality (10-12) constraints

GA simulation with the four fitness functions given in equation (19-22) is performed on the IEEE-30 bus network. Losses (P_L) are determined solely by the Newton-Raphson OPF using equation (17). The generator outputs (Pg_i) of each production unit, the total production cost (Ct) and the execution time (t) are obtained and presented in Table 4.

The results of Table 4 showed that the production cost obtained by the GA ED in the four cases minimizing the total production cost (Ct), the cost (Ct) and the power losses (P_L), the cost (Ct) and greenhouse gas emissions ($EGAS$) and cost (Ct), power losses (P_L) and greenhouse gas emissions ($EGAS$), are respectively: 608.98, 632.01, 626.03, 631.20 $ /h. The

minimum cost is obviously obtained for the only cost (*Ct*) minimizing 608.98$/h. The maximum cost is obtained for the cost (*Ct*) and P_L minimizing 632.01$/h, the cost of the third and fourth cases (626.03 and 631.20 $ /h) are less than the second case and greater than the first. So reducing greenhouse gas emissions does not cost much, i.e. compared to the first case, an increase of 2.7% for the third case and an increase of 3.5% for the fourth case.

TABLE 4. OPTIMAL POWER OUTPUT WITH LOSSES AND MINIMIZATION OF TOTAL PRODUCTION COST

Fobj	*Ct*	*Ct* + $H_{PL}P_L$	*Ct* + $H_{gas}EGAS$	*Ct* + $H_{PL}P_L$ + $H_{gas}EGAS$
Pg_1(MW)	14.64	17.29	32.97	20.08
Pg_2 (MW)	27.71	31.23	44.29	34.79
Pg_5(MW)	52.43	98.59	52.48	92.98
Pg_8(MW)	94.26	47.07	59.31	46.66
Pg_{11} (MW)	63.47	56.05	51.40	54.76
Pg_{13} (MW)	34.42	35.44	46.04	36.50
feval ($/h)	**609.13**	**2379.6**	**1643.7**	**3470**
PG (MW)	**286.9299**	**285.67**	**268.94**	**285.77**
Ct ($/h)	**608.9807**	**632.011**	**626.0307**	**631.1995**
P_L (MW)	**3.6528**	**2.4**	**3.19**	**2.41**
EGAS (Kg/hr)	----	--------	**0.1898**	**0.2016**
t(s)	**351.0081**	**398.7354**	**371.3106**	**388.7645**

Newton Raphson's power flow calculation for the optimum productions found by the IEEE-30 bus ED by GA process in the four cases gives the voltages (modulus and phase) for each case and are listed in Table 5.

TABLE 5. OPF RESULTS FOR THE TEST NETWORK WITH OPTIMAL PRODUCTIONS OBTAINED BY THE GA.

fobj		*Ct*		*Ct* + $H_{PL}P_L$		*Ct* + $H_{gas}EGAS$		*Ct*+$H_{PL}P_L$+ $H_{gas}EGAS$	
Bus	**Type**	**V (pu)**	**Teta (°)**	**V (pu)**	**Teta (°)**	**V (pu)**	**Teta (°)**	**V (pu)**	**Teta (°)**
1	1	1.0600	0	1.0600	0	1.0600	0	1.0600	0
2	2	1.0430	-0.0012	1.0430	-0.4277	1.0430	-0.0560	1.0430	-0.0560
3	0	1.0297	-0.4078	1.0305	-0.7293	1.0298	-0.5117	1.0298	-0.5117
4	0	1.0221	-0.3839	1.0229	-0.7763	1.0222	-0.5106	1.0222	-0.5106
5	2	1.0100	-0.1038	1.0100	-3.3633	1.0100	-0.5523	1.0100	-0.5523
6	0	1.0173	-0.2128	1.0177	-0.7913	1.0173	-0.3884	1.0173	-0.3884
7	0	1.0070	-0.7218	1.0077	-2.3905	1.0071	-1.0084	1.0071	-1.0084
8	2	1.0100	0.2040	1.0100	-0.0906	1.0100	0.0209	1.0100	0.0209
9	0	1.0165	1.2567	1.0173	0.5609	1.0168	1.0185	1.0168	1.0185
10	0	1.0107	-1.3804	1.0103	-1.8172	1.0107	-1.5716	1.0107	-1.5716
11	2	1.0128	7.7196	1.0147	6.4044	1.0134	7.3254	1.0134	7.3254
12	0	1.0508	-1.5156	1.0520	-1.2407	1.0510	-1.6017	1.0510	-1.6017
13	2	1.0710	1.0127	1.0710	2.0218	1.0710	1.0005	1.0710	1.0005
14	0	1.0321	-2.3839	1.0334	-2.1912	1.0323	-2.4817	1.0323	-2.4817
15	0	1.0242	-2.3584	1.0248	-2.2504	1.0243	-2.4686	1.0243	-2.4686
16	0	1.0267	-1.7272	1.0270	-1.7445	1.0268	-1.8566	1.0268	-1.8566
17	0	1.0101	-1.6983	1.0099	-2.0068	1.0101	-1.8705	1.0101	-1.8705
18	0	1.0070	-2.7401	1.0073	-2.8206	1.0071	-2.8782	1.0071	-2.8782
19	0	1.0000	-2.7677	1.0001	-2.9627	1.0001	-2.9228	1.0001	-2.9228
20	0	1.0019	-2.4784	1.0018	-2.7340	1.0020	-2.6425	1.0020	-2.6425
21	0	0.9990	-1.9542	0.9986	-2.3647	0.9990	-2.1407	0.9990	-2.1407
22	0	0.9999	-1.9720	0.9996	-2.3739	1.0000	-2.1570	1.0000	-2.1570
23	0	1.0067	-2.7135	1.0071	-2.7719	1.0068	-2.8466	1.0068	-2.8466
24	0	0.9919	-2.8347	0.9920	-3.1231	0.9920	-2.9996	0.9920	-2.9996
25	0	0.9993	-3.5737	0.9992	-3.9477	0.9994	-3.7429	0.9994	-3.7429
26	0	0.9813	-4.0088	0.9812	-4.3829	0.9814	-4.1779	0.9814	-4.1779
27	0	1.0131	-3.7409	1.0129	-4.1671	1.0131	-3.9127	1.0131	-3.9127
28	0	1.0170	-0.5580	1.0173	-1.0618	1.0170	-0.7347	1.0170	-0.7347
29	0	0.9931	-4.9958	0.9928	-5.4227	0.9931	-5.1676	0.9931	-5.1676
30	0	0.9815	-5.8972	0.9812	-6.3245	0.9815	-6.0689	0.9815	-6.0689

The OPF calculation results show that all bus voltages are close to 1pu, with the same a minimum voltage value of 0.9813, corresponding to a voltage drop of 0.0187 pu, which is very low. The ED allows power to be distributed appropriately, with voltages within the permissible limits.

E. ED with minimized total costs, losses and/or greenhouse gas emissions from an overloaded network

In this part, the ED is realized with the total costs production (*Ct*), losses (P_L) and/or greenhouse gases emission (*EGAS*) minimization of overloaded network. The multi-objective functions are given by the same equations in part C (19-22) subject to equality (6) and inequality (10-12) constraints

GA simulation with the four objective functions given in equation (19-22) is performed on the overloaded IEEE-30 bus network. Also the losses (P_L) are determined by the Newton-Raphson OPF using equation (17). The generator outputs (*Pgi*) of each production unit, the total production cost (*Ct*) and the execution time (*t*) are obtained and presented in Table 6.

The results of table 6 showed that the production cost obtained by the GA-ED of overloaded network, in the four cases minimization (total production cost (*Ct*), cost (*Ct*) and the power losses (P_L), cost (*Ct*) and greenhouse gas emissions (*EGAS*) and cost (*Ct*), power losses (P_L) and greenhouse gas emissions (*EGAS*)), are respectively: 1345.3, 1369.4, 1369.6, 1362.7 $/h. The minimum cost is obviously obtained for the first case of only cost (*Ct*) minimizing 1345.3$/h. The maximum cost is obtained for the second and third cases (*Ct* + $H_{PL}PL$, *and Ct*+ $H_{gas}EGAS$) 1369.4, 1369.6$/h respectively, the forth case is upper the first and lower than the second and the tird 1362.7 $/h. So, even with an overloaded network, reducing greenhouse gas emissions does not cost much, i.e. compared to the first case, an increase of 1.28% for the third case and an increase of 1.775% for the fourth case.

TABLE 6. OPTIMAL POWER OUTPUT WITH LOSSES AND MINIMIZATION OF TOTAL PRODUCTION COST

Fobj	*Ct*	*Ct* + $H_{PL}P_L$	*Ct* + $H_{gas}EGAS$	*Ct*+$H_{PL}P_L$+ $H_{gas}EGAS$
Pg_1(MW)	**49.25**	**30.04**	**67.44**	**39.09**
Pg_2 (MW)	**58.03**	**96.43**	**81.44**	**88.93**
Pg_5(MW)	**117.79**	**150.00**	**111.30**	**150.00**
Pg_8(MW)	**144.35**	**119.27**	**124.02**	**117.31**
Pg_{11} (MW)	**138.10**	**103.25**	**105.44**	**102.49**
Pg_{13} (MW)	**69.76**	**75.74**	**87.24**	**76.93**
feval ($/h)	**1345.478**	**7255.0275**	**2684.3**	**8677.6**
PG (MW)	**577.28**	**574.75**	**576.89**	**547.76**
Ct ($/h)	**1345.3**	**1369.4**	**1369.6**	**1362.7**
P_L (MW)	**10.6**	**8.06**	**10.34**	**8.09**
EGAS (Kg/hr)	--------	------	**0.2452**	**0.2632**
t(s)	**404.1147**	**407.3103**	**432.6234**	**423.1467**

Newton Raphson's power flow calculation for the optimum productions found by the IEEE-30 bus ED by GA process in the fourth cases gives the voltages (modulus and phase) for each case and are listed in Table 7.

The OPF calculation results show that all bus voltages are close to 1pu, with the minimum voltage value of 0.9190, corresponding to a voltage drop of 8.1% lower than the large

voltage limits of 10%. The ED allows power to be distributed appropriately, with voltages within the permissible limits.

TABLE 7. OPF RESULTS FOR THE OVERLOADED TEST NETWORK WITH OPTIMAL PRODUCTIONS OBTAINED BY THE GA IN THE FOURTH CASE.

Bus	Type	|V| (pu)	Teta (°)	Pl (MW)	Ql (MVar)	Pg (MW)	Qg (MVar)	Qinj (Mvar)
1	1	1.0600	0	0	0	1.5000	0	0
2	2	1.0430	-0.5379	21.70	12.7	81.7220	33.98	0
3	0	1.0232	-1.4150	2.4	1.2	0.0035	0	0
4	0	1.0141	-1.5542	7.6	1.6	-0.0083	0	0
5	2	1.0100	-4.1841	94.2	19.0	149.991	29.57	0
6	0	1.0089	-1.3726	0	0	0.1384	0	0
7	0	0.9983	-3.6980	22.8	10.9	0.0102	0	0
8	2	1.0100	-0.2192	30.0	30.0	114.0673	12.69	0
9	0	0.9793	0.9873	0.0	0	1.7019	0	0
10	0	0.9776	-4.3917	5.8	2.0	0.0819	0	3
11	2	0.9631	13.7318	0.0	0	103.0741	15.15	0
12	0	1.0388	-3.7244	11.2	7.5	0.0386	0	3
13	2	1.0710	1.7043	0	0.0	78.9489	5.25	0
14	0	1.0085	-5.7519	6.2	1.6	0.0093	0	0
15	0	0.9954	-5.9193	8.2	2.5	0.0062	0	3
16	0	1.0021	-4.6734	3.5	1.8	0.0244	0	0
17	0	0.9772	-5.0134	9.0	5.8	0.0560	0	3
18	0	0.9682	-7.0842	3.2	0.9	0.0115	0	0
19	0	0.9576	-7.3241	9.5	3.4	0.0421	0	0
20	0	0.9613	-6.7197	2.2	0.7	0.0203	0	3
21	0	0.9599	-5.7817	17.5	11.2	0.0992	0	3
22	0	0.9612	-5.7936	0	0	0.0062	0	0
23	0	0.9692	-7.0290	3.2	1.6	0.0069	0	3
24	0	0.9478	-7.6484	8.7	6.7	0.0488	0	4.3
25	0	0.9579	-8.9103	0	0	0.0049	0	0
26	0	0.9290	-10.2447	3.5	2.3	0.0065	0	0
27	0	0.9785	-8.9124	0	0	0.0008	0	0
28	0	1.0047	-1.9218	0	0	-0.0174	0	0
29	0	0.9405	-11.8514	2.4	0.9	0.0024	0	3
30	0	0.9178	-13.9703	10.6	1.9	0.0147	0	0

V. CONCLUSION

The genetic algorithm has been successfully applied to solve the ED problem with consideration of equality and inequality constraints. The results obtained clearly show the effectiveness of the GA in solving the ED problem in terms of minimizing the multi-objective function, i.e. fuel cost, power active losses and gas emission. Taking into account certain constraints such as current flow limits and protection constraints in our optimization model will improve its applicability in real-world situations.

The Kron's formula, gives a less accurate estimate of losses less than a third of that obtained by OPF. When we need approximate results, Kron's formula gives an acceptable total cost ED in a short time.

In normal loaded network ED, all bus-bars voltages are close to 1pu, a very low voltage drop of 0.0171 pu. The ED makes it possible to distribute power appropriately, with voltages within the admissible limits and reducing total production costs (Ct = 608.98$/h). Reducing greenhouse gas emissions does not cost much, i.e. compared to the first case, an increase of 2.7% for the third case and an increase of 3.5% for the fourth case. The ED allows power to be distributed appropriately, with voltages within the permissible limits.

So, even with an overloaded network, reducing greenhouse gas emissions does not cost much, i.e. compared to the first case, an increase of 1.28% for the third case and an increase of 1.775% for the fourth case.

The OPF calculation results show that all bus voltages are close to 1pu, with a voltage drop of 8.1% lower than the large voltage limits of 10%. The ED allows power to be distributed appropriately, with voltages within the permissible limits.

VI. REFERENCIES

[1] Lahlou Hidra, Kenza Ydjedd, A. Bouzidi, "Le dispatching économique dans les réseaux électriques par les algorithmes génétiques ", Master 2, Université de Bejaia, 2022.

[2] A. BOUZIDI, " Modélisation et simulation des réseaux électriques ", Cours Master2 Réseaux électriques, faculté deTechnologie, Université de Bejaia, 2015.

[3] Truong-Son Cao,Thi-Thanh-Thuy Nguyen,Van-Son Nguyen, "Performance of Six Metaheuristic Algorithms for Multi-Objective Optimization of Nonlinear Inelastic Steel Trusses", Buildings 2023, 13(4), 868.

[4] El-Ghazali Talbia, Matthieu Basseurc, Antonio J. Nebro and all, "Multi-objective optimization using metaheuristics: Non-standard algorithms", International Transactions in Operational Research 19(1-2), March 2012.

[5] Abdullah Konak, David W. Coit, Alice E. Smith, "Multi-objective optimization using genetic algorithms: A tutorial", Reliability Engineering & System Safety, Elsevier, Vol. 91, Iss. 9, Sept. 2006, pp. 992-1007

[6] Muwaffaq I. Alomoush, "Complex power economic dispatch with improved loss coefficients", Energy Systems volume 12, pages1005–1046 (2021)

[7] Iasonas Kouveliotis-Lysikatos, Nikos Hatziargyriou, "Fully distributed economic dispatch of distributed generators in active distribution networks considering losses", IET Generation, Transmission & Distribution, Vol. 11, Iss. 01 February 2017.

[8] Benrabeh Djaidir, Ismail Ziane, Abdelkader Rouibah, "Renewable Energy Integration In Unbalanced Three Phase Power Flow using Gauss-Seidel and Newton-Raphson Methods", International Journal of Advanced Studies in Computers, Science and Engineering, Vol. 11, N° 10, (2022): 8-16.

[9] Daniel, L., Chaturvedi, K.T., Kolhe, M., "Genetic Algorithm for Economic Load Dispatch with Microgrid to Save Environment by Reduction of CO2 Emission", Conference paper, Springer, Singapore, March 2023.

[10] Masoud Dashtdar, Aymen Flah, "Solving the environmental/economic dispatch problem using the hybrid FA-GA multi-objective algorithm", Energy Reports, Volume 8, November 2022, Pages 13766-13779.

[11] Ijaz Ahmed, Muhammad Rehan, Abdul Basit and Keum-Shik Hong, "Greenhouse gases emission reduction for electric power generation sector by efficient dispatching of thermal plants integrated with renewable systems", PMC, Scientific Reports, 2022.

[12] Innocent E. Davidson, Kamati N. I. Mbangula, "Dynamic voltage stability studies using a modified IEEE 30-bus system, 2016 IEEE 16th International Conference on Environment and Electrical Engineering (EEEIC), 2016.

Analysis of Space Vector Identification Method in Series Active Filters for Electrical Power Quality Improvement

Mustapha Asnoun [1], Rahma Kachenoura [2], Adel Rahoui [1,3] , Brahim Brahimi [4]

[1] *L2CSP Laboratory, Mouloud Mammeri University of Tizi-Ouzou, BP 17 RP, 15000 Tizi-Ouzou, Algeria*

mustapha.asnoun@ummto.dz, adel.rahoui@ummto.dz

[2] *LATAG Laboratory, Mouloud Mammeri University of Tizi-Ouzou, BP 17 RP, 15000 Tizi-Ouzou, Algeria*

r.kachenoura@gmail.com

[3] Ecole Nationale Supérieure des Travaux Publics Francis Jeanson, Rue Sidi Garidi BP 32 Kouba, 16051 Algiers, Algeria

[4] *Electrical Engineering Department, Mouloud Mammeri University of Tizi-Ouzou, BP 17 RP, 15000 Tizi-Ouzou, Algeria*

brahimibrahim@gmail.com

***Abstract*—The increasing use of non-linear loads has raised concerns about disturbances in electrical networks. This paper focuses on the analysis and enhancement of electric power quality through the application of a series active filter (SAF). A method for identifying electrical disturbances, known as the Space Vector Method, is investigated. Furthermore, two control strategies for the SAF hysteresis control and space vector pulse-width modulation control control are presented. Simulation tests are carried out to analyze the two studied control strategies.**

Keywords: **Hysteresis control, pulse-width modulation (PWM) control, quality of energy, series active filter (SAF), space vector.**

I. INTRODUCTION

Ensuring the quality of electrical power is a major concern for electricity providers. While continuity of service was the primary customer satisfaction criterion in the past, recent technological advancements have placed a new spotlight on energy treatment. Today, power quality involves not only the continuity of service but also the waveform's integrity. The quality of electrical energy, crucial for the smooth electrical loads operation, has shown significant deterioration due to the growing use of non-linear loads, leading to issues such as harmonic distortions, voltage unbalances, momentary interruptions, voltage sags, and temporary overvoltages [1].

In response to these challenges, various solutions have been developed. Traditional methods involve compensating reactive power with capacitor banks to improve the power factor and using passive filters like LC circuits to mitigate harmonic currents. Modern pollution control methods, however, offer enhanced effectiveness. These methods employ active filters based on semiconductor components, such as IGBTs and MOSFETs. These active filters can be categorized into two types: parallel active filters to improve current quality and series active filters (SAFs) to enhance voltage quality. A combination of both filters, known as unified power quality conditioning, has also been investigated [1], [2].

This paper focuses on one of these modern solutions, the implementation of the space vector method in SAFs, aiming to improve the quality of electrical power by addressing the challenges posed by non-linear loads under nonideal grid voltage conditions. We'll explore the principles, methodologies, benefits of this innovative approach.

The rest of this paper is organized as follows. Section II presents the structure and the studied control strategies of the SAF. In Section III, electrical disturbance identification methods are described. In Section IV, the hysteresis and pulse-width modulation (PWM) control strategies of the SAF are investigated through simulation tests and the obtained results are analyzed and compared. Section V concludes this paper.

II. SAF-BASED DEPOLUTION SOLUTION

Since the proposal by H. Sasaki and T. Machida in 1971 [1], active power filters for harmonics compensation in electrical networks have been a subject of study. Initially, active filtering was a theoretical concept. However, as power semiconductor technology rapidly advanced, it found application in harmonics compensation, often paired with PWM techniques. With the progress made in theoretical research, active filters were brought to practical implementation. By the 1990s, there was a resurgence of interest in active filters, driven by studies demonstrating their superior performance in harmonics compensation when compared to traditional passive LC filters.

A. SAF Structure and Basic Principle

Series active filters are controlled voltage sources strategically positioned in the electrical circuit between the power grid and the sensitive load, with the primary objective of

safeguarding the latter. These filters consist of two fundamental units:

The *control part* of the series active filter is responsible for tasks such as identifying disruptive voltages, regulating injected voltages, and managing inverter switches. This control is often achieved using PWM techniques.

The *power part* encompasses essential elements, including a three-phase voltage inverter with PWM control, energy storage components integrated into a DC power supply system, a second-order output filter, and three single-phase voltage injection transformers.

Series active filters operate as a dedicated solution designed to shield sensitive loads from undesirable voltage fluctuations that originate within the electrical network. These filters are strategically placed in series between the compromised network and the target load, utilizing injection transformers as voltage sources.

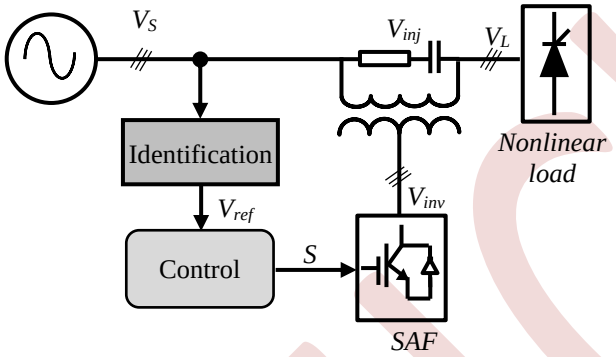


Figure 1. SAF.

Figure 1 represents the studied system, which consists of a perturbed electrical network (V_S) affected by a non-linear load (V_L) and a 1:1 ratio transformer. The primary is connected to the series active filter, providing inverter voltage V_{inv}, and the secondary is linked to an *RC* filter, supplying a voltage V_{inj}.

B. SAF Control Schemes

1) Hysteresis control

Hysteresis control is a nonlinear control technique that relies on the difference between the reference voltage and the voltage generated by the inverter. This difference is compared to a tolerance range known as the hysteresis band. When the error exceeds the upper or lower limits of the band, a control signal is sent to keep the error within this range [3].

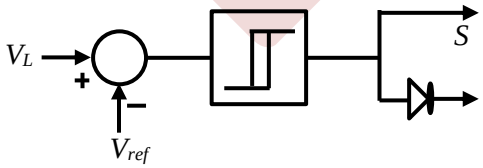
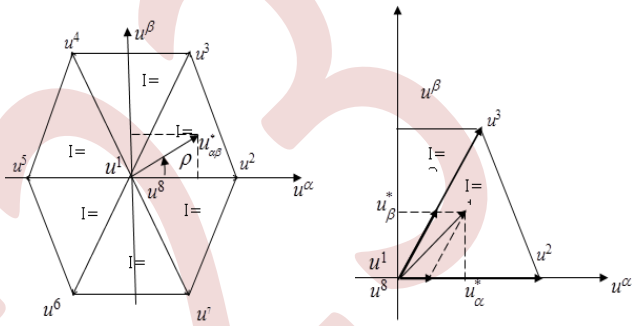


Figure 2. Hysteresis control scheme of the SAF.

Sizing this regulator essentially involves setting the width of this band, and a practical rule is to make it equal to 5% of the nominal voltage. However, it does not guarantee compliance with the maximum switching frequency of semiconductors in every case [4]. The advantage of hysteresis control lies in its unlimited speed, ease of implementation, robustness, and good dynamics.

2) Space Vector PWM control

The Space-vector PWM (SVPWM) method is widely employed in inverter control because it can increase the maximum output voltage value of the inverter while reducing harmonic distortion compared to the sinusoidal PWM method. Several algorithms utilize SVPWM to control inverters or rectifiers. The objective of all modulation strategies is to minimize switching losses and harmonics while ensuring precise control.



Command vector in the frame αβ Decomposition of a command vector

Figure 3. SVPWM principle.

III. ELECTRICAL DISTURBANCE IDENTIFICATION METHODS

Understanding the classification characteristics is crucial for identifying and analyzing different disturbances, as the effectiveness of active filters largely hinges on isolating these disruptive signals. It's essential to identify these signals so that they can be countered by injecting signals with opposite amplitude and phase. The reliability of the identification method ensures proper compensation, which, in turn, leads to an enhancement in the quality of the network signal. The proposed method for disturbance identification is known as the Space Vector Method.

A. Definition and History

The Space Vector Transformation represents an interesting approach to analyzing electrical power quality issues. This method offers a distinctive advantage: it's applicable to all types of disturbances and relies on only two parameters for analysis, a complex quantity known as the vector space and a real quantity called the homopolar component. This approach simplifies the analysis of electrical disturbances by focusing on these two quantities, making the analysis process efficient while encompassing a broad spectrum of electrical power quality concerns [5]. In an undisturbed three-phase system, the homopolar component remains at zero, causing the space vector to trace a circular path in the complex plane. However, any perturbation in the waveforms of the three-phase quantities results in changes in the trajectory of the space vector and/or the homopolar component. These alterations are used to detect, identify, classify, and characterize the measured disturbances. By tracking variations in the space vector trajectory and the homopolar component, it becomes possible to identify the disturbances impacting the three-phase electrical system.

Symmetrical components, first introduced by Fortescue in 1918, are the foundation of the Fortescue transformation, a method applicable to the phasors of sinusoidal functions. This technique enables the analysis of asymmetric three-phase systems under sinusoidal conditions. Lyon later adopted Fortescue's transformation and modified it to accommodate time-varying quantities, irrespective of the conditions, whether they are sinusoidal or not [6]. Considering the grid voltage vector $V_S = [v_a\ v_b\ v_c]^T$, the Lyon transformation gives the following decomposition :

$$\begin{bmatrix} v_d(t) \\ v_i(t) \\ v_0(t) \end{bmatrix} = \frac{1}{3}\begin{bmatrix} 1 & a^2 & a \\ 1 & a & a^2 \\ 1 & 1 & 1 \end{bmatrix}\begin{bmatrix} v_a(t) \\ v_a(t) \\ v_a(t) \end{bmatrix} \quad (1)$$

where $a = e^{-j\frac{2\pi}{3}}$. j is the complex operator.

The normalization coefficient of 1/3 is chosen to ensure the preservation of amplitudes between the three-phase systems before and after the transformation. If $v_d(t)$, $v_i(t)$, and $v_i(t)$ are real-valued, the direct and inverse components of the Lyon transformation, $v_d(t)$ and $v_i(t)$, are complex conjugates. These quantities are redundant and convey the same information. In fact, to fully describe the three real scalar quantities of the original three-phase system, only one complex scalar quantity and one real scalar quantity are required [7]. Subsequently, Clark adopted Lyon's transformation with the objective of eliminating the previously mentioned redundancy, resulting in the creation of the following matrix.

$$\begin{bmatrix} v_\alpha(t) \\ v_\beta(t) \\ v_0(t) \end{bmatrix} = \frac{1}{3}\begin{bmatrix} 1 & -\frac{1}{2} & -\frac{1}{2} \\ 1 & \frac{\sqrt{3}}{2} & -\frac{\sqrt{3}}{2} \\ \frac{1}{2} & \frac{1}{2} & \frac{1}{2} \end{bmatrix}\begin{bmatrix} v_a(t) \\ v_a(t) \\ v_a(t) \end{bmatrix}. \quad (2)$$

The matrix obtained is now in real values, mirroring the three components of the transformed three-phase system $v_\alpha(t)$, $v_\beta(t)$, and $v_0(t)$. Its initial two components constitute the space vector, and the homopolar component is given by $v_0(t)$.

B. Space Vector Characteristics in presence of disturbances

1) Fundamental disturbances

When exclusively focusing on the fundamental frequency component ω_0, the quantities of a three-phase system are assumed to be sinusoidal with the same angular frequency ω_0. Consequently, each quantity can be represented as the sum of two phasors, each multiplied by complex exponential functions of angular frequency $\pm\ \omega_0$ [8].

$$\begin{aligned} v_a(t) &= V_a\cos(\omega_0 t + \varphi_a) \\ &= \left(\frac{v_a}{2}e^{j\varphi_a}\right)e^{j\omega_0 t} + \left(\frac{v_a}{2}e^{-j\varphi_a}\right)e^{-j\omega_0 t}. \end{aligned} \quad (3)$$

When represented in the complex plane, these phasors rotate at the same angular frequency $\pm\ \omega_0$, but in opposite directions. The space vector, being a linear function of the three-phase quantities, can also be presented as the sum of one phasor rotating counterclockwise and another phasor rotating clockwise.

$$\vec{v}(t) = v_p(t)e^{j\omega_0 t} + v_n(t)e^{-j\omega_0 t} \quad (4)$$

where $v_p = |v_p|e^{j\varphi_p}$ and $v_n = |v_n|e^{j\varphi_n}$.

They are, respectively, the positive and negative phasors. In the general case where the two phasors have different amplitudes and phases, the space vector takes the form of an ellipse in the complex plane with the following parameters.

$$\begin{cases} r_{maj} = |v_p| + |v_n| \\ r_{min} = |v_p| - |v_n| \\ \varphi_{inc} = (\varphi_n + \varphi_p)/2 \end{cases} \quad (5)$$

where r_{maj} is the major radius, r_{min} is the minor radius and φ_{inc} is the inclination angle.

2) Fundamental disturbances

In the presence of harmonics, the Space Vector can be expressed as a sum of vectors rotating at different frequencies $\pm k\omega_0$.

$$\vec{v}(t) = \sum_{k=0}^{+\infty}\left[v_{pk}(t)e^{jk\omega_0 t} + v_{nk}(t)e^{-jk\omega_0 t}\right] \quad (6)$$

where k is the harmonic order of the harmonics present in the phase quantities. On the other hand, the homopolar component can be represented in the classical form of a Fourier transform.

3) Space vector simulation using Matlab

In this section, two examples of applying the space vector transformation for the analysis of electrical energy quality are presented. The simulations were performed using Matlab-Simulink. The first example illustrates voltage sags, and the results are shown in the following figures. This disturbance is characterized by a voltage drop on all three phases, with a magnitude of 50% of the nominal voltage, which is 220√2 V, as seen in Figure 4.

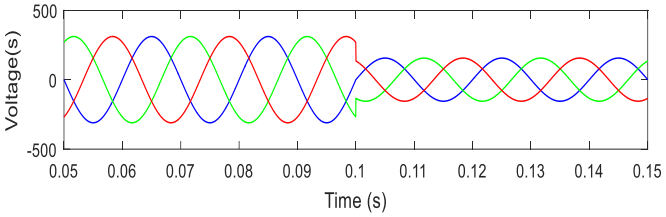


Figure 4. Measured voltage sag.

The space vector result is represented in Figure 5 throughout the entire voltage sag period from 0.5s to 1s. It follows a circular shape with a shape index SI = r_{maj}/r_{min}= 1.

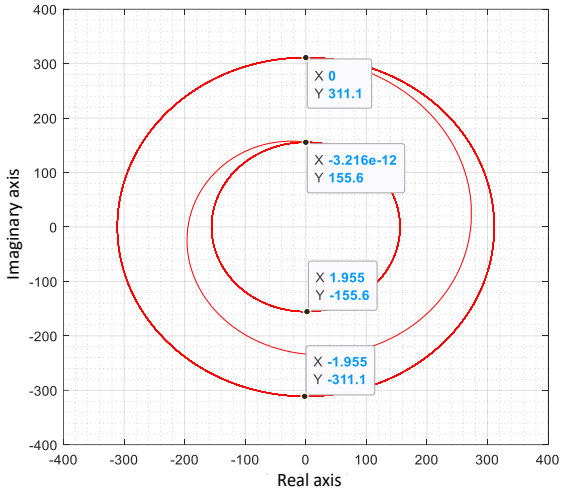


Figure 5. Space vector in the complex plane.

The second example presents the results of harmonic disturbances. Figure 6 represents the 5th order harmonic.

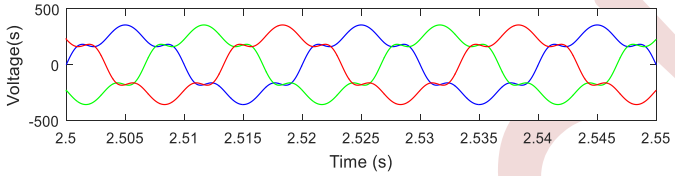


Figure 6. 5th order harmonic disturbance.

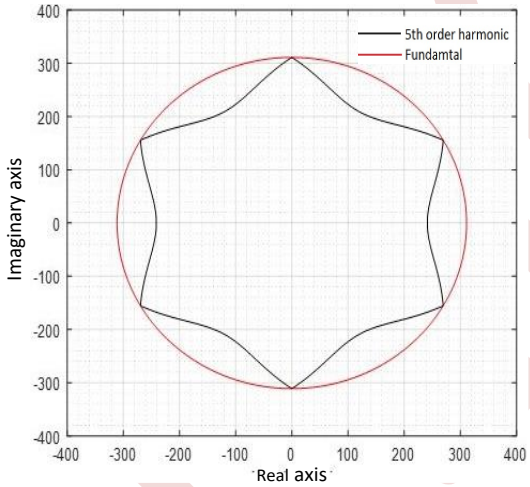


Figure 7. Space vector for 5th harmonic order.

Different types of disturbances are typically analyzed and quantified using specific methods, often necessitating the use of various parameters. Concerning disturbances with significant amplitude variations, such as voltage sags, interruptions, and overvoltages, techniques for amplitude estimation, detection, classification, and characterization are applied. For disturbances related to waveform irregularities, like harmonics, estimation tools such as Fourier series and Fourier transform are employed.

IV. Simulation Result

The studied structure comprises a three-phase voltage source, an *RL* load, and a series active filter, including a power section that consists of a series transformer, voltage inverter, and output filter. Additionally, there is a control section employing hysteresis or space vector PWM.

The primary purpose of the series active filter is to ensure voltage stability at the terminals of sensitive loads, regardless of the grid's condition. To validate this study, three tests have been conducted. Namely, 50% symmetrical voltage drop, 50% overvoltage, and then a harmonic disturbance. It has been observed that the filter's response is instantaneous, irrespective of the control method used hysteresis or space vector PWM.

Figures 8, 9, and 10 show the results obtained when a 50% three-phase voltage sag occurs in the grid voltages, a 50% three-phase overvoltage occurs in the grid voltages, and a 20% injection of the 5th harmonic, respectively.

Figure 10 illustrates spectral analyze of the distorted grid voltage V_S and the obtained load voltage V_L when SAF is operated using PWM control and hysteresis control.

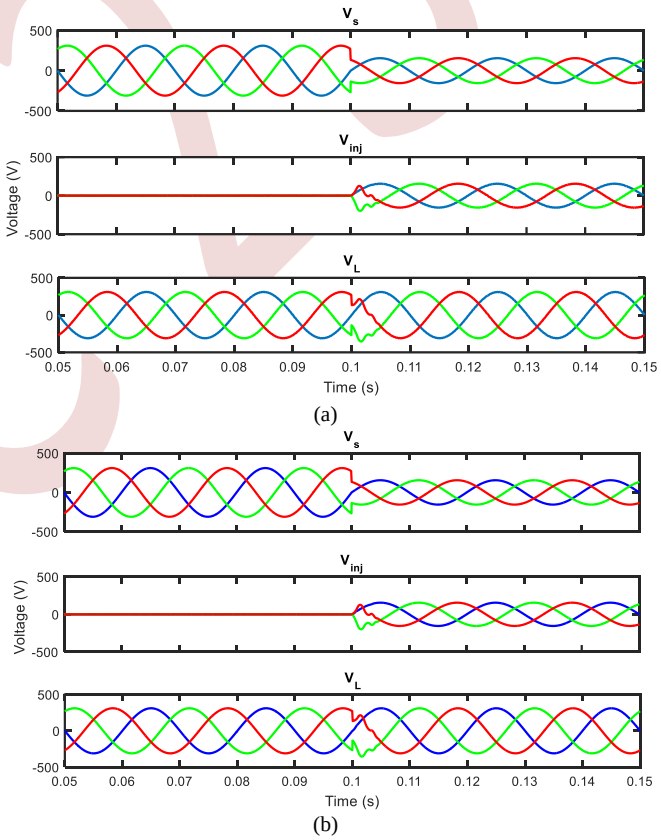


Figure 8. Control performance comparison under 50% voltage sag: (a) PWM control and (b) hysteresis control.

The simulation results demonstrate that applying hysteresis control and SVPWM method for a series active filter yields similar performance in terms of managing voltage sags and overvoltages. Both approaches exhibit comparable response times to these disturbances.

However, when considering harmonic distortion tests, it's worth noting that hysteresis control exhibited slightly better performance in terms of transient response compared to SVPWM.

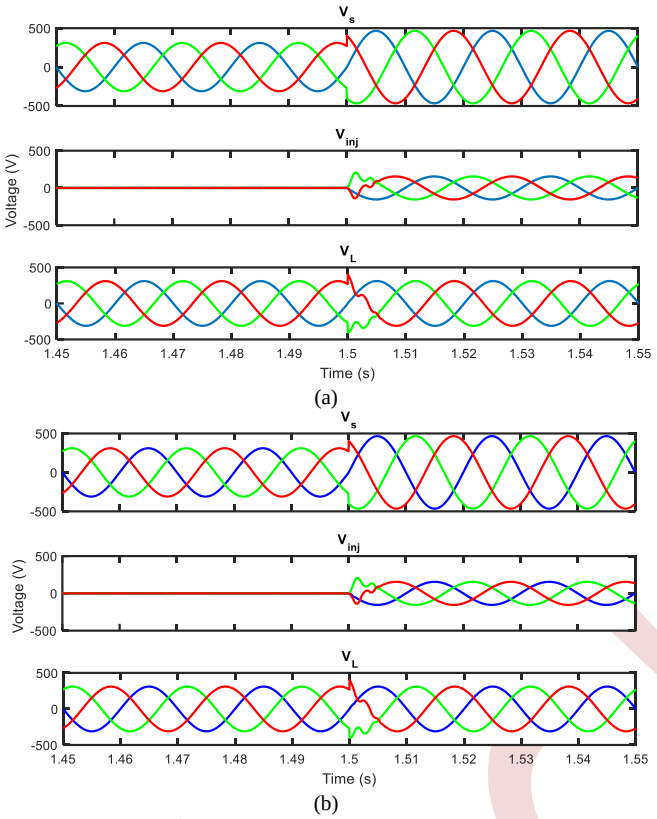


Figure 9. Control performance comparison under 50% overvoltage: (a) PWM control and (b) hysteresis control.

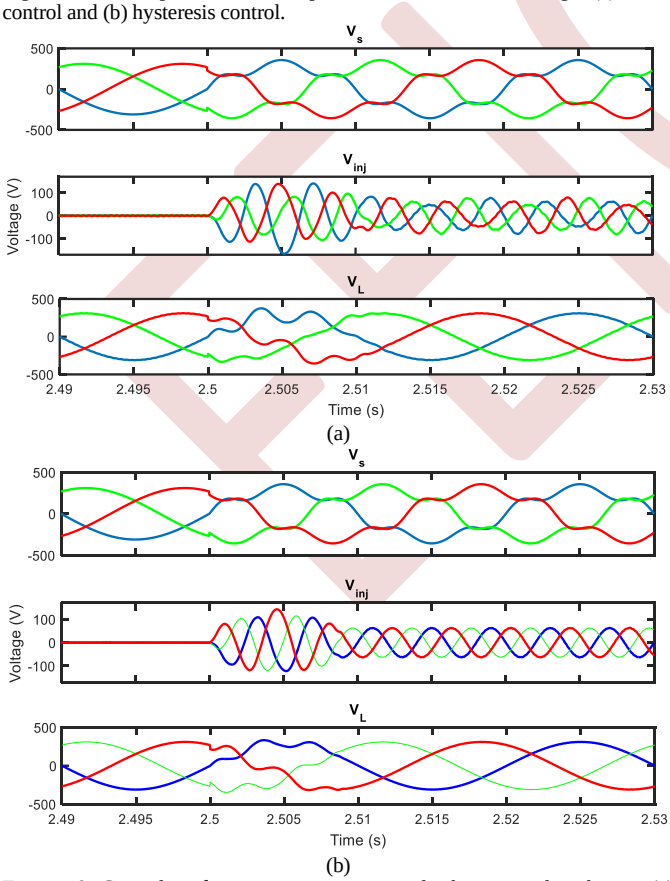


Figure 10. Control performance comparison under harmonic disturbance: (a) PWM control and (b) hysteresis control.

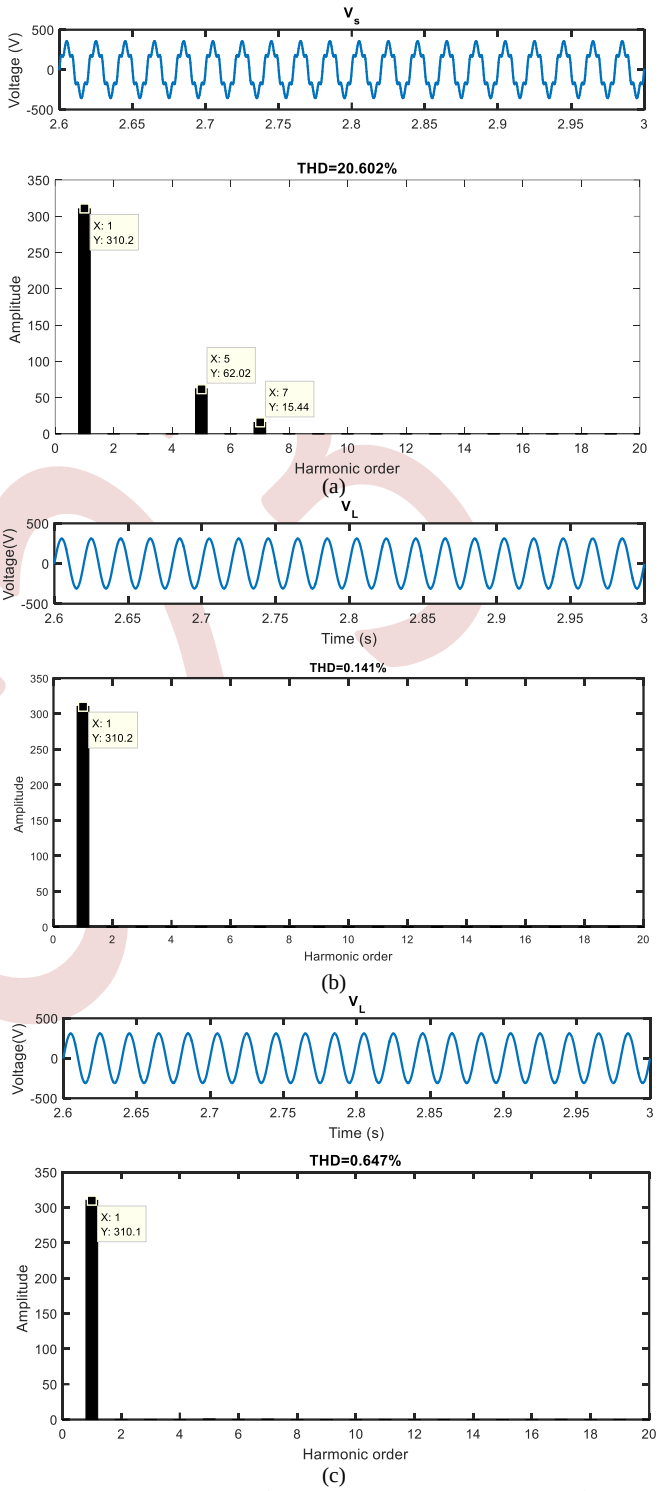


Figure 10. Spectral analysis of: (a) distorted grid voltage V_S, (b) filtered V_L obtained with PWM control and (c) filtered V_L obtained with hysteresis control.

To further validate this approach, a spectral analysis of the load voltage V_L has been conducted. It was observed that the Total Harmonic Distortion (THD) with Hysteresis Control is higher than that with SVPWM. The reasons for this improvement lie in the fact that SVPWM controls the inverter's output spectrum by controlling the switching frequency. This

precise control allows for accurate reconstruction of low-rank components.

In summary, while both Hysteresis Control and Space Vector PWM yielded similar results in managing voltage sags and surges, Space Vector PWM demonstrated significant superiority in reducing harmonic distortions.

V. CONCLUSION

This work has focused on the theoretical analysis of electrical energy quality and its enhancement using SAF structures. The Space Vector Method has been introduced for identifying disturbances affecting the quality of electrical energy. SAF control has been specifically examined through two methods, hysteresis, an easily implementable method that may lack precision as it operates within a tolerance band, and SVPWM, a slightly more challenging and costly method but offering finer control as it operates at a constant switching frequency. Both methods have demonstrated their ability to provide a similar response from the filter in terms of speed and quality for fundamental disturbances. However, in the case of harmonic disturbances, SVPWM control has proven to be more effective. In conclusion, improving the quality of electrical energy through a series active filter relies on the selection of an appropriate control strategy for the power inverter.

REFERENCES

[1] D. Li, T. Wang, W. Pan, X. Ding, and J. Gong, "A comprehensive review of improving power quality using active power filters," *Electric Power Systems Research*,Vol. 199, Oct. 2021.

[2] A. Gaillard, "système éolien basé sur une MADA : contribution à l'étude de la qualité de l'énergie et de la continuité de service," *PhD Thesis in Electrical Engineering*, Henri Poincaré University, Nancy1, Apr. 2010.

[3] A.M. Muftah, "Structures et stratégies de commande des filtres actifs parallèle et hybride avec validations expérimentales," *PhD Thesis in Electrical Engineering*, Henri Poincaré University, 2008.

[4] H. Laurent, C. Doncarli, "Stationarity index for abrupt changes detection in the time-frequency plane," *IEEE Signal Processing letters*, vol. 5, no. 2, Feb. 1998.

[5] V. Ignatova, P. Granjon and S. Bacha, "Space Vector Method for Voltage Dips and Swells Analysis," *IEEE Transactions on Power Delivery*, vol. 24, no. 4, pp. 2054-2061, Oct. 2009.

[6] J. Mikulović, T. Šekara, and M. Forcan, "Power definitions for three-phase systems in terms of instantaneous symmetrical components," *International Journal of Electrical Power & Energy Systems*, vol. 147, 108808, May 2023.

[7] W.-F. Zhang and Y.-H. Yu, "Comparison of Three SVPWM Strategies," *Journal of Electronic Science and Technology of China*, vol. 5, no 3, 2007.

[8] T Toumi, A Allali, A Meftouhi, O. Abdelkhalek, A Benabdelkader, and M. Denai, "Robust control of series active power filters for power quality enhancement in distribution grids: Simulation and experimental validation," *ISA Transactions*, vol. 107, Dec. 2020.

Investigation about Ferranti Effect and Challenge to Harmonics Suppression in a Specific Long Power Transmission Line

T. Ainouche[1], Y. Belkhiri[2], H. Moulai[1] and N. Yousfi[3]

[1] *Laboratory of Characterisation and Diagnosis of Power Equipments, Faculty of Electrical Engineering, USTHB, BP 32, Bab Ezzouar, Algiers, Algeria*

E-mail address: hmoulai@usthb.dz

[2]*Electrical engineering department, Faculty of Technology, Batna University, Algeria*

E-mail address: y.belkhiri@g.essa-alger.dz

[3]*Algerian National Electricity Transmission Company, Gué de Constantine, Algiers, Algeria*

***Abstract*— This work is devoted to overvoltage transient's propagation through unloaded relatively long transmission lines where the Ferranti effect phenomenon appears as a mean influent parameter. This phenomenon generates especially harmonics pollution and leads to inopportune flashovers and equipments failure. We have then the aim to dimension a power reactive compensation by installing adequate shunt inductance in order to attenuate the receiving end voltage and the superimposed harmonics.**

Keywords: **Over-Voltage Transients; Ferranti Effect; Total Harmonic Distortion; Reactive power compensation.**

I. INTRODUCTION

Transmission line parameters including series resistances, series reactance and shunt susceptance are important inputs to various power system programs and applications [1, 2]. The problem of designing insulation for transient voltages is complicated by the great variety of transient and meteorological conditions that the line experiences and by statistical fluctuations in the insulation strength itself [2]. Transients appear in all shapes and with different amplitudes. Each type of transient may occur during most types of meteorological conditions, all of which affect the flashover strength differently [3].

For single and three-phase power systems with sinusoidal voltages and sinusoidal currents, quantities such as active power, reactive power, active current, reactive current, power factor, etc. are based on the average concept. Many contributors have attempted to redefine these quantities to deal with three-phase systems with unbalanced and distorted currents and voltages [4].

The larger transients occur more rarely than the smaller ones, and the greatest possible transients may have an extremely low probability of occurring in actual service. Often, the expense of insulation is sufficient to withstand such a transient may be so great that it becomes more practical and economic to take the risk, clear the infrequent fault, and reclose[1]. When reclosing breakers are utilized, flashovers on transmission lines do not usually result in permanent failure or in unacceptable stability problems.

The probability of successful reclosing is quite high, thus encouraging efforts toward designing the lines to meet a given reliability criterion rather than attempting to ensure that no flashover will ever occur [2].

However when the length of the lines of transport or, in a more general way, the distance between the power stations of production and the centers of consumption, become higher than a few hundred kilometers of other electro-technical phenomena can reduce the transmissible maximum power appreciably [2, 3]. These phenomena are related on the one hand on the voltage drop in the lines and to the need for preserving the stability of the network during the most frequent disturbances such as for example the defects of insulation on line.

When a line is lowly loaded or empty it behaves like a capacitor. The reactive power supplied to the network ($C\omega U^2$) is higher than 180 kVAR / km for a 220 kV line. And as the line is loaded, the flow of current in the direct inductance line will consume reactive power equivalent to $3l\omega I^2$.When we reach the current value as that $3l\omega I^2 = C\omega U^2$, then the balance of reagent line is zero [2, 5]. The power that flows in the line when this balance is zero is called reactive characteristic power Sc; witch is:

$$Sc = 3VI = \frac{U^2}{Zc} \qquad (1)$$

Where Zc is the characteristic impedance of the line.

Therefore, the study related to the over-voltages is necessary in order to ensure the safe operation.

II. Major Problems of Long Lines

As an example of the Algerian power grid, during the visit of the line maintenance team of GRTE at the place indicated by the default locator of the departure 220 kV NAAMA to SAIDA, it was noted what follows:

Flashover marks on the anchorage pylon No. 25 between the continuity junction (Phase 4) and the pylon girder.

The protection of the circuit breaker D60 operates an opening of single Phase 4 - Earth, then a reclosing of the faulty phase. But immediately, the fault evolves between phases 0 and 4, and therefore it was immediately followed by a three phase breaking.

On the perturbo-graphy recorded on the section of the studied line (Figure 1), we can see well that the flashover took place on phase 4, where the circuit breaker detected an over-current which lasted 90 ms before it opens.

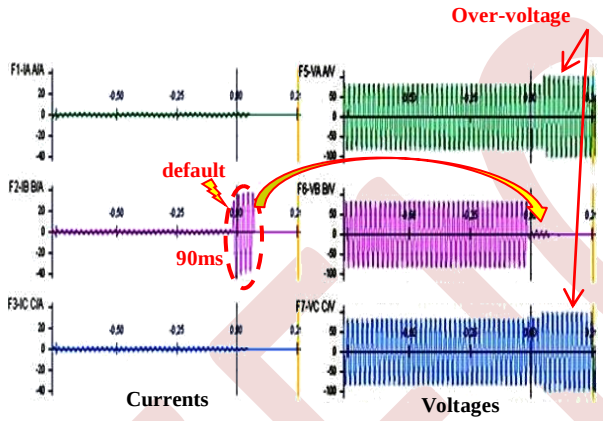


Fig.1. Perturbography of the recorded flashover.

III. Line Conditions and Model

Figure 2 shows the single phase line operating diagram of the studied electrical network (220kV, Saida - Naama - Bechar). this line is 285 km length between Saida – Naama, and 305 km between Naama and Bechar. It consists of seven buses, nine lines, two intermediate power stations (NAAC and BEC), one post of 220 kV in Saida and two substations of 220/60/30 kV in Naama and Bechar.

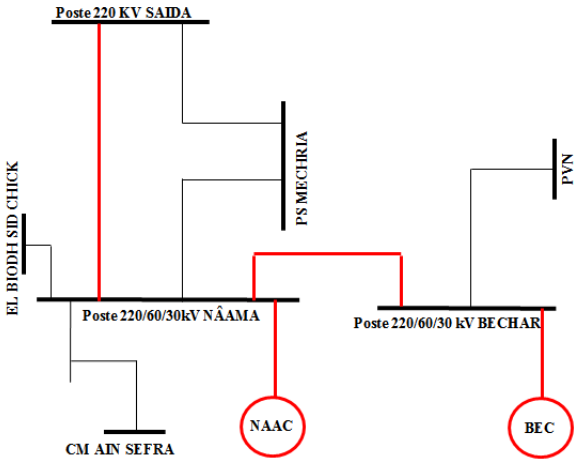


Fig. 2. An operating single line diagram of the studied electrical network.

Figure 3 shows an equivalent single phase diagram in π of the transmission line.

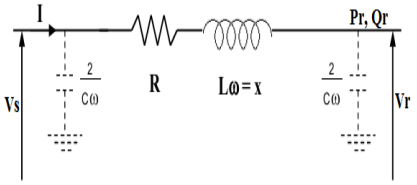


Fig. 3. Diagram in π of the transmission line.

- Vr and Vs represents the sending end voltage and receiving end voltage of the line.
- R, L and C are the cyclic impedances of the direct regime of the line.
- Pr and Qr are respectively the active and reactive power at the output of the line.

The line equations system of the quadripole connected in π is:

$$\begin{cases} Vs = A.Vr + \sqrt{3}B.Ir & \text{(phase/phase)} \\ Is = C.Vr + D.Ir & \text{(phase/ground)} \end{cases} \quad (2)$$

Whith:

$$\begin{cases} A = D = 1 + \left(\dfrac{1}{2} Y.Z\right) \\ B = Z \\ C = Y\left(1 + \left(\dfrac{1}{4} Y.Z\right)\right) \end{cases} \quad (3)$$

IV. Total Harmonic Distortion

Periodic voltage and current distorted waveforms can be presented by the sum of a series of multiple frequency terms of varying magnitudes and phases [6]. This expresses the Fourier theorem, whereby a complex wave form is expressed as

$$m(t) = a_0 + \sum_{n=1,2,3...} \left[a_n \cos(nwt + \alpha_n)\right] \quad (4)$$

Where:

- a_n is the magnitude of the n^{th} harmonic frequency
- ω is the fundamental frequency and
- α_n is the phase shift of the nth harmonic.

The Total Harmonic Distortion (THD) is computed using the following formula:

$$THD = \frac{\left(\sum_{n=2}^{\infty} V_n{}^2\right)^{1/2}}{V_1} \quad (5)$$

Where:

- V_1 is the fundamental voltage
- V_n is the n^{th} harmonic voltage.

The distortion power factor describes how the harmonic distortion of a load current decreases the average power transferred to the load.

$$\text{Distortion Power Factor} = \frac{1}{\sqrt{1+THD_i{}^2}} = \frac{I_{1rms}}{I_{rms}} \quad (6)$$

THD_i is the total harmonic distortion of the load current. This definition assumes that the voltage remains undistorted (sinusoidal, without harmonics) [4, 6]. This simplification is often a good approximation in practice.

I_{1rms} is the fundamental component of the current and I_{rms} the total current - both are root mean square-values.

The result when multiplied with the Displacement Power Factor (DPF) is the overall true power factor or just power factor correction (PFC):

$$\text{PFC} = DPF \frac{I_{1\ rms}}{I_{rms}} \quad (7)$$

V. Power Factor Correction Importance

Power Factor Correction (PFC) is defined as the ratio of the real power (P) to the apparent power (S), or the cosine (for pure sine wave for both current and voltage) that represents the phase angle between the current and voltage waveforms (Figure 4). The power factor correction can vary between 0 and 1, and can be either inductive (lagging, pointing up) or capacitive (leading, pointing down) [2]. In order to reduce an inductive lag, capacitors are added until PFC almost equals 1.

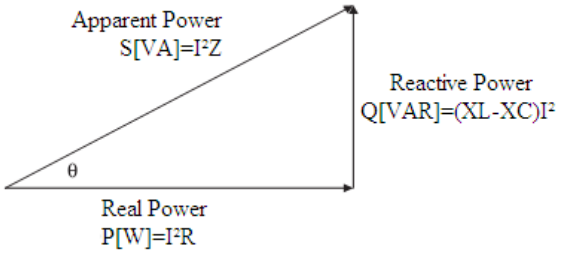


Fig. 4. Power Factor Triangle (Lagging)

Shunt inductive compensation is used either when charging the transmission line, or, when there is very low load at the receiving end. Due to very low, or no load, very low current flows through the transmission line [2]. Shunt capacitance in the transmission line causes voltage amplification (Ferranti Effect) [3].

Power factor correction provides many benefits [2]:

- Increase system capacity
- Improve the voltage
- Reduce the heat losses
- Reduce the amount of electric power used

VI. Ferranti Effect Compensation and Filtering

Long transmission lines are the seat of a substantial quantity of charging currents. If such a line is opened or very weakly loaded at the receiving end, the voltage at this end may become greater than the voltage at the departure [3, 7, 8]. This is known as Ferranti effect. It is due to the voltage drop across the line inductance (due to charging current) which is in phase with the source voltage [3, 7]. Therefore, both capacitance and inductance are responsible on the production of this phenomenon.

The capacitance (and charging current) is negligible in short lines but significant in medium lines and appreciable in long lines. Therefore, this phenomenon occurs in medium and long lines [7]. Figure 5 shows the Fresnel diagram on the Ferranti effect.

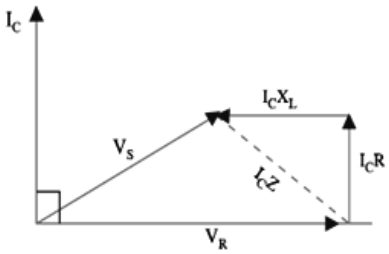


Fig. 5. Fresnel diagram (Ferranti effect).

It is clear from the Fresnel diagram that the voltage generated by the source Vs when the line is open is small than the reception voltage Vr [3]. Where Ic is the current absorbed by the capacitor.

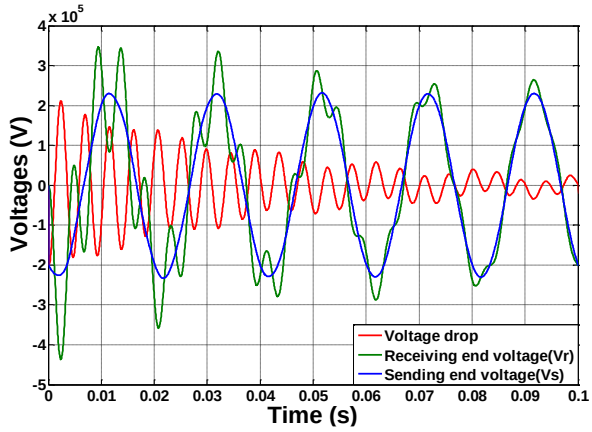


Fig. 6. Voltage drop of the sending end voltage (Vs) and receiving end voltage (Vr) without load.

Figure 6 shows the variation of the sending end voltage and receiving end voltage without load where the Ferranti effect appears clearly. By simulation of the voltage drop between the two ends, we can see that the transient is higher than 200kV. And, by using the reactive compensation as shown in Figure 7, between 0.1s and 0.2s, this enabled us to mitigate the voltage drop at 40kV and to maintain it constant.

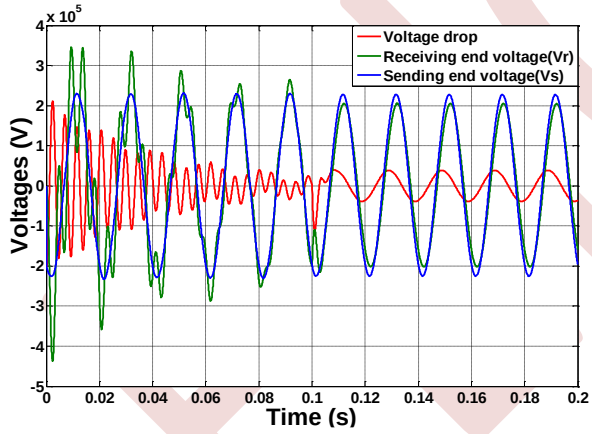


Fig. 7. Voltage drop of the sending end voltage (Vs) and receiving end voltage (Vr) with load and compensation between 0.1s and 0.2s.

Figure 8 shows the variation of the sending end voltage and receiving end voltage with filtering and without load. And, by simulation of the voltage drop between the two ends, we can see that the transient overvoltage when filtering the harmonics of the first order is higher than 200kV. On the other hand, when using the filtering and the reactive power compensation as shown in Figure 9 between 0.1s and 0.2s, we have maintained the voltage drop at 40kV.

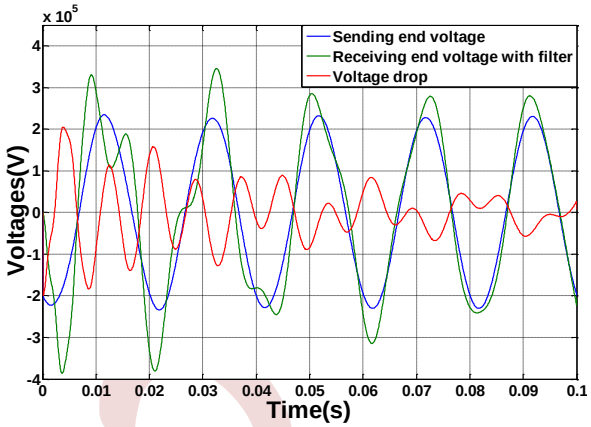


Fig. 8. Voltage drop of the sending end voltage (Vs) and receiving end voltage (Vr) with filtering and without load.

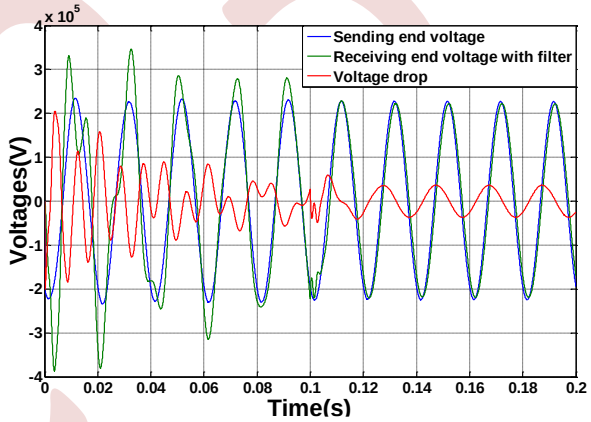


Fig. 9. Voltage drop of the sending end voltage (Vs) and receiving end voltage (Vr) with load, filtering and compensation between 0.1s and 0.2s.

VII. Conclusion

As a conclusion, we can say that in the specific studied case, the unloaded transmission line may cause, in specific conditions, a transient over-voltage where the receiving end voltage may become double of the sending end voltage. This is generally the case of unloaded very long transmission lines.

To compensate this phenomenon and in order to eliminate the consecutive harmonics, adequate shunt inductors and filters of harmonics are connected with success across the transmission line. Moreover, the proposed technique responds fast, less than half cycle duration.

REFERENCES

[1] Pritindra Chowdhuri "Power System Transients" The Electric Power Engineering Handbook, Edited by L.L. Grigsby CRC Press LLC, 2001

[2] E Kuffel, W S Zaengl and J Kuffel, '' High voltage engineering fundamentals'', Newnes, Butterworth-Heinemann, Second Edition, 2000.

[3] T. Ainouche, H. Moulai, S. Belkhir, F. Soukeur, L. Louaked, ''Study of Flashover Occurrence in Conductor Pylon Configuration in High Voltage Long Lines'', 4th International Conference On Electrical Engineering., ICEE2012, Algiers, 8-9 May 2012.

[4] Fang Zheng Peng; Ott, G.W., Jr.; Adams, D.J." Harmonic and reactive power compensation based on the generalized instantaneous reactive

power theory for three-phase four-wire systems "IEEE Transactions on Power Electronics, VOL. 13, pp 1174-1181, No. 6, November 1998.

[5] A. C-Leveque, B. Parisot, C. D. Lebranchu,D. S. Nguefeu, E. Jp. Taisne, P. Boussard « Technical specification, calculation and dimensioning of the compensation means » power grid manager, SONELGAZ-GRTE, reference book, Compensation Design V2.1.

[6] Islam, K.M.; Samra, A.H. " Effect of condensers on harmonic propagation in AC power system" Southeastcon '95. 'Visualize the Future'., Proceedings., IEEE Conference Publications, pp 425 – 428, 26-29 March 1995.

[7] B.L. Theraja, A.K. Theraja, "A Textbook of Electrical Technology, Vol III, Chap. 41, pp.1603-1682, S. SHAND edition (2009).

[8] A. Omboua, ''Alimentation de faibles charges directement des lignes à haute tension'', Doctorat Thesis, University of Liege, Belgium, December 2002.

EEIC'23

Estimation of the Schavemaker arc model parameters for high-voltage circuit breakers

Fatiha Latri [1], Ahmed Gherbi [2], Mahamad Nabab Alam [3]

[1] *Laboratory QUERE, Department of Electrical Engineering, University of SETIF1, SETIF, Algeria*
samia_latri@yahoo.fr

[2] *Laboratory LAS, Department of Electrical Engineering, University of SETIF1, SETIF, Algeria*
gherbi_a@univ-setif.dz
address

[3] *Department of Electrical Engineering, NIT Warangal, India*
mnalam@nitw.ac.in

***Abstract*— The Schavemaker arc model is a good arc model which can be used to represent the nonlinear arc conductance inside the high-voltage circuit breakers, during the interruption process. This work aims to determine the most suitable optimization method to determine precise values of its parameters from short-line fault measurements performed on high-voltage circuit breakers. For this purpose, unconstrained local and global optimization methods were used to minimize the error between the measured and the simulated arc voltage and arc current curves. Some of these methods were used in previous works.**

For numerical simulation, the Schavemaker arc model was first built in Matlab/Simulink and then inserted in the test-circuit which allows short-line fault simulation.

The simulation results show that the heuristic methods namely the particle swarm optimization technique, the genetic algorithm and the simulated annealing method perform better than the other used methods, however there is no a single method that is efficient for all the HV circuit breakers. For the 245kV and the 123kV circuit breakers, the genetic algorithm technique is the most suitable, while for the 145kV circuit breaker; the simulated annealing method is the most appropriate.

***Keywords:* High-voltage circuit breakers, Black box arc models, Parameter estimation.**

I. INTRODUCTION

High-voltage (HV) SF_6 circuit breakers are the main protection devices in HV networks, they currently dominate the HV circuit breakers market for voltages between 72.5kV and 800kV, thanks to the remarkable arc extinguishing properties of the SF_6 gas [1]. When a fault occurs, the circuit breaker contacts separate when approaching current-zero, the electric arc that appears between them is extinguished by the SF_6 gas. Successful interruption is obtained if the dielectric regeneration rate is greater than the evolution of the transient recovery voltage (TRV). The time period when the transient voltage and the post-arc current occur is in the range of microseconds to milliseconds. In some special cases, establishing or interrupting a short-circuit current is a difficult task for the HV circuit breaker, the interruption of a short-line fault (SLF) is among these cases. The SLF occurs on the overhead line relatively close to the circuit breaker terminal and creates, after the current interruption, a very steep voltage oscillation at the line side of the circuit breaker [2]-[3]. To be sure that the circuit breaker is able to interrupt this type of default, it must be tested in a high-power laboratory. However the tests are expensive and time-consuming, the black-box arc models are used to study the arc-circuit interaction during the interruption process in order to extend the information obtained during the test and better understand the complex phenomena taking place [4].

The black box arc models are mathematical description of the arc behavior. The basic black-box arc models were proposed by Cassie and Mayr by considering some physical assumptions, thereafter that many modifications of these arc models were proposed in order to well reproduce the measured data [5]-[6]-[7]. Nowadays, the KEMA and the Schavemaker arc models are the most used in the literature because they show good correspondence between the measured and simulated curves before current-zero. The schavemaker arc model has the advantage to be simpler than the KEMA arc model which consists of three submodels in series.

For a correct study of the arc-circuit interaction during the interruption process, it is not only important to choose a black box arc model that describes well such behavior but also to determine its unknown parameters as accurately as possible, from the measured arc voltage and arc current curves, because imprecise parameters can affect the predictive capability of the arc model [8]. For the AC HV circuit breakers, the following MATLAB optimization algorithms were used to minimize the error between the measured and the simulated curves; the simplex search Nelder-Mead algorithm (fminsearch) [9], the nonlinear least square function (lsqnonlin) [10], the genetic algorithm (GA) [11]-[12] and the simulated annealing (SA) algorithm.

In this work, the Schavemaker arc model is chosen to simulate the dynamic behavior of the electric arc inside the HV SF6 circuit breakers, during the interruption process. In addition of the methods cited above, the particle swarm optimization (PSO) technique, the pattern search algorithm (PS) and the quasi-Newton line search algorithm (fminunc) are used to extract its parameters from three 90% SLF measurements, performed successively on the 245kV/50kA/50Hz (CB245), 145kV/31.5kA/60Hz (CB145) and 123kV/31.5kA/60Hz (CB123) circuit breakers [9]. The obtained results are compared to determine the most suitable optimization method for a correct arc circuit interaction study.

This paper is organized as follow: Section 2 introduces the Schavemaker arc model. Section 3 describes the parameter determination procedure. Section 4 gives an overview on the used optimization methods. Section 5 presents the comparison of the simulation results. Finally, section 6 provides the conclusion of the work.

II. SCHAVEMAKER ARC MODEL

The Schavemaker arc model is a Mayr-type arc model described by the following differential equation [7]

$$y(t,\theta) = \frac{d\ln g}{dt} = \frac{1}{\tau}\left(\frac{ui}{P_0 + P_1 ui} - 1\right) \quad (1)$$

Where,

u	arc voltage, in volts
i	arc current, in amperes
g	arc conductance, in siemens
τ	time constant, in seconds.
P_0	cooling power constant (originating from the design of the circuit breaker) in Watt.
P_1	cooling power constant (regulates the influence of the electrical power input on the cooling power).
θ	vector of the unknown parameters (τ, P_0 and P_1).

As in the high currents area, the arc voltages computed with (1) were lower than the measured ones; the arc model was adapted in the following way

$$y(t,\theta) = \frac{d\ln g}{dt} = \frac{1}{\tau}\left(\frac{ui}{\max(U_{arc}|i|,\ P_0 + P_1 ui)} - 1\right) \quad (2)$$

U_{arc} is the constant arc voltage in the high currents area, in volts.

The Schavemaker arc model has three parameters to be determined; τ, P_0 and P_1. The parameter U_{arc} can be used to have a constant arc voltage in the high currents area.

III. PARAMETER ESTIMATION PROCEDURE

In this work, seven routines based on unconstrained optimization algorithms were designed to estimate the parameters of the Schavemaker arc model, the procedure followed is as follows

1) The measured arc voltage and arc current curves needed for the evaluation and the validation of the parameter estimation routines describe the arc behaviour during the interruption process; they are obtained from a high-power laboratory. The measured arc voltage $u_m(t)$ and arc current $i_m(t)$ curves corresponding to CB245, CB145 and CB123[9] are presented respectively in *Fig. 1, 2* and *3.*

2) The arc conductance and the electric power were computed point by point from $u_m(t)$ and $i_m(t)$

$$g_m(t) = \frac{i_m(t)}{u_m(t)} \quad (3)$$

$$w = u_m(t).i_m(t) \quad (4)$$

1) The differential of the arc conductance was computed from $g_m(t)$

$$y_m = \frac{d\ln(g_m(t))}{dt} \quad (5)$$

2) (1) was rearranged as

$$y(t,\theta) = \frac{d\ln g}{dt} = \frac{1}{\tau}\left(\frac{w}{P_0 + P_1 w} - 1\right) \quad (6)$$

3) The expression of the objective function was written using (5) and (6), by applying the method of ordinary least squares

$$E(\theta) = \sum_{j=1}^{n-1}\left[y_{mj} - y_j(t,\theta)\right]^2 \quad (7)$$

Here, n is the number of observation points.

4) Unconstrained optimization was performed on the parameters to minimize the objective function in (7).

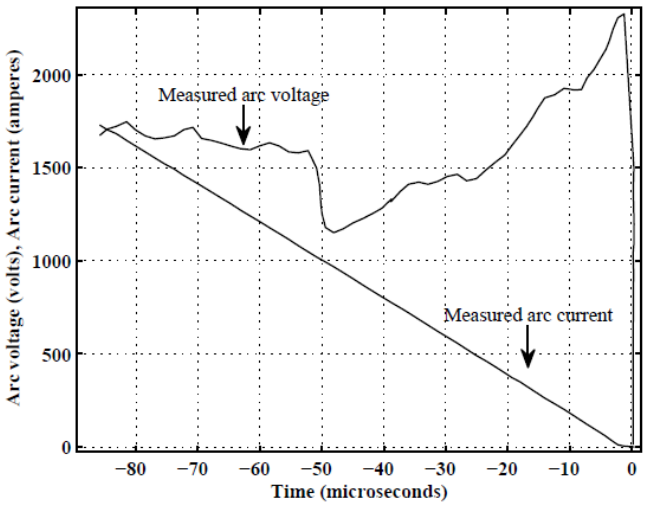


Figure 1. Measured arc voltage and arc current traces before current-zero (CB245)[9].

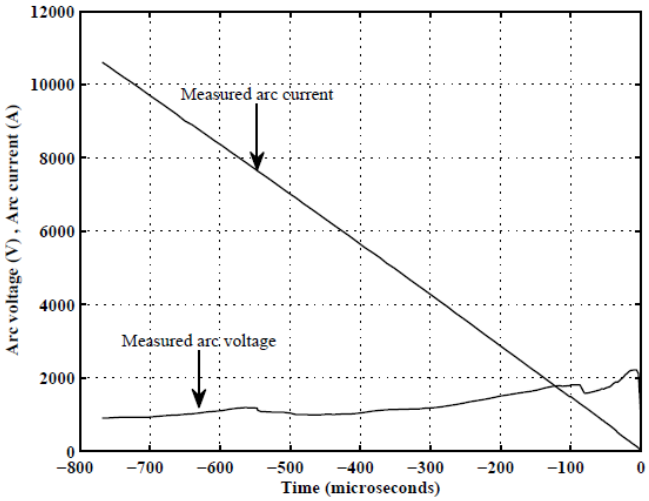


Figure 2. Measured arc voltage and arc current traces before current-zero (CB145)[9].

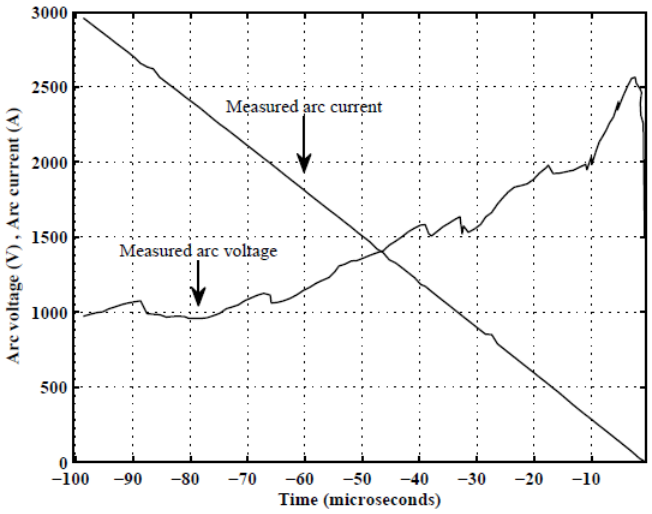


Figure 3. Measured arc voltage and arc current traces before current-zero (CB123)[9].

IV. Optimization Algorithms

The problem described by (7) is an unconstrained single-objective optimization problem; local and global optimization algorithms are used to solve it.

The local optimization algorithms consist to find a local minimum in the basin of attraction of the starting point. This local minimum can be a global minimum if initialization is performed carefully. In the other hand, the global optimization algorithms search for global minimum through more than one basin of attraction [13].

In this work, the used global optimization algorithms are PSO, GA, SA and PS, while the used local optimization algorithms are those of fminsearch, lsqnonlin and fminunc.

PSO technique is a stochastic optimization technique based on swarm intelligence; it is able to optimize non-linear and multidimensional problems. Its basic principle is inspired by the motion of bird flocks and schooling fish, which while searching for food, they transmit the information. Conducted by the good information the birds will go to the place where the food is.

The individuals are called particles and the population is named swarm.

The movement of a particle is influenced by its inertia, its personal best position (pbest) and the global best position (gbest). Each particle seeks to adjust its position using the current velocity and the distance obtained from pbest and gbest.

For a D-dimensional target search and N number of particles, at iteration k, for each particle the position vector is given as

$$X_i^k = \left[X_{i1}^k, X_{i2}^k, \dots X_{iD}^k\right]^T \quad (8)$$

The velocity vector is given as

$$V_i^k = \left[V_{i1}^k, V_{i2}^k, \dots V_{iD}^k\right]^T \quad (9)$$

These vectors are updated through the dimension j according to the following equations [14]

$$V_{ij}^{k+1} = \omega V_{ij}^k + c_1 r_1^k\left(pbest_{ij} - X_{ij}^k\right) + c_2 r_2^k\left(gbest_j - X_{ij}^k\right) \quad (10)$$

$$X_{ij}^{k+1} = X_{ij}^k + V_{ij}^{k+1} \quad (11)$$

Where:

i=1, 2…, N and j=1, 2…, D;

c_1 and c_2 are positive constants, used to pull each particle to pbest and gbest;

r_1 and r_2 are two randomly generated numbers with a range [0 1];

ω is the inertia weight and it keeps balance between exploration and exploitation. The inertia weight is defined as follows

$$\omega = \omega_{max} \cdot \frac{-k \cdot (\omega_{max} - \omega_{min})}{Maxite} \quad (12)$$

ω_{min} : the initial weight.

ω_{max} : the final weight.

Maxite: the maximal number of iterations

The flow chart of the PSO technique is shown in *Fig. 4.*

GA is a stochastic search method and evolutionary algorithm, inspired from the natural selection process. GA has four operators; the initialization operator creates the initial population of solutions called individuals, each solution is associated with a fitness value. The selection operator chooses the chromosomes from the population for mating. The crossover operator is used to combine the genetic information between two chromosomes. Finally the mutation operator modifies one or more gene of a chromosome. The process is repeated over various generations [15].

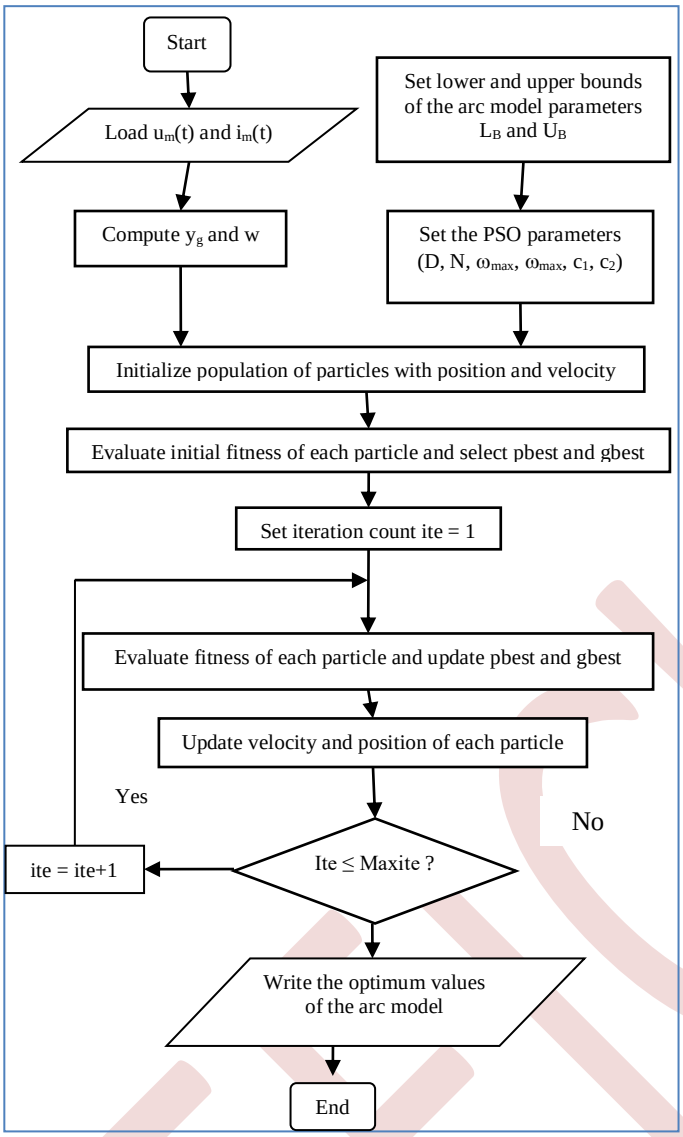


Figure 4. Flow chart of the PSO technique

SA is a metaheuristic optimization method used to approximate the global optimum of a function. It is inspired by the annealing in the metallurgy where the metal is heated to a high temperature and then slowly cooled; the structure obtained is of good quality. The SA algorithm was made by Metropolis in 1953 and then improved by other searchers. SA uses the value of the objective function; it starts with a current solution x_c of the objective function at an initial high temperature T_0, then a new solution x_1 is randomly taken from its neighborhood. The acceptance depends on the difference between the new solution and the current solution as well as the current temperature.

$$\Delta f = f(x_1) - f(x_c) \qquad (13)$$

If $\Delta f \leq 0$ the new solution x_1 replaces the current solution. Otherwise, it will be accepted probabilistically [16]. The Metropolis criterion to decide the acceptance probability is given by

$$p = \exp\left(-\frac{\Delta f}{K_B T}\right) > 1 \qquad (14)$$

Where p is the acceptance probability; Δf is the difference between the current and the neighbor solution: K_B is the constant of Boltzmann and T is the current temperature.

The general diagram of the optimization routines using the MATLAB functions; *fminsearch*, *lsqnonlin*, *fminunc*, *simulannealbnd*, *ga* and *patternsearch* is shown in *Fig. 5*.

The best fitting parameters and the computation time obtained by each optimization routine are presented in the tables I, II and III. The parameter U_{arc} was chosen, from the measured arc voltage; U_{arc} is 1420V for the CB245 (*Fig. 1*) , 1100V for the CB145 (*Fig. 2*) and 950V for the CB123(*Fig. 3*). From these results it is clear that in term of execution time the local optimization methods are faster.

V. NUMERICAL SIMULATION

For numerical simulation, the Schavemaker arc model was first built in MATLAB/Simulink and then inserted in the test-circuit (*Fig. 6)* which consists of the generator and the inductance (Ls) at the supply side of the breaker under test, the TRV network (Rs, Cs, Cd) and the artificial line (R, L , C) [3]. The test-circuit parameters can be computed for each HV circuit breaker [9].
For the CB245, Vsmax = 204.124kV (maximum amplitude), 50 Hz; Ls = 9.191 mH; Rs = 100 Ω; Cs = 60nF; Cd=1nF; L = 1.02 mH, R = 450 Ω and C = 5.03 nF.

The parameters in table I, II and III were successively used to simulate the arc-circuit interaction. The simulation results are shown in *Fig. 7* to 9.

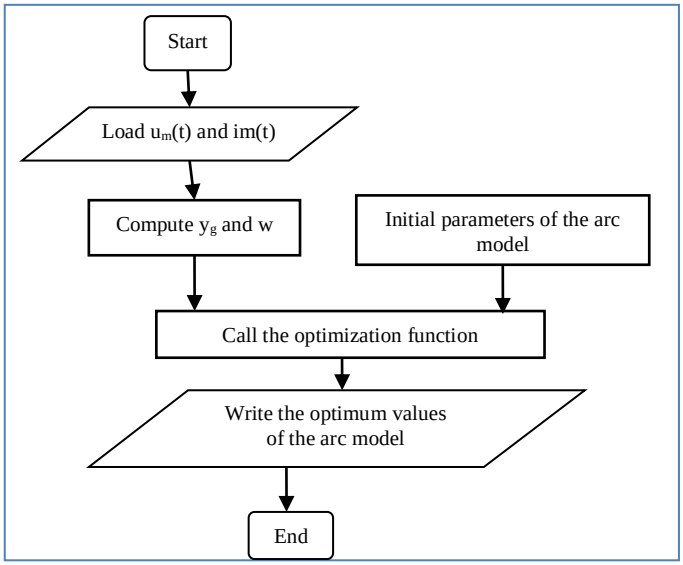


Figure 5. The general diagram of the optimization routine using fminsearch, lsqnonlin, fminunc, simulannealbnd, ga and patternsearch

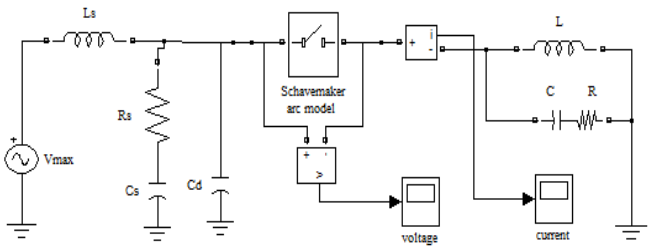


Figure 6. The test-circuit for the SLF simulation

For the CB245, only the simulated arc voltages obtained by using PSO, GA, SA and fminunc (*Fig. 7*) are well approximated to the measured arc voltage. fminsearch, lsqnonlin and PS have given a reignition rather than a successful interruption. The simulated arc voltages obtained by using SA and fminunc are almost superposed

For the CB145, only the simulated arc voltages obtained by using PSO, GA and SA (*Fig. 8*) are well approximated to the measured arc voltage. fminsearch and lsqnonlin have given a reignition rather than a successful interruption.

For the CB123, only the simulated arc voltages obtained by using PSO, GA and SA (*Fig. 9*) are well approximated to the measured arc voltage. fminsearch, lsqnonlin, fminunc and PS have given almost the same results.

TABLE I. PARAMETER ESTIMATION RESULTS (CB245)

Algorithm	τ(µs)	P_0 (W)	P_1	computation time (s)
fminsearch	0.681	54194	0.9668	0.068
lsqnonlin	0.681	54230	0.9668	0.47
PS	0.629	47373	0.9728	2.57
fminunc	0.286	15917	0.9930	0.32
PSO	0.25	13581	0.995	10.48
GA	0.3	17553	0.99151	2.31
SA	0.297	16719	0.99278	14.95

TABLE II. PARAMETER ESTIMATION RESULTS (CB145)

Algorithm	τ(µs)	P_0 (W)	P_1	computation time (s)
fminsearch	$9.9\text{x}10^{-8}$	0.0061	1	0.078
lsqnonlin	$4.4\text{x}10^{-5}$	2.6565	1	0.46
PS	0.18553	11972	0.9972	2.27
fminunc	0.17946	11500	0.9976	0.23
PSO	0.27	12000	0.999	7.04
GA	0.27107	11873	0.9964	2.06
SA	0.27008	11550	0.999	3.35

TABLE III. PARAMETER ESTIMATION RESULTS (CB123)

Algorithm	τ(µs)	P_0 (W)	P_1	computation time (s)
fminsearch	0.18096	14510	0.99799	0.093
lsqnonlin	0.18087	14498	0.998	1.86
PS	0.1839	14920	0.99772	3.05
fminunc	0.17434	13640	0.99841	0.32
PSO	0.27	14000	0.995	8.35
GA	0.27006	13254	0.995	1.59
SA	0.27	13996	0.995	5.32

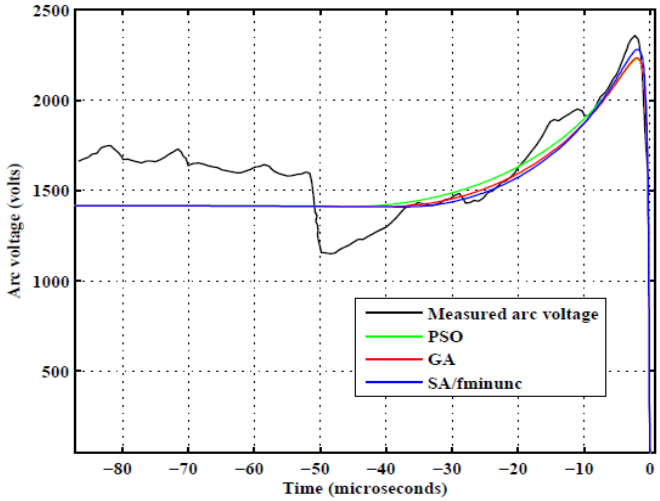


Figure 7. The simulated arc voltages using PSO, GA, SA and fminunc(CB245).

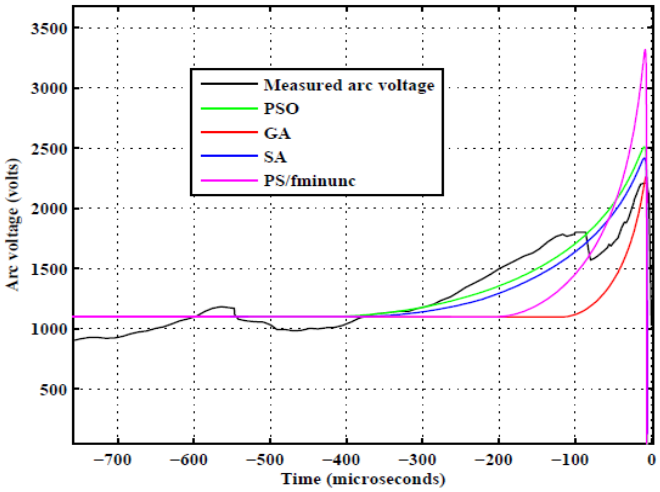


Figure 8. The simulated arc voltages using PSO, GA, SA, PS and fminunc (CB145).

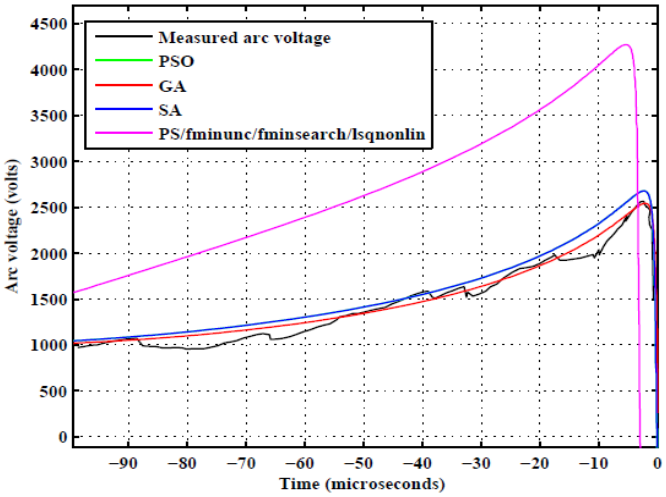


Figure 9. The simulated arc voltages using PSO, GA, SA, PS, fminunc, fminsearch and lsqnonlin (CB123).

In order to determine the most efficient optimization method for each circuit breaker subjected to SLF test, the Rout Mean Square Error (RMSE) is computed, by using (15), between the measured arc voltage $u_m(t)$ and the simulated arc voltage $u_s(t)$ obtained by using PSO, GA, SA and fminunc (Table IV).

$$\mathrm{RMSE} = \left(\frac{1}{n}\sum_{j=1}^{n-1}(u_{mj} - u_{sj})^2\right)^{1/2} \qquad (15)$$

From these results, it is clear that for the CB245 and the CB123, the GA technique is the most suitable, while for the CB145; the SA method is the most appropriate.

TABLE IV. RMSE CORESPONDING TO THE USE OF PSO, GA, SA AND FIMINUNC.

RMSE	**PSO**	**GA**	**SA**	**fminunc**
(CB245)	522.03	518.32	531.23	530.50
(CB145)	848.97	2043.30	589.21	6682.35
(CB123)	1094.10	690.70	1090.80	328281.93

VI. CONCLUSION

Through this work, the Schavemaker arc model was chosen to simulate the nonlinear arc conductance inside the high voltage circuit breakers. Unconstrained local and global optimization methods were used to estimate its unknown parameters from short-line fault measurements performed successively on a 245kV, 145kV and 123kV high-voltage circuit breakers.

The used local optimization methods were the simplex search Nelder-Mead algorithm of fminsearch, the large-scale algorithm based on the trust-region reflective Newton method of lsqnonlin and the quasi-Newton line search algorithm of fminunc. Although these methods converge faster, they have not given, in most of cases, precise values of the arc model parameters.

The used global optimization methods were the particle swarm optimization technique and the following MATLAB optimization algorithms; the genetic algorithm, the simulated annealing algorithm and the pattern search algorithm. These methods have given good parameter values, except the pattern search method.

However, there is no a single method that is appropriate for all the HV circuit breakers subjected to SLF test. For the 245kV and the 123 kV circuit breakers, the genetic algorithm technique is the most suitable while for the 145kV circuit breaker; the simulated annealing method is the most appropriate. Nevertheless, the most suitable method for any HV circuit breaker can be selected among the heuristic methods namely particle swarm optimization technique, the genetic algorithm and the simulated annealing algorithm.

ACKNOWLEDGMENT

Thanks are due to Prof. René Peter Paul Smeets, Innovation and Technology Specialist with KEMA Laboratories of CESI Group for the permission to use the measured curves corresponding to the 245kV, 145kV and 123kV circuit breakers, published in [9].

REFERENCES

[1] J. Liu, S. G.M. Huang, Y. Geng, "A novel smart grid high-voltage circuit breaker for smart grid applications", IEEE transactions on smart grids,vol.2 No 2, 2011, pp. 254-264.

[2] A. Ahmethodzic, R.P.P Smeets, S. Nishiwaki, "Design improvement of a 245 kV SF6 Circuit breaker with double speed mecanism through current-zero analysis", IEEE Transaction on Power Delivery", vol.25 No 4. October 2010, pp. 2496-2503

[3] L. van der Sluis, Transients in Power Systems, 1st ed, John Wiley & Sons, 2001, pp.97-105

[4] P.H. Schavemaker, L. van der Sluis, R.P.P. Smeets and V. Kertész, "Digital testing of high-voltage circuit breakers, IEEE Computer Applications in Power, Vol. 13, No. 2, April 2000, pp. 52-56.

[5] A. Khakpour, S. Franke, D. Uhrlandt, S. Gorchakov and R.P. Methling, "Electrical arc model based on physical parameters and power calculation"; IEEE Transaction on plasma science, Vol. 43 No 8, August 2015, pp. 2721 -2729.

[6] T. Ohtaka, V.Kertesz and R.P.P. Smeets, "Novel black box arc model validated by high-voltage circuit breaker testing", IEEE Transaction on Power Delivery, Vol. 33 No 4, Aug. 2018, pp. 1835-1844.

[7] P. H. Schavemaker, and L. van der Sluis, "An improved Mayr-type arc model based on current-zero measurement"; IEEE Transaction on Power Delivery, Vol. 15 No 2, April 2000, pp. 580-584.

[8] G. Maximov, V. Venegas, J. L. Guardado, S. E. Melgoza and D. Torres, "Asymptotic methods for calculating electric arc model parameters", Electr Eng, Jan. 2012, pp. 89 -96.

[9] P.H. Schavemaker, "Digital testing of high-voltage SF6 circuit breakers", Ph.D. dissertation, Electrical Engineering, TU Delft, Delft, Netherlands, 2002

[10] L.R Orama, and B. Rodriguez, "Numerical arc model parameter extraction for SF6 circuit breaker simulations", International conference on Power Systems Transients, IPST 2003, New Orleans, USA, pp. 1-5.

[11] V. Rashtchi, A. Lotfi, and A. Mousavi, "Identification of KEMA arc model parameters in high voltage circuit breaker by using of Genetic Algorithm", 2nd IEEE International Conference on Power and Energy, 2008, Johor Baharu, Malaysia, pp. 1515-1517.

[12] T.Chmielewski, T. Kuczek1, and P.Oramus1, "Optimization of electric arc model parameters based on simplex annealing and genetic algorithms", MATEC Web of Conferences 252, 05001 (2019)

[13] D. Boudjehem and N. Mansouri, "A two phase local global search algorithm using new global search strategy" Journal of Information and Optimization Sciences, June 2013, pp. 425-436.

[14] Q. Bai , "Analysis of Particle Swarm Optimization algorithm", Computer and Information Science Vol. 3, No. 1, February 2010, pp. 180-184.

[15] Z. S. Abo-Hammour, O. M.K. Alsmadi, A. M. Al-Smadi, M. I. Zaqout and M. S. Saraireh, "ARMA model order and parameter estimation using genetic algorithms", Mathematical and Computer Modeling of Dynamical Systems, Vol. 18, No. 2, April 2012, pp. 201–221.

[16] T. Binder, C. Heitzinger and S. Selberher, "A Study on global and local pptimization techniques for TCAD analysis tasks" IEEE transactions on computer-aided design of integrated circuits and systems, vol. 23, no. 6, June 2004,814-822

Planning study for electrical substations in Algeria

Farah Laib[1], Athmane Bouzidi[1]

[1]Laboratoire de Génie Electrique, Faculté de Technologie, Université de Bejaia, 06000 Bejaia, Algeria

farah.laib@univ-bejaia.dz, athmane.bouzidi@univ-bejaia.dz

***Abstract*— Electrical energy demand is constantly increasing, and current production capacities are insufficient to meet this huge demand, particularly during peak periods and periods of high consumption. Algeria has no choice but to face up to this challenge by drawing up an investment plan accompanied by a medium- and long-term technical and economic study. Dynamic management of the power network through planning must take into account all the parameters linked to generation, transmission and consumption, while imposing adjustments designed to ensure the quality and stability of the power system. These objectives can only be achieved through the use of decision-support tools. This work consists in the realization of the Algerian substation planning model, which allows to determine the investment cost and the expansion capacity of the existing substations, as well as the location, allocation and size of the selected and non-selected new substations, while verifying the equality and inequality constraints to ensure that the loads are adequately supplied.**

Keywords: **Electrical Substations, Planning, Optimization, Transmission Networks, Economic Cost.**

I. INTRODUCTION

The energy sector, and in particular the electricity sector, is the lifeblood of a country's economy, in the sense that its growth conditions a nation's social and demographic development and growth. Today, electricity is an essential consumer good that cannot be stored. Supply must be able to satisfy demand at all times, so we could say that the power grid is driven by consumption due to social, economic and industrial activities. A balance must be struck between the generation capacities and transmission and distribution networks available in the medium and long term, on the one hand, and the evolution of future electricity demand, on the other.

Electricity network planning involves planning new generation plants, various network extensions and the sizing of structures such as lines, transformers and substations. Power system planning takes into account a number of objectives which must be optimized simultaneously, and which are often contradictory. These objectives include, on the one hand, minimizing operating costs (line losses) and investment costs (construction of new facilities), and on the other hand, improving reliability, safety of people and property, quality and continuity of supply, and taking into account multiple environmental factors [1].

The high degree of interdependence between network elements means that transmission and distribution networks have to be separated. This means that the planning problem can be dealt with independently, and decisions can be taken for each sub-problem separately. The latter must be consistent to avoid errors in the planning studies, which can lead to erroneous decisions and considerable financial losses. Consequently, it is necessary to take account of uncertainties and random factors in long-term network evaluation calculations. Thus, it is necessary to develop new planning tools with mathematical methods that take into account all the uncertainties of social, economic and industrial electrical variables and their consequences on the power network [2].

This work consists in the realization of the Algerian substation planning model, which allows determining the investment cost and expansion capacity of existing substations, as well as the location, allocation and size of selected and non-selected new substations, while verifying the equality and inequality constraints to ensure that loads are adequately supplied.

II. SUBSTATION PLANNING

As the demand for electric load continues to increase, it is crucial that sub-transmission networks are capable of consistently supplying power to the distribution system. Failure to do so would result in a loss of network reliability and effectiveness [3, 4].

A. Description of the case study

Substation expansion planning can be defined as an optimization problem in which all investment costs, as well as operating costs, must be minimized. The expansion capacities of existing substations, the location and size of new substations and the required uptime must be defined so that loads can be adequately supplied [5]. The final solution is given by:

- The expansion capacity of all existing positions.
- Assignment and size of all new substations.
- Investment costs.

The planner must decide on the best choice, which implies choosing the lowest cost.

Overall costs can be divided into two main terms **[6]**:

1) The cost associated with the downstream network

Mainly depends on the cost of the feeder, i.e. it depends on the cost per unit length.

2) The cost associated with the HV substation

Divided into three main terms:

- Land cost is higher near load nodes (Independent term in MVA);

- The cost of equipment is due to transformers, switchgear, etc. for each substation, which is proportional to the capacity of that substation (Dependent term in MVA);

- The cost of losses, which is considered an operational cost.

Consequently, the cost associated with the HV substation is the sum of the preceding costs

$$C_{sub_HV} = C_{land} + C_{equipments} + C_{losses} \quad (1)$$

B. Mathematical formulation

The problem is formulated as a mathematical optimization problem; furthermore, it is assumed that the cost of the downstream network is simply proportional to the distance from the load node to the feeder station [7, 8].

a. Objectif function: This is the sum of the cost of the downstream network and the cost of the HV substations.

$$C_{total} = C_{down_line} + C_{stat} \quad (2)$$

1) Downstream network cost C_{down_line}

$$C_{down_line} = \sum_{i=1}^{Nl}\sum_{j=1}^{Ns} g_l(i)X(i,j)D(i,j)S_l(i) \quad (3)$$

N_s & N_l : Number of stations and load nodes respectively;

$g_l(i)$: Cost of load node *i*;

$X(i,j)$: Decision variable (1 if load access *i* is supplied by feeder *j* otherwise 0);

$D(i,j)$: Distance between load nodes *i* and station *j*;

$S_l(i)$: Amplitude of load nodes *i* in (MVA) .

2) Cost of HV substations C_{stat} is the sum of the fixed cost and the variable cost

$$C_{stat} = C_{stat_fix} + C_{stat_var} \quad (4)$$

$$C_{stat_fix} = \sum_{j=1}^{Ns} g_s^f(j)X_s(j) \quad (5)$$

$$C_{stat_var} = \left(g_s^v(j)\left(\sum_{i=1}^{Nl} X(i,j)S_l(i) - C_{exis}(j)\right)\right) \quad (6)$$

$g_s^f(j)$: Fixed cost of substation *j* (nil for existing substations);

$X_s(j)$: Binary integer (1 if substation *j* is selected otherwise 0);

$g_s^v(j)$: Variable cost of substation *j*;

$C_{exis}(j)$: Existing capacity of substation *j* (nil for new substations).

b. Length constraint: If a load is supplied by a substation far from the load node, the voltage drop may exceed a permissible value. We can define this constraint as follows:

$$X(i,j)D(i,j) \le D\max \; \forall i = 1,...,Nl; \forall j = 1,...,Ns \quad (7)$$

$D\max$: Maximum distance a load can be supplied by a substation.

c. Capacity constraint: All loads supplied by a j substation must be less than or equal to the substation's maximum capacity. We can define this constraint as follows:

$$\sum_{i=1}^{Nl} X(i,j)S_l(i) \le S_j \max \; \forall j = 1,...,Ns \quad (8)$$

III. PRESENTATION OF NETWORK STUDIED AND ITS CHARACTERISTICS

The simulation is carried out in MATLAB according to the following algorithm, and is applied to the case of an Algerian generation and transmission network with 59 accesses, 10 generators and 83 branches (5 transformers and 78 lines) with a load of 684.10 MVA (6,841pu). The network comprises five existing substations (1 to 5) and a further 21 are considered as new candidate substations.

The aim is to determine the HV substations required for the loads to be fully satisfied.

IV. PROPOSED ALGORITHM

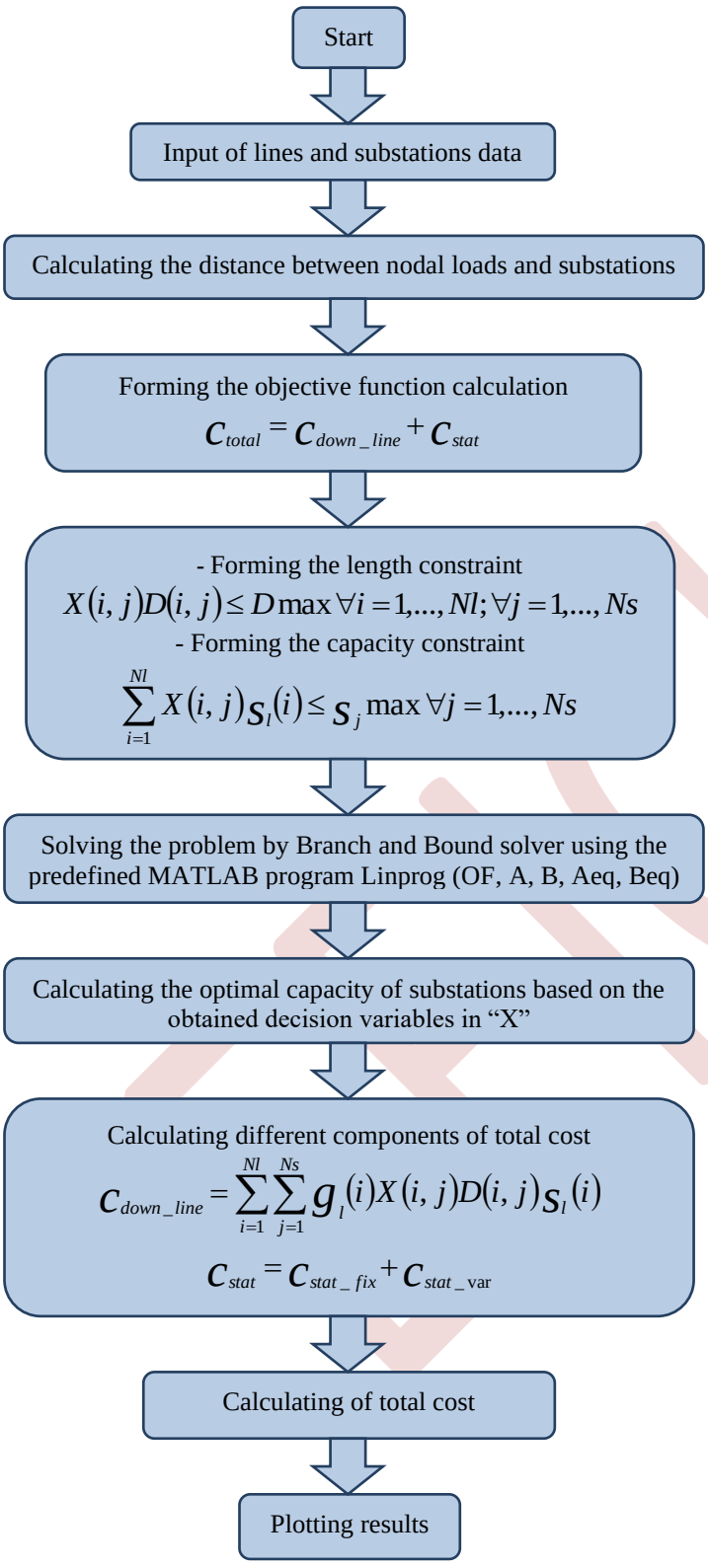


Fig 1: Organigram of electrical substations planning method

VI. APPLICATION AND RESULTS

The algorithm calculates the geographical position and optimal capacity of all existing and candidate substations after expansion, as well as the assignment of load nodes to substations, while calculating the various investment, operating and total costs to be minimized.

TABLE I. COSTS VALUES

Costs values (DA)			
C_{stat_var}	C_{stat_fix}	C_{down_line}	C_{total}
-3.00E+006	51.00E+006	85.32E+006	13.33E+007

This table presents various costs calculated after the simulation. It includes the variable static cost, the fixed static cost, as well as the downward line cost, all of which contribute to the total cost resulting from the sum of these costs.

TABLE II. OPTIMUM POSITION AND CAPACITY OF SUBSTATIONS INSTALLED AFTER EXPANSION

Substation Number	Position		Optimal Capacity (Pu)
	X (Km)	Y (Km)	
6	1	42	2.8
12	23	30	3.0
17	48	47	2.0

The second table highlights the three selected substations (numbered 6, 12, & 17) along with their geographical positions. Furthermore, it presents the optimal capacity of each substation after expansion, as clearly depicted in Fig 2.

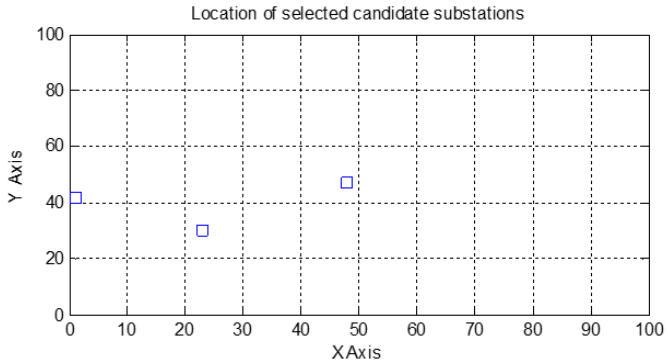


Fig 2: Location of selected candidate substations

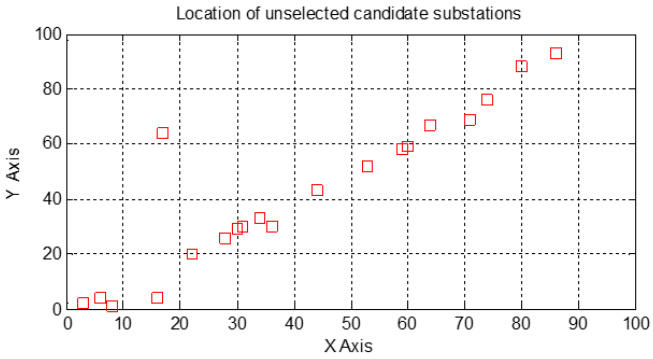


Fig 3: Location of unselected candidate substations

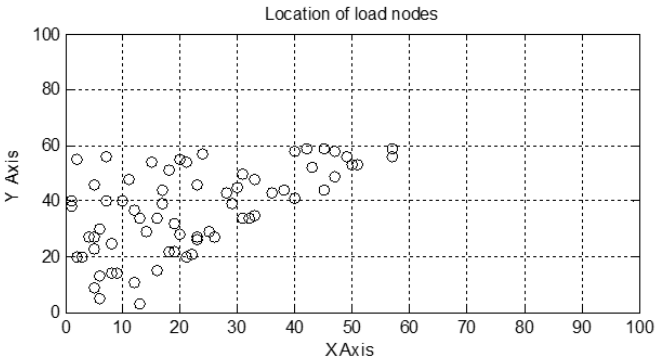


Fig 4: Location of load nodes

Figure 3 displays the geographical locations of the remaining 18 substations that were not selected from the initial 21 proposed substations. Additionally, Fig 4 highlights the geographical locations of all the load nodes that need to be assigned to the three selected substations to ensure their adequate power supply.

TABLE III. LOAD NODES CONNECTED TO SUBSTATION 6, 12 &17

Load nodes connected to substation 6				Load nodes connected to substation 12				Load nodes connected to substation 17			
Node	Position		Load (Pu)	Load Node	Position		Load (Pu)	Node	Position		Load (Pu)
	X (Km)	Y (Km)			X (Km)	Y (Km)			X (Km)	Y (Km)	
1	1	38	0.1	8	5	9	0.1	52	24	57	0.1
2	1	40	0.1	9	5	9	0.1	57	30	45	0.1
3	2	20	0.1	15	6	5	0.1	59	31	50	0.1
4	2	55	0.1	16	6	13	0.1	62	33	48	0.1
5	3	20	0.1	17	6	13	0.1	63	36	43	0.1
6	4	27	0.1	22	8	14	0.1	64	38	44	0.1
7	4	27	0.1	24	9	14	0.1	65	40	41	0.1
10	5	23	0.1	25	9	14	0.1	66	40	58	0.1
11	5	23	0.1	29	12	11	0.1	67	40	58	0.1
12	5	27	0.1	31	13	3	0.1	68	42	59	0.1
13	5	27	0.1	34	14	29	0.1	69	43	52	0.1
14	5	46	0.1	36	16	15	0.1	70	45	44	0.1
18	6	30	0.1	37	16	34	0.1	71	45	59	0.1
19	6	30	0.1	38	17	39	0.1	72	47	49	0.1
20	7	40	0.1	40	18	22	0.1	73	47	58	0.1
21	7	56	0.1	42	19	22	0.1	74	49	56	0.1
23	8	25	0.1	43	19	32	0.1	75	50	53	0.1
26	10	40	0.1	44	20	28	0.1	76	51	53	0.1
27	10	40	0.1	46	21	20	0.1	77	57	56	0.1
28	11	48	0.1	48	22	21	0.1	78	57	59	0.1
30	12	37	0.1	49	23	26	0.1				
32	13	34	0.1	50	23	27	0.1				
33	13	34	0.1	51	23	46	0.1				
35	15	54	0.1	53	25	29	0.1				
39	17	44	0.1	54	26	27	0.1				
41	18	51	0.1	55	28	43	0.1				
45	20	55	0.1	56	29	39	0.1				
47	21	54	0.1	58	31	34	0.1				
				60	32	34	0.1				
				61	33	35	0.1				

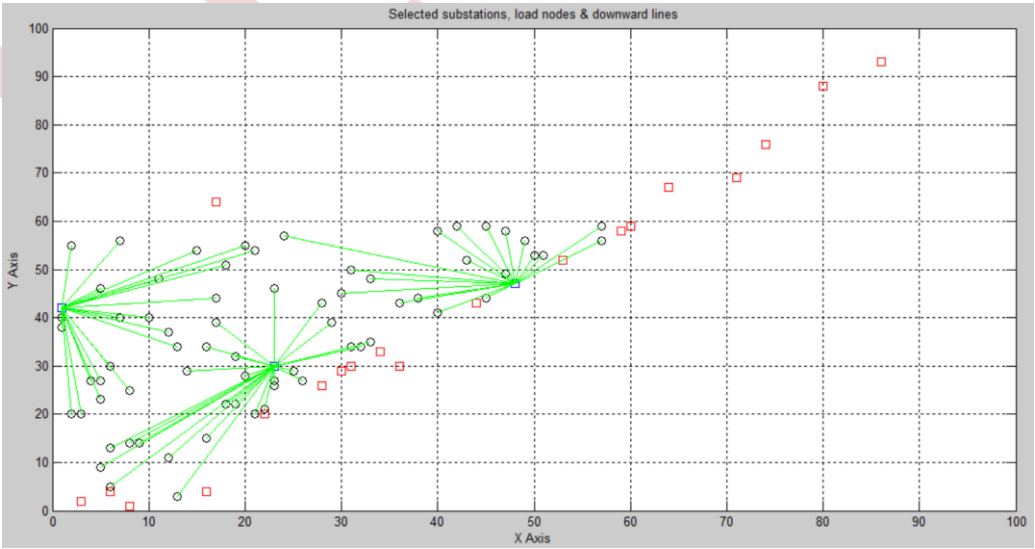


Fig 5: Selected substations, load nodes & downward lines

Table 3 provides a breakdown of the load node distribution across the three selected substations (6, 12 & 17), while adhering to two essential constraints. Firstly, the distance constraint limits the distance between load nodes assigned to the same substation to 50 kilometers. Secondly, the substation capacity constraint is set at 3 pu, indicating which substation is assigned to each load node, along with the geographical position and the associated load for each node. Figure 5 complements this information by illustrating the downward lines, depicting the connections between the load nodes and their corresponding substations.

VII. CONCLUSION

Electricity network planning aims to meet the general objectives defined by the sector strategy. Maximizing access to electricity in a given territory, within a given timeframe, for a given level of subsidy.

The planning of substations in Algeria is of crucial importance for the optimization of the country's electrical network. It brings about several major advantages, including the improvement of network reliability, the integration of renewable energies, the increase in transport capacity, the reduction of energy losses, demand management, network flexibility, and security. Moreover, it stimulates economic development by ensuring a stable energy supply while complying with specific regulations and standards in the electric power sector. This strategic planning plays a key role in the modernization and sustainability of the electrical sector in Algeria.

The obtained results could be utilized by the national dispatch center to inform their planning and deployment analyses of new substations. This usage would aid in evaluating investment costs, the expansion capacity of existing substations, determining the locations, distribution, and sizing of new substations, whether selected or not. This will facilitate optimal decision-making regarding the installation of substations, thus ensuring appropriate power supply to load nodes.

Among the conceivable perspectives, it is possible to add a constraint related to pollution. This would imply that the sum of polluting emissions from the existing substations, added to the sum of polluting emissions from the new substations, must remain below an acceptable threshold. This measure would be integrated into the constraints already taken into account in the substation planning process, in order to address the growing concerns regarding environmental sustainability.

REFERENCES

[1] H. DUTRIEUX, "Methods for multi-year planning of distribution networks. Application to the technical-economic analysis of intermittent renewable energy integration solutions", PhD thesis in electrical engineering, Central School of Lille, 2015.

[2] M.C ALVAREZ-HERAULT, "Future distribution network architectures in the presence of distributed generation", PhD thesis in electrical engineering, Grenoble Polytechnic Institute, 2009.

[3] T. Gönen, IJ. Ramirez-Rosado, "Review of distribution system planning models: a model for optimal multistage planning", IEE Proc Gener Transm Distrib 133(7), 1986.

[4] M.H. ABDI, H. HOSSEINI, A. JALILVAND, "Sub-transmission substation expansion planning considering load center uncertainties of size and locaion", Electrical power and energy systems, 2019.

[5] MS SEPASIAN, H. SEIFI, AA. FOROUD, SH. HOSEINI, EM. KABIR, "A new appoach for substation expansion planning", IEEE trans power system, 2006;21(2);997_1004.

[6] G W. Peng, W. Liu, "A new method for substation planning problem based on weighted kmeans", Springer, Berlin, 2009.

[7] H. Seifi, M.S. Sepasian, "Substation Expansion Planning", in H. Seifi, M.S. Sepasian, (Eds.): "Electric Power System Planning: Issues, Algorithms and Solutions" Springer Berlin Heidelberg, 2011, pp. 105-132.

[8] C. SHILAJA, "Real substation expansion planning using firefly algorithm", European journal of molecular & clinical medicine, ISSN 2515-8260 Volume 08, Issue 1, 2021.

Impact of the fault location and machine damping on the transient stability of an electrical power network

Souad Idri[1], Radia Abdelli [2], Farid Hamoudi [3]

[1]*Laboratoire de maitrise des énergies renouvelables (LMER). University A. Mira de Bejaia, 06000 Bejaia, Algeria*
souad.idri@univ-bejaia.dz
[2] *Laboratoire de Technologie Industrielle et de l'Information (LTII), University of Bejaia, Bejaia, Algeria*
Radia.abdelli@univ-bejaia.dz
[3] *Laboratoire de maitrise des énergies renouvelables (LMER). University A. Mira de Bejaia, 06000 Bejaia, Algeria*
farid.hamoudi@univ-bejaia.dz

***Abstract-- T*ransient stability may be defined as the ability of a power system to maintain machines' synchronous operation when subjected to large disturbances. From the system theory one can see that power system transient stability is a strongly nonlinear, high dimensional problem. To assess it accurately, one therefore has to resort to numerical integration methods, referred to as "time domain" (TD) methods. In this study, a software package is developed in MATLAB environment to analyze the transient behavior of the 9-bus system and while analyzing the effects of fault position, machine damping and critical clearing time. A three phase fault is introduced at three different locations and with different machines damping values.**
From the obtained results one can see that transient stability is greatly affected by the type, and location of a fault and the machine damping.

Keywords: **Transient stability, short circuit fault, synchronous machine, Power flow, clearing time, damping.**

I. INTRODUCTION

Transient stability is an important consideration that must be dealt with during the design of power systems. In the design process, time-domain simulations are conducted to assess the stability of the system under various conditions and when subjected to various disturbances.

Since it is not practical to design a system to be stable under all possible disturbances, design criteria specify the disturbances for which the system must be designed to be stable. The criteria disturbances generally consist of the more statistically probable events, which could cause the loss of any system element and typically include three-phase faults cleared in normal time and line-to-ground faults with delayed clearing due to breaker failure. In most cases, stability is assessed for the loss of one element (such as a transformer or transmission circuit) with possibly one element out-of-service in the predisturbance system. In system design, therefore, a wide number of disturbances are assessed and if the system is found to be unstable (or marginally stable) a variety of actions can be taken to improve stability [1].

Transient stability of a power system is its ability to maintain synchronous operation of the machines when subjected to a large disturbance. The occurrence of such a disturbance may result in large excursions of the system machine rotor angles and, whenever corrective actions fail, loss of synchronism results among machines.

The transient stability is categorized into two major classes: inter-area, which refers to when a group of coherent units lose their synchronization with other groups, and the other class is when a single generator loses synchronization in respect to the rest of the system [2]

The power system is a highly nonlinear system that operates in a constantly changing environment; loads, generator outputs, topology, and key operating parameters change continually. When subjected to transient disturbance, the stability of the system depends on the nature of the disturbance as well as the initial operating condition. The disturbance may be small or large. Small disturbances in the form of load changes occur continually, and the system adjusts to the changing conditions.

The system must be able to operate satisfactorily under these conditions and successfully meet the load demand. It must also be able to survive numerous disturbances of a severe nature, such as a short-circuit on a transmission line or loss of a large generator. Following a transient disturbance, if the power system is stable, it will reach a new equilibrium state.

Stability analysis of power systems involves the computation of the nonlinear transient dynamic trajectory of the postfault system, which depends on the initial operating conditions, the nature and duration as well as magnitude of the perturbation.

The deviation of the synchronous machine rotor angle during transient period is used as an index to assess its ability to maintain or restore equilibrium between electromagnetic and mechanical torques by analyzing the electromechanical oscillations inherent in power systems.

Several classes of methods are developed to obtain transient stability limits of power systems. Time-domain simulation (TDS) methods via numerical integration are largely used in transient stability study. Numerical methods, by solving the second order nonlinear differential swing equation, using time-domain numerical integration are the most accurate and very efficient given their ability to analyze very complex nonlinear mathematical models. This is, because they take into account all the phenomena present in the system. The main drawback of these approaches is that they are time consuming and require the whole system of equations for assessing stability of large power systems [3-6].

Other aspect of transient stability assessment is to consider the parameters which influence it. Researchers have been writing their observations and findings to address this problem.

For instance, [7] elaborates the effect of different parameters of power system on transient stability, like Fault Clearing Time (FCT), location of fault, Generator Armature Resistance based on numerical integration to compute the critical clearing time (CCT) accurately.

Similarly, [8] studied transient stability for various load configurations and power transfer limitations for transient and post transient period. In [9] stability based on Critical Moment is assessed by comparing dc power flow model and transient stability analysis method (TSA) can be performed qualitatively using time-domain simulations (TDS) based on integration methods, which yield yes or no answer, whether synchronous generators maintain synchronism or not [10,11].

The primary concern in the stability analysis is to verify the synchronism of the generator machines in a short period of time after the occurrence of a disturbance and the determination of the critical clearing time of the fault.

The objective of this study is to obtain time solution for the individual generators rotor angles and relative rotor angle after the transient is introduced. These time solutions are called "swing curves".

II. POWER SYSTEM MODELING AND ANALYSIS OF A MULTIMACHINE SYSTEM

To obtain a time solution for the rotor angle, we need to develop expressions for the mechanical and the electrical powers. The classical model of synchronous machine may be used to study the stability of the power system for a period of time during which the system dynamic response is dependent largely on the stored kinetic energy in the rotating masses.

Transient stability problem with n machines can be modeled by a set of oscilltation equations one for each machine of the system. These equations can be expressed by a set of first order differential equations as follow:

$$M_i \frac{d\omega_i}{dt} + D_i\omega_i = P_{mi} - P_{ei} \quad (1)$$

$$\frac{d\delta_i}{dt} = \omega_i(t) - \omega_s \quad (2)$$

Where:

M_i: Inertia constant of the ith machine, t : time in seconds, D_i : damping constant of the ith machine,ω_i: angular speed at each instant, P_{mi}: mechanical input power of the ith machine, P_{ei}: active electric power injected in to the network by the ith machine, δ : angular position of the axis of the ith machine with respect to an axis rotating at synchronous speed, ω_s: synchronous speed.

The above set of equations is a set of n-coupled equations nonlinear second order differential equations.
These can be written in the form: [12]

$$x' = f(x, x_0, t) \quad (3)$$

Where x is a vector of dimension (2n x 1).

$$x' = [\omega_1, \delta_1, \omega_2, \delta_2 \dots \dots \dots \omega_n, \delta_n]$$

And f is a set of nonlinear functions of the elements of the state vector x**Erreur ! Signet non défini.**

Active electrical power injected in to the network at node i by the ith machine is given by:

$$P_{ei} = R_e E_i I_i^* \quad (4)$$

$$P_{ei} = E_i^2 G_{ii} + \sum_{\substack{j=1 \\ j\neq i}}^{n} E_i E_j Y_{ij} cos\left(\theta_{ij} - \delta_i + \delta_j\right) \quad (5)$$
$$i=1 \dots n$$

Since the transfer admittance between nodes i and j, Y_{ij} is by definition given by:

$$Y_{ij} = G_{ij} + jB_{ij} \quad (6)$$

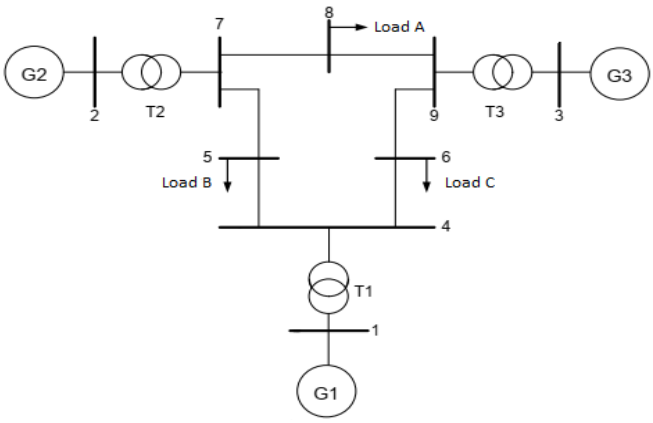
The equation above is rewritten as follow:

$$P_{ei} = E_i^2 G_{ii} + \sum_{\substack{j=1 \\ j \neq i}}^{n} E_i E_j \left[B_{ij} sin(\partial_i - \partial_j) + G_{ij} cos(\partial_i - \partial_j) \right], i = 1, \dots, n \quad (7)$$

It should be noted that prior to the disturbance $P_{mi0} = P_{ei0}$ are given by the pretransient conditions.

III. CASE STUDY

This study focuses on transient stability analysis of a nine-bus power system under symmetrical fault. Numerical integration method of the swing equation is implemented using MATLAB software. The results of this analysis are represented as swing curves. The network examined includes three generators, each connected to buses 1, 2 and 3 by power transformers, which contribute to the power supply of three loads A, B, C connected respectively to nodes 8, 5and 6. The configuration and the system data of the nine bus system were taken from reference [12]. Validity of the developed software is checked with some of the results given in the reference [12]. A line diagram of this network is shown in figure 1.



1. Figure 1. Configuration of IEEE 9 Bus System

Before solving the swing equation, a power flow program is performed using Newton's Raphson method to determine the steady state operating conditions of the power system network. A software code for transient stability in power systems using the classical model of the machine is performed.

This code is simulating the swing curve for a power system. The swing curve shows the variation of the rotor angle of a synchronous generator with respect to time after a disturbance.

The simulation considers the effect of a fault and subsequent clearing of the fault after a specified time. The values of the fault clearing time (FCT), the fault duration (FD), the critical clearing time (CCT), and the time step (ts) are all specified in the code.

IV. RESULTS AND DISCUSSION

For the rotor angle analysis, we consider a three-phase fault occurring at time 0.1s at the level of bus9, such that the fault is close to generator 3, the fault is eliminated after 3 cycles by opening the line [6-9] and the critical clearing time is determined by increasing the fault application duration just before the system becomes unstable.

The system response is given for different values of fault clearing time and different machines damping values.

To verify whether the system is stable or unstable for the particular transient under study, it is sufficient to carry out the time solution for one swing only. If the rotor angle or the angle difference reaches a maximum value and then decrease, the system is stable; if any of the angle difference increase indefinitely the system is unstable because at least one machine will lose synchronism.

A. First case, Damping D=0, and a fault clearing time t= 0.150 s.

Fig. 2 (a) and (b) show the individual generator angles and the difference angles with gen 1 (as reference). In this case, the system is stable for a fault clearing time (FCT) of 0.150s and without considering damping. Fig. 3 (a) and (b) show the evolution of the individual generator angles and the difference angles for a FCT of 0.318s. At this time the system becomes unstable.

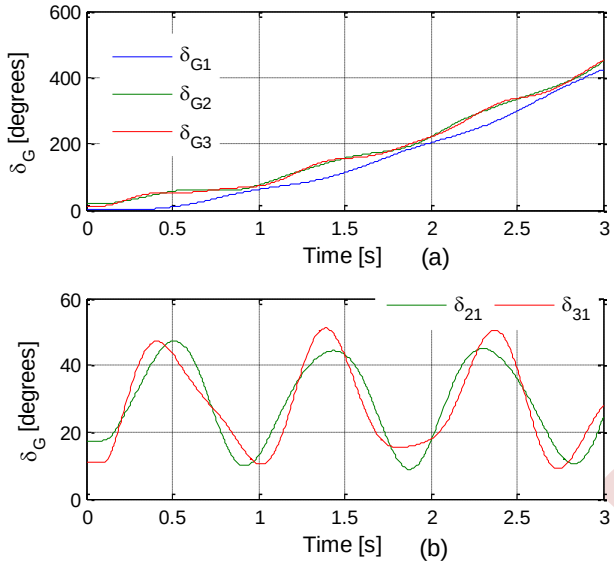


Figure 2. Transient response for a) rotor angular for individual generators and b) relative angular position (fault clearing FCT=0.150s, D=0).

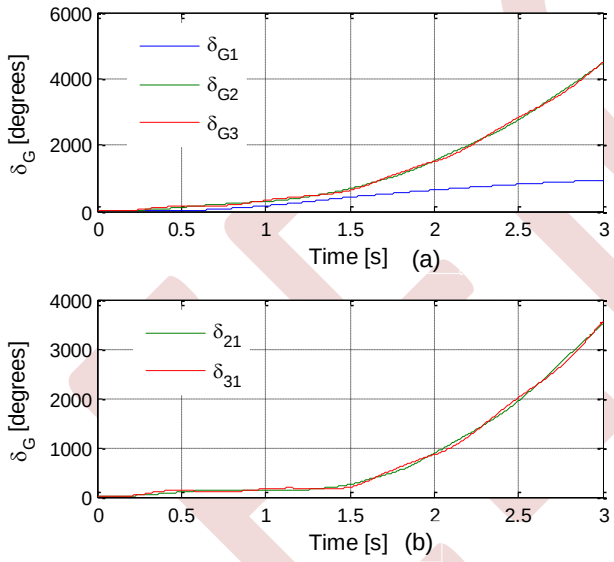


Figure 3. Transient response for a) rotor angular for individual generators and b) relative angular position (fault clearing FCT=0.318s, D=0).

B. Second case, Damping D=1, and a fault clearing time t= 0.150 s.

The results shown in figure 4 (a) and (b) for a the same FCT of 0.150s the system remains stable and figure 5 (a) and (b) for FCT 0.353s, the system becomes instable.

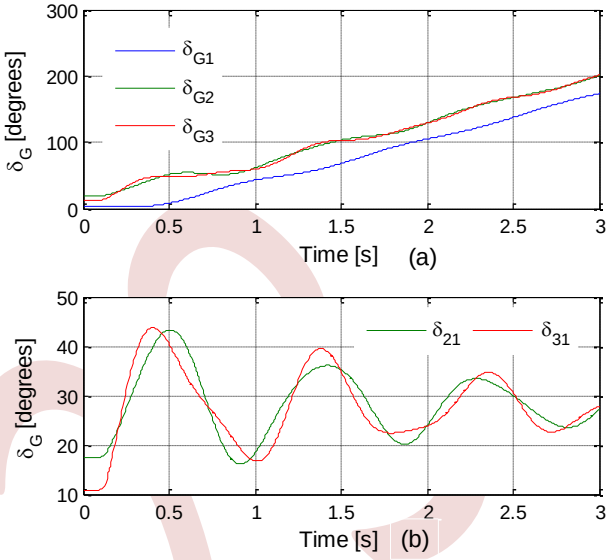


Figure 4. Transient response for a) rotor angular for individual generators and b) relative angular position (fault clearing FCT=0.150s, D=1).

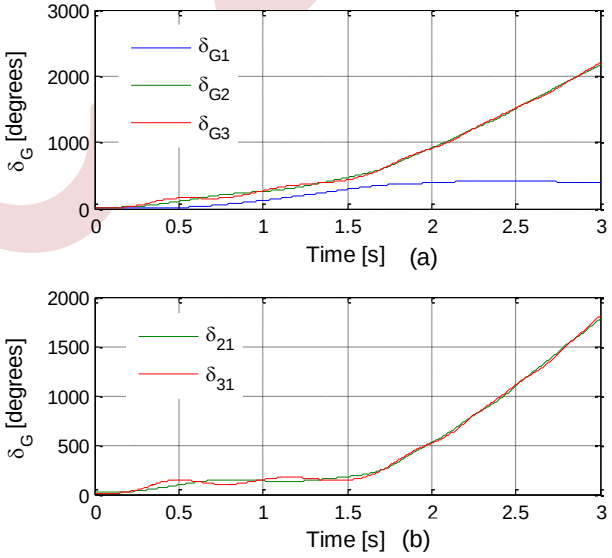


Figure 5. Transient response for a) rotor angular for individual generators and b) relative angular position (fault clearing FCT=0.353s, D=1).

C. Third case, Damping D=2, and a fault clearing time t= 0.150 s.

Fig. 6 (a) and (b) show the system responses for a FCT of 0.150 s, where we can see that the system is stable. In this case, the maximum angle difference is about 40°, this is the value of δ_{21} at t=0.50s.

Fig. 7 (a) and (b) show the system responses for an FCT value of 0.390 s. At this point the system is critically stable. The system becomes unstable for FCT = 0.391s.

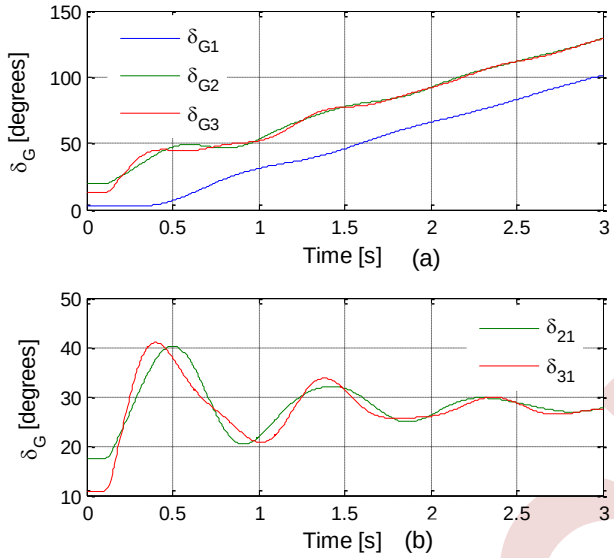


Figure 6. Transient response for a) rotor angular for individual generators and b) relative angular position (fault clearing FCT=150s, D=2).

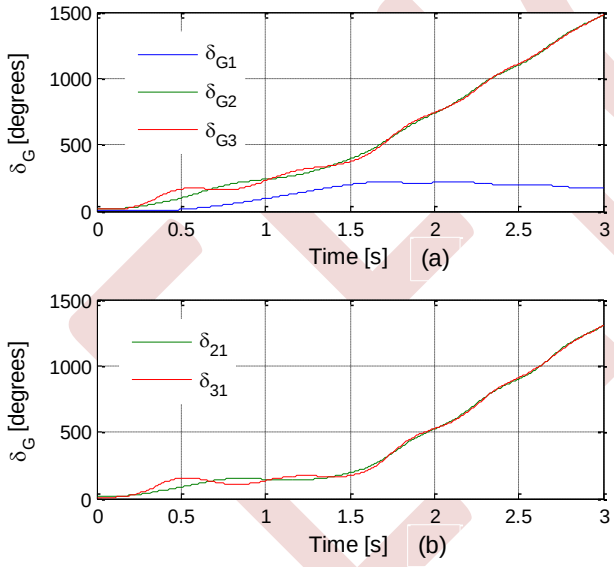


Figure 7. Transient response for a) rotor angular for individual generators and b) relative angular position (fault clearing FCT=0.391s, D=2).

D. Critical clearing time for different fault locations in IEEE 9-BUS

In this subsection, the impact of fault location in transient stability after a three phase fault introduced is considered. The three buses concerned are Bus 9, 7 and 4. The fault is introduced at t=0.1s, and eliminated after 3 cycles. To determine the critical clearing time for each location fault, the simulation is repeated till the system loses synchronism, and then the critical clearing time (CCT) is obtained.

The simulation results giving the critical clearing time with and without integrating damping coefficient are given in table 1.

TABLE1. CRITICAL CLEARING TIME FOR DIFFERENT DAMPING VALUES AND DIFFERENT FAULT LOCATIONS

Line	Fault bus number	D=0	D=1	D=2
		CCT(s)	CCT(s)	CCT(s)
5 - 7	7	0.268	0.306	0.344
6 - 9	9	0.317	0.352	0.390
4 - 6	4	0.418	0.462	0.700

The critical conditions obtained are very closest to those obtained by [11].

Also, obtained results, show that the damping coefficient has an important effect on transient stability improvement, since the critical clearing time increases with increasing damping value. When the fault is near to a generator bus, the electrical power generated by the corresponding generator becomes zero or near to zero as the fault is feed by affected generator.

When the fault is far from the generator bus, inter-machine oscillations occur in all 3 machines while accelerating speed and change of rotor angle depends on the machine inertia and distance to the fault [13].

V. CONCLUSION

In this paper, transient stability analysis is studied under three-phase balance fault and tested on the IEEE-9 bus power system under prefault and faulted conditions. Time domain simulation is used for analyzing the swing behavior of the system and to assess the stability of the system when subjected to various disturbances at different locations with and without integrating damping machines coefficient.

A power flow analysis is performed to determine the initial operating conditions just before the disturbance affect the system.

During transient stability analysis it was shown that increasing FCT increases the rotor angle difference. Moreover, the results of different case studies of fault location on power system show that fault clearness after CCT makes the system unstable while fault clearness before CCT keeps the system in synchronism. Also, The obtained results show that the machine damping improve critical clearing time and thus the stability of the system.

REFERENCES

[1] P. Kundur, "Power System Stability and Control" , EPRI Power System Engineering Series (Mc Graw-Hill, New York, 1994).

[2] M. Abedini, M. Davarpanah, M. Sanaye-Pasand, S.M. Hashemi, R. Iravani, "Generator out-of-step prediction based on faster- han-real-time analysis: concepts and applications" , IEEE Trans. Power Syst. 33 (4) (2018) 4563–4573 July.

[3] Peter W. Sauer, M. A. Pai, Joe H. Chow, " Power System Dynamics and Stability", John Wiley & Sons Ltd, 2018.

[4] Y. Dong, H.R. Pota, "Fast transient stability assessment using large step-size numerical integration", IEE PROCEEDINGS-C1991; 138:377-83. Doi: https://doi.org/10.1049/ip-c.1991.0047.

[5] Samita Padhi, Bishnu Prasad Mishra, "Numerical Method Based Single Machine Analysis for Transient Stability", International Journal of Emerging Technology and Advanced Engineering 2014;4:330-35.

[6] Fu Su, Baohui Zhang, Songhao Yang, Huaiyuan Wang, "A Novel Termination Algorithm Of Time-Domain Simulation For Power System Transient Stability Analysis Based On Phase-Plane Trajectory Geometrical Characteristic", IEEE5th International Conference on Electric Utility Deregulation and Restructuring and Power Technologies 2015.1422-26. Doi: https://doi.org/10.1109/DRPT.2015.7432455.

[7] M. Amroune, T. Bouktir, "Effects of different parameters on power system transient stability studies", Journal of Advanced Sciences and Applied Engineering, Vol.1, pp. 28-33, 2014.

[8] Mark Gordon,"Impact of load behavior on transient stability and power transfer limitations", IEEE Power Engineering Society General Meeting, 2009 https://doi.org/10.1109/PES.2009.5275908.

[9] AJun Yan, Yufei Tang, HaiboHe, and Yan Sun, "Cascading failure analysis with DC power flow model and transient stability analysis", IEEE Transactions on Power System, VOL. 30, N°. 1, pp. 285-297, January 2015.

[10] CIGRE. Review of On-line Dynamic Security Assessment Tools and Techniques, 2007.

[11] Chiang HD, "Direct methods for stability analysis of electric power systems", New Jersey: Wiley, 2011.

[12] P. M. Anderson and A. Fouad, "Power System Control and Stability" IEEE Press Poxer engineering series, John Wiley and sons, Inc. Publication 2003.

[13] N. S. K. Jayasekara Menike, "Computer simulation of transient stability of power systems", 2004, Electronic and Theses and dissertations, 1522 University of Windsor.

Optimal Placement of TCSC for Optimizing Active and Reactive Power Using AAC PSO Algorithm

Mohamed Amir Labed [1], Mohamed Benidir [2], Hocine Sekhane [3]

[1] *Department of electrical engineering.*
Brothres Mentouri Constantine 1 University, Constantine, Algeria
mohamedamir.labed@student.umc.edu.dz

[2] *Department of transport engineering.*
Brothres Mentouri Constantine 1 University, Constantine, Algeria
mcbenidir@yahoo.fr

[3] *Department of electrical engineering.*
20 August 1955 Skikda University, Skikda, Algeria
docsekhoc@gmail.com

***Abstract*— In the realm of power system optimization, this conference paper delves into the strategic integration of Thyristor-Controlled Series Compensator (TCSC) devices for the optimal enhancement of both active and reactive power, as well as substantial voltage improvement. in the IEEE 30-bus system. Leveraging the Adaptive Acceleration Coefficients Particle Swarm Optimization (AAC PSO) algorithm, our study meticulously explores the most effective placement of TCSC devices. The research not only advances the understanding of TCSC deployment but also pioneers the utilization of AAC PSO, a cutting-edge optimization algorithm. Utilizing the MATPOWER framework, a comprehensive analysis of the IEEE 30-bus system is conducted, demonstrating significant improvements in both active and reactive power and voltage stability. This work contributes valuable insights to the domain of power system engineering, showcasing a novel approach to enhance the efficiency and stability of complex power networks.**

***Keywords:* Optimization, TCSC, IEEE 30-bus system, AAC PSO, MATPOWER, Voltage stability.**

I. INTRODUCTION

Various methods and equipment such as Flexible Alternative Current Transmission Systems (FACTS) devices are reported to manage the active power flow [1]. FACTS devices control the line power flow without any changes in the grid topology, leading to improved performance, increased power transmission capacity, and reduced power grid congestion. Due to the considerable costs of FACTS devices and the maximum usage of their capabilities, the optimal location of such devices should be determined accurately [2-5].

Particle Swarm Optimization (PSO) is a powerful metaheuristic method for optimization derived from the demeanor of bird flocking or fish schooling. This approach involves a group of particles working to find the most optimal solution in a given problem space by iteratively adjusting their positions and velocities guided by their individual experience and the finest experiences of their neighbors [6].

In power flow calculations, PSO dynamically adjusts the system's parameters, such as voltage magnitudes and phase angles, to minimize the objective function, typically representing active and reactive power mismatches. By iteratively optimizing these parameters, PSO converges toward a solution that satisfies power balance equations, ensuring a stable and efficient power flow within the electrical network.

In this conference paper, our focus lies on the strategic integration of Thyristor-Controlled Series Compensator (TCSC) as a Flexible AC Transmission System (FACTS) device, aiming to enhance both active and reactive power performance while minimizing losses and ensuring voltage stability within the IEEE 30-bus distribution system. Leveraging the power of the Adaptive Acceleration Coefficients Particle Swarm Optimization (AAC PSO) algorithm, we embarked on a comprehensive analysis.

Our study delves into the comparison between the system's fundamental state, absent the TCSC device, and the optimized scenario achieved through 15 executions of AAC PSO. This comparative approach sheds light on the significant improvements brought about by our methodology, elucidating

the transformative impact of integrating TCSC and employing advanced optimization techniques in modern power systems.

II. PROBLEM FORMULATION

A. TCSC Modelisation

Thyristor-Controlled Series Compensator (TCSC) fundamentally operates by compensating for the inductive voltage drop in power lines through the application of capacitive voltage, mitigating the impact of power transmission line reactance. This process enhances line load ability and contributes to an optimized power transmission system.

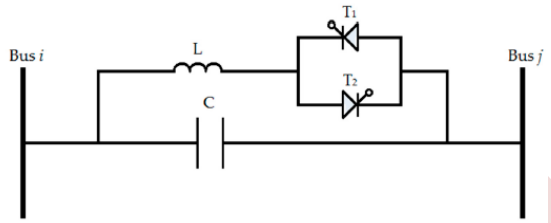


Figure 1. A model of a Thyristor-Controlled Series Compensator.

The active and reactive power flow equations in a transmission line can be determined as follows [7]:

$$P_{ij} = V_i^2 G_{ij} - V_i V_j \left(G_{ij} \cos\delta_{ij} + B_{ij} \sin\delta_{ij}\right) \quad (1)$$

$$Q_{ij} = -V_i^2 \left(B_{ij} + B_{sh}\right) - V_i V_j \left(G_{ij} \sin\delta_{ij} - B_{ij} \cos\delta_{ij}\right) \quad (2)$$

Where $P_{i,j}$, $Q_{i,j}$ are active and reactive powers respectively from bus *i* to bus *j*, V_i, V_j is voltage in the bus *i* and *j*, δ_{ij} is the phase angle difference between the voltage at bus *i* and *j*, G_{ij} and B_{ij} represent transfer conductance and transfer susceptance respectively between bus *i* and bus *j*.

Equations (3) and (6) show the active to reactive power flow equations in the presence of a TCSC:

$$P_{ij}^c = V_i^2 G'_{ij} - V_i V_j \left(G'_{ij} \cos\delta_{ij} + B'_{ij} \sin\delta_{ij}\right) \quad (3)$$

$$Q_{ij}^c = -V_i^2 \left(B'_{ij} + B_{sh}\right) - V_i V_j \left(G'_{ij} \sin\delta_{ij} - B'_{ij} \cos\delta_{ij}\right) \quad (4)$$

$$P_{ji}^c = V_j^2 G'_{ij} - V_i V_j \left(G'_{ij} \cos\delta_{ij} + B'_{ij} \sin\delta_{ij}\right) \quad (5)$$

$$Q_{ji}^c = -V_j^2 \left(B'_{ij} + B_{sh}\right) + V_i V_j \left(G'_{ij} \sin\delta_{ij} - B'_{ij} \cos\delta_{ij}\right) \quad (6)$$

P_{ij}^c and Q_{ij}^c are active and reactive powers respectively from bus *i* to bus *j* after inserting TCSC.

Active and reactive power losses on the line (P_l, Q_l) can be assessed through the following approach:

$$P_l = P_{ij} + P_{ji} \quad (7)$$

$$Q_l = Q_{ij} + Q_{ji} \quad (8)$$

Where:

$$P_l = G'_{ij} \left(V_i^2 + V_j^2\right) - \left(2 V_i V_j G'_{ij} \cos\delta_{ij}\right) \quad (9)$$

$$Q_l = -\left(V_i^2 + V_j^2\right)\left(B'_{ij} + B_{sh}\right) + \left(2 V_i V_j B'_{ij} \cos\delta_{ij}\right) \quad (10)$$

Where:

$$B'_{ij} = \frac{-(x_{ij} - x_c)}{r_{ij}^2 + (x_{ij} - x_c)^2} \quad (11)$$

$$G'_{ij} = \frac{r_{ij}}{r_{ij}^2 + (x_{ij} - x_c)^2} \quad (12)$$

G'_{ij} and $'B_{ij}$ represent the new transfer conductance and transfer susceptance respectively between bus *i* and bus *j*.

B. Adaptive acceleration coefficient AAC PSO algorithms

The Particle Swarm Optimization (PSO) algorithm was first introduced in 1995, which can be seen as a global search technique. In this algorithm, each particle, denoted by *i*, has a velocity vector (*Vi*) and a position vector (*Xi*) [8]. It can be modeled by the following equations:

$$V_i^{k+1} = \omega V_i^k + c_1 r_1 \left[P_{best}^k - X_i^k\right] + c_2 r_2 \left[G_{best}^k - X_i^k\right] \quad (13)$$

$$X_i^{k+1} = X_i^k + V_i^{k+1} \quad (14)$$

Where ω, *r*, are inertia weight and random values between 0 and 1 respectively, c_1 and c_2 acceleration coefficients, G_{best} is the global best position and *k* is the iterations number.

This paper proposes novel PSO strategy that utilize time-varying acceleration coefficient (c_1 and c_2) to improve the global search performance. The primary concept behind employing PSO with time-varying acceleration coefficients is to increase the global search during the initial phase of the optimization process [6].

This is accomplished by altering c_1 and c_2 over time in such a way that the cognitive component decreases while the social component increases [9].

The AAC-PSO acceleration coefficient formula and constants [10]:

$$c_1 = c_{min} + (c_{max} - c_{min}) e^{-\left(\frac{4 \times k}{k_{max}}\right)^2} \quad (15)$$

$$c_2 = c_{max} - (c_{max} - c_{min}) e^{-\left(\frac{4 \times k}{k_{max}}\right)^2} \quad (16)$$

With

$$c_{min} = c_{max} = 0.5 \quad (17)$$

C_{min} , C_{max} the constants of the AAC-PSO method, k , k_{max} represent the iteration number and the maximum number of iterations, respectively.

III. TEST RESULTS AND DISCUSSIONS

The IEEE 30-bus network, pivotal in our study, comprises 30 buses, 6 committed generators, and 21 loads, split into 21 fixed and 0 dispatchable types. The network also includes 2

shunts, regulating voltage, and 41 branches enabling power flow, along with 4 transformers for voltage level adjustments.

In the initial phase of our analysis, we utilized the basic Newton-Raphson method without optimization to examine the power flow. Using MATPOWER data, we obtained results pertaining to voltage levels, as well as active and reactive power losses. Subsequently, to identify the optimal placement for the TCSC device, ensuring the most effective optimization of power flow and voltage stability, we employed the AAC PSO algorithm. This advanced algorithm was run through 100 iterations and 15 executions, enhancing the precision and efficiency of our study.

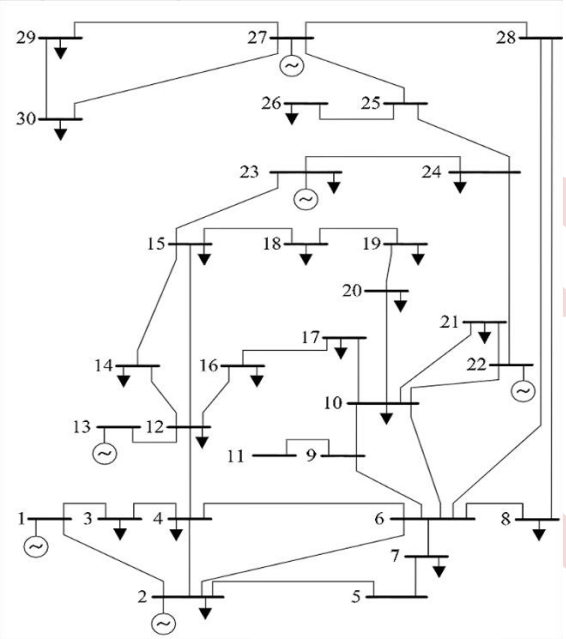


Figure 2. IEEE 30-bus test system.

Figures 3 and 4, respectively, illustrate the active and reactive power losses as functions of the number of executions, employing the AAC PSO algorithm for precise analysis and optimization.

As shown in Figures 3 and 4, it is evident that execution number 11 and 15, respectively, yield the most favorable outcomes for minimizing active and reactive power losses.

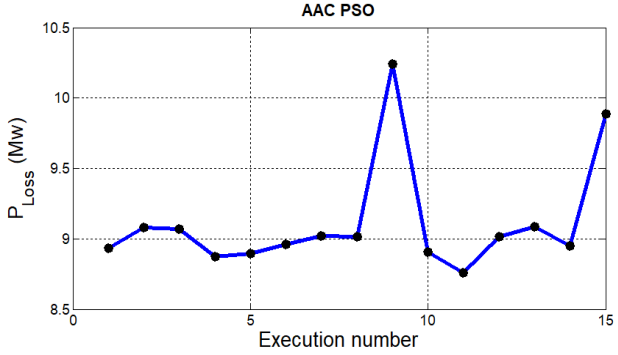


Figure 3. Curve of active power losses versus the number executions.

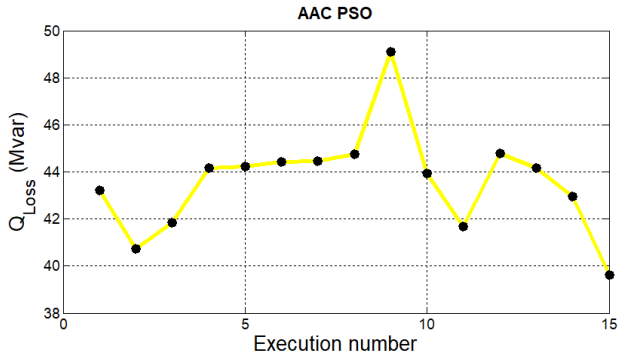


Figure 4. Curve of reactive power losses versus the number executions.

In order to compare the voltage stability before and after implementing our optimization algorithm and inserting the TCSC device, Figures 5 present the obtained results.

We mention that the optimal location for the TCSC is between bus numbers 27 and 28, as determined by execution number 11. We have chosen this case as our reference best case to compare it with the basic case.

It is clear that optimizing power flow using the AAC PSO algorithm with the integration of the TCSC significantly impacts voltage stability.

The voltage fluctuated significantly, ranging from 1.08 pu to 0.99 pu, indicating an unstable distribution. However, after integrating the TCSC, this range noticeably narrowed to 0.99 pu and 1.02 pu, exepting only 2 buses (11 and 12) confirming the enhanced voltage stability achieved through this optimization approach.

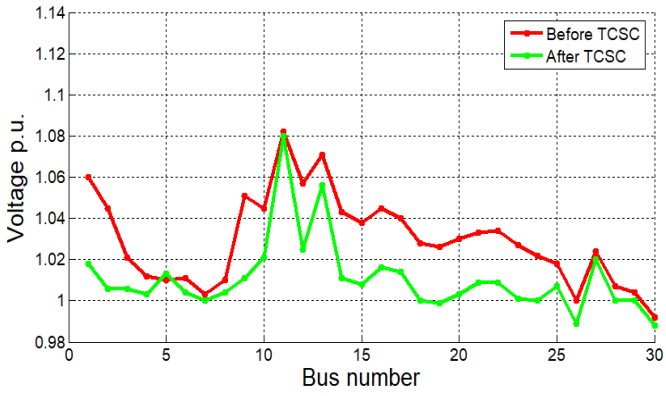


Figure 5. Improved voltage profile.

Table 1 displays the values of active and reactive power losses before and after implementing our optimization method and inserting the TCSC device.

Figure 6 provides a comparison of values in percentage for each case.

Table 1 and figure 6 illustrate the influence of the optimization algorithm method and the FACTS device on the substantial minimization of active and reactive power losses.

TABLE I. TOTAL ACTIVE AND REACTIVE POWER LOSSES WITH DIFFRENTE CASES.

Cases	Total Active Power Losses Mw	Total Reactive Power Losses Mvar
Basic Case	17.557	67.690
With Optimization +TCSC	8.7609	41.6921

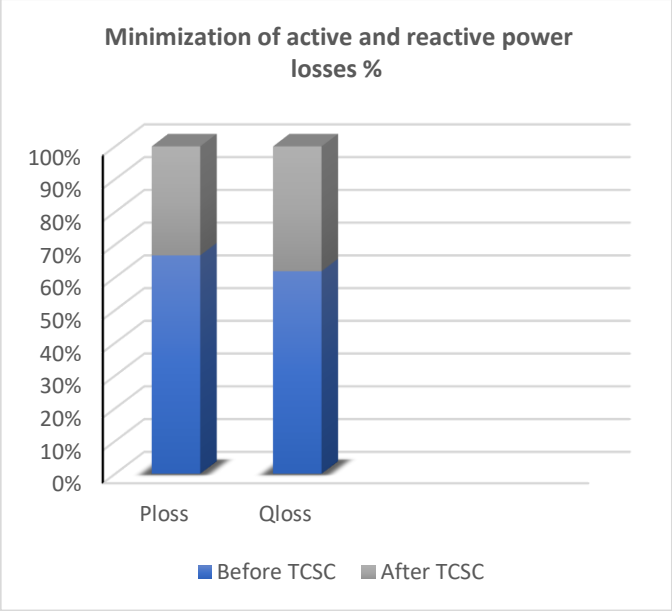


Figure 6. Minimization of active and reactive power losses in percentage.

IV. CONCLUSION

In conclusion, our study delved into the intricate realm of power system optimization, specifically focusing on the integration of the Thyristor-Controlled Series Compensator (TCSC) device with the innovative Adaptive Acceleration Coefficients Particle Swarm Optimization (AAC PSO) algorithm. Through meticulous analysis and rigorous testing on the IEEE 30-bus system, our research achieved remarkable results.

The implementation of the AAC PSO algorithm, coupled with the strategic insertion of the TCSC device, led to significant advancements in both active and reactive power losses. Our method not only optimized power flow but also substantially enhanced voltage stability, a critical factor for a resilient power grid. The achieved voltage stability within the range of 0.99 pu to 1.02 pu, evident in the minimized range, aligns with the regulatory norms of $\mp 5\%$ for voltage regulation in distribution systems demonstrating the efficacy of our approach. This substantial reduction in voltage variation signifies the effectiveness of the TCSC integration, ensuring a more stable and regulated distribution system.

In essence, our research presents a pioneering synergy between advanced optimization algorithms and FACTS devices, offering a promising avenue for future developments in the field of power systems engineering. This work not only contributes valuable insights but also sets a benchmark for the integration of innovative techniques, paving the way for more resilient and efficient power grids in the future.

REFERENCES

[1] Kumar, A.; Srivastava, S.C.; Singh, S.N. A zonal congestion management approach using AC transmission congestion distribution factors. Electr. Power Syst. Res. 2004.

[2] Mori, H.; Goto, Y. A parallel tabu search based method for determining optimal allocation of FACTS in power systems. In Proceedings of the International Conference on Power System Technology, Perth, Australia, 4–7 December 2000.

[3] Singh, S.N.; David, A.K. Congestion management by optimising FACTS device location. In Proceedings of the International Conference on Electric Utility Deregulation and Restructuring and Power Technologies, London, UK, 4–7 April 2000.

[4] Gerbex, S.; Cherkaoui, R.; Germond, A.J. Optimal location of multi-type FACTS devices in a power system by means of genetic algorithms. IEEE Trans. Power Syst. 2001, 16.

[5] Kumar, A.; Sekhar, C. Congestion management with FACTS devices in deregulated electricity markets ensuring loadability limit. Int. J. Electr. Power Energy Syst. 2013.

[6] Labed M.A., Zellagui M., Benidir M., Sekhane H., Tebbakh N. "Optimal hybrid photovoltaic distributed generation and distribution static synchronous compensators planning to minimize active power losses using adaptive acceleration coefficients particle swarm optimization algorithms", Electrical Engineering & Electromechanics, 2023, no. 6, pp. 84-90.

[7] Nguyen, T. T., & Mohammadi, F. (Year). Optimal Placement of TCSC for Congestion Management and Power Loss Reduction Using Multi-Objective Genetic Algorithm. Sustainability 2020, 12(7), 2813.

[8] Lasmari A., Zellagui M., Chenni R., Semaoui S., El-Bayeh C.Z., Hassan H.A. Optimal energy management system for distribution systems using simultaneous integration of PV-based DG and DSTATCOM units. Energetika, 2020, vol. 66, no. 1, pp. 1-14.

[9] Chaturvedi K.T., Pandit M., Srivastava L. Particle swarm optimization with time varying acceleration coefficients for non-convex economic power dispatch. International Journal of Electrical Power & Energy Systems, 2009, vol. 31, no. 6, pp. 249-257.

[10] Ziyu T., Dingxue Z. A Modified Particle Swarm Optimization with an Adaptive Acceleration Coefficients. 2009 Asia-Pacific Conference on Information Processing, 2009, pp. 330-332.

V

ELECTROMAGNETIC FIELD AND COMPATIBILITY (EMC)

Sommaire

V.1 The effect of horizontally stratified ground on the Lightning electromagnetic field calculated by the 3D-FDTD method **218**

V.2 Design of three permanent magnets drum separator for the extraction of fine iron particles **226**

V.3 Dynamic hysteresis loops using the Jiles Atherton Model based on Loss-surface formulation **230**

V.4 Semi-analytical model of an electromagnetic energy harvester **234**

V.5 Simulation of a non-destructive testing process equipped with a ferromagnetic core probe **239**

V.6 Extracting of ultrasonic pulse generated by piezoelectric material using machine learning **243**

V.7 Recovery of electromechanical vibratory energy from electromagnetic shock absorbers of vehicles **248**

The Effect of horizontally stratified ground on the Lightning electromagnetic field calculated by the 3D-FDTD method

Ahmed Ziane[1], Kaddour Arzag[2], Zin-eddine Azzouz[1]
[1]University of of Science and Technology of Oran, Algeria, BP 1505 EL M'naouer Oran 31000, Algeria.
Email: ahmed_ziane74@yahoo.com

[2]University of Saida. "BP 138 Cite En-Nasr, Saida 20000", Algeria
Email:: ar_kado2006@yahoo.fr .
[3]University of of Science and Technology of Oran, Algeria, BP 1505 EL M'naouer Oran 31000, Algeria.
Email:: zinazzouz@yahoo.fr.

***Abstract*---The aim of this paper is to study the influence of the two layers horizontally stratified soil on the electric and magnetic fields generated by a lightning stroke to the ground surface. Calculations are carried out using the Finite Difference Time Domain (FDTD) method in three Dimensions (3D) associated with an engineers' models of lightning return stoke current representation. This models are the modified transmission line with linear decay (MTLL) and the modified transmission line with exponential decay (MTLE). Results are obtained using a calculating code developed on Fortan. The electric and magnetic components are calculated on and below the ground. A comparison between the obtained results for two cases of stratified ground and using the two MTL models is done and discussed.**

Keywords: **Lightning, Electromagnetic Field, Finite-Difference Time-domain (3D_FDTD)Method, Horizontal Stratified Ground. MTL models.**

I. INTRODUCTION

The electromagnetic field radiated from a lightning strike to ground has recently been the subject of research within the scientific community. The characterization of this field requires knowledge of the spatiotemporal distribution of the current along the lightning channel [1]. The correct determination of this current distribution makes it possible to correctly evaluate the electromagnetic field generated by this phenomenon [2] ,[3] ,[4].

In this article, we will present an analysis of the electromagnetic field associated with a soil configuration. this configuration is relative to a horizontally stratified[5],[6] and the electromagnetic field components are evaluated above and below the ground[7] ,[8] ,[9]. The calculations are carried out by THE NUMERICAL IMPLEMENTATION of finite differences time domain method in the three-dimensional (3D-FDTD), [10], [11] ,[12] ,[13] we adopted in this work the conditions with ABSORBING LIMITS (1ST ORDER MUR), with a speed of propagation of lightning along the channel equal to 1.5 m/µs.

In addition, among the conditions with absorbent limits (2nd order Mur, UPML (Uniaxial Perfect Matched Layer), PML (Perfectly Matched Layers) and Liao conditions) [14],[15],

For this purpose, a numerical calculation code has been developed on FORTRAN dedicated to evaluation and analysis as well as determination of disturbances electromagnetic radiation at lightning in the presence of a horizontally stratified

II. FINITE DIFFERENCE TIME DOMAIN METHOD (FDTD)

The Finite Difference Time Domain (FDTD) method is a numerical method for solving time-dependent differential equations. It allows the calculation and analysis of the wave propagation of the electromagnetic field generated by lightning.

The application of this method to Maxwell's equations in the time domain was first developed in the field of electromagnetism by *Yee* in 1966 [16], and subsequently generalized by *Taflove* [17]. Currently, it is considered among the most powerful methods for the numerical resolution of Maxwell's equations in the time domain. Indeed, the latter has attracted the attention of many researchers (*Hagness et al*. [18] and *Sillvan* [19]) in fields involving electromagnetic wave propagation phenomena.

Furthermore, the method (FDTD) was used to calculate ([20, 21, 22, 23, 24,11]) the electromagnetic field radiated by a lightning strike from a perfectly conductive ground and

more recently in the presence of a soil of finite conductivity ([25,10,26,27, 28,]).

The finite difference method is very effective in solving Maxwell's equations in the time domain. It is characterized by its precision and flexibility [29]. In addition, it allows direct consideration of the nature of the soil.

Moreover, to study the propagation of electromagnetic field components using the FDTD method in an unbounded space, it is essential to choose boundary conditions of the working domain.

Note that the FDTD method was used for the first time in the calculation of the electromagnetic field generated by lightning by *Baba and Rakov* [30].

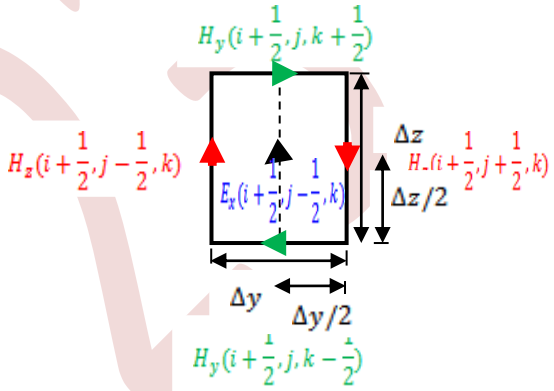
Below we present the different mathematical formulations describing the electromagnetic field components in three dimensions expressed in Cartesian coordinates associated which are obtained by the application of the FDTD method on the Maxwell's equation.

$$E_x^n\left(i+\frac{1}{2},j,k\right)\frac{1-\frac{\sigma\left(i+\frac{1}{2},j,k\right)\Delta t}{2\varepsilon\left(i+\frac{1}{2},j,k\right)}}{1+\frac{\sigma\left(i+\frac{1}{2},j,k\right)\Delta t}{2\varepsilon\left(i+\frac{1}{2},j,k\right)}}E_x^{n-1}\left(i+\frac{1}{2},j,k\right)+\frac{\frac{\Delta t}{\varepsilon\left(i+\frac{1}{2},j,k\right)}}{1+\frac{\sigma\left(i+\frac{1}{2},j,k\right)\Delta t}{2\varepsilon\left(i+\frac{1}{2},j,k\right)}}\left[\frac{H_z^{n-\frac{1}{2}}\left(i+\frac{1}{2},j+\frac{1}{2},k\right)-H_z^{n-\frac{1}{2}}\left(i+\frac{1}{2},j-\frac{1}{2},k\right)}{\Delta y}-\frac{H_y^{n-\frac{1}{2}}\left(i+\frac{1}{2},j,k+\frac{1}{2}\right)-H_y^{n-\frac{1}{2}}\left(i+\frac{1}{2},j,k-\frac{1}{2}\right)}{\Delta z}\right] \quad (1)$$

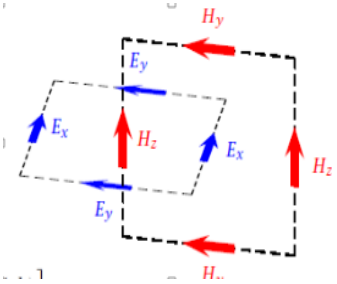
In the same way, we obtain the components of the electric field and by the following relations:

$$E_y^n\left(i,j+\frac{1}{2},k\right)\frac{1-\frac{\sigma\left(i,j+\frac{1}{2},k\right)\Delta t}{2\varepsilon\left(i,j+\frac{1}{2},k\right)}}{1+\frac{\sigma\left(i,j+\frac{1}{2},k\right)\Delta t}{2\varepsilon\left(i,j+\frac{1}{2},k\right)}}E_y^{n-1}\left(i,j+\frac{1}{2},k\right)+\frac{\frac{\Delta t}{\varepsilon\left(i,j+\frac{1}{2},k\right)}}{1+\frac{\sigma\left(i,j+\frac{1}{2},k\right)\Delta t}{2\varepsilon\left(i,j+\frac{1}{2},k\right)}}\left[\frac{H_z^{n-\frac{1}{2}}\left(i,j+\frac{1}{2},k+\frac{1}{2}\right)-H_z^{n-\frac{1}{2}}\left(i,j+\frac{1}{2},k-\frac{1}{2}\right)}{\Delta z}-\frac{H_y^{n-\frac{1}{2}}\left(i+\frac{1}{2},j+\frac{1}{2},k\right)-H_y^{n-\frac{1}{2}}\left(i-\frac{1}{2},j+\frac{1}{2},k\right)}{\Delta x}\right] \quad (2)$$

$$E_z^n\left(i,j,k+\frac{1}{2}\right)=\frac{1-\frac{\sigma\left(i,j,k+\frac{1}{2}\right)\Delta t}{2\varepsilon\left(i,j,k+\frac{1}{2}\right)}}{1+\frac{\sigma\left(i,j,k+\frac{1}{2}\right)\Delta t}{2\varepsilon\left(i,j,k+\frac{1}{2}\right)}}E_z^{n-1}\left(i,j,k+\frac{1}{2}\right)+\frac{\frac{\Delta t}{\varepsilon\left(i,j,k+\frac{1}{2}\right)}}{1+\frac{\sigma\left(i,j,k+\frac{1}{2}\right)\Delta t}{2\varepsilon\left(i,j,k+\frac{1}{2}\right)}}\left[\frac{H_y^{n-\frac{1}{2}}\left(i+\frac{1}{2},j,k+\frac{1}{2}\right)-H_y^{n-\frac{1}{2}}\left(i-\frac{1}{2},j,k+\frac{1}{2}\right)}{\Delta x}-\frac{H_x^{n-\frac{1}{2}}\left(i,j+\frac{1}{2},k+\frac{1}{2}\right)-H_x^{n-\frac{1}{2}}\left(i,j-\frac{1}{2},k+\frac{1}{2}\right)}{\Delta y}\right] \quad (3)$$



(a)



(b)

Figure 1.: Geometry showing the position of the electric field and the magnetic field [31]
(a): Position of the electric field relative to the magnetic Fields loop.
(b): Position of electric and magnetic fields in the cell

Figure 1 presents the position of the electric and magnetic field components according to the cells obtained by the work space discritization.

A. *Current at The Base of The Lightning Channel*

The model used to represent the current at the base of the lightning channel is that of *Heidler* [32] (for the subsequent lightning return stroke Eq. 4). Table 1 summarize the parameters values used in Eq. 4.

$$i(0,t)=\frac{i_{01}}{\eta_1}\frac{\left(t/\tau_{11}\right)^{n_1}}{1+\left(t/\tau_{11}\right)^{n_1}}\exp\left(\frac{-t}{\tau_{12}}\right)+\frac{i_{02}}{\eta_2}\frac{\left(t/\tau_{21}\right)^{n_2}}{1+\left(t/\tau_{21}\right)^{n_2}}\exp\left(\frac{-t}{\tau_{22}}\right) \quad (4)$$

Where i_{01} and i_{02} are the current amplitudes, τ_{11} and τ_{12} are the front-time constants, and τ_{21} and τ_{22} are the decay time constants, while n_1 and n_2 are exponents.

$$\eta_1 = \left[-\left(\frac{\tau_{11}}{\tau_{12}}\right)\left(n_1.\frac{\tau_{12}}{\tau_{11}}\right)^{\frac{1}{n_1}}\right], \eta_2 = \left[-\left(\frac{\tau_{21}}{\tau_{22}}\right)\left(n_2.\frac{\tau_{22}}{\tau_{21}}\right)^{\frac{1}{n_2}}\right] \quad (5)$$

TABLE 1. Parameters of The Lighting Current Source.

Parameter	value
i_{01}	10.7 kA
τ_{11}	0.25 µs
τ_{12}	2.5 µs
i_{02}	6.5 kA
τ_{21}	2.1 µs
τ_{22}	230 µs
n_1	2
n_2	2

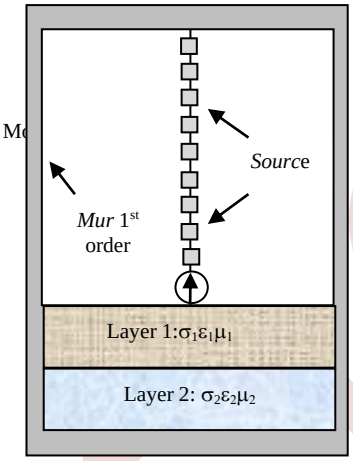


Figure 2. Schematic representation of the lightning channel above a horizontally stratified ground.

Figure 2 shows the schematic representation of the lightning channel above a horizontally stratified ground. The lightning channel is excited in its base by a current source.

B. Model of The Lightning Current Along The Channel

The lightning channel is represented by distributed current sources along the channel and placed in the form of a vertical vector (Figure 2). Each current source is activated by the arrival of the current wave at the point concerned. The calculations are performed using the FDTD-3D method with a lightning current propagation speed along the channel equal to $1.5\ 10^8\ m/s$.

The spatiotemporal distribution of the return stroke current along the lightning channel is calculated using the engineering models MTLE and MTLL.

C. Geometry of the problem

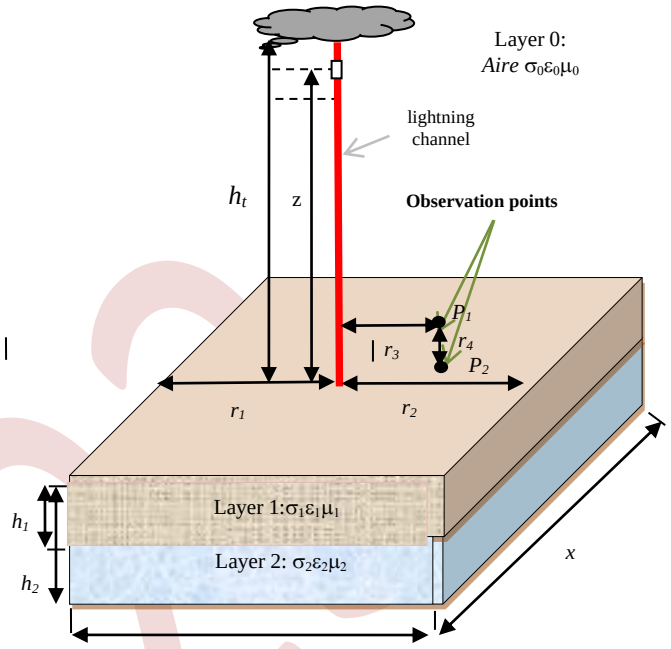
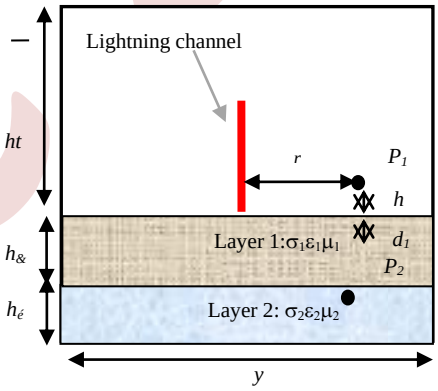
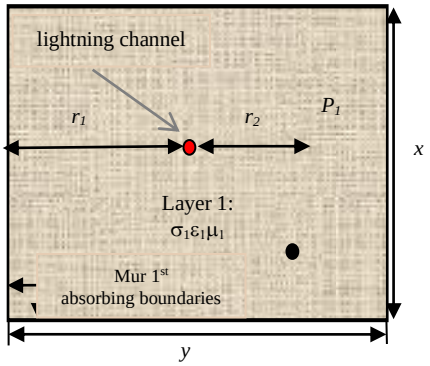


Figure 3. Geometry adopted for the lightning electromagnetic fields computation



(a) Side view



(b) Top view

Figure 4 . Position of the observation points (a) side view and (b) Top view

III. THE CONFIGURATION OF THE HORIZONTAL STRATIFIED SOIL

in this section, evaluation, the electromagnetic field is generated by lightning, so the influence of the presence of a horizontally stratified ground on the calculation of this field having a height H = 7500 m . However, due to the discretization adopted in the direction z (z = 10 m), In addition, simulations are performed for two soil conductivity cases as presented in Table 2, the first MTLE case is a soil conductivity σ1=0.001, σ2=0.01 S/m, the second MTLL case is a soil of conductivity σ1=0.01, σ2=0.001 S/m, . In addition, the soil is characterized by a relative permittivity ε1= ε2=10, a relative permeability μ1=μ1=1 and a depth of 122 m.

This system is accommodated in working volumes with lengths $x \times y \times z$. The computation of the electromagnetic fields is carried out by solving the Maxwell's equations using the three dimension finite difference time-domain method 3D-FDTD [10],[12],[25],[34],[35]],[36].

This computation is based on the discretization of the working volume into cubic or parallelepiped parts with length Δx, Δy and Δz, and a time discretization of the time domain into time increments Δt. In this work the Mur absorbing boundary conditions are applied to the six limits of the working volume in order to avoid unwonted reflection.

Figure III, presented above, describes the geometry of the problem studied in this part. The values of the various parameters of this figure will be given below in the phase of the simulation parameters.

IV. Simulation settings

The vertical lightning channel having an altitude of 7km is located at the center of the horizontal xy plane above the ground surface,

- The observation point has a distance r_d=70 m from the lightning channel,
- Volume of the workspace of 150×200×7122m.
- Parallelepiped air discretization cells: 2.5×2.5×10 m,
- Parallelepiped discretization cells for the ground: 2.5×2.5×0.5 m, for a depth of 2 m below the ground surface, and 2.5×2.5×5 m for the rest of the depth. *Time step : 1 ns,
- The parameters relating to the current are recorded in table 1, with v = 130 m/μs.
- The spatiotemporal distribution of the return arc current is carried out using the MTLL model (with H = 7500m), as well as the MTLE model (with λ=2000 m),The soil conductivity values are recorded in Table 2.

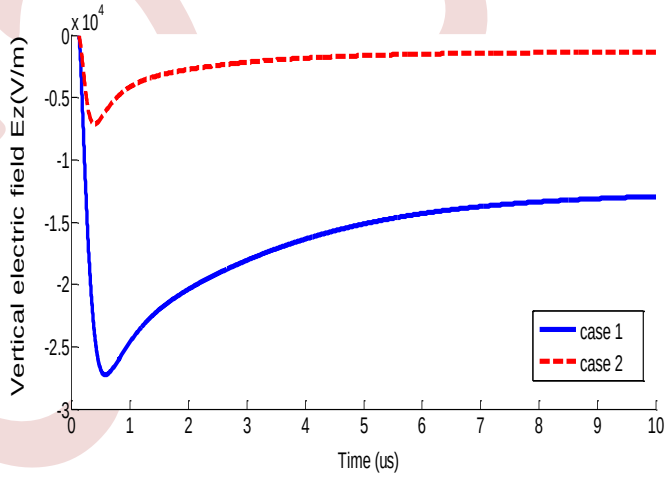
TABLE 2. Electrical Parameters Relative toThe Ground Two-Layer Stratified Vertical Stratification.

	Layer 1		Layer 2	
	Settings	Values	Settings	Values
Case1	$\sigma(s/m)$	0.001s /m	$\sigma(s/m)$	0.01
	ε_r	10	ε_r	10
Case 2	$\sigma(s/m)$	0.01s /m	$\sigma(s/m)$	0.001
	ε_r	10	ε_r	10

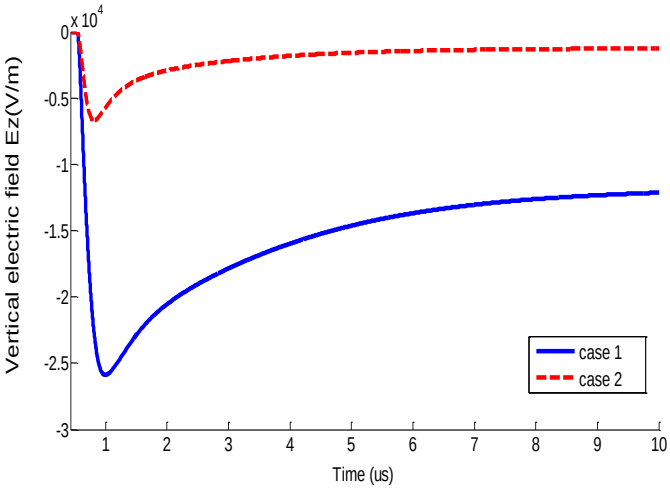
V. SIIMULATION RESULTS

A. *Ectromagnetic Field Calculated Above The Ground*

The temporal variations of the vertical and horizontal components of the electric field, as well as that of the azimuthal component of the magnetic field [37], [38], are presented in figures 5, 6 and 7 respectively.

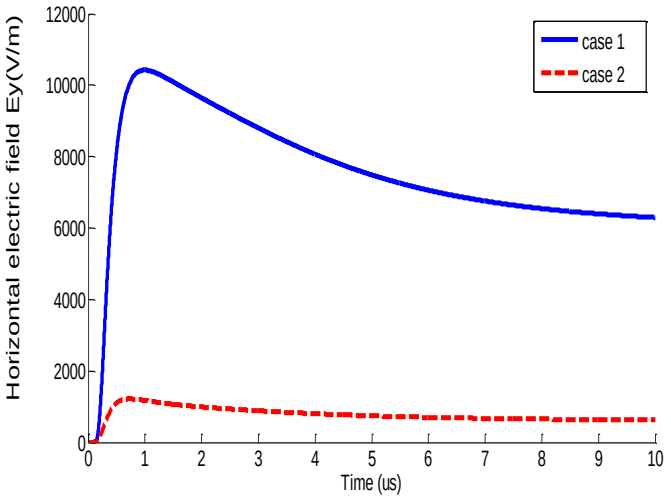


(a)

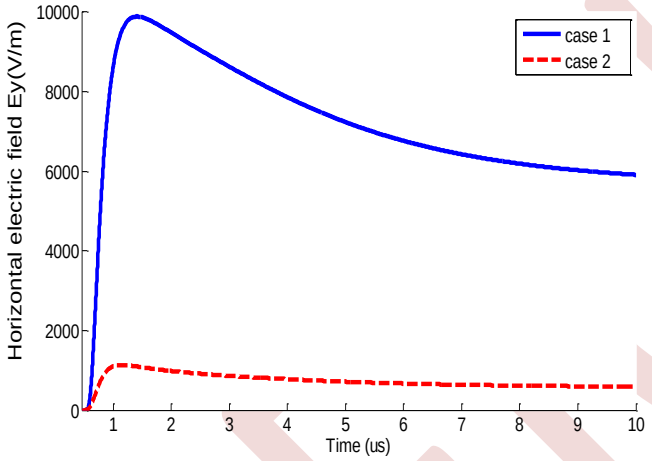


(b)

Figure 5. Temporal variations of the vertical electric field (a)MTLE model, (b) MTLL model

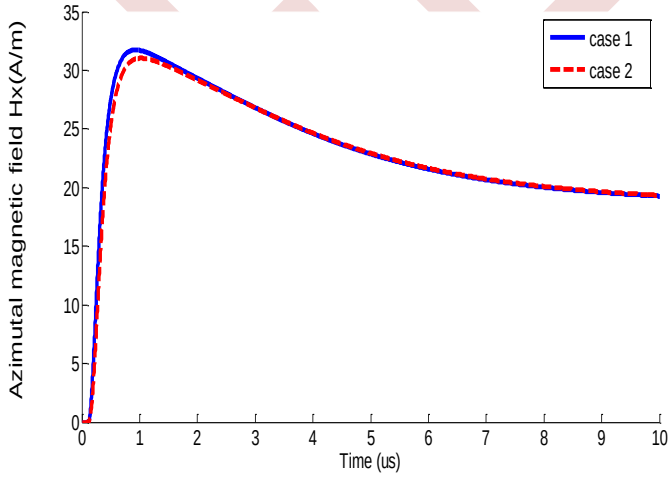


(a)

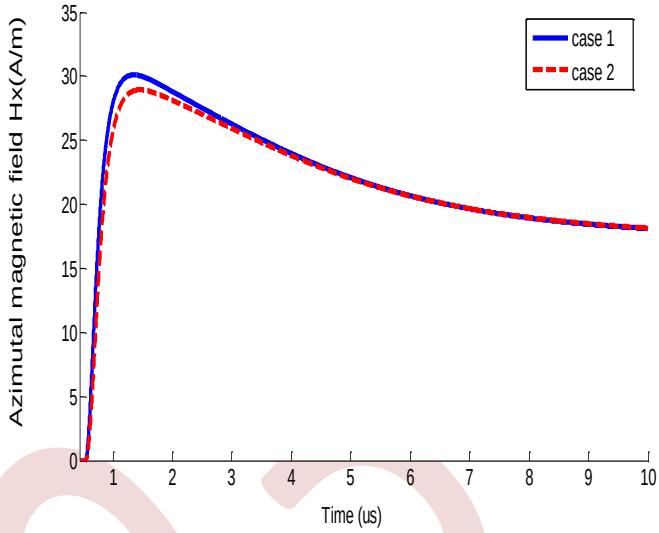


(b)

Figure 6 . Temporal variations of the horizontal electric field (a)MTLE model, (b) MTLL model



(a)



(b)

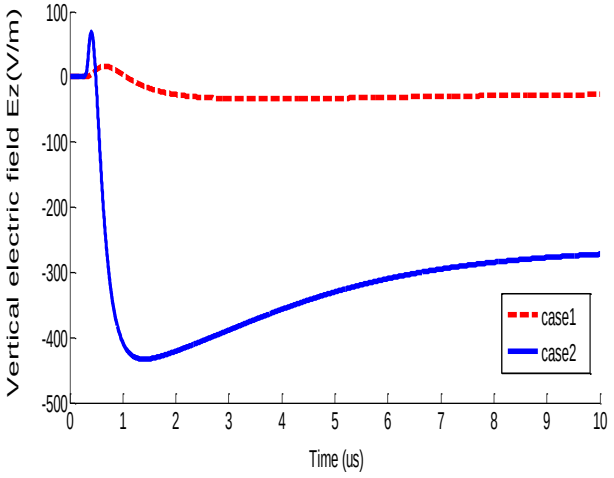
Figure 7. Temporal variations Azimuthal magnetic field (a) MTLE model, (b) MTLL model

The analysis of the waveforms relating to the vertical and horizontal components of the electric field, presented in figures 5 and 6 respectively, shows that the amplitudes of these waveforms are significantly affected by the change in the conductivity of the two layers of the stratified soil.

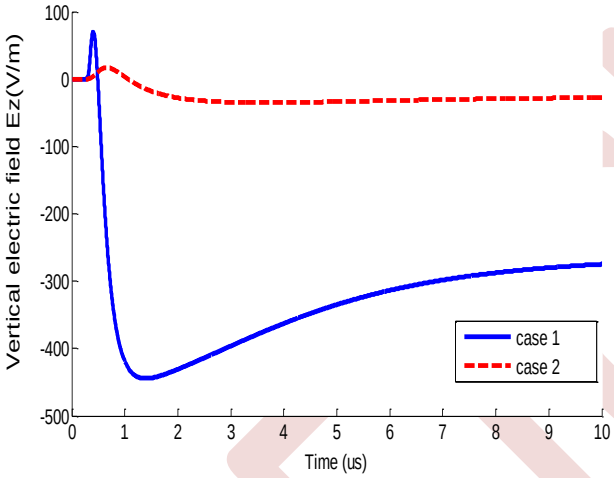
The maximum amplitudes of the magnetic field presented in figure 7, are slightly affected by the variation in the conductivity of the stratified soil. The results obtained using the MTLE model are characterized by an increase in the amplitudes compared to those obtained using the MTLL model.

B. Electromagnetic Field Calculated Below Ground

In figures 8, 9 and 10 we present respectively the appearances of the temporal variations of the vertical electric field, the horizontal electric field and the azimuthal magnetic field, obtained using the FDTD-3D method and the two current models of return arc MTLE and MTLL, calculated below the ground at a height of 10 m and at a distance of 70 m from the lightning channel.

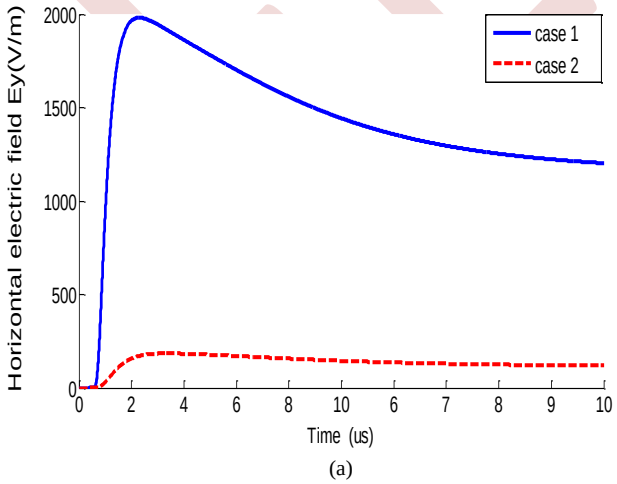


(a)

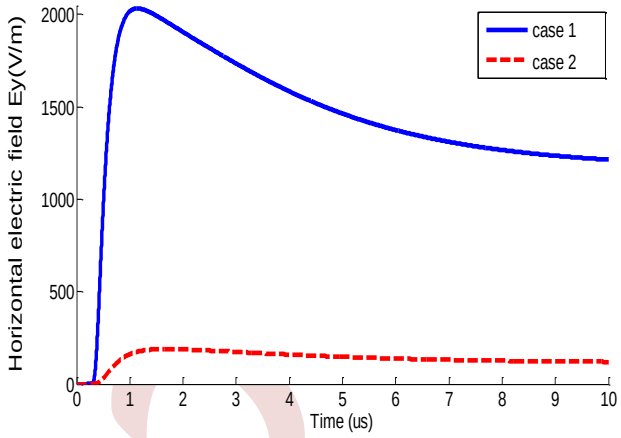


(b)

Figure 8. Temporal variations of the vertical electric field
(a) MTLE model (b) MTLL Model

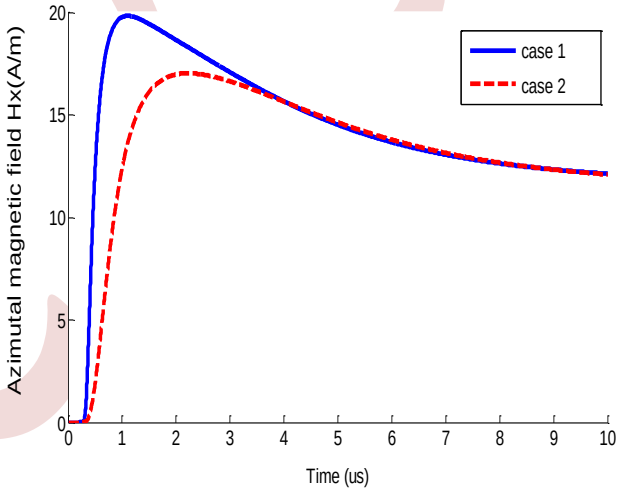


(a)

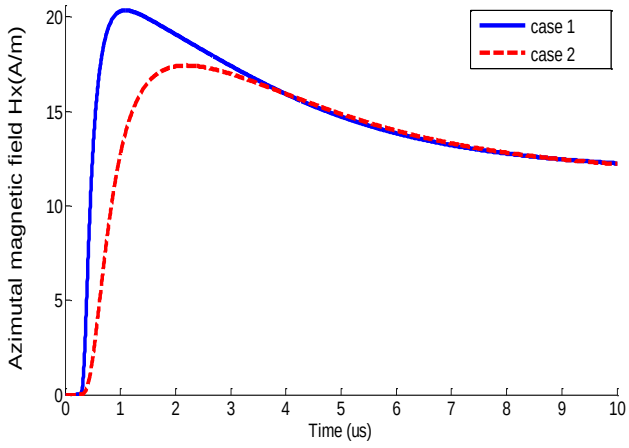


(b)

Figure 9. Temporal variations of the horizontal electric field
(a) MTLE model (b) MTLL Model



(a)



(b)

Figure 10. Temporal variations of the azimuth magnetic field
(a) MTLE model, (b) MTLL model

According to the results obtained, it can be seen that the vertical electric field presented in figure 8 is significantly affected by the variation in the values of the conductivity of the soil layers, and that it is characterized by a change in polarity (from positive sign to negative sign).

The horizontal electric field (Figure 9) is in turn significantly influenced from the amplitude point of view.

For the azimuth magnetic field, the corresponding waveform of which is shown in Figure 10, is affected at the level of the maximum amplitude and at the level of the rise time of the field pulses.

The difference between the curves of the fields obtained, by exploiting the MTLL model, and those obtained using the MTLE model is negligible.

VI. CONCLUSION

We conclude, in this study of the electromagnetic field generated by lightning in the presence of a horizontally stratified ground realized by a three-dimensional method of fine difference domain time (3D-FDTD). The spatio-temporal distribution of the lightning current along the lightning channel was using distributed current sources engineer model . In addition, we developed a calculation code on FORTRAN based on the 3D-FDTD method associated with the MUR absorption limit conditions. Finally, we performed a comparison between the electromagnetic field components obtained by the implementation of the MTLE and MTLL model.

Subsequently, we can note after the comparison that our simulation results, in particular the waveforms of the vertical electric field and the magnetic field, resulting from the 3D-FDTD calculation, are satisfactory on the amplitude plane and the waveform plane.

From these results obtained by the implementation of the FDTD-3D approach, we conclude that the influence of the horizontally stratified ground the vertical and horizontal components field at above ground are more affected by this variation in conductivity by the presence of two layers soil of horizontally stratified

which the component azimutal magnetic results in the slightly greater increase in waveform amplitude of the MTLL method compared to that of MTLE

Thus, the components of the vertical, horizontal electric field and azimuth magnetic field are affected by the variation of the soil conductivity value, that is to say by stratification of the soil which causes a temporal variation of the amplitude of the waveform on these fields which make by comparison between the MTLE with MTLL method.

REFERENCES

[1] M.A. Uman « The lightning discharge », Dover Publications, INC, Mineola, New York, 2001.

[2] F. Rachidi " effets électromagnétiques de la foudre sur les lignes de transmission aériennes : modélisation et simulation", thèse N° 974 (1991), Ecole Polytechnique Fédérale de Lausanne (Suisse).

[3] V. A. Rakov, and M.A. Uman, Review and evaluation of lightning return stroke models including some aspects of their application, IEEE Transactions on Electromagnetic Compatibility, 40 (4), 403-26, 1998.

[4] A.Mimouni " Analyse des problèmes de compatibilité électromagnétique par modélisation et simulation du rayonnement électromagnétique de la foudre", Thèse de Doctorat es-sciences, Université des Sciences et de la Technologie d'Oran Mohamed Boudiaf 2007.

[5] K. Arzag, B. Ghemri, Z. Azzouz "Lightning electric and magnetic fields computation using the 3D- FDTD method and electromagnetic models in presence of different ground configurations", IEEJ Tranactions On Power and Energy, Vol. 138, No. 5, pp 315-320, Mai , 2018.

[6] D.Abdi, Z. Azzouz, A. Mimouni "Influence of a Multilayer Soil Model on Calculation Accuracy of Lightning-Induced Currents on a Buried Cable", International Review of Electrical Engineering (IREE) Vol.12, No.5, pp 450-459, · October 2017

[7] Y. Baba and V. A. Rakov "Electric and magnetic fields predicted by different electromagnetic models of the lightning return stroke versus measurement", IEEE Transactions on Electromagnetic Compatibility. Vol. 51, No. 3, pp. 479 – 487, August 2009.

[8] Y. Baba and V. A. Rakov, "Electromagnetic computation methods for lightning surge protection studies", Singapore : Wiley-IEEE Press, 2016.

[9] A. Ziane and K. Arzag and Z. Azzouz and A. Mimouni "Analysis the Radiated Electromagnetic Field of Lightning in Presence of a Two Layers of Vertically Stratified Ground" The 12thNational Conference on High Voltage Engineering Univesite sidi belebas djillali liabes Algeria *October 04–06, 2022*

[10] K. Arzag, Z. Azzouz, Y. Baba, B. Ghemri, "3D Computation of lightning electromagnetic fields in the presence of a horizontally stratified ground", International Journal of Power and Energy Systems, Vol. 37, No. 4, pp. 120-128, 2017.

[11] K. Arzag, Z. Azzouz, Y. Baba and B. Ghemri, "3-D FDTD Computation of the electromagnetic fields associated with lightning strikes to a tower climbed on a trapezoidal mountain" IEEE Transactions On Electromagnetic Compatibility, Vol. 61, No. 3, pp. 606-616, June 2019.

[12] K. Arzag, Z. Azzouz, B. Ghemri, "3D-FDTD computation of lightning return stroke current and associated electromagnetic field using electromagnetic models", International Review of Electrical Engineering (IREE), Vol. 11, No.5, pp. 517-525, Oct. 2016.

[13] A. Ziane, K. Arzag , Z. Azzouz "Computation of Electromagnetic Field Generated by Lightning strikes to a Tall Object in Presence of a Vertically Stratified Ground Using the 3D-FDTD Method", International Review of Electrical Engineering (IREE), Vol. 16, No. 3, pp 257-266, June 2021.

[14] G. Mur "Absorbing boundary conditions for the finite difference approximation of the time domain electromagnetic field equations", IEEE Transactions on Electromagnetic Compatibility, Vol. 23, No. 4, pp. 377-382, 1981.

[15] K. Arzag, Z. Azzouz, B. Ghemri "Lightning radiation evaluation using electromagnetic models" Journal of Electrical Systems Vol. 14, No. 2, pp. 53-63 · June 2018.

[16] K. S. Yee "Numerical solution of initial boundary value problems involving Maxwell's equations in isotropic media," IEEE Trans. Antennas and Propogation., vol. AP-14, n. 3, May, 1966, pp. 302–307.May 1966.

[17] A. Taflove, M. E. Brodwin, "Numerical solution of steady-state electromagnetic scattering problems using the time dependent Maxwell's equations", IEEE transactions on microwave theory and techniques, vol. 23, no.8, p.623-630, august 1975.

[18] A. Taflove, S.C. Hagness, "Computational electrodynamics: the finite difference time domaine method", second Edition Artech House; Boston, USA, 2000.

[19] D.M Sillivan, Electromagnetic simulation using the FDTD method" , IEEE Pressries on RF microwaves technology, 2000.

[20] Y. Baba, V.A. Rakov "On the interpretation of ground reflections observed in small scale experiments simulating lightning strikes to

towers," IEEE Transactions on Electromagnetic Compatibility, Vol. 47, No. 3, 2005, pp. 533-54.
[21] K. Arzag, Z. Azzouz, B. Ghemri, "Lightning electromagnetic pulse simulation using 3D-FDTD method (comparison between PEC and UPML boundary conditions)" International Conference on Lightning Protection (ICLP2016), paper n° 5 12, 25-30 Portugal, Sept. 2016.
[22] Y. Baba, V.A. Rakov "On the mechanism of attenuation of current waves propagating along a vertical perfectly conducting wire above ground: application to lightning," IEEE Transactions on Electromagnetic Compatibility, Vol. 47, No. 3, 2005, pp. 521-532.
[23] C. A. F. Sartori, J. R. Cardoso "An analytical-FDTD method for near LEMP calculation," IEEE Transactions on Magnetics, vol. 36, No. 4, 2000, pp. 1631-1634.
[24] C. Yang, B. Zhou "Calculation Methods of Electromagnetic Fields Very Close to Lightning," IEEE Trans. Electromagnetic Compatibility, Vol. 46, N° 1, 2004, pp 133-141.
[25] K. Arzag, B. Ghemri, Z. Azzouz, Lightning Electric and Magnetic Fields Computation using the 3D-FDTD Method and Electromagnetic Models in Presence of Different Ground Configurations, IEEJ. Trans. On Power and Energy, Vol. 138, No. 5, pp 315-320, Mai, 2018.
[26] A. Mimouni, Z. Azzouz, O. Harraz, B. Ghemri and A. Cherifi "Modeling and simulation of lightning electromagnetic fields using an hybrid method for poorly conducting ground case", International Review of Electrical Engineering (IREE), Vol. 1, N°. 5, pp.594-602, 2006.
[27] Z. Azzouz, A. Mimouni, B. Ghemri and A. Cherifi "Analysis of radiated-lightning electromagnetic fields above imperfect ground Using a Quasi-FDTD HYBRID Method", Accepted for publication in ACTA Electrotechnica et Informatica.
[28] B. Ghemri, Z. Azzouz, A. Mimouni, A. Cherifi "Méthode hybride pour le calcul du champ électromagnétique associé à un coup de foudre validation expérimentale", 4th International Conference on Electrical Engineering 07 - 08 November 2006, Batna.
[29] F. Rachidi Haeri " Effet électromagnétique de foudre sur les lignes de transmission aérienne : modélisation et simulation " Thèse doctorat Es-Science , EPFL Lausanne, Suisse , 1991.
[30] Y. Baba, and V.A. Rakov ''On the transmission line model for lightning return stroke '',Geophysical research Letters. vol. 30, n. 24, 2294 doi 10.1029/2003GL018407, 2003.
[31] Y. Baba, and V.A. Rakov "Electromagnetic method for lightning surge protection", Edition Wiley, 2016.
[32] F. Heidler "Analytic lightning current functions for LEMP calculations" Proceeding 1985. International Conference on Lightning Protection (ICLP), pp. 63-66, Munich, Germany, September 1985.
[33] A. Mimouni, F. Rachidi, and M. Rubinestein, "Electromagnetic field of a lighting return stroke in presence of a stratified ground," ,IEEE Transaction Electromagnetic Compatibility, vol.56, no.2, pp. 413-418, Apr.2014.
[34] K. Arzag Z. Azzouz Y.Baba "3D-FDTD Computation of Lightning Electromagnetic Fields in the Presence of a Mountain and a River" XV SIPDA International Symposium on Lightning Protection, 30 Sep.- 04 Oct. 2019, Sao Paulo, Brasil.
[35] K. Arzag, Z. Azzouz, and B. Ghemri "Modeling and simulation of the lightning return stroke current using electromagnetic models and the 3D-FDTD method" Proceeding of International Conference on Recent Advances in Electrical Systems ICRAES'2016, Hammamet, Tunisia, pp. 360-364, December 2016.
[36] A.Ziane, Z.Azzouz, A.Mimouni, B.Ghemri"10 ème conférence sur le génie électrique Bordj El Bahri (CGE'10) (17-18 avril 2017).
[37] K. Arzag Z. Azzouz B. Ghemri"Analysis of the Under-ground azimutal Magnetic Field Generated by Lightning Strikes to a Tower Instaled on a Mountain Using the 3D-FDTD Method", Proceeding of International Conference on Recent Advances in Electrical Systems ICRAES'2019, Hammamet, Tunisia, December 2018.
[38] K. Arzag, Z. Azzouz, and B. Ghemri, 3D FDTD Calculation of Electric fields due to Lightning Strikes to a Tower Situated on a Mountain in Presence of a Vertical Stratified Ground, in Proc. 2018. International Conference on Recent Advances in Electrical Systems, Hammamet, Tunisia, pp. 247-250, Dec. 2018.

Design of Three Permanent Magnets Drum Separator for the Extraction of Fine Iron Particles

Abdallah Belounis[1,2], Rabia Mehasni[1], Oussama Belguet[1]

[1]*Electrical Laboratory of Constantine (LEC), Constantine, Algeria*

[2]*20thAugust 1955 University, Skikda, Algeria*

abdallah.belounis@lec-umc.org rabia.mehasni@umc.edu.dz oussama.belguet@lec-umc.org

***Abstract*—The aim of this work is the design of a drum magnetic separator (DMS) with only three NdFeB permanent magnets of size $10^{-2}\times1.2\times10^{-2}\times10^{-1}m^3$ and residual magnetic flux density B_r=1.1T intended for the extraction of iron particles of fine size from materials transported by a conveyor belt. Such design was done in two stages where firstly we looked for the best positioning of the group of three magnets (initially the angle between two neighbors is 45°) in respect to the entrance of the material in the drum region. In the second stage, we kept the best position of the middle magnet and we searched for the best spacing angle between it and each neighbor. The searching process was based on the estimation and comparison between the particle capture efficiencies computed for several cases of magnets arrangement. To know the particle final site that permits the checking of its capture, we computed its trajectory. For this, we solved the particle dynamic governing equation where a computing program based on the coupling of finite element (FE) and Runge-Kutta (RK4) numerical methods was developed and used.**

***Keywords:* Drum Magnetic Separator, Finite Element Modeling and Simulation, Particle Trajectory.**

I. INTRODUCTION

Magnetic separation is a technique based on the application of a magnetic field to extract magnetic objects from dry or wet non-magnetic materials. It is largely used in mining industry, metallic waste sorting and liquid and gas purification processes [1-3]. To achieve efficient separation, the device to be used must be well-designed [4-8]. The problem of separation (capture) of magnetic particles by using permanent drum separators was treated in [4]. In such separator, several arrangements of different numbers of permanent magnets were proposed and treated.

In this work, and to reduce the investment cost and drum monitoring constraints, we were interested in the design of a magnet drum separator containing only three NdFeB permanent magnets intended for the extraction of fine iron particles (assumed of cubic shape of size $10^{-6}\times10^{-6}\times10^{-6}$ m^3 and relative magnetic permeability μ_{rp} = 80). The treated material that contains the particles to be extracted is transported to the drum through a conveyor belt with controlled speed (see Figure. 1).

The design process consists of two stages. In the first stage, we looked for the best positioning of all the three magnets along the half-perimeter of the drum that is in contact with the conveyor belt where the capture of particles can be occurred. In fact, we deal with six cases of the three magnets positioning for which we always keep the same angle (45°) between the middle one and the others.

At each time, we change the position of the three magnets by shifting the entire group by an angle of 15° from a reference line (see Figure. 1). To research the best positioning of the magnets among the treated cases, we compare between the capture efficiencies (particle capture). These later were obtained from the computation of the particle trajectories for different ranges of the moving speed of the conveyor belt.

In the second stage, we search for the best shifting angle between the middle magnet and the two others. For this, we fix the middle magnet in its best position found in the first stage and we change every time the shifting angle, we compute and compare the separation efficiency until the obtaining of the best result.

To reduce the computing cost we limited the searching process to four cases of shifting angles 35°, 40°, 45° and 50°.

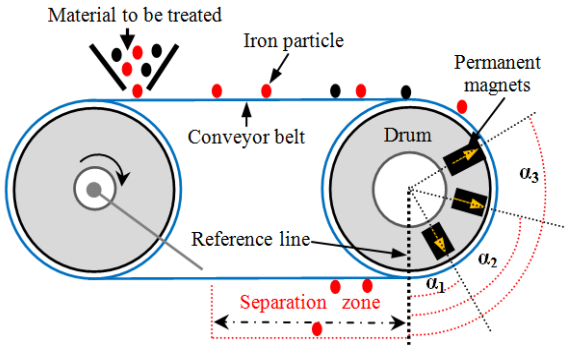


Figure 1. 2D view of the considered magnet drum separator.

As we have processed in the first stage, the investigation of the optimal positioning of the three magnets was based on the computation of the particle trajectories that provide all information on their capture.

To compute a particle trajectory, one can solve its dynamic governing equation [4]. Because we are interested in a qualitative result here, we have only taken into account the magnetic force and that of gravity. To take into account the non-linearity of the particle dynamic equation and the geometrical complexity of the study domain, a numerical resolution was achieved. Assuming that the magnetized fine particles not disturbs the applied magnetic field on one hand and the device has very important depth according to the direction perpendicular to the study plane on the other hand, a reduced 2D resolution program based on the coupling of the FE and RK4 methods has been developed and used [4].

II. MODELING EQUATIONS

A. *Magnetic Field and Applied Magnetic Force*

In our study, the magnetic field is generated by permanent magnets. To compute the distribution of such field, we have solved the magneto-static equation given by [4]

$$\vec{\nabla} \wedge \left(\frac{1}{\mu}\vec{\nabla} \wedge \vec{A}\right) = \frac{1}{\mu_a}\vec{\nabla} \wedge \vec{B}_r \quad (1)$$

Here $\vec{A}$ is the magnetic vector potential, $\vec{B}_r$ is the magnets residual flux density, μ is the magnetic permeability ($\mu = \mu_0\mu_r$, μ_0 is the magnetic permeability of vacuum, μ_r is the relative magnetic permeability), μ_a is the magnetic permeability of the permanent magnet ($\mu_a = \mu_0\mu_{ra}$, μ_{ra} is the relative magnetic permeability of the permanent magnet).

The magnetic force applied on a magnetized particle is given by [4], [8]

$$\vec{F}_m = \mu_0 V_p (\vec{M} . \vec{\nabla})\vec{H} \quad (2)$$

where $\vec{M}$ is the particle magnetization, $\vec{H}$ is the magnetic field strength and V_p is the particle volume.

B. *Force of Gravity and Dynamic Equation*

Under the effect of the gravity field, the moving particle is also subject to a gravitational force given by

$$\vec{F}_g = m\vec{g} \quad (3)$$

where m is the particle mass and $\vec{g}$ is the gravity acceleration.

By considering the two previously mentioned forces, the motion of the particles is then governed by [4], [8]

$$m\frac{d\vec{v}_p}{dt} = \vec{F}_m + \vec{F}_g. \quad (4)$$

Here $\vec{v}_p$ the particle velocity.

III. COMPUTING RESULTS

A. *Magnetic Filed and Applied Magnetic Force Density*

To check the exact and precision of both the developed mathematical models and computing program on one hand and to show the possible separation of magnetized particles when they pass in the vicinity of the drum on the other hand, we have computed the distributions of the magnetic field and the magnetic force density in the useful part of the study domain.

The results obtained for the case of positioning angles of the magnets α_1=90°, α_2=135° and α_3=180° (see Figure. 1) are presented in Figure 2.

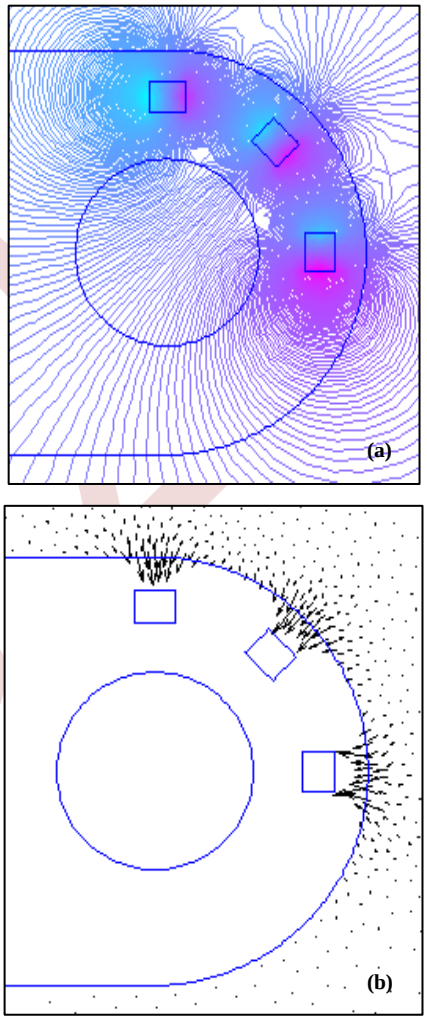


Figure 2. Distributions of the magnetic field and magnetic force density in the vicinity of the drum. (a) magnetic vector potential, (b) magnetic force density.

In Figure 2 (a), we see clearly the periodic and symmetric distribution of the magnetic vector potential, which is in concordance with the chosen polarity of the magnets.

These particularities of the obtained result approve the accuracy and precision of the computing process.

On Figure 2 (b), we see that an attractive force exists in the environment of the drum which means that if a particle crosses this region, it will be captured.

Such a force is very high close to the permanent magnets and decreases when we displace away from them. If we

change the positions or the size of the magnets, the distribution of the force changes.

B. Particle Trajectories

In order to define the best positioning of the group of the three permanent magnets (aim of the first stage) in the proposed drum separator, we computed the trajectory of one particle (assumed cubic of fine size) carried by the belt with its linear speed. Such a computation has given for different belt speeds and magnets positioning the results presented in Figure 3.

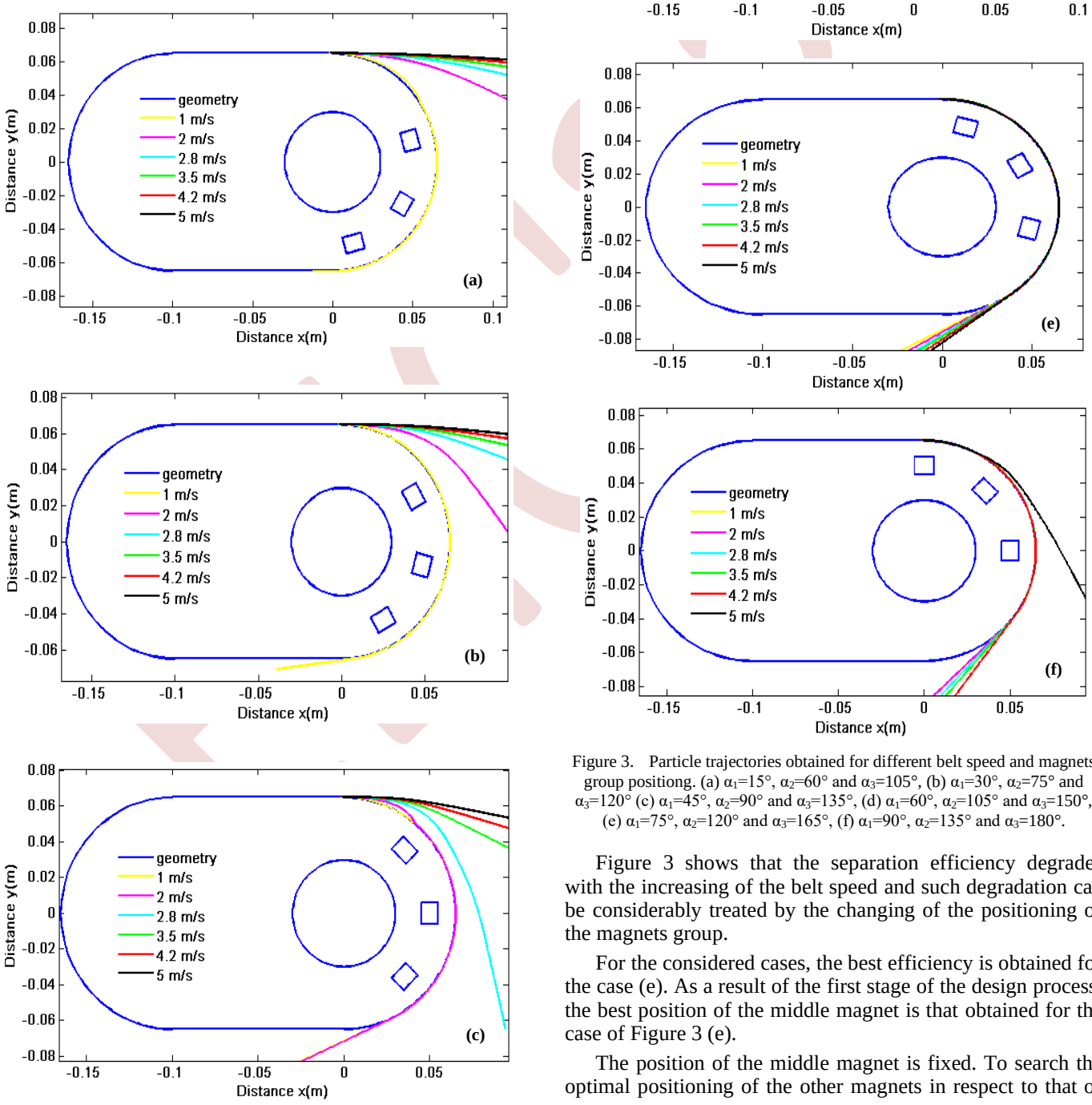


Figure 3. Particle trajectories obtained for different belt speed and magnets group positiong. (a) α_1=15°, α_2=60° and α_3=105°, (b) α_1=30°, α_2=75° and α_3=120° (c) α_1=45°, α_2=90° and α_3=135°, (d) α_1=60°, α_2=105° and α_3=150°, (e) α_1=75°, α_2=120° and α_3=165°, (f) α_1=90°, α_2=135° and α_3=180°.

Figure 3 shows that the separation efficiency degrades with the increasing of the belt speed and such degradation can be considerably treated by the changing of the positioning of the magnets group.

For the considered cases, the best efficiency is obtained for the case (e). As a result of the first stage of the design process, the best position of the middle magnet is that obtained for the case of Figure 3 (e).

The position of the middle magnet is fixed. To search the optimal positioning of the other magnets in respect to that of

the middle one, a series of computation of the particle trajectory for different belt speeds and positions of the other magnets has been achieved.

For this, and to reduce the computing cost, we have limited the computation to four cases.

For the same conditions concerning the FE and RK4 running processes, we have obtained the results presented in Figure 4.

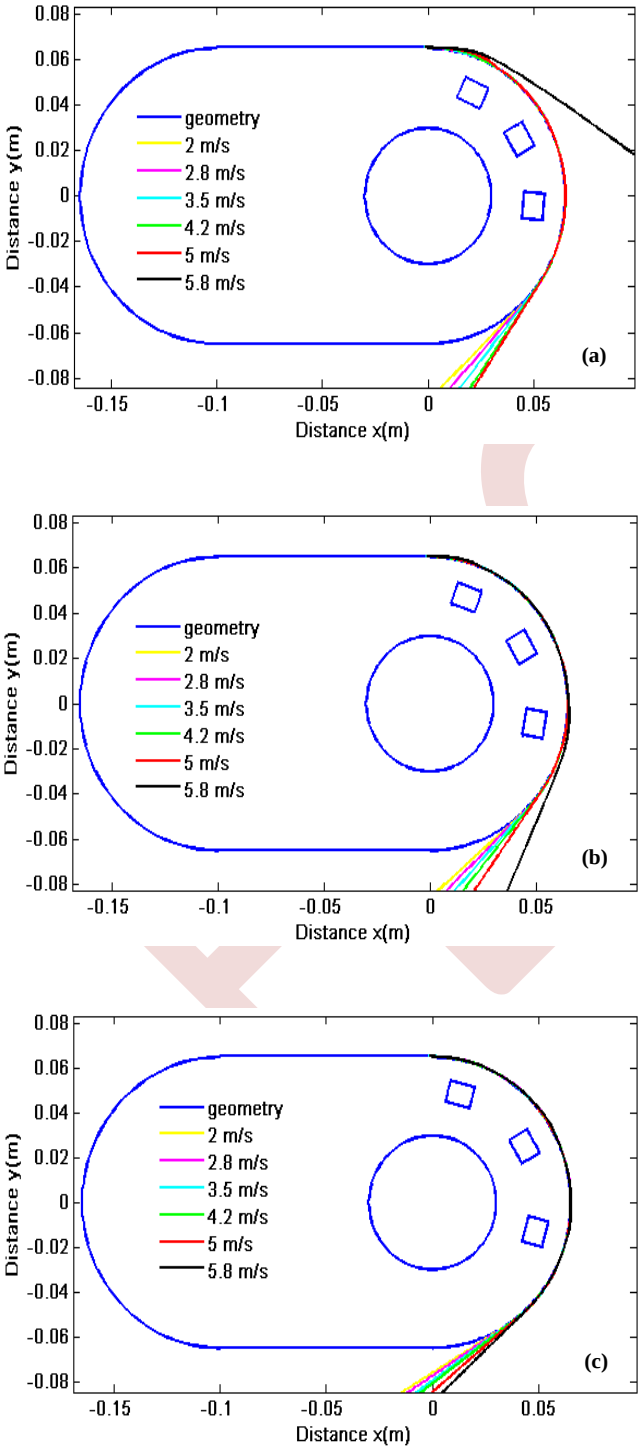


Figure 4. Particle trajectories obtained for different belt speeds and magnets positionning. (a) α_1=85°, α_2=120° and α_3=155°, (b) α_1=80°, α_2=120° and α_3=160° (c) α_1=75°, α_2=120° and α_3=165°, (d) α_1=70°, α_2=120° and α_3=170°.

Figure 4 shows that the best separation efficiency is obtained for the case (c). In this case, high separation performances are obtained for a speed belt V_b = 5.8 m/s.

IV. CONCLUSION

This study represents a contribution to the optimization of the magnet drum separators. Basing on previously achieved works, we have researched for an optimal configuration of a magnet drum with only three magnets which permits a considerable reducing of the investment cost and operating constraints. In the achieved computations only magnetic and gravitational forces have been taken into account. The fine size of the considered particles and the qualitative nature of searched results have permitted a 2D resolution of the separation problem. The obtained results have shown that for a given size of particles and used magnets, high efficient separation can be realized by an optimal choice of both the magnets positions in respect to the supplying of the material to be treated and the conveyor belt speed.

REFERENCES

[1] Ying Zhao, Beidou Xi, and all, Removal of phosphate from wastewater by using open gradient superconducting magnetic separation as pretreatment for high gradient superconducting magnetic separation, Separation and Purification Technology Vol. 86 pp. 255–261. 2012.

[2] Nakul Dholu, James. R. Nagel, and all, Eddy current separation of nonferrous metals using a variable-frequency electromagnets, KONA Powder and particle Journal No 34, 2017, pp 241-247.

[3] James. R. Nagel, and all, Electrodynamic sorting of industrial scrap metal, KONA Powder and particle Journal No 37, 2020, pp 258-264.

[4] M. Ouili, R. Mehasni, M. Feliachi, and all, "A simultaneous separation of magnetic and conductive particles in a designed permanent magnet drum separator'', IJAEM, 61, pp 137–155. 2019.

[5] S. S. Leong, Z. Ahmad, S. C. Low, J. Camacho, J. Faraudo, J. K. Lim, "Unified view of magnetic nanoparticle separation under magnetophoresis,'' Pubs.acs.org/Langmuir, 36, pp. 8033−8055, 2020.

[6] J. Lunacek, M. Lesnak, and all, "Efficiency of high gradient magnetic separation applied to micrometric magnetic particles,'' Separation Science and Technology, 50, pp. 2606–2615, 2015.

[7] D. Lu, J. Liu, Z. Cheng, and all, "Development of an open-gradient magnetic separator in the aerodynamic field", Physicochem. Probl. Miner. Process., 56(2), pp. 325-337, 2020.

[8] A. Belounis, R. Mehasni, M. Ouili, M. E.H. Latreche, "Optimization of the capture element for an OGMS based on the 3D computation of the magnetic particle behavior'', IJAEM, vol. 48, pp 387-397, 2015.

Dynamic hysteresis loops using the Jiles Atherton Model based on Loss-surface formulation

Sofiane AIDEL [1], Mourad HAMIMID [1]

[1 2] *Laboratoire de Physique Des Matériaux, Rayonnements et Nanostructures, University Mohemed El Bachir El Ibrahimi of Bordj Bou Arreridj, El-Anasser 34030, Algeria*

sofiane.aidel@univ-bba.dz

***Abstract*— This paper proposes a new extension of the Jiles-Atherton (J-A) hysteresis model that allows for its use in both quasi-static and dynamic regimes. While the quasi-static J-A model is effective in characterizing hysteresis behavior regardless of frequency. However, the Jiles-Atherton model is limited in its ability to calculate iron losses in electrical machines when they operate under varying supply voltage frequencies. To overcome this challenge, we introduce a dynamic model that takes into account two critical counter-field effects, namely eddy currents and excess field. The excess field is obtained from the Loss-Surface (L-S) model. This formulation depends on two crucial parameters, which are calculated by using the Fmincon algorithm to solve a quadratic function. To validate the proposed extension, experiments were conducted using 3% Fe-Si sheets. The results of these measurements are then compared with the predicted results of the dynamic model. Notably, the results demonstrate an agreement between the model and the experimental data, especially in the context of low- and medium frequency. This research makes a significant contribution to the understanding and modeling of hysteresis phenomena in electrical machines that operate under dynamic regime conditions.**

***Keywords:* Hysteresis, Jiles-Atherton model, Excess field, loss-surface.**

I. INTRODUCTION

Optimal electromagnetic device design is closely tied to the selection of iron core materials. These materials have a vital role in directing the magnetic flux density, leading to the emergence of a non-linear phenomenon called hysteresis. Fundamentally, this phenomenon manifests as heat in ferromagnetic materials, which are frequently employed in electromagnetic devices. Several models have been developed to describe and evaluate hysteresis loops under quasi-static and dynamic regimes [1-5]. Some of these models provide an energetic explanation of this phenomenon, including the energetic model [6, 8] and the Jiles Atherton model [9-10]. The Jiles Atherton (J-A) model is notably well-suited for the modeling of quasi-static hysteresis. To extend the applicability of the quasi-static model to dynamic regimes, various methods have been employed that involve adding two additional factors: the counter-field eddy current and the excess field [11-12]. The primary aim of this paper is to predict the dynamic behavior of hysteresis loops subjected to various frequencies.

This proposition is founded on the J-A model and employs the Berttoti approach to compute energy losses. Magnetic energy losses are typically classified into two groups: a frequency-independent hysteresis contribution, known as W_{hys}, and a frequency-dependent dynamic contribution, termed W_{dyn}. The calculation of the energy loss W_{dyn} integrates both eddy current and excess field formulations.

The excess field formulation is obtained from the model presented in reference [13], with its equation bearing a resemblance to that of the loss surface model. To validate the proposal, it was applied and compared to measurements conducted on a sample containing 3% Fe-Si over a frequency range.

II. QUASI-STATIC J-A MODEL

The J-A model enables the modeling of the hysteresis loop phenomenon from a physical approach in ferromagnetic materials. In the modified inverse quasi-static J-A model, the magnetic flux density B is considered as an independent variable which is based on the modified direct one [14]. The hysteresis loop was represented by putting the underlying phenomenon into a clear first-order differential equation.

$$\frac{\mathrm{d}\,\mathrm{M}}{\mathrm{d}\,\mathrm{B}} = \frac{\xi}{\mu_0\left(\mathrm{k}\delta + (1-\alpha)\xi\right)} \tag{1}$$

$$\xi = \delta \mathrm{kc}\frac{\mathrm{dM_{an}}}{\mathrm{dH_e}} + \left(\mathrm{M_{an}} - \mathrm{M}\right) \tag{2}$$

$$\mathrm{H_e} = \mathrm{H} + \alpha \mathrm{M} \tag{3}$$

$$\frac{\mathrm{dM_{an}}}{\mathrm{dH_e}} = \frac{\mathrm{M_s}}{\mathrm{a}}\left(1 - \coth\left(\frac{\mathrm{H_e}}{\mathrm{a}}\right)^2 - \left(\frac{\mathrm{a}}{\mathrm{H_e}}\right)^2\right) \tag{4}$$

$$M_{an} = M_s\left(\coth\left(\frac{H_e}{a}\right) - \frac{a}{H_e}\right) \quad (5)$$

Where H_e, M_{an}, and M_s are, respectively, the effective field, the anhysteretic magnetization, and the saturation, magnetization. *a*, α, *c*, and *k* and are the model parameters where *a* represent quantified domain wall density. α is the parameter of inter-domain coupling. *c* is the coefficient magnetization reversibility and *k* represents quantified energy to break the pinning site in ferromagnetic materials, these parameters have to be determined from measured hysteresis characteristics. δ is a directional parameter taking the values +1 for $dB/dt>0$ and -1 for $dB/dt<0$.

III. DYNAMIC MODEL

A. Loss-surface model

This model provides acceptable accuracy for the real behavior of the phenomenon [13], but it is based on two contributions, static and dynamic. The first is the more sensitive part of the model, taking into account the *B* induction and the history of the magnetization, and the other is linked to the *B* induction and its temporal variation *dB/dt*, making it possible to reproduce the dynamic behavior of the material as a function of the excitation frequency and waveform. This contribution contains all the dynamic effects: macroscopic induced currents, nucleation, displacement, and deformation. Its identification is based mainly on a single characteristic surface H_{mes0} *(B, dB/dt)* determined experimentally:

$$H(B, \frac{dB}{dt}) = H_{sta}(B, \text{history}) + H_{dyn}(B, \frac{dB}{dt}) \quad (6)$$

H_{stat} is represented by a scalar hysteresis model in which two terms are considered an anhysteretic field juxtaposed with a friction field which accounts for the roughness of the terrain in which the walls move. The roughness of the ground in which the walls move. This part requires two inputs: a major quasi-static cycle performed at saturation induction and a few cycles at lower inductions a few cycles at lower inductions [15]. $H_{dyn}(B, dB/dt)$ This term is calculated from the surface H_{mesdyn} *(B, dB/dt)* extracted from the surface H_{mes0} *(B, dB/dt)* after subtraction of the quasi-static contribution. Its shape is regular, with no surface discontinuity, and is approximated by portions of polynomials [16].

$$H_{dyn}(B, \frac{dB}{dt}) = \left(C_1 + C_2 \text{sign}\left(\frac{\partial B}{\partial t}\right)B\right)\frac{\partial B}{\partial t} \quad (7)$$

B. Dynamic J-A with Loss-Surface extension

The main idea of this paper is the integration of the dynamic term into the effective field of the J-A model, which takes into account the term of eddy current and effect excess field, by the following equation:

$$He = H + \alpha M - \left(K_1 + \delta K_2 B_s(t)\right)\frac{dB_s}{dt} \quad (8)$$

Where K_1 and K_2 represent the coefficient terms of eddy current excess filed.

The classical eddy-current field is given as [17]:

$$H_{edd} = K_1 \frac{dB_s}{dt} \quad (9)$$

K_1 is a coefficient related to the physical and geometrical parameters of the material and is given by [18]:

$$K_1 = \frac{\sigma d^2}{2\beta} \quad (10)$$

Where, σ is the conductivity of the material, *d* and β are parameters related to the geometry of the material. In the case of a sheet, *d* corresponds to the thickness of the sheet, and β is a form factor.

IV. RESULTS AND DISCUSSIONS

To validate this proposition, hysteresis measurements of sheets made from non-oriented electrical steel are employed. These sheets made from 3% Fe-Si materials, have laminations that are 0.35 mm thick, 15 mm width, and a mass density of 7650 kg/m3. The Epstein frame is utilized for the hysteresis loop measurements. With primary coils that have 640 turns and secondary coils that have 320 turns, this device functions as a transformer. Magnetic cores typically measure 147 mm in length. The parameter values of the quasi-static J-A model were identified by using the Fmincon procedure, at a low frequency (10 Hz) and they are illustrated in Table I. The measured and modeled hysteresis loops are shown in Figure 1.

TABLE I. QUASI-STATIC J-A PARAMETERS

J-A parameters	***Values***
Ms (A/m)	$1.19\ 10^6$
a(A/m)	*56.14.*
k(A/m)	*60.1*
α	$1.95\ 10^{-4}$
c	$1.33\ 10^{-4}$

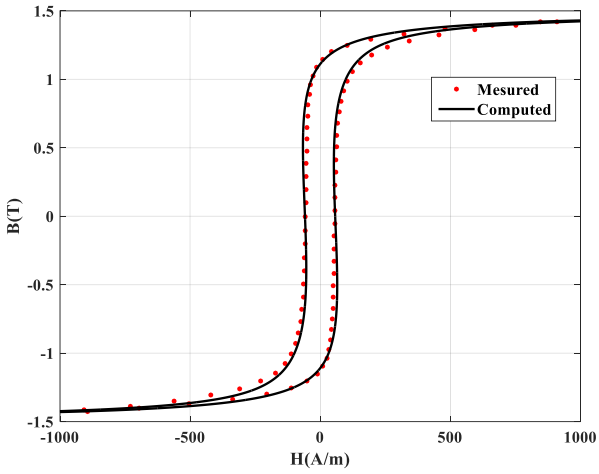


Figure 1. Computed and measured loop at 10 Hz

To extend the J-A in a dynamic regime, by using Eq-8, the same parameters of quasi-static are used in this work. These quasi-static parameters in Table I are constant and unchanged. the results are compared with hysteresis loops measured for three arbitrary frequencies 10,100,200 and 300 Hz, as shown in Figure 2. This model gives acceptable results. This has been done depending on the dynamic parameters shown in Table II.

TABLE II. DYNAMIC PARAMETERS

Parameters	***Values***
K_1	0.0417
K_2	0.0224

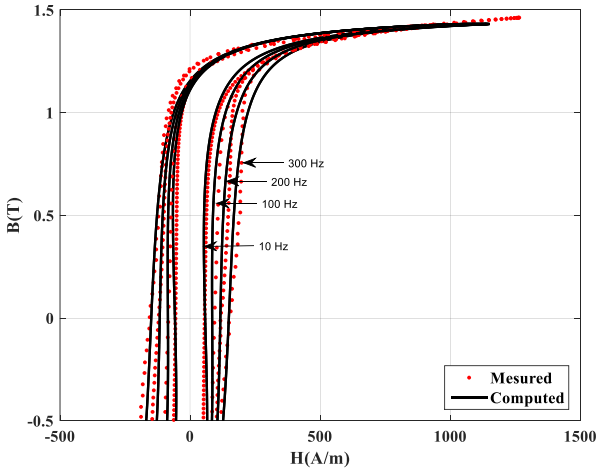


Figure 2. Computed and measured loops at different frequencies.

Figure 4 shows the energy losses modeled and measured for various frequencies, it is clear that the results of the calculated energy losses using equation (8) compared to the experiment. The accurate assessment of the magnetic field, as depicted in Figure 3, significantly contributes to the determination of energy losses in both quasi-static and dynamic regimes.

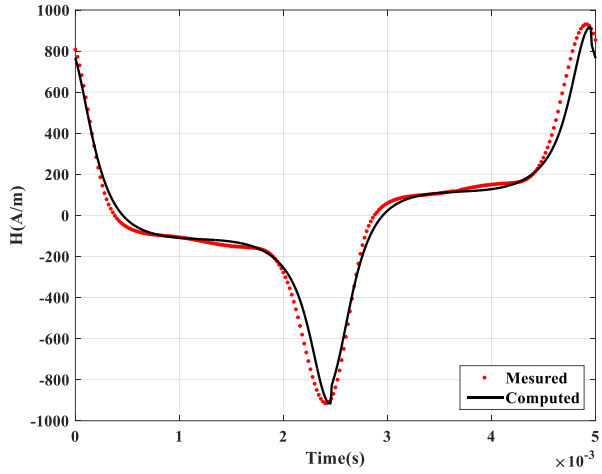


Figure 3. Computed and measured magnetic field at 200 Hz

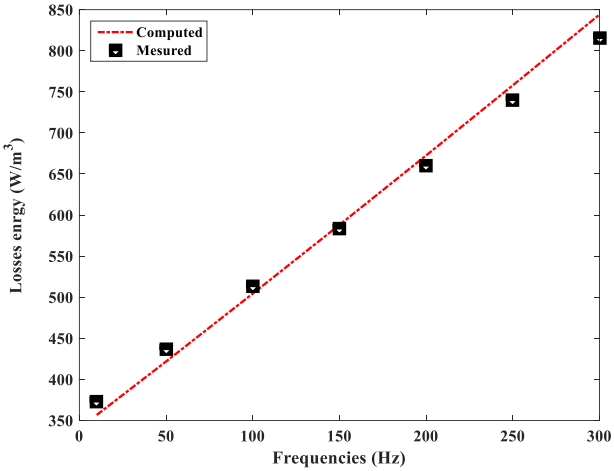


Figure 4. Comparison of the computed losses energy with measured

V. CONCLUSION

By incorporating a new formulation based on the dynamic loss surface model, the expression of the excess field is refined, leading to precise assessments of the energy losses and accurate representations of the shapes of the hysteresis loops. The computed and measured loops at different frequencies demonstrate the agreement between the calculated energy losses using equation (8) and the experimental results. The precise assessment of the magnetic field significantly contributes to the determination of energy losses in both quasi-static and dynamic regimes, particularly when compared to experimental measurements at low and medium frequencies of 300 Hz. The central approach in this study is based on the dynamic variation of the excess field, which is closely linked to the characteristics of the loss surface. In particular, the results highlight the remarkable effectiveness of the Jiles Atherton

model in describing dynamic phenomena. Two new parameters are introduced into the dynamic equation, one linked to the eddy current field and the other depending on the excess field. This innovative proposal enables the acquisition of hysteresis loop shapes that closely resemble the observed data.

REFERENCES

[1] P. Steinmetz Chas, "On the law of hysteresis," IEEE Proceeding, vol. 72, pp.197 –221, 1984.

[2] J. W. Macki, P. Nistri, and P. Zecca, "Mathematical models for hysteresis". SIAM review, vol. 35 no, 1, pp, 94-123, 1993.

[3] I. D. Mayergoyz, Mathematical models of hysteresis and their applications. Academic press. 2003.

[4] J. Tellinen, "A simple scalar model for magnetic hysteresis," IEEE Transactions on Magnetics, vol. 34, no 4, pp. 2200-2206. 1998.

[5] D. Makaveev, L, Dupre, M, DE wulf, *et al*, "Dynamic hysteresis modeling using feed-forward neural networks," Journal of magnetism and magnetic materials, vol. 254, pp. 256-258, 2003.

[6] H. Hauser, " Energetic model of ferromagnetic hysteresis". Journal of Applied Physics, vol.75, no. 5, pp. 2584-2597, 1994.

[7] M. Hamimid, S. M. Mimoune, and M. Feliachi, "Dynamic formulation for energetic model compared with hybrid magnetic formulation of ferromagnetic hysteresis". International Journal of Numerical Modelling: Electronic Networks, Devices and Fields, vol. 30 no.6, pp. e2225, 2017.

[8] A. Hammouche, M. Hamimid, A. Kansab, and B. Belmadani, "Integration of Energetic Model for Ferromagnetic Hysteresis in Finite Volume Method for Electromagnetic Field Calculation". Instrumentation Mesures Métrologies, vol. 20 no.1, 2021.

[9] M. Hamimid, S. M. Mimoune, and M. Feliachi, "Hybrid magnetic field formulation based on the losses separation method for modified dynamic inverse Jiles–Atherton model". Physica B: Condensed Matter, vol. 406 no.14, pp. 2755-2757. 2011.

[10] D. C. Jiles, "Modelling the effects of eddy current losses on frequency dependent hysteresis in electrically conducting media," IEEE Transactions on Magnetics, vol. 30,no. 6, pp.4326-4328, 1994.

[11] I. Belgasmi, and M. Hamimid, "Accurate Hysteresis Loops Calculation Under the Frequency Effect Using the Inverse Jiles-Atherton Model," Advanced Electromagnetics, vol. 9, no.2, pp. 93-98, 2020.

[12] A. P . S. Baghel, S. K. Shekhawat, S.V. Kulkarni, I. Samajdar, "Modeling of dynamic hysteresis for grain-oriented laminations using a viscosity-based modified dynamic Jiles–Atherton model," Physica B: Condensed Matter, vol.448, pp. 349-353, 2014.

[13] T. Chevalier, A. Kedous-Lebouc, B. Cornut, and C. Cester, "A new dynamic hysteresis model for electrical steel sheet," Physica B: Condensed Matter, vol.275 no.1-3, pp. 197-201. 2000.

[14] M. Hamimid, M. Feliachi, and S. M. Mimoune, "Modified Jiles–Atherton model and parameters identification using false position method". Physica B: Condensed Matter, vol.405, no.8, pp.1947-1950, 2010.

[15] O. Messal, F. Dubas, A. Kedous-Lebouc, C. Chillet, , and C. Espanet. "Pertes magnétiques des systèmes électromagnétiques: Circuit magnétique équivalent & modèle ls, " In Symposium de Genie Electrique, 2016.

[16] T. Gautreau, "Estimation des pertes fer dans les machines électriques: modèles d'hysteresis Loss Surface et application aux machines synchrones à aimants, " Doctoral dissertation, Grenoble INPG, 2005.

[17] N. Sadowski, N.J. Batistela, J.P.A. Bastos, M. Lajoie-Mazenc, "An inverse Jiles-Atherton model to take into account hysteresis in time-stepping finite-element calculations," IEEE Transactions on Magnetics, vol.38, no. 2, pp. 797-800, 2002

[18] D.C. Jiles, "Modelling the effects of eddy current losses on frequency dependent hysteresis in electrically conducting media," IEEE Transactions on Magnetics, vol.30, no. 6, pp. 4326-4328, 1994

Semi-analytical model of an electromagnetic energy harvester

Badea idir [1] , Bachir maouche [2], Sakina zerguini [3]

[1] *Electrical engineering laboratory, Faculty of Technology, university of Bejaia 06000, Algeria*
Badea.idir@univ-bejaia.dz

[2] *Electrical engineering laboratory, Faculty of Technology, university of Bejaia 06000, Algeria*
Bachir.maouche@univ-bejaia.dz

[3] *Electrical engineering laboratory, Faculty of Technology, university of Bejaia 06000, Algeria*
Sakina.zerguini@univ-bejaia.dz

***Abstract*— This contribution presents an electromagnetic energy harvester based on a multi-pole magnet to harvest energy from ambient vibrations. The harvester consists of a cylindrical housing, a copper coil, and NdFeB (N35) permanent magnets. The physical modeling of the EMEH has been demonstrated through a series of mathematical equations in which we develop a direct semi-analytical model of a voltage-induced system. The formulation is based upon the use of coupled electric circuits, in which the Crank-Nicholson formula is used to derive the transient behavior. The model is implemented and simulated using MATLB environment, and finally, the results are discussed.**

***Keywords:* electromagnetic energy harvester, multi-pole magnet, semi-analytical, coupled circuits.**

I. INTRODUCTION

Nowadays self-powering of wearable electronic devices attracts the attention of many researchers. The huge demand for such devices has contributed to their rapid proliferation but posed a great challenge for long-lasting power supply. The problem of sustainable supply can be solved by using the approach of ambient energy harvesting.

Among different ambient sources, solar cells offer excellent power density in direct sunlight but produce very low power in dim ambient light. Significant amount of electrical power is possible to harvest from wind and ocean energy[1,2]. Still the conversion procedure is very complex and cumbersome.

Nevertheless, vibration as an energy source is very small in scale, low in cost, independent on weather conditions, suitable for inside remote sensing and human wearable devices there are different vibration-based energy harvesters incorporating electromagnetic, piezoelectric and electrostatic.

But the vibration frequencies available in the environment And human body are usually very low (below 10 Hz). Electromagnetic harvesters are suitable in these cases considering their simple structure, portability and low resonance frequency. In this paper, an electromagnetic vibration energy harvester is presented; it consists of a multi-pole magnet moving through a coil.

II. SYSTEM DESCRIPTION

A. harvester design

Fig.1 shows a schematic diagram of the proposed harvester. It's structure consists of a cylindrical housing, a wire-wound copper wrapped horizontally around the iner cylinder, with Nb number of turns, has a length of lb, average radius of each turn rb. and a middle active mass which is a ring type NdFeB magnet of N-35 grades ,of Length la, radius ra, which is aligned along the Y-axis,. When an external mechanical vibration is applied to the structure, the middle magnet start to oscillate, so an AC voltage will be induced in the coil. The harvester works as a transducer that converts the mechanical motion to desired electrical energy. According to Faraday's law of induction [5], as the magnet is In motion and the conductor (coil) is at rest or vice versa, an electric field arises in the neighborhood of the magnet, producing a current.

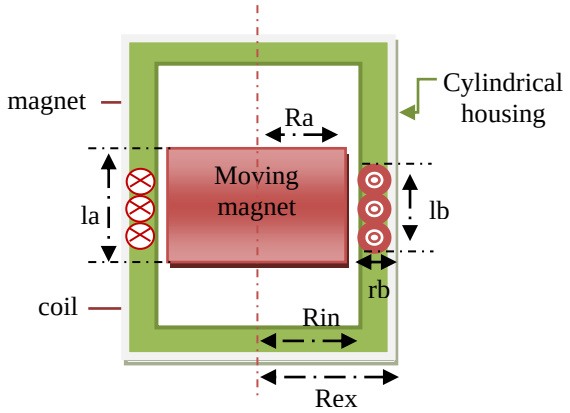


Figure 1. Harvester schematic diagram

B. Electromagnetic background

The system is considering as an axisymmetric configuration, the magnetic vector potential and the electric current density are reduced to their angular components as shown in Fig. 2.

To describe the phenomena that govern the system, the general Maxwell model is reduced to two coupled equations given as follows:

$$\begin{cases} \mathrm{div}\left(\vec{\mathrm{grad}}\,\mathrm{A(p)}\right) = -\mu_0\,\mathrm{J} & \text{(a)} \\ \vec{\mathrm{J}} = -\sigma\left(\dfrac{\mathrm{dA}}{\mathrm{dt}} + \vec{\mathrm{grad}}\,\mathrm{V}\right) & \text{(b)} \end{cases} \quad (1)$$

Where A[T.m] is the magnetic vector potential, J[A/m^2] the conduction current density, V[V] the electric scalar potential,σ[Ω.m]$^{-1}$ the electric conductivity, and μ_0 the magnetic permeability[H/m],[3,4].

Equation (1a) specifies the relationship between the magnetic vector potential A and its source (current density J), (1b) expresses the induction phenomenon.

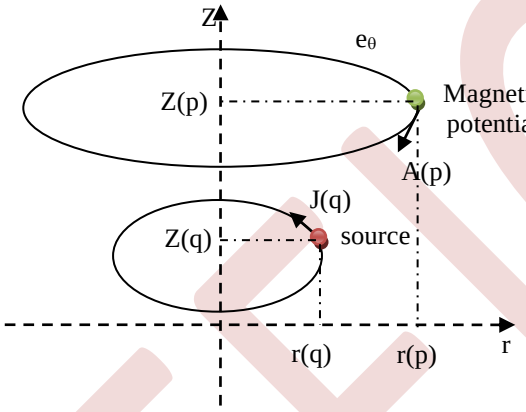


Figure 2. Axisymetrical representation

The solution of (1a) in the vacuum corresponds with the Biot and Savart formula, the development of this formula along the contour of the loop q relatively to the point p, Fig. 2 leads to (2a) and (3) according to elliptic integrals [6].

The spatial variation of the electric scalar potential is expressed in terms of the applied or induced voltage u(p) at the terminals of the turn as shown in (2b):

$$\begin{cases} \mathrm{A(p)} = \dfrac{\mu_0}{2\pi}\mathrm{G(p,q)I(q)} & \text{(a)} \\ \vec{\mathrm{grad}}\,\mathrm{V}\cdot\vec{\mathrm{e}}_\theta = -\dfrac{\mathrm{u(p)}}{2\pi\mathrm{r(p)}} & \text{(b)} \end{cases} \quad (2)$$

Where G(p,q) represents the response of the system at point p(r,z) to Dirac's distribution located at point q and called Green's function. E_1 and E_2 are elliptic Legendre functions of first and second kind, r(p) and r(q) are the respective radial co-ordinates of the transmitter and receiver points(p,q). z(p) and z(q) are their respective heights, with respect to Fig. 2.

G(p,q) is given as follows:

$$\begin{cases} \mathrm{G(p,q)} = \sqrt{\dfrac{\mathrm{r(q)}}{\mathrm{r(p)}}}\mathrm{E}\left[\mathrm{k(p,q)}\right] & \text{(a)} \\ \mathrm{E}\left[\mathrm{k(p,q)}\right] = \dfrac{\left(2-\mathrm{k}^2\right)\mathrm{E}_1(\mathrm{k}) - 2\,\mathrm{E}_2(\mathrm{k})}{\mathrm{k}} & \text{(b)} \\ \mathrm{k(p,q)} = \sqrt{\dfrac{4\mathrm{r(p)r(q)}}{\left[\mathrm{r(p)}+\mathrm{r(q)}\right]^2 + \left[\mathrm{z(p)}-\mathrm{z(q)}\right]^2}} & \text{(c)} \end{cases} \quad (3)$$

Replacing (2a) of the magnetic vector potential as well as that of the scalar potential (2b) in (1b), we manage to express the generalized electromagnetic equation according to the currents and the voltage of the various points (p,q) taking into account the relationship between current density and its intensity ($\mathrm{J} = \mathrm{I}/\mathrm{s}$).

$$\frac{2\pi\,\mathrm{r(p)}}{\mathrm{s}\sigma}\mathrm{I(p)} + \mu_0\mathrm{r(p)}\frac{\mathrm{d}}{\mathrm{dt}}\left\{\mathrm{G(p,q)I(q)}\right\} = \mathrm{u(p)} \quad (4)$$

Deriving the equation above, we come to the following expression:

$$\frac{2\pi\,\mathrm{r(p)}}{\mathrm{s}\sigma}\mathrm{I(p)} + \mu_0\mathrm{r(p)}\mathrm{G(p,q)}\frac{\mathrm{dI(q)}}{\mathrm{dt}} + \mu_0\mathrm{r(p)}\mathrm{I(q)}\frac{\mathrm{dG(p,q)}}{\mathrm{dt}} = \mathrm{u(p)} \quad (5)$$

We're only interested in the radial component, which is associated with axial velocity, assuming that:

$$\begin{cases} \dfrac{\mathrm{dG(p,q)}}{\mathrm{dt}} = \mathrm{v_z}\,\mathrm{G^{Br}(p,q)} & \text{(a)} \\ \mathrm{v_z} = \dfrac{\mathrm{dz}}{\mathrm{dt}} & \text{(b)} \\ \mathrm{G^{Br}(p,q)} = \dfrac{\mathrm{dG(p,q)}}{\mathrm{dz}} & \text{(c)} \end{cases} \quad (6)$$

G^{Br} is expressed in terms of z as follows:

$$\mathrm{G^{Br}(p,q)} = \frac{\mathrm{z(p)}-\mathrm{z(q)}}{\mathrm{r(p)}\sqrt{\mathrm{r(p)r(q)}}}\left[\frac{2-\mathrm{k}^2}{1-\mathrm{k}^2}\mathrm{E}_2(\mathrm{k}) - 2\mathrm{E}_1(\mathrm{k})\right]\mathrm{k} \quad (7)$$

Equation (5) is rewritten as:

$$\frac{2\pi\, r(p)}{s\sigma} I(p) + \mu_0 r(p) G(p,q) \frac{dI(q)}{dt} + \mu_0 r(p) I(q) G^{Br}(p,q) = u(p) \quad (8)$$

III. SEMI-ANALITYCAL MODEL

In the harvester the magnet creates a permanent magnetic field. In motion the magnet is represented by the Amperian model with Na number of turns and equivalent current given by:

$$I_a = \frac{B_r h}{\mu_0} \quad (9)$$

Where Br is the residual magnetic flux, and h the length of the magnet.

A. Spatial discretization

The geometry of the system is divided into circular elements. The magnet is divided into Na number of turns and the coil into N_b number of turns with equal elementary section (S_b).

The geometrical discretization of (8) shows:

$$\frac{2\pi r_b(p)}{s_b \sigma_b} I_b(p) + 2\pi r_b(p) \frac{d}{dt}\left(\frac{\mu_0}{2\pi} \sum_{q=1}^{Nb} G_{bb}(p,q) I_b(q) \right) + 2\pi r_b(p) v_z \frac{\mu_0}{8\pi} \sum_{q=1}^{Na} G_{ab}^{Br}(p,q) I_a(q) = -u_b(p) \quad (10)$$

Given that the coil turns are in series,the voltage induced across the coil is the sum of all the elementary voltages u(p) and the current is the same in each elementary coil, the equation above becomes:

$$\left(\sum_{p=1}^{Nb} \frac{2\pi r_b(p)}{s_b \sigma_b} \right) I_b + \left(\mu_0 \sum_{p=1}^{Nb} r_b(p) \sum_{q=1}^{Nb} G_{bb}(p,q) \right) \frac{dI_b}{dt} + \frac{\mu_0 I_a}{4} v_z(t) \sum_{p=1}^{Nb} r_b(p) \sum_{q=1}^{Na} G_{ab}^{Br}(p,q) = -U_b \quad (11)$$

σ_b and r_b are respectively electric conductivity and coil radius, v_z is the magnet velocity, where u_b is the induced output voltage.

The equation system above is assimilated to an RL electric circuit with resistance and self-inductance such that:

$$L \frac{dI_b(t)}{dt} + R I_b(t) + U_b(t) = V_{em}(t) \quad (12)$$

Identifying the two equations (11) and (12), we obtain:

$$\begin{cases} R = \sum_{p=1}^{Nb} \frac{2\pi r_b(p)}{s_b \sigma_b} \\ L = \sum_{p=1}^{Nb} 2\pi\, r_b(p) \frac{\mu_0}{2\pi} \sum_{q=1}^{Nb} G_{bb}(p,q) \\ V_{em}(z,t) = \frac{\mu_0 I_a}{4} v_z(t) \sum_{p=1}^{Nb} r_b(p) \sum_{q=1}^{Na} G_{ab}^{Br}(t,p,q) \end{cases} \quad (13)$$

R and L are the resistance and inductance of the coil, where V_{em} is the electromotive force recovered.

The model thus defined in (12) is valid for any type of electric charge. In this proposal, we limit ourselves to a resistive load Rex ($U_b = R_{ext} I_b$) such that (12) is rewritten as follows:

$$\frac{dI_b(t)}{dt} + \frac{1}{\tau} I_b(t) = \frac{1}{L} V_{em}(t) \quad (14)$$

Whereτ is the circuit time constant given by : $\tau = \frac{R_{ext} + R}{L}$

B. Temporal discretization

The temporal discretization of (14) at the middle point using the Crank Nicholson formula [7] provides:

$$\left.\frac{\partial I_b}{\partial t}\right|_t + \left.\frac{\partial I_b}{\partial t}\right|_{t-\Delta t} = \frac{I_b(t) - I_b(t-\Delta t)}{2\Delta t} \quad (15)$$

So that the discretization of induced current I_b is given as:

$$I_b(t) = \frac{\Delta t \tau_e}{(2\tau_e + \Delta t) L} \left[V_{em}(t - \Delta t) + V_{em}(t) \right] - \left(\frac{2\tau_e - \Delta t}{2\tau_e + \Delta t} \right) I_b(t - \Delta t) \quad (16)$$

IV. SIMULATION AND RESULTS

For the various parameters shown in the table below taken from an article given as a reference1, we simulate the geometry of the system as well as the voltage and current recovered at the movement, for several number of magnets without ,or ,with spacer between them.

TABLE I. SIMULATED PARAMETERS

Parameter	**Value/material**
Number of magnet	1-2-3-4-5
Magnet material	NdFeB (N35)
Residual flux density	0.37T
Moving magnet size(mm^2)	10*30
Magnetic permeability(H/m)	$4\pi 10^{-7}$
Frequence(Hz)	6
Coil material	Copper
Electric Conductivity(Ω/m)	$59.6\ 10^6$
Coil size	4*5
Spacing between coil and moving magnet (mm)	1
Spacer between magnets(mm)	5

A. *Geometrical model*

The figure below shows the geometry of the system with two opposites fixed magnets, and Nb number of coil turns

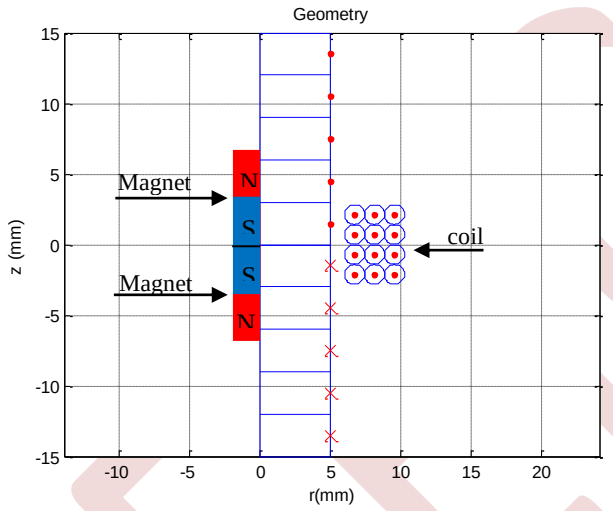


Figure 3. Geometrical structure of the system with two opposites fixed magnets.

After having visualized the geometry of the system, we move on to the simulation of the movement.

The magnet moves sinusoidally through the coil. The figure below shows the initial (maximum) and final (minimum) positions of the magnet, the displacement z(t),velocity v(t) and the acceleration a(t) are also visualized as it shows in Fig. 2.

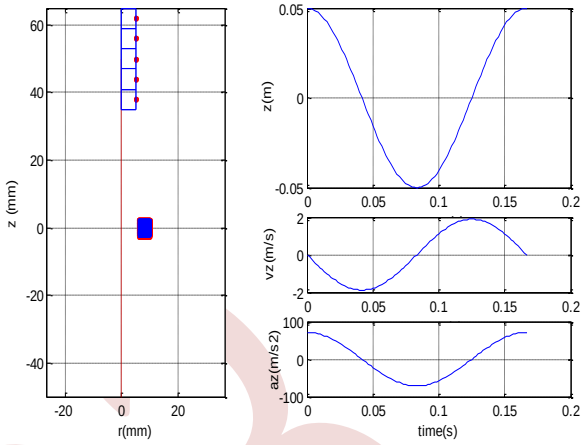


Figure 4. Simulated moving magnet through coil

B. *Simulation and validation*

➢ Induced voltage without spacer

The figure below shows the induced voltage for 1,3,4 number of magnets in opposite directions with no space between them.

The distance between north and south poles gradually reduces. As a result, the flux line areas become squeezed. Therefore, for Nb number of coil turns, some of the coil part receives very weak flux force consequently; the output of the energy harvester reduces very rapidly above a certain number of magnets. In this case, the average value increases from 0.6V for one magnet to 1.11V for three magnets. Above three magnets, the average value decreases that are similarly results obtain in [1].

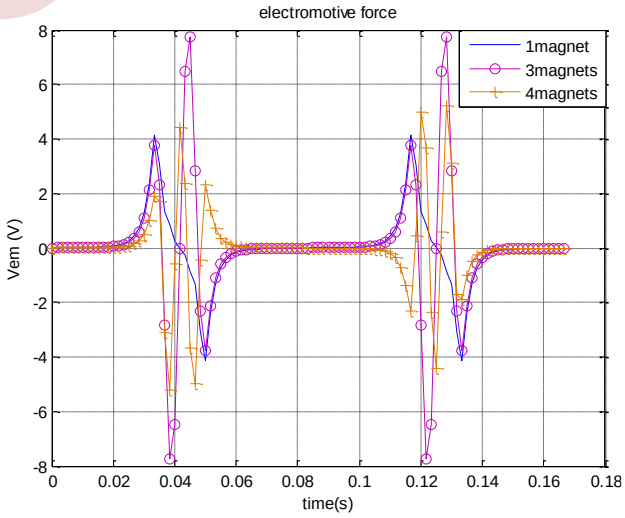


Figure 5. Simulated induced voltage 1,3,4 magnets without spacer

➢ Induced voltage with spacer

Fig. 6 shows the induced voltage for a 1,4,5 number of magnets in opposite directions with space between them.

In this case, the average value increases from 0.6V for one magnet to 1.2V for four magnets. Above four magnets, the average value decreases. With space between magnets the induced voltage increase, comparing to induced voltage without spacer.

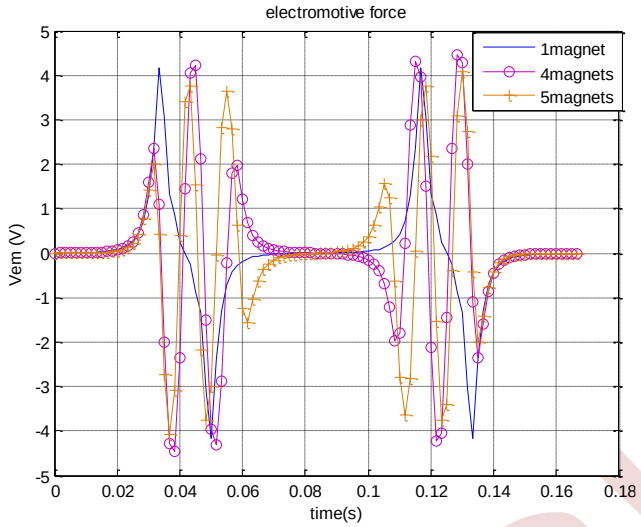


Figure 6. Simulated induced voltage 1,4,5 magnets with spacer

- Induced current without spacer

The figure below shows the induced current for 1,3,4 number of magnets in opposite directions with no space between them. In this case, the average value increases from (5.77 10^{-4}A) for one magnet to (10^{-3}A) for three magnets. Above three magnets, the average value decreases.

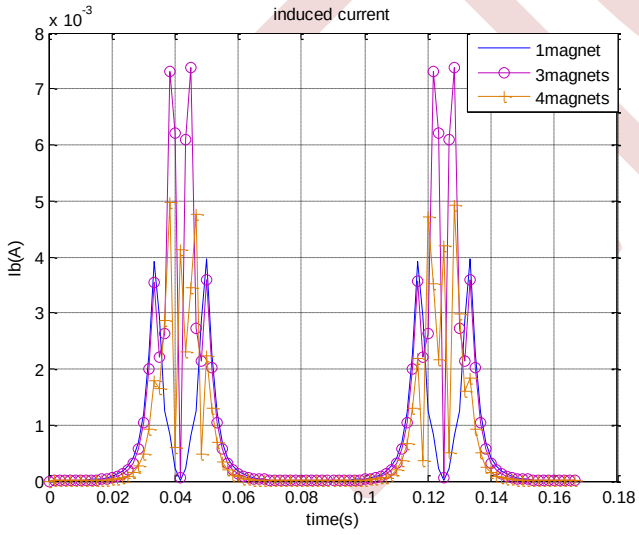


Figure 7. Simulated induced voltage,1,3,4 magnets without spacer

- Induced current with spacer

Fig.8 shows the induced current for a 1,4,5 number of magnets in opposite directions with no space between them.

In this case, the average value increases from (5.77 10^{-4}A) for one magnet to (9.7 10^{-4}) for four magnets. Above that, the average value decreases.

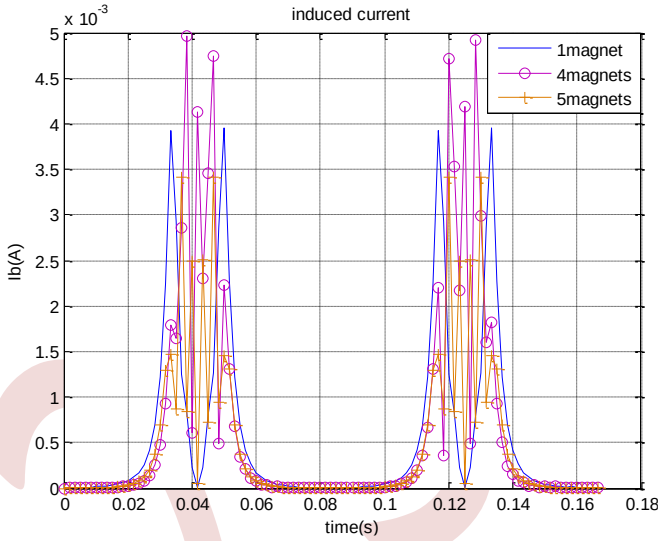


Figure 8. Simulated induced current,1,4,5 magnets with spacer

V. CONCLUSION

This Study illustrates that the outputs (voltage, current) of a multi-pole energy harvester could be augmented by dividing the moving mass (magnet) into more parts rather than using only one part, also using a gap (spacer) between the magnets increases the harvesting values.

However, beyond a certain number of magnet division the effect is reversed, the values decrease, this is why we must suggest optimization method.

REFERENCES

[1] A. Munaz, B. C. Lee, and G. S. Shung, "A study of an electromagnetic energy harvester using multi-pole magnet,", Korea, Sensors and Actuators A 201,pp.134– 140, 2013 .

[2] A. Haroun, I. Yamada, and S. Wariswa, "Study of electromagnetic vibration energy harvesting with free/impact motion for low frequency operation,", Tokyou,pp.389– 402, 2015 .

[3] B. Maouche, R. Alkama,and M. Feliachi, "Semi-analytical calculation of the impedance of a differential sensor for eddy current non-destructive testing,",Algeria, pp.573–580, 2009.

[4] B. Maouche, M. Feliachi, N. Khenfer, "A half-analytical formulation for the impedance variation in axisymmetrical modelling of eddy current non destructive testing", Eur Phys J Appl Phy,vol33,pp.59-67, 2006.

[5] A. R. Foisa, C. Hang,and G. C. Bean, "Multi-frequency electromagnetic energy harvester using a magnetic spring cantilever," Korea, Sensors and Actuators A 182,pp.106– 113, 2012.

[6] S. Zerguini, B. Maouche, M. Latreche,and M. Feliachi, "A coupled fictitious electric circuit's method for impedance of a sensor with ferromagnetic core calculation. Application to eddy currents non destructive testing," Phys. J. Appl.Phys.bejaia, 2009.

[7] K. M.khadalbajoo, A. Awasthi, "A numerical method based on Crank-Nicolson scheme for Burgers' equation,", India,Applied Mathematics and Computation 182, pp.1430–1442, 2006.

Simulation of a non-destructive testing process equipped with a ferromagnetic core probe

Sakina Zerguini, Ahmed Kasdi, Bachir Maouche
Laboratoire de Génie Electrique de Bejaia, Faculté de Technologie, Université de Bejaia, Bejaia 06000, Algeria
sakina.zerguini@univ-bejaia.dz
ahmed.kasdi@univ-bejaia.dz
bachir.maouche@univ-bejaia.dz

***Abstract*— In different industrial sectors, the need for controlling complex structures while improving economic efficiency results in designing innovating, adequate advanced probes. In this paper, we present a simulation of a dual-function sensor using the method of eddy current non – destructive testing (NDT- EC). We also developed a model which predicts the apparent changes in the impedance of an absolute ferrite-cored probe in axially symmetric configurations. The developed model is not only applied to calculation of probe's impedance in the presence of a defect inside the load but it is also applied to determine geometrical and physical characteristics of eddy current non-destructive testing (ECNDT) device. The model is implemented within a software tool developed in COMSOL environment.**

Key words: Non Destructive Testing, Evaluation, Eddy Currents, absolute Sensor, ferromagnetic core, electromagnetic Impedance.

I. INTRODUCTION

The eddy current phenomenon is widely used in the field of non-destructive testing of conductive materials. In this work, the sensor is a solenoid inductor having a ferrite core. This type of probe is useful when the creation of an important locally uniform magnetic field is required for piece evaluation.

In fact, a coil carrying an alternating current generates currents themselves creating a magnetic flux which opposes the generating flux modifying the magnetic field of the system. Consequently, it is the study of the variation of the impedance or the variation of the voltage induced at the terminals of the coil which will provide the necessary elements of control because the path, distribution and intensity of the currents eddy do not only depend on the excitation conditions (electrical and geometric parameters of the winding), but also on the physical and geometric characteristics of the target. We can therefore see that a fault, constituting an electrical discontinuity disrupting the circulation of eddy currents, could cause a variation in impedance at the level of the excitation coil.

The model presented in this article is based on Maxwell's equations and the transition relations between media by choosing the vector potential formulation. The resolution of the equations obtained is carried out by the finite element method developed by the COMSOL multi physics software.

II. SYSTEM DESCRIPTION

We present in figure 1, an axially symmetrical geometric configuration of an axially symmetric electromagnetic system including a source of domain Ω_s which delivers a sinusoidal tension, a ferrite core Ω_m, and a massive piece of domains Ω_c

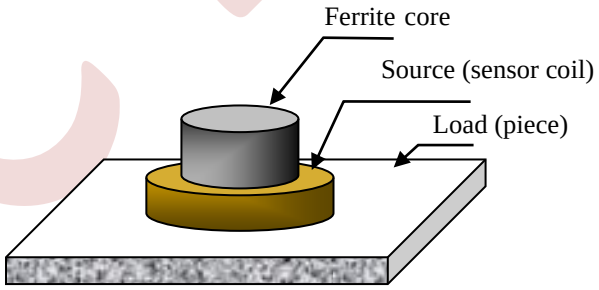


Figure 1. Ferrite core probe – piece configuration–

A. Electromagnetic background

To describe the phenomena that govern the system, the general Maxwell model is reduced to two coupled equations given as follows:

$$\begin{cases} \vec{\nabla} \wedge \left(\frac{1}{\mu}\left(\vec{\nabla} \wedge \vec{A}\right)\right) + \sigma \frac{\partial \vec{A}}{\partial t} + \sigma \vec{\nabla} V = J_s \\ \vec{\nabla}.\vec{A} = 0 \end{cases} \quad (1)$$

Where A[T.m] is the magnetic vector potential, J_s[A/m^2] the conduction current density, V[V] the electric scalar potential, σ[Ω.m]$^{-1}$ the electric conductivity, and μ_0 the magnetic permeability[H/m],[1, 2]

In the case of a sinusoidal excitation, by using the complexes, we can replace $\frac{\partial}{\partial t}$ by $j\omega$:

$$\begin{cases} \vec{\nabla} \wedge (\frac{1}{\mu}(\vec{\nabla} \wedge \vec{A})) + \sigma j\omega \vec{A} + \sigma \vec{\nabla} V = J_s \\ \vec{\nabla}.\vec{A} = 0 \end{cases} \quad (2)$$

The sensor impedance Z is determined from the vector potential A, obtained by the resolution of the equation system (2) [3].

$$Z = \frac{i\,\omega N^2}{I_s} \int \vec{A} d\vec{l} \quad (3)$$

Where N: number of turns of the sensor coil.

III. SIMULATION AND RESULTS

The sensor is an exciting coil of internal radius of 1 mm, of radial thickness of 0.75 mm, an axial length of 2 mm. The ferrite core has a radial thickness of 0.9 mm, an axial length of 3 mm and relative permeability of 100. The sensor and ferrite core are normal to the plate and has a thickness of 1.55 mm, conductivity of 1 MS/m and a relative permeability of 1. It is supposed to have an infinite length (Fig. 2, 3) [4, 5].

The distribution of the induction currents can be approached by circular turns, the revolution axis of which is that of the sensor.

In the present work, the system of equations (2) is implemented in Comsol Multiphysics, which solves the problem using the finite element method.

The boundary conditions applied in the simulation are those of Dirichlet. We calculate the variations of impedance due to the presence of conductive plate (Fig. 2), then to the presence of holes in this plate (Fig 3). The case study is axisymmetric.

We show in Fig. 4 the simulation results by tracing the magnetic flux density in the presence of a defect in the piece.

Table 1 show the variation of resistance and reactance as function of frequency results, stemming from the proposed model in presence of ferrite core due to the presence of circular defect in the piece. We considered the defect on the superior face of 50% of depth and 1.5 mm of diameter (Fig. 3).

The model may be used to determine the geometrical and physical proprieties of work piece. In this context, we give the evolution of variation of the resistance and the reactance according to the thickness of the plate as well as the curve of Lissajous giving the reactance according to the corresponding resistance (Figs. 5-7) for the three frequencies of inspection.

In the same way, figures (8-10) collect the evolution of variation of the resistance and the reactance according to gap (lift-off) between sensor and plate as well as the curve of Lissajous giving the reactance according to the corresponding resistance.

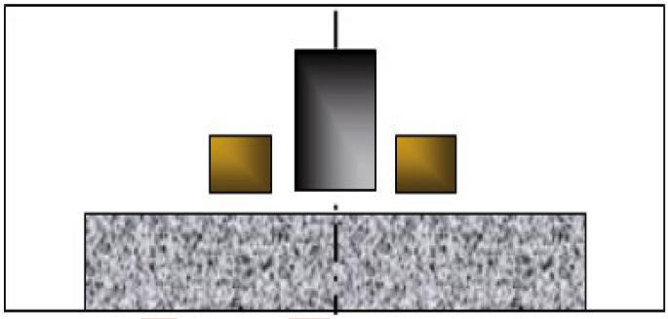


Figure 2. Piece without defect.

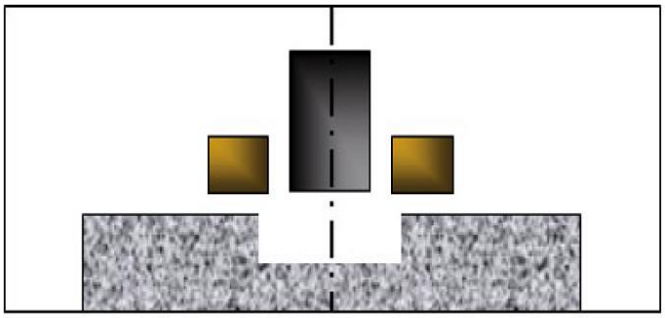


Figure 3. Piece with defect.

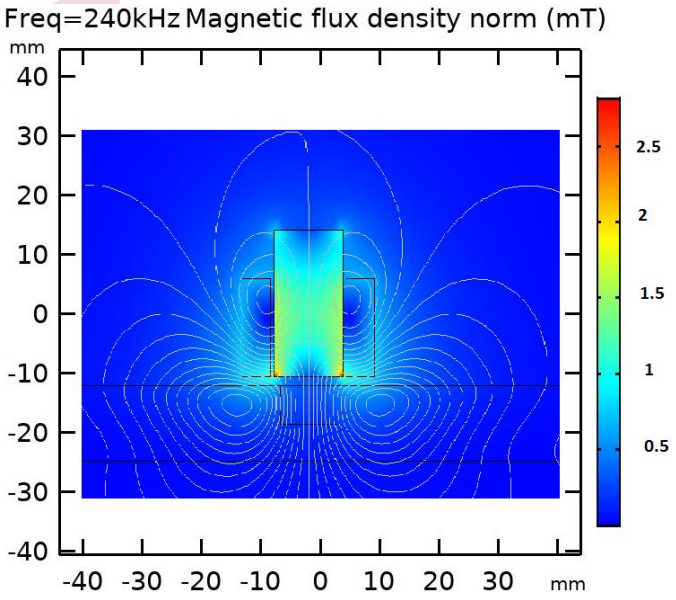


Figure 4. Magnetic Flux Density in the presence of the defect (*f*=240kHz)

TABLE I. VARIATION OF SENSOR RESISTANCE AND REACTANCE AS FUNCTION OF FREQUENCY

Freq (kHz)	ΔR_{10} (Ω)	ΔX_{10} (Ω)
100	9,735	-13,794
240	20,315	-47,05
500	35,818	-116,34

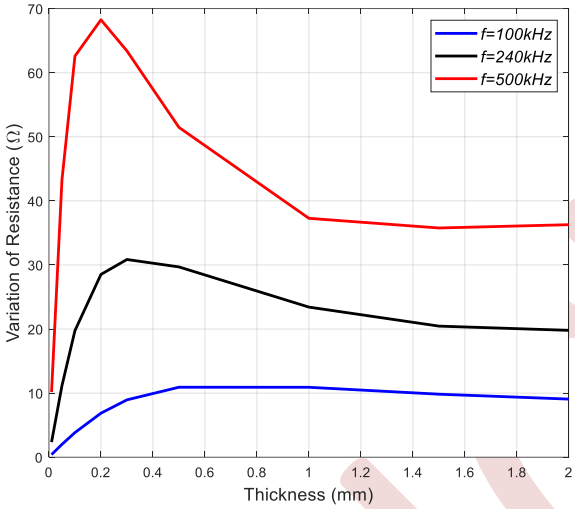


Figure 5. Variation of Sensor Resistance according to the thickness of the plate.

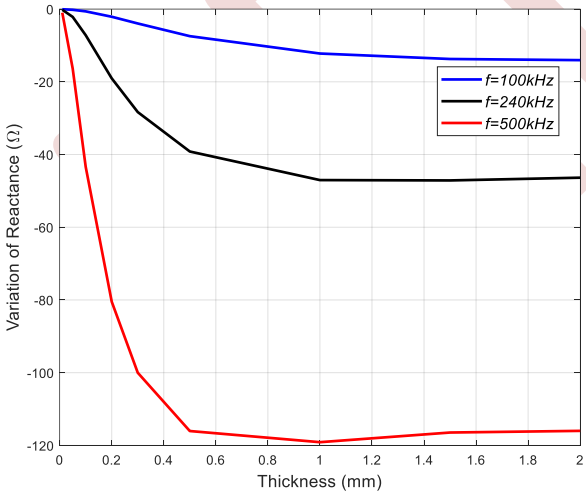


Figure 6. Variation of Sensor Reactance according to the thickness of the plate.

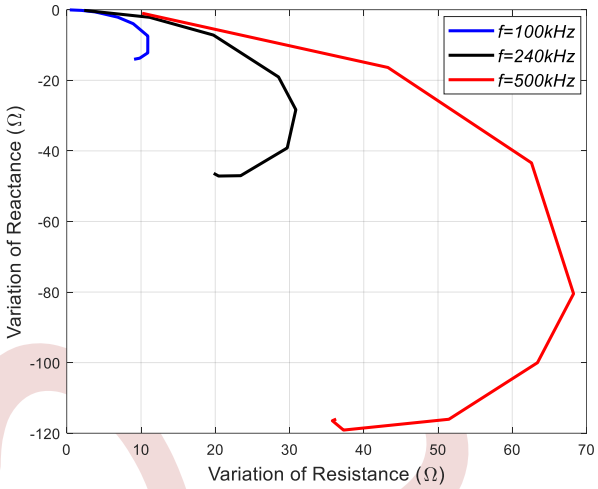


Figure 7. Variation of Sensor Reactance according to the Sensor Resistance.

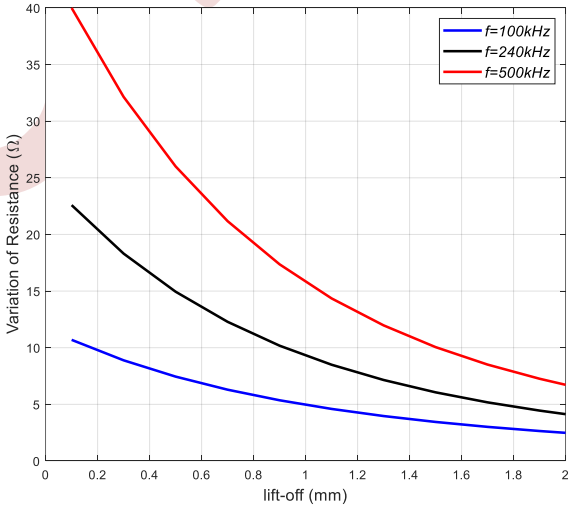


Figure 8. Variation of Sensor Resistance according to a variable lift-off

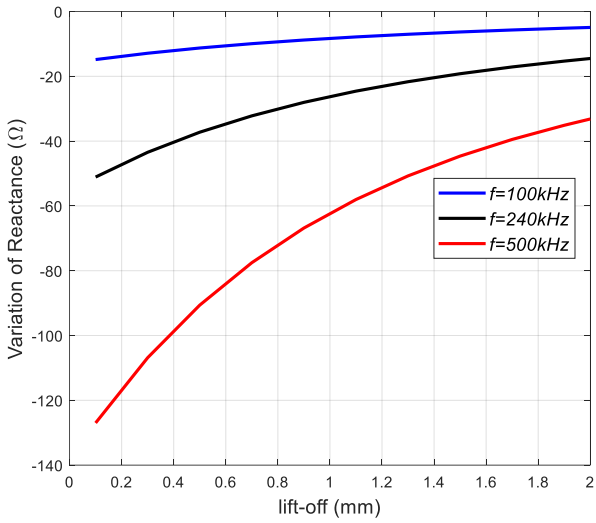


Figure 9. Variation of Sensor Reactance according to a variable lift-off

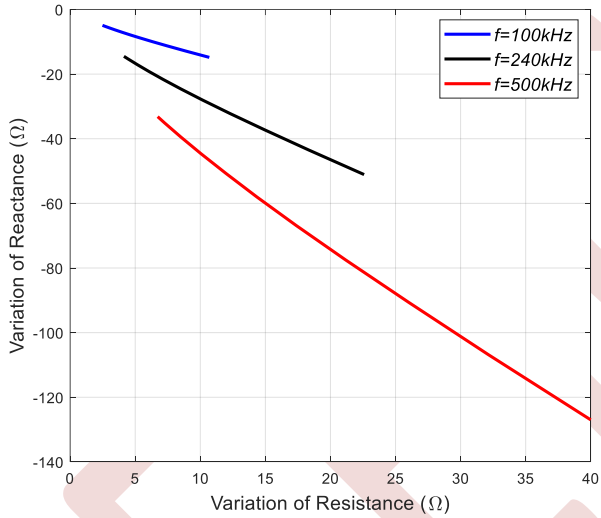


Figure 10. Variation of Sensor Reactance according to the Sensor Resistance.

IV. CONCLUSION

This article is dedicated to the development of a model explaining the geometric and electromagnetic characteristics of non-destructive eddy current testing devices.

Indeed, we present a model allowing the calculation of the impedance of a dual-function absolute sensor with ferromagnetic core in the presence of healthy non-magnetic parts or with defects. The electromagnetic problem was formulated by choosing the electromagnetic vector potential as the state variable while taking into account the properties characterizing the materials. This model is based on the finite element method for resolution developed by COMSOL Multi Physics, which leads to direct identification of the piece to be controlled.

REFERENCES

[1] B. Maouche, R. Alkama et N. Khenfer "Modélisation Semi-Analytique du Contrôle Non Destructif par Courants de Foucault à capteur Absolu", 3rd conference on Electrical Engineering, octobre 2004, pp. 149-152.

[2] B. Maouche, M. Feliachi, N. Khenfer,″A half-analytical formulation for the impedance variation in axisymmertical modeling of eddy current non destructive testing″, Eur. Phys. J. Appl. Pys. 33 (2006), pp. 59-67.

[3] Y. Bihan, "Lift-off and tilt effects on eddy current sensor measurements: a 3-D finite element study." The European Physical Journal-Applied Physics 17.1 (2002), pp. 25-28.

[4] B. Maouche,R. Alkama, and M. Feliachi, "Semi-analytical calculation of the impedance of a differential sensor for eddy current non-destructive testing,", Algeria, (2009), pp.573–580.

[5] S. Zerguini, B. Maouche, M. Latreche & M. Feliachi. "A coupled fictitious electric circuit's method for impedance of a sensor with ferromagnetic core calculation. Application to eddy currents non destructive testing''. The European Physical Journal-Applied Physics, 48(3) (2009), 31202.

Extracting of Ultrasonic Pulse Generated by Piezoelectric Material Using Machine Learning

Amel Mechnane[1], Hichem Hafdaoui[2], Djamel Benatia[1]

[1] *Electronics Department (LEA Laboratory), Faculty of Technology, University of Batna 2, (Mostefa Benboulaid), Algeria*

[2] *Centre de Développement des Energies Renouvelables, CDER, 16340, Algiers, Algeria*

mechneneamel@gmail.com

***Abstract*— In this paper, we propose a new numerical method for ultrasonic pulse detection of an acoustics microwaves signal during the propagation of acoustics micro-waves generated by piezoelectric substrate LiNbO3 Cut Y-X in ultrasonic transducer. We have used machine learning (ML) by support vector machines (SVM), the originality of this method is it provides the accurate values and help us to identify undetectable waves that we cannot identify with the classical methods; in which we classify all the values of the real part and the imaginary part of the coefficient attenuation with the acoustic velocity in order to build a model from which we note the Ultrasonic Pulse or microwaves acoustics (bulk waves). By which we obtain accurate values for each of the coefficient attenuation and acoustic velocity. This study will be very interesting in modeling and realization of acoustics microwaves devices (ultrasound) based on the propagation of acoustics microwaves.**

Keywords: Ultrasonic; Piezoelectric material; Support Vector Machines (SVM); Classification.

I. INTRODUCTION

This this work is devoted to the modeling of acoustic microwaves in piezoelectric structures; It was at the beginning of the 1950s that all electronic components were manufactured on the basis of semiconductor elements making it possible to generate an electric current (carrying information). After the discovery of piezoelectricity, a very important property, it results in an electrical polarization of the material under the action of a mechanical stress and vice versa by a deformation of this material when if excited by an electric field. In the first case, we recognize the direct piezoelectric effect discovered by the brothers Pierre and Jacques Curie in 1880, and in the second case (the opposite effect), it is the indirect piezoelectric effect established by Gabriel Lippman based on calculations thermodynamics and confirmed by the Curie brothers. Subsequently, work was continued giving rise only to theoretical work concerning crystalline structures.

In 1910, Woldemar Voigt of the Lehrbuch der Kristallphysik [1] published an article, which gives the twenty piezoelectric crystal classes, mentioning for the first time the piezoelectric constants in the tensorial formalism. The search for more efficient materials has interested various research groups around the world for the development of ferroelectric materials, such as barium titanate, PZTs and materials with a high electro-elastic coupling coefficient such as Lithium Niobate, which are moreover today reference materials. Since the 1950s, applications with ultrasound in medicine (Radiating structures and ultrasound, Doppler Effect) or in therapy (destruction of stones by shock wave) have emerged. The piezoelectric material is a crystal that deforms when it undergoes an electric voltage. In this case, the electrical signal is converting into an elastic signal propagating with speeds identical to those of supersonic waves. The waves which propagate on the surface of the material, they are called surface waves [2, 3], they are only detectable for a single acoustic velocity. For other velocity, we can find surface waves called pseudo surface waves.

Other types of waves, called bulk waves and surface waves [4, 5], in the field of application, bulk waves are used in ultrasonic; there are several works on the detection bulk acoustic microwaves [5-7]. In our case, we propose another approach for the modelling of the acoustic microwaves with a complementary vision to the literature mentioned above. In this approach, we interested especially in the detection of ultrasonic pulse by the use of (SVM) as detection tool in order to mark the mode of a bulk waves.

In this work, we searched for all acoustic velocity and attenuation coefficients relying on fundamental relations and we classified all the values so that we can detect ultrasonic pulse easily. Figure 1 Shows Ultrasonic Pulse generated by LiNbO3 substrate.

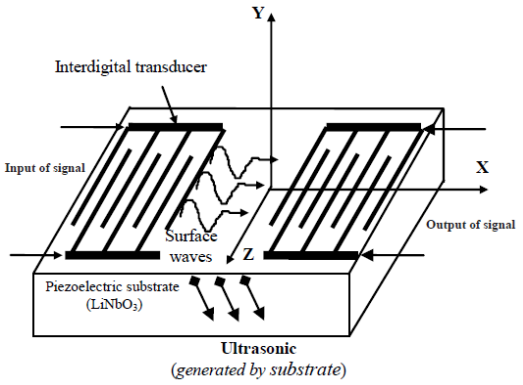


Fig 1. Ultrasonic Pulse generated by LiNbO3 substrate.

II. CONTRIBUTION

In our work, we are interested in the application of Support Vector Machine (SVM) for the detection of ultrasonic pulse. The Classification by classical neural networks presents many complications while that of Support Vector Machine (SVM) which was introduced by D. F. Specht [8] has become a reference in the field of neural classification because of their properties for classification issues. In SVMs, we find several advantages in that they do not suffer from the problem of local minima and that learning is very fast since the network is created after a single pass over the training set [8]. On the other hand, there are some disadvantages concerning the number of hidden neurons which is equal to the number of samples of the training especially in the case of a very large training set without forgetting the choice of the smoothing parameter which can affect the generalization of the network. Work has been proposed to solve the problem of generalization as well as that of the choice of parameters in probabilistic neural networks. Thus, M. Kim [9] proposed a new architecture to improve the generalization of the standard PNN. In the literature [10, 11], LVQ (Learning vector quantization) algorithms have been used for learning PNNs in order to make the network size smaller. Other variants of the PNNs are the fuzzy PNN and the stochastic optimization for the choice of the parameters of the PNN [12] only allow a partial resolution of the problem. RKPNNs methods (PNNs with rotational kernel) [13] have good generalization qualities compared to SVMs in the case of a reduced number of classes [14, 15] but learning is very slow, even for small sets of learning and the network does not support the addition of new classes of samples, in this case the whole learning process must be repeated with a new set. The learning algorithm reduces the number of hidden neurons, without affecting the network architecture; this means that adding new samples or classes is possible at any time and without redoing the learning from the beginning.

III. PHENOMENOLOGICAL TENSORIAL PIEZOELECTRIC EQUATIONS

The signal to be treated will be applied to the electrodes of the transducer that generates the distortions (compression and dilatation), so a piezoelectric wave is generated and propagated in the X direction. We consider the space coordinates as follows:

$$X=X_1,\ Y=X_2,\ Z=X_3$$

The mechanical state of the medium is defined by two magnitudes of tensorial type, the stress *Tij* and the mechanical deformation (Strain) *Sij (i, j=1, 2, 3).*

The electric state of the medium is defined by two vectors, the electric field E_k and the electric induction D_i. The stress tensor and the electric induction are defined like follows [16]:

$$T_{ij} = C_{ijkl}S_{kl} - e_{kij}E_k \quad (1)$$

$$D_i = e_{jkl}S_{kl} + \varepsilon_{ik}E_k \quad (2)$$

With *i, j, k, l= 1, 2, 3*, where

ε_{ik}: permittivity tensor (F/m)

e_{jkl}: piezoelectric tensor (c/m)

C_{ijkl}: elastic tensor (N/m^2)

The strain is bound to the relative displacements of the particles of the material environment is defined by:

$$S_{ij} = \frac{1}{2}\left(\frac{\partial U_i}{\partial X_j} + \frac{\partial U_j}{\partial X_i}\right) \quad (3)$$

where U_i represents the elastic displacement of the particle (*i=1, 2, 3*).

Note that, in the quasistatic approximation, an electric field of component can be defined by [17,18]:

$$E_i = -\frac{\partial U_4}{\partial X_i} \quad (4)$$

where U_4 is the electric potential (with *i=1, 2, 3*)

On the other hand, in the quasistatic approximation, the Maxwell's equation amounts to the Poisson's equation [18].

$$div\vec{D} = \frac{\partial D_i}{\partial X_i} \quad (5)$$

The movement of the particles under the action of stress (constraints), is described by the following differential equation (Newton's 2nd law) [19]

$$\nabla T = \rho\frac{\partial^2 Uj}{\partial t^2} \quad (6)$$

where ρ is the mass density of medium.

Replacing respectively equations (3) and (4) in equations (1) and (2), we obtain

$$T_{ij} = C_{ijkl} \cdot \frac{1}{2}\left(\frac{\partial U_j}{\partial X_k} + \frac{\partial U_k}{\partial X_j} \right) + e_{kij} \cdot \frac{\partial U_4}{\partial X_k} \quad (7)$$

$$D_{ij} = e_{ikl} \cdot \frac{1}{2}\left(\frac{\partial U_j}{\partial X_k} + \frac{\partial U_k}{\partial X_j} \right) - \varepsilon_{ik} \cdot \frac{\partial U_4}{\partial X_k} \quad (8)$$

Replacing (7) and (8) in (5) and (6), we obtain

$$C_{ijkl} \frac{\partial^2 u_k}{\partial X_i \partial X_l} + e_{lij} \frac{\partial^2 U4}{\partial X_k \partial X_i} = \rho \frac{\partial^2 U_j}{\partial^2} \quad (9)$$

$$e_{ikl} \frac{\partial^2 U_k}{\partial X_i \partial X_l} - \varepsilon_{ik} \frac{\partial^2 U4}{\partial X_k \partial X_i} = 0 \quad (10)$$

Equations (9) and (10) are the piezoelectric tensorial equations, they characterize electroelastic coupling between the elastic displacement vector of components U_1, U_2, U_3 and the electric potential U_4.

IV. General from of the Solution

The piezoelectric wave is the solution of the elastic and electric equations that satisfy elastic and electric boundary conditions. When these waves attenuate exponentially inside the piezoelectric material, they are known as surface waves and if this is not the case they are known as bulk waves. Consider the following form of the surface wave (partial wave) :

$$U_i = u_i \exp(j\beta\alpha_i Y) \exp - j(\omega t - \beta(1 + j\gamma)X) \quad (11)$$

where *ui* (*i=1, 2, 3*) are the displacement amplitudes, u_i (*i=4*) is the amplitude of the electric potential, *k* is the constant of propagation, the α_i are the penetration coefficients of the wave inside the piezoelectric substrate, γ is the coefficient of longitudinal attenuation and ω is the angular pulsation.

We will be interested in the coefficient α_i. With a chosen YX-cut LiNbO3 (Lithium Niobate).

Equations (9) and (10) can be written in a matrix form as

$$[A][U] = [0] \quad (12)$$

where [A] is a matrix (4x4), the elements of this matrix depend on the features of the piezoelectric material (C_{ijkl}, ε_{ik} *and* e_{lij}) as well as of penetration coefficient α and of the acoustic velocity V_S.

The determinant of the matrix [A] must be zero to ensure a nontrivial solution, it can be written as

$$\sum_{i=0}^{8} \beta_i \alpha^i = 0 \quad (13)$$

where B_i depends on the features of the piezoelectric material (C_{ijkl}, ε_{ik} *and* e_{lij}) and of the acoustic velocity V_S. The determinant of the matrix [A] must be zero, we have eight complex roots (*i=1, . . ., 8*):

$$\alpha_i = a_i + jb_i \quad (14)$$

where a_i is the real part and b_i is the imaginary part, with $a_m=a_{m+1}$ and $b_m=b_{m+1}$

where *m=1, 3, 5, 7.*

In the surface mode (or Rayleigh wave) the α_i (*i=1, . . ., 4*) are conjugated by pairs and only the complex roots with negative imaginary part are taken into consideration (for convergence reasons).

Let us first neglect the longitudinal attenuation (γ =0) and insert equation (14) in equation (11), to obtain:

$$U_i = u_i \exp - (b_i k.Y) \exp - j[\omega t - k(X + a_i Y) \quad (15)$$

If we go inside the crystal (Y tends to -∞), the wave U_i tends to zero. This corresponds to surface acoustic waves (SAW). In the opposite case (Y tends to +∞), U_i tends to infinity (+∞) (without physical signification).

Remarks

If $\alpha_{re}^{(i)} = 0$ and $\alpha_{im}^{(i)} > 0$, ultrasonic pulse will be obtained and for a good detection of ultrasonic pulse we should have (Real part equals zero and the maximum positive value of imaginary part (Table 1).

V. Results and Discussion

Fig 2 shows the classification using SVM; for each value of coefficient attenuation α1, we observe that Ultrasonic Pulse has 5 values, Fig 3 shows the classification using SVM but in this case, the classification factor is acoustic velocity Vs and this stage helps to know acoustic velocity Vs which corresponds to each value of coefficient attenuation α1, But in the attenuation α2 we note that; Ultrasonic Pulse is not detected, (Fig 4), in this case we are not required to use the classification of acoustic velocity Vs.

In the attenuation α3 we note that the ultrasonic Pulse is not detected (Fig 5) (Table 1), in this case, we are not required to use the classification of acoustic velocity Vs. Fig 6 shows the classification using SVM; for each value of coefficient attenuation α4, we observe that Ultrasonic Pulse has 4 values,

Fig 7 shows classification for acoustic velocity corresponds to each value of coefficient attenuation α4. (Table 1)

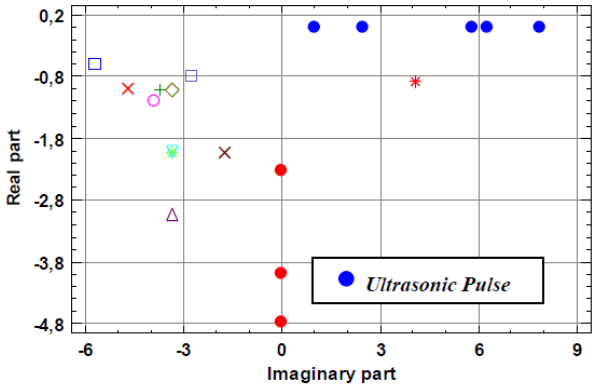


Fig 2. SVM classifier for α1.

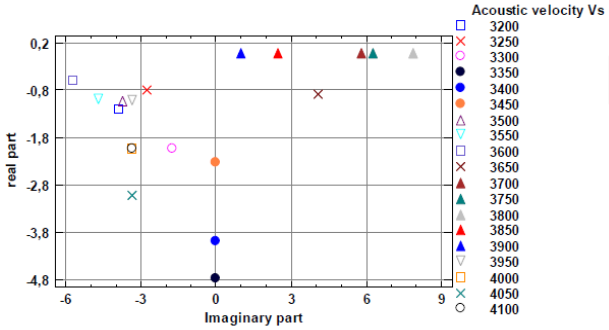


Fig 3. SVM classifier for α1- Classification factor Vs

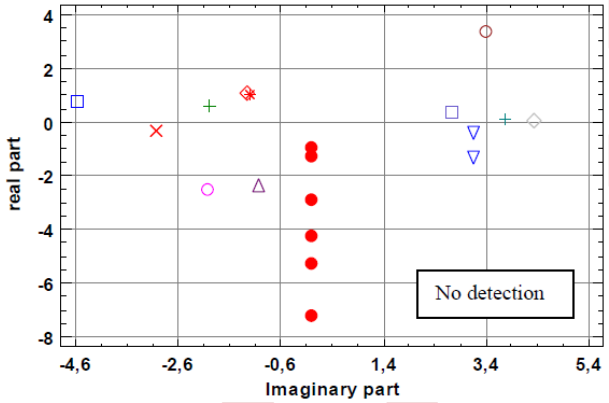


Fig 4. SVM classifier for α2.

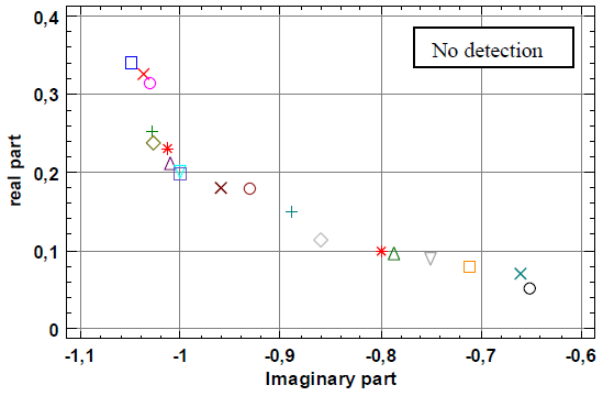


Fig 5. SVM classifier for α3.

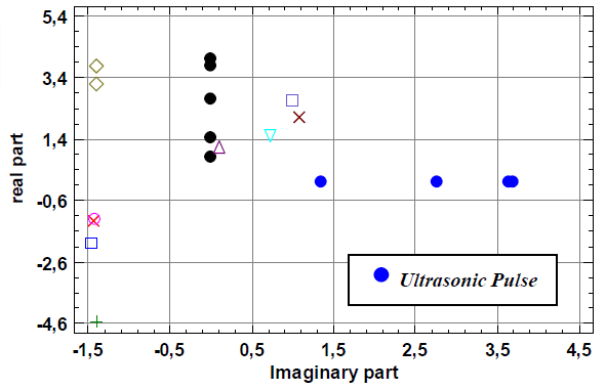


Fig 6. SVM classifier for α4.

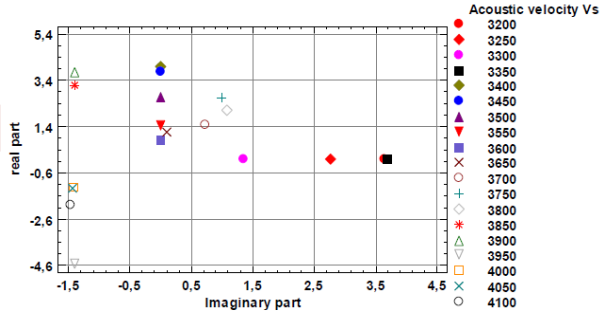


Fig 7. SVM classifier for α4- Classification factor Vs

TABLE I. SUMMARIZES THE FULL WORK

Coefficient attenuation	Real part	Imaginary part	Acoustic velocity Vs (m/s)	Ultrasonic Pulse
α1	0	5,78765	3700	Detection
	0	6,25443	3750	Detection
	0	7,8765	3800	**Good Detection**
	0	2,4543	3850	Detection
	0	1,00001	3900	Detection
α2	No Values	No Values	No Values	No detection
α3	No Values	No Values	No Values	No detection

α4	0	3,65	3200	Detection
	0	2,765	3250	Detection
	0	1,34571	3300	Detection
	0	3,7	3350	**Good Detection**

VI. CONCLUSION

Our paper was the subject of a modeling of the propagation of acoustic microwaves in piezoelectric structures, firstly at the level of the detection of partial ultrasonic pulse by the behavior of the attenuation coefficients (graphic results) and secondly by the association of Support Vector Machine for better precision. In our work we have explained the phenomenon of ultrasonic pulse by relying on two models: The first is based on numerical results at the level of the attenuation coefficients, namely the variations of their real and imaginary parts as a function of the acoustic velocity, provide us with information on the presence of partial microwaves, thus making it possible to distinguish easily the different modes of propagation in particular ultrasonic pulse. The second model is based on the application of Support Vector Machine (SVM) in order to accurately detect ultrasonic pulse during the propagation of acoustic microwaves in a piezoelectric substrate (example: LiNbO3). We used classification by support vector machine as a means of numerical analysis in which we classified all the values of the real part and imaginary part of the attenuation coefficient according to the acoustic velocity thus leading to the construction of a very precise model for the detection of ultrasonic pulse. Our method (second model) is applicable for any piezoelectric material of the same crystallographic class, it is enough just to change the characteristic parameters of the material considered (elastic tensor, piezoelectric tensor and dielectric tensor).

ACKNOWLEDGMENT

The authors acknowledge the support received by LEA Laboratory, Electronics Department, Faculty of Technology, University of Batna 2 through funding from the Ministry of higher education and scientific research.

REFERENCES

[1] N. i Fan : "Analyse et simulation de résonateurs piézoélectriques pour des applications de filtrage", Thèse de Doctorat, Université de Limoges, 2009.

[2] D. Royer et E. Dieulesaint : "Ondes élastiques dans les solides", Tome 1, "propagation libre et guidée", Ed. Masson, Paris, 1996.

[3] D. Benatia : "Modélisation des ondes de volume rampantes sous la surface (SSBW) par une technique mixte ondelettes et fractales", Thèse de Doctorat d'Etat. Université de Constantine, institut d'électronique, Décembre 1999.

[4] E. Dieulesant et D. Royer : "Ondes élastiques dans les solides", (Edition Masson et compagnie, 1974).

[5] D. Benatia and M. Benslama: "Analysis of Leaky and Bulk Acoustic Microwaves by Wavelet Technique," Journal of Communications in Numerical Methods in Engineering, 2000, Vol. 16, pp. 165-175.

[6] K. H. Yen, K. F. Lau and R. S. Kagiwada : "Recent advances in shallow bulk acoustic wave devices", Proc. IEEE Ultrasonics Symposium, 1979, pp. 776-785.

[7] Hichem, Hafdaoui, and Benatia Djamel. "A comparative study for two LiNbO3 cuts (YZ and YX) in detecting bulk acoustic microwaves using Probabilistic Neural Network." Engineering Science and Technology, an International Journal 21.3 (2018): 527-531.

[8] D. F. Specht : "Probabilistic neural networks", Neural networks, 1990, Vol. 3, No. 1, pp. 109– 118.

[9] M. W. Kim and M. Arozullah: "Generalized probabilistic neural network based classifiers", International Joint Conference on, 2002, Vol. 3, pp. 648–653.

[10] V. Georgiou, P. Alevizos, and M. Vrahatis: "Fuzzy Evolutionary Probabilistic Neural Networks", Artificial Neural Networks in Pattern Recognition, 2008, pp. 113–124.

[11] P. Burrascano: "Learning vector quantization for the probabilistic neural network", IEEE Transactions on Neural Networks / a Publication of the IEEE Neural Networks Council, 1991, Vol. 2, No. 4, pp. 458-461.

[12] I. De Falco, A. Della Cioppa and E. Tarantino: "Facing classification problems with Particle Swarm Optimization", Applied Soft Computing, Juin 2007, Vol. 7, pp. 652–658.

[13] I. Galleske and J. Castellanos : "A rotated kernel probabilistic neural network (RKPNN) for multiclass classification", in Proceedings of the Artificial and natural neural networks 7th international conference on Computational methods in neural modeling – Vol. 1, Berlin, Heidelberg, 2003, pp. 152–157.

[14] I. Galleske and J. Castellanos: "A rotated kernel probabilistic neural network (RKPNN) for multiclass classification", Computational Methods in Neural Modeling, 2003, pp. 1040–1045.

[15] D. K. Kim, D. H. Kim, S. K. Chang and S. K. Chang: "Modified probabilistic neural network considering heterogeneous probabilistic density functions in the design of breakwater", KSCE Journal of Civil Engineering, Vol. 11, No. 2, 2007, pp. 65-71.

[16] Hafdaoui, H., Mehadjebia, C., & Benatia, D. (). Using Probabilistic Neural Network (PNN) for Extracting Acoustic Microwaves (BAW) in Piezoelectric Material. In International Conference in Artificial Intelligence in Renewable Energetic Systems, 2017, pp. 308-315.

[17] Hichem, H., & Djamel, B. A comparative study for two LiNbO3 cuts (YZ and YX) in detecting bulk acoustic microwaves using Probabilistic Neural Network. Engineering Science and Technology, an International Journal, 21(3), 2018, pp527-531.

[18] Kurjak, A., & Chervenak, F. A. (2017). Donald School Textbook of Ultrasound in Obstetrics & Gynaecology. JP Medical Ltd.

[19] Lam, C. S., Gao, A., Lin, C. M., & Zou, J. (2018, March). A review of Lamé and Lamb mode crystal resonators for timing applications and prospects of Lamé and Lamb mode PiezoMEMS resonators for filtering applications. In Proc. 7th Int. Symp. Acoustic Devices Future Mobile Commun. Syst (pp. 1-12).

Recovery of electromechanical vibratory energy from electromagnetic shock absorbers of vehicles

Badis Bouchebbah[1], Bachir Maouche[2]

[1] *Laboratoire de Génie Electrique de Bejaia, Faculté de Technologie, Université de Bejaia, 06000 Bejaia, Algeria*
badis.bouchebbah@univ-bejaia.dz

[2] *Laboratoire de Génie Electrique de Bejaia, Faculté de Technologie, Université de Bejaia, 06000 Bejaia, Algeria*
bachir.maouche@univ-bejaia.dz

Abstract—The objective of this paper is to develop an electromechanical model to analyze the Electromagnetic Energy Recovery Dampers (EERD) for automotive applications in order to quantify the power of different vibration cycles caused by road irregularities. The system (EERD) converts kinetic energy from vibrations into electrical energy. The model developed is based on the governing magnetic field equation expressed in terms of magnetic vector potential, solved using the coupled circuit method and then combined with the electromagnetic and mechanical equations obtained after modeling the vehicle's damper. The coupling is carried out by the magnetic force and by an external mechanical force due to the movements of the moving part. Vibration cycles are transmitted to the device in the form of vertical displacements. The results obtained mainly represent the vehicle's damping rate and the electrical power recovered.

Keywords: **Vehicles, Electromagnetic damper, Electromechanical vibration energy.**

I. INTRODUCTION

Thanks to the technological advances of recent years, humanity has created and improved ways of facilitating and enhancing his daily life in all areas by overcoming some of the most recurrent problems. Among these problems are those linked to shock, noise and vibration encountered in industrial machinery, bridges and buildings, but also in means of transport, particularly vehicles.

Dampers have become an indispensable part of a vehicle's mechanical structure. They reduce the vibrations of the object or isolate the object from vibrations by dissipating energy to improve its life by guaranteeing more efficient operation safety and comfort of passengers.

The electromagnetic damper which is the subject of the present work is a device which aims to minimize the amplitude of vibrations resulting from road irregularities by magnetic attraction and recover vibratory energy in the form of electrical energy.

The research carried out to date is essentially based on the finite element method for the calculation of electromagnetic quantities [3], [4], [5]. In this work, we propose a different approach based on the coupled circuit method [1].

This article is divided into three sections. The first section description of the system (EERD), the second section is devoted to the electromagnetic modeling of the suspension and the mechanical modeling of the oscillations and the forces of repulsion and attraction. The final section is devoted to the MATLAB simulation of the electromagnetic suspension.

II. GEOMETRIC DESCRIPTION

We have a system consisting of a car coil spring, a wheel with a fixed degree of freedom that doesn't move, and an axially magnetized magnet concentric with a coil. The isolated system oscillates in one degree of freedom. The z(t) coordinate indicates the amplitude deviation from stable equilibrium. The geometry and study range of the electromagnetic damper are shown in "Fig. 1".

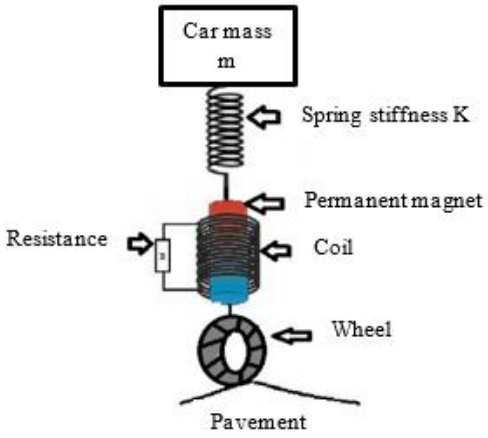


Figure 1. Mechanical model of the damped system

TABLE 1. SIMULATION PARAMETERS

	Parameters	Value
Mechanical parameters	Speed bump length (L_0)	1 m
	Speed bump height (H)	0.5 m
	Vehicle speed (v)	30 km/h
	Stiffness K	$2\ 10^5$ N/m
	Force applied to damper	40 sin(26.7t) kN
Electromagnetic parameters	Magnet width	10 cm
	Magnet length (l)	15 cm
	Remanent field of magnet	2 T
	The equivalent current in the magnet (Ieq)	$2.38\ 10^3$ A
	Average coil radius	10 cm
	Coil length	25 cm
	Number of turns (Ns)	1750 turns
	Coil position	5.5 cm
	Coil conductivity σ	$6\ 10^7$ siemens
	Battery capacity (C)	36000 F

The mechanical system representing a quarter of the vehicle "Fig.1" is made up of the vehicle mass m, the rigidity of the vehicle suspension K, a permanent magnet and a coil. When the permanent magnet changes position vertically, it creates a variation in the magnetic field, which induces a variable electric current in the coil, which must be rectified and stored in the capacitor. The diagram in "Fig. 2"shows the circuit's various operating modes.

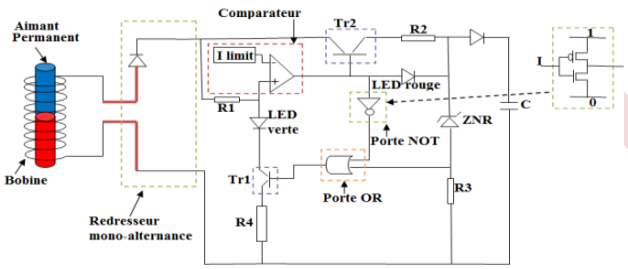


Figure 2. Schema for recovering the electrical energy generated by the magnet

III. ELECTROMAGNETIC AND MECHANICAL MODELING

The mathematical modeling of (EERD) takes into account the interaction between the mechanics of the magnet's motion, the electrical equation drawn from the circuit formed by the receiver coil, and the electromagnetic phenomena within the system.

A. Electromagnetic equation

In our situation, the Amperian approach is favored, there is therefore no magnetic material and the field is due exclusively to an equivalent current.

$$\begin{cases} \vec{\mathrm{rot}}(\vec{B}) = \mu_0 \vec{J}_{eq} & (a) \\ \vec{J}_{eq} = \vec{\mathrm{rot}}(\vec{M}) & (b) \end{cases} \quad (1)$$

Starting from Maxwell's equations, neglecting the displacement current, and taking into account the equivalent current density, the governing magnetic field equations in terms of magnetic vector potential are given in 2D cylindrical coordinates as follows:

$$\begin{cases} \mathrm{div}\left(\vec{\mathrm{grad}}(A)\right) = -\mu_0 J & (a) \\ \frac{J}{\sigma} + \frac{dA}{dt} - v_z B_r = -\vec{\mathrm{grad}}V \cdot \vec{e}_\theta & (b) \end{cases} \quad (2)$$

The solution to the equation (2.a) is given by the Biot and Savart formula for the magnetic vector potential.

$$A(p) = \frac{\mu_0}{4\pi} \int_{\tau_0} \frac{J(P_0)dv_0}{|\vec{P}-\vec{P}_0|} \quad (3)$$

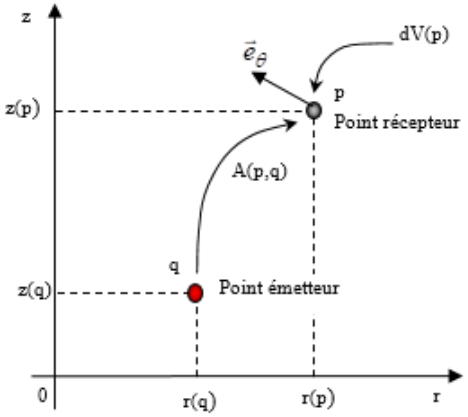


Figure 3. Electromagnetic effect between any two points

Where μ_0 and σ are the permeability and conductivity, respectively, of the conducting medium, J_{eq} represents the equivalent current density of the magnet, A the magnetic potential generated by the magnet, P0 the position of the source, P the position of the charge, (r_0,z_0) the coordinates of the source, (r,z) the coordinates of the charges and k is a geometric factor.

Br is the radial component of the magnetic field such that:

$$B_r = \frac{dA}{dz} \quad (4)$$

V is the electric scalar potential, which is written as a function of the voltage across a turn of the coil as follows:

$$\vec{\mathrm{grad}}V \cdot \vec{e}_\theta = -\frac{u}{2\pi r} \quad (5)$$

The development of the integral of relation (3) in the case of an axisymmetric system leads to the expression of the magnetic

potential as a function of the elliptic Legendre integrals respectively of first $E_1(k)$ and second species $E_2(k)$[1],[6].

$$A(r,z) = \frac{\mu_0}{2\pi} I(r_0,z_0) \sqrt{\frac{r_0}{r}} \left[\frac{(2-k^2)E_1(k) - 2E_2(k)}{k} \right] \quad (6)$$

We then deduce the expression of the radial component of the magnetic induction.

$$B_r(r,z) = \frac{\mu_0 I_0}{8\pi} \frac{z-z_0}{r\sqrt{rr_0}} \left[\frac{2-k^2}{1-k^2} E_2(k) - 2E_1(k) \right] k \quad (7)$$

With

$$k = \sqrt{\frac{4rr_0}{(r+r_0)^2+(z+z_0)^2}} \quad (8)$$

$$\begin{cases} E_1(k) = \int_0^{\pi/2} \frac{d\varphi}{\sqrt{1-k^2\sin^2\varphi}} & (a) \\ E_2(k) = \int_0^{\pi/2} \sqrt{1-k^2\sin^2\varphi}\, d\varphi & (b) \end{cases} \quad (9)$$

B. Electrical equation

The electrical equation modeling the recharging of the capacitor:

From (2.b), by introducing the expression of the gradient of the electric potential V as a function of the voltage (u) at the terminal of each turn (5), we arrive at the electric equation at the terminal of each turn of the coil.

$$2\pi r \left(\frac{J}{\sigma} + \frac{dA}{dt} - v_z B_r \right) = u \quad (10)$$

As the coil turns are in series, it is then sufficient to sum the elemental voltages of each turn to obtain the terminal voltage of the entire coil, and the equation (10) becomes:

$$L\frac{dI(t)}{dt} + RI(t) + U(t) = V_{em}(t) \quad (11)$$

$$\begin{cases} R = \sum_{i=1}^{N} \frac{2\pi r_i}{s\sigma} & (a) \\ L = \frac{1}{I} \sum_{i=1}^{N} 2\pi r_i A_i^{cc} & (b) \\ V_{em}(t) = 2\pi v_z(t) \sum_{i=1}^{N} r_i Br_i^{mc}(t) & (c) \end{cases} \quad (12)$$

Introducing the relationship between current and voltage across a capacitor (equation 13), we obtain the general equation of the electric circuit (equation 14)

$$I = C\frac{dU}{dt} \quad (13)$$

$$LC\frac{d^2I(t)}{dt^2} + RC\frac{dI(t)}{dt} + I(t) = C\frac{dV_{em}(t)}{dt} \quad (14)$$

Where s is the section of the turns of the coil, σ the conductivity of the coil, (I) the current passing through the coil, L the inductance of the coil, U the voltage at the terminal of the capacitor, C the capacitance of the capacitor, A^{cc} is the magnetic potential resulting from all the turns on the i^{th} turn, Br^{mc} is the radial component of the induction produced by the magnet on the i^{th} turn, r_i is the radius of the i^{th} turn, v_z is the speed of the magnet and V_{em} is the fem induced by the movement of the magnet.

C. Mechanical equation

The equation of motion of the above system is given by:

$$m\ddot{z}(t) + F_L(t) + Kz(t) = F_{ext}(t) \quad (15)$$

Where z(t) represents the position of the magnet over timeand F_{ext} represents the force due to road irregularities. In the case of a speed bump, the $F_{ext}$is modeled by a half-sinusoid [2]:

$$F_{ext} = k'h_0 \sin\left(\frac{\pi}{L_0} vt\right) \quad (16)$$

Where *v* represents the vehicle speed, L_0 represents the length of the speed bump, h_0 its height and k' an amplitude factor.

D. Electromechanical equation

Electromechanical interaction is represented by the Laplace force $F_L$who is the electromagnetic force exerted by a magnetic field on a conductor traversed by a current, its expression for a single turn is:

$$F_L = 2\pi r I B_r \quad (17)$$

Replacing (17) in (15) and superimposing the forces exerted on all the turns gives (18).

$$m\ddot{z}(t) + \sum_{i=1}^{N} \left(2\pi r_i I(t) \frac{dA_i^{mc}(z,t)}{dz} \right) + kz(t) = F_{ext}(t) \quad (18)$$

Where A^{mc} is the magnetic potential created by the magnet and perceived by the coil.

IV. APPLICATION ANDRESULTS

After considering the axial symmetry of the EERD, the generator can be simplified into an axially symmetric 2D model in cylindrical coordinates.

The diagram used to represent the coil and magnet in MATLAB is shown in the "Fig.4".

The simplified electrical circuit is schematized in the following "Fig.5".

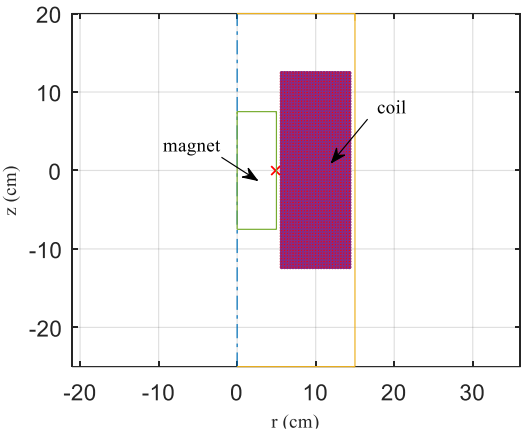


Figure 4. Simplified facial section of a magnet and coil

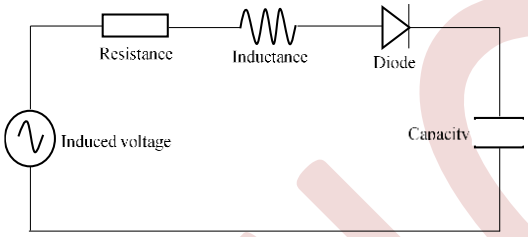


Figure 5. Equivalent circuit under load

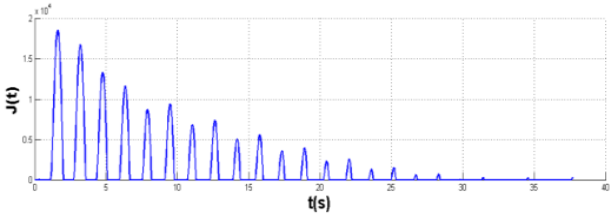


Figure 6. Current density in the coil under load

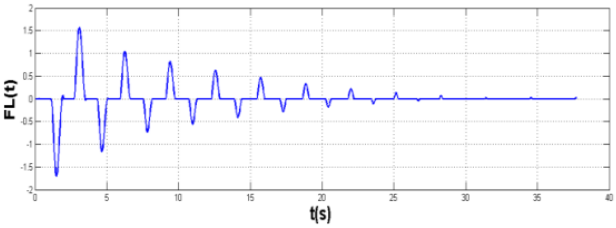


Figure 7. Laplace force under load

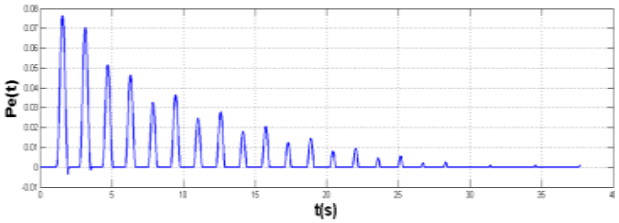


Figure 8. Electrical power dissipated under load

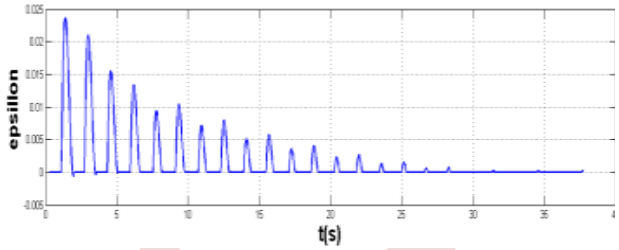


Figure 9. Damping coefficient

Note that the current remains positive because of the rectifier, and decreases as the capacitor is charged, until it cancels out when the capacitor is fully charged. As for the LAPLACE force, it changes sign so as to oppose the magnet's movement at all times, and cancels out when the current is zero.

The damping coefficient is the capacity of the current to oppose the magnet's movement through the LAPLACE force and is defined as being proportional to the ratio of the Laplace force to the magnet's speed. It always remains positive, unlike the LAPLACE force, and cancels out when the current is zero.

V. CONCLUSION

The work undertaken within the framework of this article concerns the recovery of electromechanical vibration energy from electromagnetic shock absorbers of vehicles.

After simulation, we clearly observe the presence of damping due to the current induced in the coil. However, the damping remains very low and insufficient to completely eliminate vibrations, it will then be necessary to think about optimizing the parameters of the model produced or exploring other magnet-coil configurations.

REFERENCES

[1] B. Maouche, "Elaboration de modèles par les Grandeurs Electromagnétiques couplées, Application au controle par courant de Foucault," Thèse de doctorat en sciences, Université Farhat Abbas Sétif, 2007.

[2] M. Mezoudj, "Analyse du comportement vibratoire d'un véhicule à la rencontre d'un obstacle (dos-d'âne)," mémoire présenté pour l'obtention du diplôme de Magister en Mécanique, Université de Batna, avril 2010.

[3] M. Zaouia, N. Benamrouche, A. Djerdir, "Study and Analysis of an Electromagnetic Energy Recovery Damper (EERD) for Automotive Applications," 2012 XXth International Conference on Electrical Machines, 2012.

[4] H. Mohellebi, M.E. Latrèche, et M. Féliachi, "Coupled axisymmetric analytical and finite element analysis of induction devices having moving parts," IEEE Transactions on Magnetics, vol. 34, no. 5, pp. 3308–3310, sept. 1998.

[5] M. Chaves, J. Maia, J. Esteves, "Analysis of an Electromagnetic Automobile Suspension System," in Proc. ICEM08, Paper ID 1285, Portugal, 2008.

[6] E. Durand, "Magnétostatique," Université de Paris –VI, 1969.

EEIC'23

VI

ELECTROSTATICS AND HIGH VOLTAGE ENGINEERING (EHVE)

Sommaire

VI.1 Light emission calibration technique for high voltage discharge currents measurement in liquid dielectrics **254**
VI.2 Comparative analysis of defect detection in electric cables by analyzing potential and electric field distribution on the outer cable surface **258**
VI.3 Influence of geometric parameters on the K factor of the current-voltage characteristic of DC corona discharge. **264**
VI.4 Evaluating the lifetime of polyvinyl chloride insulation under sinusoidal voltage stress **270**
VI.5 Controlled discharge of filters media surface **278**
VI.6 Physical study of an electrically aged silicone insulator under pollution **283**
VI.7 Experimental study of a vibratory-type triboelectric charging device **289**
VI.8 Study of space charge current in power cables using the alternating thermal wave method **294**
VI.9 A graphical tool for the tracking of a single particle in an electric field **298**
VI.10 Simulation of lightning strikes on photovoltaic farms **302**
VI.11 Electric field behavior of a water droplet on the surface of polymer insulators under ac stress using finite element method **308**
VI.12 Influence of the number of superhydrophobic coating layers on their electrical performance **314**
VI.13 Electric field and potential quantification on a deposit of drops covering a superhydrophobic surface under AC voltage **318**
VI.14 Optimizing the two-plane electrostatic precipitator with a small blade for airborne particulate matter filtration **325**
VI.15 Aging of composite insulators under desert conditions **330**

Light emission calibration technique for high voltage discharge currents measurement in liquid dielectrics

Hocine Moulai[1], Abderrahmane Beroual[2], Azzeddine Nacer[1]

[1] *USTHB, FEI, LSEI, BP 32, Bab Ezzouar, Algeria*

hmoulai@usthb.dz

[2]*Laboratoire Ampère, Ecole centrale de Lyon, 36 Av. Guy de Collongue, Ecully, 69134, France*

abderrahmane.beroual@ec-lyon.fr

***Abstract*—The use of a very fast recording oscilloscope (bandwidth 350MHz) enabled us to obtain qualitative results with regard to transient currents and correlated emitted lights corresponding to streamers propagation and their transition to breakdown inside the dielectric liquids under direct current (DC) or industrial voltage (AC, 50Hz), in a point-plane electrode system. The proposed technique is non intrusive. It consists on using the luminous signals of discharges to determine the currents and energies with more accuracy without risking the deterioration of any equipment.**

***Keywords:* Light emission, current, discharges, liquid dielectrics.**

I. INTRODUCTION

Most of power equipments (transformers, bushings, cables, breakers…) are filled of insulating liquids especially mineral oils that ensure at the same time both electrical insulation and heat evacuation. In general, the life period of power equipments is equal to the one of its insulation, and it necessarily depends on dielectric strength of the used insulators. During the operating of these equipments, the oil is submitted to different stresses: electrical, mechanical and thermal that can affect its characteristics

The survey of streamers in dielectric liquids has been the subject of many works [2-6]. Most of these works are dedicated to the measurement of the velocities, currents and emitted lights in divergent electrode systems (tip-plane in particular) under impulse voltages. The streamers have been classified according to their shapes and their modes of propagation dependently on the electrodes polarity [7]. Four modes of propagation have been observed in positive point polarity and three modes in negative point. Contrarily to other liquids where positive and negative events are different, the steamers in mineral oil can have similar shapes in the two polarities.

Electrical discharges can be partial or complete and evolves inside a solid, liquid or gaseous dielectric that present a default (cavity, detachment …) when a sufficient voltage level is applied. Generally, these discharges correspond at a primary stage to breakdowns in gases occluded in the defaults. Several measurement techniques have been proposed for the purpose. They are based on the use of electric (currents, charges, voltages …) [8-10], acoustic [11-13], luminous [14] and UHF radiated signals [15] that characterize them in the aim of real time diagnosis techniques development, and environmental and medical applications [2]. Measurements of the electric parameters are relatively riskier for the equipments from the fact that streamers at their initiation are characterized by very weak currents whereas breakdown reaches highly intensities. Another approach of identification and discrimination between streamers of weak energy and arcs of high energy level proves out to be necessary.

II. TECHNIQUES AND EXPERIMENTAL PROCESS

The experimental device (Fig. 1) consists of an alternative voltage source (220V/50kV, 50Hz), a tip-plane electrodes system placed vertically inside oil filled cylindrical cell made of Pyrex (500ml). The plane electrode is made of brass of diameter 40 mm. It is covered by an insulating barrier of 1.2 mm of thickness enabling to avoid any damage due to sudden arcing occurrence. The point electrode made of tungsten has a radius of curvature of 10µm, and the electrodes gap is varied from 2 to 18.5 mm.

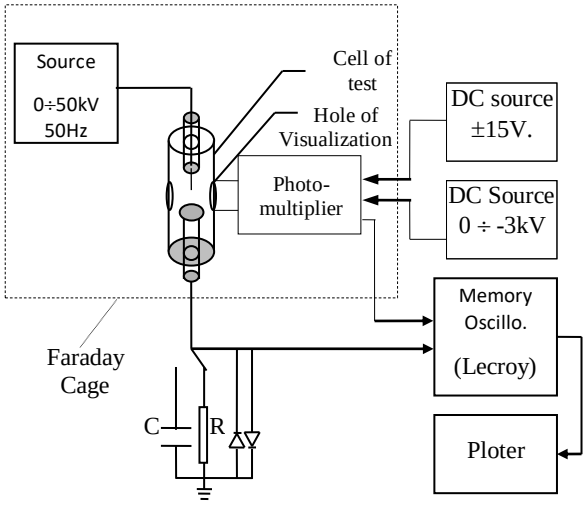


Figure1. Experimental Device

The current (charge) is measured through the voltage sag across a non inductive resistance (respectively capacity) placed in series in the circuit of test, while the emitted light is detected thanks to a photomultiplier (Hamamatsu type). The two signals are recorded simultaneously with the help of a memory digital oscilloscope (Lecroy 9450, 350 MHz). The oscilloscope input is protected with two fast diodes (AN4148, 100mA, 4ns, 100V) placed in head to head in parallel with this resistance.

The voltage is varied between a threshold that we suppose minimal of generation where at the most 2 streamers are generated during one hour of voltage application, and a maximal threshold over which at least 50% of the recorded streamers lead to arcing. It is uniformly varied from 2.0±0.2kV/s. A largest possible current range has been thus obtained: From levels corresponding to the weakest energies until those of high energy, leading directly to arcing.

The breakdown voltage threshold is defined as the lowest applied voltage level for which at least one streamer from a series of 20 successively generated leads to breakdown. It is also possible to establish the variations of the harmonic field threshold on the point electrode by using a hyperboloid approximation:

$$E_h = \frac{2.U}{r_p.\ln(4.d/r_p)} \qquad (1)$$

Where U is the applied voltage, rp the radius of curvature of the point electrode and d the gap distance.

III. Current Measurement

The streamers current is measured through a 50Ω non inductive resistance. It is placed between the plane electrode and earth, and connected to the 50 Ω input of a memory digital oscilloscope (Lecroy 9450, bandwidth 350MHz). The oscilloscope input is protected by two fast diodes (1N4148, 100mA, 4ns, 100V) connected in head to head.

The trigger level of the oscilloscope is chosen the lowest possible in order to record the lower manifestation of streamer as avoiding inopportune triggering of the oscilloscope owed to partial discharge currents through the external walls of the test cell. This level is as much more elevated than the electrodes gap distance and the applied voltage are increased.

In most cases, the oscilloscope is used in mode sequences recording simultaneously the 20, 50 or 100 first events. For the present case, this number is fixed to twenty from the fact that all types of current susceptible to appear at a given voltage level are recorded. On the other hand, while taking a greater number, the recorded signals can be truncated in part and can lose in accuracy.

The streamers appearance under DC voltage is not regular with time, especially when the applied voltage level is relatively low. Some streamers (at the most 5) are generated after the five first minutes following the voltage application, and then to mark a relatively long time, of about 30 minutes before the apparition of other streamers. At higher voltages, the streamers appear more regularly.

The experimental device used for DC measurements is almost similar to the one presented in figure 1. It is constituted from a voltage source, a testing cell and a system of measurement and recording of currents, charges and emitted lights associated to the propagation of streamers. The DC source consists of a generator (SAMES type) providing a variable voltage between 0 and 150 kV. In our experiments it is varied by steps of 2kV/s. The voltage is varied from a minimal threshold assumed to be a minimal of generation where less than 2 streamers were generated during an hour of voltage application, and a maximal threshold over which at least 50% of the recorded streamers lead to arcing. The testing cell is mainly constituted of a point-Plane divergent field electrode system.

IV. Emitted Light Detection and Calibration

The light emitted by the streamer is detected with the help of a photomultiplier (Hamamatsu) provided with a very over-sensitive photodiodes grid, polarized by a DC generator ±15V. The obtained electrical signal is amplified with the help of a HV negative DC which voltage varies between (0÷ -3000 V).

The maximal amplification of the signal is obtained around 1.8 kV when the grid of photodiodes is placed at 10 cm from the issuing source of light (i.e. the streamer). Beyond this voltage level, the photomultiplier saturates. In order to capture in totality the emitted lights, we coated the outside face of the test cell by a white lacquer and let a same measurements window than the grid of photodiodes (42x4.5mm^2). The two latter are brought closer one from the other in order to obtain a maximum of luminous sensitivity of the used equipment.

Until now the works devoted to the streamers emitted lights gave this parameter in arbitrary units. In order to have an idea on its amplitude, we proceeded to a standardization of the measurement device in equivalent light units to the electric data really measured by the oscilloscope. The grid of photodiodes plays the role of a photometric cell measuring the illumination emitted by the luminous source represented by the streamer.

The calibration of the measurement device has been made by enlightening the photodiodes grid by a known light source (neon) emitting a luminous flux "F_x", placed facing the grid of photodiodes at a distance "d_G ". By applying the relation:

$$E_C = \frac{F_X}{4.\pi.d_G^2} \qquad (2)$$

One obtains an illumination E of 68.18 Lx corresponding to a voltage of 9.8mV measured by the oscilloscope. The system being linear, one obtains therefore the following calibration: e_c=7Lx/mV.

While considering the streamer as a source of light concentrated on the point-plane axis, the distance d'_G between this axis and the grid of photodiodes being maintained fixed to 110 mm, the flux unit on this axis would be:

$$f_X = 4.\pi.e_C.d_G'^2 = 1Lum/mV. \qquad (3)$$

The luminous flux being supposed distributed uniformly around the streamer, from the fact of the axi-symmetry of the

system, one can determine the luminous intensity: $i_e = f_x / 4.\pi$ and one obtains the equivalence: $i_e = 0.027\,Cd/mV$.

V. Emitted Light and Current Shapes under AC

Streamer propagation in liquid dielectrics is mainly characterised by current flow between the two electrodes and light emission which are almost well correlated. Negative streamers are characterised by discrete current and light pulses which are irregularly spaced. Figure 2 represent a typical negative streamer current with its corresponding light emission signal. Positive streamers are characterized by an increasing continuous component which reaches its maximal value when arrived on the plane earthed electrode. On this continuous component are superimposed very fast pulses which are regularly spaced.

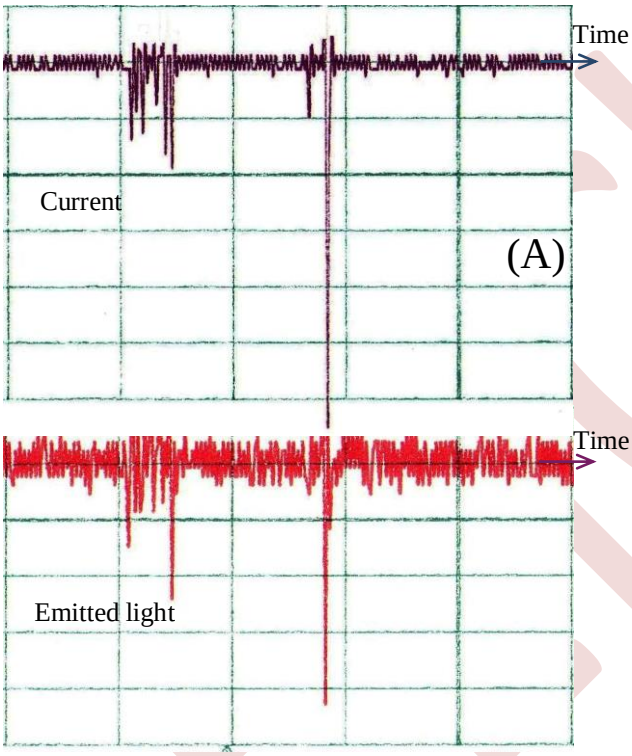


Figure 2. Typical negative streamer current (upper signal) and corresponding light emission (lower signal) variations with time in transformer mineral oil. Alternating applied voltage: U=25kV, Gap distance: d=5 mm, Point electrode radius: r_p=10µm. Scale: Current: 0.75 mA/div, Emitted light: 0.6Cd/div, Time : 5µs/div.

The greatest magnitudes are recorded in tetra-ester compared to transformer mineral oil. Different shapes of current and light can be observed depending on the applied voltage level and the corresponding alternation. In figure 3 is represented a typical positive streamer current with its corresponding emitted light.

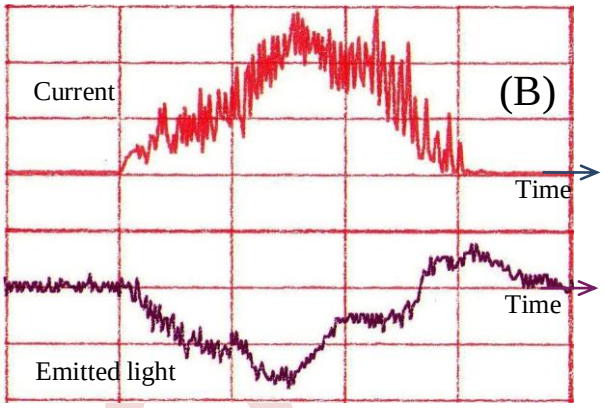


Figure 3. Typical positive streamer current (upper signal) and corresponding light emission (lower signal) variations with time in transformer mineral oil. Alternating applied voltage: U=20kV, Gap distance: d=5 mm, Point electrode radius: r_p=10µm. Scale: Current: 1.5 mA/div, Emitted light: 1.2 Cd/div, Time: 5µs/div.

VI. Emitted Light and Current Shapes under DC

In general, positive and negative streamers currents and their corresponding light emissions are perfectly correlated in shape and amplitude. However, in mineral oil submitted to negative polarity voltage, if the current is null between two successive pulses, the corresponding emitted light present a continuous component increasing with time from a pick to the succeeding one. Figures 4 and 5 show the different shapes of emitted light and current observed in mineral transformer oil under positive and negative polarity with the same electrodes geometry.

Similar observations have been reported in mineral oil for long gap distances under impulse voltage [16]. Current pulses without corresponding light pulses have also been recorded when the applied voltage is relatively weak. These two phenomena have been observed at the phase corresponding to the end of the streamer propagation.

Under the two polarities, the currents and their corresponding light emissions are constituted of very brief discrete pulses which duration is of about 20 to 40ns for the first pulses and 50 to 200ns for the latest ones. Generally, the amplitude of these pulses increases with time. It is however difficult to settle a repetitive variation law of the amplitude of these emitted lights and currents.

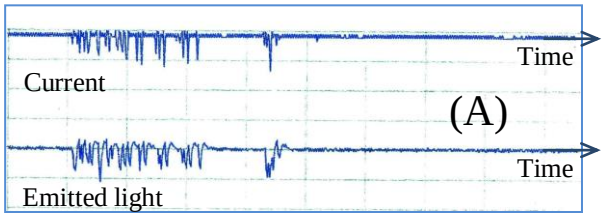


Figure 4. Typical positive streamer current (upper signal) and corresponding light emission (lower signal) variations with time in transformer mineral oil. DC applied voltage: U=50kV, Gap distance: d= 10 mm, Point electrode radius: r_p=10µm. Scale: Current: 1. 5 mA/div, Emitted light: 3Cd/div, Time: 10µs/div.

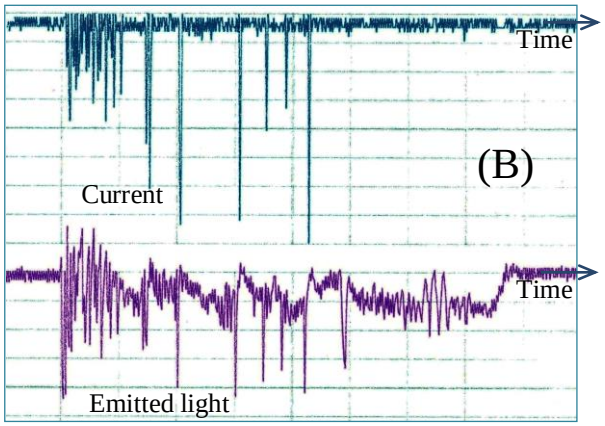


Figure 5. Typical negative streamer current (upper signal) and corresponding light emission (lower signal) variations with time in transformer mineral oil. DC applied voltage: U=50kV, Gap distance: d= 10 mm, Point electrode radius: r_p=10µm. Scale: Current: 1. 5 mA/div., Emitted light: 1.2 Cd/div, Time: 10 µs/div.

From a set of 20 streamers obtained successively in the same applied conditions, the currents and the light emissions, well that similar in the shape, present neither the same number of peaks nor the same amplitude. The disposition of accumulated charge in the liquid after a previous streamer would influence on the necessary energy to the development of the following streamer.

The streamers corresponding to the generally recorded currents and light emissions are relatively of weak energy, and none of them leads to arcing. When the latter occurs, the streamer light emission shape changes fundamentally.

It presents a continuous component whatever is the polarity of the tip. The shape of the current and then the corresponding streamer changes depending on whether this latter succeeds or no to arcing. Its velocity, being correlated to its shape, would be then more important when it is followed by an arc occurrence.

VII. CONCLUSION

Streamers currents and emitted lights are well correlated whatever are the applied voltage levels or nature, the geometric dimensions and the investigated liquid. They are both constituted from fast pulses which are in certain conditions superimposed on a continuous component corresponding to the streamer growth. The continuous component waveform variations can indicate the general streamer propagation way and velocity.

The emitted light recording is more useful than currents from the fact that it represents a non intrusive technique which is also not affected by the high electromagnetic interferences due to power stations environment. On the other hand, emitted light signals are more complete and informative of the streamer dynamics and the physic-chemical processes that are responsible on its propagation.

REFERENCES

[1] J. F. Kolb, R. P. Joshi, S. Xiao and K. H. Schoenbach (2008), *Streamers in water and other dielectric Liquids*, J. Phys. D: Appl. Phys., Vol 41, p. 234007 (22pp)

[2] P. Bruggeman and C. Leys (2009), *Non-thermal plasmas in and in contact with liquids*, J. Phys. D: Appl. Phys., Vol 42, p. 053001(28pp)

[3] R. P. Joshi and S. Mededovic Thagard (2013), *Streamer-Like Electrical Discharges in Water: Part I. Fundamental Mechanisms*, Plasma Chem. Plasma Process, Vol 33, p. 1–15

[4] M. Pompili, C. Mazzetti and R. Bartnikas (2008), *PD Pulse Burst Behavior of a Transformer Type Synthetic Organic Ester Fluid*, IEEE Trans. on Diel. and Electr. Ins., Vol 15, p. 1498-1506

[5] M. Pompili, C. Mazzetti and R. Bartnikas (2009), *Comparative PD pulse burst characteristics of transformer type natural and synthetic ester fluids and mineral oils*, IEEE Trans. on Diel. and Elect. Ins., Vol 16, p. 1511-1518

[6] T. M. Do, O. Lesaint and J. L. Augé (2008), *Streamers and Partial Discharge Mechanisms in Silicone Gel Under Impulse and AC Voltages*, IEEE Trans. on Diel. and Elect. Ins., Vol 15, p. 1526-1534

[7] A. Beroual et al (1998), *Propagation and structure of streamers in liquid dielectrics*, IEEE Elect. Ins. Magazine, Vol 14, p. 6-17

[8] T. K. Abdel-Galil, A. H. El-Hag, A. M. Gaouda, M. M. Salama and R. Bartnikas (2008), *De-noising of Partial Discharge Signal Using Eigen-decomposition Technique*, IEEE Trans. on Diel. and Elect. Ins., Vol 15, p. 1657-1662

[9] S. Wenrong, L. Junhao, Y. Peng and L. Yanming (2008), *Digital Detection, Grouping and Classification of Partial Discharge Signals at DC Voltage*, IEEE Trans. on Diel. and Elect. Ins., Vol 15, p. 1663-1674

[10] H. Zhang, T. R. Blackburn, B. T. Phung and D. Sen (2007), *A Novel Wavelet Transform Technique for On-line Partial Discharge Measurements, Part 2: On-site Noise Rejection Application*, IEEE Trans. on Diel. and Elect. Ins., Vol 14, p. 15-22

[11] R. M. Sharkawy, T. K. Abdel-Galil, R. S. Mangoubi, M. M. Salama and R. Bartnikas (2008), *Particle Identification in Terms of Acoustic Partial Discharge Measurements in Transformer Oils*, IEEE Trans. on Diel. and Elect. Ins., Vol 15, p. 1649-1656

[12] S. M. Markalous, S. Tenbohlen and K. Feser (2008), *Detection and Location of Partial Discharges in Power Transformers using Acoustic and Electromagnetic Signals*, IEEE Trans. on Diel. and Elect. Ins., Vol 15, p. 1576-1583

[13] J Lopez-Roldan, T Tang and M Gaskin (2008), *Optimisation of a Sensor for Onsite Detection of Partial Discharges in Power Transformers by the UHF Method*, IEEE Trans. on Diel. and Elect. Ins., Vol 15, p.1634-1639

[14] D. Amarasinghe, U. Sonnadara, M. Berg and V. Cooray (2007), *Correlation between Brightness and Channel Currents of Electrical Discharges*, IEEE Trans. on Diel. and Elect. Ins., Vol 14, p. 1154-1160

[15] S. Coenen, S. Tenbohlen, S. M. Markalous and T. Strehl (2008), *Sensitivity of UHF PD Measurements in Power Transformers*, IEEE Trans. on Diel. and Elect. Ins., Vol 15, p. 1553-1558

[16] N. V. Dung, H. K. Høidalen, D. Linhjell, L. E. Lundgaard and M. Unge (2013), *Effects of reduced pressure and additives on streamers in white oil in long point-plane gap*, J. Phys. D: Appl. Phys., Vol 46, p. 255501 (16pp)

Comparative Analysis of Defect Detection in Electric Cables by Analyzing Potential and Electric Field Distribution on the Outer Cable Surface

Meziani Madjid [1], Teguar Madjid [2], Mekhaldi Abdelouahab [2]

[1] *FGEI,Université Mouloud Mammeri de Tizi-Ouzou, Tiziouzou, Algeria*

madjid.meziani@ummto.dz

[2] *Laboratoire de Recherche en Electrotechnique, Ecole Nationale Polytechnique d'Alger, B.P 182, El-Harrach, Algeria*

madjid.teguar@g.enp.edu.dz, abdelouahab.mekhaldi@g.enp.edu.dz

***Abstract*—In this study, our main objective is to improve the detection of imperfections in polymeric insulation by thoroughly examining the distribution of electric potential and electric field along the external surface of electrical cables. We specifically focus on two distinct anomalies present within the internal insulation of a medium voltage cable model of 12 kV. To achieve this aim, we utilized advanced numerical simulations with the Comsol Multiphysics software, conducting a comprehensive comparative analysis in two distinct scenarios: one involving healthy insulation and the other simulating the presence of water tree and air defects. Our meticulous analysis of the results reveals minimal response variations for defect lengths less than 1.5 mm. However, a significant difference in detectable defect lengths between water tree defects and air defects is evident, primarily influenced by the defect's dielectric constant. Specifically, for shorter defects, space charge was introduced into the internal insulation, leading to localized disruptions in the electrostatic equilibrium of the defect. Consequently, this disruption yields a distinctive response in terms of potential and electric field outside the cable. A thorough examination of this signal allows us to precisely map the distribution of the electric field within the internal insulation. Furthermore, our observations underscore that the concentration of electric field and potential values primarily clusters at the water trees tips. This emphasizes the effectiveness of the technique, relying on the dynamic movement of space charges, in facilitating the detection and precise localization of minor defects.**

***Keywords:* Underground Electrical Cables, Dielectric Insulation, Water Trees, Air defects, Space Charge, Diagnosis, Non-Destructive Testing, Numerical Modeling.**

I. INTRODUCTION

The failures of underground electrical distribution cables pose a serious threat to the reliability of the electrical infrastructure. Replacement must be carried out selectively due to the high associated cost [1] [2].

Despite the improvements made to mitigate the impact of water trees in modern cables, the problem still persists, underscoring the importance of addressing it. Aging, which reduces dielectric strength and also leads to the breakdown of the dielectric function of power cable insulation, primarily occurs due to the presence of partial discharges and water treeing phenomena. Therefore, their detection is necessary for predicting and ensuring the reliable operation of insulation health. However, it is essential to use diagnostic techniques to accurately assess the level of damage within a cable [3]. Various technologies and tests are available for the evaluation of underground cables [4-7], but there is often a weak correlation between diagnostic results and actual deterioration [1] [3]. Due to its random nature, water tree modeling is a relatively recent field made possible only through computer-assisted analysis [2]. Numerical modeling of water trees and analyzing the distribution of the electric field within an insulation containing water trees are of real importance in estimating the stresses exerted by water trees in the internal insulation [8]. The implementation of our numerical model using Comsol Multiphysics aims to assess the distortion of the electric field caused by dielectric defects while also evaluating these defects and the possibility of detecting them. To achieve this goal and evaluate the internal insulation health of the cable model used in this study, it is essential to measure the electrical quantities on the outer surface of the cable. In this context, we recorded variations in the electric field and potential along the outer circumference of the cable. The values observed in the presence of defects were compared to the initial values in the case of a healthy insulation. Additionally, for the purpose of characterizing and distinguishing specific dielectric irregularities, two separate fault categories were selected. A comparative analysis was then carried out by examining the signals recorded along the cable's outer circumference in two scenarios: one involving the existence of an air defect and the other with the presence of a water tree. Moreover, we introduced the concept of space charge to study its behavior in detecting minor defects. It is

noteworthy that extensive experimental work has been carried out on non-destructive testing using space charge, owing to the significant correlation established by various authors [9-12] between the accumulation of space charge and the presence of water treeing in the insulation of electrical cables.

The objective of this study is to provide a detailed understanding of the electrical behavior and the impact of space charge on defect detection in electrical cable insulation, with a specific focus on water trees.

II. MODELING OF INDIVIDUAL SEMI-ELLIPTICAL SHAPE DEFECT

In our simulation, we opted for a model of water trees with homogeneous electrical properties, characterized by a permittivity of 5 [13][14] and a conductivity of 10^{-6} S/m [15][16]. In this case, the water tree is modeled as a semi-elliptical shape, with one of the axes parallel to the direction of the electric field shown in Fig. 1.

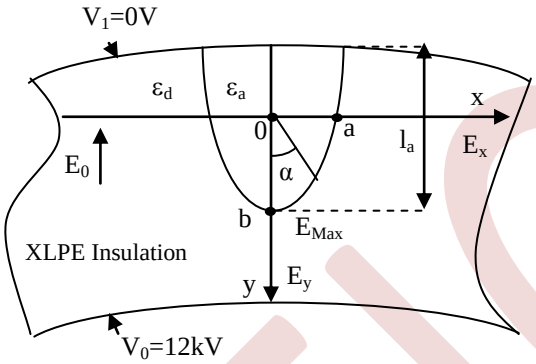


Figure 1. Maximum dielectric strength value obtained at point b, the apex of the ellipse along the ordinate axis (oy), for $\alpha=\pi/2$

The concentration of the field at the tips of the water trees is attributed to their elliptical shape (e), as given by (2) [15]:

$$e = \left(1 - \frac{b^2}{a^2}\right)^{1/2} \quad (1)$$

$$E_{max} = \frac{\left(\frac{\varepsilon_a}{\varepsilon_d}\right)}{1 + \left(\frac{\varepsilon_a}{\varepsilon_d} - 1\right)/k_f} E_0 \quad (2)$$

with:

$$k_f = \frac{1}{\left(\ln\left(\frac{1+e}{1-e}\right) - 2e\right)\left(\frac{1-e^2}{2e^3}\right)} \quad (3)$$

$$E_0 = V_0/d \quad (4)$$

d is the thickness of the insulation, V_0 and E_0 are the applied electric field and voltage respectively.

III. GOVERNING EQUATIONS

The values of the electric field $\vec{E}$ were computed in electrostatic state by using the following equations:

$$\vec{E} = -\vec{\nabla} V \quad (5)$$

$$\vec{\nabla}.\left(\varepsilon_0 \varepsilon_r \vec{\nabla} V\right) = -\rho_V \quad (6)$$

Where, $\varepsilon_0=8.85*10^{-12}$ F/m is the vacuum permittivity, ρ_v the space charges density, V is the electric potential; $\vec{E}$ is the electric field.

Due to the linearity and the isotropic material of the medium, equation (6) becomes:

$$\nabla^2 V = -\rho_V / \varepsilon_0 \varepsilon_r \quad (7)$$

The boundary conditions for the configuration shown in Fig.1 are: Dirichlet boundary conditions have been set on the surfaces S_1 (V_0= 12 kV) and S_2 (V_1= 0 kV).

IV. SIMULATION RESULTS

Fig. 2 illustrates the field distribution within the insulation, showing the deformation of electric field lines and their concentration at the tips of the trees.

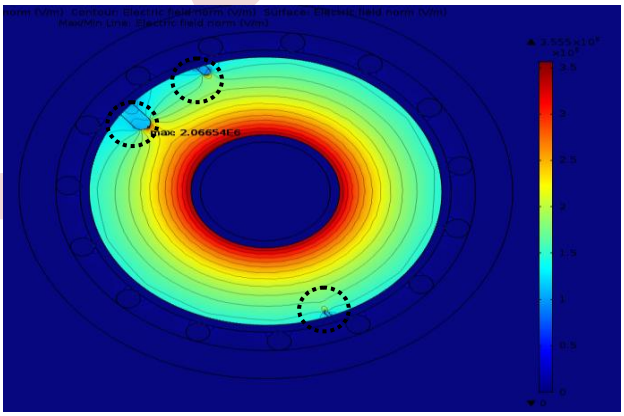


Figure 2. Distribution of the electric field in different layers of the cable in the presence of water trees

The electric field undergoes alterations due to the dielectric nature of the water trees, exhibiting a high intensity at the tips of the trees. The maximum value is 2.066kV/mm. The variation of this value depends on the length of the water trees l_a and its permittivity ε_a [17]. It also relies on the ellipticity of the water tree (e), as clearly depicted in Fig.1.

A. *Presence of water trees in the internal insulation of the cable*

In this section, we examined the correlation between the length of the water tree and the ability to detect this defect. To do so, we considered three different values for the length of the

water tree, namely: l_{a1}, l_{a2}, and l_{a3}, with values of 0.5 mm, 0.9 mm and 1.5 mm, respectively, as shown in Fig. 2.

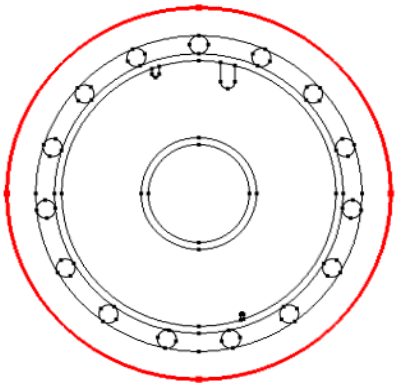


Figure 3. Highlighted in red: tracing along the outer perimeter of the cable

Fig. 3 illustrates the periphery of the cable where the various curves of the electric field and potential have been visualized.

Fig. 4 shows the variation of the electric field, while Fig. 5 illustrates the variation of the electric potential obtained along the outer circumference of the cable.

The defect with a length l_3 of 1.5mm generates a peak electric field of 2272.2V/m, as shown in both Fig. 4 and 5 under a voltage of 12.56V. These electric field values are determined along the outer circumference of the cable. These results in a variation in electric field ΔE of 492V/m compared to the initial average value of approximately 1780V/m. Indeed, the use of a proximity sensor makes it easy to detect this defect. However, the two defects with lengths of 0.5mm and 0.8mm, respectively, are difficult to detect from the exterior surface of the cable.

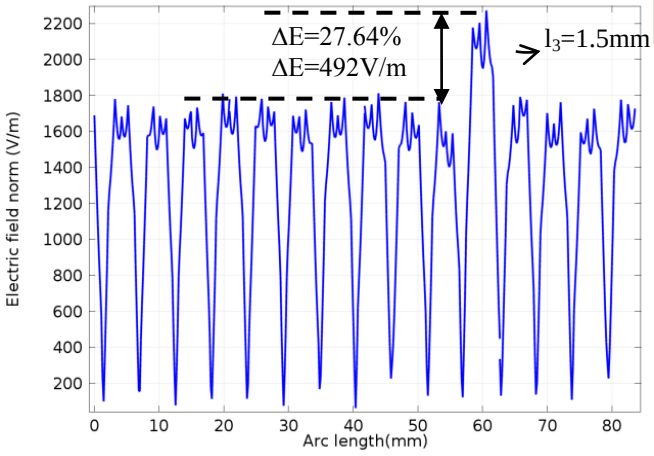


Figure 4. Distribution of the electric field with water treeing defect

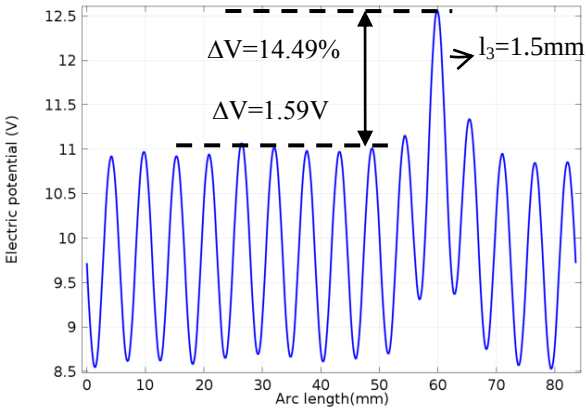


Figure 5. Distribution of the electric potential with water treeing defect

B. Presence of air defects in the internal insulation of the cable

In this section, our focus is specifically directed toward the detection of air defects, with the aim of conducting a comparative analysis between water-filled trees (consisting solely of water-filled cavities) and air defects (composed exclusively of air). To achieve this objective, the geometric shape and positioning of water and air defects remain unchanged, maintaining their semi-elliptical configuration, while the air defects are characterized by a relative dielectric constant of 1.

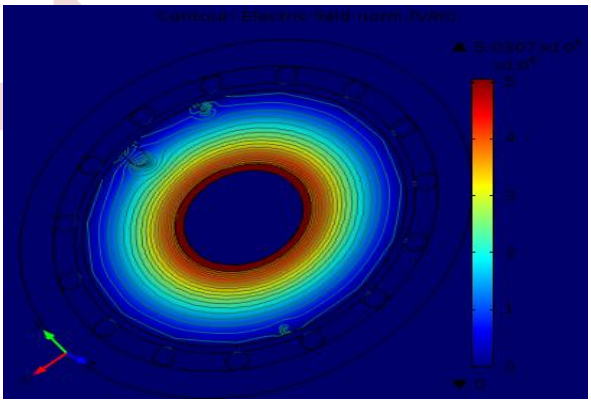


Figure 6. Distribution of the electric field in different layers of the cable in the presence of air defects

The equipotential lines approach and concentrate where the air defects are located. Considering that any convergence of equipotential lines is associated with an increase in electric field intensity, its maximum value is 2.246 kV/mm, as illustrated in Fig. 6. Additionally, there is a local decrease in the electric field at the end of the air defects, with a minimum value of 0.5 kV/mm. Furthermore, since the air is characterized by low dielectric constant, the electric field is greater inside and weaker outside of these defects. Note that equipotential lines extend into the air defects.

Both Figs. 7 and 8 depict the distribution of electric field and electric potential in the presence air defects. The defect

generates a peak electric field of 1500 V/m and a voltage of 10V. These values are lower than the initial values without defects, which are around 1760 V/m. The variation in the field and potential quantities, ΔE of 11.08%, and ΔV of 7.22%, respectively.

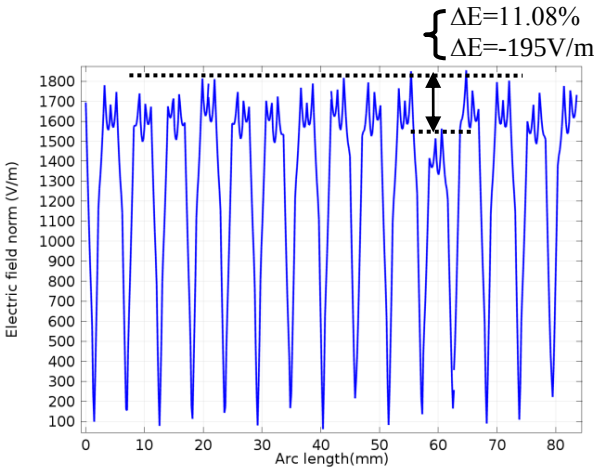


Figure 7. Distribution of the electric field in the presence of air defect

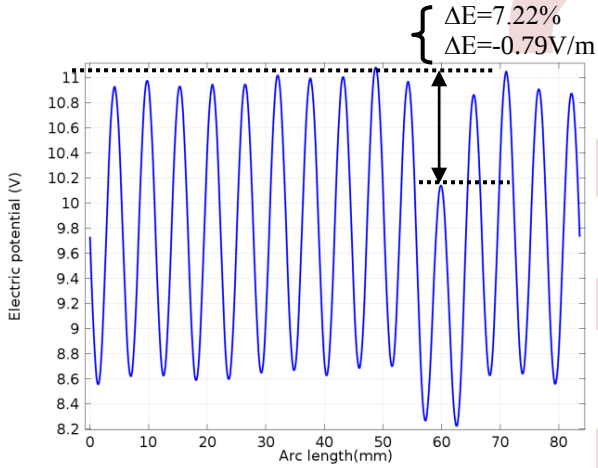


Figure 8. Distribution of electric potential in the presence of air defect

C. Simultaneous presence of water trees and air defects

From Fig. 9, depicting the variation of the electric field, we can distinguish the peaks corresponding to the two air defects and the peak of the electric field associated with the water treeing. Indeed, the maximum value of the field for the water treeing exceeds the initial value without defects, while for the air defects, this maximum value remains lower than the initial value in the case of healthy insulation. This difference can be explained by the concentration of the electric field inside the air defects, whereas in the case of the water treeing, the field concentrates at the tips.

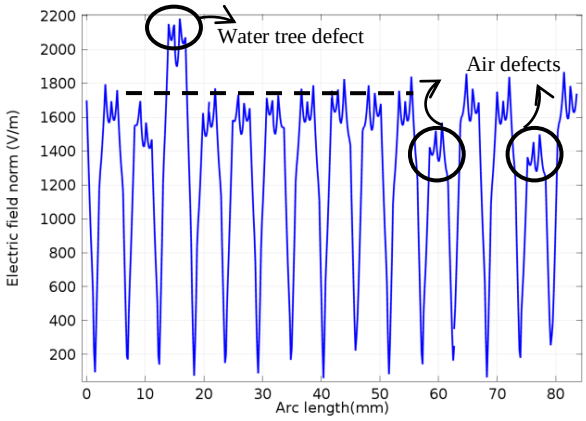


Figure 9. Distribution of the electric field in presence of both, water trees and air defect

D. Space charge and water tree detection

An optimal design of electrical cables generally requires a uniform internal electric field. However, this field can be distorted due to the presence of space charges. Furthermore, changes in the distribution of these charges, caused by degradation, will reveal the degree of deterioration through their measurement. This approach can also be applied in diagnostic techniques [4]. Thus, closely monitoring the space charge is often crucial in assessing insulation performance. That is why we set out to introduce this space charge into the internal insulation of the cable, in order to closely observe the variations in electric field and potential along the cable's outer circumference. In this section, we incorporated the influence of the space charge on the three lengths of water trees previously chosen in the preceding section. The objective was to assess the impact of the space charge on the detection of small defects, particularly those of short length. Fig. 10 displays the variations in the electric field, while Fig. 11 illustrates the variation of the electric potential along the outer circumference of the cable in the simultaneous presence of water trees and space charge. In the presence of space charges, the variation in field and potential magnitudes (ΔE= 96.59%, ΔV= 62.34%) is much more significant than the initial values without a defect. The presence of space charges thus leads to a substantial increase in the electrical stress on the insulation, as confirmed by Figs. 10 and 11.

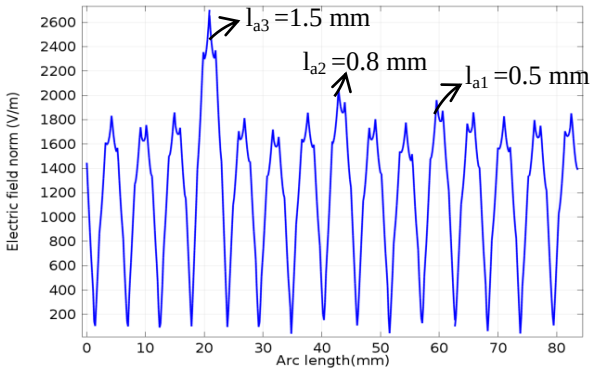


Figure 10. Distribution of the electric field in the presence of space charge as seen from the outer surface of the cable.

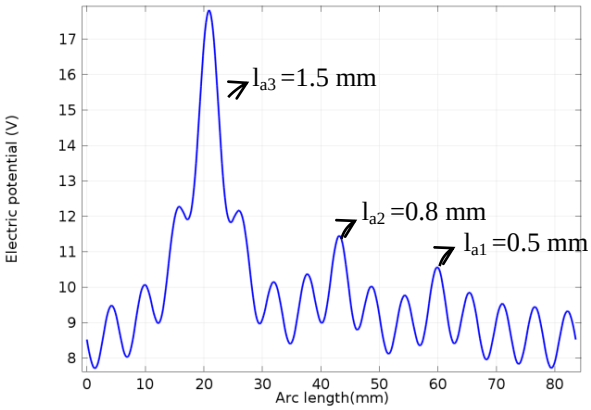


Figure 11. Distribution of the electric field in the presence of space charge as seen from the outer surface of the cable

E. Impact of space charge quantity on the detection of water trees

In order to validate the authors' experiments regarding the detection of water treeing through the measurement of space charge, seen as a non-destructive control method, particular attention is given to the amount of space charge and its impact on the amplification of the internal field at the tips of the water trees, thereby influencing defect detection. To this end, four charge values have been selected, namely: 0.1C/m^3, 0.2C/m^3, 03C/m^3, and 04C/m^3. Fig. 12 displays the variation in the electric field, while Fig. 13 illustrates the variation of the electric potential along the outer circumference of the cable for four different space charge quantities. The modification of charges locally disrupts the electrostatic equilibrium within the insulation, resulting in a measured response in terms of voltage or electric field along the outer circumference of the cable.

Analyzing this signal allows for deducing the distribution of the electric field and the space charge density within the insulation. Figs. 12 and 13 illustrate how increasing the space charge amplifies the field at the tips of the water trees, thereby facilitating the identification of their location. Ultimately, the behavior of the space charge proves to be a useful means for diagnosing faults in electrical cables.

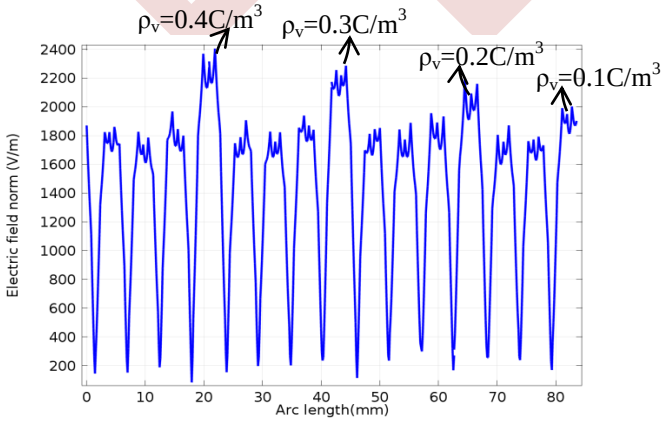


Figure 12. Variation of the elecric field as a function of the amount of space charge

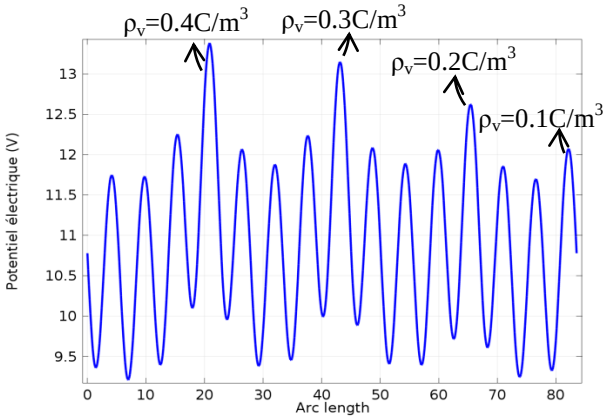


Figure 13. Variation of the potential as a function of the amount of space charge

V. CONCLUSION

Through numerical simulations, we analyzed the response in terms of electric potential and field in the presence of defects in the internal insulation of an electrical cable. This response, expressed as variations in electric potential and field along the outer circumference of the cable, allowed us to distinguish between air defect and water trees defect, based on their differences in electrical permittivity. The main objective was to assess the ability of a proximity sensor to detect small defects. Three defects of different lengths, namely 0.5 mm, 0.8 mm, and 1.5 mm, were considered. The results showed that only the 1.5 mm water tree was detected, emphasizing the influence of space charge on the insulation behavior in the presence of defects. To measure the effect of introducing this space charge on the detection of 0.5 mm and 0.8 mm defects, a quantity of 0.1 C/m³ was introduced into the cable insulation. The results of investigation confirmed the correlation between space charge and the detection of water trees, revealing that the electric field and potential reach maximum values at the peaks of the water trees, where the space charge is present. The increase in the value of this space charge, going from 0.1 C/m³ to 0.4 C/m³, allows us to observe that the augmentation of space charge leads to an increase in the electric field at the tip of the water tree structure. This increase results in the detection of the small water tree, initially measuring 0.5 mm in length, through the observed field amplification along the outer circumference of the cable. In conclusion, our simulation results confirm that measuring this space charge represents an effective non-destructive diagnostic method for detecting water trees.

REFERENCES

[1] I. Paprotny, P. K. Wright, R. M. White, J. Evans, T. Devine, "Fault Analysis in Underground Cables", Final Project Report, CIEE Electric Grid Research, University of Californian, Berkeley, 2012.

[2] Q. Chen, "*Water-Tree Modelling and Detection for Underground Cables*", Thesis in electrical engineering , Clemson University, 2017.

[3] M. J Given, R. A Fouracre, S. J MacGregor, M. Judd, H. M Banford, "Diagnostic Dielectric Spectroscopy Methods Applied to Water-treed Cable", IEEE Trans. Dielectr. Electr. Insul., Vol. 8, pp. 917-920, No.6, 2001.

[4] Tatsuo Takada, Naohiro Hozumi, "Space Charge Measurements as a Diagnostic Tool for Power Cables", IEEE Power Engineering Society Winter Meetin, 23-27 January, Singapore, 2000.

[5] T. Kurihara, T. Okamoto, T. Tsuji, K. Uchida, M. H. Kim, N. Hozumi, "Fundamental Study on Residual Charge Detection with Pulse Voltages as Diagnostic Method of Water Tree-Degraded XLPE Cables", IEEE International Conference on Condition Monitoring and Diagnosis, 23-27 September, Bali, Indonesia, 2012.

[6] K. Suenaga, K. Uchida, N. Hozumi, "Location of Water Tree Degraded Point Along XLPE Cable Line Using DC Voltage", International Conference on Condition Monitoring and Diagnosis, Beijing, China, April 21-24, 2008.

[7] T. Kurihara, T. Okamoto, M. H. Kim, N. Hozumi, T. Tsuji and K. Uchida "Measurement of Residual Charge using Pulse Voltages for Water Tree Degraded XLPE Cables Diagnosis", IEEE Transactions on Dielectrics and Electrical Insulation Vol. 21, No. 1; pp. 321-330, 2014

[8] L. Andrei, I. Vlad, F. Ciuprina, "Electric Field Distribution in Power Cable Insulation Affected by Water Trees", 9th international symposium on advanced topics in electrical engineering, Bucharest, Romania, 7-9, 2015.

[9] Y. Li, J. Kawai, Y. Ebinuma, Y. Fujiwara, Y. Ohki, Y. Tanaka and T. Takada", "Space charge behavior under ac voltage in water-treed PE observed by the PEA method", IEEE Trans. Dielectr. Electr. Insul., Vol. 4, No.1, pp. 52-57, 1997.

[10] J.H. Lee, S.M. Cho, I-K. Song, "Correlation between the AC breakdown strength and space charge distribution of water tree aged XLPE", IEEE Conf. Electr. Insul. Dielectr. Phenomena (CEIDP), Atlanta, GA, USA, Vol. 2, pp. 657-660, 1998.

[11] Y. Ohki, Y. LI, J. Kawai, Y. Ebinuma, Y. Fujiwara, "Space Charge behavior under AC voltage application in water-treed polyethylene observed by the pulsed electroacoustic method", IEEE Conf. Electr. Insul. Dielectr. Phenomena (CEIDP), San Francisco, USA, pp. 52-57, 1996.

[12] K. Suzuki, Y. Tanaka, T. Takada, Y. Ohki, C. Takeya, "Space Charge Distribution Measurement in XLPE Cable for Detection of the Water Tree Location", IEEE Conf. Electr. Insul. Dielectr. Phenomena (CEIDP), , pp. 630-633, 1999.

[13] I.Radu, M.Acedo, P.Notingher, F.Frutos, J.C.Filippini "A stady on the dependence of water tree permittivity with time" Ann. Report Conf. Elect. Insul. Dielect. Phenom, pp.762-765,Vol.2, 1996.

[14] T. Toyoda, S. Mukai, Y. Ohki, Y. Li, T.Maeno "Conductivity and permittivity of water tree in polyethylene", IEEE Conf. Electr. Insul. Dielectr. Phenomen, Vol.2, pp.577-580, 1999.

[15] J.L. Chen and J.C. Filippini, "The morphology and behavior of the water tree", IEEE Trans. Dielectr. Electr. Insul., Vol. 28, No. 2, pp. 271-286, 1993

[16] T.Czaszejko "3D Electrical Network Model of Water Tree" Conference on Electrical Insulation and dielectric Phenomena, pp.799-802, Vol.2, 1996.

[17] I. Radu, P.V. Notingher and J.C. Filippini, "Influence of water trees on the electric field distribution and breakdown in the point-point geometry", J. Electr., Vol.48, pp. 165-178, 2000.

Influence of geometric parameters on the K factor of the current-voltage characteristic of DC corona discharge.

Chouali Sabrina[1], Kasdi Ahmed[1], Atroune Salah[1], Dascalescu Lucian[2]

[1] *Electrical Engineering Laboratory, Faculty of Technologie, University A. Mira of Bejaia, Algeria*

sabrina.chouali@univ-bejaia.dz

ahmed.kasdi@univ-bejaia.dz

salah.atroune@univ-bejaia.dz

[2] *Institut PPRIME, CNRS - Université de Poitiers – ENSMA, IUT, Angoulême, 16000, France.*

lucian.dascalescu@univ-poitiers.fr

***Abstract*—This article provides a comprehensive analysis of the current-voltage characteristics associated with corona discharge in a wire-plane configuration. Townsend's law ($I=K\times V\times(V-V_0)$) has been employed to explore and evaluate the impact of various parameters on positive corona discharge.**

From the curves, it was found that the geometric K factor is significantly influenced by both wire diameter and inter-electrode distance. Indeed, a reduction in the inter-electrode distance and a small curvature radius lead to higher discharge currents. This result is also illustrated by the use of the design-of-experiments approach, which enables us to determine the trend in K-factor variation for other values of the two parameters studied.

Keywords: **Corona discharge, I-V characteristic, Design of experiments, Onset voltage.**

I. INTRODUCTION

Electrical phenomena have captivated the curiosity of scientists since the earliest days of human civilization. Throughout history, physicists have tirelessly sought to unravel the mysteries behind these phenomena. Among the various electrical manifestations, the corona discharge stands out as a particularly intriguing natural phenomenon with optical, acoustic, and electrical dimensions.

What makes corona discharge so interesting is its property of being easily produced under controlled conditions, ensuring stability and reproducibility. This is why researchers in a variety of fields have been particularly interested in exploring its potential applications.

Corona discharge has found practical use in a large number of electrostatic processes [1-2]. These applications include dust precipitation [3], the separation of granular mixtures [4-5] and the treatment of polyethylene films for cable insulation [6-7]. However, optimising the configuration and operating parameters of corona discharge systems is essential to effectively manage production costs [8].

Therefore, many studies have focused on the electrode systems used in corona discharge installations. Various types of corona electrodes have been developed, including point-to-plane [9] blade-to-plane [10], wire-to-plane [11], bipolar wires-to-plane [12], multipoint-to-plane [13], wire-cylinder [14], wire-cylinder-to-plane [15], and blade-plane electrodes [16]. Among these configurations, wire-to-plane electrodes are the most commonly employed due to their simplicity and cost-effectiveness. In this setup, the corona discharge occurs between a grounded collector plane and a wire electrode.

The current-voltage characteristic is one of the main ways of describing corona discharge. This relation presents a particular model in which the current increases progressively from the corona discharge initiation voltage until it attains the breakdown voltage. Researchers have extensively studied the current-voltage characteristics of corona discharge for both positive and negative discharges [17-18], carrying out numerous studies under various operating conditions and with different electrode geometries.

K. Meziane and al [19] investigated the corona discharge in blade-to-plane configuration. In their experimental study, they explored the impact of various geometric parameters on the formation of positive and negative corona discharges. These parameters include the inter-electrode distance, the spacing between the blades and the number of discharge blades.

Ouatah and al [20] explored the effect of ambient temperature and electrode gap on the current of a negative corona discharge in a rod-plane electrode configuration, and aimed to explore the impact of ambient temperature and electrode gap on a negative DC discharge in a rod-plane geometry. The study revealed that Townsend's formula

(I=$K.V.(V$-V_0)) proved to be the most appropriate model to describe the discharge behaviour. Experimental results showed that, when the same voltage level was applied to the high-voltage electrode, the discharge current increased with increasing temperature and decreased with increasing gap between the electrodes.

In the case of the wire-to-plane electrode configuration, Ait Said and al. [8] carried out a detailed analysis of the behavior of DC corona discharge in air. They explored the wire-to-plane geometry and employed formulae such as $I = K.V(V - V_0)$ and $I = A.(V - V_0)^m$ to determine various corona discharge parameters for both positive and negative polarities . Through curve fitting, they demonstrated that geometric factors K and A, as well as the exponent m, are significantly influenced by the number of discharging wires.

Aissou and al [17] presented a study on the influence of relative humidity (R_H) on the current-voltage characteristics of positive and negative corona discharges.

In their study they examined the impact of relative humidity (R_H) on the current-voltage characteristics of positive and negative corona discharges. Significantly, increasing R_H resulted in a large decrease in corona current for a given applied voltage. However, wire diameter also had an effect on these characteristics. Specifically, the initial voltage V_0 increased with increasing wire diameter 2R, while the corona current decreased with the same increase in 2R. In fact, the exponent m showed an inverse relationship with variations in wire diameter, decreasing as the wire diameter increased. It should be noted that negative values of current density and electric field were observed to be higher than positive values for the same applied voltage.

Ait Said and al [18] studied the current-voltage characteristic of the corona discharge in a wires-to-plane configuration. They carried out measurements that revealed a square-law equation between the corona current and the applied potential. To analyse the current-voltage characteristic and the mobility of the charge transporters, they used Cooperman's model [21] for the wire-to-plane system. It appeared that this characteristic was significantly influenced by the relative humidity of the surrounding air.

The main aim of this article is to study the current-voltage characteristics (I–V) of corona discharge in wire-plane geometry. The study will explore the impact of inter-electrode spacing and active electrode wire diameter on the I–V characteristic, and in particular on the geometric K factor.

II. MATERIALS AND METHODS

A. *Experimental set-up*

The wire-to-plane configuration considered in the present study is schematized in Fig. 1. The active electrode (ionizing wire) (1) consists of a nickel wire with a small radius of curvature R_w located at a distance H from the passive electrode (set of planes grounded plane) (3). The nickel wire is fixed by two insulating supports (2) at height H relative to the plane. The active electrode is raised to positive or negative potential. A set of plate electrodes (3), composed of a measuring plane (3a) surrounded by two grounded guard plates (3b), is placed at a distance h from the wire. The three plates are separated by very small spacers to ensure the continuity of the electric field. A current collector (S), incorporated in the center of the measurement plane (3a), is connected to a current measuring device (4) by a coaxial cable (5). These electrodes rest on two plates; one is insulating while the other is conductive and connected to the ground, all resting on a wooden support (6).

B. *Measurement of the current-voltage characteristic*

Analysis of the current-voltage characteristic of corona discharge is crucial to understanding its electrical behavior and optimizing the design of devices that exploit this phenomenon. A test method is used to measure this characteristic. This method involves gradually increasing the voltage V_a applied to the active electrode (1), starting from a value V_1 below the threshold voltage V_S required to trigger the corona effect and continuing until a value V_2 greater than V_S is reached. This characteristic is measured by measuring the electric current as a function of the voltage applied progressively up to the value V_2 on the measurement plane (3a).

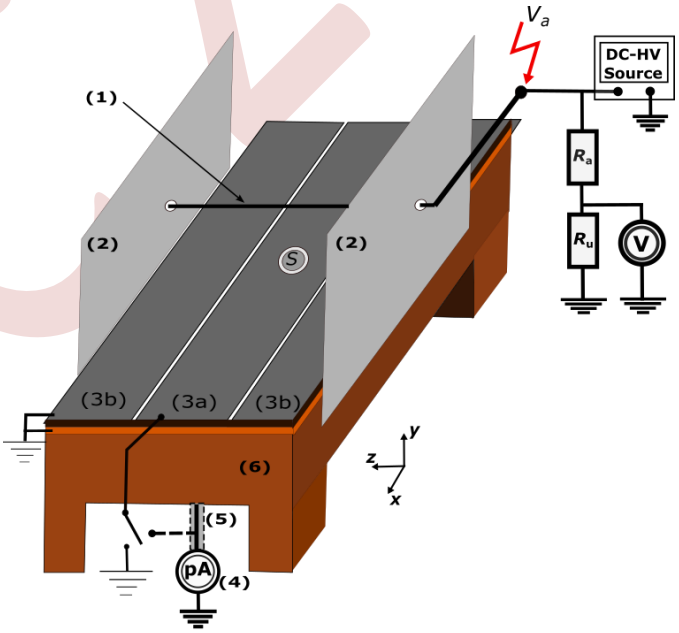


Figure 1. General view of the experimental set-up.

The current-voltage characteristic of the corona discharge obeys Townsend's formula, which bears his name. Initially, he used this law inside a coaxial cylindrical wire [22]. After several attempts, he found that this law could also be used for wire-plane geometry [23]. According to this law, the corona discharge current varies as a function of the applied voltage as follows:

$$I = K.V(V - V_0) \qquad (1)$$

Equation (1) establishes a relationship between several variables: the corona discharge current (I), the supplied voltage

(V), the corona onset voltage (V_0), and the dimensional constant (K). This constant depends on a number of factors, including the distance between the electrodes, the radius of the wire electrode, the mobility of the charge carriers in the drift zone, the humidity of the air, and other geometric characteristics.

III. Results and discussion

A. *Current – voltage characteristic*

The current-voltage characteristic curve of the positive corona discharge is shown in Figs. 2 and 3, and follows Townsend's quadratic law (1).

The current-voltage characteristics of the corona discharge were measured and calculated for the different parameters studied for the wire-plane configuration. When the applied voltage is weak, there is no current detected. However, when the voltage rises to the corona discharge initiation voltage V0, a current starts to circulate from the wire to the plane due to the ionization of the air around the electrode. At high voltage, the current increases rapidly.

B. *The influence of height on the current-voltage characteristic*

Fig.2 illustrates the influence of the wire-plane height on the current-voltage characteristic of the corona discharge. For a fixed radius of curvature and a positive applied voltage. It can be seen that the discharge current is greater and increases more rapidly with a low applied voltage for small inter-electrode distances. This is due to the concentration of charges in the plane. This has been confirmed by other geometries such as the dual geometry, as demonstrated in the following article [15].

C. *Influence of wire bending radius on current-voltage characteristic*

The impact of the wire's radius of curvature on the current-voltage characteristics is illustrated in Fig. 3. As can be seen from this graph, a smaller radius of curvature generates a lower initial voltage V_0 and a large increase in current. In fact, the wire behaves more like a point for smaller radius of curvature, generating an incredibly high electrical field at its end. This increase in electric field strength ionises the surrounding air, making it conductive and allowing the current to flow more easily between the electrodes.

D. *Variation of the K factor*

Fig. 4 describes a linear relationship between I/V and $(V\text{-}V_0)$ for all inter-electrode distances. The curves were fitted to create straight lines with an equation: $y = a * x$, where the slope 'a' represents the geometric parameter 'K' of the Townsend relationship from equation (1). From Fig. 4, it can be observed that the value of K varies inversely with variations in inter-electrode height. As the inter-electrode height increases, the K factor decreases.

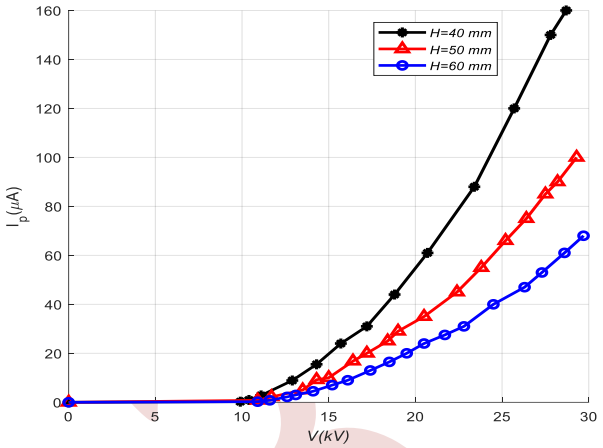


Figure 2. Current-Voltage characteristics for different values of the inter-electrode distance H (R_w = 0.15mm)

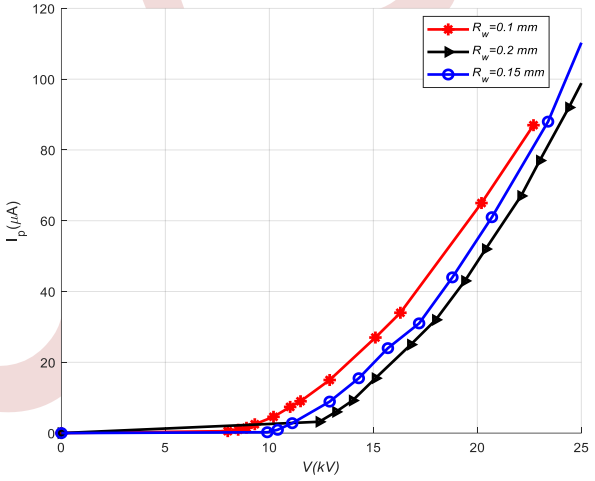


Figure 3. Current-Voltage characteristics for different values of wire radius R_w (H=40mm)

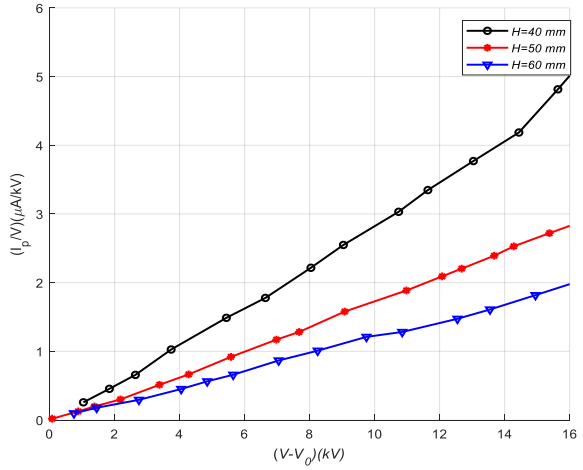


Figure 4. The dependence of the positive current-voltage ration I–V with the difference-voltage V-V_0 for different values of the inter- electrode distance H (R_w=0.2mm,).

The variation of the geometric parameter *K* according to the wire diameter and inter electrode distance *H* are shown in Figs. 5 and 6, respectively. It is apparent that when the value of *H* is lowest, the value of *K* is highest. Townsend's formula coefficient *K* is inversely proportional to *H*, similar result has already been found in rod-grid electrode systems and Rod-Plane Electrode Configuration [20][26]. Subsequently can be observed that the parameter *K* varies as the radius of curvature changes, and that its value increases as the radius of curvature increases further. For greater heights, the factor *K* stabilizes and remains relatively constant.

The values of the *K* parameter have been summarized in Table 1 for different corona discharge parameters, specifically radius of curvature and inter-electrode height.

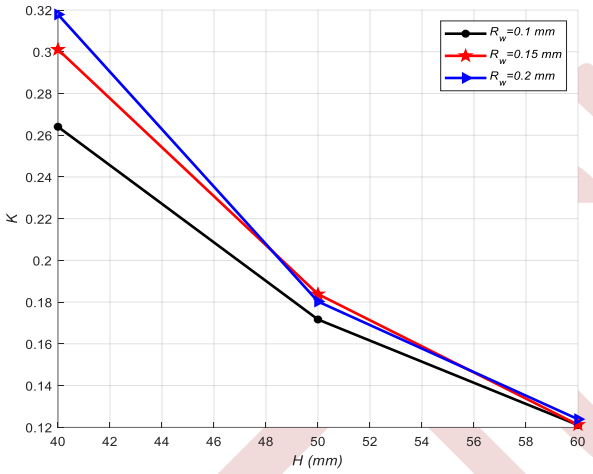


Figure 5. Variation of the *K* factor as a function of the inter-electrode distance *H*.

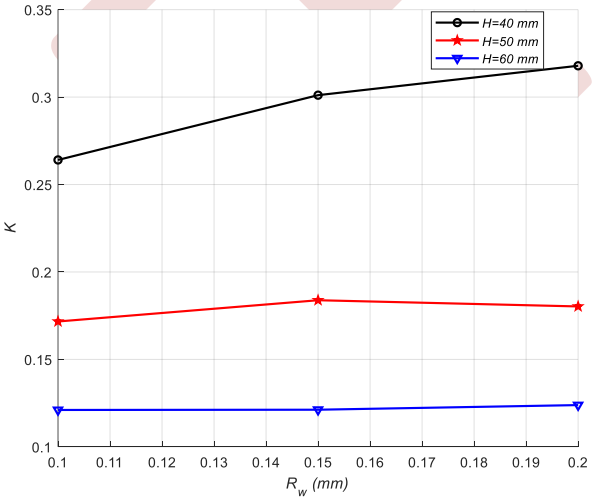


Figure 6. Variation of the k factor as a function of wire diameter.

TABLE I. RESULTS OF FACTOR *K* FOR VARIOUS OF WIRE DIAMETERS AND INTER ELECTRODES DISTANCE.

		H		
	K	40	50	60
R_w	0,1	**0.2641**	**0.1717**	**0.1211**
	0,15	**0.3011**	**0.1838**	**0.1212**
	0,2	**0.3179**	**0.1803**	**0.1239**

E. The experimental design method

Ronald A. Fisher developed the design of experiments approach in the early 20th century, and it has proved very useful in many areas of science, electrostatics included. Using statistical ideas, this experimental approach allows efficient experiments to be designed, analysed and interpreted, leading to a better understanding of complex electrostatic phenomena [24-25].

To extend our study we have used the design of experiment approach as it allows to reduce the number of experiments and to give a large value of parameters within a given interval, for this we have used the MODDE software which is a statistical modelling and data analysis tool. It is mainly used in the field of research and statistical analysis to help researchers and analysts model and understand the relationships between variables in a data set.

The variation of the *K* factor as a function of the height and radius of curvature of the electrode is shown graphically in Fig. 7. The value of the *K* factor shows a significant tendency to increase as the height decreases and the radius of curvature is clearly increased. And that the k-factor range is greater for larger inter-electrode distances.

Fig. 8 illustrates the variation of factor *K* in relation to the inter-electrode distance. This representation highlights a decrease in *K* within the distance range of 40 to 60 mm. Indeed, a larger distance results in a more dispersed distribution of the electric field, while a shorter distance leads to a more concentrated electric field. This increased concentration of the electric field promotes the formation of the corona discharge, resulting in an increase in the current on the plane and, therefore an increase in the K factor.

Fig. 9 gives the variation of the *K* factor as a function of the wire radius. It highlights an interesting observation: the value of the K factor reaches its maximum when the radius of curvature, noted Rf, is the highest. This result indicates that larger bending radii lead to greater stability in the *K*-factor. Specifically, the *K* factor is between 0.15 and 0.184 for a radius of curvature of between 0.1 and 0.2 mm.

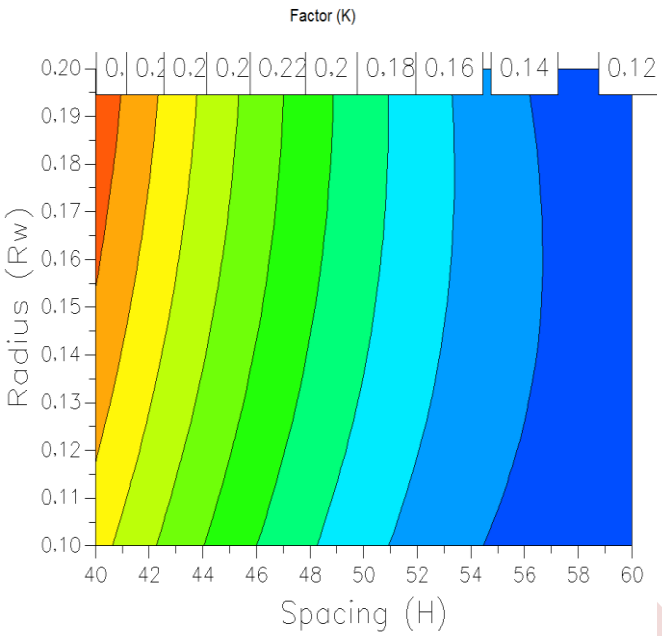


Figure 7. Contour plots of the response *K* calculated with MODDE® for the two studied parameters.

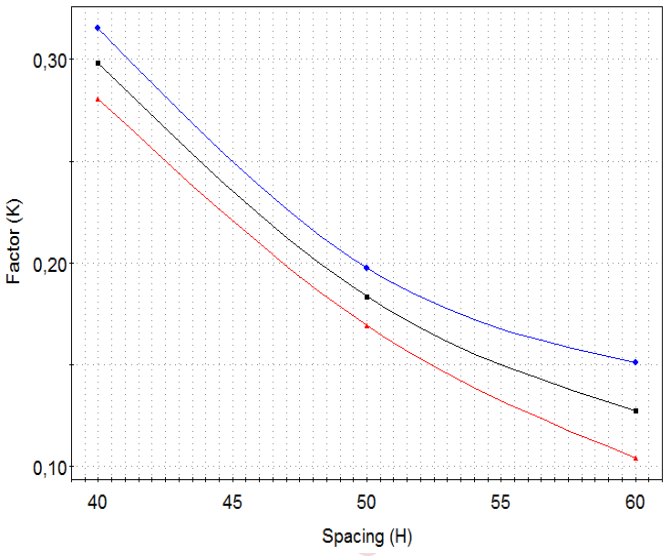


Figure 8. MODDE® predicted variation on the *K* factor as function of inter-electrode distance *H*.

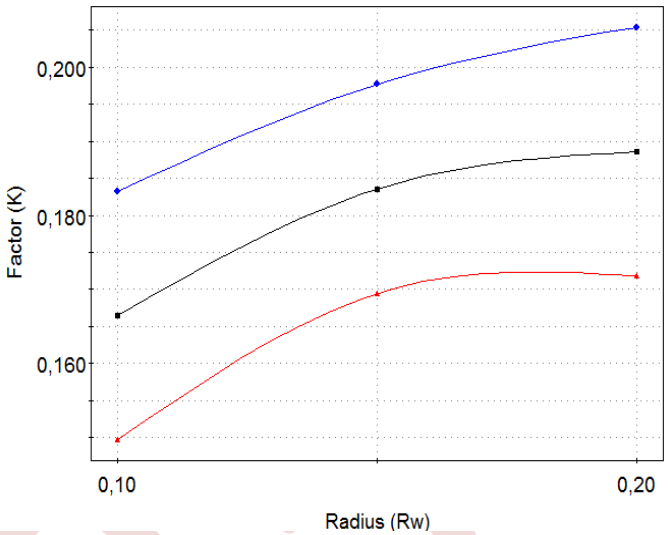


Figure 9. MODDE® predicted variation on the *K* factor as function of wire's radius

IV. CONCLUSION

In conclusion, this research has conducted an in-depth analysis of the current-voltage characteristics associated with corona discharge in a wire-plane configuration. We employed Townsend's law to investigate the influence of the *K* factor on various parameters, including the inter-electrode distance and wire curvature radius, concerning the current-voltage relationship. The results we obtained unveiled notable trends in the behavior of corona discharge.

The results indicate that the corona discharge current increases as the inter-electrode distance decreases and as the wire radius curvature decreases. In addition, the *K* factor shows higher values when the inter-electrode distance is minimized and the wire diameter is maximized.

To complete our results, we adopted Ronald A. Fisher's experimental design methodology. This approach enabled us to collect data over a range of values, allowing us to confirm the consistency of our conclusions. In summary, this study represents a significant contribution to our understanding of corona discharge phenomena in wire-plane geometry, highlighting the critical role played by factors such as inter-electrode spacing, wire radius of curvature and K-factor in developing the current-voltage characteristic.

In accord with previous studies, our results are in line with the previously reported knowledge of corona discharge phenomena, reaffirming the importance of factors such as electrode spacing, wire curvature radius and *K*-factor in defining the current-voltage characteristics in the wire-plane configuration.

REFERENCES

[1] A. Kasdi, "Etude théorique et expérimentale de la décharge couronne bipolaire". PhD Thesis, University A. Mira of Bejaia, 2007.

[2] M. Kachi, L. Dascalescu, Corona discharges in asymmetric electrode configurations, J.Electrost. 72 (1) (2014) 6–12, https://doi.org/10.1016/j.elstat.2013.11.001

[3] A. Kasdi, Computation and measurement of corona current density and V–I characteristics in wires-to-plates electrostatic precipitator, J. Electrost. 81 (2016) 1–8, https://doi.org/10.1016/j.elstat.2016.02.005

[4] L.M. Dumitran, P.V. Notingher, L. Dascalescu, Electrostatic separation of polymeric granular mixtures from medium and low voltage cables, in: The 9th International Symposium on Advanced Topics in Electrical Engineering, 2015, pp. 507–510. May 7-9, Bucharest, Romania.

[5] H. Louati, A. Tilmatine, R. Ouiddir, A. Alibida, N. Zouzou, New separation technique of metal/polymer granular materials using an electrostatic sorting device, J. Electrost. 103 (2020, https://doi.org/10.1016/j.elstat.2019.103410

[6] M.C. Plopeanu, L. Dascalescu, B. Neagoe, A. Bendaoud, P.V. Notingher, Characterization of two electrode systems for corona-charging of non-woven filter media, J. Electrost. 71 (2013) 517–523, elstat.2012.12.002, https://doi.org/10.1016/j.elstat.2012.12.002

[7] A. Messaoudene, L. Dascalescu, B. Bendahmane, Influence of high voltage waveform and frequency on the elimination of electric charges at the surface of polypropylene films, Rev. Roum. Sci. Techn. ´Electrotechn. ´Energ. 67 (2022) 3–7.

[8] H. Ait Said, H. Nouri, Y. Zebboudj, Analysis of current-voltage characteristics in the wires-to-planes geometry during corona discharge, Eur. Phys. J. Appl. Phys. 67, 30802 (2014),https://doi.org/10.1051/epjap/2014140089

[9] K. Adamiak, P. Atten, Simulation of corona discharge in point–plane configuration, Journal of ElectrostaticsVolume 61, Issue 2, June 2004, Pages 85-98, https://doi.org/10.1016/j.elstat.2004.01.021

[10] A. Reguig, "Contribution à l'étude expérimentale et numérique de la décharge couronne dans différents types de configurations d'électrodes". PhD Thesis, University Djillali Liabes of Sidi Bel-Abbes, 2017

[11] Y. Zebboudj, "Measurements of current and electric field distributions beneath a positive DC wire-to-plane corona using a linear biased probe", IEE Proc. –Sci. Meas. Technol., vol. 147, N°2, PP. 74-80, 2000. https://doi.org/10.1016/j.elstat.2015.05.019

[12] A. Kasdi, Y. Zebboudj, H. Yala, Calculation and measurement of electric field under HVDC transmission lines, EPJ Applied Physics 37 (2007) 323–329, https://doi.org/10.1051/epjap:2007026

[13] O. Chibane, A. Rahmani, K. Smili, B. Bendahmane, L. Dascalescu, A. Kasdi,Experimental characterization of multi-wire corona electrode configurations,J. Electrost. 111 (2021), https://doi.org/10.1016/j.elstat.2021.103575.

[14] A. Kasdi, Y. Zebboudj and H. Yala, Numerical Simulation of Corona Discharge using Comsol Multiphysics, 1st International Conference on Electrical Energy and SystemsOctober 22-24th,2013.

[15] A.Kasdi, S.Chouali,,A,Bekakria, L.Dascalescu, Experimental and numerical modeling of DC corona discharge in Wire-Cylinder-Plane configuration, Journal of Electrostatics 123 (2023) 103814 https://doi.org/10.1016/j.elstat.2023.103814

[16] J. Wu , P. Traore , C. Louste , D. Koulova , H. Romat , Direct numerical simulation of electrohydrodynamic plumes generated by a hyperbolic blade electrode, Journal of Electrostatics Volume 71, Issue 3, June 2013, Pages 326-331, https://doi.org/10.1016/j.elstat.2012.10.011

[17] M. Aissou, H. Aitsaid, H. Nouri, Y. Zebboudj, Effect of relative humidity on current–voltage characteristics of monopolar DC wire-to-plane system, J. Electrost. 76 (2015) 108–114,

[18] H. Ait Saida,, M. Aissou, H. Nouri and Y. Zebboudj, Analysis of the Current–Voltage Characteristic during the Corona Discharge in Wires-To-Planes Electrostatic Precipitator under Variable Air Humidity, ACTA PHYSICA POLONICA A,N3, Vol. 135 (2019), http://doi.org/10.12693/APhysPolA.135.320

[19] Meziane Kaci, Hakim Ait Said, Abdelkrim Laifaoui, Massinissa Aissou, Hamou Nouri, and Youcef Zebboudj, Investigation on the Corona Discharge in Blade-to-Plane Electrode Configuration, GENERAL AND APPLIED PHYSICS, Braz J Phys (2015) 45:643–655.

DOI 10.1007/s13538-015-0357-4

[20] El Hanafi OUATAH, Soufiane MEGHERFI, Boukhalfa BENDAHMANE, and Youcef ZEBBOUDJ , Effect of Room's Temperature and Electrode Gap on Current of Negative Corona Discharge in Rod-Plane Electrode Configuration, Mathematical Modelling of Engineering Problems, Vol. 9, No. 2, April, 2022, pp. 298-304.

https://doi.org/10.18280/mmep.090202

[21] G. Copermann, IEEE Trans. Ind. Appl. 17, 236 (1981)

[22] M. Townsend, Electricity in Gases (Oxford University Press, 1915), pp. 375–376

[23] E. Badareu, I. Popescu, Gaz ionisés: d´décharges ´électriques dans les gaz (Dunod, Paris, 1965)

[24] S. Atroune and al.,Comparative experimental study of triboelectric charging of two size classe of granular plastics Part. Sci. Technol. (2015)

[25] A.Atroune and al, A vibratory-type triboelectric charging device design of experiments based modelling for controllable and uncontrollable parameters effect study, Journal of Electrostatics Volume 123, May 2023, 103816, https://doi.org/10.1016/j.elstat.2023.103816 .

[26] Yamada, K. (2004). An empirical formula for negative corona discharge current in point-grid electrode geometry. Journal of Applied Physics, 96(5): 2472-2475. http://dx.doi.org/10.1063/1.1775301

Evaluating the Lifetime of Polyvinyl Chloride Insulation under Sinusoidal Voltage Stress

Abdelkrim LAIFAOUI[1], Hakim AIT SAID[1,2], Jean Michel REBOUL[3] and Mohand Seghir HERZINE[1]

[1]*Electrical Engineering Laboratory, University of Bejaia, Bejaia, 06000 Algeria*

jean-michel.reboul@unicaen.fr

[2]*Electrical Engineering and Automatic Department, University of Relizane, Relizane, 48000 Algeria*

hakim.aitsaid@univ-relizane.dz

[3]*Laboratoire Universitaire des Sciences Appliquées de Cherbourg, University of Caen basse - Normandie, France*

jean-michel.reboul@unicaen.fr

***Abstract*— This study analyzes the electrical aging of polyvinyl chloride sheath samples based on lifetime curves. Tests were carried out by subjecting the samples to 12 levels of alternating sinusoidal voltage, ranging from 15.5 kV to 40 kV. A total of 600 measurements were made. The results obtained were analyzed using the Weibull method, then validated using the chi-square test with 90% confidence intervals. The study provides a better understanding of the dielectric behavior of PVC under sinusoidal electrical stress and allows estimating the lifetime of PVC sheaths under real operating conditions**

***Keywords:* Aging, Inverse power model, Electrical endurance coefficient.**

I. INTRODUCTION

Solid insulators, of which polyvinyl chloride (PVC) is one example, play an essential role in insulation systems for high and medium voltage applications. PVC is a widely used amorphous thermoplastic polymer, known by its common abbreviation, PVC. Its technical versatility and economic cost make it a common choice for insulation in many electrical power generation and transmission equipment. However, despite its undeniable advantages, dielectric materials such as PVC do have their drawbacks, which include significant dielectric losses at specific voltage levels. Knowledge of the dielectric strength of these materials is therefore essential to ensure their appropriate use in medium or high voltage devices, enabling efficient transmission and distribution of electricity.

The ageing of a material is an inescapable phenomenon that results in a slow and irreversible change in its properties over time. Several complex mechanisms are involved in this process, including oxidation, hydrolysis and photoxidation. [1].

In the context of power cables, electrical ageing is closely linked to that of the material used for insulation. As years of operation accumulate, changes, whether chemical or physical, take place and alter the electrical properties of solid insulators. These changes can lead to a reversible or irreversible loss of functional properties, or even to the dielectric breakdown of insulating materials [7].

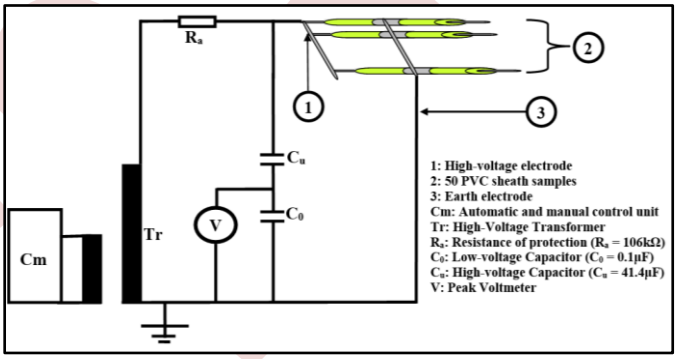


Figure 1. Electrical ageing test device

These changes can lead to a reversible or irreversible loss of functional properties, or even to the dielectric breakdown of insulating materials [7].



Figure 2. PVC sheath and electrodes

The life of a cable is generally shorter when the applied electric field is high. The physical mechanisms responsible for short-term failure are complex, encompassing concepts such as thermal, electromechanical and electrical failure. In contrast, long-term electrical breakdown is the result of a slow process involving the evolution of the dielectric's physicochemical properties.

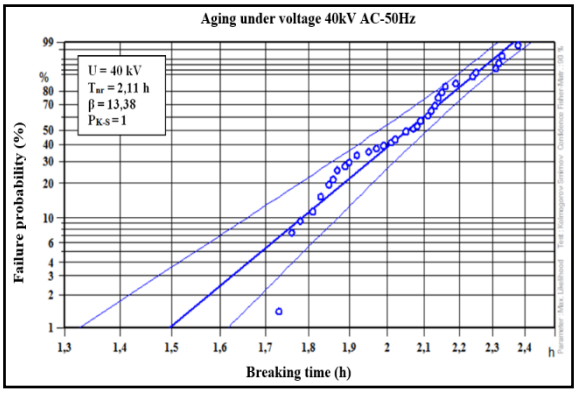


Figure 3. Ageing under sinusoidal voltage 40kV

These aspects are particularly crucial in the field of high voltage, where the reliability and durability of electrical systems are major concerns.

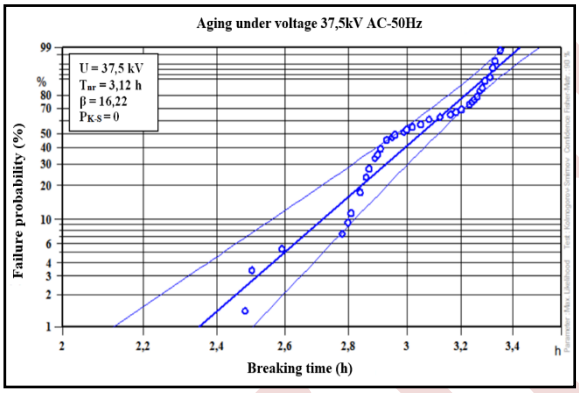


Figure 4. Ageing under sinusoidal voltage 37.5kV

This study looks specifically at the electrical ageing of PVC sheaths used for electrical insulation in high-voltage applications. The aim is to analyse the evolution of the properties of these sheaths over time, with particular emphasis on lifetime curves. The tests were carried out by subjecting samples of PVC sheaths to 12 levels of sinusoidal alternating voltage, ranging from 15.5 kV to 40 kV. A total of 600 measurements were taken, providing significant data on the behaviour of these materials in the face of electrical ageing.

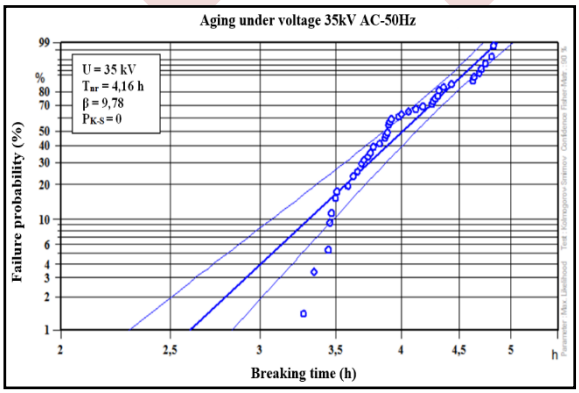


Figure 5. Ageing under sinusoidal voltage 35kV

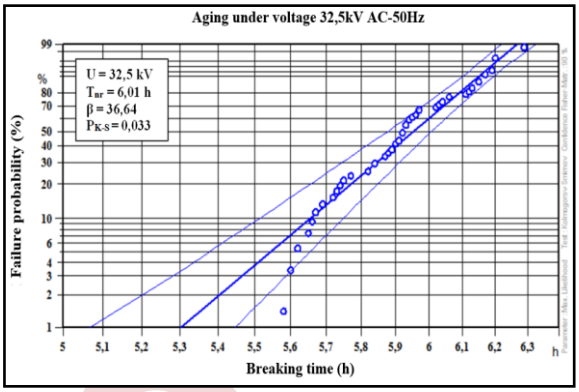


Figure 6. Ageing under sinusoidal voltage 32.5kV

The results were processed using the Weibull method, a statistical approach commonly used to analyse the reliability of materials [8]. The results obtained were validated using the chi-square test, which relies on 90% confidence intervals to guarantee the robustness of the statistical analysis [9].

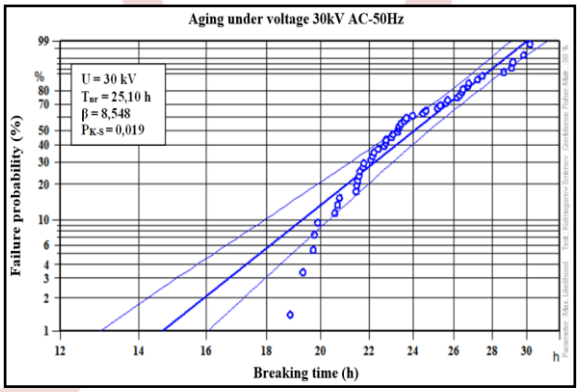


Figure 7. Ageing under sinusoidal voltage 30kV

This research is of great importance to the electrical power sector, as it contributes to a better understanding of the behaviour of PVC insulation under long-term electrical stress. Ultimately, a better understanding of these processes will enable the design of more reliable and durable electrical systems, while optimising maintenance operations and reducing operating costs.

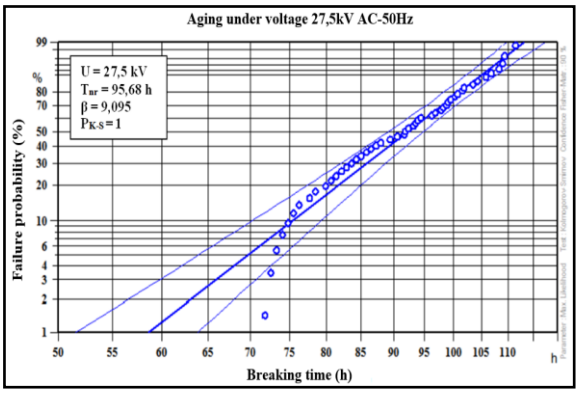


Figure 8. Ageing under sinusoidal voltage 27.5kV

The electrical ageing of polyvinyl chloride (PVC) sheaths under sinusoidal AC voltage will be at the heart of this study. It is essential to note that dielectric breakdown is a random phenomenon, implying the need to conduct experiments on a significant number of samples to obtain reliable results. The most appropriate model for characterising dielectric breakdown statistically is the Weibull model, which will be used in our analysis.

Repeating these tests on a large number of samples and applying a reliability model such as Weibull's will give us a better understanding of the behaviour of PVC sheaths subjected to sinusoidal alternating voltages. This knowledge is essential for improving the reliability of electrical systems using these insulating materials and will contribute to more efficient maintenance operations, while reducing operating costs.

II. EXPERIMENTAL SET-UP

A. Material studied

The material we studied came from the company Electro-Industriel ENEL, located in Azazga, Algeria. The samples we used were polyvinyl chloride (PVC) sheaths with an internal diameter of 4 mm and a thickness of 1.5 mm. These PVC sheaths are flexible, have no weave and are classified as type B. They are yellow in colour and have a thermal class of A, which means they can be used in a temperature range from -20°C to 105°C, as shown in Figure 2.

These PVC sheaths offer additional mechanical protection, making them suitable for environments where thermal stresses are low. They are also used as electrical insulators in machinery, transformers and various electronic applications, including domestic appliances and other electrical devices.

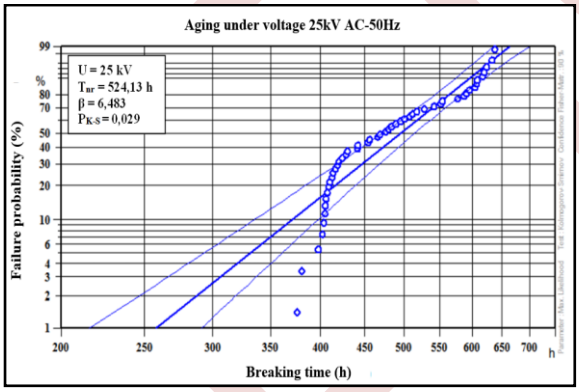


Figure 9. Ageing under sinusoidal voltage 25kV

They are also used as insulators in low and medium voltage cables, contributing to the safety and reliability of electrical systems.

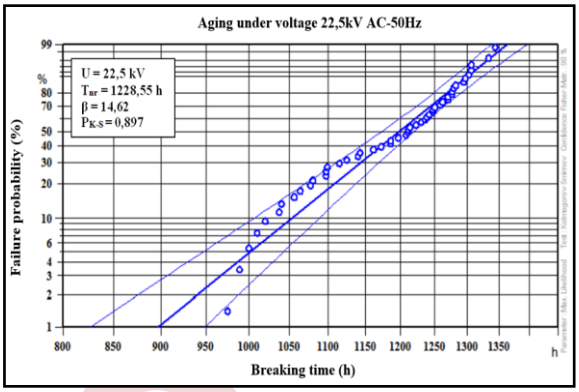


Figure 10. Ageing under sinusoidal voltage 22.5kV

B. Experimental device

To measure the breakdown voltage at AC voltage, we used the device shown in Figure 1, which consists of the following components:

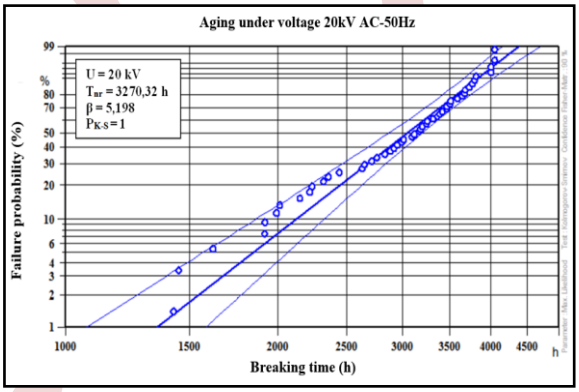


Figure 11. Ageing under sinusoidal voltage 20kV

- A high-voltage source: Our voltage source consisted of a 0.8/135 kV HV transformer (T100), capable of supplying a voltage ranging from 0 to 100 kV for AC voltage tests and from 0 to 135 kV for DC voltage. This transformer was equipped with both automatic and manual control, with several voltage ramp-up speed options.
- A capacitive voltage divider: For AC voltage measurements, we used a capacitive voltage divider, with capacitances of C0=0.1 µF and Cu=41.4 µF. For DC measurements, a resistive voltage divider was used, with resistors of R0=0.1 MΩ and Ru=250 MΩ.
- A peak voltmeter: We used a MU11 type peak voltmeter, with a digital display, to measure high AC or DC voltages, depending on the electrical circuit.
- A protection resistor: A protection resistor (R=106 kΩ) was introduced to limit the current.
- A support frame for the sample electrodes: This frame was designed to hold the PVC sheath samples in place. It was equipped with 50 sample-electrode elements.

- A high-voltage electrode: An aluminium electrode was inserted inside the PVC sheath to act as a high-voltage electrode.
- An earth electrode: A cylindrical aluminium electrode, wrapped around the outside of the sheath, was used as the earth electrode.
- Protective cage: The entire device, including the samples, was surrounded by a protective cage to ensure the safety of the operators.

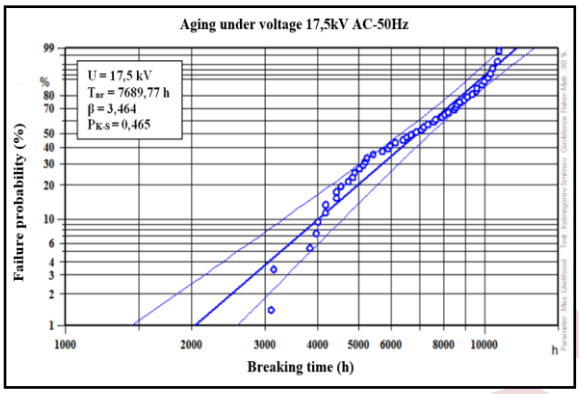


Figure 12. Ageing under sinusoidal voltage 17.5kV

This device enabled us to carry out breakdown voltage tests on the PVC sheath samples under controlled and reproducible conditions, which is essential for analysing the electrical ageing of these materials.

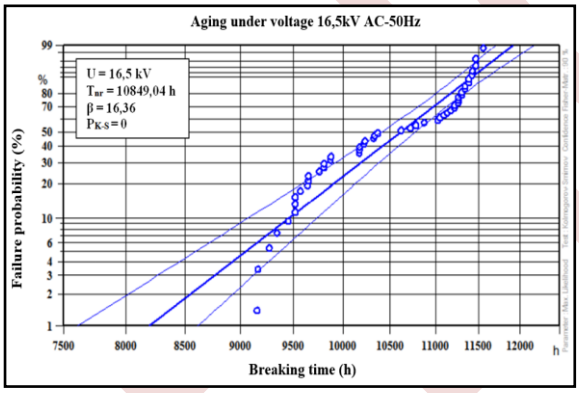


Figure 13. Ageing under sinusoidal voltage 16.5kV

C. Test procedures

The test process involves placing the sample between two electrodes and applying a constant sinusoidal AC voltage until breakdown occurs. After each breakdown, we recorded the value of the breakdown time using a programmable counter. Since breakdown times can be significant, we accumulated breakdown times for each voltage level. All tests were carried out in the open air and at room temperature in the laboratory.

The tests were carried out at various sinusoidal AC voltages, including 40, 37.5, 35, 32.5, 30, 27.5, 25, 22.5, 20, 17.5, 16.5 and 15.5 kV. It is important to note that precautions have been taken to ensure the reliability of the measurements, including:

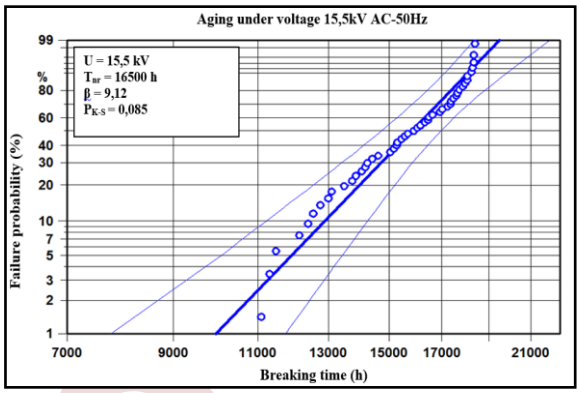


Figure 14. Ageing under sinusoidal voltage 15.5kV

- Electrode construction: The high-voltage and earth electrodes have been designed to have geometries similar to those of the PVC samples. The internal diameter of the high-voltage electrode is almost identical to that of the PVC sheath, with no gap between them. The inside diameter of the earth electrode is almost identical to the outside diameter of the sheath. The high-voltage electrode is in the form of a cylindrical tube with a diameter of 3.95 mm and a length of 85 cm. The earth electrode is a coaxial cylindrical tube, 4.2 cm long, with an internal diameter of 7.1 mm and an external diameter of 3.2 cm.
- Earth electrode: The earth electrode has been designed to eliminate edge and spike effects when applying voltage.
- Prevention of air ignition: To prevent bypass by air ignition, the earth electrode is positioned in the middle of the PVC sheath, and the length of the samples has been chosen accordingly.
- Selection of breakdowns: Only breakdowns occurring between the PVC sheath and the earth electrode were taken into account. Any breakdown occurring at the end of the earth electrode was excluded from the analysis.

These precautions were taken to guarantee accurate and reproducible measurements, thereby ensuring the validity of our study of the electrical ageing of PVC sheaths.

III. RESULTS

A. Statistical analysis

The Weibull statistical model [8-12] was used to process the fracture time results, as it is well known for its ability to determine a fracture threshold when necessary. To estimate the parameters of this model, we opted for the maximum likelihood method [11-13], which takes into account repeated rupture values within the same series of measurements.

One of the essential steps in the statistical analysis was the calculation of confidence intervals [11,12,14-17]. Based on these intervals, we were able to decide whether or not it was necessary to look for a breakpoint representation. Another crucial stage in the analysis concerned the goodness-of-fit tests.

When a large number of samples are involved, the chi-square test [17-20] is the most appropriate.

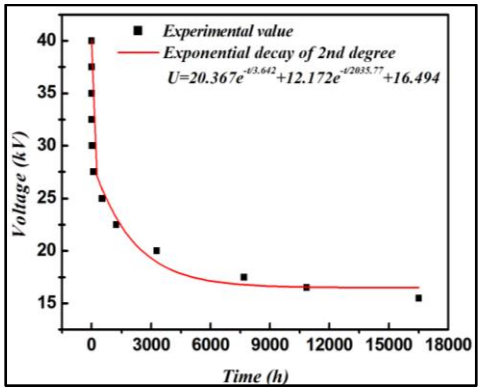


Figure 15. Electrical endurance characteristic of PVC sheath at AC-50 Hz

Using the median ranks method [11,12,21-24] with 90% confidence intervals, we drew two-parameter Weibull plots. These plots are shown in Figures 3 to 14.

The two-parameter Weibull statistical model, adapted to the study of fracture time, can be formulated as follows [12]:

$$P(t) = 1 - exp\left[-\left(\frac{t}{t_{nr}}\right)^{\beta}\right] \quad (1)$$

With:

- P(t): Failure probability,
- t: Measured failure time,
- tnr: Nominal break time which represents the scale parameter β: Shape parameter.

Table I shows the results for the nominal breaking time and the shape parameter.

TABLE I. STATISTICAL ANALYSIS RESULTS

Voltage level (kV)	Shape parameter β	Breakdown time (h)	P_{khi-2}
40	13.38	2.11	0.0020
37.5	16.22	3.12	0.0088
35	9.78	4.16	0.1259
32.5	36.64	6.01	0.0002
30	8.548	25.10	0.1314
27.5	9.095	95.68	0.0013
25	6.483	524.13	0.0219
22.5	14.62	1228.55	0.0001
20	5.198	3270.32	0.0009
17.5	3.464	7689.77	0.0005
16.5	16.36	10849.04	0.0007
15.5	9.12	16500	0.0004

B. Electrical endurance of PVC sheaths

The determination of the lifetime of solid insulating materials is based on long-term electrical ageing tests [25]. The experimental results have been used to establish the V-t characteristic, which shows the relationship between breakdown voltage and the duration of voltage application. These results are presented in the form of curves in Figures 15 and 16. Figure 15 uses a linear scale, while Figure 16 presents the data on a bilogarithmic scale.

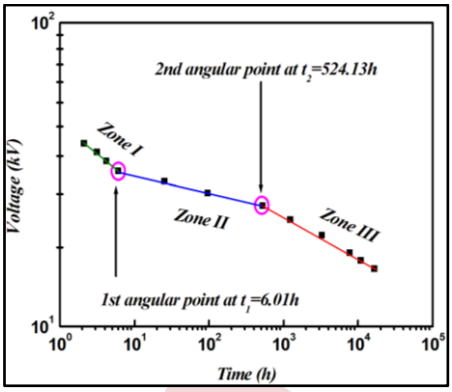


Figure 16. Electrical endurance curve of PVC sheath at AC-50 Hz

IV. DISCUSSION

All the two-parameter Weibull plots, representing the breakdown time distributions, lie partially or entirely within the confidence intervals, as indicated by the dotted lines. The width of these intervals is more significant for lower rupture probabilities.

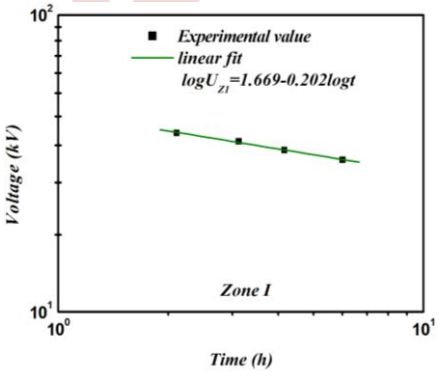


Figure 17. Zone I and its characteristics

For each voltage level, no point with a low probability of rupture lies outside the confidence interval on the left. Consequently, the search for a breakpoint is not justified. It is therefore appropriate to restrict ourselves to two-parameter Weibull plots rather than three-parameter plots.

The width of the confidence intervals is more pronounced for low rupture probabilities. According to Chauvet [26], the shape parameter is smaller for voltage levels of 20, 25 and 17.5 kV/s. This means that, below these voltage levels, the results are more dispersed than for the other levels.

The results of the chi-square test are satisfactory, allowing us to validate the two-parameter Weibull method we used to analyse our experimental results.

The curve in Figure 15 shows that the fit of the experimental points can be represented by a second-order decreasing exponential function. The empirical equation that best describes our experimental results is:

$$U = 20.36\, e^{-t/3.64} + 12.17\, e^{-t/2035.77} + 16.49 \quad (2)$$

The curve in Figure 16 can be divided into three distinct line segments, separated by two angular points, namely Zone I, Zone II and Zone III. Each of these zones follows an inverse power model.

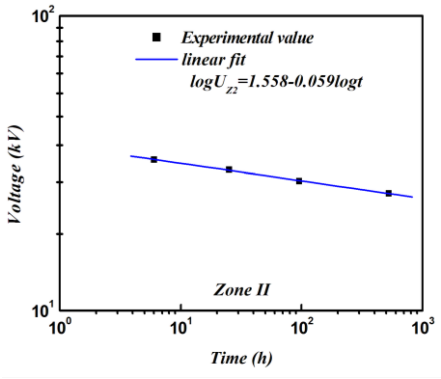


Figure 18. Zone II and its characteristics

The first zone is characterised by an electrical endurance coefficient of 4.95. In the second zone, this coefficient is 16.949, and in the third zone it reaches 7.194. The two angular points occur after 6.01 hours and 524.13 hours of ageing. These points mark significant changes in the behaviour of the PVC material studied [27].

It should be noted that the inverse power model is commonly used in studies on the electrical ageing of solid insulators [28,29]. This model is widely applied because of its simplicity and effectiveness. It is described by the following relationship [30,31]:

$$t = kU^{-n} \quad (3)$$

With:

t: lifetime,
U: applied electrical voltage,
k: parameter to be determined from tests,
n: electrical endurance coefficient, also to be determined experimentally.

We can therefore express equation (3) as follows:

$$Logu = Logk - \frac{1}{n} Logt \quad (4)$$

Figure 17 illustrates zone I of the electrical endurance characteristic of the material studied. This zone is associated with youth defects, which occur rapidly after the material has been energised at very high voltage gradients. The size of these defects, often extrinsic, can result in the presence of abnormal impurities in the dielectric, and plays a significant role [1]. During the manufacturing process, the application of a high amplitude electric field for a few tenths of a second can eliminate products with anomalies of a certain order, corresponding to large defects [1,12]. In zone I, the lifetime, expressed by the inverse power model, is governed by the following equations:

$$t_{Z1} \approx 20{,}886 \,.\, 10^{3} U^{-4{,}95} \text{ years} \quad (5)$$

Zone II, shown in Figure 18, reflects the statistical dispersion of intrinsic defects in the material. These defects may be the result of microcavities formed due to insufficient control during polymerisation or interrupted cross-linking during crystallisation of the material from its amorphous phase. During the extrusion operation, impurities, whose maximum size is limited only by the filters, may be injected randomly into the insulating volume, showing a statistical dispersion in terms of size and number [1,12]. In zone II, the lifetime can be modelled using the following equations:

$$t_{Z2} \approx 29{,}125 \,.\, 10^{21} U^{-16{,}949} \text{ years} \quad (6)$$

Finally, zone III, shown in Figure 19, reflects the actual ageing of the material, characterised by the systematic creation of new defects under the prolonged effect of the stresses to which it is subjected. In addition, other major defects in the insulator appear under the ageing conditions adopted. These failures are a sign of wear in the insulating layer [1,12]. Various processes can occur, such as a worsening of the slope corresponding to accelerated ageing of the material (oxidation, thermal degradation, etc.). Ultimately, this resembles the formation of a new insulator [12,32].

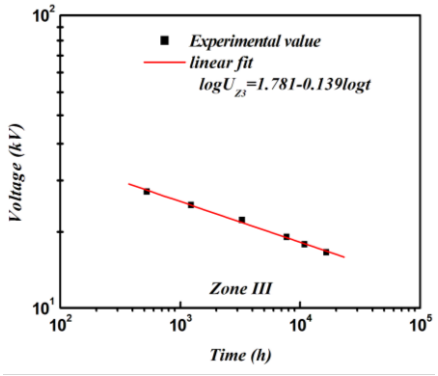


Figure 19. Zone III and its characteristics

Thus, in this zone III, the lifetime of the material can be expressed by the following equations:

$$t_{Z3} \approx 742{,}07 \,.\, 10^{6} U^{-7{,}194} \text{ years} \quad (7)$$

It is in Zone III that the service life of our PVC sheaths is defined, corresponding to a service life of up to 30 years for electrical power transmission and distribution cables [7,12].

Using equation (7), the voltage calculated for a service life of 30 years, i.e. 262800 hours, is as follows:

$$U = 10{,}658 \text{ kV} \quad (8)$$

Based on these calculations, it can be stated that, theoretically, our PVC sheaths can be used as insulation in all electrical equipment operating at sinusoidal AC voltages with a maximum amplitude equal to or less than 10 kV.

The two angular points separating the three zones reflect changes in the behaviour of the material studied [1,12].

These results obtained during the study of the electrical ageing of PVC sheaths, in this case the lifetime characteristic of

this material, are in line with numerous studies in the literature. Indeed, the electrical endurance curve of polymers does not generally present a straight line, but rather several segments or linear zones with very different slopes [25,32-34]. Nedjar demonstrated the existence of 3 zones when studying polyurethane [1] and only 2 zones in the case of polyester-imide [1,25]. In the case of polyimide films, Hirose reported the existence of 3 zones [35], while Zoledziowski and Sierota [36] showed the presence of 4 linear zones in the case of epoxy resin. The same phenomenon is observed when the failure rate is plotted as a function of ageing time. The result is a bathtub-shaped curve with an initial zone of rapid decay, a zone of early defects, followed by a zone of growth, and finally a zone of ageing defects. This phenomenon has been reported in the literature by several authors [1,12,32,37-38].

V. CONCLUSION

The study reveals that the electrical endurance curve of PVC sheaths consists of three linear segments, each characterised by a distinct slope. The first zone is associated with early defects in the insulation, involving extrinsic defects. The second zone, also known as the Weibull zone, reflects the random dispersion of intrinsic defects in the material. Finally, the third zone represents the actual ageing of the material.

It is in this last zone that we can determine the field of application of our material. The results of our study indicate that our PVC sheaths can be used as insulation in all electrical equipment operating at sinusoidal alternating voltage with a maximum amplitude equal to or less than 10 kV.

In addition, the electrical endurance curve shows two angular points, highlighting a change in the behaviour of the insulation. This feature is consistent with the inverse power model, which is commonly observed in studies of the electrical ageing of solid insulators.

The results of this study provide valuable information on the behaviour of PVC sheaths subjected to electrical stress. They contribute to a better understanding of their service life and their potential use in various types of electrical equipment. This knowledge is essential to guarantee the reliability of electrical installations and the long-term safety of operations.

REFERENCES

[1] M. Nedjar, "Evaluation de la tenue diélectrique à court et à long termes des polymères utilisés dans les dispositifs haute tension", Thèse doctorat, Université de Tizi Ouzou, Algérie, 2003.

[2] R. Fournié, "Les isolants en électrotechnique, essais et mécanismes de dégradation, applications industrielles", édition Eyrolles, Paris, 1990.

[3] J. Verdu, "Vieillissement des plastiques", édition Eyrolles, 1984.

[4] K.D. Walter, J.F. Johnson, J. Tanaka, "Polymer Degradation and its Measurement", Chapter 5, Engineering dielectrics, Vol. II-A, Electrical properties of solid insulating materials : measurement techniques, Editor R. Bartnikas, 1987, pp. 313-439.

[5] D. Bouguedad, "Influence du vieillissement thermique sur les propriétés de l'éthylène propylène diène monomère (EPDM)", Thèse doctorat, Université de Tizi Ouzou, Algérie 2010.

[6] C. Laurent, "La rupture diélectrique dans les polymères", REG, N° 10, 1985, pp. 745-755.

[7] N. Lahoud, "Modélisation du vieillissement des isolants organiques sous contrainte électrique. Application à la fiabilité des matériaux", Thèse de doctorat, Université Toulouse III-Paul Sabatier, France, 2009.

[8] W. Weibull, "A statistical distribution function of wide applicability", J. Appl. Mechanics, Vol. 18, pp. 293-297, 1951.

[9] V. Englund, R. Huuva, S.M. Gubanski and T. Hjertberg, "High efficiency voltage stabilizers for XLPE cable insulation", Science Direct: Polymer Degradation and Stability No. 94, pp. 823–833, 2009.

[10] K. Wu, Y. Wang, Y. Cheng, L.A. Dissado and X. Liu, "Statistical behavior of electrical breakdown in insulating polymers", J. Appl. Phys., Vol. 107, 064107, pp. 064107-1-064107-6, 2010.

[11] A. Laifaoui, J.M. Reboul, M.S. Herzine and al, "Breakdown strength measurements on cylindrical polyvinyl chloride sheaths under AC and DC voltages", Dielectrics and Electrical Insulation, IEEE Transactions on, 2014, vol. 21, no 5, pp. 2267-2273.

[12] A. laifaoui, "Etude de la tenue diélectrique des gaines en polychlorure de vinyle sous tension alternative et continue", Thèse doctorat, Université de Bejaia, Algérie, 2016.

[13] A.C. Cohen, "Maximum likelihood estimation in the Weibull distribution based on complete and on censored samples", Thechnometrics, Vol. 7, No. 4, pp. 579-588, 1965.

[14] J.F. Lawless, "Confidence interval estimation for the Weibull and extreme-value distribution", Thechnometrics, Vol. 20, No. 4, pp. 355-363, 1978.

[15] J.F. Lawless, "Construction of tolerance bounds for the extreme-value and Weibull distributions", Thechnometrics, Vol. 17, No. 2, pp. 255-261, 1975.

[16] G.C. Stone and R.G. Van Heeswijk, "Parameter estimation for Weibull distribution", IEEE Trans. Electr. Insul., Vol. 12, No. 4, pp. 253-261, 1977.

[17] P. Chapouille, R. de Paizzis, "Fiabilité des systèmes", Édition Masson, 1965.

[18] R. Lacoste, E. Loudghiri, J. Meric, "Sur la notion du gradient de seuil dans le phénomène de rupture diélectrique des isolants solides soumis à des rampes de tension", REG, 10/85, Octobre 1985, pp. 769-775.

[19] C. Chauvet, C. Laurent, "Weibull statistics in short-term dielectric breakdown of thin polyethylene films", IEEE Trans. On Elect. Insul., Vol. 28, N°1, February 1993,pp. 18-29.

[20] L. Simoni, "Dielecttrici proprieta e comportamento nel tempo", Universitaria Editrice, Bologna, 1974.

[21] L.A. Dissado and J.C. Fothergill, "Electrical Degradation and Breakdown in Polymers", Collection: IEE materials and devices series, 9. Editor: G.S. Stevens, Peter Peregrinus Ltd, London, 1992.

[22] W.D. Wilkens, "Statistical methods for the evaluation of electrical insulating systems", chap. 7, Engineering Dielectrics, Vol. II-B, Electrical properties of solid insulating materials: Measurement techniques, Editor R. Bartnikas, pp. 491-529, 1987.

[23] M. Ugur, A. Kuntman and A. Ersoy, "A study on the ageing process for polyester resin using improved Weibull statistics", Electr. Eng., No. 85, pp. 283–288, 2003.

[24] E. Tuncer, D.R. James, I. Sauers, A.R. Ellis and M.O. Pace, "On dielectric breakdown statistics", J. Phys. D: Appl. Phys. Vol. 39, pp. 4257–4268, 2006.

[25] M. Nedjar, "Weibull Statistics In Electrical Aging of polyesterimide Under AC Voltage", Journal of Applied Polymer Science, Vol. 116, 1593–1596, 2010.

[26] C. Chauvet, "Mise au point d'une méthodologie pour les essais de rupture à court terme en vue de la caractérisation des isolants synthétiques", thèse de doctorat, Université Paul Sabatier, Toulouse, 1992.

[27] A. Laifaoui, J.M. Reboul, M. Aissou et al, "Etude du vieillissement électrique des gaines en polychlorure de vinyle sous tension alternative sinusoïdale", 9ème conférence de la Société Française d'Electrostatique, 27-29 août 2014, Toulouse, France, Proceedings SFE'2014, ISBN 978-2-9549467-0-2, EAN 9782954946702, pp. 121-126.

[28] C. Guillermin, "Vieillissement électrique et thermique d'un composite résine époxy de-silice : étude des charges d'espace et de la conduction", Thèse de doctorat, Université Joseph Fourier Grenoble I, France, 2004.

[29] L. Boukezzi, "Influence du vieillissement thermique sur les propriétés du Polyéthylène Réticulé Chimiquement utilisé dans l'isolation des câbles de haute tension", Thèse doctorat, Ecole Nationale Polytechnique, Algérie 2007.

[30] F.W. Peek, "Dielectric phenomena high voltage engineering", MC Graw Hill, 1929.

[31] C. Dang, J.L. Parpal, J.P. Crine, "Electrical aging of extruded dielectric cables: review of existing theories and data", IEEE Transactions on Dielectrics and Electrical Insulation, Vol. 3, N°. 2, pp 237- 247, 1996.

[32] CIGRE, Groupe de travail 21-09, "Guide pratique d'utilisation des lois statistiques de Weibull dans l'étude de fiabilité des câbles", 1984.

[33] Y. Kako, K. Tsukui, S. Hirabayashi, K. Kimura, H. Mitsui, F. Natsume, "Endurance à la tension et processus de dégradation des isolations de machines tournantes à haute tension", Conférence Internationale des Grands Réseaux Electriques, 15 avril 1978.

[34] G. Katsuta, "A study on long-term characteristics of xlpe cables", journées d'etudes internationales sur les cables d'energie à isolant synthetique, pp. 232-237, 1991.

[35] H. Hirose, "A method to estimate the lifetime of solid electrical insulation", IEEE Trans on Elect. Insul, Vol. 22, N°6, pp. 745-753, 1987.

[36] S. Zoledziowski, A. Sierota, "Physical and statistical aspects of breakdown characteristics of solids dielectrics", IEE Dielectric Materials Measurments and Applications, pp. 84-87, 1992.

[37] A. Kelen, "Agening of insulating materials and equipement insolation in service and in tests", IEEE Trans on Elect. Insul, Vol. EI-12, N°1,, pp. 55-60, 1977.

[38] R. Langlois-Berthelot, "Durée de vie, fiabilité, disponibilité des matériels", édition Dunod, 1968.

EEIC'23

Controlled Discharge of Filters Media Surface

Akila Messaoudène [1], Boukhalfa Bendahmane [1], Allaoua Rahmani [1], Lucian Dascalescu[2]

[1]*Laboratoire de Génie Electrique de Bejaia, Université de Bejaia 06000, Algérie*
akila.messaoudene@univ-bejaia.dz
boukhalfa.bendahmane@univ-bejaia.dz
allaoua.rahmani@univ-bejaia.dz
[2]*PPRIME Institute, UPR 3346 CNRS - University of Poitiers – ENSMA, IUT, Angoulême, France*
lucian.dascalescu@univ-poitiers.fr

***Abstract*—Textile materials such as thin films or fibers have an important place in a large number of industrial sectors. These industries are often faced with problems introduced by the electrostatic charge and discharge phenomena of these textiles. The challenge is to neutralize the electrical charges. The objective of this work is to apply a simple and effective neutralization method based on a corona discharge generated from a triode system.**

Keywords: **AC corona discharge, Neutralization, Nonwoven media.**

I. INTRODUCTION

Dielectric materials have large applications in the most varied industrial fields. however, these insulating materials such as granules, powders or fibrous materials have a marked capacity to accumulate electrical charges. The search for an adequate solution, particularly on an industrial scale, to neutralize these charges is at the origin of this work. The objective is the active neutralization of non-woven filters media based on the principle of ionization of ambient air by corona effect generated in a triode configuration. Several methods of electric charges eliminating have been presented in the literature [1-12].

The effectiveness of the proposed neutralization process is evaluated from the surface potential profile.

II. MATERIALS AND METHODS

The experiments were carried out on white and blue non-woven filters media. They are cut into samples measuring 110 mm x 100 mm. The tests are carried out in ambient atmospheric air, at a relative humidity between 40% and 48% and at a temperature varying between 25°C and 28°C (Fig.1 and Fig. 2).

The experimental setup shown in Fig.3 consists of three stations which are:

- The charge deposition station, consisting essentially of a triode-type electrodes system with a wire-grid-plane configuration. The active electrode is powered by a DC power source.

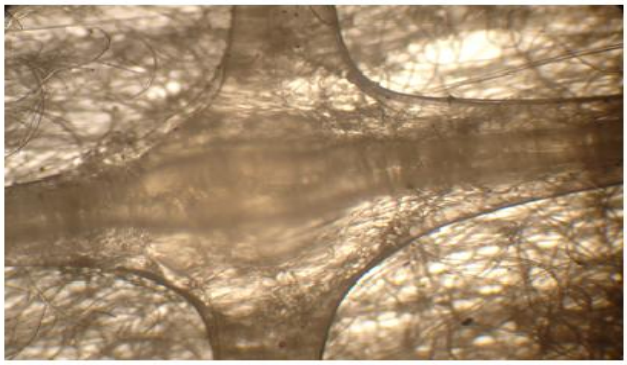
- The measurement and data acquisition station, where the surface potential is measured with a contactless probe coupled to an electrostatic voltmeter.

- The charge neutralization station, consisting of a triode-type electrodes system, where the active electrode is powered by a sinusoidal alternating voltage at industrial frequency.

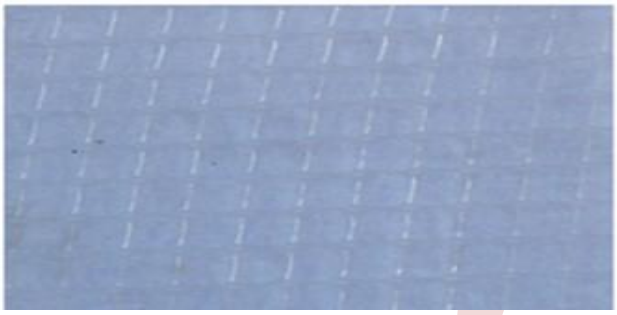
The charging station consists of a dual electrode and the grid electrode (Fig.3a). The dual electrode is composed of a thin tungsten wire, 120 mm long, with a diameter of 0.2 mm, suspended by two metal rods from a metal cylinder with a diameter of 26 mm. The assembly is brought to a direct potential of negative polarity, produced by a SPELLMAN direct DC high voltage source, 100 kV, 3 mA. A grid with rhombically shaped aluminum mesh is inserted at an equal distance between the wire and the surface of the plane. The distance between the wire and the plane is 30 mm. The grid electrode is connected to earth by a resistance Rg = 100 MΩ in series with a micro-ammeter measuring a current of intensity Ig. For an Ig intensity fixed by the constant voltage Vs of the high voltage supply, a well-defined constant potential $Vg = Rg \times Ig$ is imposed between the grid and the grounded plate electrode.

The measuring station is illustrated in the Fig.3b The measurements of the potential at the media surface after charging or after discharging are carried out using an electrostatic voltmeter (model 341B), equipped with an electrostatic probe (model 3450, Trek, Inc., Medina, NY) [13,14], and recorded via an electrometer (model 6514, Keithley Instruments, Cleveland, OH), which is connected to a computer. The acquisition and processing of experimental data are performed using a virtual instrument (LabView).

The discharging station consists of another triode device composed by a high-voltage dual electrode and a grid electrode connected directly to the ground (Fig.3c) [15-17]. The active electrode was connected to the high voltage amplifier 30 kV, 20 mA (Model 30/20A, Trek Inc., Medina, NY) connected to the frequency generator to generate a sinusoidal waveform voltage and frequency industrial (model FG300, Yokogawa, Japan).

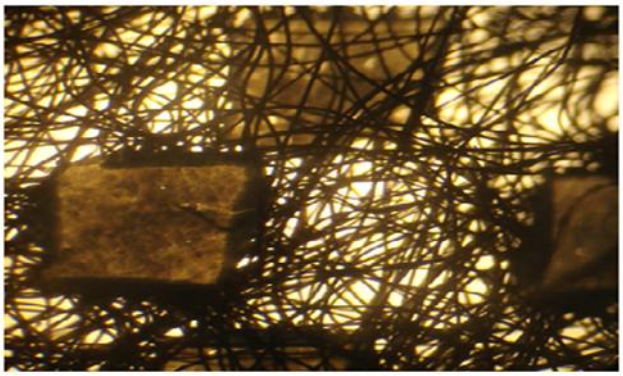


(a)



(b)

Figure 1. (a) Fibrous structure of the white non-woven media, (b) Image of one side of the white non-woven media



(a)



(b)

Figure 2. (a) Fibrous structure of the blue non-woven media, (b) Image of one side of the blue non-woven media

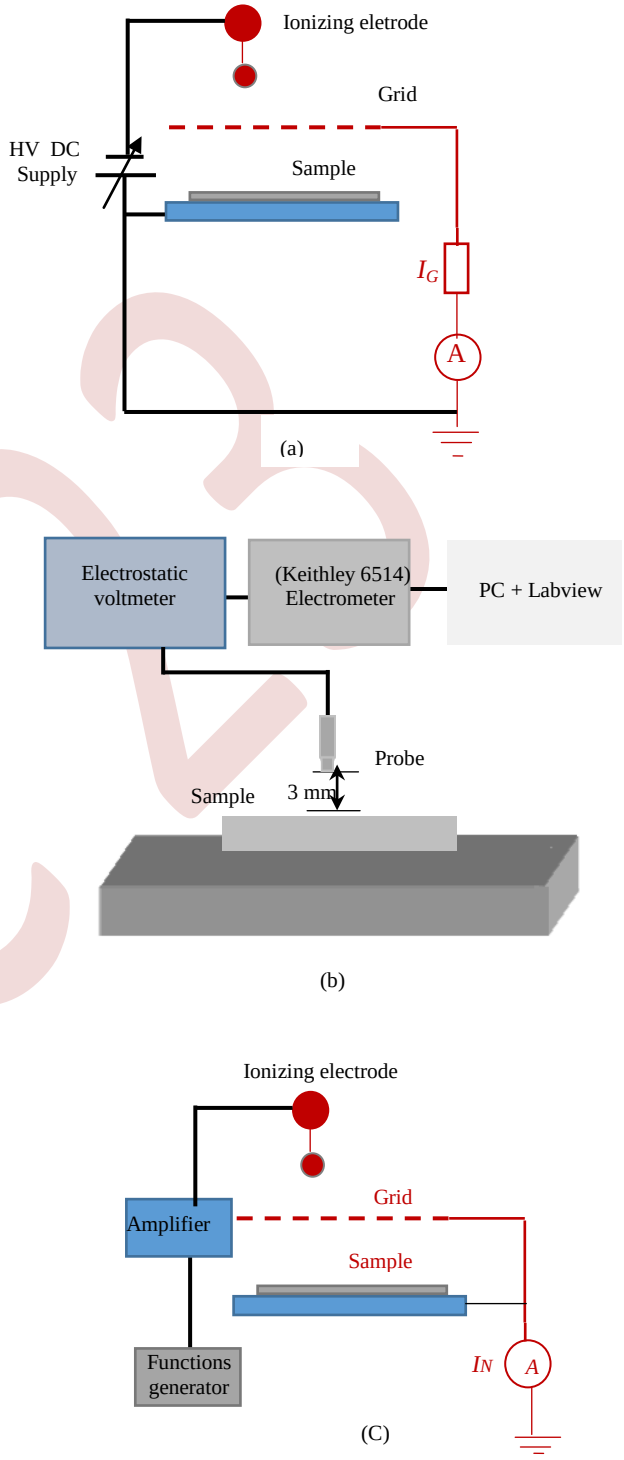


Figure 3. (a) Charging station, (b) Measuring station, (c) Neutralizing station

Two operating neutralization modes have been tested: static mode, the sample is centered just below the neutralizer and will be exposed for a well-defined time t_n to the bipolar ions generated by the ionizer and scanning mode, for which the sample passes under the corona electrode with a predefined speed of 3 cm/s. In the following I_N is the neutralization current. The surface potential profiles are obtained by measuring the potential at the surface along the central axis of the sample.

III. RESULTS AND DISCUSSION

Fig.4 and Fig.5 present the surface potential profiles after the deposition of charges on the surface of the blue and white fibrous filter media, with a grid potential of -2.5 kV. The samples were exposed to the ions generated by the corona discharge of negative polarity for 10 seconds, then transferred to the measuring station for the recording of the profile of the surface potential of the deposited charges.

The surface potential profiles of the charge deposition show the non-uniformity of the deposited charge and this is due to the non-homogeneous structure of the fibrous media. These curves also show that the maximum value of the surface potential is obtained for the white fibrous media. This maximum essentially is fixed by the dielectric strength of the air, and this means that the amount of charges deposited is limited. The values of the surface potential are different despite the same charging conditions. This can be explained by the relative humidity of the ambient air which affects the threshold for the onset of the corona discharge, as well as the limit charge level of the sample [18, 19].

The Fig.6 shows the surface potential profiles before and after two successive neutralizations in static mode and in scanning mode of the same sample of the blue fibrous filter media, where the deposition was carried out with a grid potential Vg = -2.5 kV.

The first neutralization was carried out with an intensity I_N = 10 µA in static mode for t_n = 10s. It was followed by a second neutralization in scanning mode characterized by an intensity I_N = 50 µA, at a scanning speed V_b = 3 cm/s. The second naturalization is more effective. Neutralization efficiency is achieved after the second pass, where the resulting surface potential profile is flattened. In fact, successive neutralizations increase the duration of exposure to the flow of bipolar ions.

Fig.7 illustrates the effect of two repetitive neutralizations on a white non-woven fibrous filter media charged to a grid potential Vg = -2.5 kV. A first neutralization was carried out in static mode by exposing the material to the alternating corona discharge for a time tn= 10 s. On the other hand, the second neutralization is in scanning mode where the sample scrolls under the crown electrode at a speed of 3 cm/s. After the second neutralization, a reduced residual potential is noticed near the central zone of the sample.

From the neutralization profiles, it appears that the amplitude of the residual surface potential is inversely proportional to the number of successive neutralizations. The effect of the first neutralization is to reduce the charge surface potential, especially near the center where the potential is generally maximum. The effect of other neutralizations is to reduce residual surface potential and tend to deflect neutralizing ions to unneutralized areas of the fibrous media surface. Thus, an increasingly large area of the sample will be neutralized after each neutralization. This means that successive neutralizations provide a larger neutralized surface at a lower residual potential.

Fig.8 shows that the neutralization rate increases with the neutralization intensity. The neutralization rates are higher for high voltages which can ionize the air surrounding the active electrode and generate a greater number of bipolar ions according to the half-cycles of the alternating voltage [20]. Indeed, for high neutralization intensities, an intense electric field in the wire-grid interval accelerates charges in the direction of the sample to neutralize its charged surface. The neutralization rate is proportional to the intensity of the alternating corona current.

The results shown in Fig.9 highlight the fact that the neutralization is less efficient for high scanning speeds. Indeed, the increase in speed means that the sample is exposed for a shorter duration to the alternating corona discharge, which decreases the chances of neutralizing the charges injected into the volume of the material at different energy levels during the deposit of charges. The longer exposure to the alternating corona discharge is necessary to liberate the charges trapped in deep within the porous structure of the fibrous media, thereby increasing the probability that the residual charges will be neutralized by the bipolar ion packets alternately generated by the corona discharge.

IV. CONCLUSION

The proposed active and controlled neutralization method is based on a triode-type electrode configuration. This process is simpler and guarantees effective neutralization. The presence of the grid connected to ground prevents the appearance of a potential of opposite sign.

The analysis of the potential distribution on the surface of the white and blue non-woven media makes it possible to evaluate the different parameters which contribute to greater neutralization efficiency:

1. Neutralization intensity is the dominant factor in the case of active and controlled neutralization. The neutralization rate is proportional to this factor.

2. A slow scanning speed provides a longer neutralization time, which increases the chances of neutralizing residual charges.

3. Successive neutralizations are the solution to improve the neutralization rate.

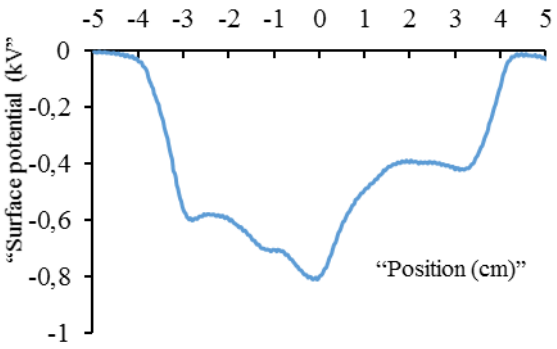


Figure 4. Deposit profile, blue filter media

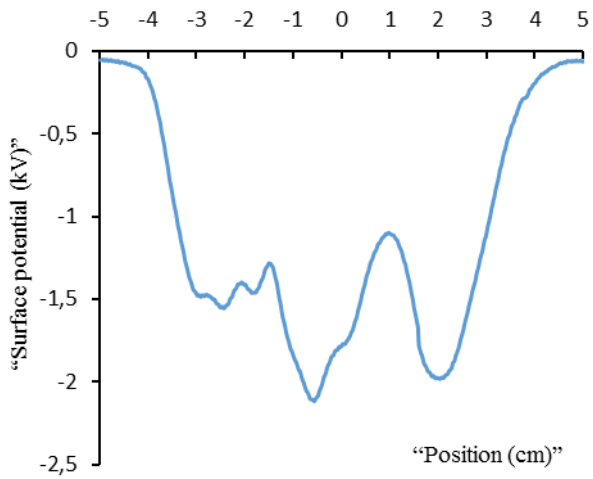


Figure 5. Deposit profile, white filter media

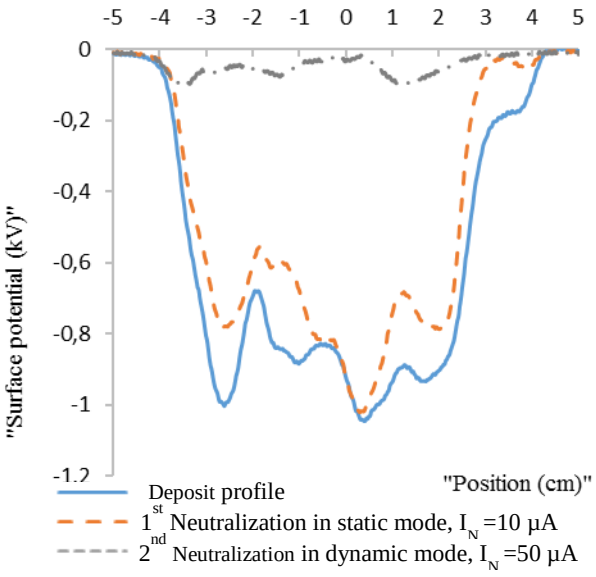


Figure 6. Deposit profile, white filter media

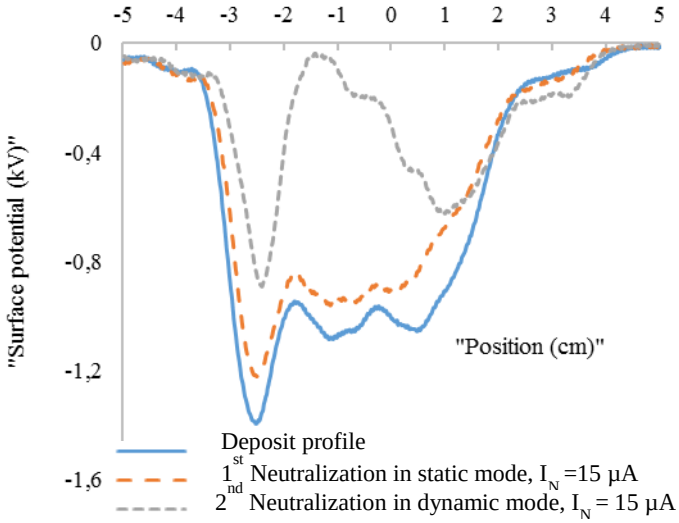


Figure 7. Deposit profile, blue filter media

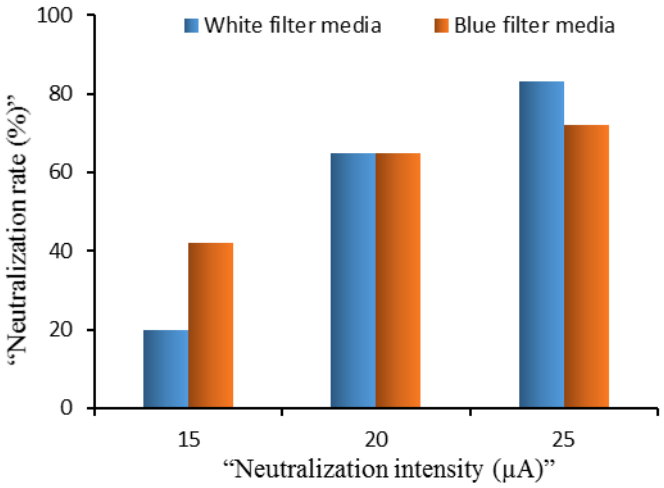


Figure 8. Neutralization rate as a function of the neutralization intensity

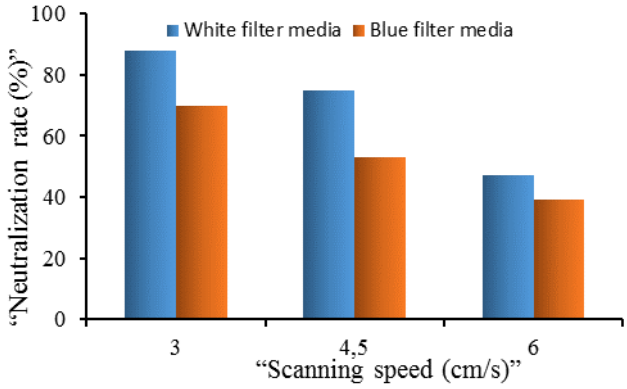


Figure 9. Neutralization rate as a function of the scanning speed

REFERENCES

[1] J. S. Chang, "Neutralization theory of static surface charge by an ionizer under wide gas pressure environments, " IEEE Trans. Ind. Appl, vol. 37, pp. 1641–1645, 2001.

[2] M. Kachi. and L. Dascalescu, "Corona-discharge-based neutralization of charged granular insulating materials in contact with an electrode of opposite polarity, " J. Electrostat, vol.76, pp. 246 – 253, 2015.

[3] A. Antoniu, B. Tabti, M. C. Plopeanu , and L. Dascalescu, "Accelerated discharge of corona-charged non-woven fabrics," IEEE Trans. Ind. Appl, vol. 46, pp. 1188–1193, 2010.

[4] C. Gibbons, "Method of Altering Electrostatic Charge on an Insulating Material," US Patent 3,470,417, 9/30/1969.

[5] M. Kachi, M. Nemamcha, L. Herous, and L. Dascalescu, "Neutralization of charged insulating granular materials using corona discharge," J. Electrostat, vol. 69, pp. 296-301, 2011.

[6] A. Antoniu, A. Smaili, I-V. Vacar. M. C. Plopeanu, and L. Dascalescu, "Sinusoidal and triangular AC high-voltage neutralizers for accelerated discharge of non-woven fibrous dielectrics," IEEE Trans. Ind. Appl, vol .48, pp. 857-863, 2012.

[7] M. Kachi, L. Dascalescu, L. Herous, and M. Nemamcha, "Experimental study of charge neutralization at the surface of granular layers ofinsulating material," IEEE Trans. Ind. Appl, vol. 48, pp. 691-698, 2013.

[8] B.Yahiaoui, M. Megherbi, B. Tabti, and L. Dascalescu, "Sinusoidal, triangular or square alternating voltages neutralization of electrostatics charges on the surface of polypropylene nonwoven fabric," IEEE Trans. Ind. Appl, vol. 51, pp. 685-691, 2015

[9] A. Messaoudènne, M. R. Mekideche, B. Bendahmane, B. Tabti, K. Medles, and L. Dascalescu, "Experimental modeling and optimization of the active neutralization of a PP film, using design of experiments methodology," IEEE/IAS Ann. Meet., Baltimore, MD, Sept. 30 – Oct. 1, 2019.

[10] K. Rouagdia, L.Dascalescu, " Robust optimum operating conditions for AC corona neutralization of insulating materials," Rev. Roum. Sci. Techn. – Électrotechn. Et Énerg., vol.65, 1-2, pp. 5–10, 2020.

[11] A. Messaoudène, L.Dasscalescu, A. Rahmani, B. Bendahmane, " Discharge of polypropylene films surface negatively charged, "2nd International conference on advanced electrical engineering (ICAEE 2022), Constantine (Algeria), October 29-31, 2022.

[12] M. A. Noras, "Non-contact surface charge/voltage measurements capacitive probe-principle of operation," Trek Application Note, number 3001, pp. 1–8, 2002.

[13] P. Molinié, and P. Llovera, "Surface potential measurements : implementation and interpretation," 8th Int. Conf. on Dielectric materials, measurements and applications, IEE Conference Publication, No 473, pp. 253-258, 2000.

[14] A. Messaoudène, M.R.Mekidèche, B.Bendahmane, B. Tabti, L. Dascalescu, "Caractérisation Expérimentale de la neutralisation active et contrôlée des films en polypropylène, 11ème Conférence de la Société Française d'Electrostatique : SFE 2018, Grenoble (France), 29-31 Aout 2018.

[15] B. Bendahmane, A. Messaoudène, L. Dascalescu, "Alternating Current Corona of Charged Filters Media, " IEEE 3rd International Conference on Dielectrics, Valencia (Spain), 5-31 July 2020.

[16] A. Messaoudène, A. Rahmani, B. Bendahmane, " Evaluation of filter media charge by DC corona discharge." III International scientific conference on Electrical and Power Engineering and Electromechanics (EPEE 2023), Odessa (Ukraine), June 15, 2023.

[17] B. Tabti, M. Mekideche, M.C. Plopeanu, M. Dumitran, A. Antoniu, and L. Dascalescu, " Fators that influence the decay rate of the potential at the surface of non-woven fabrics after negative corona discharge deposition ,"IEEE Trans. Ind.Appl., vol.46, pp. 1586-1592, 2010.

[18] B. Tabti, B. Yahiaoui, B. Bendahmane, and L. Dascalescu, "Charge dynamic characteristics of negative corona charged fibrous dielectric materials at low air humidity," IEEE Trans. Diel. Elect. Insul., vol. 21, pp.829-835, 2014.

[19] A. Messaoudène, M.R.Mekidèche, B.Bendahmane, B. Tabti, L. Dascalescu, " Experimental study of controlled active neutralization of polypropylene films, " J. Electrostat, vol.103, 103400, 2020.

[20] A. Messaoudène, L. Dascalescu, B. Bendahmane, " Discharge by AC corona of positively charged polypropylene films." International scientific conference on Electrical and Power Engineering and Electromechanics (EPEE 2022), Ukraine, May 12,2022.

Physical Study of an Electrically Aged Silicone Insulator Under Pollution

Nacera Rouha [1], Fatma Bouchelga[2], Nouredine Ouchenir [1], Saadi Remache [1]

[1]*Laboratoire de Génie Electrique, faculté de Technologie, Université de Bejaia, 06000 Bejaia, Algérie*

nacera.rouha@univ-bejaia.dz

[2] *Laboratoire de Génie Electrique, faculté de Technologie, Univesité de Ghardaia, 04700, Ghardaia, Algerie*

fatma.bouchelga@uni-ghardaia.dz

***Abstract*— This paper deals with the physical characterization of an electrically aged silicone insulator under pollution. In this context, an experimental study on Silicone Rubber films used for the coating of the insulator systems, confronted with the external pollution aggression is undertaken. We investigated the electrical aging effect on the Silicone's loss of hydrophobicity according to the declination of the insulation surface. At first, accelerated testing under alternating 50 Hz homogeneous electrical field, were conducted on both polluted and clean silicone. Then, it comes to determine the contact angle θ and hence the silicone hydrophobicity index (HI) to decide on its state, this for different angle α of silicone insulation surface declination. The following influence parameters are taken into account: the size of the water drops, their electrical conductivity, their distribution, and the material surface condition (virgin and aged under 50 Hz alternating voltage in the case of both a clean surface and surface polluted with conductive wet solution). Furthermore, a characterization of the material electrical performance is carried out by measuring the dielectric strength, the capacitor, the loss factor and the permittivity before and after aging produced by a series of surfacic breakdown. The obtained results showed that the electrical aging caused an alteration of the hydrophobic character as well as the dielectric properties of the material.**

Keywords: **Silicone, Hydrophobicity, Ageing, Pollution.**

I. INTRODUCTION

Outdoor insulators flashover is one of the challenging problems that affect not only the electrical energy quality, but also the equipments durability of high voltage lines [1, 2]. Again, this fact is aggravated by the insulators contamination when the overhead transmission lines are exposed to natural and industrial pollution [3, 4], particularly in wet weather. Indeed, sudden variations in temperature, morning dew, rain, melting snow are all elements that promote the deposition of water droplets on the external insulators surfaces of transmission networks. The presence of these water droplets on their surface is one of the main factors involved in the aging mechanism.

Under an electric field influence, a water droplet can deform and disturb this one by the creation of an intense local field in its immediate surroundings. This intense local field can lead to an extension of the droplets, thereby reducing the isolation distance [5]. This can cause partial discharges which can develop into an electric arc and lead to the insulator flashover. The recourse to hydrophobic materials remains the way to overcome this problem. The silicone is the ideal material used for coating insulators systems, which is the latest solution adopted to overcome the outdoor insulators flashover problems. The choice of the silicone is justified by its low hydrophobic index (HI) which gives a good surface appearance devoid of erosion signs, and its high dielectric properties attested by its good electrical withstand, which allows improving isolator system performances, this is coupled with a good thermal stability. The silicone hydrophobicity gives it superior performance to resist wetting due to its low surface free energy. This property reduces the leakage currents and minimizes the probability of the dry bands appearance [5]. However, the loss of hydrophobicity decreases the insulating properties of the insulator [6, 7] as well as its pollution resistance performance [8, 9], as it influences the aging process of polymeric insulators, thus reducing their lifetime [10, 11].

In this work we investigate the hydrophobicity loss of electrically aged silicone according to the declination of the insulation surface. It comes to examine the behavior of water droplets on the surface of the silicone elastomer, used for the coating of the insulator systems, confronted with the external pollution. This amounts to determine the contact angle θ for different angle α of silicone insulation surface declination, which is completed by measuring the surface and transverse resistivities ρ_s and ρ_t respectively, the dielectric strength E_l, the capacitor C_x, the loss factor tgδ and the permittivity ε_r, before and after aging. This experimentation is carried out under the effect of some influence parameters.

II. EXPERIMENTAL TECHNIQUES

This experimentation is carried out on silicone samples of (200x100x10 mm^3) in dimension, having different surface

state; virgin, electrically aged in clean surface (dry) and electrically aged under wet pollution of conductivity σ_p = 5 mS and σ_p =0.2 mS. The electrical aging of the silicone samples is performed using laboratory accelerated testing under ramp alternating 50 Hz homogeneous electrical field, at climb rate of 2 kVmax/s. Series of 100 surfacic breakdowns are carried at electrodes gaps d = 10 cm.

To investigate the hydrophobicity loss of electrically aged silicone according to the declination of the insulation surface, we use the Drop Shape Analyzer DSA30 device (Fig. 1) to analyze the shape of the drop and measure its contact angle θ, which allows determining the hydrophobicity index HI of the analyzed material. Beforehand, we data set on the PC linked to this device, the drop volume which will be deposited on the silicone sample surface placed on a holder plane with an adjustable declination α at will ($0° \leq \alpha \leq 180°$). An integrated camera captures the drop image. The built software processes the data, and the water drop image is displayed on the PC screen with the determined contact angles θ (Fig. 2). These tests are carried out for four water drops sizes (0.1 µl to 0.4 µl), two water drops distributions on surface (linear and zigzag) and two water drops conductivities (σ =5 mS and σ= 0.2 mS). The code (XYZ) is adopted to define the studied variants. X = 1, 2, 3 and 4 for the drops volumes of 0.1, 0.2, 0.3 and 0.4 µl respectively; Y = 3 and 4 for the conductivities σ = 0.2 mS and σ = 5 mS respectively and Z = 5 and 6 for a linear and zigzag drops distribution respectively.

To characterize the silicone electrical performances under electrical stress, the measurements of the surface and transverse resistivities ρ_s and ρ_t respectively, the dielectric strength E_l, the capacitor C_x, the loss factor tgδ and the permittivity ε_r before and after aging are performed, to decide on its state, this for each case considered above.

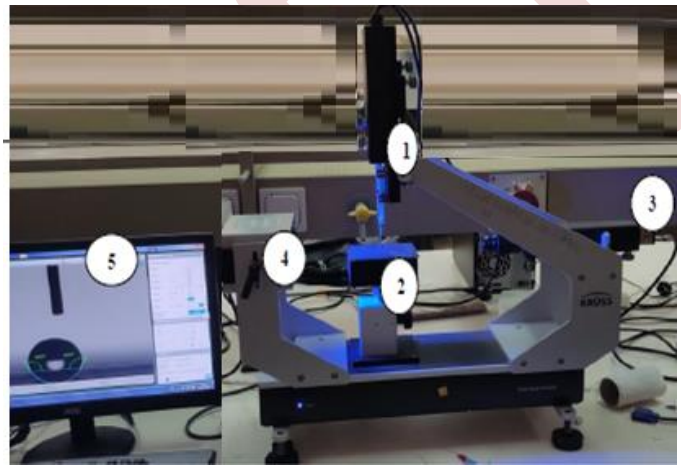


Figure 1. Drop Shape Analyzer DSA30

1 : Liquid solution tank and pipette

2 : plane holder

3 : camera

4 : torch

5 : Data setting PC

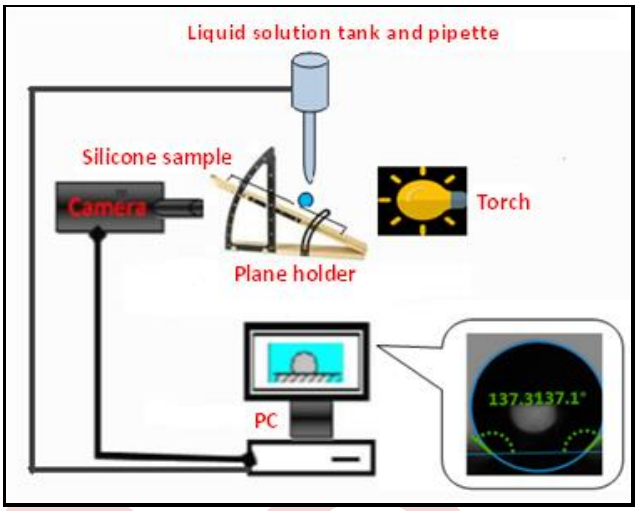


Figure 2. Experimental setup

III. EXPERIMENTAL RESULTS

The silicone hydrophobicity is affected by its surface electrical aging, whether dry or polluted (Fig. 3). Note that silicone's hydrophobicity loss is more marked in the dry ageing case compared to the wet one. The wet polluting layer would fade the discharge thermal energy, consequently mitigating the hydrophobicity loss. However, high conductivity of the polluting solution further degrades this property.

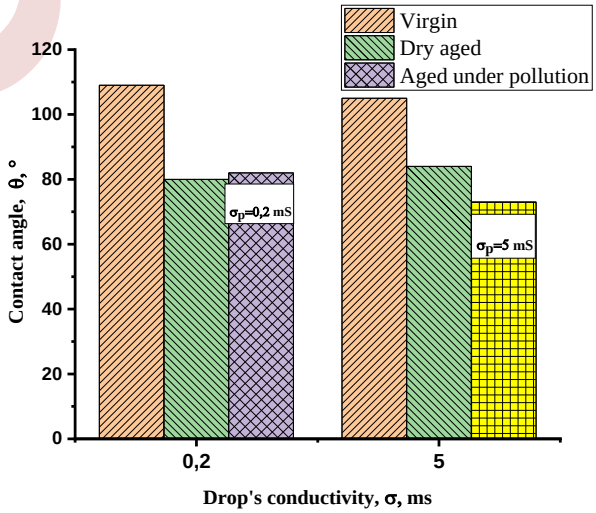
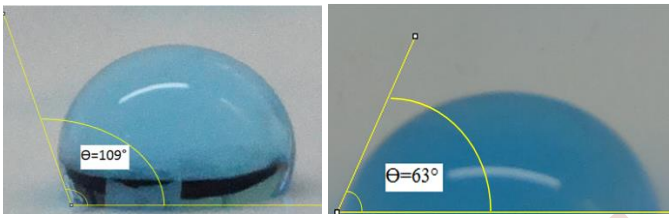


Figure 3. Contact angle versus conductivity α=0° (1Y5).

We can thus deduce that in the youthful state of the material (virgin state), the latter enjoys good hydrophobicity. On the other hand, at its aging on site caused by the multiple undergone flashover (dry aged state) and the environmental conditions imposed by the operating site on which depends the pollution degree which can be low or high (aged states under pollution at σ_p = 0.2mS and σ_p = 5 mS respectively), causes

the reduction of this property, without however going to its complete degradation. Horizontally (α = 0°), virgin silicone presents discrete droplets whose contact angle is obtuse (98 ° ≤ θ ≤ 109º). This value indicates a low wetting of this surface, to which corresponds a hydrophobicity index HI = 1 and this for all the water drops envisaged cases of volume, conductivity and distribution. While HI increases with the material aging and more with associated wet conductive polluting layer, the water droplets on the silicone surface retains its rounded shape, which testifies to the silicone good hydrophobic character (Fig.4.a, b. and c).



(a) (b)

(c)

Figure 4. Contact angle of a water droplet deposited on the silicone surface at α=0°

(a): vierge (135); (b): dry aged (435); (c): aged under pollution σ_p = 0.2 mS (336).

However, it should be noted that the effect of the water drops distribution on the silicone plate surface, both virgin and aged, is not significant (Fig.5).

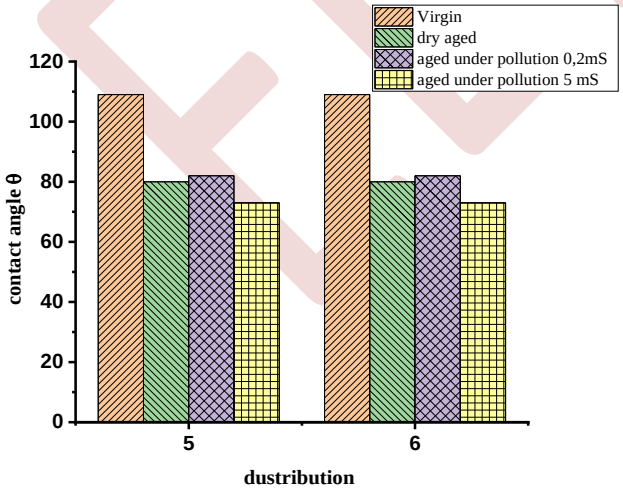


Figure 5. Contact angle θ versus the water drops distribution at α=0°, (5):linéaire and (6): zigzag

The measurement results illustrated in the figures (6, 7 and 8) show that the contact angle θ increases as the declination angle α increases, this is true whatever the variant (X , Y, Z) considered.

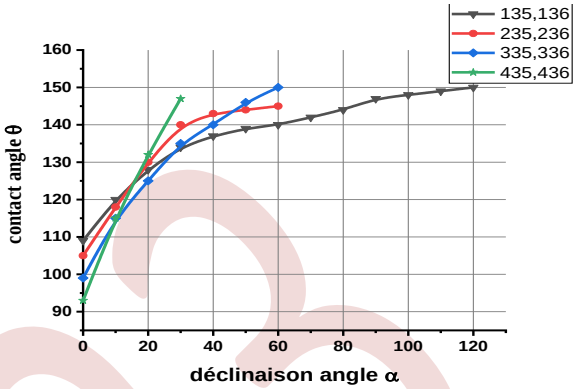


Figure 6. Contact angle θ versus the declination angle α for different drop volumes, σ = 0.2 mS and a linear or zigzag distribution in the case of silicone virgin state

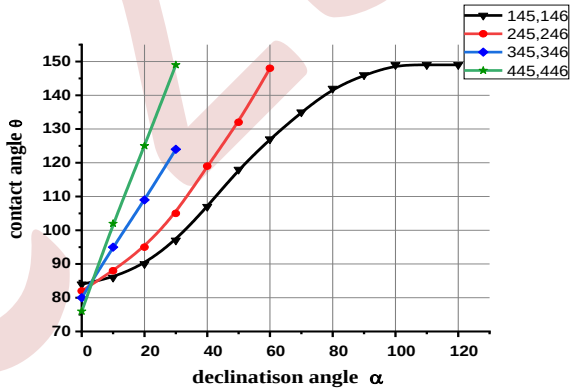


Figure 7. Contact angle θ versus the declination angle α for different drop volumes, σ = 5 mS and a linear or zigzag distribution in the case of silicone's dry-aged state

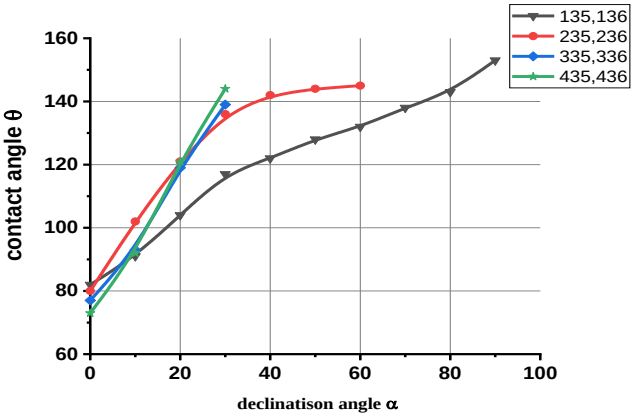


Figure 8. Contact angle θ versus the declination angle α for different drop volumes, σ = 0.2 mS and a linear or zigzag distribution in the case of silicone aged under pollution σ_p = 0.2 mS

In the virgin state, as dry aged one, of the silicone plate, the water drops of small volume (0.1 µl) simulating a fine rain, remain stuck on the plate surface even when the latter is vertical (α = 90 °), and even reversed (α = 120 °), (Fig. 6 and 7). In the aged state under pollution of the silicone plate, we note, however, the ejection of the water drop of volume = 0.1 µl, by sliding on the silicone plate surface for large declination α, and this depending on the polluting solution conductivity [12]. For higher drop volumes (> 0.1 ml), it slides under its weight effect, for smaller declinations of the surface, this, regardless of the surface state (virgin or aged), the polluting solution conductivity and the considered distribution (linear or zigzag).

The silicone degrades under the sliding discharge effect. That is reflected by the alteration of its electrical quantities: the surface and transverse resistivities, the longitudinal dielectric strength, the capacity, the permittivity and the loss factor.

In its virgin state, silicone has good surface and transverse resistivity, however, aging in its clean state, as well as under pollution, reduces the value of these two electrical quantities (Table I).

TABLE I. SILICONE SURFACE AND TRANSVERSE RESISTIVITY AT VIRGIN, AGED IN CLEAN STATE AND AGED UNDER POLLUTION STATE

Resistivity ($\Omega.m.10^9$) / **Silicone state**	**ρs**	**ρt**
Virgin	13.76	1.61
Electrically aged in clean surface	1.75	0.31
Electrically aged under wet pollution	1.094	0.25

Clean silicone has good dielectric strength. However, under pollution, it loses its performance as the conductivity and the volume of the deposited pollution increase (Table II).
The sliding discharge resulting from the applied electric field stress caused the material surface degradation, leaving visible carbonization traces, deeper with the increase in the polluting layer conductivity (Fig. 9). The carbon layer thus deposited increases the silicone surface conductivity, which directly affects its longitudinal dielectric strength.

TABLE II. SILICONE LONGITUDINAL DIELECTRIC STRENGTH E_L VERSUS THE INVOLVED PARAMETERS XYZ

Silicone state	**Clean**	**Polluted (XYZ)**									
		135	136	145	146	235	236	245	246	335	445
E*l* **(kV/cm)**	9.1	7.8	6.7	7.6	7.3	7.2	6.6	6.7	6.8	6.9	6.5

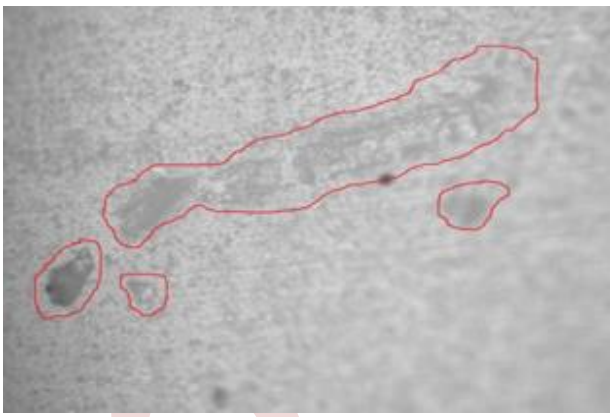
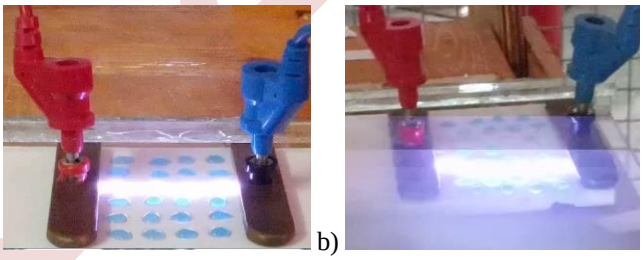


Figure 9. Silicone's optical microscope photograph after the electric discharge passing

Note also that the silicone longitudinal dielectric strength under conductive wet pollution is greater when the pollution drops follow a linear distribution, relative to a zigzag one. This is because in the case of linear distribution, the discharge follows a preferential path by slipping between the drops rows (Fig. 10.a). In the case of a zigzag distribution, it overhangs the drops which have a conductivity greater than the clean silicone surface (Fig. 10.b).



a) b)

Figure 10. Photograph of the arc on the polluted silicone surface in

(a): linear and (b): zigzag distribution

Silicone electrical aging results in a reduction in its capacity and permittivity, combined with an increase in the loss factor in the case of a polluted surface. This observation joins those made for the silicone electrical resistivities and dielectric strength which we attribute to the damage left by the discharge on its surface, further aggravated by the conductivity of the polluting factor (Table III).

TABLE III. CAPACITY, PERMITTIVITY AND LOSS FACTOR OF SILICONE AT U=100V AND F=50HZ

Silicone state	**Cx (pF/m)**	**εr (F/m)**	**Tgδ**
Virgin	11.85	4	$6.6x10^{-2}$
Electrically aged in clean surface	10.86	3.68	$6.74x10^{-2}$
Electrically aged under wet pollution	9.99	3.38	$1.368x10^{-1}$

IV. DISCUSSION

It follows from this study that, both in the cases of dry-aged silicone and silicone aged under conductive wet pollution (simulating an insulator in service), the declination α = 30° corresponds to the optimal profile of the silicone insulator exposed to an environment with moderate or high pollution and/or rainfall.

The silicone surface is affected by aging as well at dry conditions as under pollution. However, a high conductivity of the polluting solution further degrades its electrical and physical properties and the water drops conductivity can contribute; the superficial conductivity increases the discharge energy. Silicone carbonizes and the carbon deposit, in turn, causes an increase of the discharge energy. This vicious process accelerates the material degradation.

The intense energy of the sliding discharge causes a severe surface damage of the material when it runs through the preferential electrically weak zones. The sample surface depolishing involves, on the one hand, an electrical proprieties degradation of the material such as the surface and transverse resistivities ρ_s and ρ_t respectively, the dielectric strength E_l, the capacitor C_x, the loss factor tgδ and the permittivity ε_r and on the other hand, the hydrophobicity loss. However, the moisture mitigates the thermal effect of the discharge and, in corollary, slows down the physical and electrical silicone degradation relatively to silicone aging in dry conditions.

The physical and electrical silicone degradation could be explained by the following mechanisms:

- Electrical aging affects the silicone surface state, which carbonizes following the electrical discharge passage, giving it a matt and porous appearance. This degradation is due to the oxidation of the silicone occurring under the corona effect at the electric field application.
- The silicone degradation under the applied field stress effect can be directly linked to the material embrittlement following the operated phase change, the oxidation mechanism produced at a molecular scale and the surface alteration due to the intense discharge energy, which results in a decrease in its electrical and physical performances [13, 14]. Phase changes and breaks in molecular chains leading to the release of gaseous hydrogen are then revealed by FTIR and XRD analyzes of the silicone [13, 14], explaining the deterioration of its mechanical, and electrical properties and thereby the increase in its hydrophobicity index (HI) due to the alteration of its apolar character.

Actually, the apolar nature of virgin silicone prevents it from making electrostatic interactions with water, of the permanent dipole / permanent dipole type (Keesom forces), and the low surface energy of the silicone material relative to the more high liquid energy (water), is then expressed by the water molecules stacking on top of each other giving it this hydrophobic appearance. Under the electrical aging effect, silicone partially loses its apolar character, allowing it to create hydrogen bonds with water molecules which are very polar, and seeks to interact with polar molecules to regain chemical stability, this leads to greater migration of water molecules to the material surface, thereby increasing its hydrophobicity index.

The low hydrophobicity of the electrically aged silicone sample is also explained by the balance of surface tension forces γ_{SL}, γ_{LV}, γ_{SV}, where the tension $\gamma_{SV\ (solid\ /\ vapor)}$ is lower than the tension $\gamma_{SL\ (solid\ /\ liquid)}$ which tends to increase the area between the material wall and the liquid.

V. CONCLUSION

The hydrophobic nature of the silicone increases as the declination of its surface increases. The best profile of the silicone skirt insulator corresponds to an optimal declination angle of its surface α= 30°, seeing that it offers the best hydrophobicity index HI, responding both to cases where the insulator is exposed to an environment with moderate or severe pollution and to one with average or high rainfall, or even to a mixed-conditions environment.

The silicone electrical aging alters its hydrophobicity and electrical quantities such as the surface and transverse resistivities ρ_s and ρ_t respectively, the dielectric strength E_l, the capacitor C_x, the loss factor tgδ and the permittivity ε_r. This fact is compounded by a conductive pollution deposit which promotes birth arcing at the water droplets concentration points where the produced sliding discharge energy deteriorates locally the material.

The hydrophobicity loss can be explained by the balance of surface tension forces, the loss of the apolar character of the aged silicone, to which are added the material embrittlement following the operated phase change, the oxidation mechanism produced and the surface alteration under the effect of the intense discharge energy, which results in a decrease in silicone electrical and physical performances.

REFERENCES

[1] Z. Guan, X. Wang, X. Bian, L. Wang and Z.Jia, "Analysis of causes of outdoor insulators damages on HV and UHV transmission lines in China", Electrical Insulation Conference *(*EIC*)*,Philadelphia, USA, June 8-11, 2014.

[2] R.S. Gorur, E.A. Chemey, R. Hackam, T. orbeck, "The electrical performance of polymeric insulating materials under accelerated aging in a fog chamber", IEEE Transactions on Power Delivery, Volume 3, No. 3, pp 1157-1164, July 1988

[3] I. Kimoto, T. Fujimurax, "Performance of isolators for direct current transmission line under polluted conditions", IEEE, Trans, On PAS, Vol. Pas-92 N°3, pp 934-949, May June 1973

[4] A. Mekhaldi, S. Bouazabia, "Conduction phenomena on pollution insulating surface under AC high voltages3", 9è Int. Sym. HV Eng. Autriche, 1995

[5] V. Mohan, K. Chandrasekharan, K. Padmanabhan: " Marangoni effects under electricfields", Adv. Space Res., 1983, 3, (5), pp. 177–180

[6] R. S. Gorur, J. W. Chan, 0. G. Amburge, "Surface hydrophobicity of polymers used for outdoor insulation", IEEE Transactions on Power Delivery, Vol. 5, No. 4, pp 1923-1933, November 1990

[7] S. H. Kim, E. A. Cherney, R. Hackam, K. G. Rutherford, "Chemical changes at the surface of rtv silicone rubber coatings on insulators

during dry-band arcing", IEEE Transactions on Dielectrics and Electrical Insulation Vol. 1 No. 1, pp 106-123, February 2004

[8] J. F. Hall, "History and bibliography of polymeric insulators for outdoor applications", IEEE Trans. Power Deliv., 8, (1), pp. 376–385, 1993

[9] Y. Zhu, M. Otsubo, C. Honda, "Loss and recovery in hydrophobicity of silicone rubber exposed to corona discharge", Polym. Degrad. Stab., 2006, 91, (7), pp. 1448–1454

[10] R. Raja Prabu, S. Usa, K. Udayakumar, M. Abdullah Khan and S.S.M. Abdul Majeed, "Electrical insulation characteristics of silicone and EPDM polymeric blends. I", IEEE Trans. Electr. Ins., EI Vol. 14, Issue 5, pp1207-1214, October 2007

[11] H.F. Neff, A.M.N. Lima, E.U.K. Melcher, C.S. Moreira, A.G.S. Barreto Neto, J.W . Precker, "An electro-thermal approach to dielectric breakdown in solids: application to crystalline polymer insulators", Dielectrics and Electrical Insulation, IEEE Transactions on, Volume: 17 Issue 3, pp 872 – 880, June 2010

[12] N. Rouha, F. Bouchelga[2], A. Saiche, N. Ouchenir, S. Remmache, "In search of the optimal declination of the silicone insulator profile", ISH Symposium, Glasgow, UK, August 28-September 1, 2023

[13] N. Rouha, , K. Djenkel, K. Kettir, "Physico-Chemical study of Electrically Degraded Silicone", AES Symposium, Malaga, Spain, July 2016

[14] N. Rouha, , M. Djafri, S. Kernane, "Thermal Treatment Effect on Silicone Degradation Under Electrical Stress", 4th World Congress and Expo on Recycling, Rome, Italy, july 2017

EEIC'23

Experimental study of a vibratory-type triboelectric charging device

Salah Atroune[1], Nabil Taib[2],

[1] Laboratoire de Génie Electrique de Bejaia, Faculté de Technologie, Université de Bejaia, Bejaia 06000, Algeria
salah.atroune@univ-bejaia.dz

[2] Laboratoire de Technologie Industrielle et de l'Information, Faculté de Technologie, Université de Bejaia, Bejaia 06000, Algeria
nabil.taib@univ-bejaia.dz

Abstract— **A high electrical charge to mass ratio of the particulates is a crucial for the successful electrostatic separation of granular plastic waste mixtures. The aim of the present study is to optimize the operation of a vibratory-type triboelectric charging device for two types of the plastic granules: Acrylonitrile Butadiene Styrene (ABS) and High Impact Polystyrene (HIPS).The triboelectric charger is composed of an electromechanically vibrated metal plate covered with a thin sheet of Polyethylene Terephthalate (PET). The feed rate, the displacement velocity of the particles, and the length of the vibrating plate are the studied controllable variables of the process. A series of tribo-charging experiments were conducted on ABS and HIPS granules originating from industrial waste, with a particle size of 1 to 2 mm. The performance of the vibratory-type-triboelectric charging device is evaluated by measuring the electrical charge acquired by the granules. The response surface methodology is employed for the optimization of the process.**

Keywords: **electrostatic separation, triboelectricity, charge per mass ratio,**

I. INTRODUCTION

Periodic renewal of electrical and electronic equipment is a major way to improve their performances. The consequence of this renewal is the accumulation of massive stocks of end-of-life materials, which are converted into waste streams, which cause serious environmental issues [1]. The recycling of Waste Electrical and Electronic Equipment (WEEE) is currently part of the eco-conception approach aimed at optimizing the end-of-life management of these products. The WEEE contain many valuable materials [2,3], including plastics, which have seen explosive growth in recent decades due to their low cost, durability, and lighter weight than competing materials. Triboelectrostatic separation is an effective method that is widely used in the recycling industry to recover valuable plastics [4-6]. The difference in surface properties of the various plastics enables their electric tribocharging in view of the selective sorting in a high-intensity electric field [3,6], such as the one generated between the electrodes of a free-fall electrostatic separator. The dry electrostatic processing of plastic particles [5-7], has several notable advantages such as high efficiency, low cost, and the capability of processing a relatively wide range of materials [5-8]. A tribocharger is device used to charge different materials through contact or friction [1,8,9]. Triboelectric charging is due to two types of collisions: between two particles or between a particle and the walls of the device [2,7,10,11]. The charged mixture is then separated under the action of the intense horizontal electric field created by the two vertical electrodes of a free-fall separator [12]. The problem is that part of the initially charged product is not found in the compartment reserved for it. This is due to the fact that not all the particles are sufficiently charged, and the force of gravity exerted on them surpasses the electrostatic force. As a matter of fact, the movement of plastic particles introduced into an intense electric field does not depend on the amount of charge but on the charge per mass ratio [13]. The objective of this work is to validate an experimental procedure for the optimization of vibratory-type triboelectric charging processes. The design of experiments methodology was used to identify the operating conditions of the device for obtaining the highest possible electrical charge per mass ratio in the case of ABS and HIPS granules recovered from industrial waste and characterized by a particle size ranging from 1 to 2 mm.

II. EXPERIMENTAL DEVICE

The experimental triboelectric device used is presented in Fig.1. The standard plate of a vibratory feeder (Vibra France, model APB4=30) has been replaced by a stainless-steel plate with length l_0 = 230 mm, width l =100 mm and height h =30 mm, covered with a thin layer of PET (0.2 mm). To prevent charge accumulation at its surface, the vibrated metallic plate is connected to the ground. A second vibrating feeder (Fischer Bioblock, model DR 100) is used to control the feed rate ϕ [g/s] of the plastic pellets on the

PET covered vibrated plate. The charge acquired by the plastic pellets is measured by collecting them at the outlet of the plate in a Faraday pail.

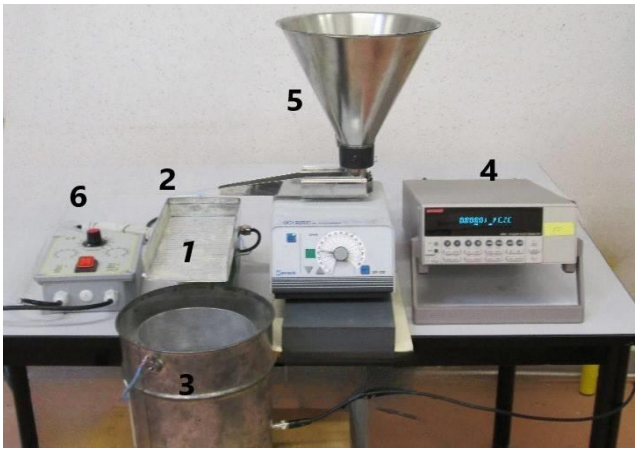


Fig. 1. Experimental setup for the study of the tribo-charging process of granular materials: (a) Schematic representation, (b) Photograph of the laboratory equipment: (1) Vibratory device; (2) PET sheet cover of the vibrating plate; (3) Faraday pail; (4) Electrometer (Keithley, model 3514); (5) Vibratory device for feed rate control;(6) Vibration amplitude controller.

III. MATERIALS AND METHOD

A series of experiments were carried out on samples of 100 g of either ABS or HIPS granules (Fig.2), with an average pellet size of 1 to 2 mm, originating from out-of-use computer casings, after shredding and grinding. The plastic granules were provided by a WEEE recycler (APR2, Bonnières sur Seine, France).

The study of feed rate ϕ effect was conducted with 100 g samples of ABS and 100 g samples of HIPS, at three constant values of the displacement velocity v: 5.67 cm/s, 7 cm/s, and 9.1 cm/s, under stable atmospheric condition (humidity RH=53% ±2%, temperature T=19.3° ±1°C). The length of the tray being L = 23 cm.

The study of displacement velocity v effect was performed on the L = 23 cm vibrating tray, with the same quantities of materials, under similar ambient conditions, at three constant values of the feed rate ϕ: 2.86 g/s, 3.86 g/s and 5 g/s.

New samples were used in each experiment concerning the effects of granule feed rate and granule velocity. For the study of the effect of vibrated plate length L, the same sample was passed one to five times in the tribocharger, corresponding to L = 23 cm; 46 cm; 69 cm; 92 cm; 115 cm (feed rate: 3.8 g/s; displacement velocity: 7.7 cm/s).

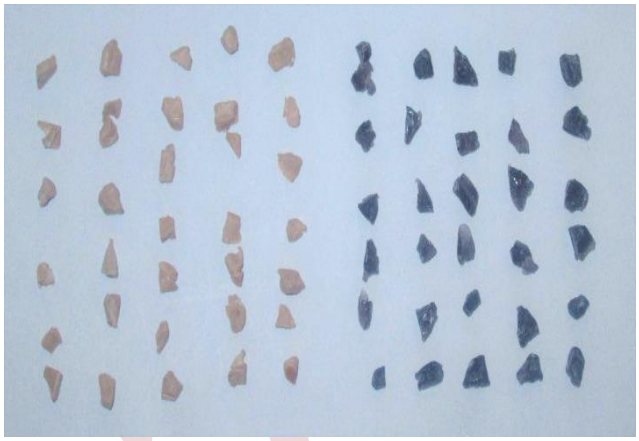


Fig. 2. Photograph of the materials used in the experiments: ABS on the left side, HIPS on the right side

To model the process and determine the optimal operating parameters of the tribocharger the design of experiments methodology was used [14]. A composite factorial experimental design [15] was conducted to obtain the response "y" of the process, given by the following general formula:

$$y = a_0 + a_1x_1 + a_2x_2 + a_3x_3 + a_{11}x_1^2 + + a_{22}x_2^2 + a_{33}x_3^2 + a_{12}x_1x_2 + a_{13}x_1x_3 + a_{23}x_2x_3 \quad (1)$$

With a_i and a_{ij} are the coefficients of the quadratic model and x_i, i = 1, 2, 3 are the normalized centered values of each factor u_i.

$$x_i = (u_i - u_{ic}) / \Delta u_i = u^* \quad (2)$$

$$u_{ic} = (u_{ima} + u_{imin})/2; \quad \Delta u_i = (u_{i\,max} - u_{i\,min})/2 \quad (3)$$

For the factors considered in this study (v, ϕ and L), the quadratic response model of the specific charging acquired by the ABS and HIPS pellets takes the following form:

$$y = a_0 + a_1 v^* + a_2 \phi^* + a_3 l^* + a_{11} v^{*2} + + a_{22} \phi^{*2} + a_{33} l^{*2} + a_{12} v^* \phi^* + a_{13} v^* l^* + a_{23} \phi^* l^* \quad (4)$$

The analysis of the obtained experimental results was performed with the software MODDE 5.0 (Umetrics 1999) [16]. It calculates the a_{ij} coefficients of the mathematical model and determines the best factor settings to optimize the procedure. The program evaluates two statistical criteria: the "goodness of the adjustment" (R^2) and the "quality of the prediction" (Q^2). The numerical values of R^2 and Q^2 must be close to the unity for a good model.

IV. **Experimental modeling of the tribo-charging process**

The results of the experiments performed according to the design of experiments methodology on samples of 100 g of ABS pellets and 100 g of HIPS pellets of sizes 1 to 2 mm are presented in Table 1. Each measured point corresponds to the average of three trials, performed under stable atmospheric conditions of humidity *RH*= 61%, ± 2% and temperature *T*= 21° ±1C.

The mathematical models obtained using MODDE 5.0 software are given in by equations (5) and (6) for ABS and HIPS respectively. The obtained charge per mass ratio models depend on *v*, ϕ and *L* parameters.

ABS: Goodness of fit: R^2 = 0.984 and Goodness of prediction: Q^2 = 0.918

$$Q/m = 1.17986 - 0.03816\, v^* + 0.004098\phi^* + 0.07899 L^* - 0.05677 v^{*2} - 0.02261\phi^{*2} + 0.05141\, v^* L^* \quad (5)$$

HIPS: Goodness of fit: R^2 = 0.984 and Goodness of prediction: Q^2 = 0.902

$$Q/m = -1.24331 - 0.00807\, v^* + 0.19388\phi^* - 0.10652 L^* - 0.10132\, v^{*2} - 0.083204\, L^{*2} + 0.01631\, v^* L \quad (6)$$

Table 1: Charge per mass ration (*Q/m)* of ABS and HIPS granules, for the 17 runs of the composite experimental design

N°	Velocity *v* [cm/s]	Feed rate ϕ [g/s]	Tray length *L* [cm]	Charge/masse ABS *Q/m* [nC/g]	Charge/masse HIPS *Q/m* [nC/g]
1	6	2.6	46	1.097	-1.345
2	9.4	2.6	46	0.816	-0.646
3	6	5	46	0.947	-0.860
4	9.4	5	46	0.805	-0.777
5	6	2.6	92	1.116	-1.687
6	9.4	2.6	92	1.241	-1.496
7	6	5	92	1.324	-1.827
8	9.4	5	92	1.062	-1.123
9	6	3.8	69	1.153	-1.04
10	9.4	3.8	69	1.226	-1.166
11	7.7	2.6	69	1.202	-1.58
12	7.7	5	69	1.141	-0.971
13	7.7	3.8	46	1.055	-1.083
14	7.7	3.8	92	1.438	-1.649
15	7.7	3.8	69	1.188	-1.249
16	7.7	3.8	69	1.17	-1.33
17	7.7	3.8	69	1.201	-0.915

A. Effect of velocity

In Fig. 3.a and Fig. 3.b, the specific charge per mass ratio of ABS and HIPS granules is presented as a function of granule displacement velocity. The model shows an approximately linear rise in the charge per mass ratio from *v* = 6 cm/s to v = 7.7 cm/s. With a displacement speed of 7.5 cm/s, the maximum value of the ABS charge per mass ratio is 1.20 nC/g. However, for HIPS, this maximum is -1.29 nC/g for a displacement speed of 7.7 cm/s. Hence, the variation of the charge to mass ratio is slightly different for the two materials.

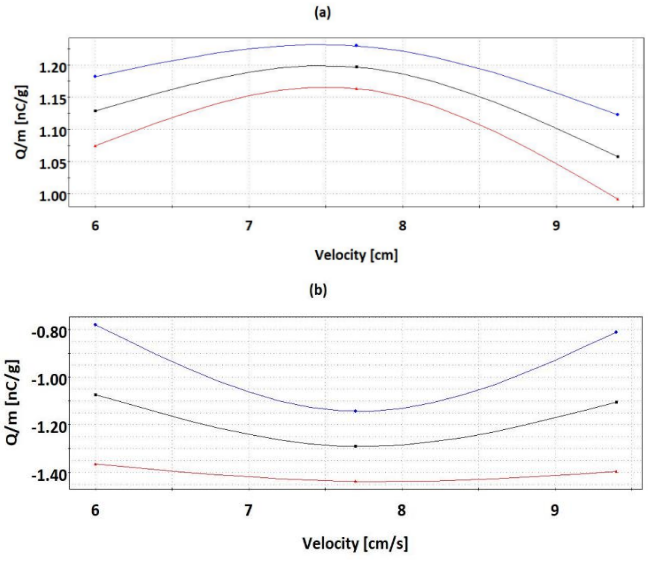


Fig.3. *Modde 5.0 predicted variation on the charge per mass ratio as function of velocity, for (a) ABS and (b) HIPS*

This trend of increasing charge per mass ratio is justified by the movement of granules with shorter jumps and a higher number of collisions with the vibrating plate. For ABS and HIPS, the charge per mass ratio declined at speed values beyond 7.5 cm/s and 7.7 cm/s, respectively. Higher velocities imply higher jumps and more energetic collisions between the granules, but fewer hits mean that the granules are accumulating less charge

B. Effect of feed rate

The charge per mass ratio of the ABS pellets, shown in Fig. 4.a, rose with increasing pellets feeding rate on the vibrating plate from 2.6 g/s to 3.8 g/s before falling sharply. On the other hand, the charge per mass ratio of the HIPS granules decreased linearly with an increase in the rate at which the granules were fed to the vibrating plate as illustrated Fig. 4.b.

The mathematical model indicates that the highest absolute value of the charge per mass ratio was for ABS 1.20 nC/g at a feed rate of 3.6 g/s and for HIPS -1.6 nC/g at a feed rate of 2.6 g/s, These outcomes are attained for length L=69 cm and v = 7.7 cm/s. The fact that the granules have less impacts on the vibrating plate can explain why specific charge decreases at increasing granule deposition velocities.

C. *Effect of length L*

As expected, the charge per mass ratio increased with the vibrating plate length L. The same result was observed for both ABS and HIPS, as shown in Fig 5.a and Fig 5.b. This leads to predicting that a vibrating plate length of 92 cm would yield the best results, with charge per mass ratios of 1.30 nC/g for ABS pellets and -1.65 nC/g for HIPS pellets.

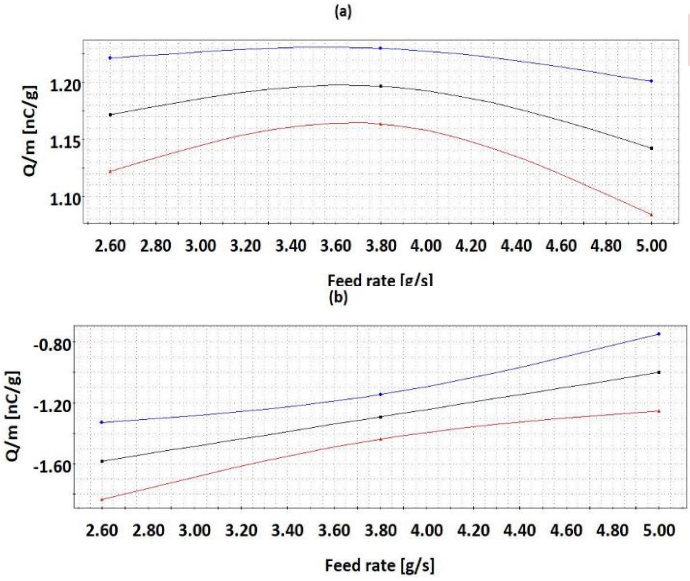


Fig.4. *Modde 5.0 predicted variation of the charge to mass ratio as function of feed rate for (a) ABS and (b) HIPS.*

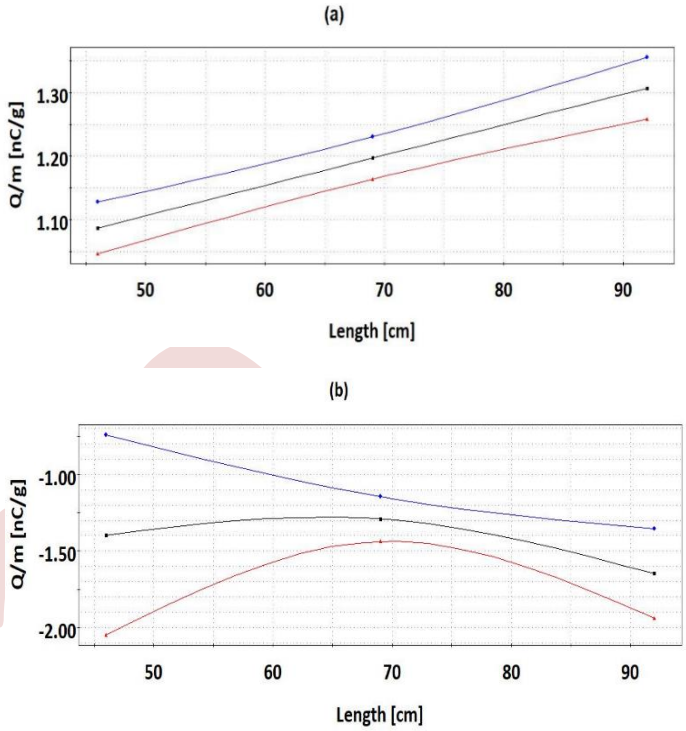


Fig.5. *Modde 5.0 predicted variation of the charge per mass ratio as function length, for (a) ABS and (b) HIPS.*

D. Velocity and feed rate interaction

Contour plots provided by MODDE.5.0 and depicted in Fig.6 highlight the effects of the two control variables: the velocity v of particle movement on the vibrating plate and the rate ϕ of granule deposition on the vibrating plate.

In the case of ABS granules, shown in Fig.6.a, the model predicts the highest charge per mass ratio of 1.177 nC/g for velocities range values between 6.70 cm/s and 8.30 cm/s, with a feed rate varying between 2.6 g/s and 4.5 g/s.

For the HIPS material, shown in Fig.6.b, the model predicts the highest charge per mass ratio value of -1.58 nC/g, for velocities ranging between 6.5 cm/s and 9.1 cm/s, with a feed rate varying between 2.6 g/s and 3 g/s.

This result can be explained by the synergetic action of the two control variables in the mentioned intervals, to generate collisions of the granules and the vibrating plate efficiently enough to obtain energetic and repetitive impacts that induce a rather high charge per mass ratio.

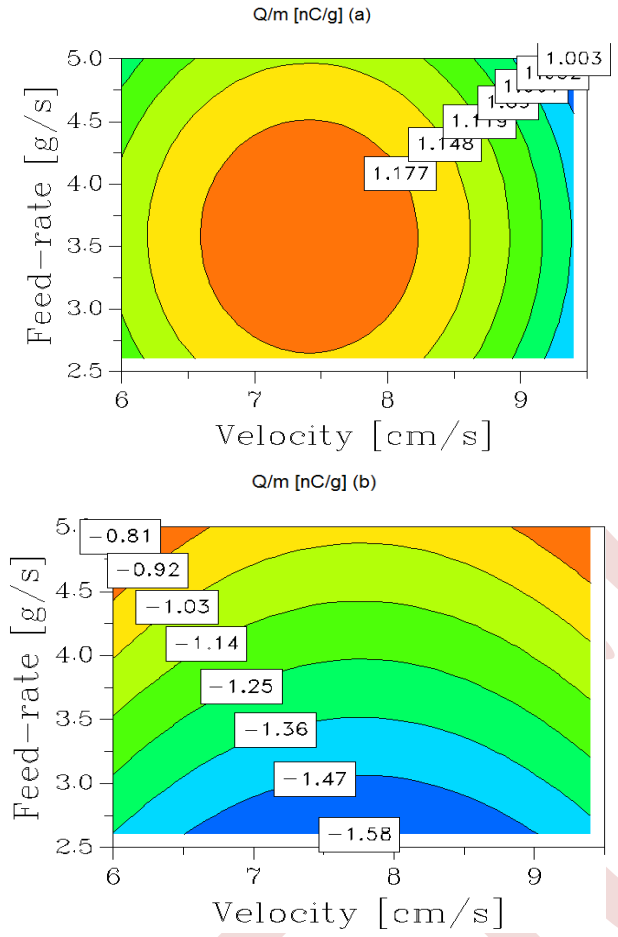


Fig.6. *Contour plots of the response Q/m charge per mass ratio calculated with MODDE 5.0 for (a) ABS and (b) HIPS.*

V. Conclusions

This paper is dedicated to model an experimental procedure on the triboelectricity of ABS and HIPS materials based on "design of experiments" approach. This model allows a better understanding of the behavior of the different parts involved in the vibratory-type triboelectric charger of ABS and HIPS granules, and the thin PET plate covering the vibrating plate.

The presented vibrating charger is a very conclusive device in terms of charge transfer by triboelectricity. It is subject to several controllable parameters, and that can influence this charge transfer.

The control and the correlation between velocity and feed rate parameters generate a rather satisfactory charge transfer between the granular materials and PET plate.

The charge per mass ratio increases with the controllable length parameter of the vibrating plate to the limit of saturation of the plastic particles, after which the exchange of charge between the two materials ceases.

The design of experiments methodology may prove to be useful for conducting in-depth research on the impact of determinable parameters on the transfer of charge per mass ratio in such devices.

References

[1] G. Wu, J. Li, Z. Xu, Triboelectrostatic separation for granular plastic waste recycling: A review, Waste Management, 33.(2013), 585-597.

[2] T. Zeghloul, A. Mekhalef Benhafssa, G. Richard, K. Medles,L. Dascalescu, Effect of particale size on the tribo-aero-electrostatic separation of plastics. Journal of Electrostatics. 88.(2017),24-28.

[3] J. Li, Z. Xu, Compound tribo-electrostatic separation for recycling mixed plastic waste, Journal of Hazardous Materials.367.(2019), 43-49.

[4] G. Buda, A. Samulia, S. Atroune, M. Bilici, L. Dascalescu, Set point identification of a tribocharging process for mixed granular solids. Journal of Electrostatics. 71. (2013), 407-412.

[5] L. Dascalescu, T. Zeghloul, A. Iuga, Electrostatic separation of metals and plastics from waste electrical and electronic equipment In WEEE Recycling. Reserch, Development, and Policies (A. Chagnes, G. Cote, E. Ekberg, M. Nilsson, T. Retegan, Eds), Elsevier, Amsterdam, 2016, pp. 75-106

[6] S. Atroune, A. Tilmatine, R. Alkama, A. Samuila, L. Dascalescu, Comparative experimental study of triboelectric charging of two size classe of granular plastics. Particulate Science and Technology, 33(6). (2015), 652-658.

[7] P. M. Ireland, K. Nicholson, Analysis and comparison of partical tribochargers. Minerals Engineering. 24 (2011), 914-922.

[8] A. Benabderrahmane , T, Zeghloul, W. Aksa, A. Telmatine, K. Medles, L. Dascalescu. Shredding as simultaneous size-reduction and tribo-charging operation for improved performance of an electrostatic separation process for granular plastic wastes. Particulate Science and Technology, 38. (2020), 827-834.

[9] R. Messafeur, I. Mahi, R. Ouiddir, K. Medles, L. Dascalescu, A. Tilmatine. Tribo-electrostatics separation of quaternary granular mixture of plastics. Particulate Science and Technology, 37. (2019), 764-769.

[10] M. Blajan, A.Iuga, L.Dascalescu. Triboelectrification of granular plastics wastes in vibrated zigzag-shaped square pipe in view of electrostatics separation. IEEE Transaction on Industry Applications, 46.(2010),1558-1563.

[11] P. M. Ireland. Triboelectrification of particulate flows on surface: Part I experiments. Powder Technol. 198.(2010),189-198.

[12] A. Benabboun, A.Telmatine, Y. Brahami, S. Bendimerad, M. Miloudi, K. Medles. Experimental investigation of electrostatic separators of plastic particles using different charging devices. Particulate Science and Technology, 49. (2014), 464-468.

[13] Y. Higashiyama, Y. Ujiie, K. Asano. Triboelectrification of plastic particles on vibrating feeder laminated with plastic film. Journal of Electrostatics. 42. (1997), 63-68.

[14] N.L. Frigon, D. Mathews. Practical guide to experimental design.New York,NY/ Wiley, (1996).

[15] L. Eriksson, E. Johansson, N. Kettaneh-Wold, C. Wikstrom, S.Wold. Design of experimrnts: Principles and applications. Stockholm: Learnways AB. (2000).

[16] Umetrics AB MODDE 5.0. User guide and tutorial, Umetrics, Umea, Sweden, 1999.

Study of space charge current in power cables using the alternating thermal wave method

I.BRAKNA [1],J.M.REBOUL [2] , M.AISSOU [1,3], A.LAIFAOUI [3]

[1] *Laboratoire intelligent structures, Ain Temouchent, Algeria*

braknaikram@gmail.com

[2]*Laboratoire Universitaire des Sciences Appliquées de Cherbourg Ecole d'ingenieurs de Cherbourg Universite de Caen Basse-Normandie Cherbourg, France*

jean-michel.reboul@unicaen.fr

aissoumass@gmail.com

[3]*Laboratoire de Génie Electrique Université Abderrahmane Mira, Bejaia, Algérie*

abdelkrim2002@yahoo.fr

***Abstract*— The alternative thermal wave method (ATWM) has several advantages over other techniques. It is non-destructive, allowing materials to be assessed without damaging them, and it is relatively fast and easy to use. This paper focuses on the development of a new approach to measuring the ATWM by heating the copper armour on an 18/30 kV medium-voltage cable aged for 1300 hours.**

Keywords: The Alternating Thermal Wave Method, Space charge, Power cable.

I. INTRODUCTION

The Alternating Thermal Wave Method involves the generation of thermal waves, which are periodic temperature variations that propagate through a material [1]. The Alternating Thermal Wave Method allows for the non-destructive testing of materials, it is a valuable tool in research and industry for characterizing materials.

The Alternating Thermal Wave Method has a wide range of applications in various fields. Additionally, the Alternating Thermal Wave Method allows for rapid and accurate measurements, providing valuable data in a short amount of time. However, it is important to note that the Alternating Thermal Wave Method also has some limitations. It requires specialized equipment and expertise to perform the measurements, which may limit its accessibility. Furthermore, the accuracy of the measurements can be affected by factors such as sample thickness and surface conditions. Despite these limitations, the Alternating Thermal Wave Method remains a valuable technique for thermal analysis and measurement in various fields.

The Alternating Thermal Wave Method (ATWM) is a technique that has been developed for space charge measurements. This method utilizes thermal analysis and simulations to improve data processing and provide accurate measurements of space charge. The ATWM has undergone recent improvements to enhance its effectiveness in measuring space charge [2]. Space charge measurements are important in various fields, including materials science, electrical engineering, and physics. Understanding the distribution and density of electric fields and space charges in solid materials is crucial for optimizing their performance and reliability. Additionally, space charge measurements are essential in studying the behaviour of electrons and ions in the space charge region, which has implications for plasma physics and other related fields.

The ATWM offers several advantages for space charge measurements. It allows for the measurement of space charge limited currents through films, providing insights into their electrical properties [3]. The ATWM's ability to improve data processing through thermal analysis and simulations further enhances its accuracy and reliability in space charge measurements. Overall, the Alternating Thermal Wave Method is a valuable tool for researchers and scientists seeking to understand and analyze space charges in various materials and systems. It uses an alternating current to heat the cable core and control measurements at different temperatures. One application of the ATWM is in the measurement of current due to space charge present in PVC sheaths after aging under AC sinusoidal high voltage [4].

II. PRINCIPLE OF THE METHOD

The Alternating Thermal Wave Method (ATWM) is a useful technique for measuring space charge in thin polymer films with metallic vacuum deposits on each side acting as electrodes. The electrodes are short-circuited by a current amplifier.

The method involves generating a thermal wave using a thermoelectric module applied to one side of the film, then scanning successive layers using increasing penetration depths [5]. Attenuated sinusoidal temperature waves penetrate the sample, and the wavelength and attenuation factor depend on the frequency and thermal properties of the material [6]. Only space charges within the penetration depth of the thermal wave are affected by the induced pyroelectric current and can be measured by the current amplifier [7].

The TEM operates in the frequency range 0.1 Hz - 100 Hz.

III. TEMPERATURE DISTRIBUTION IN ATWM CONDITIONS

The experimental current response of the sample depends on the distribution of the time derivative of temperature. In the case of the one dimensioned structure (the electrode diameter greater than the sample thickness), the experimental current i(t) obeys the following equation [8]:

$$i(t) = -\alpha_x C_0 \int_0^d E(x) \frac{\partial T(x,t)}{\partial t} dx \quad (1)$$

Where α_x is the thermal coefficient of variation of the capacitance, d the thickness of the sample, $C_0$the capacitance, $E(x)$ the electric field due to the space charge distribution, $\partial T(x,t)/_{\partial t}$ the time derivative of the temperature in the sample.

The heat equation (2) is solved for the one-dimensioned medium with specific boundary conditions [9]:

$$\frac{\partial T(x,t)}{\partial t} = a \frac{\partial^2 T(x,t)}{\partial x^2} \quad (2)$$

Where a is the thermal diffusivity $m^2/_s$.

IV. EXPERIMENTAL PROCEDURE

To measure the current due to space charge in a single-pole 18/30 kV PRC power cable, 45 cm long.

The cable was subjected to a DC voltage of 70 kV at ambient temperature (25°C) for 1,300 hours at the Bejaia Electrical Engineering Laboratory (LGEB).

We set up a new measuring bench at the laboratory (LUSAC) in Cherbourg, which consists of a voltage transformer that supplies a current (a few A) to heat the copper shielding of the cable. A current amplifier is connected between the core and the external semi-conductor of the cable figure (1).

The response of the cable is then measured.

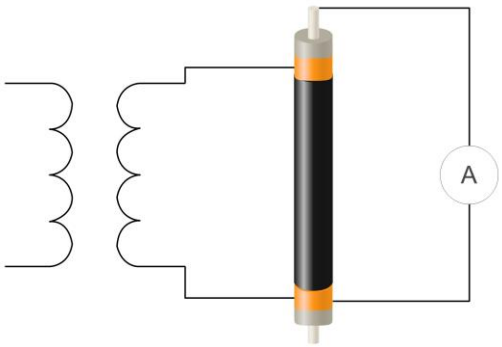
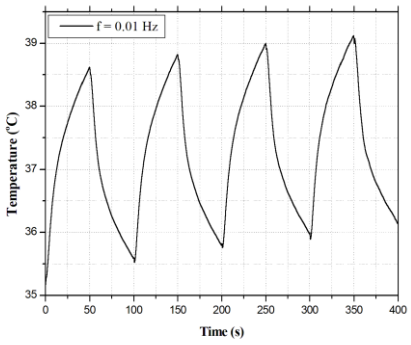


Fig 1. Schematic diagram of the experimental set-up.

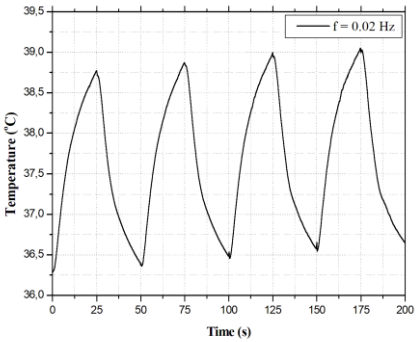
V. RESULTS AND DISCUSSION

The heat source is modulated at a specific frequency, creating alternating thermal waves in the material. We obtained the following results:

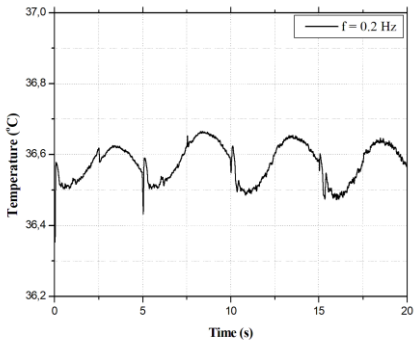
A. TEMPERATURE



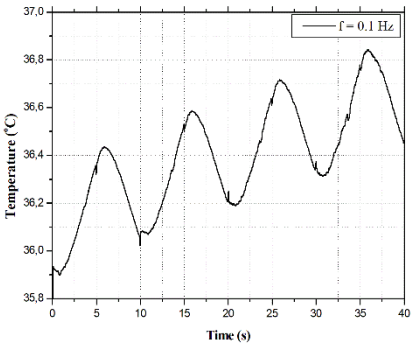
a)



b)



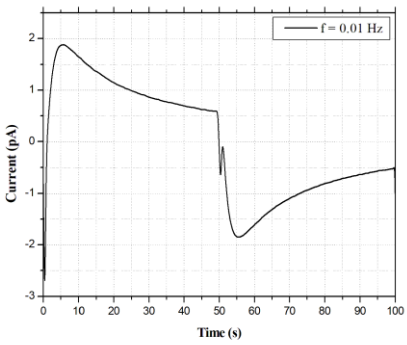
c)



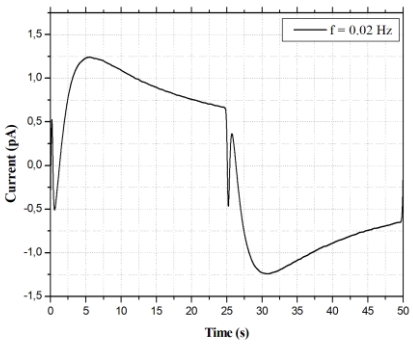
d)

Fig 2. Experimental temperature variation as a function of frequency : a) 0.01 Hz , b) 0.02 Hz , c) 0.2 Hz , d) 0.1 Hz .

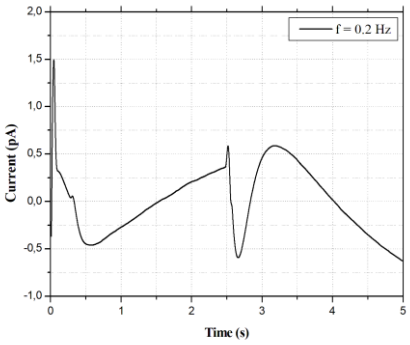
B. CURRENT



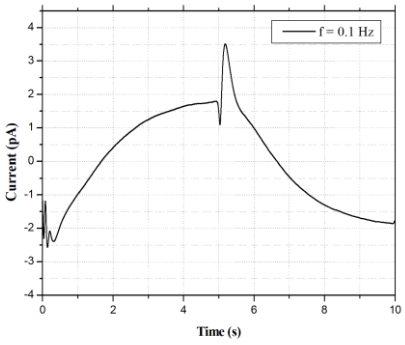
a)



b)



c)



d)

Fig 3. Variation in ATWM current as a function of frequency : a) 0.01 Hz, b) 0.02 Hz , c) 0.2 Hz , d) 0.1 Hz.

The figures 2 and 3 show the experimental currents and temperatures for each frequency (0.02,0.01,0.1,0.2 Hz).

In figure 2 ,we can see that as the frequency decreases, the wavelength of the thermal waves increases. This means that the thermal waves have more time to interact with the electrical charges in the material. These interactions lead to an increase in temperature amplitude.

The heating temperature should not exceed 40 degrees Celsius, as a high temperature can cause the cable's insulation layer to break, allowing electrical charges to flow through.

Figure 3 shows that the amplitude of the ATWM current increases during heating due to the presence of the space charge and decreases during cooling.

VI. CONCLUSION

The test set developed uses thermal excitation to evaluate cables.

Using the Joule effect to generate thermal excitation in the cable armour enables cables to be tested more accurately and more quickly, while limiting temperature changes to 40 degrees to avoid damaging the cable.

The use of ATWM has important applications in the cable industry, particularly in assessing performance, resistance to temperature change and durability. This is particularly useful in environments where cables are subjected to harsh conditions.

REFERENCES

[1] J.-M. Reboul et R. Carin, « Space-charge measurement in polymer films by the new alternating thermal wave method », Polym. Int., vol. 51, no 11, p. 1190–1197, 2002. doi : 10.1002/pi.863.

[2] J. M. Reboul et F. Mady, « Space charge measurements by the alternating thermal wave method : thermal analysis and simulations for data processing improvement », dans Proc. 2004 IEEE Int. Conf. Solid Dielectrics, Toulouse, France. IEEE. doi : 10.1109/icsd.2004.1350339.

[3] J. M. Reboul, « Thermal waves interferences for space charge measurements in dielectrics », dans 2011 IEEE 14th Int. Symp. Electrets ISE 14, Montpellier, France, 28–31 août 2011. IEEE, 2011. doi : 10.1109/ise.2011.6084983.

[4] J. M. Reboul, A. Cherifi et R. Carin, « A new method for space charge measurements in dielectric films for power capacitors », IEEE Trans. Dielectrics Elect. Insul., vol. 8, no 5, p. 753–759, 2001. doi : 10.1109/94.959694.

[5] J. M. Reboul, M. Rouff et R. Carin, « Characterization of dielectric films for power capacitors by space charge technique », dans Conf. Rec. 2002 IEEE Int. Symp. Elect. Insul., Boston, MA, USA. IEEE. doi : 10.1109/elinsl.2002.995942.

[6] J. M. Reboul, F. Mady, M. Rouff et R. Carin, « A new technique for a complete study of space charge », dans IEEE 7th Int. Conf. Properties Appl. Dielectric Mater., Nagoya, Japan. IEEE. doi : 10.1109/icpadm.2003.1218466.

[7] J. M. Reboul, « Fast plotting electric field in poled dielectrics using thermal step method », dans 2016 IEEE Int. Conf. Dielectrics (ICD), Montpellier, France, 3–7 juill. 2016. IEEE, 2016. doi : 10.1109/icd.2016.7547561.

[8] J.-M. Reboul, « Diagnostics on cylindrical case film capacitors by space charge current signatur », dans 2008 13th Int. Symp. Electrets ISE 13, Tokyo, Japan, 15–17 sept. 2008. IEEE, 2008. doi : 10.1109/ise.2008.4814047.

[9] J. Castellon et al., « Industrial installation for voltage-on space charge measurements in HVDC cables », dans Fourtieth IAS Annu. Meeting. Conf. Rec. 2005 Industry Appl. Conference, 2005., Hong Kong, China. IEEE. doi : 10.1109/ias.2005.1518496.

A Graphical Tool For The Tracking of A Single Particle In An Electric Field

Kachi Miloud, Bechkoura Hana, Mouhoub Sarra, Bouchelkha Abdelhafid

Electrical engineering laboratory, University of 8 May 1945 - Guelma, PO.B 401, Guelma, Algeria.

kachi.m@univ-guelma.dz

bechkoura.hana@univ-guelma.dz

mouhoub.sarra@univ-guelma.dz

bouchelkha.abdelhafid@univ-guelma.dz

***Abstract*—In this paper, a computer vision-based code intended to track a particle in an electric field is presented. The developed code focuses on a single particle's movement due to the electric field in an electrostatic application. The particle's trajectory is defined using its position in the treated frame from a video acquired by a fixed camera. In planar configuration, it is even possible to calculate the particle speed if real dimensions are given. Three situations are presented throughout this paper: electric curtain, plane to ground electrode, and roll to ground electrode. In all situations, the code performs well and is able to define the particle's trajectory. Examples of speed calculation are also presented in the two cases: electric curtain and plane-to-ground electrode.**

***Keywords*:** computer vision, particle tracking, electric field, particle trajectory, electrostatic applications.

I. INTRODUCTION

In the last decades, computer vision has significantly evolved and, most importantly, has become accessible through free and open-source libraries in different programming languages. This allowed the development of multiple kinds of applications, ranging from simple image treatment to a more complicated systems such as autonomous cars, drones, and many other engineering areas. The association with artificial intelligence offers limitless possibilities for computer vision and opens the area to advanced applications such as detection and classification, tracking of the object in complex conditions, prediction, and many other possibilities [1–5]. Among possible applications, the assessment of the performance of an electrostatic separation process by mapping the particle's distribution and counting recovered quantities has been carried out [6].

In electrostatic applications, particles are subjected to electric forces to make them move in some direction. During the development of such a process, the particle movement, including trajectory, is an important source of information on the performance of the developed application. Eye observation of the movements is not really helpful to evaluate the performances and the obtained results. For that reason, numerical calculation of the particle trajectory is one of the approaches followed in attempts to visualize the particle's behavior [7 – 11]. However, as these numerical studies are mostly difficult to implement, computer vision can be an alternative tool to extract information about movement from a simple recorded video or live recording camera. Over the years, advanced solutions have been developed to visualize particle movement, even in three-dimensional space, such as the particle tracking velocimetry (PTV) technique [12]. However, these techniques are so expansive because they require high-speed cameras, lasers, multicamera, and so on. The tracking of a single particle moving at relatively low speed can be easily realized using a standard camera at 30 fps to 200 fps. With proper coding, it is possible to construct a cost-effective solution to the particle tracking problem.

In this paper, a developed code is presented along with its application to a real particle movement resulting from an electric force. The code offers several functions, including dimension definition and speed calculation. The user graphically interacts with the code through a user interface. The aim is to apply these computer vision algorithms to track a single particle's movement in an electrostatic process. The developed code follows the particle's position and is able to calculate its speed if dimensions are defined.

II. ALGORITHM AND CODE DESCRIPTION

The developed Python code is based on the free and open-source computer vision Open CV library [13]. It is intended to be used with videos captured by a static camera. The main idea behind the code is the treatment of the recorded video frame after frame to define the moving object's coordinates. Once defined, the link between these coordinates with a straight line leads to the visualization of the object's trajectory. This goal can be achieved by applying the basics of computer vision algorithms to extract such information about the moving object.

Figure 1 shows the code's graphical interface during a video treatment. The buttons on the right are commands to different functions, such as video path, scale and distance entrance, start tracking, showing results and so on. Various options are offered to the user on the left side, such as reading mode and filter.

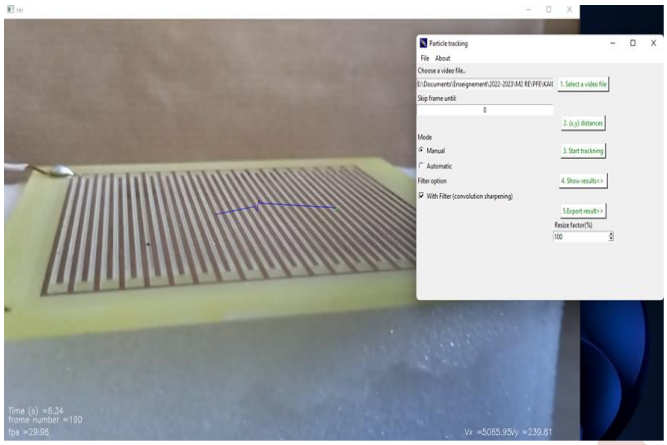


Figure 1. Main interface and results of particle trajectory over a standing wave electric curtain. Bottom left corner brings additional information about the video.

Figure 2 shows the code structure and steps followed to track the moving particle's position. Each frame of the video is subject to a series of functions to detect particles in motion. The first and most important function is the background removal, which essentially turns any pixels that do not change over time into black. This function allows detection of the object, which will be turned white. The result of the background removal function is a mask in which the object is white. Figure 3 represents an example of the resulting mask of a particle above the electric curtain. As observed, only moving particles are in white. This allows the determination of white color contours and, thus, the particle position. Additional treatments are necessary to enhance object detection, such as thresholding and image sharpening using a convolution filter. The thresholding allows suppression of objects, shadows, or any unwanted region. On the other hand, image color sharpening is realized by a 2D convolution filter, which consists of convolving the image with a kernel. The kernel is simply an array of coefficients. For example, the applied sharpening kernel takes the form:

$$kernel = \begin{bmatrix} 0 & -1 & 0 \\ -1 & 5 & -1 \\ 0 & -1 & 0 \end{bmatrix} \quad (1)$$

After treatment, the code checks for the existence of any white objects and defines the contours of the region. This leads to the location of the particle's coordinates. Finally, the link between the defined coordinates gives the particle trajectory. If a scale is defined for the treated geometry, the code is capable of calculating the particle speed and displacement. For that reason, the user has the option to enter known geometry dimensions that will be used to convert pixels to a given distance unit. The speed in both directions *x* and *y* is calculated simply by $V_x = \frac{dx}{dt}$ and $V_y = \frac{dy}{dt}$.

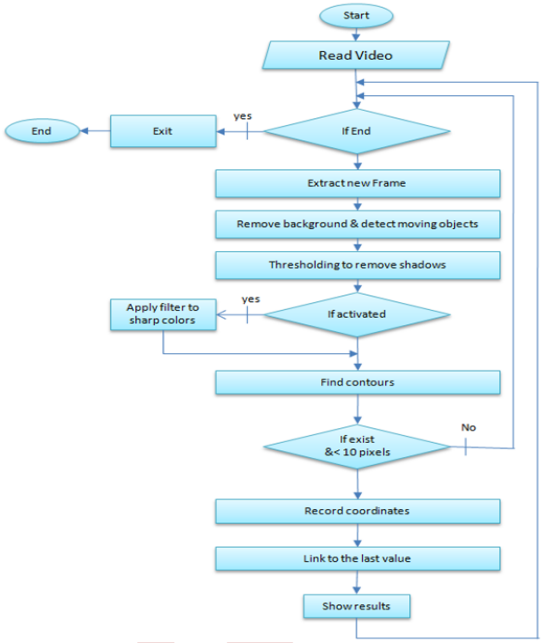


Figure 2. Flowchart of the code for particle detection and tracking using OpenCV-python.

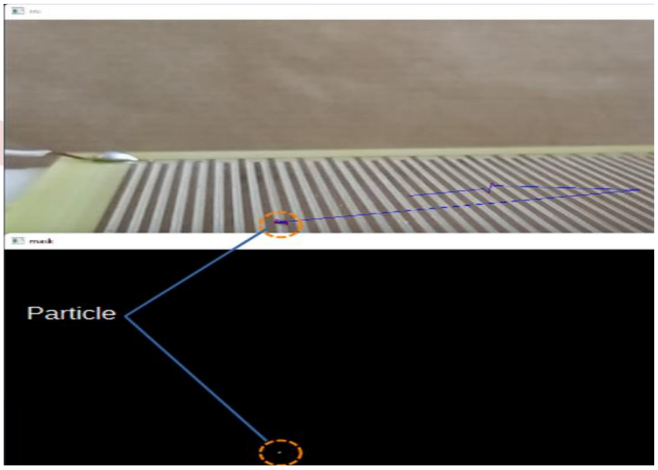


Figure 3. The frame and the corresponding mask, showing the particle in white.

III. MATERIALS AND METHODS

The particles used during experiments are acrylonitrile butadiene styrene (ABS) and high impact polystyrene (HIPS) materials of around 1 mm size. The tracking is based on observing the behavior of the particle in the electric field generated by different electrodes. These electrodes consist mainly of three devices, namely the electric curtain, plane-to-ground capacitance, and roll-to-ground electrodes. The recorded videos are acquired by a standard 30 fps camera.

A. *Electric curtain*

The electric curtain is an electrostatic device often used to clean surfaces and transport particles [11]. The used electric curtain is a biphasic type, which consists of a series of two alternatingly adjacent electrodes (see Figure 1) connected to two sinus waveform voltages of 1 kV amplitude and shifted by π.

B. *Plane to ground configuration*

The plane to ground electrode configuration is formed by a metal plate of 10 cm x 15 cm size suspended over a large metallic grounded surface at 2 cm height. The plate is connected to a positive DC high voltage power supply. The voltage amplitude is changed until the levitation of the particle.

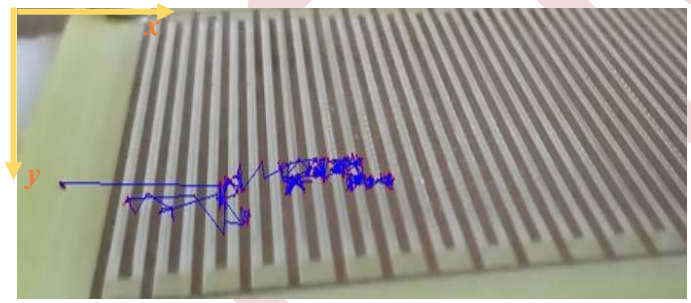
C. *Roll to ground configuration*

The roll is a metallic stainless steel made cylinder of 13 cm diameter and 14.5 cm length suspended over a grounded surface at 2 cm height. The roll is driven by an electric motor at a fixed rotating speed of 47 rpm.

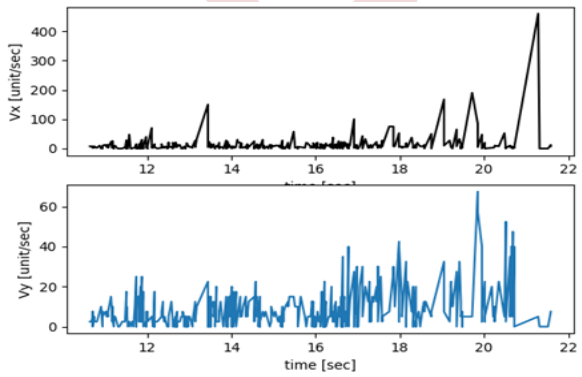
IV. Results And Discussion

A. *Electric curtain*

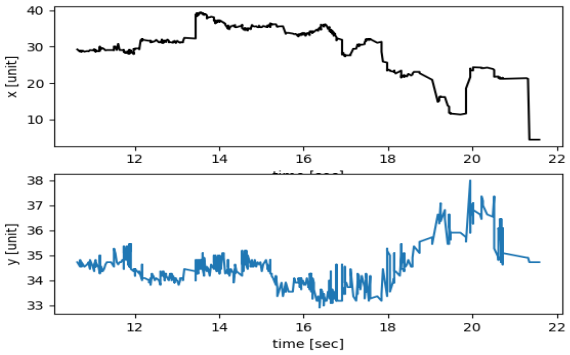
Figure 4 represents the results of particle motion analysis in the case of a double phase standing wave electric curtain. The small movements were detected, even those due to the particle's vibrations around the same position. As clearly shown by these results, the particle movement is composed of vibration and displacement over small distances (Figure 4.a), in the millimeter range (Figure 4.c). The corresponding speed over the *x* axis is much higher than the speed following the *y* axis, which is clearly noticeable in the trajectory (Figure 4.b).



(a)



(b)

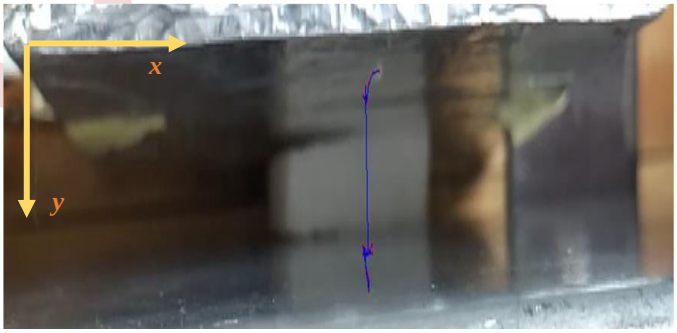


(c)

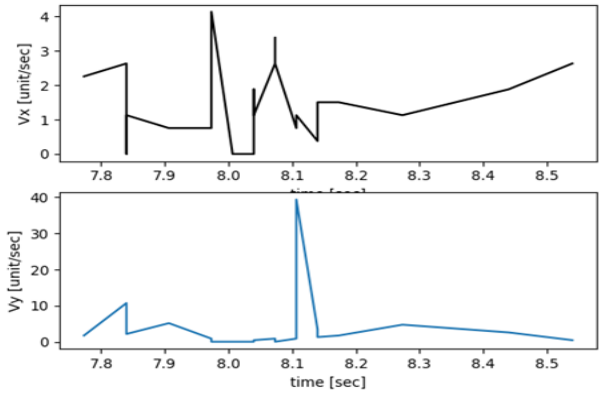
Figure 4. Particle movement above a standing wave electric curtain: (a) trajectory, (b) speed (in mm/sec), and (c) displacement (in mm).

B. *Plane to ground electrode*

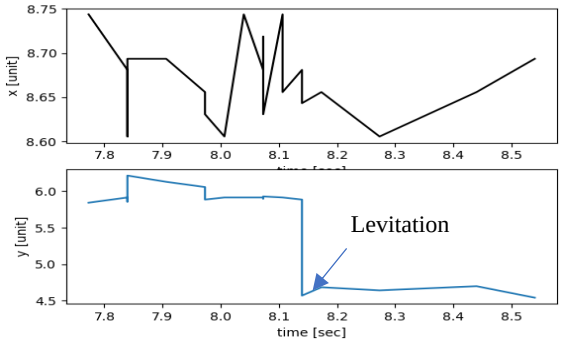
Figure 5 shows the results of a single particle movement between two plane electrodes. Indeed, the program is capable of tracking particle displacement and thus estimating its speed. The particle carries a small vibration-like movement before it levitates towards the upper HV electrode at around 8.15 seconds. In a plane electrode the electric field is uniform between the energized electrode and the ground, which leads to a constant electric force. As expected, the particle is attracted by the HV electrode following nearly a straight line. Even with the plane electrode, there is a small horizontal displacement, in the order of millimeters, along the x axis (Figure 5.c).



(a)



(b)



(c)

Figure 5. Particle movement in plane configuration: (a) trajectory, (b) speed (cm/sec) and (c) displacement (in cm).

C. Roll to ground configuration

Figure 6 depicts the particle's trajectory placed under a rotating roll suspended over a grounded plane. The result shows the particle's behavior from levitation until adherence and traveling with the rotating roll. From left to right in the figure, the pictures show particle displacement, corresponding to frames 1, 4, and 14, respectively. The last picture corresponds to the entire recorded trajectory of the particle. The recorded trajectory can be divided into two separate regions with different acting forces. The first is the space between the ground and the roll, in which the particle is subject to several kinds of electric and non-electric forces. The position of the moving particle in this region is mainly controlled by electric forces but also by the particle weight. The resulting forces attract the particle towards the high field intensity region of the cylinder. The second part of the trajectory in which the particle is stuck to the roll is mainly controlled by the electric forces (image force, coulomb force) and the centrifugal force. The particle is attached to the roll as long as the attracting electric forces are higher than the centrifugal force.

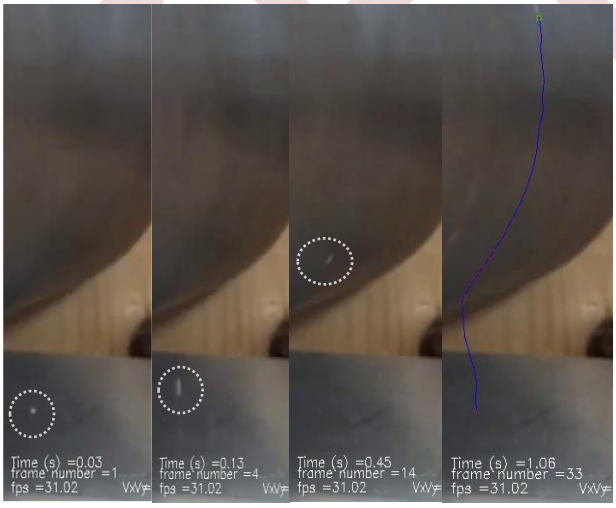


Figure 6. Particle's trajectory in roll to ground electrode. From left to the right: extracted frames from the video and the recorded particle trajectory.

V. CONCLUSION

A custom-developed piece of software to track single particle motion in an electrostatic application is presented. The software, with a graphical user interface, is capable of tracking position and calculating particle speed in the case of planar configuration if the user delivers scale dimensions. The code is still under development and needs more refinement, such as equivalence between the image and the real-space coordinates. As a perspective, the estimation of the electric charge value of the tracked particle based on its movement and electric voltage value will be implemented.

REFERENCES

[1] A. Esteva et al., "Deep learning-enabled medical computer vision," *npj Digit. Med.*, vol. 4, no. 1, Art. no. 1, Jan. 2021, doi: 10.1038/s41746-020-00376-2.

[2] X. Li and Y. Shi, "Computer Vision Imaging Based on Artificial Intelligence," *Proc. - 2018 Int. Conf. Virtual Real. Intell. Syst. ICVRIS 2018*, pp. 22–25, 2018, doi: 10.1109/ICVRIS.2018.00014.

[3] D. D. Rhoads, "Computer Vision and Artificial Intelligence Are Emerging Diagnostic Tools for the Clinical Microbiologist," *J Clin Microbiol*, vol. 58, no. 6, p. 10.1128/jcm.00511-20, May 2020, doi: 10.1128/jcm.00511-20.

[4] V. Kakani, V. H. Nguyen, B. P. Kumar, H. Kim, and V. R. Pasupuleti, "A critical review on computer vision and artificial intelligence in food industry," *J Agric Food Res*, vol. 2, p. 100033, Dec. 2020, doi: 10.1016/j.jafr.2020.100033.

[5] D. Walters, "Computer vision," in Encyclopedia of Computer Science, GBR: John Wiley and Sons Ltd., 2003, pp. 431–435.

[6] M. Kachi, A. Moussaoui, F. Beloucif, and M. Remadnia, "Using computer vision to assess an electrostatic separation process," in 2022 2nd International Conference on Advanced Electrical Engineering (ICAEE), Oct. 2022, pp. 1–4. doi: 10.1109/ICAEE53772.2022.9961966.

[7] L. Calin et al., "Controlling Particle Trajectory in Free-Fall Electrostatic Separators," IEEE Transactions on Industry Applications, vol. 44, no. 4, pp. 1038–1044, Jul. 2008, doi: 10.1109/TIA.2008.926690.

[8] J. Li, H. Lu, Z. Xu, and Y. Zhou, "A model for computing the trajectories of the conducting particles from waste printed circuit boards in corona electrostatic separators," Journal of Hazardous Materials, vol. 151, no. 1, pp. 52–57, Feb. 2008, doi: 10.1016/j.jhazmat.2007.05.045.

[9] S. Vlad, A. Iuga, and L. Dascalescu, "Numerical computation of conducting particle trajectories in plate-type electrostatic separators," IEEE Transactions on Industry Applications, vol. 39, no. 1, pp. 66–71, Jan. 2003, doi: 10.1109/TIA.2002.807218.

[10] B. S. Choi and C. A. J. Fletcher, "Turbulent particle dispersion in an electrostatic precipitator," Applied Mathematical Modelling, vol. 22, no. 12, pp. 1009–1021, Dec. 1998, doi: 10.1016/S0307-904X(98)10034-3.

[11] H. Bechkoura, N. Zouzou, and M. Kachi, "Mechanics of Particle Motion in a Standing Wave Electric Curtain: A Numerical Study," *Atmosphere*, vol. 14, no. 4, Art. no. 4, Apr. 2023, doi: 10.3390/atmos14040681.

[12] M. Kreizer, D. Ratner, and A. Liberzon, "Real-time image processing for particle tracking velocimetry," *Exp Fluids*, vol. 48, no. 1, pp. 105–110, Jan. 2010, doi: 10.1007/s00348-009-0715-5.

[13] G. Bradski, "The OpenCV Library," Dr. Dobb's Journal of Software Tools, 2000. (Library available at: https://opencv.org/ or https://pypi.org/project/opencv-python/).

Simulation of Lightning Strikes on PhotoVoltaic Farms

Kamal Nacereddine , Ahmed Boubakeur , Abdelouahab Mekhaldi , Madjid Teguar & Hossine Moulai

Ecole Nationale Polytechnique, Laboratoire de Recherche en Electrotechnique, Algiers, Algeria

kamal.nacereddine@g.enp.edu.dz; ahmed.boubakeur@g.enp.edu.dz; abdelouahab.mekhaldi@g.enp.edu.dz; madjid.teguar@g.enp.edu.dz;

Université des Sciences et de Technologie HB, LCDEP, Faculté d'Electronique et d'Informatique, Algiers, Algeria

moulaih@yahoo.fr

***Abstract*— This paper presents a novel approach to the simulation of the most common type of Cloud to Ground lightning strikes applied to a Photovoltaic farm with the view to validating its lightning protection system generally based on the electro geometric model as prescribed in the relevant international standards.**

It will be limited to the study of the electrostatic field distribution generated by a downward stepped leader progressing towards a large PV Farm with a focus on its effect on the power electronics converters operating under lightning stress conditions.

The Simulation was programmed using MATLAB's Partial Differential Equations (PDE) Toolbox based on the Finite Elements Analysis.

***Keywords:* Lightning Simulation, PV Farm Lightning Protection System, Finite Elements Method.**

I. INTRODUCTION

Despite over a century of research in lightning discharges, there is hardly any aspect of this field that is fully understood for it not to require further research.

This paper introduces a novel simulation of the Cloud to Ground Negative (CGN) lightning stroke based on the resolution of the electrostatic Poisson equation, using the Finite Elements Method (FEM), implemented on MATLAB.

In the first part of this work, we will describe our recently developed CGN lightning model which reflects our understanding of the latest developments in the scientific knowledge about lightning discharges as published in the specialist documentation by expert researchers in this still extremely active field of research [1-8].

The model's ambition is to provide us with a tool that simulates as many aspects as possible of the lightning discharge processes. In its current implementation, the model will only simulate the final stage of cloud charge separation, the stepped leader initiation and its downward progression and will stop just before its interception by the upward leader.

The second part will be an application of the model to the protection of a medium sized photovoltaic (PV) farm where the Lightning Protection System (LPS) is sized using the electro geometric model (EGM) as described in the relevant applicable national and international standards [9-12].

We will conclude with a discussion of the simulation results and the necessary future development of our model in the light of those results and work on mitigating as much as feasible of its many current limitations.

II. NOVEL SIMULATION MODEL OF CGN LIGHTNING STRIKES

A. Lightning simulation models classification

In a paper cited in [1], Rakov and Uman have defined four model classes based on what is considered to be the most salient aspect of lightning, that is the return stroke. These are: the gas dynamic, the electromagnetic, the distributed circuits and the engineering models.

Each one of the above types is generally concerned with solving a certain type of equations and each existing or new lightning return stroke model will fall within one or infringe on several of those types [1].

Our model, based on resolving Maxwell's equations, can be described as an electromagnetic type simulation model. It can also be extended to other types at different stages of its future development.

B. Simulation model presentation

For a CGN lightning model to be deemed comprehensive, it will have to address the main processes involved, namely:

- Cloud charge formation and separation
- Leader's initiation
- Stepped leader progression
- Stepped leader interception by upward leader(s)
- Return stroke(s) and associated dart leader(s)
- Ensuing processess: K, J, continuous current, etc.[5].

None of the above-mentioned items is satisfactorily understood due mainly to the variety and extreme complexity of the processes involved. Furthermore, it is now well established that most, if not all the upper atmosphere electric phenomena like sprites, elves, etc. are just part of one bigger

picture of atmospheric discharge phenomenon as illustrated on Fig.1.

Our model will try to address the first three items listed above based on pioneering work by some eminent names [2-4] and on more recent effort by equally prestigious names in the profession [5-8].

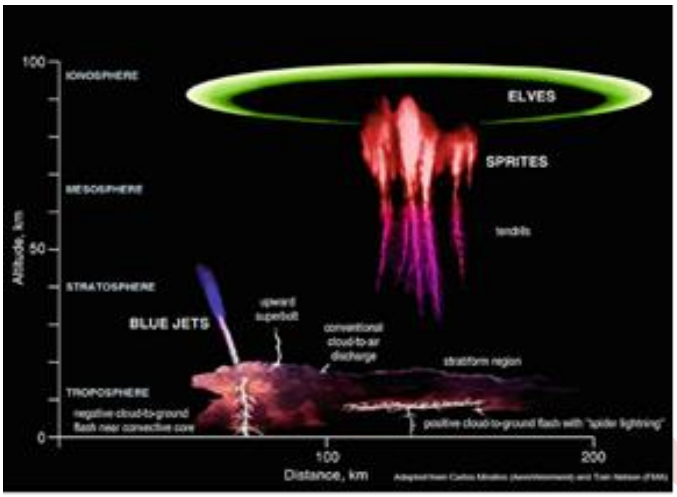


Figure 1. An illustration of atmospheric discharges with different kinds of transient luminous events https://www.nssl.noaa.gov/education/svrwx101/lightning/types/

1) Cloud charge separation

The sheer size, complexity and ephemeral nature of thunderclouds renders their study extremely difficult. The electrical and thermodynamic processes within the cloud are closely interlinked as the charge generation and separation are related to the interactions between different cloud particles populations in different thermo-hydrodynamic states [5].

As this simulation is limited to the CGN, we have used considerations thoroughly discussed in [5-8] which in turn refer largely to [2-4], to end with the model shown in "Fig. 2".

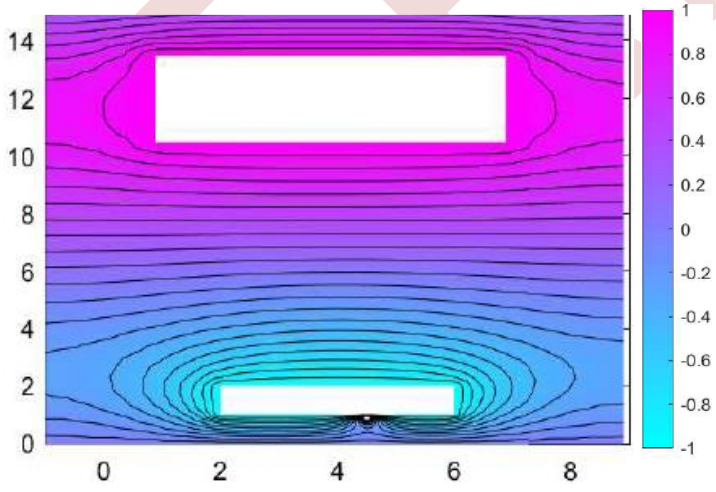


Figure 2. Cloud charge separation before leader initiation

"Fig. 2", represents a mature cloud cell immediately before a CGN leader initiation where the main positive charge is occupying the upper region, the main negative charge mainly concentrated at the bottom of the thundercloud and a relatively smaller positive charge adjacent to it conferring to the thundercloud its tripolar topology.

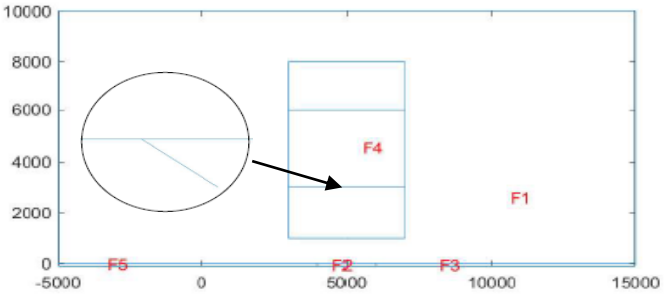


Figure 3. Initiation of the downward stepped leader

2) Leader initiation

The presence of a pocket of positive charge in the vicinity or within the negative charge area will intensify the electric field in the space between them. This forms the conditions that will aid the initiation of the first step of the downward leader as shown on "Fig. 3".

3) Stepped Leader downward progression

Once initiated and if the conditions for a stepped leader progression are met then a second, third and nth step is formed until the leader's channel reaches a distance from the ground where it will be intercepted by an upward leader.

Various models for leader stepped progression are presented in the literature of which we selected the following for their relative similarity with our model.

In [13], V. Cooray and Aravelo link the stepping process to the lightning discharge's peak current and in [14], Beroual et al simulate the leader to a circuit formed by a succession of RLC links each one constituting a step.

For Syssoev et al in [15], the step-formation process is modeled to begin with the appearance of space stems and some of them evolve into space leaders. As for M'ziou et al in [16], they propose a hybrid method, which is a combination between the Simpson method and finite difference time domain (FDTD) method for evaluating the radiated electromagnetic field.

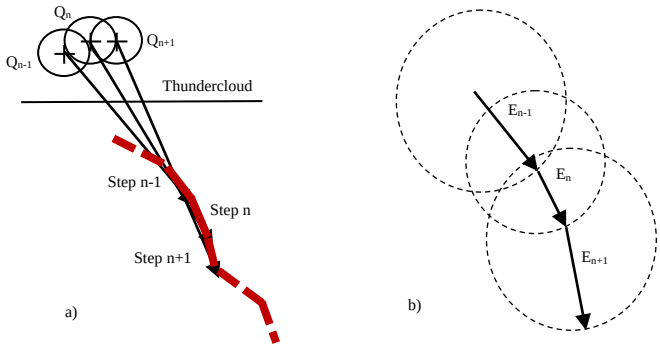


Figure 4. Leader step formation process

Our approach is similar to the one adopted in [13] but instead of linking the stepping process to the peak current, we make the assertion that the stepping nature of the downward leader is due to fluctuations of the charge center position resulting from the turbulent charge generation and separation taking place within the thundercloud.

The main assumption made in developing our step formation process, is that the leader tip is subjected to two fields (forces):

- one ambient due to the presence of the main negative charge at the bottom of the cloud and by influence its image on the ground.
- another field due to the fluctuations of the same negative charge around the position of its 'epicenter' within the cloud.

On fig.4.a, we show how the leader tip jumps from its (n-1) to the nth, then to the (n+1) position in response to slight fluctuations of the negative charge and fig. 4.b, shows the direction of the resulting field at each step.

C. Program flowchart

In fig.5 below, we present a flowchart of the model clarifying its organization:

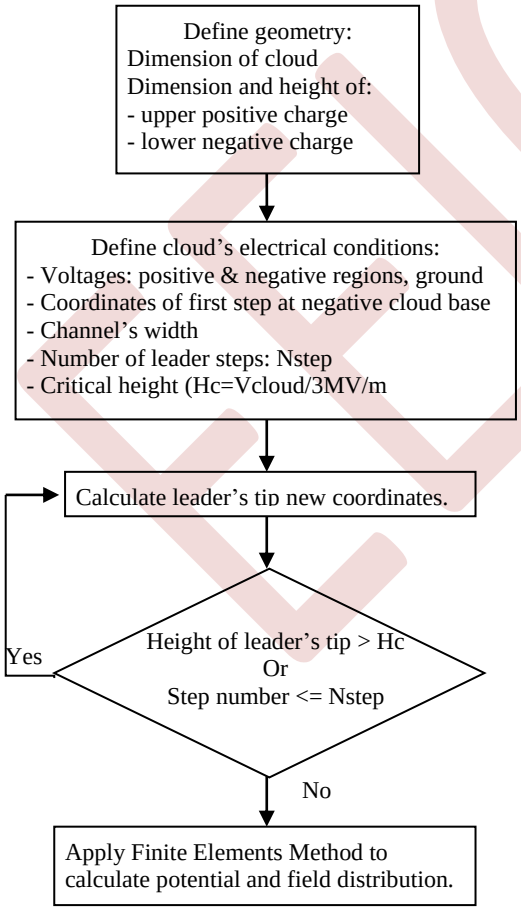


Figure 5. Flowchart of the simulation model

D. Electrical Potential and field computation using the Finite Element Method (FEM)

The FEM is a proven method for resolving Partial Derivative Equations (PDEs) especially for curved, complex geometries where other simpler calculation methods are difficult to apply. It is generally rarely used in open geometries because of the need to define boundary conditions very accurately but the increase of computers power and the development of extremely powerful software packages and methods have significantly extended its application domain [17-19].

We have used MATLAB's PDE application and PDE ToolBox, to program our simulation model.

Once the domain configuration is defined as per the flowchart in fig. 5, our program defines the geometry to be able to complete the meshing or subdivision of the entire domain into subdomains or elements.

We then allocate physical properties to the various areas constituting the domain and define the boundary conditions on selected edges for a well-posed MEF problem.

We present in fig. 6 below, an application of our simulation model.

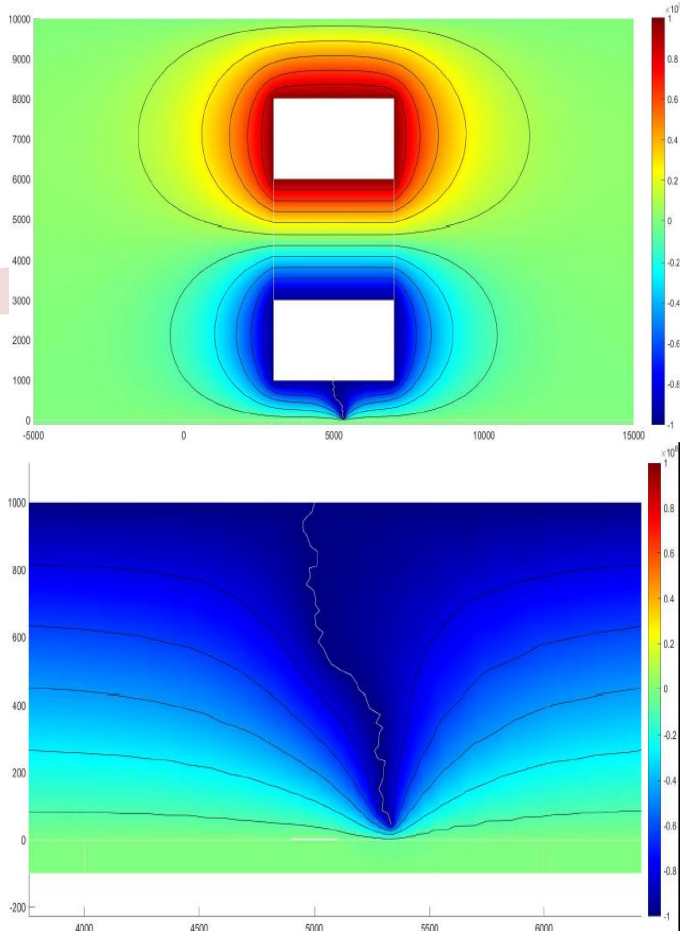


Figure 6. Calculation example using the simulation model; Top: Electric potential distribution in the domain created by the charge separation; Bottom: Zoom in the region between underside of cloud and ground.

III. APPLICATION OF THE SIMULATION MODEL TO A PHOTOVOLTAIC FARM

A. PV farm Lightning Protection System (LPS)

The first step in any lightning protection exercise is a thorough risk assessment in accordance with IEC-62305-2 or IEEE/NFPA equivalent in north America, which provides a procedure for the evaluation of risk (based on different types of loss) to a structure, due to lightning flashes to earth. For example, in large-scale PV applications, the economic losses may be the dominating factor that determine which type of surge protection should be employed [20].

Fig. 7 shows a typical grid connected PV farm layout consisting of PV panels strings, inverter room and connection to the grid.

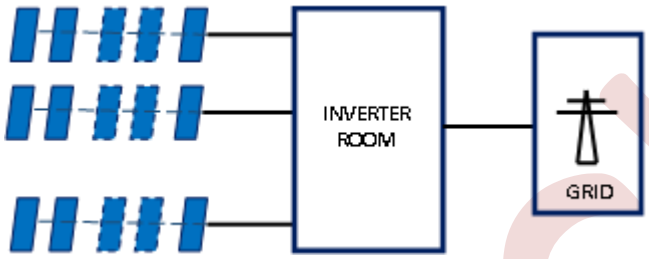


Figure 7. Typical grid connected PV farm

B. The Electro Geometric Model (EGM) applied to the protection of PV farms

Once the results of the risk assessment are known, and if those results recommend the provision of an LPS, then the protection methods prescribed in the standards will be implemented.

Amongst the protection methods applied, the EGM is the most popular especially for electrical transmission and distribution networks for which it was originally designed.

The EGM uses the rolling sphere concept which stipulates that a circular arc of radius 45.7 m would closely define the boundary of the protection zone [20-22]. This result can be visualized by imagining a sphere of 45.7-m radius rolling over the earth surface, wall, and air terminals. Objects touched by the rolling sphere are susceptible to be struck while those not touched will be protected [10, 20-22].

The rolling sphere method has been included in the NFPA with the 46-m sphere radius and has also been accepted by IEC [10], which defines four protection levels of 99%, 97%, 91%, and 84% which using CIGRE log-normal lightning stroke current distribution, corresponds to 2.9 kA, 5.4 kA, 10.1 kA, and 15.7 kA, respectively and the rolling sphere radii for the corresponding classes become 20 m, 30 m, 45 m, and 60 m, respectively [10].

With more recent advances in our understanding of discharge physics of long air gaps and consequently of the lightning attachment mechanism, several limitations of the rolling sphere method become apparent of which [10],

- The sphere radius is only a function of the critical current and not the height of the rod, ground wire, or the building on which air terminals are installed.
- The rolling sphere method does not account for the effect of the building topology on the lightning exposure of an air terminal.

C. Simulation model application

We will be applying our simulation model to the two IEC extreme radii values of 20m and 60m by adjusting the critical height Hc accordingly.

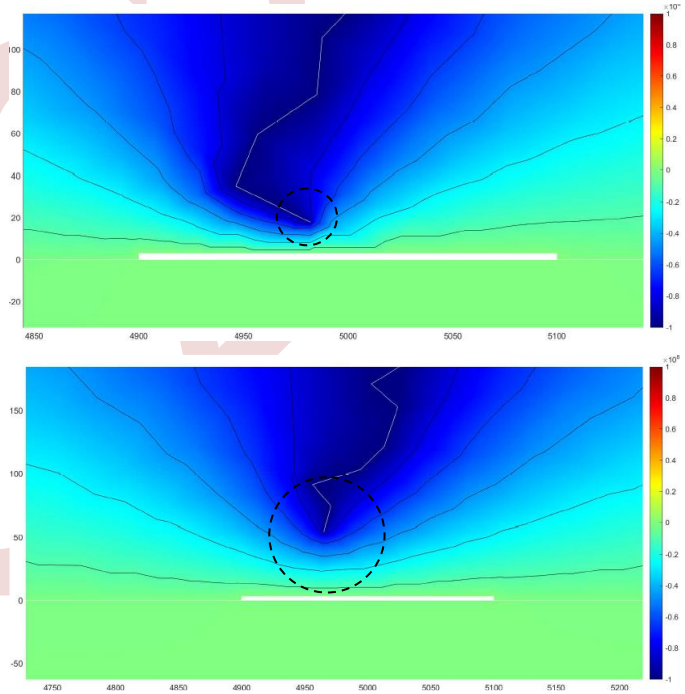


Figure 8. Simulation of a CGN on a solar farm. Top: protection radius=20m, Bottom: protection radius=60m.

Fig. 9 shows the most onerous situations when lightning strikes at either ends of an inverter:

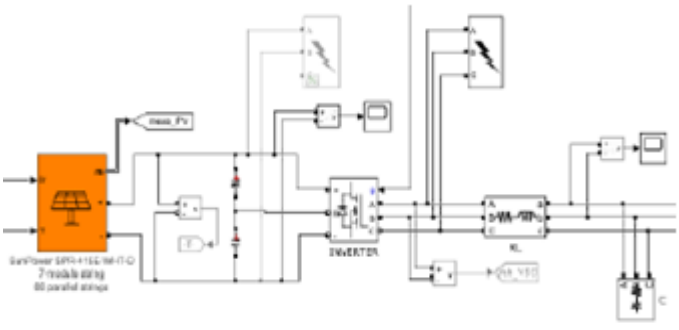


Figure 9. Simulation of a direct stroke on the DC side or the AC side of the inverter

The simulation of a direct impact on the DC side or the AC side of the inverter was carried out using MATLAB/Simulink and confirmed the generally accepted finding that a strike on the grid side of the inverter results in higher voltage levels implying larger surge protection ratings.

On Fig. 10, the Inverter's output voltage before and after a lightning strike is shown:

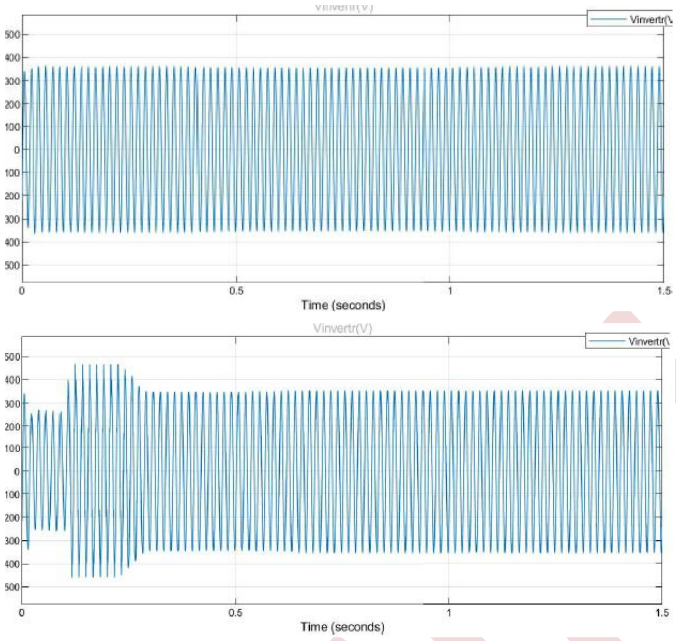


Figure 10. Inverter;s output voltage, Top: Before ligthtning impact; Bottom: After impact at 0.02s.

D. Comments on simulation results

Protection radii are correlated with the striking distance concept, the smaller the protection radius the smaller the striking distance as shown on fig. 8.

Both top and bottom simulations in fig. 8 confirm that the PV installations are adequately protected as a direct lightning stroke is likely to hit one of the air terminals if those are correctly sized, spaced and earthed as required by the applicable standards.

Simulation of a direct lightning strike near the Inverter's terminals has confirmed that resulting over voltages will lead to the selection of larger surge protection devices to adequately protect the Inverter and other associated equipment.

IV. CONCLUSION

The novel simulation model of the negative cloud to ground lightning strikes presented in the first part of this paper, does not have the pretention of equaling or even approaching the depth or reach of references cited in [11 to 13].

It does however have the ambition of setting the scene for studying the atmospheric discharge phenomenon as a whole, by addressing every one of its processes individually and understanding how they interrelate to form the bigger picture.

We deeply believe that the most powerful tool in our possession is to try to simplify the concepts as much as possible. For example: explaining the tortuosity of the stepped leader by the fluctuations of the charge epicenter's position within the cloud has allowed us to obtain realistic lightning channel forms compared to the literature.

Our model has also proven its usefulness when applied to lightning protection by addressing at least one of the electro-geometric model's limitations as it can take into consideration the particularities of the structure to be protected.

As any lightning simulation model must address the challenging lightning protection issues, the model was applied to the protection of major power conversion equipment within a PV farm and has shown the necessity to take into consideration the lightning impact on sizing surge protection devices.

In our next research effort, we will model what is generally considered to be the defining aspect of lightning: the return stroke, based on cloud and ground charges dynamics.

REFERENCES

[1] V. A. Rakov and F. Rachidi, "Overview of Recent Progress in Lightning Research and Lightning Protection", IEEE Transactions on Electromagnetic Compatibility, Vol. 51, No. 3, August 2009, pp.428-442

[2] Schonland, B.F.J.; Malan, D.J.; Collens, H. Progressive lightning II. Proc. R. Soc. A Math. Phy. 1935, 152, 595–625.

[3] K. Berger, "Novel observations on lightning discharges: Results of research on Mount San Salvatore", I .J. Frankl. Inst. 1967, 283,pp. 478–525.

[4] V. Mazur and L. H. Ruhnke, "Heinz-Wolfram Kasemir: His Collected Works", the American Geophysical Union, 2012, Section III-1: The Thundercloud, pp-278.279, Section III-3 Charge distribution in thunderstorm, pp.301-307.

[5] V. A. Rakov and M. A. Uman, "Lightning Physics and Effects", University Press, Cambridge, 2003, pp.108-213

[6] V. Cooray, F. Rachidi and M. Rubinstein "Lightning Electromagnetics Volume 2: Electrical processes and effects 2nd Ed. The Institution of Engineering and Technology 2022

[7] V. Mazur, "Principles of Lightning Physics", IOP Publishing Ltd 2016, pp. 6-1 to 6-18.

[8] P. Lalande, A. Bondiou-Clergerie, G. Bacchiega, I. Gallimberti, "Observations and modeling of lightning leaders", Elsevier SAS, C. R. Physique 3 (2002), pp. 1375–1392

[9] V.A. Rakov, V. Cooray, A. Piantini, A. Hussein, F. Rachidi et al, "Lightning Parameters for Engineering Applications", Working Group C4.407 CIGRE August 2013 pp. 81-91

[10] A. A. M. Rizk,"Modeling of lightning exposure of buildings and massive structures"IEEE Transactions on power delivery, Vol. 24, No.4, pp. 1987-1998, October 2009

[11] F. Heidler, "Lightning protection of structures and electrical systems inside of buildings", in Lightning Interaction with Power Systems Volume 2: Applications, A. Piantini, The Institution of Engineering and Technology 2020, pp. 227-270.

[12] W. Brooks, D. H. Barnett, W. A. Harrison, D. Hattz, J. Mankowski et al, "Investigation of Lightning Attachment Risks to Small Structures Associated With the Electrogeometric Model (EGM)", 0093-3813 © 2020 IEEE.

[13] V. Cooray, L Arevalo, "Modeling the Stepping Process of Negative Lightning Stepped Leaders ", Atmosphere 2017, 8, 245; doi:10.3390/atmos8120245, www.mdpi.com/journal/atmosphere

[14] A. Beroual1, J-H. Rakotonandrasana1 and I. Fofana, "Predictive Dynamic Model of the Negative Lightning Discharge Based on Similarity with Long Laboratory Sparks– Part 2: Validation", IEEE Transactions on Dielectrics and Electrical Insulation Vol. 17, No. 5; October 2010, pp 1562-1568.

[15] A. A. Syssoev, D. I. Iudin, A. A. Bulatov, and V. A. Rakov, "Numerical simulation of stepping and branching processes in negative lightning leaders",unpublished.

[16] N. M'ziou L. Mokhnache A. Boubakeur R. Kattan, '' Validation of the Simpson-finite-difference time domain method for evaluating the electromagnetic field in the vicinity of the lightning channel initiated at ground level'', IET, Transmission, Generation and Distribution vol.3, N°3, pp.279-285, March 2009.

[17] A. La Fata, M. Nicora, D. Mestriner, R. Aramini, R. Procopio et al, "Lightning Electromagnetic Fields Computation: A Review of the Available Approaches", Energies 2023, 16, 2436.

[18] M.N.O. Sadiku, Computational Electromagnetics with MATLAB, Fourth Edition, Taylor & Francis Group, LLC, 2019.

[19] D. W. Pepper, J. C. Heinrich, The Finite Element Method Basic Concepts and Applications with MATLAB, MAPLE, and COMSOL, Taylor & Francis Group, LLC, 2017.

[20] C. A. Charalambous, N. D. Kokkinos, and N. Christofides, "External Lightning Protection and Grounding in Large-Scale Photovoltaic Applications", IEEE Transactions on Electromagnetic Compatibility, 2013.

[21] E. Pons and R. Tommasini, "Lightning Protection of PV Systems", 978-1-4673-5556-8/13/$31.00 ©2013 IEEE

[22] K. Damianaki, C. A. Christodoulou, C-C. A. Kokalis, A. Kyritsis, E. D. Ellinas et al, ''Lightning Protection of Photovoltaic Systems: Computation of the Developed Potentials'', Appl. Sci. 2021, 11, 337.

Electric Field Behavior of Water Drop on Polymer Insulators Surface under AC Stress Using Finite Element Method

Fatiha Aouabed [1], Abdelhafid Bayadi [2], Rabah BOUDISSA [3]

[1] *Department of Electrical Engineering*
University of M. El-Bashir El-Ibrahimi
BORDJ BOU ARRERIDJ- Algeria
fatiha.aouabed@univ-bba.dz

[2] *Department of Electrical Engineering*
University of F. Abbas
Setif – 1- Algeria

[3] *Department of Electrical Engineering*
University A. MIRA
BEJAIA- Algeria

***Abstract*— The main objective of this work is to study the behaviour of the electric field near a water droplet on a polymer insulating surface under AC voltage. The studies are carried out using a polymer insulator with five sheds. This software uses the finite element method to calculate the electric field and electric potential along the silicone insulator. The water droplet is placed at different positions on the insulator shed. The electric field values under AC voltage are measured using COMSOL Multiphysics software. It can be seen from the simulations that the effect of the presence and the positions of the water droplets significantly affect the electric field. The contact angle between the surface of the insulator and the water droplet impacts the electric field. Therefore, it is essential to study the behavior of water droplets and the contact angle on the electric field stress. The results show that the presence of water droplets and the contact angle considerably affects the values of the electric field.**

***Keywords:* Polymer insulator, Water droplets, COMSOL Multiphysics, AC voltage, Electric field, Contact angle.**

I. INTRODUCTION

Insulators are crucial components in electric power transmission and distribution systems. Their mechanical and electrical quality significantly impacts the network's integrity. While they represent a small portion of the capital cost (5-8%), they are responsible for a large portion of line interruptions (70%) and maintenance costs (up to 50%) [1]. To enhance the reliability of power networks, optimized designs for outdoor insulators, capable of withstanding heavy icing and pollution, are essential. Traditional ceramic materials have been used for over a century but have limitations in polluted environments. Polymer insulators, with superior dielectric properties, lightweight, maneuverability, and cost-effectiveness, therefore they are steadily capturing a larger market share [2]

Although research on composite insulators in polluted conditions has a thirty-year history, there is a lack of systematic studies on how water droplets affects electric potential and field distribution along these insulators. This is one issue addressed in the report.

Y. Mizuno et al [3], conducted tests on silicone rubber specimens and observed that the breakdown voltage decreased immediately after contamination with water droplets. They also noted that the duration and value of the breakdown voltage depended on the duration of contamination. Interestingly, after five days of contamination, the breakdown voltage returned to nearly the same level as that of clean silicone rubber.

Wang Jianwu et al [4] conducted experiments and simulations using water droplets of varying volumes to investigate their effect on electrical distribution. They found that as the droplet volume increased, the electric field also increased, and leading to the formation of a corona discharge at the triple point (air, water droplets, and insulating surface). Consequently, the attainable electric potential in the region of the voltage droplets decreased.

Measuring electric fields around practical insulators, especially under polluted surface conditions, is challenging. Experimental setups such as the electrostatic probe can be used, but they are prone to mistakes. This situation could potentially be improved by using a more advanced electric field detection system [5, 6].

Therefore, many researchers have used numerical simulation techniques using commercially available electromagnetic software that approaches are more cost-effective, thus avoiding costly and complex laboratory experiments that are often difficult to perform.

Numerical analysis methods, such as finite difference method (FDM), charge simulation method (CSM), finite element method (FEM) [6], and boundary element method (BEM) are used to calculate the electric field distribution of the insulators can be used to calculate the E-field and electrical voltage distribution along polymer insulators [7,8].

The research paper focuses on calculating the potential and electric field distributions along the creepage line of non-ceramic insulators. A two-dimensional electric field analysis software package, COMSOL Multiphysics, based on the finite element method (MEF).

II. SIMULATION PROCEDURES

To study the influence of water droplets on the distribution of the field and the electrical voltage, a simulation of 2D has been created using the COMSOL Multiphysics software.

The study considered various parameters that influence the distribution of the electric field and electrical voltage, including: Contact angle, volume and shape of the droplets, position of the water droplets and the number of water droplets.

In the simulations presented, two cases were considered: the first concerns the plane–plane electrode system (Fig. 1), and the second concerns a real insulator (Fig. 2).

The insulator considered in this study and for the entire research program is a standard 18 kV outdoor silicone rubber insulator. It has about 366 millimeters long and comprised five sheds different with a diameter of 90mm and 50mm, spaced 40mm apart along the isolator. The sheath thickness is approximately 5mm. The insulation sheath is made of silicone rubber. A fiber-reinforced glass core with an 18mm diameter and a length of 160mm, attached with two metal fittings (figure 2) [8, 9].

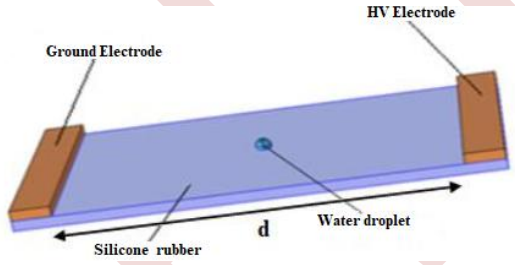


Figure 1. Structure of the simulation

A. Equations for electric field and potential

Our experiments aim to study the distribution of voltage on the chains of the insulators. Maxwell's equations were used to calculate the potential and electric field. Using these, the electric potential created by an electric field is written as follows:

$$\overrightarrow{E} = -\nabla V \quad (1)$$

By using, Maxwell's theorem defined as:

$$\nabla E = \frac{\rho}{\varepsilon} \quad (2)$$

Where ρ is the charge density, ε is the permittivity of dielectric material, and εr is the relative permittivity of the dielectric material.

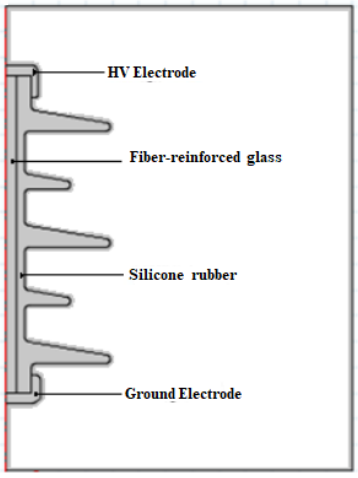


Figure 2. Structure of a silicone rubber insulator

The Poisson equation can be obtained by substituting equation (1) into (2) as

$$\nabla^2 V = -\frac{\rho}{\varepsilon} \quad (3)$$

The Laplace equation can be obtained by making the space charge, ρ = 0.

$$\nabla^2 V = 0 \quad (4)$$

In the field of electrostatics, the electrical conductivity, σ, is 0 for ideal insulating regions, and σ = ∞ for ideal conducting regions.

B. Characteristics of an insulator in comsol multiphysics

We defined the different regions of the model studied in COMSOL Multiphysics by introducing their respective relative permittivity's, εr, and electrical conductivities, σ are defined in Table 1. The two dielectric materials were assigned, namely silicone for the insulator sheath and plate. A 18-kV voltage was applied to the high-voltage electrode.

TABLE I. SUMMARY OF COMPONENTS IN COMSOL SIMULATION.

Material	Relative Permittivity, ε_r	Conductivity, σ (S/m)
Silicone	3.9	1×10^{-14}
Glass Fibre	4.2	1×10^{-14}
Forged steel	1	5.9×10^{7}
Water droplets	81	180×10^{-6}

III. RESULTS AND DISCUSSIONS

After using the model given in figure 2, the simulation results of the potential and the electric field are summarized in figure 4.

Only the first shed has been chosen for a better and easier understanding, I have observed the electric field distribution along it. The Electric field values along the first shed between the black points in figure 3 have been calculated and drawn in in figure 5.

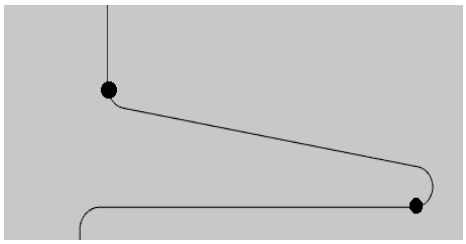
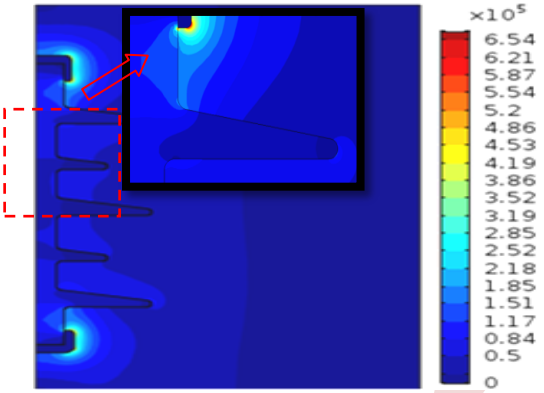
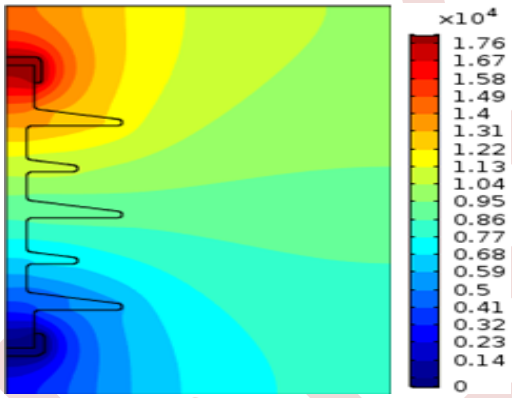


Figure 3. Exterior line created on the first shed



(a) Electric field distribution



(b) Electrical potential

Figure 4. Electric field and voltage distributions on a clean insulator

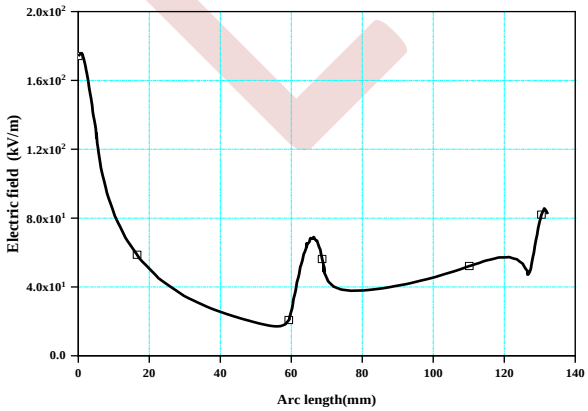


Figure 5. Distribution of the electric field along the reference line (without water drops)

A. Influence of the water Droplet at Different Positions

The position of the water droplet on the first shed of the considered insulator is done in an uncontrolled manner. Now a water droplet is placed on the first shed of the insulator and moved to the end of the shed. To simulate this random presence of the water droplet, we will study the effect of the water droplet at different positions on the electric field distribution during its displacement. Figure 6 illustrates these different positions.

Figure 7 illustrates the distribution of the electric field near the water drop on the insulator shed. It is observed that the electric field inside the water droplets is zero. Therefore, it is important to study the behavior of the electric field near the water droplet.

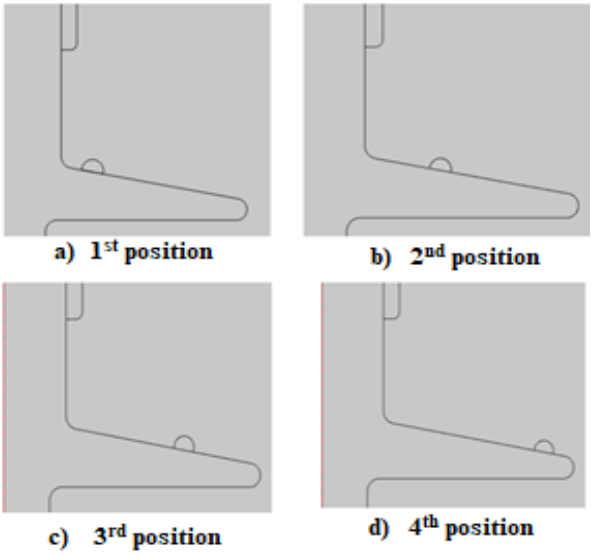


Figure 6. water droplets at different positions on an insulator shed

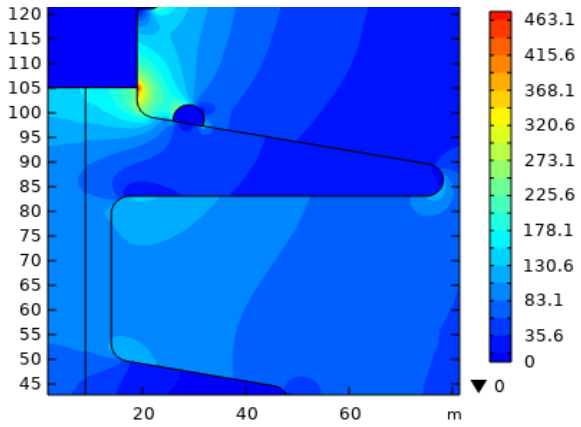


Figure 7. Distribution of the electric field near the water droplet

For the analysis, we consider the maximum values of the electric field in proximity to the water droplet at various positions. There are significant changes in the electric field

distribution near the water droplet. The maximum values of the electric field near a water drop are shown in table 2.

TABLE II. MAXIMUM OF THE ELECTRIC FIELD VALUE NEAR THE WATER DROPLET ACCORDING TO ITS POSITION IN 2D

Water droplet position	Maximum of the electric field values near a water droplet (kV / cm)
1	3.32
2	2.10
3	1.32
4	0.56

When a water droplet is present, the electric field intensity is higher at the contact angle between the water, the insulator and the air (triple point). A single of water drop was considered to find the behavior of the electric field near it. The simulation of the distribution of the electric field due to the presence of a water droplet on an insulator surface was carried out using the finite element method (FEM).

When the water drop position changes along the shed, the electric field around the water drop obviously changes. The results show that the maximum electric field E value gradually decreases along the shed (fig.8). The maximum electric field E value decreased from 3.32 kV/cm to 0.56 kV/cm.

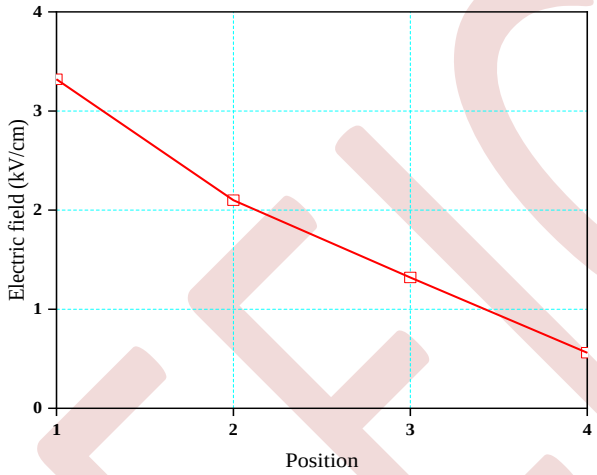


Figure 8. Maximum of the electric field values near the water drop at different positions in 2D

B. *Hanging water droplets*

This section pertains to the analysis of electric field distributions acquired in the presence of the water drop hanging at the edge of the first shed (fig 9). The objective is to assess whether these distributions provide insight into the impact of water drop hanging (rain) on the insulator.

Figure 9 illustrates the distribution of the electric field lines along the first shed including the hanging water droplet. The distributions of the components of the electric field for the cases with and without hanging water droplet were calculated and presented in figure 10. It is to be noticed a change in the value of the electric field from 6.8 kV /cm (without hanging) to 8.05 kV/cm (with hanging).

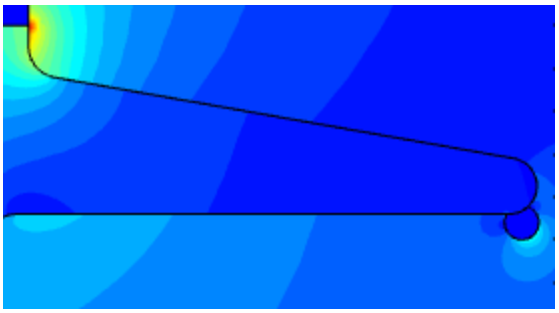


Figure 9. Electric field near the hanging drop

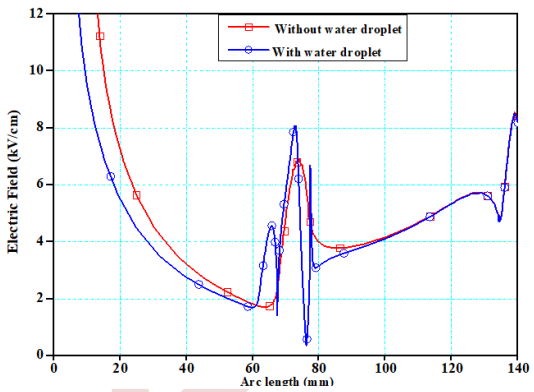


Figure 10. Electric field with and without hanging water droplet

C. *Effect of several water drops*

The primary aim of this simulation is to investigate the influence of water droplets on the distribution of the electric field and voltage along the creepage path of the silicone insulator. The insulator design consists of silicone material with a creepage distance of 750 mm between two supports, one being the high-voltage electrode and the other the earth electrode, both constructed from copper. During the simulation, an 18 kV voltage is applied to the high-voltage electrode to evaluate the insulator's performance in the presence of water droplets.

Figure 11(a) and 11(b) show the equipotential lines near the polymer insulator model under dry and wet surface conditions for direct comparison. The lines are drawn at a 6% voltage interval, thus producing a total of 25 equipotential lines in the simulation results. As can be seen in both graphs, the contour lines are concentrated generally around the metal electrodes, indicating high field regions on the polymer insulator. Under wet surface conditions, the equipotential lines are more evenly distributed than those on the clean surface, giving a better distribution of the field along the creepage line of the insulator. This behaviour can be explained by the presence of the resistive water drops which help to redistribute the concentrated contours over a larger surface.

Figure 12 shows the comparison of the calculated voltage distributions along the leakage line in the two surface conditions. Creepage distances are measured along the polymeric surface, starting at the high voltage, and moving to the grounded terminal.

As expected, it was predicted that the maximum electrical potential values are found near the high voltage electrode and commence to decrease until its cancellation when approaching the ground electrode. Although nonlinear potential distribution along a creepage line of the two cases, no significant different can be seen between a voltage without and with water droplets (fig.12). Therefore, there is no noticeable effect of water droplets on the insulator's voltage distribution along the surface [9-11].

Figure 13 presents the variation of electric field distribution for different cases (with drops, without drops). We note the elevation of the field values in the presence of water droplets compared to the case without them. Also, large drops cause a high increase in the compared to small drops. Furthermore, the maximum electric field intensity appears at the water-air-insulator triple point, because of the presence of electric discharges in this zone.

So we conclude that the water droplets, have an obvious effect on the distribution of the electric field along the insulator surface, without forgetting the increase in the electric field intensity generated by the increase of the number of drops water on its surface.

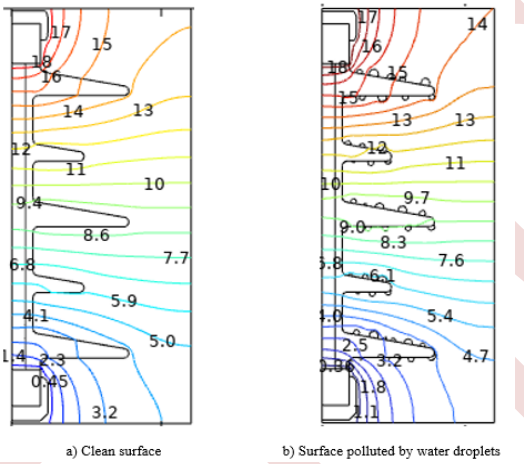


Figure 11. Equipotential around the polymer insulator

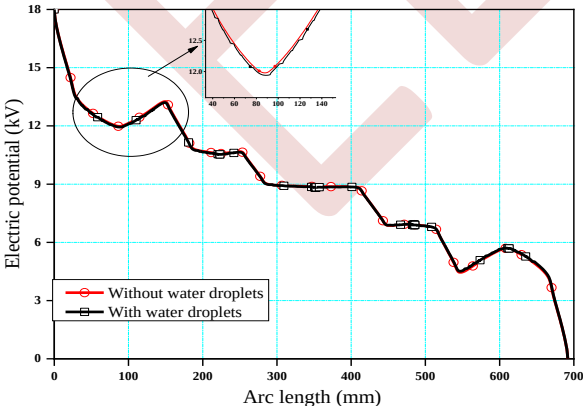


Figure 12. Electric potential along the insulator

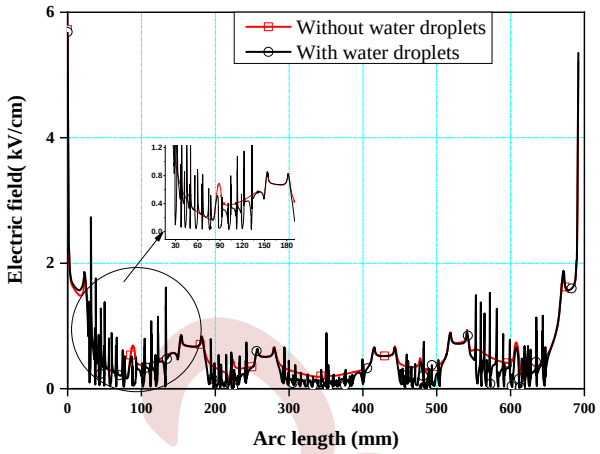


Figure 13. Electric field along an insulator

D. Effect of contact angle

For a water droplet on the insulating surface, the highest electric field strength is at the interface between the drop of water, the air and the insulating surface. It is of practical importance to know the enhancement of the electric field at various contact angles of the water droplet.

Under different stages of hydrophobicity of the silicone sheet surface, the contact angle of the water drop varies. Four typical values of the contact angle are considered for comparison, which are 120, 90, 60 and 30 degrees. The contact area in this study is defined as a circle 4 mm in diameter. The relative permittivity of the drop of water is 81 and its conductivity is equal to 180 µS/cm.

Figure 14 shows the view of equipotential contours and electric field lines around the water droplets for these four cases. The water droplet is positioned on the center of the silicone rubber plate. Solid lines represent equipotential contours; filled lines are used for electric field lines. The angle Θ indicates the contact angle between the water drop and the dielectric surface. The contact angle is an important factor in describing the hydrophobic capacity of the insulator. It is noticed that the water droplet with a larger contact angle causes more distortion in the configuration of equipotential contours. Figure 14a and Figure 14b show the spherical drop which gives the contact angle of 90° and more. This indicates that the surface is hydrophobic and has a low surface energy. Figure 14c and figure 14d show a small contact angle of less than 90° between the surface of the dielectric and a drop such as a flattened drop. This means that the surface is hydrophilic and has a large surface energy.

The maximum values of the electric field intensity on the surface of the water drop with different contact angles are given in Table 3. Figure 15 shows the relationship between the electric field amplification factor and the contact angle.

TABLE III. THE MAXIMUM ELECTRIC FIELD VALUES ON THE SURFACE OF THE WATER DROPLETS WITH DIFFERENT CONTACT ANGLES

Contact angles Θ(°)	**30**	**60**	**90**	**120**
The maximum electric	6,83e2	7,81e2	1,13e3	1,62e3

field (kV/m)				

The results in figure 15 show that the amplification of the electric field increases with increasing contact angle. The relationship between them is almost linear.

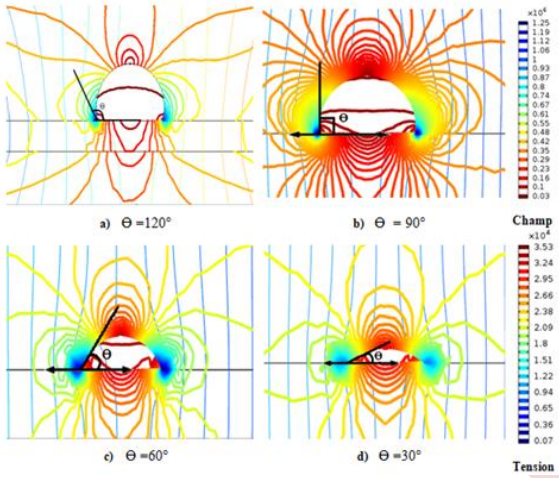


Figure 14. Equipotential contours and field lines around water droplets with variable contact angle.

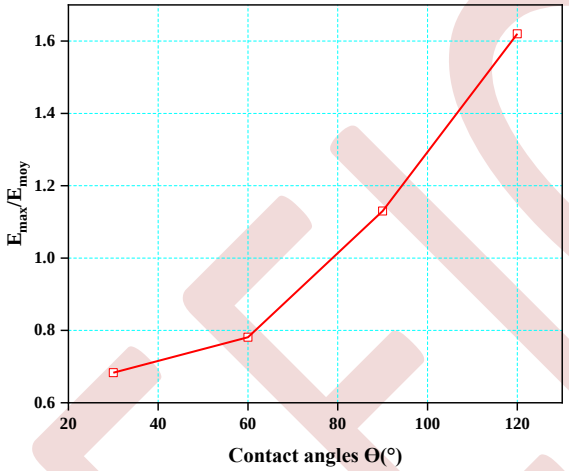


Figure 15. Maximum electric field according to the different contact angles on the insulation surface

IV. CONCLUSION

The objective in this article was to study the characteristic of the electric field distribution on the hydrophobic silicone surface covered with water drops. We simulated a real insulator in 2D, using COMSOL Multiphysics 5.6. This software uses the finite element method to calculate the electric field and electric potential along the silicone insulator.

We conclude that the presence of these drops on the surface of the silicone insulator causes an increase in the electric field intensity exactly at the triple point (air, water drop and insulator). This increase affects its surface and can cause it to lose its hydrophobic property and lead to its degradation.

Factors such as the contact angle and the position of the water droplets have a significant effect on the amplification of the electric field at the insulator surface.

REFERENCES

[1] Choi, I.H.; Kim, T.K.; Yoon, Y.B.; Kim, T.; Nguyen, H.T.T.; Yi, J. A " Study on the Lifetime Assessment Ways andVarious Failure Types of 154 kV Porcelain Insulators Installed in South Korea ". Trans. Electr. Electron. vol.19, pp.188–194, Mater.2018.

[2] Gorur, RS, Cherney , EA & Burnham, JT , "Outdoor Insulators, Ravi S. Gorur Inc Phoenix, "Arizona 85044, USA 1999.

[3] Y. Mizuno, M. Iwatani, M. Nagata K. Naito, K. Kondo, S. Ito, "Behavior of Water Droplets on Silicone Rubber Sheet under AC Voltage Application", IEEE, vol. 10, no. 1, pp. 7803-503, 1999-1998.

[4] W. Jianwu, W. Xishan, L. Lei, L. Haiyan, "Study of Discharge Process and Characteristics of Discrete Water Droplets on the RTV Hydrophobic Surface in the Non-uniform Electric Field", International Conference on Power System Technology, pp. 1-6, 2006.

[5] Wei H. J., Jayaram S., and Cherney E. A., "A study of electrical stress grading of composite bushings by means of a resistive silicone rubber coating," Journal of Electrostatics, vol. 63, pp. 273-283, 2005.

[6] Rong Z., Yun Z., Wei-Yuan C., and Bo Zhang, "Measurement of electric field distribution along composite insulators by integrated optical electric field sensor," IEEE Transactions on Dielectrics and Electrical Insulation, vol. 15, pp.302-310, 2008.

[7] Rasolonjanahary, J.L.; Krahenbuhl, L.; Nicolas, A. "Computation of electric fields and potential on polluted insulators using a boundary element method ". IEEE Trans. Magn. 1992, 28, 1473–1476.

[8] 19. Yializis, A.; Kuffel, E.; Alexander, P.H. An Optimized Charge Simulation Method for the Calculation of High Voltage Fields. IEEE Trans. Power Appar. Syst. 1978, 97, 2434–2440. [CrossRef]

[9] Doshi T, Gorur RS, Hunt J "Electric field computation of composite line insulators up to 1200 kV AC ". IEEE Trans Dielectr Electr Insul 18(3):861–867 2011.

[10] Y. Zhu, K. Haji, M. Otsubo, C. Honda and N. Hayashi, "Electrohydrodynamic behaviour of water droplet on an electrically stressed hydrophobic surface," Journal of Applied Physics 39 1970-75, 2006.

[11] Arshad, A. Nekahi, S. G. McMeekin and M. Farzaneh "Effect of pollution severity and dry band location on the flashover characteristics of silicone rubber surfaces " Electrical Engineering volume 99, pp. 1053–1063, 2017.

[12] I. S. Jacobs and C. P. Bean, "Fine particles, thin films and exchange anisotropy," in Magnetism, vol. III, G. T. Rado and H. Suhl, Eds. New York: Academic, 1963, pp. 271–350.

[13] K. Elissa, "Title of paper if known," unpublished.

[14] R. Nicole, "Title of paper with only first word capitalized," J. Name Stand. Abbrev., in press.

[15] Y. Yorozu, M. Hirano, K. Oka, and Y. Tagawa, "Electron spectroscopy studies on magneto-optical media and plastic substrate interface," IEEE Transl. J. Magn. Japan, vol. 2, pp. 740–741, August 1987 [Digests 9th Annual Conf. Magnetics Japan, p. 301, 1982].

[16] M. Young, The Technical Writer's Handbook. Mill Valley, CA: University Science, 1989.

Influence of the number of superhydrophobic coating layers on their electrical performance

Sara Alouache [1], Abdellah Medjdoub [1]

[1]Laboratory of Electrical Engineering, Department. University A. Mira de Bejaia, 06000 Bejaia, Algeria

Sara.alouache@univ-bejaia.dz

Abdellah.medjdoub@univ-bejaia.dz

***Abstract*—The accumulation of pollution on the surfaces of electrical insulators is one of the major problems in the operation of electricity networks. This pollution reduces the value of the flashover voltage, thereby affecting the reliability of the system.**
To alleviate this problem, superhydrophobic coatings, with a contact angle of a drop of water greater than 150°, help to minimize the deposition of any form of moisture on the insulator
The aim of this work is to develop a superhydrophobic surface as an insulator and investigate the effect of the variation in the number of superhydrophobic layers on the evacuation voltage of the water droplets outside the insulation
The obtained results show that an increase in the number of layers of the superhydrophobic insulating surface generates a decrease in the exhaust voltage of the water droplets of the insulation surface.

***Keywords:* insulation, superhydrophobic surface, water droplets, multilayer surface, droplet evacuation voltage, alternating voltage.**

I. INTRODUCTION

Insulators are one of the most important components of electrical power transmission lines, supporting and separating high-voltage conductors as they transmit electrical energy along the network [1]. The major problem threatening the reliability and operation of electrical power transmission is the contamination of insulators throughout the transmission chain [2] by the deposition of natural or industrial pollutants [3].
When these pollutants absorb moisture, they form a conductive layer, which enables the propagation of leakage current across the surface of the insulator [4-5]. So, the presence of water droplets resulting from rain or fog serves as an extremely sensitive environmental factor that influences their stability and deteriorates their electrical performances [6-7] [8].
In the pursuit of enhancing the reliability of electrical power systems, numerous researchers have been dedicated to the development of materials suitable for external insulators. This progress has transitioned from the substitution of glass with ceramics and has prompted consideration for composite insulators possessing hydrophobic characteristics. [9]. Nonetheless, owing to their elevated surface energy levels, they tend to readily accumulate coatings from rain and assorted pollutants, which consequently diminishes their dielectric strength, particularly in harsher environmental conditions [10- 11].
Reducing the surface energy of insulating materials could be extremely beneficial in reducing the adhesion between the water drops and the surface of the insulator. Fortunately, the development of superhydrophobic surfaces has become possible due to progress within the realm of surface science and by drawing inspiration from the characteristics exhibited by the flora and fauna in nature. [12]. they show remarkable performance in terms of self-cleaning and non-drizzleability thanks to their wide contact angle with water above 150°.This allows the drop to roll easily and evacuated out of the insulating surface, takes with it the particles of deposited pollutants that it encounters on its way and thus clean the surface.
Numerous research efforts have been dedicated to the utilization and fabrication of such surfaces, Sartaj Singh et all [13] developed hydrophobic and superhydrofobic surfaces from the candle flame, the carbon slurry was deposited on the glass blades; they studied the mechanical durability of the coatings prepared with the peeling technique, and measured the WCA after each peeling, it was noted that the glass slurries with a higher roughness offer a high resistance to the removal of carbon scrape. Allahdini, A [10], have manufactured superhydrophobic coatings based on silicone for high-voltage applications, these surfaces have shown excellent self-cleaning properties, non-smoothing due to the high value of its contact angle and its very low hysteresis, a QUV test has been performed to evaluate its resistance to weather conditions, the results showing that the superhidrophobe coating retains its properties after 100 hours of exposure. Shichao Wei [14] investigated the dynamic behavior of water droplets on hydrophobic and superhydrophobic surfaces under a high alternating electric field, resulting in an improvement in bypass voltage due to the dewetting effect of the

superhydrophobic surface, where water droplets slid off the tilted superhydrophobic surface before arriving at bypass voltage, while those deposited on the hydrophobic surface remained stuck even at a decaying field intensity. Simulation results revealed that water droplets under the influence of an electric field stretched and formed a liquid bridge, the coalescence of water droplets being caused by the surface tension force and the electric force. S. Alouache et all [15] used simulations to predict the movement and direction of evacuation of a group of water drops deposited on a superhydrophobic multilayer surface without and with the presence of a dielectric insulating cover with variable permittivity, and analyzed their impact on the electric field and potential distribution. They concluded that the variation in the number of drops deposited on a multi-layer superhydrophobic insulating surface, as well as the permittivity of the cover, have an influence on the distribution of the electric field and potential.

Several approaches have been proposed to build this type of surface. One involves the modification of low surface energy materials or chemical groups on rough surfaces to minimize liquid-solid contact, according to Cassier-Baxter [16].

The present work consists of developing a multi-layer superhydrophobic coating for use as an insulator and studying the effect of the variation in the number of superhydrophobic layers on the exhaust voltage of water droplets outside the alternating voltage insulators.

II. EXPERIMENTAL PART

A. Sample preparation:

For the first coating layer, a quantity of gel was spread over a glass plate of dimensions (12 x5 x0.5) cm, in a uniform and manual way until a very thin layer was obtained. In order to obtain the coating, another quantity of the same product is carbonized.

The coating layer is formed when the glass plate coated with a thin layer of product is brought closer to the carbonization flame of the latter in a regular way to obtain a uniform structure. Figure.1 shows the glass plate completely blackened and covered with straw. After washing it with tap water.

The other coating layers are obtained in the same way, but at 24-hour intervals.



Figure 1. Essential steps in the manufacture of a superhydrophobic coating on a glass plate.

B. Measurement Station:

In our work to evaluate the condition of our prepared samples, the measurement and monitoring of the exhaust voltage of the water droplets deposited on the insulating surface is carried out. The measuring station of the High Voltage Laboratory at the University of Bejaia consists of a high voltage transformer that delivers a voltage of 135 KV to its secondary and a current of 80 mA, a capacitive voltage divider, and a current damping resistance. It is also connected to a peak voltmeter and a camera to capture the exhaust voltage of water drops.

The superhydrophobic layer coated glass plate is deposited below 1cm by two stainless steel electrodes. One is connected to the output of the transformer (high voltage electrode), the other and the grounding, they are parallelepipedic shape of dimensions (12x3x0.8) cm. separated with a 4 cm leak line Figure 2.

The maximum number of water drops deposited on the superhydrophobic surface is 5 drops, and are located along the leak line of the insulation Figure 3.

The water drops are deposited on the multi-layer superhydrophobic surface using a graduated micropipette to select their volume, which is fixed at 50 µL in this study.

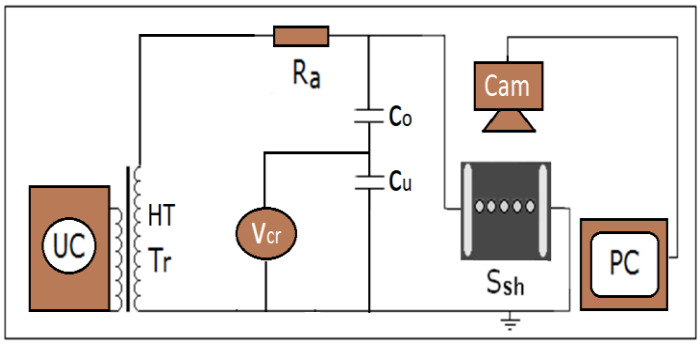


Figure 2. Scheme for measuring the exhaust voltage of water droplets outside the insulating surface and for visualizing their expulsion (Tr: Transformer, UC: control device, Ssh: superhydrophobic surface, Cam: camera, PC: Computer screen).

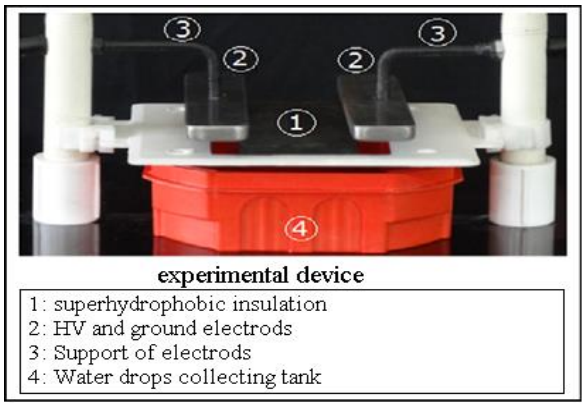


Figure 3. Experimental model.

II. RESULTS AND DISCUSSION:

The movement of the water drop along the surface is mainly caused by electrostatic force.

The electrostatic force is described by the coulomb force linked to the movement of free charges in the medium, as well as the dielectrophoretic force and the electrostriction force which is neglected due to the field uniformization generated between the two electrodes.

According to Figure (4) the expulsion of water drops outside the superhydrophobic insulating surface is due to the combination of the coulomb force and the force of attraction being exercised between the water droplets in a row placed between the two high voltage and ground electrodes in the middle of the insulation.

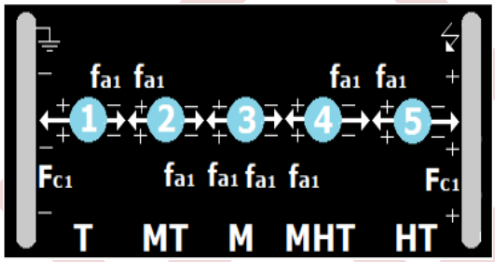


Figure 4. Total of forces exerted on a water drop deposit (FCI: Coulomb force, Fai: mutual force of attraction)

This row consists of 5 drops of water. A growing tension is applied and follows the order and direction of expulsion of this row outside the multi-layer surface ranging from 1 to 4 layers.

The evolution of the expulsion voltage of the 5 water drops depending on the variation in the number of layers of the superhydrophobic insulation is shown in Figure 5. For a surface treated by a single layer, the first drop expelled from the insulation is that in the immediate vicinity of the high voltage electrode with a lower voltage of the order of 10.36 kv, in the second place the drop located next to the ground electrodes with a voltage 17.13 kv, then followed by the drop G2 out with a tension slightly higher than that of G5. According to the value of the measured voltage, the G4 drop (V = 32.67 kv) is ranked fourth, so it comes out before the G3 drop that comes out last with a voltage of 36.1 kv. We observe the emergence of a series of practically equivalent movements regardless of the number of layers of the superhydrophobic insulation.

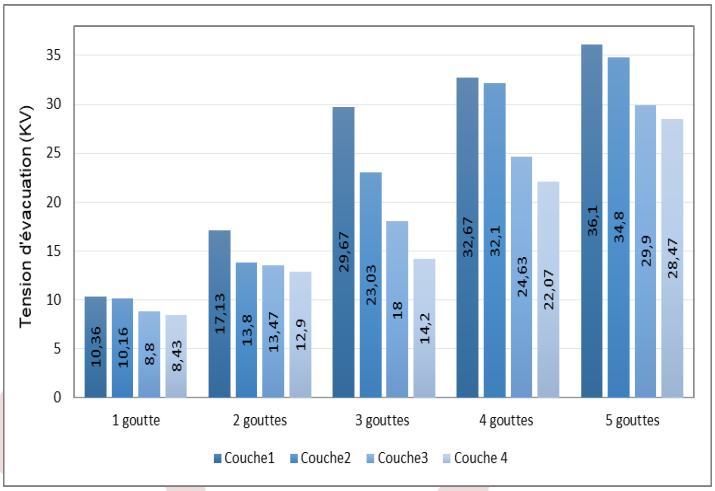


Figure 5. Exhaust voltage of 5 drops of water outside the surface of the multi-layer superhydrophobic insulation (1 to 4 layers) under alternate voltage.

Figure (6) shows the evolution of the evacuation tensions of the 5 drops of water deposited on the surface as a result of the change in the number of superhydrophobic layers, the results show a decrease in their values with the increase in the amount of layers of the superhydrofobic surfaces.

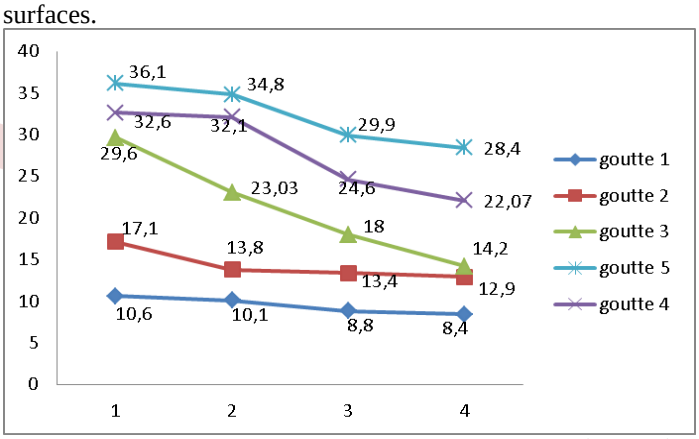


Figure 6. Water drop expulsion voltage depending on the number of layers of the superhydrophobic insulation.

A comparison of the voltages obtained between the evacuation of droplets deposited on a 1 layer surface and those deposited upon a 4 layers surface illustrated in figure (7). Note that the expulsion voltage of the resulting 4-layer water drops is reduced to that resulting from a single-layer

insulation.

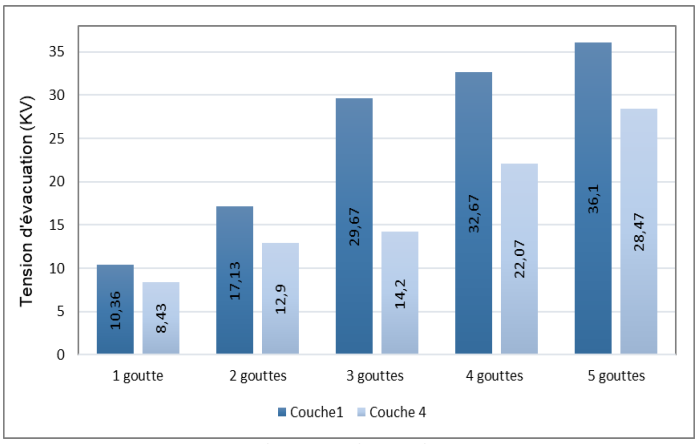


Figure 7. Exhaust voltage of 5 drops of water from the superhydrophobic insulating surface of 1 and 4 layers under the effect of an alternate electric field.

Figure (8) shows the evolution of the evacuation voltage of the first and last drop outside the insulating surface, there is a decrease in the deviation value between the disappearance of the 1st and the last drops with the increase in the number of layers of the surface or it is observed that for the first layer the deference of the voltage is 25.7 kv then decreases to 24.6 kv for the 2 layer surface, the addition of a third layer reduces this difference to 21.1 kv, and it continues to decline to approximately 19.9 kv for a number of Layers equal to 4 layers

.

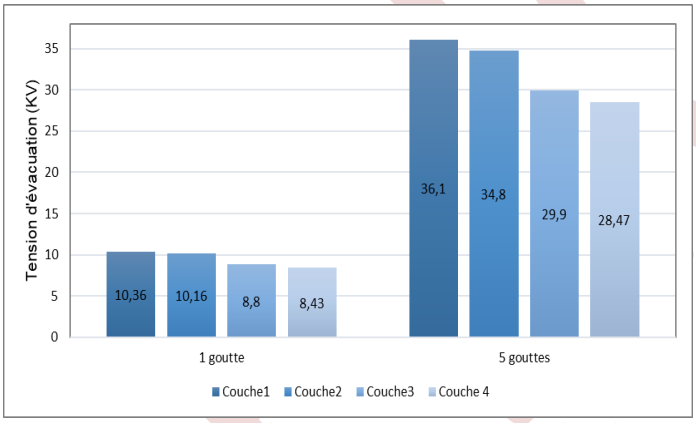


Figure 8. Exhaust voltage of drop 1 and drop 5 outside the surface of the multi-layer superhydrophobic insulation (1-4 couches).

CONCLUSION

In order to improve the electrical performance of a superhydrophobic insulation for application to high-voltage insulators, multi-layer superhydrofobic surfaces have been developed. A monitoring of the expulsion voltage of the 5 drops of water deposited on the insulation leak line showed that:

The increase in the number of superhydrophobic layers leads to a decrease in the expulsion voltage of water drops outside the insulating surface.

Increasing the number of layers of the superhydrophobic insulation reduces the gap in expulsion voltage between the first and last drop ejected from the surface.

This demonstrates the effectiveness of superhydrophobic surfaces in improving the electrical performance of insulating surface.

REFERENCES

[1] J. F. Hall, "History and Bibliography of Polymeric Insulators for Outdoor Applications", IEEE Trans. Power Delivery, Vol. 8, No. 1, pp. 376-385, 1993.

[2] M. Wakhidin and Suwarno, "Effects of Artificial Tropical Climate Aging on Insulation Performance of Silicone Rubber Polymeric Insulators," Proc. 2nd Int. Conf. High Volt. Eng. Power Syst. Towar. Sustain. Reliab. Power Deliv. ICHVEPS 2019, pp. 4–9, 2019.

[3] Ali Ahmed Salem, Kwan Yew Lau, Zulkurnain Abdul Malek, Wenbin Zhou, Salem Al-Ameri, Samir A. Al-Gailani, Rahisham Abd Rahman, "High Voltage Polymer Insulators Performance in Wet Pollution Survey", Polymers 2022, 14, 1236.

[4] Salem, A.A.; Abd Rahman, R.; Jamail, N.A. New Approach for Monitoring Contamination Level on Outdoor Insulator Based on Harmonics Components of the Leakage Current. In Proceedings of the 2021 IEEE International Conference on the Properties and Applications of Dielectric Materials (ICPADM), Johor Bahru, Malaysia, 12–14 July 2021; pp. 418–421.

[5] Mukherjee, P.K.; Ahmed, A.; Singer, H. Electric field distortion caused by asymmetric pollution on insulator surfaces. IEEE Trans. Dielectr. Electr. Insul. 1999, 6, 175–180. [CrossRef].

[6] Z. Jiang, X. Jiang, Z. Zhang, Y. Guo, Y. Li, Investigating the effect of rainfall parameters on the self-cleaning of polluted suspension insulators: insight from southern China, Energies 10 (2017) 1–13, 601.

[7] S. Ilhan, A. Ozdemir, S.H. Jayaram, E.A. Cherney, Numerical and experimental investigation of the effects of pollution on glass suspension-type insulators, IEEE Trans. Dielectr. Electr. Insul. 22 (5) (2015) 2987–2994.

[8] A. Banik, A. Mukherjee, and S. Dalai, "Development of a pollution flashover model for 11 kV porcelain and silicon rubber insulator by using COMSOL multiphysics," Electrical Engineering, vol. 100, no. 2, pp. 533-541, 2018/06/01 2018.

[9] K. Hamour, F. Bouchelga, R. Boudissa, S. Kornhuber, KD Haim, Optimization of the longevity of the superhydrophobic insulator by expulsion of any wet deposits with low alternative electric field, Electrostatics Journal 105 (2020) 103451.

[10] Allahdini, A., Momen, G., & Jafari, R. (2019). Fabrication of a durable superhydrophobic coating for high voltage glass insulators. In *CIGRE Canada Conference* (Vol. 2019). CIGRE Canada.

[11] T. Sakoda, K. Tabira, T. Miyake, N. Hayashi, K. Haji, Y. Aka, T. Anjiki, T. Fukano, Discharge behavior and dielectric performance of artificially polluted hydrophobic silicone rubber, J. Electrost. 93 (2018) 97–103.

[12] Yufeng Li, Haiyun Jin, Shichao Nie, Peng Zhang, Naikui Gao; Dynamic behavior of water droplets and flashover characteristics on a superhydrophobic silicone rubber surface. *Appl. Phys. Lett.* 15 May 2017; 110 (20): 201602. https://doi.org/10.1063/1.4983714.

[13] Singh S, Kumar V, Kango S, Verma R and Sharma N 2022 Fabrication and evaluation of superhydrophobic surfaces using carbon soot and different adhesives Int. J. Surf. Eng.Interdiscip.Mater.Sci.101–13.DOI:10.4018/IJSEIMS.304807

[14] Wei, S., et al.: Dynamic behavior of water droplets on wetted super-hydrophobic surfaces under a high AC electric field. AIP Adv. 9(6),065307 (2019).

[15] S.Alouache, F.Bouchelga, K.Hamour, Simulation of electrical field and potential on multilayer superhydrophobic insulation with water drops under DC voltage, Conference Proceedings of ICAEE 2022.

[16] Liu, S., et al.: Simultaneous optimization of the surface hydrophobicity and surface charge distribution of insulating materials. *Macromol. Mater. Eng.* **307**(2), 2100655 (2022). https://doi.org/10.1002/mame.202100655.

Electric field and potential quantification on a deposit of drops covering a superhydrophobic surface under AC voltage

Fatma. BOUCHELGA[1,2], Nacera. ROUHA[2], Khaled. HAMOUR[2], Stefan.KORNHUBER[3]

[1]*Department of Automatics and Electromechanics, Faculty of Science and Technology University of Ghardaia, Algeria*

Bouchelga.fatma@univ-ghardaia.dz

[2] *Laboratory of Electrical Engineering, Department of Electrical Engineering, University A. Mira of Bejaia, 06000 Bejaia, Algeria*

[3] *University of Applied Sciences, Theodor - Koerner - Allee 16 Zittau 8800, Germany*

***Abstract*— The main objective of this research is to carry out a numerical study on the electro-hydrodynamic behavior of water drops, with fixed electrical conductivity in motion along the creepage distance of a superhydrophobic insulation put under HVAC, that is carried out using the configuration of the field and the electric potential. Several factors are examined, such as, the presence and absence of a dielectric cover, its relative permittivity and that of the superhydrophobic layer, number of layers, volume and number of water drops. It follows from this study, conformity between the numerical and experimental results. In addition, the presence of the cover does not have an influence on the direction of the drops' expulsion from the surface; on the other hand, it affects the evacuation order of the latter. It is to be noted that the relative permittivity of the insulating cover does not have a great effect on the ejection of the drops. Also, we noticed that the number and volume of water drops affect the distribution of electrical field. However, the number of superhydrophobic layers doesn't exercise a big difference.**

***Keywords:* Superhydrophobic insulation, electric field, water drops, AC voltage, COMSOL Multiphysics.**

I. INTRODUCTION

Overhead lines and substations of electricity transmission networks face various constraints. Among which, the pollution of insulators which is one of the most important factors affecting the quality and reliability of energy transmission. Contamination of insulators can be considered as a continuous or irregular discharge of impurities from different sources. These can come from vapor emanated from evacuation devices (industrial or urban pollution), or from fine salt particles (marine pollution) located in coastal areas, or even from sand particles [1]. In reality, the formation of water drops on the insulator's surface is sometimes the origin of serious disturbances on electrical networks. Indeed, the presence of these water drops implies a reduction in the electrical performance of the insulators and can lead, in some circumstances, to the appearance and development of a flashover arc. The flashover voltage of insulators covered with these water drops is significantly lower than that of clean ones.

The electrical performance of hydrophilic insulation protecting global electrical networks is enormously affected by wet pollution because of the ease and speed of their wetting in rainy weather or condensation. This leads to the breakdown of service continuity, aging, failure and degradation of these elements [2 - 6]. In order to reduce the rate of such disturbances, hydrophobic insulations have been proposed. Despite the very strong increase in their electrical performance compared to ceramics, they deteriorate in service under conditions of very recurring high humidity. To avoid the harmful effect of flashover of these hydrophilic and hydrophobic insulations under humid pollution's conditions, several researchers have therefore taken inspiration from nature in order to develop artificial insulating materials with a superhydrophobic surface and zero wetting degree [2 - 6].

The application of superhydrophobic surfaces is important to ensure operational safety and operational efficiency of electrical power transmission networks, so it is not surprising that these components must meet particularly high reliability requirements.

The results of previous experimental works, relating to the electrohydrodynamic movement of a set of water drops, resting on the surface of an insulation based on superhydrophobic soot and put under alternating voltage, have highlighted a mode of evacuation groupo-individual and bidirectional of the water drops whatever the type of arrangement, the volume and the electrical conductivity of the water drops as well as the degree of coverage of the insulation. Concerning the direction of their evacuation, those located in the area surrounding the high voltage electrode pass through it and those deposited in the area close to the grounded electrode pass through the latter. Those in the middle row of the insulation are distributed in such a way that the number of water drops passing through the

HV electrode is slightly greater than that of the drops passing through the G electrode [2].

Hence, the objective sought through this present study consists of predicting the direction of movement of these water drops by means of the distribution of the intensity of the resulting alternating electric field and potential at their level. Measuring electric fields around practical insulators is difficult and becoming increasingly complicated. Experimental setups such as the electrostatic probe can be used, but are subject to periodic errors, although this can be improved by using a more advanced field detection system. Several researchers have employed numerical simulation techniques using commercially available electromagnetic software that appears more practical and less expensive, in order to avoid costly and complex laboratory tests that are often difficult to perform. In this simulation study, influencing parameters such as the volume of water droplets, the number of superhydrophobic soot coating layers of the insulation as well as the permittivity of the dielectric cover of the tested material were taken into consideration.

II. EXPERIMENTAL MODEL

In order to prepare the superhydrophobic insulating surface tested experimentally in our previous model simulated in this study, the first layer of superhydrophobic coating is deposited; this is obtained by first spreading, manually and uniformly a quantity of fresh silicone gel in the form of a very thin on the upper face of a glass plate (Fig. 1a). Secondly, another quantity of the same product is placed on a piece of wood and set on fire (Fig. 1b). Finally, the glass plate, with dimensions 120 mm x 50 mm x 5 mm, is brought close to the flame to cover it with soot emanating from the carbonization of the silicone (Fig. 1b). Figure 1c shows the plate completely blackened and cleaned with tap water. The following layers are applied in the same way as the first one but at time intervals lasting around 24 hours. The number of layers is varied between 1 and 4. Their structure is illustrated in Figure 2a and 2b respectively. These images were obtained using a profilometer (Fig. 3). It is worth noting a slight increase in the uniformity of the same color (for example: orange color) with the increase in the number of layers, in other words the tops of the superhydrophobic insulation asperities are erected practically at the same level above the insulation (Fig. 2b).

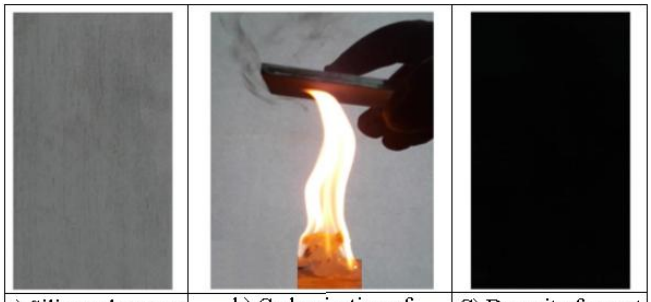


Figure 1. Steps for preparing superhydrophobic multilayer insulation

The contact angle was measured at the high voltage laboratory in Zittau (Germany) using a goniometer. The value of the static contact angle of water drop is of the order of 160°. It is practically identical for two volumes (V_d = 5 and 10 µl) and regardless of the number of superhydrophobic soot layers n_c varying from 1 to 4 (Figs. 4 and 5). On the other hand, Figure 6 shows that for the same quantity of carbon (C), those of oxygen (O) and silicon (Si) are slightly lower in the case of a layer of soot (Fig. 6a) than in the case of 4 layers (Fig. 6b).

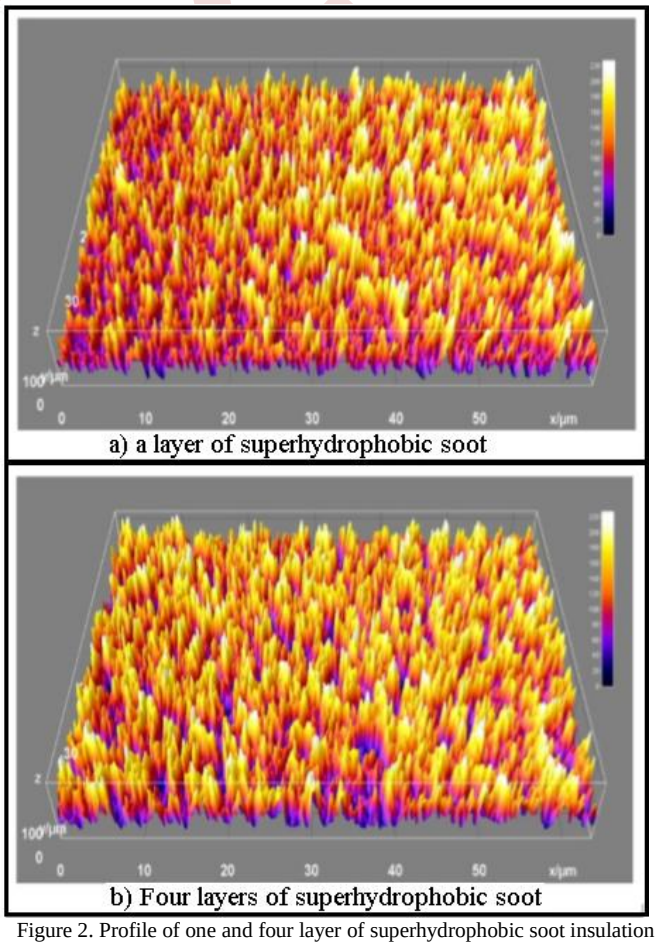


Figure 2. Profile of one and four layer of superhydrophobic soot insulation



Figure 3. Photo of a profilometer from the HV laboratory in Zittau (Germany)

The modeling and simulation technique used in this study is based on the finite element method using COMSOL Multiphysics software. The geometric model used is based on the experimental model (Fig. 7a) previously studied in reference [2]. Figure 7 (b, c, d and e) shows the simulation model. This is designed as a simplified model of a glass surface with a superhydrophobic upper side. Two flat electrodes are placed at both ends of the insulating surface, so as to obtain a homogeneous E field in the air. The distance separating the two electrodes is taken equal to 10 cm. The surface of the glass has the dimensions (16 x 0.5) cm^2, those of the superhydrophobic layer: (16 x 0.01) cm^2 and those of the insulating cover are: (16 x 0.5) cm^2. Those of the flat electrodes are: (3 x 1.2) cm^2, they are suspended 1 cm above the superhydrophobic insulating surface. The physical properties of the materials used in this model are summarized in Table 1.

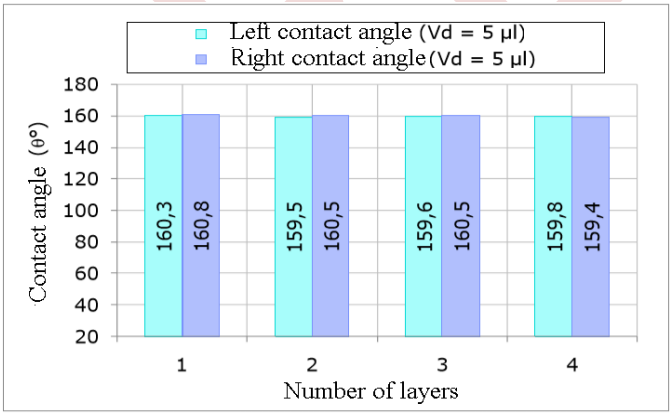


Figure 4. $\theta = f(n_c)$ for a volume of water drop equal to 5 µl

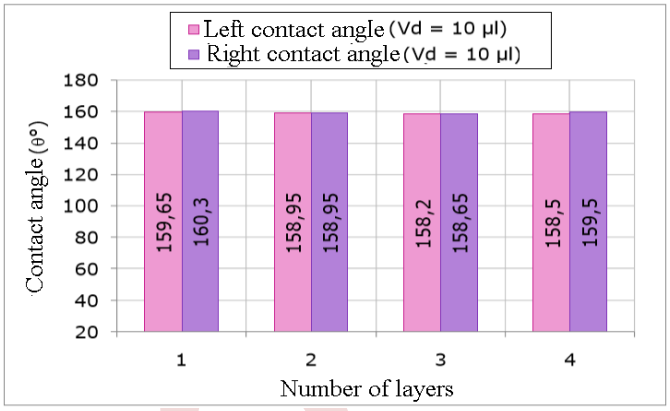


Figure 5. $\theta = f(n_c)$ for a volume of water drop equal to 10 µl

The electrodes made during our previous work [2] are parallelepiped in shape and very rounded at their ends. Their characteristics are illustrated in Figure 7a. They are suspended from the surface of the superhydrophobic insulation using two eyebolts. The size of this gap is chosen to facilitate the evacuation of large water drops from the surface of the insulation and their recovery by the green tray and their reuse. During our study, the variable parameters of influence of the electric field and potential, such as the degree of insulation coverage (without coverage Fig. 7b) or with dielectric coverage with variable permittivity ε_r (Fig. 7c), the number of superhydrophobic layers of soot coating of the insulation or its thicknes e_i (Figs. 7b and 7c), the volume of water drops (Figs. 7d and 7e) as well as the level of alternating voltage applied to the insulation have been taken into consideration.

TABLE. 1; Physical properties of materials used in the model

Material	**Relative permittivity**	**Electrical conductivity (S/m)**
Air	1	10^{-14}
Copper	1	5.99×10^{7}
Glass	5.5	10^{-14}
Superhydrophobic layer	1	10^{3}
Water	81	20×10^{-6}
Dielectric cover	20 à 160	10^{-12}

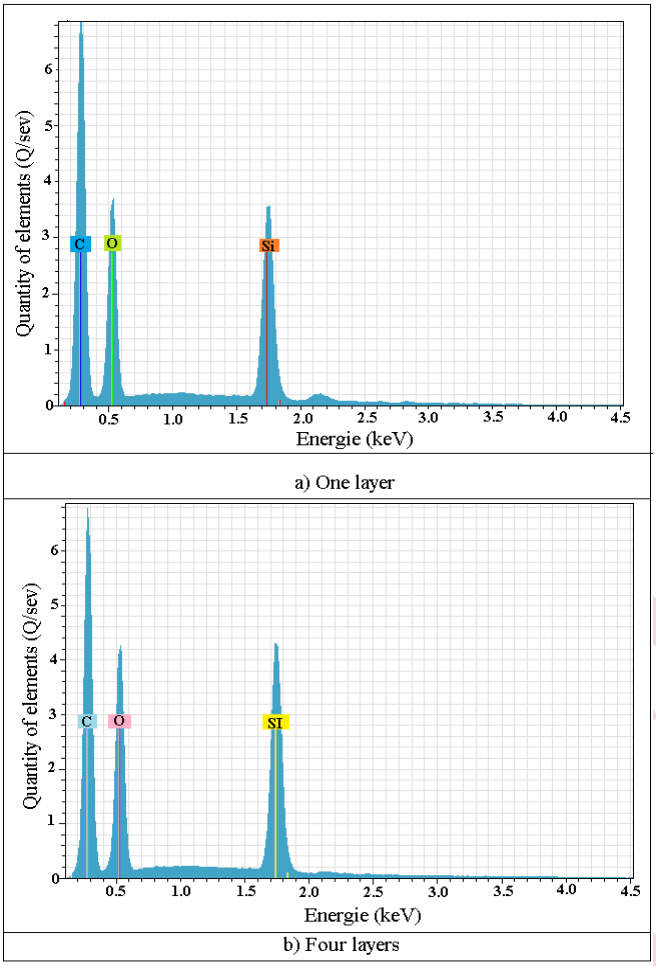


Figure 6. Chemical composition of soot-based superhydrophobic insulation

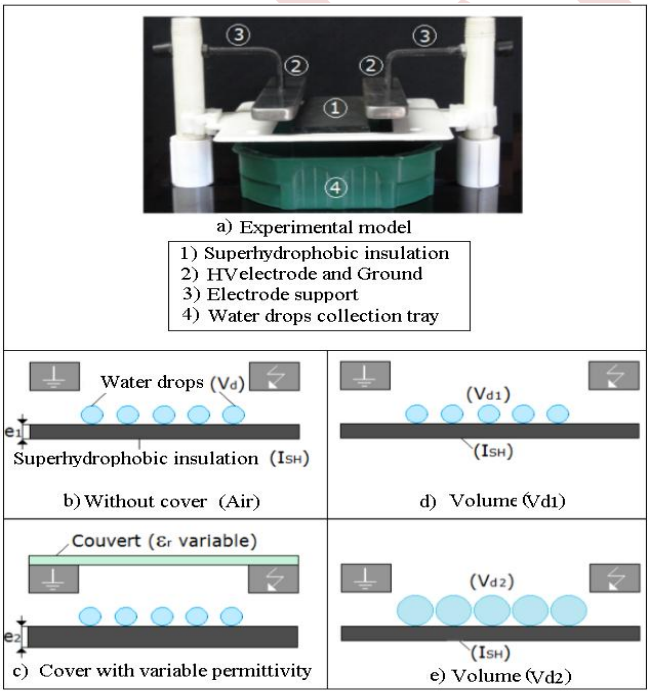


Figure 7. Experimental and simulation model

III. RESULTS AND DISCUSSIONS

A. Variation in the number of water drops, permittivity of the insulation cover and number of superhydrophobic layers

Dans le cadre de ce travail, le nombre maximal de gouttes d´eau déposées sur l'isolation superhydrophobe horizontale est égal à 5. Ces gouttes d'eau sont disposées en ligne droite perpendiculaire aux électrodes haute tension (HV) et terre (G). Cette rangée est placée au milieu de la surface de l'isolation superhydrophobe (Fig. 8).

In the context of this work, the maximum number of water drops deposited on the horizontal superhydrophobic insulation is equal to 5. These water drops are arranged in a straight line perpendicular to the high voltage (HV) and grounded (G) electrodes. . This row is placed in the middle of the superhydrophobic insulation's surface of the (Fig. 8).

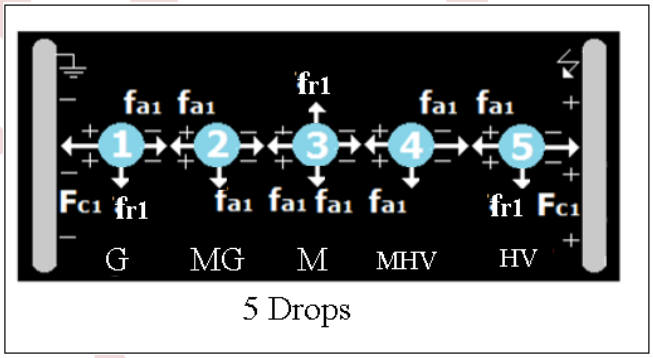


Figure 8. Set of electric forces exerted on a deposit of 5 water drops under positive alternation of AC voltage and under arrangement in straight lines (A_d) (F_{ci}: Coulomb force, F_{ai}: Force of mutual attraction, F_{ri}: Force of repulsion mutual)

The first drop is placed in the vicinity of the grounded electrode (G), the second one (MG) between the middle of the insulation (M) and the grounded side, the third one in the middle of the insulation, the fourth one (MHV) between the middle of the insulation and the high voltage electrode and finally the fifth one (HV) in the vicinity of the electrode under voltage.

In this study, we will try to predict the order and direction of the five water drops' movement by means of the distribution of the resulting electric field along them. The simulation results of the distribution of the potential and the electric field on a variable number of water drops, covering an insulation of one or four layers of superhydrophobic soot coating without or with variable permittivity cover are summarized in Figures 9 to 14. The applied voltage to the insulation is equal to 25 kV.

Figures 9 and 10, result in an amplification of the intensity of the electric field with the increase in the number of water drops from 1 to 5, independently of the degree of insulation's dielectric coverage. However, the resulting electric field is higher in the case of insulation with cover (370 kV/cm in the case of a single drop) than without it (345 kV/cm in the case

of a single drop), whatever the number of water drops considered in this study.

For a well-determined number of drops, for example 5 drops, we can qualitatively predict the direction and order of evacuation of them according to the intensity of the resulting electric field, it is illustrated respectively by Figures 9b3 and 10b3. For example, according to figure 9b3, we obtain the following series: G_1(g); G_5(HV); G_4(MHV); G_2(MG) and G_3(M). This evacuation sequence implies that the drop G_1, which generates a field of higher intensity (E_1 = 600 kV/cm in one of the ends of the drop), leaves the surface first and moves towards the electrode earth (G).

Then comes the turn of the drop G_5 with an electric field intensity slightly lower than that of G_1 (E_2= 550 kV/cm in one of the ends of the drop), but much greater than that of the others, therefore in the direction of the high voltage (HV) electrode. According to the value of the resulting field intensity, the drop G_4 (E_4 = 500 kV/cm) is classified in third position, so it is the one which will exit outside the device passing through the HV electrode. This will be followed by the evacuation of the G_2 drop via the grounded electrode. Finally, the G_3 drop comes out lastly, passing through the high voltage electrode. We see the appearance of a similar motion sequence (G_1(G); G_5(HV); G_4(MHV); G_2(M) and G_3(MG)) for superhydrophobic insulation with coverage (Fig. 10b3).

It follows from this fact that our simulation results of the movement of water drops are conform to those established experimentally in the cases of 25 drops or 5 drops arranged perpendicular or parallel to the electrodes [8] independently of the presence or absence of insulation cover. It appears from the characteristic $E_r = f(n_c)$, that the intensity of the electric field resulting (E_r) from an insulation with 4 layers of superhydrophobic soot (Fig. 11) is slightly greater than that of the field resulting from a single-layer insulation (Fig. 9) regardless of the number of drops deposited on the surface of the insulation. Figures 12 and 13 show the evolution of the intensity of the resulting electric field for a fixed value of relative permittivity ε_r of the dielectric cover and for a single water drop in the case of one and four layers of superhydrophobic soot. This is results in a very slight decline in the intensity of the electric field resulting with the increase in the relative permittivity of the cover and the number of superhydrophobic soot's layers independently of the number of drops covering the insulation. It should be noted the similarity of the effect of the number of water drops on the electric field resulting in these figures which was previously reported. Thus the effect of the number of layers of superhydrophobic soot on the quality of the roughness of the insulation surface is in accordance with the results of our simulation.

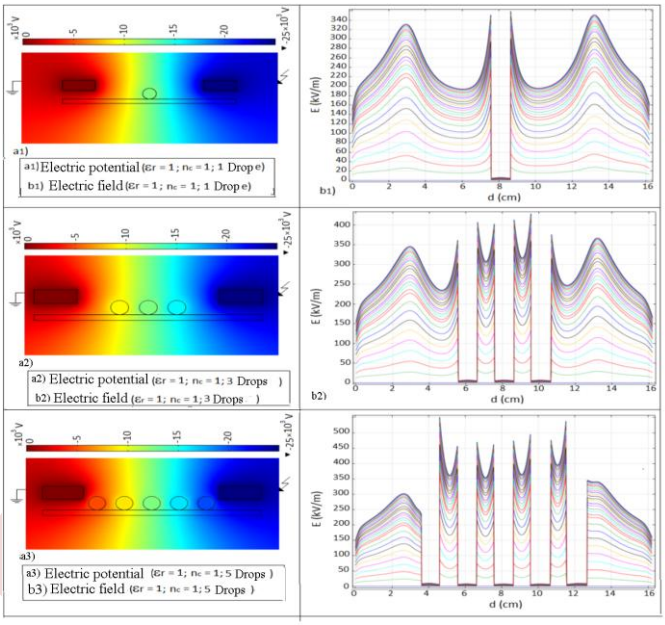


Figure 9. Distribution of potential and electric field on a variable number of drops deposited on insulation without cover (n_c = 1; σ_v = 5.5 µS/cm; V_d = 100 µl; U_a = 25 kV)

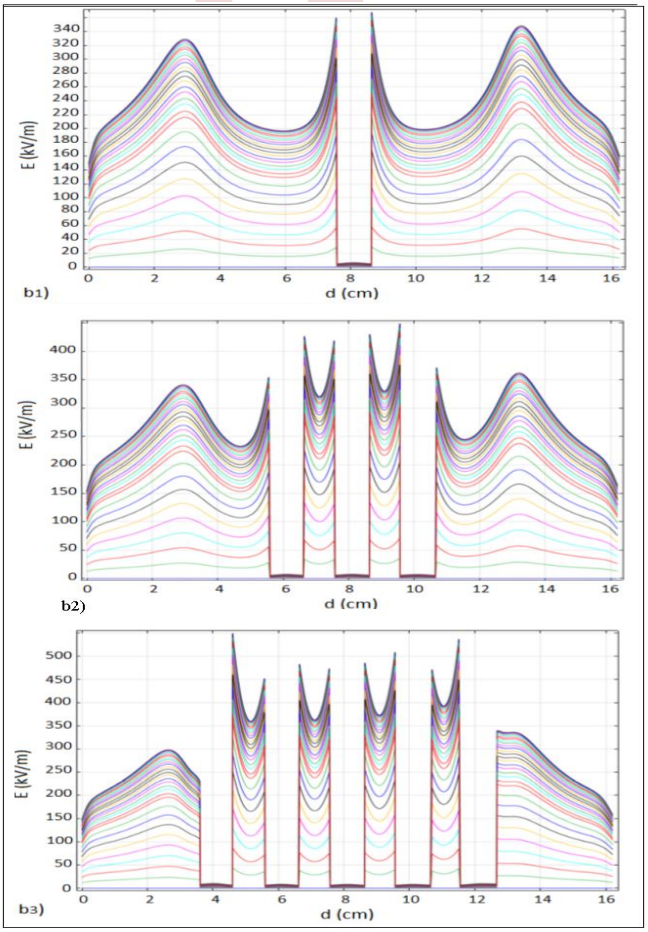


Figure 10. Electric field distribution as a function of the number of water drops of insulation with cover (n_c = 1; ε_r = 20; σ_v = 5.5 µS/cm; V_d = 100 µl; U_a = 25 kV)

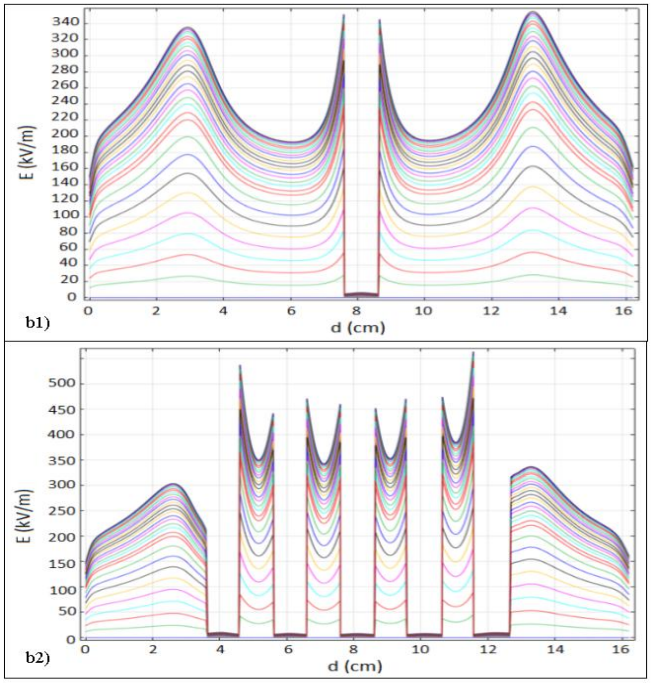


Figure 11. Distribution of the electric field over a variable number of water drops of insulation without cover (n_c = 4; ε_r = 20; σ_v = 5.5 µS/cm; V_d = 100 µl; U_a = 25 kV)

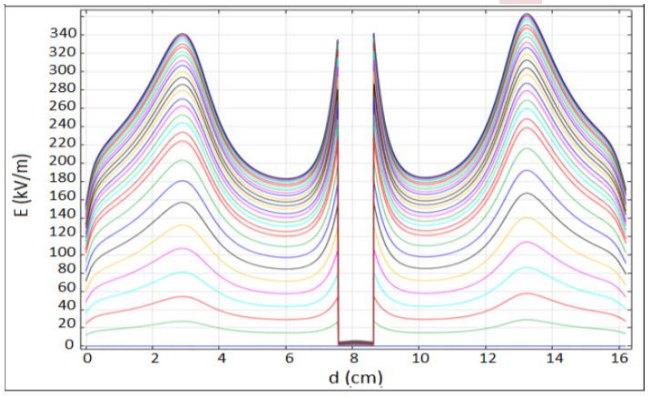


Figure 12. Distribution of the electric field on 1 water drop from insulation with cover (n_c = 1; ε_r = 160 ,σ_v = 20 µS/cm; V_d = 100µl; U_a = 25 kV)

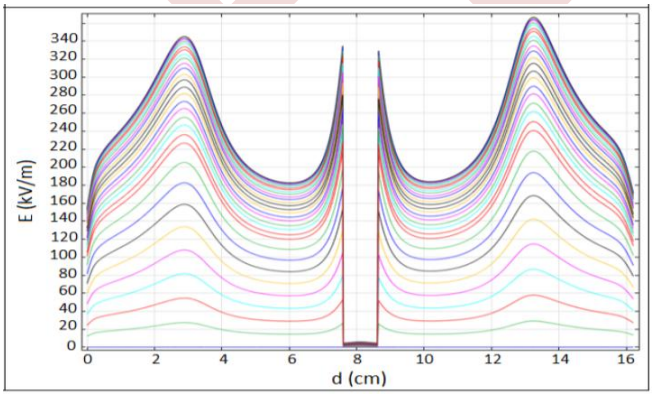


Figure 13. Distribution of the electric field on a drop of water from insulation with cover (n_c = 4; ε_r = 160 ,σ_v = 20 µS/cm; V_d = 100 µl; U_a = 25 kV)

B. Volume of the water drops resting on the superhydrophobic insulation without cover

Figure 14 describes the appearance of the intensity of the resulting electric field as a function of the volume of any number of water drops. This is results in an increase in the intensity of the electric field with that of the volume regardless of the number of drops considered in this study. It should be noted that the simulation results of the effect of the water drops' volume on the intensity of the electric field are not consistent with those obtained experimentally [2, 8] because theoretically, when the volume increases, the electrical field and the applied voltage increase, unlike in the experiment, where the applied voltage to expel the water drop decreases with the increase in volume of the drops (Fig 15).

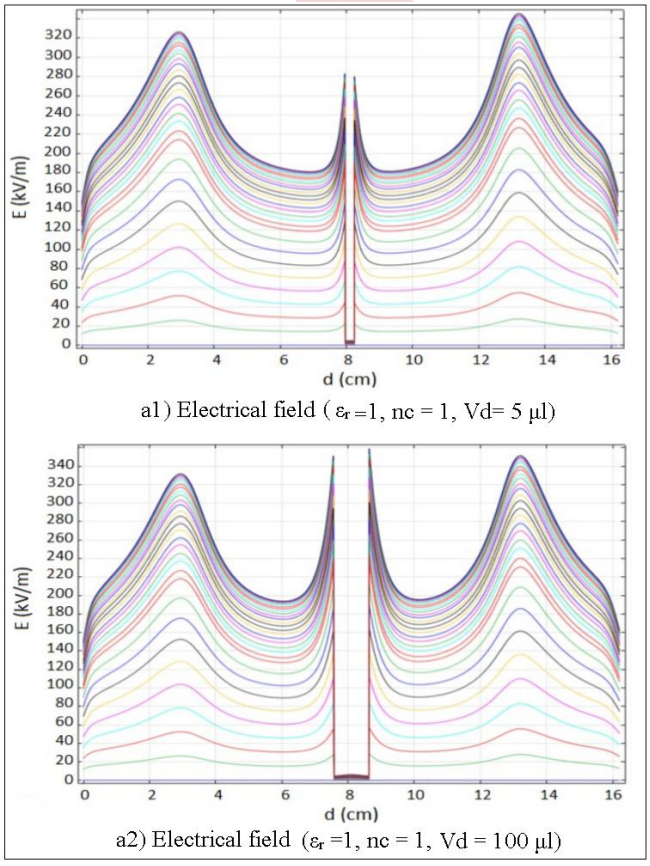


Figure 14. Distribution of the electric field on a drop of variable volume on a superhydrophobic insulation (ε_r = 1, σ_v = 5,5 µS/cm, $_{ts}$ = 10 s, U_a = 25 kV, d = 10 cm)

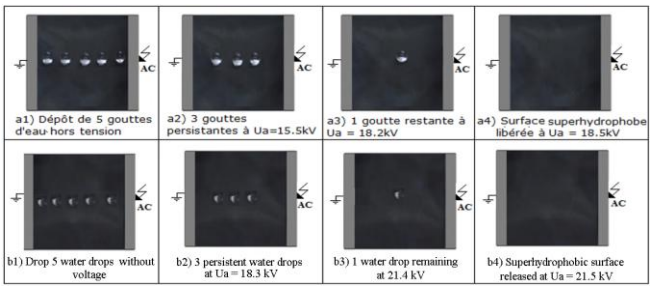


Figure 15. Steps for expelling a row of 5 drops from the middle of the insulation: a (V_d = 80 µl) et b (V_d = 10 µl)

IV. CONCLUSION

The results emanating from this investigation allowed us to quantify by simulation the intensity of the electric field and the potential resulting from a deposition of water drops of variable number and volume, resting on a superhydrophobic multilayer insulating surface with dielectric cover with different relative permittivities, and subjected to a variable AC voltage. These results are summarized as follows:

- The COMSOL software allows us to qualitatively predict the direction and the order of expulsion of a deposit of 5 water drops on a superhydrophobic insulation by means of determining the intensity of the electric field resulting at the level of these ones;
- The increase in the number of water drops leads to an increase in the intensity of the resulting electric field regardless of the number of superhydrophobic layers of the insulation;
- The growth in the number of superhydrophobic soot layers causes a slight increase in the intensity of the electric field;
- An increase in relative permittivity creates a very slight decline in field intensity regardless of the number of water drops covering the superhydrophobic insulation;
- The intensity of the electric field increases with that of the volume, whatever the number of drops resting on the insulation;
-The presence of a solid cover causes the strengthening of the electric field lines between it and the tops of the water drops, which results in an increase in the electric field;
- The results from this simulation are consistent with those established experimentally except for the volume of water drops where the results are in clear contradiction.

REFERENCES

[1] P. Xiao, H. He, J. He, C. Cheng and M. Xiao, "Experimental Study on the Flashover Characteristics of Polluted Insulators under Short-tail Lightning Impulse Waveform", 2018 IEEE International Conference on High Voltage Engineering and Application (ICHVE), 2018, pp. 1-4, doi: 10.1109/ICHVE.2018.8641922.

[2] K. Hamour, F. Bouchelga, R. Boudissa, S. Kornhuber, K.D. Haim, "Optimization of the superhydrophobic insulation longevity by expulsion of any wet deposit with a weak alternating electrical field", Journal of electrostatics 105 (2020) 103451.

[3] J. Liu, S. Zhou, Y. Yan, H. Zheng, S. Liu, ''Study on droplet movement on superhydrophobic surfaces under electric fields'', in: 19th International Conference on Electronic Packaging Technology (ICEPT18), 2018, pp. 681–686. Chicago (USA).

[4] K. Hamour, S. Soudani, B. Smati, F. Bouchelga, R. Boudissa, St. Kornhuber, K. D. Haim, ''Contribution to the optimization of the electrical performance of a superhydrophobic insulation covered with water drops under DC voltage'', J. Electrost. 102 (2019) 103375, 1 - 9.

[5] X. Wang, X. Li, Q. Lei, W. Li, Y. Wu, ''Influence of alternating current (AC) corona discharge on the superhydrophobicity of SiO2/fluorosilicone resin nano-composite coating'', Appl. Surf. Sci. 478 (2019) 642–650.

[6] Wei, H. Jin, H. Zhou, K. Yang, N. Gao, W. Li, ''Dynamic behavior of water droplets on wetted superhydrophobic surfaces under a high AC electric field'', AIP Adv. 9 (2019), 065307, 1-6.

[7] A. B. Gurav, S. S. Latthe, C. Kappenstein, S. Mukherjee, A. V. Rao, and R. S. Vhatkar, "Porous water repellent silica coatings on glass by sol–gel method," Journal of Porous Materials, vol. 18, no. 3, pp. 361-367, 2011.

[8] M. Haddadi et N. Hallouane., "Effet des paramètres électrogéométriques des gouttes d'eau recouvrant une isolation superhydrophobe sur sa performance électrique sous tension alternative 50 Hz ", PFE, , Université de Bejaia, juin 2019.

Optimizing the Two-Plane Electrostatic Precipitator with a Small Blade for Airborne Particulate Matter Filtration

HEBBAR Nihed [1], AISSOU Massinissa [2], AIT SAID Hakim [3]

[1,2]*University of Belhadj Bouchaib, Ain temouchent , Algeria*
nihedhebbar26@gmail.com
aissoumass@gmail.com
[3]University of Ahmed Zabana , *Relizane , Algeria*
hakim.aitsaid@univ-relizane.dz

Abstract— **Ambient air pollution, due to high concentrations of small particles and fine particles, and the main environmental risk for health, causes many premature deaths each year in the world, for this researchers sand to a method of dust removal to save the world is indeed electro filtration. The main objective of our work is to deepen the knowledge on the corona dischargein a son-plane precipitator. The experiments carried out allowed the study of the electrical parameters as well as the influence of the internal conditions into the electro-filter. Airborne particle matter (PM) is a major environmental and health problem. Two-plane electrostatic precipitators (ESPs) with small blades provide a convenient method for filtering PM in a variety of applications. With a focus on electrode arrangement, corona discharge, and cleaning processes, this research attempts to investigate strategies for improving the performance of such ESPs. Experimental findings show how these optimization strategies can improve PM filtering efficiency.**

Keywords: **Small blade arrangement, Corona discharge, electrostatic precipitator (ESP)**

I. INTRODUCTION

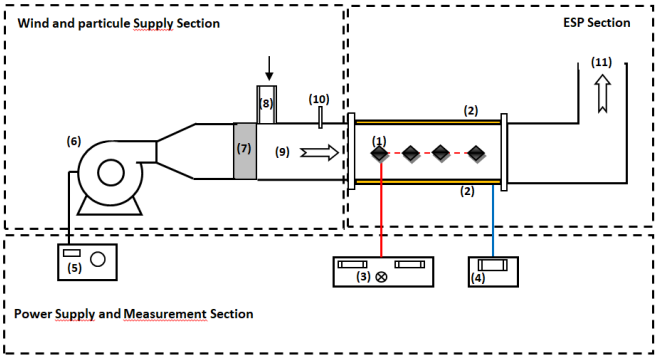
The removal of particulate matter from exhaust gases is accomplished by using electrostatic precipitators (ESPs), which are crucial equipment utilized in a variety of industrial applications. By using charged electrodes to create an electric field, ESPs work on the electrostatic attraction principle, which causes particles to move and adhere to collecting plates. Electrode polarity, electrode number, and electrode layout are some of the variables that affect how effective ESPs are. The effect of electrode configuration, particularly the two-plan arrangement, together with the quantity of electrodes and polarity, on the effectiveness of ESPs is the main topic of this study. Understanding these parameters' implications is essential for improving ESP performance and cutting down on environmental pollutants. We examine an experimental study of an electrostatic precipitator type tiny blade two planes with the filtration of small particles into the diameter is 10um for both polarity 'positive and negative'. The suggested design optimization for a two-plane electrostatic precipitator with a small blade particulate filtration is a viable approach to raising the efficiency of ESPs in particulate matter filtration. This design allows for a high energy by making it easier for the field lines to be oriented toward the collection plan. If the active electrode (the blade) voltage is the blade tip is sufficiently big, the air ionizes and turns into conductive, resulting in the creation of a strongly curved area between electrodes. Therefore, there is a non-uniform electric field linked to the corona discharge. The corona's type is based on the active electrode's polarity. If the blade's voltage in relation to the plane electrode is positive, [18-20] when the blade is operating at a negative voltage, the corona is referred to as negative corona, not positive corona. The corona discharge's current-voltage characteristic 'positive and negative polarities' due to the bulk and there is a difference in velocity between charge ions and electrons. The corona discharge current-voltage characteristics have been characterized by a number of empirical formulations involving various electrode arrangements in terms of geometry. [21]

II. EPERIMENTAL SETUP AND APPARATUS

A. Eperimental apparatus

The electrostatic precipitator type small blade two planes with filtration of particles 10um in positive and negative polarity experimental setup consists of two parallel electrodes connected to the ground, in stainless steel rectangular planes (collecting electrodes) of length 220 mm, width 170 mm, and thickness 2mm. The distance between two successive active

electrodes was kept constant at 20 mm, while the gap between active and passive electrodes was kept constant at 50 mm. A lab-scale ESP, an air blower, a particle loader, a high-voltage power supply, and an electrical monitoring system are all part of the system. The blower introduces dry air mixed with dust into the tunnel generated by the blower, which is subsequently introduced into the ESP.



(1) Discharge Blades, (2) Collection plates, (3) DC Power Supply, (4) Ampermeter, (5) Blower Supply, (6) Blower, (7) Honeycomb, (8) Inlet Particle, (9) Inlet Dust Sampler, (10) Velocity Measurement Probe, (11) outlet Air.

Figure 1. The experimental model

III. RESULTS AND DISCUSSION

The influence of the ESP design on the current-voltage characteristics is explored in this section. To begin, the ideal operating conditions for the ESP was found by altering the design and operational conditions, such as the number of electrodes and the applied voltage. Corona current-voltage should be measured before using the ESP. In order to assess the features were measured. The current was measured at the plates for collecting. All testing were conducted in a controlled environment (20-25°C, 40-50 RH %).

A. Current Voltage Characteristics

The effect of the electrostatic precipitator (ESP) design on current-voltage characteristics is an important factor to consider while maximizing the ESP's performance. The ESP's optimum operating conditions can be established by adjusting design and operating factors such as the number of electrodes and the applied voltage. The influence of polarity on the electrostatic precipitator (ESP) is an important factor to consider while maximizing the device's performance.

The voltage given to the electrodes causes the air between the electrodes to electrically breakdown, a process known as a "corona." Because a negative corona sustains a larger voltage than a positive corona before sparking occurs, the electrodes are frequently given a negative polarity. [1]

$$I=K\times V\times (V-V_0) \quad (1)$$

Where:

$$K= (4\pi\varepsilon_0\mu)/ [h^2 \log (d/ r_0)] \quad (2)$$

where I is the corona current, V the applied corona voltage, V_0 the corona threshold voltage and K a dimensional constant depending on the outer cylinder radius R, the wire electrode radius r_0 and the charge carriers mobility in the drift region μ. [4]

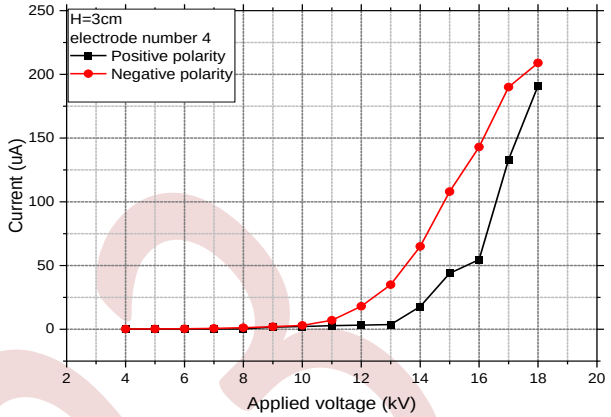


Figure 2. Current-voltage characteristic of positive and negative corona discharge

Finally, the polarity of the electrodes in an electrostatic precipitator can alter the device's performance. A negative polarity is usually chosen because it can support a larger voltage before sparking occurs than a positive polarity. Furthermore, a positive polarity electrostatic precipitator can produce ozone, which is detrimental to organisms. Indeed, in negative polarity, significant part of the charge carriers in the drift region are electrons whose mobility is much higher than those of positive and negative ions [4].

B. Current Voltage Characteristics

The distance between an electrostatic precipitator's electrodes and collecting plates has a considerable impact on its performance. In general, the greater the distance between the electrodes and the collecting plates, the lower the collection efficiency. This is due to the fact that the electric field intensity diminishes as the distance between the electrodes and collecting plate's increases. [5] Another reason why a larger distance between the electrodes and collecting plates may be desirable is to reduce the risk of back corona. Back corona is a phenomenon that can occur when the electric field strength is too high. Back corona causes the particles to be re-entrained into the flue gas stream, which reduces the collection efficiency of the ESP. [6] The optimal distance between the electrodes and collecting plates of an ESP depends on a number of factors, including the type of particles being collected, the size and concentration of the particles, the desired collection efficiency, and the allowable pressure drop. [7] Cooperman [8-10] was a pioneer in establishing the law for corona initiation in ESPs. He presents the current-voltage law, which is identical to Townsend's law.

The figures 3 and 4 show the effect of the distance between blades-planes in both polarities such as the corona discharge is greater in H=2cm. It was also observed that the range of stable operating voltages decreased as the electrode gap decreased. This is driven by both the onset voltage and the spark-over

voltage. The DC current through the inter-electrode gap is a nonlinear function of the applied voltage [18].

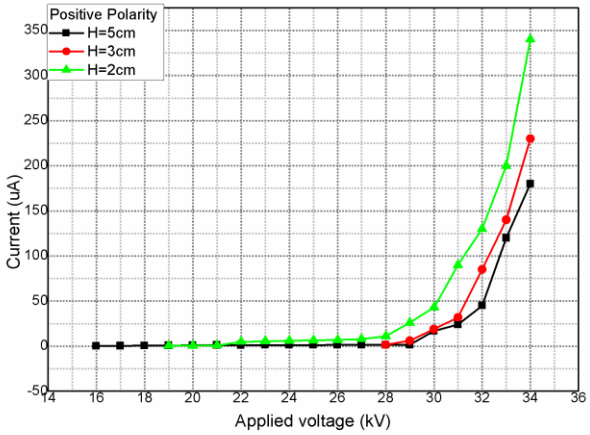


Figure 3. Current-voltage characteristic of positive corona discharge in various blade- plates distance

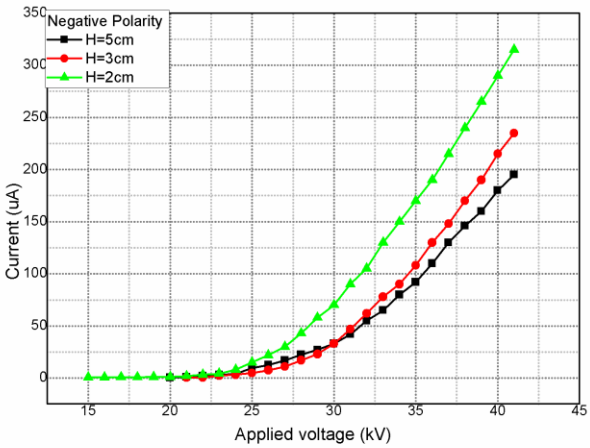


Figure 4. Current-voltage characteristic of negative corona discharge in various blade- plates distance

C. The Electrode Number Effect

An increase in the number of active electrodes will lead to an increase in the corona discharge current. This is because each small blade has its own ionization region, and the overlapping ionization regions of multiple electrodes will create a stronger electric field, which in turn will lead to a higher discharge current. The passage also mentions that the negative corona discharge current is higher than the positive corona discharge current for the same applied voltage. This is due to two factors [2]. The positive inception voltage is higher than the negative inception voltage. This means that a higher voltage is required to initiate a positive corona discharge than a negative corona discharge. The mobility of the negative ions is higher than the mobility of the positive ions. This means that the negative ions can move more freely in the electric field, which leads to a higher discharge current. In the case of blades-to-planes geometries, the presence of multiple discharging wires and two grounded planes creates a stronger electric field and a larger ionization region. This leads to a further increase in the corona discharge current. [2]

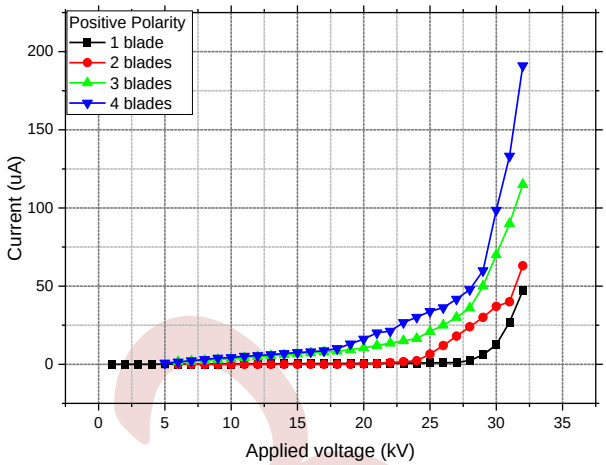


Figure 5. Current-voltage characteristic of positive corona discharge in various number electrodes

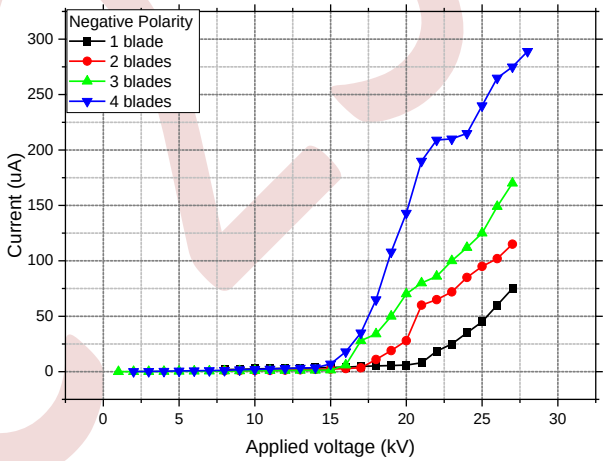


Figure 6. Current-voltage characteristic of negative corona discharge in various number electrodes

D. Electric field And Dust Collected Plates

In this section, particles dust are injected into the inlet of the electrostatic precipitator,with various applied potentienl and for both polarities, If the applied voltage increases the efficiency filtration became more performance, especially when V=20kV . [11-13] The collection efficiency is more Important with negative polarity than negative polarity, the collection particles cement in the extremities is more performance . Therefore, the greatest collection efficiency can be obtained with high voltage applied to the precharger and large particles. Although an increase in corona voltage can also improve the efficiency of the module, exceedingly high voltage will increase the amount of ozone. Therefore, in the design of practical precipitator, an appropriate charge voltage should be determined through experiments according to the requirements and specific conditions. [14-16] Such as the collection efficiency is calcuted with

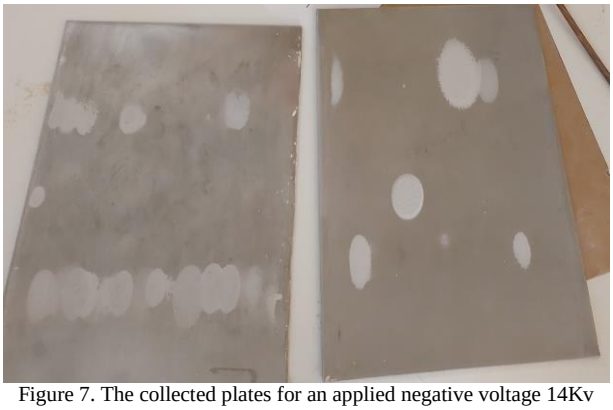


Figure 7. The collected plates for an applied negative voltage 14Kv

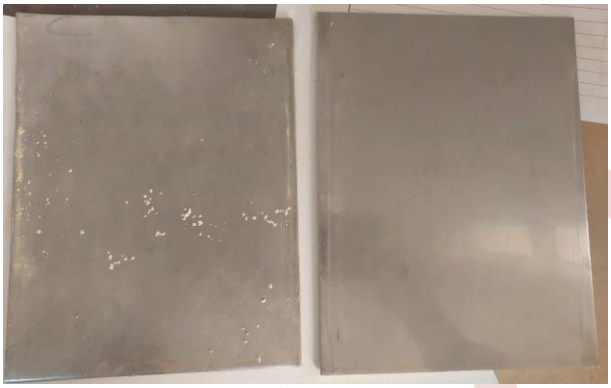


Figure 8. the collected plates for an applied positive voltage 14kV

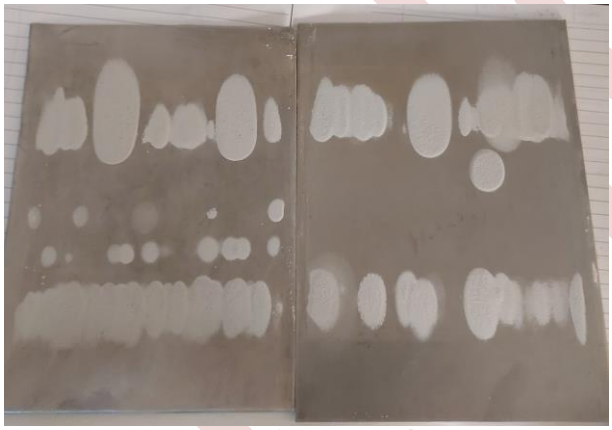


Figure 9, the collected plates for an applied negative voltage 17kV



Figure 10**.** The collected plates for an applied positive voltage 17kV

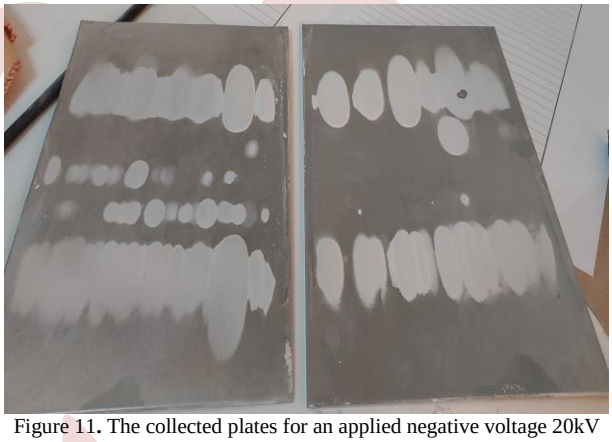


Figure 11**.** The collected plates for an applied negative voltage 20kV

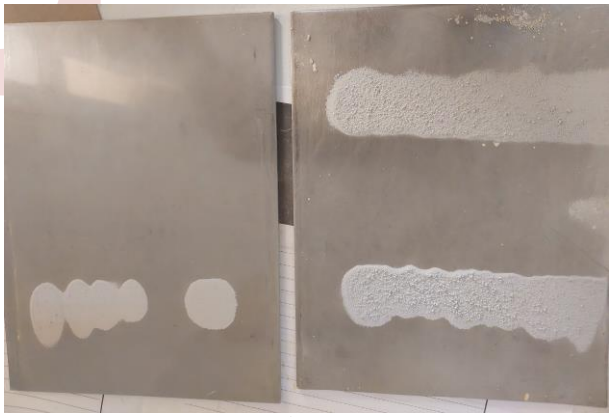


Figure 12. The collected plates for an applied positive voltage 20kV

IV. CONCLUSION

One of the industrial-scale particulate collecting technologies that is widely utilized to meet particulate emission regulations is electrostatic precipitation [17]. The current-voltage measurement method is effective for distinguishing the performance of the configuration filter 'small blades -planes' for fine particle precipitation. The

combination of electrodes improves the electrostatic filter's efficacy, especially in negative polarity.

The purpose of this study is to develop a discharge model that incorporates all of the parameters involved, such as the geometry of the inter-electrode space, the shape of the applied wave, and the ambient conditions, in order to obtain a more adequate precipitation efficiency in a PES in small blades-planes configuration. to conduct an experimental study of the corona discharge by determining the critical electrical parameters inside the electrostatic precipitator in small blades-planar configuration, taking into account geometrical parameters (inter-electrode type of injected dust particles, etc.), and to observe the behavior of the corona discharge parameters by varying the applied electric potential

ACKNOWLEDGMENT

The authors would like to acknowledge the help and encouragement they have received from colleagues and col-laboratory during the course of writing this article.

REFERENCES

[1] H. Nouri, N. Zouzou, E. Moreau, L. Dascalescu and Y. Zebboudj, « Effect of relative humidity on current–voltage characteristics of an electrostatic precipitator », *J.l of Electrostatics*, vol. 70, n° 1, p. 20–24, feb. 2012.

[2] H. Ait Said, H. Nouri and Y. Zebboudj, « Effect of air flow on corona discharge in wire-to-plate electrostatic precipitator », *J. of Electrostatics*, vol. 73, p. 19–25, feb. 2015.

[3] E.O. Selim, R.T. Waters, Static probe for Electrostatic field measurement in the presence of space charge, IEEE, Transactions on industry applications, vol 1A-16, No. 3, 1980.

[4] Hakim Ait Said, Massinissa Aissou,Hamou Nouri and Youcef Zebboudj «Effect of Wires Number on Corona Discharge of an Electrostatic Precipitators »J.of Electrical Systems , 10-4 p. 392-405 ,jan 2014.

[5] Cooperman, P., Spontaneous ionization of gases at high temperature, IEEE Trans. Ind. Appl., 1974, vol. 10, no. 6, pp. 520-523.

[6] Yala, H., Zebboudj, Y., Finite-element solution of monopolar corona in a coaxial system, Eur. Phys. J. AP, 2002, vol. 19, no. 2, pp. 123-129.

[7] Conesa A., J., Sánchez, M., The current–voltage characteristics of corona discharge in wire to cylinder in parallel electrode

[8] Shale, C., C., Holden, J., The role of wire size in negative electrical discharge at high temperature. Industry and General Applications, IEEE Trans. Ind. Gen. Appl., 1969, vol. 5, no. 1, pp. 34-39.

[9] M. Ni *et al.*, « Experimental investigation on the characteristics of ash layers in a high-temperature wire–cylinder electrostatic precipitator », *Separation and Purification Technology*, vol. 159, p. 135–146, feb. 2016.

[10] S. Arif, D. J. Branken, R. C. Everson, H. W. J. P. Neomagus, L. A. le Grange et A. Arif, « CFD modeling of particle charging and collection in electrostatic precipitators », *J. of Electrostatics*, vol. 84, p. 10–22, dec. 2016.

[11] Kanazawa S, Ohkubo T, Nomoto Y, Adachi T. Submicron particle agglomeration and precipitation by using a bipolar charging method. *J Electrostat*. 1993; 29(3): 193-209.

[12] Mainelis G, Willeke K, Adhikari A, Reponen T, Grinshpun SA. Design and collection efficiency of a new electrostatic precipitator for bioaerosol collection. *Aerosol Sci Technol*. 2002; **36**(11): 1073-1085.

[13] Mizuno A. Electrostatic precipitation. *IEEE Trans Dielectr Electr Insul*. 2000; **7**(5): 615-624.

[14] M. Gao, Y. Zhu, X. Yao, J. Shi, W. Shangguan, Dust removal performance of two-stage electrostatic precipitators and its influencing factors, Powder Technology 348 (2019) 13–23.

[15] Jaworek, A. Marchewicz, A.T. Sobczyk, A. Krupa, T. Czech, Two-stage electrostatic precipitator with co-and counter-flow particle prechargers, Journal of Electrostatics, 87(2017)180-194.

[16] U. Khaled, A. Beroual, F. Alotaibi, Y. Khan, A. AI-Arainy. Experimental and analytical study on the performance of novel design of efficient two-stage electrostatic precipitator. IET Science, Measurement & Technology, 12(2017)486-491.

[17] F. Kherbouche, Y. Benmimoun, A. Tilmatine, A. Zouaghi and N. Zouzou, « Study of a new electrostatic precipitator with asymmetrical wire-to-cylinder configuration for cement particles collection », *J. of Electrostatics*, vol. 83, p. 7–15, oct. 2016.

[18] M. Townsend, Electricity in Gases. (Oxford University Press, 1915)

[19] L.B. Loeb, Electric Coronas—Their Basic Physical Mechanisms (University of California Press, Berkeley, 1965)

[20] B.L. Henson, J. Appl. Phys. 15, 52709 (1981)

[21] G.F.L. Ferreira, O.N. Oliveira, J.A. Giacometti, J. Appl. Phys. 59, 30–45 (1986)

Aging of composite insulators under desert conditions

SAHLI ZAHIR

Laboratoire de Génie Electrique, université de Bejaia, Bejaia, Algérie
zahir.sahli@univ-bejaia.dz

Abstract— **large-scale energy-efficient projects involving the exploitation of the solar energy potential of the deserts of North Africa and the Middle East in order to sustainably supply neighboring regions (particularly Europe) with renewable electricity are emerging. Each km^2 of desert receives annually solar energy equivalent to 1.5 million barrels of oil. Covering 0.3% of the planet's deserts with solar thermal power plants would make it possible to cover the planet's electricity needs. Exploiting this energy potential requires the construction of transmission lines and electrical substations in desert regions with a hostile climate.**

With the advancement of chemical engineering many newer insulation material have been developed that advantages over older materials which are still in use. Polymeric materials are also one of them it is intensively used in the transmission lines due to its number of advantages over ceramic insulators. From materials point of view their invention can not be marked as new, but their use in insulation system is not older than 30 years. The polymeric insulator has a fiber rod structure covered with weather resistant rubbers and fillers and fitted with end fittings. Such a type of insulator is also called composite insulator. The most critical thing to be considered in outdoor insulators is the interface between the solid insulting body and the surrounding air. The problem appears at the interface because it is the interfering point of air and the solid insulator. This problem arises due to the effects of pollution, rain, dust, salt, corona, arcing over surfaces, nitric acid in air, etc.

Since their appearance, composite insulators have suffered from aging problems so this time is not enough to guarantee that they can sustain in desert environments for long time where sand wind is frequent and long period sunshine (UV and high daytime temperatures).

Keywords: **Composite insulators, Silicon rubber, aging, UV, loss of hydrophobicity, wind erosion.**

Introduction

The aging (environmental stresses) is a major problem of composite insulators now-a-days. The main thing in aging is to predict how, when and with what speed it occurs and under what conditions it can lead to failure and what overall average expected life of a composite insulator is. For this many researchers have been done.

In addition to electrical stress, heat, light, sand wind and moisture produced by environment effect the insulation in service. Heat , sand wind and UV produce surface cracking and erosion. In absence of light, most polymers are stable for very long periods at ambient temperatures. The effect of sunlight is to accelerate the rate of oxidation. Photo oxidation leads to chain scission of hydrophobic methyl groups leading to the production of aldehydes, ketones and carbolic acids at the end of polymer chains. The breakdown may be comparatively mild, affecting only side groups, or it may be of a severe nature, causing a reduction in the size of macromolecules. Considering that even one chain scission per molecule in a polymer with a molecular weight of 100,000 destroys its technical usefulness [1]. The moisture goes into these cracks and finally causes a flashover under of the rod.

Ultraviolet light is one of the major factors responsible for degradation of polymer insulators. Main sources of ultraviolet light are: sun, corona formation and dry-band arcing activities on insulator surface. The energy from sunlight that is destructive to polymers is between 320 and 270 nm. This destructive energy constitutes less than five percent of the total radiation reaching the surface of the planet. The absorption of this UV radiation results in mechanical and chemical degradation of the polymer structure which can affect the dielectric and weathering properties of that polymer. The rate at which the degradation occurs depends on the intensity and wavelength of the radiation. These factors vary with season, elevation, latitude and the time of the day. The degrading effects of these radiations are accelerated further if there is sand wind associate to high daytime temperatures. It therefore, suggests that polymer compounds for use in desert environments should be evaluated in the combined presence of UV radiation and send wind at temperatures exceeding 50°C.

The effects of UV radiation, send wind and temperatures on a polymer include crazing, chalking or cracking of the surface, discoloration and loss of hydrophobicity, leakage current, and flashover voltage under artificial pollution and Hardness measurement these are discussed in following sections.

I. DESERT FACTORS INVOLVING IN AGING OF POLYMERIC INSULATORS

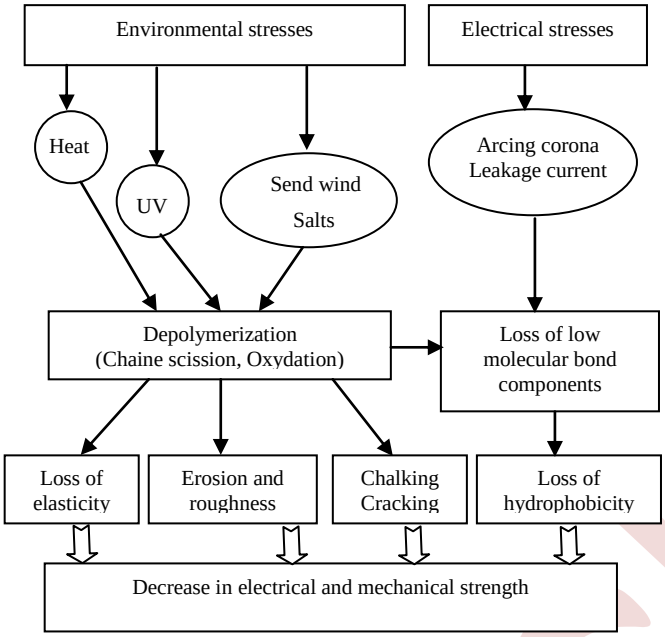


Figure 1. Chain of causation.

The absorption of UV radiation, combined with heat and sand wind, results in mechanical and chemical degradation of the polymer structure, which can affect the dielectric properties of that polymer as show in figure 1.

II. EXPERIMENTAL SETUP

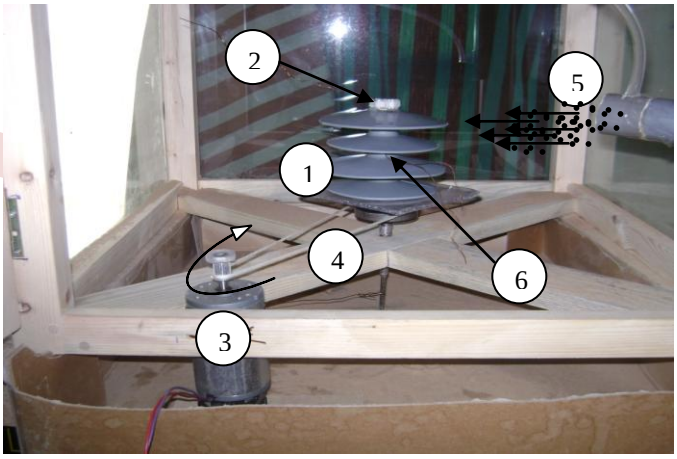
A. Desert environment aging chamber

To simulate the weather cycles at Algerian desert environment a multi stress environmental chamber was developed. The chamber is an oven 60cm X 80cm X 60cm which regulates the temperature at 50°C. One 60 cm long UVA-340 lights are used to simulate 1 mW/cm^2 UV radiation, at the wavelength in a range of 300- 400 nm. Samples are subjected to UV light normally for 1000 h. it is well known that 200 h of test period is equivalent to 1 year of actual outdoor exposure considering only the UV wavelength (300－400 nm) that is mainly related. (figure 2)

To reproduce the same conditions as a sandstorm, a source of air current projects grains of sand which flow in free fall from a tank towards the insulator under test. The diameter of the sand grains and the air flow speed are chosen to reproduce the extreme conditions to which insulators operating in desert regions are subjected. For homogenization of the sand projection, the insulator is kept in rotation at a constant speed of 40 rpm via a direct current motor; this mechanism is housed in a closed glass cell as show in the figure 3. The device is inserted into the oven in figure 2.



Figure 2. Multi stress environmental chamber.



1-Sample 2- HV electrode 3- DC Motor

4-Drive belt 5-Air and sand flow 6-Ground electrode

Figure 3. Laboratory model to simulate sand wind.

B. Techniques used for analysis

Aging phenomena can be detected by different methods. These methods are very useful to detect and to classify aging with non-destructive methods. After the installation of insulators in the aging chamber, the exact knowledge of the degradation state and residual life of the material used in a specific insulation can be detected by measuring the flashover voltage under contamination condition, leakage currents,

hydrophobicity measurement, loss factor measurement, Hardness and roughness.

1) Visual observation

There are different methods for visual observation by observing with naked eye. Another advance method for visual observation is taking snapshoot of image by a high resolution digital camera.

2) Contact angle measurement technique

There are different methods for measuring the contact angle of a hydrophobic material, but one of the most common is the hanging drop method, which consists of:

- Prepare a surfactant liquid solution. The most common is de-ionized water with a small amount of surfactant, such as fluorinated surfactant PFPE.
- Place a drop of liquid on the material using a micropipette.
- Measure the shape of the drop using an image taken by a camera or microscope. It is important to take the measurement before the drop evaporates.
- Use software to calculate the contact angle of the material based on the shape of the drop.

3) Loss factor (TAN(δ)) measurmentntact

The dielectric loss factor measurement relies contact angle measure results and is used to interpret the deterioration of silicone rubber and EPDM. As the value of the contact angle decreases, the dielectric loss increases.

4) Leakage currant and flashover voltage measurments

The pollution layer covering the insulating surface between the electrodes was prepared by mixing an appropriate amount of NaCl to distilled water depending on the required level of pollution severity. In order to simulate wet pollution (fog, drizzle), we use an atomizer which projects fine and homogeneous water droplets.

The AC test source consists of a HV transformer. The test voltage was increased at constant speed of the slope until the flashover of the insulators surface. This process was repeated for different values of pollution severity. The flashover voltage reported in this work is the average of twenty measurements for the same pollution degree. The leakage current was measured using a storage oscilloscope connected to a computer using a shunt resistor.

5) Roughness measurements

Roughness measurement is a measurement technique that quantifies the surface texture of a material. Roughness is defined as the set of irregularities in the surface of a material, which can be measured in terms of height, amplitude, wavelength, frequency and direction.

The roughness measuring station used is composed of a roughness meter type Surftest-201 Mitutoyo (SJ-201M).

6) Hardness measurements

The principle of this test is the rebound of a calibrated spherical carbide projectile at a determined speed on the material to be tested (the harder the material, the greater the rebound height). When the projectile hits the surface, surface deformation results in loss of kinetic energy. This energy loss is calculated via speed measurements. The device measures the ratio of rebound speed to impact speed. The signal voltage is proportional to the projectile speed; signal processing by the electronic system provides the hardness reading which is displayed on the screen.

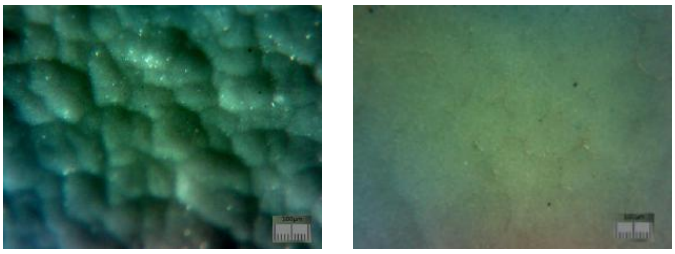
III. RESULTS OBTAINED FROM DIFFERENT TECHNIQUES

Normally, the first condition that indicates the aging of insulator is loss of gloss and discoloration. When visually observing the surface of the samples aged under ultraviolet rays and temperature, several significant changes can be noticed. First, the surface color became duller and less shiny. We notice that these samples have started to lighten, and this discoloration increases as the exposure time increases. Cracks also appeared, indicating a loss of flexibility of the material (Figure 4). Erosion is a degradation mode caused due to sandstorm activity. It is an irreversible degradation of the surface of the insulator that occurs by major loss of material (that is more than 1 mm). It significantly reduces the thickness of the polymer sheath that prevents ingress to the core rod. Erosion can be localized, uniform or tree shaped. In Figure 5, we observe the polished surface of the silicone insulator after aging; this generates weight loss.

We note on the two images (figure 6) taken with the scanning electron microscope (SEM) a tearing of material fragment and the formation of borrowings of tree structures due to surface electrical discharges. Tracking is caused by leakage current activity, which is made possible by exposure to UV heat and wind sand. This is an irreversible deterioration by the formation of paths starting and developing on the surface of insulators. These tracks have the appearance of carbon tracks which cannot be easily removed and are conductive even under dry conditions [2].



Figure 4. Visual observation of sample discoloration after aging.



Before aging After aging

Figure 5. View of the insulator surface under optical microscope.

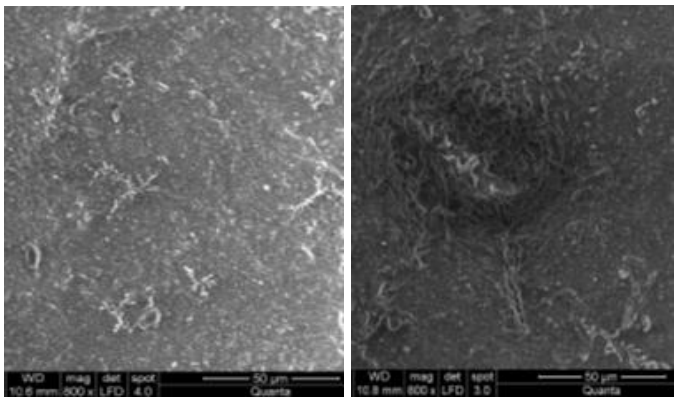


Figure 6. View of the insulator surface under SEM.

Hydrophobicity of any material is its resistance to flow of water on its surface. The hydrophobicity of silicone rubber materials is measured through measuring contact angles between the material and water drops on its surface.

The histogram in Figure 7 represents the contact angle measured as a function of the aging time. Note a slight increase at the start of exposure that coincides with the softening period of our material (Figure 8), followed by a constant decrease to reach 26.36% after 1000 hours of exposure. [3]

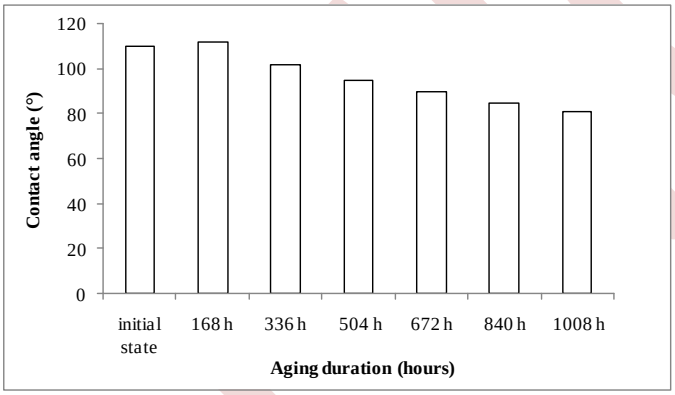


Figure 7. Contact angle of samples as a function of aging time.

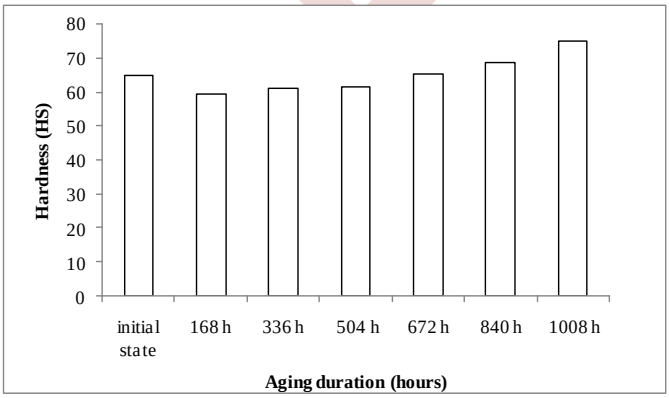


Figure 8. Hardness of samples as a function of aging time.

The roughness criterion considered shows a clear increase during the first two weeks of exposure then they stabilize at lower levels (figure 9). In our case, we can explain it by a partial chemi-crystallization within the material following the partial ordering of the molecular chains during solidification that occurs after the softening of the silicone following its exposure to ultraviolet rays combined with a temperature of 50°. [3,4]

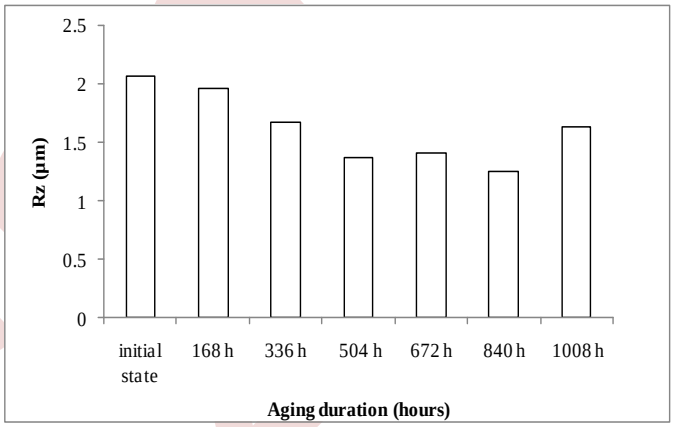


Figure 9. The average profile height of the samples as a function of aging time.

According to the results of the flashover voltage curves as a function of exposure time (figure 10 and 11), the aging of polymer insulators strongly depends on the exposure time to ultraviolet rays. Note an almost linear decrease and the aging peak is not reached after 1008 hours of UV exposure at a temperature of 50°C.

Hydrophobicity is the wetting property of rubber material because of which it resists formation of film of water by forming beads of water, thus denying a path for leakage current and associated arcing. Loss of hydrophobicity results in the formation of hydrophilic surface. The more the exposure time increases and for increasingly smaller voltages and under the effect of the electric field, the electric forces exerted on the pollution droplets are sufficient to counter the hydrophobic phenomena of the insulator silicone and droplets align then spread across the surface of the insulator to form a conductive electrolyte channel that the arc will follow for bypass.

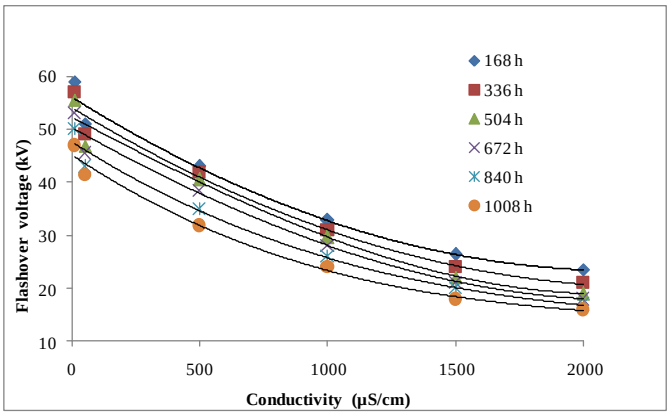


Figure 10. Flashover voltage of samples as a function of pollution conductivity. Aging duration (hours)

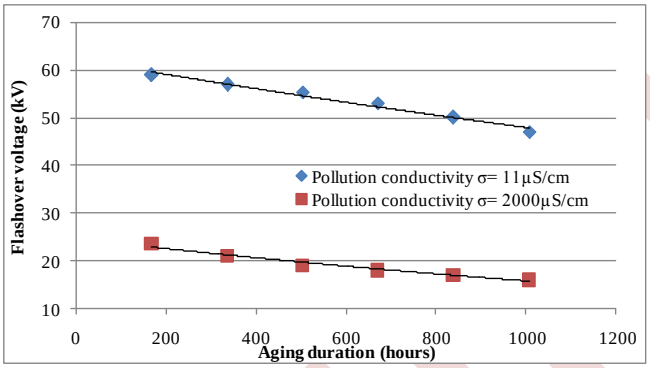


Figure 11. Leakage current of samples as a function of pollution conductivity.

Measuring the leakage current is a key criterion for the characterization of a hydrophobic material. The less hydrophobic the material, the greater the wettability of the surface of the material, the greater the leakage current.

Figure 12 shows the variations of leakage current as a function of the pollution conductivity, for each aging period and for an applied voltage of 15 kV, it can be seen that the values of the leakage current increase as the conductivity increases (virgin and aged sample). The leakage current values for the aged samples are significantly higher than that of the virgin sample.
We notice that the increase in the conductivity of the pollution on the surface of the samples increases the leakage current that is predictable, and that the increase in the time of exposure of the samples to UV and sand wind also increases the leakage current for the same degree of pollution severity. From the fact that the leakage current increases as a function of UV exposure time under well-controlled laboratory conditions, it can be concluded that wettability is greater and the samples have partially lost their hydrophobicity.[5,6]

Also, note that the leakage current curves as a function of exposure time (Figure 13) have a quasi-linear trend and maximum aging is not reached after 1008 hours of.

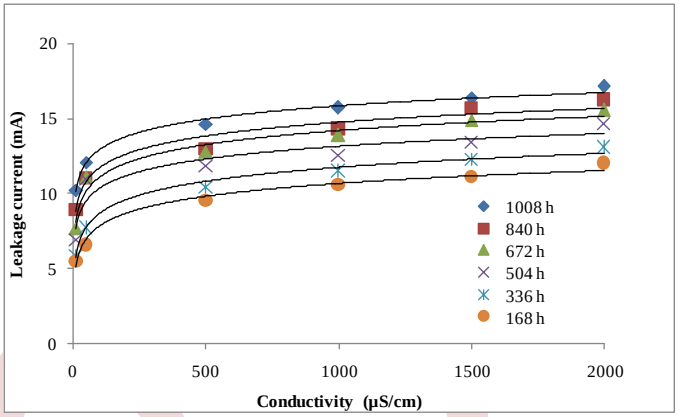


Figure 12. Leakage current of samples as a function of pollution conductivity.

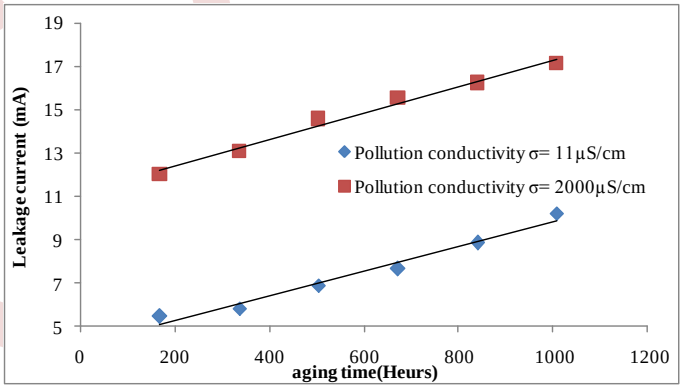


Figure 13. Leakage current of samples as a function of aging time.

As previously found, that pollution, humidity and UV combine to sand wind and high temperature could originate surface discharges, and then could damage Silicone Rubber. The damage could be detected by measuring and analyzing the pattern of the surface discharge that occurred. Measurement of the AC leakage current and flashover voltage under pollution provide significant correlation with surface damage.

Conclusion

Composite insulators are lightweight and have demonstrated exceptional performance at outstanding levels of pollution withstand voltage characteristics and impact resistance. They have been widely used.

To study the degradation of organic insulating materials following their prolonged use, exposure tests to external stresses and indoor accelerated aging tests are unavoidable.

Wind erosion is a natural process that commonly occurs in deserts, on sand dunes and on coastal beaches. When combined

with ultraviolet light, it becomes one of the main factors responsible for the degradation of polymer insulation.

The UV and sand wind effect on changing the contact angle of silicon rubber surface is very noticeable.
It has been observed that increased exposure to UV and sand wind results in increased leakage current as well as surface roughness.

A silicone rubber compound for high-voltage applications needs to be developed through detailed and comprehensive analysis of its properties and behavior under conditions similar to those encountered in the field.

REFERENCES

[1] Multistress Aging of Polymeric Insulators in various Environmental Conditions, www.east.asu.edu/ctas/multistress/Papers/ nsf-2-5.pdf.

[2] Tanmoy Rath , Yongjin Li "Nanocomposites based on polystyrene-b-poly(ethylene-r-butylene)-b-polystyrene and exfoliated graphite nanoplates: Effect of nanoplatelet loading on morphology and mechanical properties" Composites Part A: Applied Science and Manufacturing, Volume 42, Issue 12, December 2011, Pages 1995-2002.

[3] Tomas Gustavsson, "Silicon Rubber Insulators. Impacts of Material formulation in Costal Environment", Ph. D. Thesis (Chalmers University of Technology, Gutenberg, Sweden,2002

[4] Nopporn Chaipanit, Chaiwat Rattana Khongive and Raji Sundararajan, Accelerated multistress aging of polymeric insulators under San Francisco coastal environment (IEEE 2000 annual report conference on Electrical insulation and Dielectric Phenomena (2000)).

[5]

Israrullah, M. Amin, A. Mahmood, A. Khattak, "Accelerated Multi Stress Aging and Life Estimation of Polymeric Insulators" 2020 17th international Conferences.

[6] I. Joneidi, A.Majzoobi, A. Shayegani-akmal "aging evaluation of silicone rubber insulators using leakage current and flashover voltage analysis", IEEE Transaction on Dielectrics and Electrical Insulation, 2013.

VII

POWER ELECTRONICS AND APPLICATIONS (PEA)

Sommaire

VII.1 Effect of bandwidth of spiral micro coil on electrical parameters **337**
VII.2 Intelligent and robust control for direct gridconnected pv system powered arc welding machine **343**
VII.3 Flyback DC-DC micro-converter with integrated octagonal monolithic planar micro-transformer **349**
VII.4 Integrated square on-chip inductor for photovoltaic converter applications . . . **355**
VII.5 Modeling of octagonal planar microtransformer for DC-DC converter applications **361**

Effect Of Bandwidth of Spiral Micro Coil On Electrical Parameters

Benazzouz Younes, Djilalia Guendouz

Department of instrumentation maintenance, M.B Oran 2 University, Algeria

benazzouzyounes14@gmail.com

lila.guen@yahoo.fr

***Abstract*— In this work, the focus is on the design and characterization of the planar micro coil. Its purpose is to store electrical energy, making it commonly utilized in micro converters. In most studies of micro converters, the electrical performances of the integrated micro coil are limited. This is due to its electrical resistance, a consequence of inadequate dimensioning of its geometric parameters.**

To reduce the effect of electrical resistance, the operation will occur on the bandwidth of the planar spiral micro coil. Two types of planar inductors have been considered: inductance with constant turn width, and inductance with variable turn width. Several geometric and electrical parameters are taken into account to optimize their performance. A comparative study was conducted to show the influence of geometric parameters on electrical behavior.

***Keywords:* Integrated passive components, Spiral micro coil, Geometric parameter, Inductance coil, Resistance coil.**

INTRODUCTION

The integration of passive components allowed the miniaturization of electronic circuits and the evolution of power electronics which greatly expanded. This miniaturization has pushed towards developing distributed architectures, and embedded systems on System on-chip, containing several components.

The integration of the active and passive power components as well as the miniaturization of these structures, allow a maximum reduction of the space requirement while guaranteeing an acceptable level of efficiency. This optimization is particularly relevant in the context of wireless power transfer (WPT) systems for miniaturized implantable sensors [1].

Two criteria will guide the sizing of the integrated coils constituting devices and integrated circuit technologies. The first is the geometric form or topology of the structure, and the second is related to the nature of the materials used to manufacture different parts of the component [2]. These two criteria will affect the value of inductance, stored energy, and losses in the core and the conductor [3] [4] [5].

The efficiency of a coil is very linked to its geometric parameters, which depend on its topology and the materials used. In this paper, an efficient and precise method of calculating the inductance and resistance of a coil is presented; making it possible to improve the quality factor. It will be possible either by: increasing the value of the inductance or decreasing the value of the resistance. The goal is to increase the cross-section of the conductive wire as its length is increased. A comparative study between a conventional coil and a variable-width coil will validate the outcome.

I. *INDUCTANCE WITH CONSTANT TURN WIDTH*

1.1 Inductance expression

The electrical characteristics of a spiral planar topology are based on the geometric data that characterize it [6], [7], several expressions giving the inductance values for different spiral shapes have been proposed by different authors. The Mohan expression [8] has been used, which is accurate and applies to a variety of topologies. The generic expression for Mohan's inductance is:

$$L = \frac{\mu_0 n^2 d_{avg}\, C1}{2}(ln\,(C2/\rho) + C3\rho + C4\rho^2) \quad (1)$$

Where the average diameter d_{avg} and the form factor are generally defined as follows:

$$d_{avg} = \frac{d_{out}+d_{in}}{2} \quad (2)$$

$$\rho = \frac{d_{out}-d_{in}}{d_{out}+d_{in}} \quad (3)$$

Where d_{in} is the inner diameter, d_{out} is the outer diameter μ0 is the vacuum permeability and n is the turn number.

The coefficients C1, C2, C3, and C4 for different forms are given in Table 1:

TABLE I. COEFFICIENTS FOR THE ANALYTICAL CALCULATION OF INDUCTANCE [8]

Form	C1	C2	C3	C4
Square	1,27	2,07	0,18	0,13
Hexagonal	1,09	2,23	0	0,17
Octagonal	1,07	2,29	0	0,19
Circular	1	2,46	0	0,2

1.2 Choice of the topology

To choose the topology best suited to the objectives, several criteria were considered:

- The angles present in the square, hexagonal and octagonal topologies do not favor a homogeneous distribution of the current in the conductor at the angles. The lines of current accumulating inside the angle would increase the current density inside compared to the outside, which could increase the resistance (*R*) of the turns.
- For a given size and identical geometry, the circular structure makes a better L/R ratio achievable, compared to the alternative structures. The length of a coil, proportional to its resistance, is, for example, greater for a square geometry (4n d_{avg}) than for a circular shape (nπ d_{avg}), which will increase the resistance of the turn and decrease the *L/R* ratio. The length of the coil can also be calculated from the length of the Archimedean spiral of the polar equation (ρ = a θ).

-

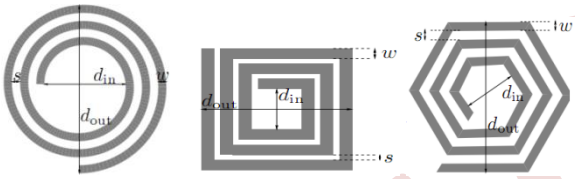


Figure 1. Different shapes of constant width turn.

To check that the circular shape is actually the one for which the *L/R* ratio is maximum at equivalent dimensions (outside diameter *dout* = 600 µm, turn width w =14µm, turn height t =180 µm, space between turns s =3µm), The inductance of a circular and square shape was calculated from expression (1) and referring to Table 1, as well as their resistance:

TABLE II. RATIO L/R AS A FUNCTION OF THE SPIRAL SHAPE

	Inductance nH	**Resistance mΩ**	**L / R H/Ω**
Square turn	79,3	142,47	5,57. 10-7
Circular turn	62.5	110,97	5,63.10-7

Although the inductance of a circular turn is lower than that of a square turn, its perimeter is also smaller for the circular topology. In the end, the *L/R* ratio of a circular topology is significantly larger than for a square's topology.

1.3 The filling rates

In the most recent work, the coil's outer diameter is determined based on the magnetic circuit's dimensions. With a fixed outer diameter, inner turns have weaker surface, leading to reduced inductance and resistance towards the center, altering the L/R ratio significantly.

Therefore, the dimensions of the coil should be chosen to maximize inductance and minimize total resistance [9], which is achieved at an optimal filling rate. For a circular configuration of turns, the influence of the number of turns on the *L/R* ratio was studied. For this, the following parameters were chosen:

Outer diameter: d_{out} = 600 µm

Turn width w =14µm, space between turns s = 3 µm

Copper height =180 µm.

These parameters are used to calculate the inner diameter as a function of the filling rate by the following expression:

$$d_{in} = d_{out} - 2nw - 2(n-1)s \qquad (4)$$

Equation (1) makes it possible to deduce the inductance *L* and the value of the corresponding resistance is given by the classic formula:

$$R = \frac{\rho_{cu} l_T}{s} = \frac{\rho_{cu} n\, \pi\, d_{avg}}{wt} \qquad (5)$$

The conductor resistivity (copper) chosen being equal to:

$$\rho_{cu} = 1.7\ 10^{-8} \Omega m$$

S: conductor section ($S = w.t$)

l_T: total length of the copper wire used to make the micro coil.

n: the number of turns in the coil.

The result of the calculation makes it possible to obtain the evolution of the *L/R* ratio as a function of the interior filling rate of the turn (*L/R* = f(n)) given in Figure 2:

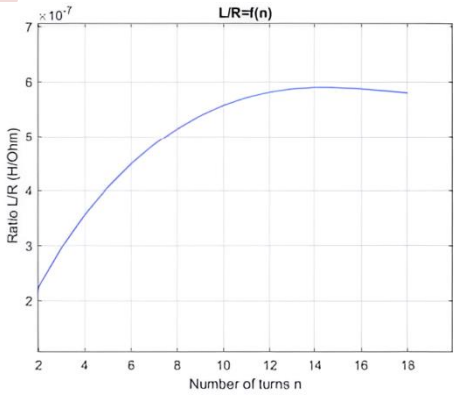


Figure 2. Variation of the ratio *L/R* according to the turn number.

For example, it is noted that for turns 2 to 15 the *L/R* ratio increases with the number of the turns, then beyond n equal 15, the *L/R* ratio begins to decrease, the spiral is full to the center for 18 turns, the three internal turns therefore, provide more resistance than inductance, therefore there is no need to fill the spiral to the center.

This type of dimensioning; used in several papers [10], [11], therefore considers constant turn width dimensioned considering the skin thickness at the frequency considered. Once the inductance value has been deduced from

the specifications, the turn's number can be deduced from expression (1), and the resistance of the coil follows directly from this dimensioning. It will be even greater for an increase in the winding length, as a function of the number of turns.

II. *VARIABLE COIL WIDTH INDUCTOR*

2.1. Benefits

Sometimes, the values of the inductance and the resistance of the coil deduced from the analytical expressions do not coincide with the experimental results and therefore, depart from the objectives set initially.

The idea is to start from a given minimum resistance per turn, then determine the total number of turns by considering a limit not to be exceeded.

The width of the conductor's windings (w) should be gradually increased as a function of the radius of the turn considered to compensate for the increase in resistance due to the increase in its perimeter as the turn moves away from the center.

The resistance per turn will be constant and the total resistance of the coil will be reduced for a given number of turns. This method offers the benefit of maximizing the utilization of the conductor's volume over the entire winding. In the absence of a magnetic circuit, the concentration of the magnetic field in the coil center generates a worse distribution of the current within the central turns than for the peripheral turns, especially for a high frequency.

For a variable width coil, however, a narrower width is used for the central turns than for those at the periphery, resulting in a more homogeneous current distribution as the turns move away from the center.

2.2. Calculation of the progression of the turn width

The first step is to determine the progression of the turn's width to ensure constant resistance per turn. Given the small dimensions considered of the planar spiral micro coil, its configuration can be assimilated by concentric circles; where R_0 is the inside radius of the turn:

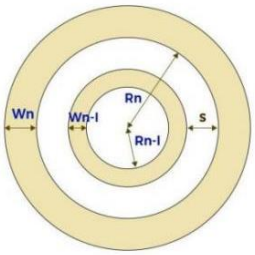


Figure 3. Variable width turns on the radius.

From the geometry of Figure 3 the radius of each turn is deducted:

$$R(1) = R_0$$
$$R(2) = R(1) + w(1) + s$$
$$R(3) = R(2) + w(2) + s$$
$$R(3) = R(1) + w(1) + w(2) + 2s$$
$$R(n) = R(n-1) + w(n-1) + s$$
$$R(n) = \sum_{i=1}^{n-1} (w(i) + s) + R_0 \qquad (6)$$

From equation 5, the resistance per turn is:

$$R_{I\,spire} = \frac{\rho_{cu} 2\pi R(1)}{w(1)t} = \frac{\rho_{cu} 2\pi R(2)}{w(2)t} = \frac{\rho_{cu} 2\pi R(n)}{w(n)t} \qquad (7)$$

The turn width relation is deducted:

$$w(n) = \frac{w(n-1)R(n)}{R(n-1)} \qquad (8)$$

Either by replacing the radius of the turn with its expression (6):

$$w(n) = \frac{w(n-1)[R(n-1)+w(n-1)+s]}{R(n-1)} \qquad (9)$$

So, for calculation of the turn progression, the following algorithm can be used:

Calculation of the progression of the radius per turn:

$$\mathrm{R}(n) = \begin{cases} \mathrm{R}_0 = \frac{d_{\mathrm{in}}}{2} \text{ if n=1} \\ \sum_{i=1}^{n-1} (w(\mathrm{i}) + \mathrm{s}) + \mathrm{R}_0 \text{ otherwise} \end{cases} \qquad (10)$$

- Calculation of the progression of the turn width:

$$w(n) = \begin{cases} w_0 \text{ if n=1} \\ \frac{w(n-1)[\mathrm{R}(n-1)+w(n-1)+s]}{\mathrm{R}(n-1)} \\ \text{or } w(n-1)\frac{\mathrm{R}(n)}{\mathrm{R}(n-1)} \end{cases} \text{ otherwise} \qquad (11)$$

The variation of the radius *R(n)* as a function of the turn number is given in Figure 4:

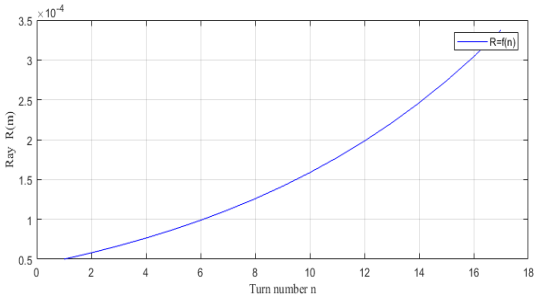


Figure 4. The coil radius as function of the coil turn number.

The radius of the turn gradually increases from its initial value R_0

$$R(1) = R_0 = d_{in}/2 = 50\ \mu m$$

a change of $R(n)$ that depends on the number of the turn, until it reaches its ultimate limit value.

$$R(n) = \frac{d_{out}}{2} - w(n)$$

At the same time, we can represent *w(n) = f(n):* in the progression in Figure 5

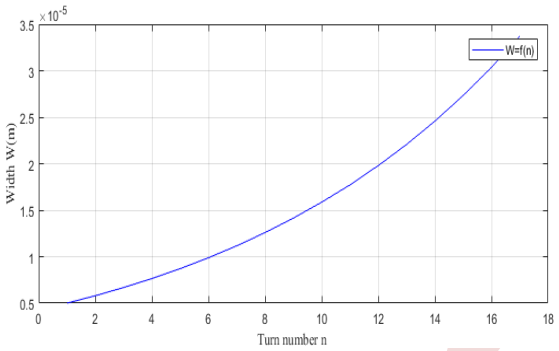


Figure 5. Width as a function of the coil turn number.

Also, the turn width increases from its initial value *w(1) = w_0 = 5µm*, as a function of the number of the turn and reaches a value that satisfies equation 11. Note that for calculation, only the dimension of the diameter d_{in} is necessary; d_{out} depends on the turns number *n* chosen.

A comparative study of the dimensioning of the two cases of coil width (constant and variable) is carried out using the same parameters: d_{in} and d_{out}.

According to curve 5, the number of turns that can be deposited without exceeding the limit value (from the outer border, d_{out}) will be for n = 15. At this position, the radius will have reached a value of R(15) = 271.0834 µm, and the width will be w(15) = 27.10834 µm.

$$d_{out}/2 = R(15) + w(15) = 298{,}1917\ \mu m$$

This corresponds to the point where a certain margin is added to avoid copper directly at coil border. This ensure that dout / 2 = 300 µm, aligning well with the requirements imposed on the dimensioning of the coil with a constant width.

III. *COMPARISON OF CONVENTIONAL AND VARIABLE WIDTH DIMENSIONING*

A variable width coil has the advantage of better control of the total resistance for a given surface, but the fact that the width of turns increases as one moves away from the center does not allow drawing as many turns in the same surface as in a conventional design, so the inductance will be lower. Since the resistance is low, it makes sense to study the impact of this design on the *L/R* ratio compared to a conventional design.

3.1. Inductance calculation

Expression (1) calculates the value of the inductance for a given number of turns (n) and a given shape (C1, C2, C3, C4), the parameter d_{avg} being defined by expression (2). On the other hand, expression (3) of the parameter ρ is no longer valid since the width of the turns varies. Otherwise, as noticed in some reference articles using variable width study [12], the value of the inductance would be the same in both cases of constant and variable width, which is not the case.

For that, the general expression of the form factor ρ is used by replacing d_{out} (or d_{in}) by expression (4) to make the important parameter intervene: the width of the coil, which gives:

- For a conventional dimensioning:

$$\rho = \frac{nw+(n-1)s}{d_{avg}} \qquad (12)$$

- Variable width dimensioning

$$\rho = \frac{\sum_{i=1}^{n} w(i)+(n-1)s}{d_{avg}} \qquad (13)$$

3. 2. Calculation of the total resistance of the coil

- For a conventional dimensioning:

$$R_T = \frac{\rho_{cu} n\pi d_{avg}}{wt} \qquad (14)$$

- Variable width dimensioning

$$R_T = \frac{\rho_{cu} 2\pi}{t}\left[\sum_{i=1}^{n} \frac{R(i)}{w(i)}\right] \qquad (15)$$

Or, since the resistance per turn is the same:

$$R_T = n\frac{\rho_{cu} 2\pi}{t}\frac{R(i)}{w(i)} \qquad (16)$$

The alternating resistance for high frequencies will be calculated at frequencies above 1MHz to study the behavior of this type of dimensioning considering the skin effect (δ) and proximity effect:

- For a conventional dimensioning

$$R_T = \frac{\rho_{cu} l_T}{w\delta(1-e^{-t/\delta})} \qquad (17)$$

- Variable width dimensioning

$$R_T = \frac{n\rho_{cu}2\pi R(i)}{w(i)\delta(1-e^{-t/\delta})} \quad (18)$$

With, the skin thickness expression:

$$\delta = \sqrt{\frac{\rho_{cu}}{\pi \cdot \mu \cdot f}} \quad (19)$$

3.3. Analytic results

Table 3 presents the values of the electrical characteristics of 3 types of coil configuration illustrated in Figure 6 and:



Figure 6. Coils with different geometric parameters.

The current distribution at 100MHz in the turns of presented dimensions differs in the center of the coil. It is relatively uniform for designs 2 and 3 as one moves away from the center of the coil.

Thus, the skin effect and the proximity effect are also reduced by reducing the volume of the conductor as it gets closer to the center of the coil, where the concentration of the magnetic field lines is high.

What is the most predominant geometric parameter?

For design 1: d_{out} = 600 µm, d_{in}= 100µm , n = 15, w = 14µm, t = 180 µm , s= 3 µm.

For design 2: d_{out} = 600 µm, d_{in} = 100µm , n = 31, w=5µm, t = 180 µm , s= 3 µm.

For design 3 : d_{out} = 600 µm , d_{in}= 100µm , n =15 , $w(1)$= 5 µm , t= 180 µm , s= 3 µm.

After calculation, the electrical parameters of each design are found using the equations of the electrical parameters and the values of the geometric parameters:

TABLE III. ELECTRICAL PARAMETERS OF EACH DESIGN

	Design 1	**Design 2**	**variable Design**
Inductance *L* (nH)	66,24	282,92	46,337
Resistance DC *R* (mΩ)	110,97	643,53	88,96
Resistance (100MHz) (mΩ)	3040,33	17630,84	2372,44
***L/R* DC (H/Ω)**	563,22 .10-9	441 .10-9	516,75 .10-9
***L/R*(100MHz) (H/Ω)**	20,56 .10-9	16,1 .10-9	19.38.10-9

According to Table 3, for the same geometric parameters: d_{in}, d_{out}, t, and s, it is noted that the inductance of design 2 is greater compared to the other models (4 to 6 times more), which is due to a high number of turns, but the resistance in this design, in DC or alternative, is very high (6 to 7.5 times more), the latter led to a significant reduction in the *L / R* ratio.

On the other hand, it is noted that the *L / R* ratio of Design 1 is the greatest, this is due to the fact, on one hand, that the width of the turns has been dimensioned to be equal to twice the skin thickness, which allows not to be bothered by it while allowing to obtain a larger conductor section. There is only the proximity effect which generates a non-homogeneous current density on the internal turns. In addition to the advantage of low resistance due to its wide turns.

In the air, for designs without magnetic circuit, design 1 (with wide turns) is then the best topology to adopt.

The variable width design also gives a higher *L/ R* ratio than design 2 and is close to design 1, and the fact that the resistance in the latter is low compared to the designs (1,2).

IV. *EXPERIMENTAL RESULTS*

Micro coils were manufactured at Laplace laboratory. The realization consists of a deposit of copper conductor on a substrate. The planar coil windings are protected by an insulator (SiO2) before being deposited on a substrate such as Kapton or PCB (Figure 7). Their characterization was made using the test bench 'LRC meter 4194'.

Figure 7 shows the micro coils realized. The dimensions of different shapes are as follows:

- For conventional micro coil: *dout* =10mm, *din* = 1mm, *n* = 3, *w* = 0,9, mm t = 35µm, s= 0,9mm
- For variable bandwidth micro coil: d_{out} =10mm, d_{in} =1mm, n = 3, w(1) = 0,3, mm t = 35µm, s=0,9mm.

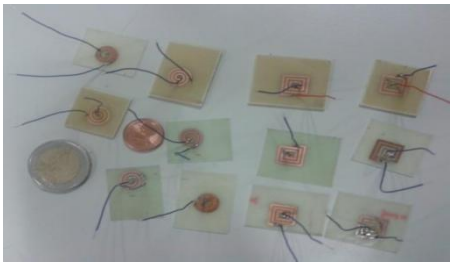


Figure 6. Different topologies of micro coils produced.

Table 4 shows the measurement results and analytic calculation for the standard circular inductor and variable width micro inductor of Figure 8.



Figure 7. Circular micro coils measured.

TABLE IV. MEASUREMENT RESULTS AND ANALYTIC CALCULATION

	Electrical parameters	**Constant bandwidth**	**Variable bandwidth**
Simulation	*L* (nH)	38.404	34.95
	R (mΩ)	27.975	15.467
Measure	*L* (nH)	23. 58	21.38
	R (mΩ	32.7	19.56

The spiral planar conductors were realized on Kapton. First, an attempt was made to compensate for the bonding resistance in order to obtain an accurate value of the series resistance of the spiral planar coil. For this reason, the measurement results gave slightly higher values for the resistances. The presence of a substrate such as Kapton could also have increased the gap between the measurement and analytical values.

As clarified previously, the inductances of a constant bandwidth coil are greater than a variable bandwidth coil because there is more copper from the center to the end of the coil, but the resistance of the variable bandwidth is weaker than conventional coil, which allows obtaining a better ratio L/R.

V. *CONCLUSION*

It can be concluded that the dimensioning by considering a variable turn width allows us to obtain a good *L/R* ratio in the air (even if it is not the best among the proposed dimensions) while reducing as much as possible the total resistance. It considered an essential criterion when it comes to converting energy.

In the air, wide turns (design 1) offer low resistance and a better *L/R* ratio compared to design 2 despite the low value of the inductance which can be improved by the presence of a magnetic circuit.

A study is underway to determine the influence of the presence of a magnetic core (closed or around the coil), which allows the obtention of a better *L/R* ratio.

The interest of the magnetic circuit is also weighted by its characteristics and in particular by iron losses that it can generate, which are linked to the method of production.

The presence of a magnetic circuit could change the balance sheet concerning these dimensions and allow conclusions on the topology of the spirals to be adopted, with or without a magnetic circuit toward the desired characteristics.

Compared to the characteristics sought for an inductance, it is preferable to favor the DC resistance to the HF components.

The study of the coil with a magnetic circuit will designate the spiral topology which has the best *L/R* ratio and low resistance for a similar inductance value, for use in the transformer.

ACKNOWLEDGEMENTS

I would like to warmly thank the staff of the Laplace laboratory of Paul Sabatier University, (Toulouse France) and especially Mr V. Bley for their help in making these prototypes and their permanent availability.

REFERENCES

[1] BISWAS, Dipon K., TASNEEM, Nishat T., et MAHBUB, Ifana. Optimization of miniaturized wireless power transfer system to maximize efficiency for implantable biomedical devices. In: 2019 IEEE Texas symposium on wireless and microwave circuits and systems (WMCS). IEEE, 2019. p. 1-6.

[2] BOUYGHF, Hamid, BENHALA, Bachir, et RAIHANI, Abdelhadi. Analysis of the impact of metal thickness and geometric parameters on the quality factor-Q in integrated spiral inductors by means of artificial bee colony technique. International Journal of Electrical and Computer Engineering (IJECE), 2019, vol. 9, no 4, p. 2918-2931.

[3] D. Zhang, et al., "Common Mode Circulating Current Control of Interleaved Three-Phase Two-Level Voltage-Source Converters with Discontinuous Space-Vector Modulation," 2009 IEEE Energy Conversion Congress and Exposition, Vols 1-6, pp. 3906-3912, 2009.

[4] Z. Yinhai, et al., "A Novel SVPWM Modulation Scheme," in Applied Power Electronics Conference and Exposition, 2009. APEC 2009. Twenty-Fourth Annual IEEE, 2009, pp. 128-131.

[5] [6] Wibben J. and Harjani R., A High-Efficiency DC-DC Converter Using nH Integrated Inductors, IEEE Journal of SolidState Circuit, Vol 43, (2008), 844-854

[6] ALDOUMANI, Maha, YUCE, Baris, et ZHU, Dibin. Using the Variable Geometry in a Planar Inductor for an Optimised Performance. Electronics, 2021, vol. 10, no 6, p. 721.

[7] NABAVI, Seyedfakhreddin et BHADRA, Sharmistha. Efficient and Easy to Fabricate Silicon-Based Planar Micro-Coils for Wireless Power Transfer Applications. IEEE Sensors Journal, 2021, vol. 22, no 3, p. 1980-1989.

[8] Mohan S., (1999) "The design, modeling, and optimization of on-chip inductor and transformer circuit", Doctoral dissertation, Stanford University (1999).

[9] JUN, Byoung Ok, KIM, Han-Joon, HEO, Su Jin, et al. Miniaturized Self-Resonant Micro Coil Array with A Floating Structure for Wireless Multi-Channel Transmission. Advanced Science, 2021, vol. 8, no 24, p. 2102944.

[10] E. Haddad C. Martin, C. Joubert, B. Allard, M. Soueidan, M. Lazar, C. Buttay, B. Payet-Gervy, Modeling, fabrication and characterization of planar inductors on YIG substrates, Advanced Materials Research. Trans Tech Publication, Vol. 324, pp:294-297, 2011.

[11] Daniel L, (1999) "Design of micro-fabricated inductors, Power Electronics", IEEE Transactions on Volume 14, Issue 4.

[12] Hayet Kharbouch, A. Hamid, T. Lebey, "Using the variable width in a planar inductor on Kapton for optimizing its performance", Turkish Journal of Electrical Engineering & Computer Sciences, Vol 25, pp: 3798- 3810, 2017.

Intelligent and Robust Control for Direct grid-connected PV System powered Arc Welding Machine

Salah Eddine Halledj[1, 2], Amar Bouafassa[1]

[1] *National Polytechnic School of Constantine,Ali Menedjeli,Constantine, 25000, Algeria*

[2] *Research Center in Industrial Technologies CRTI, P.O. Box 64, Cheraga 16014, Algiers, Algeria*

eddinesalah031@gmail.com

amar.bouafassa@gmail.com

***Abstract*— In this paper, a heuristic trained adaptive neuro fuzzy inference system (ANFIS) estimator is presented to extract the maximum voltage point from single stage grid connected photovoltaic system powering arc welding power supply. Intending to ameliorate maximum power delivered by solar cells, a hybrid controller is developed. The intelligent ANFIS is trained by particle swarm optimization (PSO) in order to produce the optimal connection weight coefficients for obtaining the reference voltage; this reference is needed to directly control the three-phase inverter without any intermediate boost converter. Moreover, to meet different power quality indices of the proposed grid, a robust based fractional-calculus order sliding mode controllers is proposed to regulate PV voltage, AC gridand arc welding power supply. The obtained simulation results demonstrate an enhancement in MPPT convergence and weld bead quality, meeting all the international IEEE standards.**

Keywords— Fuzzy neural network, Fractional calculus, sliding mode control, Grid, Particle swarm optimization, Photovoltaic system, Welding.

I. INTRODUCTION

Welding is a manufacturing method in which two or more metals are fused together using heat to produce a join metal [1]. It can achieved using different types such as solid state welding, gas welding and arc welding. Recently, arc welding process has received increasing attention and appeal because of its flexibility and high energy efficiency [2]. Controllingthe electrode wire is a major difficulty in arc welding development because of unrestrained heat which can induce arc voltage fluctuations. Thereby, the load current of AWPS should be controlled and limited during loading procedure.

In literature, various arc welding installations were used to interface with the main grid, starting with uncontrollable diode bridge rectifiers. This topology has been widely utilized in manufacturer but they suffered from high total harmonic distortion THD value and low power factor (PF) [3]. In order to address these issues, a various installations based AWPS have been presented such as power factor correctors and active power filters [4, 5]. These power electronic devices were used to ensure pure sinusoidal shape of input current, reduce THD and increase power factor to unity [6]. It has alsobeen deduced from current literature that there is a few researchers have investigated a three phase inverter basedAWPS. In [7] authors developed a new installation paradigm of AWPS with phase shunt filter, this schema has been regulated by two separated controllers; ACO-ANN and direct power control (DPC), the suggested system powered using double stage grid-connected PV system. Behind this idea, the aim of this article is to design and develop low cost renewablebased PV power distribution network (single stage) powering arc welding machine regulated by one hybrid robust and intelligent controller in order to improve various power grid indices.

Currently, grid-connected PV system becomes a hotspot topic of many research works. The main principles of the subject are: the reduction of THD [7], the control of reactive power [8] and the maximum power point extraction fromsolar cells [9]. In order to optimize energy efficiency of solar cells, various MPPT strategies have been implemented such as incremental conductance, perturb and observe, fuzzy logic technique, feedforward neural network, sliding mode control and so on. Compared with traditional approaches, FLC and ANN have accurate performance tracking under sudden change of irradiation and temperature. However, FLC needs expert knowledge based systems, which is difficult aspect in design, whereas ANN requires a long time for training and large memory storage [10].

Merging both FLC and ANN comprises interesting training capabilities. Here ANFIS [11] is one of the most favorable MPPT technique that merge the benefits of two artificial intelligence approaches into single approach. ANFIS works based on fuzzy system tuned by neural network [12]. The

learning process of ANFIS is a challenging aspect for the researchers. The recent metaheuristic algorithms like particle swarm optimization (PSO), genetic algorithm (GA) and ant colony optimization (ACO) are utilized to address optimization issues [13]. In comparison to other optimization strategies, PSO has an easier mathematical computation, faster convergence rate, does not need initial parameters and training rate. Based on these reasons, PSO is the best choice to train ANFIS for economical control design.

In control point of view, the main challenging in single stage grid integrated PV system is that the three phase invertermust be directly controlled without any intermediate circuit.In literature, a simple PI regulator is extensively utilized because it is simple and easy to implement but it alwayssuffers from internal disturbances and nonlinearity behavior.

The principle contributions of this paper are mentioned as follows:

1- Design and simulate a single stage grid integratedPV system feded arc welding machine rather than double stage one in order to reduce the cost
2- Develop PSO trained ANFIS MPPT algorithm, this structure has two inputs (temperature, irradiation) and one output (PV reference voltage).
3- Replace the PI controller in voltage control loop by fractional order SMC to improve the performance tracking of d axis rotating current.

The framework of this article is structured as follows: section II describes different parts of the total configuration of single stage grid integrated PV system feded arc welding machine, section III shows the control structure of PV system, utility grid and arc welding power supply respectively and in details. Section V presents the results for proposed application under different environment and arc welding process. Section VI concludes the work.

II. SYSTEM DESCRIPTION

The suggested single stage grid connected PV system powered arc welding machine is depicted in Fig. 1. It contains of a 250 KW *SUN POWER SPR 415E-WHT-D* photovoltaic system, two DC link voltage, a three phase DC-AC converter, a 25KV grid and arc welding power supply AWPS. The DC capacitors are needed to keep the PV voltage unchanged and RLC harmonic filter coupler is used to suppress the harmonics in the injected current. In control point of view, PSO-ANFIS is used to estimate V_{ref} from PV array, fractionalorder sliding mode control is applied to predict the desired reactive current I_{dref}. In order to control arc welding power supply, a cascaded sliding mode and PI controllers are proposed rather than PI+ hysteresis as in [5],[7]. Table I lists the numerical all the parameters of PV system.

TABLE I. PV ARRAY SPECIFICATION

Parameter	Value
Maximum power at standard temperature	414.8 w
Parallel strings	88
Series modules per string	7
Short current	6.09 A
Open voltage	85.3 V

III. CONTROL PARADIAGM

A. MPPT control based PSO trained ANFIS

ANFISis a type of artificial intelligence approach that combine ANN with FLC. In fact, ANFIS uses benefits of bothANN and FIS approaches in one hybrid system. It was proposed by Jang applies gradient and least square algorithms for learning procedure. Actually, the main drawbacks of classical ANFIS are: confined in local minimum or maximum point and slow convergence. In order to address these issues, a particle swarm optimization is applied for improving convergence speed as well as reaching the global minimum ormaximum points. By selecting the appropriate personal and global training rates, PSO will ensure convergence as well as stability. As results, the particles should move through the best solution for a given problem, whereas the global minima of the corresponding cost function can be found based on previous positions of the swarm. The velocity and position of each element are calculated according to (1) and (2):

$$V_n = wV + C_1(P_b - P) + C_2(g_b - P) \quad (1)$$

$$P_n = P + V_n \quad (2)$$

Where $P_b, g_b, C_1, C_2, V_n, V, P_n$ and p refer to the best particle's position, best solution have obtained, individual acceleration, social acceleration, new particle's velocity, actual velocity, new position and actual position respectively and inertia weight w will be updated in the following manner:

$$w = w_{damp} * w \quad (3)$$

Where: w_{damp} refers to damping ratio.

Generally, ANFIS structure has five layers, which are known as fuzzification block, rule based system block, normalization layer, defuzzification block, and summation layer respectively.

In this work, the parameters of ANFIS system are tuned via PSO. The main aim of PSO is to predict the optimized parameters.

These optimal coefficients are utilized by I/O membership functions to reach the best ANFIS structure. The proposed best ANFIS steps are described in details in Fig. 3.Consequently, the performance of PSO trained ANFISattained better than GA-ANFIS because of lower root mean square error and lesser error as shown in Fig. 2b. After executing PSO-ANFIS system error mean, error standard deviation and mean square error are computed and they have values of 0.2197, -0.00143 and 0.046 respectively for all trained information (Figs. 2a, 2c)

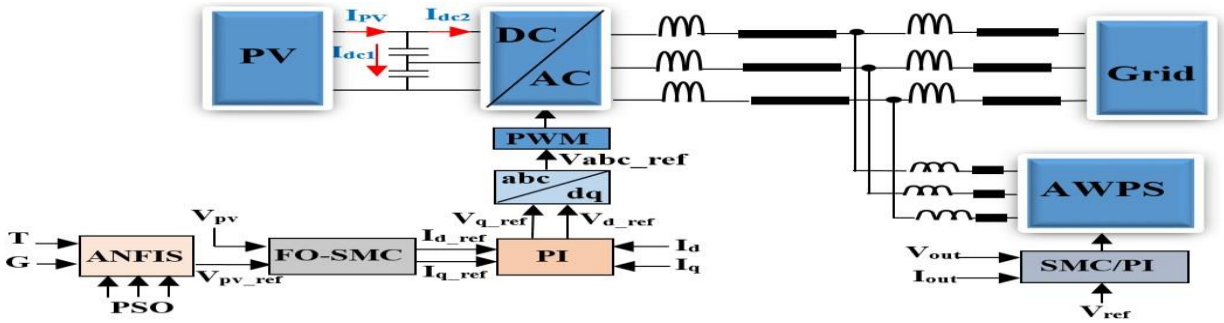


Figure 1: Single stage grid connected PV system powered AWPS

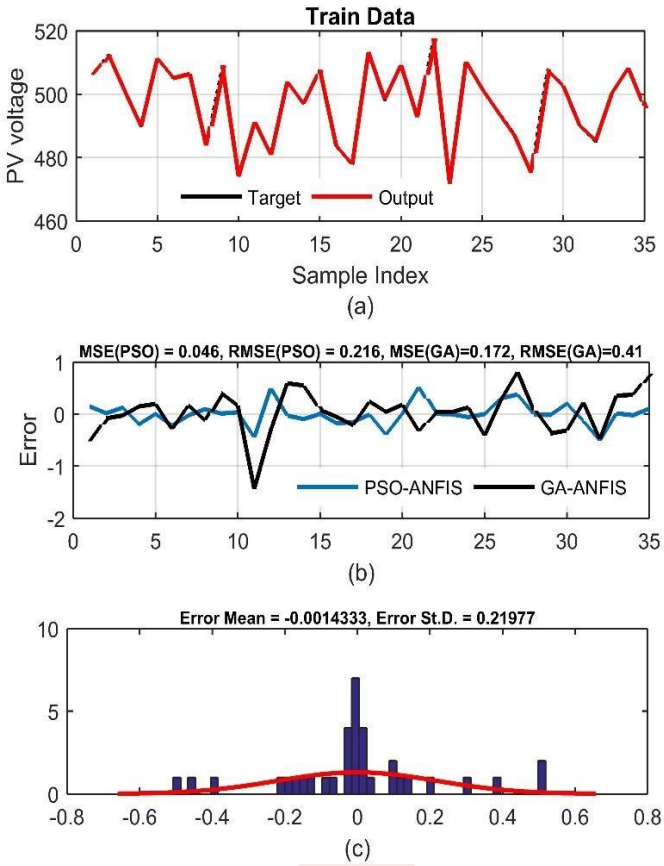


Figure 2: PSO trained ANFIS performance

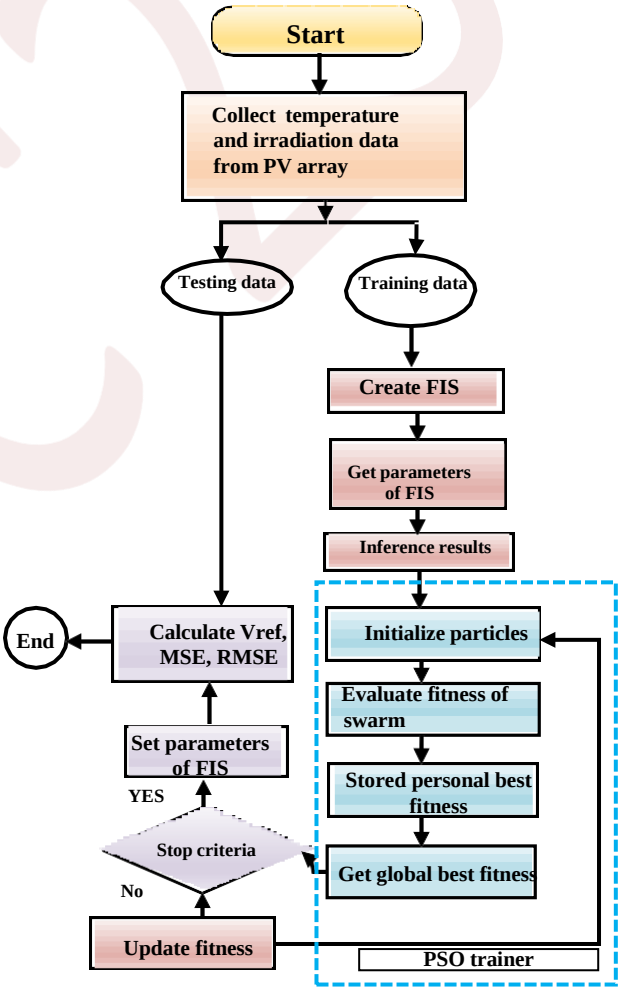


Figure 3: Flowchart of PSO trained ANFIS

B. Control of direct grid integrated PV system

The mathematical description of direct grid-PV system can be expressed as follows:

$$I_{dc1} = i_{pv} - I_{dc2} \tag{4}$$

$$C\frac{dV_{pv}}{dt} = i_{pv} - i_{dc2} \tag{5}$$

$$V_{abc} - e_{abc} = R_1 i_{abc} + L_1 \frac{di_{abc}}{dt} \tag{6}$$

In order to transform abc frame into dq frame, (6) becomes :

$$V_{qd} - e_{qd} = R_1 i_{qd} + L_1 \frac{di_{qd}}{dt} + L_1 \begin{bmatrix} -w\, i_q \\ w\, i_d \\ 0 \end{bmatrix} \tag{7}$$

Separating (7) will give qd state space equation as

$$L_1 \frac{di_d}{dt} = -R_1 i_d + w\, L_1 i_q - e_d + V_d \quad (8)$$

$$L_1 \frac{di_q}{dt} = -R_1 i_q - w\, L_1 i_d - e_q + V_q \quad (9)$$

Where: $V_{q,d}$ refers to control variable of inverter.

In this part, we will present in details the design procedure of inner-outer loop controllers of direct grid-PV system. The inner loop refers to fractional order sliding mode control and the outer loop represents PI control.

Using switching functions $S_{qd} = P\, S_{abc}$ of inverter, (5) becomes as:

$$C\, \frac{dV_{pv}}{dt} = I_{pv} - \frac{3}{2}(i_d S_d + i_q S_q) \quad (10)$$

i_{qref} should be zero and (10) can be expressed as

$$C\, \frac{dV_{pv}}{dt} = I_{pv} - \frac{3}{2} i_{dref} S_d \quad (11)$$

Intending to obtain I_{dref}, a fractional order sliding mode control is proposed. Now , let define error variable e and sliding surface s as:

$$e = V_{pv} - V_{pvref} \quad (12)$$

$$s = C_1 e + C_2 D^{u-1} \frac{de}{dt} \quad (13)$$

To reach convergence, $\frac{ds}{dt}$ should satisfy (14) as

$$\frac{ds}{dt} = -K_1 sign(s) - K_2 s = M(s) \quad (14)$$

Where: D^u is fractional order differentiator (Oustaloup filter),$C_{1,2} > 0$, $K_{1,2} > 0, 0 < u < 1$.

Differentiating (13) gives:

$$\frac{ds}{dt} = C_1 \frac{de}{dt} + C_2 D^{u-1} \frac{d^2 e}{dt^2} \quad (15)$$

After calculating$\frac{d^2 e}{dt^2}$, (15) can be expressed again as:

$$\frac{ds}{dt} = C_1 \frac{de}{dt} + C_2 D^{u-1} \left(\frac{3S_d}{2C} \frac{dI_{dref}}{dt} - \frac{di_{pv}}{Cdt}\right) \quad (16)$$

Using (14), we get:

$$C_1 \frac{de}{dt} + C_2 D^{u-1} \left(\frac{3S_d}{2C} \frac{dI_{dref}}{dt} - \frac{di_{pv}}{Cdt}\right) = M(s) \quad (17)$$

I_{ref} can be expressed as:

$$I_{dref} = \frac{2C}{3C_2 S_d} \int_0^t \left[\frac{C}{C_2} \frac{di_{pv}}{dt} + D^{1-u}(M(s) - C_1 \frac{de}{dt})\right] dt \quad (18)$$

To analyze the stability of grid connected PV system, we can try laypunov stability theorem as verification tool. Let define the candidate as:

$$V(s) = \frac{1}{2} s^2 \quad (19)$$

Making the derivative of V gives

$$\frac{dV}{dt} = s \frac{ds}{dt} = s\, M(s) = -K_1 |s| - K_2 s^2 < 0 \quad (20)$$

Based on (20), the system is asymptotically stable.

For qd current loop, a simple discrete PI controller is used for controlling both I_q, I_d and generating the appropriate V_{qd}.

A. Arc welding machine control

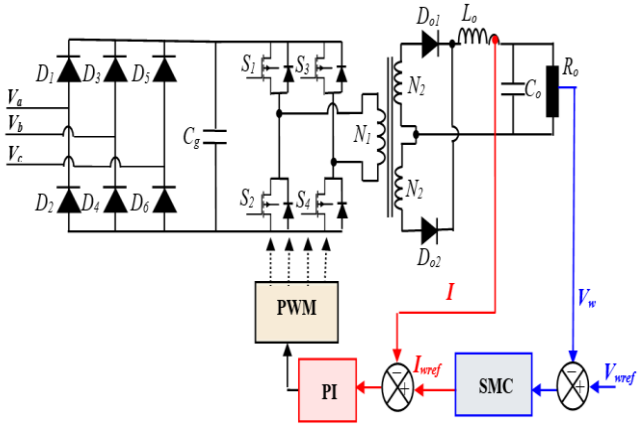


Figure 4: control paradigm of AWPS

Arc welding power supply is power electronic device known as phase shift full bridge center-tapped converter. It is used in order to step down the voltage from three phase rectifier to the desired arc voltage during the normal operation. Moreover, the arc current should also be regulated to ensure a good processing of AWPS as depicted in Fig. 4.

In order to obtain C_0 and L_0 values, (21) and (22) are required:

$$L_0 = \frac{V_0(0.5 - D)}{f_w \partial I_{L0}} \quad \forall\, D = \frac{V_0 N_1}{2V_{in} N_2} \quad (21)$$

$$C_0 = \frac{V_0(1 - 2D)}{32 f_w^2 L_0 \partial V_0} \quad (22)$$

Where: D refers to duty cycle of AWPS, $\frac{N_1}{N_2}$ is ratio of transformer, f_w represents the switching frequency ($f_w = 50\, KHZ$), $\partial I_{L0}(5\%)$, ∂V_0 are output ripple current and voltage respectively. The values of C_0, L_0 are set 4uF and 8uH.

The proposed control paradigm is based on two controllers:

(i) a sliding mode controller for regulating the arc welding voltage.

(ii) a PI controller for tuning and limiting arc current of AWPS.

Starting with SMC loop, the proposed sliding surface can be written as :

$$S_w = V_{wref} - V_w + K_3 \int_0^t (V_{wref} - V_w) dt \quad (23)$$

The control law of SMC (I_{ref}) is suggested as follows:

$$I_{ref} = V_{wref} - V_w + K_4 sign(S_w) \quad (24)$$

For the current loop, the output of PI controller for K^{th} sampling time can be expressed as:

$$O_{pi}(K) - O_{pi}(K-1) = K_5\big(e_I(k) - e_I(K-1)\big) + K_6 e_I(K) \quad (25)$$

Where: $e_I(k) = I_{ref}(k) - I(k)$

IV. Simulation Results

The proposed application has been tested via MATLAB/SIMULINK. The proposed MPPT controller is compared with well known perturb and observe MPPT method under various irradiation levels as shown in Fig. 5. Secondly, intending to verify the performance of fractional order sliding mode control, we present the grid system response. Finally, we present the responses of AWPS under SMC/PI controller and compare the results with traditional PI/hysteresis control.

A. Photovoltaic system performance

Figs. 6,7 and 8 present generated reference voltage from MPPT algorithm, output PV voltage and output PV power respectively.

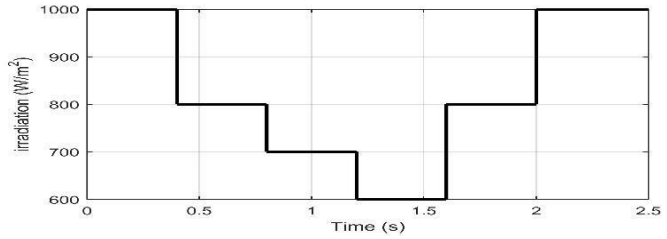


Figure 5: irradiation level

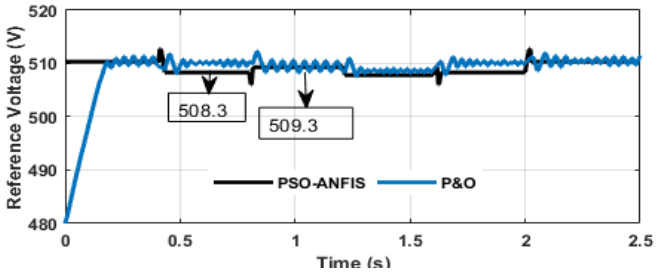


Figure 6: the generated reference voltage from MPPT method

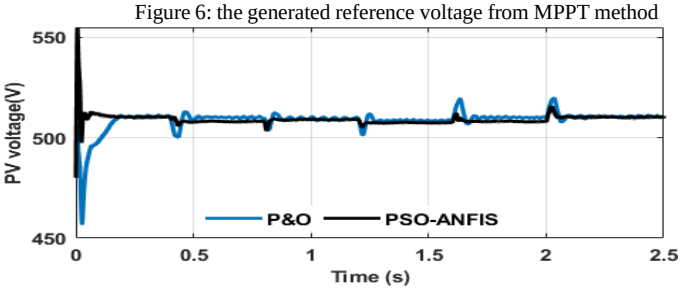


Figure 7: photovoltaic voltage

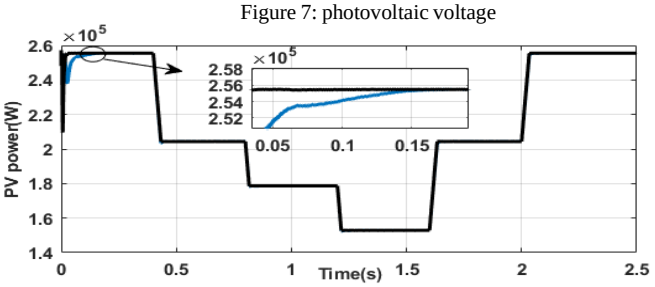


Figure 8: Photovoltaic power

Based on various irradiation variations, the suggested PSO trained ANFIS demonstrated a better control performance than P&O, where PSO-ANFIS finds the MPP points in 0.01 s whereas P&O takes 0.15 s as shown in Fig. 8. In addition, PSO-ANFIS shows a good response in term of accuracy and rippling compared to P&O as depicted in Figs. 6, 7.

B. Grid system performance

In order to verify the robustness of FOSMC-PI controller under different irradiance conditions. We need to show some different control signals and power quality indices of inverter and utility grid. As it can be observed from Fig. 9, q-axis current has been successfully forced to zero. The proposed controller FO-SMC has steady state error of 0.01 which is lesser than the value of PI controller (0.05). For d-axis current, the measured d-axis current has tracked the generatedI_{dref} from FO-SMC. The proposed robust controller reduced overshoot, undershoot, oscillation and enhanced the speed of convergence compared to simple PI control as depicted in Figs. 10, 11. As we can see from Fig. 12 the power of PV cell is perfectly transferred into utility grid without any loss and distortion. Moreover, the total harmonic distortion of gridcurrent has been perfectly reduced into 1.29% because of the single stage grid-PV topology and fractional order sliding mode control strategy as depicted in Fig. 13.

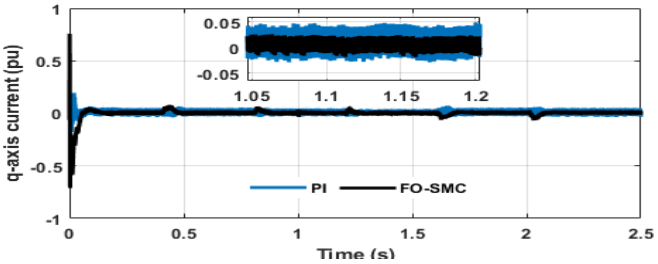


Figure 9: q-axis current

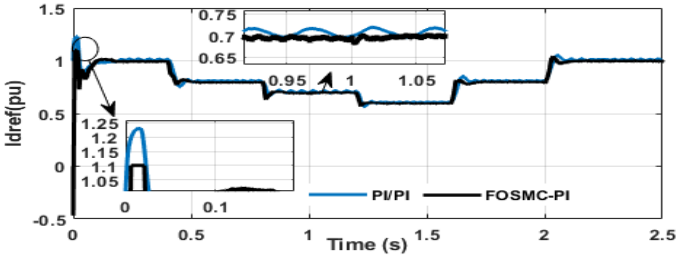


Figure 10: d-axis reference current

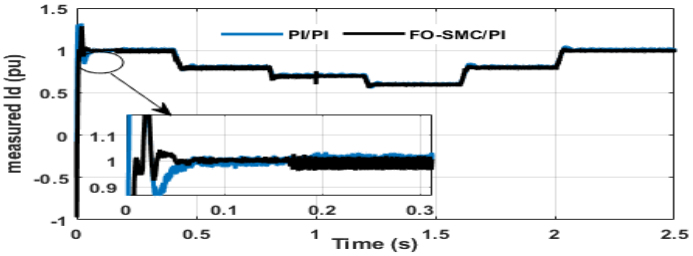


Figure 11: measured d-axis current

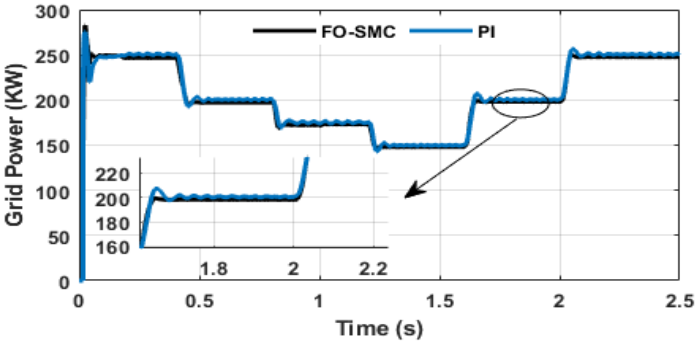


Figure 12: Grid power

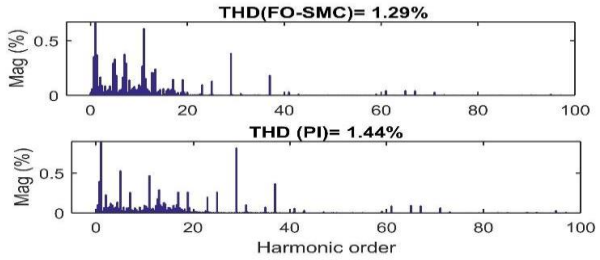


Figure 13: Total harmonic distortion of grid current

C. *Arc welding performance*

The system described in Fig. 4 is tested during a rated load via a cascaded sliding mode and PI controllers. A 20 V reference voltage is applied to ensure a high arc current that is required in welding process. The obtained simulation results are depicted in Figs. 14 and 15. he dynamic characteristic of AWPS has been improved, where the output voltage and current are controlled to follow the desired values. The settlingtime of the proposed control paradigm is 0.02 s whereas the PI+ hysteresis controller takes 0.5 s to reach the reference amount as depicted in Figs. 22, 23.

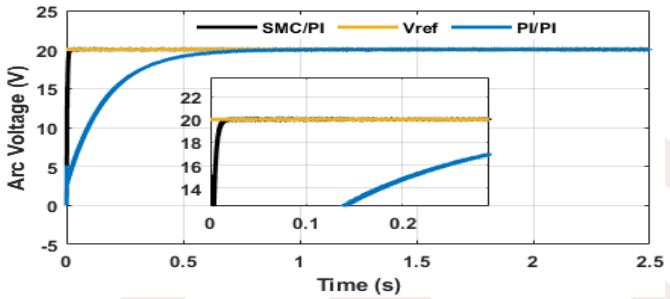


Figure 22: arc welding output voltage

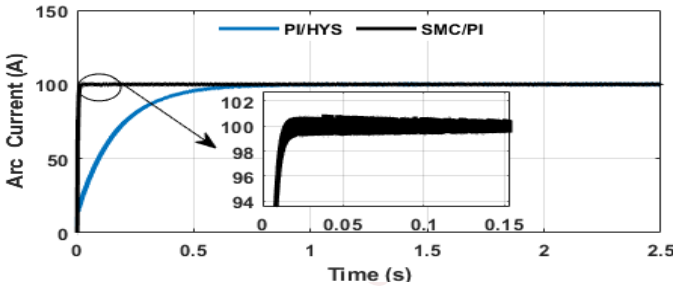


Figure 23: arc welding output current

V. CONCLUSION

In order to reduce the control complexity of double stage grid topology, we have proposed new controller based on intelligent and robust strategies of direct grid integrated PV system powered arc welding power supply. The MPPT algorithm has achieved using PSO trained ANFIS. This MPPT seeker follows maximum voltage point efficiently under various irradiation levels. Furthermore, the proposed FO- SMC/PI is used for regulating current/voltage of inverter-grid system, ensuring the robustness under parametric changes andproviding a satisfactory dynamic performance. The obtained simulation results show preferable dynamic performance compared to traditional control strategy in term of efficiency, response time and robustness. Moreover, all the power qualityindices of the proposed application meet international standards like IEEE 519 and EN 61000.

APPENDIX

A. FO-SMC control design: $u = 0.1, C_1 = 100, C_2 = 1,$ $K_1 = 110,\ K_2 = 180.$

B. Arc welding control design

- SMC: $K_3 = 33.3,\ K_4 = 100.$
- PI:$K_5 = 2.33,\ K_6 = 0.006.$

REFERENCES

[1] J. Li, F. Cao, and Y. Shen, "Effect of welding parameters on friction stir welded Ti–6Al–4V joints: temperature, microstructure and mechanical properties," *Metals*, vol. 10, no. 7, p. 940, 2020.

[2] A. V. Frolov, "The Experience of the Portal Machine Control System Modernizing for Automatic Arc Welding and Surfacing in a Shielded Gas," in *Current Problems and Ways of Industry Development: Equipment and Technologies*, Springer, 2021, pp. 622–631.

[3] S. Rymar, A. Zhernosekov, and V. Sidorets, "Effect of single-phase power sources of welding arc on electric mains," *Paton Weld. J.*, vol. 12, pp. 9–15, 2011.

[4] M. Hojabri, M. Hojabri, and A. Toudeshki, "Third-order passive filter improvement for renewable energy systems to meet IEEE 519-1992 standard limits," 2015, pp. 199–204.

[5] A. Bouafassa, L. M. Fernández-Ramírez, and B. Babes, "Power quality improvements of arc welding power supplies by modified bridgeless SEPIC PFC converter," *J. Power Electron.*, vol. 20, no. 6, pp. 1445– 1455, 2020.

[6] N. Hamouda, B. Babes, A. Boutaghane, S. Kahla, R. Amraoui, and M. Mezaach, "Improving the Power Quality of the Arc WeldingSupply using an Active Power Filter," presented at the 6th International Conference on Welding, Non Destructive Testing and Materials Industry (IC-WNDT-MI'18), 2018.

[7] B. Babes, A. Boutaghane, and N. Hamouda, "A novel nature-inspired maximum power point tracking (MPPT) controller based on ACO-ANNalgorithm for photovoltaic (PV) system fed arc welding machines," *Neural Comput. Appl.*, vol. 34, no. 1, pp. 299–317, 2022.

[8] L. Alhafadhi and J. Teh, "Advances in reduction of total harmonic distortion in solar photovoltaic systems: A literature review," *Int. J. Energy Res.*, vol. 44, no. 4, pp. 2455–2470, 2020.

[9] G. M. T. Nguyen and K. Uchida, "Active and reactive power control techniques based on feedback linearization and fuzzy logic for three-phase grid-connected photovoltaic inverters," *Asian J. Control*, vol. 17, no. 5, pp. 1522–1546, 2015.

[10] R. W. Kotla and S. R. Yarlagadda, "A Novel Enhanced Active Power Control Maximum Power Point Tracking Algorithm for Photovoltaic Grid Tied systems," *Adv. Electr. Comput. Eng.*, vol. 21, no. 3, pp. 81– 90, 2021.

[11] R. T. Moyo, P. Y. Tabakov, and S. Moyo, "Design and modeling of the ANFIS-based MPPT controller for a solar photovoltaic system," *J. Sol. Energy Eng.*, vol. 143, no. 4, 2021.

[12] H. Abu-Rub, A. Iqbal, S. M. Ahmed, F. Z. Peng, Y. Li, and G. Baoming, "Quasi-Z-source inverter-based photovoltaic generation system with maximum power tracking control using ANFIS," *IEEE Trans. Sustain. Energy*, vol. 4, no. 1, pp. 11–20, 2012.

[13] A. M. Eltamaly, "A novel particle swarm optimization optimal control parameter determination strategy for maximum power point trackers of partially shaded photovoltaic systems," *Eng. Optim.*, vol. 54, no. 4, pp. 634–650, 2022.

Flyback DC-DC Micro-Converter with Integrated Octagonal Monolithic Planar Micro-Transformer

Mokhtaria Derkaoui[1]*, Yamina Benhadda[2]

[1]*LARATIC laboratory, Higher National School of Telecommunications & ICT (ENSTTIC-Oran), Algeria*
[2]*LEPA laboratory, University of Sciences and Technology of Oran (USTO- MB), Algeria*
** mokhtaria.derkaoui@ensttic.dz*

***Abstract*—The work presented in this paper presents the design of an integrated flyback DC-DC micro-converter operating at high frequencies. The flyback converter consists of only one transformer. The integrated micro-transformer in the flyback micro-converter is composed of two planar stacked coils with spiral octagonal geometry. Basing on Mohan's method, the geometrical parameters are evaluated. The different parasitic effects created in the stacked layers are grouped perfectly in the equivalent electrical circuit. To validate the electrical model, the simulation of the flyback micro-converter containing the equivalent electrical circuit of the micro-transformer is established, using Psim 9.0 software.**

Keywords*:*Flyback Micro-Converter; Integration; Micro-Transformer; Monolithic; Planar

I. INTRODUCTION

The objective of the integration of passive components is to make the converter fully integrated and stand-alone. The majority of surface is occupied by discrete passive components. To overcome this problem, the integrated components were introduced [1-2]. Planar micro-transformers are currently extensively used in integrated circuits in many systems for several RF applications [3-4]. The integration allows to compact the small size components with better efficiency and low fabrication costs [5-6]. The easier technique for reducing sizes is to increase the operating frequency. Increasing the frequency has an impact for inductive components as the inductance, the size and the current. At high frequencies, inductive components can have a smaller size and hence smaller inductance [7-8]. The aim of our work is the design of a DC-DC micro-converter containing an octagonal planar spiral micro-transformer. The micro-converter is operating for low powers and high frequencies. The dimensioning of different geometric and electric parameters is required to integrate the micro-transformer in the micro-converter [9-10]. The simulations of the global integrated structure of DC-DC flyback micro-converter validate the studies.

II. FLYBACK MICRO-CONVERTER PRESENTATION

The converter is the main step of the design and dimensioning of passive components. We have opted for a flyback DC-DC converter (Fig.1) for it contains just one transformer. The Flyback operation is based on the energy transfer from primary to secondary through a transformer [3].

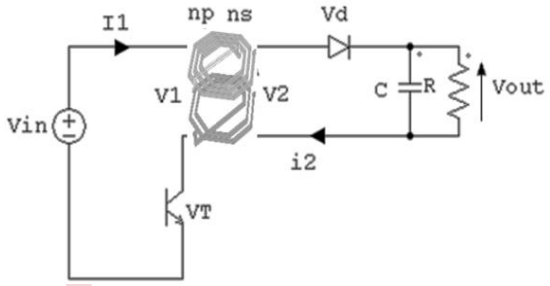


Fig.1. Electrical circuit of DC-DC flyback converter with planar monolithic micro-transformer

Our target is to integrate completely the converter and to reduce its sizes. From the main parameters of the DC-DC flyback micro-converter (Input voltage V_{in}=12V, Output voltage V_{out} =5V, Duty cycle α=0.5, Output power P_{out}=5W, Operating frequency f =1GHz), we calculate the primary and secondary inductances (L_p, L_s) of the micro-transformer and their turn ratio m (1-3) [2].

$$L_p = \frac{V_{in}^2.\alpha^2}{2.f.P_{out}} \quad (1)$$

$$m = \frac{\alpha}{1-\alpha}.\frac{V_{out}}{V_{in}} \quad (2)$$

$$L_s = m^2.L_p \quad (3)$$

In this work, the integrated micro-transformer is composed of two octagonal spiral stacked planar coils (Fig.2.a). The octagonal micro-transformer is defined by geometrical parameters. The outer diameter is equal to 500 µm, the angles are equivalent to multiples of 45 degrees. The coils are in copper stacked on dielectric layer of silicon nitride Si_3N_4, magnetic layer of ferrite NiFe and substrate layer of silicon Si. When the micro-transformer operates at 1 GHz of frequency, the coupling capacitances are created in parallel with inductances and in different layers. The

equivalent electrical circuit of the micro-transformer displays the different parasitic effects created in the different layers at high frequencies (Fig.2.b).

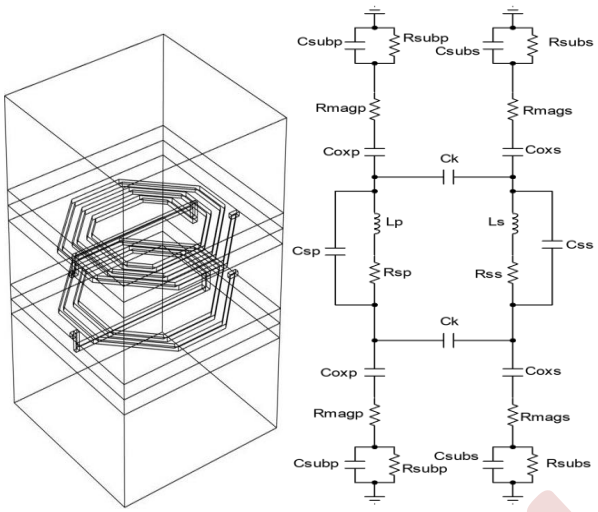


Fig.2. (a) Integrated octagonal spiral planar micro-transformer model, (b) Equivalent electrical circuit [4][10]

We find in literature several expressions that allow us to calculate the turn's number of micro-coils according to the inductance, we opted for Mohan's method [9] (4-5).

$$n_p = \sqrt{\frac{2 \cdot L_p}{\mu_0 \cdot d_{avg} \cdot C_1 \cdot \left\{\ln\left(\frac{C_2}{\rho}\right) + C_3 \cdot \rho + C_4 \cdot \rho^2\right\}}} \quad (4)$$

$$n_s = \sqrt{\frac{2 \cdot L_s}{\mu_0 \cdot d_{avg} \cdot C_1 \cdot \left\{\ln\left(\frac{C_2}{\rho}\right) + C_3 \cdot \rho + C_4 \cdot \rho^2\right\}}} \quad (5)$$

$$d_{avg} = \frac{d_{out} + d_{in}}{2} \quad (6)$$

$$\rho = \frac{d_{out} - d_{in}}{d_{out} + d_{in}} \quad (7)$$

The coefficients C_1, C_2, C_3 and C_4 are defined for our octagonal geometry as C_1= 1.07, C_2= 2.29, C_3= 0, C_4= 0.19. d_{avg} is the average diameter and ρ is the form factor.

Primary and secondary total length lt_p, lt_s, spacing s_p, s_s and width w_p, w_s are related to the inner and the outer diameter (8-11);

$$l_{tp} = n_p \cdot d_{avg} \cdot N \cdot \tan\frac{\pi}{N} \quad (8)$$

$$l_{ts} = n_s \cdot d_{avg} \cdot N \cdot \tan\frac{\pi}{N} \quad (9)$$

N is the number of sides which is 8 in our case.

$$2 \cdot n_p \cdot w_p + 2 \cdot (n_p - 1) \cdot s_p = d_{out} - d_{in} \quad (10)$$

$$2 \cdot n_s \cdot w_s + 2 \cdot (n_s - 1) \cdot s_s = d_{out} - d_{in} \quad (11)$$

The magnetic core volume (12) is related to the total magnetic stored energy W_t (13) and the maximum energy volume density W_{vmax} (14). Therefore, 0.050 mm^3 of ferrite NiFe is necessary to store 1.2 nJ of energy.

$$V = \frac{W}{W_{vmax}} = 5.025\ 10^{-11} m^3 \quad (12)$$

$$W_t = \frac{1}{2} \cdot L_s \cdot i_{out}^2 = 1.2\ 10^{-9} J \quad (13)$$

$$W_{vmax} = \frac{B_{max}^2}{2 \cdot \mu_{NiFe}} = 23.88\ J/m^3 \quad (14)$$

Maximal saturation induction B_{max}= 0.3 T

The electrical parameters of the equivalent electrical circuit, primary and secondary magnetic resistance R_{magp}, R_{mags}, substrate resistance Rsubp, R_{subs}, oxide capacitance C_{oxp}, C_{oxs}, substrate capacitance C_{subp}, C_{subs}, spacing capacitance C_{sp}, C_{ss}, coupling capacitance C_{Kp}, C_{Ks}, serial resistance R_{sp}, R_{ss}, are calculated as follows [6-8].

$$R_{magp} = 2 \cdot \rho_{NiFe} \cdot \frac{e_{NiFe}}{w_p \cdot l_{tp}} \qquad R_{mags} = 2 \cdot \rho_{NiFe} \cdot \frac{e_{NiFe}}{w_s \cdot l_{ts}} \quad (15)$$

Ferrite resistivity ρ_{NiFe}= 10^3 Ω.m

$$R_{subp} = 2 \cdot \rho_{Si} \cdot \frac{e_{Si}}{w_p \cdot l_{tp}} \qquad R_{subs} = 2 \cdot \rho_{Si} \cdot \frac{e_{Si}}{w_s \cdot l_{ts}} \quad (16)$$

Silicon resistivity ρ_{Si}= 18.5 Ω.m

$$C_{oxp} = \frac{1}{2} \cdot \varepsilon_{Si_3N_4} \cdot \frac{w_p \cdot l_{tp}}{t_{gap}} \qquad C_{oxp} = \frac{1}{2} \cdot \varepsilon_{Si_3N_4} \cdot \frac{w_s \cdot l_{ts}}{t_{gap}} \quad (17)$$

t_{gap} is the spacing between primary and secondary coils, relative permittivity of Si_3N_4 equals to 6.

$$C_{subp} = \frac{1}{2} \cdot \varepsilon_{Si} \cdot \frac{w_p \cdot l_{tp}}{e_{si}} \qquad C_{subs} = \frac{1}{2} \cdot \varepsilon_{Si} \cdot \frac{w_s \cdot l_{ts}}{e_{si}} \quad (18)$$

Relative permittivity of silicon is 11.8

$$Cs_p = \varepsilon_{Si3N4} \cdot \left[\frac{t}{\delta} + 0.15\frac{t}{\delta} + 2.8\left(\frac{s_p}{\delta}\right)^{0.222}\right] \cdot l_{tp}$$

$$Cs_s = \varepsilon_{Si3N4} \cdot \left[\frac{t}{\delta} + 0.15\frac{t}{\delta} + 2.8\left(\frac{s_s}{\delta}\right)^{0.222}\right] \cdot l_{ts} \quad (19)$$

$$C_{kp} = \varepsilon_{Si3N4} \cdot \left[\frac{w_p}{\delta} + 0.15\frac{w_p}{\delta} + 2.8\left(\frac{t_{gap}}{\delta}\right)^{0.222}\right] \cdot l_{tp}$$

$$C_{ks} = \varepsilon_{Si3N4} \cdot \left[\frac{w_s}{\delta} + 0.15\frac{w_s}{\delta} + 2.8\left(\frac{t_{gap}}{\delta}\right)^{0.222}\right] \cdot l_{ts} \quad (20)$$

$$Rs_p = \rho_{cu} \cdot \frac{lt_p}{w_p \cdot t} \qquad Rs_s = \rho_{cu} \cdot \frac{lt_s}{w_s \cdot t} \quad (21)$$

Copper resistivity ρ_{Cu} = 1.7 10^{-8} Ω·m and t is the coil thickness.

III. INTEGRATED MICRO-TRANSFORMER CHARACTERIZATION

Scattering parameters characterize the electrical behaviour of the integrated planar micro-transformer. From the electrical model (Fig.2.b), we obtain the S-parameters' matrix and also the Z-parameters [12-14]. S_{11} and S_{22} represent the reflection coefficients of the primary and secondary coils of micro-transformer. They are directly related to the impedance. S_{12} and S_{21} represent the transmission coefficients, they are commonly called gain or attenuation. The simulation was performed in the range of frequency between 100 MHz and 10 GHz.

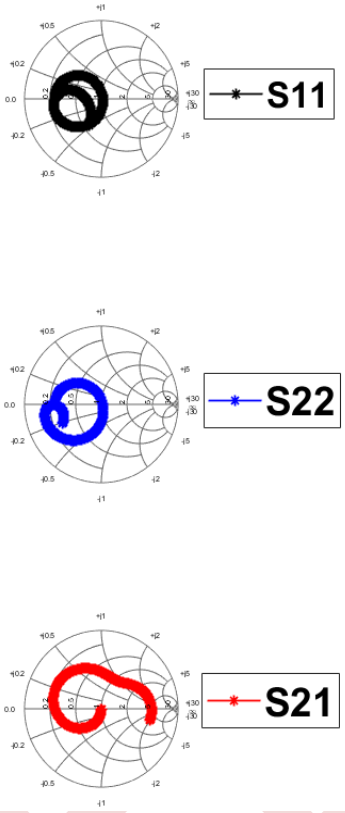


Fig.3. Scattering parameters S_{11}, S_{22} and S_{21} of on-chip micro-transformer

As shown in Fig.3, the S-parameters are represented in Smith chart. The curves of S_{11} and S_{22} display an inductance characterization. S_{11} shows a nearly short circuit at low frequencies (100 MHz). Therefore, S_{22} shows a very low impedance over the whole frequency range. The micro-transformer have a self-resonance frequency of about 2.3 GHz.

Fig.4 shows the real part and the imaginary part of S_{11} and S_{22} of the impedance as a function of frequency. The real part represents the resistance, the imaginary part represents the reactance. The self-resonance frequency is at 2.3 GHz. In that frequency the micro-transformer windings become purely resistive. Before the resonance frequency, the windings have an inductive behaviour and beyond it, the behaviour becomes capacitive.

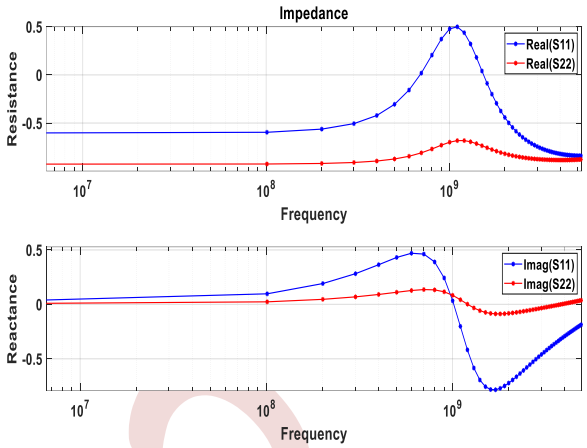


Fig.4. Impedance of on-chip micro-transformer versus frequency

The coupling factor k, given by (22) [4], is shown on Fig.5 versus frequency. A k-factor of the micro-transformer is equal to 0.9 at the operating frequency 1GHz.

$$k = \sqrt{\frac{\mathrm{Imag}(Z_{12}).\mathrm{Imag}(Z_{21})}{\mathrm{Imag}(Z_{11}).\mathrm{Imag}(Z_{22})}} \qquad (22)$$

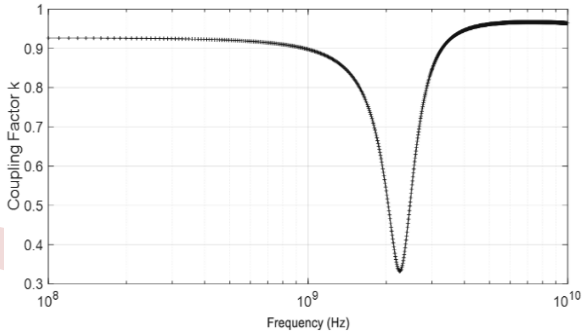


Fig.5. Coupling factor k versus frequency

The quality factor expresses losses in the micro-transformer, it is analysed using (23) [6][8],

$$Q_p = \frac{\mathrm{Im}(Z_{11})}{\mathrm{Re}(Z_{11})} \qquad Q_s = \frac{\mathrm{Im}(Z_{22})}{\mathrm{Re}(Z_{22})} \qquad (23)$$

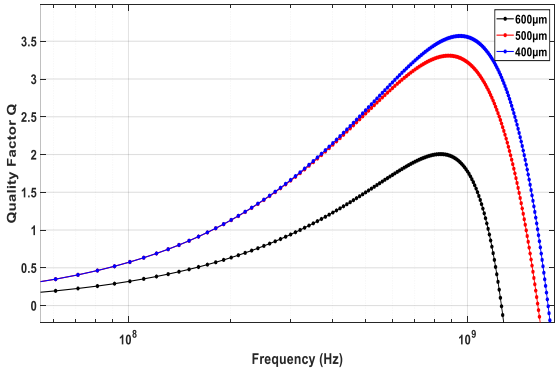


Fig.6. Quality factor versus frequency with different outer diameters

Fig.6 illustrates the measurement results with different outer diameters. We observe that the quality factor increases when the outer diameter decreases. The maximum values of the quality factors remain unchanged before the partial operating frequency. Thus, the Q factor is superior for the smaller micro-transformer when the frequency increases.

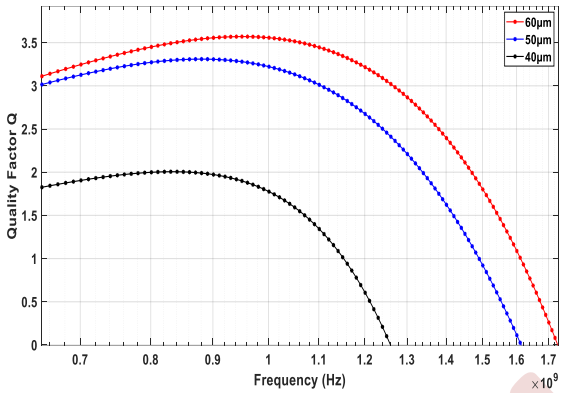


Fig.7. Quality factor over frequency with different width traces

Fig.7 illustrates the measurement results with different width. We observe that the Q factor is smaller when the traces are thinner. For lower frequencies the 60µm wide micro-transformer has a better Q-factor and the resonance frequency is close to the operating frequency, however the quality factor of the 40µm wide micro-transformer presents an important resonance frequency. The increase of the Q-factor for thin width traces is compensated by a reduction on the equivalent capacitance, which is related to the surface occupied by the micro-transformer.

IV. MICRO-TRANSFORMER MODEL VALIDATION

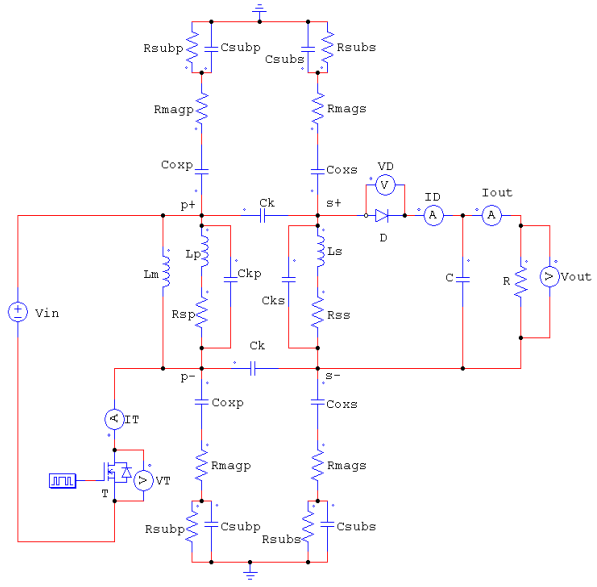


Fig.8. DC-DC flyback micro-converter with the integrated micro-transformer

In this section, we accomplish the simulation on DC-DC flyback micro-converter to check the integrated micro-transformer operation. Fig.8 shows the DC-DC flyback micro-converter containing the integrated micro-transformer equivalent electrical circuit. To complete the simulations, we need to calculate the load resistance R, load capacitance C and the magnetizing inductance L_m (24-26)

$$R = \frac{V_{out}}{i_{out}} \tag{24}$$

$$C = \frac{V_{in}}{32 \cdot L \cdot \Delta V_{out} \cdot f^2} \tag{25}$$

$$L_m = n_p^2 \cdot \frac{\mu_{NiFe} \cdot d_{out}^2}{2 \cdot e_{NiFe}} \tag{26}$$

After simulation on TINA software 9.0, the different curves are represented; the output voltage and current (V_{out}, I_{out}) (Fig.9), the transistor and diode voltages (V_T, V_D) and currents (I_T, I_D) (Fig.10), primary and secondary voltages (V_1, V_2) and currents (I_1, I_2) (Fig.11).

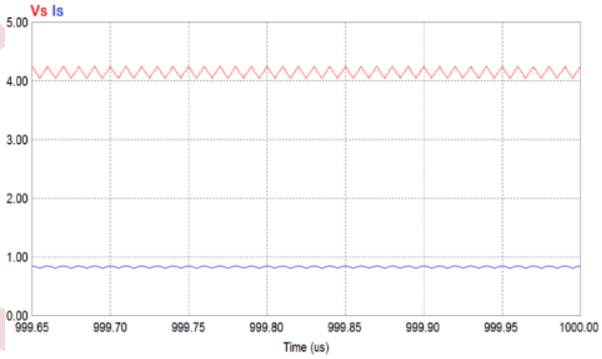


Fig.9. Output voltage and current of flyback micro-converter with the integrated micro-transformer

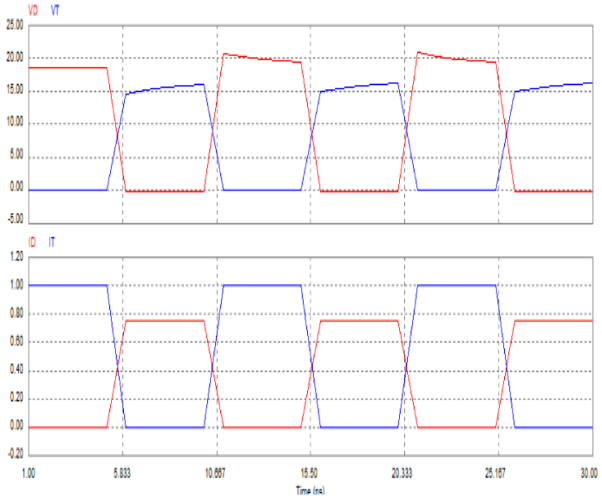


Fig. 10. Voltage and current of both transistor and diode of flyback micro-converter with the integrated micro-transformer

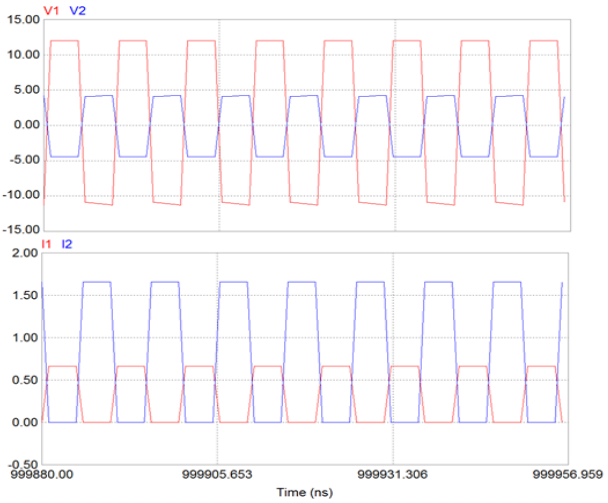


Fig. 11. Voltage and current of both primary and secondary coils of integrated micro-transformer in flyback micro-converter

The obtained simulation results show that the output voltage V_{out} achieved is 4.25 V and the output current I_{out} is 0.85 A. The values are close to the main parameters (V_{out} = 5 V and I_{out} = 1A) of the DC-DC flyback micro-converter. This deline is due to the magnetic core losses in ferrite layers, the Joule losses in conductor coils, the capacitive losses between coils and also to the voltage drop across the transistor and diode. The primary coil V_1 acheives 12 V and the secondary V_2 is about 5 V. When the transistor is closed, the primary is directly connected to the input voltage source and the primary current increases storing energy in the magnetic layer of micro-transformer. When the transistor is opened, the diode become forward and the secondary allows the current to flow from the micro-transformer. The results confirm that micro-converter operates correctly and the dimensioning of the micro-transformer is well done.

Efficiency η calculated by (27) represents the ratio of the output and input power of the micro-converter [17-18]. In Fig.12, we notice that the output power 5 W of the DC-DC flyback micro-converter, containing the integrated micro-transformer, corresponds to an efficiency of 76.5%. Therefore, the micro-transformer dimensioning results are compatible with the integration in electronics and they are in accordance with the literature [11][15].

$$\eta = \frac{(V_{out} \cdot I_{out}) - (R_{seq} \cdot I_{out}^2) - (V_{in}^2 / R_{seq})}{V_{out} \cdot I_{out}} \quad (27)$$

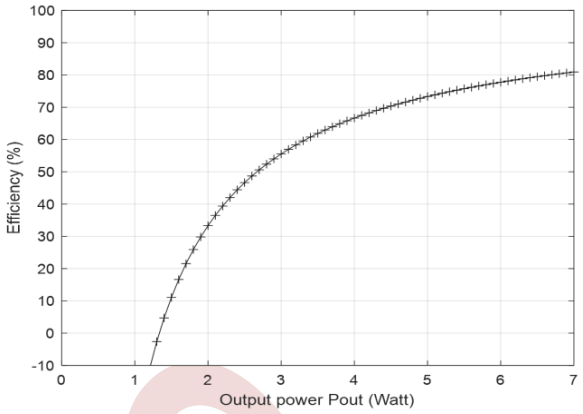
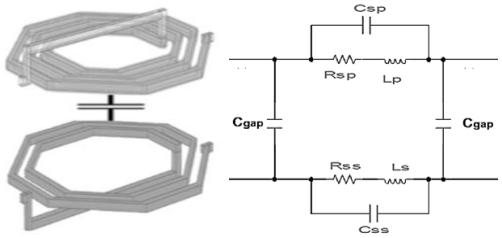


Fig.12. Flyback DC-DC micro-converter efficiency versus output power

To fully integrate the flyback micro-converter, we can consider the micro-transformer coupling capacitance as the load capacitance of the micro-converter (Fig.13). The capacitor is located between metal spiral layers. It is considered as an integrated MIM (Metal-Insulator-Metal) capacitor. We compared between putting the dielectric material or the air between the coils of the micro-transformer. The capacitance is given by (28).

$$C_{gap} = \varepsilon_0 \cdot \varepsilon_r \cdot \frac{d_{out}^2}{t_{gap}} \quad (28)$$

The integration of the micro-transformer with the load capacitance of the micro-converter leads to create an integrated component called LCT (Inductor-Capacitance-Transformer). The inductor in this case is created from the leakage inductance [16-19].



(a) (b)

Fig. 13. (a) Micro-transformer coupling capacitance as load capacitance of the micro-converter, (b) Equivalent circuit

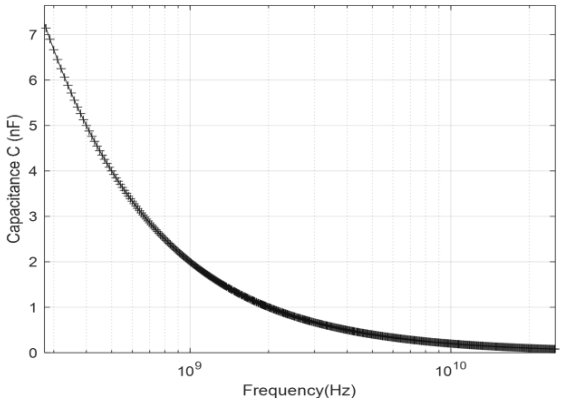


Fig. 14. Capacitance between the coils of the micro-transformer versus frequency

Fig.14 shows that the increase of the frequency permits to decrease the capacitance. Adding dielectric material allows to increase the capacitance.

V. CONCLUSION

This paper presents the design of a Flyback DC-DC micro-converter containing an integrated spiral planar octagonal micro-transformer. The first considered parameter was the shape of the coils. Octagonal spiral planar is the geometry of the stacked micro-transformer. This work is planned for the application requiring a conversion of energy of low power and high frequency. We have fulfilled the geometric dimensioning using the Mohan's method, which is used for planar polygonal shapes. We have extracted the different electric parameters of the equivalent electrical circuit, which determines the parasitic effects created in stacked layers and generated at high frequency. The Q factor is an important characteristic for the coils behavior, it present the energy dissipation. To validate our study, we have integrated the electrical circuit of the micro-transformer into a flyback micro-converter to test the good operation of the component. We conclude that the simulation results are in accordance with the literature and compatible with the integration in electronics.

REFERENCES

[1] G. Lv *et al*., "A High-Efficiency Double-Side Silicon- Embedded Inductor for Integrated DC–DC Converter Applications," in *IEEE Transactions on Electron Devices*, vol. 68, no. 9, pp. 4801-4804, Sept. 2021, doi: 10.1109/TED.2021.3096923.

[2] X. Xing, N. X. Sun, and B. Chen, "High-Bandwidth Low-Insertion Loss Solenoid Transformers Using FeCoB Multilayers", IEEE Transaction on Power Electronics, vol. 28, no. 9, pp. 4395 – 4401, 2013.

[3] Hao Wu, Michael Lekas, Ryan Davies, Kenneth L. Shepard, Noah Sturcken, "Integrated Transformers With Magnetic Thin Films", IEEE Transaction on Magnetics, vol. 52, no. 7, pp. 8401204, 2016.

[4] E. S. Lee, J. H. Park, M. Y. Kim and S. H. Han, "An Integrated Transformer Design With a Center-Core Air-Gap for DAB Converters," in *IEEE Access*, vol. 9, pp. 121263-121278, 2021, doi: 10.1109/ACCESS.2021.3108837.

[5] M. Li, Z. Ouyang and M. A. E. Andersen, "Discovery of the Nearly Zero Flux Between Two Parallel Conductors in Planar Transformers," in *IEEE Transactions on Power Electronics*, vol. 37, no. 1, pp. 714-723, Jan. 2022, doi: 10.1109/TPEL.2021.3093171.

[6] L. Zheng, R. P. Kandula, K. Kandasamy and D. Divan, "New Modulation and Impact of Transformer Leakage Inductance on Current-Source Solid-State Transformer," in *IEEE Transactions on Power Electronics*, vol. 37, no. 1, pp. 562-576, Jan. 2022, doi: 10.1109/TPEL.2021.3101811.

[7] M. Lan *et al*., "An Improved Six-Port Equivalent-Circuit Model for Millimeter-Wave On-Chip Transformers With Accurate Coupling Factor Modeling," in *IEEE Transactions on Microwave Theory and Techniques*, vol. 69, no. 9, pp. 3989-4000, Sept. 2021, doi: 10.1109/TMTT.2021.3092342.

[8] K. Youssouf *et al*., "Design and Study of Interleaved and Face to Face Magnetic Microtransformers," in *IEEE Transactions on Electron Devices*, vol. 61, no. 8, pp. 2873-2878, Aug. 2014, doi: 10.1109/TED.2014.2329334.

[9] S. Mohan, C.P.Yue, M. del Mar Hershenson, S. Wong, and T.H. Lee, "Modeling and characterization of on-chip transformers," International Electron Devices Meeting *1998*, Technical Digest, IEEE, 1998, pp. 531-534.

[10] G. Lv *et al*., "A High-Efficiency Double-Side Silicon- Embedded Inductor for Integrated DC–DC Converter Applications," in *IEEE Transactions on Electron Devices*, vol. 68, no. 9, pp. 4801-4804, Sept. 2021, doi: 10.1109/TED.2021.3096923.

[11] D. Dinulovic, M. Shousha, M. Haug, S. Beringer and M. C. Wurz, "Comparative Study of Microfabricated Inductors/Transformers for High-Frequency Power Applications," in *IEEE Transactions on Magnetics*, vol. 53, no. 11, pp. 1-7, Nov. 2017, Art no. 4700107, doi: 10.1109/TMAG.2017.2734878.

[12] N. Zeidi, S. Kaziz, M. Hadj Said, L. Rufer, A. Cavallini, F. Tounsi, " Partial discharge detection with on-chip spiral inductor as a loop antenna", Review of Scientific Instruments 92, 094701 (2021)

[13] E. M. Dede *et al*., "Thermal Design, Optimization, and Packaging of Planar Magnetic Components," in *IEEE Transactions on Components, Packaging and Manufacturing Technology*, vol. 11, no. 9, pp. 1480-1488, Sept. 2021, doi: 10.1109/TCPMT.2021.3105003.

[14] L. Ying, H. Chunyue, Z. Xin, L. Tianming, G. Guangkuo, X. Guoji, T. Wenliang, "Influence of Compliant Layer Thickness on Stress and Strain of Solder Joints in Wafer Level Chip Scale Package under Thermal Cycle", IEEE 15th International Conference on Electronics Packaging Technology, 577-582, 2014.

[15] I. MS, MRK. Akanda, "3D Temperature Distribution of SiC MESFET Using Green's Function", Electrical and Computer Engineering, IEEE. 13-16, 2010

[16] Z. Ouyang and M. A. E. Andersen, "Overview of planar magnetic technology-fundamental properties", *IEEE Trans. Power Electron.*, vol. 29, no. 9, pp. 4888-4900, Sep. 2014.

[17] M. K. Ranjram, I. Moon and D. J. Perreault, "Variable-inverter-rectifier-transformer: A hybrid electronic and magnetic structure enabling adjustable high step-down conversion ratios", *Proc. 18th Workshop Control Model. Power Electron.*, pp. 1-8, Jul. 2017.

[18] H. K. Krishnamurthy et al., "A digitally controlled fully integrated voltage regulator with on-die solenoid inductor with planar magnetic core in 14-nm tri-gate CMOS", *IEEE J. Solid-State Circuits*, vol. 53, no. 1, pp. 8-19, Jan. 2018.

[19] S. A. Ansari, J. N. Davidson, M. P. Foster, and D. A. Stone, "Design and Analysis of a Fully-integrated Planar Transformer for LCLC Resonant Converters," in 2021 23rd European Conference on Power Electronics and Applications (EPE'21 ECCE Europe), 2021: IEEE, pp. P. 1-P. 8.

Integrated Square On-Chip Inductor for Photovoltaic Converter Applications

Mokhtaria Derkaoui[1]*, Yamina Benhadda[2]

[1]*LARATIC Laboratory, National Higher School of Telecommunications & ICT of Oran, Algeria*
[2]*LEPA Laboratory, University of Sciences and Technology of Oran, Algeria*

*mokhtaria.derkaoui@ensttic.dz

***Abstract*—The research of this paper concerns the study of an integrated square on-chip inductor in a DC-DC Buck converter connected to a photovoltaic module. The topology of the inductor is chosen for its ability to provide improved performance and high inductance value. The paper presents the integrated inductor geometrical and electrical dimensioning. The equivalent electrical circuit of on-chip inductor with different added layers is described. The finite elements method is used to illustrate the current density and temperature distribution in the on-chip spiral inductor. The simulation of the DC-DC Buck converter with PV panel is validated using the integrated inductor to show its performances. The study combines theoretical analysis, modeling and simulation techniques to evaluate the performance and effectiveness of the square on-chip inductor topology. The results obtained provide valuable insights into the design and operation of the integrated inductor based PV system.**

***Keywords:* DC-DC Buck Converter; Inductor; Integration; On-Chip; PV**

I. Introduction

Solar energy is an important renewable energy source that is environmentally friendly and its applications in photovoltaic (PV) systems are increasing [1-2]. The electric power generated by a photovoltaic system is influenced by solar radiation and temperature variations [3-4]. The maximum power produced by photovoltaic (PV) module is delivered to the load by adjusting the voltage through a DC-DC converter [5]. DC-DC converters play a crucial role in these systems by simplifying the conversion and distribution of power [6-7]. This miniaturization of converters has pushed towards developing distributed architectures and embedded systems for on-chip systems containing several components [8-9]. Therefore, the integration of the passive components of these converters becomes an inevitable solution in order to reduce sizes and cost [10-11]. On-chip integrated planar inductors remove several inconveniences, at recent years [12-13]. The aim of this paper is to address the challenges in PV systems containing a DC-DC converter with an integrated on-chip inductor. We propose a comprehensive study on the topology of the square spiral planar inductor integrated in a DC-DC Buck converter, which offers improved performance and a high inductance value. The model presented in this study includes geometric and electric characteristics to develop analytical equations for the inductor topology. Besides, we focus on implementing a PV system for the DC-DC converter, which integrates the proposed square inductor. This control strategy aims to operate the PV panel at its maximum power point, optimizing the overall energy conversion efficiency of the system. The performance of the integrated on-chip inductor in the converter is validated using specialized software. The simulations allow us to evaluate the effectiveness and efficiency of the designed integrated inductor in the DC-DC Buck converter and its application in photovoltaic systems.

II. Methodology and Modelling of DC-DC Buck Converter

The DC-DC Buck converter can decrease the input voltage (Fig.1). It is frequently used in photovoltaic applications due to its high efficiency and easy implementation. In order to enhance the efficiency of PV systems, DC-DC converters are employed between the solar panels and the loads [6]. These converters enable the adaptation of input resistance to the output resistor, thus optimizing power transfer. The block diagram of a typical photovoltaic system is illustrated in Fig.2.

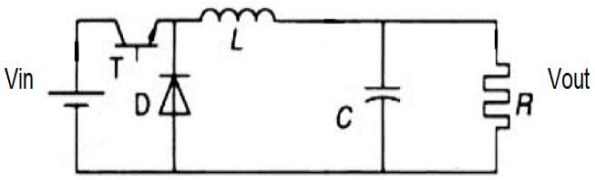


Fig.1. Conventional DC-DC Buck Converter

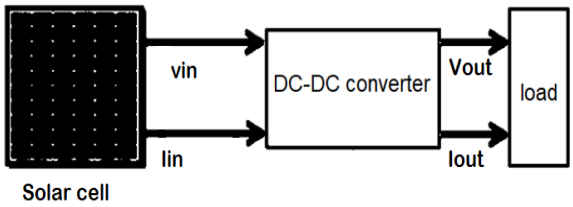


Fig.2. Block diagram of Photovoltaic system

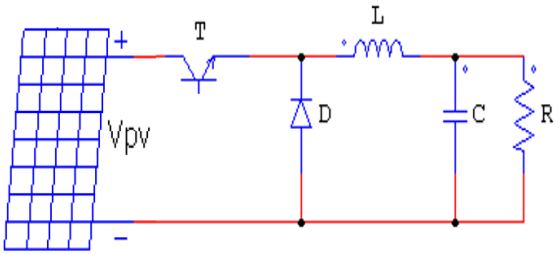


Fig.3. PV panel integrated with DC–DC Buck converter

As shown in Fig.3, DC-DC Buck converter consists of PV voltage source, inductor L, capacitor C, load resistor R and also both transistor and diode operating as switches.

The objective of this study is to reduce the size of the converter and preserve its performances. The mainly problem is to reduce the size of the inductor. The dimensions of the on-chip inductor to be integrated in the DC-DC Buck converter will be determined by the characteristics indicated in Table 1.

Table 1. Converter specifications

Input voltage V_{in}	5 V
Output voltage V_{out}	2.5 V
Output power P_{out}	1 W
Operating frequency f	500 kHz

The global model of a PV cell includes a diode connected in parallel with a current source, in addition to series and parallel resistances (Fig.4) [3]. The technical characteristics of the PV panel are determined in Table 2.

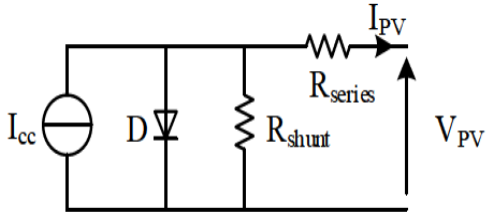


Fig.4. Equivalent circuit of PV cell

Table 2. PV panel technical characteristics

Maximum working voltage	12 V
Maximum current	0,5 A
Maximum power	3 W
Minimum working voltage	1 V
Maximum power tolerance	15%
Working temperature	-45°C to +85 °C

The average output current is given by (1).

$$I_{out} = \frac{P_{out}}{V_{out}} \quad (1)$$

The peak amplitude of the current flowing through the inductor is given by (2).

$$(\Delta I_L) = I_{Lmax} - I_{Lmin} = \frac{V_{in}}{4 \cdot L \cdot f} \quad (2)$$

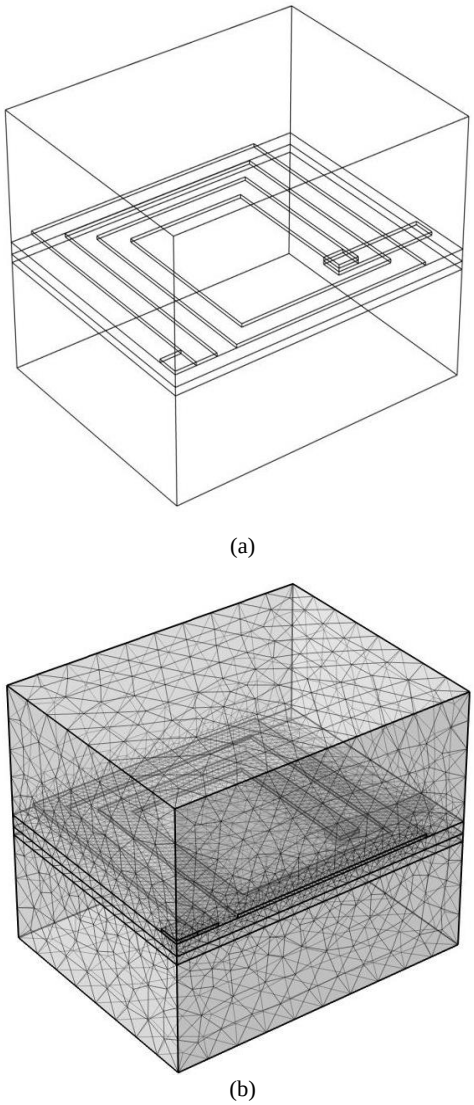
The relation between the current supplied by the cell I_{PV} and the voltage across the cell V_{PV} is given by (3) [2].

$$I_{PV} = I_{cc} - I_{sat}\left[\exp\left(\frac{q \cdot V_{PV}}{n \cdot K \cdot T_c} + I \cdot R_{series}\right) - 1\right] \quad (3)$$

I_{sat}: junction saturation current
K: Boltzmann constant
T_c: cell temperature
q : electron charge
n: non-ideality factor of the junction

III. Dimensioning of the integrated on-chip inductor

The integrated planar inductor consists of a square spiral coil in copper (Cu). The planar spiral coil is superimposed on NiZn ferrite layer and isolated from there by SiO_2 silicon dioxide layer. All these different layers with different materials are superimposed on silicon layer (Si), which serves as a substrate (Fig.5).



(a)

(b)

Fig.5. (a) Square on-chip inductor 3D view, (b) Mesh

The required NiZn ferrite volume for the energy storage is given by (4).

$$V_{indu} = \frac{W_{indu}}{W_{vmax}} \quad (4)$$

W_{indu} and W_{vmax} represent the total magnetic stored energy (5) and the maximum volume density of energy (6) [12].

$$W_{indu} = \frac{1}{2} \cdot L \cdot I_{out}^2 \quad (5)$$

$$W_{vmax} = \frac{B_{max}^2}{2 \cdot \mu_0 \cdot \mu_{rNiZn}} \quad (6)$$

B_{max}= 0.3 T

μ_{rNiZn}= 1500

Therefore, 9.8125 mm^3 of NiZn is necessary to store 1 µJ of energy in the inductor.

The integrated square planar spiral inductor is characterized by geometrical parameters (Table 3), the angles are limited to multiples of 45 degrees.

Table 3. Geometrical parameter values

Geometrical parameters	Values
Outer diameter d_{out}	3 mm
Inner diameter d_{in}	1.2 mm
Turns number n	2
Coil thickness t	34 µm
Coil width w	25 µm
Coil total length l_t	9 mm
Coil spacing s	2.17 µm

The equivalent electrical circuit extracted from Fig.5 determines the electrical behavior of the integrated planar inductor. Different structures have been proposed for the integrated inductors, however the most successful design is illustrated in Fig.6, which has been widely studied [12-14]. The circuit contains different electrical parameters that define each material layer. They are calculated by (7-13) and the different values are grouped in Table 5.

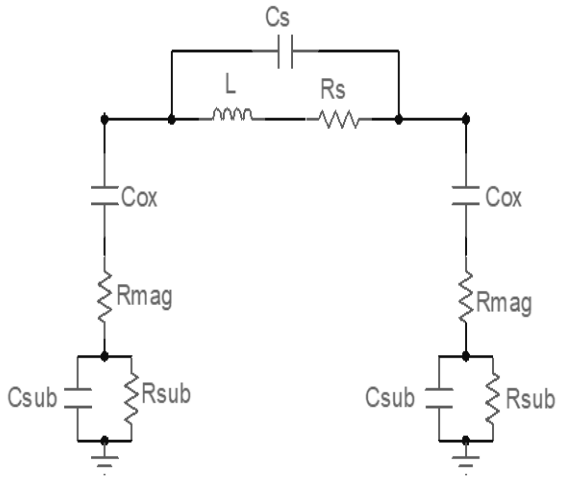


Fig.6. Lumped elements equivalent electrical circuit

The inductance value is calculated using Wheeler method (7) [10].

$$L = k_1 \cdot \mu_0 \cdot \frac{n^2 \cdot \left(\frac{d_{out}+d_{in}}{2}\right)}{1+k_2 \cdot \left(\frac{d_{out}-d_{in}}{d_{out}+d_{in}}\right)} \quad (7)$$

k_1 and k_2 represent the coefficients used in Wheeler expression for different coil topologies

Table 4. k_1 and k_2 coefficients values

Form	k_1	k_2
Square	2.34	2.75
Hexagonal	2.33	3.82
Octagonal	2.25	3.55

$$Rs = \rho_{cu} \cdot \frac{lt}{w \cdot t} \quad (8)$$

$$R_{mag} = 2 \cdot \rho_{NiZn} \cdot \frac{t_{mag}}{w \cdot lt} \quad (9)$$

$$R_{sub} = 2 \cdot \rho_{Si} \cdot \frac{t_{Sub}}{w \cdot lt} \quad (10)$$

$$C_{sub} = \frac{1}{2} \cdot \varepsilon_0 \cdot \varepsilon_{rSi} \cdot \frac{w \cdot lt}{t_{sub}} \quad (11)$$

$$C_{ox} = \frac{1}{2} \cdot \varepsilon_0 \varepsilon_{rSiO2} \cdot \frac{w \cdot lt}{t_{ox}} \quad (12)$$

$$C_s = \frac{1}{2} \cdot \varepsilon_0 \varepsilon_{rair} \cdot \frac{t \cdot lt}{s} \quad (13)$$

Where, t_{mag} is the ferrite thickness, t_{sub} is the substrate thickness and t_{ox} is the oxide layer thickness.

$\rho_{NiZn} = 1000\ \Omega \cdot m$

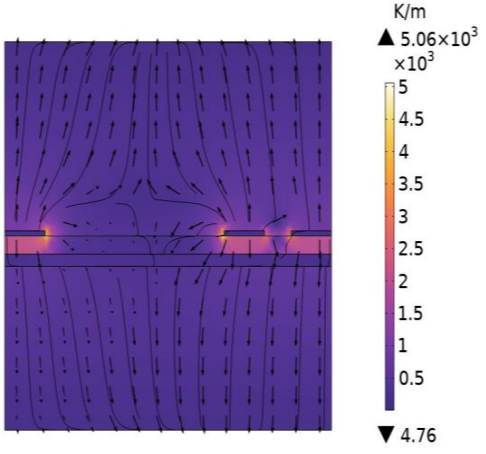
$\rho_{Cu} = 1.7 \cdot 10^{-8}\ \Omega \cdot m$

$\rho_{Si} = 18.5\ \Omega \cdot m$

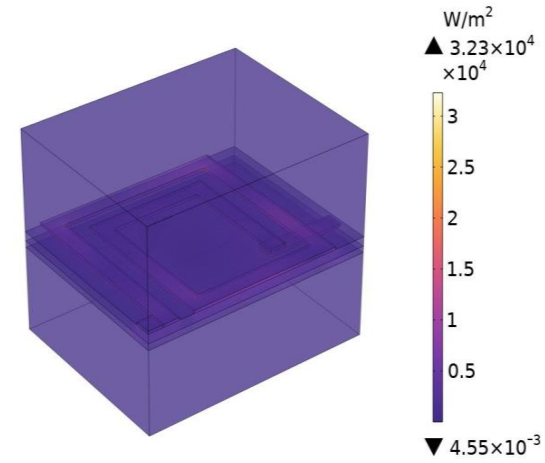
$\varepsilon_{rSi} = 11.8$

Table 5. Electrical parameters values

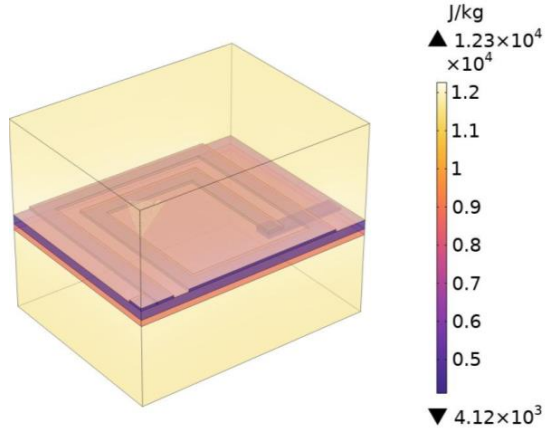
Electrical parameters	Values
Inductance L	3.125 µH
Serial resistance Rs	0.75 Ω
Magnetic resistance R_{mag}	2.8 MΩ
Substrate resistance R_{sub}	2.86 Ω
Substrate capacitance C_{sub}	17.43 pF
Oxide capacitance C_{ox}	11.149 Pf
Coil capacitance Cs	0.338 pF



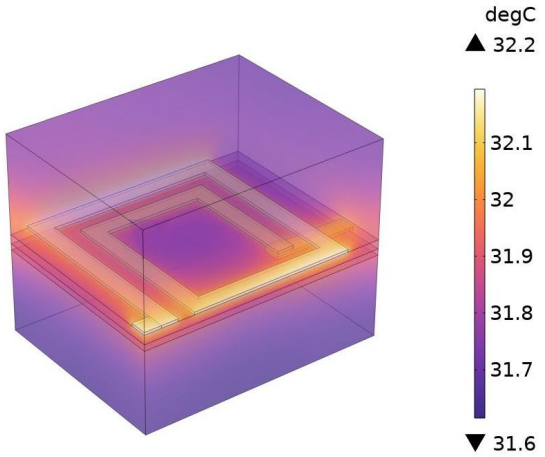
(a)



(b)

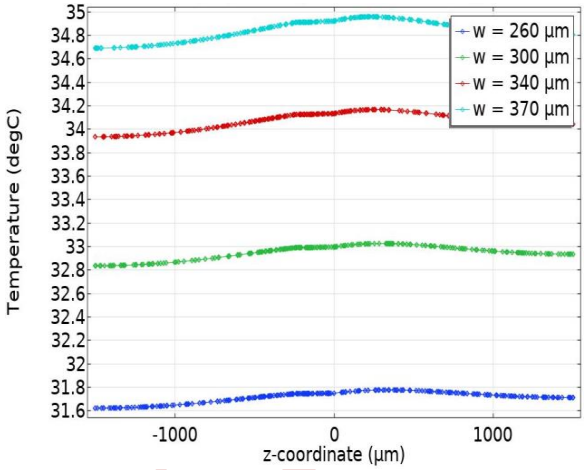


(c)

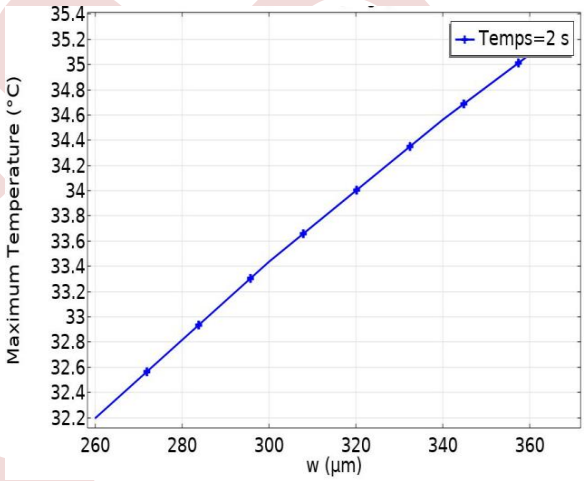


(d)

Fig.7. (a) Temperature gradient, (b) Total heat flow (c) Enthalpy, (d) Temperature



(a)



(b)

Fig.8. (a) temperature distribution in the inductor for different widths, (b) Maximum temperature versus width

Simulation was done by finite element method software to observe temperature gradient, total heat flow, enthalpy and temperature distribution in the inductor at the operating frequency of 500 kHz (Fig.7). Besides, the impact of the width on temperature.

IV. Simulation of DC-DC Buck Converter for Photovoltaic Applications

The PV panel allows to convert the thermal energy into electricity. Fig.9 shows the circuit diagram of the DC-DC Buck converter containing the PV panel and the equivalent electrical circuit of the integrated on-chip inductor. This structure allows the efficient conversion of the output variable from the photovoltaic cell to a chosen output voltage and current level.

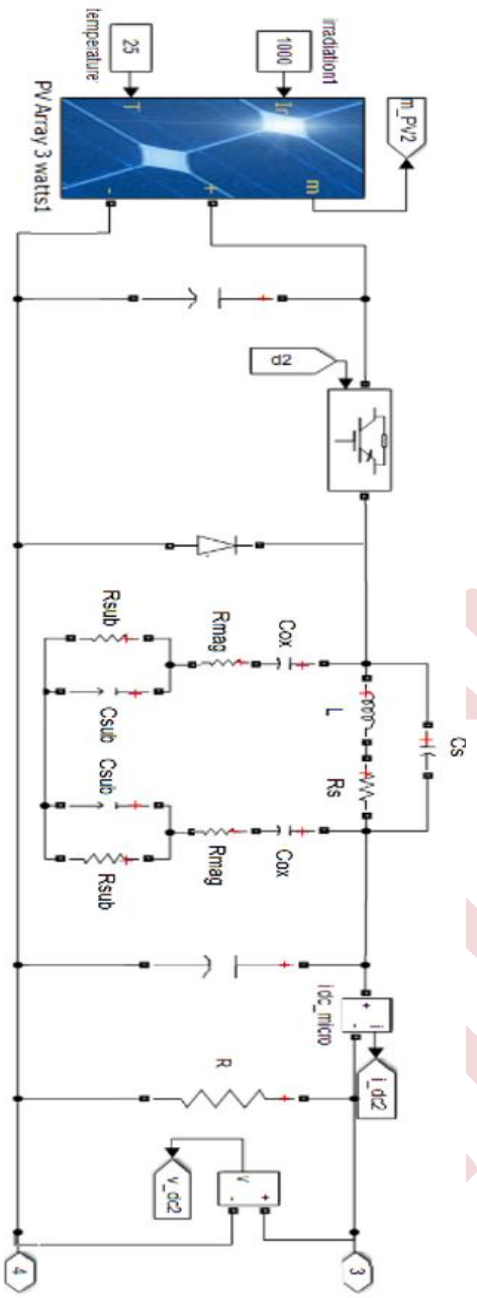
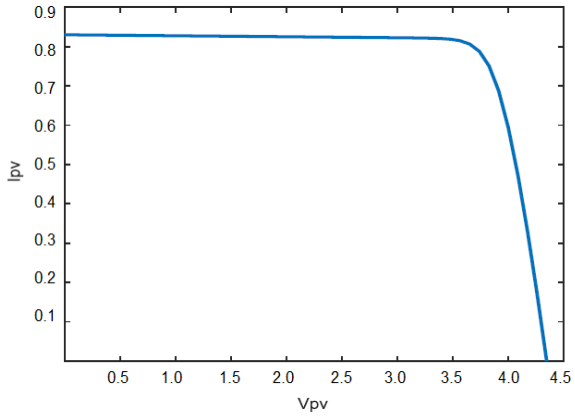
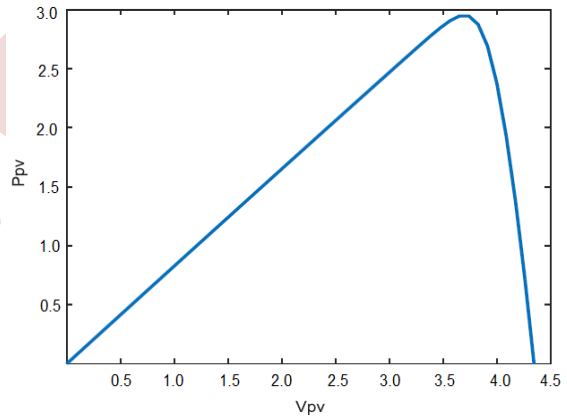


Fig.9. Photovoltaic system using DC-DC Buck converter with integrated on-chip inductor

Simulated results of the DC-DC Buck converter at a switching frequency of 500 kHz are presented in Fig.10. We notice that the maximum photovoltaic current achieves 0.8 A and the power is about 2.9 Watt for a voltage of 3 V. These results show that the integrated on-chip planar inductor works well. Hence, we can confirm that the geometrical and electrical dimensions are well defined.



(a)



(b)

Fig. 10. (a) I-V and (b) P-V Characteristics of Solar Cell

V. Conclusion

In this paper, we have presented the dimensioning, the modeling and the simulation of the square on-chip planar inductor integrated in DC-DC Buck converter using for PV system. Simulations were established to evaluate the photovoltaic panel behaviour. The simulations were conducted under a temperature of 25°C and constant irradiation of 1 kW/m². We have extracted geometrical and electrical parameters of the integrated square planar inductor basing on the specifications of DC-DC Buck converter. By using a software simulation, we have extracted converter output current and power waveforms. The results obtained in this work serve as a valuable reference for the inductor integration into photovoltaic applications. The square on-chip planar inductor was found appropriate for operating the DC-DC Buck converter combined with photovoltaic generator. We conclude that the results of dimensioning in this work are interesting indeed.

REFERENCES

[1] J. J. Khanam, S. Y. Foo, Modeling of a photovoltaic array in MATLAB simulink and maximum power point tracking using neural network, Electrical & Electronic Technology Open Access Journal, vol. 2, no. 2, 2018.

[2] R. Gladwin Antony, *et al*, "Design of Solar Charging Case for Mobile Phones," Journal of Physics: Conference Series (International Conference on Physics and Energy), vol. 2040, 2021.
[3] O. Ibrahim, N. Z. Yahaya, Matlab/Simulink Model of Solar PV Array with Perturb and Observe MPPT for Maximising PV Array Efficiency, 2015 IEEE.
[4] N. Belhaouas, M.S. Ait Cheikh, A. Malek, C. Larbes, Matlab-Simulink of photovoltaic system based on a two-diode model simulator with shaded solar cells, Revue des Energies Renouvelables, vol. 16, no.1, pp 65 – 73, 2013.
[5] K. V. G. Raghavendra, *et al*, "A Comprehensive Review of DC–DC Converter Topologies and Modulation Strategies with Recent Advances in Solar Photovoltaic Systems," electronics, vol. 31, n. 9, p 1- 41, 2020.
[6] S. Saravanan, N.R. Babu, "A modified high step-up non-isolated DC–DC converter for PV application," Journal of Applied Research and Technology, vol. 15, n.3, p 242–247, 2017.
[7] G. Pratapsinh Parmar and D. Urvashi Patel, "A Review on DC-DC converters for Photovoltaic system," IJIREEICE, vol. 3, no. 12, pp. 143– 146, Dec. 2015.
[8] M. R. Benzidane, *et al*, "Miniaturization and Optimization of a DC–DC Boost Converter for Photovoltaic Application by Designing an Integrated Dual-Layer Inductor Model," Transactions on Electrical and Electronic Materials, vol. 23, p 462–475, 2022.
[9] Zaghba, A. Borni, A. Bouchakour, N. Terki, Buck-boost converter system modelling and incremental inductance algorithm for photovoltaic system via Matlab/Simulink, Revue des Energies Renouvelables SIENR'14 Ghardaïa (2014) , pp 63 – 70.
[10] Derkaoui M, Benhadda Y, Hamid A, Temmar A. (2021) Design and modeling of square planar inductor and transformer in monolithic technology for RF systems. J Electr Eng Technol 16:1481–1493.
[11] Aldoumani, M.; Yuce, B.; Zhu, D. Using the Variable Geometry in a Planar Inductor for an Optimised Performance. Electronics 2021, 10, 721.
[12] Derkaoui, M.; Benhadda Y.; Chaabene G.; Spiteri P.; "On-Chip GaN Planar Transformer Design for Highly Integrated RF Systems", Journal of Circuits, Systems and Computers, Vol. 32, No. 09, 2350149 (2023).
[13] Benhadda, Y., Derkaoui, M., Mendaz, K., Kharbouch, H., Spiteri, P. "Design for Integrated Planar Spiral Inductor for MEMS", Periodica Polytechnica Electrical Engineering and Computer Science, (2023).
[14] M. H. Bechir, *et al*, "Planar inductor equivalent circuit model taking into account magnetic permeability, loss tangent, skin and proximity effects versus frequency,"Analog integrated circuits and signal processing, vol.88, n.1, p 105–113, 2016.

Modeling of Octagonal Planar Microtransformer for DC-DC Converter Applications

Mokhtaria Derkaoui[1]*, Yamina Benhadda[2]

[1]*LARATIC laboratory, Higher National School of Telecommunications & ICT (ENSTTIC-Oran), Algeria*
[2]*LEPA laboratory, University of Sciences and Technology of Oran (USTO- MB), Algeria*
** mokhtaria.derkaoui@ensttic.dz*

***Abstract*—The work presented in this paper concerns the modeling of an octagonal microtransformer integrated in Flyback converter. The microtransformer is composed of two spiral planar stacked coils. An optimal geometry of the planar coils are the important difference regarding the microtransformer topologies for high frequencies. In this work, a comparison was first restricted to a square and an octagonal geometry of coils. Then, a study on the microtransformer topology was presented regarding to a spiral coils. Besides, the modeling through electromagnetic and thermal simulations was carried out. Furthermore, a validation of the equivalent electrical model was validated.**

Keywords--Converter; Integration; Microtransformer; Planar; RF

I. INTRODUCTION

Power electronics has never stopped to advance, since its appearance. This discipline exists in the majority of electrical systems. Passive energy storage elements are widely used in RF ICs circuits and one of the important passive components is the transformer. Before, it was realized as discrete components. However increasing demands on the RF applications, the integrated transformers appear. The integration allows a realization of compact high frequency circuits with a high level of integrity along with low production costs [1-3].The use of transformers is tricky because their modeling and optimization is difficult. Integrated transformers are used for impedance matching, differential conversion, voltage-controlled oscillators, low noise amplifiers, power amplifier and mixers [4-5]. Several works have made it possible to evaluate the different layout of transformers, but few of them have presented a simple model that allows rapid optimization of transformers [6-7].

II. PRESENTATION OF FLYBACK CONVERTER

Flyback converter is composed of one transformer and few active and passive components (Fig.1). The principle of the Flyback operation is based on the energy transfer from primary to secondary through a transformer.

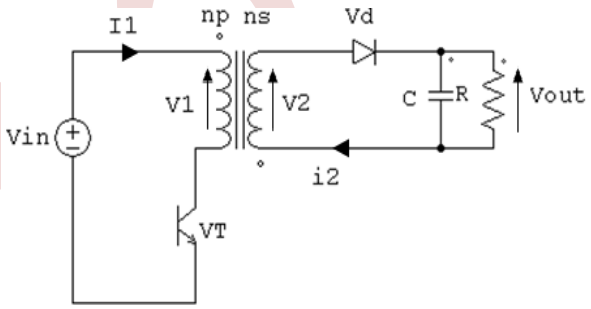


Fig.1. Schematic diagram of Flyback converter

The study in this paper is oriented towards the integration of a planar microtransformer in Flyback converter. The microtransformer is composed of two coupled spiral planar coils superimposed on different layers of the different materials (Fig.2).

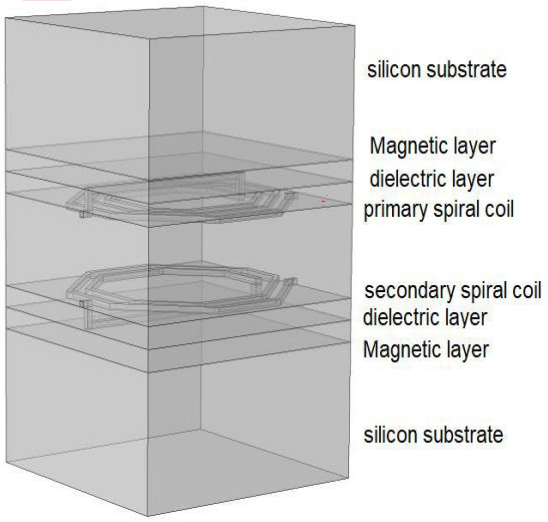


Fig.2. Cross section of the integrated planar spiral microtransformer

It is important, thus, to present the π equivalent electrical model which demonstrates the electrical behavior of the integrated microtransformer for an operating frequency of 1GHz (Fig.3). The circuit contains different electrical parameters that define each layer. The coil is represented by the self-inductances L_p and L_s of the line in series with the series resistances R_p and R_s and both in

parallel with series capacitances C_{sp} and C_{ss}. Oxide capacitances C_{oxp} and C_{oxs} of the dielectric layers. Magnetic resistances modeling magnetic losses R_{magp} and R_{mags}. Coupling capacitance between the top and bottom coils of the microtransformer C_k. Substrate resistances R_{subp}, R_{subs} and capacitances C_{subp}, C_{subs} [8-10].

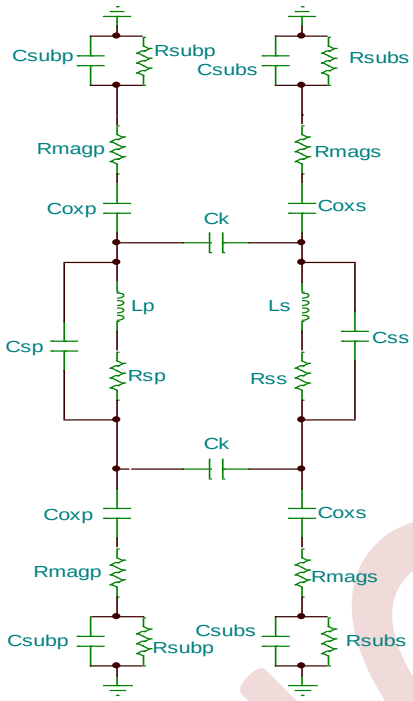
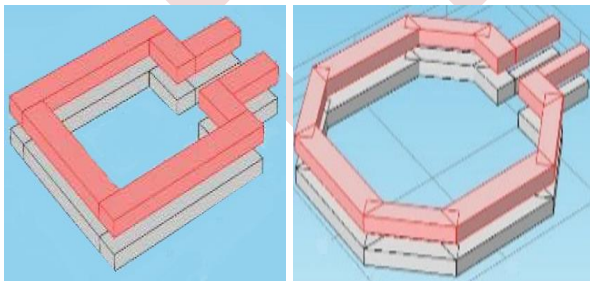


Fig.3. π equivalent electrical circuit of the microtransformer [8]

III. COMPARISON OF GEOMETRICAL SHAPES

The coil's shape, as circular and polygonal, is an important feature regarding the transformer topologies. In this work, comparison was hence restricted to a square (Fig.4.a) and an octagonal planar microtransformer (Fig.4.b) the angles are limited to multiples of 45 degrees. We have opted for an outer diameter of 500 µm and a width of 50 µm. Those two transformers present the same diameter and the same width.



(a) (b)

Fig.4. Square (a) and octagonal (a) planar spiral microtransformer

Primary and secondary inductances are determined by the Z-parameters (Equation 1) [7][12]. The measurement results for square and octagonal microtransformers are shown in Fig.5.

$$L_p = \frac{\mathrm{Im}(Z_{11})}{\omega} \qquad L_s = \frac{\mathrm{Im}(Z_{22})}{\omega} \tag{1}$$

The two microtransformers present the same spiral width and the same diameter. It is noticed in Fig.5 that for the same diameter, square coils present a higher inductance value. This difference is due to the greater total length that the square device presents.

Primary and secondary quality factor are determined by the Z-parameters (Equation 2) [7][12]. The measurement results for square and octagonal microtransformers are shown in Fig.6.

$$Q_p = \frac{\mathrm{Im}(Z_{11})}{\mathrm{Re}(Z_{11})} \qquad Q_s = \frac{\mathrm{Im}(Z_{22})}{\mathrm{Re}(Z_{22})} \tag{2}$$

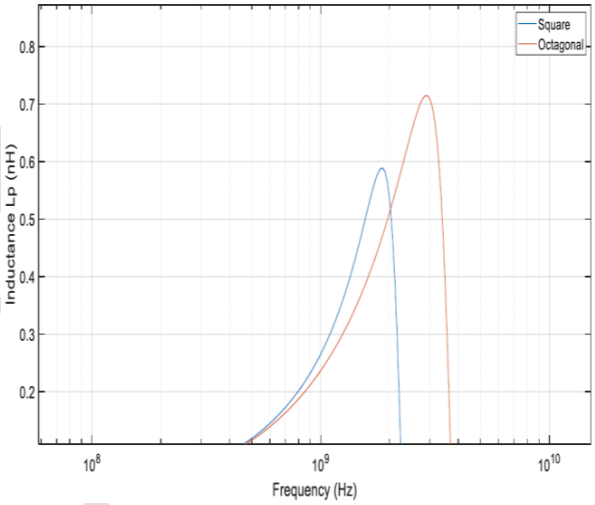


Fig.5. Inductances of square and octagonal microtransformers.

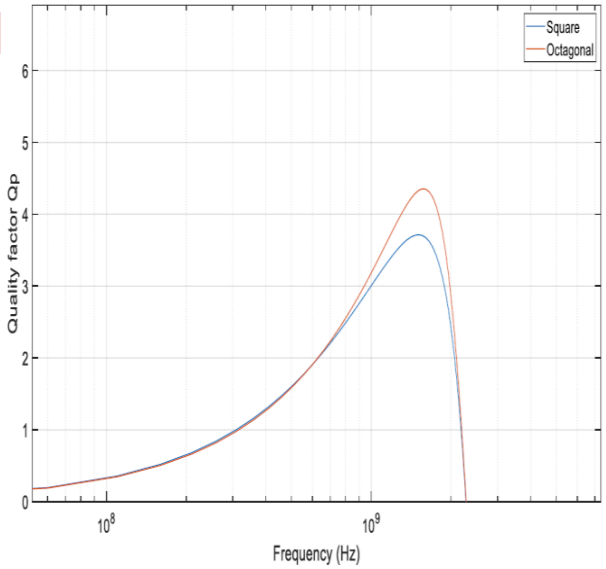
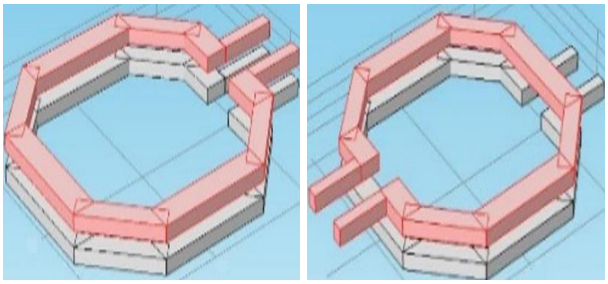


Fig.6. Quality factors of square and octagonal microtransformers.

It is noticed in Fig.6 that for the same diameter, the octagonal microtransformer has lightly better quality factor. This means that the reduction of this topology brings to the resistance and capacitance of the coils is proportionally more substantial than the reduction on the inductance.

IV. FEED LINES POSITION



(a) (b)

Fig.7. Non-flipped (a) and flipped (b) microtransformer topologies.

The primary and secondary coils are superimposed and they are completely covered, so their feed lines overlap (Fig.7.a). Fig.7.b shows the flipped microtransformer which consists in a 180-degrees rotation of one of the coils. The uncovered zones of the feed lines tend to weaken their coupling. The choice between these configurations should be made in function of their performance.

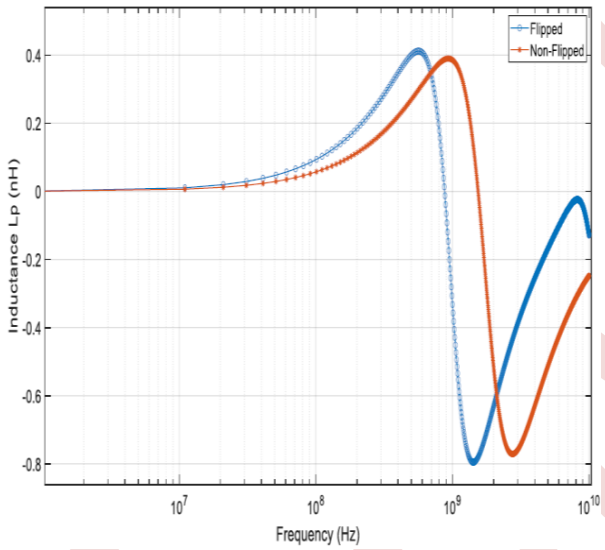


Fig.8. Flipped and non-flipped inductances.

The measurement results for flipped and non-flipped microtransformers are presented in Fig.8. The curves illustrate an important reduction of the resonant frequency with the flipped topology. In low frequencies, the inductances remain unchanged and the magnetic coupling is weaken, this decrease results typically from the augmented oxide and substrate capacitance that the flipped topology presents. For frequencies greater than 1 GHz, the magnetic coupling is significantly lower. Therefore, the flipped transformer demonstrates a lower minimum insertion loss, however the non-flipped transformer presents a proper performance for a wider band.

V. CHARACTERIZATION OF THE MICROTRANSFORMER

From the electrical model (Fig.3), scattering parameters characterize the electrical behaviour of the microtransformer completely [9][14]. As shown in Fig.9, the curves of S11 and S22 display an inductance characterization. S11 shows a nearly short circuit at low frequencies (100MHz). Therefore, S22 shows a very low impedance over the whole frequency range. The transformer have a self-resonance frequency of about 2,3 GHz. S12 and S21 represent the transmission coefficients, they are commonly called gain or attenuation. The simulation was performed in the range between f=100MHz and f=10 GHz.

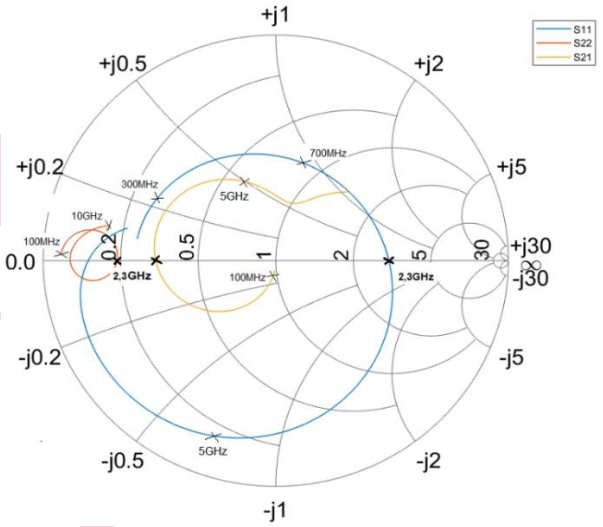


Fig.9. Scattering parameters S11, S22 and S21 of the microtransformer

The coupling coefficient k of the octagonal microtransformer is given by (Equation 3) [8];

$$k = \frac{M}{\sqrt{L_p.L_s}} = \sqrt{\frac{(Y_{11}^{-1}-Z_{11}).Z_{22}}{Im(Z_{11}).Im(Z_{22})}} \quad (3)$$

M is the mutual inductance between the two coils (Equation 4) [8];

$$M = \sqrt{(Y_{11}^{-1} - Z_{11}).\frac{Z_{22}}{\omega^2}} \quad (4)$$

Fig.10 shows the coupling coefficient k versus frequency. A k-factor of 0.9 at the operating frequency (1GHz) is a very high value for the microtransformer.

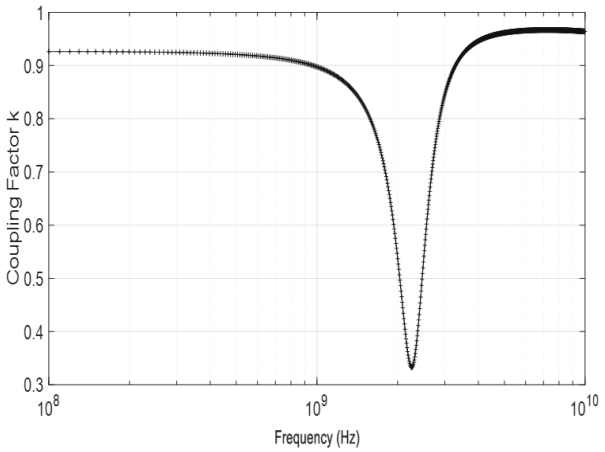


Fig.10. Coupling coefficient k over frequency

VI. GEOMETRIC DIMENSIONS OF COILS

It is necessary to study the sizing of the coils and to show the impact of the different geometric dimensions on the transformer performances. Fig.11 illustrates the measurement results with different outer diameters. We observe that the quality factor increases when the outer diameter increases. The maximum values of the quality factors remain unchanged before the partial operating frequency. Thus, the Q factor is superior for the smaller microtransformer when the frequency increases.

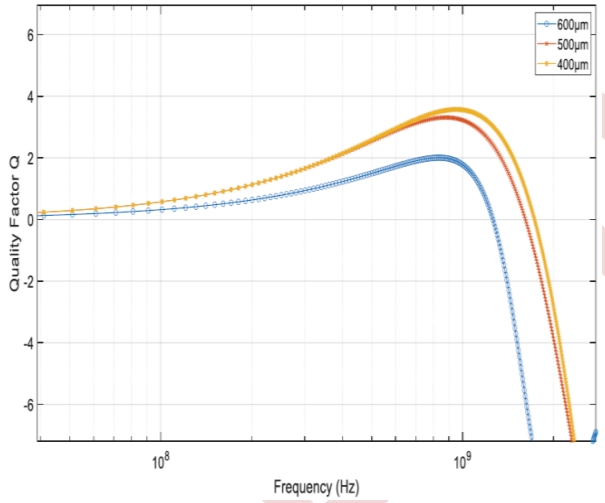


Fig.11. Quality factor over frequency with different outer diameters

Fig.12 illustrates the measurement results with different width. We observe that the Q factor is higher when the traces are thinner. For lower frequencies the 60µm wide transformer has a better Q, however the quality factor of the 40µm wide transformer is superior for higher frequencies. The increase of the Q factor for thin width traces is compensated by a reduction on the equivalent capacitance, which is related to the surface occupied by the microtransformer.

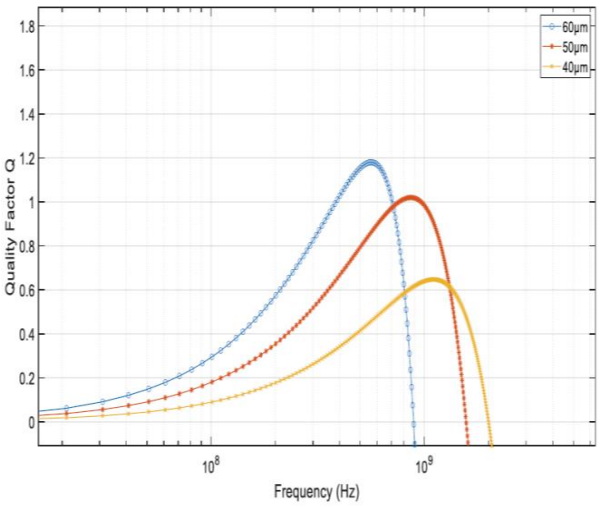


Fig.12. Quality factor over frequency with different width traces

VII. SIMULATION OF THE FLYBACK CONVERTER

In order to validate our model, we simulated the operation of Flyback converter containing the integrated microtransformer, by PSIM 9.0 software (Fig.13). The specifications of conditions are as follows :

Input voltage: V_{in} = 12 V

Output voltage: V_{out}= 5 V

Output power: P_{out} = 5 watt

Operation frequency: f = 1 GHz

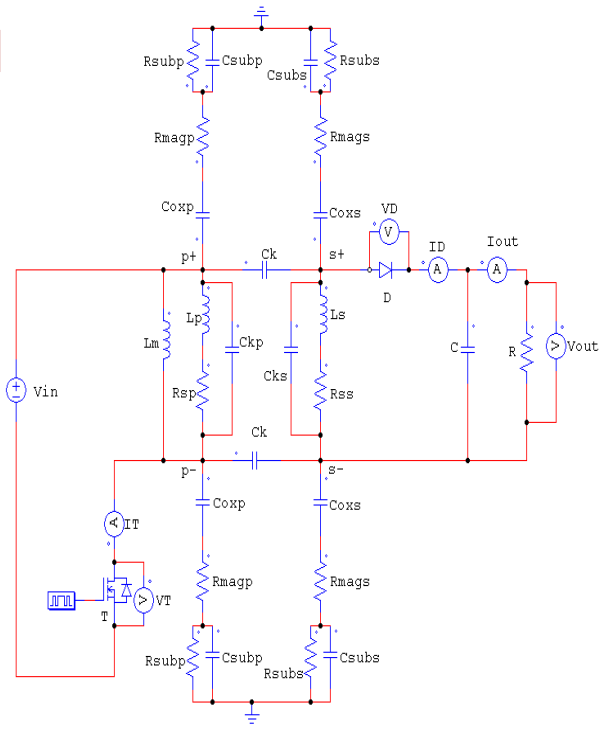


Fig.13. Flyback with the integrated microtransformer

Fig.14 shows the output voltage and current waveform of the Flyback converter.

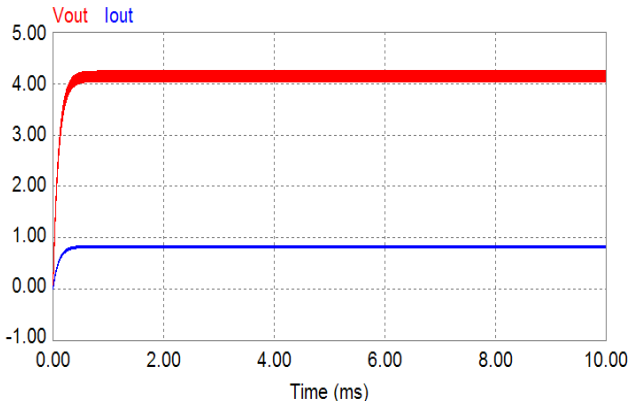


Fig.14. Output voltage and current of flyback with the integrated microtransformer

We notice in Fig.14 that it exist two regimes of converter operation: transient and steady state. The output voltage and current are 4.24 V and 0.84 A instead of 5 V and 1 A respectively. This decrease is due to drop voltage across the diode and the transistor, the resistive losses in the conductors and then the magnetic core losses. The output power corresponds to 3.6 W instead of 5 W.

VIII. ELECTROMAGNETIC AND THERMAL EFFECTS

By using COMSOL Multiphysics 6.0 software, which is based on finite elements method, 3D electromagnetic and thermal effects simulations (Fig.15) are done on the octagonal microtransformer at frequency of 1 GHz.

The Maxwell equations [6][15] are the partial derivatives that link the magnetic phenomena characterized by the magnetic induction B and the magnetic field H, to the electrical phenomena characterized by the electric induction D and the electric field E, the current densities J and the densities of free electric charges *ρe* (Equations 5 to 8);

$$\nabla \times \vec{E} = -\frac{\partial \vec{B}}{\partial t} \quad (5)$$

$$\nabla \times \vec{H} = \sigma \cdot \vec{E} + \frac{\partial \vec{D}}{\partial t} \quad (6)$$

$$\nabla \cdot \vec{D} = \rho_e \quad (7)$$

$$\nabla \cdot \vec{B} = 0 \quad (8)$$

$\vec{E}$: Electric field [V/m],

$\vec{B}$: Magnetic flux density [T],

$\vec{D}$: Displacement field [C/m²],

$\vec{H}$: Magnetic field [A/m].

Equation (9) calculates the distributed temperature in the microtransformer [16].

$$\rho \cdot C_p \cdot \frac{\partial T}{\partial t} - \nabla(k\nabla T) = q \quad (9)$$

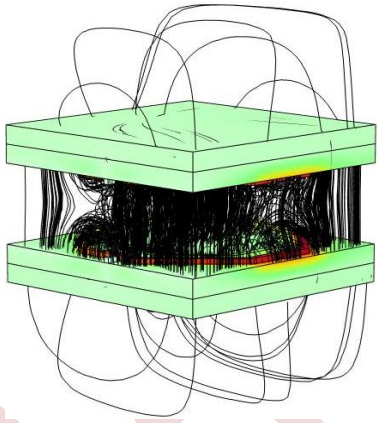
T: Calculate temperature

ρ: Density [kg/m³]

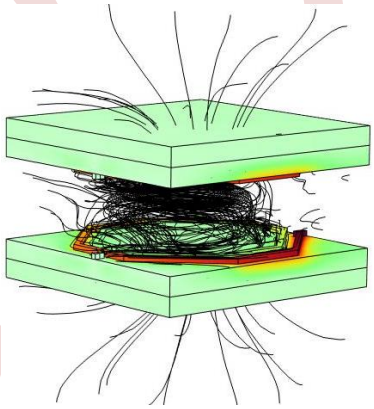
C_p: Heat capacity [J/K.kg]

k: Thermal conductivity [W/m.K]

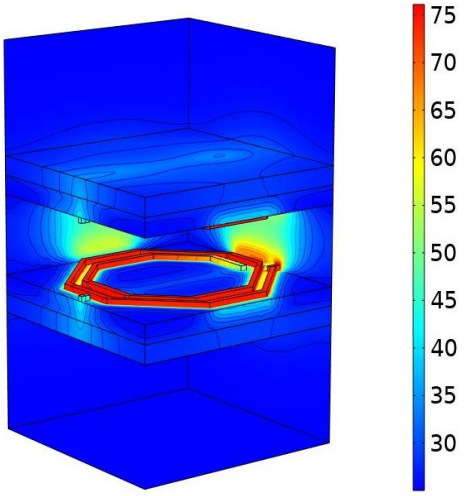
q: Heat source



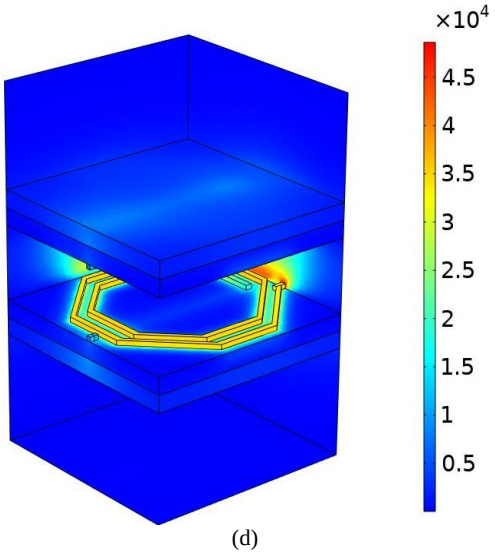
(a)



(b)



(c)



(d)

Fig.15. Different effects in the octagonal microtransformer: (a) Distribution of magnetic field lines, (b) Power flow, (c) Temperature distribution, (d) Enthalpy

Fig.15 illustrates the distribution of magnetic field lines, the power flow, temperature distribution and the enthalpy in the octagonal microtransformer. We notice that the high permeability of the magnetic core in ferrite NiZn allows to confine the majority of the magnetic field lines and the power flow in order to limit to disturb the close components adjacent to the microtransformer. The magnetic core allows also to decrease the temperature and the enthalpy caused by the current circulation which creates the Joule effects in the coils.

IX. CONCLUSION

This paper presents the modeling of RF octagonal microtransformer integrated in Flyback converter. The first considered parameter was the shape of spiral coils. Octagonal spiral microtransformer presents a higher quality factor than the spiral square form. Furthermore, the effect of the feed lines position of the two spiral coils is important. It was observed that the flipped microtransformer can achieve lower losses, however the non-flipped topology presents a high magnetic coupling. Moreover, the insertion of magnetic core in ferrite with high permeability allows to confine the magnetic field lines, to limit the spread of the heat and decease the temperature in order to avoid to disturb the close components in the integrated circuits. In the last step of this work, the equivalent electrical circuit of the microtransformer was integrated in the converter in order to test the good operation and to validate the results. We conclude that the results of simulations obtained throughout this paper are compatible with the integration in electronics and there are an accordance with the literature.

REFERENCES

[1] Mina Danesh and John R. Long, Differentially Driven Symmetric Microstrip Inductors, IEEE Trans. Microwave Theory and Techniques, vol. 50, Jan. 2002

[2] M. D'Amore, F.Maradei, S. Cruciani, M. Feliziani, "High frequency performance of carbon nanotube-based spiral inductors", EMC Europe –Int. Symposium on EMC, Bruges, Belgium, Sept. 2-6, 2013

[3] J. W. Hooker et al., "An Empirical Expression to Predict the Resonant Frequencies of Archimedean Spirals," IEEE Trans. Microw. Theory Tech., vol. 63, no. 7, pp. 2107–2114, Jul. 2015

[4] Yang-Hun Yun, Te-Yu J. Kao, K.O. Kenneth, "Variable inductors in CMOS for millimeter-wave applications", IEEE Electron Device Letters, Vol. 33, No. 7, July 2012

[5] S. Abi, H. Bouyghf, A. Raihani, B. Benhala, "Swarm intelligence optimization techniques for an optimal RF integrated spiral inductor design," in 2018 International Conference on Electronics, Control, Optimization and Computer Science (ICECOCS), Kenitra, Morocco, 1–7, 2018

[6] Omar ElSherbiny, Subhanwit Roy, Sadaf Charkhabi, Adam R. Carr, Andee M. Beierle, Nigel F. Reuel, Nathan M. Neihart, "Physically Inspired Circuit Model for Systematic Analysis of Resonant Ion Sensor ",978-1-7281-3320-1/20, IEEE Xplore 2020

[7] Vasjanov, A.; Barzdenas, V. A Review of Advanced CMOS RF Power Amplifier Architecture Trends for Low Power 5GWireless Networks. Electronics 2018, 7, 271

[8] Lim, A.; Tan, A.; Kong, Z.H.; MA, K. A Design Methodology and Analysis for Transformer-Based Class-E Power Amplifier. Electronics 2019, 8, 494

[9] Kaymaksut, E.; Zhao, D.; Reynaert, P. Transformer-Based Doherty Power Amplifiers for mm-Wave Applications in 40-nm CMOS. IEEE Trans. Microw. Theory Tech. 2015, 63, 1186–1192

[10] Zhang, D.; Yu, H.; Kumar, T.B.; Men, K.; Lu, M.; Yu, X.; Design of Millimeter-wave Transformer Balun with Isolation Circuit in Silicon Based Technology. In Proceedings of the International Symposium on Integrated Circuits (ISIC), Singapore, 12–14 December 2016; pp. 1–3

[11] Mariappan, S.G.; Moazenzadeh, A.; Wallrabe, U. Polymer Magnetic Composite Core Based Microcoils and Microtransformers for Very High Frequency Power Applications. Micromachines 2016, 7, 60

[12] C.H. Liu, H.D. Chang, K.H. Li, C.H. Lin, C.J. Hsu, T.Y. Lin, H.H. Chou, Adaptable and integrated packaging platform for MEMS-based combo sensors utilizing innovative wafer-level packaging technologies, in IEEE Electronic Components and Technology Conference (ECTC) (2013), pp. 1675–1681

[13] Haitao Gan, On-Chip Transformer Modeling, Characterization, and Applications in Power AND Low Noise Amplifiers, Doctoral dissertation, Department of Electrical Engineering, Stanford University, March 2006

[14] P. Pereira, M. H. S. Fino, F. V. Coito, M. V. Neves, "RF integrated inductor modeling and its application to optimization-based design," Analog Integrated Circuits and Signal Processing, 73, 47–55, 2011

[15] D. Karaboga, B. Akay, "A comparative study of Artificial Bee Colony algorithm," Applied Mathematics and Computation, 214(1), 108–132, 2009

[16] O. El-Gharniti, E. Kerherve, and J. B. Begueret, "Characterization of si-based monolithic transformers with patterned ground shield," in IEEE Radio Frequency Integrated Circuits (RFIC) Symposium, 2006.

VIII

RENEWABLE AND SUSTAINABLE ENERGY (RSE)

Sommaire

VIII.1 Direct vector control and particle swarm optimisation in dual star induction generator . . . 369
VIII.2 Energy management of a non-autonomous photovoltaic station for hybrid vehicle loading . . . 375
VIII.3 Management of a hybrid system of renewable energies in pumping . . . 381
VIII.4 A control strategy of dual stars induction generator with power limitation . . . 387
VIII.5 A finite state machine based energy management for fuel-cell hybrid vehicle . . . 393
VIII.6 Robust control of dfig wind turbines in sub/super-synchronous operation using integral backstepping controller . . . 399
VIII.7 Control of a wind turbine based on dfig by improved direct torque control using fuzzy logic . . . 404
VIII.8 Enhancing photovoltaic array performance through optimizing power during mismatch conditions under Series-parallel (SP) and Total Cross-Tied (TCT) configurations . . . 408
VIII.9 Sizing and energy management of a multi-source pumping system . . . 413
VIII.10 Characterization and mitigation of multipeak phenomena in photovoltaic systems under environmental conditions and electrical fault . . . 419
VIII.11 Power management strategy for stand-alone DFIG-based wind turbine with battery storage . . . 423
VIII.12 Enhancing wind energy conversion system efficiency with fuzzy logic controllers for doubly fed induction generators . . . 429
VIII.13 Enhancement DTC control for SEIG in variable-speed wind turbines, associated with a energy storage system . . . 435
VIII.14 Fuzzy logic MPPT algorithm for standalone photovoltaic water pumping system using separately excited DC motor . . . 441
VIII.15 Artificial intelligence technique to compare between the performance of different technologies of PV Modules in the photovoltaic systems . . . 447
VIII.16 Wind energy conversion system based on dual stator windings permanent magnet synchronous generator fed by multilevel converter . . . 451

VIII.17 Grid-connected multi-source energy systems: control and management **458**
VIII.18 Comparative analysis of P&O, PSO, and ANN methods for MPPT in photovoltaic systems **464**
VIII.19 Energy management strategy of PV system with battery supercapacitor hybrid energy storage for stand-alone applications **469**
VIII.20 Energy management for renewable electricity production system including hybrid hydrogen sub-system **474**
VIII.21 Model predictive for enhancing resistive droop control stability in isolated AC microgrid **480**
VIII.22 Study and manufacture of a parabolic solar concentrator with automatic tracking - Experimental tests **484**
VIII.23 Robust input-output linearizing and decoupling control of wind turbine based on DFIG under variable wind speed **490**
VIII.24 Optimal location and sizing of DG using fuzzy logic for improving voltage profile and reducing power losses **496**
VIII.25 Enhancement of fuzzy direct torque control performances for doubly fed induction generator wind turbines **501**
VIII.26 Power management for Hybrid Electric Vehicles (HEVs) based on Permanent Magnet Synchronous Motors (PMSMs) using passivity control **506**

Direct Vector Control and Particle Swarm Optimisation in Dual Star Induction Generator

Katia Benamara, Hocine Amimeur, Yanis Hamoudi

Laboratoire de Maîtrise des Energies Renouvelable (LMER), Bejaia, Algeria

katia.benamara@univ-bejaia.dz

hocine.amimeur@univ-bejaia.dz

yanis.hamoudi@univ-bejaia.dz

***Abstract*—This paper deals with the modeling and the control of a dual stator induction generator (DSIG) integrated into a wind energy conversion system with a variable speed wind turbine. DSIG is increasingly used because of its advantages in better reliability and supply division. Direct field-oriented control was therefore employed in this work and incorporated into the generator to control the torque and flux. Conventional setting of the PID controller gain usually results in significant overshoot, so modern heuristic approaches such as the particle swarm optimization (PSO) algorithm are used to improve the capability of traditional techniques, this will facilitate the determination of design parameters and reduce computation time. Simulation results based on MATLAB/Simulink are presented and discussed.**

***Keywords:* Dual star induction generator, direct vector control, particle swarm optimization.**

I. INTRODUCTION

Following strong industrialization, electric energy will always be an energy that humanity cannot do without it. Fossil fuels have long been used in the production of electrical energy, these fossil fuels are causing harmful damage to the environment. To meet the high demand for energy and at the same time keep the environment safe, the majority of countries have opted for the use of renewable energies. These energies are inexhaustible, clean, and do not create greenhouse gases, unlike fossil fuels. Among the renewable energies, wind energy is experiencing significant growth and is considered a mature and economical technology [1].

The power rating of an AC drive system can be increased by using a multiphase drive system that has more than three phases in the stator of the machine. Multiphase drive systems offer several advantages over conventional three-phase drives, such as reduced rotor harmonic currents, power segmentation, and high reliability. This is why multiphase induction machine drives are mainly used in high-power and/or high-current applications, such as electric ship propulsion, locomotive traction, and electric/hybrid vehicles. A very interesting multiphase solution discussed in the literature is the double stator (double three-phase) induction machine (DSIM) having two sets of three-phase windings spatially offset by 30 electrical degrees [2].

Vector control was originally introduced by Blascke in 1972. However, it was only possible to implement and use it with the advances in micro-electronics. It requires calculations of Park transforms, evaluation of trigonometric functions, integrations, regulations, etc., which could not be carried out using pure analog. In this paper, direct vector control was used, where the flux is regulated by feedback and is estimated and reconstituted from the stator currents and the pulsation [3].

PID (Proportional-Integral-Derivative) controllers have been widely used for speed and position control in diverse applications. To improve the capabilities of traditional PID parameter tuning techniques, several intelligent approaches have been approached to improve PID tuning, such as those using genetic algorithms (GA) and particle swarm optimization (PSO). With the advance of computational methods, optimization algorithms are often proposed to tune the control settings to find optimal performance [4].

This work aims to analyze the use of direct vector control and particle swarm optimization in a dual stator induction generator.

II. MODELING OF THE WIND ENERGY CONVERSION SYSTEM

The wind energy conversion chain studied includes, in addition to the DSIG, inverters 1,2, the DC link voltage, inverter 3, and connection to the grid via a filter. Inverters 1 and 2 are used to control the speed and flux of the generator. This control is based on the MPPT algorithm. Inverter 3 controls the DC link voltage, the active and reactive power exchanged with the grid, and sets the current at the correct frequency using PI controllers. Figure 1 shows the scheme of the system under study.

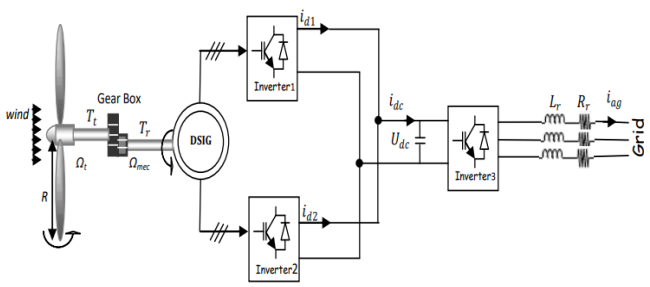


Figure 1. Block diagram of the wind power system based on DSIG.

a. Modeling of the Wind Turbine

The transmitted power, P_t, captured by the wind turbine, is given by expression (1).

$$P_t = 0.5C_p(\lambda)\rho S V^3. \quad (1)$$

Where C_t is the power coefficient, S is the area swept by the blades, ρ the air density, and V is the wind speed. The torque of the turbine is the ratio of the transmitted power to the shaft speed, Ω_t. It is given by:

$$T_t = \frac{P_t}{\Omega_t}. \quad (2)$$

The gearbox adapts the generator to the turbine. The generator torque T_g and the speed Ω_t are given by:

$$T_g = \frac{T_t}{G}, \Omega_t = \frac{\Omega_{mec}}{G}. \quad (3)$$

The mechanical equation can be expressed as:

$$J p\Omega_{mec} = T_{em} - T_g - f\Omega_{mec}. \quad (4)$$

The power coefficient is the aerodynamic efficiency of a wind turbine and its evolution is specific to each turbine and wind speed. It depends on the blade pitch angle β and the speed ratio λ which is expressed by:

$$\lambda = \frac{R\Omega_t}{V}. \quad (5)$$

Where R is the blade radius.

$$C_p = \left[0.5\left(\frac{116}{\lambda'}\right) - 0.4\beta - 5\right]\exp\left(-\frac{21}{\lambda'} + 0.0068\lambda\right). \quad (6)$$

With, $\lambda' = [\frac{1}{\lambda+0.08\beta} - 0.035(\beta^3+1)]^{-1}$.

For the value $\beta = 0$, the graph of $C_p(\lambda)$, given in Fig. 2, is plotted using expression (6). The conversion device extracts

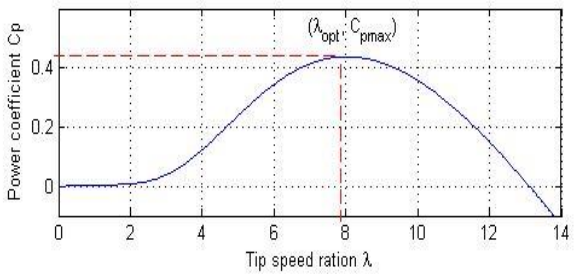


Figure 2. Graph of C_p function λ

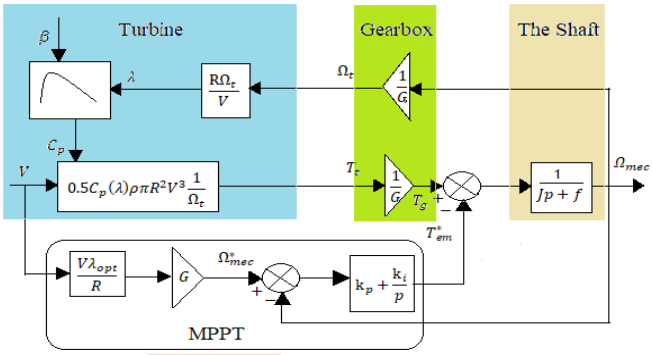


Figure 3. Block diagram of the turbine model with variable speed control

less power than is theoretically recoverable because of the non-zero speed of the air masses upstream of the turbine. This presents a theoretical limit known as the Betz limit, which corresponds to a C_{pmax} [5].

The maximum power point tracking (MPPT) algorithm permits to maximization of the electric power extracted from the wind energy. The tip speed ratio should be kept around its optimal value, λ_{opt}. The reference speed Ω^*_{mec} can be written as:

$$\Omega^*_{mec} = \frac{R\lambda_{opt}}{V}G. \quad (7)$$

The block diagram of the turbine model with the control of the speed is represented in Fig. 3.

b. Modelling of the DSIG

The generator comprises a rotor winding and two stator windings which are moved at an electrical angle. The stator windings are 180 degrees apart and are supplied by a balanced voltage system. The rotor is of the squirrel cage type and comprises conductor rings that short-circuit the conductor bars at each end of the rotor. The mathematical model of the generator is derived from Park's theory to simplify the differential equations [6].

The electrical equations of the DSIG along the direct and quadrature axes (d, q) related to the field are given by [7]:

$$\begin{cases} v_{d1} = r_1 i_{d1} + p\varphi_{d1} - \omega_e\varphi_{q1}. \\ v_{q1} = r_1 i_{q1} + p\varphi_{q1} + \omega_e\varphi_{d1}. \\ v_{d2} = r_2 i_{d2} + p\varphi_{d2} - \omega_e\varphi_{q2}. \\ v_{q2} = r_2 i_{q2} + p\varphi_{q2} + \omega_e\varphi_{d2}. \\ v_{dr} = r_r i_{dr} + p\varphi_{dr} - (\omega_e - \omega_r)\varphi_{qr} = 0. \\ v_{qr} = r_r i_{qr} + p\varphi_{qr} + (\omega_e - \omega_r)\varphi_{dr} = 0. \end{cases} \quad (8)$$

The expressions for stator and rotor flux linkages are:

$$\begin{cases} \varphi_{d1} = L_1 i_{d1} + L_m(i_{d1} + i_{d2} + i_{dr}). \\ \varphi_{q1} = L_1 i_{q1} + L_m(i_{q1} + i_{q2} + i_{qr}). \\ \varphi_{d2} = L_2 i_{d2} + L_m(i_{d1} + i_{d2} + i_{dr}). \\ \varphi_{q2} = L_2 i_{q2} + L_m(i_{q1} + i_{q2} + i_{qr}). \\ \varphi_{dr} = L_r i_{dr} + L_m(i_{d1} + i_{d2} + i_{dr}). \\ \varphi_{qr} = L_r i_{qr} + L_m(i_{q1} + i_{q2} + i_{qr}). \end{cases} \quad (9)$$

The electromagnetic torque is evaluated as:

$$T_{em} = P\frac{L_m}{L_m + L_r}(i_{q1} + i_{q2})\varphi_{dr} - (i_{d1} + i_{d2})\varphi_{qr}. \quad (10)$$

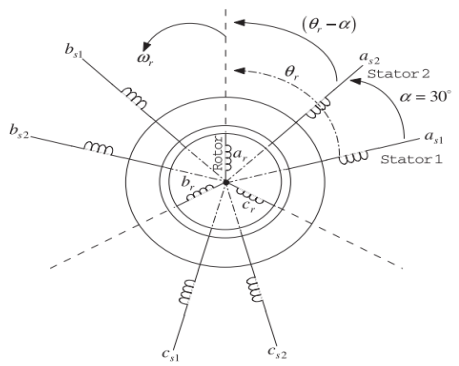


Figure 4. Schematic of dual stator induction generator.

The active and reactive power at the stator as well as those provided for the grid are defined as:

$$\begin{cases} P_s = v_{ds1}i_{ds1} + v_{qs1}i_{qs1} + v_{ds2}i_{ds2} + v_{qs2}i_{qs2}. \\ Q_s = v_{qs1}i_{ds1} - v_{ds1}i_{qs1} + v_{qs2}i_{ds2} - v_{ds2}i_{qs2}. \end{cases} \quad (11)$$

III. Direct Field-Oriented Control of DSIG

Vector control achieves a natural decoupling of flux and torque control, as in the case of a separately excited DC machine. The control strategy is specific to a drive and a given load specification [8]. Controlling the MASDE by flux orientation consists of regulating the flux by one component of the current and the torque by the other component.

To do this, we need to choose a control law and a system of axes that will ensure the decoupling of flux and torque.

However, by choosing the orientation of the rotor flux along the d axis $(\varphi_{dr} = \varphi_{qr})$ and $\varphi_{qr} = 0$, we will have the following form of electromagnetic torque form:

$$T_{em} = \left(P\frac{L_m}{L_m+L_r}\right)\left(\frac{i_{q1}+i_{q2}}{\varphi_r}\right) = k''\varphi_r i_q. \quad (12)$$

With $k'' = P\frac{L_m}{L_m+L_r}$ and $i_q = i_{q1} + i_{q2}$.

For the choice of flux orientation in the MASDE, we opt for the choice of rotor flux orientation $(\varphi_{dr} = \varphi_{qr})$ and $\varphi_{qr} = 0$, because this results in a variable speed drive where the

electromagnetic flux and torque are independently controlled via the stator currents [3].

For direct vector control, the rotor flux module will be controlled by feedback. To this end, a rotor flux estimator φ_r is implemented from measurements of i_{ds} and i_{sq} and the rotor current pulsation ω_r imposed on the machine [8]. The MFOC coupling block diagram is shown in Fig. 5.

IV. Tunning PID Controller Using Particle Swarm Optimization

PSO, as an optimization tool, provides a population-based search procedure in which individuals, called particles, change their position (state) as a function of time. In a PSO system, particles fly in a multi-dimensional search space. During the flight, each particle adjusts its position according to its own experience (this value is called P_{best}), and according to the

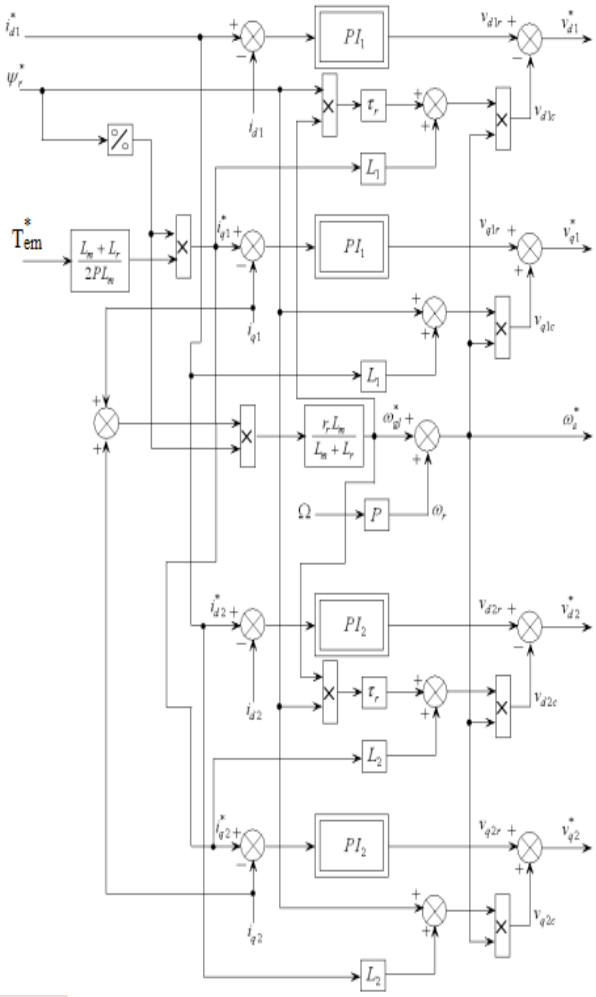


Figure 5. Schematic representation of the decoupling block of MFOC.

experience of a neighboring particle (this value is called G_{best}), using the best position encountered by itself and its neighbor. This modification can be represented by the concept of speed. The following equation can modify the speed of each agent:

$$v^{k+1} = w.v^k + c_1.rand(P_{best} - x^k) + c_2.rand(G_{best} - x^k). \quad (13)$$

Using the equation above, a certain speed that gradually approaches P_{best} and G_{best} can be calculated. Using the equation above, a certain velocity can be calculated which gradually approaches P_{best} and G_{best}. The following equation can modify the current position:

$$x^{k+1} = x^k + v^{k+1}, k = 1,2,\dots,n. \quad (14)$$

Where $x^k$is the current searching point, x^{k+1} is the modified searching point, v^k is the current velocity, v^{k+1} is the modified velocity. P_{best} is the best solution observed by the current particle and G_{best} is the best solution of all particles, w is an inertia weight, c_1 and c_2 are two positive constants, rand is a randomly generated number with a range of [0,1].

The PSO based approach to finding the global maximum value of the objective function is shown in Fig. 6.

TABLE I. PARAMETERS OF PSO ALGORITHM

Swarm size	30
Number of maximum iteration	50
$c_1 = c_2$	2
Inertia weight w	0.9

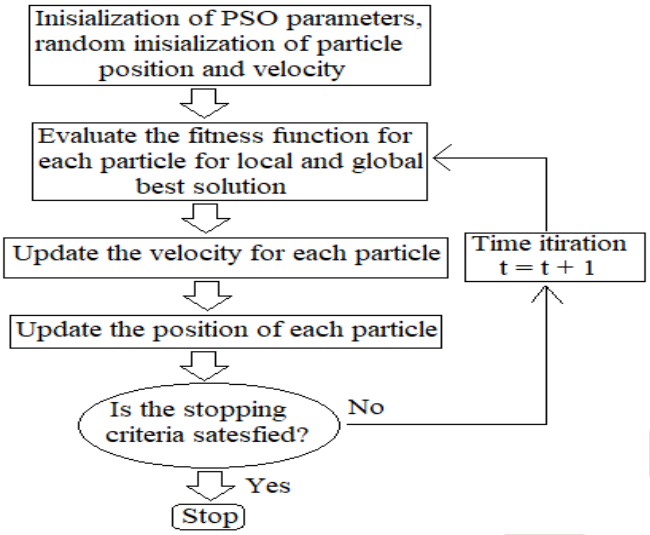


Figure 6. Flowchart of the PSO algorithm.

The PID controller is a good controller for machine control, but the problem is that the mathematical model of the installation must be known. To solve problems in the overall system, several methods have been introduced to tune the PID controller. Our proposed method uses the PSO method to determine the angular speed controller parameters (Kp, Ki, and Kd) [9].

The parameters of the PSO algorithm used in this work are shown in Table 1.

V. POWER CONTROL ON THE GRID SIDE

For grid connection, the control mode ensures that all available power extracted from the generator is correctly transferred to the grid. For the grid current vector to be in phase with the grid voltage vector, the reference reactive power Q^* must be zero. The DC link voltage control acts to provide the reference active power. The DC link voltage is governed by:

$$\frac{dU_c}{dt} = \frac{1}{c}\left(i_m - i_g\right). \quad (15)$$

The reference active power injected into the electrical supply network is given by:

$$P^* = U_c(i_m - i_c^*) = P_{dc_m} - P_{dc}^*. \quad (16)$$

Where $i_c^* = PI(U_c^* - U_c)$.

The PI controller is incorporated to maintain a constant DC link voltage.

VI. RESULTS

To verify the validity of this proposed work, a series of simulations of the behavior of the DSIG controlled by direct vector control and PSO were obtained using MATLAB/Simulink.

To gain a deeper understanding of the results achieved through the various approaches, PID-PSO and PID, it's essential to conduct a comprehensive comparison of their static and dynamic characteristics. This comparison should occur under identical operating conditions (which encompass references, and disturbance loads) and within the same simulation configuration

Speed control data from both controllers is showcased in Fig. 7, It is evident that utilization of the PID-PSO controller results in superior performance. This is characterized by a settling time without overshoot and a reduced steady-state error which is 0.3, in contrast to the PID controller with a steady-state error of 0.75. With the PID controller, there is a noticeable deviation in speed, which becomes more prominent when using the hybrid PID-PSO controller.

For this reason, the rest of this article will be connected to the presentation of other results using the proposed PID-PSO.

The figure in Fig. 8 depicts the changes in mechanical power applied to the DSIG's shaft. We observe minimal fluctuations during operation phases with mechanical speeds below the rated speed, while the power is restricted by a power-limiting mechanism when operating at speeds exceeding the nominal rating. The waveform of the electromagnetic torque generator follows its reference, Fig.9. The decoupling of the direct and quadratic rotor fluxes of the DSIG is illustrated in Fig.10. We can see that the quadratic rotor flux has zero value, as the oriented control field requires.

Fig. 11 represents the stator voltages and currents of the first star and the results for the 2nd star are similar to the 1st star. These reveal that the voltage and current are almost 180° out of phase. The evolution of DSIG stator currents in the first phase of each star at all simulation time is shown in Fig. 12 and between 18 and 18.06s, these currents are sinusoidal, displaced with $\alpha = 30°$.

The rotor current i_{ar} obtained is shown in Fig. 13, it evolves in the same way as the stator currents, but with different frequencies. Fig. 14 shows the total active and reactive stator power profiles of the DSIG. The active power has a negative sign, which means that DSIG generates this power, and the reactive power has a positive sign, which means that the machine is absorbing this energy needed for its magnetization. The DC link voltage is constant and follows its set level of 1130 V Fig.15.

The voltage and current profiles at the output of inverter 3 are given in Fig.16, it is apparent that the phase difference between the supply current and voltage is 180°, therefore the line side converter provides real power to the electrical network. The voltage and current grid and their zoom are given respectively in Fig.17. It is clear that the current has a sinusoidal form and opposite phase concerning the voltage meaning that power flows

from the aero generator to the grid. It can be seen from Fig.18 that the active and reactive grid powers follow acceptably by their references at all simulation times.

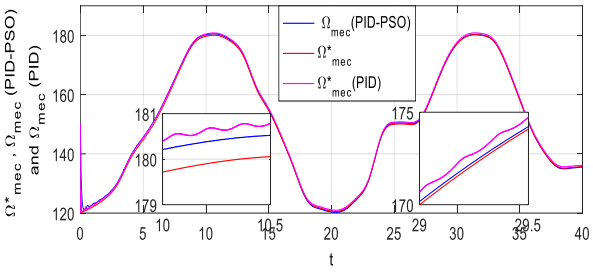


Figure 7. Random of the DSIG rotor speed.

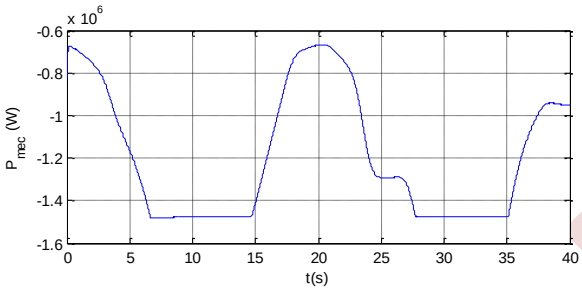


Figure 8. Wind generator mechanical power.

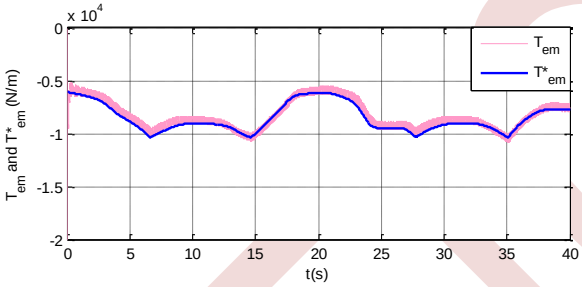


Figure 9. Generator torque.

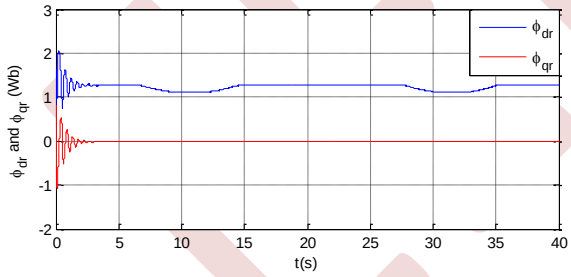


Figure 10. Direct and quadratic rotor flux.

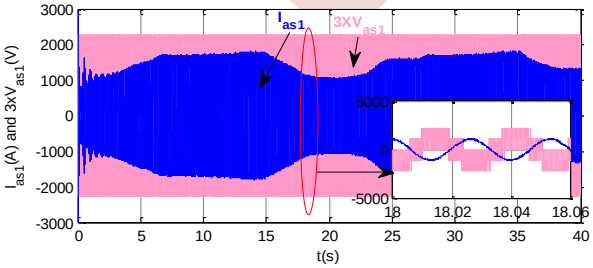


Figure 11. Stator current and voltage (phase as1).

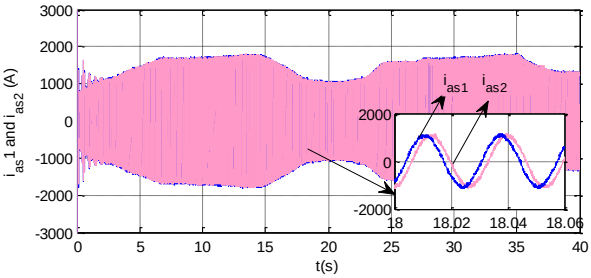


Figure 12. Stator currents (phases as1 and as2).

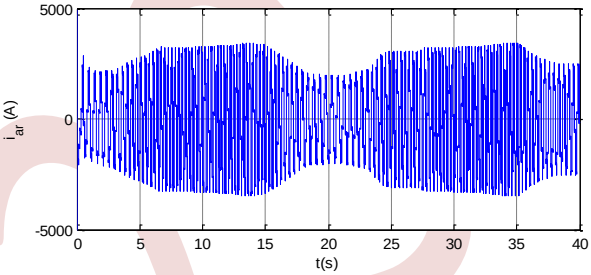


Figure 13. Rotor current.

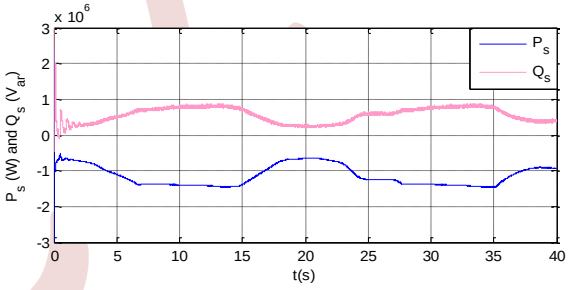


Figure 14. Stator active and reactive powers.

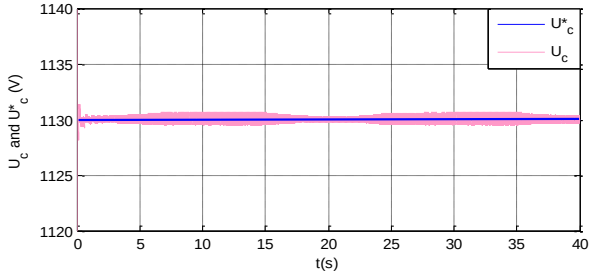


Figure 15. DC link voltage.

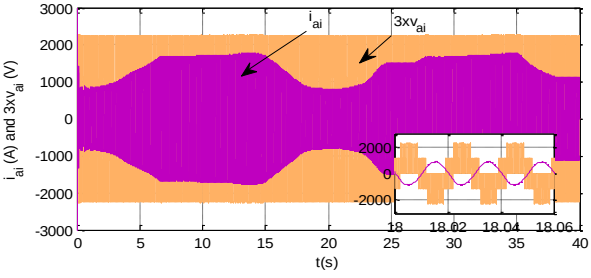


Figure 16. Current and voltage at the output of the inverter 3.

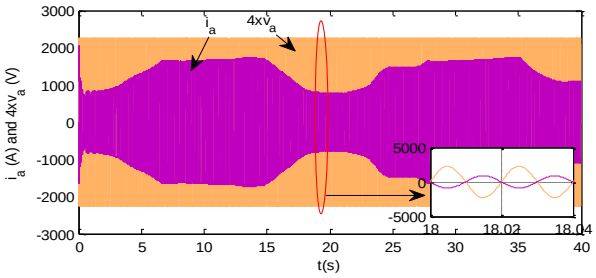


Figure 17. Grid current and voltage (phase a).

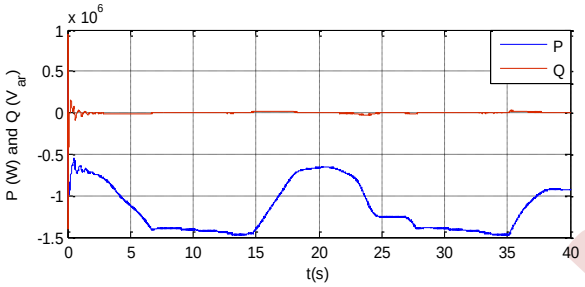


Figure 18. Grid active and reactive powers.

VII. Conclusion

An improved control of the DSIG in the wind energy conversion system connected to the grid has been presented. The PSO algorithm was proposed to optimize the PID speed controller and ensure that the DSIG speed follows its reference correctly and, that the steady-state error was reduced (0,3 for PID-PSO) Many authors have published several research papers on the vector control techniques of induction motor. And studying vector control techniques it is clear that direct vector control offers better performance than the indirect method in terms of accuracy and stability. In the remainder of the work, the method adopted is the direct vector control technique. Simulation results confirm the reliability of the techniques used, and it has been observed that the use of optimization techniques improves system efficiency.

References

[1] M. Boudarbala, B. Boussoufi, A. Lagrioui, M. Taoussi, H. Alami Aroussi, and Y. Ihedrane, "Direct and indirect vector control of a doubly fed induction generator based in a wind energy conversion system," Int. J. Electrical and Computer Engineering, vol. 9, no. 3, pp. 1531–1540, June 2018.

[2] H. Amimeur, D. Aouzellag, R. Abdessemed, and K. Ghedamsi "Sliding mode control of a dual-stator induction generator for wind energy conversion systems," Int. J. Electrical Power & Energy Systems, vol. 42 pp. 60–70, November 2012.

[3] H. Amimeur, "Contribution to the control of the double star induction machine by sliding mode control," in French, Magister dissertation, Hadj Lkhdar's University of Batna, Juin 2008.

[4] M. Iwan Solihin, L. Fook Tack, and M. Leap Kean, "Tuning of PID controller using particle swarm optimization (PSO)," in Proc. Int. Conf. Advanced Science, Engineering and Information Technology, Hotel Equatorial Bangi-Putrajaya, Malaysia, 14–15 January 2011.

[5] M. Benakcha, L. Benalia, F. Ameur, D.J. Tourqui, "Control of dual stator induction generator integrated in wind energy conversion system" in Journal of Energy Systems 2017, 1(1):21-31, DOI: 10.30521/jes.351269

[6] A. Ibrahim, Y. Jibril, G. A. Olarinoye, A. S. Abubakar, A. An Olaniyan, M. Mohammed, "A cuckoo search optimized control of dual stator induction generator in wind energy conversion system" in 2nd International Conference on Electrical Power Engineering, ICEPENG, 18 – 22 May 2021.

[7] K. Benamara, H. Amimeur, Y. Hamoudi, "Control of a dual stator induction generator integrated in a wind power system" in 1st International Conference on Renewable Solutions for Ecosystems: Towards a Sustainable Energy Transition, Djelfa University, 5 – 6 May 2023.

[8] L. Benalia, "Voltage control of double-fed induction motors," Doctoral thesis, Hadj Lkhdar's University of Batna, June 2010.

[9] Y. Bekakra, and D. Ben Attous, "Optimal tuning of PI controller using PSO optimization for indirect power control for DFIG based wind turbine with MPPT," Int. J. Syst. Assur. Eng. Manag. vol. 5, no. , pp. 219–22, July-Sept 2014.

Energy Management Of A Non-Autonomous Photovoltaic Station For Hybrid Vehicle Loading

Kamel Djermouni [1], Ali Berboucha [1], Kaci Ghedamsi [1], Djamal Aouzellag [1], Salah Tamalouzt [2]
[1] Laboratory of Renewable Energy Mastery (LMER), University of Bejaia- Algeria
kamel.djermouni@univ-bejaia.dz , ali.berboucha@univ-bejaia.dz , kaci.ghedamsi@univ-bejaia.dz , djamal.aouzellag@univ-bejaia.dz
[2] Laboratory of Industrial Technology and Information (LTII), University of Bejaia- Algeria
salah.tamalouzt@univ-bejaia.dz

***Abstract*— The aim of this paper is to develop an optimal energy management system for a non-autonomous photovoltaic station dedicated for charging a hybrid vehicle. This management is based on of a fuzzy logic controller with seven classes; the inputs of our controller are the state of charge of the battery group station and the sunshine for a day. The management system tries to consider all requirements and fit all possible case.**

***Keywords:* photovoltaic station, loading, energy management, fuzzy logic, lithium-ion batteries, hybrid vehicle.**

I. INTRODUCTION

In recent years, there has been a notable increase in the integration of renewable energy sources in electrical power systems to facilitate a cleaner and more sustainable approach to electricity generation. The renewable energy based generators (photovoltaic panels, wind turbines) have a random production, which is directly dependent upon the weather conditions (wind speed, sunshine and temperature.) [1]; to solve this problem, the energy storage is necessary for the exploitation of an intermittent production based on renewable energy [2-4]. Recent studies have shown that a storage capacity exceeding 2 or 3 days of autonomy is deemed unnecessary [5, 6]. Research interests are essentially related to the modeling [7–10], the optimization [11] and the adaptation system [12] of the photovoltaic panel supply according to the equipment needs. Other researches developed energy-management strategies so as to offer optimal function [13–15] the objective has been to help intensive penetration of photovoltaic (PV) production into the grid by proposing a peak shaving service by adding a storage system [16-17]. Energy management is still a contemporary research in the photovoltaic field. According to [18], the Fraunhofer-Institute of Solar Energy Systems has developed a new generation of battery-management system, which improves the storage lifetime and reliability of batteries. This battery-management system allows for new operating strategies not possible with conventional battery systems. In [19] an optimal energy management method for stand-alone photovoltaic system is presented. Their method exploits a predictive state of charge model to implement the control algorithm. Authors in [20] proposed an energy management control strategy for stand-alone PV system. Their strategy was based on the control of the un-directional DC–DC converter and bi-direction DC–DC converter. In [21] an energy management method that integrates maximum power tracking control, load power tracking control, fast charge with variable current and discharge control for battery is presented.

Electric vehicle charging stations have experienced great progress in recent years, the authors in [22-25] proposed some strategies for controlling an electric vehicle charging station for appropriate energy management and voltage regulation in a stand-alone micro-grid. In [26] a robust two-stage energy management of a hybrid charging station was proposed for a system composed of an electrolyze, a fuel cell and a hydrogen storage with the integration of a photovoltaic source. The authors in [27] adopted a real scenario for a multi-vector energy management system including an electrolyze for charging electric vehicles. In [28] propose an autonomous charging station based on solar energy coming from building envelopes for drones.

The aim of this work is to address the matter of producing photovoltaic electricity adapted for habitat applications, such as charging stations for electric or hybrid vehicles. This involves incorporating innovative electrochemical storage systems that use lithium-ion batteries. To achieve highly efficient and multifunctional systems, an optimization search method is used, based on fuzzy logic controller.

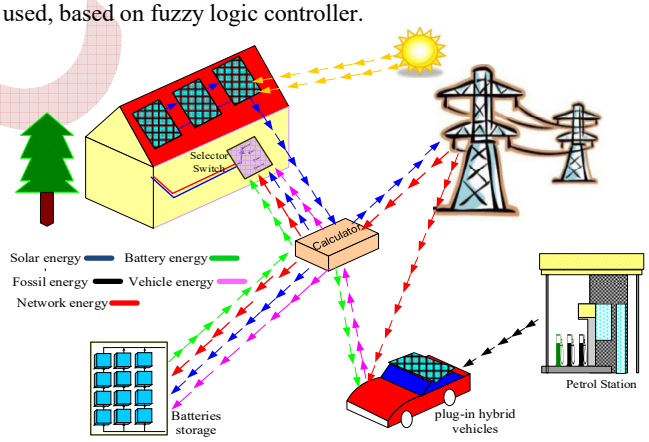


Figure 1. Energy exchange of a hybrid vehicle with different possible sources

II. DESIGN OF THE LOADING STATION

The aim is to size charging station for a hybrid vehicle with a storage capacity of 54 kWh; in the literature several authors use an overall correction coefficient K that considers: the observation uncertainty (in the order of ± 5%), module pollution over time (of the order of 5%), the integral of the crossing of the glazing module from all angles (of the order of 5%), aging of the modules (on the order of 5%), the dispersion

characteristics of the modules when they are connected in series (of the order of 5%), faradic battery performance (loss of about 10%). Taking into account all these parameters leads to a global correction coefficient (K) between 0.65 and 0.75 [22]. In this work we take a corrective coefficient K = 0.75 therefore the ability to group of batteries is 72 kWh.

III. MANAGEMENT OF PHOTOVOLTAIC SYSTEM

The main objective of designing the PV system is to ensure charging batteries of a hybrid vehicle, but good management of this facility can make very effective and versatile (home use, injection on the network, ...) by taking advantage of all the energy that can be produced by PV modules. For such management, several techniques can be used such as genetic algorithms [27], optimization by particle swarm and/or swarm of salps [30], neural networks with machine learning techniques [31] and fuzzy logic controller [32]. In this work we opted for fuzzy logic with forecasting weather conditions because of its robustness, flexibility and simplicity of implementation of the control model.

The bloc diagram of fuzzy controller proposed for the system management is shown in "figure 2". It receives as inputs sunshine *S (k)* (we did not take into account the temperature variation, since its influence on the PV power generated is very small compared to that of the sunshine) and the battery group state of charge *SOC (k)*, output will be the allowable power *FP (k)* for use outside the principal function of the system (battery charging).

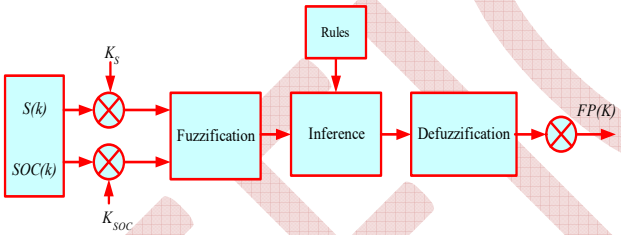


Figure 2. Block diagram of a fuzzy logic

The linguistic inputs of the fuzzy controller consist of seven fuzzy sets each, resulting in a total of forty-nine rules. These rules can be found in Table 1.

TABLE1. FUZZY RULES BASES

SOC / S	S	M_1	M_2	M_3	B_1	B_2	B_3
S	Z	Z	Z	Z	Z	Z	Z
M_1	Z	Z	Z	Z	Z	Z	S
M_2	Z	Z	Z	Z	Z	S	M_1
M_3	Z	Z	Z	Z	S	M_1	M_2
B_1	Z	Z	S	M_1	M_2	M_3	B_1
B_2	Z	S	M_1	M_2	M_3	B_2	B_3
B_3	M_1	M_2	M_3	B_1	B_2	B_3	B_3

"Figure 3" shows us the inputs *S(k)* and *SOC(k)*; and output *FP(k)* membership functions of fuzzy logic controller. Inputs are sunshine and battery group state of charge and the output of our controller is the allowable power.

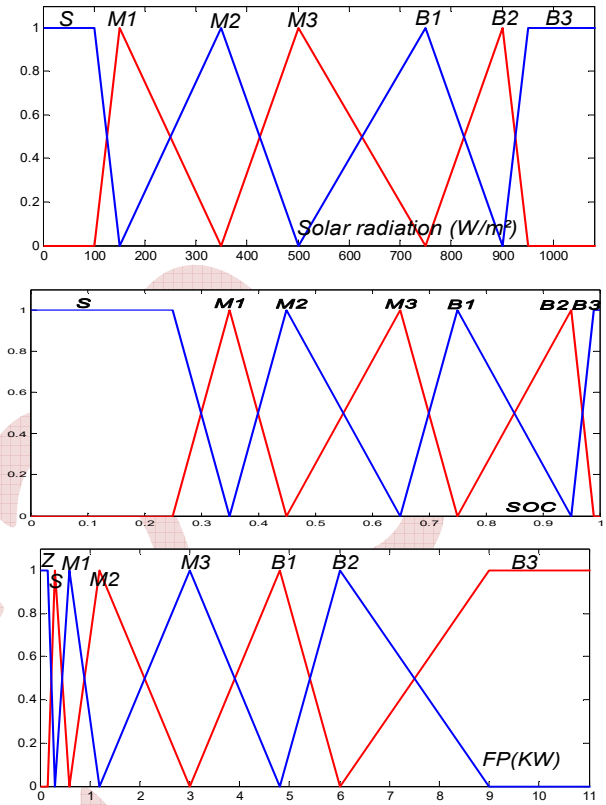


Figure 3. Membership function of each linguistic variables of the sunshine, the charge state of the battery and the output

A. Overall management Algorithm

In order to facilitate the understanding of the power management station flowchart (Figure 4), the following abbreviations were chosen:

- P_{pv} : Power produced by the PVG;
- *FP* : Power allowed by the fuzzy system to be used otherwise;
- *DP* : Power asking for domestic uses;
- P_{en} : Power exchanged with the public network;
- *PB* : Push button used to manually activate or deactivate battery charging according to the station's energy requirements and the user's will.
- D_{en}: Existence detector of public network (D_{en} = 1 if we can import energy public network, D_{en} = 0 if we cannot import energy public network or for a break or an overload against export is permitted in the latter case).

In this case the secondary function of the loading station is: domestic use and injection to the grid. For this, in addition to fuzzy management system, and in order to take full advantage of the photovoltaic generator, we have expanded our management algorithm for allowing the system to exchange energy in the maximum directions as shown in Figure 1, for better management and operation such as:

- For (*PB*=1 and *SOC*<1):
  - If the *DP* is greater than the *FP* the rest will be imported from network;
  - If the *DP* is below *FP*, surplus power will be injected into the grid if we are in the peak hours or it will be reused for battery charging;
- For (*PB*≠0 where *SOC*=1)
  $FP=P_{pv}$: All the energy produced by PVG is oriented to secondary uses:
  - If the *DP* is greater than the *FP*, lack will be imported from network;
  - If the *DP* is below *FP*, surplus power will be injected into the grid.

In this system a margin was left to the desire of the driver to use the energy stored in the vehicle batteries or produced by the panels installed on its roof as it expects by manual intervention.

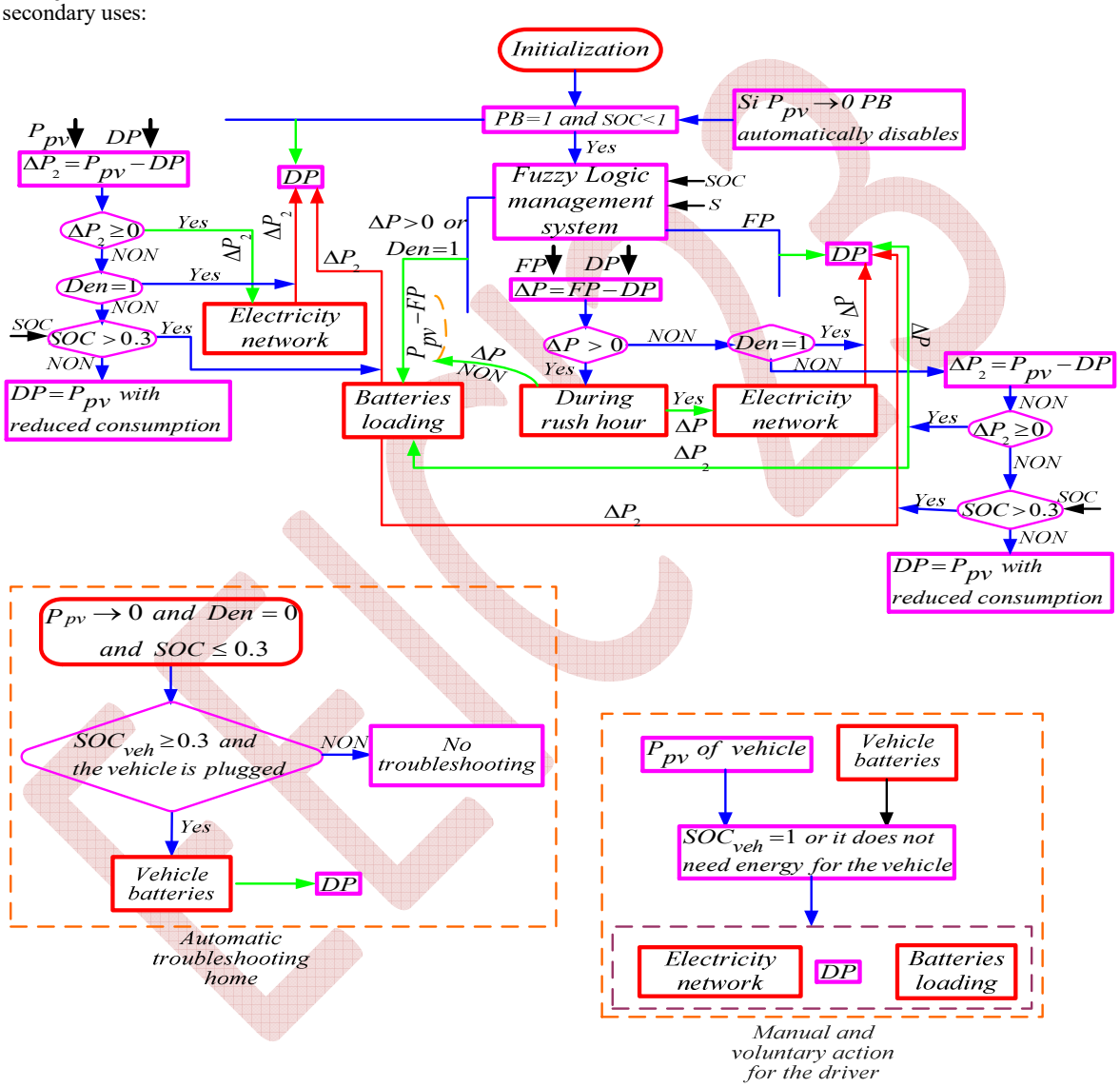
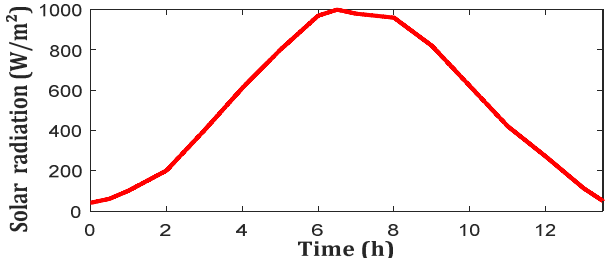


Figure 4. Flowchart of energy management

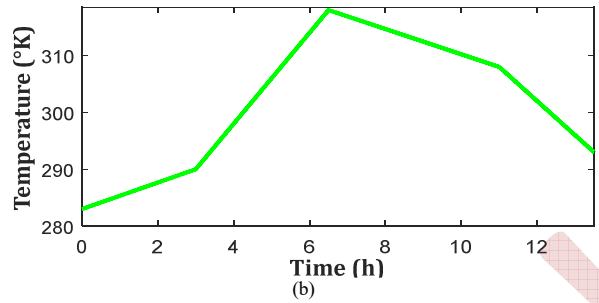
IV. SIMULATION AND INTERPRETATION OF RESULTS

To validate the efficiency of our algorithm, tests are carried out (the vehicle is disconnected for cases A to C). The maximum power of a PV module is 219.67 Watts with a current I_{ph} =8,214 A, for N_s =54 cells under normal conditions. The series and parallel resistances of PV module are respectively R_s =221,10^{-3} Ω and R_p =415.405 Ω.

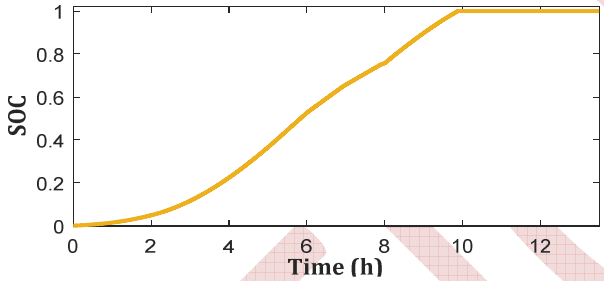
A. In the first case, it is assumed that the domestic needs are low and do not exceed 1kW, however the batteries are completely discharged (SOC_0=0), for favorable climatic conditions (an average day).



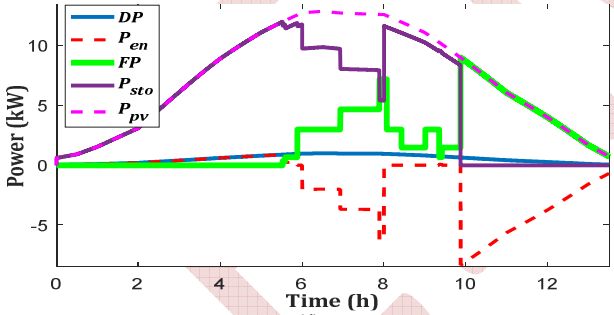
(a)



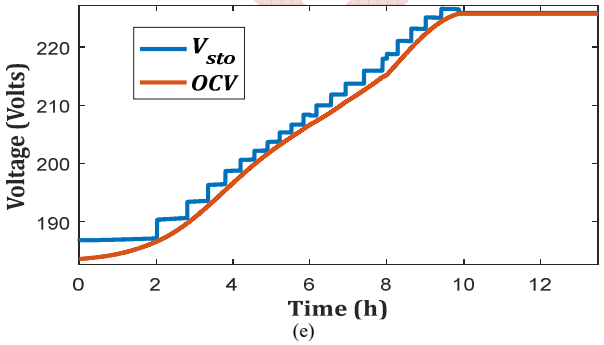
(b)



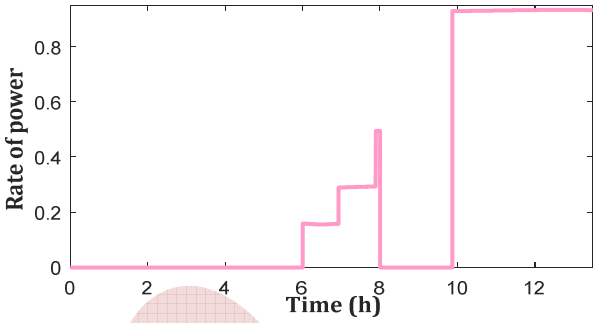
(c)



(d)



(e)



(f)

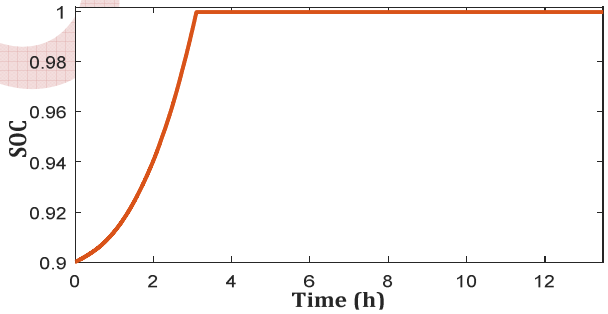
Figure 5. (a) Sunshine profile, (b) Temperature profile, (c) Batteries state of charge, (d) Domestic power needs, Power shared with the public network, Power authorized by the fuzzy manager, Power battery charging and Power produced by the PVG (e) Load voltage, (f) Power rate injected into the grid

From Figure 5 it can be noted that:

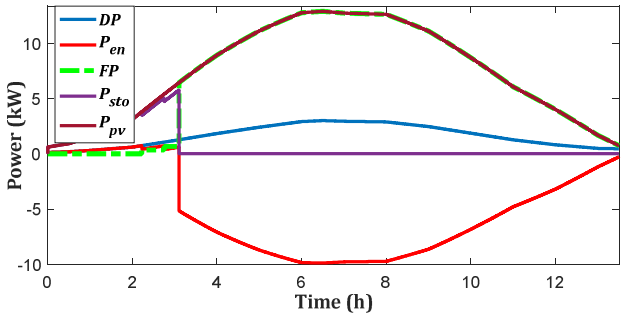
- The domestic energy needs are fully provided by public network until t = 5.52h, between 5.52h and 5.88h half of this energy is provided using the energy allowed by the fuzzy manager (*FP*) and from t = 5.88h all needs are covered it by *FP* power;

- Between t = 6 and t = 8 hours (during peak hours) the excess power authorized by the fuzzy manager is injected into the grid after t = 8h this extra is injected to force the battery charging to *SOC* = 1.

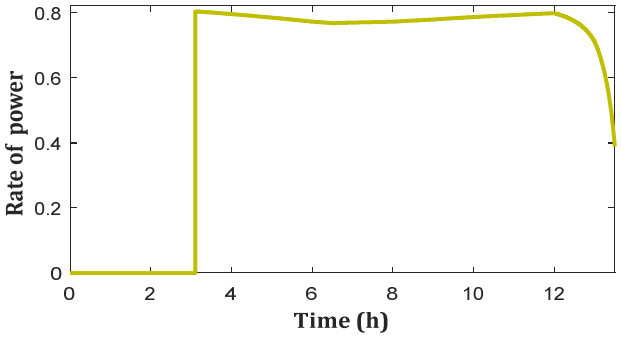
B. The same conditions in case A is taken except SOC_0=0.9 (for example, if the station is loaded)



(a)



(b)

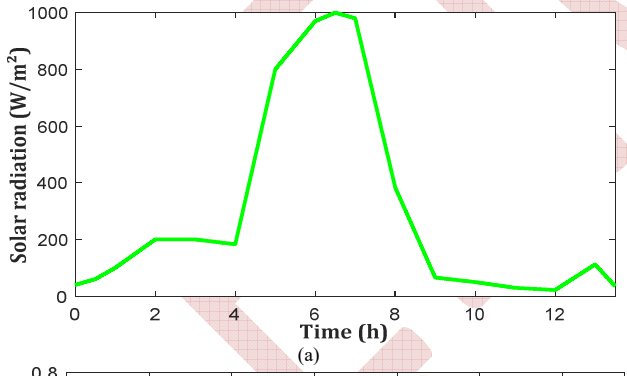


(c)

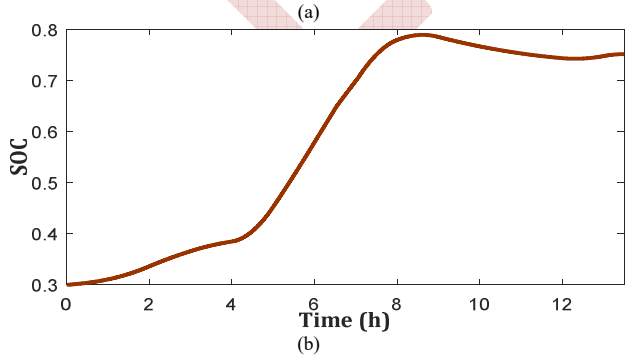
Figure 6. (a) Batteries state of charge, (b) Domestic power needs, Power shared with the public network, Power authorized by the fuzzy manager, Power battery charging and Power produced by the PVG, (c) Power rate injected into the grid

From figure 6, we notice that the fast charging of the batteries allows the fuzzy controller, during the majority of the day, to use the totality of the PV energy for supplying the domestic needs and send the surplus to the grid; the rate of power injected into the grid is improved over almost a period of 7 hours.

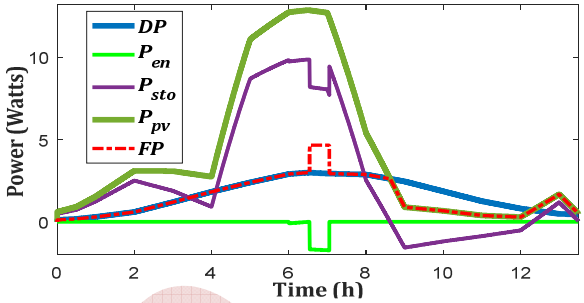
C. In this case shading defects is introduced on the PVs pannels, which causes the reduction of the PV energy production during the appearance of the defects, SOC_0=0.3 and D_{en}=0 (due to a cut or an overload), on the other hand, the export of energy is allowed to help out a neighbor during peak hours (transition to the "Smart City" or the micro-grid), for example.



(a)



(b)

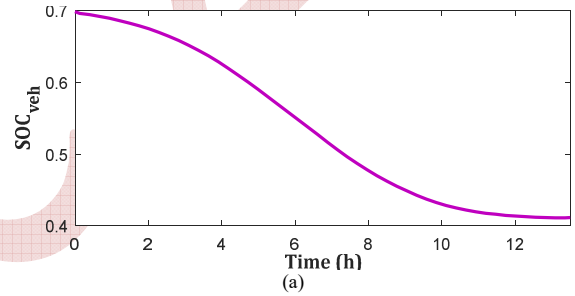


(c)

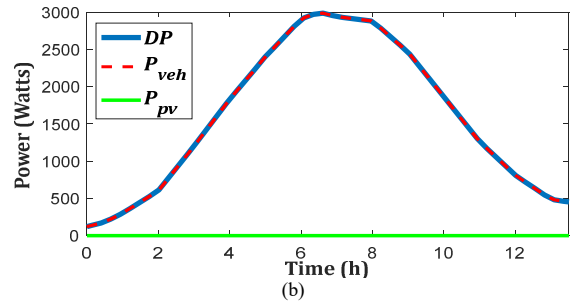
Figure 7. (a) Sunshine profile received by PVG (with defects), (b) Batteries state of charge, (c) Domestic power needs, Power shared with the public network, Power authorized by the fuzzy manager, Power battery charging and Power produced by the PVG

The main remark that can be drawn from Figure 7.c is that domestic energy needs are fully guaranteed by the energy produced by PVG most of the time, in parallel from t=8.624h, the deficit is ensured by the energy stored in the batteries, since the import of energy from the grid is not permitted.

D. In this case the power produced by the PVG is negligible domestic needs are the same as case C, SOC_0=0.3, D_{en}=0 and the vehicle is plugged in (SOC_{veh0}=0.7).



(a)



(b)

Figure 8 (a,b). Batteries state of charge, (b) Domestic power needs, Power supplied by the batteries of hybrid vehicles, and Power produced by the PVG

Since the photovoltaic energy is negligible, the battery bank is discharged and the public network is disconnected so the domestic needs are met by the energy stored in the batteries vehicle that can play this role in the special and unfavorable conditions.

V. CONCLUSION

The main objective of this paper was the design of optimal energy management for a photovoltaic personal hybrid

rechargeable vehicle charging station using one of the artificial intelligence methods, trying to reduce problems created to domestic power grids especially the overhead simultaneous connection and charging with a large number of electric vehicles. Which make the need to optimize the loading and unloading behavior of electric vehicles, due to the issue of security and economy operation of the grid. We made a sizing of our station for the most unfavorable weather conditions and the management of this energy is made through a fuzzy logic controller. The simulation results show that:

- The control system that was used with the integration of a fuzzy manager based on some prediction of climatic conditions is very effective and allows benefiting of the maximum solar energy that can be produced;
- The fuzzy logic manager allows the use of photovoltaic energy for other functions outside the main without affecting the final state of battery charge;
- The fuzzy logic manager participates effectively in good control battery charging especially for high rates of SOC (between 0.9-1) by avoiding any heating of the battery;
- A charging station designed for PHEV can be multiservice and played several roles whether the control system used is effective and can be adapted to all possible cases.

So, with the presence of adequate management systems, these small individual installations can remedy some unforeseen impacts of charging hybrid vehicles on the electrical network in addition to the economic advantages which bring, in particular, with the integration and combination between the principle of cogeneration and the notion of "Smart Home Energy", while estimating the allocation of smart-city or micro-grid systems.

REFERENCES

[1] D. Lu, H. Fakham, T. Zhou, B. François « Application of Petri nets for the energy management of a photovoltaic based power station including storage units" Renewable Energy 35 (2010) 1117–1124

[2] Chaabene, M., Ammar, M.B., Elhajjaji, A., 2007. Applied fuzzy approach for optimal energy-management of a domestic photovoltaic panel. Applied Energy 84, 992–1001.

[3] Arun, P., Banerjee, R., Bandyopadhyay, S., 2009. Optimum sizing of photovoltaic battery systems incorporating uncertainty through design space approach. Solar Energy 83 (7), 1013–1025.

[4] S. Semaoui, A. Hadj A, S. Bacha, B. Azoui "The new strategy of energy management for a photovoltaic system without extra intended for remote-housing" Solar Energy 94 (2013) 71–85 .

[5] Fu Z, Li Z, Si P, Tao F. A hierarchical energy management strategy for fuel cell/battery/supercapacitor hybrid electric vehicles. Int J Hydrogen Energy 2019;44(39):22146e59.

[6] O. Krishan, S. Suhag, A novel control strategy for a hybrid energy storage system in a grid-independent hybrid renewable energy system, Int. Trans. Electr. Energy Syst. 30 (2020).

[7] Xu Mei and al. Modelling anti-islanding protection devices for photovoltaic systems. Renewable Energy 2004;29:2195–216.

[8] Kawamura H, Naka K, Yonekura N. Simulation of I–V characteristics of a PV module with shaded PV cells. Solar Energy Mater Solar Cells 2003;75:613–21.

[9] Gergaud O, Multon B, Ben Ahmed H. Analysis and experimental validation of various photovoltaic system models In: 7th international electrimacs congress, Montre´al, August; 2002.

[10] De Soto W and al. Improvement and validation of a model for photovoltaic array performance. Solar Energy 2006;80(1):78–88.

[11] Gong Xi, Kulkarni M. Design optimization of a large-scale rooftop photovoltaic system.Solar Energy 2005;78:362–74.

[12] Kang Feel soon, Cho Su Eog, Park Sung Jun. A new control scheme of a cascaded transformer type multilevel inverter for a residential photovoltaic conditioning system. Solar Energy 2005;78:727–38.

[13] Zhao Z, Wang T, Li M, Wang H, Wang Y. Optimization of fuzzy control energy management strategy for fuel cell vehicle power system using a multi-islandgenetic algorithm. Energy Sci Eng 2020.

[14] Serpi A, Porru M. Modelling and design of real-time energy management systems for fuel cell/battery electric vehicles. Energies 2019;12(22):4260.

[15] Chaabene M, Annabi M. Dynamic thermal model for predicting solar plant adequate energy management. Energy Convers Manage 1998;39(3–4):349–55.

[16] Riffonneau, Y., Bacha, S., Barruel, F., Ploix, S., 2011. Optimal power flow management for grid connected PV systems with batteries. Sustain Energy, IEEE Transactions 2 (3), 309–320.

[17] Nge, C.L., Ranaweera, I.U., Midtgård, O.-M., Norum, L. A real-time energy management system for smart grid integrated photovoltaic generation with battery storage. Renew. Energy 130, 774–785, 2019.

[18] Kaiser, R.. Optimized battery-management system to improve storage lifetime in renewable energy systems. Journal of Power Sources 168, 58–65 , 2007

[19] Barca, G., Moschetto, A., Sapuppo, C., Tina, G.M., Giusto, R., Grasso, A.D., 2008. Optimal energy management of a photovoltaic standalone dual battery system. MELECON. In: The 14th IEEE Mediterranean Electrotechnical Conference, May.

[20] Zhu, X., Liao, Z., 2009. Energy management for stand-alone PV system. ISECS. In: International Colloquium on Computing, Communication, Control, and Management, ISBN: 978-1-4244-4246-1 IEEE, August.

[21] Qi, Z., Wang, S., Liu, G., Tian, G., 2009. Integrated control of energy management for stand-alone pv system. In: Asia-Pacific Power Energy Engine Conference, 978-1-4244-2487-0-09 IEEE, pp. 1–4.

[22] Ankush Gupta and Sathans Suhag. Charging station control strategy considering dynamic behaviour of electric vehicles with variable state of charge regulation for energy management of autonomous micro-grid. Journal of Energy Storage 59 (2023) 106460.

[23] Chao-Rong Chen, Yong-Sheng Chen, Tzu-Chiao Lin. Optimal Charging Scheduling for Electric Vehicle in Parking Lot with Renewable Energy System . 2019 IEEE International Conference on Systems, Man and Cybernetics (SMC) Bari, Italy. October 6-9, 2019.

[24] K. Dhingra, M. Singh, Handshaking of VSG with charging station to support the frequency in microgrid, Electr. Eng. 102 (2020) 2349–2362.

[25] P.H. Trinh, I.Y. Chung, Optimal control strategy for distributed energy resources in a DC microgrid for energy cost reduction and voltage regulation, Energies (Basel) 14 (2021).

[26] A. A. Dibavar and al. Two-stage robust energy management of a hybrid charging station integrated with the photovoltaic system. international journal of hydrogen energy 46 (2021) 12701-12714.

[27] Joaquim Massana and al. Multi-vector energy management system including scheduling electrolyser, electric vehicle charging station and other assets in a real scenario. Journal of Cleaner Production 380 (2022) 134996.

[28] Mo ElSayed, Ahmed Foda, Moataz Mohamed. Autonomous drone charging station planning through solar energy harnessing for zero-emission operations. Sustainable Cities and Society 86 (2022) 104122.

[29] A. Ricaud, Photovoltaic systems, Engineering School Polytech 'Savoie, 5th year, France 2011.

[30] Ibrahim AL-Wesabi and al. Hybrid SSA-PSO based intelligent direct sliding mode control for extracting maximum photovoltaic output power and regulating the DC-bus voltage. International journal of hydrogen energy 2023.

[31] Aisha Saad and al. A day-ahead multi-approach machine learningtechnique for photovoltaic power forecasting. 9th International Conference on Renewable Energy Research and Applications Glasgow, UK, Sep. 27-30, 2020.

[32] Zhao Z and al. Optimization of fuzzy control energy management strategy for fuel cell vehicle power system using a multi-islandgenetic algorithm. Energy Sci Eng. 10.1002/ese3.835. 2020.

Management of a hybrid system of renewable energies in pumping

1st Arezki Adjati [1], 2nd Toufik Rekioua [2], 3rd Djamila Rekioua [3]

[1] *Industrial and Information Technology Laboratory, Faculty of Technology, A.Mira University, Bejaia, Algeria*
arezki.adjati@univ-bejaia.dz

[2] *Industrial and Information Technology Laboratory, Faculty of Technology, A. Mira University, Bejaia, Algeria*
to_reki@yahoo.fr

[3] *Industrial and Information Technology Laboratory, Faculty of Technology, A. Mira University, Bejaia, Algeria*
dja_rekioua@yahoo.fr

***Abstract*—With uncertain and often fluctuating production capacities, so-called renewable energies are now widespread. The option of combining the wind turbine, photovoltaic (PV) and fuel cell (FC) in a hybridization system can counteract the inconvenience of a single source that obeys the stochastic nature of these energies. There is a need to develop a management algorithm that is able to "select" the source or sources to be used to meet load demand.**

***Keywords:* Photovoltaic, Wind turbine, Fuel cell, Hybrid pumping, Dual stator induction motor.**

I. INTRODUCTION

The intermittent nature of the sun and wind is one reason to combine these two renewable sources in a hybrid system. However, not having a backup source can be a handicap during cloudy days or during weak winds and will have consequences on the pumped flow. Therefore, despite the low efficiency of the electricity-hydrogen-electricity conversion process, the FC are used [1, 2]. The real need for water is a vital element of a rigorous sizing of the station. With a view to better management of the energy sources assembled in the form of a beneficial hybridization, various probable scenarios are established.

In the absence of experimentation and taking into account all possible constraints, the simulation offers results that are very close to reality. In order to provide corrections to improve the yields, the behavior of each element in relation to the other elements constituting the pumping chain is be peeled [3].

II. PRESENTATION OF THE SITE

Timimoune is 29°15' north and 0°15' east in southern Algeria. Average temperatures in this region range from 19°C in January to 45°C in July. The use of climatic data, namely relative humidity, temperature and duration of sunlight, makes it possible to estimate solar radiation. With a rate around 80%, the average annual amount of sunshine is 9.5 hours per day for the site. The various daily measurements made it possible to know the wind potential of Timimoune available during a year.

To estimate the overall irradiation of solar radiation, Mefti and Bouroubi [4] opted for the insolation fraction; Merdaoui [5] proposes to generate data of solar radiation from the duration of the insolation; Gairaa and Benkaciali [6] completed the study carried out on a horizontal plane by opting for inclinations. To cite only these, Bouchouicha [7], meanwhile, applied six types of models to express the clarity index as a function of the fraction of insolation.

TABLE I. WIND SPEEDS IN TIMIMOUNE [3, 8, 9].

Speed [km/h]	[1;5[	[5;12[	[12;19[	[19;28[	[28;38[	[38;50[
Jan.	0.2	6.6	10.9	9.8	3.2	0.3
Feb.	0.1	5.0	8.1	9.9	4.5	0.6
Mar.	0.0	2.8	9.2	11.5	6.2	1.3
Apr.	0.0	1.5	6.4	11.5	9.1	1.4
May	0.0	0.7	6	14.0	9.3	1.0
Jun.	0.0	1.1	7.8	14.3	6.3	0.5
Jul.	0.0	0.0	1.9	9.0	16.7	3.4
Aug.	0.0	1.9	11.1	15.7	2.3	0.0
Sep.	0.0	2.5	9.8	13.7	3.7	0.2
Oct.	0.0	3.3	11.7	12.4	3.5	0.1
Nov.	0.1	6.1	10.2	10.5	2.8	0.2
Déc.	0.1	7.7	10.3	10.1	2.7	0.1
Total	12	940.8	2481.6	3417.6	2100	218.4

To calculate the mean wind speed value, the statistical relationship 1 is used [3].

$$\overline{v_w} = \frac{\sum_{i=1}^{n} x_i . n_i}{\sum_{i=1}^{n} n_i} \quad (1)$$

$\overline{v_w} = 22.43 km/h = 6.23\ m/s$

Statistical data make it possible to designate photovoltaic as the main source [3].

Figure 1 summarizes the number of hours of daily sunshine in a year and figure 2 recaps the average monthly wind speed [3].

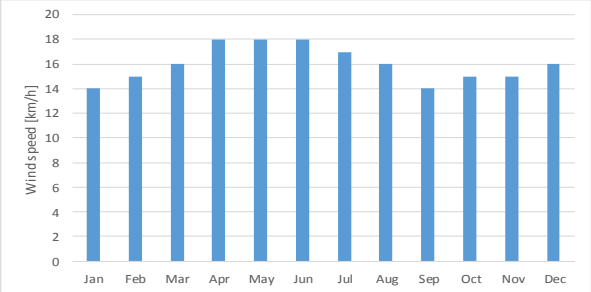


Figure 1. Hours of sunshine per day in Timimoune [3].

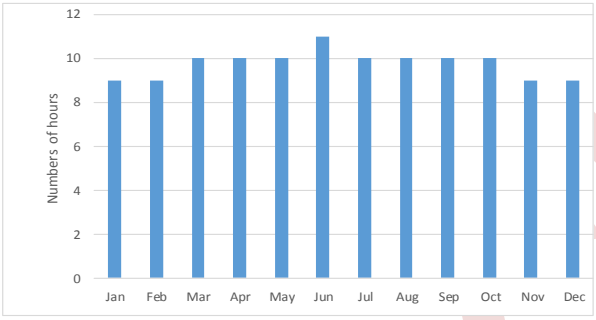


Figure 2. Timimoune region monthly wind speeds [3].

To calculate the mean wind speed value, the statistical relationship 1 is used [3].

$$\overline{v_w} = \frac{\sum_{i=1}^{n} x_i . n_i}{\sum_{i=1}^{n} n_i} \quad (1)$$

With an average wind speed of 6.23m/s and according to statistical data, photovoltaic is the main source [3].

III. PUMP SIZING

After an annual water needs assessment, a 150m3 tank ensure a 72-hour autonomy. The pumping time evaluated at 9 hours obtained for a nominal flow of 17m3/h and a total dynamic head of 30m.

The necessary electrical power depends on the efficiency of the pump and the DSIM and includes the consumption of static converters. The power of the GPV depends the losses caused by dust on the photovoltaic panels and their temperatures [10, 11].

$$P_g = \frac{\rho_{water} . g_t . TDH . Q_n}{\eta_{inverter} \eta_{DSIM} \eta_{pump} (1 - \sum losses)} \quad (2)$$

$$P_g = \frac{1000 \times 9{,}81 \times 30}{0.444(1 - 0.2)} \times \frac{17}{3600} \simeq 3912.5\ W$$

IV. SIZING OF THE PHOTOVOLTAIC GENERATOR

The determination of available solar energy is obtained by consulting the climatic data of the region, including irradiation, shadows, temperatures, fog, microclimate, etc. [3, 12, 13].

To determine the standard power of the GPV, the sizing will be carried with standardized solar panels of type SIEMENS SM 110-24 having a standard nominal power of 110Wp [3,14].

A. *Determination of the number of photovoltaic panels*

The number of panels required is:

$$N_p = \frac{P_g}{P_{OP}} \quad (3)$$

$N_p \geq \frac{3912.5}{110} = 35{,}56$. Thirty-six panels are required with a standard power of: [3, 11, 13]

$$P_{GPV} = N_P . P_{OP} \quad (4)$$

$P_{GPV} = 36 \times 110 = 3960W$

B. *DC bus voltage value*

The DC bus voltage must obey the following relationship [3]:

$$V_{bus} \geq \sqrt{2}.\sqrt{3}.V_{eff} + 2.V_{CE(IGBT)} + 2Z_{filter}\hat{\imath} \quad (5)$$

For a voltage of 240V, voltage drops in semiconductors «V_{CE} (IGBT) =3V» as well as an RL filter "L_{filter}=15mH, R_{filter}=0.5721Ω" and for an average current $\hat{\imath}$=1.23A, the DC bus voltage must be greater than 607 V. It is interesting to opt for V_{bus}=630 V, a value slightly higher than the calculated value, in order to operate under all conditions.

C. *Number of serial panels and parallel branch*

The number of photovoltaic serial panels is [3, 12, 13].

$$N_{PVser} = \frac{V_{bus}}{V_{OP}} \quad (6)$$

The nominal current of the DSIM is 6.5 A, so the number of branch of photovoltaic panels in parallel will be [3, 11, 12, 13]:

$$N_{PV//} = \frac{I_{nominal}}{I_{OP}} \quad (7)$$

V. TURBINE SIZING

The reference electrical power will be the standardized power P_{elec}=3960W.

A. *Mechanical power*

The mechanical power required to turn the blades of the wind turbine is [3, 11, 14]:

$$P_{mec} = \frac{P_{elec}}{\eta_{Multi} . \eta_{DSIG}} \quad (8)$$

B. *Determination of blade length*

The length of the blades is [3, 11, 14]:

$$R = \sqrt[3]{\frac{2P_{mec}}{\rho_{air} . \pi . C_p . v_w^2}} \quad (9)$$

Calculations give a radius of 5m and according to the characteristics of the three-blade wind turbine, the corresponding coefficients are Cp = 0.48 and λ = 8 [3, 11, 14].

C. *Blades speed*

Blades speed is:

$$N = \frac{30.\lambda.v_w}{\pi.R} \quad (10)$$

$$N = \frac{30 \times 8 \times 6.5}{\pi \times 5} = 98.36\ rpm$$

D. Multiplication Ratio

The multiplier coefficient thus obtained by:

$$K = \frac{N_s}{N} \quad (11)$$

Thus the blades of the wind turbine have a length of 5 m and a speed multiplier K = 30.5 [3, 11, 14].

VI. FUEL CELL SIZING

The FC must guarantee a voltage of 630 volts to the DC bus supplying both inverters. The voltage depends on the cells that have assembled in series and the current depends on the total surface of a cell.

For 60% efficiency, the operating voltage is 0.63V/cell and the current density is 1300mA/cm² [13].

The number of cells will be:

$$N_{cells} = \frac{U_{FC}}{U_{cell}} \quad (12)$$

The numerical application gives: $N_{cells} = \frac{630}{0.63} =$ 1000 cells and the current will therefore be:

$$I_{FC} = \frac{P_{elec}}{U_{FC}} \quad (13)$$

$I_{FC} = \frac{3960}{630} = 6.29\ A$ and the required area is:

$$S = \frac{I_{FC}}{dI_{FC}} \quad (14)$$

TABLE II. SUMMARY OF THE DIMENSIONS OF THE SOURCES [3].

Designation	Value	Designation	Value
Time of pumping	9 hours	Inverters yield	0.95
Tank volume	150 m³	DSIM yield	0.85
Debit	17 m³/h	Pump yield	0.55
Total dynamic head	30 m	Total yield	0.444
Photovoltaic generator			
Designation	**Value**	**Designation**	**Value**
normalized power	3960 W	number of panels	36
Panels in series	18	Parallel panels	2
Wind turbine		Mechanical power	5000 W
Designation	**Value**	**Designation**	**Value**
DSIG yield	0.88	Multiplier gain	0.9
multiplying factor	30.5	Blade radius	5 m
Fuel cell		Number of cells	1000
Designation	**Value**	**Designation**	**Value**
electric current	6.29 A	Surface	4.83 cm²
fuel	Hydrogen	oxidizer	Oxygen

VII. PRINCIPLE OF HYBRIDIZATION

The management of the hybrid system based on two essential axes, namely the state of filling of the water tower and that of the hydrogen bottles. According to the pre-established conditions, the Ki coefficients pre-select the renewable generators and the power of the hybrid system is [3]:

$$P_{SEH} = K_{pv} \times P_{pv} + K_w \times P_w + K_{FC} \times P_{FC} \quad (15)$$

Similarly, the load to couple is:

$$P_{Load} = K_{pmp} \times P_{pmp} + K_{lyz} \times P_{lyz} \quad (16)$$

For management purposes, the difference between the available power of the hybrid system and the power requirement of the load is [3]:

$$\Delta P_i = P_{SEH} - (2 - i) \times P_{pmp} - (i - 1) \times P_{lyz} \quad (17)$$

If "i=1", the choice will be made on the coupling of the centrifugal pump to fill the water tank and if "i=2", the choice will be made on the electrolyzer [3].

VIII. SYSTEM COMPONENTS « PV – WIND TURBINE – FC »

TABLE III. INPUTS, OUTPUTS AND SENSORS [3]

Sensors			
G_s	Sunshine	v	Speed at which the wind turbine produce
G_{min}	low sunlight	v_{max}	Stall of the wind turbine
FC_{max}	Full hydrogen cylinders	v_{min}	The wind turbine does not produce
H	tank level	H_{max}	full tank
Inputs		**Outputs**	
P_W	Wind turbine power	P_{lyz}	Electrolyzer power
P_{PV}	PV panel power	P_{pmp}	Pump power
P_{FC}	FC power	P_{SEH}	SEH power

The pumping station consists of a photovoltaic generator (GPV) powered via a "K_{PV}" contactor, a wind turbine whose "K_W" contactor allows its connection [3].

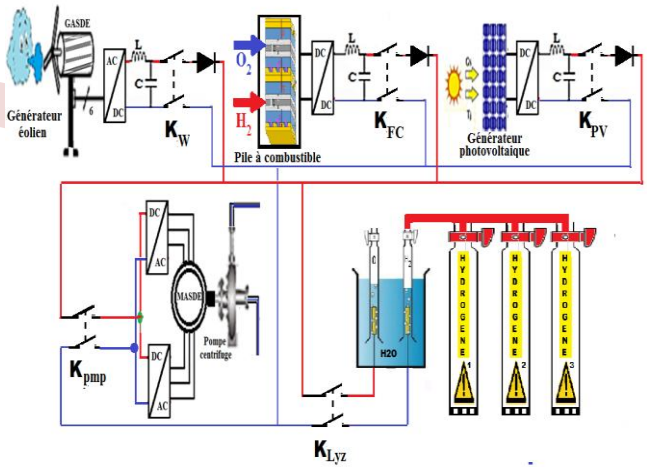


Figure 3. Installation of the pumping station [3]

The "K_{pmp}" contactor is used to couple the pump and "K_{lyz}" that of the electrolyzer. «K_{FC}» contactor implement the hydrogen storage system [3].

IX. STRATEGIES FOR MANAGING A HYBRID SYSTEM

In an SEH, the operating strategy is an algorithm that remains the key element, relating to storage management and is essential to the optimal operation of the pumping station. It is the center of continuous decision-making, concerning the

sources to be connected and the loads to couple on the scale of several hours or several days [3].

First, before the design of these specifications, it is necessary to classify the needs according to the need for operation [3].

- Whatever the conditions, the priority is to fill the water tank, necessary for the survival of the locality.
- Always use source hybridization as long as conditions allow.
- Fill the hydrogen cylinders by electrolysis of water once the water tank is filled or exclusively, in the event that the energy available is not sufficient for pumping.
- Never attach pump and electrolyzer together.
- Use excess energy for tertiary LED lighting circuits.

X. PROPOSED MANAGEMENT SCENARIO

The operating strategy established based on probable scenarios at each variation in wind speed and solar irradiation and taking into account the state of charge of the hydrogen cylinders, as well as the filling level of the water reservoir [3].

A. Mode A " $H < H_{max}$ & $FC < FC_{max}$ "

Logically the first mode denoted "Mode A", is the mode where the water tank and the hydrogen bottles are empty.

Logically the first mode denoted "Mode A", is the mode where the water tank and the hydrogen bottles are empty.

In this case, four combinations are possible between sunstroke and wind speed.

1) Mode A1 : $(G < G_{smin})$ & $(v < v_{min}\ ou\ v > v_{max})$

The sunshine is unavailable and the wind speed is inadequate for the operation of the wind turbine. No power is involved and the pump station is shut down [3].

2) Mode A2 : $(G < G_{smin})$ & $(v_{min} \leq v \leq v_{max})$

The solar panels do not provide energy; on the other hand, the wind turbine generates a power, which is according to the speed of the wind.

- Mode A2.1 : $(\Delta P_1 = P_w - P_{pmp} \geq 0)$

In this case, it must ensure that the energy available is sufficient to rotate the centrifugal pump. The wind energy through the DSIG provides the DC bus voltage of the DSIM inverters.

- Mode A2.2: $(\Delta P_1 = P_w - P_{pmp} < 0)$

The energy available is insufficient to pump the water, where now it is necessary to check whether this energy is sufficient to produce hydrogen.

  - Cas 1 : $\Delta P_2 = P_w - P_{lyz} \geq 0$

The energy provided by the wind turbine will used to produce hydrogen by electrolysis.

  - Cas 2 : $\Delta P_2 = P_w - P_{lyz} < 0$

The energy provided by the wind turbine will used to produce hydrogen by electrolysis. This energy will used for rechargeable LED lamps.

3) Mode A3 : $(G \geq G_{smin})$ & $(v_{min} \leq v \leq v_{max})$

The two renewable sources provide energy and hybridization is then carried out.

4) Mode A4 : $\boldsymbol{(G \geq G_{smin})}$ & $\boldsymbol{(v < v_{min}\ ou\ v > v_{max})}$

The PVs provide energy and the wind speed does not allow the wind turbine to generate voltage.

- Mode A4.1 : $(\Delta P_1 = P_{PV} - P_{pmp} \geq 0)$

The available energy of the sun is sufficient to turn the centrifugal pump.

- Mode A4.2 : $(\Delta P_1 = P_{PV} - P_{pmp} < 0)$

The energy available is insufficient to pump the water but can used to produce hydrogen.

  - Cas 1 : $\Delta P_2 = P_{PV} - P_{lyz} \geq 0$

The energy provided by the silicon panels will used to produce hydrogen by electrolysis.

  - Cas 2 : $\Delta P_2 = P_{PV} - P_{lyz} < 0$

The energy produced by the photon bombardment is not sufficient either for pumping or for the generation of hydrogen. The tertiary circuit of the pumping station lighting will powered.

B. Mode B " H < Hmax & FC > FCmax "

The tank is not yet full and the hydrogen cylinders are full. Four possibilities between insolation and wind speed are be counted.

1) Mode B1 : $(G > G_{smin})$ & $(v_{min} \leq v \leq v_{max})$

The available sunshine and wind speed are suitable for hybridization. The power of the hybrid system becomes: $P_{SEH} = P_{pv} + P_w$

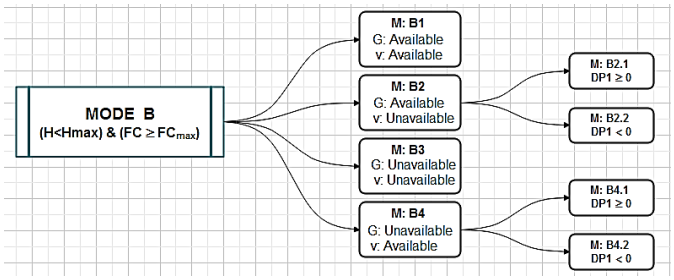


Figure 4. Synoptic diagram of mode "B" [3]

2) Mode B2 : $(G \geq G_{smin})$ & $(v < v_{min}\ ou\ v > v_{max})$

Solar panels provide energy, on the other hand, the wind turbine, for adaptation reasons, does not generate any power. The measurement of the powers involved makes it possible, among other things, to check whether the available energy is sufficient to power the DSIM or to compensate for the lack of power by engaging the FC [3].

- Mode B2.1 : $(\Delta P_1 = P_{PV} - P_{pmp} \geq 0)$

The sun's energy is used to supply the DC bus voltage for the DSIM inverters.

- Mode B2.2 : $(\Delta P_1 = P_w - P_{pmp} < 0)$

The available energy is insufficient to pump the water, where now it is necessary to put into action the fuel cell to provide the lack of power.

The power of the hybrid system becomes: $P_{SEH} = P_{pv} + P_{FC}$

3) Mode B3 : $(G < G_{smin})$ & $(v < v_{min}\ ou\ v > v_{max})$

Both renewable sources provide no energy. To pump water, the use of FC remains the only means. The power of the hybrid system becomes: $P_{SEH} = P_{FC}$.

4) Mode B4 : $(G < G_{smin})$ & $(v_{min} \leq v \leq v_{max})$

The PV does not provide energy and the wind speed generates a voltage.

- Mode B4.1 : $(\Delta P_1 = P_W - P_{pmp} \geq 0)$

The energy available from the wind turbine is sufficient to run the centrifugal pump.

- Mode B4.2 : $(\Delta P_1 = P_W - P_{pmp} < 0)$

The available energy is insufficient to pump the water but it can combined with the FC to operate the pump. The power of the hybrid system becomes: $P_{SEH} = P_W + P_{FC}$.

C. Mode C " H > Hmax & FC < FCmax "

Four combinations determine four operating modes [3].

1) Mode C1 : $(G < G_{smin})$ & $(v < v_{min}\ ou\ v > v_{max})$

The pumping station is stopped because no renewable source is available in its hostile climatic conditions.

2) Mode C2 : $(G < G_{smin})$ & $(v_{min} \leq v \leq v_{max})$

Solar panels do not provide energy, but the wind turbine generates power that depends on the speed of the wind.

- Mode C2.1 : $(\Delta P_2 = P_w - P_{lyz} \geq 0)$

In this case, it must ensure that the energy available is sufficient for the generation of hydrogen. Eole's energy provides the DC voltage needed by the electrolyzer.

- Mode C2.2 : $(\Delta P_2 = P_w - P_{lyz} < 0)$

In this case, the available energy is insufficient to produce hydrogen for the FC. The energy surplus will be used for lighting.

3) Mode C3 : $(G \geq G_{smin})$ & $(v_{min} \leq v \leq v_{max})$

The two renewable sources provide energy.

Hybridization is carried out by feeding the electrolyzer by the combination of photovoltaic and wind turbine.

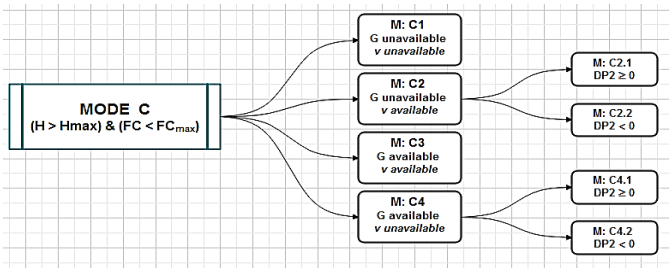


Figure 5. Synoptic diagram of mode "C" [3].

4) Mode C4 : $(G \geq G_{smin})$ & $(v < v_{min}\ ou\ v > v_{max})$

The solar panels provide energy and the wind speed does not allow the wind turbine to generate voltage.

- Mode C4.1 : $(\Delta P_2 = P_{PV} - P_{pmp} \geq 0)$

In this case, the available energy of the sun is sufficient to power the electrolyzer. The GPV provides the necessary DC voltage.

- Mode C4.2 : $(\Delta P_2 = P_{PV} - P_{pmp} < 0)$

The available energy is insufficient for the electrolyzer. Either the energy thus available will used for the tertiary circuit of the lighting, or the station will stopped.

D. Mode D " H > Hmax & FC > FCmax "

In this case, the water tank is full and the hydrogen bottles are full.

XI. RESULTS AND COMMENTS

Not being able to simulate and study the 21 cases of operation, we will remedy it by the treatment of some cases of operation of some bearings of illumination of the photovoltaic generator combined with three levels of wind speed.

The aerodynamic power provided is proportional to the cube of the wind speed and given by the relation [14]:

$$P_{éol} = \frac{1}{2}\rho\pi R^2 C_p(\lambda) v^3 \qquad (26)$$

After calculations, the turbine power will deduced by the following relationship [3]:

$$P_t = 23v^3 \quad [W] \qquad (27)$$

The rotation speed of the blades after calculations is [3]:

$$\Omega = 15.28 \times v \quad [rnd/mn] \qquad (28)$$

TABLE IV. SOME CHARACTERISTICS DEPENDING ON THE WIND SPEED

Wind speed *v [m/s]*	Turbine power P_t [w]	Blades speed [tr/mn]	Electric power $P_{élec}$ [W]
6	4968	91.68	3935
5	2875	76.4	2277
4	1472	61.12	1166

We will address the case where the water tank and the hydrogen bottles supposed not yet full [3].

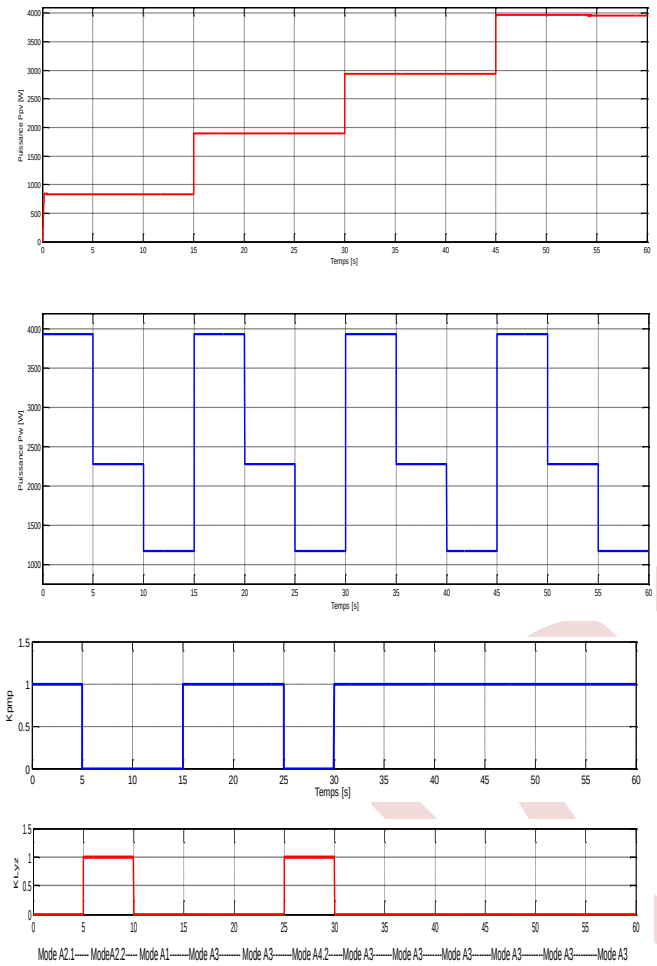


Figure 6. Power of some operating modes [3].

TABLE V. LOAD CONNECTED ACCORDING TO POWER [3].

G_s [W/m²]	P_{PV} [W]	*v* [m/s]	P_w [W]	P_{SEH} [W]	K_{pmp}	K_{Lyz}
250	833.70	6	3935	4768.70	1	0
		5	2277	3110.70	0	1
		4	1166	1999.70	0	0
500	1891.70	6	3935	5826.70	1	0
		5	2277	4168.70	1	0
		4	1166	3057.70	0	1
750	2940.80	6	3935	6875.80	1	0
		5	2277	5217.80	1	0
		4	1166	4106.80	1	0
1000	3960	6	3935	7895.00	1	0
		5	2277	6237.00	1	0
		4	1166	5126.00	1	0

The table (V) summarized the various calculations of the powers harvested according to the sunshine and the wind speed, as well as the state of the contactors activating the centrifugal pump and the electrolyzer.

XII. CONCLUSION

The design of our hybrid system aims to provide the necessary energy to the DSIM and ensure a better quality of the energy supplied.

We have proposed an automated management of our three hybrid sources that will ensure strict real-time monitoring of the pre-designed specifications.

The combination of photovoltaic and wind power provides us with an autonomy of the station. The two sources are complementary rather than competitive, and the adoption of hydrogen as backup energy is only a comfort for the pumping station.

The strategy, which we have chosen, offers us good performance of the elements involved with a better return. Added to these, the service life of the installation is improved and the pumped flow is increased.

REFERENCES

[1] L. Bemal-Agustin, R. Dufo-Lapez, "Simulation and optimization of standalone hybrid renewable energy systems", Renew. Sustain. Energy Rev., vol. 13, pp. 2111 - 2118,. doi: 10.1016/j.rser.01.010.2009

[2] J. L. Bemal-Agustin , R. Dufo-Lapez, J. Dominguez-Navarro, and J. M. YustaLoyo, "Optimal Design of a PV -Wind system for water pumping," Int. Conf, pp. 1- 6, 2008.

[3] A. Adjati, "Etude des machines asynchrones à double étoile en pompage hybride à énergies renouvelables", Doctoral thesis in science, University A. Mira Bejaia, Algeria, 2022.

[4] A. Mefti, M.Y. Bouroubi, 'Estimation et Cartographie de la Composante Globale du Rayonnement Solaire', Revue des énergies renouvelables, Valorisation, pp. 219-224. 1999.

[5] Z.Merdaoui, "Caractérisation radiométrique des sites de Bouzeréah et Ghardaia", Magister thesis, Blida university, 2007.

[6] K.Gairaa, S. Benkaciali, "Modélisation numérique des irradiations globle et diffuse au site de Ghardaia", Revue des Energies Renouvelables Vol. 11 N°1 pp 129 – 136. 2008.

[7] K. Bouchouicha, "Modelisation multispectrale des images satellitaire - application: Quantification du bilan d'énergie Sol-Atmosphère", Doctoral these in sciences USTO, Oran, 2017.

[8] N. Bailek, K. Bouchouicha, Z. Al-Mostafa, M. El-Shimy, N. Aoun, A. Slimani, S. Al-Shehri, " A new empirical model for forecasting the diffuse solar radiation over Sahara in the Algerian Big South", Renewable Energy, Volume 117, Pages 530-537, March 2018.

[9] "Simulation de données climatiques et météorologiques historiques pour Timimoun", "Timimoun _ Climat, Températures et Météo, Les meilleures périodes !", meteoblue, Accessed 01 April 2022.

[10] A. Adjati, A. Azib et T. Rekioua, "Etude d'une machine asynchrone à double alimentation en pompage photovoltaïque", Revue des Energies Renouvelables, Vol. 17 N°3 pp 411 – 418, 2014.

[11] A. Adjati, T. Rekioua, D. Rekioua, "Use of the Dual Stator Induction Machine in Photovoltaic - Wind Hybrid Pumping", Journal Européen des Systèmes Automatisés, Vol.54, N°.1, pp. 115-124, February, 2021.

[12] A. Adjati, "Etude des machines asynchrones à double étoile en pompage", Thèse de Magister de l'université A. Mira Bejaia, systèmes électro-énergétique. 2012.

[13] A. Adjati, T. Rekioua, D. Rekioua, A. Tounzi, "Study of Dual Stator Induction Motor in Photovoltaic-Fuel Cell Hybrid Pumping Application", European Journal of Electrical Engineering, 53(5): 601-608, 2020. https://doi.org/10.18280/jesa.530502.

[14] A.Guettaf; "Direct field oriented control of induction motor fed by wind turbine generator under saturation effect". Mediterranean Journal of Measurement and Control, Vol 7, N°1, pp 190-196, 2011.

A Control Strategy of Dual Stars Induction Generator with Power limitation

Kamel Hamitouche[1], Samira Chekkal[2], Djamal Aouzellag[3]

[123] *Department of electrical engineering, Faculty of technology, Renewable Energy Control Laboratory, Bejaia University, 06000 Bejaia, Algeria.*

[1] *kamel.hamitouche@univ-bejaia.dz* [2] *samira.chekkal@univ-bejaia.dz* [3] *djamal.aouzellag@univ-bejaia.dz*

***Abstract*—A limitation power control strategy associated to the field-oriented control of stand-alone dual stars induction generator (DSIG) has done in this article. The induction machine has two sets of stator three-phase windings spatially shifted by 30 electrical degrees. One supplied power to the DC load via a rectifier bridge and AC capacitors, and the other was connected to the battery banks by an inverter to store energy and restore it to regulate the power of the first star in weak wind. The power is limited by MPPT strategy to maintain power delivered to the nominal value. We develop the steady state model and show the performances of different configurations by the simulation results.**

***Keywords*: Stand-alone wind energy conversion system, DSIG, Non-identical stars, Field-oriented control, MPPT, Storage system, Power limitation.**

I. INTRODUCTION

Today in a context of global warming, renewable power generation is a suitable technology used to deliver energy locally to customers [1]. In most remote areas, wind energy is a source of electricity generation. Their exploitation for the production of electricity is very profitable, where the extension of the electricity grid would be a financial failure [2]. The applications of wind systems for isolated operation are numerous and can meet an energy need ranging from simple lighting to complete electrification of villages [3]. Wind turbines for small isolated electrical systems use small-sized electrical machines. They are a good solution for generating low-voltage electricity in isolated locations [4-6]. Synchronous and asynchronous machines under their various variants can be used. However, the low cost and standardization of induction generators have led to the large domination of induction generators [7-10]. A wide range of energy storage technologies are available today which offer a wide spectrum of performance and capacities for different applications [11].

To ensure, at all times, the sufficient energy required by the charge while maintaining a quality of the supplied energy, a storage system was carried out by the use of the batteries [12]. The study of multiphase machine drives has progressed significantly over the last century. This research has taken place in the fields of hybrid motors and railway propulsion, all-electric ships, more-electric aircraft, and wind power generation systems [13-14]. For isolated systems of relatively large power, the DSIG, compared with conventional three-phase induction generator-based structures, can be a much better alternative thanks to these numerous advantages resulting from the reduction of harmonics, reduce current without increasing voltage in each phase and power segmentation. [15-17]. Providing customers with quality voltage is the main challenge of a standalone system. The proposed stand-alone wind energy system consists of Dual Stator Induction Generator (DSIG) based variable-speed wind energy conversion, battery and charge. The source of production, i.e. wind energy, is equipped with a maximum power point tracking system (MPPT) and connected to the power DC bus. a battery is used as a storage device and is connected to the control DC bus. The conventional configuration using only induction generator in wind power applications, consists to connect the battery bank directly to the DC bus voltage by bidirectional buck-boost converter, in this configuration, the battery bank stores the excess energy when the charge demand is low [18-19]. To overcome this problem, in this paper, the battery bank is connected to a control winding through a dc/ac converter, thus the battery bank is charged at the same time as the load demand is supplied with its nominal value as long as the wind allows, furthermore, the proposed configuration allows the main converter to transfer an almost constant power. In article [20] the DSIG worked at nominal speed, in this paper the wind speed is higher and takes values exceeding the nominal value, for this, the power limitation technique is activated by the MPPT strategy. The DSIG has two sets of stator windings wound for the same number of pole pairs, their functions are different and separated, and they have no physical connection but have an electromagnetic link, one of which is called as power winding supplied 75% of the power of the DSIG to DC load via a bridge rectifier and self-excited capacitors, while the other is termed as control winding which provides 25% of the power to charge the battery bank by an inverter and restitute this energy to provide the power winding in case of weak wind as shown in Figure 1. Moreover, like the traditional IG, the rotor of the

DSIG is a cage type. It is simple, robust, and innate brushless, which can guarantee good safety and reliability.

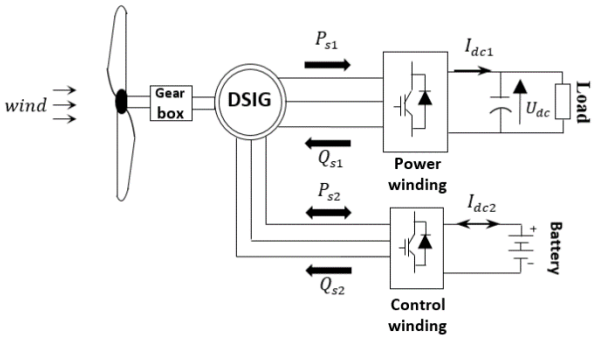


Figure. 1 Aerogenerator based on the DSIG

II. MODELING OF THE WIND TURBINE

The power of the wind transferred to the rotor is calculated as follows [21]:

$$P_t = \frac{1}{2} C_p(\lambda, \beta) \rho S V_{wind}^3 \quad (1)$$

where, ρ = 1.225 kg.m^{-3} is the mass density of the air at T~ 15°C and $C_p(\lambda, \beta)$ is the turbine power coefficient that is a function of speed ratio λ and blade pitch angle β according [22]:

$$C_p(\lambda, \beta) = C_1 . (C_2/\lambda_i - C_3\beta - C_4) . exp^{-(C_5/\lambda_i)} + C_6\lambda_i \quad (2)$$

where,

$$1/\lambda_i = 1/(\lambda + 0.08\beta) - 0.035/(\beta^3 + 1) \quad (3)$$

The parameters C_1, C_2, C_3, C_4, C_5, C_6, depend on the aerodynamic characteristics of the turbine. For a modern turbine these parameters are obtained empirically where:

C_1 = 0.5176, C_2 = 116, C_3 = 0.4, C_4 = 5, C_5 = 21, C_6 = 0.0068, these values are given for a three-bladed wind turbine, with similar aerodynamic characteristics to the wind turbine model used in this system. The value of (β=0°) is to obtain the optimal tip speed ratio (λ) [23].

The speed ratio is given by:

$$\lambda = R\Omega_t / V_{wind} \quad (4)$$

And the V_{wind} is the wind speed assumed to be constant over the entire of the surface swept by rotor blade S.

The torque produced by the wind turbine is calculated by:

$$T_t = P_t / \Omega_t \quad (5)$$

The turbine is normally coupled to the generator shaft through a gearbox whose gear ratio G is chosen in order to set the generator shaft speed within a desired speed range. Neglecting the transmission losses, the torque and shaft peed of the wind turbine, referred to the generator side of the gearbox, are given by:

$$T_g = T_t / G \quad (6)$$

$$\Omega_t = \Omega_m / G \quad (7)$$

The mechanical equation can be expressed as:

$$T_g - T_{em} = Js\Omega_m + f\Omega_m \quad (8)$$

where,

$T_{em} = T_{em1} + T_{em2}$: The electromagnetic torque of the machine which will be the sum of the electromagnetic torque of the power winding and the control winding.

The wind speed varies over time, and to ensure maximum capture of wind energy incident, the rotational speed of the wind turbine must be continuously adjusted with that of the wind. This is achieved using the MPPT technique.

A typical relationship between C_p and λ show that there is a value of λ for which C_p is maximum and that maximize the power for a given wind speed. The peak power for each wind speed occurs at the point where C_p is maximized. To maximize the generated power, it is therefore desirable for the generator to have a power characteristic that will follow the maximum C_{p_max} line [24].

With the use of this control method, wind power systems can continuously adjust its rotations speed according to incoming wind speed, the reference rotational speed Ω_m^* can be written as:

$$\Omega_m^* = \left(R\lambda_{opt}/V_{wind}\right) . G \quad (9)$$

The action of the speed corrector must achieve two tasks [25]:

- It must control the mechanical speed Ω_m in order to yet a speed reference Ω_m^*.

- It must attenuate the action of the aerodynamic torque, which is an input disturbance.

If the wind speed is measured and the mechanical characteristics of the wind turbine are known, it is possible to deduce in real time the optimal mechanical power which can be generated using the maximum power point tracking (MPPT) [26]. The optimal mechanical power can be expressed as:

$$P_{opt} = \frac{1}{2} \frac{C_{p_max}}{\lambda_{opt}^2} \frac{\rho \pi R^5}{G^3} \Omega_m^3 \quad (10)$$

The optimal torque will be given by:

$$T_{opt} = K_{opt} \Omega_m^2 \quad (11)$$

where,

$$K_{opt} = \frac{1}{2}\frac{C_{p_max}}{\lambda_{opt}^2}\frac{\rho\pi R^5}{G^3}$$

The reference electromagnetic torque of the power winding T_{em1}^* would be obtained by regulating the DC bus voltage and depend on the load value, on the other hand, the reference electromagnetic torque of the control winding T_{em2}^* would be obtained by subtracting the reference electromagnetic torque from the power winding by the total optimal torque T_{opt}^* as:

$$T_{opt}^* = T_{em1}^* + T_{em2}^* \tag{12}$$

When the power delivered by the machine exceeds its nominal value, the power limitation command is activated In order to limit electric constraints on the generator, the mechanical reference power is maintained in its nominal value:

$$P_{opt} = P_n \tag{13}$$

III. MACHINE MODEL

The dual stars induction machine model is composed of a stator with two non-identical phase windings shifted by an electric angle $\alpha = 30°$. The six stator phases are divided into two wye-connected three-phase sets. The windings of each three-phase set are uniformly distributed and have axes that are displaced 120° apart. The rotor is squirrel cage consisting of conduction bars short-circuited by a conductive ring at each end, and they simulated as three-phase windings (a_r, b_r, c_r) sinusoidally distributed and have axes that are displaced by 120° apart [27-28].

The electrical equations of the dual-stars induction generator in the synchronous reference frame $(d-q)$ are given as [29]:

$$\begin{cases} v_{ds1} = R_{s1}\iota_{ds1} + s\varphi_{ds1} - \omega_s\varphi_{qs1} \\ v_{qs1} = R_{s1}\iota_{qs1} + s\varphi_{qs1} + \omega_s\varphi_{ds1} \\ v_{ds2} = R_{s2}\iota_{ds2} + s\varphi_{ds2} - \omega_s\varphi_{qs2} \\ v_{qs2} = R_{s2}\iota_{qs2} + s\varphi_{qs2} + \omega_s\varphi_{ds2} \\ v_{dr} = R_r\iota_{dr} + s\varphi_{dr} - \omega_{sl}\varphi_{qr} \\ v_{qr} = R_r\iota_{qr} + s\varphi_{qr} + \omega_{sl}\varphi_{dr} \end{cases} \tag{14}$$

With, $\omega_{sl} = \omega_s - \omega_m$

The expressions for stator and rotor flux are:

$$\begin{cases} \varphi_{ds1} = L_{s1}\iota_{ds1} + L_m(\iota_{ds1} + \iota_{ds2} + \iota_{dr}) \\ \varphi_{qs1} = L_{s1}\iota_{qs1} + L_m(\iota_{qs1} + \iota_{qs2} + \iota_{qr}) \\ \varphi_{ds2} = L_{s2}\iota_{ds2} + L_m(\iota_{ds1} + \iota_{ds2} + \iota_{dr}) \\ \varphi_{qs2} = L_{s2}\iota_{qs2} + L_m(\iota_{qs1} + \iota_{qs2} + \iota_{qr}) \\ \varphi_{dr} = L_r\iota_{dr} + L_m(\iota_{ds1} + \iota_{ds2} + \iota_{dr}) \\ \varphi_{qr} = L_r\iota_{qr} + L_m(\iota_{qs1} + \iota_{qs2} + \iota_{qr}) \end{cases} \tag{15}$$

The electromagnetic torques are evaluated as:

$$\begin{cases} T_{em1} = P\frac{L_m}{L_m+L_r}(\iota_{qs1}\varphi_{dr} - \iota_{ds1}\varphi_{qr}) \\ T_{em2} = P\frac{L_m}{L_m+L_r}(\iota_{qs2}\varphi_{dr} - \iota_{ds2}\varphi_{qr}) \end{cases} \tag{16}$$

where, P is the number of pairs pole.

IV. FIELD ORIENTED CONTROL OF AN DSIG

The control of the two windings is different, the first star keeps the DC bus voltage constant to supply the load, and the second star charges the battery bank by the excess power supplied by the wind and converts the rectifier into an inverter to regulate the power of the first star in the event of weak wind by absorbing the energy of the battery, in this article, the power absorbed by the turbine is limited to its nominal value by the associated MPPT algorithm. The general diagram of the power regulation technique of the DSIG machine is shown in figure 2.

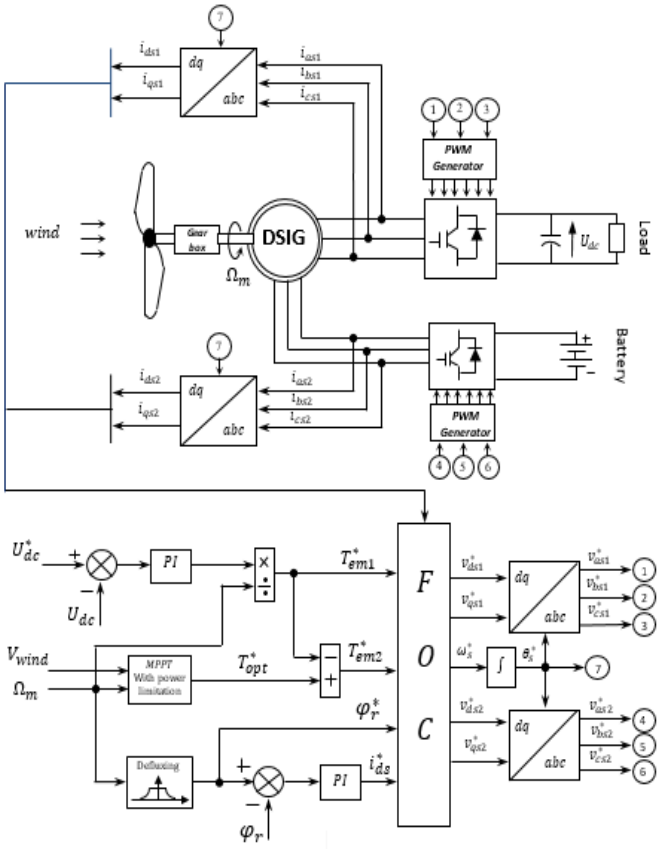


Figure. 2 Block diagram of the power control system for the DSIG

In this order, we propose to study the field oriented control (FOC) of the DSIG. The control strategy used consists to maintain the quadrature component of the flux null and the direct flux equals to the reference:

$$\varphi_{dr} = \varphi_r^* \tag{17}$$

$$\varphi_{qr} = 0 \tag{18}$$

Substituting (17), (18) into (14) Yields:

$$R_r \iota_{dr}^* = 0 \Rightarrow \iota_{dr}^* = 0 \quad (19)$$

$$R_r \iota_{qr}^* + \omega_{sl}^* \varphi_r^* = 0 \Rightarrow \iota_{qr}^* = -\frac{\omega_{sl}^* \varphi_r^*}{R_r} \quad (20)$$

The rotor currents in terms of the stator currents are divided from the rotor flux (15) as:

$$\iota_{dr}^* = \frac{1}{L_m + L_r}[\varphi_r^* - L_m(\iota_{ds1}^* + \iota_{ds2}^*)] \quad (21)$$

$$\iota_{qr}^* = -\frac{L_m}{L_m + L_r}(\iota_{qs1}^* + \iota_{qs2}^*) \quad (22)$$

We obtain the reference rotor flux expression by substitution (19) into (21):

$$\varphi_r^* = L_m(\iota_{ds1}^* + \iota_{ds2}^*) \quad (23)$$

Substitution (20) into (22) obtain:

$$\omega_{sl}^* = \frac{R_r L_m}{(L_m + L_r)} \frac{(\iota_{qs1}^* + \iota_{qs2}^*)}{\varphi_r^*} \quad (24)$$

The stator current in quadrature axis is obtain by substitution (17), (18) into (16) as:

$$\iota_{qs1}^* = \frac{1}{\varphi_r^*} \frac{(L_m + L_r)}{P\, L_m} T_{em1}^* \quad (25)$$

$$\iota_{qs2}^* = \frac{1}{\varphi_r^*} \frac{(L_m + L_r)}{P\, L_m} T_{em2}^* \quad (26)$$

The power of the star 1 is at 75% of total power of the machine, and the star 2 is at 25%, we will have: $\iota_{ds}^* = \iota_{ds1}^* + \iota_{ds2}^*$ such as: $\iota_{ds1}^* = 0.75 * \iota_{ds}^*$ and $\iota_{ds2}^* = 0.25 * \iota_{ds}^*$.

The relations between voltages and currents components are obtained by substituting (19), (21), and (23) into the stator flux equation (15) and replacing the expression into the stators voltage equation systems (14):

$$\begin{cases} v_{ds1}^* = R\iota_{ds1}^* + L_{s1} s\iota_{ds1}^* - \omega_s^*(L_{s1}\iota_{qs1}^* + \tau_r \varphi_r^* \omega_{sl}^*) \\ v_{qs1}^* = R_{s1}\iota_{qs1}^* + L_{s1} s\iota_{qs1}^* + \omega_s^*(L_{s1}\iota_{ds1}^* + \varphi_r^*) \\ v_{ds2}^* = R_{s2}\iota_{ds2}^* + L_{s2} s\iota_{ds2}^* - \omega_s^*(L_{s2}\iota_{qs2}^* + \tau_r \varphi_r^* \omega_{sl}^*) \\ v_{qs2}^* = R_{s2}\iota_{qs2}^* + L_{s2} s\iota_{qs2}^* + \omega_s^*(L_{s2}\iota_{ds2}^* + \varphi_r^*) \end{cases} \quad (27)$$

where, $\tau_r = \frac{L_r}{R_r}$: is the time rotor constant

V. SIMULATION RESULTS AND DISCUSSION

The limitation control strategy for a stand-alone variable speed wind energy supply system is performed by Matlab Simulink software, the DSIG parameters are given in table 1.

The power regulation technique is illustrated in article [20], in this paper, the wind speed exceeds the nominal speed of the machine which will induce an overproduction of the power expressed by the increase of the current, in this case the machine work in overload, to remedy this, a regulation by power limitation is activated, which is shown through the following curves. The wind profile is represented by figure 3 which will give us the speed profile of the DSIG illustrated in figure 4, under these conditions, the speed of the rotor takes values higher than the nominal speed of the machine, the regulation by power limitation is activated, the figure 5 and figure 6 which are the active power and the electromagnetic torque of the control winding follows the variation of the wind speed in order to correctly balance the power response to compensate the power missing of star 1, which provides constant power to the load, and to charge the battery bank in the other case. The active power of the star 1 remains constant and the electromagnetic torque follows the variation of wind speed represented in figure 7 and figure 8 respectively. We can clearly see that the power supplied by star 1 is limited to 3.33 kW, and that of star 2 to 1.12 kW which are the nominal values of these windings.

The DC-link voltage was successfully regulated as shown in Figure 9. despite the step variations in the generator power.

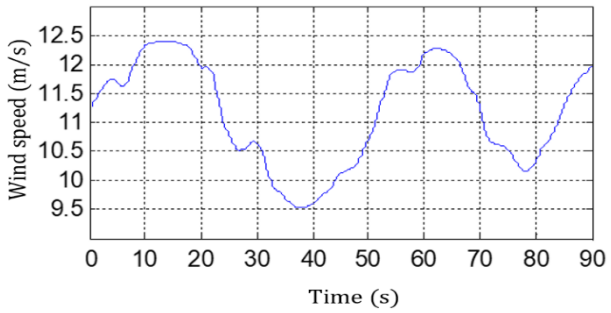


Figure. 3 Wind speed profil

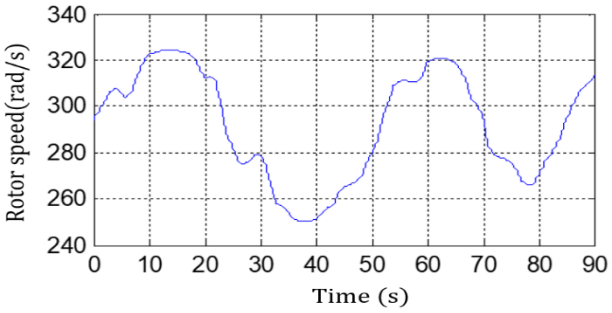


Figure.4 DSIG rotor speed

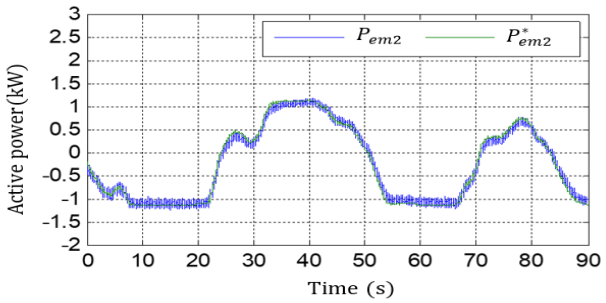


Figure 5 Active power of control winding

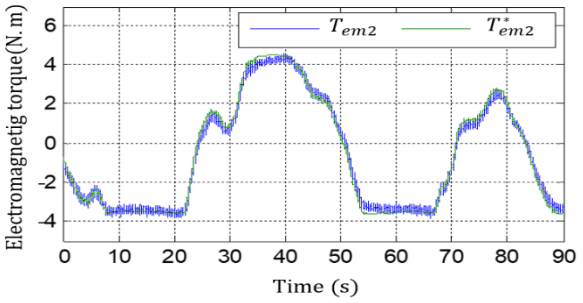


Figure 6. Electromagnetic torque of control winding

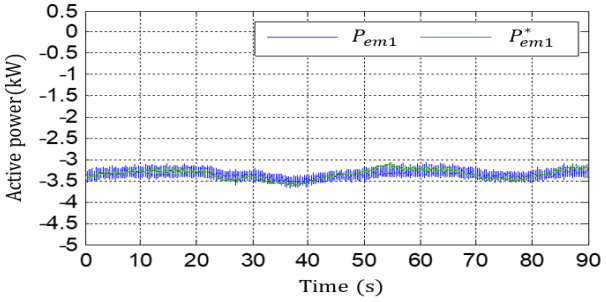


Figure. 7 Active power of power winding

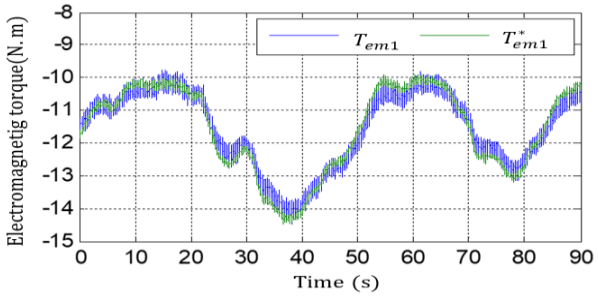


Figure 8. Electromagnetic torque of power winding

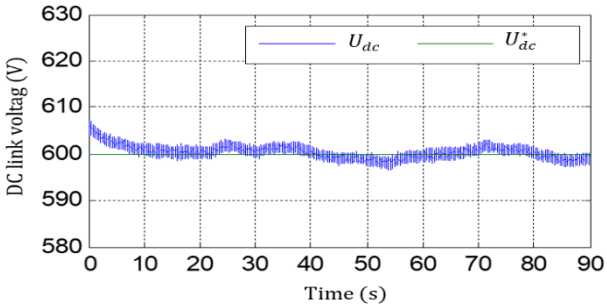


Figure. 9 DC link voltage of power winding

Table 1. DSIG parameters

Components	Rating values
Nominal power	P_n = 4.5 kW
Power winding resistance	R_{s1} =2.79 Ω
Control winding resistance	R_{s2} = 4.65 Ω
Rotor resistance	R_r = 2.12 Ω
Power winding inductance	L_{s1}= 0.0165 H
Control winding inductance	L_{s2}=0.0275 H
Rotor inductance	L_r = 0.006 H
Mutual inductance	L_m = 0.3672 H
Moment of inertia	J = 0.0625 kg .m^2
Viscous friction	f = 0.001 N m. s/rd
Rate speed	Ω_m = 293 rad/s
Number of pole pairs	P=1

VI. CONCLUSION

In this paper, a control by limitation power of DSIG with non-identical parameters and different operating mode have been presented. The simulation results of power limitation control strategy show its performance through power compensation of stator 1 with the power available in the storage battery connected to the stator 2, and a limitation power of stator 2 in case of over speed obtained by MPPT regulation. The DC bus voltage is maintained constant by using flow orientation control strategy, which can be used in variable wind speed applications.

ACKNOWLEDGMENT

The study was supported by the renewable energy's management laboratory of Bejaia university, which i would like to thank its director as well as the researchers who contribute to this work.

REFERENCES

[1] F. Hamoud, M.L. Doumbia, A. Cheriti, "Performance study of a self-excitation dual stator winding induction generator for renewable distributed generation systems", Smart Grid and Renewable Energy, 2016 7: 197-215. http://dx.doi.org/10.4236/sgre.2016.76016

[2] W.M. Lin, C.M. Hong "Intelligent approach to maximum power point tracking control strategy for variable-speed wind turbine generation system", Energy, 2010, 35(6): 2440-2447. https://doi.org/10.1016/j.energy.2010.02.033

[3] X.X. Yin, Z.D. Jiang, P. Li, "Recurrent neural network based adaptive integral sliding mode power maximization control for wind power systems", Renewable Energy,2020, 145: 1149-1157. https://doi.org/10.1016/j.renene.2018.12.098

[4] M. Benakcha, L. Benalia, D.E. Tourqui, A. Benakcha, "Backstepping control of dual stator induction generator used in wind energy conversion system", International Journal of Renewable Energy Research, 2018, 8(1): 384-395.

[5] K. Bedoud, M. Ali-rachedi, T. Bahi, R. Lakel, "Adaptive fuzzy gain scheduling of PI controller for control of the wind energy conversion systems", Energy Procedia, 2015, 74: 211–225. https://doi.org/10.1016/j.egypro.2015.07.580

[6] M. Stiebler "Wind energy systems for electric power generation", Springer series in green energy and technology, Berlin, 2008.

[7] D.Yazdani, S. Ali Khajehoddin, A. Bakhshai, G. Joos "Full utilization of the inverter in split-phase drives by means of a dual three-phase space vector classification algorithm" in IEEE Transactions on Industrial Electronics, 2009, 56(1): 120-129. https://doi.org/10.1109/TIE.2008.927405

[8] M.A. Khlifi, M. Ben Slimene, M. Ben Fredj, H. Rhaoulia, "Performance evaluation of self-excited DSIG as a stand-alone distributed energy resources" Electrical Engineering 2015, 98(2): 159–167. https://doi.org/10.1007/s00202-015-0349-y

[9] F. Bu, W. Huang, Y. Hu, K. Shi "Optimal selection of excitation capacitor for 6/3-phase dual stator-winding induction generator with the static excitation controller applied in wind power", Energy Conversion Congress and Exposition (ECCE), 2010 IEEE, pp. 2397-2402. https://doi.org/10.1109/ECCE.2010.5617905

[10] D. Wang, W. Ma, , F. Xiao, , B. Zhang, D. Liu, A. Hu "A novel stand-alone dual stator-winding induction generator with static excitation regulation", IEEE Transactions on Energy Conversion, 2005, 20(4): 826-835. https://doi.org/10.1109/TEC.2005.853744

[11] A. Chenna, D. Aouzellag, K. Ghedamsi, "Study and control of a pumped storage hydropower system dedicated to renewable energy resources", Journal Européen des Systèmes Automatisés, 2020 53 (1): 95-102. https://doi.org/10.18280/jesa.530112

[12] B. Singh, G.K. Kasal, "Solid-state voltage and frequency controller for a stand-alone wind power generating system", IEEE Trans. Power Electronics, 2008, 23(3): 1170–1177. https://doi.org/10.1109/TPEL.2008.921190

[13] F. Barrero, M.J. Duran, "Recent advances in the design, modeling, and control of multiphase machines-part I", IEEE Transactions on Industrial Electronics, 2016, 63(1): 449–458. https://doi.org/10.1109/TIE.2015.2447733

[14] M.J. Duran, F. Barrero, "Recent advances in the design, modeling, and control of multiphase machines-Part II", IEEE Trans. Ind. Electron., 2016, 63(1): 459–468. https://doi.org/10.1109/TIE.2015.2447733

[15] H. Amimeur, R. Abdessemed, D. Aouzellag, K. Ghedamsi, "Sliding mode control of a dual-stator induction for wind energy conversion systems", Electrical Power and Energy Systems, 2012, 42(1): 60-70. https://doi.org/10.1016/j.ijepes.2012.03.024

[16] D. Hadiouche, H. Razik, A. Rezzoug, "On the modeling and design of dual-stator windings to minimize circulating harmonic currents for VSI fed AC machines", IEEE Transactions on Industry Applications, 2004, 40(2): 506–515. https://doi.org/10.1109/TIA.2004.824511

[17] S. Chekkal, N.A. Lahaçani, D. Aouzellag, K. Ghedamsi, "Fuzzy logic control strategy of wind generator based on the dual-stator induction generator", International Journal of Electrical Power & Energy Systems, 2014, 59: 166-175. https://doi.org/10.1016/j.ijepes.2014.02.005

[18] E. Merabet, R. Abdessemed, H.Amimeur, F. Hamoudi, "Field oriented control of a dual star induction machine using fuzzy regulators", in 4th Int. Conf. Computer Integrated Manufacturing, 2007

[19] A.A. Tanvir, A. Merabet, "Artificial neural network and Kalman filter for estimation and control in standalone induction generator wind energy DC micro grid Energies" 2020, 13(7): 1743. https://doi.org/10.3390/en13071743

[20] K. Hamitouche, S. Chekkal, H. Amimeur, D. Aouzellag, "A new control strategy of dual stator induction generator with power regulation", Journal Européen des Systèmes Automatisés, 2020, Vol. 53, No. 4, pp. 469-478. https://doi.org/10.18280/jesa.530404

[21] A.B. Abrahamsen, N. Mijatovic, E. Seiler, T. Zirngibl, C. Traeholt, , P.B. Norgard, , N.F. Pedersen, , N.H. Andersen, , J. Østergård, "Superconducting wind turbine generators" Superconductor Science and Technology, 2010, 23(3): 034019. https://doi.org/10.1088/0953-2048/23/3/034019

[22] M.A.H. Navas, J.L.A. Puma, A.J.S. Filho, "Direct torque control for squirrel cage induction generator based on wind energy conversion system with battery energy storage system", IEEE Workshop on Power Electronics and Power Quality Applications (PEPQA), Bogota, 2015, pp. 1-6. https://doi.org/10.1109/PEPQA.2015.7168203

[23] A.M. Howlader, N. Urasaki, A.Y. Saber, "Control strategies for wind-farm-based smart grid system" IEEE Transactions on Industry Applications, 2014, 50(5):3591–3601. https://doi.org/10.1109/tia.2014.2304411

[24] K. Ghedamsi, D. Aouzellag, E.M. Berkouk, "Control of wind generator associated to a flywheel energy storage system", Renew Energy, 2008, 33(9): 2145–56. https://doi.org/10.1016/j.renene.2007.12.009

[25] F. Poitiers, M. Machmoum, "Control of a doubly fed induction generator for wind energy conversion systems", In: GE44-LARGE, Saint Nazaire, France. 2001.

[26] D. Aouzellag, K. Ghedamsi, E.M. Berkouk, "Power control of a variable speed wind turbine driving an DFIG", Renewable Energy and Power Quality Journal, 2006, Vol. 1. https://doi.org/10.24084/repqj04.220

[27] D. Hadiouche, "Contribution to the study of dual stator induction machines: Modeling, supplying and structure", (in French), Ph.D. dissertation, GREEN, Faculty Sci. Tech. Univ. Henri Poincare-Nancy I, Vandœuvre-lès-Nancy, France, 2001.

[28] R. Sadouni, A. Meroufel, "Performances comparative study of field oriented control (FOC) and direct torque control (DTC) of dual three phase induction motor (DTPIM)" International Journal of Circuits, Systems and Signal Processing, 2(6): 163-170. 2012.

[29] O. Ojo, I.E. Davidson, "PWM-VSI inverter-assisted stand-alone dual stator winding induction generator", IEEE Transactions on Industry Applications, 2000, 36(6): 1604–1611. https://doi.org/10.1109/28.887212

A Finite State Machine Based Energy Management for Fuel-Cell Hybrid Vehicle

Haroune Aouzellag [1], Bessam Amrouche [1], Koussaila Iffouzar [2]

[1]*Laboratoire de Maitrise des Energies Renouvelables (LMER), Faculté de Technologie, Université de Béjaia, 06000 Béjaia, Algeria*

haroune.aouzellag@univ-bejaia.dz , bessam.amrouche@univ-bejaia.dz

[2]*Laboratoire des Sciences Appliquées, Ecole Nationale Supérieure des Technologies Avancées ENSTA d'Alger, Algiers 16000, Algeria*

k.iffouzar@g.essa-alger.edu.dz

***Abstract*— This paper presents a fuel cell hybrid electric vehicle's energy management strategy using a finite-state machine control approach. The finite-state machine strategies are developed based on the vehicle's power demand and the energy storage system's state of charge as transitional conditions. A technique for assessing the stress caused on the fuel cell is proposed. The vehicle's electrical and mechanical elements are modeled using MATLAB/Simulink and SimPower Systems packages. The state-flow control system of MATLAB is utilized to implement the strategies.**

***Keywords*— Energy management, fuel cell, hybrid vehicle, finite state machine.**

I. INTRODUCTION

Considerable attention has been drawn to the advancements in fuel cell (FC) systems and their applications, owing to their potential for zero-emission, high efficiency compared to thermal engine and environmental friendliness [1-2]. A fuel cell is a device that converts hydrogen's chemical energy into electricity through an electrochemical reaction, with various types available. Among these, the proton exchange membrane fuel cell (PEMFC) is particularly suitable for transportation due to its low operating temperature, quick start-up, and high efficiency [3]. However, FC systems suffer from two main drawbacks: low power density and increased vehicle prices [4]. To address the low power density issue, FC vehicles incorporate auxiliary power sources like ultra-capacitors (UC) or batteries, with UCs offering numerous duty cycles and higher power density compared to batteries [5]. These UCs can supply instantaneous high power demands and recover braking energy.

For a vehicle equipped with FC/UC structure, an energy management strategy (EMS) is essential to enhance total system efficiency, reduce fuel consumption, and maintain the performance and longevity of each component. In the past, EMS has been mainly conducted using rule-based approaches. While these approaches yield satisfactory real-time results in managing power flow between sources, they require no knowledge of the mathematical model of the system and have less computation time. However, they necessitate an understanding of the field of application, operating points, and constraints of various components to set the rules ensuring high system performance. Operational restrictions for FC vehicle applications with battery or ultra-capacitor storage systems include avoiding sudden power variations for the FC, recognizing that FC systems' efficiency is low at low loads, and not allowing the battery's state of charge (SOC) to fall below 20% [6]. If the battery or ultra-capacitor feeds the traction system via a parallel structure DC converter, defining the low SOC that guarantees a high converter efficiency operation is crucial, and all these restrictions must be established by the EMS.

In this paper, we propose a finite state machine (FSM) based energy management strategy for FC/UC vehicle structures. The proposed strategy uses as the input variables the UC SOC and the power demand of the vehicle.

The results indicate that the proposed FSM energy management strategy efficiently meets the vehicle's power demand.

II. MODEL OF THE FC VEHICLE

The vehicle consists of an FC system as the principal source of energy and an UC as an energy storage system to assist FC in abrupt power transition and to recover the braking energy. Both sources are linked to the DC bus via converters, as shown in figure 1, and the later feeds the traction system via a DC/AC converter.

The FC will guarantee energy autonomy for long-distance travel, while the UC will guarantee high power density during acceleration phases.

A parallel structure is chosen for the DC/DC converter, despite its low efficiency when the duty cycle is low, but it is still a less bulky structure and has fewer components to maintain in the event of failure.

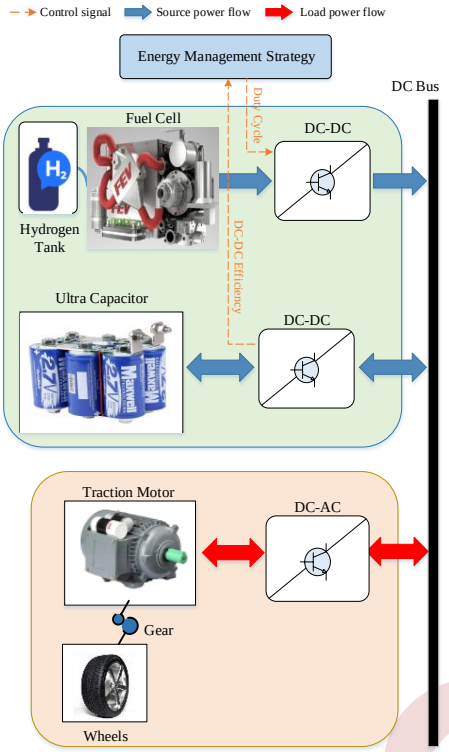


Figure 1. FC hybrid vehicle model

A. *Model of the vehicle*

In this sub-section, only the models of the energy sources are presented, the aerodynamic model of the vehicle as well as the intermediate parts is given in the reference [7-8].

1) *Fuel cell model*

The specific parameters calculation of the PEMFC are as follow:

$$V_{fc} = N_{fc}(E_{nernest} - V_{act} - V_{ohm} - V_{con}) \quad (1)$$

V_{fc} is the FC output voltage, obtained from the theoretical voltage E_{nernst}, which is subject to various voltage drops.
And Nernst voltage E_{nernst} that can be expressed as follow:

$$E_{nernest} = 1.229 + 0.85\times10^{-3}(T - 298.15) + 4.3085\times10^{-5}T\left[\ln(P_{H_2}) - 0.5\ln(P_{O_2})\right] \quad (3)$$

The gas pressure is assumed to be constant and only the electrical dynamics are taken into account in this study.
The resistive losses can be expressed as follows:

$$V_{ohm} = R_{fc}I_{fc} \quad (4)$$

The activation losses are deduced from the relationship between I_{fc} and the current density I_0. They are given by the Tafel relation as follows:

$$V_{act} = A\ln\left(\frac{I_{fc}}{I_0}\right) \quad (5)$$

The concentration polarization losses are defined as:

$$V_{con} = \frac{RT}{zF}\ln 1 - \left(\frac{I_{fc}}{I_{\lim}}\right) \quad (6)$$

TABLE 1. PEMFC PARAMETERS

Parameter	*Value*	*Unit*
Maximal Stack power	52	kW
Nominal Stack Power	37	kW
Nernst Voltage	1.28	V
Nominal Airflow rate	1698	Lpm
Nominal fuel supply pressure	H2: 3, O2: 3	bar
Nominal efficiency	55	%
Operating temperature	95	℃

A FC of 52 kW is used, as mentioned in Tab. 2, to guarantee the maximum power that can be absorbed by the traction system and to cover the various losses.
The model available in the MATLAB library is used, incorporating these parameters. This model gives the polarization curves of the FC as in Fig. 2.

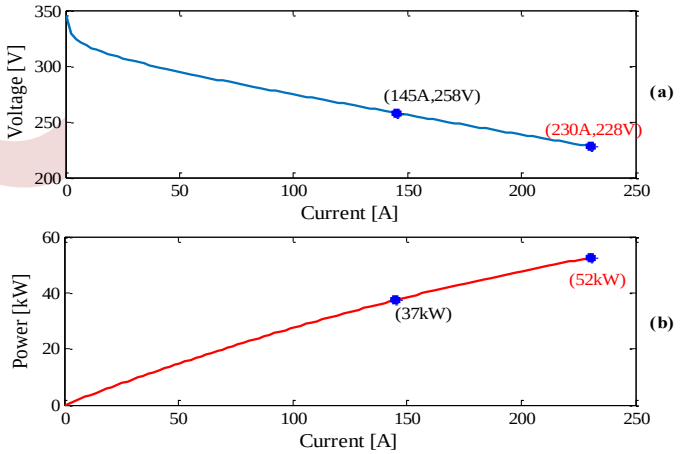


Figure 2. Polarization curves of the PEM FC

To reduce the fuel consumption, the FC system should be operated efficiently. An accurate efficiency model should be used as a reference to determine the operating constraints on the FC system. Fuel cell theoretical efficiency is defined as the ratio between FC output power and the power of hydrogen consumed, which is developed in (7) [9-10].

$$\eta_{LHV} = \frac{P_{fc}}{P_{H_2}} \quad (7)$$

The efficiency of the FC system is the product of the theoretical efficiency and the efficiency of the auxiliary systems.

$$\eta_{fcs} = \eta_{LHV} \times \eta_{aux} = \frac{V_{fc}}{1.254}\left(\frac{P_{fc} - P_{aux}}{P_{fc}}\right) \quad (8)$$

From figure 3, the maximum efficiency point occurs at the fuel cell current of 18 kW. From the power of 7.5 kW to 42.5 kW, the fuel cell system efficiency is above 50 %, which is defined as a high-efficiency region. To reduce the final hydrogen consumption, fuel cells should be operated to reach the maximum efficiency point within this region. In the high power region, the current is high and excessive heating can reduce the lifetime of the FC cells [11]. Therefore, the operation in this region should be reduced.

The hydrogen mass consumption rate can be defined by fuel cell power as the following equation [12]:

$$m_{H_2} = \int_0^t \frac{P_{fc}(t)}{\eta_{fcs}\,\rho_{H_2}}\,dt \quad (9)$$

As we can see in equation (9), the hydrogen consumption is inversely proportional to the FC system efficiency.

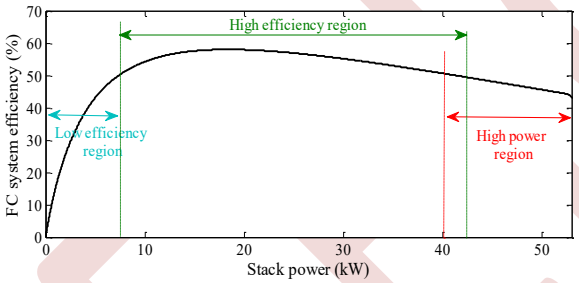


Figure 3. FC system efficiency curve along with stack power

To reduce de fuel consumption, the FC must be operating in the high-efficiency region shown in Fig. 3.

B. Model of the ultra capacitor

The UC model of MATLAB is used, which is modeled as an equivalent circuit model based on Stern model, where the voltage is obtained by the following equation [13]:

$$U_{uc} = \frac{N_s\,Q\,d}{N_p\,N_c\,\varepsilon\,\varepsilon_0\,S_{uc}} + \frac{N_c N_s 2RT_{uc}}{F}\,\text{arsinh}^{-1}\left(\frac{Q}{N_p\,N_s^2\,S_{uc}\sqrt{8\,R\,T\,\varepsilon\,\varepsilon_0\,C}}\right) \quad (10)$$

The implemented model is considered as a variable voltage given by Eq. (7), in series with an internal resistance R_{uc} as shown in figure 3. The output voltage is calculated by taking into account the losses by the Joule effect.

$$V_{uc} = U_{uc} - R_{uc} I_{uc} \quad (11)$$

The state of charge in percent can be calculated by the following expression:

$$SOC = \left(1 - \frac{\int i_{uc}\,dt}{CU_{uc,max}}\right).100 \quad (12)$$

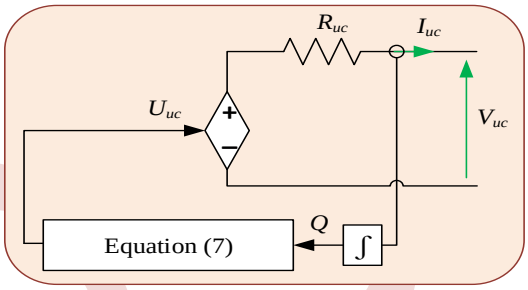


Figure 4. Simulation model of UC

C. DC/DC converters modeling

The DC/DC converters are realized using the power electronics elements of the Sim-Power system library and placed as shown in Fig. 4. The both converters used have the boost structure, with an additional switch for the UC converter to ensure current flow in both directions.

The switches (K_1 and K_{21}) are controlled by the control signals (u_1 and u_2) and current inversion in UC converter is guaranteed by the K_{22} switch associated with the u'$_2$ control signal.

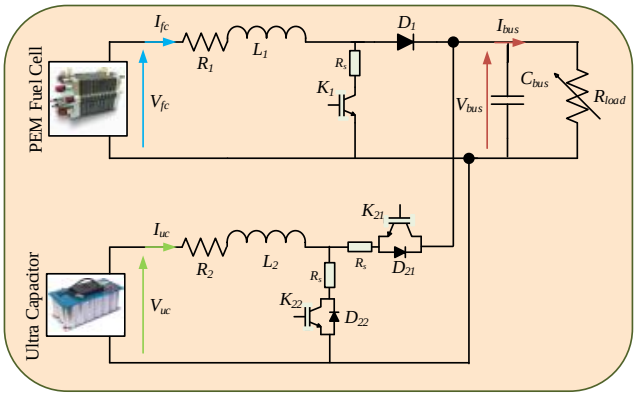


Figure 5. Sources and associated converters

The mathematical model of the converters presented in Fig. 4, in boost mode, is given by the following equations system [13]:

$$\begin{cases} L_1 \dfrac{di_{L_1}}{dt} = V_{fc} - (R_1 + R_s) i_{L_1} - (1 - u_1) V_{bus} \\ L_2 \dfrac{di_{L_2}}{dt} = V_{uc} - (1 - u_2) V_{bus} - [R_2 + R_s] i_{L_2} \\ C_{bus} \dfrac{dv_{bus}}{dt} = (1 - u_2) i_{uc} + (1 - u_1) i_{fc} \end{cases} \quad (13)$$

Tab. 2 shows the FC and UC converters parameters.

TABLE 2. DC/DC CONVERTERS PARAMETERS

Parameter	*Value*	*Unit*
R_{L1}	0.1	Ω
R_{L2}	0.1	Ω
R_s	15	mΩ
L_1	6.4	mH
L_2	3	mH
C_{bus}	560	µF
C_{fc}	10	µF

III. CONTROL OF THE DC/DC CONVERTERS

The UC converter is controlled using a double-loop proportional-integral (PI) controller to fix the DC bus voltage at 400V [13-14]. Figure 5 shows the regulation scheme of the UC converter.

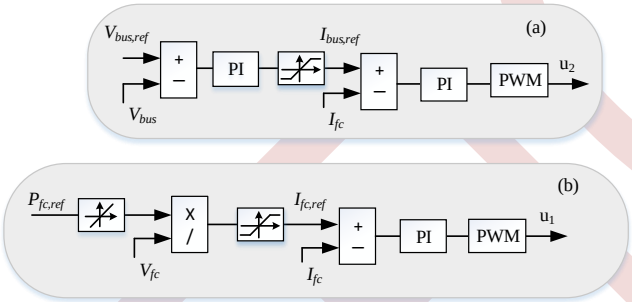


Figure 6. FC current and bus voltage control loops

IV. PROPOSED ENERGY MANAGEMENT STRATEGY

The EMS based on the state machine approach offers a straightforward development process and is independent of the system's mathematical model for tuning. However, it does require a comprehensive understanding of the energy source characteristics. Specifically, when using the state machine-based EMS, the FC reference power should be directed towards power points with optimal efficiency, as illustrated in figure 3. Additionally, for effective recovery of braking energy and to ensure a high UC converter efficiency, the UC state of charge must be limited within certain upper and lower bounds.

Figure 6 presents the SMC represented by nine states, each corresponding to various levels of the state of charge and the power demand of the vehicle. By employing this approach, the fuel cell experiences minimal stress, as the strategy generates a constant power reference within a predetermined range defined by the input bounds for each state. What can be detrimental to the fuel cell is the transition between states. To remedy this, several intermediate states have been added. According to figure 3, there are four distinct states of the power reference: zero FC power, minimal FC power (8 kW), optimal FC power (37 kW) and maximal FC power (52 kW). For example, if the power demand is around the FC low power and the UC state of charge changes from normal to low, the reference power most be increase from low point to optimum point in order to recharge the UC. The sudden transition in a short time can cause damage for the FC cells. So some states have been added as shown in Fig. 7.

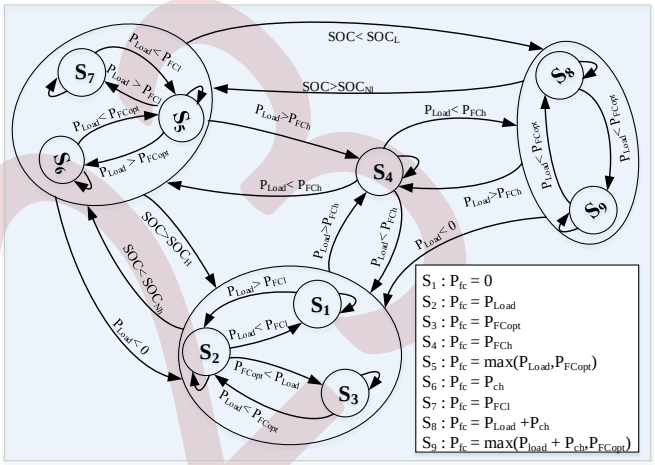


Figure 8. Finite state machine based EMS scheme

V. RESULTS AND DISCUSSIONS

There are several standardized driving cycles for testing vehicle efficiency. In this study, we will use the cycle of HWFET as illustrated in the figure 8. It operates a warmed-up engine with no stops; the average speed is 77 km/h with a top speed of 97 km/h over a 16 km distance.

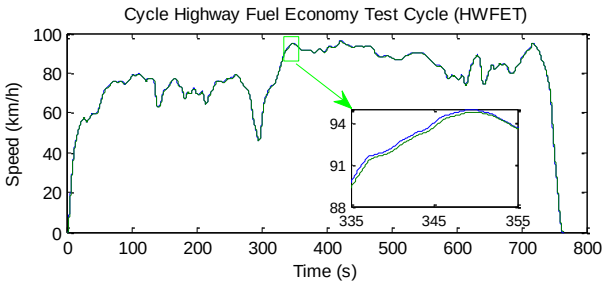


Figure 9. HWFET cycle profile and vehicle speed

The HWFET is a standard cycle used to determine a vehicle's official fuel economy ratings. It represents different driving scenarios focused on highway driving, including various acceleration, deceleration, and constant speed phases.

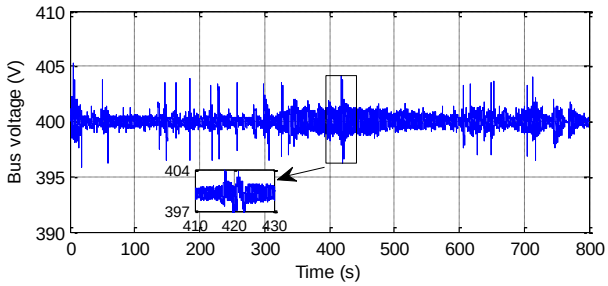


Figure 10. DC bus voltage

The DC bus voltage is kept at its reference value of 400 V by the double PI control loop. Disturbances of ±5 V are observed along the cycle, less than 5 % of the reference value. Therefore, we can conclude that this control is sufficient to guarantee a stable voltage at the input of the inverter feeding the traction machine to ensure a steady speed.

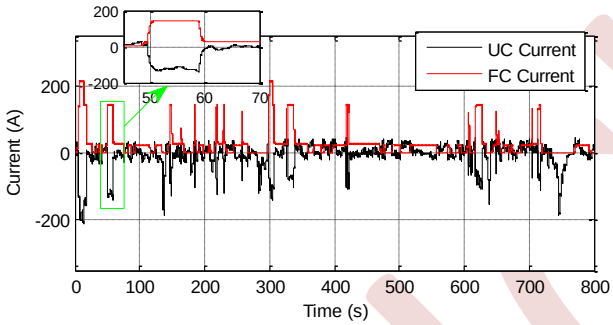


Figure 11. FC and UC currents

From the figure 10, we note that the FC current does not exceed the maximum admissible current for the fuel cell and contains less noise than the current supplied by the UC.

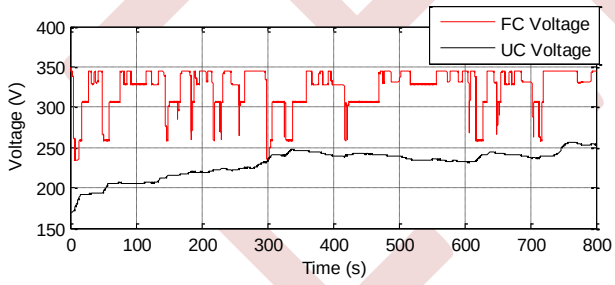


Figure 12. FC and UC voltages

Figure 11 shows the voltages of the energy sources and as we can see that the FC voltage drops when it is activated, due to the different losses presented in equation 2.

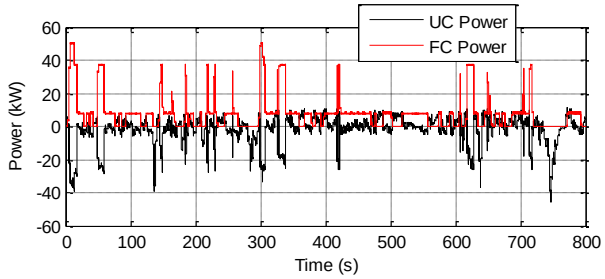


Figure 13. FC and UC powers

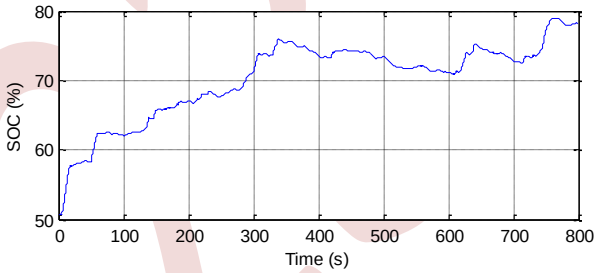


Figure 14. UC state of charge

The UC SOC at the start of the cycle is assumed to be 50% as shown in figure 13. We can see that the UC is less used by the strategy until the SOC exceeds 70%. Therefore, there are two modes of operation: when the state of charge is low [0 to 300s], the UC contributes to the supply of power peaks and this is shown by the noise present in the state of charge profile. Once the UC is charged (high SOC) [300 to 800 s], the UC supplies considerable power to the traction machine and we observe a SOC fluctuation between 75 % and 70 %.

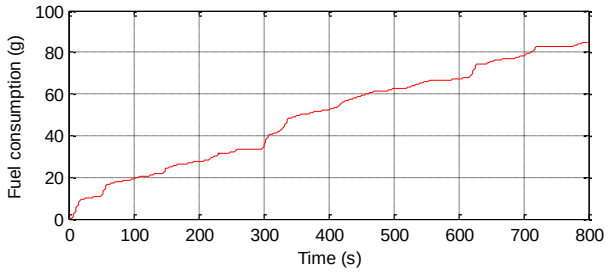


Figure 15. FC fuel consumption

Figure 14 shows the fuel consumption during the HWFET cycle. From figures 10 and 12, we observe that the FC is used at its highest efficiency region as illustrated in the figure 3.

VI. CONCLUSION

In this paper, a finite state machine-based EMS is proposed to manage the energy flow in the hybrid vehicle. The main objectives of the energy management are: firstly, reduce the fuel consumption of the fuel cell system and it is achieved by using the fuel cell in its high efficiency region. Secondly,

reduce the power transition of the control generated by the energy management that causes FC stress and it is realized by using constant states.

REFERENCES

[1] L. Fan, Z. Tu, S. H. Chan, "Recent development of hydrogen and fuel cell technologies: A review. Energy Reports," vol. 7, pp. 8421-8446, 2021.

[2] T. Selmi, A. Khadhraoui, A. Cherif, "Fuel cell–based electric vehicles technologies and challenges," Environ Sci. Pollut. Res., vol. 29, pp. 78121–78131, 2022.

[3] A. Alaswad, A. Omran, J. R. Sodre, et al, « Technical and Commercial Challenges of Proton-Exchange Membrane (PEM) Fuel Cells," Energies, vol. 14, pp. 144, 2021.

[4] F. Un-Noor, S. Padmanaban, L. Mihet-Popa, M .N. Mollah, E. A. Hossain, "Comprehensive Study of Key Electric Vehicle (EV) Components, Technologies, Challenges, Impacts, and Future Direction of Development," Energies, vol. 10, pp. 1217, 2017.

[5] D. Kumar, R. K. Nema, S. A. Gupta, "Comparative review on power conversion topologies and energy storage system for electric vehicles," Int. J. Energy Res., vol. 44, pp. 7863– 7885, 2020.

[6] S. Njoya Motapon, L. A. Dessaint, K. Al-Haddad, "A Comparative Study of Energy Management Schemes for a Fuel-Cell Hybrid Emergency Power System of More-Electric Aircraft," in IEEE Transactions on Industrial Electronics, vol. 61, pp. 1320-1334, 2014.

[7] E. D. Kostopoulos, G. C. Spyropoulos, J. K. Kaldellis, "Real-world study for the optimal charging of electric vehicles," Energy Reports, vol. 6, pp. 418-426, 2020.

[8] H. Aouzellag, K. Ghedamsi, D. Aouzellag, "Energy management and fault tolerant control strategies for fuel cell/ultra-capacitor hybrid electric vehicles to enhance autonomy, efficiency and lifetime of the fuel cell system," International Journal of Hydrogen Energy, vol. 40, pp. 7204-7213, 2015.

[9] A. Ferrara, M. Okoli, S. Jakubek, C. Hametner, "Energy management of heavy-duty fuel cell electric vehicles: model predictive control for fuel consumption and lifetime optimization," IFAC-Papers On Line, vol. 53, pp. 14205-14210, 2020.

[10] H. Aouzellag, B. Amrouche, K. Iffouzar, D. Aouzellag, "Proposed hysteresis energy management strategy based on storage system efficiency for hybrid electric vehicle," Journal of Energy Storage, vol. 54, 105259, 2022.

[11] Y. Oono, T. Fukuda, A. Sounai, M. Hori, "Influence of operating temperature on cell performance and endurance of high temperature proton exchange membrane fuel cells," Journal of Power Sources, vol. 195, 1007–14, 2010.

[12] Z. Fu et al., "Optimization based energy management strategy for fuel cell/battery/ultracapacitor hybrid vehicle considering fuel economy and fuel cell lifespan," Int. Journal of Hydrogen Energy, vol. 45, pp. 8875-8886, 2020.

[13] L. Török, S. D. Sønderskov and S. Munk-Nielsen, "Bidirectional Operation of High Efficiency Isolated DC-DC Converter in Fuel Cell Telecom Back-up Systems," 2018vIEEE International Telecommunications Energy Conference (INTELEC), pp. 1-5.

[14] M.S. Mahdavi, M. S. Karimzadeh, T. Rahimi, G. B. Gharehpetian, "A Fault-Tolerant Bidirectional Converter for Battery Energy Storage Systems in DC Microgrids," Electronics, Vol. 12, pp. 679, 2023

Robust Control of DFIG Wind Turbines in Sub/Super-Synchronous Operation Using Integral Backstepping Controller

Itouchene Hichem[*1], Amrane Fayssal[2] and Boudries Zoubir[3]

[1*] *Laboratory of Industrial Technology and Information (LII), Faculty of Technology University of Bejaia, Algeria*
hichem.itouchene@univ-bejaia.dz

[2] *LAS Research Laboratory Department of Electrical Engineering, University of Setif 1, Setif, Algeria*
amrane_fayssal@univ-setif.dz

[3] *Laboratory of Industrial Technology and Information (LII), Faculty of Technology University of Bejaia Algeria*
zboudries@yahoo.fr

***Abstract*—This paper presents a robust control strategy for Doubly Fed Induction Generator (DFIG) wind turbines in Sup/Super Synchronous operation using an integral backstepping controller (INT-BCS-Control) based on the Lyapunov function. The objective of this work is to decouple the active and reactive power of the DFIG with high robustness and enhance the performance and reliability of DFIG wind turbines operating in the Sup/Super Synchronous mode within grid-connected systems. To ensure the effectiveness of the proposed control, we present simulation results using MATLAB Simulink.**

Keywords: **wind turbines, Lyapunov function, Integral Backstepping, DFIG, robustness.**

I. INTRODUCTION

As the world industrializes and people consume more electricity, the demand for electricity is growing. Fossil fuels are the main source of electricity production, but they are a major contributor to climate change and other environmental problems [1]. Governments are investing in renewable energy sources to ensure sustainable development [2]. The renewable energy sector is becoming more competitive, and wind energy is growing the fastest in the world [3-4].

This work evaluates the impact of integral backstepping control on a wind energy conversion system based on a doubly fed induction generator (DFIG). The DFIG was chosen because it offers several advantages, including improved output power, increased efficiency, grid support capability, variable speed operation, cost-effectiveness, and reduced mechanical stress on the wind turbine. [5-6].

Backstepping control is a nonlinear control strategy that decomposes complex systems into simpler subsystems and stabilizes a desired system behavior using a Lyapunov function [6-7]. It was developed by Kokotovic in the 1990s [6] and has become a widely studied and used approach for controlling nonlinear systems [8].

This study aims to assess the impact of backstepping control on a DFIG-based wind energy conversion system, especially under parameter variations. The grid-side converter (GSC) is directly connected to the grid, while the rotor-side converter (RSC) is connected to the grid through a series of converters and transformers [9], as shown in figure 1.

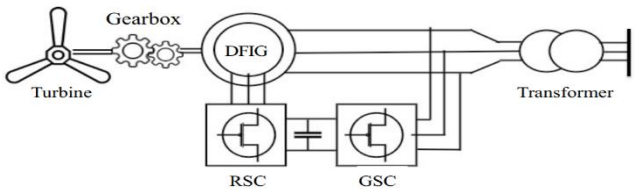


Figure .1 Architecture of wind turbine system (WTS) [10]

II. WIND TURBINE MODEL

The mechanical power of a wind turbine is proportional to the cube of the wind speed, while the torque is proportional to the square of the wind speed. This means that the mechanical power and torque of a wind turbine increase rapidly with increasing wind speed [1]. The relationship between the mechanical power and torque of a wind turbine can be expressed by the following formula [10-11]:

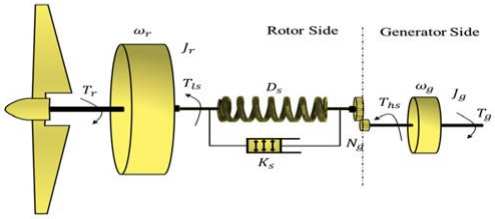


Figure .2 The structure of a wind turbine [7]

$$P_{aero} = \frac{1}{2}.\rho.\pi.R^2.v^3.C_p(\lambda;\beta) \quad (1)$$

$$T_{aero} = \frac{C_p(\lambda;\beta).\rho.\pi.R^2.v^3}{2.\Omega_{turbine}} \quad (2)$$

With the relative speed λ provided by this equation:

$$\lambda = \frac{\Omega_t.R}{V}$$

Cp can be thought of as the percentage of wind energy that is converted into mechanical energy by the turbine. A higher Cp value indicates a more efficient turbine. The power coefficient Cp can be described as follows:

$$C_p(\beta,\lambda) = \left(0.5 - 0.0167.(\beta-2)\right).\sin\left[\frac{\pi.(\lambda+0.1)}{18.5-0.3.(\beta-2)}\right] - 0.00184.(\lambda-3).(\beta-2) \quad (3)$$

Figure 3 shows how the power coefficient changes as the speed ratio (λ) and pitch angle (β) change. The figure shows that the optimal speed ratio for maximum power point tracking (MPPT) mode with β= 0° is λ_{opt} = 8.1, which gives a maximum power coefficient of $C_{p\text{-}max}$= 0.48.[11]

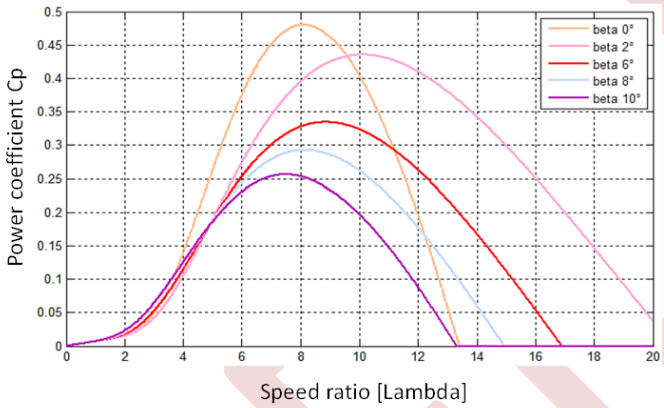


Figure .3 Power coefficient Vs Lambda

III. DFIG MODEL

The DFIG's electrical equations describe how the voltage and current at the stator and rotor terminals depend on the slip and the speed of the rotor. These equations can be used to model the electrical behavior of the DFIG and to calculate its power output and torque [10-11].

$$\begin{aligned} V_{sd} &= R_s I_{sd} + \frac{d\,\emptyset_{sd}}{dt} - \omega_s \emptyset_{sq} \\ V_{sq} &= R_s I_{sq} + \frac{d\,\emptyset_{sq}}{dt} + \omega_s \emptyset_{sd} \\ V_{rd} &= R_r I_{rd} + \frac{d\,\emptyset_{rd}}{dt} - \omega_r \emptyset_{rq} \\ V_{rq} &= R_r I_{rq} + \frac{d\,\emptyset_{rq}}{dt} + \omega_r \emptyset_{rd} \end{aligned} \quad (4)$$

With:

$$\begin{aligned} \emptyset_{sd} &= L_s I_{sd} + M I_{rd} \\ \emptyset_{sq} &= L_s I_{sq} + M I_{rq} \\ \emptyset_{rd} &= L_r I_{rd} + M I_{sd} \\ \emptyset_{rq} &= L_r I_{rq} + M I_{sq} \end{aligned}$$

Mechanical equation:

$$T_{em} = T_r + J\frac{d\Omega_r}{dt} \quad (5)$$

The state model can then be written as:

$$[\dot{X}] = [A].[X] + [B].[U] \quad (6)$$

With:

$$[X] = [I_{sd}\ I_{sq}\ I_{rd}\ I_{rq}\ ]^t$$

$$[U] = [V_{sd}\ V_{sq}\ V_{rd}\ V_{rq}\ ]^t$$

Where:

$$[A] = \begin{bmatrix} -a_1 & a\omega + \omega_s & a_3 & a_5\omega \\ -a\omega - \omega_s & -a_1 & -a_5\omega & a_3 \\ a_4 & -a_6\omega & -a_2 & -\frac{\omega}{\sigma} + \omega_s \\ a_6\omega & a_4 & \frac{\omega}{\sigma} - \omega_s & -a_2 \end{bmatrix}$$

$$[B] = \begin{bmatrix} b_1 & 0 & -b_3 & 0 \\ 0 & b_1 & 0 & -b_3 \\ -b_3 & 0 & b_2 & 0 \\ 0 & -b_3 & 0 & b_2 \end{bmatrix}$$

$$\alpha = \frac{1-\sigma}{\sigma};\ a_1 = \frac{R_s}{\sigma L_s};\ a_2 = \frac{R_r}{\sigma L_r};\ a_3 = \frac{R_r M}{\sigma L_s L_r};\ a_4 = \frac{R_s M}{\sigma L_s L_r};\ a_5 = \frac{M}{\sigma L_s};$$

$$a_{36} = \frac{M}{\sigma L_r}$$

Based on the last equations, the DFIG model in Matlab/Simulink can be simplified as shown in the following figure.

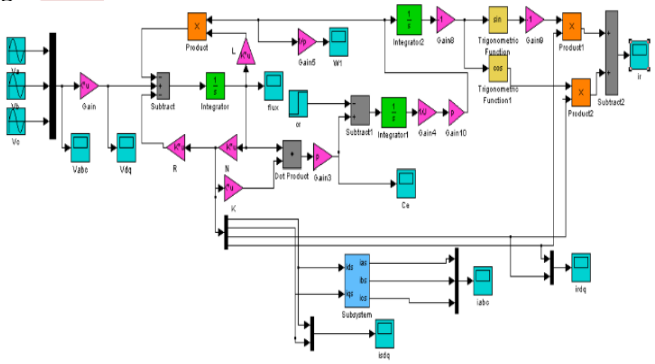


Figure .4 DFIG Module in Matlab/Simulink

IV. INTEGRAL BACKSTEPPING CONTROL

Integral Backstepping is a variation of Backstepping control that adds integral action. This makes it more robust to perturbations and can help to eliminate steady-state errors. The error variable is defined as the difference between the actual and desired states of the system. The specific definition of the error variable will depend on the application and system dynamics [11].

$$\dot{e_{01}} = e_{r1} = P_s^* - P_s \quad (7)$$

$$\dot{e_{02}} = e_{r2} = Q_s^* - Q_s$$

$$e_{01} = \gamma * \int_0^t e_{r1}(t).dt\,, \qquad \gamma > 0 \tag{8}$$

$$e_{02} = \gamma * \int_0^t e_{r2}(t).dt\,, \qquad \gamma > 0$$

Lyapunov function:

$$V(e_{r1}) = \frac{1}{2}.e_{r1}^2 + \frac{1}{2}.e_{01}^2 \tag{9}$$

$$V(e_{r2}) = \frac{1}{2}.e_{r2}^2 + \frac{1}{2}.e_{02}^2$$

Derivative of Lyapunov function:

$$\dot{V}(e_{r1}) = e_{r1}\,\dot{e_{r1}} + \gamma e_{r1}\,e_{01} \tag{10}$$

$$\dot{V}(e_{r2}) = e_{r2}\,\dot{e_{r2}} + \gamma e_{r2}\,e_{02}$$

$$\dot{V}(e_{r1}) = e_{r1}\,(\dot{e_{r1}} + e_{01})$$

$$\dot{V}(e_{r2}) = e_{r2}\,(\dot{e_{r2}} + e_{02})$$

The expression of the Backstepping stabilizer with integral action is typically taken as follows:

$$v_{rd} = -\frac{2}{3}\frac{Y}{X}\dot{Q}_s^* + R_r i_{rd} - g w_s Y * i_{rq} - \frac{2}{3}\frac{Y}{X} * (k_2\,e_{r2} + e_{02}) \tag{11}$$

$$v_{rq} = -\frac{2}{3}\frac{Y}{X}.\dot{P}_s^* + Y g w_s * i_{rd} + R_r i_{rq} + gX - \frac{2}{3}\frac{Y}{X} * (k_1\,e_{r1} + e_{01})$$

Where: $X = \frac{V_s L_m}{L_s}$, $Y = \sigma.L_r$

$$\dot{V}(e_1) = -k_1\,e_{r1}^2 \tag{12}$$

$$\dot{V}(e_{r1}, e_{r2}) = -k_1\,e_{r1}^2 - k_2\,e_2^2$$

With K_1 and K_2 being positive.

V. INTEGRAL BACKSTEPPING CONTROL

The DFIG used in this work is a doubly fed induction generator that is connected to the grid. The nominal parameters of the DFIG and the turbine parameters are given in Appendix. The Integral Backstepping Control (INT-BCS-Control) will be tested through simulation using MATLAB/SIMULINK software. The following tests will be conducted:

- References tracking and transient response.
- Robustness to perturbations.

A. References Tracking and Transient Response

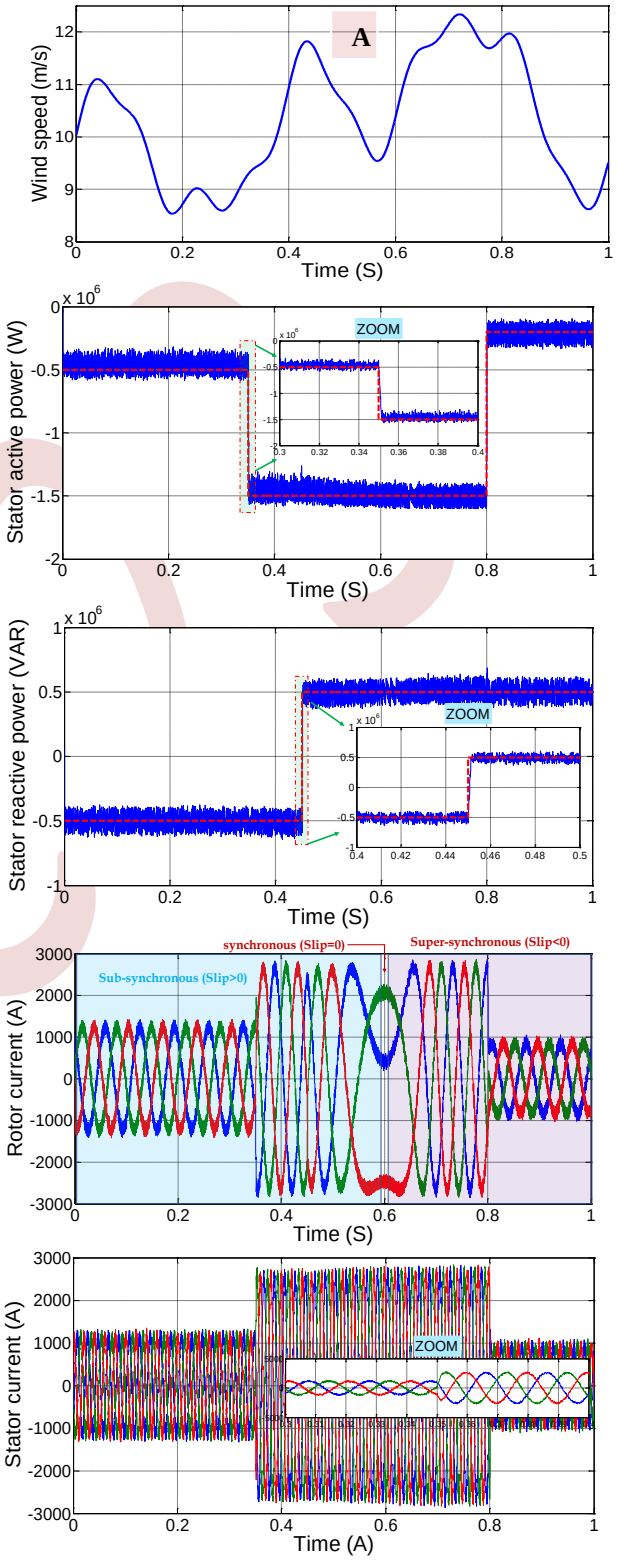


Figure 5. Simulation results of the INT-BCS-Control of DFIG at variable wind speed

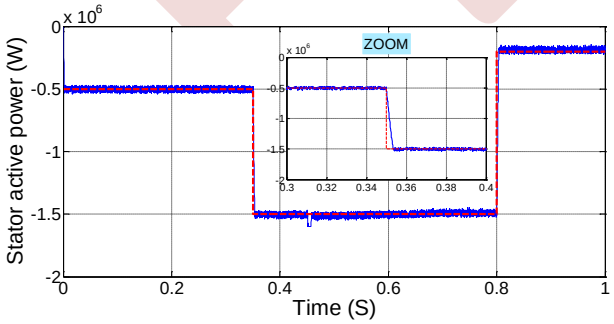
In this case, the wind turbine operates under variable wind speeds, with an average value of 10 m/s, as shown in figure 5.A. figure 5 represents the simulation results for the INT-BCS-Control of DFIG. The objective of this test is to evaluate the performance of an Integral Backstepping control system in terms of its ability to accurately track specified references.

The simulation results show that the INT-BCS-Control is a robust and effective control strategy for DFIG wind turbines. It is able to accurately track the desired references for both the stator active and reactive power, as evident from the fact that the graphs of the stator active and reactive power closely follow the reference signals. Additionally, the currents, which are proportional to the active power, also exhibit sinusoidal behavior because the INT-BCS-Control is designed to regulate the active and reactive power of the DFIG. The rotor current undergoes a smooth and controlled transition from the Sub-synchronous mode to the Super-synchronous mode of the DFIG at 0.5 seconds because the wind profile applied to the wind turbine changes at this time. The Sub-synchronous mode is the mode in which the rotor speed is less than the synchronous speed of the DFIG, while the Super-synchronous mode is the mode in which the rotor speed is greater than the synchronous speed of the DFIG.

B. Robustness To Perturbations

The robustness test was conducted by varying the parameters of the DFIG model. The stator inductance, Ls, and rotor inductance, Lr, were reduced by 10% of their rated values. This was done to analyze the performance of the system. Figure 6 illustrates the simulation results of the INTBCS-Control applied to the DFIG.

The INT-BCS-Control, exhibit good dynamic and static performance, despite variations in the DFIG parameters. This is evident in the curve shown in Figure 6. The response time of the active and reactive powers are fast and impressive, with INT-BCS-Control demonstrating a response time of 0.0007 seconds. However, it is important to note that the last nonlinear method does exhibit high-frequency oscillations, particularly in the rotor currents. This could potentially lead to problems with the power converter or the DFIG itself.



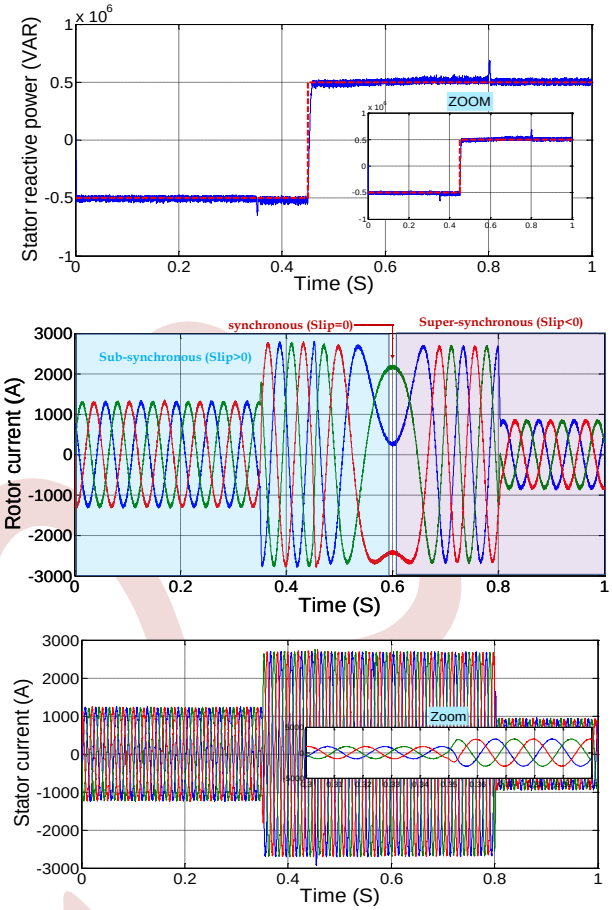


Figure 6. Simulation results of the INT-BCS-Control of DFIG at parameters variations

CONCLUSION

In this paper, a robust nonlinear control strategies is presented namely INT-BCS-Control, have been presented. These strategies enable independent control of the active and reactive stator powers of the DFIG, which is driven by a variable speed wind turbine. The results obtained from robustness tests using MATLAB/Simulink have demonstrated that the INT-BCS-Control strategy is a simple and robust control technique. This strategy has the advantage of being easily implemented in real-time and effectively eliminates static errors, while reducing the gap between measurement and reference.

Through a comprehensive study of the proposed control method in this paper and based on the simulation results using MATLAB Simulink, we can say that the INT-BCS-Control technique excels in the following aspects:

- Nonlinear control method
- Good dynamic and static performance
- Accurately tracks desired reference signals
- Effective for systems with nonlinear dynamics
- Robust against uncertainties and disturbances
- Utilizes Lyapunov stability theory for stability analysis
- Relatively complex to design and implement

ACKNOWLEDGMENT

We would like to express our sincere appreciation to everyone who contributed in various ways to this research. In addition, we would like to thank our colleagues in the electrical engineering department for their feedback and support. We are also grateful to the participants in our study, without whom this research would not have been possible.

APPENDIX

The parameters of the DFIG and Wind turbine, in SI units are:

DFIG Parameter: P_n=1.5MW, P=2, R_s= 0.012Ω, R_r=0.021 Ω, L_s= 0.0137 Ω, L_r=0.0136 Ω, L_m=0.0135 Ω, V_{dc}=1200 volt

Turbine Parameter: Np=3, R=35.25m, G=90, f_v=0.0024, J=1000Kg.m^2

REFERENCES

[1] El Mourabit Youness, Derouich Aziz, El Ghzizal Abdelaziz, Zamzoum Othmane, and El Ouanjli Najib, "Nonlinear backstepping control of variable speed wind turbine based on permanent magnet synchronous generator," International Conference on WITS, morocco, 2019,

[2] Youness El Mourabit, Aziz Derouich, Abdelaziz El Ghzizal, Najib El Ouanjli, and Othmane Zamzoum, "Nonlinear backstepping control for PMSG wind turbine used on the real wind profile of the Dakhla-Morocco city," Int Trans Electr Energ Syst, 2019,

[3] Rabiaa Mahroug, Mohamed Matallah, and Salam Abudura, "Modeling of wind turbine based on dual DFIG generators," International Journal of Power Electronics and Drive Systems (IJPEDS), vol. 13, no. 2, pp. 1170-1185, 2022.

[4] Z. Faramarzi, S. Abazari , S. Hoghoughi, and N. Abjadi, "Improved power system dynamic stability by DFIG in the presence of SSSC using adaptive nonlinear multi-Input backstepping," Journal of Operation and Automation in Power Engineering, 2022,

[5] Arafat Hossain, Rashidul Islam, Yahya Ul Haque, Jakir Hasan, Tushar Kanti Roy, and Mohammad Ashraf Hossain Sadi, "Protecting DFIG-based multi-machine power system under transient-state by nonlinear adaptive backstepping controller-based capacitive BFCL," IET Generation, Transmission & Distribution published by John Wiley & Sons Ltd on behalf of The Institution of Engineering and Technology, 2022.

[6] Mourad Yessef, Badre Bossoufi, Mohammed Taoussi, Ahmed Lagrioui and Mohammed El Mahfoud, "Evaluation of adaptive backstepping control applied to DFIG wind system used on the real wind profile of the Dakhla-Morocco city," 2021,

[7] Ahmad Parvaresh, Saber Abrazeh, Saeid-Reza Mohseni ,Meisam Jahanshahi Zeitouni, Meysam Gheisarnejad, and Mohammad-Hassan Khooban, "A novel deep learning backstepping controller-based digital twins technology for pitch angle control of variable speed wind turbine," Articl designs, vol.15, no.4, 2020;

[8] Cheriet Ahmed, Abdelkader Bekri, Hicham Gouabi, and Hamed Ali, "Nonlinear backstepping control optimized by genetic algorithm for the control of a wind turbine generator (DFIG)", International Journal of Industrial Electronics and Electrical Engineering, vol.7, iss.6, 2019,

[9] Youcef Djeriri, "Robust second order sliding mode control of doubly fed induction generator for wind energy conversion system," Article in Acta Electrotechnica et Informatica-October 2020,

[10] Salmi Hassan, Badri Abdelmajid, Zegrari Mourad, Sahel Aicha, and Baghdad Abdenaceur, "PSO-backstepping controller of a grid connected DFIG based wind turbine," International Journal of Electrical and Computer Engineering (IJECE), vol. 10, No. 1, pp. 856-867,2020,

[11] Yahya Dbaghi, Sadik Farhat, Mohamed Mediouni, Hassan Essakhi, and Aicha Elmoudden, "Indirect power control of DFIG based on wind turbine operating in MPPT using backstepping approach," vol. 11, no. 3, pp. 1951-1961, 2021,

Control of a Wind Turbine based on DFIG by Improved Direct Torque Control using Fuzzy Logic

Karim Fathi Sayeh[1], Salah Tamalouzt[1], Djamel Ziane[1,2], Younes Sahri[1], Brahim Deffaf[3], Sofia Lalouni Belaid[1]

[1] *Laboratoire de Technologie Industrielle et de l'Information (LTII), Faculté de Technologie, Université de Bejaia, Bejaia 06000, Algeria*
E mail: karimfathi.sayeh@univ-bejaia.dz, salah.tamalouzt@univ-bejaia.dz, younes.sahri@univ-bejaia.dz, lalouni_sofia@yahoo.fr

[2] *Nantes Université, Institut de Recherche en Énergie Électrique de Nantes Atlantique, IREENA, UR 4642, F-44600, Saint-Nazaire, France*
E-mail: djamel.ziane@univ-nantes.fr

[3] *Laboratoire de Maitrise des Energies Renouvelables (LMER), Faculté de Technologie, Université de Bejaia, Bejaia 06000, Algeria*
E-mail: brahim.deffaf@univ-bejaia.dz

***Abstract*— This work presents the utility of using a fuzzy logic controller to improve the performance of DTC applied to a wind turbine based on a doubly-fed induction generator (WT-DFIG). The objectives are to minimize the drawbacks of conventional DTC (C-DTC) as much as possible and to preserve its advantages, by proposing an improved DTC based on fuzzy controllers (FH-DTC). The simulation results obtained on MATLAB/Simulink showed the effectiveness of the proposed technique in minimizing the disadvantages of C-DTC, in a remarkable way, thus leading to better performance of the WT-DFIG system.**

***Keywords:* Wind turbine, DTC, DFIG, Hysteresis, Fuzzy logic controller.**

I. INTRODUCTION

Wind energy is a renewable energy source, gaining in popularity because of its ability to produce clean energy while reducing pollution and global warming. Due to its high performance, wide speed range and active and reactive power control, the doubly-fed induction generator (DFIG) is the most efficient generator for variable-speed wind farms [1].

In the mid-1980s, the direct torque control (DTC) technique was introduced [2]. Its objective is to determine the best rotor voltage vector by considering the hysteresis errors, rotor flux sector and switching tables. The presence of large ripples is the main challenge of DTC, for which various complex solutions have been proposed such as [3-6].

The main objective of this work is to present the utility of using a fuzzy logic controller to improve the performance of DTC applied to a WT-DFIG, in the different operating modes of this generator. The aims are to minimize as much as possible the disadvantages of C-DTC, even if it is possible to eliminate some, while preserving its advantages, by proposing an improved DTC based on fuzzy controllers (FH-DTC). The results of this study will be presented in the form of complete simulation results obtained using MATLAB/Simulink

The main contributions of this paper are: (1) The development of an FH-DTC scheme for DFIG wind turbines; (2) The design of fuzzy hysteresis controllers for torque and flux; (3) Performances evaluation through simulations under three WT-DFIG operating modes. This work aims to establish the viability of the proposed FH-DTC technique for high-performances DFIG-based wind energy conversion systems.

The paper is organized as follows. First, the DFIG wind turbine and conventional DTC principles are explained. Next, the proposed FH-DTC scheme and fuzzy controller designs are presented. Then, MATLAB/Simulink simulation results are analyzed to evaluate the performance of the proposed strategy under fluctuating wind speeds. Finally, conclusions are provided.

II. DESCRIPTION OF THE PROPOSED SYSTEM

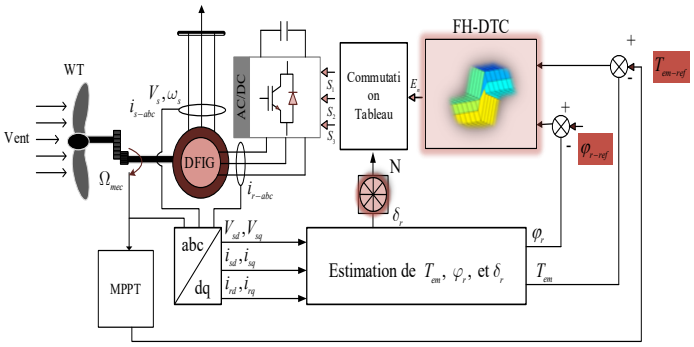


Figure 1. FH-DTC method applied to the WT-DFIG.

The Wind turbine-DFIG (WT-DFIG) system controlled by the proposed FH-DTC technique is illustrated in Fig. 1. This system comprises a DFIG, a gearbox and a wind turbine. While the DFIG rotor is connected to two level back to back power converter (an AC/DC and a DC/AC), the stator is directly connected to the AC grid. The first rotor converter is connected

to the DFIG rotor controlled by the proposed technique, the other converter is connected to the AC grid, it delivers a sinusoidal current (50 Hz) with a unity power factor.

Then the MPPT algorithm allows the system to extract maximum power when the generated power is below the rated value [7].

The mechanical power of the wind turbine is a function of wind speed v and power coefficient C_p, as presented in the following equation:

$$P_{mec}=0.5\rho\pi R^2 v^3 C_P(\lambda,\beta) \quad (1)$$

The mathematical model of the doubly fed induction generator (DFIG) in the d-q frame is given by:

$$\begin{cases} v_{sd}=R_s i_{sd}+\frac{d\varphi_{sd}}{dt}-\omega_s\varphi_{sq} \\ v_{sq}=R_s i_{sq}+\frac{d\varphi_{sq}}{dt}+\omega_s\varphi_{sd} \\ v_{rd}=R_r i_{rd}+\frac{d\varphi_{rd}}{dt}-\omega_r\varphi_{rq} \\ v_{rq}=R_r i_{rq}+\frac{d\varphi_{rq}}{dt}+\omega_r\varphi_{rd} \end{cases} \quad (2)$$

$$\begin{cases} \varphi_{sd}=L_s i_{sd}+Mi_{rd} \\ \varphi_{sq}=L_s i_{sq}+Mi_{rq} \\ \varphi_{rd}=L_r i_{rd}+Mi_{sd} \\ \varphi_{rq}=L_r i_{rq}+Mi_{sq} \end{cases} \quad (3)$$

Where

v_{sd},v_{sq},v_{rd} and v_{rq}: Stator and rotor voltages in the d-q frame respectively;

I_{sd},I_{sq},I_{rd} and I_{rq}: Stator and rotor current in the d-q frame respectively;

ω_s,ω_r: Stator and rotor phase electrical variable pulsations respectively;

R_s,R_r: Stator and rotor resistances respectively;

L_s,L_r: Stator and rotor leakage inductances respectively;

M: Stator-rotor mutual inductance.

III. Direct Torque Control

To control the DFIG, the DTC advanced approach adjusts the machine's electromagnetic torque and the rotor's magnetic flux. It was first proposed by Takahashi and Noguchi in 1986 as an alternative to field-oriented control (FOC). The aim of DTC is to directly select the AC/DC converter switching states to rapidly regulate flux and torque based on the errors between their references and estimated values. This differs from FOC which involves regulating current components through PI controllers. The principle of DTC is explained in [8]. The system under study is illustrated in Fig. 1.

The components along the α and β axes of the rotor voltages and currents are used to estimate the rotor magnetic flux, then the calculated values of the currents ($i_{r\alpha}$, $i_{r\beta}$) and the estimated flux values ($\varphi_{r\alpha}$, $\varphi_{r\beta}$) are used to estimate the electromagnetic torque. As illustrated by the equations that follow.

$$\begin{cases} \varphi_{r\alpha}(t)=\int_0^t (v_{r\alpha}-R_r i_{r\alpha}) \\ \varphi_{r\beta}(t)=\int_0^t (v_{r\beta}-R_r i_{r\beta}) \end{cases} \quad (4)$$

$$\varphi_r(t)=\sqrt{\varphi_{r\alpha}^2+\varphi_{r\beta}^2} \quad (5)$$

$$\theta_r=\tan^{-1}\left(\frac{\varphi_{r\beta}}{\varphi_{r\alpha}}\right) \quad (6)$$

$$T_{em}=P(\varphi_{r\alpha}i_{r\beta}-\varphi_{r\beta}i_{r\alpha}) \quad (7)$$

The outputs of the hysteresis controllers (electromagnetic torque controller and rotor flux controller) and the position of the rotor flux vector are used to select the optimal vector required using a switching table, As outlined in Table 1 [8].

To minimize the number of commutations in the arms of the AC/DC converter, the V0 and V7 vectors are alternated.

TABLE I. Switching Table C-DTC

$H\varphi_r$	HT_{em}	N					
		I	II	III	IV	V	VI
+1	+1	V_2	V_3	V_4	V_5	V_6	V_1
	0	V_7	V_0	V_7	V_0	V_7	V_0
	-1	V_6	V_1	V_2	V_3	V_4	V_5
-1	+1	V_3	V_4	V_5	V_6	V_1	V_2
	0	V_0	V_7	V_0	V_7	V_0	V_7
	-1	V_5	V_6	V_1	V_2	V_3	V_4

IV. The Proposed Direct Torque Control

The proposed FH-DTC uses a fuzzy logic controller, rather than two hysteresis controllers to improve C-DTC performance. The FH-DTC design process includes fuzzification, defuzzification and fuzzy logic control based on rules. The fuzzification process converts the system input variables into linguistic variables by defining membership functions for each input variable, see Fig. 2. The defuzzification process converts the fuzzy inference results into a quantifiable output. The defuzzification method chosen is Bi sector and the output is a single numerical value with 6 singleton membership functions (E1, ..., E6), see Fig. 3.

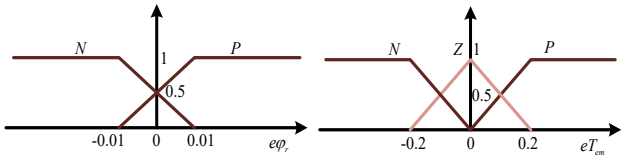


Figure 2. Inputs membership functions.

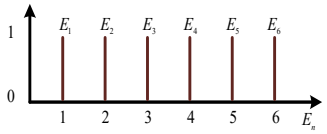


Figure 3. Output membership functions.

Finally, the fuzzy rules are designed according to a hysteresis operating principle and consist of 6 rules due to the number of membership functions per table 2 input. The inference method used to run the fuzzy logic switching controller is the Mamdani method based on Max-Min decision.

TABLE II. FUZZY RULES

eTem/eφ	P	Z	N
P	E_1	E_2	E3
N	E_4	E_5	E_6

To select the appropriate rotor voltage vector (V_n) for the inverter, it will be based on the output of the numerical error powers (E_n) and the rotor flux sector using the switching table 3.

TABLE III. SWITCHING TABLE FH-DTC

En	N					
	I	II	III	IV	V	VI
E_1	V_2	V_3	V_4	V_5	V_6	V_1
E_2	V_7	V_o	V_7	V_o	V_7	V_o
E_3	V_6	V_1	V_2	V_3	V_4	V_5
E_4	V_3	V_4	V_5	V_6	V_1	V_2
E_5	V_o	V_7	V_o	V_7	V_o	V_7
E_6	V_5	V_6	V_1	V_2	V_3	V_4

V. SIMULATION RESULTS

The effectiveness of the proposed technique is applied to control a WT-DFIG system, allowing the DFIG to operate in its three operating modes. The study is carried out using MATLAB/Simulink. Where the system parameters are described in [7].

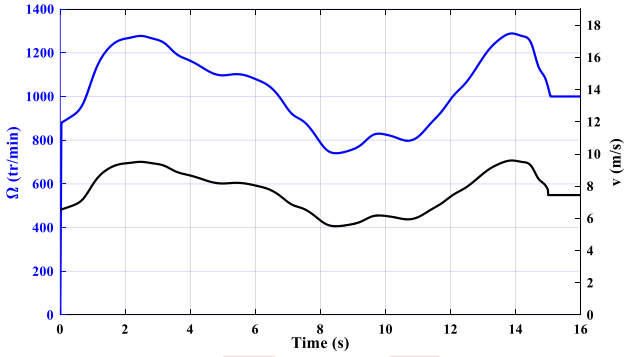


Figure 4. Ω and v responses.

Fig. 4. It represents wind speed and the mechanical speed of the DFIG, indicating that the system is operating in three modes, (sub-synchronous, synchronous and super-synchronous, respectively).

The electromagnetic torque with its reference and the rotor flux are illustrated in Figures 5 and 6, respectively. The torque is influenced by the wind speed and follows its reference. At its reference value, the rotor flux remains constant. The proposed FH-DTC control has proven its effectiveness and advantages compared to those of conventional control (C-DTC) illustrated in reference [8].

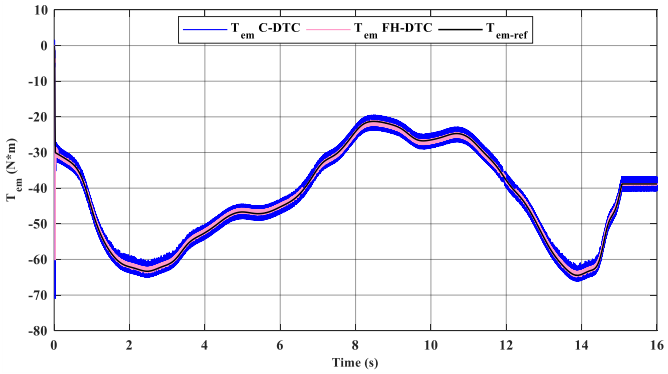


Figure 5. Electromagnetic torque and its reference.

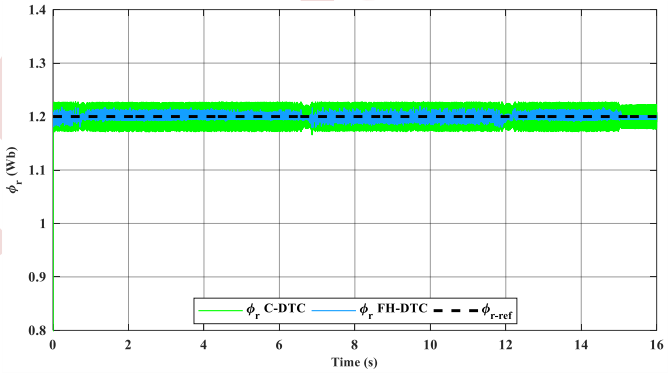


Figure 6. Rotor flux and its reference.

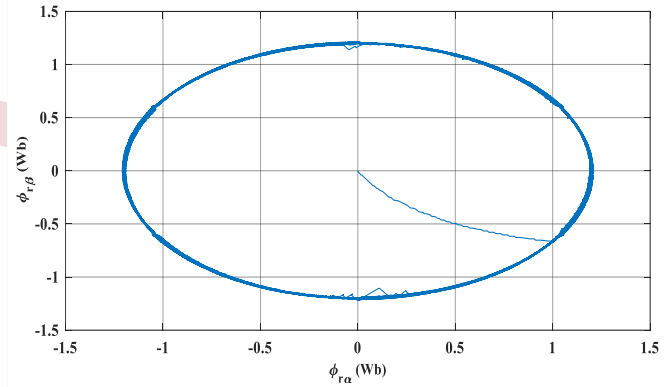


Figure 7. Rotor flux.

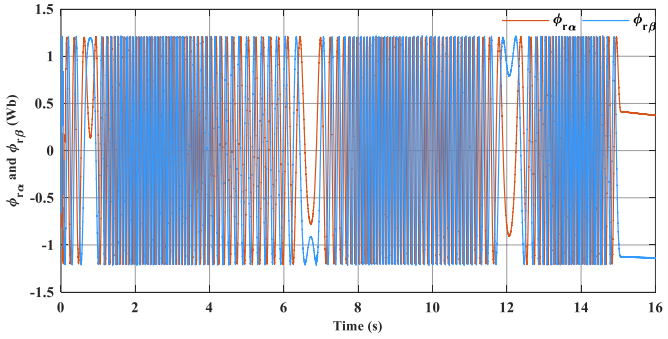


Figure 8. Waveformvof rotor flux.

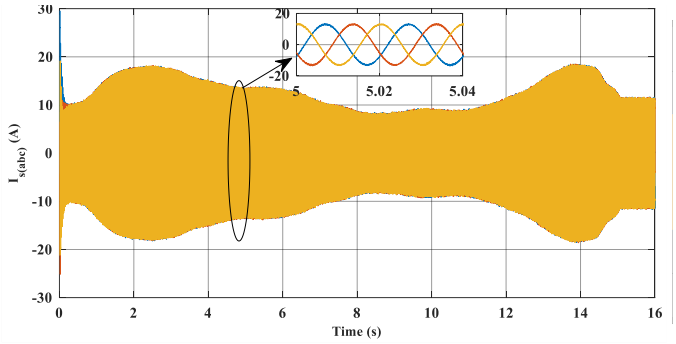


Figure 9. Stator currents.

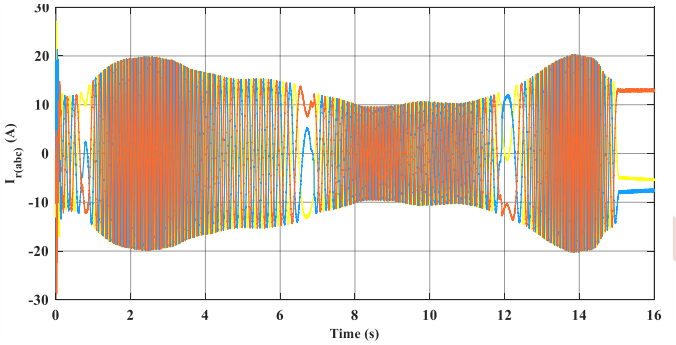


Figure 10. Rotor currents.

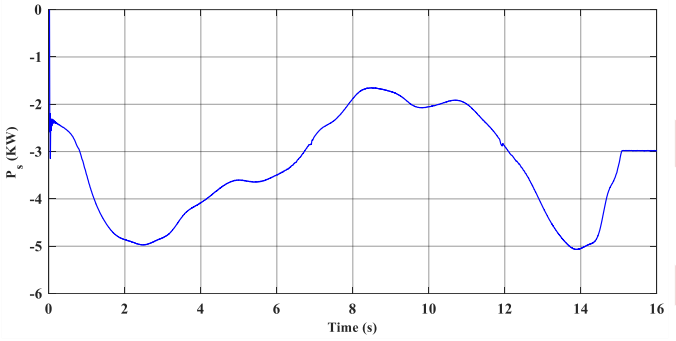


Figure 11. Stator active power.

Figs. 7 and 8 depict the circular rotor flux in the (α, β) plane. Its amplitude is a steady 1.2 Wb because its components vary sinusoidally in sub-, super-, and synchronous operation. As shown in Fig. 9, the amplitude of the generated stator currents increases with mechanical speed, while the frequency remains constant at 50 Hz during each state variation.

Fig. 10 shows that the DFIG rotor current amplitude varies with changes in mechanical speed, while the frequency directly changes with variations in mechanical slip. In synchronous mode, the rotor currents become DC with zero frequency.

The stator active power being negative (PS < 0) in Fig. 11 reveals operation as a generator, with this power being provided to the network as indicated by the negative sign.

VI. CONCLUSIONS

This paper has presented a novel direct torque control scheme using fuzzy logic control for a doubly-fed induction generator-based wind energy system. The proposed fuzzy hysteresis-based direct torque control (FH-DTC) aims to improve the performance limitations of conventional DTC strategies.

The FH-DTC represents an effective method to reduce the drawbacks of C-DTC in the WT-DFIG system. The simulation results showed that the implementation of FH-DTC will improve the system performance.

REFERENCES

[1] P.D. Singh and S. Gao, "An isolated hydro power generation using parallel asynchronous generators at variable turbine inputs using AC-DC-AC converter," 2018 8th IEEE India International Conference on Power Electronics (IICPE), pp. 1-6, December 2018.

[2] I. Takahashi and T. Noguchi, "A new quick-response and high efficiency control strategy of an induction motor," IEEE Trans. Ind. Appl., vol. IA-22, no. 5, pp. 820–827, Oct 1986.

[3] Y. Sahri, S. Tamalouzt, S. Lalouni Belaid, S. Bacha, N. Ullah, A. A. A. Ahamdi, and A. N. Alzaed, "Optimal Power Extraction in Wind Turbine System using Advanced Fuzzy 12 DTC Control of Doubly Fed Induction Generator under Random Wind Conditions," Sustainability, vol. 13, no.21, pp. 11593, 2021.

[4] H. Chojaa, A. Derouich, S. E. Chehaidia, O. Zamzoum, M. Taoussi, H. Benbouhenni, and S. Mahfoud, " Enhancement of Direct Power Control by Using Artificial Neural Network for a Doubly Fed Induction Generator-Based WECS: An Experimental Validation," Electronics, vol. 11, no. 24, pp. 4106, 2022.

[5] B. Zinelaabidine, R. Taleb, Y. Djeriri, and A. Yahdou, "A novel direct torque control using second order continuous sliding mode of a doubly fed induction generator for a wind energy conversion system," Turkish Journal of Electrical Engineering and Computer Sciences, vol. 25, no. 2, pp. 965-975, 2017.

[6] A. Wiam, M. Ourahou, B. El Hassouni, and A. Haddi, "Direct torque control improvement of a variable speed DFIG based on a fuzzy inference system," Mathematics and Computers in Simulation, vol. 167, pp. 308-324, 2020.

[7] S. Tamalouzt, T. Rekioua, R. Abdessemed, "Direct torque and reactive power control of grid connected doubly fed induction generator for the wind energy conversion," Conférence Internationale en Sciences et Technologies Electriques au Maghreb CISTEM'2014, Tunis, Tunisie, p. 1-7, November 2014.

[8] R. Cardenas, R. Pena, S. Alepuz, and G. Asher, "Overview of control systems for the operation of DFIGs in wind energy applications," IEEE Trans Ind Electron, 2013.

Enhancing Photovoltaic Array Performance through Optimizing Power during Mismatch Conditions under Series-parallel (SP) and Total Cross-Tied (TCT) Configurations

Lahlou Abad [1], Salah Tamalouzt [1], Kamel Djermouni [2], Karim Fathi Sayeh [1]

[1] *Laboratoire de Technologie Industrielle et de l'Information, Bejaia, Algeria*

lahlou.abad@univ-bejaia.dz, salah.tamalouzt@univ-bejaia.dz, karimfathi.sayeh@univ-bejaia.dz

[2] *Laboratoire de maitrise des énergies renouvelables Bejaia, Algeria*

kamel.djermouni@univ-bejaia.dz

***Abstract*—Photovoltaic (PV) systems, harnessed from the sun's energy, serve as vital components in the global shift towards sustainable energy sources. This paper presents a comprehensive investigation into the performance optimization of PV arrays operating under mismatched conditions, examining both Series-Parallel (SP) and Total Cross-Tied (TCT) configurations. The study explores the influence of variations in series and parallel resistances within PV modules on power generation. Two Maximum Power Point Tracking (MPPT) techniques are employed to enhance system efficiency. The research unequivocally demonstrates the superiority of the TCT configuration, yielding a remarkable 28-watt advantage over the SP configuration when subjected to internal resistance changes. Additionally, fuzzy logic-based MPPT exhibits exceptional responsiveness, surpassing the conventional Perturb and Observe (P&O) approach. These findings emphasize the pivotal role of system configuration and control strategies in optimizing PV array performance under varying operational conditions. This study contributes valuable insights to advance the harnessing of solar energy and underscores the significance of configuration and control methodologies in maximizing power output from PV systems.**

Keywords: **Photovoltaic systems, PV Array configuration, Maximum power point tracking.**

I. INTRODUCTION

Photovoltaic (PV) systems play a pivotal role in the global transition towards sustainable energy sources. Harnessing energy from the sun, PV arrays have proven to be a reliable and renewable source of electricity. However, the performance of photovoltaic panels is influenced by a multitude of factors, the degradation of the PV panels and system configuration being among the most important.

Several comprehensive studies have delved into the intricate realm of mismatch losses within photovoltaic (PV) systems, highlighting the multifaceted nature of this critical issue. For instance, the reference [1] conducted an insightful investigation into the mismatch problem, meticulously dissecting the deleterious effects stemming from partial shading scenarios. This study revealed the intricate mechanisms at play when shading phenomena disrupt the operation of PV arrays. Furthermore, this study [2] embarked on a rigorous exploration of the mismatch problem induced by partial shading conditions, coupling their investigation with a meticulous quantitative analysis of the ensuing power losses. In [3], the author focuses on the primary factors that underpin the occurrence of mismatch problems in PV systems. They dissected the various elements, ranging from shading effects and module degradation to circuit configuration intricacies, that collectively contribute to mismatches. Moreover, references [4] and [5] honed on improving power generation efficiency when dealing with changes in both series and parallel resistances of PV modules in a Series-Parallel configuration. Their investigations delved into the intricacies of power control strategies tailored to SP setups, acknowledging the unique challenges posed by mismatches in this specific configuration. By exploring strategies to maximize energy yield under mismatch conditions, collectively, these studies reflect a concerted effort within the research community to unravel the complexities of mismatch losses in PV systems, offering valuable insights and methodologies for optimizing performance and harnessing the full potential of solar energy.

This paper has the primary objective of introducing an in-depth investigation into the optimization of power generation in photovoltaic (PV) systems operating in the presence of mismatch conditions. The study is specifically focused on examining the impact of variations in both series and parallel

resistances within PV modules when configured in both Series-Parallel (SP) and Total Cross-Tied (TCT) configurations. Furthermore, it aims to conduct a thorough comparative analysis between these two configurations to discern their respective performance characteristics. The optimization of power generation in these scenarios is achieved through the implementation of two Maximum Power Point Tracking (MPPT) techniques, which are crucial in ensuring that the PV system operates at its highest efficiency level.

II. PV SYSTEM MODELING

The mathematical model of a photovoltaic (PV) cell is based on the physical principles governing its operation. A PV cell converts sunlight directly into electrical energy through the photovoltaic effect [6]. The primary mathematical model used to describe the behavior of a PV cell is the single diode model [7], [8], which is mostly used in literature. The selection of the one-diode equivalent circuit is based on its ability to provide faster numerical calculations while maintaining an acceptable level of accuracy. The ideal model of a PV cell can be described as a controlled current source Ipc representing the photocurrent connected with a parallel diode as depicted in Fig. 1 a, the correspondent current-voltage curve of this model is shown in Fig. 2. The one diode real model comprises a controlled current source Ipc and a diode carrying current Id. In addition, there are series and shunt internal resistances, Rs and Rsh, respectively, as presented in Fig. 1 b.

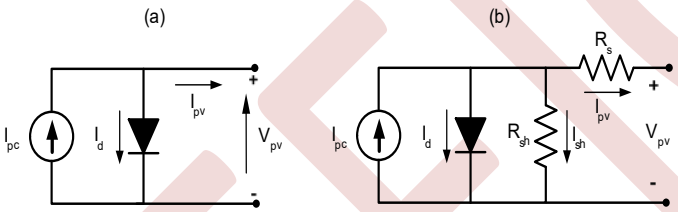


Figure 1. Equivalent electrical scheme of the PV cell.

$$I_{pv} = I_{pc} - I_d - I_{sh} \quad (1)$$

I_{pv} is the PV module current.

$$I_{pc} = \left[\left[(Suns - Suns_{ref}) * P_2\right] + \left[(T - T_{ref}) * P_3\right] + 1\right] P_1 * Suns \quad (2)$$

Where Suns represents the actual solar irradiation level (W/m^2), $Suns_{ref}$ is the nominal level of insolation, T and T_{ref} (K) are the ambient temperature and the nominal temperature, respectively, at STC $Suns_{ref}$ is equal to 1KW/m^2 and T_{ref} is 298.15K. The parameters P_1, P_2, P_3 are to be determined experimentally.

$$I_d = I_{sat}\left[exp\left(\frac{q\left(V_{pv}+(I_{pv}*R_S)\right)}{A*n_S*K*T}\right) - 1\right] \quad (3)$$

The diode current Id represents the losses due to the recombination of charge carriers in the PV cell, Vpv and Ipv are the voltage and current generated by the cell, q (C) is the electron charge, K is the Boltzmann constant (J/K), A is the diode ideality factor, n_s is the number of series connected cells, and Isat is the saturation current which is highly temperature-dependent as shown in following equation:

$$I_{sat} = P_4 T^3 exp\left(\frac{-E_g}{K*T_j}\right) \quad (4)$$

I_{sh} is the current running through the shunt resistor, R_s represents the resistance in series with the PV cell. It accounts for the resistive losses within the cell, such as the resistance of the semiconductor material and the interconnection of cells in a module, R_{sh} resistance represents the leakage paths in parallel with the PV cell. It explains the non-ideal behavior of the cell, such as surface defects or impurities that create unintended pathways for current flow [5]. This model can depict the characteristics of a photovoltaic (PV) module that incorporates a series connection of n_s individual cells Fig. 2.

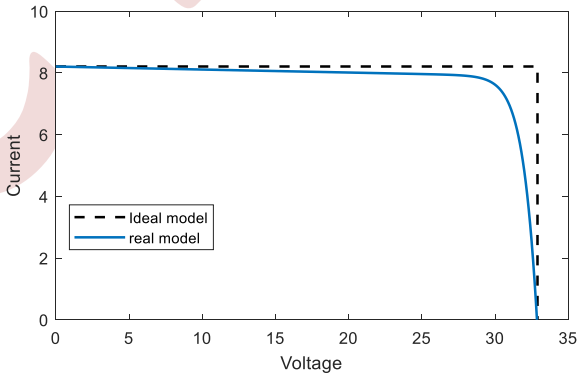


Figure 2. I-V curve of the PV cell

III. R_S AND R_{SH} EFFECT

Figs. 3 a and b present a visual representation of how both series and shunt resistors impact the output current of the PV cell. Upon careful analysis of these curves, a notable pattern emerges: the slope of the horizontal segment in the I-V curve of the PV cell exhibits an inverse relationship with the shunt resistance (Rsh). In contrast, the slope of the vertical segment in the I-V curve of the PV cell demonstrates a direct proportionality with the series resistance (Rs).

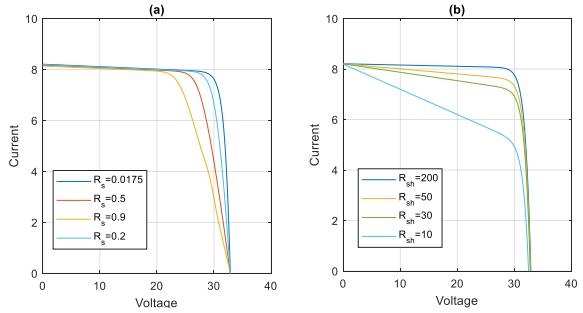


Figure 3. Effect resistor on the output current of the photovoltaic cell: (a) R_s and (b) R_{sh}.

This insightful observation can be succinctly summarized and illustrated in Fig. 4, providing a clear visual representation of the inverse relationship between shunt resistance and the slope of the horizontal I-V curve, as well as the direct relationship between series resistance and the slope of the vertical I-V curve in the PV cell.

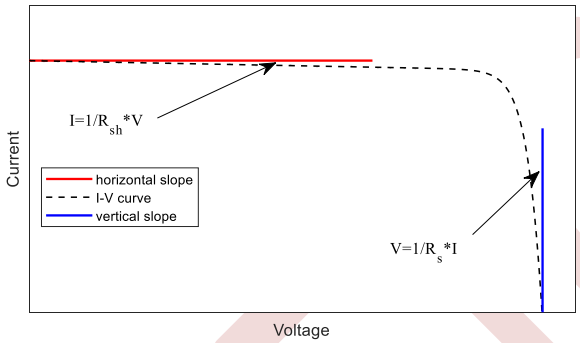


Figure 4. I-V curve with horizontal and vertical slopes.

IV. PV ARRAY CONFIGURATIONS

A. *Series-Parallel (SP) configuration*

In a Series-Parallel (S-P) PV array configuration Fig. 5 a, the photovoltaic (PV) modules are initially interconnected in series to create strings. This series connection is employed to generate a specific desired output voltage. Subsequently, these strings of modules are connected in parallel to generate the desired output current. One of the key advantages of the (SP) configuration is its ease of construction. It is a straightforward and cost-effective approach for configuring PV arrays. Moreover, it minimizes redundant connections, streamlining the overall design. This simplicity not only reduces installation costs but also enhances the reliability of the system, as fewer components mean fewer points of failure[10].

B. *Total Cross-Tied (TCT) configuration*

The Total Cross-Tied (TCT) connection scheme Fig. 5 b can be described as a configuration in which cross-ties are integrated into the series-parallel connected PV system. This particular configuration stands out as one of the most prevalent and effective approaches employed within the photovoltaic industry. Its primary purpose is to mitigate the adverse effects of partial shading on the PV array while concurrently minimizing losses when compared to other fundamental connection schemes. By incorporating cross ties into the system, the TCT configuration facilitates improved overall performance, particularly in scenarios where certain parts of the PV array are subject to shading. This design promotes the efficient utilization of available solar energy, thereby maximizing the power yield of the installation. As a result, the TCT connection scheme remains a popular choice among PV practitioners seeking to enhance the reliability and efficiency of their solar power systems [11].

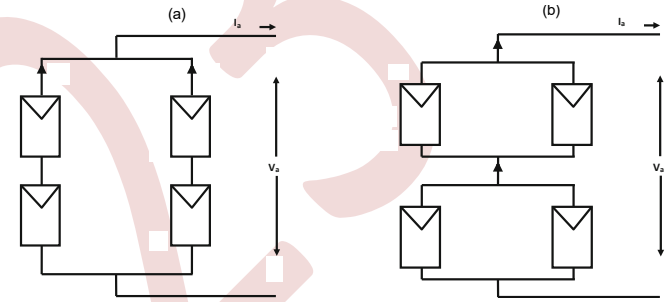


Figure 5. Schematic diagram of a PV array connected in case: (a) SP and (b) TCT configuration.

V. RESULTS AND DISCUSSION

In this section, the simulation results are presented for four modules initially connected in a series-parallel (SP) configuration and then in a (TCT) configuration. During these simulations, two of the modules were subjected to a mismatch fault. The ideal series and parallel resistance values for the modules are set as Rs=0.221Ω and Rsh=415.45 Ω, respectively. To introduce the mismatch fault, the resistance values of these two modules are modified as follows: Rs1=1.5 Ω, Rs2=1.1 Ω; Rsh1=55 Ω, Rsh2=20 Ω. A visual summary of these changes is provided in Figs 6 a and b.

Fig. 7 illustrates the I-V (current-voltage) and P-V (power-voltage) curves during the occurrence of a mismatch fault in both the series-parallel (SP) and total cross-tied (TCT) configurations. It is evident from the graph that the TCT configuration outperforms the SP configuration. In TCT, the maximum power point (MPP) reaches approximately 1068.2 W. In contrast, the MPP for the SP configuration is 1040.6 W, indicating a difference of approximately 28 W. This discrepancy underscores the effectiveness of the TCT configuration.

Figs. 8 and 9 depict the power response of four modules in an SP and TCT configuration, connected to a load through a boost converter. This boost converter is controlled by an MPPT (Maximum Power Point Tracking) block, employing two different techniques for tracking the maximum power point (MPP): The conventional Perturb and Observe (P&O) method

and a fuzzy logic approach with two input parameters, namely the error (E) and the rate of change of error (ΔE). The error is determined using the equation:

$$E = \Delta P / \Delta V \quad (5)$$

The output of the fuzzy logic is the duty cycle (D), triangular membership functions are employed for defining all three membership functions for both inputs and the output.

In Fig. 8 a, the power response of the modules in the SP configuration is shown for both the P&O and fuzzy logic methods. Fig. 8 b provides a close-up view of the power response between 0.024 s and 0.035 s. It is evident that both methods converge to the MPP with 100% accuracy during this interval. Notably, the fuzzy logic method exhibits a quicker response time, achieving a time response of 0.025 s, while the conventional P&O method takes 0.028 s to respond. This discrepancy underscores the effectiveness of the fuzzy logic method.

Moving on to Fig. 9 a, it presents the power response of the modules in a Total Cross-Tied (TCT) configuration, utilizing both the P&O and fuzzy logic methods. Fig. 9 b zooms in on the power response between 0.022 s and 0.033 s. Both methods reach the MPP, however, there is a noticeable difference in response times, with the fuzzy logic method attaining the MPP in 0.025

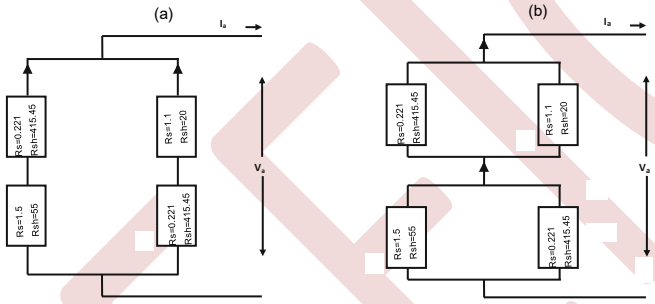


Figure 6. PV array configuration with resistance values: (a) SP configuration and (b) SP configuration.

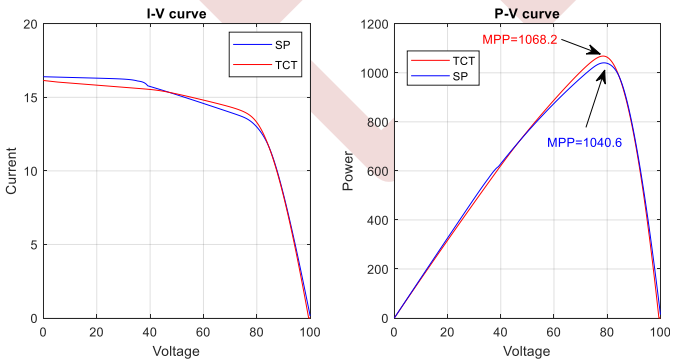


Figure 7. I-V and P-V curves with mismatch default

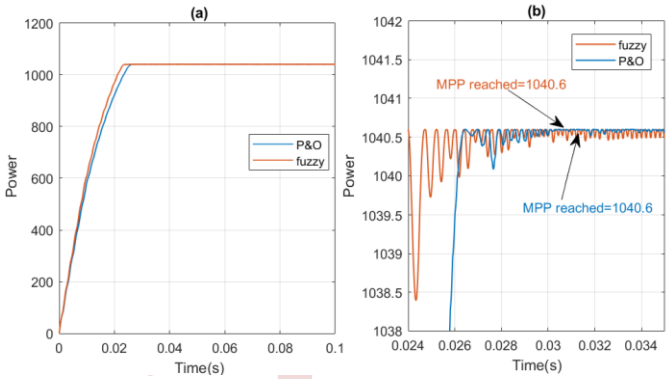


Figure 8. Power response in case of SP configuration.

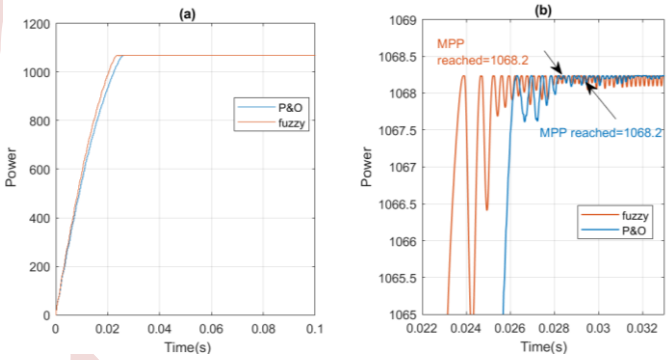


Figure 9. Power response in case of TCT configuration.

Lastly, the Total Cross-Tied (TCT) configuration has proven to be significantly more effective in generating power when compared to the Series-Parallel (SP) configuration, resulting in a noticeable power increase of 28 watts. It is worth noting that the fuzzy logic-based method exhibited a considerably faster response and performance compared to the Perturb and Observe (P&O) method.

VI. CONCLUSION

This paper delves into a comprehensive examination of a photovoltaic (PV) array's performance under mismatched conditions, conducted in both Series-Parallel (SP) and Total Cross-Tied (TCT) configurations. The findings unequivocally highlight the superiority of the TCT configuration when confronted with changes in internal resistances, manifesting as a substantial 28-watt discrepancy compared to the SP configuration. Notably, utitlizing the fuzzy logic method exhibited remarkable efficiency, demonstrating significantly faster response times when compared to the conventional Perturb and Observe (P&O) approach. This study underscores the pivotal role of configuration and control techniques in

optimizing the power output of PV arrays under varying operating conditions.

REFERENCES

[1] R. K. Pachauri et al., "Impact of partial shading on various PV array configurations and different modeling approaches: A comprehensive review," IEEE Access, vol. 8, pp. 181375–181403, 2020.

[2] Z. Wang, N. Zhou, L. Gong, and M. Jiang, "Quantitative estimation of mismatch losses in photovoltaic arrays under partial shading conditions," Optik, vol. 203, p. 163950, 2020.

[3] A. D. Dhass, N. Beemkumar, S. Harikrishnan, and H. M. Ali, "A review on factors influencing the mismatch losses in solar photovoltaic system," Int. J. Photoenergy, vol. 2022, pp. 1–27, 2022.

[4] K. Djermouni, A. Berboucha, K. Ghedamsi, and D. Aouzellag, "Optimization of a photovoltaic field during faulty and normal operation," Sol. Energy, vol. 113, pp. 171–180, 2015.

[5] N. Boutasseta, M. Ramdani, and S. Mekhilef, "Fault-tolerant power extraction strategy for photovoltaic energy systems," Sol. Energy, vol. 169, pp. 594–606, 2018.

[6] J. C. Teo, R. H. Tan, V. H. Mok, V. K. Ramachandaramurthy, and C. Tan, "Impact of bypass diode forward voltage on maximum power of a photovoltaic system under partial shading conditions," Energy, vol. 191, p. 116491, 2020.

[7] T. Khatib and W. Elmenreich, Modeling of Photovoltaic Systems Using MATLAB®: Simplified Green Codes, 1st ed. Wiley, 2016. doi: 10.1002/9781119118138.

[8] R. Kumar and S. K. Singh, "Solar photovoltaic modeling and simulation: As a renewable energy solution," Energy Rep., vol. 4, pp. 701–712, 2018.

[9] O. Bingöl and B. Özkaya, "Analysis and comparison of different PV array configurations under partial shading conditions," Sol. Energy, vol. 160, pp. 336–343, 2018.

[10] S. R. Pendem and S. Mikkili, "Modeling, simulation and performance analysis of solar PV array configurations (Series, Series–Parallel and Honey-Comb) to extract maximum power under Partial Shading Conditions," Energy Rep., vol. 4, pp. 274–287, 2018.

[11] T. S. Babu, D. Yousri, and K. Balasubramanian, "Photovoltaic array reconfiguration system for maximizing the harvested power using population-based algorithms," IEEE Access, vol. 8, pp. 109608–109624, 2020.

Sizing and energy management of a multi-source pumping system

Amrouche Karim [1], Abdelli Radia [2], Benhacine Nasr-Eddine [3]

[1]Laboratoire de Technologie Industriel et de l'Information, *Bejaia, Algeria*

karim.amrouche@univ-bejaia.dz

[2]Laboratoire de Technologie Industriel et de l'Information, *Bejaia, Algeria*

radia.abdelli@univ-bejaia.dz

Bejaia, Algeria

Benhacine.nasreddinemaster@gmail.com

***Abstract*— The growth of renewable energy development and exploitation has been strong in recent years. The multisource pumping is considered as one of the most widely adopted solutions in rural areas. The process of sizing involves determining the optimal component capacities to meet energy demands, taking into account variables such as energy source variability and load profiles. In parallel, energy management strategies are critical to balance energy supply and demand, mitigate intermittency issues, and extend the lifespan of energy storage components. This paper explores the sizing and energy management of a multi-source system comprising a photovoltaic generator, a wind turbine with MPPT methods, a battery storage and a motor pump to meet power requirements.**

***Keywords:* Photovoltaic system, Wind power system, Battery, MPPT, Pumping, Sizing, Energy management.**

I. INTRODUCTION

Our planet is being impacted by the excessive use of fossil fuels, and these finite resources are also set to dry up in the coming years. Energy and water scarcity pose significant challenges for numerous residents living in the rural and remote regions of developing countries. The issue of limited water resources in these distant areas is of paramount importance to the local populations. The pursuit of suitable remedies for this problem plays a vital role in enhancing living standards in such regions. Multi-source pumping emerges as the perfect solution for providing water supply in these remote and rural locations. [1][2]

Multi-source system with storage is proposed to reduce the overheating of the motor temperature and increase the efficiency. the storage serves as both an energy reservoir for surplus power and a backup energy source. [3] To guarantee the efficient and dependable performance of a multi-source system, it is imperative to coordinate and optimize the energy sources employed within the system. This action is achieved through the implementation of energy management algorithms, several researches have been made in the subject. [4][5][6]

In this article, we introduce a multi-source pumping system powered by solar and wind sources with battery storage. The system also incorporates an induction motor controlled through rotor flux-oriented vector control. This motor is linked to a centrifugal pump, which is coupled with a strategically placed elevated water storage tank. To maximize power extraction from both the photovoltaic panel and the wind turbine, we have employed two distinct Maximum Power Point Tracking (MPPT) techniques. Furthermore, we have integrated the necessary power converters to ensure the system's proper functionality. In order to guarantee efficient management of the available energy and meet power demands, we have carried out system sizing and developed an energy control and management algorithm.

II. DESCRIPTION OF THE SYSTEM

Figure 1 shows a block diagram of the proposed system

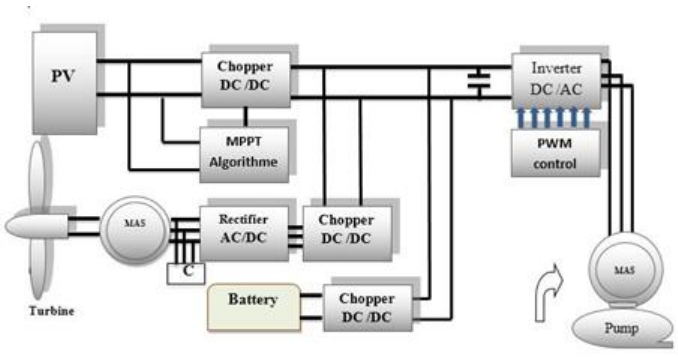


Figure 1. Proposed system scheme

The system is composed of PV Panels, a DC/DC converter with MPPT control, a wind turbine with MPPT control, an

induction motor, three phase PWM inverter and a centrifugal pump and a battery.

III. SYSTEM MODELING

A. *Photovoltaic generator*

This model is characterized by a very simple resolution. It requires only four parameters namely I_{sc}, V_{oc}, I_m and V_m. The (I_{pv}, V_{pv}) characteristic of this model is illustrated as follows [3][7]:

$$I_{pv} = I_{sc}\left[1 - C_1\left(\exp\left(\frac{Vpv}{C_2 V_{oc}}\right) - 1\right)\right] \quad (1)$$

With:

$$\begin{cases} C_1 = I_{sc}\left[1 - \left(\frac{I_m}{I_{sc}}\right)\right] e^{-\frac{V_m}{C_2 V_{oc}}} \\ C_2 = \frac{\left(\frac{V_m}{V_{oc}}\right) - 1}{\ln\left(1 - \frac{I_m}{I_{sc}}\right)} \end{cases} \quad (2)$$

B. *Turbine*

The optimal wind turbine power (with MPPT) versus time PWT(t) has the following expression [5]:

$$P_{WT}(t) = \frac{1}{2}\eta_{sc}\eta_g C_{p,opt}\rho A_{WT} V_{wind}^3(t) \quad (3)$$

with

η_{sc}, η_g static converter efficiency, generator efficiency,
$C_{p,opt}$ optimal wind turbine power coefficient (i.e. corresponding to a perfect maximum point tracker),
ρ_{air} density (kg/m^3),
A_{WT} wind turbine swept area (m^2),
V_{wind} (t) wind speed versus time (m/s)).

C. *Battery (CIEMAT model)*

The battery's model is characterized by the series connection of an electromotive force with a variable resistance, as follows [8]:

$$V_{bat} = n_b . E_b \pm n_b . R_b . I_{bat} \quad (4)$$

With n_b is cell number, V_{batt}: battery voltage, I_{batt}: battery current, E_{batt}: electromotive force.

D. *Induction machine*

The electric equations of the induction machine are written in matrix form as follows [9]:

$$\begin{bmatrix} v_{ds} \\ v_{qs} \\ 0 \\ 0 \end{bmatrix} = \begin{bmatrix} R_s & -\omega_s l_s & 0 & -\omega_s . L_m \\ \omega_s l_s & R_s & \omega_s . L_m & 0 \\ -R_r & \omega_r . l_s & R_r & -\omega_r (l_r + L_m) \\ -\omega_r . l_r & -R_r & -\omega_r (l_r + L_m) & R_r \end{bmatrix} \cdot \begin{bmatrix} i_{sd} \\ i_{sq} \\ i_{md} \\ i_{mq} \end{bmatrix} + \begin{bmatrix} l_s & 0 & L_{md} & L_{dq} \\ 0 & l_s & L_{dq} & L_{mq} \\ -l_r & 0 & L_r & 0 \\ 0 & -l_r L_{dq} & l_r + L_{mq} & \end{bmatrix} \begin{bmatrix} \frac{di_{sd}}{dt} \\ \frac{di_s}{dt} \\ \frac{di_{md}}{dt} \\ \frac{di_{mq}}{dt} \end{bmatrix} \quad (5)$$

The expression of the electromagnetic torque is:

$$T_{em} = P . L_m . (i_{md} . i_{sq} - i_{mq} . i_{sd}) \quad (6)$$

E. *Centrifugal pump*

The head-Flowrate h − Q characteristic can be expressed approximately by the following Quadratic form: [10]

$$H = a_0 \omega^2 - a_1 \omega Q - a_2 Q^2 \quad (7)$$

Where a_0, a_1, a_2 are the coefficients generally given by the manufacturers. The hydraulic power, resistive torque and the mechanic power are given by: [11]

$$P_H = \rho g Q H, \quad T_r = k_r \omega^2 + C_s \quad (8), (9)$$

The pump efficiency is defined as the ratio of the hydraulic power imparted by the Pump to the fluid to the shaft mechanical power and is given by:

$$\eta_p = \frac{\rho_H g H Q}{c\left(1 - \frac{\omega_{s1}}{\omega_s}\right)^3 \omega_s} \quad (10)$$

where Q, H , ρ, g , ω_S and ω_{Sl} are the water flow (m^3/s), the total height of the well (m), the density (Kg/m^2) and the gravity (m/s^2), the angular frequency of the supply (rad/s) and the slip speed (rad/s), respectively.

F. *Flux-Oriented Vector Control of the Squirrel Cage Induction Machine:*

The motor's equations with the constraint $\emptyset_{qs} = 0$ et $\emptyset_{dr} = \emptyset_r$ is simplified as follows:

$$\begin{cases} V_{rd} = \sigma L_s \frac{di_{sd}}{dt} + \left(R_s + \frac{M^2}{L_r^2} R_r\right) i_{sd} - \sigma L_s \omega_s i_{sq} - \frac{M R_r}{L_r^2} \emptyset_r \\ V_{rd} = \sigma L_s \frac{di_{sq}}{dt} + \left(R_s + \frac{M^2}{L_r^2} R_r\right) i_{sq} + \sigma L_s \omega_s i_{sd} + \frac{M_r}{L_r^2} \omega \emptyset_r \\ \frac{d\emptyset_r}{dt} = \frac{M}{T_r} i_{sd} - \frac{1}{T_r} \emptyset_r \\ \omega_r = \frac{M}{T_r} \frac{i_{sq}}{\emptyset_r} \\ P_{em} = \frac{T_{em} \omega_s}{p} \\ T_{em} = \frac{PM}{L_r} \emptyset_r i_{sq} \end{cases} \quad (11)$$

IV. SIZING AND MANAGEMENT

A. *Pumping system sizing*

We will take the photovoltaic generator as main source, the wind system as complementary source, batteries for compensation and a water tank to meet the water needs of a small village contains 170 family. From what we need to make a sizing of the various components of the studied system. The daily consumption of the village is therefore estimated by 72.25 m^3 so we will take a tank of 110 m^3, the dynamic level head is about 12 m and the nominal flow rate is of 25 m^3/h. The results obtained from the sizing system are presented in the Table I.

TABLE I. SIZING PUMPING SYSTEM

Symbols	Expressions	Results
Hydraulic power	$P_{hyd} = \rho g Q H$	817.5 W
Mechanical power required by the pump	$P_{mec} = \frac{P_{hyd}}{\eta_p}$	1486.36 W
Electric power	$P_{ele} = \frac{P_{mec}}{\eta_m}$	1748.66 W
Input power of the inverter	$P_{dem} = \frac{P_{ele}}{\eta_{inv}}$	1840.69 W
Necessary pumping time	$\tau_p = \frac{V}{Q}$	4.4 h
Daily electrical energy required by the load	$E_c = P_{dem}\tau_p$	8099.036 Wh/day
The power of the PV generator	$P_{PV} = \frac{E_{ele}}{\tau_p(1 - pertes)}$	2300.8625 W
Number of panels	$N_{PV} = \frac{P_{PVt}}{P_{PV}}$	21 panels
Number of panels series	$N_{PVs} = \frac{V_{dc}(1-\alpha)}{V_m}$	7 panels
Number of panels parallel	$N_{PVp} = \frac{I_{PVt}}{I_{PV}}$	3 panels
Battery capacity	$C_{bat} = \frac{E_c N_{jaut}}{V_{bat} PDD R_{bb} N_m}$	150 A.h

With: N_{jaut}: number of days of autonomy, PDD: depth of discharge, R_{bb}: battery performance, Nm: number of days in the month.

Speed reference of motor-pump: The reference speed (ω_{ref}) is determined by the total power (photovoltaic, wind, and batteries) and is given by the following relation:

$$\omega_{ref} = \omega_n \times \sqrt[3]{\frac{P_{tot} \times \eta}{P_n}} \qquad (12)$$

With: (ω_{ref}) is the rated speed of the induction motor [rad/s], P_{tot} is the total power (photovoltaic, wind, and batteries) [W], η is an efficiency of the motor-pump unit and P_n is the rated power of the motor [W].

After sizing, we need 21 panels of 120 Wc (7 in series and 3 in parallel) as main generator, while the 1KW wind system will be a complementary generator and 6 batteries will be used for compensation.

B. *Supevisor control*

To maintain a reliable water supply, it's crucial for the entire system to operate perfectly and effectively. Achieving this goal requires the optimal management of energy flow between different components. The management system plays a critical role in overseeing energy transfers among these components and in regulating the charging and discharging processes of the storage (batteries) to extend their lifespan.

From this management system, we can establish five modes of operation, which are summarized in the table II, figure 2 represent the energy management algorithm:

TABLE II. MANAGEMENT SYSTEM

Mode	Description	Action
1	Hybrid Power = Load Demand	Disconnect the battery, direct supply to the load.
2	Hybrid Power > Load Demand, State of Charge < State of Charge max	Supply the load and charge the battery.
3	Hybrid Power > Load Demand, State of Charge > State of Charge max	Disconnect the battery. Load is powered by both generators; excess energy goes to load-dumping resistor.
4	Hybrid Power < Load Demand, State of Charge > State of Charge min	Battery compensates for power deficit.
5	Hybrid Power < Load Demand, State of Charge < State of Charge min	Disconnect both battery and load.

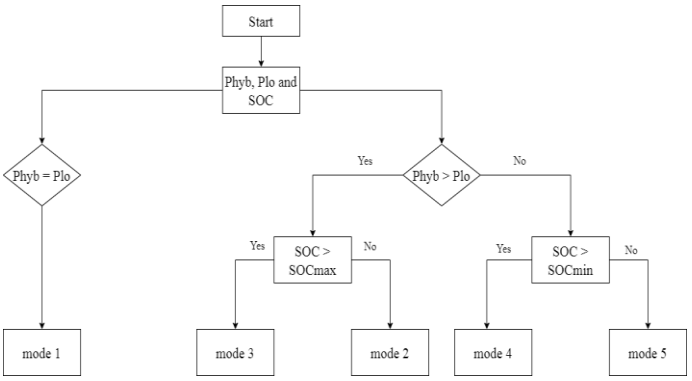


Figure 2. Proposed flowchart

V. SIMULATION RESULTS

Utilizing the previously described models and control methods, a simulation of a multisource pumping system has been developed and conducted within the MATLAB/Simulink environment.

The parameters of the wind turbine, the induction generator, the photovoltaic panel and the induction motor are given in Table III, Table VI, Table V, Table IV respectively.

TABLE III. PARAMETER OF WIND TURBINE

Rated power	1000 W
Blades	3
Blades diameters	2.26 m
Startup wind speed	3.4 m/s
Rated wind speed	12.5 m/s

TABLE IV. PARAMETER OF ASYNCHRONOS GENERATOR

Statoric resistance	5.75 Ω
Rotoric resistance	4.2 Ω
Stator inductance	0.4662 H
Rotor inductance	0.4662 H

TABLE V. PARAMETER OF THE PHOTOVOLTAIC PANEL

Maximum power	110 W
Rated current	3.15 A
Rated voltage	35 V
Short-circuit current	3.45 A
Open circuit voltage	43.5 V
Temperature coefficient of I_{SC}	1.4 mA/°C
Temperature coefficient of V_{oc}	-152 mA/°C

TABLE VI. PARAMETER OF ASYNCHRONOS MOTOR

Nominal power	1500 W
Nominal Voltage	220/380 V
Nominal Current	5.2/3 A
Rated speed	1460 tr/min
Number of poles pairs	2

Irradiation, temperature, and wind speed exhibited daily variations over the course of 12 days in October. These variations are quantified by the average values for each parameter per day, and they are visually depicted in Figure 2, Figure 3 and Figure 4.

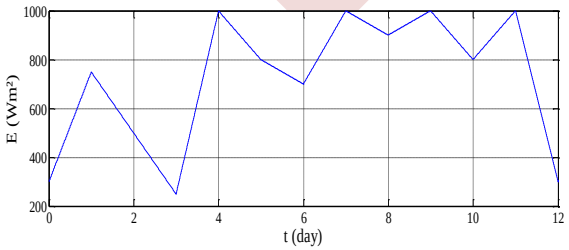


Figure 2. Solar irradiance

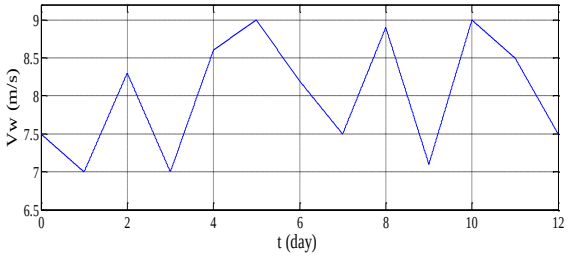


Figure 3. Wind speeds

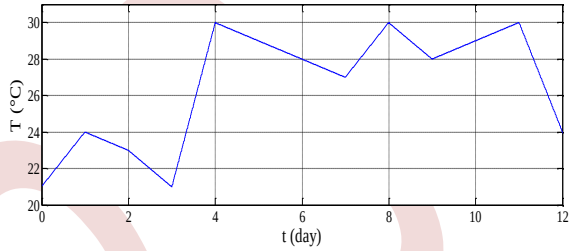


Figure 4. Ambient temperature

The figure 5 represents the powers (P_{hyb}, P_{bat}), while it is noted that the hybrid power and that of the battery (charge and discharge) are complementary.

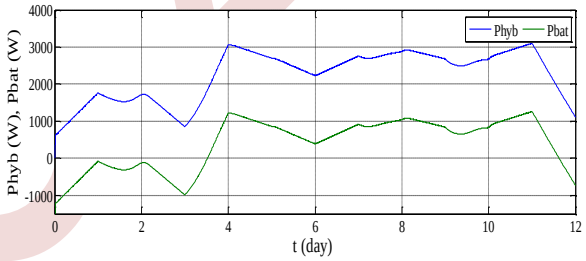


Figure 5. Hybrid and battery power

After management, Figure 6 shows that the powers (hybrid, battery) are complementary. At moments (0 to 3.5), (11.5 to 12), the battery compensates for the power deficit to supply the load ($P_{hyb} < P_{lo}$). In this case, the battery acts as a source. At the moment (3.5 to 11.5), the hybrid power is greater than or equal to the power demanded ($P_{hyb} \geq P_{lo}$), here the battery disconnects and does not contribute and the excess energy is used to charge the battery.

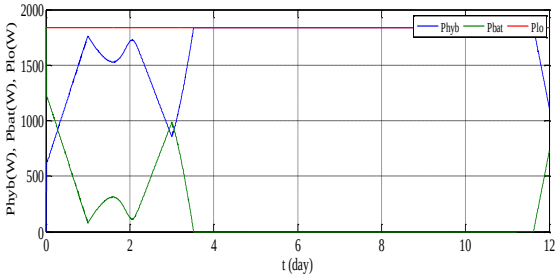


Figure 6. Hybrid, battery and load power after management

Water flow is almost constant as shown in figure 7 which means the availability of energy in all time.

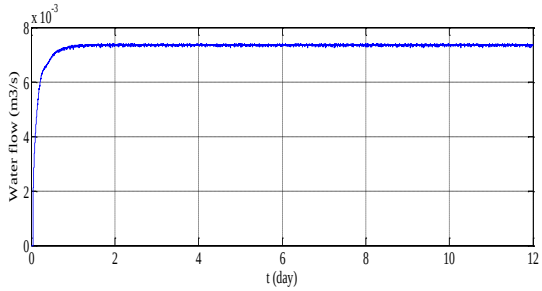


Figure 7. Water flow

It can be observed that the estimated speed evolves until it reaches the reference speed value in Figure 8, the rotor flux increases slowly until it stabilizes at its reference value of 0.7 Wb in Figure 9. The electromagnetic torque and the resistive torque are nearly equal, for each value of the resistive torque, the electromagnetic torque tends to track the value imposed by it Figure 10, the direct and quadrature currents in figure 11 and figure 12 are closely track their references, the stator current in figure 13 and figure 14 are sinusoidal.

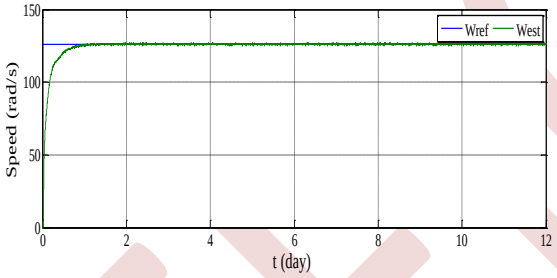


Figure 8. Reference and estimated speed

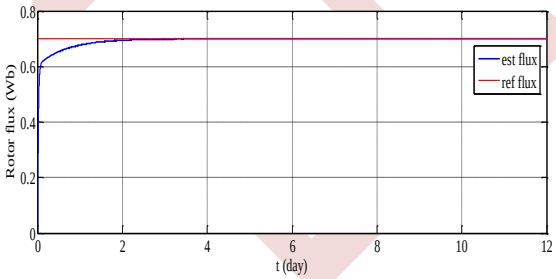


Figure 9. Rotor flux

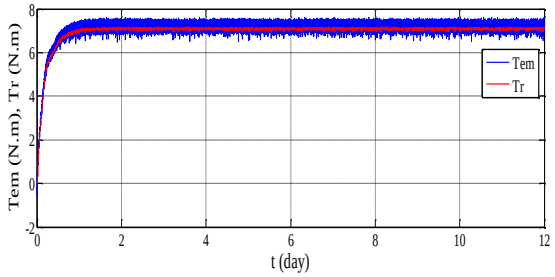


Figure 10. Electromagnetic and resistive torque

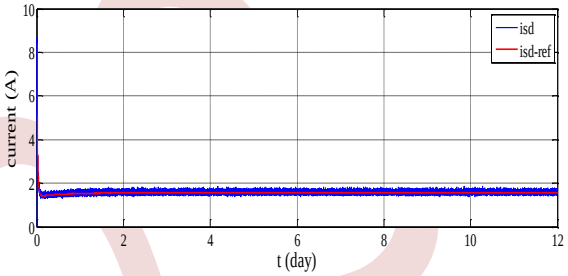


Figure 11. Currents waveform isd-ref, isd

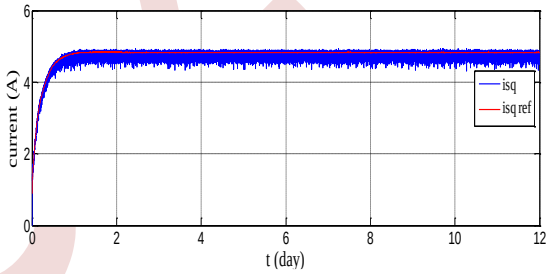


Figure 12. Current waveform isq_ref, isq

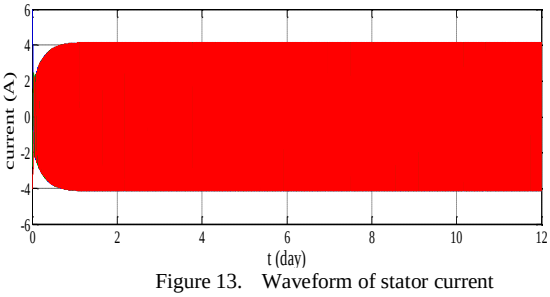


Figure 13. Waveform of stator current

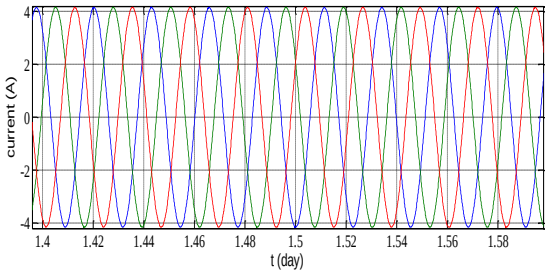


Figure 14. Zoom of waveform of stator current

VI. CONCLUSION

We have presented the necessary steps for the sizing of a multisource pumping system combining photovoltaic and wind sources with batteries, along with a strategically positioned water tank for a site located in a rural region. This system is designed to provide the required energy to power the load, also ensure a reliable water supply for the region's needs. A power management algorithm has been presented to ensure energy availability and proper operation throughout the year. After a simulation on MATLAB/Simulink. The obtained results show the efficiency and reliability of the proposed system.

REFERENCES

[1] Xiao Xu, Weihao Hu, Di Cao, Qi Huang, Cong Chen, Zhe Chen. Optimized sizing of a standalone PV-wind-hydropower station with pumped-storage installation hybrid energy system. Renewable Energy 2020; 147, pp 1418-1431.

[2] Obaid W, Hamid A, Ghenai Ch. Solar/wind pumping system with forecasting in Sharjah, United Arab Emirates. International Journal of Electrical and Computer Engineering (IJECE) 2021; 11(4), pp 2752-2759.

[3] Serir Ch, Rekioua D, Mezzai N, Bacha S. Supervisor control and optimization of multi-sources pumping system with battery storage. Int J Hydrogen Energy 2016; 41(45), pp 20974-20986.

[4] Gam O, Abdelati R, Tankari M A, Mimouni M F. An improved energy management and control strategy for wind water pumping system. Transactions of the Institute of Measurement and Control 2019; 1-15.

[5] Zaibi M, Cherif H, Champenois G, Sarenib B, Roboamb X, Belhadjc J. Sizing methodology based on design of experiments for freshwater and electricity production from multi-source renewable energy systems. Desalination 2018; 446, pp 94-113.

[6] Poompavai T, Kowsalya M. Control and energy management strategies applied for solar photovoltaic and wind energy fed water pumping system: A review. Renewable and Sustainable Energy Reviews 2019; 107, pp 108–122.

[7] Pant S, Saini R.P. Solar Water Pumping System Modelling and Analysis using MATLAB/Simulink. IEEE Students Conference on Engineering & Systems (SCES) 2020; Prayagraj, India.

[8] Laadissi1 E.M, El Filali A, Zazi M, El Ballouti A.Comparative Study Of Lead Acid Battery Modelling. ARPN Journal of Engineering and Applied Sciences 2018; 13(15), pp 4448-4452.

[9] Chouidira I, Khodja D.J, Chakroune S. Fuzzy Logic Based Broken Bar Fault Diagnosis and Behavior Study of Induction Machine. Journal Européen des Systèmes Automatisés 2020; 53(2), pp 233-242.

[10] Goppelt F, Hieninger T, Schmidt-Vollus R. Modeling Centrifugal Pump Systems from a System-Theoretical Point of View. 18th International Conference on Mechatronics - Mechatronika (ME) 2018, Brno, Czech Republic.

[11] Perissinotto R M, Monte Verde W, Biazussi J L, Vieira Bulgarelli N A, Denner Pires Fonseca W, Souza de Castro M, Erick de Moraes Franklin, Bannwart A C. Flow visualization in centrifugal pumps: A review of methods and experimental studies. Journal of Petroleum Science and Engineering 2021; 203, 108582.

Characterization and Mitigation of Multipeak Phenomena in Photovoltaic Systems Under Environmental Conditions and Electrical Fault

Abad Lahlou [1], Tamalouzt Salah [1], Djermouni Kamel [2], Sayeh Karim [1]

[1] *Laboratoire de Technologie Industrielle et de l'Information, Bejaia, Algeria*

lahlou.abad@univ-bejaia.dz

[2] *Laboratoire de maitrise des énergies renouvelables Bejaia, Algeria*

***Abstract*— Photovoltaic (PV) systems are crucial for the global transition to sustainable energy sources, but their performance is susceptible to environmental factors and electrical faults. This paper investigates the multipeak phenomena in the power-versus-voltage (P-V) characteristics of PV generators, with a focus on line-to-line (LL) faults, line-to-ground (LG) faults, and partial shading conditions (PSC). LG faults are identified as the most significant contributor to power loss, causing a substantial 50% reduction in power output compared to healthy system operation, while PSC and LL faults lead to power losses of 32% and 30%, respectively. To address these issues, we implement the Particle Swarm Optimization (PSO) algorithm for Maximum Power Point Tracking (MPPT). The PSO algorithm demonstrates remarkable accuracy and rapid response times, enhancing PV system performance under challenging conditions.**

***Keywords:* Photovoltaic systems, multipeak phenomena, power-versus-voltage characteristics, line-to-line faults, line-to-ground faults, partial shading conditions, Maximum Power Point Tracking, Particle Swarm Optimization.**

I. INTRODUCTION

Photovoltaic (PV) systems have emerged as a sustainable and efficient source of renewable energy, playing a pivotal role in the global transition toward cleaner power generation. However, these systems are not immune to challenges, and their performance can be significantly affected by environmental factors and electrical faults.

The presence of shading on the surfaces of photovoltaic (PV) arrays stands as a pervasive and extensively studied challenge within the realm of solar energy generation. This issue has garnered significant attention due to the detrimental impact it inflicts on the performance and reliability of PV systems, [1] Conducted an analysis of how shading affects PV arrays through the lens of thermodynamic laws, other studies as [2], [3] have focused their research efforts on reducing shading's impact on the power output of PV generators. They accomplished this by examining different module arrangement configurations, other researches like [4]–[8] have delved into the task of monitoring and optimizing the tracking of maximum power in PV systems when multiple peaks appear in the P-V curves. These phenomena occur due to shading effects on PV characteristics. The issue of multiple peaks in P-V (Power-Voltage) curves within photovoltaic (PV) systems is not solely attributed to shading; it can also arise from various electrical fault, [9] They introduced a tolerant control strategy designed to address the occurrence of electrical faults such as line-to-line and line-to-ground faults. These issues have the potential to induce multiple peaks in the P-V curve of the PV generator.

This research delves into the primary issues responsible for the emergence of multiple peaks in the P-V (Power-Voltage) curve of photovoltaic (PV) generators. Specifically, it examines three key factors: partial shading conditions (PSC), connectivity issues such as Line to Line (LL) and Line to Ground (LG) faults. The study is organized into four main sections. The first section provides an overview of PV system characteristics, followed by the second section which delves into the intricacies of PSC, LL, and LG problems. The third section introduces an application of Maximum Power Point Tracking (MPPT) for PV generators during the aforementioned faults. Finally, the last section offers a concise conclusion summarizing the findings.

II. PV SYSTEM CHARACTERISTICS

Photovoltaic (PV) systems serve as crucial power converters, harnessing the energy from sunlight and converting it into electrical power. In essence, a PV system can be conceptualized as an electrical current generator, as illustrated in Figure (1). At the core of understanding and characterizing a PV generator are several key parameters. These parameters are pivotal for assessing the system's performance and behaviour. The first of these is the Maximum Power Point (MPP), which represents the point at which the PV system generates the maximum electrical power output. The MPP is a critical parameter as it directly influences the system's efficiency and energy production. Another fundamental parameter is the Short Circuit Current (I_{sc}), which denotes the maximum current that can flow through the PV system when the output terminals are short-circuited. On the other end of the spectrum, the Open

Circuit Voltage (V_{oc}) represents the maximum voltage across the PV system when there is no load connected.

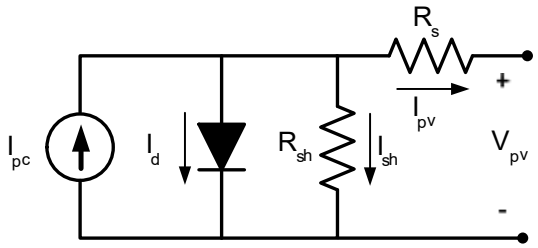


Figure 1. equivalent PV cell electrical circuit.

In Figure (2), we can observe the Current versus Voltage (I-V) curve and the Power versus Voltage (P-V) curve of a photovoltaic (PV) cell. These curves depict the electrical characteristics of the PV cell in an optimal and healthy operating condition. They provide valuable insights into how the cell's current and power output vary with changes in voltage levels, forming a critical foundation for understanding the performance of PV cells under ideal conditions.

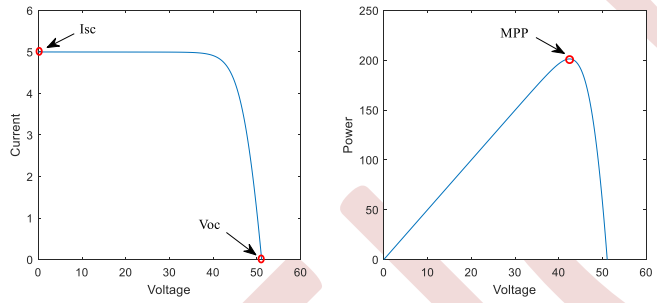


Figure 2. characteristics of the PV module.

Table 1. PV module characteristics.

Parameter	Value
Peak power (MPP)at STC	198,52 W
Voltage at MPP(V_{mpp})	42,43 V
Current at MPP (I_{mpp})	4.68 A
Short circuit current(I_{sc})	5 A
Open circuit voltage(V_{oc})	51 V
Number of series cells(n_s)	60

III. PSC, LL AND LG PROBLEMS

A. Partial shading conditions:

Partial shading is a common issue in photovoltaic (PV) arrays, resulting from factors like dirt on the front surface of PV cells, snow, leaves, or the shading caused by nearby buildings. When a cell in a string of PV cells is shaded, it produces less current compared to the other cells in the same series, leading to overheating, commonly known as a "Hot Spot." To mitigate the formation of Hot Spots due to partial shading, bypass diodes are integrated into the strings.

These diodes enable the current to circumvent the shaded module. However, this protective measure introduces a drawback, manifesting as multiple power peaks in the PV curve [9], as depicted in the accompanying figure (3).

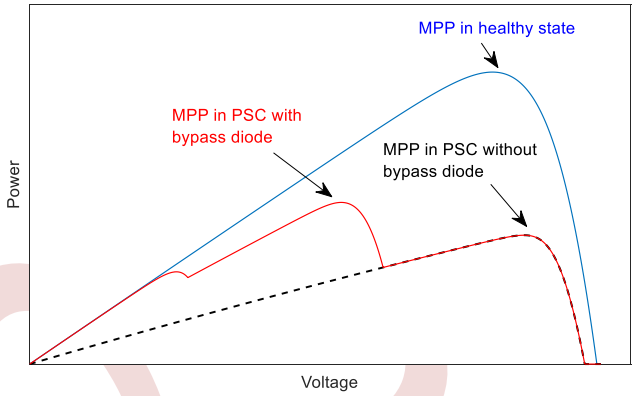


Figure 3. P_V curve in healthy and in PSC.

B. Line to Line fault:

A line-to-line fault in a photovoltaic (PV) installation represents a critical electrical issue wherein two points within the electrical circuit unintentionally come into contact, resulting in a short circuit figure (4). These faults can emerge due to a range of factors, including physical damage, corrosion, and installation errors.[10]

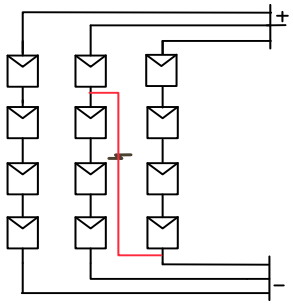


Figure 4. Line to line fault in a PV installation.

The consequences of line-to-line faults are profound, leading to significant power losses within the PV system, the figure (5) shows the P_V curve of a PV array subjected to a LL fault, showing a multipeak curve P_V characteristic of the PV array these peaks appeared due to the presence of bypass diodes.

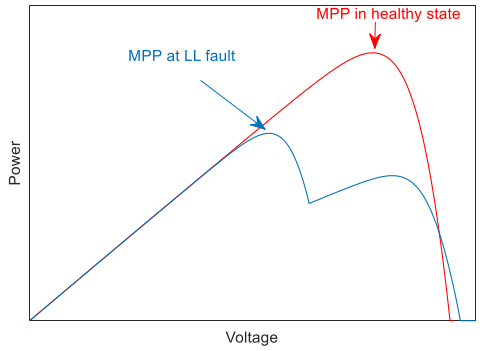


Figure 5. P_V curve in healthy state and LL fault.

C. Line to ground fault:

Line-to-Ground (LG) fault, also known as a ground fault, occurs when one of the conductors carrying electrical current unintentionally makes contact with either the earth or a conductive surface at a different electrical potential. This kind of fault can manifest for various reasons, including compromised insulation, equipment malfunction, or physical damage to the wiring. The immediate and easily observable consequence of a line-to-ground fault is a decrease in the power output of the photovoltaic (PV) array (figure). This decline transpires because the fault establishes a path of low electrical resistance, allowing current to bypass the intended electrical circuit and instead flow directly into the ground or another conducting surface. Consequently, the affected segment of the PV array generates less power.[10], [11]

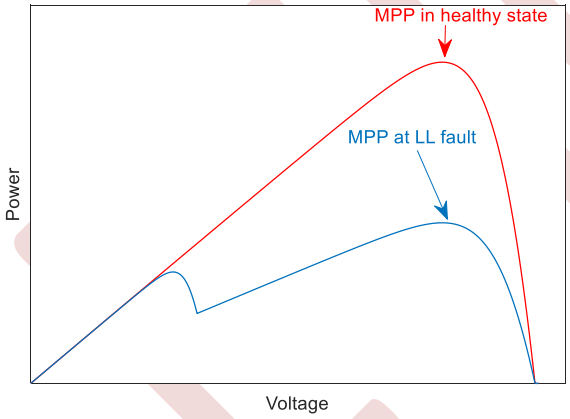


Figure 6. P_V curve in healthy and LG fault.

IV. RESULTS AND DISCUSSION

In this section, we provide the simulation outcomes for two parallel arrays, with each array consisting of three modules connected in series. The initial segment of our discussion showcases the Power-Voltage (P-V) characteristics of this configuration when subjected to PSC, LL, and LG faults. Subsequently, the second part of our analysis concentrates on Maximum Power Point Tracking (MPPT) in the context of these aforementioned fault conditions.

The figure 7 shows the P_V curves of the array under different anomalies, namely: partial shading conditions, line to line fault, line to ground fault, if we consider an efficient maximum power tracking operation, the most significant power loss arises from line-to-ground faults, resulting in a loss exceeding 50% of the power in the healthy state. In the case of partial shading conditions, more than 32% of the power is lost, while line-to-line faults lead to a 30% power loss, which is comparatively lower than the losses observed with line-to-ground faults and partial shading conditions.

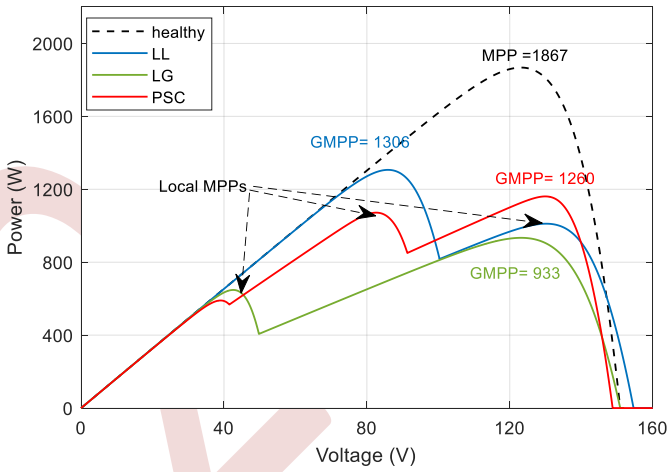


Figure 7. P_V curves under different faults.

Figures 8, 9, and 10 depict the simulation outcomes for the aforementioned array connected to a load through a buck converter. This converter is controlled by an MPPT (Maximum Power Point Tracking) module using the particle swarm optimization algorithm. In Figure 8, we examine the Power-Voltage (P-V) curve and power response of the PV system during a Line-to-Line fault scenario. Notably, the MPPT algorithm demonstrates remarkable accuracy, achieving 99.78% of the global maximum power point (GMPP) within a mere 0.033 seconds, indicating an exceptionally fast response. In this case, the duty cycle converges to 0.62. When assessing partial shading conditions (PSC), Figure 9 reveals that the system attains approximately 99.34% of the GMPP with a swift response time of 0.084 seconds and a duty cycle of around 0.39. Moving on to the Line-to-Ground (LG) fault in Figure 10, the system reaches 99.90% of the GMPP with a duty cycle of 0.35. However, the response time is slightly longer at 0.71 seconds compared to the two previous cases. These results firmly establish the efficiency of the entire system, underscoring the precision and speed of the employed MPPT algorithm. Additionally, the varying operating points of the system, characterized by three distinct duty cycles (0.69, 0.39, 0.35), demonstrate the system's capability to swiftly return to the maximum power point, further validating its effectiveness.

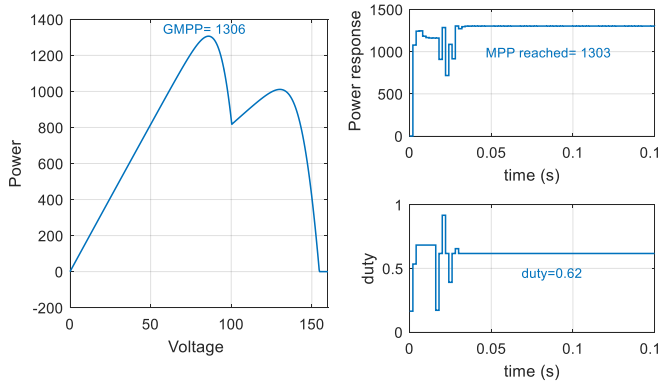


Figure 8. simulation results at LL fault.

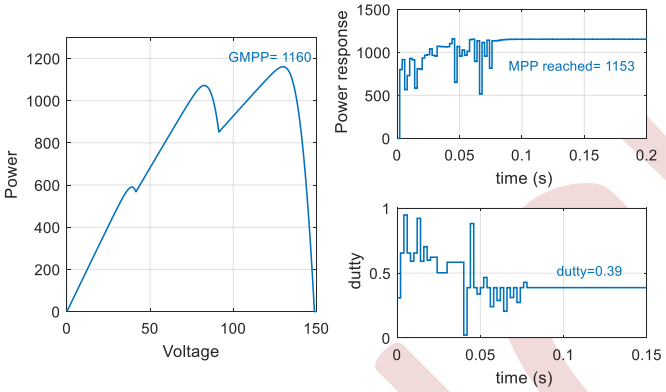


Figure 9. simulation results under PSC.

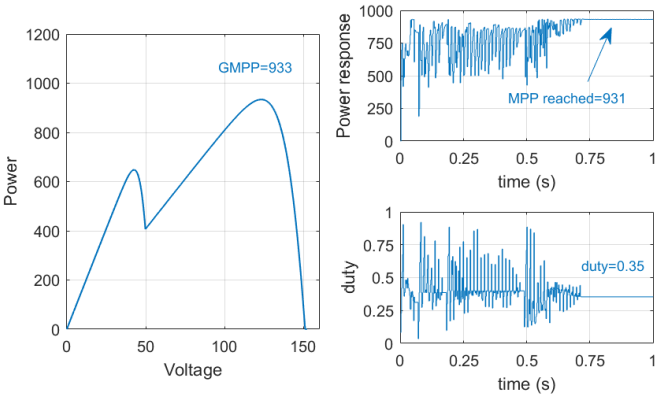


Figure 10. simulation results at LG fault.

V. CONCLUSION

This paper has provided a study of the multipeak curve within the power-versus-voltage (P_V) characteristic of PV systems, shedding light on its primary causes. Our investigation delved into three distinct issues: line-to-line faults (LL), line-to-ground faults (LG), and partial shading conditions (PSC). Through our study, we have identified LG fault as the most significant fault in term of power loss, resulting in a staggering 50% power loss when compared to the system's maximum power output in its healthy state. Meanwhile, partial shading conditions and line-to-line faults contribute to power losses of 32% and 30%, respectively.

Furthermore, our utilization of the PSO (Particle Swarm Optimization) algorithm for maximum power point tracking has yielded promising results. It has demonstrated both exceptional accuracy and rapid response times. These findings underscore the effectiveness of the PSO algorithm in optimizing the PV system's performance under challenging operating conditions.

In essence, this research not only enhances our understanding of power generation characteristics in PV systems but also highlights practical strategies for mitigating power losses and ensuring efficient operation, ultimately contributing to the advancement of renewable energy technologies.

REFERENCES

[1] F. Bayrak, G. Ertürk, and H. F. Oztop, "Effects of partial shading on energy and exergy efficiencies for photovoltaic panels," J. Clean. Prod., vol. 164, pp. 58–69, 2017.

[2] O. Bingöl and B. Özkaya, "Analysis and comparison of different PV array configurations under partial shading conditions," Sol. Energy, vol. 160, pp. 336–343, 2018.

[3] C. Saiprakash, A. Mohapatra, B. Nayak, and S. R. Ghatak, "Analysis of partial shading effect on energy output of different solar PV array configurations," Mater. Today Proc., vol. 39, pp. 1905–1909, 2021.

[4] R. Sangrody, S. Taheri, A.-M. Cretu, and E. Pouresmaeil, "An Improved PSO-based MPPT Technique Using Stability and Steady State Analyses Under Partial Shading Conditions," IEEE Trans. Sustain. Energy, 2023.

[5] K. S. Tey, S. Mekhilef, M. Seyedmahmoudian, B. Horan, A. T. Oo, and A. Stojcevski, "Improved differential evolution-based MPPT algorithm using SEPIC for PV systems under partial shading conditions and load variation," IEEE Trans. Ind. Inform., vol. 14, no. 10, pp. 4322–4333, 2018.

[6] H. Deboucha, I. Shams, S. L. Belaid, and S. Mekhilef, "A fast GMPPT scheme based on collaborative swarm algorithm for partially shaded photovoltaic system," IEEE J. Emerg. Sel. Top. Power Electron., vol. 9, no. 5, pp. 5571–5580, 2021.

[7] H. Deboucha, S. Mekhilef, S. Belaid, and A. Guichi, "Modified deterministic Jaya (DM-Jaya)-based MPPT algorithm under partially shaded conditions for PV system," IET Power Electron., vol. 13, no. 19, pp. 4625–4632, 2020.

[8] H. Deboucha, M. Kermadi, S. Mekhilef, and S. L. Belaid, "Voltage track optimizer based maximum power point tracker under challenging partially shaded photovoltaic systems," IEEE Trans. Power Electron., vol. 36, no. 12, pp. 13817–13825, 2021.

[9] N. Boutasseta, M. Ramdani, and S. Mekhilef, "Fault-tolerant power extraction strategy for photovoltaic energy systems," Sol. Energy, vol. 169, pp. 594–606, 2018.

[10] D. S. Pillai, J. P. Ram, N. Rajasekar, A. Mahmud, Y. Yang, and F. Blaabjerg, "Extended analysis on line-line and line-ground faults in PV arrays and a compatibility study on latest NEC protection standards," Energy Convers. Manag., vol. 196, pp. 988–1001, 2019.

[11] A. E. Nieto, F. Ruiz, and D. Patiño, "Characterization of electric faults in photovoltaic array systems," DYNA, vol. 86, no. 211, pp. 54–63, 2019.

Power management strategy for stand-alone DFIG-based wind turbine with battery storage

Oualid Djoudi, Sofia Lalouni Belaid, Salah Tamalouzt

Laboratoire de Technologie Industrielle et de l'Information (LTII), Faculté de Technologie

Université de Bejaia, 06000 Bejaia, Algérie

oualid.djoudi@univ-bejaia.dz, sofia.lalouni@univ-bejaia.dz, salah.tamalouzt@univ-bejaia.dz

***Abstract*— This paper deals with the control and power management of stand-alone power system based on a doubly fed induction generator (DFIG) wind turbine with battery storage system. The main objective is to supply AC loads with a constant voltage amplitude and frequency, while satisfying the load power required at any time. For this purpose, field-oriented control (FOC) is proposed to regulate the DFIG stator voltage and the DC-link voltage. On the other hand, a power management algorithm is designed to control the power flow in the DC-link in order to satisfy the load power by extracting energy from battery when wind power is insufficient. Simulation results performed with MATLAB/Simulink environment show high and satisfactory performance.**

***Keywords:* Wind power, Stand-alone DFIG, Power management algorithm, Battery storage.**

I. INTRODUCTION

Nowadays, doubly fed induction generators (DFIGs) are increasingly used in wind farms due to inexpensive power electronics, with a back-to-back converter estimated at around 30% of DFIG stator rated power [1]. A further advantage is the DFIG's ability to operate over a wide range of wind speeds [2]. In this context, a number of papers have been published on grid-connected wind energy conversion systems. However, to fully utilize the capacity of the DFIG, stand-alone mode control becomes essential due to the high sensitivity of the control operation in this scenario [3].

In autonomous mode system, the DFIG must deliver a constant voltage amplitude and frequency, irrespective of variations in wind speed and load conditions. Field oriented control (FOC) is the most frequently suggested method for stand-alone DFIG application control. For the rotor side converter (RSC), FOC strategy enables decoupled control of the voltage amplitude. In contrast, to maintain a suitable voltage frequency, a slip frequency is imposed on the rotor connections [4],[5]. Whereas, decoupled active and reactive power control is performed using FOC method for the load side converter (LSC) to regulate the value of the DC-link voltage. Results obtained with FOC method for stand-alone DFIG system in [4] and [5] demonstrate high performance and satisfactory regulation of stator voltage amplitude and frequency. Nevertheless, a major limitation of stand-alone power generation systems based on renewable energies is their intermittent nature. A power system employing an energy storage system is highly recommended in this situation. In this work, lead-acid battery is used to solve the problem of unplanned wind energy and to satisfy the load demand.

In this paper, the FOC method is proposed for both RSC and LSC controls of the stand-alone DFIG. In addition, an energy management algorithm is designed to control the energy flow in DFIG wind turbine equipped with a battery storage device supplying AC load. MATLAB/Simulink software is employed to simulate the proposed stand-alone DFIG/battery system, shown in the Figure. 1.

II. SYSTEM MODELLING

A. DFIG modeling

The DFIG electrical model expressed in the synchronous dq frame is given by the following expression.

$$\begin{cases} V_{sd} = R_s i_{sd} + \dfrac{d\phi_{sd}}{dt} - \omega_s \phi_{sq} \\ V_{sq} = R_s i_{sq} + \dfrac{d\phi_{sq}}{dt} + \omega_s \phi_{sd} \\ V_{rd} = R_r i_{rd} + \dfrac{d\phi_{rd}}{dt} - \omega_r \phi_{rq} \\ V_{rq} = R_r i_{rq} + \dfrac{d\phi_{rq}}{dt} + \omega_r \phi_{rd} \end{cases} \quad (1)$$

Where, V_{sd}, V_{sq} and V_{rd}, V_{rq} are d-q stator and rotor voltage components, respectively. i_{sd}, i_{sq} and i_{rd}, i_{rq} are d-q stator and rotor current components, respectively. ϕ_{sd}, ϕ_{sq} and ϕ_{rd}, ϕ_{rq} are d-q stator and rotor flux components, respectively. ω_s and ω_r are the stator and rotor electrical pulsations, respectively. R_s, R_r are the stator/rotor phase resistances.

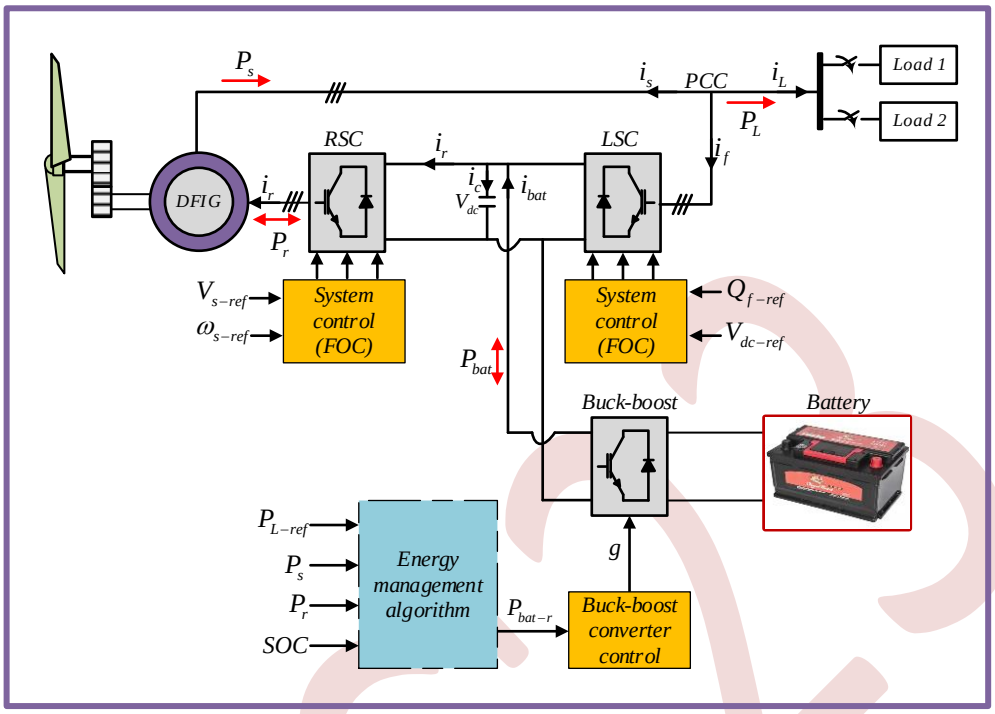


Figure 1. Proposed power system

The DFIG magnetic model is written as function of rotor/stator current, rotor/stator phase leakage inductance and mutual inductance, as shown by equation (2).

$$\begin{cases} \phi_{sd} = L_s i_{sd} + M i_{rd} \\ \varphi_{sq} = L_s i_{sq} + M i_{rq} \\ \phi_{rd} = L_r i_{rd} + M i_{sd} \\ \phi_{rq} = L_r i_{rq} + M i_{sq} \end{cases} \quad (2)$$

Equation. (3) gives the electromagnetic torque expression.

$$T_{em} = p(\phi_{rd} i_{rq} - \phi_{rq} i_{rd}) \quad (3)$$

Where, p is the pair pole number.

B. Battery modeling

The storage system is an essential element in stand-alone wind power systems due to fluctuating wind and load demand [6]. In this study, the storage system consists of lead acid battery connected to the DC link via the Buck-boost converter to manage the active power of the load. The power diagram of the lead acid battery is depicted by Figure. 2.

The battery output voltage can be calculated as follow:

$$V_{bat} = E_0 - R_{bat} i_{bat} - V_{cbat} \quad (4)$$

Where, E_0 is the empty voltage of the battery, R_{bat} is the battery internal resistance, i_{bat} is the charged and discharged current of the battery and V_{cbat} is the voltage across the capacitor.

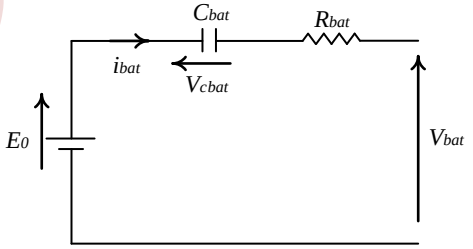


Figure 2. Lead-acid battery schematic [7]

The quantity of electricity stored by the battery during the charging phase is called the state of charge (SOC). The equation below allows to determine the battery's SOC.

$$SOC = 1 - \frac{i_{bat} * t}{C_{bat}} \quad (5)$$

With, C_{bat} is battery capacitor capacity.

III. Power Converters Control

A. Field oriented control (FOC) for RSC and LSC

In the DFIG-based grid-connected wind energy conversion system, voltage amplitude and frequency are maintained constant by the undisturbed grid. In the isolated area, the DFIG must satisfy the load's energy demand with

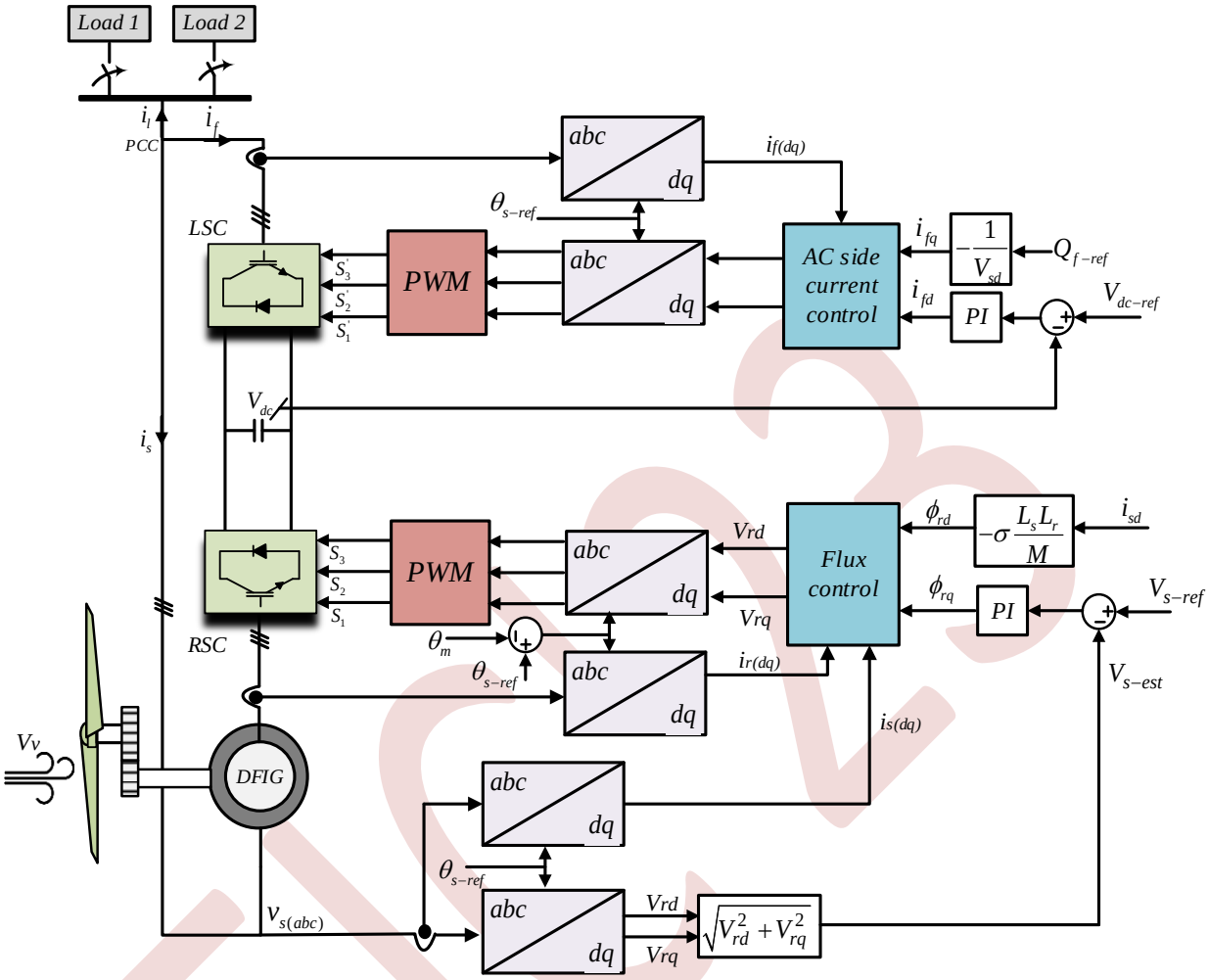


Figure 3. Schematic diagram of proposed FOC method for RSC and LSC

constant voltage amplitude and frequency. To achieve this goal, the RSC is performed to control the stator voltage amplitude and frequency. On the other hand, The LSC controls the DC-link voltage and the reactive power between the load and the generation system. Field oriented control (FOC) is employed to control RSC and LSC switches.

In the FOC method, the stator voltage amplitude is controlled by orienting the rotating reference frame along the q-axis of the stator flux. By modifying equations (1) and (2), the rotor flux can be rewritten as follows.

$$\begin{cases} \phi_{rd} = -\sigma.\dfrac{L_s.L_r}{L_m}.i_{sd} \\ \phi_{rq} = \dfrac{L_r}{\omega_s.L_m}.E_{sd} - \sigma.\dfrac{L_s.L_r}{L_m}.i_{sq} \end{cases} \quad (6)$$

On the basis of equation (6), the control of stator voltage amplitude can be achieved by controlling the q-axis rotor flux.

The control of the stator voltage frequency is obtained by adjusting the slip angle, as illustrates the equation below.

$$\theta_{sl} = \theta_{s-ref} - \theta_m \quad (7)$$

On the other hand, decoupled control is achieved using the FOC method to control the LSC's active and reactive powers separately. By orienting the rotating reference frame to the d-axis stator voltage, the LSC active power can be monitored by the d-axis LSC current. While, the LSC reactive power is adjusted by the q-axis LSC current, as specified in the following equation.

$$\begin{cases} P_f = V_{sd}.i_{fd} \\ Q_f = -V_{sd}.i_{fq} \end{cases} \quad (8)$$

The schematic diagram of the proposed FOC method for RSC and LSC is shown in Figure. 3.

B. Buck-boost converter control

The buck-boost converter is used to ensure current reversibility in the battery, which is necessary in the charging

and discharging process. The schematic diagram of the buck-boost converter is shown in Figure. 4.

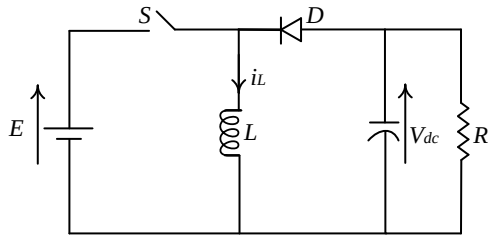


Figure 4. Buck-boost converter scheme

The following two equations govern the buck-boost converter's operating principle.

$$L\frac{di_L}{dt} = gE + V_{dc}(1-g) \quad (9)$$

$$C\frac{dV_{dc}}{dt} = -i_L(1-g) - \frac{V_{dc}}{R} \quad (10)$$

Figure 5 illustrates the switching signal generation for the bidirectional DC/DC converter to regulate the power exchanged with the battery.

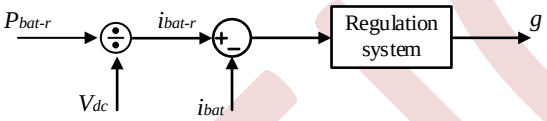


Figure 5. Battery current regulation

IV. Power Management Algorithm

The main objective of the proposed energy management algorithm is to meet load requirements by monitoring the energy flow supplied by the stand-alone DFIG-based wind turbine and the lead acid battery. The primary energy source is the wind. Due to the wind speed fluctuation, the energy management system must compensate for the lack of wind energy by drawing on the energy available in the battery. If wind energy exceeds load demand, the energy management system orders the battery to be charged by the surplus energy. Consequently, the energy management algorithm's output is the reference battery power. To determine the reference battery power, it is essential to establish the power flow in the DC-link and the point of common coupling (PCC). The following two equations define the power flow in the DC-link and the PCC, respectively.

$$i_r = i_f + i_{bat} - i_c \quad (11)$$

$$i_{bat} = i_L + i_s + i_r + i_c \quad (12)$$

The energy management result is generated with the <IF conditions, THEN decision>. Figure. 6 displays the flowchart used to manage energy flow in the proposed stand-alone DFIG/storage battery system.

V. Simulation Results and Discussion

To check the performance of the proposed control technique for the stand-alone DFIG and the validity of the suggested power management strategy, a MATLAB simulation was run with the proposed control structure (Figure 1). The wind speed profile is variable, as shown the Figure.7.

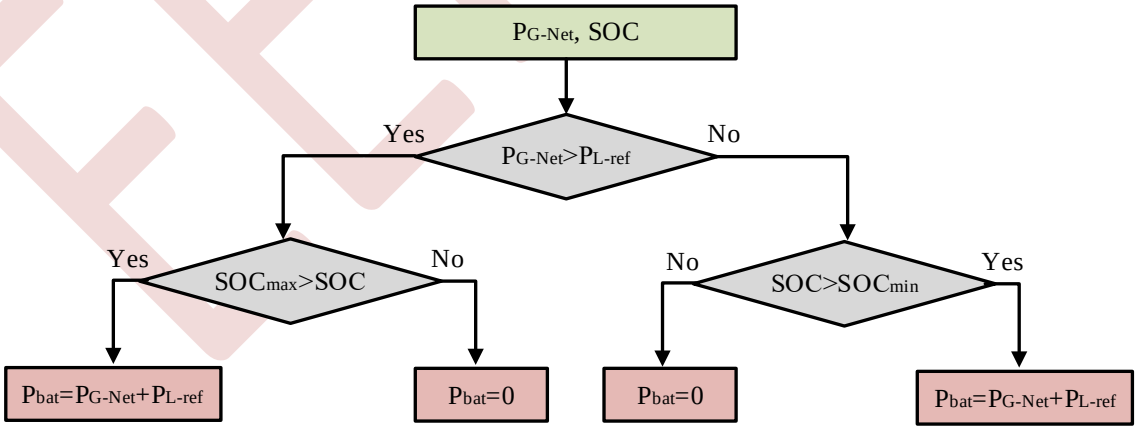


Figure 6. Power management algorithm

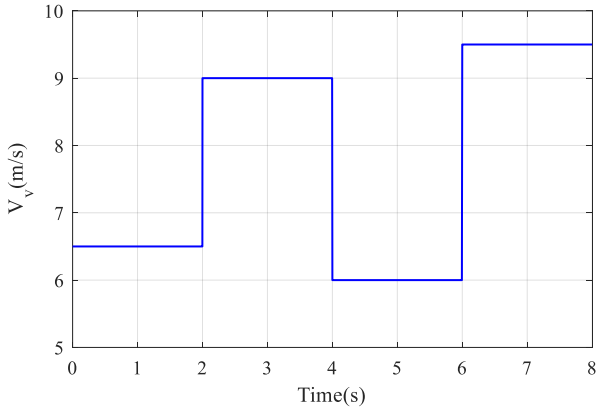


Figure 7. Wind speed profile

Figures. 8, 9 and 10 illustrate the stator voltage amplitude, the stator voltage frequency and the DC-link voltage respectively. The stator voltage amplitude and frequency demonstrate high transient and steady-state performance.

The stator voltage amplitude/frequncy and the DC-link voltage track their reference value regardless the sudden wind speed variations. Figure. 11 displays the rotor's three-phase current waveform.

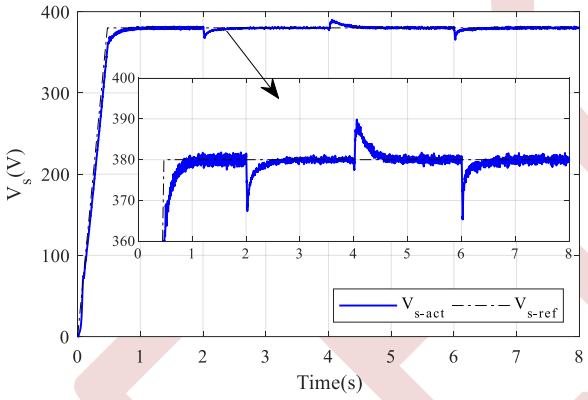


Figure 8. Stator voltage amplitude shape

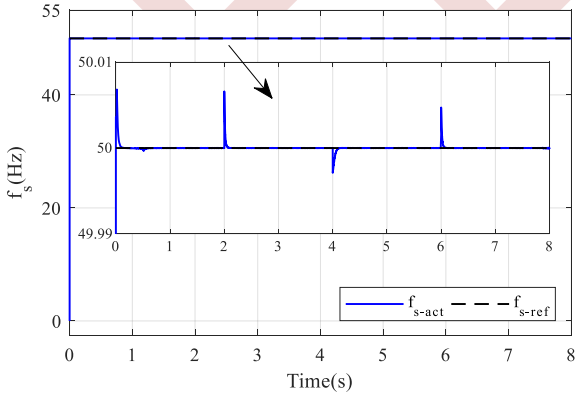


Figure 9. Stator voltage frequency shape

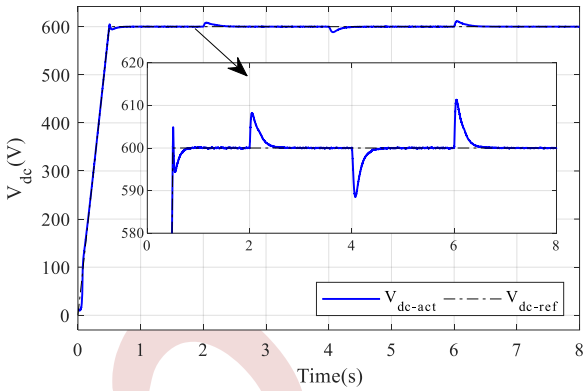


Figure 10. DC-link voltage waveform

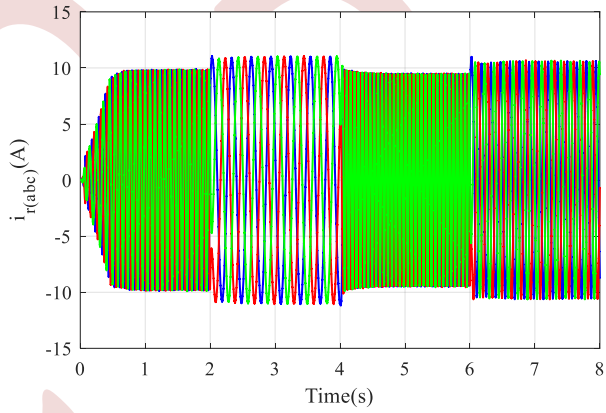


Figure 11. Rotor's three-phase current waveform

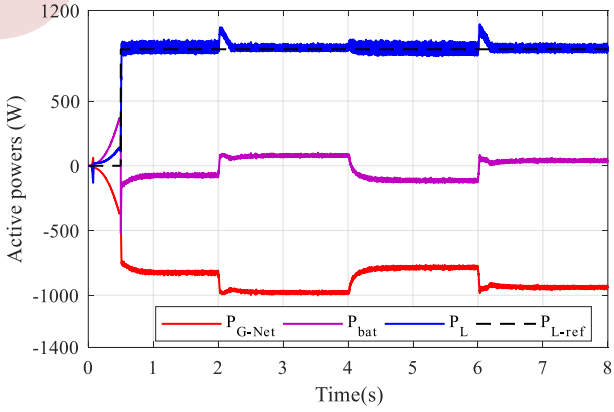


Figure 12. Active powers waveform

The power flow between the connected load and the generation system is depicted in Figure. 12. The reference load power is set to 900W after 0,5s. The load power perfectly follows its reference, despite the variation in wind speed. This is justified by the battery SOC waveform in Figure. 13. Figures 8-13 attest on the effectiveness and the validity of the proposed control strategy and the power management algorithm. The stand-alone DFIG supplies the load with constant voltage. On the other hand, load demand is ensured during the operation.

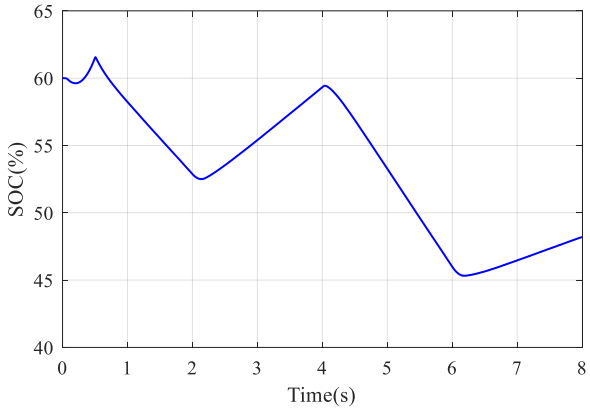


Figure 13. Battery state of charge

VI. CONCLUSION

This paper presents an effective power management for stand-alone DFIG-based wind power with battery storage system. The generation system under consideration is designed to supply an AC load with a constant voltage amplitude and frequency, while providing the energy required by the load. Numerical simulation results show high performance of the power received from the load, while the energy management process allows the desired power to be delivered at all times.

REFERENCES

[1] I. Erazo-Damián, J. M. Apsley, R. Perini, M. F. Iacchetti and G. D. Marques, "Stand-Alone DFIG FOC Sensitivity and Stability Under Mismatched Inductances," in IEEE Transactions on Energy Conversion, vol. 34, no. 2, pp. 860-869, June 2019, doi: 10.1109/TEC.2018.2869286

[2] A. Kadri, H. Marzougui, A. Aouiti, and F. Bacha J, "Energy management and control strategy for a DFIG wind turbine/fuel cell hybrid system with super capacitor storage system," in Energy, vol. 192, 2020, doi.org/10.1016/j.energy.2019.116518

[3] M. Noroozi and S. Farhangi, "Voltage and frequency stability for control of stand-alone DFIG-based wind turbine using direct voltage control method," 2014 14th International Conference on Environment and Electrical Engineering, Krakow, Poland, 2014, pp. 85-90, doi: 10.1109/EEEIC.2014.6835842

[4] R. Dev Shukla, and R.K. Tripathi, "A novel voltage and frequency controller for standalone DFIG based Wind Energy Conversion System," in Renewable and Sustainable Energy Reviews, vol. 37, pp. 69-89, 2014, doi.org/10.1016/j.rser.2014.04.069

[5] F. Abdoune, D. Aouzellag, K. Ghedamsi, " Terminal voltage build-up and control of a DFIG based stand-alone wind energy conversion system", Renewable Energy, Vol. 97, 2016, pp. 468-480, doi.org/10.1016/j.renene.2016.06.005

[6] V. Mehar Jyothi, T. Vijay Muni, and S.V.N.L. Lalitha, " An Optimal Energy Management System for PV/Battery Standalone System," in International Journal of Electrical and Computer Engineering (IJECE), vol. 6, no. 6, pp. 2538-2544, December 2016, doi: 10.11591/ijece.v6i6.11479

[7] I. Hacini, S. Lalouni, K. Idjdarene, and K. Berabez, "Energy Management of a Photovoltaic System with Hybrid Energy Storage Battery-Super capacitor," in J. Ren. Energies, vol. 1, no. 1, pp. 65-74, Sep 2023, doi.org/10.54966/jreen.v1i1.1099

Enhancing Wind Energy Conversion System Efficiency with Fuzzy Logic Controllers for Doubly Fed Induction Generators

Abdelli Radia [1], Bouzida Ahcene [2]

[1] *Laboratoire de Technologie Industrielle et de l'Information (LTII), University of Bejaia, Bejaia, Algeria*
Radia.abdelli@univ-bejaia.dz

[2]*Electrical Engineering Department, Faculty of Sciences and Applied Sciences, University of Bouira, Bouira, Algeria*
a.bouzida@univ-bouira.dz

***Abstract*—This paper presents a comprehensive study on the application of fuzzy logic controllers (FLCs) to doubly fed induction generators (DFIGs) in wind power conversion systems (WECS) With their variable speed operation and grid-friendly features, DFIGs have gained popularity as a solution for producing wind energy. However, their nonlinear and dynamic behavior under varying wind conditions presents control challenges that can be effectively addressed through nonlinear control strategies such as FLCs.**

***Keywords:* Fuzzy Logic Controller, DFIG, Wind Conversion System.**

I. INTRODUCTION

The efficiency and performance of wind turbines are pivotal to the success of wind energy projects. As wind conditions are inherently variable and unpredictable, optimizing the operation of DFIGs in wind conversion systems poses a formidable control challenge. These challenges are compounded by the nonlinear and dynamic nature of DFIGs, which necessitate advanced control strategies for effective energy capture and grid integration [1-3].

In recent years, control systems based on Fuzzy Logic Controllers (FLCs) have gained prominence as powerful tools for managing complex and uncertain processes. FLCs, inspired by human decision-making, have demonstrated their adaptability and precision in various engineering applications, including robotics, automotive systems, and industrial processes. The capacity of FLCs to handle imprecise and nonlinear data makes them an appealing choice for addressing the control intricacies associated with DFIGs in wind energy systems [4-6].

This paper explores the application of FLCs to DFIGs within the context of wind energy conversion systems. By harnessing the inherent advantages of FLCs, we seek to enhance the performance and reliability of DFIG-based wind turbines. The integration of FLCs aims to address critical aspects such as improving the system performances despite parameter variations.

This paper endeavors to underscore the pivotal role of advanced control strategies in shaping a sustainable and efficient future for wind power generation. The ensuing sections will delve into the theoretical foundations of FLCs, their design and implementation for DFIG control, and the empirical results of their application, shedding light on how FLCs contribute to the advancement of wind energy technology.

II. CONVERSION SYSTEM MODELING

The studied system involves a wind turbine that integrates a doubly fed induction generator (DFIG) directly connected to the grid via its stator, as well as a connection to a power electronic stage from its rotor. This configuration is presented in its entirety in Figure 1.

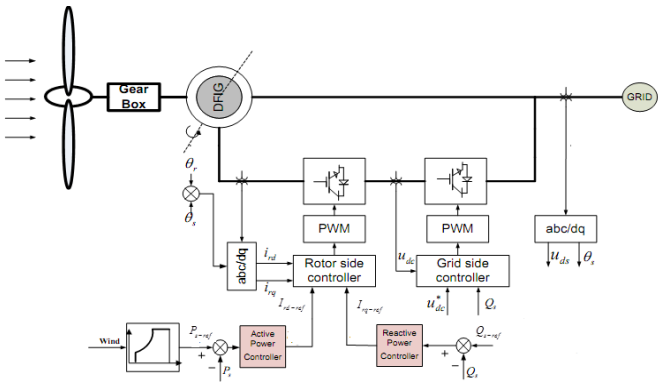


Figure 1. Studied Conversion System

The two control methods used to regulate the system on the generator side or the control of the electrical grid connection on the grid side are illustrated

A. Wind Turbine Modeling

The approximate values of aerodynamic torque T_a is given by:

$$T_a = \frac{1}{2}\rho\pi R^3 C_p(\lambda,\beta)V^2 \quad (1)$$

Where C_p is the torque coefficient, β is the blade pitch angle, λ is the tip-speed ratio, ρ is the air density, R is the blade radius and V is the wind speed.

The Maximum Power Point Tracking (MPPT) control structure adopted in this work is based on the assumption that the wind speed varies very little in steady state. To extract the maximum from the generated power, it is necessary to fix the speed ratio λ_{opt} to the value which corresponds to the maximum of the power coefficient $C_{p-\max}$. The reference electromagnetic torque must then be set to the following value:

$$T_{em-ref} = \frac{1}{2n_g\Omega_t} C_{p-\max}\rho S V_{est}^3 \quad (2)$$

B. DFIG Modeling

The stator of the machine is connected directly to the power grid but its rotor is connected via power electronics. The following equations give the mathematical model of DFIG in the (d-q) park referential:

$$\begin{cases} v_{sd} = R_s i_{sd} + \dfrac{d\Phi_{sd}}{dt} - \omega_s \Phi_{sq} \\ v_{sq} = R_s i_{sq} + \dfrac{d\Phi_{sq}}{dt} + \omega_s \Phi_{sd} \\ v_{rd} = R_r i_{rd} + \dfrac{d\Phi_{rd}}{dt} - \omega_r \Phi_{rq} \\ v_{rq} = R_r i_{rq} + \dfrac{d\Phi_{rq}}{dt} + \omega_r \Phi_{rd} \end{cases} \quad (3)$$

The equations of flux are given by:

$$\begin{cases} \Phi_{sd} = L_s i_{sd} + M i_{rd} \\ \Phi_{sq} = L_s i_{sq} + M i_{rq} \\ \Phi_{rd} = L_r i_{rd} + M i_{sd} \\ \Phi_{rq} = L_r i_{rq} + M i_{sq} \end{cases} \quad (4)$$

Where R_s, R_r are the stator and rotor resistances, L_s, L_r are cyclic stator and rotor Inductances and M is the stator-rotor mutual inductance.

Active and reactive stator powers are given by:

$$\begin{cases} P_s = v_{sd} i_{sd} + v_{sq} i_{sq} \\ Q_s = v_{sq} i_{sd} + v_{sd} i_{sq} \end{cases} \quad (5)$$

III. CONVERSION SYSTEM CONTROL

In this section, we delve into the control of the DFIG and its integration with the grid. The two strategies we introduce are both rooted in the principles of fuzzy logic.

A. DFIG Control

The strong coupling between the rotor and stator fluxes and currents is evident in equation (4), which complicate the control. The fundamental idea behind vector control is to direct the machine's flux along one of the two axes, d or q. In our case, we use an orientation on the d axis to simplify the control of active and reactive stator powers.

$$\Phi_{sd} = \Phi_s \text{ and } \Phi_{sq} = 0 \quad (6)$$

We can modify the stator voltage equations because stator resistances are ignored for medium and high-power machines.

The previous voltage and flux equations will be simplified and written as:

$$\begin{cases} v_{sd} = 0 \\ v_{sq} = v_s = \omega_s \Phi_{sd} \end{cases} \quad (7)$$

$$\begin{cases} \Phi_{sd} = \Phi_s = L_s i_{sd} + M i_{rd} \\ \Phi_{sq} = 0 = L_s i_{sq} + M i_{rq} \end{cases} \quad (8)$$

The following expressions give the power relations as a function of the rotor currents by taking into account the results of Eq.7 and Eq.8:

$$\begin{cases} P_s = -\dfrac{v_s M}{L_s} i_{rq} \\ Q_s = \dfrac{v_s^2}{L_s \omega_s} - \dfrac{v_s M}{L_s} i_{rd} \end{cases} \quad (9)$$

As we can see, the reactive power is dependent on the direct component of the rotor current i_{rd}, whereas the active power only depends on the quadrature component of the rotor current i_{rq}. The expression of the control voltages must be expressed as a function of rotor currents in order to achieve control.

$$\begin{cases} v_{rd} = R_r i_{rd} + \left(L_r - \dfrac{M^2}{L_s}\right)\dfrac{di_{rd}}{dt} - \omega_r \left(L_r - \dfrac{M^2}{L_s}\right) i_{rq} \\ v_{rq} = R_r i_{rq} + \left(L_r - \dfrac{M^2}{L_s}\right)\dfrac{di_{rq}}{dt} + \omega_r \left(L_r - \dfrac{M^2}{L_s}\right) i_{rd} + \dfrac{M v_s \omega_r}{L_s \omega_s} \end{cases} \quad (10)$$

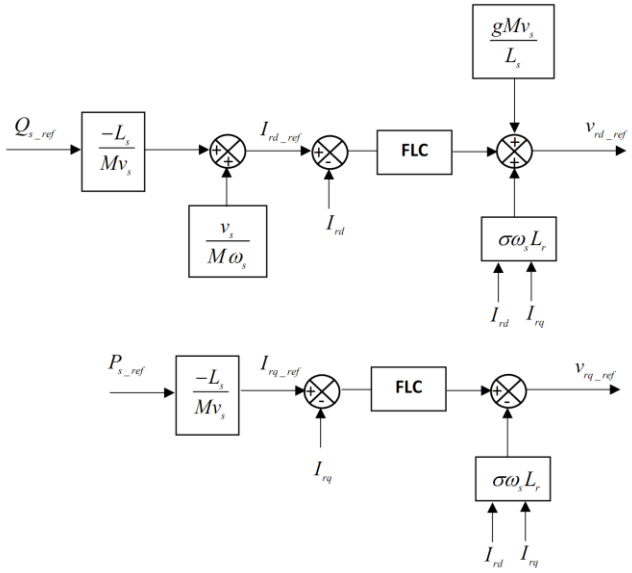


Figure 2. DFIG Control Scheme besed on a FLC PI controller

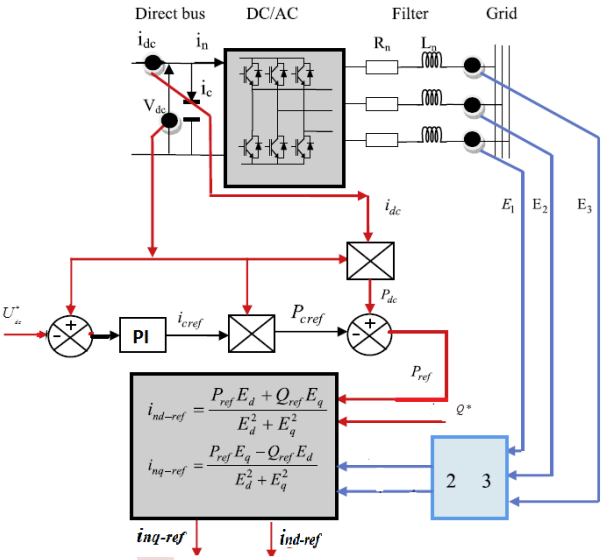


Figure 3. Grid Side Control Scheme based on a FLC PI controller

B. *Grid-Side control Scheme*

The block "Grid side controller" of figure.1 is detailed in figure.3 where the scheme of the control strategy is depicted [7, 8].

In figure.3, the inverter's control scheme and the grid link control are presented. In order to fix the power factor to the unit, the reactive power is adjusting to zero $\left(Q_{ref}=0\right)$ and the supplied active one to its reference P_{ref} which is deduced by controlling the direct bus voltage with a proportional integral corrector generating the current reference i_{c-ref} to the capacity:

$$P_{ref}=U_{dc}\left(i_{dc}-i_{c_ref}\right) \tag{11}$$

P_{ref} and Q_{ref} are given in terms of the park components of reference currents i_{nd-ref}, i_{nq-ref} by the following equations:

$$\begin{cases} P_{ref}=E_d i_{nd-ref}+E_q i_{nq-ref} \\ Q_{ref}=E_q i_{nd-ref}-E_d i_{nq-ref} \end{cases} \tag{12}$$

Where: E_d, E_q are the Park components of E_1, E_2, E_3.

The reference current expressions are given by the following equation:

$$\begin{cases} i_{nd-ref}=\dfrac{P_{ref}E_d+Q_{ref}E_q}{E_d^2+E_q^2} \\ i_{nq-ref}=\dfrac{P_{ref}E_q-Q_{ref}E_d}{V_d^2+V_q^2} \end{cases} \tag{13}$$

IV. RESULTS AND DISCUSSION

The simulation of the system under study was carried out using Matlab's Simulink environment. The wind speed was set at 9 m/s. The simulation results are presented in order to compare the use of the two PI and fuzzy controllers.

A. *Results présentation*

The curves of various quantities such as active power, reactive power, stator currents and rotor currents will be presented and commented on in this section.

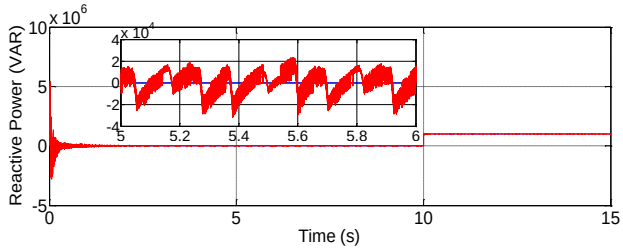


Figure 4. Stator reactive power with PI controllers

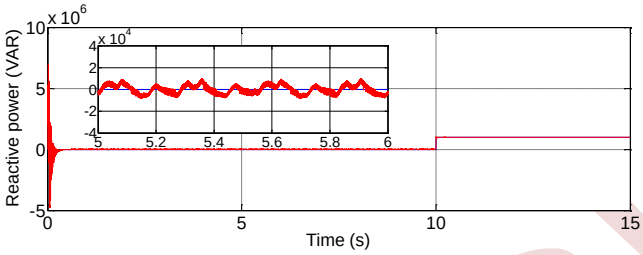


Figure 5. Stator reactive power with FLC controllers

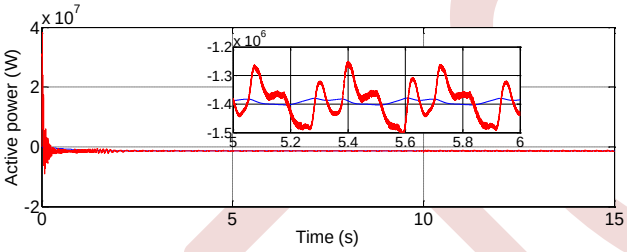


Figure 6. Stator active power with PI controllers

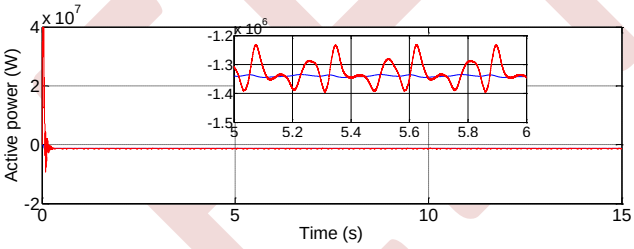


Figure 7. Stator reactive power with FLC controllers

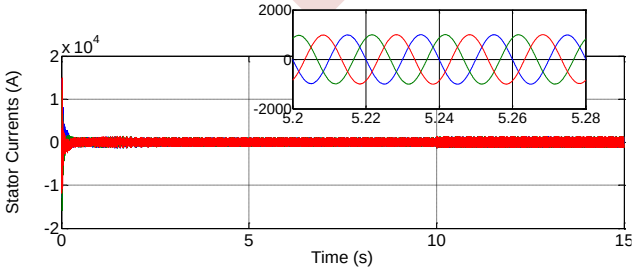


Figure 8. Stator currents with PI controllers

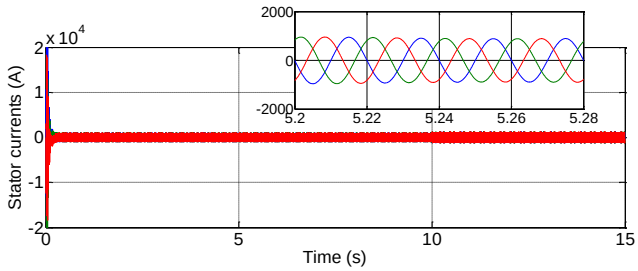


Figure 9. Stator currents with FLC controllers

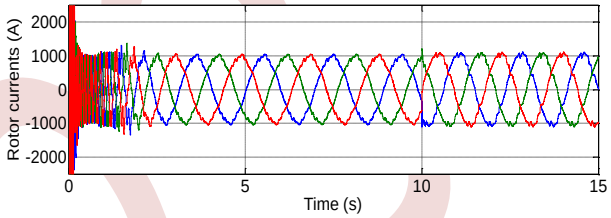


Figure 10. Rotor currents with PI controllers (with a zoom)

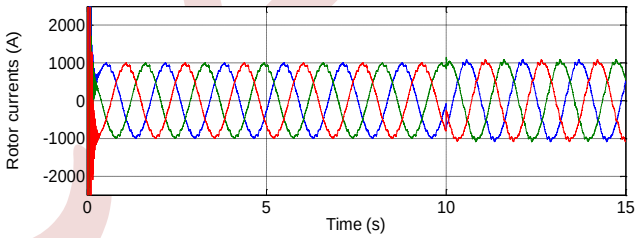


Figure 11. Rotor currents with FLC controllers

It can be seen that when using fuzzy controllers instead of PI controllers, the active and reactive power ripples around their references have been reduced by more than 27% and 39% respectively. The currents produced at the generator rotor are almost identical with a much shorter response time in the case of fuzzy controllers compared with the conventional PI controller.

B. Robustness testing

the robustness test is carried out according to the stator resistance and the rotating parts moment of inertia variations.

Firstly, the simulation of the two studied systems (with PI or FL controllers) is repeated with different values of resistance (Rs, 1.5Rs, 2Rs, 3Rs) and the obtained active power responses are superimposed on the same figure to facilitate comparison.

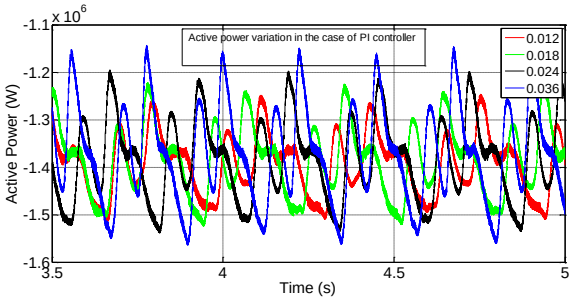


Figure 12. Zoom on the variation in active power for different Rs with PIC

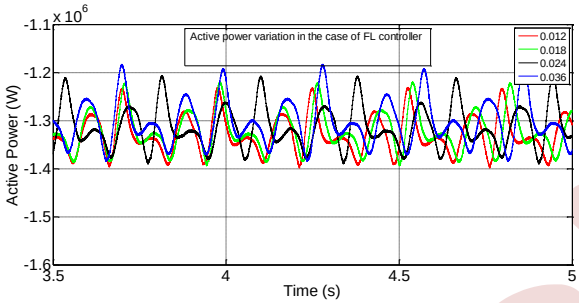


Figure 13. Zoom on the variation in active power for different Rs with FLC

Table 1 summarizes the results found. the ripples calculated as a function of each stator resistance value are given as ripple rates relative to normal operation ($R_s = 0.012\Omega$).

Table 1. Power ripples variation according to R_s variations

	$1.5R_s$	$2R_s$	$3R_s$
PIC	**+11.53%**	**+23%**	**+55.87%**
FLC	**+6.45%**	**+16%**	**+30%**

The robustness study according to the inertia coefficient variation was carried out, the models were simulated with several values of J (0.5J, J, 2J, 3J). the obtained results are presented in the following two figures and Table 2:

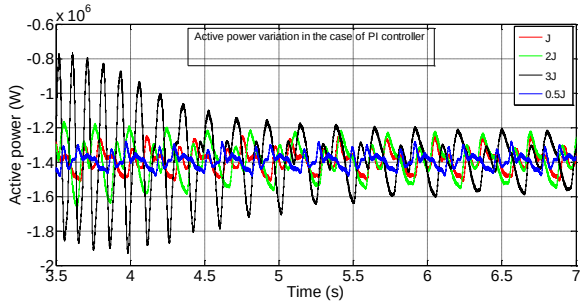


Figure 14. Zoom on the variation in active power for different J with PIC

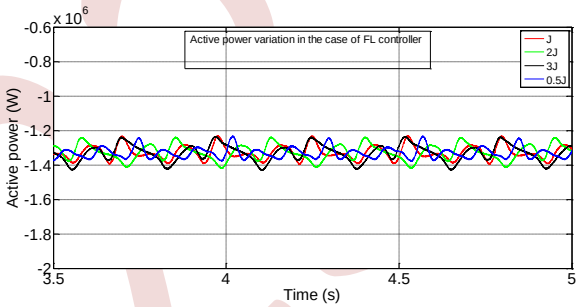


Figure 15. Zoom on the variation in active power for different J with FLC

Table 2. Power ripples variation according to J variations

	$0.5J$	$2J$	$3J$
PIC	**-12.9%**	**+41.46**	**+56.1**
FLC	**-2.4%**	**+12.25%**	**+22.6%**

we can notice the great robustness of fuzzy regulators compared to classic linear regulators in the case of variation of the parameters of the generator, this robustness is added to the good performances already noted in the comparison under normal operating conditions.

V. CONCLUSION

In the context of controlling a Doubly Fed Induction Generator (DFIG), the robustness comparison between fuzzy controllers and traditional Proportional-Integral (PI) controllers has yielded insightful results. It was found that fuzzy controllers exhibit superior robustness when facing parameter variations and uncertainties in the DFIG system. While PI controllers rely on fixed parameters and linear control strategies, fuzzy controllers adapt dynamically to changing conditions by incorporating linguistic variables and fuzzy logic rules.

REFERENCES

[1] I. K. Amin and M. N. Uddin, "Nonlinear control operation of DFIG based WECS with stability analysis," in *2017 IEEE Industry Applications Society Annual Meeting*, 2017, pp. 1-8: IEEE.

[2] I. K. Amin and M. N. J. I. T. o. p. e. Uddin, "Nonlinear control operation of DFIG-based WECS incorporated with machine loss reduction scheme," vol. 35, no. 7, pp. 7031-7044, 2019.

[3] M. J. Morshed and A. Fekih, "A nonlinear control design to improve the dynamic stability of a multi-machine power system with DFIG-based wind turbines," in *2018 Annual American Control Conference (ACC)*, 2018, pp. 6731-6736: IEEE.

[4] S. K. Raju and G. N. J. I. T. o. S. E. Pillai, "Design and implementation of type-2 fuzzy logic controller for DFIG-based wind energy systems in distribution networks," vol. 7, no. 1, pp. 345-353, 2015.

[5] A. J. A. i. M. Tamaarat and A. C, "Active and reactive power control for DFIG using PI, fuzzy logic and self-tuning PI fuzzy controllers," vol. 74, no. 2-4, pp. 95-102, 2019.

[6] H. Chojaa *et al.*, "Nonlinear control strategies for enhancing the performance of DFIG-based WECS under a real wind profile," vol. 15, no. 18, p. 6650, 2022.

[7] R. Abdelli, D. Rekioua, T. Rekioua, and A. J. I. t. Tounzi, "Improved direct torque control of an induction generator used in a wind conversion system connected to the grid," vol. 52, no. 4, pp. 525-538, 2013.

[8] R. Abdelli, D. Rekioua, T. Rekioua, A. Bouzida, and A. Tounzi, "Control of the grid-side converter in wind conversion systems with flywheel energy storage and constant switching frequency," in *2017 International Renewable and Sustainable Energy Conference (IRSEC)*, 2017, pp. 1-6: IEEE.

EEIC'23

Enhancement DTC Control for SEIG in variable-speed wind turbines, associated with a energy storage system

Kahina Berabez [1], Hacini Ismail [1], Farid Hamoudi[2] , Kassa Idjdarene[1]

[1] *Laboratoire de Technologie Industrielle et de l'Information, Faculté de Technologie, Université de Bejaia, Bejaia 06000, Algeria*

kahina.berabez@univ-bejaia.dz

ismail.hacini@univ-bejaia.dz

kassa.idjdarene@univ-bejaia.dz

[2] *Laboratoire de Maitrise des Energies Renouvelables, Faculté de Technologie, Université de Bejaia, Bejaia 06000, Algeria*

farid.hamoudi@univ-bejaia.dz

***Abstract*—This research focuses on the application of the Direct Torque Control (DTC) strategy to manage the terminal voltage of a Self-excited induction generator (SEIG) that supplies power to an autonomous load. The SEIG is connected to a three-level Neutral Point Clamped (3L_NPC) converter. The utilization of the 3L_NPC converter ensures the increase in generated voltage levels, leading to improved current waveform quality and reduces the Total Harmonic Distortion (THD) in the stator currents. To ensure a more stable and dependable power supply, this study also introduces an Energy Storage System (EESS) consisting of batteries (BT) along with a management algorithm designed to oversee power flows between different storage devices. Furthermore, the dynamic model of the SEIG incorporates the saturation effect of magnetic materials and is conducted in the (α-β) frame using the Concordia transform. The efficacy of the proposed control strategy is verified through simulation tests conducted in MATLAB/Simulink.**

***Keywords:* DTC Control, Induction Generator, Battery Storage**

I. INTRODUCTION

The utilization of induction machines in generator mode shows considerable potential for harnessing wind energy in rural and remote areas [1]. In recent years, the adoption of variable-speed wind turbines with Self-Excited Induction Generators (SEIGs) has gained prominence in standalone systems [2]. This approach offers an appealing and highly efficient solution due to their robust construction and low cost [1-2]. Nonetheless, a significant drawback of these generators is how to guarantee the stability and voltage regulation of the stator windings of this machine in the face of variations in load and/or rotation speed [1-3]. As a solution, the implementation of voltage control strategies becomes essential to maintain a consistent DC voltage irrespective of load fluctuations. These strategies involve the design of control schemes for a power converter.

Direct Torque Control (DTC) has emerged as an alternative approach in recent years, [3] and has gained prominence. Notably, this technique has proven its effectiveness in control various types of machines. For example, DTC has been successfully applied to control Doubly Fed Induction Generators (DFIG), Permanent Magnet Synchronous Generators (PMSG) [4].

One of the key advantages of DTC is its independence from the need for current control loops or speed control loops, and it does not demand any coordinate transformation. Furthermore, it is known for its robustness and its ability to provide precise control with excellent regulation of DC voltage [3-4]. The widespread adoption of the three-level inverter with the NPC structure can be attributed to its effectiveness, stemming from several advantages. These benefits include the enhancement of output waveforms, the reduction of semiconductor stress, the mitigation of voltage variations (dv/dt), which, in turn, minimizes stress on semiconductors, and a reduction in harmonic components.

On the other hand, wind energy, despite being a key renewable energy source, continues to face specific challenges when it comes to widespread implementation. One of the primary concerns revolves around the substantial variations in wind speed experienced throughout the day and year, leading to corresponding fluctuations in power generation [5]. Various proposals have been put forward to address this issue and regulate the output of wind turbines, ensuring a consistent power supply for isolated loads with a steady demand. These solutions include Electrical Energy Storage Systems (EESS), which encompass technologies designed to store electrical energy for future usage. EESS technologies play a pivotal role in contemporary energy management by addressing issues associated with intermittent renewable energy sources [5-6]. These systems store surplus electricity when supply exceeds demand and release it when demand exceeds supply, thereby enhancing

the reliability and flexibility of the energy infrastructure. Various types of EESS technologies exist, each with its own characteristics, advantages, and limitations. Some common types include: Batteries: These are perhaps the most familiar form of EESS [2-5]. The control system described in this paper has a dual purpose: firstly, to control the terminal voltage of a SEIG with the DTC control application, and secondly, to integrate an Energy Storage System (ESS) featuring batteries (BT) and a specialized management algorithm for effective power distribution among different storage devices.

this study incorporates an (EESS) that includes batteries (BT) and employs a management algorithm to oversee the distribution of power among various storage devices. The studied system has been modeled and subjected to testing using the MATLAB/Simulink software package.

II. THE STUDIED SYSTEM

The system studied in this article includes the following elements: a wind turbine, a three-phase squirrel cage asynchronous generator, a three-level neutral point clamped rectifier/inverter (3L_NPC), an autonomous load, a buck-boost converter, as well as a DC-side capacitor and a battery used as a storage system to maintain the balance between production and consumption. The proposed management program is responsible for ensuring the charging and discharging of the batteries, as well as their connection and disconnection (full charge or critical discharge).

A. Generator modeling

Considering the phenomenon of saturation, the electrical equations governing the behavior of the induction generator are expressed in the following manner [3]:

[Vs]=[A]*[I]+[B][dI/dt].

$$A = \begin{bmatrix} R_S & 0 & 0 & 0 \\ 0 & R_S & 0 & 0 \\ -R_r & \omega_r . l_r & R_r & -\omega_r . (l_r + L_m) \\ -\omega_r . l_r & -R_r & \omega_r . (l_r + L_m) & R_r \end{bmatrix} \quad I = \begin{bmatrix} i_{s\alpha} \\ i_{s\beta} \\ i_{m\alpha} \\ i_{m\beta} \end{bmatrix}$$

$$B = \begin{bmatrix} l_s & 0 & L_m + L_m' . \frac{i_{m\alpha}^2}{|i_m|} & L_m' . \frac{i_{m\alpha} . i_{m\beta}}{|i_m|} \\ 0 & l_s & L_m' . \frac{i_{m\alpha} . i_{m\beta}}{|i_m|} & L_m + L_m' . \frac{i_{m\beta}^2}{|i_m|} \\ -l_r & 0 & l_r + L_m + L_m' . \frac{i_{m\alpha}^2}{|i_m|} & L_m' . \frac{i_{m\alpha} . i_{m\beta}}{|i_m|} \\ 0 & -l_r & L_m' . \frac{i_{m\alpha} . i_{m\beta}}{|i_m|} & l_r + L_m + L_m' . \frac{i_{m\beta}^2}{|i_m|} \end{bmatrix} \quad (1)$$

B. Battery modeling

The model of battery is given in the figure 2.

The relationship between the battery voltage (V_{bat}) and the battery current (I_{bat}) is described by the following equation:

$$V_{bat} = E_b - R_i I_{bat} - V_{cvat} \quad (2)$$

The state of charge (SOC) can be expressed using the following formulation:

$$SOC = 1 - \frac{Q_d}{C_b} \quad (3)$$

C. energy management algorithm

The energy management algorithm is based on three scenarios:

If wind energy is sufficient, the wind turbine supplies energy to both the load and the battery.

If wind energy is insufficient, the load is powered by both sources simultaneously (wind turbine and battery).

If wind energy is absent (no wind), the load is solely powered by the battery

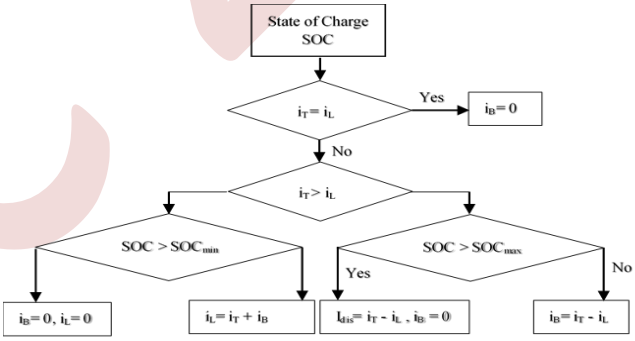


Figure 1. Flowchart depicting the Strategy for Managing Power

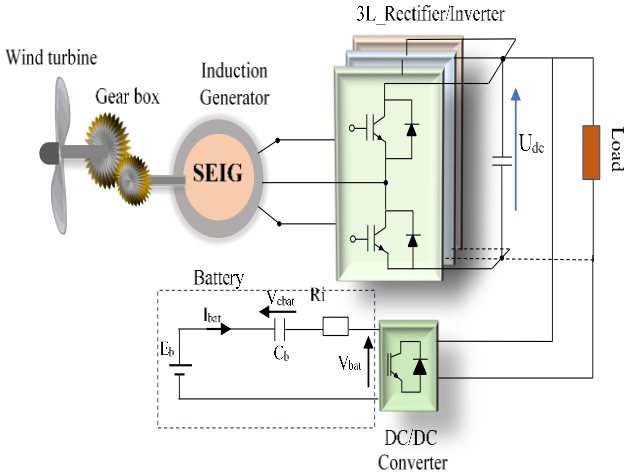


Figure 2. The studied system

III. GENERATOR CONTROL STRATEGY

The primary objective of DTC is to achieve direct torque regulation of the machine by applying the different voltage vectors from the inverter. The variables under control in this process typically include the stator flux and electromagnetic torque, both of which are typically managed through the utilization of hysteresis regulators.

The stator flux magnitude is determined using the ($\Phi_{s\alpha}$, $\Phi_{s\beta}$) components, as outlined below [3-7]:

$$\begin{cases} \Phi_{s\alpha} = \int_0^t (V_{s\alpha} - R_s i_{s\alpha})dt \\ \Phi_{s\beta} = \int_0^t (V_{s\beta} - R_s i_{s\beta})dt \end{cases} \quad (4)$$

$$\Phi_s = \sqrt{\Phi_{s\alpha}^2 + \Phi_{s\beta}^2} \quad (5)$$

The electromagnetic torque can be calculated using the stator current components ($i_{s\alpha}$, $i_{s\beta}$), the flux ($\Phi_{s\alpha}$, $\Phi_{s\beta}$), and the pole pair number (p).

$$T_{em} = p(\Phi_{s\alpha} i_{s\beta} - \Phi_{s\beta} i_{s\alpha}) \quad (6)$$

A. DTC control based on a three-level NPC converter

Enhancing the performance of DTC is achieved by implementing modifications in the inverter through the use of a three-level inverter.
Figure 3 depicts a schematic representation of a three-level neutral point clamped inverter (NPC).

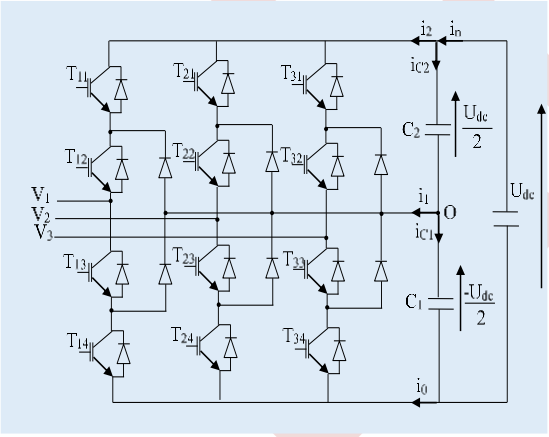


Figure 3. 3L_NPC converter

The three output voltage levels, which are -Vdc/2, 0, and -Vdc, are produced through combinations of the 12 switches within the inverter. These combinations involve the four switches within each leg, as specified in Table I [3].

$$\begin{cases} S_{ji} = 1 \ \ if \ \ T_{ji} \ \ closed \\ S_{ji} = 0 \ \ if \ \ T_{ji} \ \ open \end{cases} \quad (7)$$

With j=a, b, c and i=1,2,3,4.

TABLE I. SWITCHING STATES

S_{j1}	S_{j2}	$\overline{S_{j1}}$	$\overline{S_{j2}}$	S_j	v_{jo}
1	1	0	0	P	$U_{dc}/2$
0	1	1	0	O	0
0	0	1	1	N	$-U_{dc}/2$

The provided equation defines a connection function, denoted as F_j^h, which is attributed to each state h of arm j.

$$\begin{cases} F_j^2 = S_{j1} S_{j2} \\ F_j^1 = S_{j1} \overline{S_{j2}} \\ F_j^0 = \overline{S_{j1}\, S_{j2}} \end{cases} \quad (8)$$

The voltages of the legs can then be expressed as:

$$\begin{bmatrix} v1 \\ v2 \\ v3 \end{bmatrix} = \frac{U_{dc}}{3} \begin{bmatrix} 2 & -1 & -1 \\ -1 & 2 & -1 \\ -1 & -1 & 2 \end{bmatrix} \begin{bmatrix} F_1^2 - F_1^0 \\ F_2^2 - F_2^0 \\ F_3^2 - F_3^0 \end{bmatrix} \quad (9)$$

The spatial representation of voltage vectors is shown in Figure. 2, which forms three hexagons [3].

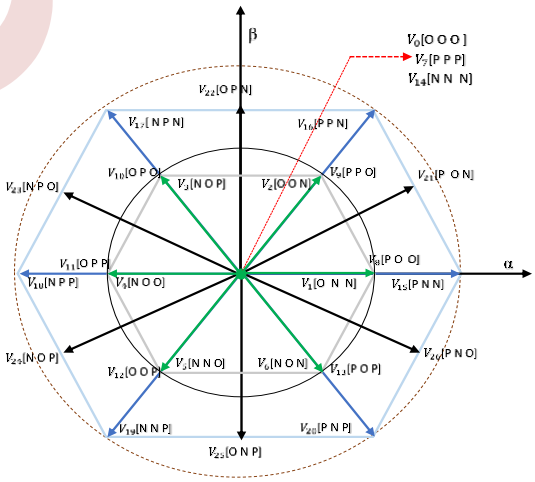


Figure 4. Voltage vectors delivered 3L_NPC converter

The control mechanism for stator flux employs a three-level hysteresis comparator, represented as (-1, 0, 1). while the control of electromagnetic torque employs a five-level hysteresis comparator, denoted as (-2, -1, 0, 1, 2) [3].

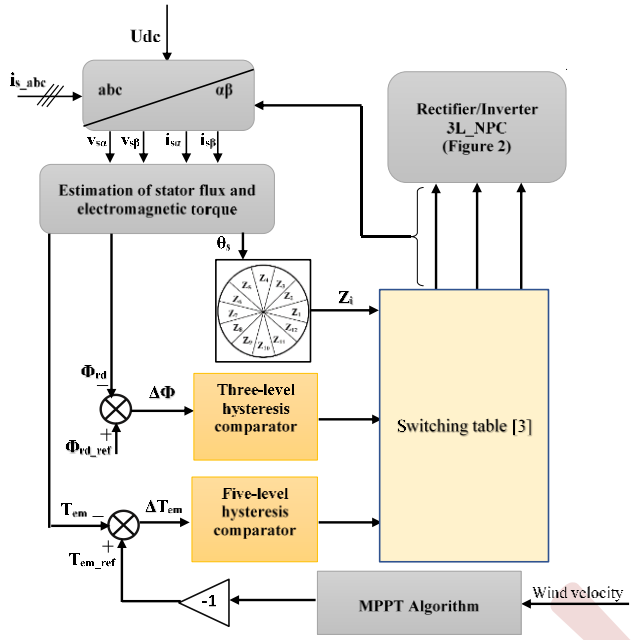


Figure 4. Structure of DTC control for SEIG by 3L-NPC converter

In order to regulate the DC voltage "Vdc " with the Buck Boost chopper, the block diagram system shown in figure 5 is employed.

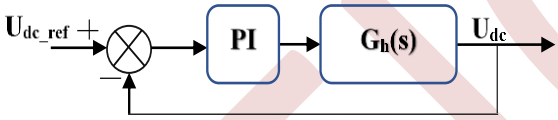


Figure 5. Diagram illustrating the Output Voltage Regulation in the Buck-Boost Chopper [2]

The transfer function Gh(s) can be expressed as follows [2]:

$$G_h(s) = \frac{V_{dc}}{V_{bat}} = \frac{\left(\alpha \frac{L}{R}\right)s + (1-\alpha)^2}{(1-\alpha)^4 \sqrt{\frac{L}{C_s}}s^2 + (1-\alpha)^2 \frac{L}{R}s + (1-\alpha)^5} \quad (10)$$

With R, L, and Cs representing the resistance, inductance, and capacitance of the buck-boost chopper circuit, respectively.

IV. SIMULATION RESULTS

An efficiency assessment of the proposed control has been conducted through MATLAB/Simulink simulations. whose main parameters for the SEIG, is given in the appendix. In this study, the DC voltage reference is maintained at a value of 465V, and the flux reference is established at 0.7Wb.

Figure 7 illustrates the variable wind speed profile. Figure 8 illustrates that the DC bus voltage is effectively regulated. It's evident that, despite fluctuations in speed and/or load, the DC bus voltage consistently closely follows its reference value.

Figures (9 –10) depict respectively the evolution of both the reference and measured stator flux, the circular movement of the stator flux. Upon analyzing the obtained results, the estimated flux closely follows its reference without any noticeable overshoot, and it exhibits remarkable insensitivity to the variations applied. The evolution of the flux $\Phi_{s\beta}$ as a function of $\Phi_{s\alpha}$ displays a perfectly circular motion (Figure 10). Furthermore, as indicated by the zoomed-in sections of the figures, a pronounced ripple is observed in the 2L-DTC, while the 3L-DTC exhibits a smoother flux profile.

Figure 11 illustrates how variations in speed and load affect the electromagnetic torque (referred to as Tem). Notably, The estimated torque tracks finely its reference. Moreover, it can be noticed that the torque ripple differs between the two converters (3L and 2L). When we zoom in on the Tem evolution, it becomes evident that 2L_DTC exhibits a high torque ripple, whereas 3L_DTC manages to reduce this ripple.

Figure 12 depict the wind, battery and load powers, the battery provides an energy source to meet the demand of the load, as shown in Figure 20 (battery charging/discharging). Wind energy has been accurately tracked based on wind speed. the state of charge of the battery during the charging/discharging mode is depicts in figure 13. In Figure 14, this current is depicted in the abc reference frame. Naturally, this current varies in response to changes in speed and load. Furthermore, its waveform is sinusoidal, as illustrated in the zoomed-in portion.

In Figure 15, a close-up view of the phase (a), of stator current for both converters are presented during a steady-state operation. It's evident that the currents exhibit a sinusoidal pattern, with the 2L-DTC showing a higher current ripple compared to the 3L-DTC.

In contrast, the stator currents exhibit of harmonic components, as demonstrated by the spectrum depicted in figure 16, with a THD-min_ of 0.77%. The histogram in figure 17 illustrates the THD values of these currents measured at various time points under different operating conditions for the two converters. It's noticeable that the 3L_DTC significantly reduces THD compared to the 2L_DTC.

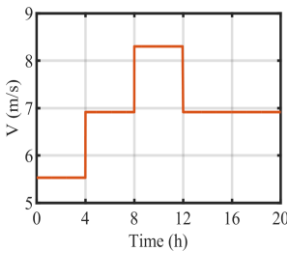


Figure 7. wind speed profile

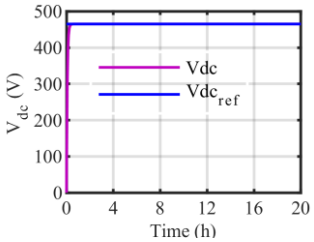


Figure8. Vdc voltage

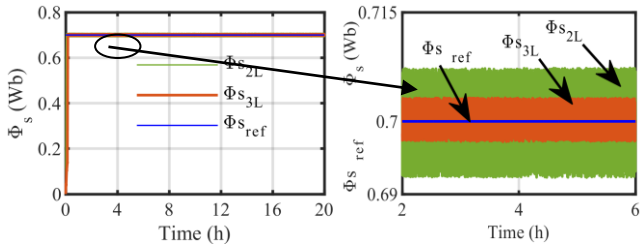


Figure 9. The stator flux magnitude with its zoom

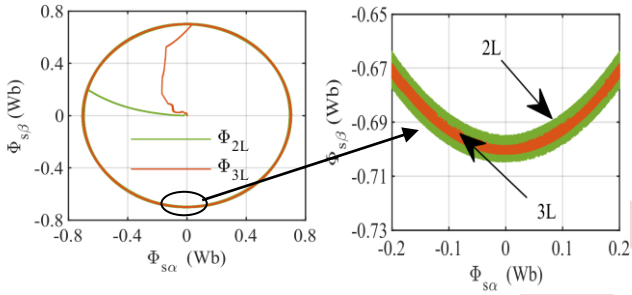


Figure10. Stator flux trajectory with zoom

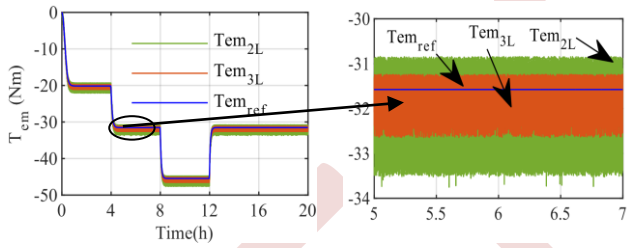


Figure 11. Electromagnetic torque evolution with its zoom

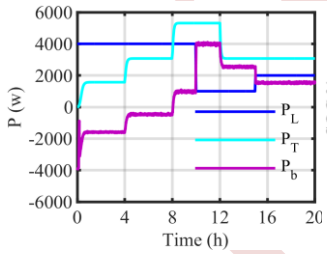


Figure 12. Wind, Battery and load powers

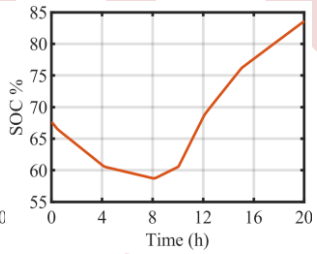


Figure13. Battery SOC

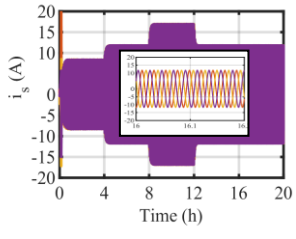


Figure14. The stator current with its zoom

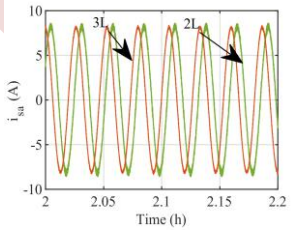


Figure15.Stator current comparison

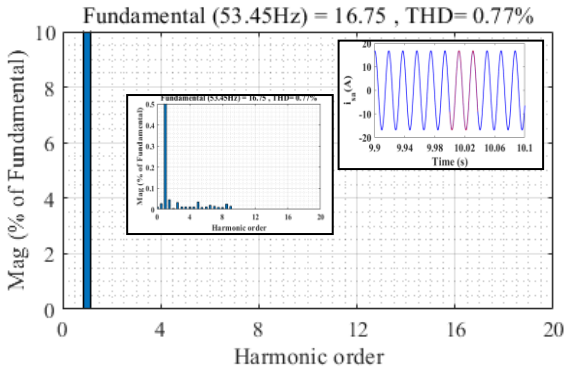


Figure16. The spectral analysis (THD)

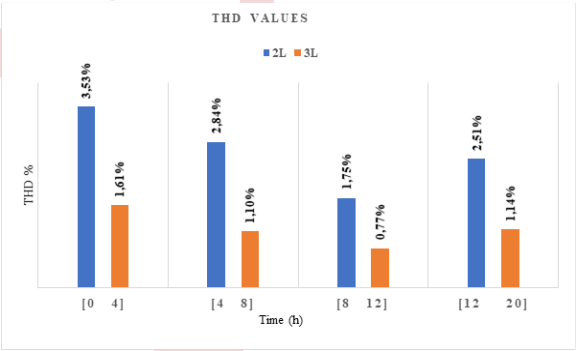


Figure17. THD values

V. CONCLUSION

In this paper, we have discussed the application of the DTC control strategy to improve the dynamic performance of a SEIG in a variable-speed wind turbine system using a 3L-NPC. This strategy enables the maintenance of the stator flux regardless of wind speed fluctuations and abrupt changes in load conditions. Additionally, it achieves the adjustment and electromagnetic torque by generating an appropriate voltage vector to ensure they closely track their respective reference values.

The advantage of a 3L-NPC converter over a two-level one in DTC control is evident in its spatial representation of voltage vectors, which offers a significant degree of flexibility in controlling a (SEIG), leading to reduced and minimizing torque and flux ripples and The THD of the stator currents in the 3L_DTC is significantly lower when compared to the 2L_DTC.

Furthermore, this study introduces an Energy Storage and Management System (EESS) along with a control algorithm to govern the power distribution among the Turbine, Load, and Batteries. The simulation results also demonstrate that the essential energy balance is consistently maintained.

ACKNOWLEDGMENT

Acknowledgement The project presented in this paper is supported by the Laboratory of Industrial Technology and the Information (LTII) of Bejaia University under the

patronage of the General Directorate of Scientific Research and Technological Development (DGRSDT), Algeria.

REFERENCES

[1] M.Bubalo, M. Bašić, D. Vukadinović & I. Grgić " Optimized isolated operation of a WECS-powered microgrid with a battery-assisted qZSI". In 2020 6th International Conference on Electric Power and Energy Conversion Systems (EPECS) (pp. 1-6). IEEE.

[2] K.Idjdarene, D. Rekioua, T. Rekioua & A.Tounzi. "Vector Control of Autonomous Induction Generator with Battery Storage System". In 2017 International Renewable and Sustainable Energy Conference (IRSEC) (pp. 1-6). IEEE.

[3] K.Berabez, F.Hamoudi, K. Idjdarene, & I.Hacini, "Advanced Terminal Voltage Control of Self-Excited Induction Generators in VariableSpeed Wind Turbines Using a Three-Level NPC Converter". Mathematical Modelling of Engineering Problems, Jun2023, Vol. 10, p805-814 (2023).

[4] O. Djoudi, S.L. Belaid, & S. Tamalouzt (2023). "Multilevel Converter and Fuzzy Logic Solutions for Improving Direct Control Accuracy of DFIG-based Wind Energy System". Periodica Polytechnica Electrical Engineering and Computer Science, 67(2), PP. 136-148 , (2023). doi.org/10.3311/PPee.21047.

[5] Y.S. Bouziane, N. Henini & A.Tlemçani,. "Energy Management of a Hybrid Generation System Based on Wind Turbine Coupled with a Battery/Supercapacitor". Journal Européen des Systèmes Automatisés, 55(5).

[6] P.K.Behera, & M. Pattnaik, "Power Distribution Control and Performance Assessment of a Wind Energy fed Microgrid Integrated with Hybrid Energy Storage System". Authorea Preprints. (2022). DOI: 10.22541/au.166999205.54316844/v1.

[7] K.Idjdarene, D.Rekioua, T. Rekioua, A.Tounzi, A, " Direct torque control strategy for a variable speed wind energy conversion system associated to a flywheel energy storage system". In 2009 Second International Conference on Developments in Systems Engineering, Dhabi, United Arab Emirates, pp. 17-22. 10.1109/DeSE.2009.47.

APPENDIX

Parameters of the SEIG:
Rated power = 5,5 kW, Frequency 50 Hz,
Rated voltage =230/400V, current =23.8/13.7 A
Rotation speed = 690 rpm, Inertia = 0.230 kg.m2
Friction =0,0025 N.m/rads^{-1}, Stator resistance Rs= 1,07131Ω
Rotor resistance R r= 1,29511 Ω, Number of pair of poles =4

Fuzzy Logic MPPT Algorithm for Standalone Photovoltaic Water Pumping System Using Separately Excited DC Motor

Samir ZOUGHAB [1], Nouri BELHAOUCHET [2], Samir SAYAH [3]

[1,2] *LAS Laboratory, Electrical Engineering Department, Faculty of Technology, Ferhat Abbas University, Setif1, ALgeria*

zoughabsamir@gmail.com, nouri_belhaouchet@yahoo.fr

[3] *QUERE Laboratory, Electrical Engineering Department, Faculty of Technology, Ferhat Abbas University, Setif 1, Algeria*

samir_pg04@yahoo.fr

***Abstract*— This paper describes an efficient control for a standalone photovoltaic (PV) water pumping system using a separately excited DC motor drive. The structure contains two power converters linked by a DC-bus capacitor. The first converter is a DC-DC boost converter; used for extracting the maximum power from the PV array by using a fuzzy logic maximum power point tracking (FL-MPPT) technique. For this converter, two control loops are used. The first loop is an outer voltage control loop, which uses a proportional-integral (PI) controller to regulate the output PV voltage at its reference value generated by FL-MPPT technique and estimate the reference inductor current. The second loop is an inner current control loop; it uses a predictive current controller which forces the inductor current to track its reference with fast dynamic response. The second converter is a DC-DC buck converter; used to supply the armature circuit with a variable voltage and drive the motor with a variable speed according to the produced PV power. The field circuit of the DC motor is connected to the DC-bus capacitor and the DC-bus voltage is regulated at a required level to ensure a constant rated magnetic flux. The reference speed is estimated from the control of the DC-bus voltage and the affinity law. The performances of the presented system are verified by digital simulation under Matlab/Simulink environment in starting, steady-state and dynamic conditions.**

Keywords: **PV water pumping system, DC-DC boost converter, DC-DC buck converter, FL-MPPT, separately excited DC motor.**

I. INTRODUCTION

In an era where sustainable and eco-friendly solutions are becoming increasingly imperative, the utilization of renewable energy sources has gained significant attention [1]. One such groundbreaking technology that has been gaining momentum in recent years is the solar photovoltaic (PV) water Pumping [1, 2]. The utilisation of the solar PV energy for water pumping reduces dependency on fossil fuels, leading to lower carbon emissions and a smaller environmental footprint [1-4]. The PV water pumping presents a promising and sustainable alternative for supplying water in various contexts, be it for agricultural, domestic, or industrial purposes [1, 5].

Standalone PV water pumping system is one of the best choices, especially in remote areas where the access to electricity is limited [6]. In this system, the PV energy is used directly from PV panels without energy storage or grid connection [3, 6, 7].

In solar PV systems, the PV array presents a nonlinear Power-Voltage characteristic which has only one peak called maximum power point (MPP); mainly depends on the atmospheric conditions (solar irradiance and temperature). In order to track this MPP, it is necessary to introduce an intermediate power conditioning unit equipped with a maximum power point tracking (MPPT) control. The most common methods to extract the available MPP from the PV array are perturb and observe (P&O) and incremental conductance (INC) MPPT techniques. These techniques use mathematical models and perturbations to find the MPP, and can suffer from oscillations around the MPP, especially under rapidly changing of atmospheric conditions or partial shading situations. This can result in frequent adjustments and decreased system efficiency [8,9]. Recently, the fuzzy logic maximum power point tracking (FL-MPPT) technique has many applications in PV systems. This technique takes a more heuristic approach and does not require a detailed model of the system [8,9,10]. It is particularly useful when dealing with complex, nonlinear systems, such as the behavior of PV array under varying conditions [8,9].

The most PV water pumping systems use a centrifugal pump driven by DC or AC motor for pumping water [11]. The DC motor is a popular and efficient choice because the DC motor-based system is relatively simple, with fewer components compared to AC motor systems, making it easier to install and maintain [2,6]. In this work, a separately excited DC motor is used to drive a centrifugal pump. The structure of system contains two power conversion stages placed between the PV array and the group moto-pump. The first stage is a DC-DC boost converter; used to extract the MPP from the PV array by using a FL-MPPT technique. The FL-MPPT technique generates the reference voltage corresponding to

MPP. Two control loops are used for this converter. The first loop is an outer voltage control loop, it uses a proportional-integral (PI) controller to regulate the output PV voltage at its reference value generated by FL-MPPT technique and estimate the reference inductor current. The second loop is an inner current control loop; it uses a predictive current controller which forces the inductor current to track its reference with fast dynamic response [12, 13]. The second converter is a DC-DC buck converter; used to drive the DC motor with variable speed according to the produced PV power. The field circuit of the DC motor is connected to the DC-bus and the DC-bus voltage is regulated at a required level to ensure a constant rated magnetic flux. The reference speed is estimated from the control of the DC-bus voltage and the affinity law. The structure of the presented system is simulated by digital simulation under Matlab/Simulink environment. The obtained results show the effeteness of this system for starting, steady-state and dynamic conditions.

The remaining of this paper is organized as follows. The system configuration is presented in Section II. Section III presents the system design. Section IV describes the operating principles of the control system. Section V discusses the obtained simulation results for different operating conditions. Some conclusions are given in the last section.

II. PV WATER PUMPING SYSTEM

The structure of PV water pumping system is presented in Fig.1. It is composed of a PV array, a separately excited DC motor which drives a centrifugal pump and two power converters coupled via a DC bus capacitor; the first is a DC-DC boost converter equipped with an FL-MPPT controller; for the extraction of the MPP. The second is a DC-DC buck converter used to drive the DC motor.

III. SYSTEM DESIGN

A. *Design of PV Array*

From the system shown in Fig. 1, the PV array is selected to feed a 5 HP separately excited DC motor. Due to losses in the conversion structure, the power of PV array at standard conditions (STC) must be greater than the rated power of the DC motor. In this system, a PV array of $P_{mpv} = 6004.29$ W maximum power is selected. It has 3 PV strings connected in parallel and each PV string has 10 identical PV modules connected in series. The specifications of each PV module are presented in table I. The parameters of the used separately excited DC motor are given by the table II.

B. *Design of DC-DC Boost Converter and DC-DC Buck Converter*

The DC-DC boost converter is used to elevate the output voltage V_{pv} , and extract the maximum power of PV array [4]. The output voltage V_{dc} of DC-DC boost converter is regulated at a required level value higher than the nominal voltage $V_a = 240$ V of the armature circuit of the DC motor. The maximum voltage of PV array at STC (solar irradiance 1000 W/m2 and cell temperature 25°C) is $V_{pv} = V_{mpv} = 263$ V and the reference of DC-bus voltage V_{dc}^* can be fixed to 300 V. The buck converter is the inter-link between the DC-DC boost converter and the DC motor; used to supply the armature circuit. The design of the used power converters are presented in table III [14].

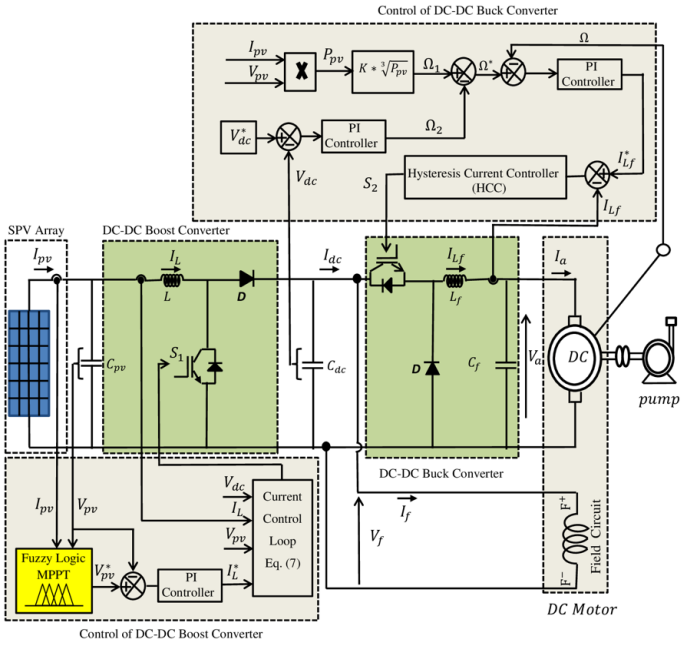


Figure 1. Structure of PV water pumping system

TABLE I. TECHNICAL CHARACTERISTICS OF PV MODULES AT STC

Specifications	Value
maximum power point P_m	200 W
open circuit voltage V_{oc}	32.9 V
short circuit current I_{sc}	8.21 A
maximum power point voltage V_m	26.3 V
maximum power point current I_m	7.61 A

TABLE II. PARAMETERS OF SEPARATELY EXCITED DC MOTOR

Specifications	Value
Rated power P_m	5 HP
Rated speed N	1750 rpm
Rated armature voltage V_a	240 V
Rated armature current I_a	21.17 A
Rated torque T	21.41 $N.m$
Rated voltage of filed-circuit V_f	300 V
Rated current of filed-circuit I_f	1.66 A

TABLE III. DESIGN OF DC-DC BOOST CONVERTER AND DC-DC BUCK CONVERTER

Component	Expression	Data	Used Value
d_1	$d_1 = \frac{V_{dc}^* - V_{mpv}}{V_{dc}^*}$	$V_{dc}^* = 300\ V$ $V_{mpv} = 263\ V$	0.123
L	$I_L = N_p * I_m$ $L = \frac{V_{mpv} * d_1}{\Delta I_L * f_1}$	$N_p = 3$ $I_m = 7.61$ $f_1 = 3000\ HZ$ $\Delta_{I_L} = 5\%\ of\ I_L$	$10\ mH$
C_{dc}	$I_{dc} = P_{mpv}/V_{dc}^*$ $C_{dc} = \frac{I_{dc} * d_1}{f_1 * \Delta V_{dc}}$	$P_{mpv} = 6004{,}29$ $V_{dc}^* = 300$ $\Delta_{V_{dc}} = 1\%\ of\ V_{dc}^*$	$274\ \mu F$
d_2	$d_2 = \frac{V_a}{V_{dc}^*}$	$V_{dc}^* = 300\ V$ $V_a = 240\ V$	0.8
L_f	$L_f = \frac{V_a * (1 - d_2)}{f_2 * \Delta I_{Lf}}$	$I_{Lf} = 21.17A$ $\Delta_{I_{Lf}} = 5\%\ of\ I_{Lf}$ $f_2 = 3000\ HZ$	$16\ mH$
C_f	$C_f = \frac{\Delta I_{Lf}}{8 * f_2 * \Delta V_a}$	$\Delta_{V_a} = 0.1\%\ of\ V_a$	$185\ \mu F$

Where;

d_1, d_2: Duty cycle of DC-DC boost converter and DC-DC buck converter, respectively.

L, L_f: Inductance of DC-DC boost converter and DC-DC buck converter, respectively.

C_{dc}, C_f: DC bus capacitor, filter capacitor, respectively.

$\Delta I_L, \Delta I_{Lf}$: Current ripple across the inductor L and L_f, respectively.

$\Delta V_{dc}, \Delta V_a$: Voltage ripple of DC bus voltage and armature voltage, respectively.

f_1, f_2: Frequency switching of DC-DC boost converter and DC-DC buck converter, respectively.

C. Design of Centrifugal Pump

For the PV water pumping system, the centrifugal pump torque T_r and the motor speed Ω are related as [14];

$$T_r = K_p * \Omega^2 \quad (1)$$

Where, k_p is the proportionality constant, it can be determined from the rated speed and the rated torque of the DC motor as:

$$K_p = \frac{T_r}{\Omega^2} = \frac{21.41}{(2 \times \pi \times 1750/60)^2} = 6.38 * 10^{-4}\ N.m/(rad/s)^2 \quad (2)$$

IV. SYSTEM CONTROL

The PV water pumping system shown in Fig. 1 has two power conversion stages. The purpose of its global control system is to ensure the extraction of the maximum power of the PV array and the control of the DC motor speed.

A. Fuzzy Logic MPPT Control

The Fuzzy logic is a type of control system that imitates human decision-making processes, making it suitable for handling complex and uncertain environments [9]. In the context of MPPT, the fuzzy logic allows to make decisions based on linguistic rules and linguistic variations [8,9]. This technique does not need system model knowledge, and can optimize the system efficiency [8,9], it allows to avoid the problems of the traditional MPPT techniques (P&O, INC). The structure of the FL-MPPT control is represented in the Fig. 2.

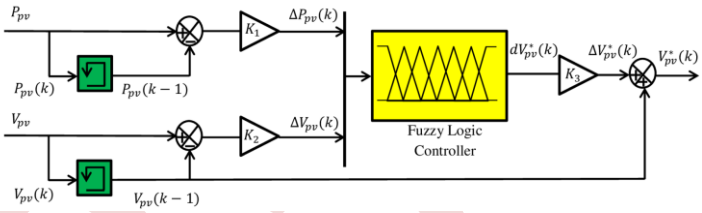


Figure 2. Structure of the fuzzy logic MPPT control

The inputs of FL-MPPT controller are the power error $\Delta P_{pv}(k)$, and the voltage error $\Delta V_{pv}(k)$. The output of this controller is considered as the reference PV voltage $V_{pv}^*(k)$, according to the equation (3) [8].

$$\begin{cases} \Delta P_{pv}(k) = K_1 \cdot \left(P_{pv}(k) - P_{pv}(k-1)\right) \\ \Delta V_{pv}(k) = K_2 \cdot \left(V_{pv}(k) - V_{pv}(k-1)\right) \\ \Delta V_{pv}^*(k) = K_3 \cdot dV_{pv}^*(k) \\ V_{pv}^*(k) = \Delta V_{pv}^*(k) + V_{pv}(k-1) \end{cases} \quad (3)$$

Where; K_1, K_2 and K_3 are the normalization factors and are crucial to the drive's static and dynamic performance [4]. The fuzzy logic controller has seven linguistic variables; these are used to form the fuzzy rules (Table IV). Fig. 3 shows the membership functions of this controller [8].

TABLE IV. TABLE OF SEVEN-CLASS INFERENCE RULE

ΔP_{pv} / ΔV_{pv}	NB	NM	NS	ZE	PS	PM	PB
NB	PB	PB	PM	ZE	NM	PB	NB
NM	PB	PM	PS	ZE	NS	NM	NB
NS	PM	PS	PS	ZE	NS	NS	NM
ZE	NB	NM	NS	ZE	PS	PM	PB
PS	NM	NS	NS	ZE	PS	PS	PM
PM	NB	NM	NS	ZE	PS	PM	PB
PB	NB	NB	NM	ZE	PM	PB	PB

Where;

NB : Negative big, NM: Negative medium, NS: Negative small, ZE: Zero, PS: Positive small, PM: Positive medium, PB: Positive big.

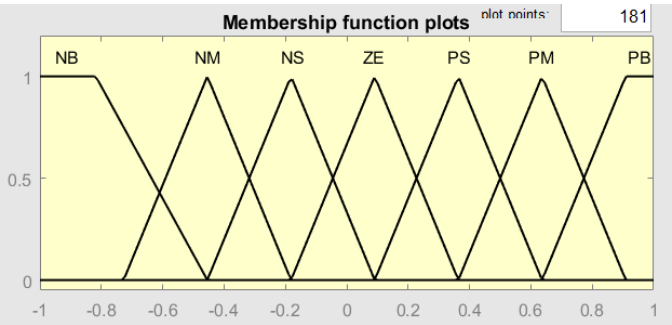


Figure 3. Memberchip functions of $\Delta P_{pv}, \Delta V_{pv}, and\ \Delta V_{pv}^{*}$.

B. DC-DC Boost Converter Control

The control system of DC-DC boost converter shown in Fig.1 uses two control loops. For the first loop (outer loop), a PI controller is used to regulate the output PV voltage at its reference value V_{pv}^{*} generated by FL-MPPT technique. This controller provides the reference inductor current I_L^{*}.

The reference inductor current is estimated as:

$$I_{L(k)}^{*} = I_{L(k-1)}^{*} + K_{ppv}\left(V_{pv-err(k)} - V_{pv-err(k-1)}\right) + K_{ipv} V_{pv-err(k)} \quad (4)$$

Where;

The error of the PV voltage is given by the expression:

$$V_{pv-err(k)} = V_{pv(k)}^{*} - V_{pv(k)} \quad (5)$$

K_{ppv} and K_{ipv} are the proportional and integral gains of the PV output voltage PI controller:

For the second (inner loop), a model predictive control (MPC) is applied to control the inductor current and generate the control signal of DC-DC boost converter. From Fig. 1, the operation of the DC-DC boost converter can be divided into two distinct phases depending on the state S_1 of switch. The first when the switch is closed ON, the inductor current crosses the electronic switch; the second when the switch is open OFF, the inductor current crosses the diode[13].

$$\begin{cases} Switch\ ON : \dfrac{d_{i_L}}{dt} = \dfrac{V_{pv}}{L} \\ Switch\ OFF : \dfrac{d_{i_L}}{dt} = \dfrac{V_{pv} - V_{dc}}{L} \end{cases} \quad (6)$$

The current dynamic equation is discretized for a sampling time T_s by using Euler forward method :

$$I_L(k+1) = I_L(k) + \frac{T_s}{L} \cdot \left(V_{pv}(k) - (1 - S_1) \cdot Vdc(k)\right) \quad (7)$$

Where, S_1 is the switching state of the electronic switch (the switch is open for $S_1 = 0$ or closed for $S_1 = 1$).

The objective of this control is to make the inductor current follow its reference by selecting the best switching states of DC-DC boost determined by evaluating the cost function J. The change in the reference current for one sampling interval can be neglected, so $I_L^{*}(k+1) \cong I_{L(k)}^{*}$. This assumption can cause one sample delay in the reference tracking, which is negligible at high sampling frequencies.

The cost function J is the absolute value of error between the predicted one $I_L(k+1)$ and the reference current $I_{L(k)}^{*}$ as [13]:

$$J = I_{L,S1=0,1}(k+1) - I_{L(k)}^{*} \quad (8)$$

Fig.4 shows the flowchart of predictive current control

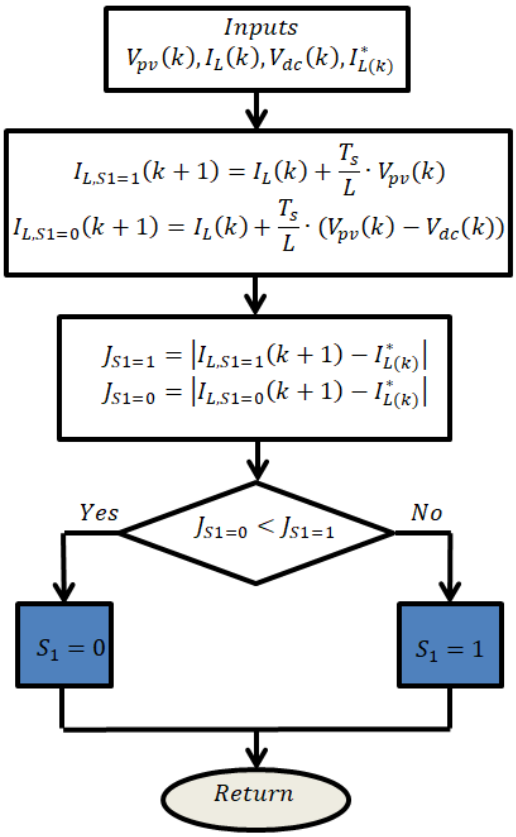


Figure 4. Flowchart of inductor current control loop.

C. DC Motor Control

As shown in Fig. 1, the field circuit is connected to the DC-bus capacitor and the armature circuit is fed by a DC-DC buck converter. According to the centrifugal pump affinity law, the output power of the PV array and speed motor are both affected by variations in the atmospheric conditions [7]. The control system of DC motor is to regulate the DC-bus voltage to a desired value and estimate the motor reference speed. This control makes the magnetic flux of field circuit regulated to its rated value and activates the DC-DC buck converter which

continuously adjusts the armature voltage according to the reference speed.

The reference speed is estimated as[7,15]:

$$\Omega^* = \Omega_1 + \Omega_2 \quad (9)$$

Where, Ω_1 is the first component of the reference speed corresponding to the PV array power, it is expressed as [7,15]:

$$\Omega_1 = K\sqrt[3]{P_{pv}} \quad (10)$$

Where, K is the constant for converting PV power into speed , P_{pv} is the power produced by the PV array.

The PI controller of the DC bus voltage estimates the second component Ω_2 of the reference speed. Ω_2 is given as[7,15]:

$$\Omega_{2(k)} = \Omega_{2(k-1)} + k_{pdc}(V_{dc_{err}(k)} - V_{dc_{err}(k-1)}) + k_{idc}V_{dc_{err}(k)} \quad (11)$$

Where, $V_{dc_{err}}$ is the error of DC bus voltage calculated as:

$$V_{dc_{err}(k)} = V^*_{dc(k)} - V_{dc(k)} \quad (12)$$

K_{pdc} and K_{idc} are the proportional and integral gains of the DC-bus voltage PI controller.

The difference between the reference speed Ω^* and sensed speed Ω is transmitted to the PI controller, which minimizes the error and provides reference inductor current I^*_{Lf} :

$$I^*_{Lf(k)} = I^*_{Lf(k-1)} + K_{p\Omega}(\Omega_{err(k)} - \Omega_{err(k-1)}) + K_{i\Omega}\Omega_{err(k)} \quad (13)$$

Where, Ω_{err} is the speed error calculated as:

$$\Omega_{err(k)} = \Omega^*_{(k)} - \Omega_{(k)} \quad (14)$$

$K_{p\Omega}$ and $K_{i\Omega}$ are the proportional and integral gains of the speed PI controller.

The inductor current I_{Lf} is forced to track its reference I^*_{Lf} by using a hysteresis comparator.

V. SIMULATION RESULTS

The feasibility of the PV water pumping system is examined by digital simulation using Matlab/Simulink environment. The different simulation tests are performed to observe the starting dynamics, the steady state response, and also the reaction of the control system for variations of solar irradiance. The reference value of the DC-bus voltage is fixed to 300 V.

A. Starting and steady state performances

The solar irradiance, the cell temperature, the electrical quantities (voltage, current, power) of PV array, the DC-bus voltage, the motor speed, the electromagnetic torque and the armature current waveforms are shown in Fig.5. It is well observed that the system has a good start dynamics; the available maximum power 6004.29 W is rapidly achieved and tracked by using the FL-MPPT technique. The corresponding maximum current and maximum voltage are $I_{mpv} = 22.83$ A , $V_{mpv} = 263$ V. In steady state, the DC-bus voltage is well regulated to its reference value 300 V, the DC motor drives the centrifugal pump with a rated speed of 1750 rpm. The electromagnetic torque reaches its rated value 21.41 Nm and the consumed armature current is of 21.17 A.

B. Performances of the System for Sudden Change of Solar irradiance

In this test, the PV array is subjected to sudden changes in the solar irradiance (1000W/m², 800W/m², 600W/m², 400W/m²). The temperature is fixed to 25°C. Fig.6 shows the solar irradiance profile, the electrical quantities of PV array, the DC-bus voltage, the motor speed, the electromagnetic torque and the armature current. It can be clearly observed that at the time of the diminution of the solar irradiance, rapid diminutions in output PV current and PV power are provoked, while the output PV power is practically not affected. The produced PV power is practically proportional with the solar irradiance. The DC-bus voltage is maintained closed to its reference value 300 V, which ensures the operation of the DC motor with a constant rated magnetic field. The diminution of the solar irradiance provokes the diminution of the motor speed, the electromagnetic torque and also the armature current.

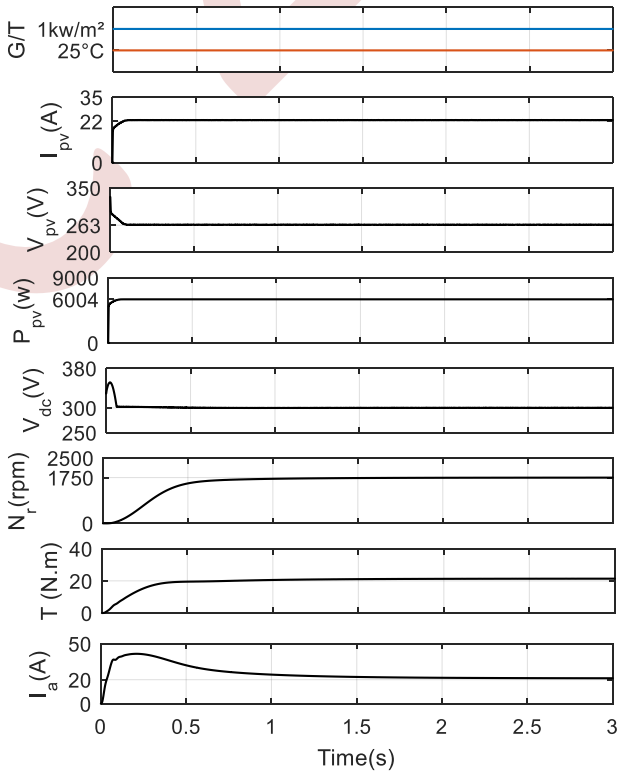


Figure 5. Performances of PV water pumping at starting and steady-state.

VI. CONCLUSION

This paper has presented a standalone PV water pumping system based on separately excited DC motor. The system contains two power conversion stages linked by a DC-bus capacitor. The first is a DC-DC boost converter controlled by

using a FL-MPPT technique; used to extract the available maximum power of the PV array. The second is a DC-DC buck converter; used to supply the armature circuit with a variable voltage and drive the motor with a variable speed according to the produced PV power. The field circuit of the DC motor is connected to the DC-bus and the DC-bus voltage is regulated at a required level to ensure a constant rated magnetic flux. The reference speed is estimated from the control of the DC-bus voltage and the affinity law. The usefulness of the PV water pumping system was fully confirmed by a digital simulation under Matlab/Simulink environment for different operation conditions. The obtained results have demonstrated that the presented system is characterized by good performances for steady-state and transient responses.

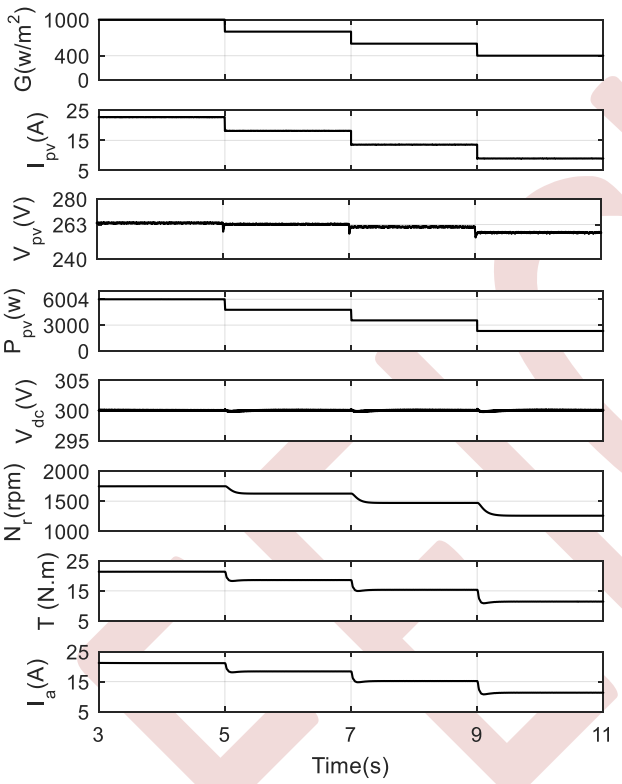


Figure 6. Performances of PV water pumping system for variable solar irradiance and fixed temperature at 25°C

REFERENCES

[1] W. S. dos Santos, P.F. Torres, A. F. Brito, A. R. A. Manito, G. F. Pinto Filho, W. L. Monteiro, and W. N. Macedo, ''A novel method to determine the optimal operating point for centrifugal pumps applied in photovoltaic pumping systems,'' Sol Energy, vol. 221, pp. 46-59, 2021.

[2] M. M. Ahmed, W. S. Hassanien, and M. A. Enany, ''Modeling and evaluation of SC MPPT controllers for PVWPS based on DC motor,'' Energy Rep, vol. 7, pp. 6044-6053, 2021.

[3] S. Bhim, U. Sharma, and S. Kumar, ''Standalone photovoltaic water pumping system using induction motor drive with reduced sensors,'' IEEE Trans. Ind. Appl, vol. 54, pp. 3645-3655, 2018.

[4] M. Errouha, A. Derouich, N. El Ouanjli, and S. Motahhir, ''High-performance standalone photovoltaic water pumping system using induction motor,'' Int. J. Photoenergy, vol. 2020, 2020.

[5] A. Narendra, N.V. Naik, A. K. Panda, and N. Tiwary, ''A comprehensive review of PV driven electrical motors,'' Sol Energy, vol. 195, pp. 278-303, 2020.

[6] R. Kumar and B. Singh, ''Single stage solar PV fed brushless DC motor driven water pump,'' IEEE J. Emerg. Sel. Top. Power Electron, vol. 5, pp. 1377-1385, 2017.

[7] S. Shukla and B. Singh, ''Reduced current sensor based solar PV fed motion sensorless induction motor drive for water pumping,'' IEEE Trans Industr Inform, vol. 15, pp. 3973-3986, 2018.

[8] B. Abdelhak, B. Abdelhalim, and B. Mostéfa, ''Comparative study of P&O-PI and fuzzy-PI MPPT controllers and their optimisation using GA and PSO for photovoltaic water pumping systems, '' Int. J. Ambient Energy, vol. 42, pp. 1746-1757, 2021.

[9] G. Gavril-Ionel, S. L. Andras, and G. Danut-Vasile, ''Benefits of fuzzy logic on MPPT and PI controllers in the chain of photovoltaic control systems,'' Appl. Sci, vol. 12, pp. 2318, 2022.

[10] Y. Unal, K. Ali, and B. Selim, ''PV system fuzzy logic MPPT method and PI control as a charge controller,'' Renew. sustain. energy rev, vol. 81, pp. 994-1001, 2018.

[11] V. C. SONTAKE, and V. R. KALAMKAR, ''Solar photovoltaic water pumping system-A comprehensive review,'' Renew. sustain. energy rev, vol. 59, pp. 1038-1067, 2016.

[12] D. Ahmad, F. Gholamreza, V. Hani, and K. Al-Haddad , ''Model predictive control design for DC-DC converters applied to a photovoltaic system,'' Int. J. Electr. Power Energy Syst, vol. 103, pp. 537-544, 2018.

[13] R. B. A. CUNHA, R. S. INOMOTO, J. A. T. ALTUNA, F.F. Costa, S.G. Di santo, and A.J. Sguarezi Filho, ''Constant switching frequency finite control set model predictive control applied to the boost converter of a photovoltaic system,'' Solar Energy, vol. 189, pp. 57-66, 2019.

[14] M. Dubey, S. K. Sharma, and R. Saxena, ''Cascaded boost buck converter for solar power driven stand-alone PMSM drive,'' Renew. Energy Focus, vol. 35, pp. 32-40, 2020.

[15] Varma, G. H. Kumar, V. R. Barry, and R. K Jain, ''A total-cross-tied-based dynamic photovoltaic array reconfiguration for water pumping system,'' IEEE Access, vol. 10, pp. 4832-4843, 2022.

Artificial intelligence technique to compare between the performance of different technologies of PV Modules in the photovoltaic systems

Hichem Hafdaoui, Nasreddine Belhaouas, El Amin Kouadri Boudjelthia, Houria Assem, Farid Hadjrioua, Nadira Madjoudj

Centre de Développement des Energies Renouvelables, CDER, 16340, Algiers, Algeria

h.hafdaoui@cder.dz – hichemhafdaoui@gmail.com

***Abstract*— In this paper we applied artificial intelligence technique (SVM Classifier) to compare between the performance of two different technology of PV modules (class to class and backsheet to glass) after five (05) months of operation in Algeria under the same weather conditions (moderate and humid climate) .Where we have a database for the outdoor monitoring of these two PV modules, consisting of data (Isc, Voc, Pmax, Imp, Vmp, Tm, T amb, G, WD, WS, Date, Time, FF) which are variables data, where the SVM creates the groups or class according to the conditions that we entered, after which it produces heatmaps that help us in reading the results and making the decision easily, unlike the classic methods which are very difficult . This method is applicable for comparison between several solar panels or several photovoltaic PV plats. It is enough just to give the database.**

I. INTRODUCTION

Solar energy is sustainable energy as it is renewable, meaning that it is energy that does not run out. It is a natural energy source and can be used to generate other forms of energy. Solar panels do not cause any noise when they convert sunlight into usable electrical energy Solar power plants and solar panels in Homes do not emit any emissions and do not cause any harmful impact on the environment.

The statistics worldwide for the capacity of PV has increased from almost zero GW in 1990 to 505 GW in 2018 [1-2] and a 102.4 GW growth in PV installation has been observed globally in 2018 alone [1,3]. Be alerted in the event of a malfunction, supervise your photovoltaic installation: it is essential to monitor solar production. Monitoring now offers many possibilities, from simple production measurement to home automation. Some manufacturers even offer support in addition to the monitoring tool: customer service, technical interventions, and additional tools to help solar professionals [4]. A. Arechkik et Al [5] Long-term performance and degradation analysis, as well as an economic investigation of three based-silicon PV technologies including amorphous silicon (a-Si), polycrystalline silicon (p-Si), and monocrystalline silicon (m-Si), The authors of [6] was includes a discussion of different MPPT techniques and performs comparison for the performance of the two MPPT techniques, the P&O algorithm, and salp swarm optimization (SSO) algorithm, in Ref [7] contains the experimental investigations of different cooling methods used for photovoltaic (PV) panels. Phase change material (PCM), thermoelectric (TE) and aluminum fins were chosen as the cooling methods, even in Ref [8] presented a deep learning-based defect detection of PV modules using electroluminescence images through addressing two technical challenges: (1) providing a large number of high-quality Electroluminescence (EL) image generation method for the limit of EL image samples; and (2) an efficient model for automatic defect classification with the generated EL image. In this work we applied Machine learning for compare between the performance of two deferent technology of PV modules (glass glass PV module and backsheet glass PV module) after five (05) months of operation in Algeria under the same weather conditions (moderate and humid climate), Table 1 Shows electrical characteristics of the two photovoltaic module.

II. MACHINE LEARNING

Machine Learning can be defined as an artificial intelligence technology allowing machines to learn without having previously been programmed specifically for this purpose. Machine Learning is explicitly linked to Big Data, since to learn and develop, computers need streams of data to

analyze and train on. In machine learning, classifying data for predictive modeling problem where a class label is predicted for a given example of input algorithms according to the dataset.

Support Vector Machine (SVM) is a linear model for classification and regression problems. It can resolve linear and non-linear problems and work well for another problem. The algorithm creates a line or a hyper-plane, which separates the data into classes. Which is simple principal of SVM.

Furthermore, the SVMs are a family of machine learning algorithms that solve problems of classification, regression or anomaly detection. They are known for their solid theoretical guarantees, their great flexibility and their ease of use even without great knowledge of data mining [9-11].

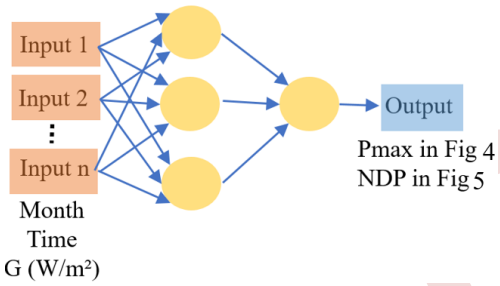


Figure 1. Architecture of SVM classifier (Neuron model)

III. METHOD OF MEASUREMENT AND DATA PROCESSING

Outdoor Data Acquisition System provides wide range of measurement conditions. Measured data contain parameters provided by different measurement units and stored. Moreover, the parameters measure is imported into common database for preparing further analysis by transformation into data structures appropriate for fast queries.

The PV modules are installed at annex of renewable energy development center CDER, Ben Aknoun City, Algeria (Latitude 36◦44'44,94''N, Longitude 3◦00'46,80 E and Altitude 236 m).

The several measurements in our laboratory was investigated based on data acquisition (Keysight 34972 A). Moreover, the system collects the measurements from the various sensors (Namely Isc, Voc, Pmax, Imp, Vmp, Tm, T amb, G, WD, WS, Date, Time, FF).



Figure 2. Data acquisition (Keysight 34972A).

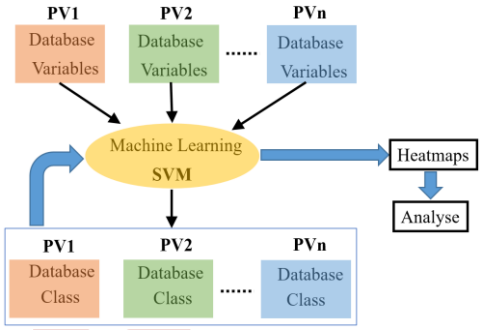


Figure 3. Diagram of method.

IV. RESULTS AND DESCUTION

In this paper, we present the compared and Machine Learning based on monitoring data of two (02) PV module of during 05 months with step of measurement of 5 min. The parameters measured in our system were the I–V curves of PV module with electrical parameters (Pmax, Isc, Voc, Imp, Vmp, FF), the temperature was measured on back side of module and weather parameters (solar irradiation on the inclined plane, ambient temperature and direction and speed of wind).

Figure 4 show the maximal power of those PV modules provided in hours and months. Figure 4 shows the evolution of the average monthly power over a day. Photovoltaic production is significant between 12H00 and 13H00. Local time is around 68% nominal power during the month of February of PV1 and 64% nominal power during the month of February of PV2. This values decreases in autumn because of the more frequent presence of clouds and the lower height of the sun. This figure also shows the monthly evolution of sunshine duration.

Figure 5 shows the daily point's numbers of measurement obtained at irradiation and specific time.

This technique allows us to identify areas of interest for performance analysis and areas that represent non-core values or isolated phenomena. Eliminating these values represents a challenge in analyzing the performance of PV systems [12,13].

Indeed, we notice the squares in dark yellow correspond to the curve of the solar irradiation of a clear sky; while the measurement points inside this bell correspond mainly to the measurements under cloudy conditions. On the other hand, very high values above 1150 W/m^2 may correspond to reflection phenomena. This presentation allows us to delimit the study area and thus reduce the values that can induce errors in the calculation of the various parameters.

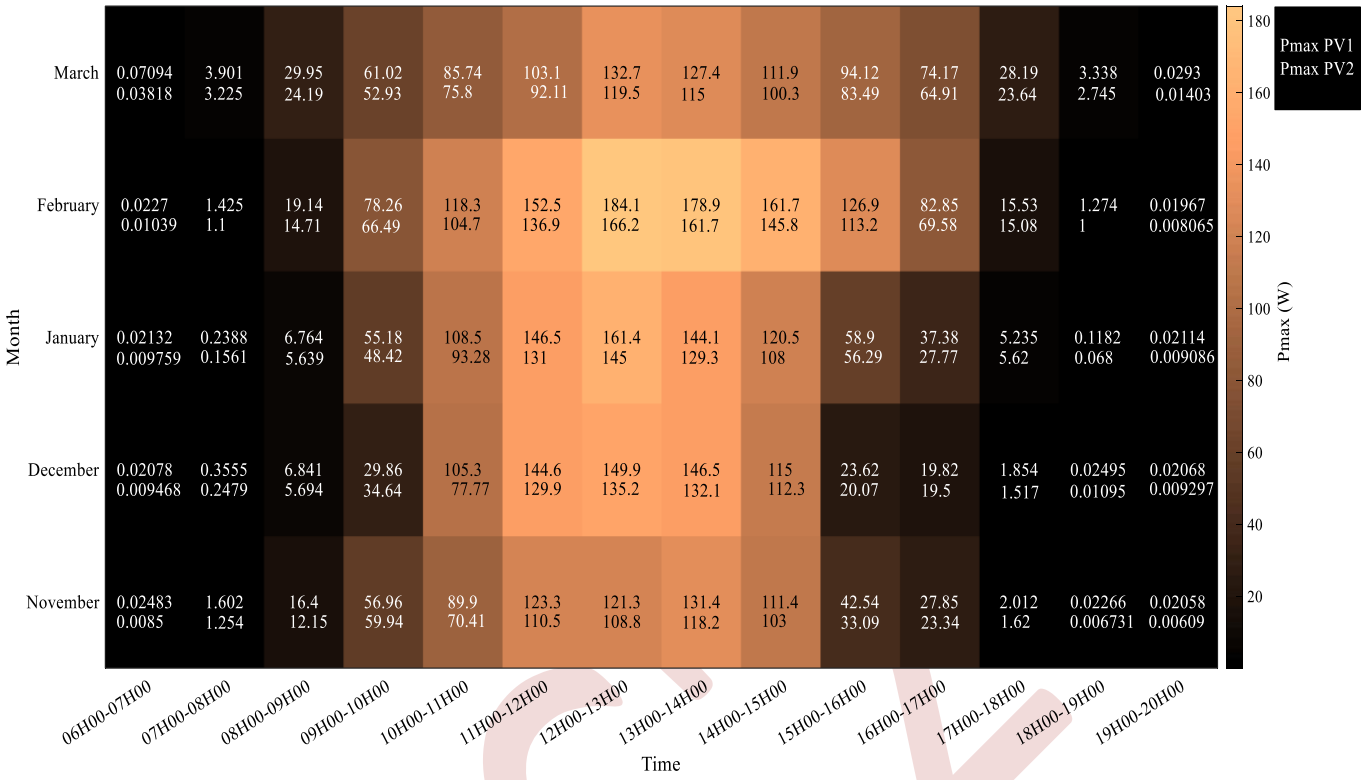


Figure 4. Maximum power supplied over a day in five (05) months.

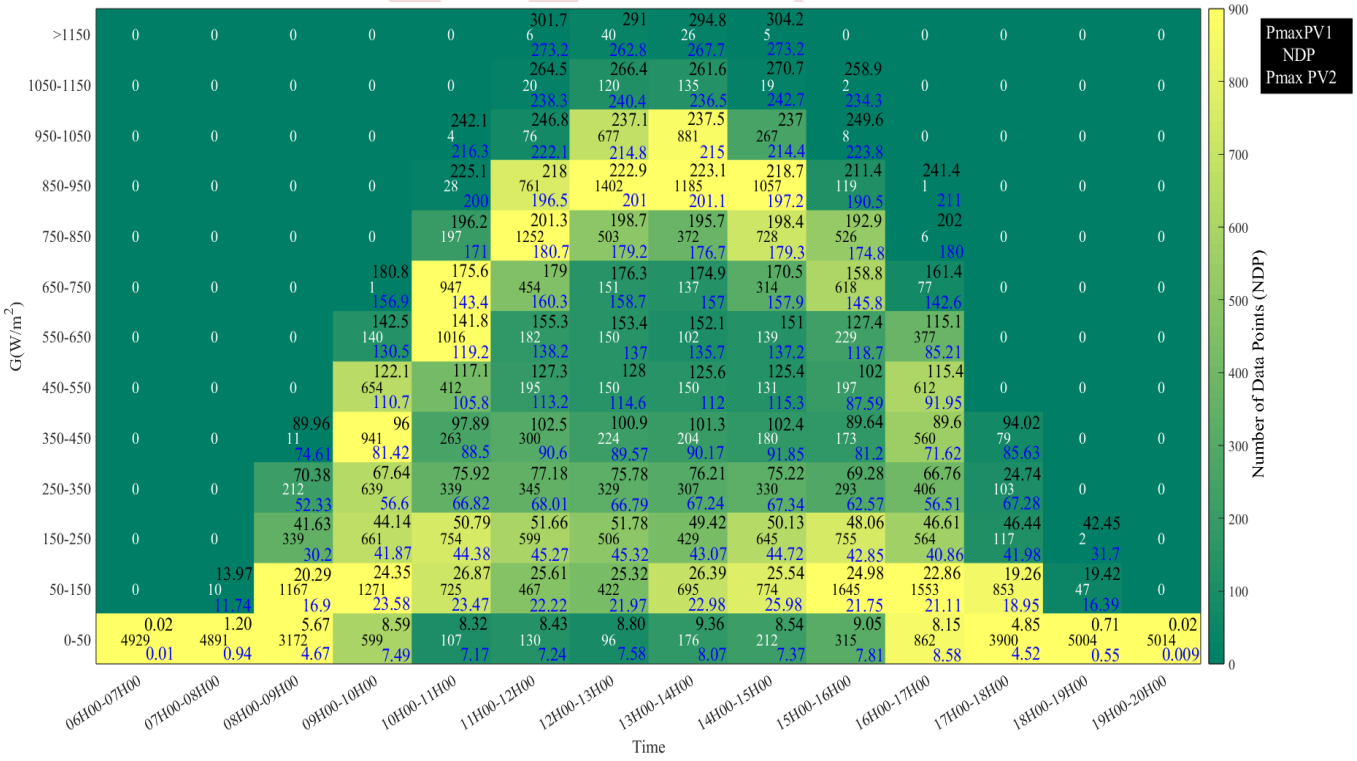


Figure 5. Number of Data points according to G (W/m^2) and Time in Five (05) months

PV 1		PV2	
Pmax	275W	Pmax	260W
Isc	9,38A	Isc	8,6A
Voc	38,5V	Voc	38
Imp	8,76A	Imp	8,1A
Vmp	31,4V	Vmp	31V

TABLE 1. ELECTRICAL CHARACTERISTICS OF THE TWO PHOTOVOLTAIC MODULE

V. CONCLUSION

This study shows the importance of machine learning and artificial intelligence in the processing of databases for monitoring photovoltaic systems. and comparison between the performance of PV power plat.

The complexity of the phenomena that influence the performance of photovoltaic systems is tamed by the targeting of common operating conditions, which constitute the dominant trends, and the isolation of marginal phenomenon.

The classification method used in this research work, allows having an overview on the behavior of photovoltaic systems, and can be used in the comparison of the different photovoltaic technologies or for an optimized sizing.

ACKNOWLEDGMENT

The authors acknowledge the support received by the Centre de Development des Energies Renouvelables through funding from the Ministry of higher education and scientific research.

REFERENCES

[1] Tara Doyle, Ryan Desharnais, Tristan Erion-Lorico, 2019 PV Module Reliability Scorecard, PVEL, 2019.

[2] Sebastijan Seme, Klemen Sredenšek, Bojan Štumberger, Miralem Hadžiselimović, Analysis of the performance of photovoltaic systems in Slovenia, Sol. Energy 180 (2019) 550–558.

[3] David A. Quansah, Muyiwa S. Adaramol, Assessment of early degradation and performance loss in five collocated solar photovoltaic module technologies installed in ghana using performance ratio time-series regression, Renew. Energy 131 (2019) 900–910.

[4] Nallapaneni Manoj Kumar, Maria Malvoni, Nikos Hatziargyriou, Shauhrat S. Chopra, Data related to crystalline photovoltaic plant performance in the semi-arid climate of India, Data Brief 31 (2020) 105696.

[5] AMEUR, Arechkik, BERRADA, Asmae, BOUAICHI, Abdellatif, et al. Long-term performance and degradation analysis of different PV modules under temperate climate. Renewable Energy, 2022, vol. 188, p. 37-51.

[6] ALI, Mohamed Hussein Mohamedy, MOHAMED, Mahmoud Mohammed Sayed, AHMED, Ninet Mohamed, et al. Comparison between P&O and SSO techniques based MPPT algorithm for photovoltaic systems. Int. J. Electr. Comput. Eng, 2022, vol. 12, no 1, p. 32-40.

[7] BAYRAK, Fatih, OZTOP, Hakan F., et SELIMEFENDIGIL, Fatih. Experimental study for the application of different cooling techniques in photovoltaic (PV) panels. Energy Conversion and Management, 2020, vol. 212, p. 112789.

[8] TANG, Wuqin, YANG, Qiang, XIONG, Kuixiang, et al. Deep learning based automatic defect identification of photovoltaic module using electroluminescence images. Solar Energy, 2020, vol. 201, p. 453-460.

[9] Ruben Ruiz-Gonzalez, Jaime Gomez-Gil, Francisco Javier Gomez-Gil, et al., An SVM-based classifier for estimating the state of various rotating components in agro-industrial machinery with a vibration signal acquired from a single point on the machine chassis, Sensors 14 (11) (2014) 20713–20735.

[10] Nahla Farid, Bassant Elbagoury, Mohamed Roushdy, et al., A comparative analysis for support vector machines for stroke patients, Rec. Adv. Inf. Sci. (2013) 71–76.

[11] HAFDAOUI, Hichem, KOUADRI BOUDJELTHIA, El Amin, CHAHTOU, Amina, BOUCHAKOUR, Salim, et al. Analyzing the performance of photovoltaic systems using support vector machine classifier. Sustainable Energy, Grids and Networks, 2022, vol. 29, p. 100592.

[12] S. Daliento, A. Chouder, P. Guerriero, A. Massi Pavan, A. Mellit, R. Moeini, P. Tricoli, Monitoring, diagnosis, and power forecasting for photovoltaic fields: A review, Int. J. Photoenergy 2017 (2017).

[13] Bert Herteleer, Bart Huyck, Francky Catthoor, Johan Driesen, Jan Cappelle, Normalised efficiency of photovoltaic systems: Going beyond the performance ratio, Sol. Energy 157 (2017) 408–418.

Wind energy conversion system based on Dual Stator Windings Permanent Magnet Synchronous Generator fed by Multilevel converter

Yazid Madi [1], Abdelhakim Dendouga [2], Djamal Aouzellag[3]
[1,3] *LMER - Laboratory, University of Bejaia 06000- Bejaia-Algérie*
E-mail : yazid.madi@univ-bejaia.dz, djamal.aouzellag@univ-bejaia.dz
[2] *I3CUB-Laboratory, University of Biskra-Biskra,-Algérie*
E-mail : hakimdendouga@yahoo.fr

Abstract— **A back-to-back power converter interface for a dual stator windings permanent magnet synchronous generator (DSWPMSG) based wind energy conversion systems is presented in this paper. The converter stage is capable to step-up the low-voltage side of standard (DSWPMSG) used in today's WECS to a medium-voltage grid side. The proposed converter is an hybrid back-to-back topology composed of two parallel connected three-phase voltage source converters (VPC) at the generator side, and a 3-level neutral point clamped converter (3-level NPC) at the grid side. The direct power control (DPC) strategy applied to the three-phase grid connected (3-level NPC) is proposed to estimate the active and reactive powers injected into the grid. The use of a multilevel converter at medium voltage at the grid side has several advantages like improved power quality; it can eliminate the low-order harmonics in the output waveform without increasing the high-order harmonics. Therefore, the harmonic fluctuation of the inverter output voltage is reduced, and the waveform level is high. The feasibility of the proposed configuration is verified by the MATLAB/Simulink.**

Keywords: **DSWPMSG, 3-level NPC, wind turbine. DPC.**

I. INTRODUCTION

Currently, renewable energies have become a crucial interest for the sustainable development of nations without having an impact on the natural resources of the countries.
Renewable energies, especially wind energy, are important energy sources because they are clean, abundance and widespread [1]. Undoubtedly, supplying the electrical grid with a continuous, smooth and balanced power, which is not affected by faults and disturbances, is one of the main objectives of the Wind Energy Conversion Systems (WECS).

Therefore, by 2030 it is foreseen to supply more than 20% of global electricity consumption through the wind [2].

Research on multi-phase machines has become largely important in the last few decades. Multi-phase PMSM are being used for high power electric drive applications like electric vehicles (EVs) [3], more electric aircrafts (MEAs), ship propulsion etc.

The multi-phase direct-driven permanent magnet synchronous generator (PMSG) is getting more application in the wind generators recently for its convenient maintenance without gearbox. In addition, multi-phase PMSG has high reliability, high power density, efficiency and good performance in fault tolerance [4 6].

Variable speed wind energy conversion system (WECS) shown in Figure. 1 consists of a wind turbine driving connected to the grid through a full scale back to back converter. Two three-phase, two-level converters are connected across generator side, and grid side consists of a single three-phase (3-level NPC). Both converters share a common DC-link in between. All the converters are IGBT based and voltage source operated. At the grid side, medium-voltage operation through a multilevel converter has a series of advantages: improved power quality (better grid code compliance), higher efficiency (lower switching frequency), lower step-up voltage requirement and lower currents for the same power level (reduction in cable and filter size). [7] Accordingly, the wind energy industry is looking for medium-voltage topologies for the newly developed multimegawatt WECS. In this paper, FOC control and DPC control in order to ensure the robustness of the wind system to be controlled while ensuring simplicity of adjustment and implementation.

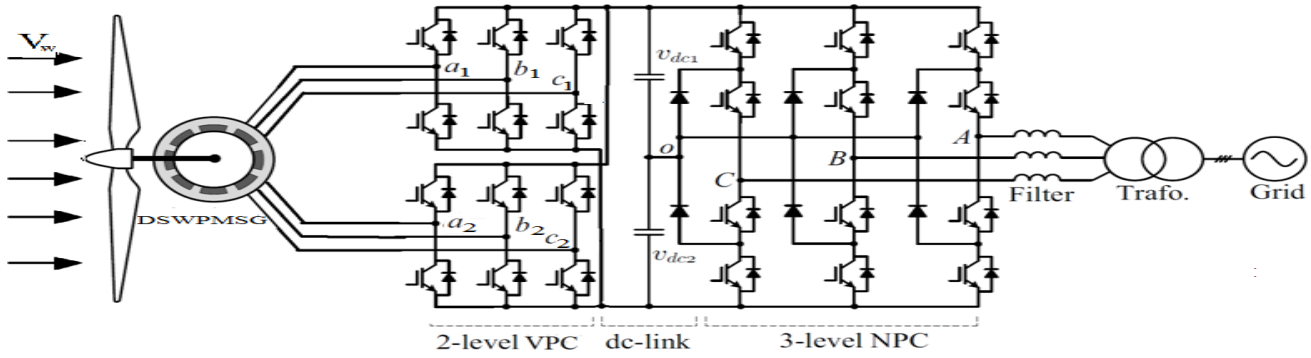


Figure. 1 Grid-connected WECS configuration of DSWPMSG

II. MODELING OF THE WIND ENERGY CONVERSION SYSTEM

A. Wind turbine optimization

Maximum power can be extracted at different wind speeds by operating the generator at an optimum speed. This can be achieved by adjusting the power co-efficient (C_p) depending on the aerodynamic conditions. Different MPPT methods can be found for variable speed WECS, among those one method is based on power speed curve of the wind turbine. In this method, maximum power, which can be obtained at different wind speeds for the particular wind turbine is calculated and a curve is plotted with respect to the speed of wind turbine. A locus of point can be tracked for different wind speeds, and a differential equation is obtained for a particular turbine. In real time, the wind speed is measured by using a wind speed sensor or an anemometer. According to plotted MPPT profile, the speed reference $\omega_m^*$is generated and provided to generator control system, which compares the speed reference with the speed measured from generator $\omega_m$to produce control signals for the power converters to achieve maximum power operation.

The relationship between the wind speed and power captured by turbine blade to convert into mechanical energy can be described as follows [8],

$$P_M = \frac{1}{2}\pi\rho R^2 V_w^3 C_p(\lambda,\beta) \quad (1)$$

where P_M is the mechanical power extracted by turbine blades, R is the radius of wind turbine, ρ is the air density, $V_w$is the velocity of wind and Cp is the power coefficient of blade and is a function of tip speed ratio λ and blade pitch angle β. C_p can be approximated by using,

$$C_p(\lambda,\beta) = C_1\left[\frac{C_2}{\lambda_i} - (C_3 + C_4)\beta - C_5\right]e^{\frac{C_6}{\lambda_i}} \quad (2)$$

With

$$\frac{1}{\lambda_i} = \frac{1}{\lambda + 0.08\beta} - \frac{0.0365}{\beta^3 + 1} \quad (3)$$

$C_1 - C_6$ values are chosen from blade element momentum [9]. Tip speed ratio λ can be defined as,

$$\lambda = \frac{\omega_t R}{V_w} \quad (4)$$

$$T_m = \frac{P_m}{\omega_m} \quad (5)$$

Figure. 2 shows that the wind turbine control strategy is divided, according to wind speed, into four regions. Region 1, the standstill region, the output of mechanical power is approximately zero. Region 2, the MPPT region, the wind turbine operates to extract optimum power during wind speed variation. Region 3, the pitched operating region, the output power from a wind turbine should be limited at rated output power using pitch control. The wind turbine must be stopped to avoid damage at high wind speed in Region 4 [10].

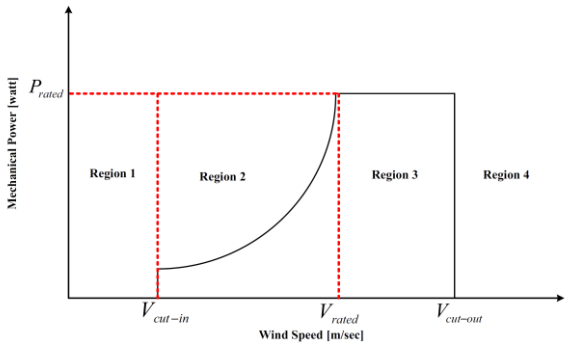


Figure. 2 Turbine operating regions.

B. DSWPMSG dynamic model

The DSWPMSG has two identical stator windings which are assumed balanced star connected. Commonly, the two sets of winding can have a phase shift 0, 30 and 60 degrees. The two sets winding are designed to the same which will have the identical parameters such as resistance and inductance Figure

3. Because of the decoupling of the magnetic circuit of the two sets windings, the mutual inductance between them can be ignored [11,12] .

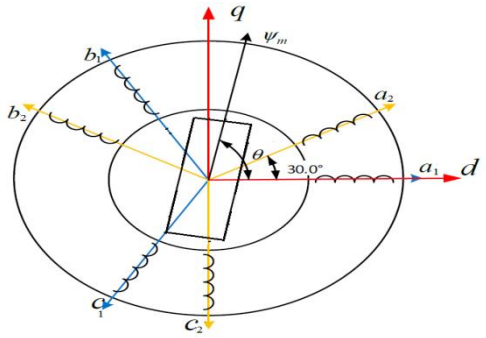


Figure 3. Winding configuration of DSWPMSG

The mathematic model of the dual stator windings PMSG can be deduced based on a reference coordinate system rotating synchronously with the magnet flux oriented as d axis. The voltage equations can be represented as,

$$\begin{cases} V_{d1} = R_S I_{d1} + L_d \frac{dI_{d1}}{dt} - \omega_s L_q I_{q1} \\ V_{q1} = R_S I_{q1} + L_q \frac{dI_{q1}}{dt} + \omega_s L_d I_{d1} + \omega_s \psi_m \\ V_{d2} = R_S I_{d2} + L_d \frac{dI_{d2}}{dt} - \omega_s L_q I_{q2} \\ V_{q2} = R_S I_{q2} + L_q \frac{dI_{q2}}{dt} + \omega_s L_d I_{d2} + \omega_s \psi_m \end{cases} \quad (6)$$

where V_{d1}, V_{d2}, V_{q1}, V_{q2}, I_{d1}, I_{d2}, I_{q1} and I_{q2} are the voltages and currents in d and q axis of two sets winding respectively, R_S is the phase resistance of the two sets winding, L_d and L_q are the inductance components in the d and q axis, ψ_m is rotor flux linkage produced by permanent magnet, ω_s is the rotor electrical angular frequency.

The electromagnetic torque T_e can be written as,

$$T_e = \frac{3P}{2}(\psi_m(I_{q1} + I_{q2}) + (L_d - L_q)(I_{d1}I_{q1} + I_{d2}I_{q2})) \quad (7)$$

Where P is pole pair of the DSWPMSG.

C. Vector Control

Vector control decouples field flux and armature flux so that they can be controlled separately to control torque or current and power or speed independently. The current control forms an inner loop while seep control forms the outer control for the case considered. The vector control is applied in the synchronous rotating frame so as to use simple PI regulators.

The vector space decomposition approach of vector control has been used to control dual three phase induction machines [13]. Though using single current controller makes the design easier and need less number of PI regulators, it can not observe the current imbalance. Therefore, to do away with this problem, dual current controller is preferred. The control schematics of the proposed system is shown in Figure. 4

The vector control of $I_d = 0$ and the current coordinate control between two sets stator windings are adopted for the torque control of DSWPMSG [14]. For surface-mounted DSWPMSG of which the d and q axis inductance are equal, $L_d = L_q$, the electromagnetic torque T_e represented as,

$$T_e = \frac{3P}{2}\psi_m(I_{q1} + I_{q2}) \quad (8)$$

The overall control equations for the current control loop resulting in the required terminal voltage are expressed as:

$$\begin{cases} V^*_{d1} = (k_{pii} - \frac{k_{ii}}{s})(I^*_{d1} - I_{d1}) - \omega_s L_q I_{q1} \\ V^*_{q1} = (k_{pii} - \frac{k_{ii}}{s})(I^*_{q1} - I_{q1}) + \omega_s L_d I_{d1} + \omega_s \psi_m \\ V^*_{d2} = (k_{pii} - \frac{k_{ii}}{s})(I^*_{d2} - I_{d2}) - \omega_s L_q I_{q2} \\ V^*_{q2} = (k_{pii} - \frac{k_{ii}}{s})(I^*_{q2} - I_{q2}) + \omega_s L_d I_{d2} + \omega_s \psi_m \end{cases} \quad (9)$$

The outer speed control loop is designed to run the DSWPMSG at the desired angular speed ω_m.

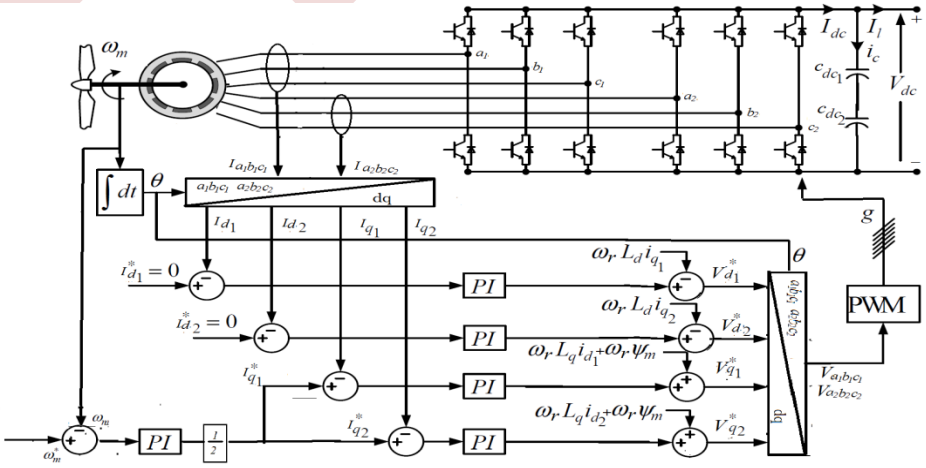


Figure. 4 Speed and current control loop for DSWPMSG

$$I_q{}^* = \left(k_{pOi} - \frac{k_{Oi}}{s}\right)(\omega_m{}^* - \omega_m) \quad (10)$$

Where k_{pii}, k_{pOi}, $k_{ii}$and k_{Oi} are the proportional and integral gain of outer current loop control and outer speed control loop of DSWPMSG, respectively.

III. MODELING AND CONTROL OF GRIDE

Modeling of grid side system consists of a three-level converter NPC , inductive filter, voltage source as grid and a dc link. A simplified model is shown in Figure. 5.

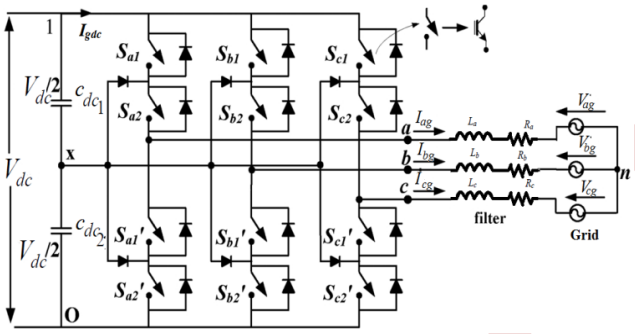


Figure. 5 Simplified model of the converter, filter and grid

A. Model of three-level NPC Converter

Multilevel converters can be availed to achieve higher voltage levels in order to improve the performance and quality of output power and voltage. Three-level neutral point clamped converter (3-level NPC) consists of twelve IGBT switches and six independent diodes. All the IGBT switches are connected with anti-parallel diodes for bidirectional operation. Output voltage waveforms (v_{a0}, v_{b0}, v_{c0}) generated by NPC converter comprises of three switching levels of amplitude V_{dc}/2 (0, V_{dc}/2, V_{dc}). The output phase voltage of the converter with respect to point 'O' can be express as follows [15].

$$v_{a0} = S_{a1}V_{c1} + S_{a2}V_{c2} \quad (11)$$

$$v_{b0} = S_{b1}V_{c1} + S_{b2}V_{c2} \quad (12)$$

$$v_{c0} = S_{c1}V_{c1} + S_{c2}V_{c2} \quad (13)$$

$V_{dc1}$and V_{dc2} are the voltages across capacitor C_1 and C_2 respectively Output AC voltages can be realized by combining equations (11)-(13) as,

$$v_{an} = \frac{V_{dc1}}{3}(2S_{a1} - S_{b1} - S_{c1}) + \frac{V_{dc2}}{3}(2S_{a2} - S_{b2} - S_{c2}) \quad (14)$$

$$v_{bn} = \frac{V_{dc1}}{3}(2S_{b1} - S_{a1} - S_{c1}) + \frac{V_{dc2}}{3}(2S_{b2} - S_{a2} - S_{c2}) \quad (15)$$

$$v_{cn} = \frac{V_{dc1}}{3}(2S_{c1} - S_{a1} - S_{b1}) + \frac{V_{dc2}}{3}(2S_{c2} - S_{a2} - S_{b2}) \quad (16)$$

B. Direct power control of 3-level NPC

The DPC is based on the direct torque control (DTC) concept in electrical machines. The intention for DPC is to control the instantaneous of active and reactive power control loops [16] as the same direction for DTC in controlling the torque and flux of induction machines. In this paper the new switching look-up table based on the differentiation of instantaneous active and reactive powers method is applied [17]. The instantaneous input active and reactive power of the 3-level NPC in a stationary $\alpha\beta$-reference frame can be express as follows.

$$\begin{cases} P_{inst} = \frac{3}{2}(V_\alpha I_\alpha + V_\beta I_\beta) \\ Q_{inst} = \frac{3}{2}(V_\beta I_\alpha - V_\alpha I_\beta) \end{cases} \quad (17)$$

One of the 3-level NPC inverter's main tasks is to balance the upper and lower capacitor voltages. The imbalance of upper and lower capacitor voltages (V_{c1} and V_{c2}) may occur due to the application of short amplitude of voltage vectors. Each of the short amplitude of the voltage vector (inner hexagon) consists of double switching states as shown in Figure. 6. The switching states are divided into *P*-type and the other is *N*-type. Both types of switching states have different effects on the capacitor voltage. The application of the *P*-type switching state will decrease the lower capacitor, V_{dc2} while the *N*-type will increase the upper capacitor voltage, V_{dc1}. The problem of capacitor voltage imbalance is necessary to be addressed for preventing a short circuit that produces system instability, high switching loss, and high dv/dt [18]. Hence, to ensure satisfactory performance and reliability of 3-level NPC, voltages across the two dc-link capacitors must be kept balanced.

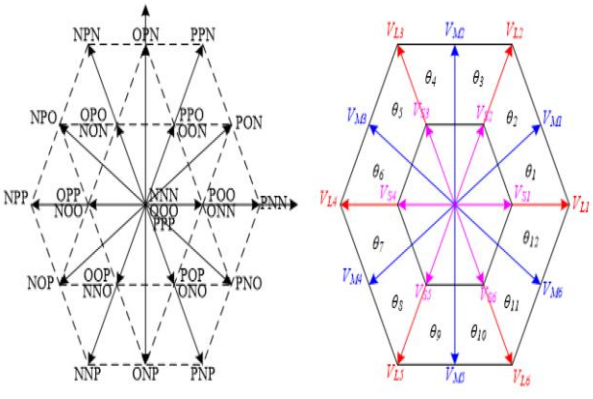


Figure 6. Space voltage vector of the 3-level NPC

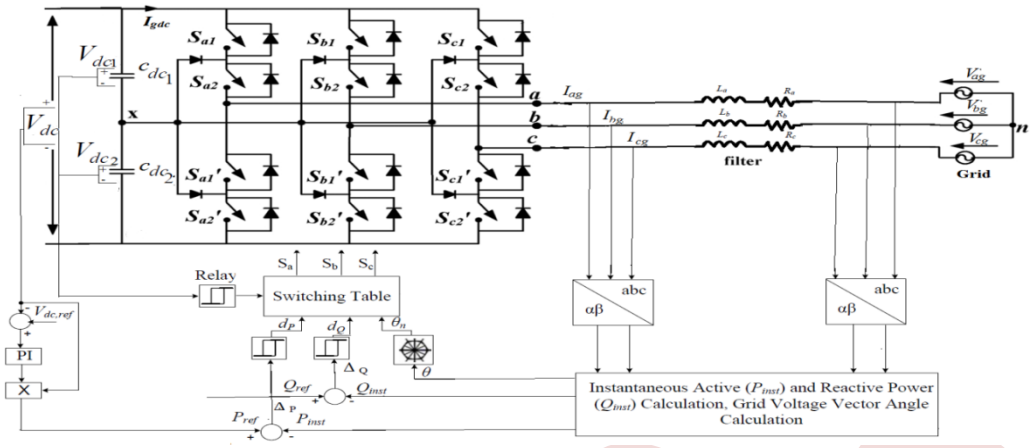


Figure7. Block diagram of the DPC strategy for 3level NPC connected to grid

Table 1. Switching table for 3-level-NPC

Power error status			Sector position (θ_n) and converter voltage vector (V_n)											
d_P	d_Q	B_S	θ_1	θ_2	θ_3	θ_4	θ_5	θ_6	θ_7	θ_8	θ_9	θ_{10}	θ_{11}	θ_{12}
0	0	-	V_{L_1}	V_{M_1}	V_{L_2}	V_{M_2}	V_{L_3}	V_{M_3}	V_{L_4}	V_{M_4}	V_{L_5}	V_{M_5}	V_{L_6}	V_{M_6}
0	1	-	V_{M_1}	V_{L_2}	V_{M_2}	V_{L_3}	V_{M_3}	V_{L_4}	V_{M_4}	V_{L_5}	V_{M_5}	V_{L_6}	V_{M_6}	V_{L_1}
1	0		V_{S_5}	V_{S_5}	V_{S_6}	V_{S_6}	V_{S_1}	V_{S_1}	V_{S_2}	V_{S_2}	V_{S_3}	V_{S_3}	V_{S_4}	V_{S_4}
		1	OOP	OOP	POP	POP	POO	POO	PPO	PPO	OPO	OPO	OPP	OPP
		0	NNO	NNO	ONO	ONO	ONN	ONN	OON	OON	NON	NON	NNO	NNO
1	1		V_{S_4}	V_{S_4}	V_{S_5}	V_{S_5}	V_{S_6}	V_{S_6}	V_{S_1}	V_{S_1}	V_{S_2}	V_{S_2}	V_{S_3}	V_{S_3}
		1	OPP	OPP	OOP	OOP	POP	POP	POO	POO	PPO	PPO	OPO	OPO
		0	NNO	NNO	NNO	NNO	ONO	ONO	ONN	ONN	OON	OON	NON	NON

* B_S = Balancing status

Table 1 presents the new switching table for the three-level NPC converter which is developed by analyzing the effect of each four group voltage vector on the changes in active and reactive powers.

The three-phase supply voltage and current are measured to estimate the instantaneous active P_{inst} and reactive powers Q_{inst}. Meanwhile, the reference active power P_{ref} is produced by multiplying the dc-link output voltage V_{dc} with the output from the *PI* controller while the reference reactive power Q_{ref} is set to zero in order to demonstrate a unity power factor operation. Subsequently, the command active power P_{ref} and reactive power Q_{ref} value are subtracted with calculated active and reactive power to produce the instantaneous active power error and reactive power error denoted by ΔP and ΔQ respectively. The error signals are processed by two hysteresis controllers to produce the power error status signals shown by d_P and d_Q in Figure 7.

IV. Simulation Results And Discussion

The simulation system, which is designed to verify the availability of the proposed WECS and control scheme, is investigated based on the Matlab/Simulink. The electrical parameters for the proposed system are listed in Table 2.

Table 2 Parameters of the proposed system

Parameter		Unit
Rated Power	2	MW
Number of pole pairs, P	48	-
d axis inductance, L_d	2.54e-4	mH
q axis inductance, L_q	2.54e-4	mH
Stator phase winding resistance, R_s	3.52e-3	Ohm
DC bus voltage(V)	2000	V
C_{dc1} , C_{dc1}	400e-4	F

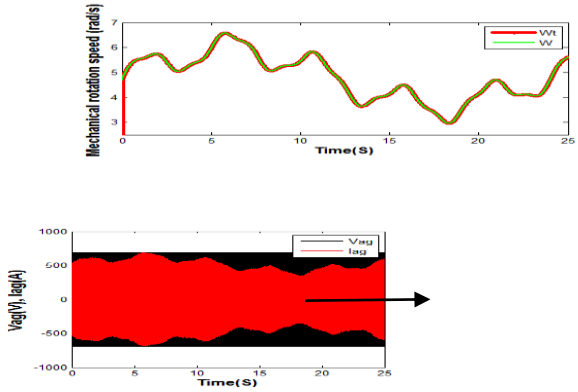
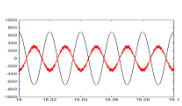


Figure 8. Simulated waveforms of generator speed for change in wind speed



(a)

(c)

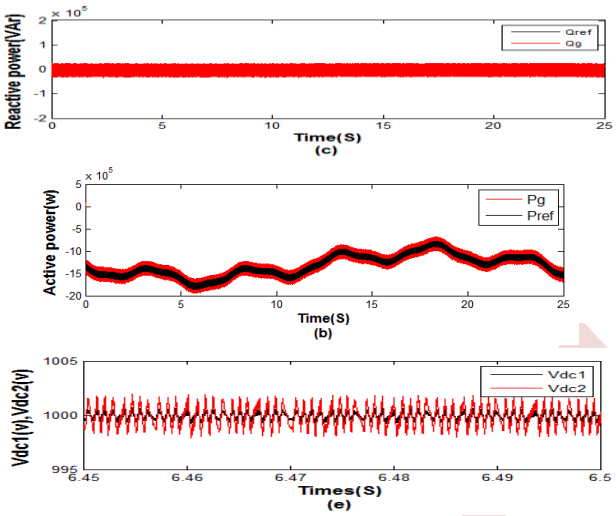


Figure 9 Simulation results of the DPC control algorithm.

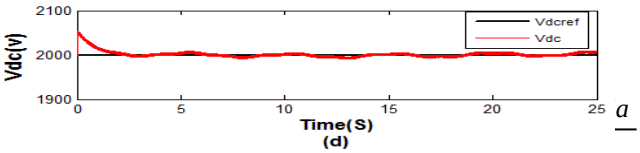
Figure 8. shows the generator speed control for variation in wind speeds by using vector control, reference speed for generator control at different wind speeds is obtained from MPPT.

Figure 9.a shows the grid voltage V_{ag} and phase current I_{ag} injected to the grid, A phase shift is observed almost zero resulting in a power factor unitary. The evolution of the instantaneous active power represented in Figure 9.b the active power follows the reference power, also notes that the reactive power follows the reference power which is zero Figure 9.c. According to the results found in the presence of a fluctuating wind, the regulation of the DC bus voltage is well controlled as shown in Figure 9.d. It can be seen from Figure 9.e. that the DPC strategies can keep the voltages of the two capacitors at their reference.

V. CONCLUSION

This paper has presented an improvement of the hybrid back-to-back power converter interface for a dual stator windings permanent magnet synchronous generator DSWPMSG based wind energy conversion systems, two parallel connected three-phase voltage source converters at the generator side, and 3-level NPC at the grid side,

The main results of this work are as follows:



a

- Good tracking of the different electrical and mechanical quantities with a very acceptable ripple rate given the high power of our system.
- The quality of the waves of the three-phase electrical currents injected into the grid and the operation with a power factor almost equal to unity offers this control employed to take its place among the best algorithms used in the field of WECS control.

REFERENCES

[1] L. Sagbansua, F. Balo, Decision making model development in increasing wind farm energy efficiency, Renew. Energy 109 (2017) 354–362.

[2] A.K. Aliyu, B. Modu, C.W. Tan, A review of renewable energy development in Africa: a focus in South Africa, Egypt and Nigeria, Renew. Sustain. Energy Rev.(2017).

[3] Luming Cheng; Yi Sui; Ping Zheng; Zuosheng Yin; Chuanze Wang "Investigation of low space harmonic six-phase PMSM with FSCWS for electric vehicle applications" IEEE Transportation Electrification Conference and Expo, Asia-Pacific (ITEC Asia-Pacific) 07-10 August 2017.

[4] Liserre M, Cardenas R, Molinas M, et al, "Overview of Multi-MW Wind Turbines and Wind Parks," IEEE Transactions on Industrial Electronics,vol. 58, no 4, pp. 1081-1095, April 2011

[5] Shen J, Miao D, "Variable Speed Permanent Magnet Synchronous Generator Systems and Control Strategies," Transactions of China Electrotechnical Society, vol. 28, no 3, pp. 1-8, March 2013.

[6] Modepalli K, Parsa L, "Offshore wind energy systems using high frequency isolated current-fed modular converters," IEEE Industrial Electronics Society (IECON 2015), 2015

[7] J. Rodríguez, L. G. Franquelo, S. Kouro, J. I. León, M. Pérez, R. Portillo, and M. A. Prats, "Multilevel converters: an enabling technology for high power applications," *Proceedings of the IEEE*, vol. 97, no. 811, pp. 1786–1817, November 2009.

[8] B. Wu, Y. Lang, N. Zargari, S. Kouro, Power Conversion and Control of Wind Energy Systems, John Wiley & Sons, 2011.

[9] R. Lanzafame, M. Messina, Fluid dynamics wind turbine design: Critical analysis, optimization and application of bem theory, Renewable energy 32 (14)(2007)2291-2305

[10] H.H. Mousa, A.-R. Youssef, E.E. Mohamed, Model Predictive Speed Control of Five-Phase PMSG Based Variable Speed Wind Generation System, 2018 Twentieth International Middle East Power Systems Conference (MEPCON) (2018) 304–309.

[11] Jiawen Li; Heng Nian; Yipeng Song "Dual stator windings PMSG fed by half controlled converters for wind power application" IEEE 2011 International Conference on Electrical Machines and Systems (ICEMS) 20-23 Aug. 2011

[12] Hoem, Q.M.M. Control of Six-Phase Machines. Master's Thesis, Norwegian University of Science and Technology, Trondheim, Norway, June 2009.

[13] Radu Bojoi, Alberto Tenconi, Giovanni Griva, and Francesco Profumo" Vector Control of Dual-Three-Phase Induction-Motor Drives Using Two Current Sensors" 1284 IEEE TRANSACTIONS ON INDUSTRY APPLICATIONS, VOL. 42, NO. 5, SEPTEMBER/OCTOBER 2006.

[14] Indupuri Sai Babji Kumar, Bindu S" Direct control technique for PMSG based Variable speed Wind Applications" International Conference on Electrical, Electronics, and Optimization Techniques (ICEEOT) – 2016.

[15] K.A. Chinmaya, G.K. Singh" Modeling and experimental analysis of grid-connected six-phase induction generator for variable speed wind energy conversion system" Electric Power Systems Research 166 (2019) 151–162

[16] D. Semenov, B. Tian, Li Sun and G. Mirzaeva, "Advanced fault-tolerant current control of five-phase PMSM for mining applications," *2016*

IEEE Industry Applications Society Annual Meeting, 2016, pp. 1-7, doi: 10.1109/IAS.2016.7731918.

[17] Azziddin M. Razali, Nor Azizah Yusoff, Kasrul Abdul Karim, Auzani Jidin, Tole Sutikno " A new switching look-up table for direct power control of grid connected 3L-NPC PWM rectifier" International Journal of Power Electronics and Drive Systems (IJPEDS) Vol. 12, No. 3, September 2021, pp. 1413~1421 ISSN: 2088-8694, DOI: 10.11591/ijpeds.v12.i3.pp1413-1421

[18] M. Lu, J. Hu, R. Zeng, W. Li and L. Lin, "Imbalance Mechanism and Balanced Control of Capacitor Voltage for a Hybrid Modular Multilevel Converter," in *IEEE Transactions on Power Electronics*, vol. 33, no. 7, pp. 5686-5696, July 2018, doi: 10.1109/TPEL.2017.2743780.

EEIC'23

Grid-Connected Multi-Source Energy Systems: Control and Management

Amina CHENNA [1], Djamal AOUZELLAG [2], Kaci GHEDAMSI [3]

Laboratoire de Maitrise des Energies Renouvelables, Faculté de Technologie, Université de Bejaia 06000, Algérie

Université de Bejaia 06000, Algérie

amina.chenna@univ-bejai.dz, djamal.aouzellag@univ-bejai.dz, kaci.ghedamsi@univ-bejaia.dz

***Abstract*— Over the last twenty years, clean energy sources such as wind, hydro, and solar power have made substantial progress in line with the global objective of "green recovery. The integration of more than one renewable energy source and the inclusion of backup sources and storage systems are among the measures to overcome the variability and intermittency nature of renewable energy sources (RES). This article examines a hybrid structure, combining wind, hydro with the addition of a battery energy storage system to supply power to the grid. The energy management strategy is presented, and various operating modes. The energy management strategy is usually integrated with optimization to ensure the continuity of grid and to decrease the cost of energy production. Simulation results obtained on the basis of the dynamic models of renewable energy sources are given, for different operating points, to validate the performance of the proposed system.**

Keywords: **Hybrid renewable energy system; Wind turbine; Hydropower systems; Battery energy storage; Converter control system.**

I. INTRODUCTION

In recent decades, a significant increase in electricity consumption has been driven by population growth, technological progress, and the development of new infrastructure. The production of renewable energy has been extensively developed in recent years. Of course, the capturing and the storing RE requires several technological supports, and the technological development supports these [1, 2] energy conversions. Energy Storage (ES) systems can drive strong renewable incorporation since the intermittent electricity generated in excess can be captured and released as additional capacity to the grid when it is necessary. In this context, several researchers have dealt with the RE hybridization scheme with different combinations of energy resources.

The numerous researchers have explored the hybridization of renewable energy (RE) through various combinations of energy resources. These systems are appealing because individual sources can synergize to offer more dependable power to customers compared to a single-source system. To enhance the continuity of power supply to local loads, it is crucial to establish compatibility between Wind Energy Conversion Systems (WECS) and Hydropower System (HS) and PV systems compatible and additional energy storage systems [3,4].

In the literature, various configurations have been examined, with the most prevalent ones being renewable battery or renewable-battery-diesel setups used to supply electrical power to remote communities [4, 5].

In temperate areas or near water dams or seawater, where the wind resource is not adequate, adding PV/ hydropower plant and battery to DG systems leads to the reduction of DG operation time and corresponding fuel consumption. For example: [6] They studied on a PV-Battery-DG system designed to supply power to two villages in Malaysia. Their analysis included a comparison of diesel-only, hybrid diesel-renewable, and renewable-battery configurations. The optimized hybrid configuration was determined to be more cost-effective in one of the two locations and 15% costlier than the diesel-only system in the second location [7].

The objective of ensuring energy supply security entails, firstly, reducing dependence on imports through the expansion of renewable sources and improved energy efficiency. Secondly, it involves diversifying the sources of energy supply. The aim is to explore the feasibility of enhancing the integration of renewable energy grid infrastructures to achieve safety and flexibility goals.

The topic of this article is the transformation of a renewable energy generator into an active generator by using energy storage systems. A hybrid power system is studied in the article. It consists a Wind Energy Conversion System (WECS) (as primary energy source), a hydropower system (HPS) (as second energy source), Battery Energy Storage (BES). The components of the system, including the wind turbine system (WT) with PMSG and Machine Side Converter MSC, the hydro-turbine system (HT) with PMSG and MSC, and battery bank BES converter, and) and the grid converter, are all connected to a shared DC bus. The architecture of the Hybrid system studied has been presented in figure (1).

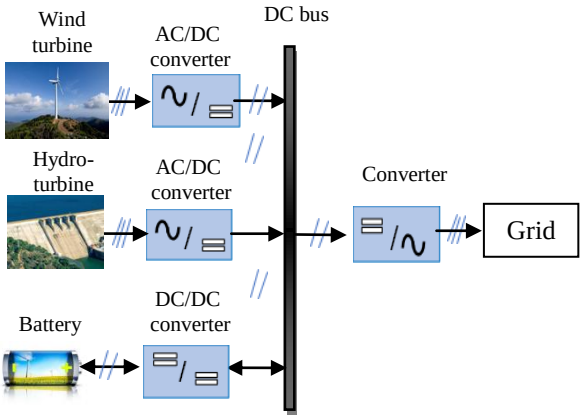


Figure 1. The architecture of the hybrid system studied

II. MATHEMATICAL MODELS OF THE MAIN COMPONENTS OF HRES

The considered system consists of: Wind Energy Conversion System (WECS) and Hydropower System (HS), and Battery Energy Storage (BES) and a diesel generator set (DGS).

A. *Modeling of the WG:*

The power coefficient with the 2 MW power is given by the expression [8]:

$$C_p(\lambda,\beta) = 0.5\left(116\,\frac{1}{\lambda_i} - 0.4\,\beta - 5\right)e^{-21\frac{1}{\lambda_i}} \qquad (1)$$

Where:

$$\frac{1}{\lambda_i} = \frac{1}{\lambda + 0.08\beta} - \frac{0.035}{\beta^3 + 1}$$

The maximum power from the wind turbine, is obtained for $C_{p.max}$=0.593 and for λ_{opt}=5.6 this point corresponds at the Maximum Power Point Tracking (MPPT) in shown in figure 3.

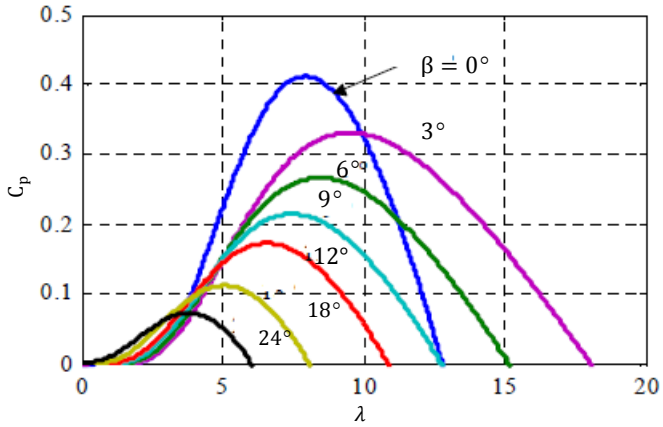


Figure 2. Cp- λ Curve

B. *Modeling of the Hydraulic Turbine (HT)*

The expression for available hydraulic energy is proportional to the height of the fall and the water flow rate:

$$P_{HT} = \rho_{HT}.Q_{HT}.g.h \qquad (2)$$

The mechanical power and the mechanical torque of the hydraulic turbine are given by:

$$\begin{cases} P_{HT.m} = \rho_{HT}.Q_{HT}.g.h.\eta_{HT} \\ C_{HT.m} = \frac{P_{HT.m}}{\Omega_{HT}} \end{cases} \qquad (3)$$

Where:

Q_{HT}: is the flow water (kg/m3)

g : Acceleration due to gravity (m/s2)

h : Available head (m)

η_{HT}: Hydraulic turbine efficiency

Ω_{HT}: Hydraulic turbine rotational speed (rad /s).

Expression (3) shows that for a given water flow rate, there is an optimal rotational speed at which the efficiency of the hydraulic turbine is maximum (η_{max}), corresponding to maximum hydraulic power ($P_{HT.m}$).

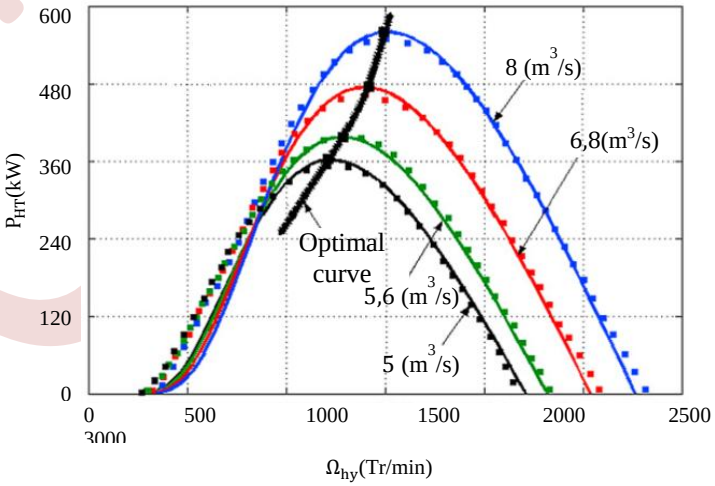


Figure 3. Hydraulic turbine characteristics

C. *Mathematical model of PMSG*

The PMSG, model in the park reference frame, is described by [9-10]:

$$\begin{cases} V_d = R_s I_d - p\Omega_w L_q I_q + L_d \frac{dI_d}{dt} \\ V_q = R_s I_q + p\Omega_w (L_d I_d + \phi_f) + L_q \frac{dI_q}{dt} \end{cases} \qquad (4)$$

Where:

R_s is the stator winding resistance, p is the pair pole number of the synchronous generator, I_d and I_q are, respectively, the direct and quadratic current.

The direct and quadratic magnetic fluxes are given by (the excitation flux ϕ_f is constant):

$$\begin{cases}\phi_d = L_d I_d + \phi_f \\ \phi_q = L_q I_q\end{cases} \quad (5)$$

The electromagnetic torque is also expressed as fellow:

$$C_{em} = p(\phi_d I_q - \phi_q I_d) \quad (6)$$

The active and reactive powers are given according to:

$$\begin{cases}P = V_d I_d + V_q I_q \\ Q = V_q I_d - V_d I_q\end{cases} \quad (7)$$

D. PMSG current regulation:

PMSG currents are regulated by hysteresis controllers, which allow keeping the current wave into range defined around the reference value. When current wave reached the band limits, the hysteresis controller generate a logic signal (0 or 1) (Figure 4). So, for (j=1, 2, 3) we have:

$$\begin{cases}F_j = 1 \text{ if } i^*_{mj} - i_{mj} \geq \Delta i \\ F_j = 0 \text{ if } i^*_{mj} - i_{mj} \leq \Delta i\end{cases} \quad (8)$$

With Δi is the hysteresis band defined in the controller.

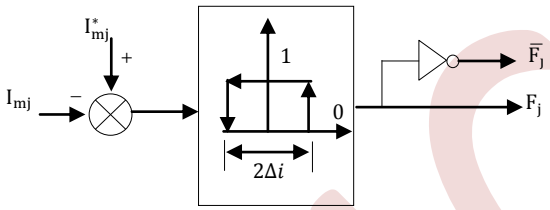


Figure 4. Hysteresis regulation principal

E. Mathematical Models of Battery Energy System:

A variety of battery models exist that predict battery behavior. The storage system includes a lead-acid banc battery and DC-DC buck-boost bidirectional the first task of this system is to maintain a DC Link voltage at the desired value whatever the variation in the load (Figure 5). The batteries are connected in series/parallel to achieve the desired capacity and voltage.

$$soc = 100\left(1 + \frac{\int I_{Bat} dt}{Q}\right) \quad (9)$$

Where:

I_{Bat}: is the battery charging current and Q: is the battery capacity.

F. Control of Bidirectional DC/DC Converter for Battery System

The bidirectional converter control strategy has two objectives: the first is to control the direction of the power flow. That is, to decide when the battery will play the role of an energy source, and when it is rather in charging mode (energy storage), all this depending on the evolution of the state of the hybrid system. The converter operates in buck mode (batteries charging) when switch S1 is closed and switch S2 is open. Otherwise (switch S1 is open and switch S2 is closed), the converter operates in boost mode (battery discharging).

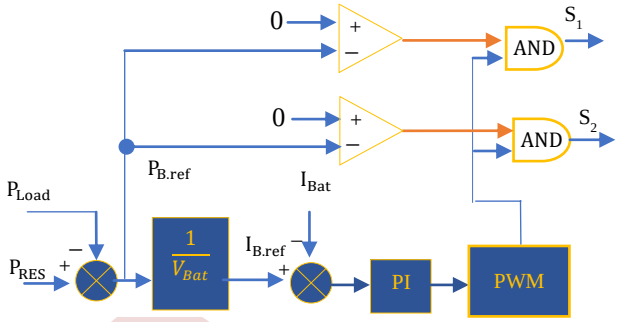


Figure 5. Control of switching signals for bidirectional DC/DC converter for battery system

The power absorbed (or returned) at the battery is expressed by:

$$\begin{cases}P_{Bat.ref} = P_{RES} - P_{grid} \\ P_{RES} = P_{WT} + P_{HT}\end{cases} \quad (10)$$

Where: P_{RES} : the renewable energy source power

III. ENERGY MANAGEMENT STRATEGY (EMS)

The aim of the energy management system is to maintain the balance between the energy produced by the renewable energy sources and the energy demanded by the electrical grid and energy storage, while protecting the storage units from excessive charge or discharge. The energy management strategy is represented by figure (8).

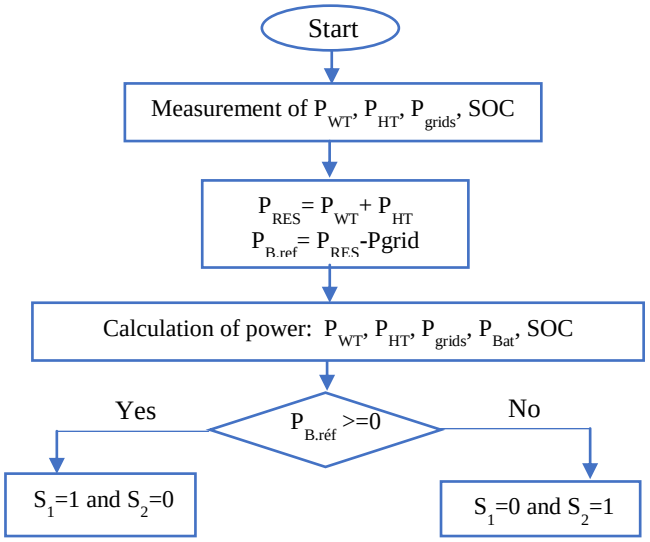


Figure 6. DC bus energy management diagram

If the total power generated by the RES ($P_{RES} = P_{WT} + P_{HT}$) is greater than the load demand (P_{grid}), the surplus power will charge the battery when the condition is fulfilled. The battery can be charged until it will be fully charged. If the total power generated by the RES is lower than the load demand (P_{grid}), The batteries will be discharged in order to reduce or compensate for the power deficit.

The charge and discharge process are monitored, and limits are imposed based on the value of SOC (between 40% and 80%, which corresponds to voltages of 460.8 V and 230.4 V, respectively).

IV. SIMULATION RESULTS

The mathematical models of individual parts of the hybrid renewable energy system (HRES) and the applied control systems have been implemented in the simulation program, which was formulated in a MATLAB/Simulink environment. The results of simulation are obtained for grid power reference $P_{grid\text{-}ref}$= 750kW (Figure 7.a). Table 1 gives the parameters for the HRES.

TABLE I. PARAMETER OF SIMULATION

name	Table of parameter		
	Parameter	Value	unit
Wind turbine	Nominal Power	660	kW
	Turbine Radius	20.41	m
	Inertia	222 963	Kg.m²
	Friction coefficient	743.21	N.m.s/rad
PMSG	Frequency	50	Hz
	Stator winding resistance	0.01	Ω
	Stator inductance	0.001	H
	Rotor inductance	0.001	H
	Excitation Flux	2.57	Wb
	Number of pole pairs	64	
Hydraulic turbine/PMSG	Nominal Power	500	kW
	Nominal power of the PMSG	500	kW
	Frequency	50	Hz
Batteries banc	Nominal voltage	576	V
	Nominal capacity	1000	Ah
	SOC (Max-min)	80%-40%	
	Smoothing inductance	20	mH
	DC/DC converter switching frequency	5	kHz
DC-Bus	voltage	1000	V
	Smoothing inductance	2	mH
	capacity	0.001	F
Electrical Grid	Voltage	690	V
	Filter inductance	0.001	H
	Filter resistance	0.001	Ω
	Frequency	50	Hz

The DC common connection point collects all the energy from the wind and hydro systems. The produced energy is available at the DC bus and is used, the remaining energy is used to recharge the batteries; in the presence of a surplus of production. When the energy produced by renewable sources is insufficient to power the grid, the storage system is activated to meet the needs of the grid. Indeed, this profile represents an approach to the fixed consumption of a 750kW electrical network over a day. The system inputs are: the daily wind speed, the water flow given in the figure (7, b and c).

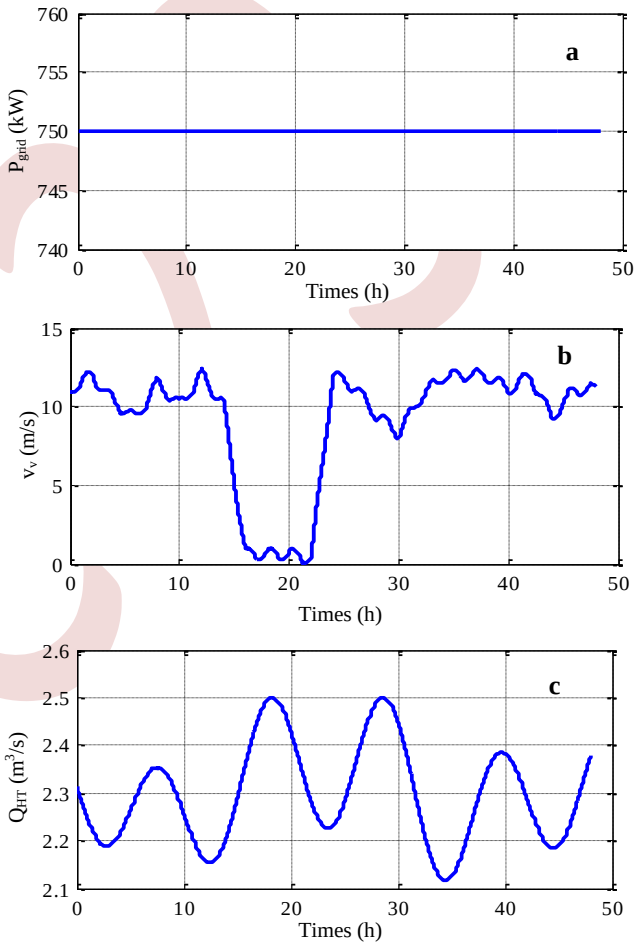


Figure 7. (a) Electric grid power reference, (b) Wind speed profile, (c) Water flow of the hydraulic turbine

The powers produced by the renewable energy systems (RES) are illustrated in Figures (8 a and b). For wind speeds below 3.5 m/s between 16:00 and 22:00, the wind power is zero.

Based on the simulation results, it is observed that the DC-DC converters and MPPT controllers perform their roles correctly to extract the maximum power from the wind energy conversion systems and the hydraulic energy conversion systems, respectively

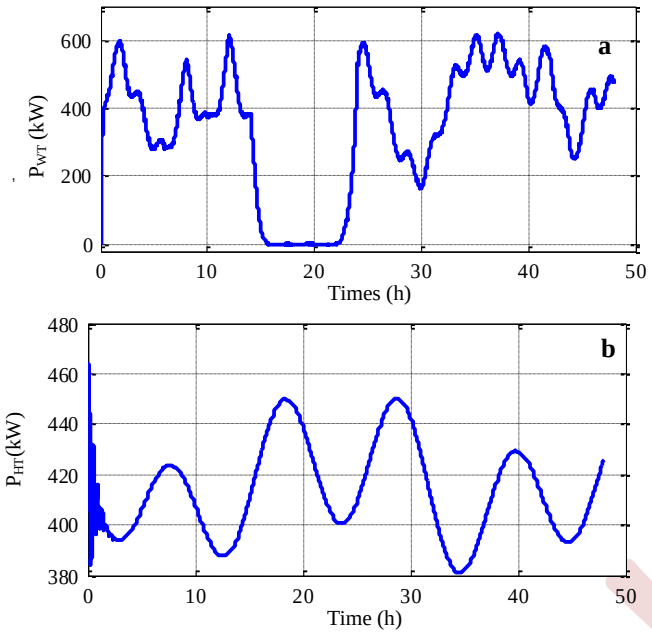


Figure 8. (a) Power of wind turbine, (b) Power of hydraulic power

Figure (9 a, b) shows the DC-voltage and the total power (P_T) collected by the common DC bus. The batteries, through the bidirectional converter, ensure that the voltage at the common DC connection point (Figure 9 a) remains constant. This achieves the balance between production and consumption, as the batteries charge or discharge depending on the difference between the renewable power supplied and the power consumed by the network.

The current and reference current of the battery's banc are presented in Figure (9 a). Between 16:00h and 22:00h, the power delivered by SCEE is zero, which means that the renewable power produced is less than the power demanded by the grid. In this case, the batteries discharge to cover the production deficit, which is justified by a negative current and a negative battery bank power (Figure 9 a, Figure 10).

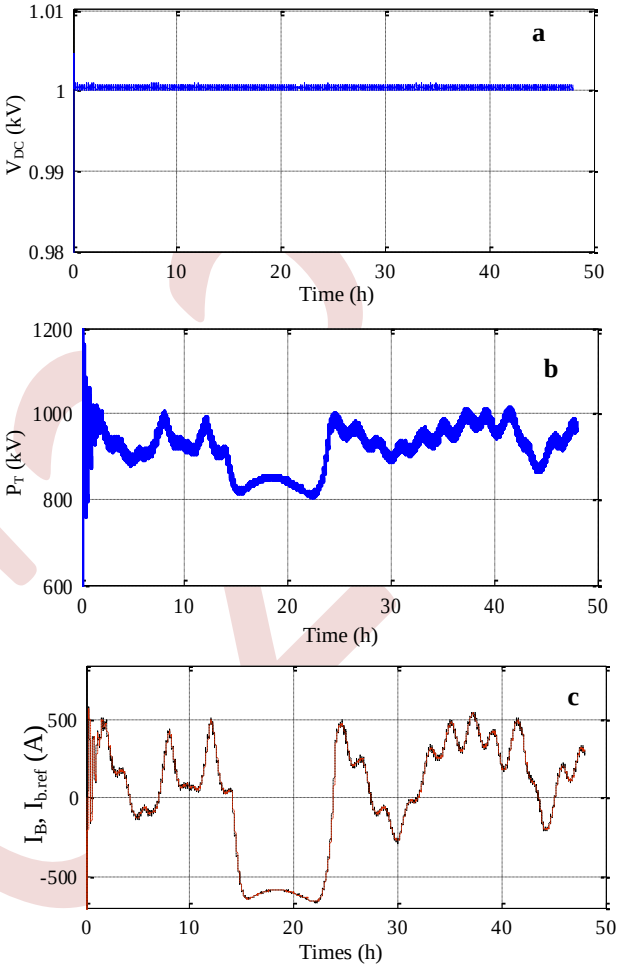


Figure 9. (a) DC-Voltage, (b): DC-Power, (c) Current of the BES

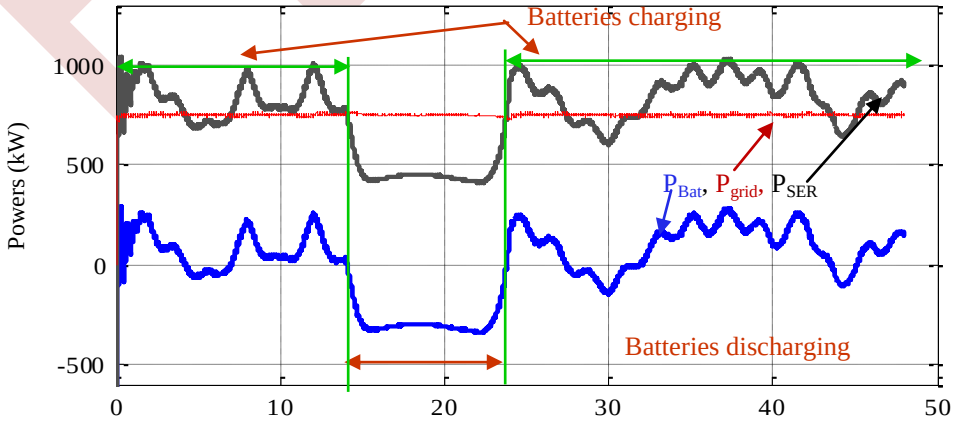


Figure 10. Powers of the hybrid system

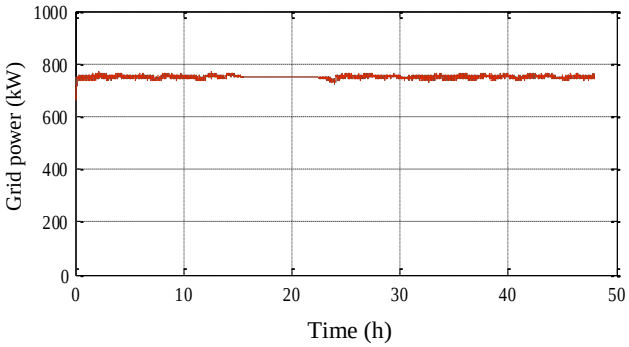


Figure 11. Grid power

Based on Figure (10), two modes of operation of the battery's banc can be distinguished:

- Between [0h-14h] and [23h-48h], the power produced by the SER is greater than the power demanded by the electrical grid. In this case, the surplus power is absorbed by the battery storage bank.
- Between [14h-23h], the power produced by the SER is less than the power demanded by the load. In this case, the battery bank discharges to the DC bus to provide the missing power.

The grid-side power perfectly follows the power demanded by the electrical grid (Figure 11).

V. CONCLUSION

In this work, the power management of a hybrid renewable energy system (HRES) has been carried out.

The developed power management strategies allow the proper operation of both the wind energy system and the hydropower system under different environmental conditions, while maintaining the grid-side power demand at the required level. In order to store the surplus power, the converter system with battery energy storage.

In the case of surplus power from the wind turbine system or hydraulic turbine panels system, the excess power will be stored in the battery system. The simulation results obtained under Matlab\Simulink\Sim-Power-System show the validity and good performance of the hybrid wind/hydro-power system in the presence of a storage system with lead-acid electrochemical batteries.

ACKNOWLEDGMENT.

We would like to thank the Directorate general for scientific research and technological development for funding our Laboratory.

REFERENCES

[1] L. Xu,.and all, "An improved optimal sizing method for wind-solar-battery hybrid power system". IEEE Trans. Sustain. Energy **2013**, 4,pp. 774–785, 2013. DOI:10.1109/TSTE.2012.2228509

[2] A. Sangwongwanich, and all, "Development of flexible active power control strategies for grid-connected photovoltaic inverters by modifying MPPT algorithm". In Proceedings of the IEEE 3rd International Future Energy Electronics Conference and ECCE Asia, Kaohsiung, Taiwan, 3–; pp. 87–92, 7 June 2017. DOI: 10.1109/IFEEC.2017.7992423

[3] F. Kahwash, and all, " Integration and optimisation of high-penetration Hybrid Renewable Energy Systems for fulfilling electrical and thermal demand for off-grid communities, Energy Conversion and Management 236 (2021), pp.1-19, 25 March 2021.
https://doi.org/10.1016/j.enconman.2021.114035

[4] P. Royand all, "Recent Advances of Wind-Solar Hybrid Renewable Energy Systems for Power Generation", A Review. IEEE Open J. Ind. Electron.. 2022, 3, pp.81–104, : 24 May 2023. https://doi.org/10.3390/eng4020084

[5] C. Dario, and all, "Hybrid solar, wind, and energy storage system for a sustainable campus: A simulation study", Science and Technology for Energy Transition 78, 13 (2023), pp.1-12, 2023. https://doi.org/10.2516/stet/2023008

[6] LM. Halabi, and al, "Performance analysis of hybrid PV/diesel/battery system using HOMER: a case study Sabah, Malaysia". Energy Convers Manag 2017; 144: pp. 322–39, 15 July 2017.
https://doi.org/10.1016/j.enconman.2017.04.070

[7] C. Tiansheng, and all, "Technoeconomic Analysis and Optimization of Hybrid Solar-Wind-Hydrodiesel Renewable Energy Systems Using Two Dispatch Strategies", International Journal of Photoenergy, pp.1-20, 2023. https://doi.org/10.1155/2023/3101876

[8] A. Ramli, "étude, commande et supervision d'un parc de sources d'energie decentralisées", Universite A.MIRA-BEJAIA, these doctorat, 2017.

[9] S. Zhang, and all, "Design of a robust grid interface system for PMSG-based wind turbine generators", IEEE TRANSACTIONS ON INDUSTRIAL ELECTRONICS 2011, VOL. 58, NO. 1, pp.316–328, 2011. DOI: 10.1109/TIE.2010.2044737

[10] [27] L. Jean Paul, and all,"Commande numérique des machines synchrones (Digital control of synchronous machines). Techniques d'Ingenieur ", ,(1999), Reference D3644.

Comparative Analysis of P&O, PSO, and ANN Methods for MPPT in Photovoltaic Systems

Meryem Lagoune[1], Samia Latreche[1], Badreddine Babes[2], Mabrouk Khemliche[1]

[1]*Automatic Laboratory of Setif, Electrical Engineering Department, Ferhat Abbas Setif1 University-UFAS Setif, Algeria*
meryemagon964@gmail.com, ksamia2002@yahoo.fr, mabroukkhemliche@univ-setif.dz
[2]*Research Center In Industrial Technologies CRTI P.O. box 64, Cheraga 16014 Algiers, Algeria*
elect_babes@yahoo.fr

***Abstract*—Solar photovoltaics (PV) have proven to be the most reliable source of solar energy collection. The output of a solar PV system is determined by solar radiation and temperature, which fluctuate throughout the day. Consequently, the maximum power point (MPP) on the solar PV output characteristics curve varies. Different Maximum Power Point Tracking (MPPT) approaches are employed to track the MPP and collect the maximum power from PV systems. This research presents a comprehensive simulation-based analysis comparing three widely used MPPT algorithms: perturb and observe (P&O), particle swarm optimization (PSO), and an artificial neural network-based MPPT technique implemented using MATLAB Simulink. These MPPT algorithms are used to control the duty cycle of a DC-to-DC Boost converter. The performance of the three algorithms is evaluated in terms of tracking speed, accuracy, and efficiency. Under conditions of partial shade and rapidly changing irradiance, the MPPT based on ANN algorithm demonstrates superior tracking efficiency compared to the PSO and P&O algorithms.**

***Keywords:* Maximum Power Point Tracking, Photovoltaic, Particle Swarm Optimization, Perturb and Observe.**

I. INTRODUCTION

In recent years, solar photovoltaic (PV) technology has emerged as the most practical choice for electricity generation. Depletion of fossil fuel sources and growing environmental concerns related to fossil fuel use have driven the widespread adoption of solar PV for energy generation. PV-generated electricity is clean, quiet, and requires minimal maintenance. Various factors, including temperature, solar irradiation, and shading conditions, affect the energy generation of PV modules [1]. The voltage-current (V-I) characteristics of PV modules are nonlinear, and the voltage-power (V-P) characteristic curve has a single point where it produces maximum power (Pmax). This maximum power point (MPP) varies with ambient conditions, resulting in a mismatch between load and source characteristics, leading to reduced power output. Maximum power point tracking (MPPT) is a technique that optimizes the PV module's operation to match the load characteristics, minimizing power losses [1,2]. The MPPT controller adjusts the duty cycle of a DC-DC converter, which serves as an interface between the load and the PV modules.

Numerous MPPT strategies are available in the literature to extract maximum power from PV modules for various applications. Commonly used MPPT techniques include Perturb and Observe (P&O), Fractional Short Circuit Current (FSCC), Incremental Conductance (IC), among others. Additionally, sophisticated soft computing-based MPPT methodologies such as Artificial Neural Networks (ANN), Fuzzy Logic approaches, and Particle Swarm Optimization (PSO) have been developed. The MPPT controller aids in adjusting the duty cycle of a DC-DC converter, which acts as the interface between the load and the PV modules.

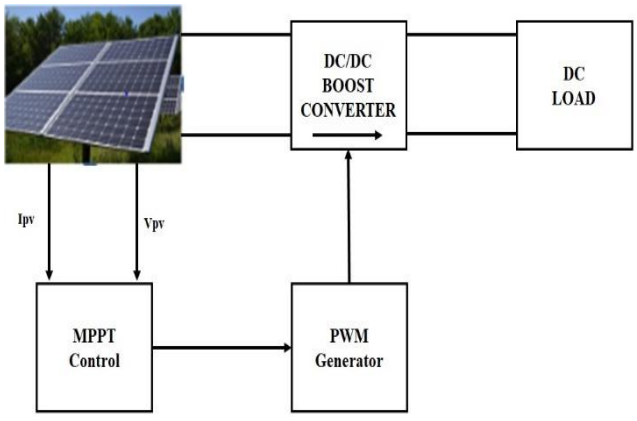


Figure 1. MPPT Control for PV System.

In this study, we compare three MPPT approaches: PSO, ANN, and P&O, under standard test conditions (STC) as well as variable irradiance conditions.

II. SYSTEM MODELLING AND SIMULATION

The primary component of a PV cell is a p-n junction created within a thin semiconductor wafer. Solar energy is promptly converted into electricity through the photovoltaic effect. The electrical properties of a PV cell are nonlinear and heavily influenced by temperature and solar irradiation [3].

In this study, the single-diode model is selected for its simplicity and accuracy. This model can be electrically represented by an analogous circuit, as shown in Figure 2, comprising a photocurrent source connected in series with a diode, a shunt resistance (Rsh), and a series resistance (Rs).

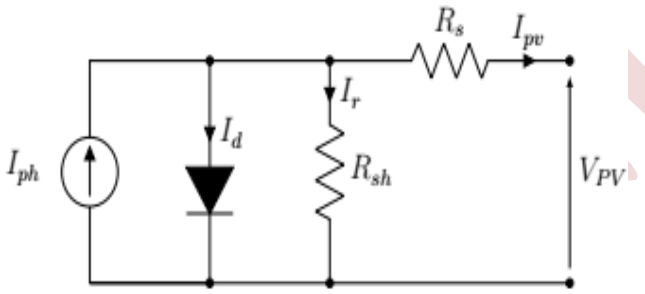


Figure 2. Equivalent circuit of a PV cell.

The relation of the equivalent circuit of the PV system is as follows,

$$I_{pv} = I_{ph} - I_d - I_r = I_{ph} - I_0\left(e^{\frac{V_{pv}+R_s I_{pv}}{nV_t}} - 1\right) - \frac{V_{pv} + R_s I_{pv}}{R_{sh}} \quad (1)$$

And

$$V_t = \frac{KT}{q} \quad (2)$$

Modeling photovoltaic cells involves several key parameters. These include Ipv and Iph, representing the cell's output and light-produced currents, respectively.

The Shockley formula models Id, while Ir is derived from shunt resistance. I_0 signifies the reverse saturation current of the diode, and Vpv represents cell output voltage. Parasitic resistances, Rs (series) and Rsh (shunt), affect electrical characteristics. Additionally, Vt (thermal voltage) and nn (diode ideality factor) play roles, and physical constants, such as the Boltzmann constant K and elementary charge q, are used. Cell temperature T is expressed in Kelvin.

These parameters are essential for accurate modeling and characterization of photovoltaic cells.

III. MPPT CONTROL FOR PV SYSTEM

An MPPT unit, equipped with an appropriate control algorithm, is a power conversion system that enables the extraction of maximum power from a PV array. It achieves this by adjusting either the current drawn from the PV array or the voltage across it to operate at or near the Maximum Power Point (MPP), thereby maximizing the supplied power. To enhance the energy efficiency of PV arrays, various MPPT algorithms, each with different levels of complexity, accuracy, efficiency, and implementation challenges, have been developed [4-5].

A. PERTURB AND OBSERVE ALGORITHM

The P&O-MPPT method is commonly used due to its low cost, simple structure, and minimal measurement requirements [6]. Figure 4 illustrates the P&O method using a flowchart,

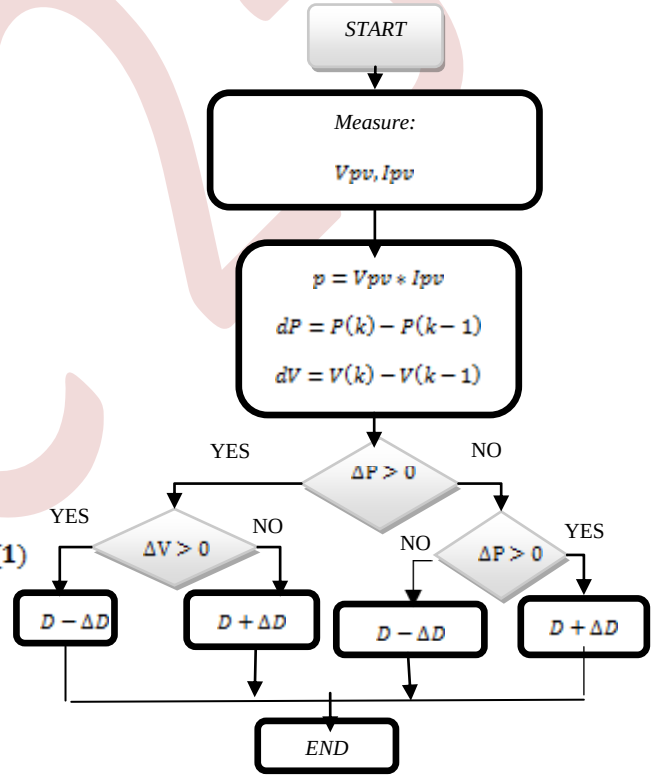


Figure 3. Flowchart for P&O Algorithm

B. NEURAL NETWORK-BASED MPPT TECHNIQUE

The ANN-MPPT method is trained using MATLAB and the Levenberg-Marquardt method. The Levenberg-Marquardt approach enables the rapid and precise resolution of nonlinear least squares issues. We chose the Levenberg-Marquardt method for training the neural network because of the highly nonlinear nature of temperature and irradiance effects on output power and voltage. The construction of the neural network-based MPPT for a PV array follows the phases outlined in the following sections [7].

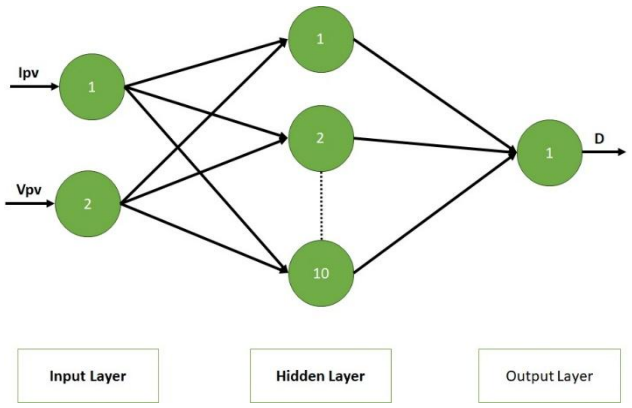


Figure 4. The Neural Network Architecture.

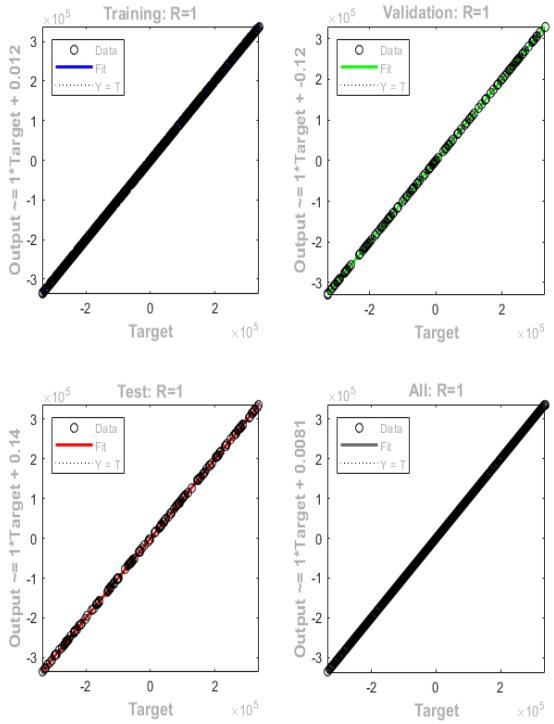


Figure 5. The Neural Network Regression

C. Particle Swarm Optimization (PSO)

The PSO-MPPT method is based on the behavior of flocks of birds and involves a multidimensional swarm of particles, where each particle represents a solution. These particles continuously adjust their positions to find the optimal location based on their past experiences and interactions with neighboring particles. The position of each particle is influenced by both the best-performing particle in its vicinity (Pbest_i) and the best solution found by the entire population of particles (Gbest) [8].

To achieve this, each particle's movement is controlled by adjusting its velocity, which is increased or decreased based on the comparison between its current position value and the best value. If the current position is inferior to the best value, the velocity increases, and vice versa.

The particle's position (xi) is modified according to the following equation [13-14],

$$x_i^{k+1} = x_i^k + v_i^{k+1} \qquad (3)$$

Where (vi) represents the velocity and is obtained as follows,

$$v_i^{k+1} = w v_i^k + c_1 r_1 \{P_{best\,i} - x_i^k\} + c_2 r_2 \{G_{best} - x_i^k\} \qquad (4)$$

with c1 and c2 are acceleration coefficients, w denotes the inertia weight, and r1, r2 are random values drawn from the uniform distribution U. Figure 6 illustrates the PSO flowchart,

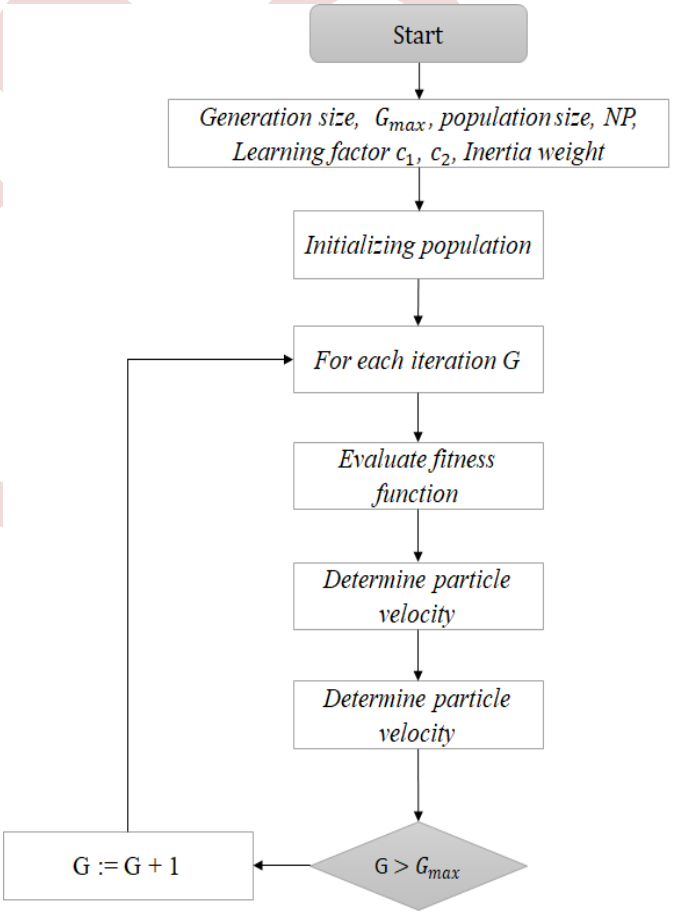


Figure 6. Flowchart for PSO Algorithm.

IV. SIMULATION RESULTS

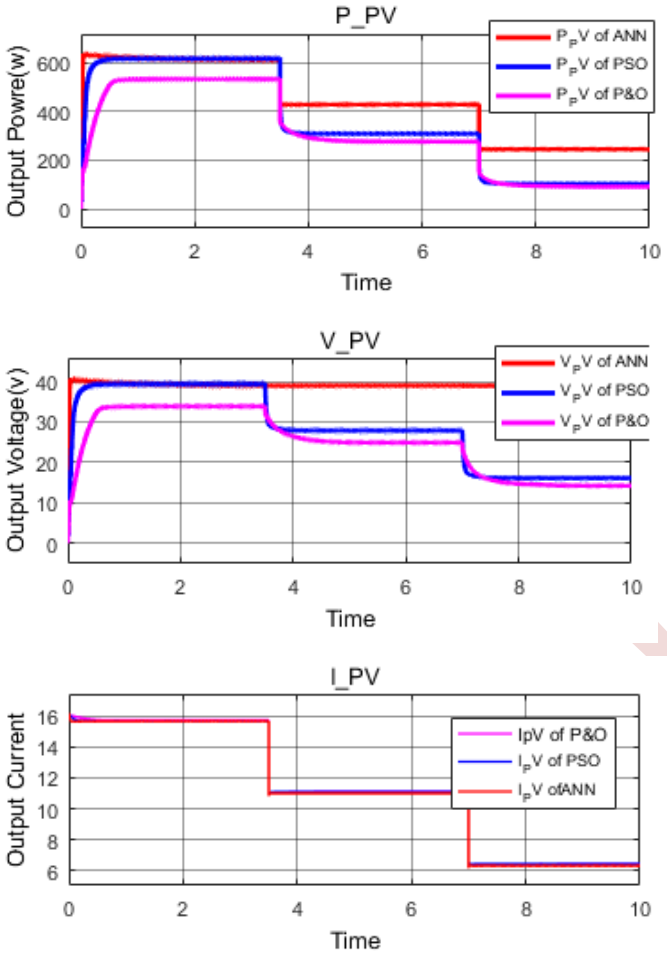


Figure 7. Comparison of P_PV ,V_PV, I_PV from PSO, ANN and P&O

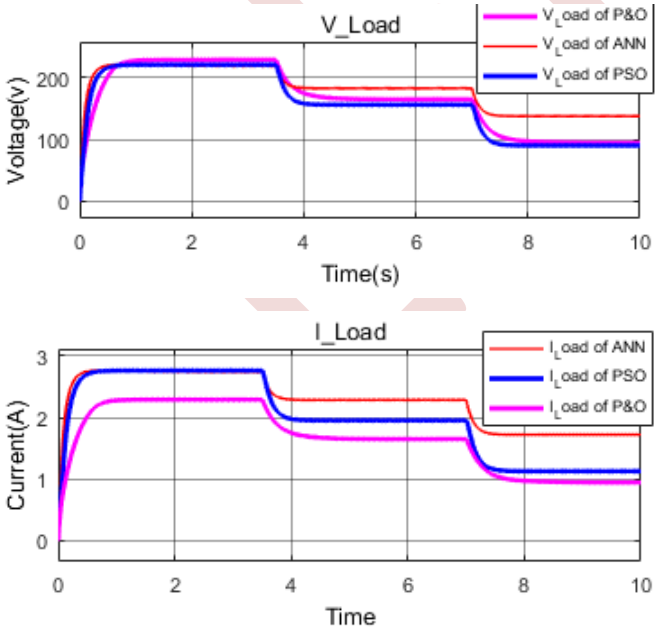


Figure 8. Comparison of I_Load, V_Load, from PSO, ANN and P&O

V. CONCLUSIONS

In conclusion, this paper has introduced and compared two distinct Maximum Power Point Tracking (MPPT) techniques, namely an ANN-based approach and a PSO-based method, both aimed at optimizing the power output of photovoltaic energy conversion systems under varying atmospheric conditions. These techniques have been rigorously evaluated and compared against the conventional Perturb and Observe (P&O) method. Using the ANN algorithm, we achieved faster convergence to the maximum point compared to the PSO and P&O methods. Furthermore, the ANN algorithm demonstrated minimal fluctuation at steady state, resulting in significant power savings

REFERENCES

[1] Ali Omar Baba; Guangyu Liu; Xiaohui Chen. Classification and Evaluation Review of Maximum Power Point Tracking Methods School. Of Automation, Hangzhou Dianzi University, Hangzhou 310018, China;2020

[2] Gursoy, M.; Zhuo, G.; Lozowski, A.G.; Wang, X. Photovoltaic Energy Conversion Systems with Sliding Mode Control. Energies 2021, 14, 6071.

[3] Leopoldo Gil-Antonio 1,2 , Belem Saldivar 1,3,* , Otniel Portillo-Rodríguez 1,* , Juan Carlos Ávila-Vilchis 1 and Pánfilo Raymundo Martínez-Rodríguez 4 and Rigoberto Martínez-Méndez 1. Flatness-Based Control for the Maximum Power Point Tracking in a Photovoltaic System. Energies 2019, 12, 1843

[4] B. Yang, T. Zhu, J. Wang, H. Shu, T. Yu, X. Zhang, W. Yao, and L. Sun, ''Comprehensive overview of maximum power point tracking algorithms ofPVsystemsunderpartialshadingcondition,''J.CleanerProd.,vol.268, Sep. 2020, Art. no. 121983

[5] .Worku, M.Y.; Hassan, M.A.; Maraaba, L.S.; Shafiullah, M.; Elkadeem, M.R.; Hossain, M.I.; Abido, M.A. A Comprehensive Review of Recent Maximum Power Point Tracking Techniques for Photovoltaic Systems under Partial Shading. Sustainability 2023, 15,

[6] Kumar, M.; Panda, K.P.; Rosas-Caro, J.C.; Valderrabano-Gonzalez, A.; Panda, G. Comprehensive Review of Conventional and Emerging Maximum Power Point Tracking Algorithms for Uniformly and Partially Shaded Solar Photovoltaic Systems. IEEE Access 2023, 11, 31778–31812. [CrossRef]

[7] Roy,R.B.;Rokonuzzaman,M.;Amin,N.;Mishu,M.K.;Alahakoon,S.;Rahman,S.;Mithulananthan,N.;Rahman,K.S.;Shakeri, M.; Pasupuleti, J. A Comparative Performance Analysis of ANN Algorithms for MPPT Energy Harvesting in Solar PV System. IEEE Access 2021, 9, 102137–102152. [CrossRef]

[8] Muhannad Alshareef 1, Zhengyu Lin 1,* , Mingyao Ma 2 and Wenping Cao 1. Accelerated Particle Swarm Optimization for Photovoltaic Maximum Power Point Tracking under Partial Shading Conditions. Energies 2019, 12, 623

[9] F. Bait, S. Latreche, and M. Khemliche, "Simulation of different faults in photovoltaic installation," in 2022 19th IEEE International Multi-Conference on Systems, Signals and Devices, SSD 2022, May 2022, pp. 1130–1138, doi: 10.1109/SSD54932.2022.9955851.

[10] S. Latreche, A. E. Badoud, and M. Khemliche, "Implementation of MPPT algorithm and supervision of shading on photovoltaic module," Engineering, Technology and Applied Science Research, vol. 8, no. 6, pp. 3541–3544, Dec. 2018, doi: 10.48084/etasr.2354

[11] S. Latreche, A. Khenfer, and M. Khemliche, "Sensors placement for the faults detection and isolation based on bridge linked configuration of photovoltaic array," Electrical Engineering and Electromechanics, vol. 2022, no. 5, pp. 41–46, Sep. 2022, doi: 10.20998/2074-272X.2022.5.07

[12] Y. Lahiouel, S. Latreche, and H. Afghoul, "Experimental realization using a dSP ACE card of the PI control for an active power filter," in 2022 19th IEEE International Multi-Conference on Systems, Signals and Devices, SSD 2022, May 2022, pp.53–57, doi: 10.1109/SSD54932.2022.9955690

[13] H. E. Amara, S. Latreche, M. A. Sid, and M. Khemliche, "Sliding mode observer and event triggering mechanism co-design," Engineering, Technology and Applied Science Research, vol. 10, no. 2, pp. 5487–5491, Apr. 2020, doi: 10.48084/etasr.3285

[14] Lahiouel Y., Latreche S., Khemliche M., Boulemzaoud L. Photovoltaic fault diagnosis algorithm using fuzzy logic controller based on calculating distortion ratio of values. Electrical Engineering Electromechanics, 2023, no.4, pp. 40-46. doi:https://doi.org/10.20998/2074-272X.2023.4.06

EEIC'23

Energy Management Strategy of PV System with Battery Supercapacitor Hybrid Energy Storage for Stand-alone Applications

Hacini Ismail[1], Sofia Belaid[1], Kassa Idjdarene [1], Kahina Berabez [1]

[1] *Laboratoire de Technologie Industrielle et de l'Information, Faculté de Technologie, Université de Bejaia, Bejaia 06000, Algeria*

ismail.hacini@univ-bejaia.dz, sofia.lalouni@univ-bejaia.dz, kassa.idjdarene@univ-bejaia.dz, kahina.berabez@univ-bejaia.dz

***Abstract*— A hybrid energy storage system using the combination of batteries and super capacitors is an attractive solution. Batteries are used to meet long-term power needs, while super capacitors are used to meet instantaneous power demand. This article deals with the management of a battery - super capacitor hybrid energy storage for autonomous applications. A new energy management strategy is developed to manage power flows between storage devices. The simulation results demonstrate the effectiveness of the proposed energy management strategy under sudden changes in power generation and load demand.**

***Keywords:* Hybrid Energy Storage, Batteries, Supercapacitor.**

I. INTRODUCTION

Due to its low cost, the lead-acid battery is the most widely used energy storage element. They have a high energy density so that they can deliver energy efficiently for a long time, but have a low power density, therefore limited charge and discharge rates and a short lifespan [1]. Large power fluctuations reduce battery life due to increased charge and discharge cycles which can affect PV system performance. To overcome these difficulties and make the PV system robust to the unwanted effects of power fluctuations, super capacitors (SC) are now used. Compared with battery, SC has high power density but low energy density and has high charge and discharge rate [2]. Thus, these properties of SC are effectively used to mitigate transient power fluctuations. Batteries used in renewable energy storage systems can have multiple irregular charge/discharge cycles. This can also have a negative effect on battery life and can increase installation costs. To solve this problem, researchers have proposed hybrid energy storage systems (HESS) and new energy management strategies to improve battery life. Various hybrid energy storage control strategies are proposed in [3][4], for power sharing between battery and super capacitor. The active HESS system allows both the battery and the supercapacitor to be operated at different voltages, allowing for better utilization of the individual components. An active HESS configuration makes the best use of the available supercapacitor energy [5]. In [6], rule-based methods are adopted and verified by simulation results. The control scheme proposed in this paper effectively presents the control of bidirectional DC-DC converters for power sharing between the battery and the super capacitor by allowing low frequency power fluctuations provided by the battery and harsh transients provided by the super capacitor. This document is organized as follows: After the Introduction section, a description of the system is given in section 2. The control and management of the DC bus is discussed in section 3. In section 4, the simulation results representing the analysis of the SCs-battery combination are discussed. Section 5 concludes the article.

II. SYSTEM DESCRIPTION

The studied standalone PV system is composed of photovoltaic panels, batteries, and supercapacitors connected to a common DC bus through DC-DC converters (Figure 1). The batteries are defined as high-energy, low-power devices. The Batteries are designed for storing electrical energy in order to use it later. This source has a large mass energy and provides energy storage and slow dynamics of the system. The battery energy storage system is an effective means to smooth out the power fluctuations. The supercapacitor, with its rapid dynamics, can be added to smooth out rapid fluctuations in PV power and short-term loads. Supercapacitors have characteristics opposite to those of batteries. They are characterized by their high specific power due to the low internal resistance and low voltage. SCs are capable of very fast charges and discharges and they have a very large number of cycles without degradation and with a high efficiency. The Central capacities of the bus filter the power fluctuations from static converters adopted. System stability can be affected by the loss of instant balance between supply and load. Therefore, an energy management algorithm is mandatory. The battery and supercapacitors have been combined in parallel. The control system presented in this work is designed to leverage the fast charge and discharge capability of supercapacitors to alleviate battery constraints due to instantaneous power demands.

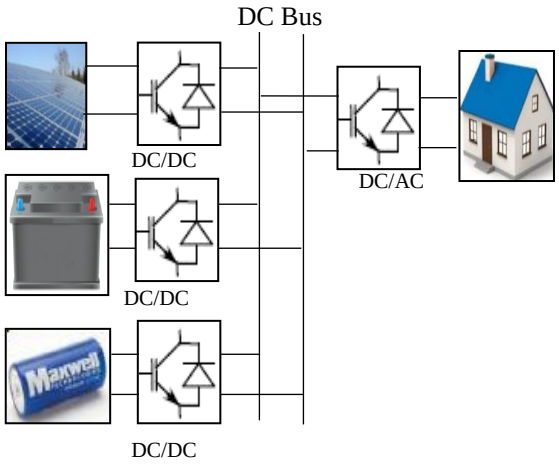


Figure.1. Configuration of the hybrid PV-battery-super capacitor system.

A. Hybrid energy storage

Hybrid batteries and super capacitors are two different energy storage technologies, but it is possible to combine them to create a hybrid energy storage system. This combination can offer certain advantages, such as improved energy density, longer lifespan, and enhanced performance compared to using each technology separately

B. super capacitor energy storage

super capacitors are added as a storage element for its high-power devices, Among the models presented in the scientific literature, the two-branch model is used in this work. Figure 2 depicts an equivalent electric circuit with two RC branches, which was proposed by Zubieta and Bonert [7].

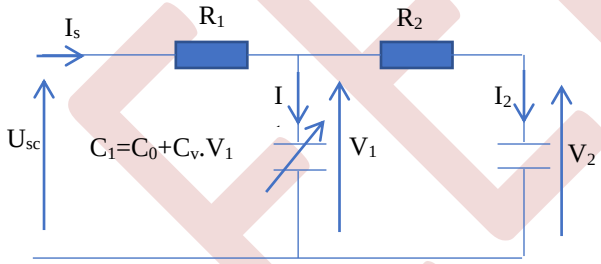


Figure.2 Supercapacitor simplified circuit

The main capacitance C_1, called differential capacitance, depends on the voltage V_1. It consists of a constant capacity C_0 (in F) and a constant parameter C_v (in F/v) and it is written as:

$$C_1 = C_0 + C_v.V_1 \quad (1)$$

The following equation expresses the voltage of the equivalent circuit of the SC :

$$U_{sc} = N_s Vsc = N_s.V_1 + R_1 \frac{I_{sc}}{N_p} \quad (2)$$

Where U_{sc} and V_{sc} are pack voltage and elementary voltage of the super capacitors respectively. I_{sc} and i_{sc} are pack current and elementary current of the super capacitors respectively. Ns and Np are the number of series/ parallel branches of the SC connections. The voltage V_2 in the secondary capacity C_2 is expressedby:

$$V_2 = \frac{1}{C_2}\int i_2 dt = \frac{1}{C_2}\int \frac{1}{R_2}(V_1 - V_2)dt \quad (3)$$

The current i1 flowing in C1 is given by:

$$i_1 = i_{sc} - i_2 \quad (4)$$

The current i1 is denoted also in terms of the instantaneous charge Q_1 and C_1 as:

$$i_1 = C_1\frac{dV_1}{dt} = \frac{dQ_1}{dt} = (C_0 + C_V C_1)\frac{dV_1}{dt} \quad (5)$$

where the charge Q_1 is given by:

$$Q_1 = C_0 V_1 + \frac{1}{2}C_v V_1^2 \quad (6)$$

Then voltage V_1 is defined as follows:

$$V_1 = \frac{-C_0 + \sqrt{C_0^2 + 2.C_v Q_1}}{C_v} \quad (7)$$

C. Battery Energy Storage

A battery energy storage system consists of series and parallel chains of batteries. There are several lead-acid battery models, and their implementation is difficult because many parameters must be considered. The RC model is used in our study. this last also known as the simple model includes E, the emf that models the no-load voltage of the battery, an internal resistance R_s and a capacitor Cbat modelling its internal capacitance.

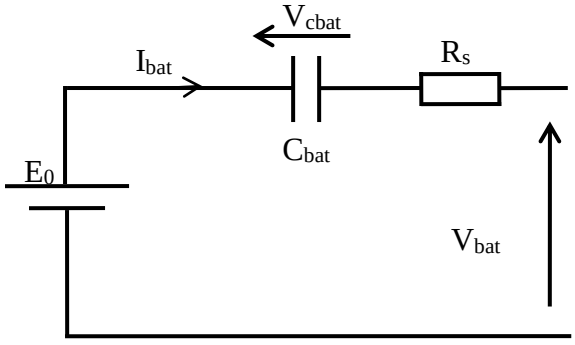


Figure.3 RC model of the battery

Thus, the expression of the voltage V_{cbat} according to the current I_{bat} is given by the following:

$$V_{bat} = E_0 - R_s I_{bat} - V_{cvat} \quad (8)$$

The battery's state of charge (SOC) is defined by the following equation:

$$SOC = 1 - \frac{Q_d}{C_{cbat}} \quad (9)$$

With:
C_{bat}: the nominal capacity (Ah) of the battery;
Q_d: the amount of charge missing in relation to Cbat. The value of Cbat is given by the following expression:

$$Q_d = Q_{d0} - I_{bat}.t \quad (10)$$

$$C_{bat} = \frac{Q_d}{V} = \frac{I_{bat}.t}{V} \quad (11)$$

D. Battery-Supercapacitors Combination

As shown in Figure. 1, the battery and supercapacitors have been combined in parallel. The two converters DC/DC and AC/DC are supposed ideal, without losses. The DC-bus voltage V_{dc} is taken to 465 V. This work presents a control system that is designed to profit the rapid charge and discharge capability of the SCs in order to decrease the battery stresses due to instantaneous power demands. The goal of the combination between the battery and the SCs is to make the super-capacitors provide the power transients and to smooth the high-power demands applied to the battery during autonomous operation.

III. ENERGY CONTROL AND MANAGEMENT STRATEGY

Modern batteries have a higher energy storage density but a relatively slow response rate. On the other hand, supercapacitors have a low power density but a rapid response rate. Therefore, in the design of the EMS (Energy Management System) control, the supercapacitor must be responsible for rapid transient energy exchange, while the battery must support energy charge or discharge in a relatively stable regime. The result is a control design as illustrated in Figure 4.

The PI controller calculates the DC bus reference current, I_{dcref}, to maintain the DC bus voltage at its reference value, Vref.

Then, a low-pass filter is applied to obtain the battery reference current, I_{batref}, while the remainder is used as the supercapacitor reference current, I_{scref}. At all times, the sum of the reference currents, I_{scref} and I_{batref}, must be equal to I_{dcref}.

The DC bus voltage can be modeled by the following equation:

$$C_{dc}\frac{dv_{dc}}{dt} = I_{scdc} + I_{batdc} + I_{pvdc} - I_{load} \quad (12)$$

The flowchart in Figure. 5 shows how the EMS works by displaying the reference currents of the batteries and the SCs for various SOC instances.

The reference current of DC bus is null when the power source produce the power needed by the load.

The SOC_{sc} and SOC_{bat} must be between 30% and 90% in the normal situation of state of charge of batteries and supercapacitors.

The reference current of the SCs must be null if the reference current of the DC bus is negative (when the energy source output exceeds the load power) and the SOC of the SCs is >90% percent (SCs are saturated). SCs begin to charge if this is not the case.

The reference current of the SCs must be null if the reference current of the DC bus is positive (when the source energy fails to provide the appropriate power) and the SOC of the SCs is less than 30%. If not the case, SCs begin to charge.

If the reference current of DC bus is negative (when the power source gives higher than the load power) and the SOC of batteries is >90% (SCs was saturated) the reference current of batteries must be null. If not the case, batteries begin to charge.

If the reference current of DC bus is positive (when the power source fails to give the desired power) and the SOC of batteries is <30% the reference current of batteries must be null. If the SOC_{bat} is >30% batteries begin to discharge.

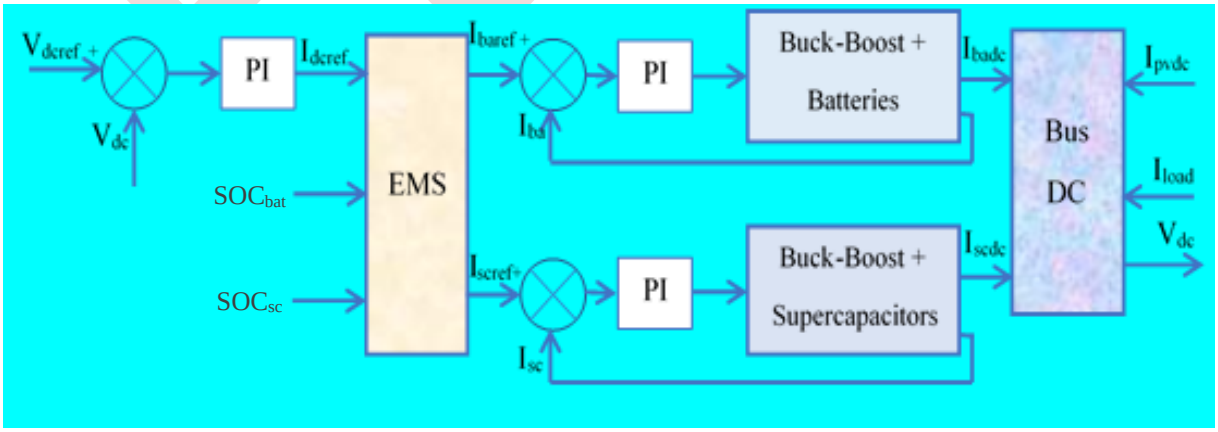


Figure.4. Block diagram of DC bus control.

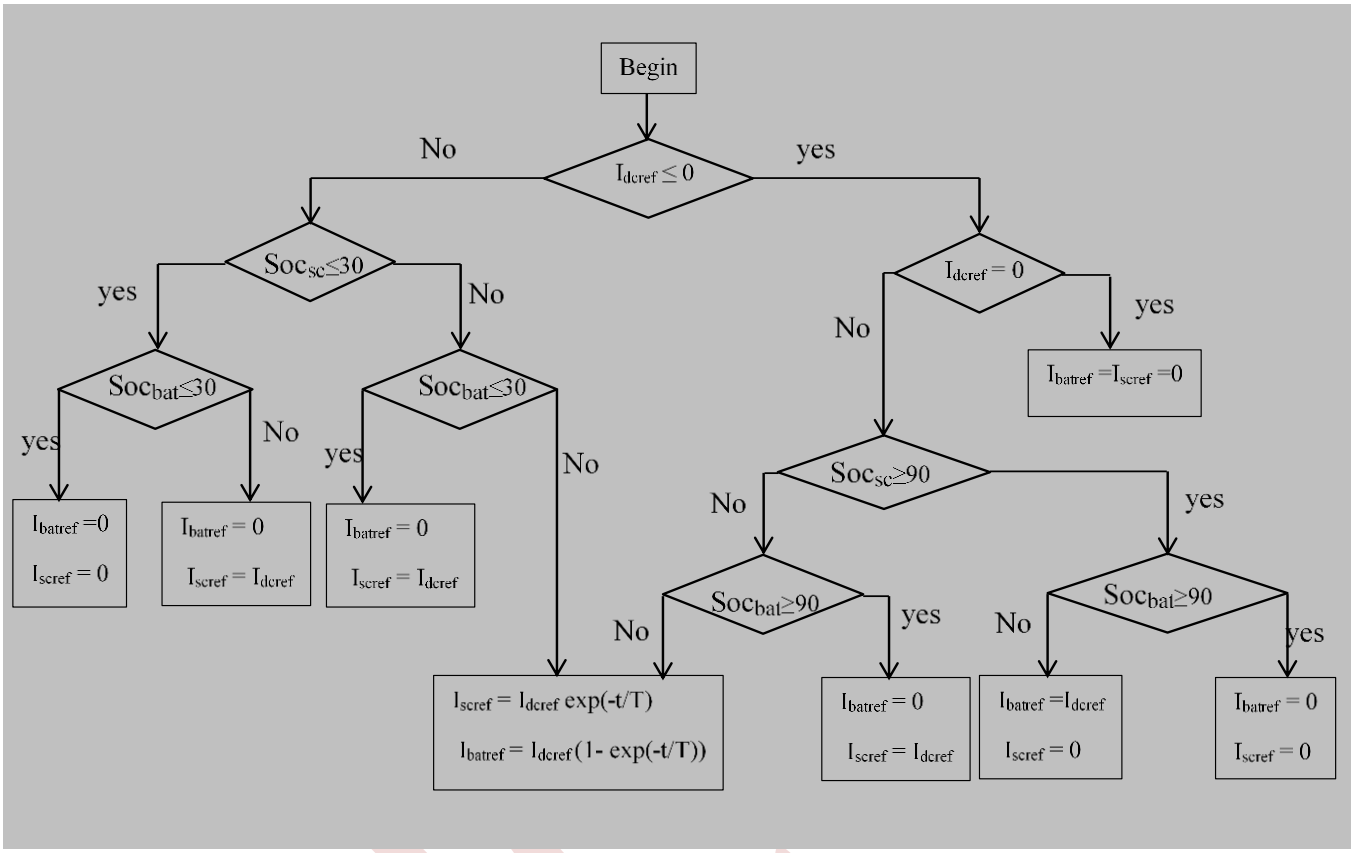


Figure.5. Flowchart of the distribution of the reference sources of the energy storage system

IV. SIMULATION AND RESULTS

The studied system was implemented with different operating conditions in the MATLAB/SIMULINK environment.

To ensure continuous supply to the load and prevent damage to the batteries and supercapacitors, we must maintain the State of Charge (SOC) of the SCs (SOC_{sc}) and the batteries (SOC_{bat}) at acceptable levels. The low charge rate for both batteries and SCs is set at 30%, and the high charge rate is 90%

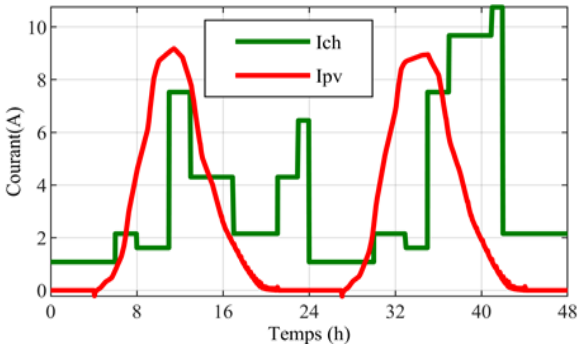


Figure.6. The current of the load and the PV source.

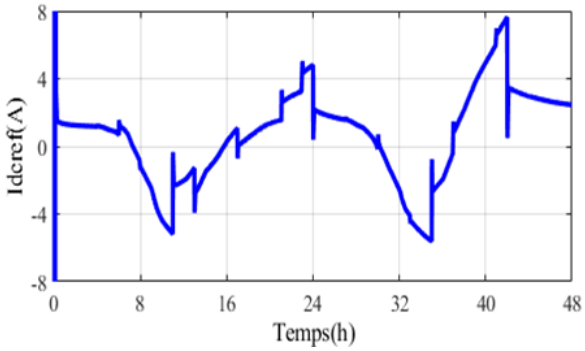


Figure.7. DC bus current

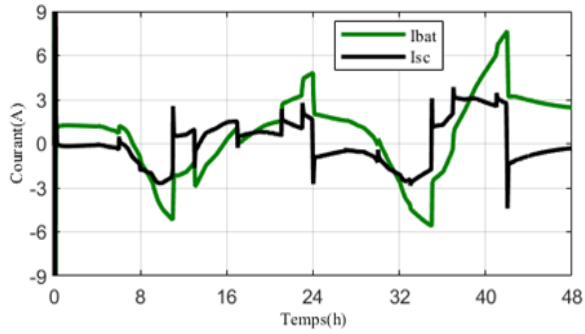


Figure.8. Battery and super capacitor current

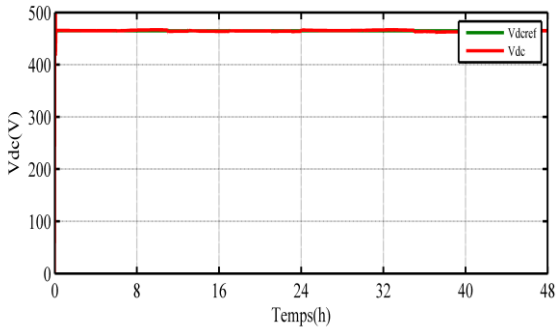


Figure.9. DC bus voltage

The charging current is illustrated in Figure 6. The distribution of the charging current between the battery and the supercapacitor, based on the strategy defined above, is shown in Figures 7 and 8. During the initial period from 0 to 6 hours, the power required falls within the battery's allowable power range, so only the battery provides energy, and the supercapacitor does not share any power. During the remaining period, the load demand changes suddenly, and the supercapacitor comes into play. Fig 5 demonstrates how the supercapacitor assists the battery in meeting the load demand when sudden changes in load power occur.

CONCLUSION

Battery hybridization with supercapacitors is an effective means of reducing stress on the battery. Therefore, the use of supercapacitors is beneficial for improving the battery's lifespan and efficiency. An energy management strategy aimed at sharing the power demand of the load between the battery and the supercapacitor is also presented, ensuring that both operate within their allowed range and at their optimal efficiency.

ACKNOWLEDGMENT

The project presented in this paper is supported by the Laboratory of Industrial Technology and the Information (LTII) of Bejaia University under the patronage of the General Directorate of Scientific Research and Technological Development (DGRSDT), Algeria.

REFERENCES

[1] Zineb Cabrane, Mohammed Ouassaid, Mohamed Maaroufi1, « Battery and supercapacitor for photovoltaic energy storage: a fuzzy logic management »,IET Renew. Power Gener., Vol. 11, pp. 1157-1165, 2017.

[2] Kollimalla SK, Mishra MK, Narasamma NL. , « Design and analysis of novel control strategy for battery and supercapacitor storage system », IEEE Trans Sustain Energy 2014.

[3] S. Sikkabut et al, « "Control of High-Energy High-Power Densities Storage Devices by Li-ion Battery and Supercapacitor for Fuel Cell/Photovoltaic Hybrid Power Plant for Autonomous System Applications», IEEE Transactions on Industry Applications, vol. 52, pp. 4395-4407, October. 2016.

[4] Wang Y, Liu C, Pan R, et al, « Modeling and state-of-charge prediction of lithium-ion battery and ultracapacitor hybrids with a co-estimator», J. Energy 2017.

[5] Logerais, P.O.; Riou, O.; Camara, M.A.; Durastanti, J.F. Study of photovoltaic energy storage by supercapacitors through both experimental and modeling approaches. J. Sol. Energy 2013.

[6] Wang Y, Zhang X, Liu C, et al, « Multi-timescale power and energy assessment of lithium-ion battery and supercapacitor hybrid system using extended Kalman filter», J Power Sources 2018.

[7] L. Zubieta and R. Bonert, "Characterization of double-layer capacitors for power electronics applications," IEEE Trans. Ind. Appl., vol. 36, no. 1, pp. 199-205. 2000.

Energy management for renewable electricity production system including hybrid hydrogen sub-system

Nourredine ZIDANE , Sofia Lalouni Belaid

Laboratoire de Technologie Industrielle et de l'Information (LTII), Faculté de Technologie. Université de Bejaia. Algérie
nourredine.zidane@univ-bejaia.dz, sofia.lalouni@univ-bejaia.dz

***Abstract*— This paper presents an optimal energy management method for a hybrid renewable power generation system with hydrogen storage, based on a fuzzy controller and local controls for each converter. The system consists of photovoltaic solar panels as the primary energy source, a fuel cell, an electrolyzer, hydrogen storage tanks, batteries and electrical converters. The energy management method is based on a fuzzy logic algorithm to manage the excess energy from the solar panels and satisfy the load while taking into account the cost and lifetime of the system. Simulation results show that the proposed management method limits the current/voltage constraints, that extends the life of the hydrogen sub-system, and reduces the total cost of the system while ensuring the load demand requirement.**

***Keywords:* — Hydrogen energy system, Photovoltaic energy, Fuzzy logic controller, Energy management.**

I. INTRODUCTION

The intermittent nature of solar energy requires further study to meet the energy needs of consumers. Although solar photovoltaic is a clean energy resource, its power output is dependent on meteorological conditions, makes the production estimate inaccurate. Storing excess energy and using it at times of shortages makes solar systems a more competitive energy source.

Conventional battery storage remains expensive, but hydrogen energy storage systems have proved to be promising and competitive for the future [1,2]. On the other hand, appropriate energy management is needed in all hybrid systems to satisfy the energy demanded by the load when the photovoltaic panels cannot produce energy for a period of time. References [3,4,5] have shown some examples of energy management, the purpose was to verify the performance of the hydrogen hybrid system at all times and for long periods of time, e.g. months, years or even during the lifetime of the hybrid system. However, the costs of using the components or an analysis of their costs were not taken into account in the management system. A management method was made in [6] to optimize energy production, this management method did not take into account the costs, but the author developed an economic variable to evaluate the total cost of the system.

In this work, the cost of using energy sources was calculated and taken into account, and some of the parameters used in the management system were optimized using a fuzzy controller. These costs are updated every year according to the lifetime of each element, so that the management system improves the life of the system. The study is carried out over one year, including an estimate of the number of fuel cells, electrolysers and batteries required for a 20-year life of the overall system shown in Fig. 1.

II. STAND-ALONE HYBRID SYSTEM

The selected power system configuration is shown in Fig 1. The hybrid system consists of a photovoltaic generator, an electrolyzer, hydrogen tanks and a fuel cell interconnected to the DC bus by DC/DC converters. A battery provides the transient energy demand and peak loads required during peak consumption; the battery provides all other load variations.

A. Solar photovoltaic panels

Photovoltaic solar energy is the main energy source of the autonomous system presented in our study. The production of electrical energy based on photovoltaic solar energy is done by solar panels, the latter are made up of solar cells connected in series/parallel to provide the desired voltage and current. A solar cell is manufactured at the junction base of a semiconductor material.

The electrical energy coming from the photovoltaic generator is given by the Eq. 1 and Eq. 2 [7,8].

$$P_{PV} = i_{PV}.V_{PV}.\eta_{PV} \quad (1)$$

$$i_{PV} = i_L - i_0\left[\exp\left(\frac{q\left(V_{PV}+R_S i_{PV}\right)}{AKT}\right)-1\right]-\frac{V_{PV}+i_{PV}R_S}{R_{Sh}} \quad (2)$$

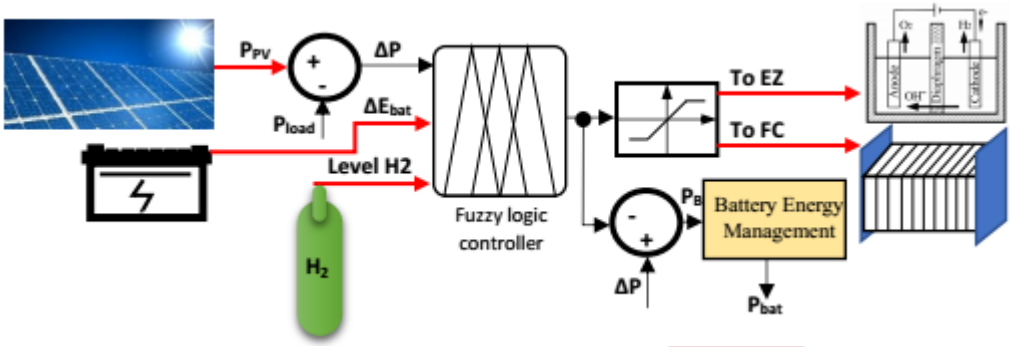


Figure 1. Overall energy management system.

Where V_{PV} and i_{pv} are the solar cell voltage and current, respectively, i_L is the current source, R_{Sh} and R_{Se} are the internal shunt and series resistances, A is the ideality factor of the pen junction, K is the Boltzman constant, T is the cell temperature, i_0 is the diode reverse saturation current, and q is the electron charge.

B. *Fuell Cell dynamic model*

There are currently different types of fuel cells and a great deal of research has been carried out on the equivalent electrical model depicted in Fig. 2. [9,10].

The output voltage V_{FC} of a single cell can be defined in (3)

$$V_{FC} = E_{Nernst} - V_d - V_{ohm} \tag{3}$$

Where E_{Nernst} is the thermodynamic potential of the cell and it represents its reversible voltage; V_{ohm} is the ohmic voltage drop [9,10,11].

$$E_{Nerst} = 1,229 - 0,85.10^{-3}(T - 298,15) + 4,31.10^{-5}.T\left[\ln(pH_2) + \frac{1}{2}\ln(pO_2)\right] \tag{4}$$

$$\frac{dV_d}{dt} = \frac{1}{C} i_{FC} - \frac{1}{\tau} V_d \tag{5}$$

$$V_{ohm} = i_{FC}(R_M + R_C) \tag{6}$$

Where pO_2, pH_2 is the partial pressure (atm) of oxygen and hydrogen respectively, i_{FC} is fuel cell actual current (A), C is the equivalent electrical capacitance (F), T is the membrane temperature (°K), $R_{M\ is}$ equivalent membrane resistance (Ω), Rc is membrane equivalent contact resistance and τ is the FC electrical time constant (s), defined as [9,10]:

$$\tau = C.\left(\frac{V_{act} + V_{con}}{i_{FC}}\right) \tag{7}$$

Where V_{act} is the voltage drop due to the activation of the anode and of the cathode and $Vcon$ represents the voltage drop resulting from the concentration or mass transportation of the reacting gases [8,9].

$$V_{act} = -\left[\zeta_1 + \zeta_2.T + \zeta_3.T.\ln(Co_2) + \zeta_4.T.\ln(i_{FC})\right] \tag{8}$$

$$V_{con} = -B.\ln\left(1 - \frac{J}{J_{\max}}\right) \tag{9}$$

Where: $\mathcal{E}_1$, $\mathcal{E}_2$, $\mathcal{E}_3$ and $\mathcal{E}_4$ are parametric coefficients based on electrochemical kinetics and thermodynamic laws, J is actual FC current density (A/cm²), [10].

The gas concentration can be calculated using the following equation. For oxygen [10], for example, we have:

$$Co_2 = \frac{Po_2}{\left(5,08.10^6.e^{-(498/T)}\right)} \tag{10}$$

C_{O2} concentration of oxygen in the catalytic interface of the cathode (mol/cm³), C_{H2} concentration of hydrogen in the catalytic interface of the anode (mol/cm³)

The amount hydrogen consumed by the fuel cells (M_{FC}) can be calculated using equation (11)

$$M_{FC} = 3600.\frac{i_{FC}.m_{H2,act}}{2.F.m_{H2,th}} \tag{11}$$

Where $m_{H2,th}$ is the theoretical hydrogen flow rates through the FC, $m_{H2,act}$: are the and actual hydrogen flow rates through the FC.

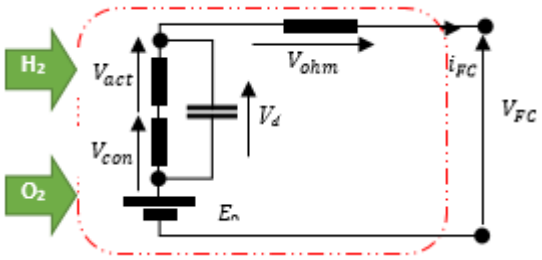


Figure 2. Simplified circuit of the Fuel Cell.

C. *Electrolyzer*

In this work, the hydrogen production rate of the electrolyzer is calculated from Faraday's law.

The hydrogen produced in the electrolyzer, n_{H2} (mol/s) is given in (12) [12,13].

$$n_{H_2} = \frac{n_F . n_c . i_e}{2.F} \quad (12)$$

Where n_c is the number of cells in series; i_e (A) is the electrolyzer current (C/mol), F is the Faraday constant; and n_F is the Faraday efficiency, can be expressed by (13) [12].

$$n_F = 96,5.\exp\left(\frac{0,09}{i_e} - \frac{75,5}{i_e^2}\right) \quad (13)$$

D. Battery

The battery is an essential storage device for storing electrical energy for maximum use of intermittent renewable resources. In this work, the battery is used as an auxiliary source to improve the flexibility, speed and lifetime of the PEM fuel cell. Eq. 14 gives the amount of energy stored in battery [14,15].

$$E_b = \int \left(P_{b.dish\arg} - P_{b.ch\arg} . n_b\right).dt \quad (14)$$

Where $P_{b.disharg}$ represents battery power when it is discharging, $P_{b.charg}$ represents battery power when it is charging and η_b is the efficiency of the battery.

The state of charge of the battery is calculated in Eq (15) [15].

$$SOC(\%) = 100\left(1 - \frac{\int i_{bat}.dt}{Q}\right) \quad (15)$$

Where Q (Ah) is the maximum battery capacity, and i_{bat} is the battery current.

E. hydrogen tank

The hydrogen produced by the Electrolyser is stored in liquid or gaseous form in storage tanks. The tank pressure is calculated by the following equation [16,17,18].

$$P_{tank} - P_{tank,init} = z\frac{N_{H_2}.R.T_{tank}}{M_{H_2}.V_{tank}} \quad (16)$$

F. Power electronics converters

The amplitude of the PV output voltage is variable and depending on the energy received, a DC/DC converter is used to stabilize the output voltage. To charge and discharge the storage battery, a bi-directional DC/DC converter is used. The PEMFC and the Electrolyser are controlled by a DC/DC converter.

III. MANAGEMENT STRATEGY APPLIED

The Energy Management System (EMS) needs to control the power flow between the PV system, electrolyzer, fuel cell, battery storage and the load. It's designed to meet charging needs throughout the day and after sunset while preserving the components of the hybrid system.

In this work, the fuzzy controller delivers the current references of the hydrogen subsystem, these references are injected to the local controls of the DC/DC converters, a local control to ensure the regulation of the proton exchange membrane fuel cells (PEMFC) and the electrolyzer current has been adopted.

A. Fuzzy control of a PEMFC and Electrolyzer

The fuzzy control system aims to anticipate the start/stop of the FC and the electrolyser and to improve their respective lifetimes by taking into account the current stress. Pout is designed as the output variable of the fuzzy control system. The architecture of the FLC is shown in Fig 3.

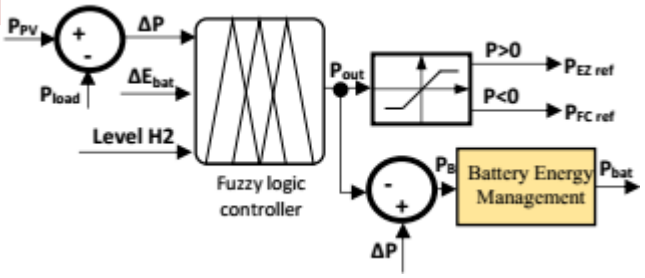


Figure 3. Fuzzy logic supervisor and controlled system.

The battery is used as a back-up source to absorb and compensate the energy in the DC bus. Then it undergoes a significant number of charge/discharge cycles, and to preserve its lifetime by limiting its minimum discharge to Soc_{min}=40% and its maximum charge to Soc_{max}=100%. The battery energy management complementary is depicted in Fig 4.

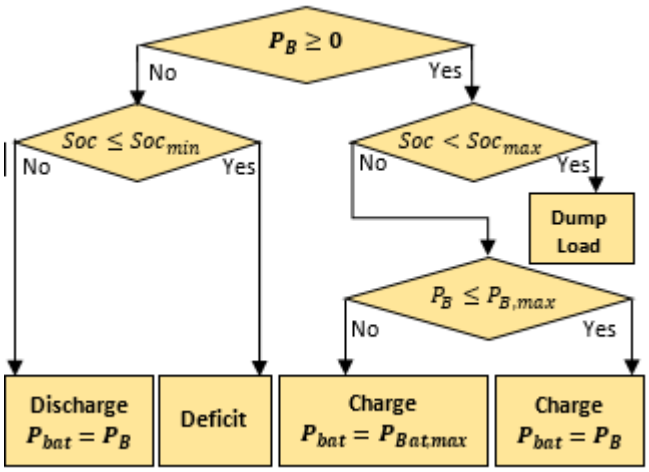


Figure 4. Flowchart of the battery energy management algorithm.

B. Fuzzy logic controller variables

The variables of the fuzzy logic controller are:

ΔP(t): the difference between Ppv(t) and Pload(t). A positive value of ΔP(t) designates an increment of the net power at times (t), while a negative value indicates a deficiency from the net power.

ΔEbat(t): the battery SOC at time t. The energy evolution along a period ΔT can be defined by Eq. (17) and Eq. (18) [19].

$$\Delta E_i(t) = \int_{t}^{t+\Delta T} P_i(t)dt \qquad (17)$$

$$\Delta E_i(n.\Delta T) = \int_{(n-1)\Delta T}^{n.\Delta T} P_i(t)dt \approx P_i\left[(n-1)\Delta T\right]\Delta T \qquad (18)$$

Trapezoidal and triangular membership functions are used for the linguistic variable's input/output of the fuzzy control system as shown in the Fig 5. The aim is to simplifying computer calculations on the FC, and the electrolyzer control signal.

In order to keep the effectiveness of the controller fuzzy in terms of rules and decisions, we use different language variables. ΔE(t) used seven linguistic variables (Fig 5(a)). ΔEbat(t) is represented by three inguistic variables (Fig 5(b)). Level H2 has three linguistic variables (Fig 5(c)). The output, P_{out} is represented with five linguistic variables (Fig 5(d)).

Finally, Table 1 shows the basis of the control rules for the three controller inputs, which will concretize the defined evaluation criteria.

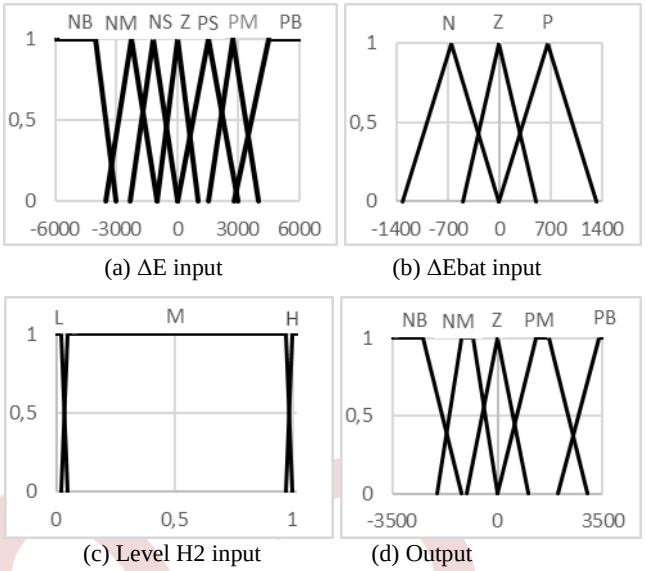
TABLE I. CONTROL RULE BASE

ΔE		NB	NM	NS	Z	PS	PM	PB
ΔE_{Bat}	L_H2							
N	L	Z	Z	Z		Z	PM	PB
	M	NB	NB	NB		Z	Z	PB
	H	NB	NB	NB			Z	
Z	L	Z	Z	Z		PM	PM	PB
	M	NB	NB	NM	Z	Z	PM	PB
	H	NB	NB	NM			Z	
P	L					PM	PB	PB
	M		Z			PM	PB	PB
	H						Z	

IV. SIMULATION AND RESULTS

The proposed method was carried out and simulated under the MATLAB-Simulink environment, the structure and sizing of the hybrid system was the subject of previous work [20].

The management system provides power references via a fuzzy controller, these power references converted to current references, used to battery controller and EZ current via a DC/DC converter.



(a) ΔE input (b) ΔEbat input

(c) Level H2 input (d) Output

Figure 5. Membership functions.

The PEMFC and EZ unit lifetime is shown in Fig. 6, as a function of the HS life time. When the FC reaches a nominal voltage 18% lower than the nominal start-up voltage, the element is replaced.

The storage level of hydrogen tanks during the four seasons of the year is shown in Fig. 7. A total discharge of the hydrogen tank is allowed, as the hydrogen level and the number of cycles do not influence the life of the tank. It is clear that the demand is largely satisfied, in summer and spring, the hydrogen level in most cases exceeds 40%. In winter and autumn, however, there are days when the tank is empty.

Figure. 8 shows the powers evolution during the four seasons of the year of Delta P (difference between the PV generated and required load power), the power supplied to the EZ, the power evolution of the supply battery and the energy generated by the fuel cells. To better visualize the evolution of the HS power during the four seasons presented in Fig. 8, a zoom has been presented in Fig. 9. It can be seen that the battery plays the role as an energy damper during peak production and it allowed to reduce the peaks currents supposed to be sent to EZ, on the other hand, this battery plays the role as an energy compensator during high demands, and allows the major power for the charge to be shared with PEMFC.

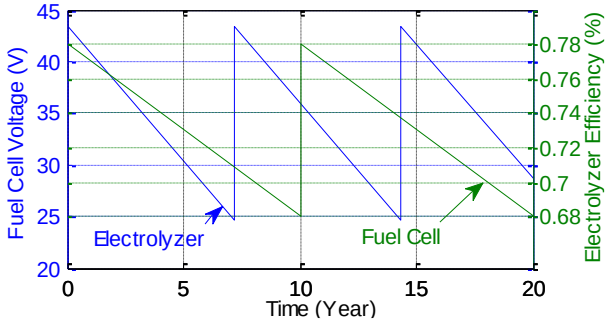


Figure 6. Unit life of the PEMFC and EZ.

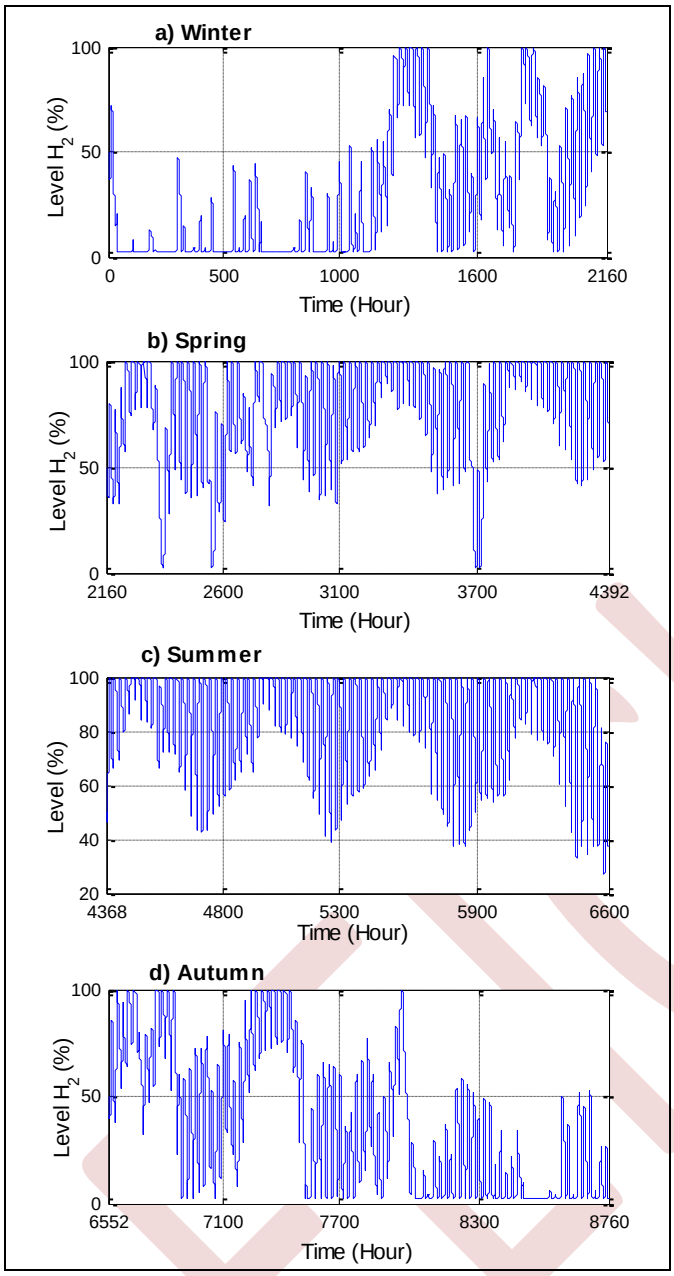


Figure 7. Storage level of hydrogen tanks.

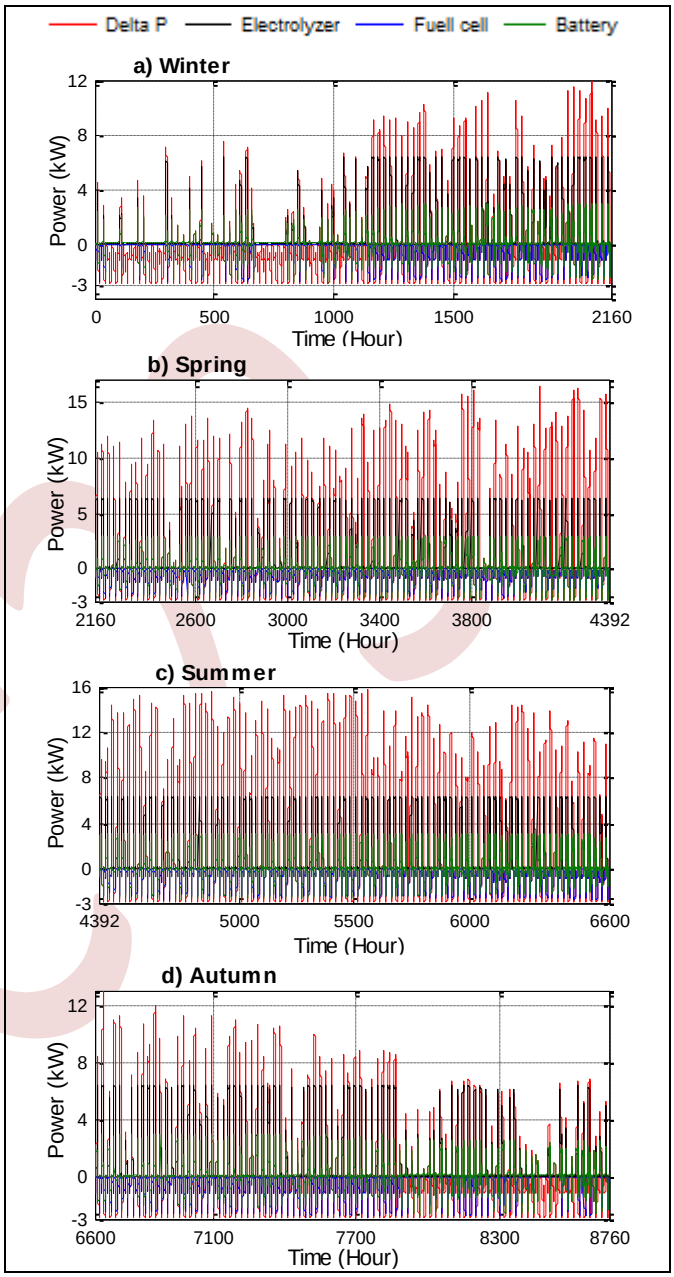


Figure 8. Powers evolution during the four seasons (Delta P, EZ, FC and battery).

V. CONCLUSION

An energy management method for a hybrid renewable energy system including a hydrogen subsystem as energy storage was simulated under the Matlab-Simulink environment. The objective was to test in real time the management method with a fuzzy controller based on the maximum current/voltage value of the PEM and the electrolyser. The simulation results show a significant improvement in the current/voltage peaks of the PEM and EZ compared to conventional management. The fuzzy logic management method takes into account the variation in the energy produced, the variation in the energy stored in the battery and the level of the hydrogen.

In addition, the use of a battery as an energy buffer makes fuzzy logic management more important in controlling the PEM and EZ currents, thus avoiding operation at maximum power at times of consumption or production peaks. The robustness and reliability of this proposed method has been evaluated and simulated under Matlab-Simulink.

This method allowed us to evaluate the different conditions of intermittency of renewable energy sources that the hydrogen hybrid system and its control system have to face. Finally, the proposed method allowed us to manage the instantaneous energy according to the energy produced, the consumption and the life span of the most expensive elements, thus extending the life span of the overall system.

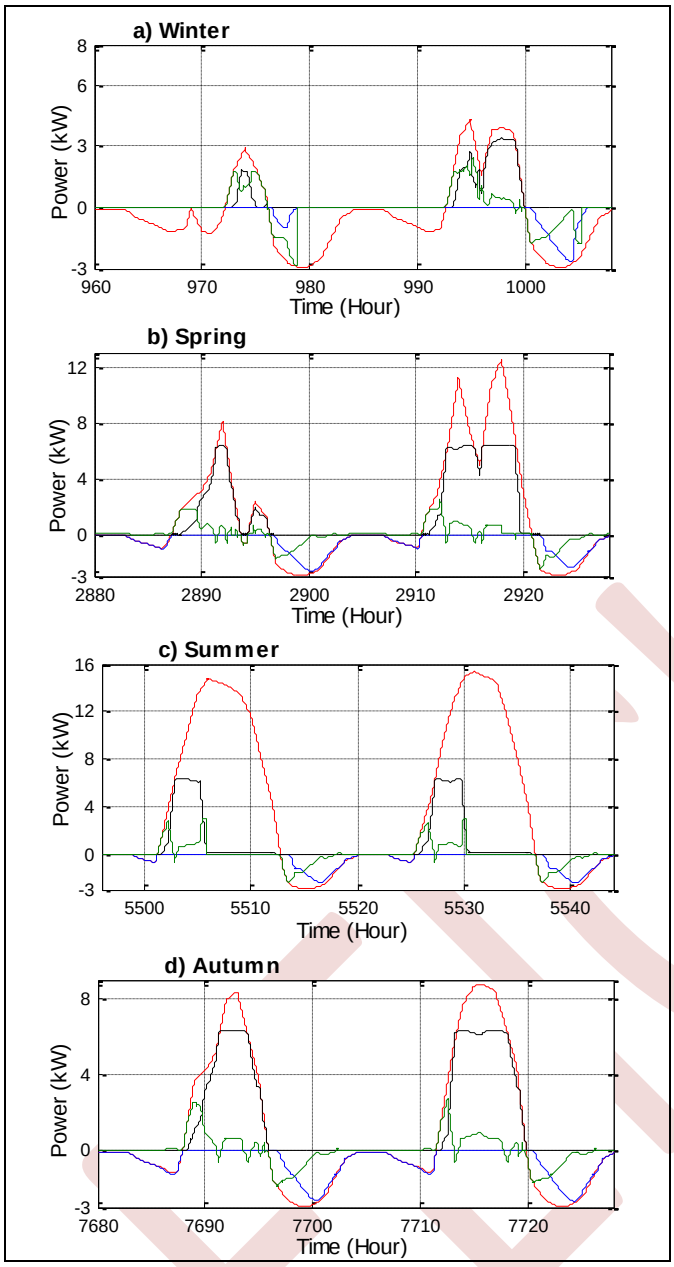


Figure 9. Zooms of powers evolution of the HS during the two days, for the four seasons.

REFERENCES

[1] A. Magrini, S. Lazzari, L. Marenco, G. Guazzi, "A procedure to evaluate the most suitable integrated solutions for increasing energy performance of the building's envelope, avoiding moisture problems," International Journal of Heat and Technology, 35(4), pp. 689-699, 2017.

[2] Ivalin, P., Paolo, G., "Power-to-hydrogen as seasonal energy storage: an uncertainty analysis for optimal design of low-carbon multi-energy systems," Applied Energy, 274, pp. 115197, 2020.

[3] Lux B, Pfluger B. "A supply curve of electricity-based hydrogen in a decarbonized European energy system in 2050," Applied Energy; pp. 269: 115011, 2020.

[4] Dash V, Bajpai P. "Power management control strategy for a stand-alone solar photovoltaic-fuel cell–battery hybrid system," Sustainable Energy Technologies and Assessments;9, pp. 68–80, 2015.

[5] Higuita C. M, Agbossou K, Kelouwani S, Dubé Y. "Experimental evaluation of a power management system for a hybrid renewable energy system with hydrogen production," Renewable Energy;113:1086–1098, 2017.

[6] Sadigh Behzadi M, Niasati M. "Comparative performance analysis of a hybrid PV/FC/battery stand-alone system using different power management strategies and sizing approaches," Int J Hydrogen Energy;40 (1): 538–548, 2015.

[7] Tabanjat A, Becherif M, Hissel D, Ramadan H. S. "Energy management hypothesis for hybrid power system of H2/WT/PV/GMT via AI techniques," Int J Hydrogen Energy;43 (6):3527–3541, 2018.

[8] S. Lalouni. Belaid, "Improved IM DTC by using a Fuzzy Switching Table in PV Applications," Elektrotehniški vestnik, 88, 1-2, pp. 26–32, 2021.

[9] J. F. Z. Zerhouni, M. Telidjane, "Branchement direct d'une pile à combustible à membrane échangeuse de protons à une charge et modelisation, " Rev. Roum. Sci. Techn. – Électrotechn. et Énerg, 60, 4, pp. 387–396, 2015.

[10] 21. M. Uzunoglu, O.C. Onar, M.S. Alam, "Modeling, control and simulation of a PV/FC/UC based hybrid power generation system for stand-alone applications," Renewable Energy, 34, pp. 509–520, 2009.

[11] 22. M.J. Khan, M.T. Iqbal, Dynamic modeling and simulation of a small wind–fuel cell hybrid energy system, Renewable Energy, 30, pp. 421–439, 2005.

[12] L. Xueqin, W. Yinbo, L. Jie, Z. Yangyang, C. Chao, W. Peisong, M. Lingzheng, "Energy management of hybrid electric vehicles: A review of energy optimization of fuel cell hybrid power system based on genetic algorithm," Energy Conversion and Management, 205, pp. 112474–500, 2020.

[13] A. Kadri, H. Marzougui, A. Aouiti, F. Bacha, "Energy management and control strategy for a DFIG wind turbine/fuel cell hybrid system with super capacitor storage system," Energy, 192, pp. 116518–57, 2020.

[14] T. Wang, Q. Li, X. Wang, Y. Qiu, M. Liu, X. Meng, L. Jincheng, W. Chen, "An optimized energy management strategy for fuel cell hybrid power system based on maximum efficiency range identification," Journal of Power Sources, 445, pp. 227333–44, 2020.

[15] J. Liu, S. Cao, X. Chen, H. Yang, J. Peng, "Energy planning of renewable applications in high-rise residential buildings integrating battery and hydrogen vehicle storage," Applied Energy, 281, pp. 116038–54, 2021.

[16] A. A. Ahmed, R. Hegazy, A. Mohammad Ali, "Enhancing the operation of fuel cell-photovoltaic-battery-supercapacitor renewable system through a hybrid energy management strategy," International Journal of Hydrogen Energy, 46, 8, pp.6061–75, 2021.

[17] P. Bhat Nempu, N. Sabhahit Jayalakshmi, "A new power management strategy for PV-FC-based autonomous DC microgrid," Archives of Electrical Engineering, 67, 4, pp. 815–828, 2018.

[18] L. Gerlach, T. Bocklisch, "Experts versus Algorithms? Optimized Fuzzy Logic Energy Management of Autonomous PV Hybrid Systems with Battery and H2 Storage," Energies. 14, 6, pp. 1777, 2021.

[19] Chaouali, W. B. Salem, D. Mezghani, A. Mami, "Fuzzy Logic Optimization of a Centralized Energy Management Strategy for a Hybrid PV/PEMFC System Feeding a Water Pumping Station," International Journal of Renewable Energy Research, 8, 4, pp. 2190–98, 2018.

[20] N. Zidane, S. Lalouni, "*Optimal sizing of hybrid PV/FC/EZ/BAT system using* LPSP *concept*", 5th International Conference on Electrical Engineering in Boumerdes, Algeria, ICEE'2017.

Model Predictive For Enhancing Resistive Droop Control stability In Isolated AC Microgrid

Larbi Bousbia[1], Riad Toufouti[2],

[1,2] Department of Electrical Engineering,University of mohamed cherif messaadia, Souk ahras, Algeria

[1] l.bousbia@univ-soukahras.dz [2] riad.toufouti@univ-soukahras.dz

***Abstract*—This work presents Finite Control Set Model Predictive Control (FCS-MPC) applied in the primary microgrid control layer based on resistive droop control technique. Due to its appropriateness with the microgrid line impedances, furthermore, predictive control replaces the voltage and current loops in linear controls. Which gives the system fast responses, stabilizes voltage and frequency, as well as guarantees good power sharing among parallel inverters. The simulation results demonstrate the strongest capability of the proposed control to keep the voltage and frequency deviations within acceptable limits, all with accurate power sharing and high voltage quality.**

Keywords: **Isolated Microgrid, Resistive Droop Control, Finite Control Set Model predictive, Power sharing.**

I. INTRODUCTION

The microgrid system serves as a link connecting various forms of distributed energy resources (DERs), including but not limited to fuel cells, micro turbines, photovoltaics (PV), and wind turbines, with the primary grid. The microgrid can be described as a versatile electrical network composed of diverse DERs, power electronic converters, energy storage systems, and various load types. These components operate cohesively alongside an energy management system, control mechanisms, and protective measures.Microgrids (MG) provide a myriad of benefits, including reduced carbon emissions, effective solutions for addressing power quality concerns, enhanced grid reliability, improved market strategies, optimized energy scheduling, and more efficient power delivery to rural communities[1].

The microgrid (MG) is typically linked to the primary grid through a point of common coupling (PCC). It functions in either grid-connected mode, where the frequency and voltage levels are dictated by the primary grid, or in islanded mode. Islanded mode can occur intentionally or unintentionally due to network faults. In islanded mode, precise control of frequency and voltage becomes crucial to ensure the system operates effectively[2].All with a guarantee of accurate power sharingamong the parallel-connected inverters that interface with the distributed generators (DGs).

Islanded microgrids are particularly susceptible to disturbances, leading to increased challenges in controlling the MG. To address these challenges, a hierarchical control structure has been introduced, consisting of three control levels: primary, secondary, and tertiary control. The primary control focuses on power sharing, voltage and frequency regulation within the MG[3].Parallel connections in isolated microgrids enhance reliability by allowing multiple power sources to work together. This configuration improves power sharing, increases overall system capacity, and ensures a stable and resilient energy supply[4].Various control structures are implemented to operate parallel-connected inverters, which can be categorized as centralized, such as master-slave control, and decentralized, like droop control techniques. The latter is widely used in the scientific community due to its ability to operate without the need for communication among the parallel-connected inverters

A droop control strategy is implemented by adjusting the output frequency and voltage of inverters in response to the active and reactive power they deliver. This adjustment is based solely on local measurements, which enhances its reliability, flexibility, and eliminates issues related to the physical location of units[5].In contrast to the conventional droop approach, the resistive droop method (P-E/Q-F) adjusts the voltage based on active power and the frequency based on reactive power, aligning with the resistive characteristics commonly found in microgrid line distributions [6].Nonetheless, the droop approach does suffer from several drawbacks that limit its application, including slow transient response, deviations in voltage and frequency, and dependence on the output inverter's impedance.

The finite control set model predictive control (FCS-MPC) is a promising option for primary microgrid control. It offers improved dynamic response, a discrete nature similar to electronic device converters, and straightforward implementation[7]. This makes it highly effective in enhancing transient response and ensuring the stability of both voltage and frequency.It employs a filter in conjunction with a discrete-time converter model to predict the system's output behavior for all possible input combinations through predefined cost function [8].

The rest of the paper is organized as follows:Section 2: Description of the microgrid system in isolated mode under study, along with the resistive droop approach. Section 3: Provide the FCS-MPC model predictive concept with a

comprehensive mathematical model of VSI converter and LC output filter.Section 4:The simulation result and discussion. The conclusion of paper in Section 5.

II. THE ISOLAND MICROGID SYSTEM AND RESISTIVE DROOP APPROACH

A. The Island Microgrid

Figure 1 presents two distributed generators (DGs) connected in parallel to the point of common coupling (PCC). For feeding a common load .Each DG is interfaced with a voltage source converter (VSI) consisting of a two-level, three-phase inverter. The output of each VSI is connected to an LC filter designed to eliminate high-frequency components.The Z-line impedances are assumed to be similar and exhibit resistive behavior.

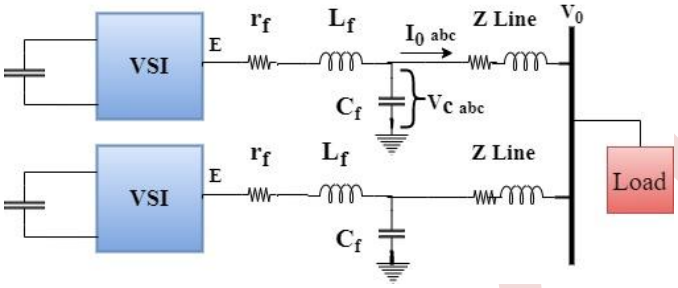


Figure 1. The island microgrid under study.

B. The Resistive Droop Approach

The droop control method is widely embraced within power systems and serves as a vital element in the primary control systems of microgrids. It plays a significant role in ensuring the efficient and stable operation of inverters operating in parallel. This is achieved by maintaining voltage and frequency deviations within acceptable limits while also guaranteeing precise power distribution among the parallel-connected distributed generators (DGs).The resistive droop control method, denoted as (P-E/Q-F), represents one among various types of droop control strategies. This approach takes into account the predominantly resistive characteristics of the impedance lines within the system. It determines the flow of power based on these considerations.

$$Q = \frac{-EV_0}{R}\sin\delta \approx \frac{-EV_0}{R}\delta \quad (1)$$

$$P = \left(\frac{EV_0}{R}\cos\delta - \frac{V_0^2}{R}\right) \approx \frac{V_0}{R}(E - V_0) \quad (2)$$

where, E represents the output voltage of the inverter, while V_0denotes the voltage at the Point of Common Coupling (PCC). R signifies the output resistance of the inverter, and δ represents the phase voltage difference between E and V_0,ofen called the power angle. From equations (1) and (2), it clear that active power is primarily influenced by the inverter voltage amplitude E, while the power angle δ regulates reactive power. Hence, the voltage reference for the inverter can be expressed in the following manner.

$$F = F_n^* + m_p(Q - Q^*) \quad (3)$$

$$E = E_n^* - n_q(P - P^*) \quad (4)$$

where,$P^*$and Q^*denote the nominalactive and reactive power reference. F and Esignify the nominal frequency and the output voltage amplitude, respectively. While P and Q represent the actual real and reactive power output power.E_n^* and F_n^* are the magnitude and frequency references.m_p and n_q denote the proportional drooping frequency and voltage ,respectively. These parameters are subsequently designed as functions of the nominal power rating of the inverter.

III. FINITE CONTROL SET MODEL PREDICTIVE

The Model Predictive FCS-MPC approach is based on the minimization of a designed cost function, aiming to provide an optimal output. This approach involves anticipating future values within a predefined time horizon by utilizing the mathematical model of the system[9].

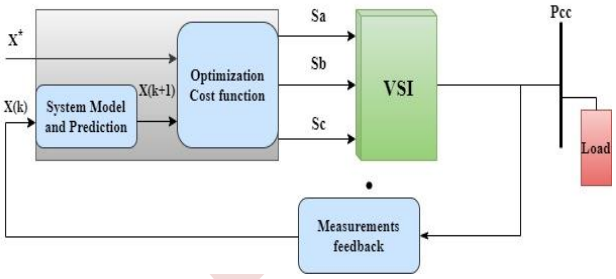


Figure 2.The FCS-MPC model predictive structure.

The model predictive use the feedback measurement x(k) and the model of system to predict the future value x(k+1) and through the cost function .where x^* is the reference value.

$$J = (x^* - x(k+1))^2 \quad (5)$$

A. Predictive Voltage Control

The control performed in αβ frame, and the x* is the voltage reference generated by the resistive droop, while x(k) is the voltage measured across the filter capacitor(V_C) Fig .1. Also the switching signals resulting from the cost function, determine the output Voltage of the Voltage Source Inverter (VSI), which provided as follows:

$$V_i = \frac{2}{3}V_{dc}e^{i(j-1)\frac{\pi}{3}}, \qquad j = 0; \ldots\ldots; 7 \quad (6)$$

Where V_i is output voltage vector of the VSI inverter, with Two of them having zero voltage.

The mathematical model of the isolated microgrid system under investigation can be developed using the following equations:

$$C\frac{dV_c}{dt} = I_f - I_0 \quad (7)$$

$$V_i = V_c + V_f + R_f I_f \quad (8)$$

Where,I_f and V_f denote the current and the voltage inductor, respectively.I_0 represent the load current .whileV_c and V_i signify the capacitor voltage and the output voltage inverter terminal. According to that the system state space model represented as:

$$\frac{dx}{dt} = Ax + B_1 V_i + B_2 I_0 \quad (9)$$

$$x = \begin{bmatrix} I_f \\ V_c \end{bmatrix}, A = \begin{bmatrix} \frac{-R_f}{L_f} & \frac{-1}{L_f} \\ \frac{1}{C_f} & 0 \end{bmatrix}, B_1 = \begin{bmatrix} \frac{1}{L_f} \\ 0 \end{bmatrix} B_2 = \begin{bmatrix} 0 \\ \frac{-1}{C_f} \end{bmatrix} \quad (10)$$

The system model in discrete time expressed as:

$$X(K+1) = A_d X(K) + B_{1d} V_i(k) + B_{2d} I_0(K) \quad (11)$$

Where

$$A_d = e^{A T_s},\ B_{2d} = \int_0^{T_s} e^{A\tau} B_1 d\tau, B_{2d} = \int_0^{T_s} e^{A\tau} B_2 d\tau$$

By approximating the exponential term and manipulating the previous equations, we can express the predicted capacitor voltage as follows:

$$V_c(k+1) = V_c(k) + \frac{T_s}{C_f}\left(I_f(K) - I_0(K)\right) \quad (12)$$

And the cost function in αβ frame expressed as:

$$j = \left(V^*_{c\alpha\beta} - V_{c\alpha\beta}(k+1)\right)^2 \quad (13)$$

Where $V^*_{c\alpha\beta}$ and $V_{c\alpha\beta}(k+1)$ are the resistive droop voltage reference and the anticipated future capacitor voltage, respectively .the result of cost function determine the voltage inverter vector that must applied on the output inverter.

IV. SIMULATION RESULT

To evaluate the proposed control approach, the islanded microgrid, as described in section two, was simulated using MATLAB Simulink software. Multiple scenarios were executed to showcase the control scheme's stability, robustness, and effectiveness in both transient and steady-state conditions across linear load conditions.Also the load step change test to validate the resistive droop control capability. the simulations parameters of system depicted in TABLE I .

TABLE I. SIMULATION PARAMETERS

	Simulation parameters		
	Power stage	***value***	***unit***
	Nominal RMS voltage	220	(V)
	Nominal frequency	50	f(Hz)
	DC voltage	700	(V)
	Filter inverter side	2.10^{-3} , 0.5	Lf(H),R(Ω)
	Filter capacitor	60	C (f)
	Load1equal Load 2	10 , 6	P(kw), Q(kvar)
	Line impedance VSI1 R , L	0.2 , 0.1e-3	(Ω), (H)
	Line impedance VSI2R , L	0.2 , 0.1e-3	(Ω), (H)
	Droop coeffetion m_p , n_q	3.10^{-4} ,-5.10^{-4}	
	Sampling time	25. 10-6	(s)

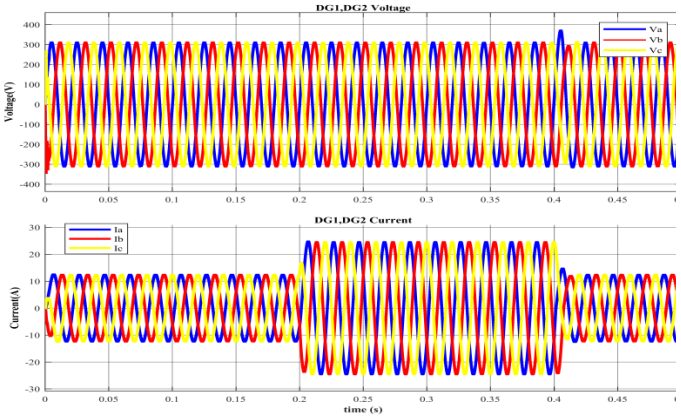


Figure 3. DG1,DG2 voltage and current.

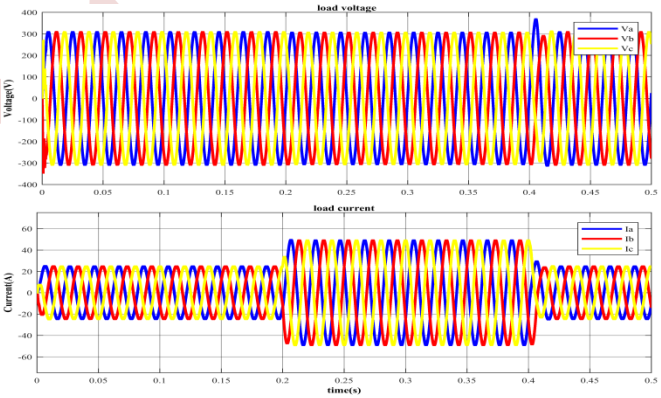


Figure 4. load voltage and current.

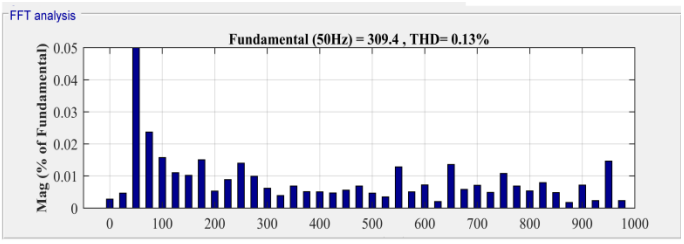


Figure 5.Total Voltage Harmonic Distortion (THD) .

To assess the performance of the isolated microgrid, the simulation was divided into three phases. In the first phase, at time zero (0) seconds, a 10 kW and 6 kVAR RL load was

connected to the microgrid system. The voltage at the output of each inverter and on the load side, as shown in Figure 3 and Figure 4, remained stable, maintaining a fixed value of 311V. These voltage waveforms also exhibited sinusoidal characteristics with a Total Harmonic Distortion (THD) of 0.13%, as depicted in Figure 5. Additionally, it is worth noting that the total load current was equally distributed between the two inverters.

At 0.2 seconds, the load was doubled by connecting the second RL load, and it was disconnected at 0.4 seconds. Consequently, the current doubled in both DGs and on the load side while maintaining the voltage and frequency at their nominal values. This demonstration highlights the exceptional performance of the FCS-MPC (Model Predictive Control) model in stabilizing the voltage at the Point of Common Coupling (PCC).

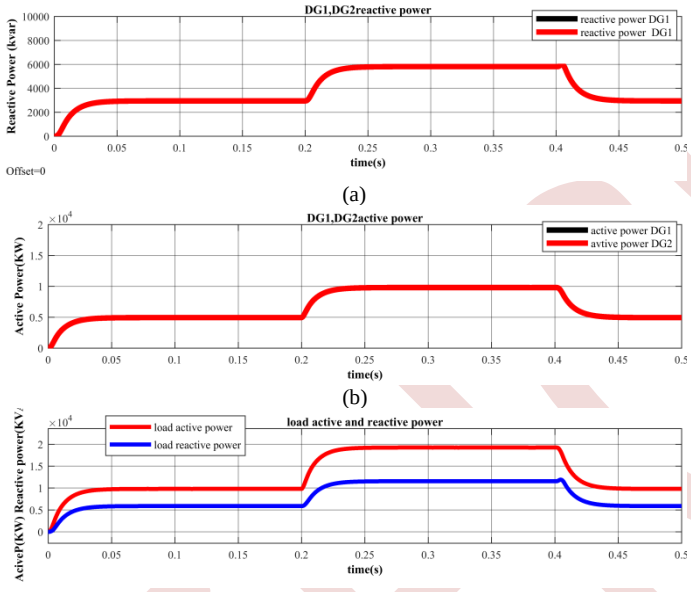


Figure 6.The output DGs and the load active and reactive power.

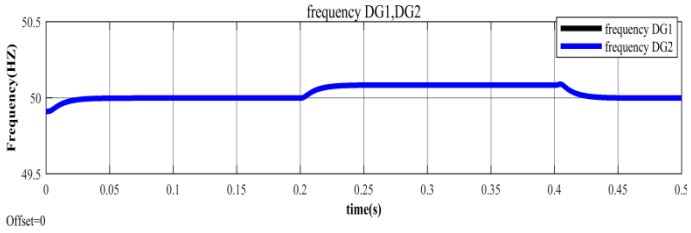


Figure 7.DG 1,DG2 frequency deviation.

Figure 6(a) illustrates the active power in both DG1 and DG2, showcasing precise power sharing between them. Additionally, Figure 6(b) displays the reactive power, further demonstrating the balanced operation of the system. In Figure 6(c), the active and reactive load throughout the simulation phases are depicted, with the load power equalling the sum of the two DG powers. These results collectively underscore the effectiveness and robust capabilities of the resistive droop control method under varying load conditions. Also figure 7. Shown the small frequency deviation under load step change which proven the resistive droop concept.

I. CONCLUSION

In this study, our investigation focuses on the utilization of the FCS-MPC (Model Predictive Control) approach within the primary islanded microgrid layer as a voltage controller.The primary objectives are to enhance the transient response of the system and ensure the stability of voltage and frequency while maintaining precise power sharing among the distributed generators (DGs). This control strategy is based on the adoption of resistive droop control, which serves as a fundamental component in achieving these goals.

The simulation results clearly showcase the exceptional performance of the proposed control strategy in terms of system stability, robustness, as well as the quality of power. Moreover, the results present the excellent compatibility of the resistive droop control with microgrid systems.

REFERENCE

[1] H. A. Rahman, M. S. Majid, A. R. Jordehi, G. C. Kim, M. Y. Hassan, and S. O. Fadhl, "Operation and control strategies of integrated distributed energy resources: A review," *Renewable and Sustainable Energy Reviews*, vol. 51, pp. 1412-1420, 2015.

[2] J. M. Guerrero, M. Chandorkar, T.-L. Lee, and P. C. Loh, "Advanced control architectures for intelligent microgrids—Part I: Decentralized and hierarchical control," *IEEE Transactions on Industrial Electronics*, vol. 60, pp. 1254-1262, 2012.

[3] A. Mohd, E. Ortjohann, D. Morton, and O. Omari, "Review of control techniques for inverters parallel operation," *Electric Power Systems Research*, vol. 80, pp. 1477-1487, 2010.

[4] A. Tuladhar, H. Jin, T. Unger, and K. Mauch, "Parallel operation of single phase inverter modules with no control interconnections," in *Proceedings of APEC 97-Applied Power Electronics Conference*, 1997, pp. 94-100.

[5] J. M. Guerrero, N. Berbel, L. G. de Vicuña, J. Matas, J. Miret, and M. Castilla, "Droop control method for the parallel operation of online uninterruptible power systems using resistive output impedance," in *Twenty-First Annual IEEE Applied Power Electronics Conference and Exposition, 2006. APEC'06.*, 2006, p. 7 pp.

[6] J.-J. Seo, H.-J. Lee, W.-W. Jung, and D.-J. Won, "Voltage control method using modified voltage droop control in LV distribution system," in *2009 Transmission & Distribution Conference & Exposition: Asia and Pacific*, 2009, pp. 1-4.

[7] S. Vazquez, J. I. Leon, L. G. Franquelo, J. Rodriguez, H. A. Young, A. Marquez, *et al.*, "Model predictive control: A review of its applications in power electronics," *IEEE industrial electronics magazine*, vol. 8, pp. 16-31, 2014.

[8] H. S. Khan, M. Aamir, K. Kauhaniemi, M. Mumtaz, M. W. Hassan, and M. Ali, "Improved finite control set model predictive control for distributed energy resource in islanded microgrid with fault-tolerance capability," *Engineering Science and Technology, an International Journal*, vol. 24, pp. 694-705, 2021.

[9] J. Rodriguez, M. P. Kazmierkowski, J. R. Espinoza, P. Zanchetta, H. Abu-Rub, H. A. Young, *et al.*, "State of the art of finite control set model predictive control in power electronics," *IEEE Transactions on Industrial Informatics*, vol. 9, pp. 1003-1016, 2012.

Study and manufacture of a parabolic solar concentrator with automatic tracking Experimental tests

MEBARKI Youcef, Laboratory LMER University A. Mira of Bejaia, Algeria
youcef.mebarki@univ-bejaia.dz

***Abstract*— The work carried out concerns a thermal and experimental study of conversion of solar energy into thermal energy using a parabolic concentrator. The orientation of the concentrator to solar radiation is ensured by an automatic tracking system. The prototype used to perform the tests essentially comprises: A solar reflector which is a parabola reflecting solar radiation and an absorber consists of a copper coil tube that will be the focus at which the rays will focus of the sun. The results obtained are important, we reached a temperature exceeding 380°C on the surface of the absorber.**

Keywords: solar radiation, parabolic concentrator, receiver, absorber, reflector, heat transfer fluid.

I. INTRODUCTION

Currently, several countries in the world are experiencing an unprecedented crisis in meeting their needs for energy products, such as oil or natural gas, because of the war in Ukraine. The major concern of these countries is the production of electricity and heating. Many countries around the world have begun to invest in renewable energies in order to minimize dependence on fossil fuels, in particular wind turbines, thermal concentrators and photovoltaics commonly called solar energy. However, investment in the latter mainly depends on the rate of sunshine during the year, as Algeria is one of the sunniest countries in the world which led us to become interested in this area [1, 2]. Generally, the studies already carried out mainly concern the capture of solar rays and their transformation into electrical energy. However, there are research studies which aimed to create a concentrator of solar rays whose thermal energy produced will be used for purposes other than the production of electricity. This work is dedicated to the creation of the parabolic solar concentrator with absorber equipped with automatic tracking, it concerns several disciplines namely thermal transfer, mechanics, electronics, and artificial intelligence.

II. MECHANICAL MANUFACTURE

II.1 The reflector

We took a parabolic plate, on which we glued, with thermal glue, mirrors which we cut into small squares so that they fit the rounded shape of the interior surface of the parabola. These mirrors have their shiny sides facing the sun. We chose mirrors because their reflection rate is 99.9%.

Table 1

Physical characteristics of the reflector	
big diameter	d = 0.9 m
little diameter	h = 0.08m
The opening angle	$\Psi_p = 38.95°$
Focal distance	f = 0.6328 m
Opening surface	$A_a = 0.6361\ m^2$
Mirrorless mass	m = 4.3kg

II.1.1Concentrator

This parameter indicates the quantity of energy concentrated at the collector. There are two types of solar concentration: geometric concentration (surface) and optical concentration (flux).

II.1.1.1 Geometric concentration

Defined by the ratio of the surface of the opening of the collector (Aa) and that of the receiver Ar: The higher the geometric concentration, the more the temperature increases.

$$Cg = \frac{A_a}{A_r} \qquad (1)$$

II.1.1.2 Optical concentration

It's the ratio between the energy on the surface of the absorber and energy of the opening of the parabolic [3]:

$$C_o = \frac{Ir}{Ia} \qquad (2)$$

Ir : The energy received on the opening of recepter.
Io : The energy received on the opening of paraboloid.
The concentration of parabolic concentrator is given by [3] :

$$C = 4.\frac{\sin^2\psi}{\theta^2} \qquad (3)$$

La concentration maximale $C_{max} = 46250$ pour $\psi = 90°$

II.1.2 The energy received when a paraboloid opens

This energy being the quantity of light reflected by the entire surface of the parabola, we must consider a differential region integrable over the entire surface of the parabola.

The differential surface is [4]: $dA_s = I.ds$

ds : longueur différentielle d'arc de la parabole.

I : longueur d'une bande différentielle sur la surface d'une cuvette parabolique.

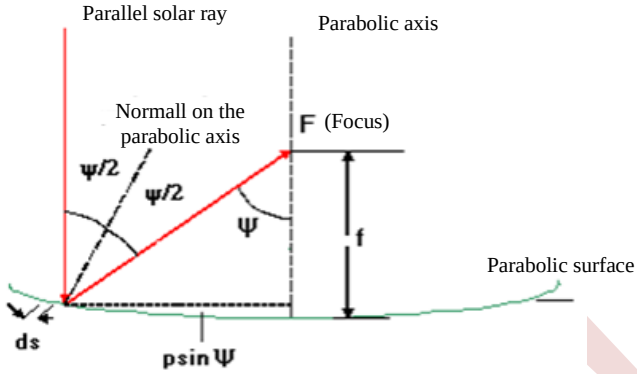


Fig. 1 Reflection of a parallel ray

$$ds = \frac{p \sin(d\psi)}{\cos(\frac{\psi}{2})} \quad (4)$$

The angle dψ is small, we set sindψ = dψ the equation becomes:

$$ds = \frac{p(d\psi)}{\cos(\frac{\psi}{2})} \quad (5)$$

$$dA_s = \frac{I.p.d\psi}{\cos(\frac{\psi}{2})} \quad (6)$$

All the reflected radiant flux (dIa) of this differential sector at the focal point is [4]:

$$dI_a = dA_s.I_b.\cos\left(\frac{\psi}{2}\right) = I.p.I_b.d\psi \quad (7)$$

Replacing p by its value, we find:

$$dI_a = \frac{2.f.I.Ib.d\psi}{(1+\cos\psi)} \quad (8)$$

$$I = \frac{4.\pi.f.\sin\psi}{(1+\cos\psi)^2} \quad (9)$$

The energy received when a paraboloid opens is [6]:

$$I_a = \int \frac{8.\pi.Ib.f^2\sin\psi.d\psi}{(1+\cos\psi)^2} \quad (10)$$

II.1.3 Solar power absorbed by the opening of the receiver

Arriving at the opening, this power is reduced due to losses. It is given by the following formula [4]:

$$Q_a = I_b . A_a . \alpha . \rho . \tau \quad (11)$$

Where

$$\eta_{op} = A_a . \alpha . \rho . \tau \quad (12)$$

The equation (11) becomes :

$$Q_a = \eta_{op}.I_b \quad (13)$$

ηop: Optical efficiency of the concentrator.

Ib: Energy received when the concentrator opens.

τ: Receiver transmission coefficient.

α: Receptor absorption coefficient.

ρ: Reflection coefficient of the parabola.

II.3 Absorber

The absorber must have good thermal conductivity and a good melting or degradation point, which is why we chose copper as the material for the absorbing device (thermal conductivity 386 W/m.K, melting point 1083 °C) [5]. The absorber is made up of a copper coil which is placed in a chimney pipe tube, insulated with glass wool to ensure good insulation, we then added pieces of aluminum foil between the absorber and the interior wall of the tube to take advantage of the cumulative temperature. The copper coil is 6mm in diameter and 1m in length, we modeled it to have a coil of 60mm in diameter and 15cm in length, the latter and put in a chimney pipe of 80mm in diameter and 20cm long, everything is put in another tube of the same material but 110mm in diameter and 20cm. The geometric concentration of this model is:

$$Cg = \frac{Aa}{Ar} = \frac{0.6361}{0.00282} = 225.008 \quad (14)$$



(a)



(b)

Fig. 2 a) drawing of the absorber, b) real image of the absorber

Table 2 Physical characteristics of the absorber

Absorber characteristics	
Coil diameter	d_2 = 0.06 m
Coil length	l_2 = 0.15 m
Capture surface	A_r = 0.002827 m^2
Mass of empty absorber	M_a = 0.5 Kg

II.1.4 Pursuit mechanism

The vertical rotation system is provided by an electric motor equipped with a drive chain. We added a support to provide better stability and resistance against swaying caused by the wind.



Fig. 3 Real image of the system

concentrator The modeling of the elements of the system was carried out using the SolidWorks mechanical design and manufacturing software, the assembly of these elements is done while respecting the given constraints in order to obtain the desired mechanism.



Fig. 4 Modeling of the prototype produced BAY SOLIDWORKS

III. POWER CORRESPONDING TO THERMAL LOSSES

Once the solar energy arrives at the opening surface of the receiver, its temperature is above the ambient temperature, this variation causes heat losses, defined by convection, by radiation and by conduction. The power corresponding to the thermal losses is given by the following expression [7]:

$$\mathbf{Qp = Qp\ .cv + Qp.r + Qp.cd} \quad (15)$$

Qp: Power corresponding to thermal losses.
Qp.cv: Losses by convection.
Qp.r: Radiation losses.
Qp.cd: Conduction losses.

III.1 Losses by convection

It is the loss of heat to the surrounding air when the air comes into contact with the surface of the body. The speed of heat reduction by contact with cold air is further linked to the speed of the air and its direction on the site. These losses are proportional to the surface of the receiver and to the difference between the surface temperature of the absorber and the ambient air [31].

$$\mathbf{Q_{pcv} = h_{cv}\ .\ A_{\gamma}\ .(T_r - T_a)} \quad (16)$$

A_{γ}: Receiver opening surface
T_r : Receiver temperature
T_a : Ambient temperature
h_{cv}: Convection transfer coefficient
The convection transfer coefficient is given by [8].

$$\mathbf{h_{cv}} = \frac{N_u\ .\lambda}{d^2} \quad (17)$$

$$N_u = 0.664 (R_e)^{1/2} (P_r)^{1/3} \quad (18)$$

$$R_e = \frac{V.d^2}{v} \quad (19)$$

V: Wind speed.
λ: Thermal conductivity of air.
v: Air viscosity.
d^2: Diameter of the receiver.

III.2 Radiation losses

These losses depend on the shape of the receiver but more particularly on the temperature of the receiver. They are proportional to the emissivity of the absorber [7].

$$Q_{p.r} = \varepsilon.\sigma.A_{\gamma}(T_r{}^4 - T_{sk}{}^4) \quad (20)$$

ε: Emissivity factor of the absorber.
σ: Stefan –Boltzmann constant (5.670×10^{-8} W/m^2.K^4)
Tsk: Sky temperature.
Usually we take the sky radiation temperature 6°C lower than the ambient temperature [1]. $\mathbf{T_{sk} = Ta - 6}$

III.3 Conduction losses

These losses are linked to the nature of the equipment used, generally small compared to losses by convection or radiation, they can be associated with losses by convection in most cases.

$$Q_{p.cd} = \lambda.A_{\gamma}.(T_r - T_a) \quad (21)$$

IV. AUTOMATIC TRACKING SYSTEM

Our prototype is designed to have tracking on both axes, vertical and horizontal, we have dimensioned and machined parts and mechanisms which ensure these movements. Automation is ensured thanks to motors actuated by contactors (Arduino relay module) which are controlled by an Arduino card which receives and converts the signals from the light sensors which we have fixed on the reflector. Figure III.5 is a synoptic diagram which generalizes the implementation of our work. Photoresistors give an analog value which will be input to the Arduino card, then the latter makes a comparison using the uploaded program. The Arduino card controls the opening and closing of the Arduino relay modules, which allows the two motors to be activated to have an ideal orientation in the sun.

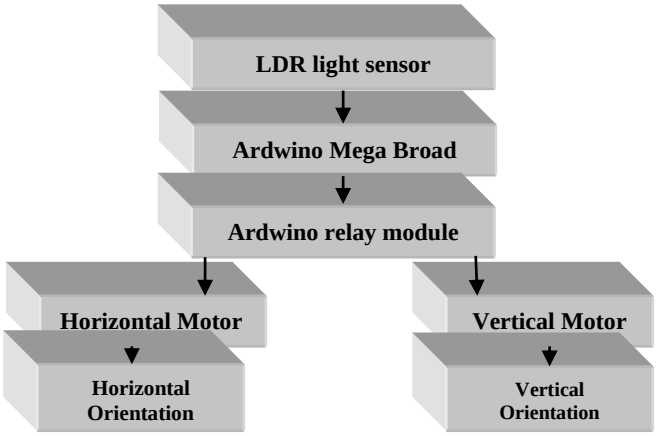


Fig. 5 Synoptic diagram of solar tracking

IV.1 Arduino

relay module A relay module is a controllable switch which makes it possible to make a connection between the control part and the power part. It allows you to close or open a contactor on a power circuit based on a signal between 0 and 5V. The relay consists of an electromagnet and a mechanical contactor. When the current is high enough on the input terminal, the solenoid magnetizes which forces the contactor to close the power circuit. As there is no mechanical connection between the control circuit and the power circuit (magnetic actuation), there is galvanic isolation between the two circuits; which helps protect the control circuit.

IV.2 Programming software

The Arduino module programming software is a free, multi-platform Java application serving as a code editor and compiler, which can transfer the FIRMWAE and the program through a serial link (RS-232, Bluetooth or USB depending on the module) [8]. The programming language used is C++, compiled with avr-g++ 3, and linked to the Arduino development library, allowing the use of the card and its inputs/outputs. The implementation of this standard language facilitates the development of programs on Arduino platforms, for anyone who masters C or C++.

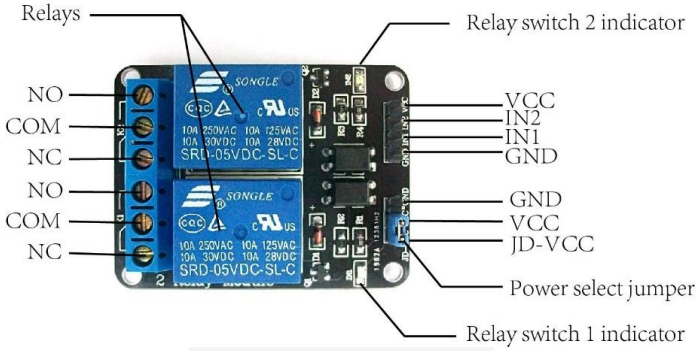


Fig. 6 Arduino relay module

V. TESTING AND INTERPRETATION OF RESULTS

V.1 Conduct of the experiment

By using thermocouples and measuring temperatures with a digital millimeter, we recorded five different temperatures at the same time, namely, the ambient temperature, the temperature inside and at the opening surface of the absorber. The temperature of the fluid at the inlet and outlet of the absorber We used water as a heat transfer fluid to carry out the tests, these took place in two different locations and each under these conditions.

V.2 First test

This will take place on 08/22/2022 in El kseur, Algeria, from 10:45 until 11:45. Measurements are taken every 5 minutes with a flow rate of 0.0016 l/s. The sky was rather clear and the wind was strong.

• The geographical coordinates of El kseur
- Latitude: 36°40′45″ North
- Longitude: 4°51′19″ East
- Altitude relative to sea level: 84 m

V.2.1 Results of first test

Table 3 Measurement results from 22/08/2022

Hour	Ta	Te	Ts	Tab	Ti
10 :49	32	28	39	76	55
10 :54	35	26	40	80	71
10 :59	35	26	42	85	79
11 :04	36	28	47	110	83
11 :09	37	31	48	114	86
11 :14	37	32	50	114	88
11 :19	37	31	54	125	87
11 :24	38	31	50	120	87
11 :29	38	33	51	116	84
11 :34	38	33	53	109	81
11 :39	39	34	53	125	82
11 :44	40	34	52	104	80
11 :49	40	34	50	112	82
11 :54	40	34	51	103	81

V.2.2 Comments

Figure 7 shows the evolution of the different temperatures as a function of time; we note that the variation of the ambient temperature and that of the water entry is almost constant. After 30 seconds of exposure to solar rays, the temperature at the opening surface of the absorber reaches 76°C, inside 55°C, when the water outlet temperature reaches 39°C . After 30 minutes, these temperatures reach their maximum values, i.e. 125°C at the opening surface, 88°C inside the absorber and 54°C for the water at the outlet. Then they suffered

disturbances, more precisely the temperature at the opening surface.

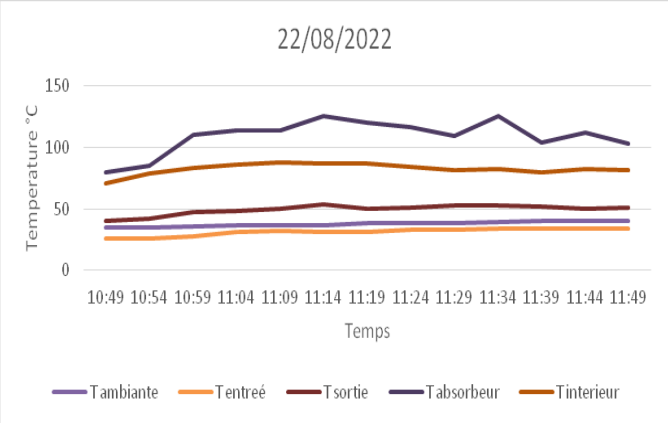


Fig. 7 Graph of temperature evolution as a function of time on 22/08/2022

V.2.3 Interpretation

We noticed that the temperatures recorded were disturbed after 30 minutes of the experiment, this is due to the strong wind present this day despite the sunshine. The unfavorable conditions and the results obtained were not satisfactory, which led us to do another test.

V.3 Second test

This test was carried out on 09/08/2022 at the University of Bejaia from 12:00 p.m. and 2:05 p.m. Measurements are taken every 10 min with a flow rate of 0.0022 l/s. The sky was partly overcast and the wind was moderate.

•The geographical coordinates of the city of Bejaia [9]:

– Latitude: 39°54′26″ North

– Longitude: 116°23′50″ East

– Altitude relative to sea level: 49 m

V.3.1 Results second test

Table 4 Measurement results from 08/09/2022

Hour	Ta	Te	Ts	Tab	Ti
12:05	30	32	38	102	43
12:15	32	26	38	100	70
12:25	33	32	47	124	80
12:35	30	29	50	116	84
12:45	31	30	50	113	85
12:55	31	32	52	110	83
13:05	32	36	56	113	86
13:15	33	34	62	126	85
13:25	33	34	63	116	86
13:35	34	34	68	121	99
13:45	34	36	57	105	84
13:55	34	36	62	127	81
14:05	35	36	61	122	87

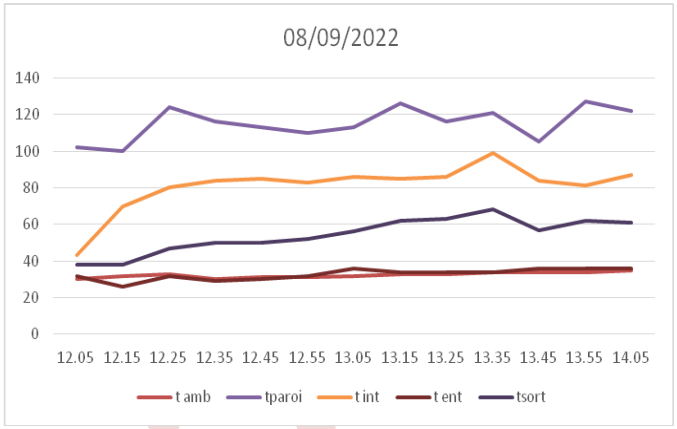


Fig. 8 Graph of temperature evolution as a function of time on 08/09/2022

V.3.2 Comments

The ambient temperature and the water inlet temperature follow a close to linear pace. For 30 seconds of exposure to solar rays, the temperature at the opening surface reaches 102°C, 43°C inside the absorber and 38°C at the water outlet. The best temperatures obtained are as follows: – 127°C at the opening surface. – 99°C inside the absorber. – 68°C at the water outlet.

V.3.3 Interpretation

This last test brought us better results despite the partially overcast sky. This leads us to say that this system is more sensitive to wind than to diffuse radiation.

V.4 Temperature at the surface and inlet of the absorber without water flow

The temperature at the opening surface reached 382°C which is higher than that measured at the front which reached 333°C. The temperature inside the absorber reached 241°C.



Fig. 9 Temperature on the surface and inside the absorber

VI. CONCLUSION

This project is entitled study and improvement of a parabolic concentrator with absorber, equipped with an automatic tracking system. The goal was to implement an automatic tracking system and to create an absorber which will improve the efficiency of the system. The major objectives were the

replacement of the actuator with an electric motor, the creation of a new, more efficient absorber and the writing of a new program which offers better stability and monitoring of solar radiation. This project is multidisciplinary, it combines electronics, automation, thermal transfer, mechanical construction and artificial intelligence. The results obtained were quite satisfactory, since the automatic tracking is more stable and more precise, and the temperature values obtained are excellent. In fact the temperatures of the absorber are close to 400°C, with this temperature 04 times more the boiling temperature of water at 01 atmosphere is very high, could be used for other purposes, it is a source significant energy. Thus the outlet temperatures of the heat transfer fluid are improved. It has been shown, following experiments carried out in different conditions and with different parameters, that these systems depend on several factors, the most important of which are the variation in solar illumination, the geometry of the reflector, and the material used.

REFERENCES

[1] O. GAMMA, «Study and production of a thermodynamic photovoltaic hybrid test bench», Master's dissertation, Nationale Colege of Polytechnique 10, Avenue, El-Harrach, 2008.

[2] N. Nadir, «Search for optimal operating conditions of a solar dryer", Master's dissertation, KASDI Merbah Ouargla University 2012.

[3] D. Kedwards, L. Marlot. «Solar Sensors», Edition S CM Paris 1979.

[4] B.Stine. Michael Geyer, «Power from the sun», Lyle centre for regenerative studies 2001.

[5] Y. MEBARKI copy of course given for master students 2 electrical machines «Heating and cooling of electromechanical sharehold», at the University of Bejaia Algeria 2020.

[6] UH. Kurzweg and IP. Benson. «Iso-Intensity absorber Configurations For parabolic Concentrators», Solar energy Vol 29 No.2.pp167-174,1982.

[7] S. Bonned and A. Alaphilippe, «Thermodynamic conversion of solar energy in low or medium power installations». R. Energy 11th international thermal days. pp. 73-80. 2003.

[8] Summary of the IEC 60584-1 standard on thermocouples, reference tables and functions B

[9] A. Guillaume, «Modeling, dynamic simulation, experimental validation and energy optimization of a solar absorption cooling unit», Doctoral Thesis, University of Pau and Pays de l'Adour, November 28, 2011.

Robust Input-Output Linearizing and Decoupling Control of Wind Turbine Based on DFIG under Variable Wind Speed

Itouchene Hichem [1*], Boudries Zoubir [2], Amrane Fayssal [3], Issaadi Idris [4]

[1*] *Laboratory of Industrial Technology and Information (LII), Faculty of Technology University of Bejaia, Algeria*
hichem.itouchene@univ-bejaia.dz

[2] *Laboratory of Industrial Technology and Information (LII), Faculty of Technology University of Bejaia Algeria*
zboudries@yahoo.fr

[3] *LAS Research Laboratory Department of Electrical Engineering, University of Setif 1, Setif, Algeria*
amrane_fayssal@univ-setif.dz

[4] *LAS Laboratory, Department of Electrical Engineering, Faculty of Technology University Setif-1, Campus El Bez, Setif 19137, Algeria*
idris.issaadi@univ-setif.dz

***Abstract*— In this research paper, we introduce a nonlinear control technique for the Doubly Fed Induction Generator (DFIG) used in wind power systems, namely the Input-Output Linearizing and Decoupling Control (I/OLDC). This method aims to decouple the active and reactive powers of the DFIG. To demonstrate the effectiveness of the proposed techniques, simulation results are showcased within the MATLAB Simulink environment.**

***Keyword*— Wind turbine, DFIG, I/OLDC, robustness.**

I. INTRODUCTION

Among various forms of renewable energy, wind power is regarded as one of the most auspicious and promising sources of sustainable energy globally. Over the past few years, the number of wind power plants installed worldwide has surged by over 30% [1, 2].

At present, the Double Fed Induction Generator (DFIG) is recognized as a top-tier, advanced technological and cost-effective option for harnessing wind energy across the majority of global wind farms [3]. Additionally, it enables the direct linkage of the stator to the grid and the management of power transmission by manipulating rotor currents through an inverter/rectifier linked to the rotor [3-4], This configuration is illustrated in figure 1.

Recently, various nonlinear control methods employing the Double Fed Induction Generator (DFIG) have been introduced in literature, including approaches like the sliding mode control (SMC) technique [5-6]. Nevertheless, a primary concern associated with this control strategy is the occurrence of chattering phenomenon. To resolve this problem, we introduce a more robust control technique, specifically input-output linearizing and decoupling control (I/OLDC), since these types of methods have become pivotal in tackling global renewable energy challenges [4-1].

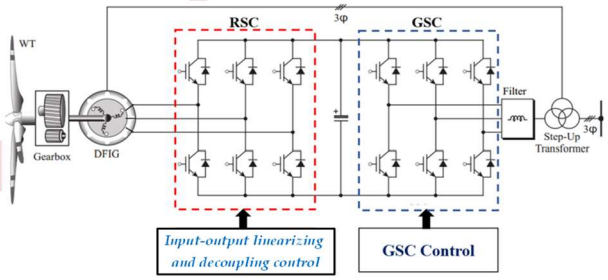


Figure 1. Bloc diagram of WECS based on DFIG.

II. MODEL OF TURBINE

We can provide a model for wind turbines as illustrated in figure 2, and the design of these turbines varies based on the specific model and manufacturer.

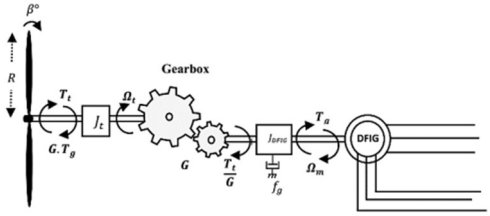


Figure 2. Mechanical model of a wind energy conversion system

The input power of the wind turbine usually is:

$$P_v = \frac{1}{2}[\rho.\pi.R^2.v^3] \quad (1)$$

With: $\rho = 1.225\ \text{kg}.m^{-3}$: air density, R: radius of turbine, V: wind speed (m/s).

The wind turbine's mechanical power output is:

$$P_{aero} = C_p.P_v = \frac{1}{2}.C_p(\lambda;\beta).\rho.\pi.R^2.v^3 \quad (2)$$

$$\lambda = \frac{\Omega_t.R}{V}$$

$$T_{aero} = \frac{P_{aero}}{\Omega_{turbine}} = \frac{C_p(\lambda;\beta).\rho.\pi.R^2.v^3}{2.\Omega_{turbine}} \quad (3)$$

Where: C_p represents power coefficient; λ: relative speed; β: pitch angle (deg); Ω_t: turbine speed (rad/s);

C_p Can be described as:

$$C_p(\lambda,\beta) = 0.5176\left(\left[\frac{116}{\lambda_i}\right] - 0.4\,\beta - 5\right)e^{-\left[\frac{21}{\lambda_i}\right]} + 0.0068\,\lambda) \quad (4)$$

Where: $\lambda_i = \left(\frac{116}{\lambda+0.08\beta} - \frac{1160.035}{\beta^3+1}\right)^{-1}$

The maximum value of C_p ($C_{p\max}$= 0.5483) is attained when the blade pitch angle (β) is set to 0° and the tip speed ratio (λ_{opt}) is set to 6.4, as demonstrated in figure 3.

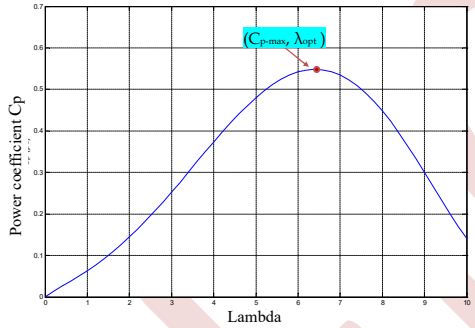


Figure 3. Power coefficient variation Cp against tip speed ratio λ.

Notably, this point corresponds to the maximum power point tracking (MPPT) condition, as reported in reference [7].

III. THE DFIG MODEL

The DFIG's electrical equations are written as follows [9].

$$V_{sd} = R_s\,I_{sd} + \frac{d\,\emptyset_{sd}}{dt} - \omega_s\,\emptyset_{sq} \quad (5)$$

$$V_{rd} = R_r\,I_{rd} + \frac{d\,\emptyset_{rd}}{dt} - \omega_r\,\emptyset_{rq}$$

$$V_{sq} = R_s\,I_{sq} + \frac{d\,\emptyset_{sq}}{dt} + \omega_s\,\emptyset_{sd} \quad (6)$$

$$V_{rq} = R_r\,I_{rq} + \frac{d\,\emptyset_{rq}}{dt} + \omega_r\,\emptyset_{rd}$$

With:

Stator flux components:

$$\emptyset_{sd} = L_s\,I_{sd} + L_m\,I_{rd} \quad (7)$$

$$\emptyset_{sq} = L_s\,I_{sq} + L_m\,I_{rq}$$

Rotor flux components:

$$\emptyset_{rd} = L_r\,I_{rd} + L_m\,I_{sd} \quad (8)$$

$$\emptyset_{rq} = L_r\,I_{rq} + L_m\,I_{sq}$$

DFIG electromagnetic torque:

$$T_{em} = \frac{3}{2}P * \frac{L_m}{L_s}(\emptyset_{sq}I_{rd} - \emptyset_{sd}I_{rq}) \quad (9)$$

Mechanic equation:

$$T_t = T_{em} + J\frac{d\Omega_r}{dt} + f_r\Omega_r \quad (10)$$

Stator active and reactive power:

$$P_s = (3/2)[V_{sd}\,I_{sd} + V_{sq}\,I_{sq}] \quad (11)$$

$$Q_s = (3/2)[V_{sq}\,I_{sd} - V_{sd}\,I_{sq}]$$

The rotor-side converter is controlled in a synchronously rotating d-q axis frame, with the d-axis oriented along the stator flux vector position. The effect of the stator resistance can be neglected, and the stator flux can be held constant as the stator is connected to the grid. Consequently [9]:

$$\emptyset_{sq} = 0, \quad \emptyset_{sd} = \emptyset_s \quad (12)$$

$\emptyset_{sq} = 0$ If the resistances of the phases are neglected, we can express the stator voltage:

$$V_{sd} = 0\ ;\ V_{sq} = V_s = \omega_s\emptyset_s \quad (13)$$

In this case, the torque is given by:

$$T_{em} = -\frac{3}{2}\,P\,\frac{L_m}{L_s}(\emptyset_{sd} * I_{rq}) \quad (14)$$

After applying the conditions found in equation (10), we obtain the rotor flux and stator current equations as follows.

$$\emptyset_{sd} = \emptyset_s = L_s * I_{sd} + L_m * I_{rd} \quad (15)$$

$$\emptyset_{sq} = 0 = L_s * I_{sq} + L_m * I_{rq}$$

$$I_{sq} = -\frac{L_m}{L_s} * I_{rq} \quad (16)$$

$$I_{sq} = -\frac{L_m}{L_s} * I_{rq}$$

The DFIG's active and reactive powers can be expressed as:

$$P_s = -\left[\frac{3}{2}\right].\left[\frac{L_m}{L_s}\,V_s\,I_{rq}\right] \quad (17)$$

$$Q_s = \left[\frac{3}{2}\right].\left[\frac{V_s}{L_s * \omega_s} - \frac{L_m}{L_s}\,I_{rd}\right]V_s\,I_{rd}$$

The electromagnetic torque and is given by:

$$T_{em} = -\frac{3\,L_m}{2L_s}\,P\,\emptyset_S\,I_{rq} \quad (18)$$

IV. INPUT-OUTPUT LINEARIZING CONTROL OF THE DFIG

Given the system by [1] as shown in figure 6.

$$x = f_n(\dot{x}) + g.u$$
$$y = h(x) \quad (19)$$

where x is state vector; u and y are respectively the input and output; f_n, g and h are smooth vector fields and scalar function respectively.

The input-output linearizing control schematic.

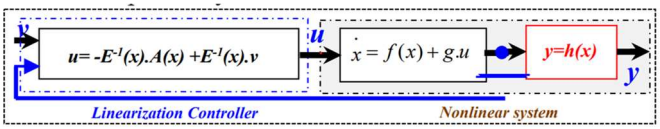


Figure 4. A DFIG's simplified model.

Referring to equation 11, the currents (I_{sd}, I_{sq}, I_{rd}, and I_{rq}) are linear dependent respectively. As a result, we opt for the state vector of the DFIG as follows:

$$x = [x_1 \quad x_2]^T = [I_{rd} \quad I_{rq}]^T \quad (20)$$

The Input variables are the rotor voltages:

$$u = [u_1 \quad u_2] = [V_{rd} \quad V_{rq}]^T \quad (21)$$

The output variables are the active and reactive stator powers:

$$x = \begin{bmatrix} y_1 \\ y_1 \end{bmatrix} = \begin{bmatrix} h_1(x) \\ h_2(x) \end{bmatrix} = \begin{bmatrix} P_s \\ Q_s \end{bmatrix} \quad (22)$$

The derivative of active and reactive power is given by:

$$\dot{y}_1 = \dot{h}_1(x) = -\frac{3}{2}\frac{L_m}{L_s}V_s\dot{I}_{rq}$$
$$\dot{y}_2 = \dot{h}_2(x) = -\frac{3}{2}\frac{L_m}{L_s}V_s\dot{I}_{rd} \quad (23)$$

By substituting (17) to (9), we find:

$$\emptyset_{rd} = \sigma L_r I_{rd} + \frac{L_m}{L_s}\emptyset_s$$
$$\emptyset_{rq} = \sigma L_r I_{rq} \quad (24)$$

Where: $\sigma = 1 - \left(\frac{L_m^2}{L_r L_s}\right)$, is the dispersion coefficient of Blondel.

By replacing (24) in (8), we find:

$$V_{rd} = R_r I_{rd} + \sigma L_r \frac{d}{dt} I_{rd} - g\omega_s \sigma L_r I_{rq}$$
$$V_{rq} = R_r I_{rq} + \sigma L_r \frac{d}{dt} I_{rq} - g\omega_s \sigma L_r I_{rd} + \frac{gL_m V_s}{L_s} \quad (25)$$

From (25), the following equations hold:

$$f_1(x) = -\frac{R_r}{\sigma L_r} I_{rd} + g\omega_s I_{rq}$$
$$f_2(x) = -g\omega_s I_{rd} - \frac{R_r}{\sigma L_r} I_{rq} - \frac{gL_m V_s}{\sigma L_s L_r} \quad (26)$$

And

$$g = \begin{bmatrix} g_1(x) & 0 \\ 0 & g_2(x) \end{bmatrix} = \begin{bmatrix} \frac{1}{\sigma L_r} & 0 \\ 0 & \frac{1}{\sigma L_r} \end{bmatrix}$$

We replace (26) in (23), and then we have:

$$\dot{y}_1 = \dot{h}_1(x) = -\frac{3}{2}\frac{L_m}{L_s}V_s\left(f_2 + \frac{V_{rq}}{\sigma L_r}\right)$$
$$\dot{y}_2 = \dot{h}_2(x) = -\frac{3}{2}\frac{L_m}{L_s}V_s\left(f_1 + \frac{V_{rd}}{\sigma L_r}\right) \quad (27)$$

We can rewrite (27) in the form:

$$\begin{bmatrix} \dot{y}_1 \\ \dot{y}_2 \end{bmatrix} = A(x) + D(x)\begin{bmatrix} u_2 \\ u_1 \end{bmatrix} \quad (28)$$

Since the decoupling matrix D(x) is nonsingular, the control law is given as:

$$\begin{bmatrix} V_{rd} \\ V_{rq} \end{bmatrix} = D^{-1}(x)\left[-A(x) + \begin{bmatrix} v_2 \\ v_1 \end{bmatrix}\right] \quad (29)$$

The Proportional-Integral (PI) controller achieves the tracking of the stator powers. Hence, the new input "v" is given by [10, 11]:

$$\begin{bmatrix} v_2 \\ v_1 \end{bmatrix} = \begin{bmatrix} \dot{y}_1^* - k_{p1}e_1 - k_{i1}\int e_1 dt \\ \dot{y}_2^* - k_{p2}e_2 - k_{i2}\int e_2 dt \end{bmatrix} \quad (30)$$

Where e1 is the error between the desired and the measured active power, and e_2 is that relates to the reactive power:

$$e_1 = y_1^* - y_1 = P_s^* - P_s$$
$$e_2 = y_2^* - y_2 = Q_s^* - Q_s$$

V. Simulation Results

The outcomes of the simulation results using Matlab/Simulink software are illustrated in figures 9 and 10. The wind-power generation system's electrical performance was examined under changing wind speeds through two distinct types of tests:

- Reference Tracking Test:
  a) Scenario 01: Random wind speed
  b) Scenario 02: Step wind speed
- Robustness Test.

The parameters for the DFIG (1.5MW) and wind turbine (1.5MW) employed in this study were provided as follows:

- DFIG Parameter: P_n=1.5MW, P=2, R_s= 0.012Ω, R_r=0.021 Ω, L_s= 0.0137 Ω, L_r=0.0136 Ω, L_m=0.0135 Ω, V_{dc}=1200 volt
- Turbine Parameter: Np=3, R=35.25m, G=90, f_v=0.0024, J=1000Kg.m^2

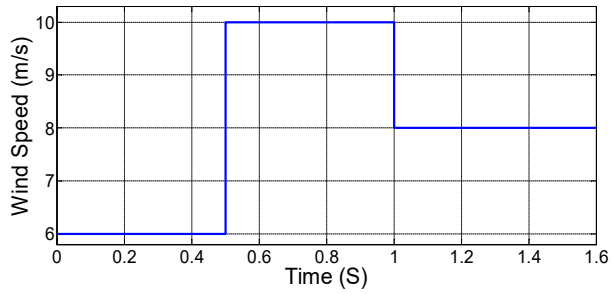
A. Reference Tracking Test

In this test, the wind turbine operates under varying wind speeds, and the MPPT strategy is employed to generate the reference active power. Meanwhile, the reference reactive power is set to zero to ensure unity of power factor, to confirming the effectiveness of the proposed control method. We suggest the following two scenarios.

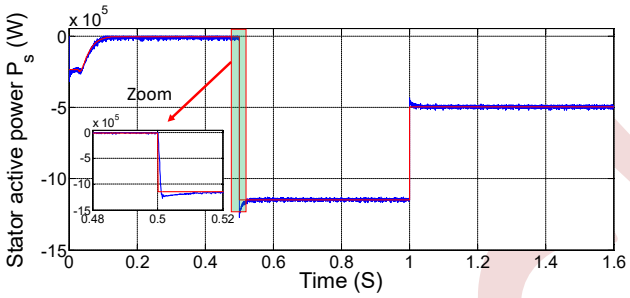
Through the simulation results shown in Figure 5, we observe that both the active and reactive powers follow their references accurately, despite the changing wind speed (random and step). The direct and quadrature components of rotor

currents exhibit the same pattern as the reactive and active powers respectively.

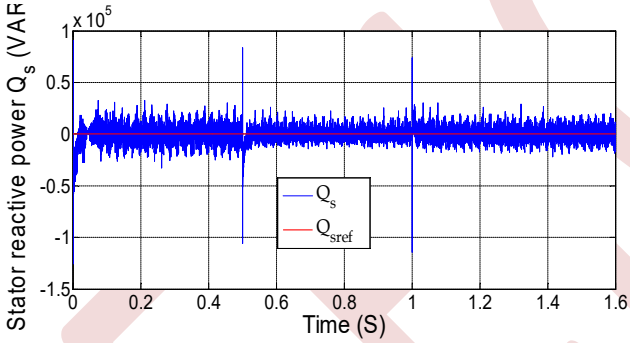
1- Step wind speed



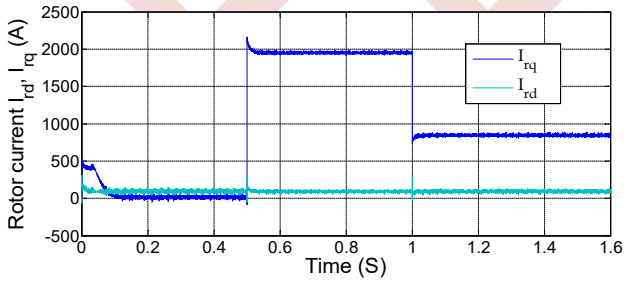
a) Wind speed



b) Stator active power



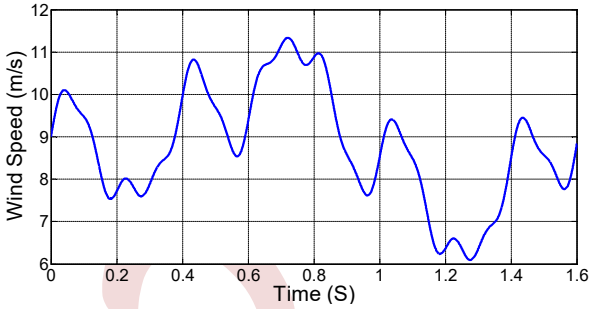
c) Stator reactive power



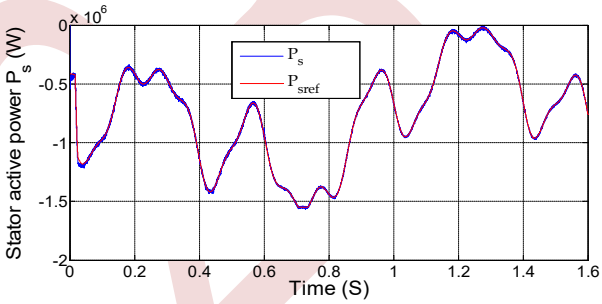
d) Rotor current Ird, Irq

Figure 5. Simulation results of the proposed control for DFIG under step wind speed

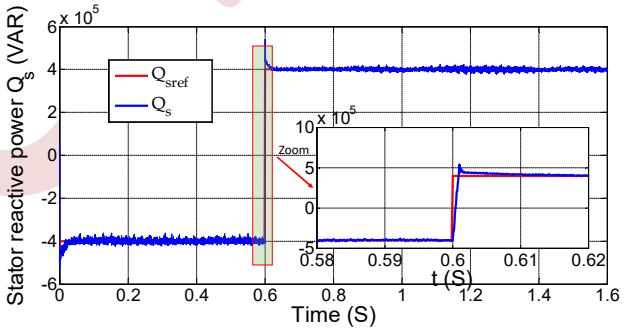
2- Random wind speed



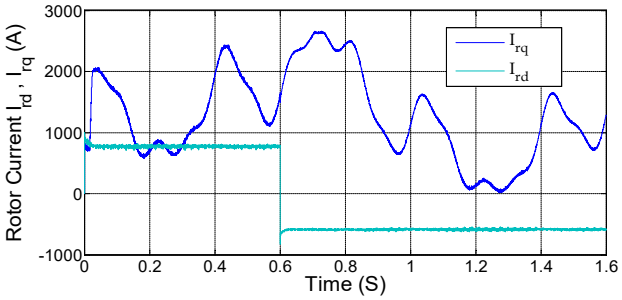
a) Wind speed



b) Stator active power



c) Stator reactive power



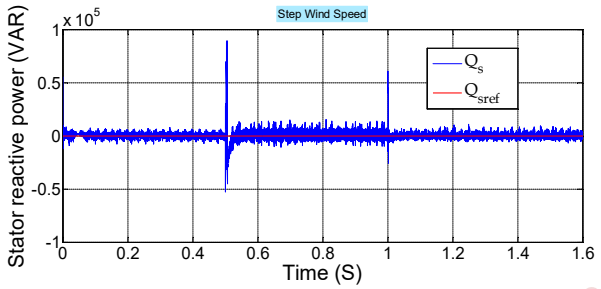
d) Rotor current Ird, Irq

Figure 6. Simulation results of the proposed control for DFIG under random wind speed

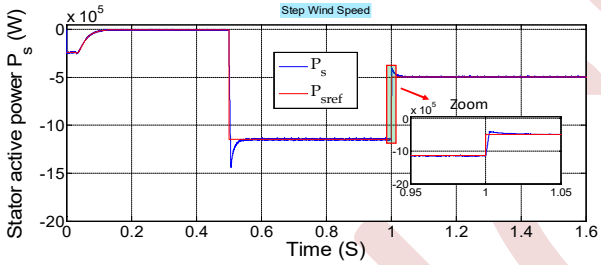
B. Robusteness Tracking Test

In this test, we vary the parameters of the DFIG to ensure the effectiveness of the input-output linearization control. To conduct this test, we:

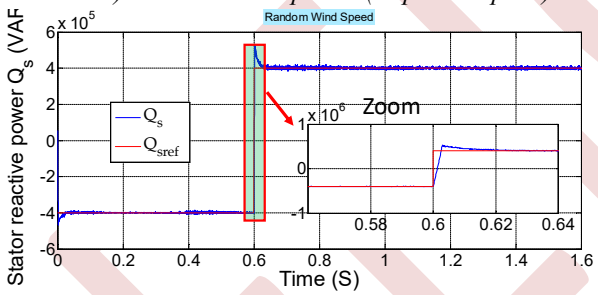
- Enhance the rotor resistance R_r by doubling its nominal value (warming-up of rotor windings).
- Reduce the mutual inductance L_m by half of its nominal value (inductance saturation).



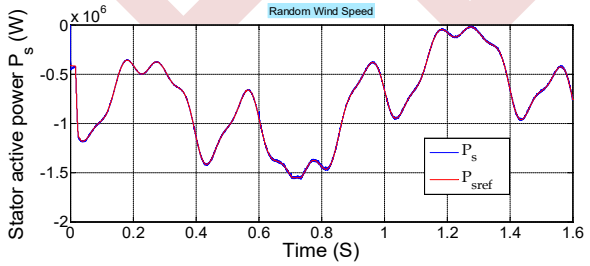
a) Stator reactive power (step wind speed)



b) Stator active power (step wind speed)



c) Stator reactive power (random wind speed)



d) Stator active power (random wind speed)

Figure 7. Simulation results of the robustness test for the proposed DFIG control.

Through the analysis of the simulation results, it becomes evident that the introduced control strategy demonstrates a high degree of robustness, even when confronted with significant variations in the parameters of the Doubly Fed Induction Generator (DFIG). The control unit's ability to maintain effective performance in the face of such parameter fluctuations underscores its stability and adaptability. This is a significant finding, as it validates the control strategy's potential to ensure consistent and reliable operation of the DFIG system.

CONCLUSION

In this work, a non-linear control strategy has been presented that relies on applying input-output linear control to the rotor-side converter (RSC) of a DFIG, aiming to separate the active and reactive powers under changing wind speed conditions. Through the simulation results presented above, the proposed control strategy demonstrated its effectiveness and robustness even in the presence of parameter variations. Furthermore, this control algorithm is extremely simple and robust, with the added advantage of being easily implementable in real-time. Based on previous knowledge and simulation results, some key characteristics of input-output control can be mentioned, which are:

- Utilizes input-output linearization to achieve decoupling between active and reactive powers
- Improved control performance and power quality by separately regulating active and reactive powers
- Relatively moderate complexity due to mathematical transformations and control design
- Effectively handles variable wind speeds and changes in system parameters
- Feasible for real-time application with proper hardware and control implementation
- Suitable for DFIG wind turbines in various wind conditions.

ACKNOWLEDGMENT

I would like to thank all the individuals who have supported and encouraged me during this research endeavor, and I would like to acknowledge the efforts of the researchers who contributed to this work. Their expertise and collaboration have enriched the study, and I am grateful for their valuable insights and ideas.

REFERENCES

[1] Fayssal Amrane, Azeddine Chaiba, and Bruno Francois, "Improved Adaptative Nonlinear Control for Variabl Speed Wind-Turbine fed by DirectMatrix Converter," Rev. Roum. Sci. Techn Électrotechn. et Énerg, Vol. 68, 1, pp. 58-64, 2023.

[2] Salah Tamalouzt, "Performances of direct reactive power control technique applied to three level-inverter under random behaviour of wind speed," Rev. Roum. Sci. Techn.– Électrotechn. et Énerg, vol. 64, no. 1, pp. 33-38, 2019.

[3] Zouheyr Dekali, Lotfi Baghli, and Abdelmadjid Boumediene, "Experimental implementation of the maximum power point tracking algorithm for a connected wind turbine emulator, Rev. Roum. Sci. Techn.– Électrotechn. et Énerg, vol. 66, no. 2, pp. 111-117, 2021.

[4] Youcef Djeriri , and Hamza Mesai Ahmed, "Robust nonlinear control of wind turbine driven doubly fed induction generators," Heritage and Sustainable Development, vol. 2, no. 1, pp. 17-29, 2020,

[5] Sadegh Ebrahimkhani, "Robust fractional order sliding mode control of doubly-fed induction generator (DFIG)-based wind turbines," ISA Transactions, vol. 63, no. 2, pp. 343-354, 2016.

[6] Brice Beltran, Mohamed El Hachemi Benbouzid, Tarek Ahmed-Ali, "Second-order sliding mode control of a doubly fed induction generator driven wind turbine," IEEE Transactions on Energy Conversion, vol. 27, no. 2, pp. 261-269, 2012.

[7] Fayssal Amrane, Azeddine Chaiba, Badreddine Babes, and Saad Mekhilef , "Design and Implimentation of High Performance Fied Oriented for Grid-Connected Doubly Fed Induction Genenerator Via Hysteresis Rotor Current Controller," Rev. Roum. Sci. Techn Électrotechn Énerg. vol. 61, no. 4, pp. 319–324, Bucarest, 2016.

[8] S. Mekhilef D. Aouzellag, K. Ghedamsi, and E.M. Berkouk, "Network power flux control of a wind generator," Renewable Energy, vol. 34, pp. 615-622,

[9] Sara Mensou, Ahmed Essadki, Issam Minka, Tamou Nasser, and Badr Bououlid Idrissi, "Backstepping Controller for a Variable Wind Speed Energy Conversion System Based on a DFIG," vol. 978, no. 1, 2017.

[10] Luhua Zhang, Xu Cai, and Jiahu Guo, "Simplified input-output linearizing and decoupling control of wind turbine driven doubly-fed induction generators," International Power Electronics and Motion Control Conference, pp. 632-673, 2009.

[11] Anasse Bennouk, A. Nejmi, and Mark Ramzi, "Feedback Linearization Control of Wind Turbine Based on PMSG," International Journal of Emerging Technology and Advanced Engineering, vol. 5, no. 3, pp. 433-438, 2015.

EEIC'23

Optimal location and sizing of DG using fuzzy logic for improving voltage profile and reducing power losses

Samir KENNOUCHE [1], Narimen LAHAÇANI AOUZELLAG [1], Samira CHEKKAL [1]

[1] Laboratoire de maitrise des énergies renouvelables (LMER), *Bejaia, Algeria*

samir.kennouche@univ-bejaia.dz

nlahacani@yahoo.fr

samirachekkal@yahoo.fr

***Abstract*— In order to integrate more renewable energy into the electrical power networks, power plants called decentralized generation "DG" have been chosen. In order to get the most out of these plants, it is necessary to find their ideal location at first. In this paper, the optimization of the DG location and its rate of integration in an IEEE 26 bus system is performed, with the aim of reducing the total active losses identified as the most critical impact and minimizing the deviation of voltages from the reference voltage. The optimization of the DG is obtained by applying the methods of Newton Raphson (NR) and Fuzzy Logic (FL). The modeling and simulation are done in the Matlab software.**

***Keywords:* Decentralized generation, power flow, fuzzy logic control, optimization, Newton Raphson.**

I. INTRODUCTION

The world today is drifting more and more to the integration of renewable energies into the power network, and this in the form of small power plants called decentralized generators. Decentralized production based on wind turbines is becoming competitive in terms of production costs and reduction of greenhouse gas emissions, however, their extension poses a problem in electrical networks by considering them disturbing sources in terms of production fluctuation which can be significant depending on the installation site. On the other hand, offshore systems for example have good prospects and are promising in terms of energy production capacity comparable to existing centralized systems, which is considerable and regulated. In this work, the objective is to seize the opportunity offered by its systems to integrate them into the transport network as an alternative solution.

For a better installation and operation of these DGs and for the proper functioning of power systems, the optimal location and integration rate must first be determined in order to obtain the maximum benefits.

Optimization problems present several difficulties related to the needs of the user, the characteristics of the problem to be solved and the computation time. Many works have been done on this topic, each with its own method to find the optimal location and size of the DG, and each with its own optimization method and objective. the importance of DG sources in distribution systems and reviewing the published work on optimal planning through determination of optimal locations and sizes of DG sources by minimizing single objective function (SOF) and multi-objective function (MOF) [1], exploitation of fuzzy logic to find ODGP using the power loss index PLI and the voltage sensitivity index VLI [2], A review of optimum DG placement based on minimization of power losses and voltage stability enhancement of distribution system [3], a comparison between a novel power losses sensitivity, power stability index and voltage stability index methods for DG location in radial network [4] and a proposed optimal DG allocation by minimizing active power losses and enhancing voltage stability margin considering load variation [5]. All of the above articles are either about the optimal location of DG while neglecting the integration rate, or the other way around. Their studies have focused on distribution networks, whereas in this paper the focus is on transmission networks as a proposed solution for more regulated energy.

The objective of the DG location and size optimization problem is to minimize the total active power losses and to improve the voltage profile while satisfying the equalities and inequalities constraints. In order to achieve this, the location and the rate of integration are combined simultaneously in a fuzzy logic model all that after applying the method of Newton Raphson for resolving the power flow problem.

II. METHODOLOGY

The present work consisted firstly of calculating the power flow by applying the New-ton Raphson method to determine the voltages and their phase shifts at the various bus bars, the powers generated and those transited and to evaluate the voltage drops and the active and reactive power losses through the lines, of an electrical network with a mesh structure of 26 bus power network as shown in "Fig. 1" [6].

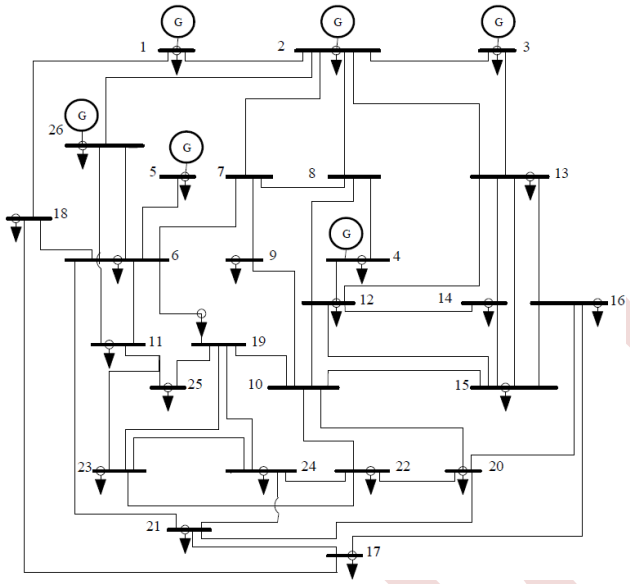


Figure 1. IEEE 26 bus system

A. *Application of the Newton Raphson method in power flow calculation*

The Newton-Raphson method requires that a system of linear equations be formed from the relationships between the variations of the active and reactive powers and also those of the real and imaginary components of the nodal voltages [7-9].

One of the most basic ways to formulate the power flow problem is to write equations that state that at each node "i" the powers generated (PGi, QGi) consumed (PDi, QDi) and transited through the branches cancel each other out.

$$\begin{aligned} P_i^s &= P_{Gi} - P_{Di} \\ Q_i^s &= Q_{Gi} - Q_{Di} \end{aligned} \quad (1)$$

The variations of the powers are the differences between the specific values (Psi) and those calculated (Pci) allowing the determination of the elements of the Jacobian "J".

$$\begin{cases} \Delta P_i = P_i^s - P_i^c = V_i \sum_{j=1}^{n} V_j \left(G_{ij} \cos\theta_{ij} + jB_{ij} \sin\theta_{ij} \right) \\ \Delta Q_i = Q_i^s - Q_i^c = V_i \sum_{j=1}^{n} V_j \left(G_{ij} \sin\theta_{ij} - j\, B_{ij} \cos\theta_{ij} \right) \end{cases} \quad (2)$$

This formulation results in a system of non-linear equations, two for each node of the network. The active and reactive powers (Pi) and (Qi) are known.

The real and imaginary components of the voltage (Vi) and (θi) are unknown for all nodes except for the reference node where the voltage is specified and held constant. This results in 2(n-1) equations to solve for the solution of the power flow problem.

The linearization of the active and reactive power equations gives the matrix system at iteration "k":

$$\begin{bmatrix} \Delta P_1 \\ \vdots \\ \Delta P_i \\ \vdots \\ \Delta P_{n-1} \\ \vdots \\ \Delta Q_1 \\ \vdots \\ \Delta Q_i \\ \vdots \\ \Delta Q_{n-1} \end{bmatrix}^{(k)} = \begin{bmatrix} \frac{\partial P_1}{\partial V_1} & \cdots & \frac{\partial P_1}{\partial V_i} & \cdots & \frac{\partial P_1}{\partial V_{n-1}} & \cdots & \frac{\partial P_1}{\partial \theta_1} & \cdots & \frac{\partial P_1}{\partial \theta_i} & \cdots & \frac{\partial P_1}{\partial \theta_{n-1}} \\ \frac{\partial P_i}{\partial V_1} & \cdots & \frac{\partial P_i}{\partial V_i} & \cdots & \frac{\partial P_i}{\partial V_{n-1}} & \cdots & \frac{\partial P_i}{\partial \theta_1} & \cdots & \frac{\partial P_i}{\partial \theta_i} & \cdots & \frac{\partial P_i}{\partial \theta_{n-1}} \\ \frac{\partial P_{n-1}}{\partial V_1} & \cdots & \frac{\partial P_{n-1}}{\partial V_i} & \cdots & \frac{\partial P_{n-1}}{\partial V_{n-1}} & \cdots & \frac{\partial P_{n-1}}{\partial \theta_1} & \cdots & \frac{\partial P_{n-1}}{\partial \theta_i} & \cdots & \frac{\partial P_{n-1}}{\partial \theta_{n-1}} \\ \frac{\partial Q_1}{\partial V_1} & \cdots & \frac{\partial Q_1}{\partial V_i} & \cdots & \frac{\partial Q_1}{\partial V_{n-1}} & \cdots & \frac{\partial Q_1}{\partial \theta_1} & \cdots & \frac{\partial Q_1}{\partial \theta_i} & \cdots & \frac{\partial Q_1}{\partial \theta_{n-1}} \\ \frac{\partial Q_i}{\partial V_1} & \cdots & \frac{\partial Q_i}{\partial V_i} & \cdots & \frac{\partial Q_i}{\partial V_{n-1}} & \cdots & \frac{\partial Q_i}{\partial \theta_1} & \cdots & \frac{\partial Q_i}{\partial \theta_i} & \cdots & \frac{\partial Q_i}{\partial \theta_{n-1}} \\ \frac{\partial Q_{n-1}}{\partial V_1} & \cdots & \frac{\partial Q_{n-1}}{\partial V_i} & \cdots & \frac{\partial Q_{n-1}}{\partial V_{n-1}} & \cdots & \frac{\partial Q_{n-1}}{\partial \theta_1} & \cdots & \frac{\partial Q_{n-1}}{\partial \theta_i} & \cdots & \frac{\partial Q_{n-1}}{\partial \theta_{n-1}} \end{bmatrix}^{(k)} \cdot \begin{bmatrix} \Delta V_1 \\ \vdots \\ \Delta V_i \\ \vdots \\ \Delta V_{n-1} \\ \vdots \\ \Delta \theta_1 \\ \vdots \\ \Delta \theta_i \\ \vdots \\ \Delta \theta_{n-1} \end{bmatrix}^{(k)} \quad (3)$$

The iterative solution can be expressed as a function of the correction vector representing the voltage and phase variation vectors, (ΔV) and $(\Delta \theta)$, such that:

$$\begin{bmatrix} \Delta V \\ \Delta \theta \end{bmatrix}^{(k)} = -\left(\begin{bmatrix} \frac{\partial P}{\partial V} & \frac{\partial P}{\partial \theta} \\ \frac{\partial Q}{\partial V} & \frac{\partial Q}{\partial \theta} \end{bmatrix}^{-1} \right)^{(k)} \begin{bmatrix} \Delta P \\ \Delta Q \end{bmatrix}^{(k)} = -(J^{-1})^{(k)} \begin{bmatrix} \Delta P \\ \Delta Q \end{bmatrix}^{(k)} \quad (4)$$

The voltage and phase vectors at iteration "k+1" can be deduced according to the expressions:

$$\begin{cases} V^{k+1} = V^k + \Delta V^k \\ \theta^{k+1} = \theta^k + \Delta \theta^k \end{cases} \quad (5)$$

After calculating the amplitudes and phases of the voltages, the active and reactive powers transmitted by the lines of the network are determined quite simply. The voltage differences and the total active power losses will then be evaluated when the network is in its initial state before the insertion of the DG.

B. *Fuzzy logic*

Fuzzy logic can model complex, non-linear relationships between variables, which is essential in many real-world optimization problems where traditional linear approaches may not be suitable.

1) *The interest of using the fuzzy logic in optimization:* Is by the fact that it is similar to human reasoning based on the use of simple mathematics for non-linear, integrated and complex systems, as it is known for its high accuracy and fast operation [10].

- Multi-objective Optimization: Fuzzy logic is well-suited for multi-objective optimization, where multiple conflicting criteria need to be considered simultaneously. It allows for the ranking and selection of solutions that tradeoff between conflicting objectives in a more human-centric manner.
- Robustness: Fuzzy logic-based optimization can be robust against small variations and disturbances in the input data, making it suitable for applications where stability and resilience are important.

Fuzzy logic has no well-defined mathematical relationship, but uses inferences with several rules, based on linguistic variables. Based on these inferences, it is possible to take into account the experiences acquired gained by the operators of technical processes based on three steps:

2) *The fuzzification:* which is a conversion of input variables (which are physical quantities) into fuzzy quantities.
3) *The establishment of rules:* linking outputs to inputs, called fuzzy inference.
4) *The defuzzification:* which is the opposite operation of the fuzzification, it consists in transforming linguistic variables into real or numerical variables [11-13].

Fuzzy logic will be applied to optimize the location and the integration rate by minimizing the total losses and also the maximum deviation between the voltages at the different bus-bars and the voltage at the slack bus.

- Controller inputs: The first input to the fuzzy control is for the total power losses (TPL). Five fuzzy sets from universe of discourse to represent linguistically the five stats of active power losses in per unit (pu) from 0 to 1.The total active power losses TPL are evaluated by calculating the difference between the sending active power ($P_{sending}^{(m)}$) and the receiving active power ($P_{receiving}^{(m)}$) for each line, denoted (m), according to equation (6):

$$TPL = \sum_{m=1}^{n-1} \left(P_{sending}^{(m)} - P_{receiving}^{(m)}\right) \quad (6)$$

The second input of the fuzzy command is the maximum deviation $VDmax$ between the voltages at the various bus-bars (V_i) and that of the reference (V_{ref}). Five fuzzy sets from universe of discourse to represent linguistically the five stats of the maximal voltage difference in per unit (pu) from 0 to 0.1.The maximum deviation $VDmax$is calculated for only PQ buses following this expression:

$$VDmax = \max(V_{ref} - V_i) \quad (7)$$

- Controller output: The output of the fuzzy control is the location index of the DG. Going from 0 to 1 it's going from the best location to the worst one. Five fuzzy sets from universe of discourse to represent linguistically the five stats of the index so define the location and sizing of DG.

- Fuzzy Logic Control Rule: The fuzzy control system is developed using two inputs and one outputs with the outputs further detailed into different operating options. Some of the examples of the generated rules for the fuzzy logic control system are as follows with TABLE I illustrating the fuzzy control rules captured from the program developed.

TABLE I. LOGICAL INFERENCE RULES

VDmax / TPL	SL	MSL	ML	MMJL	MJL
SD	***VGL***	***GL***	***ML***	***ML***	***BL***
MSD	***VGL***	***GL***	***ML***	***BL***	***BL***
MD	***GL***	***ML***	***ML***	***BL***	***BL***
MMJD	***ML***	***BL***	***BL***	***BL***	***VBL***
MJD	***BL***	***BL***	***VBL***	***VBL***	***VBL***

- Surface viewer of the fuzzy logic control: The objective of the implementation of the coordinated control by fuzzy logic is to obtain an index calculated by the method of the center of gravity by combining between the two inputs in their admissible limits. "Fig. 2" shows the surface visualization of the control output of the fuzzy logic system.

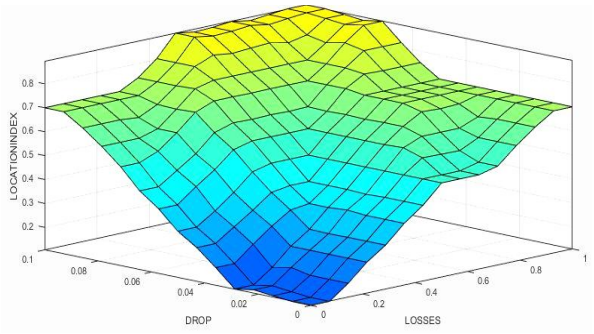


Figure 2. Surface viewer of the fuzzy logic control output

III. RESULTS AND DISCUSSION

The proposed method is applied to the studied network; voltage deviations and total active power losses vary with variations in DG location and integration rate. "Fig 3" shows that the lowest total active power losses were recorded for a location at the 9th bus-bar and with an integration rate of 25% of the total load.

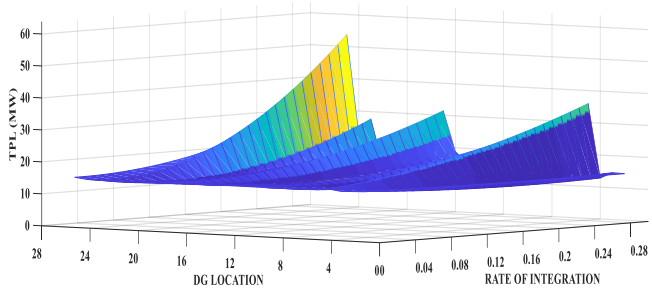


Figure 3. Power losses area

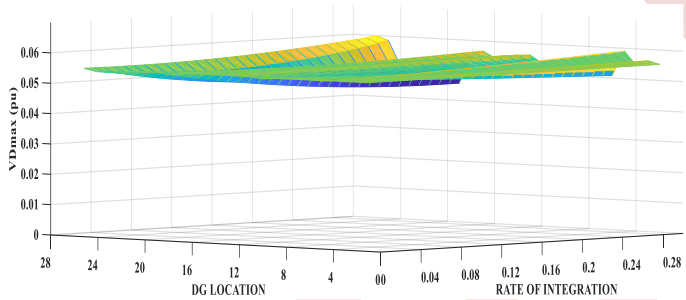


Figure 4. Area of maximum voltage deviation

"Fig 4" shows that the minimum value of the maximum deviation between the voltages at the different bus-bars and the reference voltage is recorded in the 19th bus-bar and at an integration rate of 29% of the total load.

"Fig 5" shows the obtained curve of the index calculated as a function of the total losses and the maximum deviations for the studied network, with the following objective function:

$$F(x) = \min(TPL, VDmax) \quad (8)$$

The index sought represents the minimum value. "Fig 5" shows that the minimum index is obtained for an optimal location at the 19th bus-bar with an optimal integration rate of 20% of the total load which represents a power of 252.60 MW.

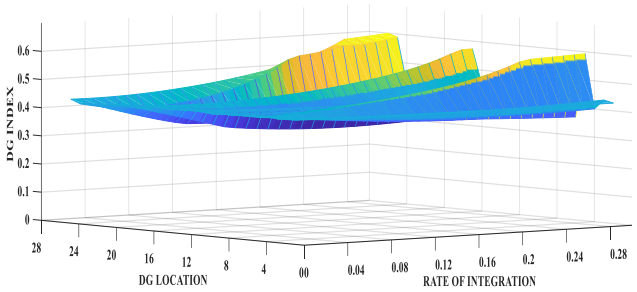


Figure 5. DG location index surface

Applying the results obtained on the network, the power of the DG is injected, as a negative load, to the bus 19. Its influence is significant as shown in TABLE II, where a comparison of the results before and after the optimization is grouped, while exposing in the second column of the table the minimization of the two parameters each in a separate way, the results are obtained by an iterative method changing the location and size of the DG with a fixed step.

In the third column, for the optimization of the DG location, the minimizations of the active powers losses as well as of the voltage deviation were the two objectives to be achieved.

TABLE II. COMPARISON BEFORE AND AFTER DG OPTIMIZATION

	Without DG (NR method)	***With DG Without Optimization (DG bus, size)***	***With DG With optimization (FL) (DG bus, size)***
Total Power Losses (pu)	0.1539	0.1128 (9th, 20%)	0.1289 (19th, 20%)
Maximum Voltage Deviation (pu)	0.0552	0.0457 (19th, 29%)	0.0465 (19th, 20%)

"Fig 6" illustrates the influence of the DG on the bus-bar voltage level. An improvement of the voltage level at all bus-bars is noticed and considerably those connected to the 19th bus-bar, the location of the DG.

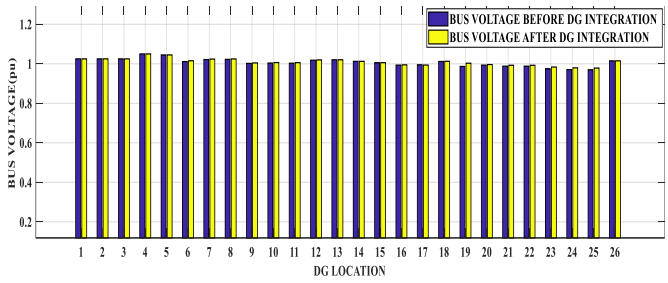


Figure 6. Voltage magnitudes before and after insertion of the DG

"Fig 7" illustrates the power generated in the grid before and after the insertion of the DG. It shows the decrease of the

conventional generation in the grid after the connection of the DG, which is the objective since the beginning.

The generator bus-bars have maintained their power supplies to the grid, while the reference bus-bar has significantly decreased its production, as it is responsible for the power balance in the grid.

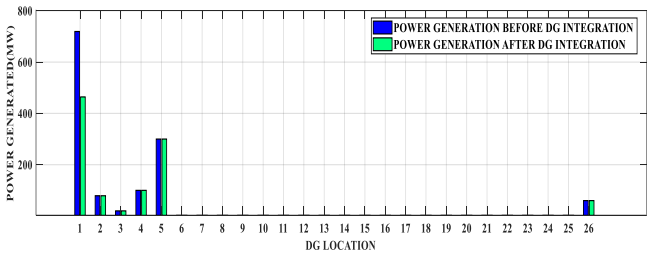


Figure 7. Power generated before and after DG insertion

IV. CONCLUSION

We carried out a calculation of the distribution of powers which allows the balance between the production and the demand for electrical energy, in order not to exceed the limit values of thermal stability, the maintenance of the voltages at the bus bars between the tolerated limits and avoid excessive power losses in the lines, thereby extending the life of network equipment.

In this paper, an optimization of the location and integration rate of the distributed generation using fuzzy logic has been done. The simulation was applied for an IEEE 26 bus system and the results are confirmed.

The connection of the DG to the network has considerably lowered the total active power losses and voltage drops. So just with the optimization of the DG, a positive effect on the parameters of the network has been recorded.

REFERENCES

[1] M. Abdel-Salam, M. T. El-Mohandes, A. M. Yousef, and R. Ramadan, "Optimal Sizing and Locations of DG Sources in Distribution Systems: A Review of Different Techniques," 2019 21st Int. Middle East Power Syst. Conf. MEPCON 2019 - Proc., pp. 383–391, 2019.

[2] S. Huddar, B. Kantharaj, K. R. Mohan, S. B. Patil and R. Magadum, "Optimal Location and Sizing of DG using Fuzzy logic,"International open access Journal of Modern Engineering Research (IJMER),pp.59-64, 2014.

[3] U. Sultana, A. B. Khairuddin, M. M. Aman, A. S. Mokhtar, and N. Zareen, "A review of optimum DG placement based on minimization of power losses and voltage stability enhancement of distribution system," Renew. Sustain. Energy Rev., vol. 63, pp. 363–378, 2016..

[4] V.V.S.N. Murty, A. Kumar. "Optimal placement of DG in radial distribution systems based on new voltage stability index under load growth," Journal of Theoretical and Applied In-formation Technology, pp.246–256, 2014.

[5] B. Poornazaryan, P. Karimyan, G.B. Gharehpetian, M. Abedi, "Optimal allocation and sizing of DG units considering voltage stability, losses and load variations," Electrical Power and Energy Systems, pp.42-52, 2015.

[6] D. V. Tien, P. Hawliczek, R. Gono and Z. Leonowicz,"Analysis and Modeling of STATCOM for Regulate the Voltage in Power Systems," 18th International Scientific Conference on Electric Power Engineering (EPE), 2017.

[7] M. Crappe, "Electric Power Systems," ISTE and John Wiley & Sons, 2008.

[8] P.S.R. Murthy,"Power System Analysis," BS Publications, 2007

[9] D. Das, "Electrical Power Systems," New Age International Publishers, 2006.

[10] 13. F. Behrooz and all,"Review of Control Techniques for HVAC Systems—Nonlinearity Ap-proaches Based on Fuzzy Cognitive Maps", Energies, 2018.

[11] B. Jin, L. Zhang, Q. Chen, and Z. Fu, "ScienceDirect Energy management strategy of fuzzy logic control for fuel cell truck," Energy Reports, vol. 9, pp. 247–255, 2023.

[12] S. Chekkal, N. Lahaçani Aouzellag, D. Aouzellag and K. Ghedamsi, "Fuzzy logic control strategy of wind generator based on the dual-stator induction generator," Electrical Power and Energy Systems,pp.166–175,2014.

[13] T. J. Hashim and A. Mohamed, "Fuzzy Logic Based Coordinated Voltage Control for Distribution Network with Distributed Generations," International Journal of Electrical, Computer, Energetic, Electronic and Communication Engineering, Vol.7, 2013.

Enhancement of Fuzzy Direct Torque Control Performances for Doubly Fed Induction Generator Wind Turbines

Karim Fathi Sayeh[1], Salah Tamalouzt[1], Djamel Ziane[1,2], Kamel Djermouni[3], Brahim Deffaf[3], Sofia Lalouni Belaid[1]

[1] *Laboratoire de Technologie Industrielle et de l'Information (LTII), Faculté de Technologie, Université de Bejaia, Bejaia 06000, Algeria*
E mail: karimfathi.sayeh@univ-bejaia.dz, salah.tamalouzt@univ-bejaia.dz, lalouni_sofia@yahoo.fr

[2] *Nantes Université, Institut de Recherche en Énergie Électrique de Nantes Atlantique, IREENA, UR 4642, F-44600, Saint-Nazaire, France*
E-mail: djamel.ziane@univ-nantes.fr

[3] *Laboratoire de Maitrise des Energies Renouvelables (LMER), Faculté de Technologie, Université de Bejaia, Bejaia 06000, Algeria*
E-mail: kamel.djermouni@univ-bejaia.dz, brahim.deffaf@univ-bejaia.dz

***Abstract*— Direct torque control (DTC) is an advantageous strategy for controlling doubly-fed induction generator (DFIG) wind turbines, providing simple, robust control and fast dynamic response. However, conventional DTC (C-DTC) suffers drawbacks including torque/flux ripples. This paper investigates a fuzzy logic 12 sector-enhanced DTC (FH12-DTC) approach to improving DFIG wind turbine performance by overcoming C-DTC limitations. MATLAB/Simulink simulations compare FH12-DTC and C-DTC applied to a DFIG wind turbine across operating modes. Results show that FH12-DTC effectively reduces torque and flux ripples compared to C-DTC. The simulations demonstrate fuzzy control can significantly enhance DTC for DFIG-based wind turbines by minimizing the disadvantages of conventional DTC while retaining its benefits.**

Keywords: **Wind turbine, DTC, DFIG, Hysteresis, Fuzzy logic control.**

I. INTRODUCTION

Wind power has emerged as a vital renewable energy source owing to its clean energy production and mitigation of pollution and climate change. Doubly-fed induction generators (DFIGs) have become prevalent in variable-speed wind farms due to their excellent performances, wide operating range, and active/reactive power controllability [1]. However, controlling DFIGs presents challenges.

Direct torque control (DTC) was introduced in the mid-1980s [2] as a technique to select optimal rotor voltage vectors for doubly-fed induction generators. DTC uses hysteresis controllers on torque and flux errors along with a switching table based on the flux sector to determine the proper voltage vector. While providing simple, robust control, conventional DTC suffers from major torque and flux ripples that degrade performance [3-6].

The primary aim of this paper is to develop and evaluate a fuzzy logic controller to enhance direct torque control (DTC) of doubly-fed induction generator (DFIG) wind turbines. The proposed approach, called fuzzy logic 12 sector DTC (FH12-DTC), aims to minimize the disadvantages of conventional DTC (C-DTC) including torque/flux ripples and variable switching frequency while retaining benefits like fast dynamic response and simple control structure. Simulations in MATLAB/Simulink compare FH12-DTC and C-DTC performance across different DFIG operating modes. The results will demonstrate the ability of fuzzy control to significantly improve C-DTC by reducing its limitations.

The contributions of this paper are outlined as follows:

- Developing a fuzzy logic 12 sectors direct torque control (FH12-DTC) strategy for doubly-fed induction generator (DFIG) wind turbines;
- Designing fuzzy hysteresis controllers to replace the conventional flux and torque hysteresis controllers;
- Evaluating the performance of FH12-DTC through simulations across different DFIG operating modes.

This paper is organized as follows. First, modeling of DFIG wind turbines and conventional DTC is provided. The proposed FH12-DTC scheme and fuzzy controller designs are then explained. Next, MATLAB/Simulink simulations compare FH12-DTC and conventional DTC performance under varying wind speeds. Finally, conclusions summarize the results.

II. DESCRIPTION OF THE PROPOSED SYSTEM

Figure 1 illustrates the wind turbine-driven doubly-fed induction generator (WT-DFIG) system controlled by the fuzzy logic

direct torque control (FH12-DTC) method. The system consists of a wind turbine, gearbox, and a DFIG. The DFIG has a rotor connected to two level power converters - an AC/DC converter and a DC/AC converter. The stator is directly connected to the AC grid. The rotor-side converter is linked to the DFIG rotor and is regulated by the FH12-DTC technique. The grid-side converter connects directly to the AC grid to deliver pure sinusoidal current at 50 Hz frequency and unity power factor. Additionally, the system uses a maximum power point tracking (MPPT) algorithm to maximize power extraction when the generated power is below rated power.

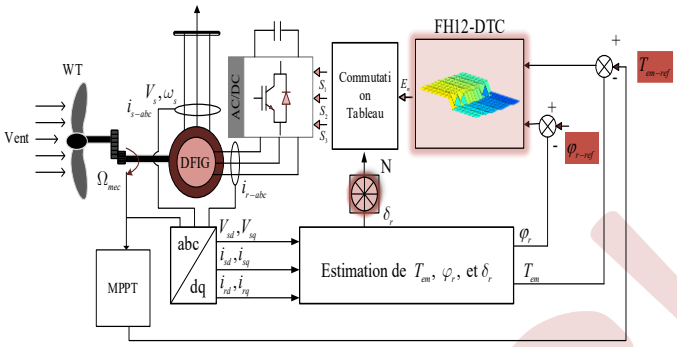


Figure 1. FH12-DTC method applied to the WT-DFIG.

The mechanical power of the wind turbine is a function of wind speed v and power coefficient Cp, as presented in the following equation:

$$P_{mec}=0.5\rho\pi R^2 v^3 C_P(\lambda,\beta) \quad (1)$$

The mathematical model of the doubly fed induction generator (DFIG) in the d-q frame is given by:

$$\begin{cases} v_{sd}=R_s i_{sd}+\frac{d\varphi_{sd}}{dt}-\omega_s\varphi_{sq} \\ v_{sq}=R_s i_{sq}+\frac{d\varphi_{sq}}{dt}+\omega_s\varphi_{sd} \\ v_{rd}=R_r i_{rd}+\frac{d\varphi_{rd}}{dt}-\omega_r\varphi_{rq} \\ v_{rq}=R_r i_{rq}+\frac{d\varphi_{rq}}{dt}+\omega_r\varphi_{rd} \end{cases} \quad (2)$$

$$\begin{cases} \varphi_{sd}=L_s i_{sd}+Mi_{rd} \\ \varphi_{sq}=L_s i_{sq}+Mi_{rq} \\ \varphi_{rd}=L_r i_{rd}+Mi_{sd} \\ \varphi_{rq}=L_r i_{rq}+Mi_{sq} \end{cases} \quad (3)$$

Where

v_{sd},v_{sq},v_{rd} and v_{rq}: Stator and rotor voltages in the d-q frame respectively. I_{sd},I_{sq},I_{rd} and I_{rq}: Stator and rotor current in the d-q frame respectively. ω_s,ω_r: Stator and rotor phase electrical variable pulsations respectively.

R_s,R_r: Stator and rotor resistances respectively. L_s,L_r: Stator and rotor leakage inductances respectively. M: Stator-rotor mutual inductance.

III. Direct Torque Control

To control the DFIG, the DTC technique regulates the machine's electromagnetic torque and rotor flux. First proposed by Takahashi and Noguchi in 1986, DTC offers an alternative to field-oriented control (FOC) by directly selecting AC/DC converter switching states to quickly control flux and torque based on errors between their references and estimated values. This differs from FOC which uses PI controllers to regulate current components. The principle of DTC is explained in [7]. The system under study is illustrated in Fig. 1.

The α-β components of the rotor voltages and currents are used to estimate the rotor flux. The calculated currents ($i_{r\alpha}$, $i_{r\beta}$) and estimated flux values ($\varphi_{r\alpha}$, $\varphi_{r\beta}$) are then used to estimate the electromagnetic torque using equations (4-7).

$$\begin{cases} \varphi_{r\alpha}(t)=\int_0^t (v_{r\alpha}-R_r i_{r\alpha}) \\ \varphi_{r\beta}(t)=\int_0^t (v_{r\beta}-R_r i_{r\beta}) \end{cases} \quad (4)$$

$$\varphi_r(t)=\sqrt{\varphi_{r\alpha}^2+\varphi_{r\beta}^2} \quad (5)$$

$$\theta_r=\tan^{-1}\left(\frac{\varphi_{r\beta}}{\varphi_{r\alpha}}\right) \quad (6)$$

$$T_{em}=P(\varphi_{r\alpha} i_{r\beta}-\varphi_{r\beta} i_{r\alpha}) \quad (7)$$

The outputs of the hysteresis controllers (torque and flux controllers) and rotor flux vector position determine the optimal switching vector selection from the switching table (Table 1) [8].

TABLE I. Switching Table C-DTC

$H\varphi_r$	HT_{em}	N					
		I	II	III	IV	V	VI
+1	+1	V_2	V_3	V_4	V_5	V_6	V_1
	0	V_7	V_0	V_7	V_0	V_7	V_0
	-1	V_6	V_1	V_2	V_3	V_4	V_5
-1	+1	V_3	V_4	V_5	V_6	V_1	V_2
	0	V_0	V_7	V_0	V_7	V_0	V_7
	-1	V_5	V_6	V_1	V_2	V_3	V_4

IV. The Proposed Fuzzy Logic 12 Sectors Direct Torque Control

The proposed fuzzy logic 12-sectors DTC (FH12-DTC) is inspired by [3]. It utilizes a fuzzy logic controller instead of two hysteresis controllers to improve conventional DTC (C-DTC) performance. The FH12-DTC design involves fuzzification, defuzzification, and rule sets.

Fuzzification converts the input variables into linguistic variables by defining membership functions for each, as shown in Fig. 2. Defuzzification converts the fuzzy inference results into a quantifiable output using the Bisector method. The output is a single numerical value with 10 singleton membership functions (E1, ..., E10), illustrated in Fig. 3.

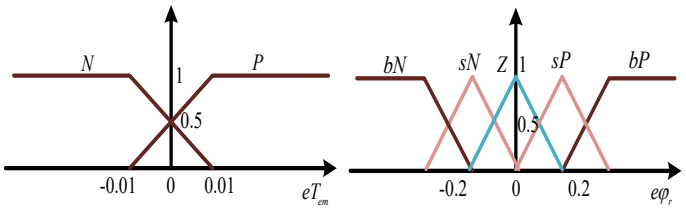


Figure 2. Inputs membership functions.

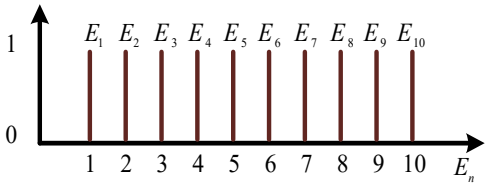


Figure 3. Output membership functions.

The fuzzy logic switching controller uses 10 rules based on the number of inputs membership functions (Table 2). The rules follow a hysteresis operating principle. The Mamdani inference method with Max-Min decision making is used to run the fuzzy controller.

TABLE II. FUZZY RULES

eφ/eTem	bP	sP	Z	sN	bN
P	E_1	E_2	E_3	E_4	E_5
N	E_6	E_7	E_8	E_9	E_{10}

To select the appropriate rotor voltage vector (V_n) for the inverter, it will be based on the output of the numerical error powers (E_n) and the rotor flux sector using the switching table 3.

TABLE III. SWITCHING TABLE FH12-DTC

E_n	θ_n											
	θ_1	θ_2	θ_3	θ_4	θ_5	θ_6	θ_7	θ_8	θ_9	θ_{10}	θ_{11}	θ_{12}
E_1	V_2	V_3	V_3	V_4	V_4	V_5	V_5	V_6	V_6	V_1	V_1	V_2
E_2	V_2	V_2	V_3	V_3	V_4	V_4	V_5	V_5	V_6	V_6	V_1	V_1
E_3	V_0	V_7	V_7	V_0	V_0	V_7	V_7	V_0	V_0	V_7	V_7	V_0
E_4	V_1	V_1	V_2	V_2	V_3	V_3	V_4	V_4	V_5	V_5	V_6	V_6
E_5	V_6	V_1	V_1	V_2	V_2	V_3	V_3	V_4	V_4	V_5	V_5	V_6
E_6	V_3	V_4	V_4	V_5	V_5	V_6	V_6	V_1	V_1	V_2	V_2	V_3
E_7	V_4	V_4	V_5	V_5	V_6	V_6	V_1	V_1	V_2	V_2	V_3	V_3
E_8	V_7	V_0	V_0	V_7	V_7	V_0	V_0	V_7	V_7	V_0	V_0	V_7
E_9	V_7	V_5	V_0	V_6	V_7	V_1	V_0	V_2	V_7	V_3	V_0	V_4
E_{10}	V_5	V_6	V_6	V_1	V_1	V_2	V_2	V_3	V_3	V_4	V_4	V_5

V. SIMULATION RESULTS

The proposed FH12-DTC technique is validated through simulation of a wind turbine driven doubly-fed induction generator (WT-DFIG) system. The technique is implemented in MATLAB/Simulink to control the DFIG across its three operating modes. The WT-DFIG system parameters are as specified in reference [8]. This simulation-based study demonstrates the effectiveness of FH12-DTC for DFIG control.

Fig. 4 shows the wind speed and mechanical speed of the DFIG, indicating operation in three modes - sub-synchronous, synchronous, and super-synchronous.

The electromagnetic torque and its reference along with the rotor flux are shown in Figs. 5 and 6. The torque follows the reference and is influenced by wind speed changes. The rotor flux remains steady at its reference value. The proposed FH-DTC control demonstrating its effectiveness over conventional DTC methods by reduce the ripples.

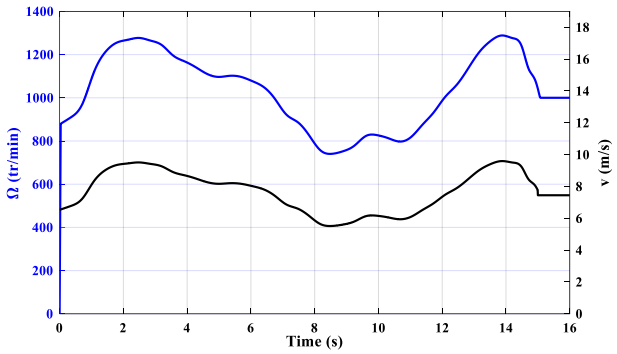


Figure 4. Ω and v responses.

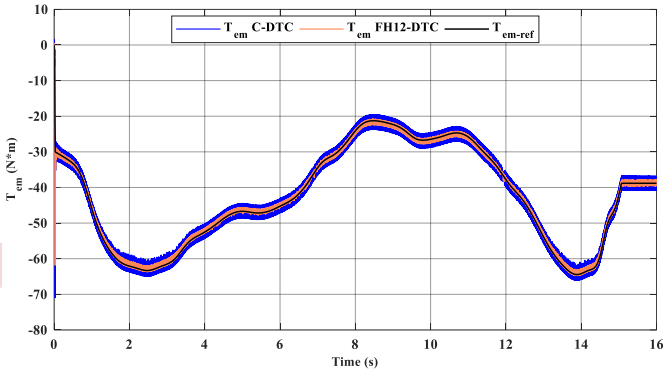


Figure 5. Electromagnetic torque and its reference.

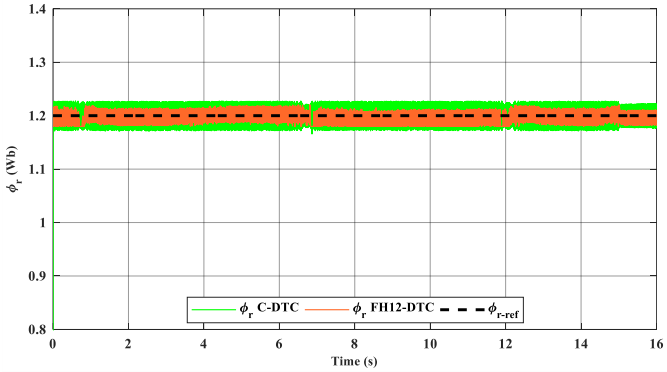


Figure 6. Rotor flux and its reference

Figs. 7 and 8 illustrate the circular rotor flux trajectory in the (α, β) plane. The flux amplitude stays constant at 1.2 Wb as the

components vary sinusoidally in the sub-, super-, and synchronous modes.

As seen in Fig. 9, the stator current amplitude increases with mechanical speed while the frequency is maintained at 50 Hz during the transitions between states.

Fig. 10 indicates the DFIG rotor current amplitude varies with speed changes, and the frequency directly changes with slip variations. In synchronous mode, the rotor currents become DC with zero frequency.

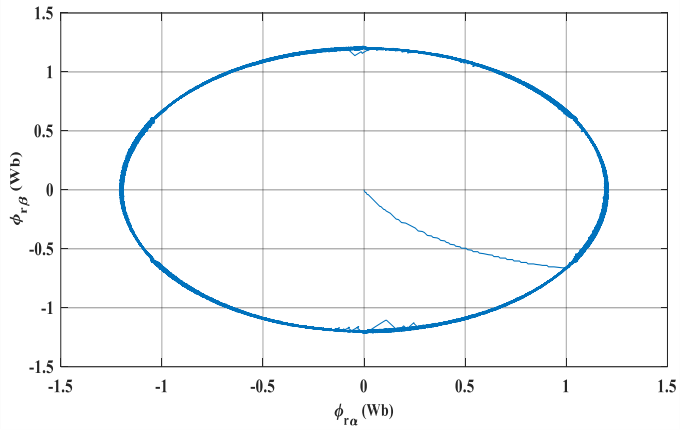


Figure 7. Rotor flux

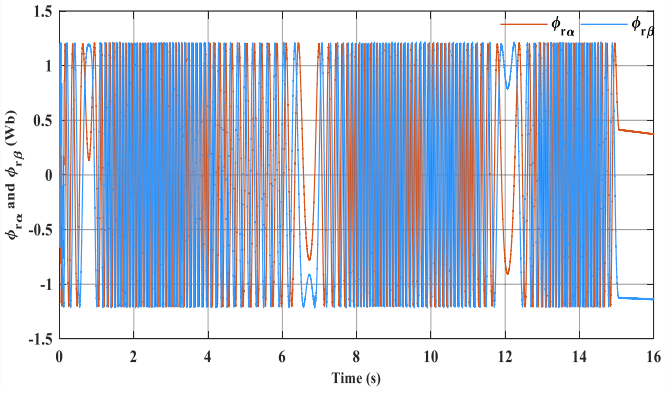


Figure 8. Waveformvof rotor flux.

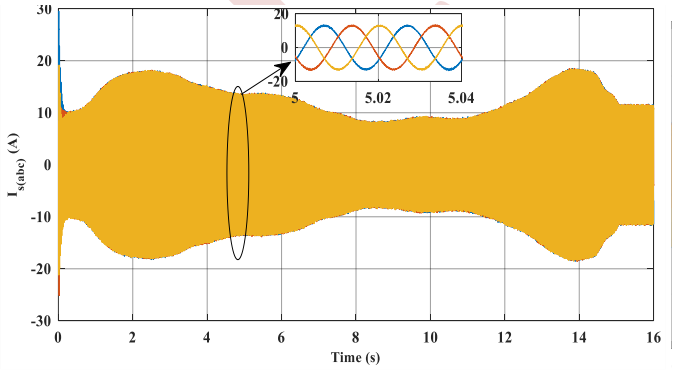


Figure 9. Stator currents.

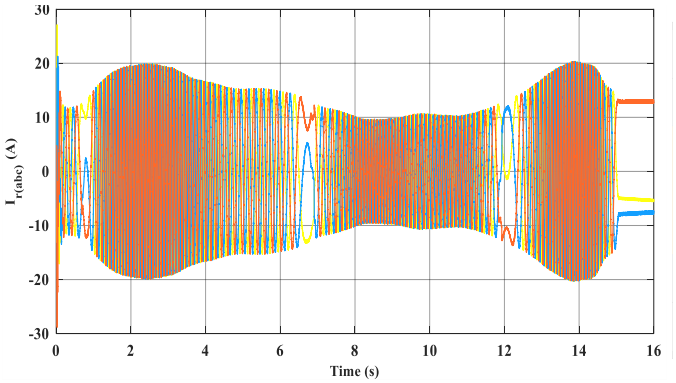


Figure 10. Rotor currents.

In Fig. 11, the negative stator active power ($P_S < 0$) confirms operation as a generator, with this power being fed to the grid as shown by the negative sign.

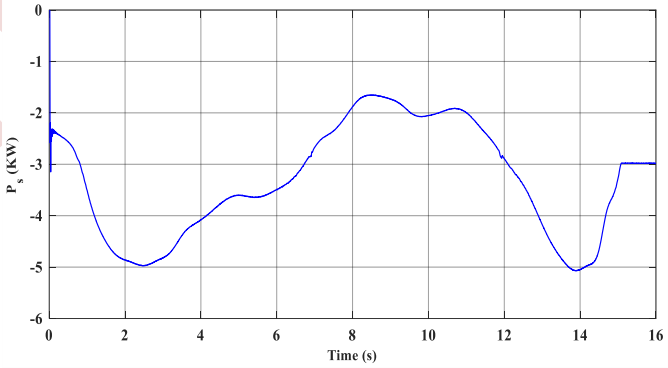


Figure 11. Stator active power.

VI. CONCLUSIONS

This work proposed and validated through simulation a novel direct torque control strategy applying fuzzy logic 12 sectors DTC (FH12-DTC) to enhance conventional DTC for doubly-fed induction generator wind turbines. The objectives were improving DTC by minimizing its major torque and flux ripple while retaining its advantages. Comprehensive simulations under varying wind speeds demonstrated FH12-DTC is a practicable approach for high-performance DFIG operation with substantially reduced ripples and excellent torque and flux tracking.

REFERENCES

[1] P.D. Singh and S. Gao, "An isolated hydro power generation using parallel asynchronous generators at variable turbine inputs using AC-DC-AC converter," 2018 8th IEEE India International Conference on Power Electronics (IICPE), pp. 1-6, December 2018.

[2] I. Takahashi and T. Noguchi, "A new quick-response and high efficiency control strategy of an induction motor," IEEE Trans. Ind. Appl., vol. IA-22, no. 5, pp. 820–827, Oct 1986.

[3] Y. Sahri, S. Tamalouzt, S. Lalouni Belaid, S. Bacha, N. Ullah, A. A. A. Ahamdi, and A. N. Alzaed, "Optimal Power Extraction in Wind Turbine System using Advanced Fuzzy 12 DTC Control of Doubly Fed Induction Generator under Random Wind Conditions," Sustainability, vol. 13, no.21, pp. 11593, 2021.

[4] H. Chojaa, A. Derouich, S. E. Chehaidia, O. Zamzoum, M. Taoussi, H. Benbouhenni, and S. Mahfoud, " Enhancement of Direct Power Control by Using Artificial Neural Network for a Doubly Fed Induction Generator-Based WECS: An Experimental Validation," Electronics, vol. 11, no. 24, pp. 4106, 2022.

[5] B. Zinelaabidine, R. Taleb, Y. Djeriri, and A. Yahdou, "A novel direct torque control using second order continuous sliding mode of a doubly fed induction generator for a wind energy conversion system," Turkish Journal of Electrical Engineering and Computer Sciences, vol. 25, no. 2, pp. 965-975, 2017.

[6] A. Wiam, M. Ourahou, B. El Hassouni, and A. Haddi, "Direct torque control improvement of a variable speed DFIG based on a fuzzy inference system," Mathematics and Computers in Simulation, vol. 167, pp. 308-324, 2020.

[7] R. Cardenas, R. Pena, S. Alepuz, and G. Asher, "Overview of control systems for the operation of DFIGs in wind energy applications," IEEE Trans Ind Electron, 2013.

[8] S. Tamalouzt, T. Rekioua, R. Abdessemed, "Direct torque and reactive power control of grid connected doubly fed induction generator for the wind energy conversion," Conférence Internationale en Sciences et Technologies Electriques au Maghreb CISTEM'2014, Tunis, Tunisie, p. 1-7, November 2014.

EEIC'23

Power management for Hybrid Electric Vehicles (HEVs) based on Permanent Magnet Synchronous Motors (PMSMs) using passivity control

Bessam AMROUCHE [1], Haroune AOUZELLAG[1], Koussaila IFFOUZAR [2], Sabrina NACEF [1], Tahar Otmane CHERIF [3] ,Kaci GHEDAMSI[1]

[1] *Laboratoire de Maitrise des Energies Renouvelables, Faculté de Technologie, Université de Bejaia, Algiers*

bessam.amrouche@univ-bejaia.dz

[2] *Laboratoire des Sciences Appliquées, Ecole Nationale Supérieure des Technologies Avancées ENSTA d'alger, Algiers* E-mail address

k.iffouzar@g.essa-alger.edu.dz

[3] *Laboratoire de Conception et Conduite des Systèmes de Production, Faculté de Génie Electrique et Informatique, Université de Tizi Ouzou, 15000,* otmane_cherif@yahoo.com

***Abstract*—This article presents a solution to a converter coordination problem in a fuel cell system, more precisely a hydrogen fuel cell associated with supercapacitors, with a view to an application to instantaneous dynamic power management. This solution is based on the use of a PI (Proportional - Integral) type nonlinear controller. Validation of this approach was carried out by simulation using Matlab/Simulink, and the results obtained from a scaled-down system confirm the feasibility of this proposed electric transportation system.**

Keywords: **Fuel-cell, super capacitors, hybrid electric vehicle, energy management strategie.**

I. INTRODUCTION

Air pollution caused mainly by conventional combustion vehicle classified as classical car and the employment of battery as the only source of energy for electric vehicles (first proposed solution) is still restricted because of its low autonomy, lifetime and charging time problems [1]. In support, the FC is as a good alternative source to its high autonomy and its zero emission of polluting gas [2, 3]. Between the different FC technologies, the Proton Exchange Membrane (PEMFC) is very useful for the transportation area [4, 5]. PEMFC offers a lot of benefits such as the working at a low temperature compared to other types of FC, low cost which is very important point, quick start up and high efficiency. Just, the FC cannot respond to fast transient peak power demand [6, 7] The vehicle speed and power fluctuations may lead to pressure oscillation and oxygen starvation in the FC membrane which can affect the cell life-time[3, 8]. To solve this problem, a hybridization with another source as UC is the most excellent solution to assist the FC source [9]. This system was used not only to cover the peak power demand, but also to recover the braking energy. Therefore, such configuration improved efficiency and satisfied the power drive demands in all driving conditions. The problem of the use of more than one energy source is the power management. In the literature, different strategies have been emerged to solve this problem. This strategies include the state machine control in tramway [10], which is a simple and well-known rule based strategy; each state is given after on heuristic or empiric past experience. In [11].

The HEV is propelled by Permanent Magnet Synchronous Motor (PMSM) connected to the wheels. The global scheme of the HEV and power system of the FC/Ucis represented in Fig. 1 [5]. The two energy sources (FC and UC) exchange power with a DC bus. For the FC, a boost converter unidirectional in current is utilized to connect the FC to the DC bus; although, the UC requires DC/DC converter bidirectional in current to supply power and to recover the breaking energy. The two inductances added as filters and to respect sources alternation. The DC bus which is a capacitor supplies the both traction machines with employing a tow levels inverter to convert the DC power into AC power. This system gives the torque control of wheels in dependently with a significantly high accuracy, which can enhance the stability of the HEV, reduce clutter caused by the mechanical part such as electrical differential and transmission shafts and give more frees space in the vehicle for UC and hydrogen tank. In an electric vehicle (EV) or hybrid electric vehicle (HEV), the PMSM is typically connected to the vehicle's wheels and is controlled by sophisticated power electronics and control systems. These systems manage the speed, torque, and energy flow between the motor, the vehicle's energy storage system (such as batteries or ultracapacitors), and the driving conditions. The paper is divided into four main parts; the first part is the modelling of the different elements of the system. The second part will deal with the control of the hybrid vehicle. The third part will deal with the control of each element of the system using passivity-based control IDA-PBC for the two sources [5] and FOC for the PMSM [12]. This work will be concluded with the interpretation of the results and the resulting conclusion.

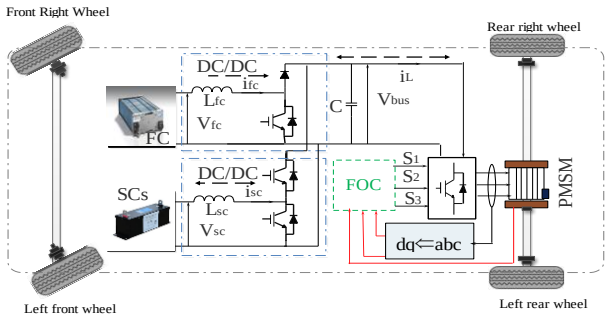


Fig. 1. Global system scheme

II. SYSTEM MODELING

For the FC, a boost converter unidirectional in current is utilized to connect the FC to the DC bus; although, the UC requires DC converter bi-directional in current to supply power and to recover the breaking energy. The two inductances (L_{fc} and L_{sc}) added as filters and to respect sources alternation. The DC bus which is a capacitor (C_{bus}) supplies the traction machine with employing a three phase inverter to convert the DC power into AC power. The machine is three-phase permanent magnet synchronous machine type which is recently used in the transportation field due to its good power, high efficiency The PEMFC is the main energy source for the vehicle. Its cell voltage and its total power are defined by the following equations [4,13]

A. *PEMFC dynamic model*

$$V_{fc} = N_0 V_{fc,cell} \quad (1)$$

$$V_{fc,cell} = E + U_{act} + U_{ohm} \quad (2)$$

$$U_{ohm} = -R_{fc}\, i_{fc} \quad (3)$$

$$U_{act} = -\frac{B}{N_0}\ln\left(C i_{fc}\right) \quad (4)$$

The expression of the Nernst equation according to JC Pamphlet is given by:

$$E_{Nernst} = E_0 + \frac{RT_{fc}}{2F}\ln\left(\frac{P_{H_2}\sqrt{P_{O2}}}{P_{H_2O}}\right) \quad (5)$$

The FC should be able to provide the power demand of the vehicle P_{dem} by taking into account the FC efficiency η_{fc}

$$\frac{q_{H_2}}{P_{H_2}} = K_{H_2} \quad (6)$$

$$\frac{q_{O_2}}{P_{O_2}} = K_{O_2} \quad (7)$$

$$\frac{q_{H_2O}}{P_{H_2O}} = K_{H_2O} \quad (8)$$

where K_{H_2} and K_{O_2} are the hydrogen and oxygen valve constants respectively. Using the ideal gas formula and writing the molar flows as q^{in}, q^{out} and q^{r}.

The fuel cell model is shown in the Fig. 2.

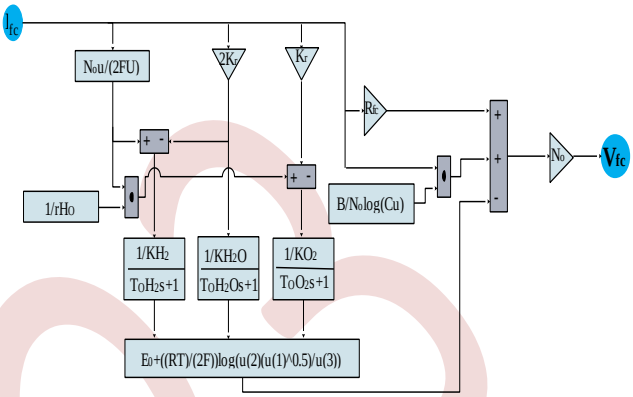


Fig. 2. Mathematical model of the fuel cell

B. *Vehicle modeling*

The vehicle is considered as a solid point moving subjected to forces along the longitudinal axis: the traction force to the advancement F_{roll}, the effort of aerodynamic resistance F_{aero} and the resistance of mounted side F_{slope} [14,15]. The resisting forces are given by the following equations::

$$F_{roll} = M_v\, g\, f_r \quad (9)$$

$$F_{aero} = \frac{1}{2}\rho A C_x V_v^2 \quad (10)$$

$$F_{slope} = M_v\, g \sin\left(\delta\right) \quad (11)$$

The fundamental principle of the vehicle dynamics is described by the following equation:

$$M_v \frac{dV_v}{dt} = F_t - F_{roll} - F_{aero} - F_{slope} \quad (12)$$

The traction force of each wheel is given by the following expression: $\frac{F_t}{2} = \frac{T}{2R_w}$ (13)

C. *SCs boost converter*

in this paper SCs are used for two types of operations, the mode of working when SCs receives the uninterrupted energies of the bus of current and the second mode when SCs gives the energies in the bus of current go on, therefore the storage elements are connected to the DC bus through a reversible power converter, The boost converter is controlled by binary input. We define λ_2 as the duty cycle of the control variable. The second sub-system is represented by an average model as follows:

$$\frac{d}{dt}\left(i_{sc}\right) = \frac{1}{L_{SC}}\left(-\left(1-\lambda_2\left(t\right)\right)v_b\left(t\right) + v_{sc}\left(t\right)\right) \quad (14)$$

$$\frac{d}{dt}v_{sc}(t) = -\frac{i_{sc}(t)}{C_{sc}} \quad (15)$$

where $v_{sc}(t)$ is the SCs voltage, v_b is the DC link voltage, i_{sc} is the SCs current, L_{SC} is the inductance of the SCs and C_{sc} is the capacity of the SCs

D. FC boost converter

a lifting converter must augment voltage v_{fc}, by what voltage, v_{fc} is often less than the voltage of bus of direct current, is controlled by binary input. Defining λ_1 as the duty cycle of control variable knowing that the currents i_{fc} and i_L are physically the same . The dynamics of the DC–DC boost power converter with an inductive load This sub-system is represented by an average model as follows :

$$\frac{d}{dt}i_{fc} = \frac{1}{L_{fc}}\left(-\left(1-\lambda_1(t)\right)v_b(t) + v_{fc}(t)\right) \quad (16)$$

$$\frac{d}{dt}v_b(t) = \frac{1}{C_b}\left(\left(1-\lambda_1(t)\right)i_{fc}(t) + \left(1-\lambda_2(t)\right)i_{sc}(t) - i_L(t)\right) \quad (17)$$

where v_{fc} is the FC voltage, i_L is the DC current delivred to the load and i_{fc} is the FC current In our work, the load is modeled by a Permanent magnet synchronous machine; the model is represented in the reference mark(d ,q).

$$\frac{d}{dt}i_L(t) = \frac{1}{L}\left(-R_l(t)i_L + v_b(t) - \varphi_f\,\omega(t)\right) \quad (18)$$

$$\frac{d}{dt}\Omega = \frac{1}{J}\left(p\left(\left(L_d - L_q\right)i_d i_q + \varphi_f i_q\right) - f\,\Omega - T_r\right) \quad (19)$$

Complete model. It follows that the complete "fuel cell - super capacitors" system is represented by the 5th order non-linear state space model :

$$\begin{cases} \frac{d}{dt}v_b(t) = \frac{1}{C_b}\left(\left(1-\lambda_1(t)\right)i_{fc}(t) + \left(1-\lambda_2(t)\right)i_{sc}(t) - i_L(t)\right) \\ \frac{d}{dt}v_{sc}(t) = -\frac{i_{sc}(t)}{C_{sc}} \\ \frac{d}{dt}i_L(t) = \frac{1}{L}\left(-R_l(t)i_L + v_b(t) - \varphi_f\,\omega(t)\right) \\ \frac{d}{dt}i_{fc} = \frac{1}{L_{fc}}\left(-\left(1-\lambda_1(t)\right)v_b(t) + v_{fc}(t)\right) \\ \frac{d}{dt}(i_{sc}) = \frac{1}{L_{SC}}\left(-\left(1-\lambda_2(t)\right)v_b(t) + v_{sc}(t)\right) \end{cases} \quad (20)$$

with state space $x(t) = \left[v_b; v_{sc}; i_L; i_{fc}; i_{sc}\right]^T$,control imputs $u(t) = \left[u_1; u_2\right]^T = \left[1-\lambda_1; 1-\lambda_2\right]^T$,measures $y(T) = x$ and v_{fc} .

the system equation (20) is called an unsettled system since the difference of ladder of time between the dynamics of voltages and the current them causes it of disturbance, to resolve this problem the system in mode controlled is forced by current by using a loop inner current. More precisely, the following PI current controllers.

$$u_1 = Ki_{fc}\int_0^t\left(i_{fc}^* - i_{fc}\right)dt + Kp_{fc}\left(i_{fc}^* - i_{fc}\right) \quad (21)$$

$$u_2 = Ki_{sc}\int_0^t\left(i_{sc}^* - i_{sc}\right)dt + Kp_{sc}\left(i_{sc}^* - i_{sc}\right) \quad (22)$$

In equations 40 and 41, u_1 and u_2 have been programmed to individually compel the i_{fc} and i_{sc} currents to obey their references i_{fc}^* and i_{sc} , resulting in an extremely rapid response time when the static error occurs. The two control laws u_1 and u_2 function as high gain feedback, the two static gains are deemed suitably strong in terms of the voltage and load dynamics, and after the transient we obtain $i_{fc}^* - i_{fc} = 0$ and $\int_0^t\left(i_{fc}^* - i_{fc}\right) = v_{fc}/v_b\,Ki_{fc}$, this means that the equation 40 becomes $u_1 = v_{fc}/v_b$ and according to the same argument the equation 41 becomes $u_2 = v_{sc}/v_b$. therefore by replacing the two new control laws and current i_{fc}^* and i_{sc}^* them in the global system we obtain the following reduced order system [16]

$$\begin{cases} \frac{d}{dt}v_b(t) = \frac{1}{C_b}\left(\frac{v_{fc}(t)}{v_b(t)}i_{fc}^*(t) + \frac{v_{sc}(t)}{v_b(t)}i_{sc}^*(t) - i_L(t)\right) \\ \frac{d}{dt}v_{sc}(t) = -\frac{i_{sc}^*(t)}{C_{sc}} \\ \frac{d}{dt}i_L(t) = \frac{1}{L}\left(-R_L(t)i_L + v_b(t) - E(t)\right) \end{cases} \quad (23)$$

according to the control by passivity and the Hamiltonian modeling the resolution of the equations of states representing the static converters [21,6] we will obtain the referential equations of the currents as

$$\begin{cases} \boldsymbol{i_{fc}^*} = \frac{v_{bus}}{v_{fc}}\left[i_L^* + \lambda\left(\left(\frac{v_{sc}}{v_{bus}} - \frac{v_{bus}}{v_{fc}}\right)\tilde{v}_{bus} - \tilde{v}_{sc}\right)\right] \\ \boldsymbol{i_{sc}^*} = -\lambda\,\tilde{v}_{bus} \end{cases} \quad (24)$$

III. CONTROL SYSTEM

A. Field oriented control of PMSM

The aim is always to assimilate the behavior of PMSM to that to the DC machine separately excited by decoupling control of torque of the flux. The model exprimed in system (23) is strongly coupled, which make it very difficult to resolve. For this the decoupling of this later is most interesting

The model of the synchronous machine in the reference rotational frame (dq) to system differential equations where

the currents i_d and i_q, are not independent one of the other. They are connected by nonlinear terms $L_q \omega i_q$ and $L_d \omega i_d$

$$\begin{cases} V_d = \left(R i_d + L_d \dfrac{d}{dt} i_d \right) - L_q \omega i_q \\ V_q = \left(R i_q + L_q \dfrac{d}{dt} i_q \right) + L_d \omega i_d + \varphi_f \omega \end{cases} \quad (25)$$

then the method of the compensation is useful has the elimination of this coupling, this last method consists has to add terms to the levels of the two axes in order to return them independent completions. The principle of this decoupling return has to define two new variables e_d and e_q of orders as follows such as

$$\begin{cases} V_d = V_{d1} - e_d \\ V_q = V_{q1} + e_q \end{cases} \quad (26)$$

with

$$\begin{cases} V_{d1} = R i_d + L_d \dfrac{d}{dt} i_d \\ R i_q + L_q \dfrac{d}{dt} i_q \end{cases} \quad (27)$$

And

$$\begin{cases} e_d = L_q \omega i_q \\ e_q = L_d \omega i_d + \varphi_f \omega \end{cases} \quad (28)$$

finally we will have both of this month who are uncoupled

$$\begin{cases} i_d = \dfrac{V_{d1}}{R_s + pL_d} \\ i_q = \dfrac{V_{q1}}{R_s + pL_q} \end{cases} \quad (29)$$

p: Operator of Laplace

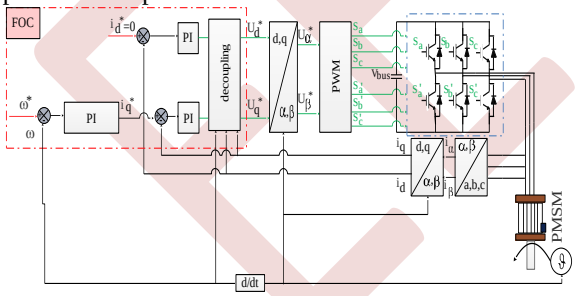


Fig. 4. Block diagram of field oriented control (FOC)

3.2 Power management strategies

The control of the two converters system has been detailed in [21] It consists on the frequency decoupling of sources according to the power requested. The DC bus filters the high frequencies, the SCs connected with its converter provides the medium frequencies and the FC ensures the low frequencies. This frequency decoupling of the sources naturally induces a power management strategy based on cascaded loops presented in Fig. 5.

Any change in the DC bus voltage is induced by power load modification. Hence, it seems recommended to control the DC bus voltage with the SCs by computing the reference current i_{sc}, and thus regulate the bus voltage to its reference. The outer voltage loop associated with the SCs management must maintain the DC bus voltage at a constant reference v_{bus} fixed at $400V$. The current loops are based on proportional-integral controller.

Knowing that the demand for DC bus assistance would result in a permanent SC discharge, which would impose an excessive capacity to provide and continuously absorb energy during rapid transient regimes. Therefore, the control system must maintain, in steady state, the SC state of charge at a desired value and avoid huge SCs voltage ripple. This requirement can be ensured by a compensation

loop whose purpose is to regulate the SCs voltage v_{sc} at their references v_{sc}^*. The compensation is assured by a proportional integral regulator. Thus the compensation loop generates a current reference i_{fc}^* with a slow dynamic. Consequently, this choice meets the frequency decoupling requirement and allows good control of the SCs to their voltage reference levels.

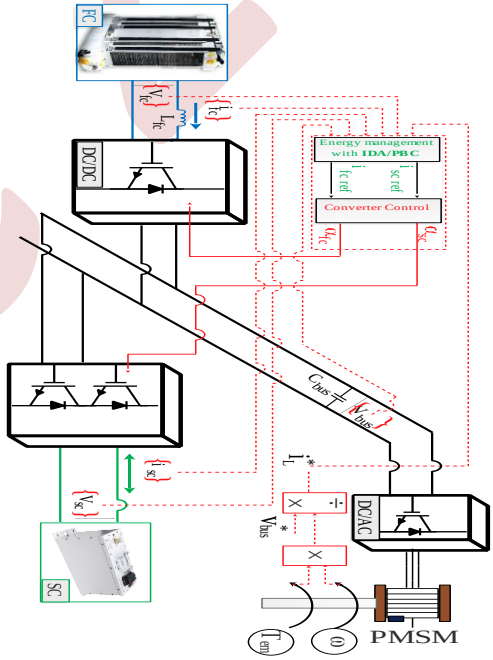


Fig. 5. Bloc diagram of the control strategy

IV. *SIMULATIONS AND RESULTS*

The analysis will focus on the Transitional FC / SC System Fig.6 shows the response of the hybrid system for both architectures to a load including positive and negative current steps (Fig.6. (a),(c),(i)). At each transient load (T = 0.1 s / 2.5 s / 6 s), the bus voltage for the two-converter structure (Figure.6 (e), (f)) is slightly transiently affected (less than 4%) but is generally well regulated. We observe a slow variation of the FC voltage, but it nevertheless remains subject to its reference. Indeed, this is made possible by the super capacitors that react

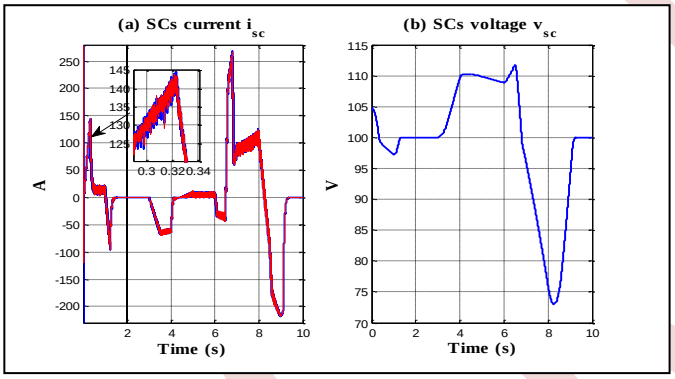
Rapidly to the sudden transients of the charging current (Fig. 6 (e)). These transients are induced by the regulation of the bus voltage and

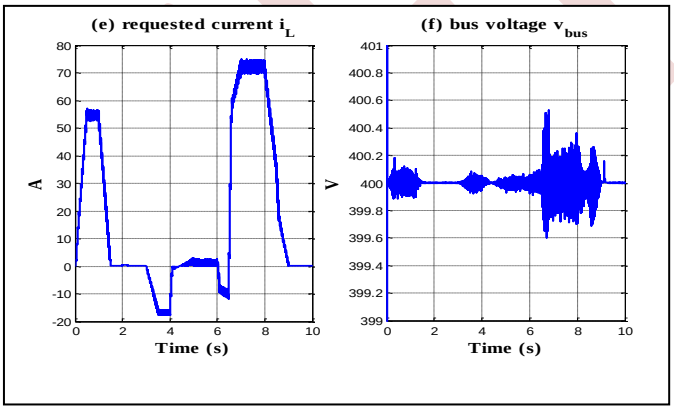
make it possible to ensure the major part of the transient component of the required power. The energy transfer from the SCs to the DC bus is therefore logical and correct and makes it possible to compensate for the energy that is not supplied by the fuel cell. This allows the cell to respond without abrupt change in its current stress to the load

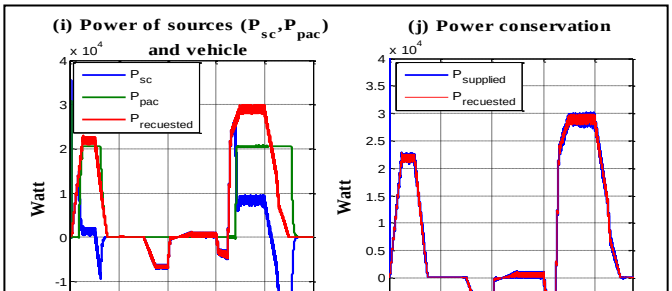
Then, as the current of the FC increases, the discharge Of the SCs characterized by the decrease of its voltage is attenuated until it cancels out (Fig. 6 (b)). There is then a regime of rebalancing (called compensation), Characterized by a recharge of the SCs at its values of Reference (V_{scref}) set at 100V.

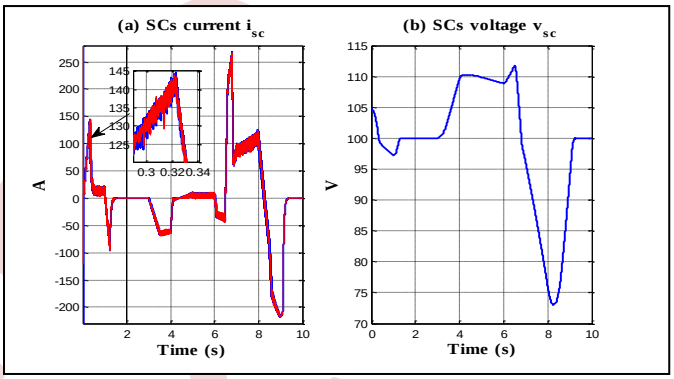
During the negative current transients of the load (at times t = 2.5 s / 6s), the load is fed by the FC but part of the excess power of this load is absorbed by the SCs (HF) .Subsequently, rebalancing (compensation) takes place because the FC progressively supplies the power required for the load, as well as that necessary to bring the voltages of the SCs back to their reference levels. In this case, it may be a power lower than that required by the load so that the voltage of the SCs decreases towards its reference level.

The recuperative functioning is envisaged in the simulation. However, the sudden drop in load power creates recuperative operation at the SCs









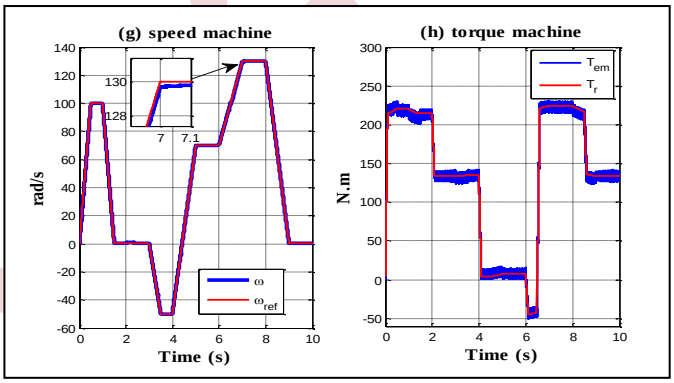


Fig. 6. Simulation system results

V. *CONCLUSION*

The integration of permanent magnet synchronous machines (PMSMs) in electric vehicles (EVs) is a significant topic in the field of electric vehicle propulsion systems and motor drive technology. PMSMs are a type of electric motor that offers several advantages for EV applications, making them a popular choice for electric propulsion. The passivity-based control method used in this article aims to define controllers that feature system . stability and performance while preventing instability or unpredictable behavior. A control strategy for an electric vehicle is essential to maximize energy efficiency, optimize the management of electrical sources and improve the overall performance of the vehicle

REFERENCE

[1] M D. Berliner, D A. Cogswell , M Z. Bazant *, R D. Braatz A Mixed Continuous-Discrete Approach to Fast Charging of Li-ion Batteries While Maximizing Lifetime IFAC-PapersOnLine 2022, Pages 305-310

[2] H. Aouzellag, B. Amrouche, k. iffouzar D. aouzellag. Proposed hysteresis energy management strategy based on storage system efficiency for hybrid electric vehicle Journal of Energy Storage, 2022, 105259
[3] Azib Toufik, Bethoux Olivier, Remy Ghislain, Marchand Claude. Saturation management of a controlled fuel-cell/ultracapacitor hybrid vehicle. IEEE Trans. Veh. Technol. 2011; 60: 4127–4138.
[4] H S Das , M Salem , M A A M Zainuri , A M Dobi , S Li , Md H Ullah . A comprehensive review on power conditioning units and control techniques in fuel cell hybrid systems Energy Reports, 2022, Pages 14236-14258
[5]A A Sinha , Sanjay , M Z Ansari , A K Shukla [c], T Choudhary . Comprehensive review on integration strategies and numerical modeling of fuel cell hybrid system for power & heat production. International Journal of Hydrogen Energy .2023
[6] B Amrouche , T O Cherif, M Ghanes, K Iffouzar, A passivity-based controller for coordination of converters in a fuel cell system used in hybrid electric vehicle propelled by two seven phase induction motor. Int. J. Hydrogen Energy 2017, 26362-26376.
[7] S Sagaria, RC Neto, P Baptista. Assessing the performance of vehicles powered by battery, fuel cell and ultra-capacitor: Application to light-duty vehicles and buses Energy Conversion and Management, 2021, 113767
[8] A Farsi, M A. Rosen Performance analysis of a hybrid aircraft propulsion system using solid oxide fuel cell, lithium ion battery and gas turbine . Applied Energy, 2023, 120280
[9] C Jia , J Zhou , H He , J Li a c, Z Wei , K Li, M Shi . A novel energy management strategy for hybrid electric bus with fuel cell health and battery thermal- and health-constrained awareness . Energy ,2023, 127105
[10] M Iqbal , M Becherif, H S Ramadan, A Badji. Energy source sizing methodology for hybrid fuel cell vehicles based on statistical description of driving cycle. Applied Energy, 2021, 117345
[8] J Yang, X Xu, Y Peng, J Zhang, P Song .Modeling and optimal energy management strategy for a catenary-battery-ultracapacitor based hybrid tramway Energy ,2019, Pages 1123-1135
[11] R T Yadlapalli , R R Alla , R Kandipati , A Kotapati. Super capacitors for energy storage: Progress, applications and challenges Journal of Energy Storage Volume 49, May 2022, 104194
[12] K Iffouzar , B Amrouche , T O Cherif, M F Benkhoris, D Aouzellag , K Ghedamsi . Improved direct field oriented control of multiphase induction motor used in hybrid electric vehicle application. Int. J. Hydrogen Energy 2017, Pages 19296-19308
[13] Q Li , H Yang, Y Han a, MLi b, W Chen. A state machine strategy based on droop control for an energy management system of PEMFC-battery-supercapacitor hybrid tramway. In. J . Hydrogen Energy 2016, 16148-16159
[14] D Rezzak a, N Boudjerda. Robust energy management strategy based on non-linear cascade control of fuel cells-super capacitors hybrid power system. In. J Hydrogen Energy 2020, Pages 23254-23274
[15] H Hu, W W Yuan , M Su , K Ou .Optimizing fuel economy and durability of hybrid fuel cell electric vehicles using deep reinforcement learning-based energy management systems. Energy Conversion and Management September 2023, 117288
[16] Hilairet M, Ghanes M, Bethoux O, Tanasa V, Barbot J-P, Normand-Cyrot D. A passivity-based controller for coordination of converters in a fuel cell system. Control Eng Pract 2013;21(8):1097e109. Pergamon.

Appendix A. Table 1: Electric characteristics of the hybrid system.

parametre	Value
Fuel cell parametre	
Open circuit voltage E	$350V$
Rated voltage	$342\,V$
Rated current	$60\,V$
Supercapacitors parametres	
Capacitance	$5\,F$
Rated voltage	$100\,V$
Rated current	$250\,A$
Optimal voltage v_{sc}^{*}	$100\,V$
Exchange current density i_0	$0.05\,A.m-2$
Molar concentration c	$1(8\,NA\,r^3)^{-1}$mol.m^{-3}
Number of layers of electrodes N_C	1
Number of parallel UC cells N_P	1
Number of series UC cells N_S	18
Molecular radius r	10^{-9}C
Charge transfer coefficient α	$0.3\,m$
Permittivity of material ε	$6.0208\,10^{-10}$F.m-1
Over potential ΔV_c	$2.7\,V$
Operating temperature TC	25 C°
Inductance and capacitie parametres	
L_{sc}	$200\,\mu H$
L_{fc}	$100\,\mu H$
Rated current L_{sc}	$250\,A$
Rated current L_{fc}	$60\,A$
Capacities C	$1\,mF$
Optimal DC bus voltage v_{bus}^{*}	$400\,V$
Parameters of the HEV model.	
Vehicle total mass	$1300\,Kg$
Rolling resistance force constant	$0.01\,s^2/m^2$
Air density	$1\,Kg.m^3$
Frontal surface area of the vehicle	$2.6\,m^2$
Tire radius	$0.32\,m$
Aerodynamic drag coefficient	0.30
Acceleration due to gravity	$9.8\,m/s^2$
parameters of PMSM	
Speed	$150\,rad/s$
Nominal torque	$250\,N.m$
R_s	$0.5\,\Omega$
$L_d = L_q$	$8.5\,mH$
φ_f	$0.1815\,Wb$
p	4
J	$0.00546\,Kg.m^2$
f	$0.0112\,m^{-1}$

IX

Robotics and Artificial Intelligence (RAI)

Sommaire

IX.1 A sampling-based approach for path planning of unmanned aerial manipulators **513**
IX.2 Multispectral stereo-vision for outdoor localization **519**
IX.3 Robust PUMA560 control with backstepping-ADRC **525**
IX.4 Optimal trajectory planning with obstacle avoidance based on water cycle algorithm for a flying robot **531**
IX.5 Remote control of mentor robot via Bluetooth **537**
IX.6 Comparative study between two parametric identification methods used to identify the building heating system **543**
IX.7 Asymptotic stabilization of a morphing drone using interconnection and damping assignment-passivity based control **549**
IX.8 A comparison of fuzzy logic and adaptative backstepping in diabetics controler **556**
IX.9 Model-based states estimation approach applied to a reconfigurable quadrotor for position and attitude tracking control **561**

A Sampling-Based Approach For Path Planning of Unmanned Aerial Manipulators

1st ZAMOUM Housseyn [1], 2nd BOUZID Yasser [2], 3rd GUIATNI Mohamed [3]

[1] *Ecole Militaire Polytechnique, Algiers, Algeria*

zamoumhousseyn@gmail.com

[2]*Ecole Militaire Polytechnique, Algiers, Algeria*

yasseremp@gmail.com

[3]*Ecole Militaire Polytechnique, Algiers, Algeria*

mohamed.guiatni@gmail.com

***Abstract*—This paper presents a new approach to path planning for unmanned aerial manipulator systems (UAMs) using Sampling-Based Methods and Random Geometric Models (RGM) to efficiently search the configuration space for feasible, collision-free paths. The RGM generates random points in the UAM's workspace to guide sampling-based algorithms in constructing graphs that link the aerial manipulator's initial and final positions. These graphs are then explored using the RRT* algorithm to find an optimal collision-free path. The effectiveness of this approach is demonstrated through different scenarios, showing that it outperforms existing path planning techniques in terms of efficiency, computing time, and robustness. The proposed framework is adaptable to various application scenarios and environments, making it a valuable tool for applications such as search and rescue missions, surveillance, and inspection tasks.**

***Keywords:* Path Planning, Sampling-Based Methods, Random Geometric Model, UAMs, UAV Manipulator.**

I. INTRODUCTION

Unmanned Aerial Vehicles (UAVs) equipped with manipulator's arms have become increasingly popular in recent years, offering a versatile and efficient solution for various applications, including pick up, place and transportation of objects, smart agriculture, object manipulation, inspection, and construction, in environments that are difficult or unsafe for humans to access [8].

Generating efficient, collision-free path for UAV manipulators is one of the main challenges in their operation, as it is critical for performing complex tasks accurately and quickly.

Recently, there has been a growing interest in the use of sampling-based algorithms to solve the problem of trajectory planning for aerial manipulators. In their work, M. Brunner et al. [1] proposed a sampling-based approach for fully-actuated MAVs that can exert forces and torques in six degrees of freedom (6- DoF). This makes them well-suited for aerial manipulation tasks that require precise control. The sampling-based approach utilized in their work does not rely on an analytical model of the interaction dynamics. This allows the approach to handle multiple and recurring contacts between the aerial manipulator and the environment. In [9] M. Yavari proposes an integrated planning strategy for object retrieval using a sampling-based approach called Lazy-Steering-RRT*. This approach plans the motion of an Unmanned Aerial Manipulator (UAM) from its starting point to a pre-grasp state while minimizing the motion of the arm. Limited-range sensors onboard facilitate on-the-fly planning using Machine-Learning-based. The authors in [2] propose a path planning approach for an aerial pick-and-place task, where an aerial manipulator is required to pick up or place an object at specified waypoints with partial state variable constraints. The proposed framework is based on the informed RRT* algorithm in a bidirectional manner and incorporates an extra merging process to integrate the trees from the start and goal points. In [3]., an airborne robotic system with two arms and a lengthy bar extension is designed for long-range manipulation in crowded settings. The authors provide detailed information on the trajectory planning performance of this system using a planner based on the Rapidly-exploring Random Tree (RRT*) algorithms. In [4]., the authors present the planning of multiple aerial manipulators for cooperative transport. The desired path for each aerial manipulator is obtained by using RRT* to transport an object to the desired position while taking into consideration the constraints of the end effector's capture point.

This paper proposes a new path-planning method for UAMs that utilizes sampling-based algorithms and the direct geometric model (DGM) and inverse geometric model (IGM) equations to describe the coupled motions between the UAV and its manipulator's arm. The proposed approach combines the strengths of sampling-based methods and the RGM, which can be used together with DGM and IGM to generate

efficiently achievable trajectories that can navigate complex and cluttered environments.

The rest of the document is organized as follows: Section 2 presents the mathematical formulation of the path planning problem and the direct and inverse geometric modelling of UAMs. In Section 3, the proposed path planning strategy and the details of the algorithm developed in this work are described. Section 4 presents the different results obtained from implementing the algorithm for several scenarios. Finally, Section 5 concludes with the results and recommendations for future research.

II. MATHEMATICAL FORMULATIONS OF THE PROBLEM

Path planning for a UAV with a manipulator's arm involves finding a collision-free path that the system can follow from an initial position to a desired goal position. The mathematical formulation of this problem can vary depending on the specific scenario and objectives, but here are some of the common mathematical formulations used in path planning:

- Let X is the state space of the planning problem.
- The states that collide with the obstacles are called $X_{obs} \subset X$, and $X_{dead} \subset X$ is the dead space or "unreachable space", the states in which an aerial manipulator cannot manipulate an object where it is unable to reach it due to limitations in its physical structure or the constraints of the task.
- Let $X_{free}=X \setminus X_{obs}$ is the set of admissible states that results for the aerial robot, the initial state is X_{star} and the desired finale state is X_{goal}.

Definition 1. A feasible path is defined for an aerial manipulator system, if it is a collision-free path and if there is a sequence of states $\sigma = [\sigma_\beta, \sigma_e]$ defined as follows:

$$\sigma : [0, 1] \times [0, 1] \longrightarrow X_{free} \times X_{free} \qquad (1)$$
$$\lambda \longrightarrow \sigma(\lambda) = [\sigma_\beta, \sigma_e]$$

with $\sigma(0, 0) = [X_{\beta,star}, X_{e,star}]$ and $\sigma(1, 1) = [X_{final}, Xgoal]$. The search for the optimal path σ_e^* and σ_β^* , which minimizes a specified cost function, $c : \Gamma \longrightarrow R+$, which connects X_{start} to X_{goal} through the free space X_{free} is the formal definition of the optimal planning problem and is expressed as follows:

$$\sigma_\beta^* = \arg\min_{\sigma \in \Gamma} \{c(\sigma_B) \mid \forall s \in [0, 1], \sigma_B(t) \in X_{free}\} \qquad (2)$$

Sampling-based methods such as RRT and RRT* are helpful for generating feasible paths that satisfy constraints such as obstacle avoidance. However, sampling-based methods cannot consider the UAV's positioning model or unreachable positions, as shown in fig.1.

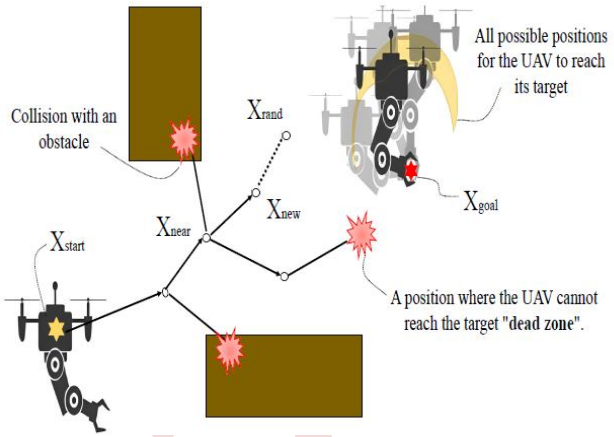


Fig.1: The challenges of path planning through the sampling approaches of an aerial manipulator.

We consider a UAM which is a combined system of a UAV and an n-DoF robotic arm. The earth fixed frame $\{I\} = (O_I, X_I, Y_I, Z_I)$, the body fixe frame $\{B\} = (O_B, X_B, Y_B, Z_B)$ attached to the centre of mass of UAV, and the $\{B_j\} = (O_j, X_j, Y_j, Z_j)$ reference frame. attached to the link j of the arm are defined in Fig. 2.

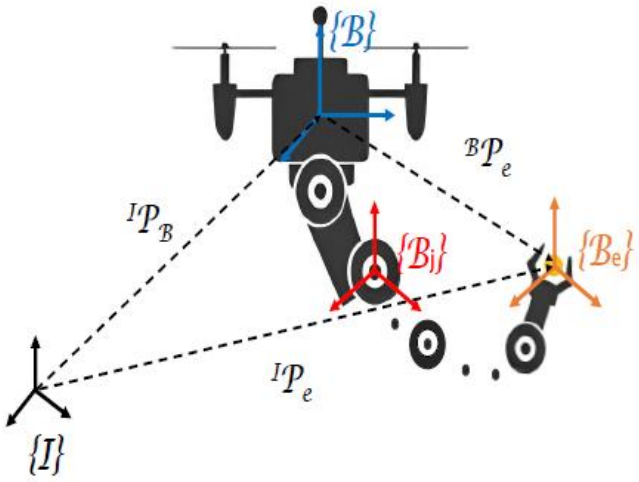


Fig.2: Configuration space of an unmanned aerial manipulator (i.e. a UAV with a robot arm with n-DoF) in our proposed configurations.

The first vector $\chi=[X_e^T \Phi_e^T]^T$, where $\Phi_e =[\phi_e \theta_e \psi_e]^T$ expressed as the generalized coordinates of the terminal organ attached to the frame $\{B_e\}$.

The second vector represented by the collection of state variables of the UAV and the arm joint as $\xi =[X_e^T \Phi_e^T Q_a^T]^T$, with $\Phi_B =[\phi \theta \psi]^T$ gives the orientation of the UAV with respect to the fixed reference frame {I}, $Q_a =[q_1 q_2 \ldots q_n]^T$ represent the joint vector of the n-DoF manipulator's arm expressed in the reference frame {B}.

A. Direct Geometrical Models

The direct geometrical problem consists in determining the

operational coordinates of the end effector, according to the movements of the UAV as well as the movement of the manipulator's joints.

Definition 2. Consider D_G as a mathematical function describing the transition from the operational coordinate space $N \subseteq R^6$ to the joint space $M \subseteq R^{6+n}$ as follows:

$$D_G : N \longrightarrow M$$
$$\xi \longrightarrow \chi = D_G(\xi) \quad (3)$$

B. Inverse Geometrical Models

The inverse geometric approach is fundamental to the control of the UAM as it allows the calculation of the UAV motions and the manipulator arm joint variables required to move the end effector to a desired position.

Definition 3. Consider I_G as a mathematical function describing the transition from the joint space M to the operational coordinate space N as follows:

$$I_G : M \longrightarrow N$$
$$\chi \longrightarrow \xi = I_G(\chi) \quad (4)$$

III. PATH PLANNING STRATEGY

In this work, path planning for a manipulator UAV using sampling and random geometric model (RGM) based methods is a technique used to generate feasible trajectories for an unmanned aerial vehicle (UAV) with a manipulator's arm.

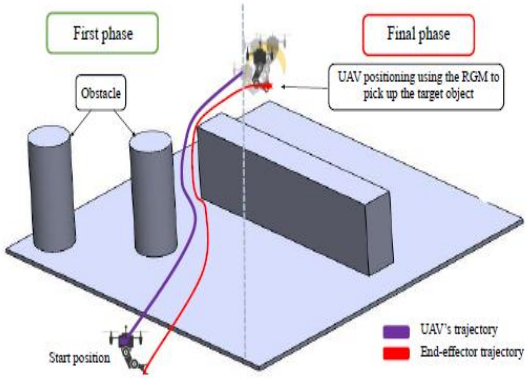
Algorithm 1: S-RGM*$(X_{\mathcal{B},\text{start}}, X_{e,\text{start}}, X_{\text{goal}}, \Phi_{e,\text{goal}}, map)$

$\mathcal{V} \leftarrow \{X_{\mathcal{B},\text{star}}, X_{e,\text{star}}\}; E \leftarrow \{\emptyset\}$;
$\mathcal{T} \leftarrow \{\mathcal{V}, E\}$;
for $k = 1$ *to* N **do**
  $X_{\mathcal{B},\text{RGM}} \leftarrow \text{RGM}(X_{\text{goal}})$;
  $X_{\mathcal{B},\text{nearest}} \leftarrow \text{Nearest}(\mathcal{T}, X_{\text{rand}})$;
  $X_{\mathcal{B},\text{new}} \leftarrow \text{Steer}(X_{\mathcal{B},\text{nearest}}, X_{\mathcal{B},\text{rand}})$;
  if $CollisionFree(X_{\mathcal{B},nearest}, X_{\mathcal{B},new}, map)$ **then**
    $X_{\mathcal{B},\text{near}} \leftarrow \text{Near}(\mathcal{T}, X_{\mathcal{B},\text{new}}, r_{RRT*})$;
    $\mathcal{T} \leftarrow \text{Add}(X_{\mathcal{B},\text{nearest}}, X_{\mathcal{B},\text{near}}, X_{\mathcal{B},\text{new}})$;
    $\mathcal{T} \leftarrow \text{Rewire}(X_{\mathcal{B},\text{near}}, X_{\mathcal{B},\text{new}})$;
  else
    $\mathcal{T} \leftarrow$ Informed RRT*;
  end
end
$\mathcal{T}^*_{\mathcal{B}}, \mathcal{T}^*_e \leftarrow \text{DualPath}(\mathcal{T}, X_{\text{goal}}, \Phi_{e,\text{goal}})$;
return $\mathcal{T}^*_{\mathcal{B}}, \mathcal{T}^*_e$;

This technique is divided into two steps, in the first step the sampling is based on RRT* to ensure optimal search in the working space where the target object is located while avoiding obstacles. In the second stage, the sampling introduces the RGM which provides information on the system geometry to guide the sampling to converge quickly to the position where the UAM is able to position its body and manipulate it with its arm to reach the target objects while ensuring a safe transition between the DGM and the IGM using the functions Dg and Ig developed in section II.

The proposed planning strategy is divided into two phases, as shown in Fig. 7. In the first phase, the search extends to the target object around the end point using RGM, as shown in Fig. 3 and 4. Once the target object is found, the algorithm proceeds to the final phase, which involves finding all possible positions of the UAM to pick up the object. All desired paths are clearly shown in Fig. 5 and 6. The Algorithm 1 presents the pseudocode for the suggested algorithm using the RGM.

In order to apply this general structure to the UAV manipulator system, some of the intermediate functionalities have been adapted to the studied problem. These particular developments will be discussed below.



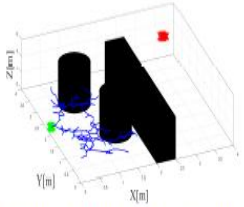


Fig. 3: During each iteration in the first phase, the search extends to the target object around the goal point using RGM.

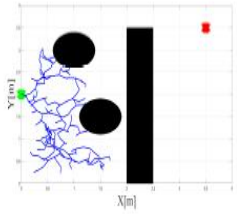


Fig. 4: 2D representation of the first phase of the search for the target object.

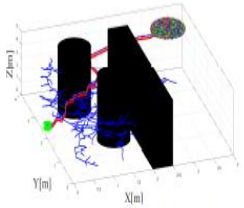


Fig. 5: When the target object is found, the algorithm ends with the final phase to find all possible positions of the UAM to pick up the object.

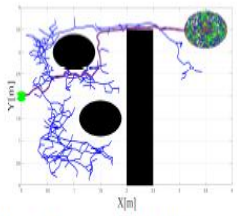


Fig. 6: 2D representation of the final phase to pick up the object.

Fig.7: The path planning phases of the aerial manipulator that must pass to pick up the object. The start and end positions of the UAM are shown in a green and red star. Each purple and red line shows the trajectory of the aerial manipulator's body and effector position, respectively.

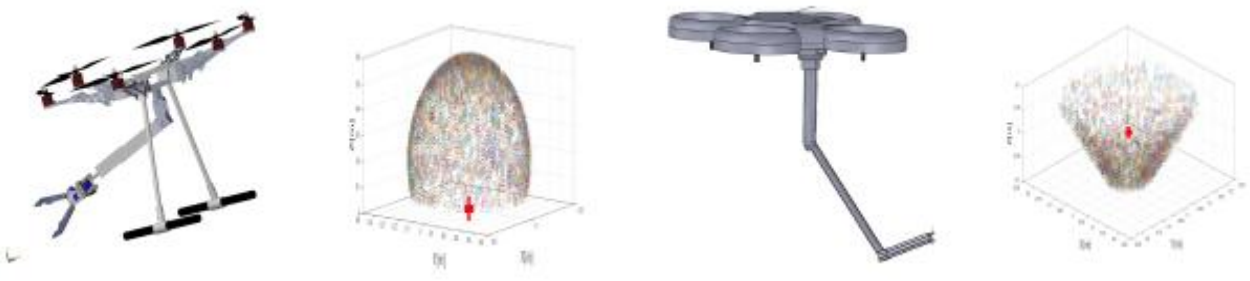


Fig.8: RGM cloud points for two types of UAM, H-RRR and Q-PRR

A. The RGM function

This function generates a random sample in the configuration space around the target object, using the IGM and a random value of Φ_B, Q_a.

The RGM uses random values of the articulation variables Q_a and the attitude of the UAM Φ_B to obtain all the possible positions of the drone so that it can be manipulated with its arm correctly (Fig.8 show the cloud of points generated by the RGM for two types of UAM, H-RRR in [5-6] and Q-PRR in [7]).

The RGM in Algorithm 2 is a compact representation of the workspace of a UAM that can be used for efficient sampling for the manipulator arm that is likely to lead to a successful trajectory to the target.

Algorithm 2: RGM(X_{goal})

$\Phi^0_{\mathcal{B},rand} \leftarrow rand(\Phi^0_{Min}, \Phi^0_{Max})$;
$\mathcal{Q}_{a,rand} \leftarrow rand(\mathcal{Q}_{a,Min}, \mathcal{Q}_{a,Max})$;
$X_{\mathcal{B},RGM} \leftarrow \mathcal{I}^+_{\mathcal{G}}(X_{goal}, \Phi^0_{\mathcal{B},rand}, \mathcal{Q}_{a,rand})$;
return $X_{\mathcal{B},rand}$;

IV. SIMULATION RESULTS AND DISCUSSION

To evaluate the efficacy of the proposed S-RGM* algorithm in path planning, we employed MATLAB as the simulation platform for this study. The simulation experiments were conducted in a three-dimensional environment, we examined a two-dimensional environment with obstacles and compared the path planning results of UAM using the RRT* and S-RGM* algorithms, analyzing search time and path length under identical conditions for the system H-RRR under identical conditions.

1) In the first case, the UAM executes a vertical maneuver (vertical takeoff) until it reaches the altitude of the desired object. Subsequently, the algorithm searches for the optimal path while maintaining a constant altitude. The algorithm undergoes 1500 iterations, and the resulting trees generated by the algorithm are illustrated in Fig.9ab.
2) In the second case, the algorithm directly pursues the optimal path, considering not only the horizontal coordinates (X and Y) but also the vertical dimension (Z). The algorithm operates for 2000 iterations, and the corresponding trees produced by the algorithm are depicted in Fig.9c-d.

By differentiating between these cases, the algorithm aims to ascertain the most efficient path for the UAM, taking into account both the horizontal and vertical aspects of the environment.

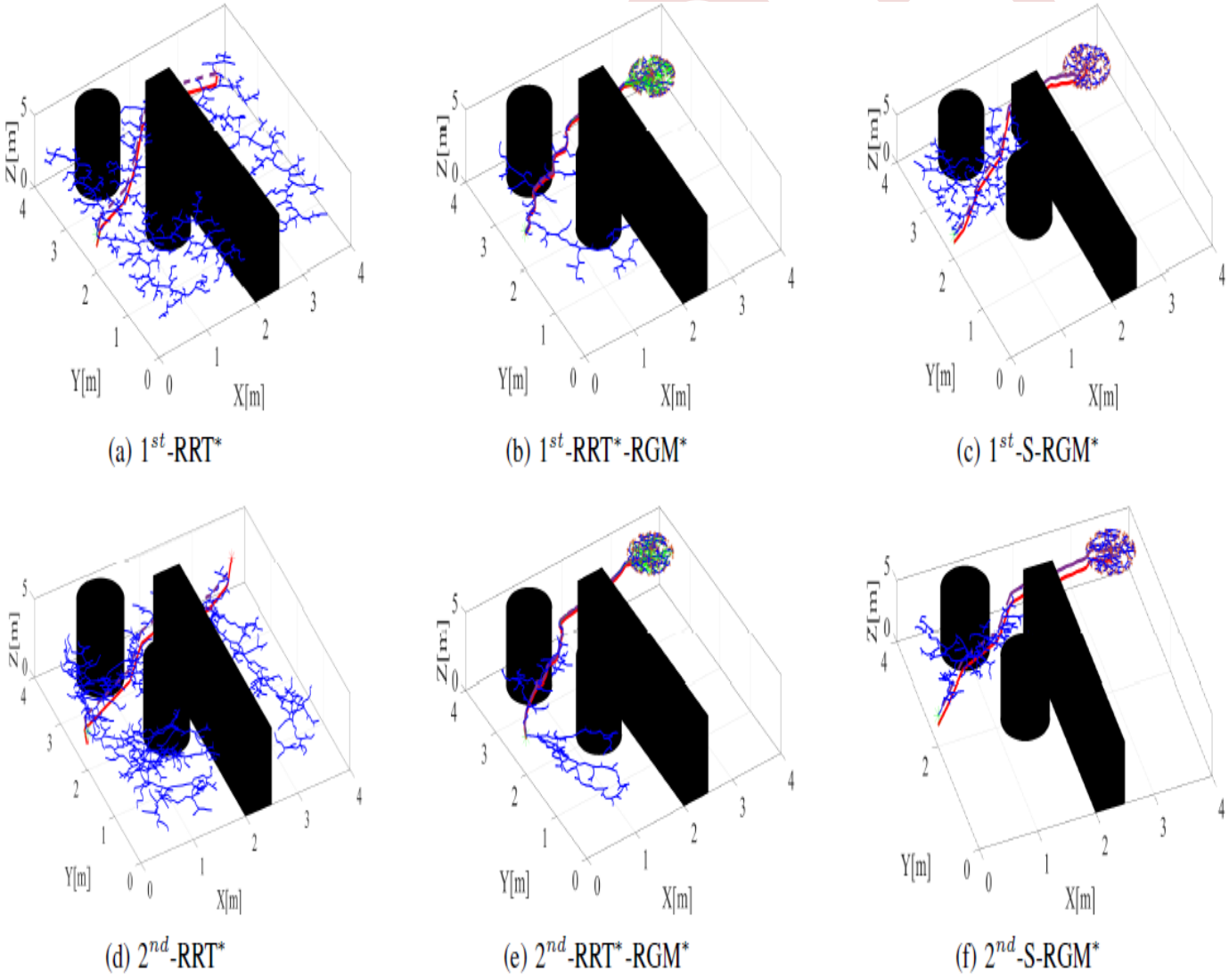
Table I provides a comprehensive analysis of the performance of three distinct approaches: RRT*, RRT*-RGM*, and S-RGM*, within the context of the second scenario. The table showcases key metrics, including the sampling time, sampling number, and path lengths for both the UAV and the manipulator arm.

In the first case, the RRT∗ approach exhibited a sampling time of 82.24 seconds, using a total of 972 samples. It resulted in a UAV path length of 4.543 meters and an ARM path length of 4.94 meters. Conversely, the RRT∗-RGM∗ approach achieved a slightly reduced sampling time of 57.78 seconds with 547 samples, producing a UAV path length of 4.20 meters and an ARM path length of 4.93 meters. Lastly, the S-RGM∗ approach showcased superior efficiency, utilizing a sampling time of 34.22 seconds with 475 samples, leading to a UAV path length of 4.00 meters and an ARM path length of 4.80 meters.

For scenario 2, the RRT* approach recorded a higher sampling time of 144.57 seconds, employing 1312 samples. This resulted in a UAV path length of 5.72 meters and an ARM path length of 6.12 meters. Conversely, the RRT*-RGM* approach demonstrated increased efficiency with a reduced sampling time of 66.47 seconds and 626 samples. The resulting UAV path length was 4.54 meters, while the ARM path length measured 4.94 meters. Similarly, the S-RGM* approach showcased notable efficiency with a sampling time of 38.38 seconds, utilizing 594 samples, resulting in a UAV path length of 4.3307634876 meters and an ARM path length of 5.08 meters.

TABLE I: Comparison performance table of three approaches RRT*, RRT*-RGM*, and S-RGM*in the second scenario.

Scenario	Approach	Sampling time[S]	Sampling number	Path length[UAV](m)	Path length[ARM](m)
1	RRT*	82.2411588	972	4.5432720327	4.9454903938
	RRT*-RGM*	57.7834467	547	4.2019639913	4.9374771523
	S-RGM*	34.2245274	475	4.0003855859	4.8003868179
2	RRT*	144.574231	1312	5.7248080639	6.1270264249
	RRT*-RGM*	66.4797705	626	4.5432720327	4.9454903938
	S-RGM*	38.3879616	594	4.3307634876	5.0809982024



(a) 1^{st}-RRT* (b) 1^{st}-RRT*-RGM* (c) 1^{st}-S-RGM*

(d) 2^{nd}-RRT* (e) 2^{nd}-RRT*-RGM* (f) 2^{nd}-S-RGM*

Fig. 9: The tow case of path planning in the scenario to pick up the object. Each purple and red line shows the trajectory of the aerial manipulator's body and effector position, respectively.

V. CONCLUSIONS

The article discusses the potential advantages of aerial robot manipulators, including their ability to manipulate objects in inaccessible, dangerous, or complex locations. The article proposes a solution for path planning using Sampling-Based Methods and the RGM. The results obtained through simulation have been satisfactory. The proposed solution provides a simple and effective way to plan trajectories for aerial robot manipulators, which could have significant.

VI. REFERENCES

[1] Brunner, Maximilian and Rizzi, Giuseppe and Studiger, Matthias and Siegwart, Roland and Tognon, Marco, "A Planning-and-Control Framework for Aerial Manipulation of Articulated Objects," *IEEE Robotics and Automation Letters*, vol. 7, 2022.

[2] Kim, Hyoin and Seo, Hoseong and Kim, Jongchan and Kim, H Jin, "Sampling-based motion planning for aerial pick-and-place," in *2019 IEEE/RSJ International Conference on Intelligent Robots and Systems (IROS)*, 2019.

[3] Caballero, Alvaro and Suarez, Alejandro and Real, Fran and Vega, Victor M and Bejar, Manuel and Rodriguez-Casta{\~n}o, Angel and Ollero, Anibal, "First experimental results on motion planning for transportation in aerial long-reach manipulators with two arms," in *2018 IEEE/RSJ International Conference on Intelligent Robots and Systems (IROS)*, 2018.

[4] Lee, Hyeonbeom and Kim, Hyoin and Kim, H Jin, "Path planning and control of multiple aerial manipulators for a cooperative transportation," in *2015 IEEE/RSJ International Conference on Intelligent Robots and Systems (IROS)*, 2015.

[5] Zamoum, Housseyn and Bouzid, Yasser and Guiatni, Mohamed, "Robust control and recursive modelling approach for hexarotor manipulator," *Proceedings of the Institution of Mechanical Engineers, Part I: Journal of Systems and Control Engineering*, 2023.

[6] "Modeling and trajectory tracking by robust control of a hexacopter with a 3-D OF manipulator arm," in *2022 2nd International Conference on Advanced Electrical Engineering (ICAEE)*, 2022.

[7] K. Bouzgou, Contribution a l'architecture, la modelisation et la commande d'un bras manipulateur aerien, Universite Paris-Saclay, 2021.

[8] Ruggiero, Fabio and Lippiello, Vincenzo and Ollero, Anibal, "Aerial manipulation: A literature review," *IEEE Robotics and Automation Letters*, pp. 1975--1964, 2018.

[9] Yavari, Mohammadreza and Gupta, Kamal and Mehrandezh, Mehran, "Interleaved Predictive Control and Planning for an Unmanned Aerial Manipulator With On-The-Fly Rapid Re-Planning in Unknown Environments," *IEEE Transactions on Automation Science and Engineering*, pp. 1-16, 2022.

Multispectral stereo-vision for outdoor localization

Fahima Benyounes [1], Abdelkrim Nemra [2]

Guidance and Navigation Laboratory
Ecole Militaire Polytechniques
Bordj El Bahri, Algiers, Algeria
benyounes.fahima@gmail.com

Guidance and Navigation Laboratory
Ecole Militaire Polytechniques
Bordj El Bahri, Algiers, Algeria
karim_nemra@yahoo.fr

***bstract*— In this paper, we propose a novel method to estimate the coordinates of points and localization in outdoor environment using computer vision. The proposed approach consists in combining visible and infrared images acquired by the Kinect sensor to localize the mobile robot to extend the utility of the Kinect sensor in outdoor environment. Our algorithm localizes a moving target using Kinect sensors (RGB camera, IR camera), using multispectral stereovision RGB/IR. MVO algorithm is based on two steps: first, 3D landmarks are localized in the word frame using multispectral images (RGB and IR images). Second, alignment of consecutive 3D landmarks will be used for mobile robot localization.**

To overcome the limitation of the multimodal visual navigation especially during navigation mode switching an extended Kalman filter (EKF) is implemented to fuse the MVO pose with the Wheel Odometry (WO) pose. The proposed approaches are validated experimentally for trajectory tracking using the mobile robot (Pioneer P3-AT) and several scenarios are considered. Good results of 3D features estimation and mobile robot localization and navigation are obtained.

Keywords—multispectral, kinect, stereo-vision, IR, RGB.

I. INTRODUCTION

3D scanning has been a very popular task in the last years. There are several technologies that could be used to capture the 3D geometry of an object (or a scene), such that: LIDAR [1], time of flight, stereo cameras, and structured light. Nevertheless, a scanner is an expensive and a big machine. On the other hand, Kinect is a low cost and handheld device capable of capturing, in real time, geometry and colors of a scene. Naturally, there is a tradeoff. The Kinect data resolution is typically 640*480. It is lower than most of the scanners. However, it is enough for several applications. Furthermore, we can infer better data from the captured one, i.e., reconstructing a surface from the depth data [2].

Laser based 3D scanners use a process called trigonometric triangulation to accurately capture a 3D shape as millions of points. Laser scanners work by projecting a laser line or multiple lines onto an object and then capturing its reflection with a single sensor or multiple sensors. The sensors are located at a known distance from the laser's source. Accurate point measurements can then be made by calculating the reflection angle of the laser light [3].

Laser scanners are very popular and come in many designs. They include handheld portable units, arm based, CMM based, long range, and single point long range trackers, but it has disadvantages also as, the price of a laser 3D scanner is expensive, some small businesses cannot afford them and non-contact 3D scanners can be very slow in scanning objects the clarity of the image may not be the best.

Stereo vision systems reconstruct 3D scenes by matching two or more images taken at slightly different viewpoints. Stereo vision systems are based on two forward-facing cameras, where each camera gives a 2D projection of a scene. The matching of image points is obtained by comparing a region in one image with matching regions in the other image and selecting the most likely match based on some similarity measure. These correctly matching points can be used to calculate the depth of the point. Depth information is used for mobile robot navigation and obstacle detection in real time applications [4].

In this paper, a novel method for multispectral visual odometry (MVO) for mobile robot localization and navigation is proposed. Unlike the classical visual Odometry [9] [10], the proposed multispectral visual odometry consists in combining visible and infrared images to localize the mobile robot in outdoor environment.

The MVO algorithm is based on two main steps, similar to the visual odometry algorithms: first, 3D landmarks are localized in the word frame using multispectral images (RGB, IR, and depth images) from the Kinect sensor. Second, in order to localize the mobile robot, constructed 3D landmarks are linked.

Multispectral stereovision RGB/IR for outdoor localization is very important to extend the utility of the Kinect sensor in outdoor environment. To improve the robustness of the proposed algorithm MVO pose is fused with the Wheel Odometry (WO) pose using an extended Kalman filter (EKF). When visual information is not available WO localization system will be used. The proposed approaches are validated and evaluated experimentally for a trajectory tracking problem with the mobile robot (Pioneer P3-AT). Many scenarios are considered in outdoor environment. Good results of 3D features estimation and mobile robot localization and navigation are obtained in whatever conditions.

A. *Previous Work:*

Many implementations of 3d estimation can be found in the literature, we cite for examples:
The problem of visual odometry for ground vehicles based on the simultaneous utilization of multispectral cameras [5].

Stereo-based 3D scanner system, which is able to acquire various resolution range data. The system consists of stereo cameras and one slit laser [6].

depth estimation techniques using cues from two images, different approaches for depth estimation like Vergence, Stereo Disparity, Stereo Matching, Familiar Size, Defocus Cue, Convex Optimization, Sum of Absolute Differences Algorithm are reviewed and finally disparity-based depth estimation using Sum of Absolute Difference (SAD) matching algorithm were proposed in this work [4].

There are also papers that talk about correction of radial distortion of the RGB camera and find the transformation matrix for the correspondence between the RGB and depth image of the Kinect v2 [7].

Following the private works we propose an algorithm for 3D estimation based on multispectral stereo vision. The propose system should be able to estimate 3D coordinate of known object in Outdoor environment, by combining the (RGB/IR) images.

II. MULTISPECTRAL SENSOR

A standard visual sensor collects red, green and blue wavelengths of light. Multispectral sensors are able to collect these visible wavelengths as well as infrared radiation and ultraviolet light (non-visible wavelengths).

There too many multispectral sensors like, laser 3D, RGB-D camera, in our work we have used Kinect v1 sensor because it's easy for manipulation and installation on windows and matlab also, cheaper compared to other multispectral sensors, it offers fast 3D information.

A. *Kinect sensor*

Kinect appeared on November 4, 2010, as an accessory to Xbox 360 Console. It is a device developed by the Prime Sense Company in collaboration with Microsoft. In January of 2012, more than 18 million units were sold. In February of 2012, a version for Windows was released [2].

The Kinect Camera (Figureure 1) has a 640 x 480 32-bit RGB color camera and a 320*240 16-bit DEPTH camera both running at 30 frames per second. The field of view (FOV) of cameras is 57º horizontally and 43º vertical. It has a motorized angle driver which can tile the both cameras 27º vertically and a microphone array which is used for detecting voice commands [8].

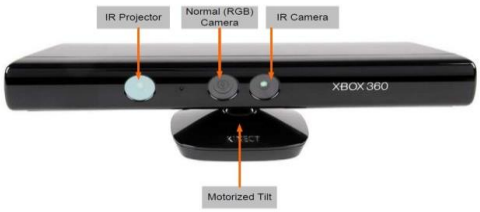


Figure.1. The Kinect sensor which was released by Microsoft. The sensor is used in Xbox 360 gaming console for control free game experience.



Figure.2. Kinect provided data: RGB image (left), DEPTH (middle) and infrared image (right).

B. *Camera model*

In order to use the Kinect readily we must calibrate it first we calibrate the two cameras alone (RGB and IR) to get the intrinsic parameters, second for determining the extrinsic parameters we consider the two cameras as a stereoscopic bench in which we interested in the distance between the two cameras (base line).

In this work we considered the left (RGB) camera as reference camera.

The relationship between the homogeneous image coordinates $\hat{x} = (u, v, 1)$ and the camera coordinates $Xc = (Xc, Yc, Zc)$ is given by $\hat{x} = I_C * Xc$.

Let $I_{C_{RGB}}$ and $I_{C_{IR}}$ be calibrations matrices of RGB camera and IR camera successively.

$$I_{C_{RGB}} = \begin{bmatrix} \alpha_u & 0 & U_0 \\ 0 & \alpha_v & V_0 \\ 0 & 0 & 1 \end{bmatrix} \qquad I_{C_{IR}} = \begin{bmatrix} \alpha'_u & 0 & U'_0 \\ 0 & \alpha'_v & V'_0 \\ 0 & 0 & 1 \end{bmatrix}$$

Where α_u, α_v correspond to the focal length U_0, V_0 the principal point coordinates. Therefore, the projections $\hat{x}_{RGB} = (U_{RGB}, V_{RGB}, 1)$ and $\hat{x}_{IR} = (U_{IR}, V_{IR}, 1)$ on the left and right cameras, respectively, are given by

$$\hat{x}_{RGB} = I_{C_{RGB}} * Xc \qquad \hat{x}_{IR} = I_{C_{IR}} * (Xc - (b_L, 0, 0)^T)$$

b_L denotes the stereo baseline.

C. *Camera parameters*

Calibration tools such as Camera Calibration Toolbox for Matlab are available to determine the intrinsic parameters of the cameras. A set of checkerboard images from both color and IR cameras are used to identify the corners of the checkerboard pattern in RGB and IR images. Then, by solving the equations from the correspondences of the corner points and by using the non-linear optimization technique to reduce the reprojection errors, the intrinsic camera parameters such as focal length, principal points, and skew can be determined [9].
Results of calibration obtained are presented in Table 1.

TABLE 1: CAMERA PARAMETERS FOR KINECT V1.

Right camera IR	***Focal length***	$\alpha_u = 526.97494$ $\alpha_v = 528.35283$

	Principal point	$u_0 = 324.17104$ $v_0 = 254.74485$
Left camera RGB	***Focal length***	$\alpha_u = 582.52835$ $\alpha_v = 584.54913$
	Principal point	$u_0 = 322.26189$ $v_0 = 240.73137$
Baseline		$b_L = 26mm$

III. MULTISPECTRAL IMAGES FOR 3D ESTIMATION

Reconstructing a three-dimensional image of a scene from a collection of two or more images taken from various angles is known as 3D reconstruction. When we have one or more 2D representations of an object and want to find the coordinates of the elements visible on these representations in a reference of the real 3D space, this is when we run into the problem of 3D estimation.

IV. 3D ESTIMATION USING MULTISPECTRAL (RGB/IR)

One of the major challenges in computer vision, and stereo vision in particular, is the correspondence/matching problem. It involves matching corresponding points in 2D that are a projection of the same 3D point in the scene. This task proved very demanding when implemented on images of the same spectral band and very challenging on images captured with sensors operating in different spectrum such as visible (RGB) and infrared (IR) [10].

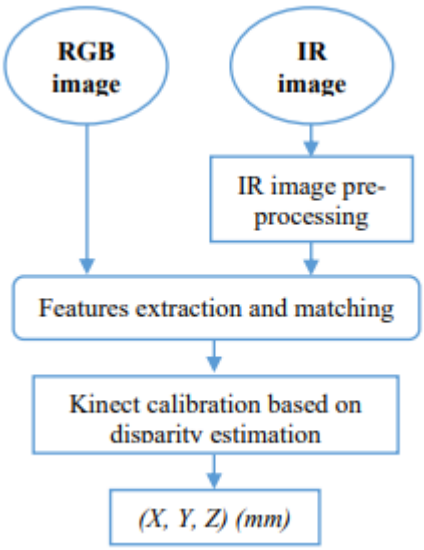


Figure.3. 3D estimation using (RGB/IR).

In our work we have to get 3 D estimation using RGB and IR images acquired from Kinect v1 sensor, and estimate the coordinates of points in outdoor averments, according to the diagram show in figureure 3.

The acquired images from Kinect are very unclear (figureure 4), why it is very hard to associated, so before any manipulation a step of processing is mandatory,

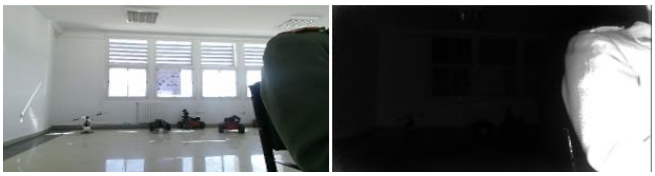


Figure.4. acquired images from Kinect (left) and infrared image (right).

A. *IR processing*

This step is used to clarify IR image, in order to facilitate features extraction and matching. Figureure 5 above shows the processing steps.

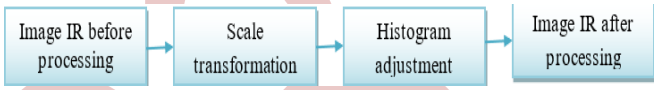


Figure.5. IR image processing steps.

B. *Feature extraction*

Feature extraction (figure 6) task has as main goal to characterize and represent a given image by a set of distinctive features. Those features should be stable enough to be repeatedly detected in each stereo image, invariant to geometric transformations and robust to noise. There are mainly local features (edges, corners…etc) and global features (image structures…etc) [11].

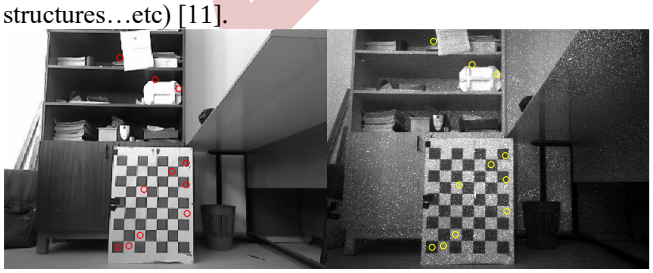


Figure. 6. feature extraction.

C. *Feature matching*

The matching process (figure 7)is achieved using the cosine similarity function that is often adopted in comparing wavelet based descriptors. Each feature in the left image at a position (x,y) is compared to all the features in the right image located within a rectangular disparity window ($Disp_x * Disp_y$) centered at (x,y). $Disp_x and\ Disp_y$ account for the maximum expected horizontal and vertical disparities respectively [12].

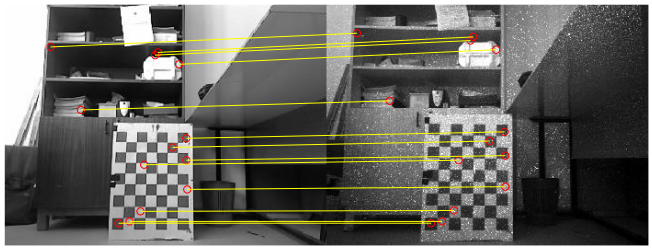


Figure .7. feature matching.

For matching this feature, we have compared between two methods of feature matching; matrix correspondence method and SURF method [12].

D. multispectral mapping

Contrary to an ordinary stereovision, involving images of the same specter, the spectral multi- stereovision cannot base on the luminous intensity itself what returns the stage of putting in difficult correspondence RGB/IR. For this problem, we planned two steps:

- Use the detector of the points of interest: as of detector surf, in this case of face, the detection is made in the image RGB and in the image IR (figureure 6). The core of SURF feature point detection is Hessian matrix. Firstly, the Gaussian filtering is applied to the image, and then the Hessian matrix is obtained by Gaussian difference method.
- Use an algorithm for the putting in correspondence based on SURF detector descriptor.

E. Surf detector:

After using feature point extraction by surf detector, the second method for make multispectral correspondence is to use SURF descriptor construction which comprises the construction of the main direction of the feature point and the surrounding image information, result of this experience is chew in figureure 8.

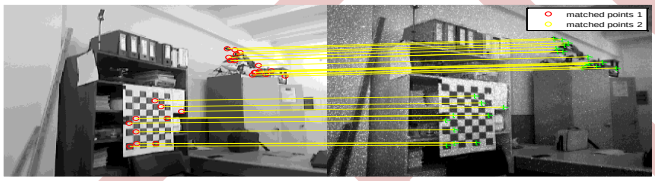


Figure. 8. Correspondence using SURF descriptor.

In our experience we have chosen SURF (Speeded Up Robust Features) detector to extract feature, for its robustness, efficiency, invariance in changing of scale, rotation and image transformation.

F. Calibration of Kinect

To estimate the depth, we tried a new approach; we know that the depth varies according to the disparity, with an equation of the form:

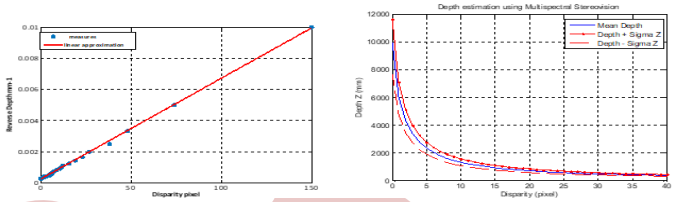
$$Z = b\frac{f}{d}$$
$$Z = C/d$$

With b the baseline, f the focal length and d disparity.

The disparity ($d = y - y'$) with y coming from the right image and y' from the left image, and $C = f * b$ (C is constant).

So we took known distances and for each distance we record the disparity (we record the coordinates of the object in the two images manually), after this operation, we draw the inverse of the depth according to the disparity.

After tracing the variation of Z-1 according to the disparity, we approximate this variation by a linear function, we got the figureure 9.



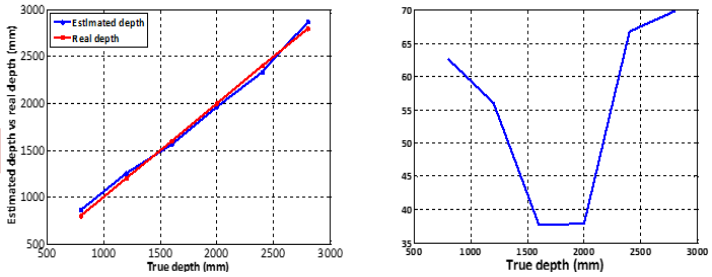
(a) (b)

Figure .9. Variation of Z-1 according to the disparity.

G. Precision evaluation

The objective of this part is to evaluate the precision of average DEPTH for ten (10) points of a surface parallel to the Kinect.

To realize this experiment we have fixed the Kinect on a support facing a checkerboard. We have moved the Kinect sensor along the Z axis and measure the real distance between the camera and points fixed on the checkerboard each time. Several tests have been carried out by moving the sighting device from 0.8 to 2.8m.



(a) (b)

Figure.10. (a) DEPTH evaluation, (b) error evaluation, vs true DEPTH (IR/DEPTH).

Figureure 10 (a) shows the average DEPTH acquired by Kinect vs true DEPTH for a single point, we started with z = 800 mm to z=2800 mm, we note that the results acquired by the Kinect follow approximately the true depth. The error increasing, when depth is between 800 mm and 1550 mm, after that it remains constant to z=2000 mm (about 30 mm). Then it increases until 70 mm when z=2800mm (figure 10 (b)).

V. DISCUSSION

The following table summarizes the results of the variance obtained in this case of the 3D estimating.

TABLE 2: THE RESULTS OF THE VARIANCE.

	Day Outdoor RGB/IR
X(mm)	σ_x =15

	$Z \in [1400\ 2200]$
Y(mm)	$\sigma_y = 20$
	$Z \in [1400\ 2200]$
Z(mm)	$\sigma_z = 37$
	$Z \in [1200\ 2400]$

Overall, the estimate of depth in outdoor is accurate.
An error of 37 mm for a distance of 2400 mm that is to say 0.37% which represents a very good precision in mobile robotics.

VI. Algorithm of Multispectral Visual Odometry (MVO)

By observing a series of images of the robot's surroundings, visual odometry is the process of calculating the robot's motion (translation and rotation with respect to a reference frame). The first two steps involve finding and matching 2D features in successive frames for each new image Ik (or image pair in the case of a stereo camera or Kinect). The term "2D/3D image correspondences" refers to image features that are the same 3D features projected onto different frames [14].
In this paper, the localization algorithm based on Multispectral Visual Odometry (MVO) using Kinect sensor is proposed for outdoor localization [15]. For every new observation given by the Kinect, a 3D estimation ($Pk\ i$) of the observed features is obtained using available images at time i. The next step of the MVO is the estimation of the robot pose (translation and rotation) by minimizing the criterion [16]:
$F(R,t) = 1\ N \sum \| (RPk\ i+1 + t) - Pk\ i \|^2\ N\ k=1$

A. MVO Algorithm based on ICP-SURF

An Iterative Closest Point (ICP) algorithm and SURF detector/descriptor are combined to minimize the criterion given in the Equation. In this instance, there are two steps in the pose estimation process. Using SURF detection and matching, the first step entails determining the correspondence between two subsequent 3D scans. The mean square error (MSE) between two consecutive scans is minimized in the second step in order to estimate the geometric transformation (rotation and translation) (Figure. 11). The ICP algorithm's computation time is greatly reduced when using the SURF descriptor for point association, and the estimated pose will quickly meet the convergence criterion. The following flowchart illustrates the idea behind the Iterative Closest SURF points (ICP-SURF) algorithm for visual odometry.

VII. Mobile robot localization using EKF-MVO

In certain scenarios, in which the visual information is not available (bad weather or dark area) few number of SURF features are detected, thus the MVO algorithm [16] provides poor localization performances.
As solution, in this paper, we propose to combine the multispectral visual odometer (MVO) pose with the mobile robot wheel odometer (WO) pose using an Extended Kalman Filter [17] [18]. The use additional sensor (WO) can maintain a suitable pose estimation and overcome MVO limitations (Figure. 12). Moreover, the proposed EKF-MVO algorithm (figure 13)

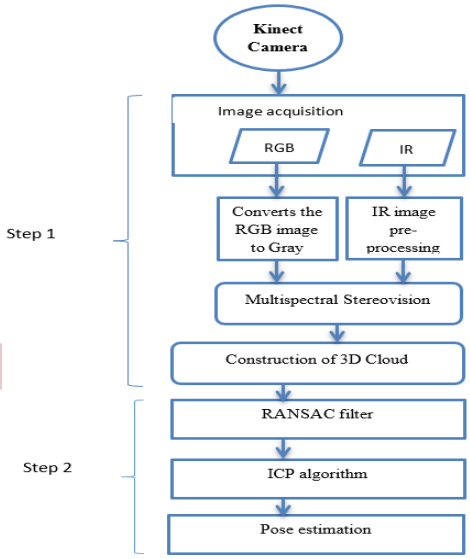


Figure.11. Multispectral Visual Odometry (MVO) algorithm using ICP-SURF algorithm

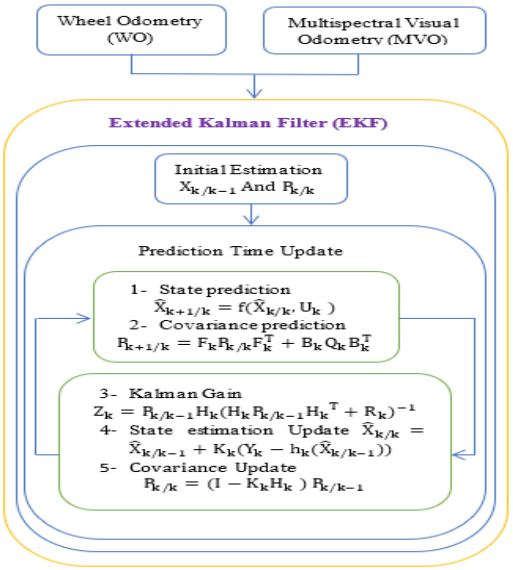


Figure.12. EKF-MVO algorithm

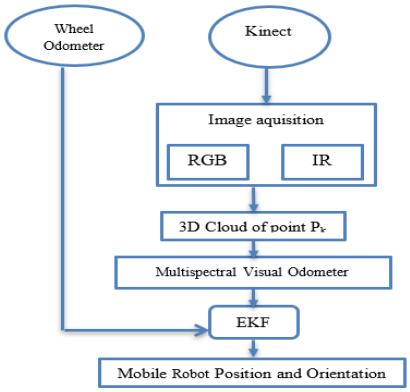


Figure.13. MVO-EKF algorithm

VIII. Results and Discussion

In section V, 3D estimation algorithm is validated and evaluated in outdoor environment. Based on this result further experiments are considered to evaluate and validate the proposed Multispectral Visual Odometry (MVO) algorithm for mobile robot localization. The localization algorithm is validated on a trajectory-tracking task, where the mobile robot with embedded Kinect sensor (Figure.14) should track accurately a desired (reference) trajectory using the proposed approach. The proposed EKF-MVO is compared to the MVO and the mobile robot Wheel Odometry (WO).



Figure.14 The mobile robot Pioneer with a Kinect Camera.

Trajectory tracking results using multispectral in outdoor environment is mainly based on RGB and IR images to estimate the mobile robot pose. From Figure. 15, we can observe that MVO localization precision is decreased significantly. In the other hand, MVO-EKF maintains a suitable localization accuracy using stereovision.

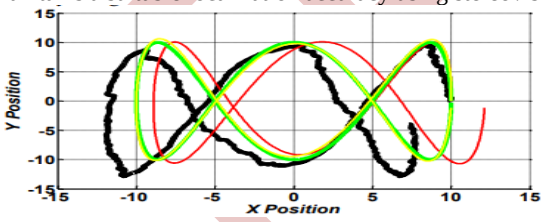


Figure.15. Trajectory tracking using MVO, EKF-MVO and Odometry for outdoor localization (RGB/IR).

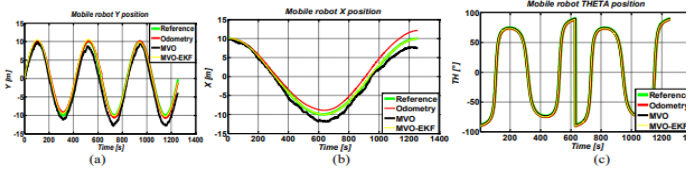


Figure.16. (a) Mobile robot X position, (b) mobile robot Y position, (c) mobile robot THETA position

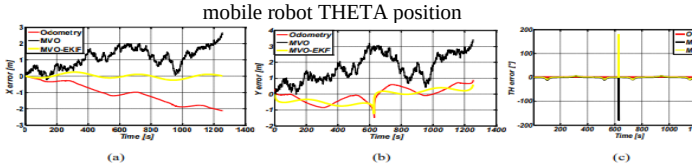


Figure17. (a) X error, (b) Y error, (c) THETA error

Figure. 16 (a, b and c) shows respectively the mobile robot position (X, Y and Theta) for different localization approaches; precision evaluation is given by Figure. 17 (a, b and c), from this figureure we can observe that even in outdoor navigation (IR sunlight disturbance) the MVO-EKF performs much better than the Odometry and the MVO.

IX. Conclusion

The objective of our work was to implement an algorithm for outdoor localization of mobile robot using camera Kinect V1, this algorithm localizes moving trage.

The proposed approach based on Multispectral Visual Odometry (MVO) use stereovision between RGB/IR images.

To overcome the limitation of the MVO especially during the navigation of our robot an extended Kalman filter (EKF) is implemented to fuse the MVO pose with the Wheel Odometry (WO) pose. The proposed localization algorithms are evaluated and validated on a trajectory tracking problem. From the experimental results, good precision of 3D estimation has been obtained by the proposed approach even in outdoor environment.

References

[1] Hang, R., Li, Z., Ghamisi, P., Hong, D., Xia, G., & Liu, Q. (2020). Classification of hyperspectral and LiDAR data using coupled CNNs. IEEE Transactions

[2] Guzsvinecz, T., Szucs, V., & Sik-Lanyi, C. (2019). Suitability of the Kinect sensor and Leap Motion controller—A literature review. Sensors, 19(5), 1072.

[3] Yuan, W., Li, R., Chen, Z., Gu, J., & Tian, Y. (2021). A comparative study on microstructure and properties of traditional laser cladding and high-speed laser cladding of Ni45 alloy coatings. .

[4] Bao, W., Lai, W. S., Ma, C., Zhang, X., Gao, Z., & Yang, M. H. (2019). Depth-aware video frame interpolation. In Proceedings of the IEEE/CVF conference

[5] Uribe-Rios, J., Marquez-Viloria, D., & Castano-Londono, L. FPGA-based Low-Cost Multispectral Camera Prototype for Precision Agriculture Applications.

[6] Liu, D., Yu, X., Wu, F., Xiao, S., Itoigawa, F., & Ono, S. (2021). Terahertz high-Q quasi-bound states in the continuum in laser-fabricated metallic double-slit arrays.

[7] Demim, F., Nemra, A., Boucheloukh, A., Kobzili, E., Hamerlain, M., & Bazoula, A. (2019). SLAM based on adaptive SVSF for cooperative unmanned vehicles in dynamic environment.

[8] Tölgyessy, M., Dekan, M., Chovanec, Ľ., & Hubinský, P. (2021). Evaluation of the azure kinect and its comparison to kinect v1 and kinect v2

[9] He, M., Zhu, C., Huang, Q., Ren, B., & Liu, J. (2020). A review of monocular visual odometry. The Visual Computer

[10] Teed, Z., Lipson, L., & Deng, J. (2022). Deep patch visual odometry.

[11] Zebari, R., Abdulazeez, A., Zeebaree, D., Zebari, D., & Saeed, J. (2020). A comprehensive review of dimensionality reduction techniques for feature selection and feature extraction. Journal of Applied Science and Technology Trends.

[12] [12] Sun, J., Shen, Z., Wang, Y., Bao, H., & Zhou, X. (2021). LoFTR: Detector-free local feature matching with transformers. In Proceedings of the IEEE/CVF conference on computer vision and pattern recognition

[13] Liu, J., & Bu, F. (2019). Improved RANSAC features image-matching method based on SURF. The Journal of Engineering, 2019(23), 9118-9122.

[14] Sitzmann, V., Thies, J., Heide, F., Nießner, M., Wetzstein, G., & Zollhofer, M. (2019). Deepvoxels: Learning persistent 3d feature embeddings. In Proceedings of the IEEE/CVF Conference on Computer Vision and Pattern Recognition.

[15] Nilwong, S., Hossain, D., Kaneko, S. I., & Capi, G. (2019). Deep learning-based landmark detection for mobile robot outdoor localization. Machines, 7(2), 25.

[16] Kim, T., & Park, T. H. (2020). Extended Kalman filter (EKF) design for vehicle position tracking using reliability function of radar and lidar. Sensors, 20(15), 4126.

[17] Gupta, A., & Fernando, X. (2022). Simultaneous localization and mapping (slam) and data fusion in unmanned aerial vehicles: Recent advances and challenges.

[18] Demim, F., Benmansour, S., Abdelkrim, N., Rouigueb, A., Hamerlain, M., & Bazoula, A. (2022). Simultaneous localisation and mapping for autonomous underwater vehicle using a combined smooth variable structure filter and extended kalman filter. Journal of Experimental & Theoretical Artificial Intelligence

Robust PUMA560 Control with Backstepping-ADRC

Safinaz Ben Messaoud [1], Mohammed Belkhiri [1,2]

[1] *Telecommunications, Signals and Systems, University Amar Telidji, Laghouat, Algeria*

s.benmessaoud@lagh-univ.dz

[2] *Modélisation, Information et Systèmes, Université de Picardie Jules Verne, Amiens, France*

m.belkheiri@lagh-univ.dz

***Abstract*— This paper presents a design approach that relies on Backstepping based Active Disturbance Rejection Control strategy for trajectory tracking control of a PUMA560 robot accounting uncertainties. The control design aims to achieve accurate trajectory tracking and disturbance rejection for unknown disturbances that may affect the performance of the plant. The system under consideration is six degrees of freedom industrial manipulator, and the performance of the control design is demonstrated on the first three joints. This paper conducts a performance comparison between conventional Backstepping control, ADRC and Backstepping- ADRC.**

***Keywords:* Backstepping, ADRC, Control, PUMA560.**

I. INTRODUCTION

In recent decades, the field of robotics technology and its practical applications has seen a notable emphasis on the development and deployment of adaptive control strategies. Robust control, Backstepping control, Active Disturbance Rejection Control (ADRC), and other similar methodologies have become prominent in this pursuit.

Uncertainties and external disturbances are inherent in the modeling and control of dynamic systems, playing a pivotal role in shaping control system performance. Extensive research efforts have been dedicated to identifying and compensating for these uncertainties, leading to the development of various control methodologies. Among these, Backstepping control has emerged as a widely adopted approach for managing uncertain systems [1-2]. However, while Backstepping effectively addresses parametric uncertainties, its performance often diminishes in the presence of complex, uncertain nonlinearities. To mitigate the performance degradation in the presence of uncertain nonlinearities, researchers often turn to adaptive control approaches [3].

To contend with systems characterized by extensive uncertainties, the Active Disturbance Rejection Control (ADRC) framework was introduced by J. Han. The core concept behind ADRC revolves around treating all unknown aspects of a system as a unified disturbance, which is continuously estimated in real-time by an extended state observer (ESO) [4-5].

Recognizing the complementary strengths of Backstepping and ADRC, researchers have begun exploring their combined application, resulting in a more potent control strategy for uncertain nonlinear systems. This combined approach offers several distinct advantages, including improved convergence to desired trajectory profiles without the need for excessively high feedback gains and the elimination of steady-state errors. These benefits have spurred considerable interest and attention from the research community [6-7].

In this paper, we delve into the integration of Backstepping and ADRC, elucidating the synergistic advantages it offers for the control of systems fraught with uncertainties and nonlinearities. The concept of Backstepping-ADRC represents a fusion of two powerful control methodologies. Backstepping control, which involves designing controllers recursively for each dynamic variable, is combined with the principles of ADRC to enhance control performance in complex systems. In this approach, the control law is systematically designed, considering the intricate system dynamics step by step. Meanwhile, the Active Disturbance Rejection Control strategy actively estimates and compensates for disturbances, ensuring robustness in the presence of uncertainties. By integrating these concepts, Backstepping-ADRC aims to achieve accurate trajectory tracking and disturbance rejection in systems with complex and interrelated dynamics.

The paper is organized in the following manner: Section 2 presents the manipulator dynamics. Section 3 outlines the proposed control design methodology. Section 4 showcases the simulation results of the proposed controller compared to the conventional Backstepping control and ADRC method. Lastly, in Section 5, conclusions are provided.

II. SYSTEM OVERVIEW

A. *Dynamics of PUMA560*

The general form of the dynamic model of a manipulator can be expressed as

$$M(q)\ddot{q} + V(q,\dot{q}) + G(q) = \tau \qquad (1)$$

The dynamic equation, referred to as the configuration space equation, is obtained by expressing the velocity-dependent term $V(q,\dot{q})$ differently, leading to matrices that solely depend on the manipulator position [8]

$$M(q)\ddot{q} + B(q).[\dot{q}.\dot{q}] + C(q)[\dot{q}^2] + G(q) = \tau \qquad (2)$$

Where τ is $n \times 1$ vector of torques, $M(q)$ is $n \times n$ inertia matrix of the manipulator, $B(q)$ is $n \times n(n-1)/2$ matrix of Coriolis torques, $C(q)$ is $n \times n$ matrix of Centrifugal torques, and $G(q)$ is $n \times 1$ vector of gravity terms.

$q : n \times 1$ is the position vector $[\dot{q}.\dot{q}]$ is $n(n-1)/2 \times 1$ vector of joint velocity products given by $[\dot{q}_1.\dot{q}_2, \dot{q}_1.\dot{q}_3, \dots, \dot{q}_1.\dot{q}_n, \dot{q}_2.\dot{q}_3, \dot{q}_2.\dot{q}_4, \dots, \dot{q}_{n-2}.\dot{q}_n, \dot{q}_{n-1}.\dot{q}_n]^T$, and $[\dot{q}^2]$ is $n \times 1$ vector given by $[\dot{q}_1{}^2, \dot{q}_2{}^2, \dots, \dot{q}_n{}^2]^T$.

More model details are available in [8].

B. Using PUMA560 as 3 degrees of freedom

The configuration space equation of a 3-DOF PUMA robot has the same configuration space equation general form as that of a 6-DOF PUMA robot. In the 3-DOF robot, the last three joints are blocked to maintain their initial states during motion.

By setting the values of these joints to zero $q_4 = q_5 = q_6 = 0$ for the configuration space equation [9], yields

$$\ddot{q} = [\ddot{q}_1\ \ddot{q}_2\ \ddot{q}_3\ 0\ 0\ 0]^T$$

$$[\dot{q}.\dot{q}] = [\dot{q}_1.\dot{q}_2\ \dot{q}_1.\dot{q}_3\ 0\ 0\ 0\ \dot{q}_2.\dot{q}_3\ 0\ 0\ 0\ 0\ 0\ 0\ 0\ 0\ 0]^T$$

$$[\dot{q}^2] = [\dot{q}_1{}^2\ \dot{q}_2{}^2\ \dot{q}_3{}^2\ 0\ 0\ 0]^T$$

$$B(q).\dot{q}\dot{q} = [b_{112}\dot{q}_1\dot{q}_2 + b_{113}\dot{q}_1\dot{q}_3 + b_{123}\dot{q}_2\dot{q}_3$$

$$b_{223}\dot{q}_2\dot{q}_3\quad 0\quad b_{412}\dot{q}_1\dot{q}_2 + b_{413}\dot{q}_1\dot{q}_3\quad 0\quad 0]^T$$

And

$$C(q)\dot{q}^2 = [c_{12}\dot{q}_2^2 + c_{13}\dot{q}_3^2\quad c_{21}\dot{q}_1^2 + c_{23}\dot{q}_3^2$$

$$c_{31}\dot{q}_1^2 + c_{32}\dot{q}_2^2\quad 0\quad c_{51}\dot{q}_1^2 + c_{52}\dot{q}_2^2\quad 0]^T$$

The angular acceleration is determined to be

$$\ddot{q} = M^{-1}(q)\left[\tau - \left(B(q)\dot{q}\dot{q} + C(q)\dot{q}^2 + G(q)\right)\right] \qquad (3)$$

Let

$$I = \tau - \left(B(q)\dot{q}\dot{q} + C(q)\dot{q}^2 + G(q)\right) \Rightarrow \ddot{q} = M^{-1}(q)I \qquad (4)$$

Then

$$I_1 = \tau_1 - [b_{112}\dot{q}_1\dot{q}_2 + b_{113}\dot{q}_1\dot{q}_3 + b_{123}\dot{q}_2\dot{q}_3]$$

$$-[c_{12}\dot{q}_2{}^2 + c_{13}\dot{q}_3{}^2] \qquad (5)$$

$$I_2 = \tau_2 - [b_{223}\dot{q}_2\dot{q}_3] - [c_{21}\dot{q}_1{}^2 + c_{23}\dot{q}_3{}^2] - g_2 \qquad (6)$$

$$I_3 = \tau_3 - [c_{31}\dot{q}_1{}^2 + c_{32}\dot{q}_2{}^2] - g_3 \qquad (7)$$

$$I_4 = \tau_4 - [b_{412}\dot{q}_1\dot{q}_2 + b_{413}\dot{q}_1\dot{q}_3] \qquad (8)$$

$$I_5 = \tau_5 - [c_{51}\dot{q}_1{}^2 + c_{52}\dot{q}_2{}^2] - g_5 \qquad (9)$$

These equations suggest that to maintain zero values for the last three dynamics, it is preferable to set $I_4 = I_5 = I_6 = 0$.

Consequently, the control torques of the last three joints are held as

$$\tau_4 = [b_{412}\dot{q}_1\dot{q}_2 + b_{413}\dot{q}_1\dot{q}_3] \qquad (11)$$

$$\tau_5 = [c_{51}\dot{q}_1{}^2 + c_{52}\dot{q}_2{}^2] + g_5 \qquad (12)$$

$$\tau_6 = 0 \qquad (13)$$

Therefore, it can be concluded that the last three joints are constrained to remain in their initial states.

III. CONTROLLER DESIGN

A. Active Disturbance Rejection Control design

Let the model (1) with three links in the following form be considered

$$\tau = M(q)\ddot{q} + B(q).[\dot{q}.\dot{q}] + C(q)[\dot{q}^2] + G(q) + \Delta(t) \qquad (14)$$

$$y = q \qquad (15)$$

$\Delta(t) \in \mathbb{R}^n$ is the external disturbances. $y \in \mathbb{R}^m$ is a measurable output of the system. The focus is on the investigation of trajectory tracking, where

a desired trajectory, denoted as $q_d \in \mathbb{R}^n$, is specified. This desired trajectory is characterized by continuous differentiability of at least class C^2. The objective is to achieve

$$\lim_{t\to\infty} q - q_d = 0 \qquad (16)$$

$$\lim_{t\to\infty} \dot{q} - \dot{q}_d = 0 \tag{17}$$

In addressing this issue, the controller is designed following the principles of the ADRC paradigm [10]. The initial step involves the estimation of the unmeasurable state variable $\dot{q}$ and the total lumped disturbance.

Let $x_1 = q$ and $x_2 = \dot{q}$. Then we can rewrite (14) in the normal form

$$\begin{aligned} \dot{x}_1 &= x_2 \\ \dot{x}_2 &= f(x_1, x_2, t) + b\tau \end{aligned} \tag{18}$$

Let f be differentiable and defined as $h = \dot{f}$. By defining an extended state $x_3 = f$, the extended state space equation will be

$$\begin{aligned} \dot{x}_1 &= x_2 \\ \dot{x}_2 &= f(x_1, x_2, t) + b\tau \\ \dot{x}_3 &= h(x_1, x_2, t) \end{aligned} \tag{19}$$

Where

$$f(x_1, x_2, t) = M^{-1}(x_1)(-B(x_1).[x_2.x_2] - C(x_1).[{x_2}^2] - G(x_1) - \Delta(t)) \tag{20}$$

$$b = M(x_1)^{-1} \tag{21}$$

$f(x_1, x_2, t)$ is a vector of unknown dynamics and external disturbances $\Delta(t)$.

The dynamics are determined by the following equations of the extended state observer

$$\begin{aligned} \dot{\hat{x}}_1 &= \hat{x}_2 + \beta_1(\hat{x}_1 - x_1) \\ \dot{\hat{x}}_2 &= \hat{x}_3 + b\tau + \beta_2(\hat{x}_1 - x_1) \\ \dot{\hat{x}}_3 &= \beta_3(\hat{x}_1 - x_1) \end{aligned} \tag{22}$$

This observer is expected to guarantee, that the vector $\hat{x}$ converges to x as $t \to \infty$.β_1, β_2 and β_3 are the observer gain parameters.

The ESO gains can be found using a simple pole-placement method, where the roots of a characteristic polynomial

$$\lambda(s) = s^{n+m} + \beta_1 s^{n+m-1} + \beta_2 s^{n+m-2} + \cdots + \beta_{n+m-2} s^2 + \beta_{n+m-1} s + \beta_{n+m} \tag{23}$$

Are compared to a following polynomial

$$L(s) = (s + \omega_0)^{n+m} \tag{24}$$

which places all of the observers poles in the left half plane at $-\omega_0$, making the characteristic polynomial a Hurwitz-type.

x_1 is known and measurable, so it can be used to obtain both estimates of plant dynamics. On the other hand, x_2 is not available for the measurement, so the estimate of $f(x_1, x_2, t)$ is designed using $\hat{x}_2$ vector.

The estimates of the Extended State can be used in a feedback signal to guarantee the trajectory tracking and the disturbance rejection. A control law is described as follows

$$\tau = \frac{1}{b}(\tau_0 - \hat{x}_3) \tag{25}$$

With

$$\tau_0 = K_p(x_1 - q_d) + K_d(\hat{x}_2 - \dot{q}_d) + \ddot{q}_d \tag{26}$$

τ_0 is a feedback controller. K_p and K_d are the selected controller gains.

If $\hat{x}_3 \to \Delta$, it signifies that all uncertainties, caused by both the unknown dynamics and external disturbances, can be effectively rejected by the previously described controller (25).

B. Backstepping-ADRC design

Based on the nonlinear error control law in ADRC, the Backstepping-ADRC control law is formulated with the explicit aim of enhancing the tracking performance, with the objective of ensuring that the input signal is more accurately tracked by the output signal [11].

Defining the position error as

$$e_1 = x_1 - q_d \tag{27}$$

Its dynamics is governed by

$$\dot{e}_1 = \dot{x}_1 - \dot{q}_d = x_2 - \dot{q}_d \tag{28}$$

Define the Lyapunov function for the system e_1 as

$$V_1 = \frac{1}{2}{e_1}^2 \quad (29)$$

The derivative of V_1 along the tracking error dynamics (28) is given by

$$\dot{V}_1 = e_1(x_2 - \dot{q}_d) \quad (30)$$

To render it negative definite, the following fictitious control signal is chosen

$$x_2 = \dot{q}_d - c_1 e_1 + e_2 \quad (31)$$

where $c_1 > 0$, and e_2 is the virtual control quantity. From Equation (31), we can obtain

$$e_2 = x_2 - \dot{q}_d + c_1 e_1 \quad (32)$$

Then (30) become

$$\dot{V}_1 = -c_1{e_1}^2 + e_1 e_2 \quad (33)$$

If $e_2 = 0$, $\dot{V}_1 \leq 0$, we need to design the next step. Choosing the candidate Lyapunov function as

$$V_2 = \frac{1}{2}[{e_1}^2 + {e_2}^2] \quad (34)$$

The derivative of (32) is

$$\dot{e}_2 = M^{-1}(x_1)\tau + f(x_1, x_2, t) - \ddot{q}_d + c_1\dot{e}_1 \quad (35)$$

Then we obtain

$$\dot{V}_2 = -c_1{e_1}^2 + e_1 e_2 + e_2\left(b\tau + f(x_1, x_2, t) - \ddot{q}_d + c_1\dot{e}_1\right) \quad (36)$$

To make $\dot{V}_2$ negative definite, the following fictitious control is chosen

$$\tau = \frac{1}{b}(-f(x_1, x_2, t) - e_1 + \ddot{q}_d - c_1\dot{e}_1 - c_2 e_2) \quad (37)$$

$c_1, c_2 > 0$. Subsequently, we can obtain

$$\dot{V}_2 = -c_1{e_1}^2 - c_2{e_2}^2 \leq 0 \quad (38)$$

Equation (32) can be expressed as

$$e_2 = \dot{e}_1 + c_1 e_1 \quad (39)$$

Then

$$\tau = \frac{1}{b}\left(K_p e_1 + K_d\dot{e}_1 - f(x_1, x_2, t) + \ddot{q}_d\right) \quad (40)$$

$$\begin{cases} K_p = -c_1 c_2 - 1 \\ K_d = -c_1 - c_2 \end{cases}$$

As the first two terms of (40) take the form $K_p e_1 + K_d\dot{e}_1$, they are similar to those in (25). Therefore, (40) can be integrated with (25) to create the Backstepping-ADRC control law.

IV. Simulation Results

In Matlab/Simulink, Backstepping-ADRC is applied for controlling plant (14). By comparing the tracking performance and robustness (disturbance rejection and errors) of the conventional ADRC, Backstepping, and the proposed controller, the dynamic control performance of Backstepping-ADRC is verified and analyzed according to the simulation results under external disturbances $(\Delta(t) = \dot{q}\sin q + q\cos\dot{q})$.

To ensure a robust dynamic coupling, only the first three links of the PUMA560 robot are included in the simulation model, as stated in [9].

The aim of each joint is to follow a given reference trajectory generated in operational space. The controllers (ADRC and Backstepping-ADRC) were tuned using the same set of parameters. Chosen controller gains are

$$K_p = 3,\ K_d = 6$$

and observer parameters are

$$\beta_1 = 27, \beta_2 = 243 \text{ and } \beta_3 = 729$$

Trajectory tracking: Fig. 1, Fig. 2 and Fig. 3 presents trajectory tracking of the first joint angle before and after adding uncertainty for the Backstepping controller, ADRC and Backstepping-ADRC respectively. The trajectory tracking performance of the Backstepping control exhibited remarkable accuracy, with an error as low as -0.01. In contrast, the ADRC showed a relatively larger error of approximately ± 0.05. This disparity can be attributed to the approach employed in each method. Backstepping leverages the derivative of the error directly in the control law, while ADRC relies on the estimation of x_2 due to its non measurability.

However, the integration of Backstepping and ADRC, referred to as "Backstepping-ADRC" delivers a more satisfactory trajectory tracking performance, even when

employing the same controller parameters and relying on the estimate of x_2, as mentioned earlier.

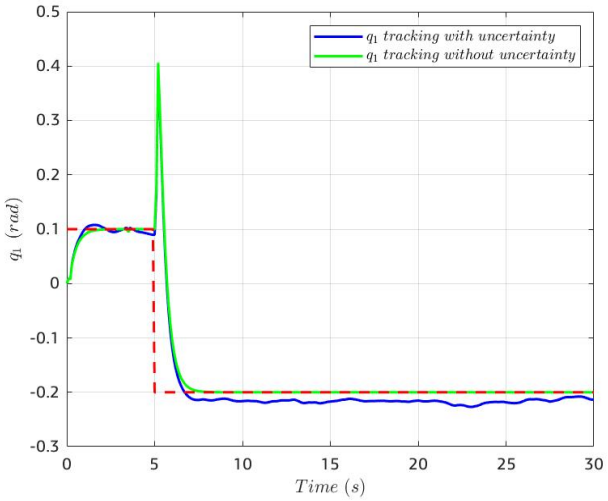


Figure 1. First joint trajectory tracking with and without uncertainty under the Backstepping control

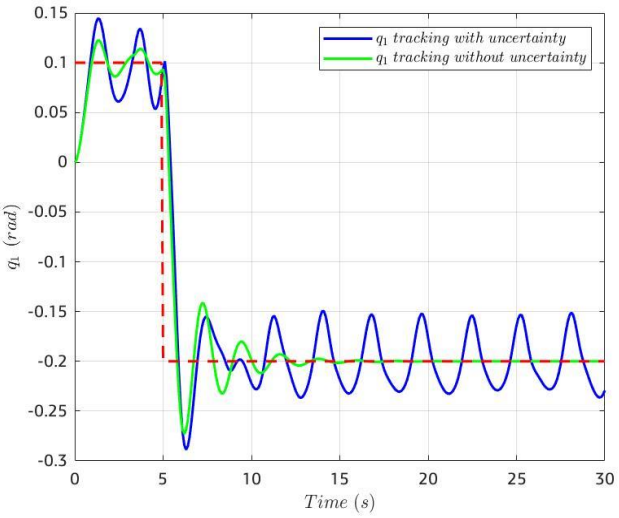


Figure 2. First joint trajectory tracking with and without uncertainty under the ADRC

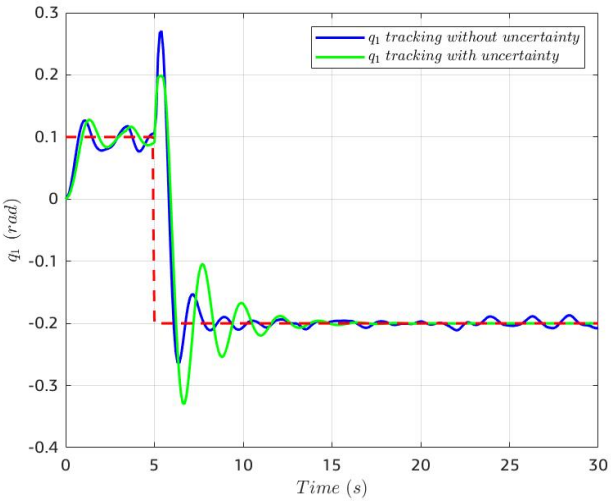


Figure 3. First joint trajectory tracking with and without uncertainty under the Backstepping-ADRC

Path errors: Figure 4 illustrates the trajectory tracking errors for the first three joints. The tracking errors were satisfactory for both Backstepping and Backstepping-ADRC.

However, in ADRC, the error is augmented due to the use of the estimated x_2.

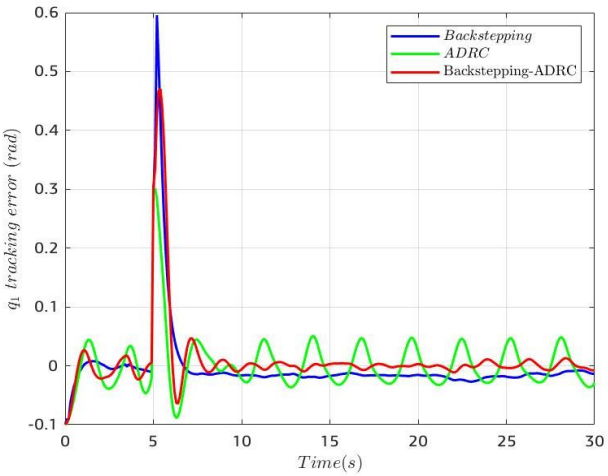


Figure 4. Trajectory tracking error for the Backstepping control, ADRC and Backstepping-ADRC

Joint angles estimation: The first three joints are shown in Figure 5 with their estimates, resulting in a perfect estimation of the observer chosen for the Backstepping-ADRC.

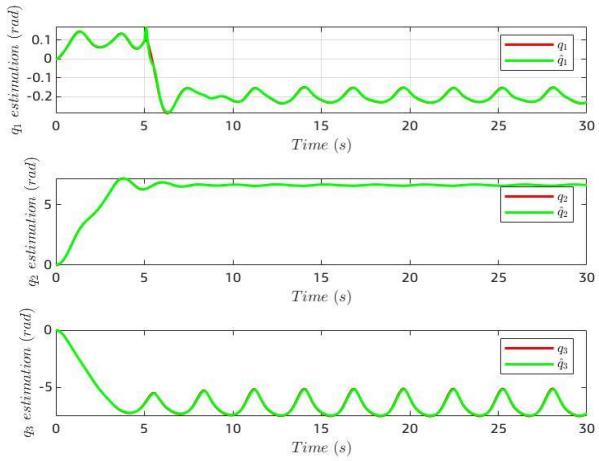


Figure 5. The first three joints estimation for the Backstepping-ADRC

Control signals: The Backstepping-ADRC control inputs are presented in Figure 6.

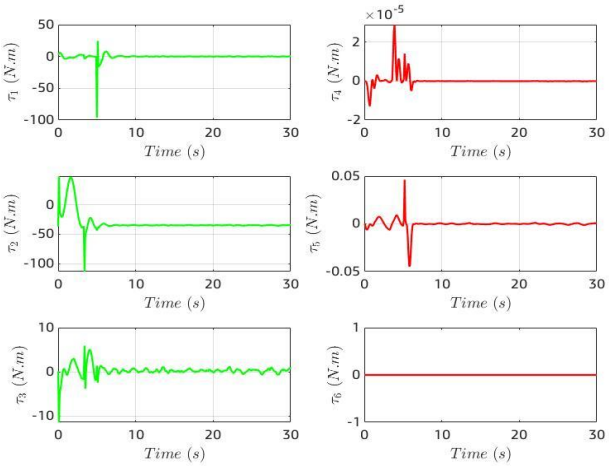


Figure 6. Control torques of the Backstepping-ADRC

V. CONCLUSION

In this paper, we proposed a method to address the impact of uncertainties in the manipulator control model, which is the integration of ADRC and Backstepping control strategies, particularly for a PUMA560 robot with a focus on its first three joints. We introduced uncertainties into the system, which added a significant layer of complexity to the control challenge. Our comparative analysis revealed that Backstepping-ADRC outperformed traditional ADRC and Backstepping control in terms of trajectory tracking. Backstepping-ADRC offers better performance in the presence of uncertainties. It combines the robust disturbance rejection capabilities of ADRC with the recursive control design of Backstepping control, resulting in improved tracking and disturbance rejection. Based on this paper, further verification of the applicability of the proposed controller for complex multi-degree-of-freedom manipulators is required.

ACKNOWLEDGMENT

We gratefully acknowledge the Directorate-General for Scientific Research and Technological Development (DGRSDT) and the Ministry of Higher Education and Scientific Research (MESRS) of Algeria for their generous support and funding.

REFERENCES

[1] Sheng, D., Wei, Y., Cheng, S., & Wang, Y. (2017). Adaptive backstepping state feedback control for fractional order systems with input saturation. IFAC-PapersOnLine, 50(1), 6996-7001.

[2] Borah, M., & Roy, B. K. (2018). Design of fractional-order hyperchaotic systems with maximum number of positive lyapunov exponents and their antisynchronisation using adaptive control. International Journal of Control, 91(11), 2615-2630.

[3] Yao, J., & Deng, W. (2017). Active disturbance rejection adaptive control of uncertain nonlinear systems: Theory and application. Nonlinear Dynamics, 89, 1611-1624.

[4] Gao, Z., Huang, Y., & Han, J. (2001, December). An alternative paradigm for control system design. In Proceedings of the 40th IEEE conference on decision and control (Cat. No. 01CH37228) (Vol. 5, pp. 4578-4585). IEEE.

[5] Huang, Y., & Xue, W. (2014). Active disturbance rejection control: Methodology and theoretical analysis. ISA transactions, 53(4), 963-976.

[6] Gao, Z. (2006, June). Active disturbance rejection control: a paradigm shift in feedback control system design. In 2006 American control conference (pp. 7-pp). IEEE.

[7] Hernández-Méndez, A., Linares-Flores, J., Sira-Ramírez, H., Guerrero-Castellanos, J. F., & Mino-Aguilar, G. (2017). A backstepping approach to decentralized active disturbance rejection control of interacting boost converters. IEEE Transactions on Industry Applications, 53(4), 4063-4072.

[8] Armstrong, B., Khatib, O., & Burdick, J. (1986, April). The explicit dynamic model and inertial parameters of the PUMA 560 arm. In Proceedings. 1986 IEEE international conference on robotics and automation (Vol. 3, pp. 510-518). IEEE.

[9] Piltan, F., Emamzadeh, S., Hivand, Z., Shahriyari, F., & Mirazaei, M. (2012). PUMA-560 robot manipulator position sliding mode control methods using MATLAB/SIMULINK and their integration into graduate/undergraduate nonlinear control, robotics and MATLAB courses. International Journal of Robotics and Automation, 3(3), 106-150.

[10] Mahmoud, M. S., & Khalil, H. K. (2002). Robustness of high-gain observer-based nonlinear controllers to unmodeled actuators and sensors. Automatica, 38(2), 361-369.

[11] Wang, L., Yan, J., Cao, T., & Liu, N. (2021). Manipulator control law design based on Backstepping and ADRC Methods. In Proceedings of 2020 Chinese Intelligent Systems Conference: Volume I (pp. 261-269). Springer Singapore.

Optimal Trajectory Planning with Obstacle Avoidance Based on Water Cycle Algorithm for a Flying Robot

Nesrine Tenniche [1], Boubekeur Mendil [2], Lyes Tighzert [3]

[1] *Laboratoire de Technologie Industrielle et de l'Information (LTII), Faculté de Technologie, Université de Béjaia, Algeria*

nesrine.tenniche@univ-bejaia.dz

[2] *Faculté de Technologie, Université de Béjaia, Algeria*

boubekeur.mendil@univ-bejaia.dz

[3] *Laboratoire de Technologie Industrielle et de l'Information (LTII), Faculté de Technologie, Université de Béjaia, Algeria*

lyes.tighzert@univ-bejaia.dz

***Abstract*—Trajectory planning presents several challenges that need to be addressed to ensure effective and reliable flying robot's motion. These challenges include collision avoidance, real-time planning, dynamics environments, and high-dimensional state spaces. Metaheuristic algorithms emerge as a promising approach for overcoming these challenges, providing a viable solution to navigate complex scenarios, optimize trajectories, and handle uncertainties effectively. In this work, a new trajectory planner based on the Water Cycle Algorithm (WCA) is proposed for a flying robot called quadrotor, to find the best possible, achievable, and optimal trajectory in a 3D environment with obstacles. The WCA algorithm, emulates the water cycle's dynamic processes, consider path length as an objective function while incorporating constraints such as collision avoidance, velocity limit, flying robot non-holonomic constrains, and time execution. The performance of the WCA was evaluated by comparing it with the Firefly Algorithm (FA) and the Particle Swarm Optimization (PSO). The obtained results demonstrated that the trajectory planned by WCA outperformed the trajectories generated by FA and PSO, in terms of path length.**

***Keywords:* Quadrotor, Trajectory Planning, Obstacle Avoidance, Optimization, Water Cycle Algorithm (WCA).**

I. INTRODUCTION

In recent years, the field of robotics has witnessed remarkable advancements, particularly in the realm of flying robots. While the applications of the flying robots continue to expand and diversify, encompassing a wide range of tasks such as object detection, aerial photography, disaster response, search and rescue operations, infrastructure inspection, and even assisting in medical deliveries, the challenge of trajectory planning remains a significant hurdle.

Hence, optimal track planning has become a significant research topic due to the increasingly complex flight missions and changing flight environments [1]. Additionally, Trajectory planning involves solving the complex task of motion planning while incorporating various constraints. This becomes particularly challenging when dealing with systems with a large number of degrees of freedom (DOF) [2], such as quadrotors which have six DOF. Moreover, Quadrotors possess distinctive characteristics such as coupling, underactuation, and nonlinearities, which contribute to the inherent complexity of trajectory planning. Consequently, successfully addressing these constraints and finding optimal paths requires sophisticated algorithms and techniques.

The trajectory tracking of quadrotors has garnered significant attention among researchers, and related works have been extensively reported in the literature. Traditional methods, including the potential field method, Dijkstra algorithm, and RRT (Rapidly-Exploring Random Tree) algorithm, have been employed for quadrotor trajectory planning. These methods typically rely on constructing the map environment for the target before initiating the trajectory planning process [3]. The potential field method has been applied in [4], for quadrotor trajectory planning under dynamic environment. The authors in [5], utilized Dijkstra's algorithm to quadrotor path planning in a closed and known environment with obstacles and boundaries, enabling obstacle avoidance and finding the shortest path from an initial to a final position. In [6], the formation landing problem of quadrotors is addressed using RRT algorithm for path planning and considering static obstacles. Simulation results show the applicability of the proposed framework in real-time.

Recently, metaheuristic algorithms enhance quadrotor trajectory planning performance and flexibility. They handle high-dimensional spaces better, ensuring smoother and more accurate tracking. A new path planning method using PSO is presented in [7] for quadrotors, aiming to optimize smooth trajectories, minimizes flight distance, and ensures collision avoidance. Simulation results demonstrates its effectiveness in generating efficient and collision-free trajectories. In [8], a Differential Evolution (DE) algorithm-Artificial Bee Colony (ABC) algorithm is proposed, to address the limitations of the traditional ABC algorithm by incorporating the diversity-enhancing mechanisms of the DE algorithm, for quadrotors path planning and obstacle avoidance in urban environments. The

proposed hybrid algorithm demonstrates superior performance over the traditional ABC and DE algorithms. Genetic Algorithm (GA) is used in [9], for quadrotors path planning. The algorithm navigation waypoints to minimize distance and avoid obstacles. Real-time experiments validate the algorithm's effectiveness. In [10], a new algorithm for path planning in quadrotors is presented, based on the teaching-learning-based optimization (TLBO) algorithm. The proposed algorithm, called Multi-subject TLBO, enhances TLBO with mutation, elite selection, and multi-subject training to improve solution quality and convergence speed. Comparative analysis and real UAV experiments confirm its effectiveness in generating optimal, collision-free paths in complex environments.

In this work, a new trajectory planner based on the WCA is proposed, for quadrotor trajectory planning. The WCA operates by representing potential solutions as water drops within a search space. This algorithm is utilized to determine the waypoints of the optimal trajectory. Each water drop corresponds to a waypoint along the trajectory between the initial and final points, and the optimization process emulates the natural movement of water drops to determine optimal paths. In this process, the objective function considers path length as a key criterion for finding the best optimal trajectories. The main objective of the proposed trajectory planner is to generate smooth and collision-free trajectory for the flying robot in an environment that includes 25 obstacles in the form of cylinders. The cylinders are used to model buildings of various heights and diameters. A comparative study was conducted with FA and PSO to validate the effectiveness of the proposed trajectory planner based on the WCA. The obtained results show that the WCA-based planner produced shorter path lengths.

The structure of this paper is as follows: Section 2 presents the quadrotor mathematical model. The trajectory planning problem is described in Section 3. Section 4 explains the WCA The obtained results are presented and discussed in Section5. Finally, Section 6 provides the conclusion of this paper.

II. QUADROTOR MATHEMATICAL MODEL

A quadrotor is a flying robot with four rotors arranged in a cross formation, possessing six DOF and controlled by four brushless direct current motors [11]. The equations of motion for a quadrotor, derived from the Newton-Euler formalism, can be represented by a set of six equations that describe both the rotational and translational dynamics of the flying robot [12].

$$\dot{p} = \frac{1}{I_x}[(I_y - I_z)qr - K_{fax}p^2 - J_r\bar{\Omega}q + U_\phi] \quad (1a)$$

$$\dot{q} = \frac{1}{I_y}[(I_z - I_x)pr - K_{fay}q^2 + J_r\bar{\Omega}p + U_\theta] \quad (1b)$$

$$\dot{r} = \frac{1}{I_z}[(I_x - I_y)pq - K_{faz}r^2 + U_\psi] \quad (1c)$$

$$\ddot{x} = \frac{1}{m}[(Cos\phi\ Sin\theta\ Cos\psi + Sin\phi\ Sin\psi)U_z - K_{ftx}\dot{x}] \quad (1d)$$

$$\ddot{y} = \frac{1}{m}[(Cos\phi\ Sin\theta\ Sin\psi - Sin\phi\ Cos\psi)U_z - K_{fty}\dot{y}] \quad (1e)$$

$$\ddot{z} = \frac{1}{m}[(Cos\phi\ Cos\theta)U_z - K_{ftz}\dot{z}] - g \quad (1f)$$

where $x, y,$ and z represent longitudinal, lateral, and vertical motions, respectively. $\phi, \theta,$ and ψ denote bank, pitch, and heading angles, while $p, q,$ and r are roll, pitch, and yaw rates, respectively. $U_z, U_\phi, U_\theta,$ and U_ψ are altitude, roll, pitch, and yaw commands, respectively. m represents the quadrotor's mass. d is the quadrotor's mass-center to propeller axis distance. $I_x, I_y,$ and I_z are the roll, pitch, and yaw inertia moment, respectively. $K_{ftx}, K_{fty},$ and K_{ftz} denote the positive drag coefficients, whereas $K_{fax}, K_{fay},$ and K_{faz} are the aerodynamic friction coefficients. The drag coefficient force is denoted as C_D, while b represents lift force coefficient. g is the gravity acceleration.

III. TRAJECTORY PLANNING PROBLEM DESCRIPTION

The quadrotor trajectory planning problem can be framed as an optimization problem, where the goal is to find the optimal waypoints for the quadrotor's flight path. To tackle this problem, a WCA is employed which will be explained in the next section.

A. Environement model

In this work, the environment model used for trajectory planning is a 3D representation that incorporates 25 obstacles represented as cylinders to accurately model buildings of varying heights and diameters. By considering the presence of these obstacles, the trajectory planner ensures that the flying robot navigates safely and avoids any potential collisions during its flight. The environment model is represented in Fig. 1, while Table I provides the coordinates of each obstacle.

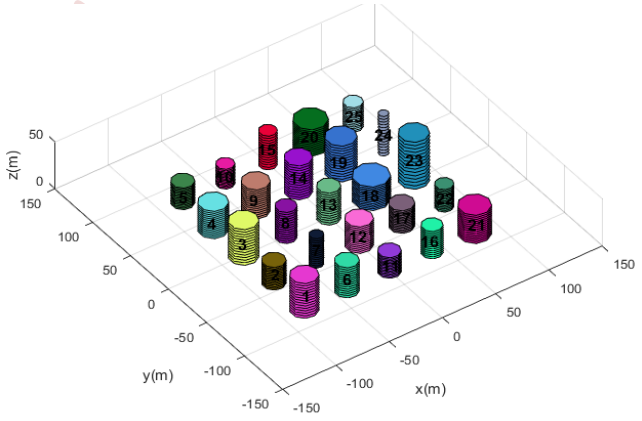


Figure 1. Environment model.

B. Constraints

The quadrotor trajectory planning involves several constraints that must be considered to ensure safe and efficient flight:

- Non-holonomic constraints

The explicit representation of the coupling between different states of the flying robot is made possible through the development of non-holonomic constraints. These constraints are utilized in quadrotor trajectory planning to ensure realistic motion, generate safe trajectories, optimize efficiency, and enable collision avoidance. From the equations of translational

dynamics, (1d), (1e) and (1f), the expressions for the non-holonomic constraints can be extracted:

$$\begin{cases} tan\theta = \dfrac{\left(\ddot{x}-\frac{K_{ftx}}{m}\dot{x}\right)C\psi+\left(\ddot{y}-\frac{K_{fty}}{m}\dot{y}\right)S\psi}{\ddot{z}+g-\frac{K_{ftz}}{m}\dot{z}} \\ Sin\phi = \dfrac{-\left(\ddot{x}-\frac{K_{ftx}}{m}\dot{x}\right)S\psi+\left(\ddot{y}-\frac{K_{fty}}{m}\dot{y}\right)C\psi}{\sqrt{\left(\ddot{x}-\frac{K_{ftx}}{m}\dot{x}\right)^2+\left(\ddot{y}-\frac{K_{fty}}{m}\dot{y}\right)^2+(\ddot{z}+g-\frac{K_{ftz}}{m}\dot{z})^2}} \end{cases} \quad (2)$$

TABLE I. OBSTACLES COORDINATES

Obstacle	**1**	**2**	**3**	**4**
Coordinate	(-78,-76,37)	(-78,-36,24)	(-78,4,38)	(-78,44,29)
Obstacle	**5**	**6**	**7**	**8**
Coordinate	(-78,83,23)	(-38,-76,32)	(-38,-36,31)	(-38,4,33)
Obstacle	**9**	**10**	**11**	**12**
Coordinate	(-38,44,31)	(-38,83,21)	(1,-76,22)	(1,-36,28)
Obstacle	**13**	**14**	**15**	**16**
Coordinate	(1,4,34)	(1,44,36)	(1,83,36)	(41,-76,29)
Obstacle	**17**	**18**	**19**	**20**
Coordinate	(41,-36,24)	(41,4,25)	(41,44,38)	(41,83,25)
Obstacle	**21**	**22**	**23**	**24**
Coordinate	(81,-76,30)	(81,-36,24)	(81,4,50)	(81,44,42)
Obstacle	**25**			
Coordinate	(81,83,26)			

- Obstacle avoidance

The height of the obstacle must be lower than the trajectory height ($H_{obstacle} \leq z$). When the trajectory passes overhead, it should not touch a building when the drone flies between structures. The safety distance is the sum of the quadrotor's radius and the obstacle's radius ($d = r_{obstacle} + r_{quadrotor}$).

- Velocity limit

For the problem of trajectory planning, a maximum velocity of 100 km/h has been selected for the quadrotor.

C. Cost function

The cost function chosen for quadrotor trajectory planning is path length, as represented by Eq. (3). By minimizing the path length, the objective is to optimize the trajectory planning of the flying robot.

$$L = \int \sqrt{\left(\left(\frac{dx}{dt}\right)^2 + \left(\frac{dy}{dt}\right)^2 + \left(\frac{dz}{dt}\right)^2\right) dt} \quad (3)$$

IV. WATER CYCLE ALGORITHM

The WCA [13], a water-based metaheuristic optimization algorithm, draws inspiration from nature by observing water cycles and the downhill flow of rivers and streams towards the sea [14]. It's specifically developed to address constrained continuous optimization problems. The WCA algorithm involves the following main steps:

1. Population

The initial population of streams, including both sea and rivers, is randomly selected as:

$$Population = \begin{bmatrix} x_1^1 & x_2^1 & x_3^1 & \cdots & x_N^1 \\ x_1^2 & x_2^2 & x_3^2 & \cdots & x_N^2 \\ \vdots & \vdots & \vdots & \cdots & \vdots \\ x_1^{N_{pop}} & x_2^{N_{pop}} & x_3^{N_{pop}} & \cdots & x_N^{N_{pop}} \end{bmatrix} \quad (4)$$

N_{pop} refers to the population size, while N represents the number of design variables.

The cost of a stream is determined by evaluating the cost function using the following formula:

$$C_i = Cost_i = f\left(x_1^i, x_2^i, \dots, x_N^i\right), \; i = 1,2,3,\dots,N_{pop} \quad (5)$$

After generating the N_{pop} streams, the best N_{sr} individuals are selected based on their fitness (minimum values), and these individuals are considered as the river and sea in the given equations:

$$N_{sr} = Number\ of\ rivers + \underbrace{1}_{\text{Sea}} \quad (6)$$

$$N_{Stream} = N_{pop} - N_{sr} \quad (7)$$

The number of streams flowing into the rivers and sea is determined by water flow intensity as follows:

$$NS_n = round\left\{\left|\frac{Cost_n}{\sum_{i=1}^{N_{sr}} Cost_i}\right| \times N_{stream}\right\}, n = 1,2,\dots,N_{sr} \quad (8)$$

NS_n represents the streams that flow into specific rivers or the sea.

2. Confluence processes

The water circulation system operates like a merging into a river, which then flows into the sea. Initially, there's a distance between the stream and the river, but they converge over time. If the river's cost is lower than the sea, they swap positions [14], and updating equations guide their flow towards the sea:

$$x_{stream}^{i+1}(t+1) = x_{stream}^{i}(t) + rand \times C \times \left(x_{sea}(t) - x_{stream}^{i}(t)\right) \quad (9)$$

$$i = 1,2,3,\dots,N_{Stream}$$

$$x_{stream}^{i+1}(t+1) = x_{stream}^{i}(t) + rand \times C \times \left(x_{river}^{i}(t) - x_{stream}^{i}(t)\right) \quad (10)$$

$$i = 1,2,3,\dots,N_{Stream}$$

$$x_{river}^{i+1}(t+1) = x_{river}^{i}(t) + rand \times C \times \left(x_{sea}(t) - x_{river}^{i}(t)\right) \quad (11)$$

$$i = 1,2,3,\dots,(N_{Sr}-1)$$

where rand is uniformly distributed random number between [0, 1],C is a constant value ranging from 1 to 2, typically taking the value 2, and t represents the iteration index.

3. Evaporation process

The evaporation plays a crucial role in preventing the algorithm from getting trapped in local optima due to overly rapid convergence. Water from streams or rivers evaporates, forms clouds, and returns as rain to create new streams when the 'evaporation condition' in the algorithm is met due to their proximity to the sea [14]. The evaporation conditions are as follows:

$$\text{if } \left\|x_{sea}(t) - x^{j}_{river}(t)\right\| < d_{max} \quad \text{or } rand < 0.1 \;,\; j = 1,2,\dots,N_{sr}-1 \qquad (12)$$

Perform raining process by Eq (15)

end

$$\text{if } \left\|x_{sea}(t) - x^{j}_{stream}(t)\right\| < d_{max} \quad \text{or } rand < 0.1 \;,\; j = 1,2,\dots,N_{sr}-1 \qquad (13)$$

Perform raining process by Eq (15)

end

where d_{max}, a value close to zero, effectively regulates the search depth in proximity to the sea.

The value of d_{max} adaptively decreases at the end of each iteration as :

$$d_{max}(t) = d_{max}(t) - \frac{d_{max}(t)}{t_{Max}} \quad ,t = 1,2,3,\dots,t_{Max} \qquad (14)$$

3. Raining process

Once the evaporation process is completed, the raining process is applied. During this process, streams of new raindrops are generated at different locations. To calculate the new positions of these newly formed streams, the following equation is employed:

$$x^{i}_{stream}(t+1) = LB + rand \times (UB - LB) \qquad (15)$$

LB and UB represent the lower and upper bounds, respectively, of a specified optimization problem.

V. SIMULATION RESULTS AND DISCUSSION

This work addresses quadrotor trajectory planning, aiming to find the optimal flight path from the starting point (-150, -150,0) to the final destination (150,150,5), within an environment containing 25 obstacles. WCA is applied to determine optimal four waypoints, considering the specified constraints and objective function. Once the optimal waypoints are obtained, the B-splines method is used to join these waypoints and create a smooth trajectory for the flying robot.

The study compared WCA with the FA and PSO algorithms using path length as the cost function. The pseudo-code of WCA is presented in Fig. 2, while those of PSO and FA were extracted from [15] and [16], respectively. The algorithms were evaluated using a population size of 50 and tested over 10 000 iterations. Specified algorithms parameters are indicated in Table II. The obtained results show that the WCA performed competitively, as depicted in Fig. 3, in terms of path length. Table III presents the path length and the optimal waypoints achieved by the three algorithms for the optimal trajectory.

Algorithm: *Water Cycle Algorithm*

1. Parameters initialization ($N_{pop}, N_{sr}, t_{Max}, d_{max}$).
2. Determine the number of streams (individuals) which flow to the rivers and sea by Eq. (7).
3. Generate an initial population using Eq. (4).
4. Define the intensity of flow using Eq. (8)
5. ***while*** t≤ t_{Max} **do**
6. **for** i=1: N_{pop}
7. Streams directly flow to the sea using Eq. (9)
8. Calculate the objective function of the stream by Eq. (5)
9. **if** Cost (New_stream) < Cost (Sea)
10. Sea = New_Stream
11. **end if**
12. Streams flow to their rivers using Eq. (10)
13. Calculate the objective function of the stream by Eq. (5)
14. **if** Cost (New_stream) < Cost (River)
15. River = New_Stream
16. **if** Cost (New_Stream)< Cost (Sea)
17. Sea= New_Stream
18. **end if**
19. **end if**
20. Rivers flow to the sea using Eq. (11)
21. Calculate the objective function of the river by Eq. (5)
22. **if** Cost (New_River)< Cost (Sea)
23. Sea= New_River
24. Check the evaporation condition using Eqs. (12) and (13)
25. **if** the evaporation condition is satisfied
26. **for** i=1: (N_{sr}-1)
27. **if** (distance (Sea and River) < d_{max} or (rand<0.1)
28. New streams are created using Eq. (15)
29. **end if**
30. **end for**
31. **for** i=1: (N_{stream})
32. **if** (distance (Sea and Stream) < d_{max} or (rand<0.1)
33. New streams are created using Eq. (15)
34. **end if**
35. **end for**
36. **end if**
37. **end for**
38. Reduce the value of d_{max} using Eq. (14)
39. ***end while***

Figure 2. Pseudo-code of WCA [14].

TABLE II. ALGORITHMS PARAMETERS

WCA parameters	N_{sr}	d_{max}	
Value	10	10^{-16}	
PSO parameters	W	C_1	C_2
Name	Inertia weight	Personal learning coefficient	Global learning coefficient
Value	1	1.5	1.5
FA parameters	γ	β_0	α
Name	Light absorption coefficient	Attraction coefficient base value	Mutation coefficient
Value	1	2	0.2

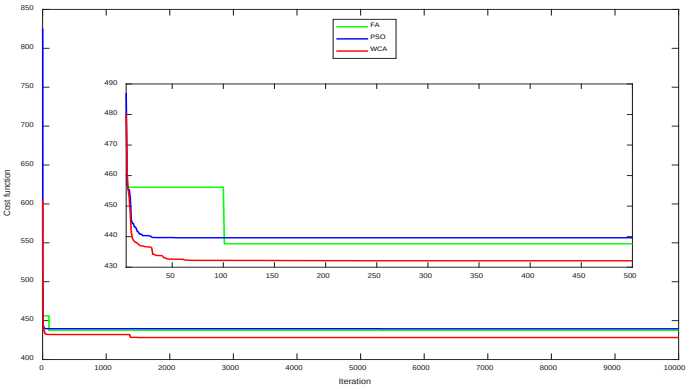


Figure 3. Cost function comparison for the three algorithms.

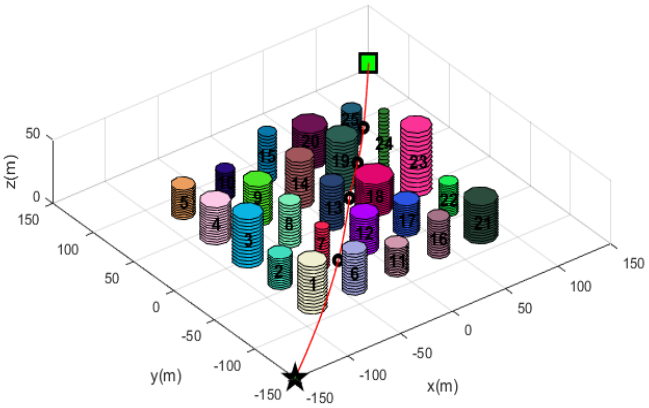


Figure 4. 3D optimal trajectory planning with WCA.

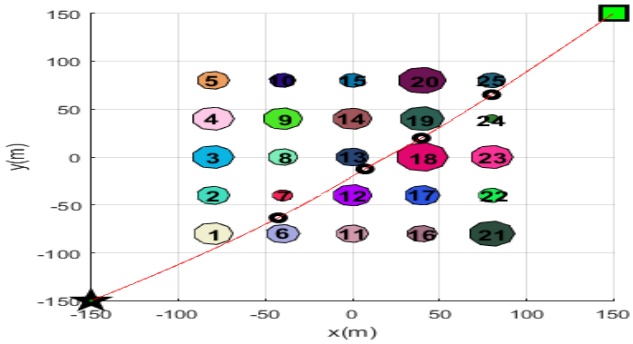


Figure 5. 2D optimal trajectory planning with WCA.

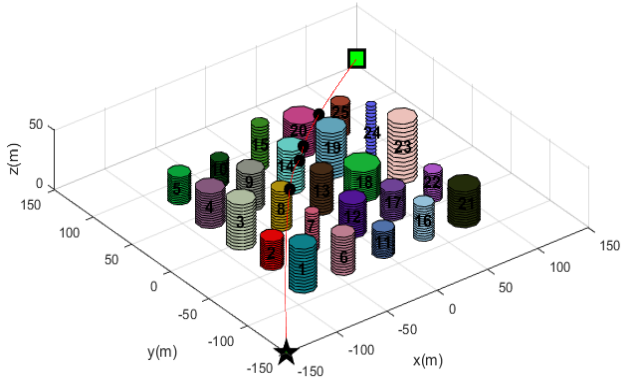


Figure 6. 3D optimal trajectory planning with PSO.

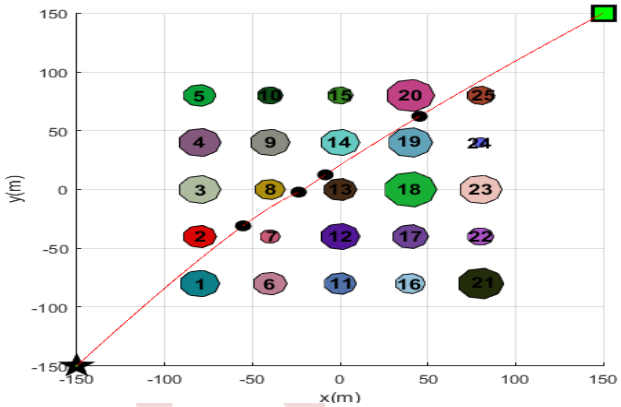


Figure 7. 2D optimal trajectory planning with PSO.

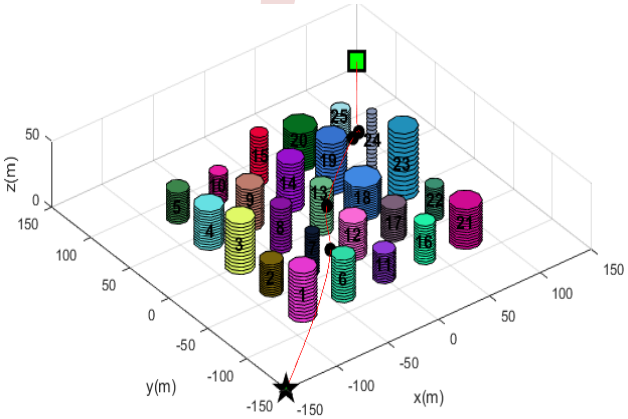


Figure 8. 3D optimal trajectory planning with FA.

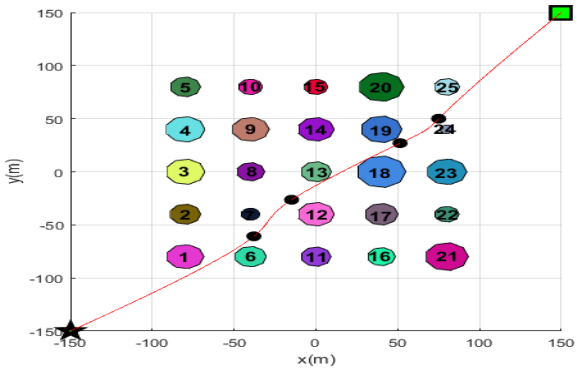


Figure 9. 2D optimal trajectory planning with FA.

TABLE III. PATH LENGTH AND WAYPOINTS COORDINATES

Algorithm	WCA	FA	PSO
Path length L (m)	428.3108	437.6651	439.6393
Waypoint 1 (m)	(-42.54, -63.4, 15.3)	(-37.96, -60.8, 25)	(-54.24, -29.88, 50.23)
Waypoint 2 (m)	(7.31, -12.46, 23.3)	(-12.71, -24.28, 34.5)	(-23.26, -1.98, 49.95)
Waypoint 3 (m)	(39.68, 19.81, 24.7)	(56.01, 30.28, 37.16)	(-8.37, 12.48, 50)
Waypoint 4 (m)	(80, 65.06, 17.67)	(70.3, 42.91, 28.52)	(46.5, 63.41, 34.58)

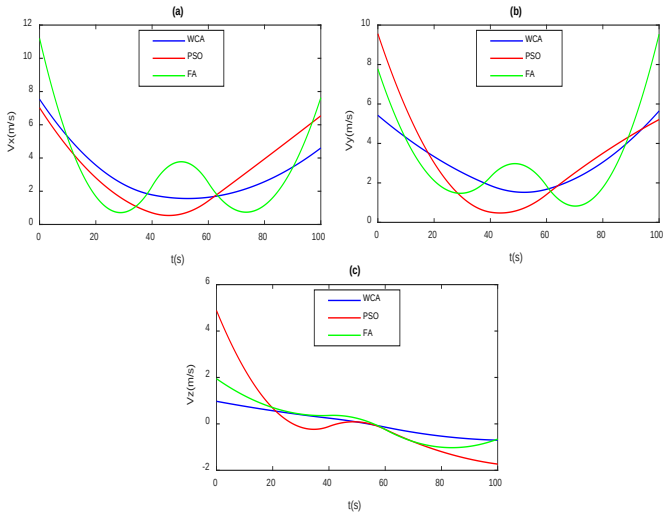


Figure 10. Quadrotor velocities V_x (a) , V_y (b) , and V_z (c) of the planned trajectory.

Fig. 4 and 5 display the 3D and 2D trajectories resulting from the WCA optimization, respectively. Remarkably, the trajectory successfully avoids contact with any obstacles and smoothly navigates above obstacle 18. This efficient path planning led to a notable path length of 428.3108 m. Similarly, the 3D and 2D planned trajectories shown in Fig. 6 and 7 were generated using the FA optimization, successfully minimizing the path length and skillfully avoiding obstacles over a distance of 437.6651 m. Lastly, Fig. 8 and 9 illustrate the 3D and 2D planned trajectories obtained from the PSO algorithm, resulting in a path length of 439.6393 m. It is evident that the WCA optimization outperformed the other algorithms, displaying its superiority in path planning with the most optimized path length. Fig. 10 represents the quadrotor velocities V_x, V_y , and V_z of the planned trajectory using the algorithms WCA, PSO, and FA.

VI. CONCLUSION AND FUTURE WORKS

In this work, a new trajectory planner based on WCA has been proposed, for a flying robot called quadrotor. The WCA has been used to represent potential solutions as water drops within a search space and determine the waypoints of the optimal trajectory. Each water drop has corresponded to a waypoint along the trajectory between the initial and final points, and the optimization process has emulated the natural movement of water drops to determine optimal paths. The proposed trajectory planner has been designed to generate smooth and collision-free trajectories for the flying robot in an environment that includes 25 obstacles in the form of cylinders. These cylinders have been used to model buildings of various heights and diameters. In order to validate the effectiveness of the proposed trajectory planner based on the WCA, a comparative study was conducted with FA and PSO. The obtained results demonstrate the success of the WCA-based planner in generating shorter path lengths.

Further work will be dedicated to tracking the planned trajectory.

REFERENCES

[1] J. Fan, X. Chen, and X. Liang, " UAV trajectory planning based on bi-directional APF-RRT* algorithm with goal-biased," *Expert Systems with Applications*, vol. 213, pp. 119137, 2023.

[2] D. Hashemi and H. Heidari, " Trajectory planning of quadrotor UAV with maximum payload and minimum oscillation of suspended load using optimal control," *Journal of Intelligent & Robotic Systems*, vol. 100, no. 3-4, pp. 1369-1381, 2020.

[3] Y. Yang, X. Xiong, and Y. Yan, " UAV Formation Trajectory Planning Algorithms: A Review," *Drones*, vol. 7, no. 1, pp. 62, 2023.

[4] A. Budiyanto, A. Cahyadi, T.B. Adji, and O. Wahyunggoro, "UAV obstacle avoidance using potential field under dynamic environment," In *2015 International Conference on Control, Electronics, Renewable Energy and Communications (ICCEREC)*, pp. 187-192, 2015.

[5] D. Gautam, C. Ha, "Control of a quadrotor using a smart self-tuning fuzzy PID controller," *International Journal of Advanced Robotic Systems*, vol. 10, no. 11, pp. 380, 2013.

[6] Y. Dong, C. Fu, and E. Kayacan, "RRT-based 3D path planning for formation landing of quadrotor UAVs," In *2016 14th International Conference on Control, Automation, Robotics and Vision (ICARCV)*, pp.1-6, 2016.

[7] Y. Hong, S. Kim, and J.Cha, "Integrated Global and Local Path Planning for Quadrotor Using Particle Swarm Optimization," vol. 53, no. 2, pp. 15621-15625, 2020.

[8] C. Haohao, Q. Xiaohui, and Y. Sen, "Obstacle Avoidance and Path Planning for Quadrotor based on Differential Evolution-Artificial Bee Colony Algorithm," In *Journal of Physics: Conference Series*, vol. 1087, no. 2, pp. 022030, 2018.

[9] M. A. Gutierrez-Martinez, E. G. Rojo-Rodriguez, L. E. Cabriales-Ramirez, L. A. Reyes-Osorio, P. Castillo, and O. Garcia-Salazar, "Collision-free path planning based on a genetic algorithm for quadrotor uavs," *In 2020 International Conference on Unmanned Aircraft Systems (ICUAS)* , pp. 948-957, 2020.

[10] V. T. Hoang and M. D. Phung, "Enhanced Teaching-Learning-Based Optimization for 3D Path Planning of Multicopter UAVs," *In International Conference on Advanced Mechanical Engineering, Automation and Sustainable Development* , pp. 753-753, 2021.

[11] N. Tenniche, B. Mendil, L. Tighzert, and M. Yazid, "Nonlinear PID Control Based On DE Algorithm for Flying Robot Trajectory Tracking," *In 4th International Conference on Technological Advances in Electrical Engineering (ICTAEE'23)*,2023, in press.

[12] H. Bouadi and F. Mora-Calino, "Direct adaptive backstepping flight control for quadcopter trajectory tracking," *In 2018 IEEE/AIAA 37th Digital Avionics Systems Conference (DASC)*, pp. 1-8, 2018.

[13] H. Eskandar, A. Sadollah, A. Bahreininejad, and M. Hamdi, "Water cycle algorithm–A novel metaheuristic optimization method for solving constrained engineering optimization problems," *Computers & Structures*, vol. 110, pp. 151-166, 2012.

[14] M. Nasir, A. Sadollah, Y. H. Choi, and J.H. Kim, "comprehensive review on water cycle algorithm and its applications," *Neural Computing and Applications*, vol. 32, pp. 17433-17488, 2020.

[15] S. M. K. Heris, "Particle Swarm Optimization in MATLAB," *Yarpiz*, 2015.

[16] S. M. K. Heris, " Firefly Algorithm (FA) in MATLAB," *Yarpiz*, 2015.

Remote control of mentor robot via Bluetooth

Oussama Sait[1], Samia Latréche[1], Mabrouk Khemliche[1],Belkacem Sait[1]

[1]*Automatic Laboratory of Setif, Electrcal EngineeringDepartment,Setif1University, Setif, Algeria*
oussamasait2017@gmail.com

[1]*Automatic Laboratory of Setif,Electrcal EngineeringDepartment,Setif1University, Setif, Algeria*
ksamia2002@yahoo.fr

[1]*Automatic Laboratory of Setif, Electrcal Engineering Department,Setif1University, Setif, Algeria*
mabroukkhemliche@univ-setif.dz

[1]*Automatic Laboratory of Setif,Electrcal Engineering Department,Setif1University, Setif, Algeria*
belkacemsait@yahoo.fr

Abstract— Controlling a robotic arm has presented a long-standing challenge. In this article, a remote control Bluetooth was developed and integrated within a six-axis robotic arm. The central components of the designed remote control Bluetooth included the MEGA Arduino microcontroller unit, the driver unit, and the power supply unit. To govern the movements of the arm's joints in various directions, six DC motors equipped with associated potentiometers for position feedback signals were employed. The Mentor robotic arm served as the test bed for evaluating this remote control Bluetooth. The controller was connected to a personal computer through its USB port. A graphical user interface window was created on the personal computer using Google App Inventor software. Commands for joint movements were transmitted to the robotic arm through a mobile phone via Bluetooth. This proposed system offers a cost-effective, energy-efficient, compact, and highly accurate remote control Bluetooth solution for complex robotic arms.

Keywords: Bluetooth, Robotic arm, Arduino, Google App Inventor.

I. INTRODUCTION

Wireless communication technologies have revolutionized the way we live, work, and communicate. They have also had a significant impact on the scientific sphere, particularly in the field of robotics. Wireless communication technologies allow robotic systems to be controlled and monitored from a distance, which makes them ideal for a wide range of applications, including education, research, and industry [1].

This paper presents the development of a remote control system for a Mentor Arm using Bluetooth and an Arduino program. The Mentor Arm is a six degree of freedom manipulator arm that can be used for a variety of tasks, such as grasping objects, manipulating tools, and performing assembly operations. The Arduino program is used to control the motors of the Mentor Arm and to receive commands from the remote control application.

The remote control application is developed using MIT App Inventor, which is a visual programming environment that allows users to create mobile apps for Android devices without writing any code. The application provides a simple and intuitive interface for controlling the Mentor Arm.

The remainder of this paper is organized into VII sections. Section II reviews related work in the field of robotics remote control applications. Section III presents a comprehensive overview of the Mentor Arm, a VI-degree-of-freedom manipulator arm used in this project. Section IV describes the tools and devices used in the project, including their specific functions and capabilities. Section V provides a detailed account of the development of the remote control application using MIT App Inventor, a visual programming environment that enables users to create Android mobile apps without writing any code. Section VI explains how these tools are integrated to achieve the project's objectives, including the design and implementation of the remote control application. Finally, Section VII concludes the paper by summarizing the key features and functionality of the final application and providing examples of how it can be used to control the Mentor Arm and execute a variety of tasks.

II. RELATED WORK

Robotic arms are programmable mechanical devices that can be used to perform a variety of tasks. They are typically composed of a series of links connected by joints, which allow the arm to move in a variety of ways. The end effector, which is the part of the arm that interacts with the environment, can be used to grasp objects, manipulate them, or perform other tasks [2], [3].

Robotic arms are used in a wide variety of applications, including manufacturing, assembly, healthcare, and research. They are becoming increasingly sophisticated and versatile, and their use is expected to continue to grow in the future [4].

In paper [5] was describes the design and implementation of a remote-controlled robotic arm with six degrees of freedom for industrial use. The robotic arm is based on the Arduino Uno microcontroller and uses six DC geared motors with the L298 motor driver. Rotary encoders are attached to each motor for

position control. Wireless communication is established between the joystick and the system.

The paper also discusses the mechanical structure of the robotic arm, which is modular in design. The basic structure of the arm consists of a base, waist, shoulder, arm, elbow, forearm, and hand. The wrist is a separate module that can be attached to the forearm.

The paper concludes by discussing the advantages of using the proposed robotic arm system. The system is relatively affordable, easy to use, and safe to operate around humans. It is also relatively small and lightweight, making it easy to move and store.

This paper [6] presents the development of a remote control system for a Mentor Arm using Bluetooth and a smart phone. The system is designed to be used in industrial and research settings to control the Mentor Arm from a distance.

The system consists of a Bluetooth module that is connected to the Mentor Arm and a Smartphone app that is used to control the arm. The smart phone app sends commands to the Bluetooth module, which then controls the motors of the Mentor Arm.

The system was tested using a variety of tasks, including moving the arm to different positions, grasping objects, and releasing objects. The system was found to be able to control the Mentor Arm accurately and reliably. The system was also found to be easy to use and safe to operate..

This paper [7] describes a system for remote control of a mobile robot using a Smartphone and Bluetooth technology. The system uses a custom-built mobile application to send control commands to the robot. The robot is equipped with an Arduino Uno microcontroller and an HC-05 Bluetooth module. The Arduino decodes the received commands and controls the robot's movements accordingly.

The system was evaluated using two robots, MOCOVE and RIZZY. MOCOVE is a two-wheeled robot with differential steering, while RIZZY is a four-wheeled robot with omnidirectional steering. Both robots were able to be successfully controlled using the Smartphone application.

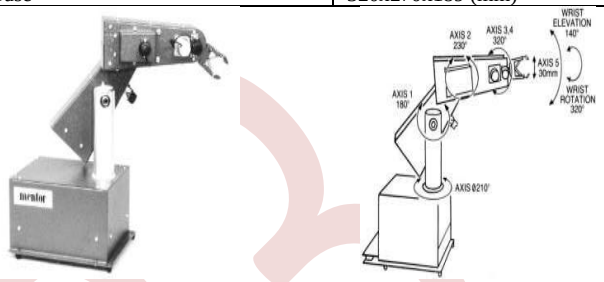
III. MENTOR DESKTOP ROBOTS

The Mentor Desktop Robot (MDR) is a six-degree-of-freedom (DOF) serial manipulator arm equipped with a gripper [8], [9]. The MDR is driven by six servo motors and controlled through a closed-loop control system. The gripper's position in space is determined by the individual axis controllers, which continuously monitor and maintain the gripper's position until a new move command is received. This articulated arm resembles the human arm and is widely used in industry .The properties of the Mentor arm robot are detailed in Tables 1 and 2 [10]. This robot can be easily programmed using WALLI software.

Table I. shows the properties of mentor robot arm [11].

TABLE I. MENTOR ARM ROBOT PROPERTIES[11].

Properties	Specification
Repeatability	2 degree
Accuracy	1.5 degree
Lifting (payload)	1000gm at full reach
Gripper	Jaw opening 45mm
Base	320x270x189 (mm)



(A) (B)

Figure 1. (A) Mentor desktop robotic, (B) Maximum allowable movement

Table II shows the structure and movement of mentor robot arm[11].

TABLE II. MENTOR ARM ROBOT MOVEMENT RANGE OF BASIC STRUCTURE [11].

Structure	Movement type	Maximum allowable
Waist	Rotation	(Θ1) 0<Θ1 ≤360°
Arm	Rotation	(Θ2) 0<Θ2 ≤180°
Forearm	Rotation	(Θ3) 0<Θ3 ≤200°
Wrist	Rotation	(Θ4) 0<Θ4 ≤360°
Shoulder	Linear	(L1) 0<L1≤8 inch
Base	Linear	(L2) 0<L2≤12 inch

IV. CONTROLLER DESIGN AND IMPLEMENTATION

In this paper the old control system of the Mentor robotic arm was replaced by a new PC-based open source controller for the same purpose.

A. The controller architecture

The following paragraphs describe the designing and implementation of the main units with their selected hardware.

The Arduino MEGA control system (Figure 2) [12] governs the movements of the six DC motors in the robotic arm via Bluetooth signals transmitted from a mobile phone using a dedicated application. The Arduino MEGA control unit requires a 5VDC power supply with a current rating of 1A.This board acts as intermediary between the mobile phone and the custom-designed control board ensures seamless communication and control.



Figure 2. Arduino Mega

The precise management of the DC motors has been achieved through motor drivers. These DC motor drivers receive control signals from the Arduino MEGA unit to power the coils of the DC motors. This action induces the rotation of the motors in the appropriate direction, enabling the robotic arm to move in accordance with the system's requirements.

DC motor drivers are typically based on the H-bridge configuration, specifically the L298N (Figure 3). This configuration allows for the delivery of higher currents to the motors while protecting the Arduino MEGA unit from back EMF (electromotive force) [13]. In this system, three L298N drivers are used, each of which is responsible for controlling two motors [14].

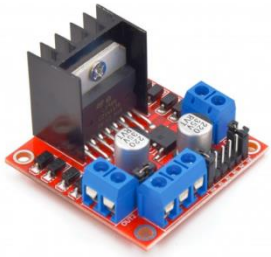


Figure 3. L298N double bridge-H

The Arduino HC-05 Bluetooth module (Figure 4) is a low-power, short-range wireless communication device that enables Arduino devices to communicate with other Bluetooth devices using the Bluetooth Serial Port Protocol (SPP) [15].



Figure 4. Bluetooth modules for Arduino

DC motors are compact, easy to control, and can be powered by batteries or power supplies. They are also relatively easy to use. This system uses the DME33S5C500A (Figure 5)[16] servo DC motor of the DME 33 series with gearbox type 5C [17],and supplied by NIDEC Servo Corporation [18], which is a geared motor with a gear ratio of 500, a rotational speed of 9 revolutions per minute (r/min), and an output power rating of 3W. It also has a continuous operational lifespan of 1000 hours.

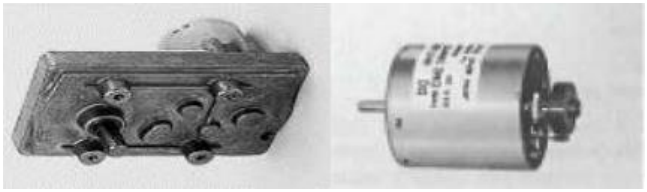


Figure 5. The DC Motor with Gearbox (DME33 series) [16].

Table III. Shows the Specifications of the DC motors used

TABLE III. SPECIFICATIONS OF THE DC MOTORS USED [16].

Product type	DC motor with 5C gearbox
Series	DME33
Model Code	SA
Gear ratio	500
Nominal voltage	12 VDC
Rated output	3.0 W
Dia. meter	420 Ma
Rated current	9 r/min
Rated speed	0.48N.m [68.05 oz-in]
Rated torque	32mm [1.26 in]
Frame size	94.5*50 mm [3.72*2.7262 in]

B. Robotic Arm Control Software

To enable remote control of our implementation, we employed a Bluetooth receiver to establish wireless communication between the Arduino and a custom Android mobile application developed using Google App Inventor.

Arduino is an open-source electronics platform based on easy-to-use hardware and software. Arduino boards are programmable with a variety of sensors and actuators, making them ideal for creating interactive devices and robots [19].

The Arduino programming environment is written in Java and allows users to write and modify programs, which are then converted into instructions that the Arduino board can understand. The Arduino programming language is derived from C and C++, but is simpler and easier to learn.

App Inventor, an online software application developed by Google Lab [20] and later taken over by MIT (Massachusetts Institute of Technology), enables Android app development through a block-based programming interface (similar to Scratch). Programming is performed online, requiring only a Gmail account and internet access. Information is stored on remote servers. The site is available in English and French, but the block functions may be less comprehensible in French.

App Inventor development is structured into two distinct phases: graphical design and block programming.

In the graphical design phase (Figure 6), users create the user interface (UI) using a variety of elements, such as buttons, text boxes, images, and cursors. The environment also offers additional features for multimedia, GPS, and Bluetooth communication. This simplified approach enables users to design intuitive UIs without requiring in-depth knowledge of traditional programming [21].

In the block programming phase, users program the app's behavior using visual code blocks. These blocks represent the mathematical, logical, and event-related functions associated with the objects used in the graphical phase. This approach takes advantage of the simplicity of object oriented programming, enabling users to create complex programs without writing any code [20].



Figure 6. Design part of our application in AppInventor

With proper use of these tools, we can create simple, effective, and visually appealing applications that meet our needs. Next, we will explain the operation of the Brick and its use in an Arduino program to control the arm.

First, we define the elements of a Bluetooth object, Bluetooth List such as available Bluetooth devices (Figure 7), then, we establish the connection between the device and the application.

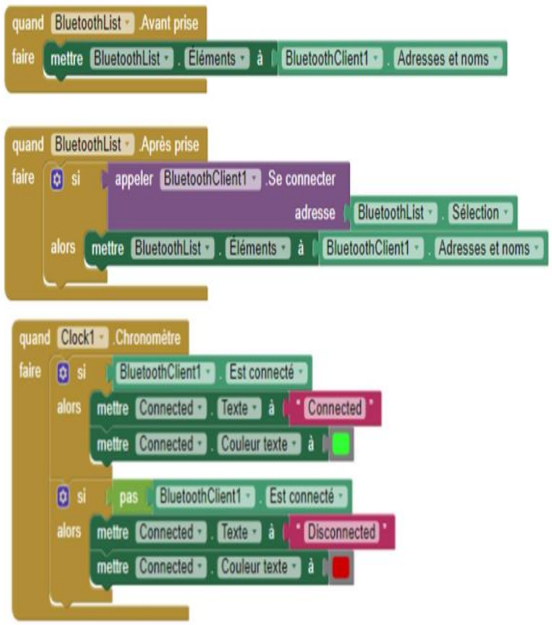


Figure 7. Definition of Bluetooth object elements

Next, we define the control blocks for our arm (Figure 8).

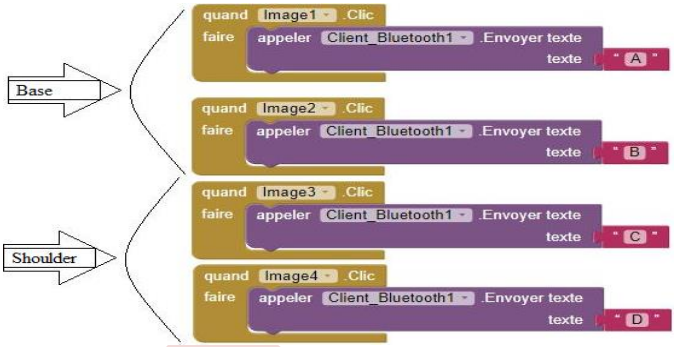


Figure 8. Basic control blocks and the shoulder

These are the blocks that control the manipulator arm six motors. If you change the cursor position, using the BluetoothSendText function, you send a text to the Arduino. This text consists of a prefix indicating which cursor has been modified (prefix "A" for the gripper to prefix "L" for the base).

V. COMMUNICATION WITH THE ARDUINO

After installing our Android application and establishing a connection with the Bluetooth module, the application sends status information to the Bluetooth module. The latter, in turn, transmits this information to the Arduino via a serial link, as illustrated in Figure 9.

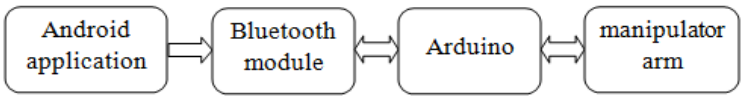


Figure 9. Simplified schematic diagram of the system

To manage communication with the HC-05 module, we established a connection by linking the board's RXpin for reception and TXpin for transmission to the corresponding ones on our Bluetooth module. Specifically, the module's RX pin is connected to the Arduino TX pin, and vice versa. App Inventor is an online software application developed by this configuration ensures bidirectional data exchange between the Arduino and the HC-05 module(Figure 10).

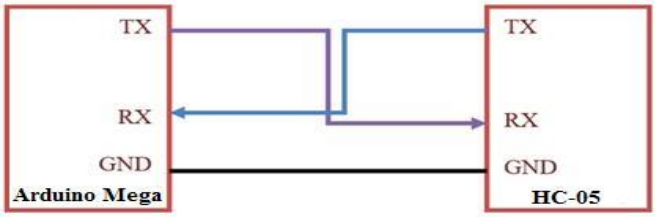


Figure 10. Communication diagram with Bluetooth module HC-05

So, each time a character/text is received, it is sent to the control board's serial port. To make the link with the application, we need to proceed by programming in C++, which translates the strings of characters received via the application into information for the manipulator arm's actuators.

Then we organize our program into a set of execution functions for each actuator (motor 1, motor 2, motor 3, motor 4, motor 5, and motor 6), which we call up using the "if" conditional tool, which each time tests the prefix sent by the application and indicates the current position and modified cursor of the selected actuator. The sub-program is defined as follows:

```
void loop() {
    if(Serial.available() > 0){
      state = Serial.read();
      flag=0;
    }
    if (state == 'A') {
        digitalWrite(IN1_1, LOW);
        digitalWrite(IN2_1, HIGH);
        delay(1000);
        if(flag == 0){
          Serial.println("LEFT");
          flag=1;
        }
    }
    else if (state == 'B') {
        digitalWrite(IN1_1, HIGH );
        digitalWrite(IN2_1, LOW);
        delay(1000);
        if(flag == 0){
          Serial.println("RIGHT");
          flag=1;
        }
```

The Serial.available ( ) function is used to obtain the number of bytes (characters) available for reading from the serial port. The Serial.read ( ) function allows us to read these. Each function must be programmed to convert the received character string into an integer, which will designate the motor's direction of travel.

The flowchart in Figure 11 summarizes wireless control.

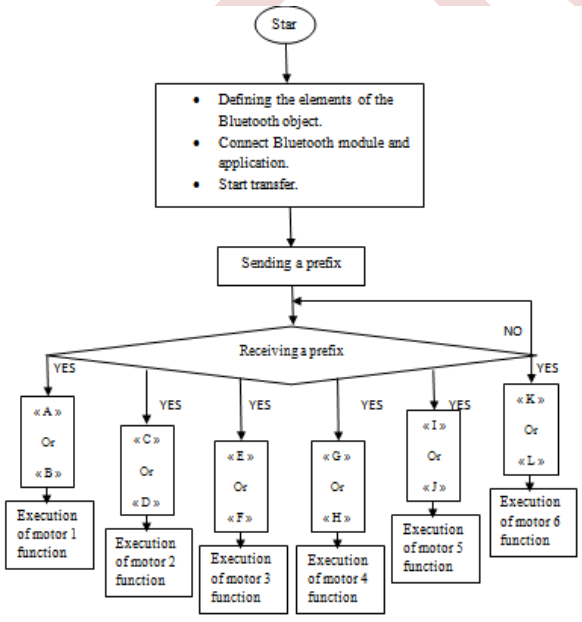


Figure 11. Logigram summarizing wireless control

The real image of our realization is shown in Figure 12. It comprises: stabilized DC power supply, robot, digital multi-meter, control board, microcomputer and cell phone.



Figure 12. Picture of our practical realization

VI. EXPERMENTS AND RESULTS

The system's accuracy and operational capability were assessed through experimentation. The remote control system for a robotic arm, utilizing Bluetooth and an Arduino Mega microcontroller, demonstrated smooth remote operation with remarkable responsiveness and control. The developed application has proven to be highly efficient, enabling precise remote control of each joint, with the ability to rotate each joint wirelessly to its maximum extent.

This experiment confirmed the robotic arm's excellent responsiveness.

VII. CONCLUSION AND FUTURE WORK

The project successfully demonstrated the feasibility of integrating wireless communication and robotics to develop a precise remote control system for a robotic arm. The system utilized Bluetooth technology, an Arduino Mega microcontroller, and a Smartphone based control interface to achieve seamless remote operation with remarkable responsiveness and control. The system is easy to use, affordable, and has been successfully tested.

This research makes a significant contribution to the field of robotics. The authors' work demonstrates the potential of wireless communication and remote control technologies to revolutionize the way we interact with robots. Their research could lead to new and innovative applications in a wide range of fields, including education, research, industry, and healthcare.

Although this work has achieved its objectives, there is still room for improvement. We offer the following suggestions:

- Use servomotors with higher motor torque.
- Use wireless commands such as Wi-Fi or GSM or LoRa to improve the robot's remote control.

REFERENCES

[1] Wireless Networks [Online] (last visited 12-aout-2023) https://www.springer.com/journal/11276

[2] Robotics. Oxford Dictionaries. Retrieved 4 February 2011.

[3] OSHA Technical Manual [Online] (last visited 2-juin - 2023)https://www.osha.gov/dts/osta/otm/otm_ iv/otm_iv_4.html

[4] W. Jacak, Intelligent Robotic Systems: Design, Planning, And Control, Kluwer Academic, ISBN: 0-306-46062-9, p. 321,2002.

[5] Md. Bony Amin, G.M. Sultan Mahmud Rana, Abdullah-Al-Farabi, A.M.M. Nazmul Ahsan, Md. Ahasan Habib, "Design and Implementation of a Remote Controlled Robotic Arm Based on Industrial Application Perspective", International Conference on Mechanical, Industrial and Materials Engineering (ICMIME2013)

[6] Johnson, M., and Williams, D. (2022). Development of a Remote Control System for a Mentor Arm Using Bluetooth and a Smartphone. IEEE Transactions on Industrial Electronics, 69(12), 8923-8932.

[7] S. N. Dhulipala, J. C. N. D. N. Prasad, and C. S. S. R. Kumar, "Robot Remote Control Using Bluetooth and a Smartphone Augmented System," in Proceedings of the 2013 International Conference on Advances in Computing, Communications and Informatics (ICACCI), 2013, pp. 2174-2179

[8] Mentor desktop robot [Online] (last visited 12-juin-2023) www.italtec.it

[9] Khan, S. M., & Khan, S. S. (2019). A Mentor Robot Arm for Teaching Robotics to Students. International Journal of Advanced Research in Electronics and Communication Engineering, 8(3), 1234-1239.

[10] Al-Salihi, M. A., & Al-Jumaily, A. A. (2017). Design and Implementation of a Mentor Robot Arm for Industrial Applications. Iraqi Journal of Science, 58(2), 633-642.

[11] Al-Jumaily, A. A., & Al-Shaher, A. M. (2016). Development of a Mentor Robot Arm for Rehabilitation Applications. International Journal of Advanced Robotics and Intelligent Systems, 5(2), 40-47.

[12] « Arduino Mega» dans Arduino. [En ligne]. Disponible à :https://www.arduino.cc/en/Main/ArduinoBoardMega

[13] A. Hughes, Electric Motors and Drives Fundamentals, Types and Applications", Jordan Hill, Oxford, UK, 2006.

[14] « LN298, dual full-bridge driver»,
https://www.sparkfun.com/datasheets/Robotics/L298 H Bridge.pdf

[15] L. Menguy. « Cinématique du point matériel » cours [Enligne]. Disponible :https://www.cpge.eu/documents/coursPCSI/mecachap1.pdf

[16] Hosham Wahballa, Abdalla Mahamed «Designing and implementation of PID controller robotic Arm» ThèseDoctorat, University of Science and Technology,Sudan 2018

[17] Mohmmed Huesien, "Design Controller System for Rbotic Arm", Vo1. 6, No. 4, pp449–463, Nov, 2016

[18] DME technical data sheet [Online] (last visited 30-juin -2023)
http://catalog.e-jpc.com/Asset/DME- Technical-Datasheet.pdf

[19] J. Bayle, C Programming for Arduino, Packt Publishing Ltd., ISBN 978-1-84951-758-4, p. 512, 2013

[20] Google. App Inventor for Android
http://appinventor.googlelabs.com/about/2010

[21] Hal Abelson. 2009. App Inventor Pilot Announcement. Retrieved Dec. 6, 2010 from http://googleresearch.blogspot.com/2009/07/app-inventorfor-android.html.

Comparative study between two parametric identification methods used to identify the building heating system

Ahmed Ouaret [1], Hocine Lehouche [2], Boubekeur Mendil [3], Hervé Guéguen [4], Siham Fredj [5]

[1,2,3,5] *Laboratoire de Technologie Industrielle et de l'Information, Faculté de Technologie, Université de Bejaia, 06000 Bejaia, Algeria;*
[4] *IETR –CentraleSupelec, Rennes, France*
ahmed.ouaret@univ-bejaia.dz

***Abstract*—With the increasing complexity of dynamical systems appearing in engineering and other scientific domains, the study of large-scale systems composed of interconnected subsystems has become an important subject of focus in various fields such as robotics, transportation networks, large space structures (solar panels, antennas, telescopes, etc.), buildings, and has led to interesting problems in parametric identification analysis, distributed control, and optimization. The objective of this work is to conduct a comparative study between two methods of parametric identification: the first one being the least squares method and the second one being the recursive least squares method, in order to identify the heating system of a room considered as a black box. The validity and performance of the proposed control system have been demonstrated through various simulations using the SIMBAD toolbox.**

Keywords— Identification; building zone; least squares; mean squared error.

I. INTRODUCTION

Linear system identification is a well-established and widely utilized technique in the field of system identification, as noted by references [1], [2], and [3]. It involves the endeavor to find a linear system that best fits a given input-output dataset. Any residual portion of the data that remains unexplained by the system is typically attributed to noise. The theory behind linear system identification has reached a level of maturity, with numerous thoroughly developed methods available in the literature. These approaches prove highly effective when the system generating the dataset is genuinely linear or can be adequately approximated as such. However, it is crucial to recognize that the assumption of linearity may not always hold true in practical scenarios. In cases where the underlying system exhibits nonlinearity, the application of linear system identification can lead to significant errors. Hence, the need for nonlinear system identification is underscored, as highlighted by references [4]-[11].

In general, nonlinear system identification can be categorized into two groups: parametric and non-parametric. When prior knowledge of the unknown system's structure is accessible, identification transforms into a parameter estimation challenge. While non-trivial, it essentially boils down to a nonlinear optimization problem. This allows for the use of a black box, gray box, or white box approach, depending on whether a general pre-defined model description or a custom-made model incorporating prior structural information is employed. On the contrary, when minimal prior information is available about the structure, identification is considered non-parametric, typically making it more challenging. This paper concentrates on applying parametric identification methods to model intricate dynamical systems.

Over the years, the identification of nonlinear systems has witnessed significant advancements through innovative parametric methods. Deep neural networks such as CNNs and RNNs, along with Support Vector Machines (SVM), have demonstrated effectiveness in modeling complex systems [12]-[14]. Additionally, generalized Volterra series and Chebyshev series have been developed to capture higher-order nonlinearities [15], [16]. However, some limitations persist, such as overfitting in neural networks and computational complexity in methods based on Volterra and Chebyshev series, necessitating ongoing research to enhance the identification of complex nonlinear systems.

In the context of this scientific article, our main objective is to apply two parametric identification methods to a building heating system in order to obtain a representative mathematical model of the system. These identification methods will enable us to determine the model parameters

based on experimental data of the system, using appropriate optimization criteria. Developing an accurate model that closely reflects the real behavior of the heating system is essential to enhance our understanding of its operation and to design more efficient and energy-saving control strategies. By leveraging these identification methods, we aim to contribute to the advancement of modeling techniques and provide a solid foundation for practical applications in energy management and performance optimization of building heating systems.

The document is structured as follows. Section II presents a case study of a building with electric heating. The two identification methods used are introduced in Section III. Section IV focuses on the application of these identification methods. Finally, the conclusion is presented in Section V.

II. CASE STUDY : BUILDING ZONE WITH ELECTRICAL HEATER

A. *Description of the zone model*

The building zone model consists of detailed envelope, simplified radiation, and simplified convection sub-models. A central node has been used to represent the resultant temperature in the zone. The different inputs and outputs of the model are illustrated in fig. 1.

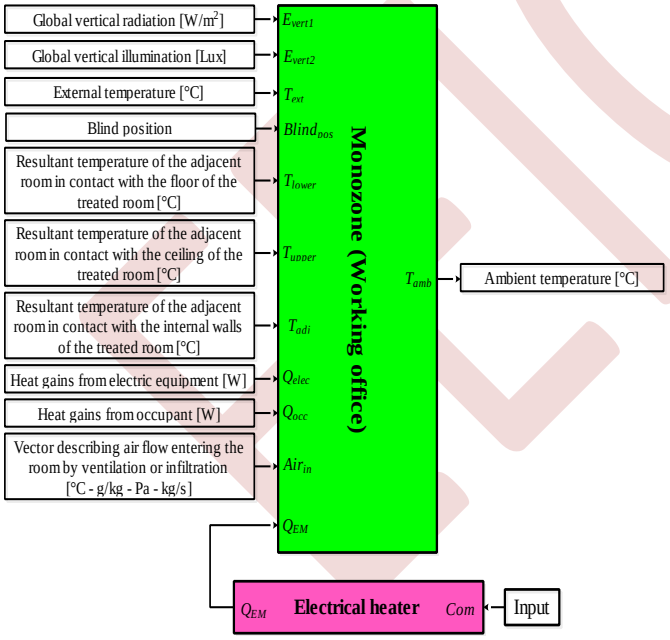


Figure 1. Simulation model of the working office with different perturbations and electric heater [17, 18]

1) *Model inputs*

- $T_{ext}[°C]$ external temperature provided by weather data files.
- $E_{vert}\left[W/m^2\right]$ and $E_{vert}[lux]$ global vertical Radiation and Illumination respectively which are obtained from the weather file.
- $Blind_{pos}$ blind position takes the value between 0 and 1.
- T_{lower}, T_{upper} and $T_{adj}[°C]$ lower, upper and adjacent temperatures that come from other zones.
- $Q_{elec}[W]$ heat gains from electrical equipment.
- $Q_{EM}[W]$ heat gains from convector or radiator.
- $Q_{occ}[W]$ heat coming from the occupants.
- $Air_{in}[°C, Pa, kg/s]$ is the flow of the air entering the room by ventilation or infiltration.

2) *Model outputs*

- $T_{amb}[°C]$ ambient temperature

B. *Model of electric heater*

The electrical heater has a normalised control input Com, limited between 0 and 1, and a heat flux output $Q_{EM}[W]$.

III. PRESENTATION OF THE TWO IDENTIFICATION METHODS USED

Identification is a crucial process in which the parameters of mathematical models are sought based on experimental data. The fundamental principle behind identification, using the least squares method, is to optimize the model's parameters in a manner that minimizes the sum of the squares of the differences between the model's predicted values and the actual observed values. This powerful technique is commonly employed to establish a model using the n^{th} order difference equation, making it well-suited for analyzing complex systems. By applying the least squares method to the identification process, we can effectively fine-tune the model to best represent the real-world system and gain deeper insights into its behavior and characteristics.

A. *Simple least squares algorithm* [3]

In the context of minimizing the quadratic criterion based on the equation error using the least squares method, let's assume that the system is strictly causal.

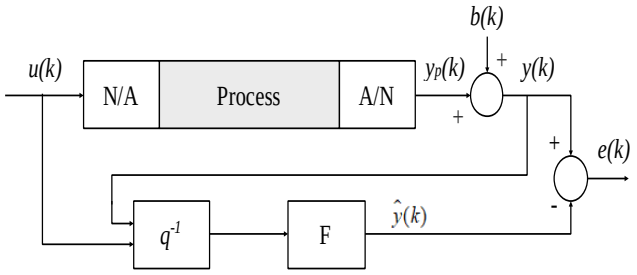


Figure 2. Equation error $e(k)$

In this case, the predicted output at instant k is :

$$\hat{y}(k) = -a_1 y(k-1) - a_2 y(k-2) - \ldots - a_n y(k-n) + b_0 u(k-d) + b_1 u(k-d-1) + \ldots + b_m u(k-d-m) \quad (1)$$

Which can be written in the following form :

$$\hat{y}(k) = \varphi^T(k)\theta$$

with : $\theta^T = [a_1, a_2, \ldots, a_n, b_0, b_1, \ldots, b_m]$

$$\varphi^T(k) = [-y(k-1) - y(k-2) - \ldots - y(k-n)\ u(k-d)\ u(k-d-1) \ldots u(k-d-m)]$$

where $\varphi^T(k)$ represents the vector of inputs and outputs and θ the vector of parameters to identify.

The equation error $e(k)$ is given by equation (2):

$$e(k) = y(k) - \hat{y}(k) = y(k) - \varphi^T(k)\theta \quad (2)$$

With $e(k)$ is the performance criterion.

By accumulating N measurements, for example, at discrete time points k = 1, 2, ..., N, equation (2) takes the form of a matrix:

$$e = Y - \phi\theta \quad (3)$$

with e is the error vector, Y is the measurement vector, Φ is the observation matrix, and θ is the parameter vector.

The quadratic prediction error criterion is written as follows:

$$J(\theta) = \sum_{k=1}^{N} e^2(k) = e^T e = Y^T Y - 2Y^T \phi\theta + \theta^T \phi^T \phi\theta \quad (4)$$

The parameter vector $\hat{\theta}$ that minimizes equation (4) cancels the gradient of J with respect to θ :

$$\left.\frac{\partial J}{\partial \theta}\right|_{\theta=\theta_0} = -2\phi^T Y + 2\left(\phi^T \phi\right)\hat{\theta} = 0 \quad (5)$$

From where one derives:

$$\hat{\theta} = \left(\phi^T \phi\right)^{-1} \phi^T Y \quad (6)$$

The estimation of the parameter vector, given by equation (6), can also be expressed in an equivalent form as follows:

$$\hat{\theta} = \left[\sum_{k=1}^{N} \varphi(k)\varphi^T(k)\right]^{-1} \left[\sum_{k=1}^{N} \varphi(k) y(k)\right] \quad (7)$$

B. Recursive least squares [3]

For computer implementation, equation (7) can be transformed into a recursive form. Considering the measurements u_p to time instant kT and using similar notations as in equation (1) :

Equation (7) gives :

$$\hat{\theta}_k = \left[\sum_{i=1}^{k} \varphi(i)\varphi^T(i)\right]^{-1} \left[\sum_{i=1}^{k} \varphi(i) y(i)\right] \quad (8)$$

In this context, $\hat{\theta}_k$ represents the estimation of θ at time kT based on the first k equations.

Equation (8) can be rewritten in the following form:

$$\hat{\theta}_k = P_k \left[\sum_{k=1}^{k} \varphi(i) y(i)\right] \quad (9)$$

where the square matrix P_k of dimension p (number of parameters) is the inverse of the information matrix.

$$P_k = \left[\sum_{i=1}^{k} \varphi(i)\varphi(i)\right]^{-1} \quad (10)$$

where : $$P_k^{-1} = \sum_{i=1}^{k} \varphi(i)\varphi^T(i) \quad (11)$$

The matrix P_{k+1}^{-1} can be recursively computed as follows:

$$P_{k+1}^{-1} = P_k^{-1} + \varphi(k+1)\varphi^T(k+1) \quad (12)$$

The parameter vector at time $k+1$ can be written as :

$$\hat{\theta}_{k+1} = \hat{\theta}_k + P_{k+1}\varphi(k+1)\left[y(k+1) - \varphi(k+1)\hat{\theta}_k\right] \quad (13)$$

To avoid inverting matrix P_{k+1}^{-1} at each iteration, one can employ the lemma of matrix inversion.

Lemma :

If A, C and $C^{-1} + DA^{-1}B$ are invertible matrices, then:

$$(A + BCD)^{-1} = A^{-1} - A^{-1}B(C^{-1} + DA^{-1}B)^{-1}DA^{-1}$$

The proof of the lemma is carried out by calculating the product of the two terms in the equation, which should be equal to the identity matrix.

Taking $A = P_k^{-1}$, $B = \varphi(k+1)$, $C = 1$, $D = \varphi^T(k+1)$ in equation (16), we obtain :

$$P_{k+1} = P_k - \frac{P_k \varphi(k+1)\varphi^T(k+1)P_k}{1 + \varphi^T(k+1)P_k\varphi(k+1)} \quad (14)$$

The recursive formulation of least squares can be :

$$P_k = P_{k-1} - \frac{P_{k-1}\varphi(k)\varphi^T(k)P_{k-1}}{1 + \varphi^T(k+1)P_k\varphi(k+1)} \quad (15)$$

$$\hat{\theta} = \hat{\theta}_{k-1} + P_k\varphi(k)\left[y(k) - \varphi^T(k)\hat{\theta}_{k-1}\right] \quad (16)$$

IV. APPLICATION OF BOTH IDENTIFICATION METHODS

A. Simulation parameters

To assess the performance and the capacity of these methods in the identification, we have simulated the case of an office occupied from 8h to 17h from with dimensions ($4m \times 4m \times 3m$) during one day, the different parameters and inputs are provided in Table I and Table II.

TABLE I. SIMULATION PARAMETERS

Geometric characteristics of the studied room	**Dimension**
Wall, floor and ceiling heat transfer coefficients	[0.25 0.0001 0.25] W/m²/k
Initial temperature	10 ºC
Reference temperature while occupancy	19 ºC
Electric heater nominal power	1500 W
Number of occupants	2
Weather data	Rennes (France)
Simulation time	1 day
Heat emission equipment per m²	1 W/m²
Fresh air supply	40 m³/h/pers 24/24h
Mean outside temperature	6.5 °C

TABLE II. THE INPUTS USED IN OUR CASE

Inputs	**Parameters**
E_vert [W/m²], *E_vert* [luxe]	Connected to weather data (Rennes)
Blind_pos	Closed during the period of occupation
Text [°C]	Connected to weather
(Tlower, Tupper, Tadj) [°C]	Temperature of lower, upper and adjacent zones
Q_elec [W]	Heat given by the electrical equipements
Q_occ [W]	Heat given by the occupants
Air in	Air conditionning vector of zone
Q_EM [W]	Power given by the heater
Control input signal	Normalised interval of the input [0,1]

B. Simulation results

After the definition of the different simulation parameters, our system was simulated as shown in fig.4. The evaluation was conducted using the mean square error, calculated using the following equation:

$$MSE = \frac{1}{N}\sum_{k=1}^{N}\left(\hat{y}(k) - y(k)\right)^2 \qquad (17)$$

where $\hat{y}(k)$ is the output of the identifier and $y(k)$ is the ambient temperature output of the system.

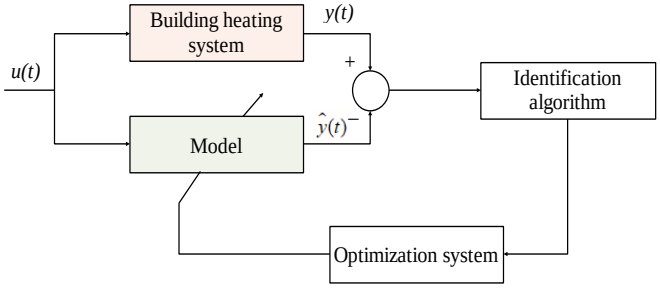


Figure 3. Parameter identification

Figures 5 and 6 display the output of the system and the model, along with the identification error obtained by applying the methods of simple least squares and recursive least squares, respectively.

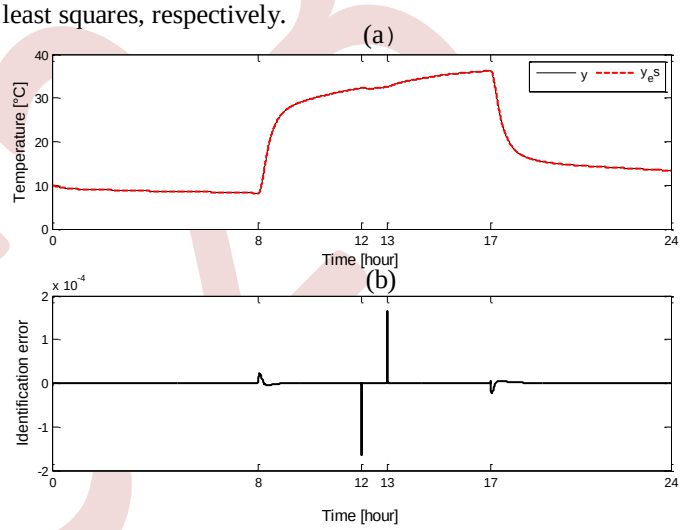


Figure 4. Identification results (a) Output od system and model (b) Identification error (MCS)

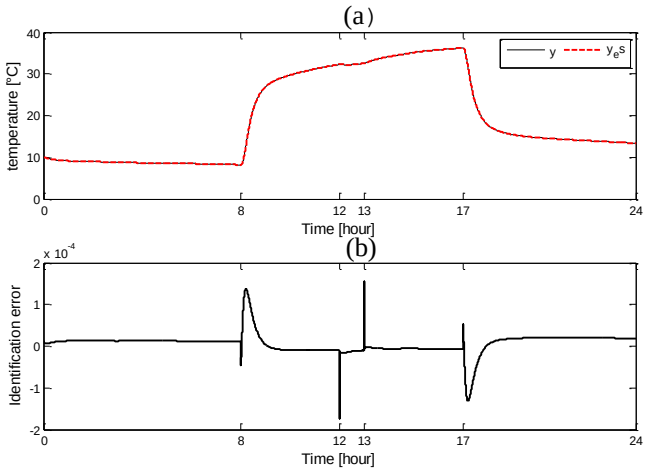


Figure 5. Identification results (a) Output od system and model (b) Identification error (MCR)

C. Numerical results

The numerical results obtained using the two identification methods are illustrated in Table 3.

TABLE III. NUMERICAL RESULTS

	MCS	**MCR**
b_1	0.000168036611084	0.000176474501491
b_2	- 0.000166797031247	- 0.000112594793487
a_1	- 1.999871857561794	- 1.981854335190126
a_2	0.999871867974605	0.981855871747247
MSE	5.564617100879375e-012	6.231912136925985e-010

The model obtained using the simple least squares method is given by the following transfer function:

$$H(z)=\frac{0.0001680366110084Z-0.000166797031247}{Z^2-1.999871857561794Z+0.999871867974605} \quad (18)$$

The model obtained using the recursive least squares method is given by the following transfer function:

$$H(Z)=\frac{0.000176474501491Z-0.000112594793487}{Z^2-1.981854335190126Z+0.981855871747247} \quad (19)$$

Discussion of the results

According to figures 5-a and 6-a, we observe that the model's output perfectly follows the system's output, with a very low mean squared error (see figures 5-b and 6-b). The numerical results from both methods show that the model parameters obtained using the two identification approaches are very close, with a slight difference in terms of mean squared error, which is very small with the simple least squares method.

In summary, we can conclude that both methods yield good identification results. The model fits the system data well, and the simple least squares method appears to be slightly more accurate in terms of mean squared error. These results confirm the reliability and effectiveness of the identification approaches used, demonstrating their relevance for this specific context.

D. Study of robustness

To evaluate the robustness of the two proposed methods for the identification of complex systems, we chose to use a random square wave signal as the test benchmark. This random square wave signal is depicted in Figure 7.

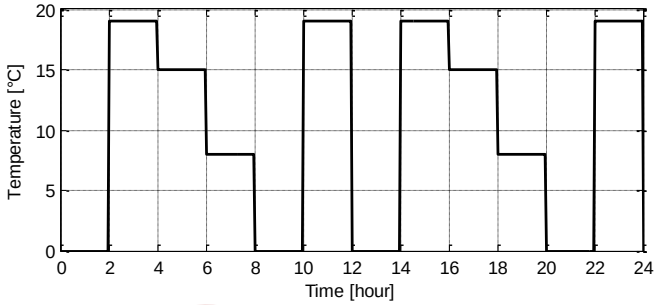


Figure 6. Input signal

The outputs of the system and the model, along with the identification error obtained using the simple least squares method, are illustrated in Figure 8.

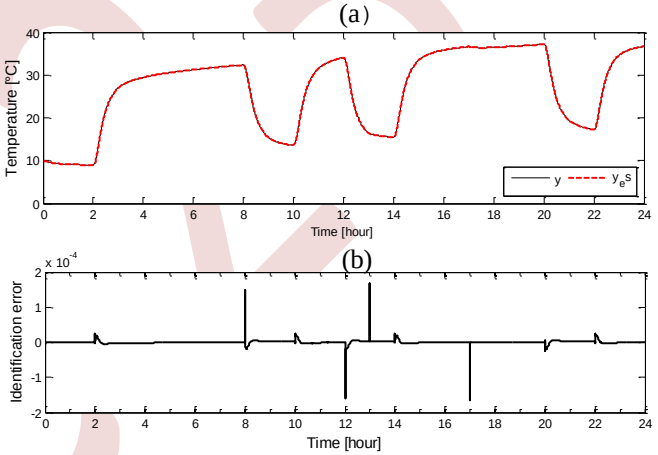


Figure 7. Identification results (a) Output od system and model (b) Identification error (MCS)

The outputs of the system and the model, along with the identification error obtained using the recursive least squares method, are presented in Figure 9.

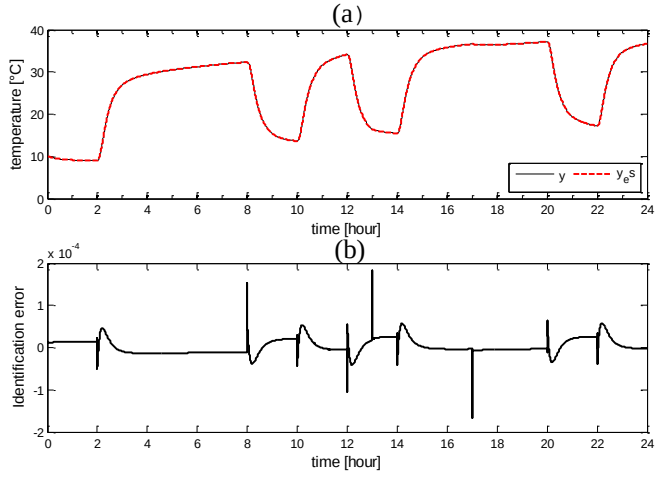


Figure 8. Identification results (a) Output od system and model (b) Identification error (MCR)

Discussion of the results

According to figures 8-a and 9-a, we observe that the model's output perfectly follows the system's output, despite variations in the input signal over time. This demonstrates the effectiveness and robustness of the two proposed methods for identifying complex systems. Figures 8-b and 9-b represent the identification errors, which are very small, indicating a strong correspondence between the model's output and the system's output. These results enhance the reliability of the used identification approaches and confirm their ability to provide accurate and consistent results, even under varying input signal conditions.

V. CONCLUSION

In this study, we investigated the application of two identification methods on a complex building heating system. The main goal was to accurately model and understand the system's behavior under varying conditions. The two methods considered were the simple least squares and recursive least squares approaches.

The results obtained from both methods demonstrated their effectiveness in identifying the heating system's parameters and predicting its output accurately. The outputs of the model closely followed the actual system's behavior, even when subjected to dynamic variations in the input signals. This highlights the robustness and reliability of both identification techniques for dealing with the complexities inherent in building heating systems.

Moreover, the low identification errors observed in the experiments indicate the strong performance of the identified models in capturing the system dynamics. This is particularly important for ensuring energy efficiency and maintaining optimal comfort levels within the building.

In conclusion, this study establishes the significance of applying accurate identification techniques for building heating systems and opens up new possibilities for enhancing the overall energy efficiency and comfort in buildings. The insights gained from this research contribute to the sustainable development of smart and energy-efficient buildings, promoting a greener and more sustainable future.

REFERENCES

[1] L. Ljung, System Identification: Theory for the User, 2nd ed. Upper Saddle River, NJ: Prentice-Hall, 1999.

[2] T. Söderström and P. Stoica, "Instrumental Variable Methods for System Identification," Journal of Process Control, Volume 69, Pages 143-160, 2018.

[3] L. Ljung, "Perspectives on System Identification," Annual Reviews in Control, Volume 44, Pages 1-16, 2017.

[4] E. W. Bai, "Non-parametric nonlinear system identification: A datadriven orthogonal basis function approach," IEEE Trans. Autom. Control, vol. 53, no. 11, pp. 2615–2626, Nov. 2008.

[5] E. W. Bai and Y. Liu, "Recursive direct weight optimization in nonlinear system identification: A minimal probability approach," IEEE Trans. Autom. Control, vol. 52, no. 7, pp. 1218–1231, Jul. 2007.

[6] E. W. Bai, R. Tempo, and Y. Liu, "Identification of nonlinear systems without prior structural information," IEEE Trans. Autom. Control, vol. 52, no. 3, pp. 442–453, Mar. 2007.

[7] D. Feng and T. Chen, "Identification of Hammerstein nonlinear ARMAX systems," Automatica, vol. 41, pp. 1479–1489, 2005.

[8] D. Feng, Y. Shi, and T. Chen, "Auxiliary model-based least squares identification method for Hammerstein output-error systems," Syst. Control Lett, vol. 56, pp. 373–380, 2007.

[9] A. Juditsky, H. Hjalmarsson, A. Benveniste, B. Delyon, L. Ljung, J. Sjoberg, and Q. Zhang, "Nonlinear block-box models in system identification: Mathematical foundations," Automatica, vol. 31, pp. 1725–1750, 1995.

[10] L. Y. Wang, G. Yin, and J.-F. Zhang, "Joint identification of plant rational model and noise distribution functions using binary-valued observation," Automatica, vol. 42, pp. 535–547, 2006.

[11] L. Y. Wang, G. Yin, and J.-F. Zhang, "Space and time complexity and sensor threshold selection in quantized identification," Automatica, vol. 44, pp. 3014–3024, 2008.

[12] Y. LeCun, Y. Bengio, and G. Hinton, "Deep learning," Nature, vol. 521, no. 7553, pp. 436-444, 2015.

[13] H. Jaeger, "The echo state approach to analyzing and training recurrent neural networks," GMD Report 148, 2001.

[14] C. Cortes and V. Vapnik, "Support-vector networks," Machine Learning, vol. 20, no. 3, pp. 273-297, 1995.

[15] L. O. Chua and T. Roska, "The CNN universal machine: an analogic array computer," IEEE Transactions on Circuits and Systems II: Analog and Digital Signal Processing, vol. 40, no. 3, pp. 163-173, 1993.

[16] M. S. Zarghami and A. C. Loukianov, "Identification of nonlinear dynamic systems using Chebyshev series," International Journal of Control, vol. 52, no. 3, pp. 499-515, 1990.

[17] A. Ouaret, H. Lehouche, B. Mendil and H. Guéguen, "Supervisory control of building heating system with insulation changes using three architectures of neural networks". Journal of the Franklin Institute, 357(18), 13362-13385, 2020.

[18] A. Ouaret, H. Lehouche, N. Ouali, H. Guéguen and B. Mendil, "Predictive functional control of building HVAC systems". The 1st Electrical Engineering International Conference EEIC'19, University of Bejaia, 2019.

Asymptotic Stabilization of a Morphing Drone using Interconnection and Damping Assignment-Passivity Based Control

Amina Belmouhoub[1][a], Yasser Bouzid[2], Slimane Medjmadj[3], Saddam Hocine Derrouaoui[4] and Mohamed Guiatni[2]

[1]*Materials and Electronic Systems Laboratory, University Mohamed El Bachir El Ibrahimi of Bordj Bou Arreridj, Algeria*
belmouhoub.amina@gmail.com

[2]*Complex Systems Control & Simulators Laboratory, Ecole Militaire Polytechnique, Algiers, Algeria*
[3]*Laboratory of Control University of Setif and University of Bordj Bou Arreridj, Algeria*
[4]*Ecole Supérieure Ali Chabati, Algiers, Algeria*

Keywords: Morphing drone, Asymptotic stability, Port-Controlled Hamiltonian form, Interconnection and Damping Assignment-Passivity Based Control.

Abstract: The main aim of this paper is to illustrate how the Interconnection and Damping Assignment-Passivity Based Control (IDA-PBC) approach has been implemented on a novel morphing drone. The purpose of the controller is to ensure accurate trajectory tracking while addressing challenges associated with controlling such systems. These drones possess a unique feature that allows them to adjust their shape during flight by rotating their arms. The dynamic modeling of the system, which takes into account changes in various geometrical parameters and also in Inertia, Center of Gravity (CoG), and allocation matrix, is mathematically described. The IDA-PBC control principle is subsequently introduced and applied to the system. Overall, the numerical simulations conducted on the system have yielded satisfactory results.

1 INTRODUCTION

In recent years, research laboratories have shown a keen interest in drones with variable geometry due to their clear superiority over other categories. These advanced systems are capable of navigating through complex and crowded environments, effectively carrying out diverse missions in challenging conditions (Belmouhoub et al., 2023b; Fabris et al., 2021; Belmouhoub et al., 2023a).

Controlling this new class of drones is a difficult task because these systems can change their shape during flight, making it challenging to design control laws. In reference (Oğuz and Oktay, 2020), authors used Proportional Integral Derivative (PID) controller to stabilize a quadrotor with forward flight. The quadrotor achieved differential morphing by lengthening or shortening its arms at different times, resulting in changes in moments of inertia. In another study (Bucki et al., 2022), researchers synthesized an infinite horizon Linear-Quadratic Regulator LQR to control the attitude of reconfigurable quadcopter that could perform four operations in three configurations: unfolded, two-arms-folded, and four-arms-folded. An adaptive controller based on Model Reference Adaptive Control (MRAC) was presented in (Desbiez et al., 2017) to control an X-morph vehicle and address uncertainties resulting from changes in inertia and center of mass. Zhao et al. in (Zhao et al., 2021) used an optimal Linear Quadratic Integral (LQI) controller to control the attitude of a two-dimensional multilinked aerial robot, while the position controller is based on a PID technique.

The conventional control approach for morphing drones does not achieve satisfactory performance due to the significant changes in the dynamics of these systems. However, implementing nonlinear modern control theory can enhance the system's performance and enable accurate tracking of challenging trajectories.

The main objective of this study is to explore the use of a nonlinear IDA-PBC controller to address the trajectory tracking problem of a morphing drone by utilizing the Port-Controlled Hamiltonian (PCH) model. The key benefit of PCH is that it is directly

[a] https://orcid.org/0000-0002-9583-3624

derived from the system's energy function, providing information about the relation between kinetic and potential energy with dynamic behavior. This information is advantageous for control design since it also offers insights into the stability properties of the system. Additionally, the fact that a Hamiltonian system conserves energy implies that the model is marginally stable, which is a desirable characteristic for controller development.

Souza et al. presented, in their work (Souza et al., 2014), an IDA-PBC control methodology to perform the path tracking of a quadrotor helicopter. Similarly, Researcher in reference (Guerrero et al., 2015b) used this technique for a specific class of underactuated mechanical system, composed by an Unmanned Aerial Vehicle (UAV) transporting a cable-suspended payload. In reference (Ryalat et al., 2015), the authors investigated the extension of the IDA-PBC method to a robustness perspective to ensure the asymptotic stability of the system in the presence of perturbations which exist in any realistic problem. The results are applied to a Quanser inertia wheel pendulum. Additionally, in (Ryalat et al., 2021), the same researcher introduced two adaptive control approaches to handle uncertainties caused by parametric and modeling errors in a class of nonlinear systems with uncertainties, and applied them to two underactuated robotic systems; the Acrobot and non-prehensile planar rolling robotic (disk-on-disk) systems. In the same context, Acosta et al. designed a controller based on IDA-PBC methodology for underactuated Aerial Manipulators (AMs) (Acosta et al., 2014).

The remainder of this paper is structured as follow: In Section 2, the dynamic modeling of the morphing drone is described. Section 3 focuses on the application of IDA-PBC to the system. The efficiency of the controller is demonstrated through numerical simulations in Section 4. Finally, a brief conclusion is provided in Section 5.

Preliminaries

Let $\mathbb{R}$ and $\mathbb{R}^n$ denote the set of real numbers and vectors respectively. The symbol $\wedge$ denotes the cross product and $O_{3\times3}$ means a 3×3-dimensional zero matrix. The gradient vector of a mapping $H : D_x \subseteq \mathbb{R}^n \to \mathbb{R}$ is denoted as: $\nabla H(x) = \begin{bmatrix} \frac{\partial H(x)}{\partial x_1} & \dots & \frac{\partial H(x)}{\partial x_n} \end{bmatrix}^T$, where n is the dimension of $x = \begin{bmatrix} x_1 & x_2 & \dots & x_n \end{bmatrix}^T \in D_x \subseteq \mathbb{R}^n$. $J_{3\times3}$ means a 3×3-dimensional matrix. The notation V^T represents the transpose of vector V.

2 MORPHING DRONE MODELING

In this section, the dynamic modeling of the morphing drone is briefly described.

2.1 Dynamic modeling

In order to describe the movement of a morphing drone in space, two reference frames are used: an inertial frame fixed to the earth's surface $E = (o_i, x_i, y_i, z_i)$, and a body frame associated with the drone's center of gravity $B = (o, x_m, y_m, z_m)$. The drone consists of a standard quadcopter with four rotating arms connected to the central body by servomotors (see Figure 1). The servomotors can rotate the arms independently to construct different configurations from the basic configuration 'X'. The four rotors generate lift forces denoted by $F_i|_{i=1\dots4}$ and have angular velocity $\omega_i(t)|_{i=1,\dots4}$. Changes in morphology during flight cause the center of gravity to shift and modify the inertia, both dependent on the rotation angles of the arms $\sigma(t)|_{i=1\dots4}$.

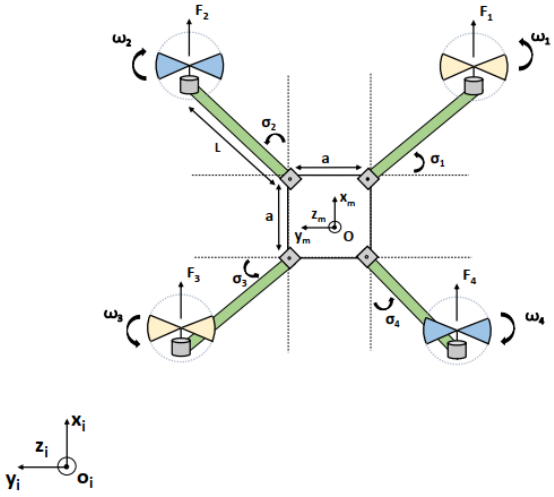


Figure 1: Structure of morphing drone.

Based on Newton-Euler formalism (Bouzid et al., 2018), we develop the system's dynamic equations. The following is a form of how the system can be written:

$$\begin{bmatrix} mJ_{3\times3}(\sigma(t)) & O_{3\times3} \\ O_{3\times3} & J_{3\times3}(\sigma(t)) \end{bmatrix} \begin{bmatrix} \ddot{\zeta} \\ \dot{\mu} \end{bmatrix} + \begin{bmatrix} \mu \wedge m\zeta \\ \mu \wedge J_{3\times3}(\sigma(t))\mu \end{bmatrix} = \begin{bmatrix} F \\ \tau \end{bmatrix} \quad (1)$$

where
$\zeta = (u,v,w)^T \in \mathbb{R}^3$ and $\mu = (p,q,r)^T \in \mathbb{R}^3$ are, respectively, linear and angular velocity vectors of the quadrotor with rotating arms in the mobile frame. m is the total mass of the vehicle. Let $\eta = (\phi,\theta,\psi)^T \in \mathbb{R}^3$ and $\xi = (x,y,z)^T \in \mathbb{R}^3$ describe the mobile's orientation and position, respectively, with respect to B. $F = (F_x,F_y,F_z)^T \in \mathbb{R}^3$ and $\tau = (\tau_x,\tau_y,\tau_z)^T \in \mathbb{R}^3$ are, respectively, the external forces and moments applied to the CoG.

The developed mathematical model expressed in vehicle coordinated q is written under a compact form using the general mechanical equation, as follows:

$$\mathcal{M}(q)\ddot{q} + \mathcal{C}(q,\dot{q})\dot{q} + \mathcal{G} = B(q)u \tag{2}$$

where, $q = [\xi,\eta]^T \in D_\xi \times D_\eta \subseteq \mathbb{R}^3 \times \mathbb{R}^3$ is the generalized coordiates, and it expresses the quadrotor position and orientation. $\mathcal{M} = \mathcal{M}^T \in \mathbb{R}^{6\times6} = \begin{bmatrix} mI_{3\times3} & 0 \\ 0 & J(\sigma(t)) \end{bmatrix} > 0$ is composed of the mass, $mI_{3\times3}$, and the inertia matrix, which depends on the variation of the angle of the arms. $\mathcal{C} \in \mathbb{R}^{6\times6} = \begin{bmatrix} 0 & 0 \\ 0 & C_{3\times3} \end{bmatrix}$ is matrix of centrifugal and coriolis effects. $\mathcal{G} \in \mathbb{R}^6 = \begin{bmatrix} 0 & 0 & mg & 0 & 0 & 0 \end{bmatrix}^T$ denote the gravitational force vector. $\mathcal{B} = I_{6\times6}$ is the input matrix.

In this paper, we have chosen six possible quadrotor configurations according to the position of the arms (X, Y, YI, H, T, O).

2.2 Problem statement

The underactuated system given by (1) can be represented in Port-Controlled Hamiltonian (PCH) form (3),

$$\Sigma : \begin{cases} \dot{x} = \left[\mathcal{J}(x) - \mathcal{R}(x)\right]\nabla_x H(x) + g(x)u \\ y = g^T(x)\nabla_x H(x) \end{cases} \tag{3}$$

where
x is the state vector and $H(x)$ represents the internal energy accumulation in the system. $\mathcal{J}(x)$ and $\mathcal{R}(x) \geq 0$ are the interconnection skew and the damping symmetric matrices, respectively, while $g(x)$ is the input matrix. u and y are defined as two power ports variables.

The main objective is to render the closed loop system assymptotically stable by changing the matrices $\mathcal{J}(x), \mathcal{R}(x)$ and $H(x)$ i.e to force the system to follow a desired system written in PCH form (4) according to the specifications of the control.

$$\Sigma_d : \dot{x} = \left[\mathcal{J}_d(x) - \mathcal{R}_d(x)\right]\nabla_x H_d(x) \tag{4}$$

3 INTERCONNECTION AND DAMPING ASSIGNMENT-PASSIVITY BASED CONTROL

The Interconnection and Damping Assignment-Passivity Based Control (IDA-PBC) technique is a well-known approach that employs the PCH system and has been effectively utilized to regulate various physical systems and practical applications. The main objective of the IDA-PBC approach is to create a state feedback controller by shaping the total energy of the system, which is the Hamiltonian, and changing the interconnection structure (Ortega et al., 2001). This control method ensures that the PCH system is stable, with the energy function serving as a Lyapunov function. Furthermore, asymptotic stability of the closed-loop is attained at the desired equilibrium by incorporating damping into the system through the damping-injection feedback controller.

The control law by IDA-PBC for the morphing drone is designed as:

$$U = -\mathcal{K}\mathcal{M}^{-1}(p - p_d) + \nabla_q \mathcal{V}(q) - \nabla_q \mathcal{V}_d(q) + \mathcal{C}\mathcal{M}^{-1}p \tag{5}$$

where $\mathcal{K} = \mathcal{K}^T > 0$ is a positive constant.

Theorem 1. *Considering the system* (1)*, the control input* (5) *ensure the tracking of the desired trajectories. i.e. the tracking error* $\equiv 0$*.*

Proof. *The Hamiltonian* $H(q,p)$ *of system* (2) *is the sum of kinetic energy* $\mathcal{T}$ *(translational and rotational) and potential energy* $\mathcal{V}$*, respectively.*

$$H(q,p) = \mathcal{T}(q,p) + \mathcal{V}(q) \tag{6}$$

which implies

$$H(q,p) = \frac{1}{2}p^T\mathcal{M}^{-1}(q)p + \mathcal{G}^T q \tag{7}$$

where p is the generalized momentum.

Based on (2)*, the dynamic of the morphing drone written in PCH model is given as follow:*

$$\begin{bmatrix} \dot{q} \\ \dot{p} \end{bmatrix} = \left(\mathcal{J}(q,p) - \mathcal{R}(q,p)\right)\begin{bmatrix} \nabla_q H(q,p) \\ \nabla_p H(q,p) \end{bmatrix} + \begin{bmatrix} 0 \\ B(q) \end{bmatrix} u \tag{8}$$

with

$$\mathcal{J}(q,p) = \begin{bmatrix} 0 & I_{6\times6} \\ -I_{6\times6} & 0 \end{bmatrix} \tag{9}$$

and

$$\mathcal{R}(q,p) = \begin{bmatrix} 0 & 0 \\ 0 & C \end{bmatrix} \tag{10}$$

Our suggestion is to use a specific energy function, which is defined as:

$$H_d(q,p) = \mathcal{T}_d(q,p) + \mathcal{V}_d(q) \tag{11}$$

We alter the internal energy function of the closed loop system to achieve the desired equilibrium configuration and ensure that the function $H_d(q,p)$ has a minimum value at (q^*,p^*), thus

$$H_d(q,p) = \frac{1}{2}(p-p^*)\mathcal{M}_d^{-1}(q)(p-p^*) + \mathcal{V}_d(q) \tag{12}$$

where $\mathcal{V}_d(q)$ and $\mathcal{M}_d = \mathcal{M}_d^T > 0$ represent the desired closed loop potential energy function and inertia matrix, respectively with

$$q^* = arg_{min}\mathcal{V}_d(q) \tag{13}$$

Remark 1. *To stabilize the vehicle and track any reference trajectory, we take the desired equilibrium configuration $(q^*,p^*) = (q_r,p_r)$ as the reference trajectories.*

In order to maintain the energy interpretation, it is also necessary that the desired closed loop system be in the port-controlled Hamiltonian representation.

$$\begin{bmatrix}\dot{q}\\ \dot{p}\end{bmatrix} = \left(\mathcal{J}_d(q,p) - \mathcal{R}_d(q,p)\right)\begin{bmatrix}\nabla_q H_d(q,p)\\ \nabla_p H_d(q,p)\end{bmatrix} \tag{14}$$

where

$$\mathcal{J}_d(q,p) = -\mathcal{J}_d^T(q,p) = \begin{bmatrix}0 & \mathcal{M}^{-1}\mathcal{M}_d\\ -\mathcal{M}^{-1}\mathcal{M}_d & \mathfrak{J}(q,p)\end{bmatrix} \tag{15}$$

and

$$\mathcal{R}_d(q,p) = \mathcal{R}_d^T(q,p) = \begin{bmatrix}0 & 0\\ 0 & B\mathcal{K}B^T\end{bmatrix} \tag{16}$$

Assumption 1. *The structure of the matrix $\left[\mathcal{J}_d(q,p) - \mathcal{R}_d(q,p)\right]$ is identical to that of the initial system.*

The PBC control input consists of two components: the first one injects damping to the system, while the second one is responsible for shaping the energy.

$$u = u_{DI} + u_{ES} \tag{17}$$

The resulting equations are obtained by substituting equation (17) *into equation* (8) *and equating them to equation* (14)*, in order to derive the controller. Thus*

$$\begin{bmatrix}0 & I_{6\times6}\\ -I_{6\times6} & -C\end{bmatrix}\begin{bmatrix}\nabla_q H(q,p)\\ \nabla_p H(q,p)\end{bmatrix} + \begin{bmatrix}0\\ B(q)\end{bmatrix}(u_{DI}+u_{ES})$$
$$= \begin{bmatrix}0 & \mathcal{M}^{-1}\mathcal{M}_d\\ -\mathcal{M}^{-1}\mathcal{M}_d & \mathfrak{J}(q,p) - B(q)\mathcal{K}B^T(q)\end{bmatrix}\begin{bmatrix}\nabla_q H_d(q,p)\\ \nabla_p H_d(q,p)\end{bmatrix} \tag{18}$$

The energy shaping term is derived from the second row.

$$\begin{aligned}u_{ES} = B^{-1}(q)(\nabla_q H(q,p) + C\nabla_p H(q,p)\\ -\mathcal{M}^{-1}\mathcal{M}_d\nabla_q H_d(q,p) + \mathfrak{J}(q,p)\nabla_p H_d(q,p))\end{aligned} \tag{19}$$

and

$$B(q)u_{DI} = -B(q)\mathcal{K}B^T(q)\nabla_p H_d(q,p) \tag{20}$$

The above control law relies heavily on the $\mathcal{M}_d$ matrix, which is essential for adapting the closed-loop behavior to the mission. This matrix includes the mass and inertia matrices that determine the behavior of the entire system.

Remark 2. *The injection of damping into the system is facilitated by $\mathcal{R}_d$ through negative feedback of the passive output, which is specifically selected in our case as $B^T\nabla_p H_d(q,p)$ (as shown in equation* (20)*). The corresponding term for damping injection can be expressed as:*

$$u_{DI} = -\mathcal{K}B^T\nabla_p H_d(q,p) \tag{21}$$

Assumption 2. *To simplify matters, the interconnection matrix remains unchanged, i.e. $\mathcal{M}_d$ is equal to $\mathcal{M}$ and $\mathfrak{J}$ is equal to zero.*

Using (12)*, we obtain*

$$u_{DI} = -\mathcal{K}\mathcal{M}^{-1}(p-p_r) \tag{22}$$

$$u_{ES} = \nabla_q\mathcal{V}(q) - \nabla_q\mathcal{V}_d(q) + C\mathcal{M}^{-1}p \tag{23}$$

By using energy shaping as a state-feedback technique, the position of the system is stabilized. To achieve asymptotic stability, damping injection is introduced via passive output feedback.

The selection of $\mathcal{V}_d$ involves choosing a quadratic function as defined in equation (24)*, which satisfies the necessary and sufficient conditions of $\nabla_q\mathcal{V}_d(q^*) = 0$ and $\partial_q^2\mathcal{V}_d(q^*) > 0$, respectively.*

$$\mathcal{V}_d(q) = \frac{1}{2}(\xi-\xi_d)^T\Gamma_\xi(\xi-\xi_d) + \frac{1}{2}(\eta-\eta_d)^T\Gamma_\eta(\eta-\eta_d) \tag{24}$$

where Γ_ξ and Γ_η denote positive definite matrices.

Using (24)*, the control of energy shaping u_{ES} becomes*

$$u_{ES} = \begin{bmatrix}-\Gamma_\xi(\xi-\xi_d) + \mathcal{G}\\ -\Gamma_\eta(\eta-\eta_d) + C\dot{\eta}\end{bmatrix} \tag{25}$$

Theorem 2. *The closed loop of system* (2) *using control law* (5) *is asymptoticaly stable*

Proof. *By employing the IDA-PBC approach as explained earlier, the closed loop system* (2)*, written using the port-controlled Hamiltonian representation*

model (8)*, can be transformed into the desired port-controlled Hamiltonian representation model* (14) *using the control law* (17)*. In this context,* u_{ES} *is defined by* (25) *and* u_{DI} *by* (22)*, subject to the conditions of Assumption 2. Additionally,* $\mathcal{V}_d(q)$ *can be expressed as* (24)*.*

$H_d(q,p)$ *is a positive definite function chosen herein as Lyapunov candidate function where the first time derivative is*

$$\dot{H}_d(q,p) = \dot{q}^T \nabla_q H_d(q,p) + \dot{p}^T \nabla_p H_d(q,p) \tag{26}$$

Using (14)*, we get*

$$\begin{aligned} \dot{H}_d(q,p) = \nabla_p H_d^T(q,p) - (\nabla_q H_d^T(q,p) \\ + \nabla_p H_d^T(q,p) B^T \mathcal{K}^T B) \nabla_p H_d(q,p) \end{aligned} \tag{27}$$

Then

$$\begin{aligned} \dot{H}_d(q,p) = -\nabla_p H_d^T(q,p) \mathcal{K}^T \nabla_p H_d(q,p) \\ \leqslant eig_{min}(\mathcal{K})(p-p_d)^T \mathcal{M}^{-1}(q)^2 (p-p_d) \end{aligned} \tag{28}$$

where $eig_{min}(.)$ *denotes the minimal eigenvalue of matrix* $\mathcal{K}$*.*
Therefore, the closed loop system is asymptotically stable

4 SIMULATION RESULTS

The simulation starts with the morphing drone flying in the 'X' configuration. The drone then changes configuration according to the table reftconfig, which was presented previously, respecting the time intervals given by $T = \begin{bmatrix} 0s & 5s & 20s & 30s & 60s & 70s & 80s \end{bmatrix}$. Each configuration is supposed to be adapted to a specific mission. To test the robustness of the system, simulations were performed with an external disturbance of $d_y = d_z = 0.1N.kg^{-1}$ in translation. Additionally, the simulations took into account the presence of uncertainties $\triangle$ related to the calculation of inertia and center of gravity of each configuration

In this scenario, we create a complex path, and the results of the simulation are presented in Figures 2 to 7. Each figure displays the progress of the vehicle's position and orientation, as well as the tracking and attitude errors and the actuator force controls, separately. In order to facilitate a more intuitive observation of the position system's trajectory tracking effect during the flight, Figure 2 depicts the three-dimensional space trajectories of IDA-PBC.

As it can be observed, the controller result in more successful tracking of the reference trajectories. From the results dipicted in Figs. 3 and 4, it is apparent that

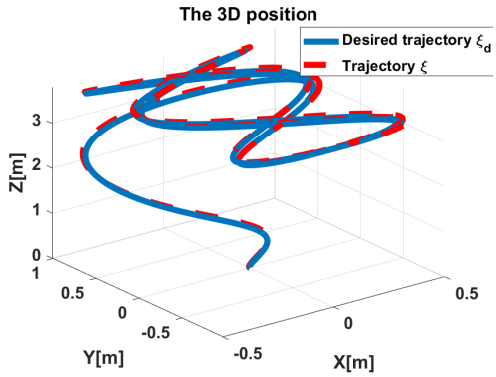


Figure 2: Absolute position of the quadrotor with disturbances.

the system's outputs converge towards the desired trajectories and exhibit good tracking. Additionally, Figures 5 and 6 indicate that the tracking errors converge to the origin and remain in a steady state in the neighborhood due to the efficiency of the controllers. The curve in Fig. 7 represents the evolution of the control inputs. As it is observed, the applied control inputs of the proposed controllers are smooth.

5 CONCLUSIONS & FUTURE WORKS

The paper introduces a new type of drone, known as the morphing drone, which can modify its shape during flight to fulfill a specific mission in a challenging environment. Additionally, a nonlinear robust controller utilizing IDA-PBC was implemented, allowing the UAV to follow the desired tracking trajectory. The proposed controller's asymptotic stability was also demonstrated through analytical means. To verify the analytic results, a simulation was run to exhibit the stability of the controller. According to the simulation results, the developed controller showed high accuracy capabilities and maintained good performance.

In our future work, we plan to approach the issue from an experimental perspective and extend our research to energy consumption and energy planning.

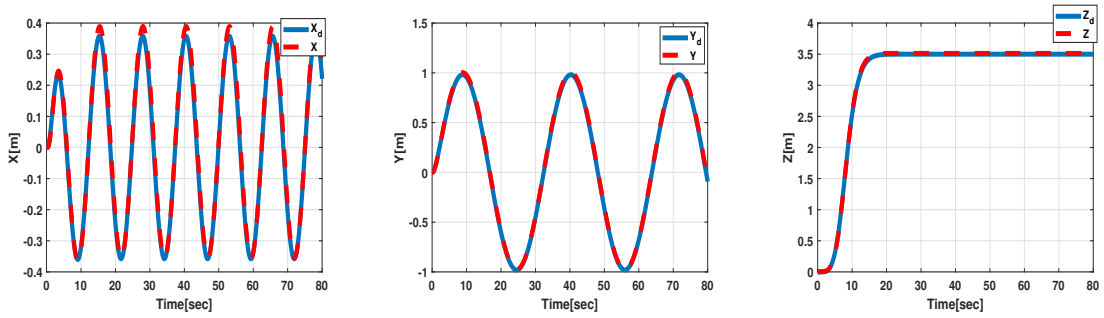


Figure 3: Trajectories of position.

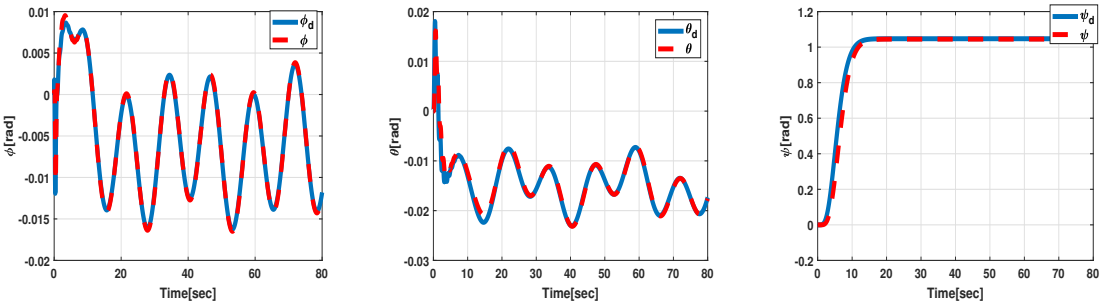


Figure 4: Euler angles.

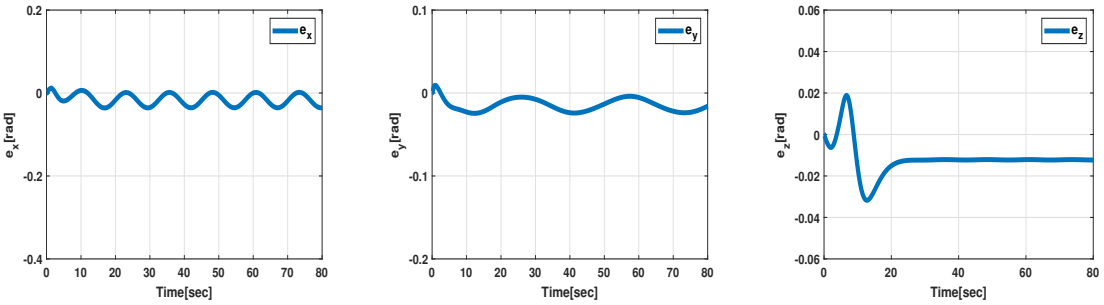


Figure 5: Quadrotor tracking errors.

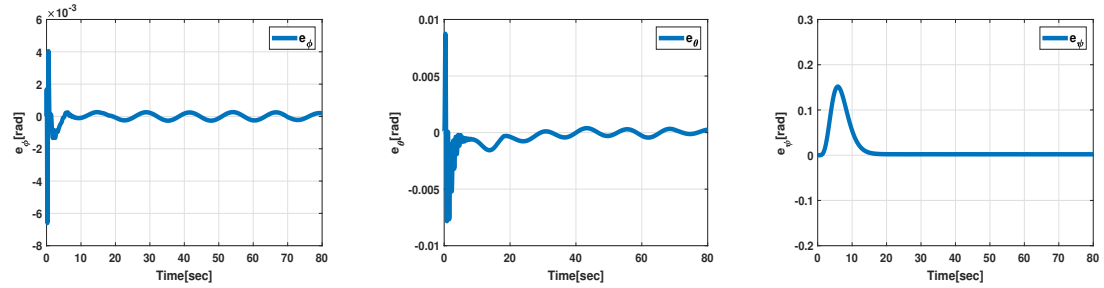


Figure 6: Quadrotor attitude errors.

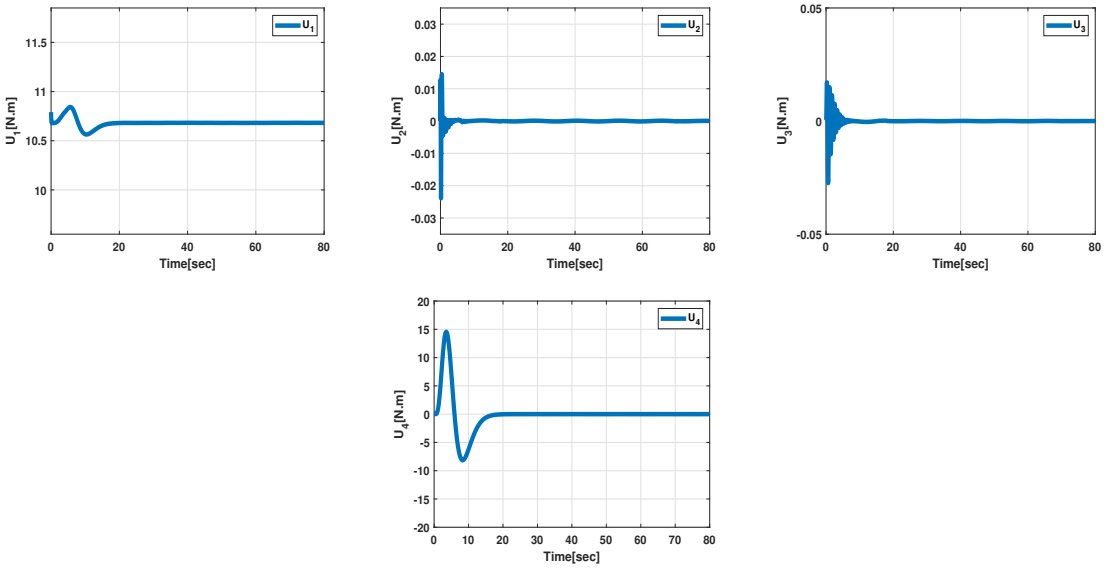


Figure 7: Evolution of control signals.

REFERENCES

Acosta, J. Á., Sanchez, M., and Ollero, A. (2014). Robust control of underactuated aerial manipulators via ida-pbc. In *53rd IEEE Conference on Decision and Control*, pages 673–678. IEEE.

Belmouhoub, A., Bouzid, Y., Medjmadj, S., Derrouaoui, S., and Guitani, M. (2023a). Backstepping control merged with disturbances observer for quadrotor with rotating arms. *Unmanned Systems*, pages 1–14.

Belmouhoub, A., Bouzid, Y., Medjmadj, S., Derrouaoui, S., Siguerdidjane, H., and Guitani, M. (2023b). Fast terminal synergetic control for morphing quadrotor with time-varying parameters. *Aerospace Science and Technology*, 141:108540.

Bouzid, Y., Siguerdidjane, H., and Bestaoui, Y. (2018). Generic dynamic modeling for multirotor vtol and robust sliding mode based model-free control for 3d navigation. In *2018 international conference on unmanned aircraft systems (ICUAS)*, pages 970–979. IEEE.

Bucki, N., Tang, J., and Mueller, M. W. (2022). Design and control of a midair-reconfigurable quadcopter using unactuated hinges. *IEEE Transactions on Robotics*.

Desbiez, A., Expert, F., Boyron, M., Diperi, J., Viollet, S., and Ruffier, F. (2017). X-morf: A crash-separable quadrotor that morfs its x-geometry in flight. In *2017 Workshop on Research, Education and Development of Unmanned Aerial Systems (RED-UAS)*, pages 222–227. IEEE.

Fabris, A., Kleber, K., Falanga, D., and Scaramuzza, D. (2021). Geometry-aware compensation scheme for morphing drones. In *2021 IEEE International Conference on Robotics and Automation (ICRA)*, pages 592–598. IEEE.

Guerrero, M., Mercado, D., Lozano, R., and García, C. (2015). Passivity based control for a quadrotor uav transporting a cable-suspended payload with minimum swing. In *2015 54th IEEE Conference on Decision and Control (CDC)*, pages 6718–6723. IEEE.

Oğuz, K. and Oktay, T. (2020). Investigation of the effect of differential morphing on forward flight by using pid algorithm in quadrotors. *Journal of Aviation*, 4(1):15–21.

Ortega, R., Van Der Schaft, A. J., Mareels, I., and Maschke, B. (2001). Putting energy back in control. *IEEE Control Systems Magazine*, 21(2):18–33.

Ryalat, M., Laila, D. S., and ElMoaqet, H. (2021). Adaptive interconnection and damping assignment passivity based control for underactuated mechanical systems. *International Journal of Control, Automation and Systems*, 19:864–877.

Ryalat, M., Laila, D. S., and Torbati, M. M. (2015). Integral ida-pbc and pid-like control for port-controlled hamiltonian systems. In *2015 American Control Conference (ACC)*, pages 5365–5370. IEEE.

Souza, C., Raffo, G. V., and Castelan, E. B. (2014). Passivity based control of a quadrotor uav. *IFAC Proceedings Volumes*, 47(3):3196–3201.

Zhao, M., Anzai, T., Okada, K., Kawasaki, K., and Inaba, M. (2021). Singularity-free aerial deformation by two-dimensional multilinked aerial robot with 1-dof vectorable propeller. *IEEE Robotics and Automation Letters*, 6(2):1367–1374.

A Comparison of Fuzzy logic and Adaptative Backstepping in Diabetics Controler

Touitou Ikram , Ziani Salim

Faculty of engineering, University of Constantine 1
Laboratory of automatic, robotic and control systems
[1]ikram.touitou@student.umc.edu.dz
[2]ziani_salim@umc.edu.dz

***Abstract*—Type 1 diabetes develops when the immune system targets and destroys the pancreatic beta cells, resulting in inadequate production of insulin a hormone essential for enabling sugar or glucose to enter cells for energy generation. In response to pancreatic dysfunction, artificial pancreases are employed to administer the necessary insulin dosage into the body. Automated controllers are utilized to maintain a harmonious equilibrium between blood glucose and insulin levels. Bergman's minimal model (BMM) is a validated physiological representation of this phenomenon. This model addresses the perturbations in blood glucose levels resulting from meal consumption. Two nonlinear control strategies are introduced: an adaptative backstepping algorithm and a Fuzzy Logic Controller (FLC). These methods are proposed for the automated regulation of blood glucose levels in individuals with Type 1 Diabetes Mellitus The outcomes of the simulations revealed that the fuzzy logic control system (FLC) outperformed the adaptative backstepping controller.**

***Keywords:* Fuzzy Logic Controller (FLC), blood glucose levels (BGL), Adaptative Backstepping.**

I. INTRODUCTION

The pancreas secretes the hormone insulin, which the body uses to control blood glucose levels. When the pancreas produces insufficient or excessive amounts of insulin, blood glucose concentrations rise or fall outside of the prescribed range. People's pancreas with Type 1 Diabetes (T1D(generates little or no insulin. They require daily insulin injections to maintain blood glucose levels. Diabetes management is necessary to stop or postpone the onset of micro vascular (retinopathy, nephropathy) and macro vascular (myocardial ischemia, stroke) complications.[1]In 2017, the American Diabetes Association (ADA) has fixed the glycemic target range (180-80) mg/dl for many non-pregnant adults with diabetes. [2]

Diabetes mellitus can be categorized into two primary types: Type 1 and Type 2. Type 1 diabetes, also referred to as 'Juvenile Diabetes,' is characterized by elevated blood glucose levels resulting from an insufficient production of insulin. This insufficiency stems from the depletion of beta cells in the pancreas, which play a crucial role in insulin synthesis. On the other hand, Type 2 diabetes develops due to either (i) insulin resistance or (ii) inadequate insulin secretion. Management of Type 1 diabetes involves administering insulin to stabilize blood glucose levels, while Type 2 diabetes is typically treated with appropriate medications. [3]

In order to prevent such severe conditions, maintaining a balanced blood glucose level is of utmost importance. While manually administering a fixed quantity of insulin can help Type 1 patients achieve normal blood glucose levels, this approach isn't practical for consistently reaching and sustaining normal levels. Additionally, this method lacks the capability to address potential disruptions in the process. As a result, a more favorable approach involves controlled infusion, facilitated by a specially designed controller that utilizes data from continuous glucose monitoring (CGM). This solution is embodied in the form of an Artificial Pancreas (AP), comprising three key components: CGM for continuous blood glucose monitoring, a controller for insulin dosing calculations, and an insulin pump for insulin delivery (figure 1). The CGM continuously tracks blood glucose levels and relays the data to the controller, which then computes the appropriate insulin dosage and communicates the necessary instructions to the insulin pump if insulin infusion is deemed necessary. [4] The main purpose of this paper is to apply Adaptative backstepping nonlinear controller based on the method of Lyapunov for automated control of blood glucose in Type 1 Diabetic Patients, in the first part. after that the application of the fuzzy logic nonlinear controller with a generated trajectory reference. The interest of fuzzy logic lies in its ability to deal with the imprecise, the uncertain and the blurred. It stems from man's ability to decide and act

appropriately despite the lack of available knowledge. After that, a comparison of the two controllers is done.

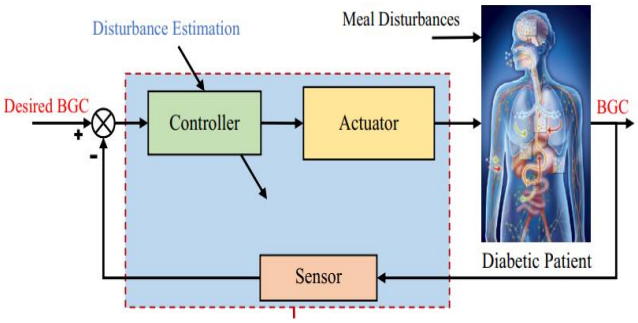


Figure 1. Closed loop controller[5].

II. SYSTEM MODELING OF BERGMAN

Bergman's model is the most popularly utilized model in the literature, and it approximates the dynamic response of a diabetic patient's blood glucose concentration to the insulin injection [6].

Bergman's model is formulated based on first-order differential equations, utilizing three state variables: the level of blood glucose concentration (G), interstitial insulin (X) situated among muscle cells, which aids in glucose uptake by muscles, and the concentration of insulin in the bloodstream (I) [7, 8]

The representation of a dynamic model for blood glucose (BG) and insulin is depicted through a set of three differential equations as outlined below: [9, 1]

$$\dot{G} = -p_1 (g(t) - gb) - x(t)g(t) + M(t) \quad (1)$$

$$\dot{X} = -p_2 x(t) + p_3 (i(t) - ib) \quad (2)$$

$$\dot{I} = -NI + \frac{1}{V_i} U_i \quad (3)$$

i : Concentration of insulin in the human body.
g : Concentration of glucose in the human body.
x: insulin "active".
P1, p2, p3, n, and ɤ, h: are characteristics of the patient of his diabetes.
ib, gb: balance, baseline level of I and G respectively.

TABLE I. PARAMETER VALUES OF SYSTEM.

parameter	values	Unity
gb	100	**Mg/dl**
ib	7.0	**mU/ml**
P_1	0.03	**Min^{-1}**
P_2	0.01	**Min^{-1}**
P_3	0.00001	**Min^{-1}**
N	0.10	**Min^{-1}**
Vi	12	**L**
G0	120	**Mg/dl**
I0	7.0	**mU/ml**
X0	0	**Min^{-1}**

M (t) represents the meal glucose disturbance and can be modeled by decaying exponential function of the following form [10]:

$$M(t) = Gin = (dg * ag) * t * \exp(-t * 40) / tmax \quad (4)$$

dgen [***g***]: Represents the amount of carbohydrates in the meal.

ag: A constant in the pattern of the expression.

tmax: Represents the time when the absorption of carbohydrates is in the peak value (max).

III. ADAPTATIVE BACKSTEPPING CONTROLLER DESING

Non-linear BS controller as implemented in [5, 11],

The adaptative backstepping technique stands as an effective control strategy for nonlinear systems. This approach employs virtual control to streamline the process of devising control regulations. Typically, intricate nonlinear systems can be restructured into multiple subsystems using the backstepping design. Subsequently, a virtual controller is formulated for each of these subsystems utilizing Lyapunov functions. Consequently, at each stage, a more manageable control law is dealt with; the overall diagram of designed controller is shown on Figure 2.

The error e1 is the difference between the reference output and actual output, which is defined as:

$$e_1 = G_1 - G_{1ref} \quad (5)$$

A. Step1

First, a candidate for the positive defnite Lyapunov function is defined as:

$$V_1 = \frac{1}{2} e_1^2 > 0 \quad (6)$$

Its derivative function is:

$$\dot{V}_1 = (\dot{G}_{ref} - \dot{G}) e_1 \quad (7)$$

First, a candidate for the positive defnite Lyapunov function is defined as:

$$V_1 = \frac{1}{2} e_1^2 > 0 \quad (6)$$

Its derivative function is:

$$\dot{V}_1 = (\dot{G}_{ref} - \dot{G}) e_1 \quad (7)$$

Using the corresponding $\dot{G}$ value from equation (1) to equation (7) results in:

$$\dot{V} = e_1 [p_1 (G - G_B) - GX + D - \dot{G}_{ref}] \quad (8)$$

Defining the following as the virtual control law makes Eq. (8) into a negative definite equation.

$$X^* = \frac{1}{G} [\dot{G}_{ref} + p_1 (G_B - G) + D - k_1 e_1] \quad (9)$$

Indeed, when Eq. (9) is replaced into Eq. (8), the desired outcome is as follows:

$$\dot{V}_1 = -k_1 e_1 < 0 \quad (10)$$

Where $k_1 > 0$, G ≠ 0.

B. Step2

We now need to identify the control to assure that X →X*.

$$V_2 = V_1 + \frac{1}{2} e_2^2 > 0 \quad (11)$$

With $e_2 = (X^* - X)$.

The Lyapunov function's derivate is:

$$\dot{V}_2 = \dot{V}_1 - \dot{e}_2 e_1 = \dot{V}_1 + (\dot{X}^* - \dot{X}) e_2 = \dot{V}_1 + (\dot{X}^* + P_2 X + P_3 (I_B - I) e \quad (12)$$

Eq. (12) becomes negative definite, if we define the following virtual control law:

$$I^* = \frac{1}{p_3} (\dot{X}^* + P_2 X + P_3 I_B + K_2 e_2). \quad (13)$$

Indeed, when Eq. (13) is replaced into Eq. (12), the desired outcome is as follows:

$$\dot{V}_2 = \dot{V}_1 - K_2 e_2 < 0, \quad (14)$$

Where $k_2 > 0$, $p_3 \neq 0$.

C. Step3

We now need to identify the control to assure that I →I*.

$$V_3 = V_1 + V_2 + \frac{1}{2} e_3^2 > 0 \quad (15)$$

With $e_3 = (I^* - I)$

The Lyapunov function derivate is:

$$\dot{V}_3 = \dot{V}_1 + \dot{V}_2 + \dot{e}_3 e_3 = \dot{V}_1 + \dot{V}_2 + (\dot{I}^* - \dot{I}) e_3 \quad (16)$$
$$= \dot{V}_1 + \dot{V}_2 + (\dot{I}^* + \mathrm{NI} - \frac{1}{v_i} U_i) e_3.$$

Eq. (16) becomes negative definite, if we define the following virtual control law:

$$U_i^* = v_i (\dot{I}^* + NI + K_3 e_3) \quad (17)$$

Indeed, when Eq. (17) is replaced into Eq. (16), the desired outcome is as follows:

$$\dot{V}_3 = \dot{V}_1 + \dot{V}_2 - K_3 e_3^2 < 0 \quad (18)$$

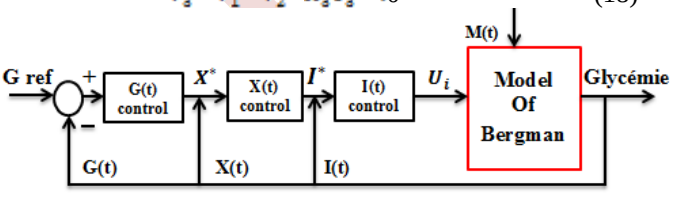


Figure 2. Block diagram of adaptive backstepping controller.

IV. FUZZY LOGIC CONTROLLER

The implementation of FLC involves tracking the internal insulin level from state variable I and blood glucose level through BG sensor. When a blood glucose level deviates from the reference, FLC delivers the necessary amount of insulin. Its simulations have been run using MATLAB's Fuzzy Toolbox.[12]

As illustrated in Figure 3, the FLC structure has organization three essential elements such as fuzzification, fuzzy inference, and defuzzification.

The first block is fuzzification, which looks up each input data element using one or more membership functions to transform it to degrees of membership. The rule base and inference base have the capacity to simulate human decision-making based on fuzzy notions, and they also have the ability to infer fuzzy control actions using fuzzy implication and the rules of inference in fuzzy logic. Defuzzification is the name given to the third procedure. In order to create a clear control signal, the resultant fuzzy set is defuzzified.

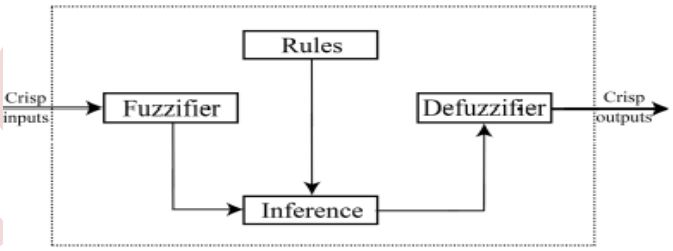


Figure 3. FLC algorithm [13]

The fuzzy logic controller in this study is predicated on two inputs: the concentration of glucose and glucose concentration change rate are given by Figure 4, Figure. 5, respectively .The amount of insulin administered is the output. The membership function (MF) type-specific fuzzy sets are defined together with the range of variation for each variable as part of the fuzzification process.

The main goal in this part is to design a pump to regulate the flow of insulin inside the body according to the level of glucose present in the blood, by controlling it with the fuzzy logic controller.

The controlled system is mathematically represented by the Bergman system. The element that controls the pump is the valve, which is called, which controls the change of glucose by pumping or determining the level of insulin entry into the body.[14]

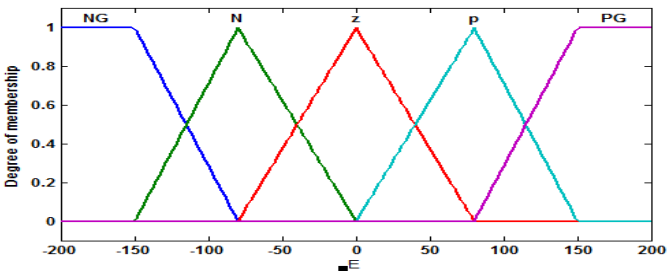


Figure 4. Input membership function of error glucose concentration.

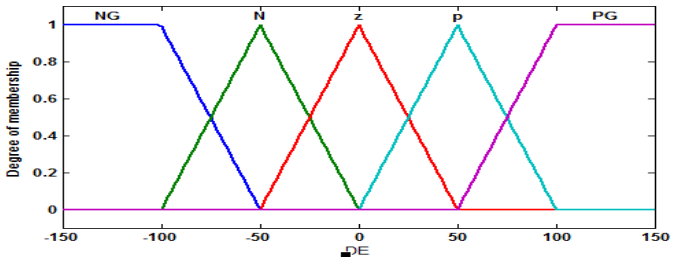


Figure 5. Input membership function of rate of error glucose concentration.

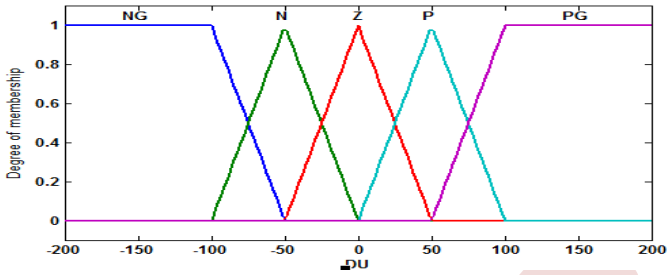


Figure 6. Output membership function.

decision or output in fuzzy linguistic variables. Fuzzy rules for blood glucose regulation are mentioned in Table II.

TABLE II. PARAMETER VALUES OF SYSTEM.

G / DG	NG	N	Z	P	PG
NG	NG	NG	NG	N	Z
N	NG	NG	N	Z	P
Z	NG	N	Z	P	PG
P	N	Z	P	PG	PG
PG	Z	P	PG	PG	PG

NG (Negative Big), N (Negative), Z (Zero), P (Positive), PG (Positive Big)

V. SIMULATION RESULTS

Discussion and testing of simulations the effectiveness of the suggested control strategy is demonstrated using the results of simulations in order to validate our work. Prior to comparing the suggested fuzzy logic controller's performance to the Adaptive back-stepping controller, an analysis of its performance is conducted. In the appendix, the BMM's rating and specifications are listed. Note that the initial glucose basal level for all simulations is GB=120 mg/dL, Ib is 7.The following figure illustrates the form of a particular amount of carbs' fluctuation over time:

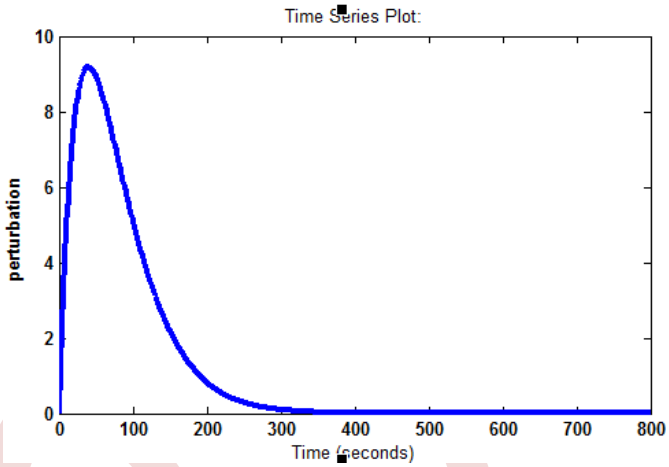


Figure 7. Disturbance of glucose

The simulation begins with high blood glucose levels and significant meal disruption, necessitating a continuous insulin infusion. As the controller increases the amount of insulin it is administering into the system, the blood glucose level immediately drops, the controller starts lowering the insulin level as seen in Figure 8.

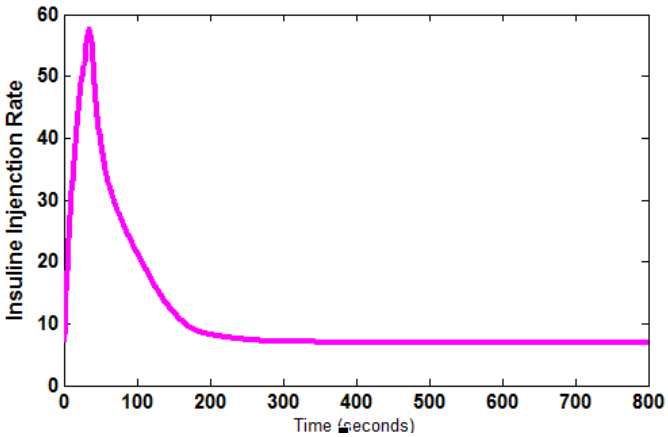


Figure 8. Insulin injections to control blood glucose.

Figure 9 illustrates the comparison of blood glucose level using fuzzy type-1and adaptative backstepping . As it can be seen in figure 9, a controller is needed to maintain the blood glucose level in the desirable range. Also, it is clear that the glucose range is decreased during the control process. Moreover, while adaptative backstepping controller showed promising results in controlling blood glucose level, fuzzy type-1 exceeds its performance in keeping the blood glucose level closer to the desired value (100[mg/dL]). As it is known, its amount initially has a sharp increase, which figure 9 clearly illustrates this pattern. Also, by conducting fuzzy type-1 the

patient will experience a lower maximum level of blood glucose concentration.

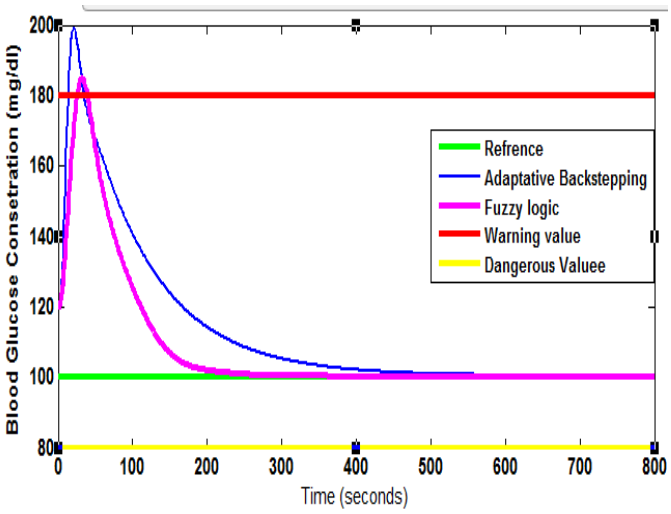


Figure 9. Glucose response of closed loop system.

VI. CONCLUSION

The concentration of glucose is controlled in this paper using fuzzy logic and a backstepping controller, and the simulation results are obtained using MATLAB SIMULINK. By comparing fuzzy logic to Adaptative backstepping controller, the main goal of this paper was to regulate the concentration of glucose in the blood, so that when it rises, the pump intervenes and injects insulin up to the normal value of glucose. The simulations and experimental results demonstrated that fuzzy control outperformed conventional backstepping systems.

REFERENCES

[1] M. Djouima, S. Drid, et D. Mehdi, « Backstepping Glycemic Control of Type 1 Diabetes for Implementation on an Embedded System », 2018.

[2] American Diabetes Association, Standards of Medical Care in Diabetes – 2017 (2017). Diabetes Care, The Journal of Clinical and Applied Research and Education, Vol. 40, Supplement 1.

[3] ''Diagnosis and classification of diabetes mellitus,'' Diabetes care, vol. 37, pp. S81–S90, Jan. 2014.

[4] M. Breton, A. Farret, D. Bruttomesso, S. Anderson, L. Magni, S. Patek, C. Dalla Man, J. Place, S. Demartini, and S. Del Favero, ''Fully integrated artificial pancreas in type 1 diabetes: Modular closed-loop glucose control maintains near normoglycemia,'' Diabetes, vol. 61, no. 9, pp. 2230–2237, 2012.

[5] R. Zahedifar, A. K.Khalaj« Control of blood glucose induced by meals for type-1 diabetics using an adaptive backstepping algorithm »i University Tehran, 2022.

[6] D. N. M. Abadi, M. H. Khooban, A. Alfi, et M. Siahi, « Design of Optimal Self-Regulation Mamdani-Type Fuzzy Inference Controller for Type I Diabetes Mellitus », *Arab J Sci Eng*, p. 10, 2014.

[7] Shiang K. D., F. Kandeel (2010). A Computational Model of the Human Glucose-insulin Regulatory System, Journal of Biomedical Research, 24(5), 347-364.

[8] Van Riel N. (2004). Minimal Models for Glucose and Insulin Kinetics. A Matlab Implementation, Eindhoven University of Technology, 1-21.

[9] K. E. Andersen and M. Højbjerre, « A Bayesian Approach to Bergman's Minimal Model », p. 8.

[10] I. Zouad, M .Alouane, «Etude et Simulation d'un système de Régulation Glucose- Insuline à base PID par MATLAB/SIMULINK», p. 27, 2016.

[11] F. Munir, I. Ahmad, and N. Naz, ''Backstepping based automatic blood glucose nonlinear controller for diabetes mellitus type 1 patients,'' Adv. Sci. Lett., vol. 22, no. 10, pp. 2652–2656, 2016.

[12] S. A. Babar, I. A. Rana, M. Arslan, et M. W. Zafar, « Integral Backstepping Based Automated Control of Blood Glucose in DiabetesMellitus Type 1 Patients », *IEEE Access*, vol. 7, p. 173286‑173293,2019, doi: 10.1109/ACCESS.2019.2951010.

[13] C-Sharp Fuzzy Logic API. Accessed: Jan. 8, 2019. [Online]. Available:https://www.codeproject.com/Articles/5092762/Csharp-Fuzzy-Logic-API

[14] D. N. M. Abadi, M. H. Khooban, A. Alfi, et M. Siahi, « Design of Optimal Self-Regulation Mamdani-Type Fuzzy Inference Controller for Type I Diabetes Mellitus », *Arab J Sci Eng*, p. 10, 2014

Model-Based States Estimation Approach Applied to a Reconfigurable Quadrotor for Position and Attitude Tracking Control

Abdenour Salmi[1], Mohamed Guiatni[1], Yasser Bouzid[1], Saddam Hocine Derrouaoui[1], Farès Boudjema[2]
[1]*Complex Systems Control and Simulators Laboratory, Ecole Militaire Polytechnique*
Algiers, Algeria
[2]*Process Control Laboratory, Ecole Nationale Polytechnique*
Algiers, Algeria

***Abstract*—**
This paper proposes the design of a controller-observer system for a reconfigurable quadrotor with foldable rotor arms that takes into account internal and external disturbances using integral sliding mode approach.Two types of observers are considered : (i) observer based Extended Kalman Filter (EKF), and (ii) Sliding mode observer (SMO). The two observers are designed in order to observe and estimate the state variables, the first one is a recursive stochastic observer whereas the second one is a robust non linear observer. A comparison is made using Matlab simulation.

***Keywords*—**
States Estimation, Reconfigurable Quadrotor, Extended Kalman Filter, Observer, Sliding Mode Observer

I. Introduction

Reconfigurable quadrotors, also known as modular or transformable quadrotors, are a type of unmanned aerial vehicle (UAV) that have the capability to change their physical configuration during flight. Unlike traditional quadrotors with fixed structures, reconfigurable quadrotors can alter their shape, size, or configuration to adapt to different tasks, environments, or mission requirements. This adaptability can be highly advantageous in various applications [1]–[7]. An excellent survey and a state-of-the-art on morphing Unmanned Aerial Vehicles (UAVs) are compiled in [8]. It arises from this survey that reconfigurable UAVs are a promising solution in the near future, since they allow increasing considerably the capabilities and performance of the conventional UAVs.
However, designing and controlling these systems can be challenging due to the complexity of managing different configurations and flight modes. Moreover, designing a state estimator for a quadrotor is a complex task that requires a good understanding of control theory, sensor characteristics, and the specific quadrotor dynamics. Additionally, the choice of observer may depend on the complexity of the system and the desired estimation accuracy.
In this paper, a controller-observer system is designed for a reconfigurable quadrotor with foldable rotor arms. The design takes into account internal and external disturbances using integral sliding mode approach. Two different observers are introduced : (i) Extended Kalman Observer (EKF), and (ii) Sliding mode observer (SMO). The two observers are designed in order to estimate the state variables, the first one is a recursive stochastic observer whereas the second one is a robust non linear observer.
This paper is organized as follows. In section II, dynamic modeling of the reconfigurable quadrotor is presented. In Section III, two model-based states estimation approaches are presented. It details the mathematical formulas of both the EKF and SMO. Section IV explains the proposed controller-observer design. Simulation results are then shown in section V. Finally, conclusions and future works are drawn.

II. Reconfigurable Quadrotor Model

A. System Description

Designing an observer for state estimation of a quadrotor involves developing a mathematical model that estimates the quadrotor's state variables (such as position, velocity, attitude, and angular rates) based on sensor measurements. Figure 1 shows a schematic model of a reconfigurable quadrotor which is designed based on the standard DJI F450 frame by integrating four additional servomotors attached to the main body to make the quadrotor arms rotate [9]–[11]. This modification makes the four arms rotatable around the central body. Thus, this UAV is able to change its flight configuration by rotating its four arms independently around a central body, thanks to its adaptive geometry. The four arms can rotate around the central body independently by changing the angles $\alpha_i (i = 1, 2, 3, 4)$. Consequently, different configurations are possible [9]–[11] and more details about the description of this system is given in reference [1].
Unlike conventional quadrotors where the center of gravity (CoG) is assumed to be located at the geometric center of the body, the folding of the reconfigurable quadrotor arms has a considerable impact on the variation of the CoG and the moments of inertia (MoIs). Thus, it is necessary to estimate these two properties in real time in order to update the model of the UAV and adjust the controller parameters accordingly [1], [10], [11]. According to the diagram in Figure 1, and using trigonometric relations, the coordinates of the CoGs of

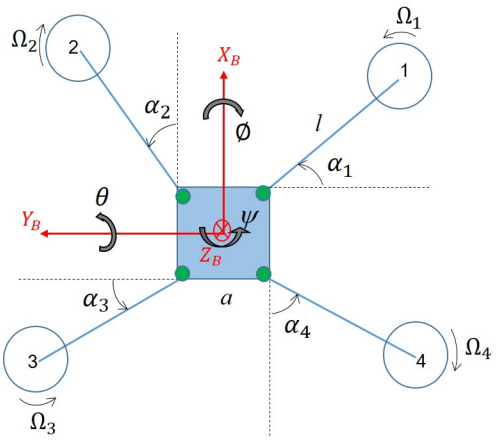


Figure 1. Schematic model of a reconfigurable quadrotor UAV.

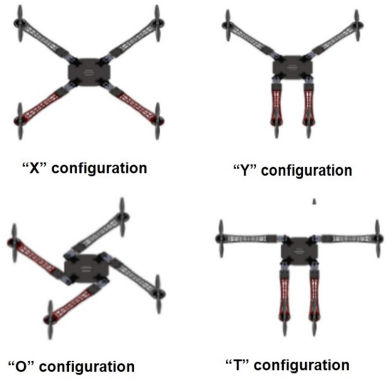


Figure 2. The reconfigurable quadrotor in some possible configurations.

the four arms and the four rotors are given as follows:

$$\begin{cases} (x_{a,1}, y_{a,1}) = (\frac{a}{2} + \frac{l}{2}S\alpha_1, -\frac{a}{2} - \frac{l}{2}C\alpha_1) \\ (x_{a,2}, y_{a,2}) = (\frac{a}{2} + \frac{l}{2}C\alpha_2, \frac{a}{2} + \frac{l}{2}S\alpha_2) \\ (x_{a,3}, y_{a,3}) = (-\frac{a}{2} - \frac{l}{2}S\alpha_3, \frac{a}{2} + \frac{l}{2}C\alpha_3) \\ (x_{a,4}, y_{a,4}) = (-\frac{a}{2} - \frac{l}{2}C\alpha_4, -\frac{a}{2} - \frac{l}{2}S\alpha_4) \end{cases} \quad (1)$$

$$\begin{cases} (x_{r,1}, y_{r,1}) = (\frac{a}{2} + lS\alpha_1, -\frac{a}{2} - lC\alpha_1) \\ (x_{r,2}, y_{r,2}) = (\frac{a}{2} + lC\alpha_2, \frac{a}{2} + lS\alpha_2) \\ (x_{r,3}, y_{r,3}) = (-\frac{a}{2} - lS\alpha_3, \frac{a}{2} + lC\alpha_3) \\ (x_{r,4}, y_{r,4}) = (-\frac{a}{2} - lC\alpha_4, -\frac{a}{2} - lS\alpha_4) \end{cases} \quad (2)$$

$C_{(.)}$ and $S_{(.)}$ are abbreviations for $\cos(.)$ and $\sin(.)$ respectively.

Therefore, based on the general expression of the global center of gravity of the multi-body system, the position of the global center of gravity of our vehicle which depends on the rotation angles α_i is determined as follows:

$$\begin{cases} x_{cog} = \frac{l(m_a + 2m_r)}{2m_t}(S\alpha_1 + C\alpha_2 - S\alpha_3 - C\alpha_4) \\ y_{cog} = \frac{l(m_a + 2m_r)}{2m_t}(-C\alpha_1 + S\alpha_2 + C\alpha_3 - S\alpha_4) \end{cases} \quad (3)$$

B. Dynamic model

The dynamic model of the reconfigurable quadrotor can be written using the state space representation as follows [1]:

$$\begin{cases} \dot{x}_1 = x_2 \\ \dot{x}_2 = f_1(X) + g_1(X)u_2 + d \\ \dot{x}_3 = x_4 \\ \dot{x}_4 = f_2(X) + g_2(X)u_3 + d \\ \dot{x}_5 = x_6 \\ \dot{x}_6 = f_3(X) + g_3(X)u_4 + d \\ \dot{x}_7 = x_8 \\ \dot{x}_8 = f_4(X) + g_4(X)u_1 + d \\ \dot{x}_9 = x_{10} \\ \dot{x}_{10} = f_5(X) + g_5(X)u_1 + d \\ \dot{x}_{11} = x_{12} \\ \dot{x}_{12} = f_6(X) + g_6(X)u_1 + d \end{cases} \quad (4)$$

where
$X = (x_1, x_2, x_3, x_4, x_5, x_6, x_7, x_8, x_9, x_{10}, x_{11}, x_{12})^T = \left[\phi, \dot{\phi}, \theta, \dot{\theta}, \psi, \dot{\psi}, x, \dot{x}, y, \dot{y}, z, \dot{z}\right]^T \in \mathbb{R}^{12}$
$U = (u_1, u_2, u_3, u_4)^T \in \mathbb{R}^4$ and
$Y = (x_1, x_3, x_5, x_7, x_9, x_{11})^T \in \mathbb{R}^6$ are the state, the control input and the output respectively.
x, y, z represent the position coordinates, while ϕ, θ, ψ are the attitude of the quadrotor and $\dot{x}, \dot{y}, \dot{z}, \dot{\phi}, \dot{\theta}, \dot{\psi}$ are their change rates respectively, while:

$$\begin{cases} f_1(X) = a_1x_4x_6 + a_4\overline{\Omega}x_4, f_4(X) = 0 \\ f_2(X) = a_2x_2x_6 + a_5\overline{\Omega}x_2, f_5(X) = 0 \\ f_3(X) = a_3x_2x_4, f_6(X) = -g \\ g_1(X) = b_1, g_4(X) = \frac{u_x}{m_t} \\ g_2(X) = b_2, g_5(X) = \frac{u_y}{m_t} \\ g_3(X) = b_3, g_6(X) = \frac{\cos x_1 \cos x_3}{m_t} \end{cases}$$

with the two virtual control inputs u_x, u_y and the total gyroscopic torques are given respectively as follow:

$$\begin{cases} u_x = C\phi S\theta C\psi + S\phi S\psi \\ u_y = C\phi S\theta S\psi - S\phi C\psi \\ \overline{\Omega} = \Omega_1 - \Omega_2 + \Omega_3 - \Omega_4 \end{cases} \quad (5)$$

and

$$\begin{cases} a_1 = \dfrac{(I_{yy}(\alpha_i) - I_{zz}(\alpha_i))}{I_{xx}(\alpha_i)}, a_4 = -\dfrac{J_r}{I_{xx}(\alpha_i)}, b_1 = \dfrac{1}{I_{xx}(\alpha_i)}, \\ a_2 = \dfrac{(I_{zz}(\alpha_i) - I_{xx}(\alpha_i))}{I_{yy}(\alpha_i)}, a_5 = \dfrac{J_r}{I_{yy}(\alpha_i)}, b_2 = \dfrac{1}{I_{yy}(\alpha_i)}, \\ a_3 = \dfrac{(I_{xx}(\alpha_i) - I_{yy}(\alpha_i))}{I_{zz}(\alpha_i)}, b_3 = \dfrac{1}{I_{zz}(\alpha_i)}. \end{cases}$$

where J_r is the rotor inertia, d represents the disturbances applied to the quadrotor.

The control inputs, u_i, $(i = 1, ..., 4)$, are given by

$$\begin{cases} u_1 = b(\Omega_1^2 + \Omega_2^2 + \Omega_3^2 + \Omega_4^2) \\ u_2 = b(y_{r1}\Omega_1^2 + y_{r2}\Omega_2^2 + y_{r3}\Omega_3^2 + y_{r4}\Omega_4^2) \\ u_3 = b(x_{r1}\Omega_1^2 + x_{r2}\Omega_2^2 + x_{r3}\Omega_3^2 + x_{r4}\Omega_4^2) \\ u_4 = d(\Omega_1^2 - \Omega_2^2 + \Omega_3^2 - \Omega_4^2) \end{cases} \tag{6}$$

in which:

$$\begin{cases} x_{ri} = x_{cog} - x_{r,i} \\ y_{ri} = y_{r,i} - y_{cog}, (i = 1, ..., 4). \end{cases} \tag{7}$$

Since, $\Omega_i \in [0, \Omega_{max}]$, $(i = 1, ..., 4)$, it follows that

$$|\overline{\Omega}| \leq 2\Omega_{max} \tag{8}$$

The pitch, roll, yaw angles and their angular rates respectively satisfy the following inequalities

$$\begin{aligned} &|\phi| < \frac{\pi}{2}, |\theta| < \frac{\pi}{2}, |\psi| \leq \pi, \\ &|\dot{\phi}| \leq \kappa_1, |\dot{\theta}| \leq \kappa_2, |\dot{\psi}| \leq \kappa_3, \end{aligned} \tag{9}$$

Using Equation (5) to extracted desired roll and pitch angles are

$$\begin{cases} \phi_d = \sin^{-1}(u_x S\psi_d - u_y C\psi_d) \\ \theta_d = \sin^{-1}(\dfrac{u_x C\psi_d + u_y S\psi_d}{C\phi_d}) \end{cases} \tag{10}$$

III. Model-based states estimation

In this section, two model-based states estimation will be investigated. The first one is the Extended Kalman Filter which is known by its simplicity and effectiveness for state estimation in nonlinear systems. It is a recursive estimation algorithm that is an extension of the traditional Kalman Filter and widely used. The second one is the Sliding Mode Observer, which provides state estimation even in the presence of uncertainties, disturbances and measurement noise.

A. Extended Kalman Filter

In 1960, R.E. Kalman published his famous paper describing a recursive solution to the discrete-data linear filtering problem [12]. The purpose in this paper is to find the best estimate of the state vector of the system of which the discrete-time nonlinear dynamic is given as:

$$\begin{cases} X_{k+1} = f(X_k, u_k, w_k) \\ Z_k = h(X_k, v_k) \end{cases} \tag{11}$$

where $f(.)$ and $h(.)$ represent the evolution function and relationship between the state vector and the measurement Z_k respectively, u_k is the control input at step k and w_k, v_k are the process and measurement white Gaussian noise vectors with zero mean and associated covariance matrices $Q = E[w_k, w_k]^T$ and $R = E[v_k, v_k]^T$ respectively .

To apply the EKF algorithm, the nonlinear system given in equation 11 must be linearized around the desired reference point $(\hat{X}, \hat{w_k} = 0, \hat{v_k} = 0)$, which gives us the following approximated linear model:

$$\begin{cases} X_{k+1} \approx f(X_k, u_k, w_k) \\ \approx f(\hat{X}_k, u_k, 0) + F_k(X_k - \hat{X}_k) + W_k(w_k - 0) \\ Z_k \approx h(X_k, v_k) \\ \approx h(\hat{X}_k, 0) + H_k(X_k - \hat{X}_k) + V_k(v_k - 0) \end{cases}$$

where the Jacobean matrices of f and h are given as follows:

$$\begin{aligned} F_k &= \left.\frac{\partial f(X,0)}{\partial X}\right|_{X=\hat{X}}, H_k = \left.\frac{\partial h(X,0)}{\partial X}\right|_{X=\hat{X}} \\ W_k &= \left.\frac{\partial h(\hat{X},w)}{\partial w}\right|_{w=0}, V_k = \left.\frac{\partial h(\hat{X},v)}{\partial v}\right|_{v=0} \end{aligned}$$

We denote $\hat{X}_{k+1/k+1}$,$\hat{X}_{k+1/k}$,$P_{k+1/k+1}$ and $P_{k+1/k}$ the posteriori state prediction vector, the priori state prediction vector, the posteriori prediction error covariance matrix and the priori prediction error covariance matrix respectively.

The steps of the recursive EKF algorithm are given by the following equations to estimate the state vector.

Prediction step:

$$\begin{cases} \hat{X}_{k+1/k} = f(\hat{X}_{k/k}, u_k, 0) \\ P_{k+1/k} = F_k P_{k/k} F_k^T + W_k Q W_k^T \end{cases} \tag{12}$$

Innovation step:

$$\begin{cases} Y_{k+1/k} = h(\hat{X}_{k+1/k}, 0) \\ S_k = (H_k P_{k+1/k} H_k^T + V_k R V_k^T) \end{cases} \tag{13}$$

Kalman filter gain matrix:

$$K_k = P_{k+1/k} H_k^T S_k^{-1} \tag{14}$$

Correction step:

$$\begin{cases} \hat{X}_{k+1/k+1} = \hat{X}_{k+1/k} + K_k(Z_k - Y_{k+1/k}) \\ P_{k+1/k+1} = P_{k+1/k} - K_k H_k P_{k+1/k} \end{cases} \tag{15}$$

B. Sliding Mode Observer

The Sliding Mode Observer (SMO) [13] is derived from (4) and has the form:

$$\begin{cases} \dot{\hat{x}}_1 = \hat{x}_2 + \mu_1 \\ \dot{\hat{x}}_2 = f_1(\hat{X}) + g_1(\hat{X})u_2 + \mu_2 \\ \dot{\hat{x}}_3 = \hat{x}_4 + \mu_3 \\ \dot{\hat{x}}_4 = f_2(\hat{X}) + g_2(\hat{X})u_3 + \mu_4 \\ \dot{\hat{x}}_5 = \hat{x}_6 + \mu_5 \\ \dot{\hat{x}}_6 = f_3(\hat{X}) + g_3(\hat{X})u_4 + \mu_6 \\ \dot{\hat{x}}_7 = \hat{x}_8 + \mu_7 \\ \dot{\hat{x}}_8 = f_4(\hat{X}) + g_4(\hat{X})u_1 + \mu_8 \\ \dot{\hat{x}}_9 = \hat{x}_{10} + \mu_9 \\ \dot{\hat{x}}_{10} = f_5(\hat{X}) + g_5(\hat{X})u_1 + \mu_{10} \\ \dot{\hat{x}}_{11} = \hat{x}_{12} + \mu_{11} \\ \dot{\hat{x}}_{12} = f_6(\hat{X}) + g_6(\hat{X})u_1 + \mu_{12} \end{cases} \tag{16}$$

where

$$\begin{cases} \mu_i = K_i sign(x_i - \hat{x}_i) \\ \mu_{i+1} = K_{i+1} sign(x_i - \hat{x}_i) \end{cases}, i = 1, 3, 5, 7, 9, 11 \tag{17}$$

K_i are positive gains.

IV. Integral Sliding Mode Control Design

Because of the complexity of reconfigurable quadrotors, we need a powerful controller to overcome the commutation between different configurations and to compensate for the partial loss of effectiveness in one of its rotors. The SMC approach is an excellent candidate for that, thanks to its strong robustness. Therefore, in this section, an Integral SMC controller is designed to control our vehicle. The structure of the proposed controller-observer is shown in Figure 3.

Let $\hat{x}_i = (\hat{\phi}, \hat{\theta}, \hat{\psi}, \hat{x}, \hat{y}, \hat{z})$, be the outputs of the observer. This section presents a sliding mode control that drive system (**??**) to track a given desired reference $x_i^d = (\phi_d, \theta_d, \psi_d, x_d, y_d, z_d)$, $(i = 1, ..., 6)$ in finite time. $\lambda_i > 0$, and $k_i > 0$ are constant control gains.

A. Position control

Let $e_i = x_i^d - \hat{x}_i$, $(i = 4, 5, 6)$, be the transnational error. Define the following sliding surface

$$s_i = \dot{e_i} + \lambda_i e_i + kp_i \int e_i \tag{18}$$

The time derivative of s_6 is

$$\begin{aligned} \dot{s_6} &= \ddot{e_6} + \lambda_6 \dot{e_6} + kp_6 e_6 \\ &= \ddot{z_d} - \dot{\hat{z}} + \lambda_6 \dot{e_6} + kp_6 e_6 \\ &= \ddot{z_d} - \frac{u_1}{m_t} C\hat{\phi}C\hat{\theta} + g + \lambda_6 \dot{e_6} + kp_6 e_6 \\ &= -k_6 sign(s_6) \end{aligned} \tag{19}$$

where $sign$ is the signum function. The input control $u1$ is extracted as

$$u_1 = \frac{m_t}{C\hat{\phi}C\hat{\theta}}(\ddot{z_d} + g + \lambda_6 \dot{e_6} + kp_6 e_6 + k_6 sign(s_6)) \tag{20}$$

We follow the same procedure to derive the virtual control inputs u_x and u_y we get

$$\begin{aligned} u_x &= \frac{m_t}{u_1}(\ddot{x_d} + \lambda_4 \dot{e_4} + kp_4 e_4 + k_4 sign(s_4)) \\ u_y &= \frac{m_t}{u_1}(\ddot{y_d} + \lambda_5 \dot{e_5} + kp_5 e_5 + k_5 sign(s_5)) \end{aligned} \tag{21}$$

The resulting closed loop dynamics is given by

$$\dot{s_i} = -k_i sign(s_i), (i = 4, 5, 6). \tag{22}$$

Consider the Lyapunov function

$$V(s_4, s_5, s_6) = \frac{1}{2}\sum_{i=4}^{6} s_i^2 \tag{23}$$

The derivative of V is computed as

$$\dot{V} = \sum_{i=4}^{6} s_i \dot{s_i} = -\sum_{i=4}^{6} k_i |s_i| < 0 \tag{24}$$

which imply that the system trajectories converge to the sliding surface in finite time and the error $e_i, (i = 4, 5, 6)$ converge exponentially to zero.

B. Attitude control

Let $e_i = x_i^d - \hat{x}_i$, $(i = 1, 2, 3)$, be the rotational error variables. Define the following sliding surface

$$s_i = \dot{e_i} + \lambda_i e_i + kp_i \int e_i \tag{25}$$

The time derivative of s_1 is

$$\begin{aligned} \dot{s_1} &= \ddot{e_1} + \lambda_1 \dot{e_1} + kp_1 e_1 \\ &= \ddot{\phi_d} - \dot{\hat{\phi}} + \lambda_1 \dot{e_1} + kp_1 e_1 \\ &= \ddot{\phi_d} - a_1 \hat{\theta}\hat{\psi} - a_4 \overline{\Omega}\hat{\theta} - b_1 u_2 + \lambda_1 \dot{e_1} + kp_1 e_1 \\ &= -k_1 sign(s_1) \end{aligned} \tag{26}$$

The input control u_2 is extracted as

$$u_2 = \frac{1}{b_1}(\ddot{\phi_d} - a_1 \hat{\theta}\hat{\psi} - \lambda_1 \dot{e_1} + kp_1 e_1 + k_1 sign(s_1)) \tag{27}$$

We follow the same procedure to derive the virtual control inputs u_3 and u_4 we get

$$\begin{aligned} u_3 &= \frac{1}{b_2}(\ddot{\theta_d} - a_2 \dot{\hat{\phi}}\hat{\psi} - \lambda_2 \dot{e_2} + kp_2 e_2 + k_2 sign(s_2)), \\ u_4 &= \frac{1}{b_3}(\ddot{\psi_d} - a_3 \dot{\hat{\phi}}\hat{\theta} - \lambda_3 \dot{e_3} + kp_3 e_3 + k_3 sign(s_3)) \end{aligned} \tag{28}$$

The resulting closed loop dynamics is given by

$$\begin{aligned} \dot{s_1} &= a_4 \overline{\Omega}\hat{\theta} - k_1 sign(s_1), \\ \dot{s_2} &= a_5 \overline{\Omega}\dot{\hat{\phi}} - k_2 sign(s_2), \\ \dot{s_3} &= -k_3 sign(s_3), \end{aligned} \tag{29}$$

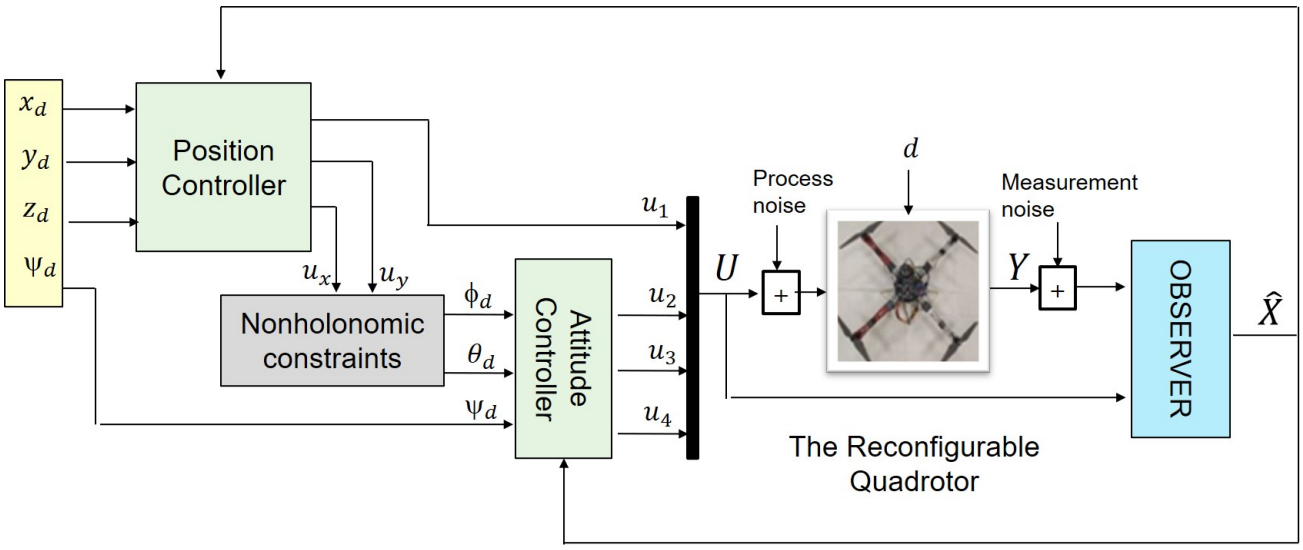


Figure 3. Controller-observer system of the reconfigurable quadrotor.

Consider the Lyapunov function

$$V(s_1, s_2, s_3) = \frac{1}{2}\sum_{i=1}^{3} s_i^2 \tag{30}$$

The derivative of V is given as follows

$\dot{V} = -k_1|s_1| - k_2|s_2| - k_3|s_3| + a_4\overline{\Omega}s_1\hat{\dot{\theta}} + a_5\overline{\Omega}s_2\hat{\dot{\phi}}$
$\leq -(k_1 - \kappa_2 a_4|\overline{\Omega}|)|s_1| - (k_2 - \kappa_1 a_5|\overline{\Omega}|)|s_2| - k_3|s_3|$
$\leq -(k_1 - 2\kappa_2 a_4\Omega_{max})|s_1| - (k_2 - 2\kappa_1 a_5\Omega_{max})|s_2| - k_3|s_3|,$

Thus, the system trajectories converge to the sliding surface in finite time and the error $e_i, (i = 1, 2, 3)$ converge exponentially to zero if the following gains are chosen such that

$$\begin{aligned} k_1 &\geq 2\kappa_2 a_4\Omega_{max}, \\ k_2 &\geq 2\kappa_1 a_5\Omega_{max}, \\ k_3 &\geq 0. \end{aligned} \tag{31}$$

V. Simulation and Discussions

In this section, several numerical simulation are performed to demonstrate the performance of the controller-observer developed for a reconfigurable quadrotor UAV. The main parameters used in this simulation are given in [1].
The integral sliding mode controller parameters are selected as follows:
$\lambda_i = (15, 15, 2, 9, 9, 2)$,
$k_i = (15, 15, 2, 6, 6, 2)$,
$kp_i = (0.6, 0.6, 0.6, 0.1, 0.1, 0.1)$, for $i = 1, 2, ..6$.
Two types of uncertainties are injected in the system to verify the robustness of the controller-observer. An internal disturbance includes the random Gaussian noise with zero mean value and process covariance $q = 10^{-2}$ and measurement covariance $r = 10^{-4}$. An external disturbance $d(t) = 0.01sin(2\pi t)$, which is assumed to be bounded $D = max(|d|) = 1$.

For EKF, the initial state and initial covariance are chosen to be $\hat{X}_{0/0} = 0_{12x1}$ and $\hat{P}_{0/0} = 1xI_{12x12}$ respectively, the covariance matrices are $Q_{12x12} = diag(10^{-2}, 10^{-2}..., 10^{-2})$,$R_{6x6} = diag(10^{-4}, 10^{-4}..., 10^{-4})$.
The parameters of the SMO are selected as follows: $K_1 = K_3 = 8, K_2 = K_4 = 0.8$, and $K_i = 1$, for $(i = 5, 6, ..., 12)$.
The desired trajectory is chosen to be rectangular.
the vehicle changes its configuration as follows : X-configuration from 0s to 40s, Y-configuration from 40s to 60s, O-configuration from 60s to 80s, T-configuration from 80s to 100s. These four configurations are shown on Figure 2.
We have simulated two cases:
-Case 1: States estimation by EKF,
-Case 2: States estimation by SMO.
Simulation results are depicted in Figures 4-7.
Figures 4 and 5 show the tracking positions, which are obtained using EKF and SMO respectively for states estimation. Figure 6 shows the evolution of control outputs and Figure7 shows the evolution of servomotors angles.

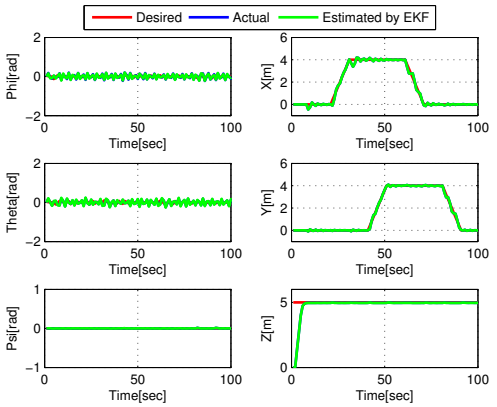


Figure 4. Positions tracking (Case 1).

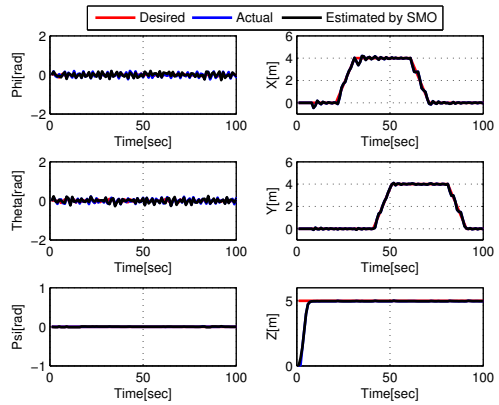


Figure 5. Positions tracking (Case 2).

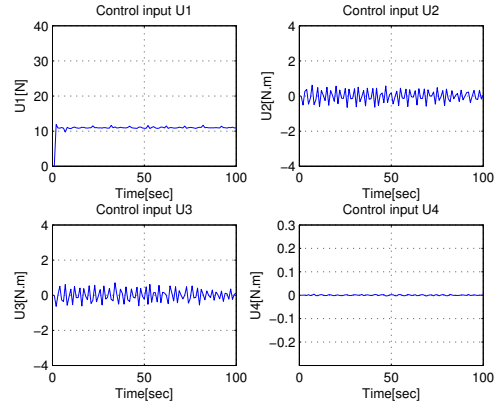


Figure 6. Control outputs.

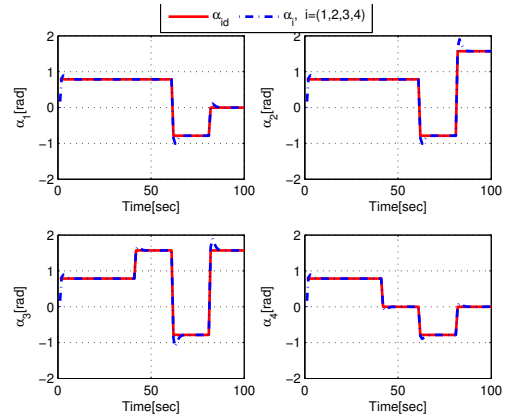


Figure 7. Evolution of servomotors angles.

VI. Conclusion

In this paper, we presented a controller-observer for altitude-attitude tracking control of a reconfigurable quadrotor tacking some flight configurations in the presence of internal and external disturbances. By assuming that not all states are measured and to avoid hardware sensors, an Extended Kalman Filter and a Sliding Mode Observer based states estimation are introduced in order to estimate the hidden state variables. Integral Sliding Mode Control was applied.

References

[1] A. Salmi, M. Guiatni, Y. Bouzid, S.H. Derrouaoui and F. Boudjema, "Fault Tolerant Control based on Thau Observer of a Reconfigurable Quadrotor with Toltal Loss of Actuator," Unmanned Systems.

[2] C. Kim, H. Lee, M. Jeong, and H. Myung, "A Morphing Quadrotor that Can Optimize Morphology for Transportation," arXiv:2108.06759 [cs], Aug. 2021, Accessed: Nov. 22, 2021. [Online]. Available: http://arxiv.org/abs/2108.06759

[3] D. Hu, Z. Pei, J. Shi, and Z. Tang, "Design, Modeling and Control of a Novel Morphing Quadrotor," IEEE Robot. Autom. Lett., vol. 6, no. 4, pp. 8013–8020, Oct. 2021, doi: 10.1109/LRA.2021.3098302.

[4] D. Yang, S. Mishra, D. M. Aukes, and W. Zhang, "Design, Planning, and Control of an Origami-inspired Foldable Quadrotor," in 2019 American Control Conference (ACC), Philadelphia, PA, USA, Jul. 2019, pp. 2551–2556. doi: 10.23919/ACC.2019.8814351.

[5] A. Fabris, K. Kleber, D. Falanga, and D. Scaramuzza, "Geometry-aware Compensation Scheme for Morphing Drones," arXiv:2003.03929 [cs], Mar. 2020, Accessed: Nov. 22, 2021. [Online]. Available: http://arxiv.org/abs/2003.03929

[6] D. Falanga, K. Kleber, S. Mintchev, D. Floreano, and D. Scaramuzza, "The Foldable Drone: A Morphing Quadrotor That Can Squeeze and Fly," IEEE Robot. Autom. Lett., vol. 4, no. 2, pp. 209–216, Apr. 2019, doi: 10.1109/LRA.2018.2885575.

[7] Xiong, H., Hu, J., Diao, X.: Optimize energy efficiency of quadrotors via arm rotation. J. Dyn. Syst. Meas. Control. 141(9) (2019)

[8] S. H. Derrouaoui, Y. Bouzid, M. Guiatni and I. Dib, "A Comprehensive Review on Reconfigurable Drones: Classification, Characteristics, Design and Control Technologies," Unmanned Systems, Vol. 9, No. 3, pp 1–27, 2021, doi: https://doi.org/10.1142/S2301385022300013

[9] S. H. Derrouaoui, Y. Bouzid and M. Guiatni, "Towards a new design with generic modeling and adaptive control of a transformable quadrotor". The Aeronautical Journal, 125(1294), pp 2169-2199, Jul 2021, doi:10.1017/aer.2021.54.

[10] Derrouaoui, S. H., Bouzid, Y., Guiatni, M., Dib, I., and Moudjari, N.,"Design and Modeling of Unconventional Quadrotors", 28th Mediterranean Conference on Control and Automation (MED), 2020, doi:10.1109/med48518.2020.9183002.

[11] Derrouaoui, S.H.; Bouzid, Y.; Guiatni, M. Nonlinear Robust Control of a New Reconfigurable Unmanned Aerial Vehicle. Robotics, 2021, 10, 76, https://doi.org/10.3390/robotics10020076.

[12] Kalman, R. E. 1960. "A New Approach to Linear Filtering and Prediction Problems," Transaction of the ASME—Journal of Basic Engineering, pp. 35-45 (March 1960).

[13] Abhisek K. Behera, Saikat Mondal, Bijnan Bandyopadhyay ; A decoupled design of a robust sliding mode observer; Automatica Volume 148, February 2023, 110799.

X

SIGNAL AND IMAGE PROCESSING (SIP)

Sommaire

X.1 A new algorithm for extracting fetal (fECG) signal from abdominal (aECG) using wavelet transform **568**
X.2 A comparative study of local binary pattern and local ternary pattern for fault detection in induction motors **577**
X.3 Speech denoising based on empirical wavelet transform and adaptive threshold **581**
X.4 Efficient ECG signal denoising technique based on the empirical mode decomposition method and the discrete wavelet transform **586**
X.5 Efficient gear fault detection in rotating machines through envelope-derivative operator analysis **591**
X.6 Comparative evaluation of YOLOv5 and YOLOv8 across diverse datasets . . . **595**

A new algorithm for extracting fetal (fECG) signal from abdominal (aECG) using wavelet transform

Lilia Radjef [1], Tahar Omari [1], Mohamed Salah Benlatreche[2], Ahmed el amine Tayeb Cherif [1], Khaoula Ladgi[1]

[1] *Ingénieurie Des Systèmes électriques Departement, Faculty of Technology, Ingénierie des Sytémes et des Telecommunication Laboratory, Boumerdes University, Algeria*

[2] *Centre Universitaire Abdel Hafid Boussouf Mila, Algeria*
l.radjef@univ-boumerdes.dz
tahar.omari@univ-boumerdes.dz

***Abstract*— The fetal electrocardiogram (fECG) is a non-invasive technique for monitoring the electrical activity of the fetus during pregnancy. Reading the (fECGs)s remains crucial in detecting defects or anomalies in fetal health. However, the processed signals are generally superimposed on the maternal signal (mECG) and noise. In this study, we propose a new algorithm to extract the (fECG) from the abdominal (aECG) signal based on biorthogonal wavelet 2.4. The (ECG)s signals are obtained from the open-access database "Abdominal and Direct Fetal ECG Database" available on Physiobank. After the (ECG)s signals pre-processing with a band-pass filter of 3-30 Hz. An 8-level wavelet decomposition is used to extract the (mECG), a 6-level reconstruction is applied to detect the maternal (QRS)s, and R-peaks are detected by applying an envelope. Maternal heart rate (MRC) is calculated by detecting the envelope peaks. Adaptive thresholding is then applied to the detected envelope peaks. This allows each pulse to be covered by a specific window that locates only the maternal (mECG). Multiplication of the abdominal signals by these windows directly produces the fetal (fECG) signals. This algorithm was evaluated by assessing the sensitivity and accuracy of maternal and fetal R-wave detection. The mean sensitivity and accuracy of the maternal (mECG) were (98.8%) and (97.6%) respectively, with 83 out of 83 beats correctly detected. The mean sensitivity and accuracy of (fECG) were 94.9% and 93.2%, respectively, with 110 out of 116 beats correctly detected. The results obtained show a satisfactory recording performance.**

***Keywords:* Fetal Electrocardiogram (fECG), Maternal Electrocardiogram (mECG), Abdominal Electrocardiogram (aECG), Signal Processing, Wavelet Transform, (fECG) Extraction.**

I. INTRODUCTION

Monitoring fetal cardiac activity, as reflected by a fetal electrocardiogram (fECG), is crucial to assess the condition of the fetal heart during pregnancy [1]. To identify factors that affect fetal and maternal health and to prevent intrauterine death or permanent damage [2]. Since Cremer's work in 1906 [3], various invasive and non-invasive methods of fetal monitoring have been proposed to provide information about the condition of the fetus, including, fetal phonocardiography (fPCG) [4-5], fetal echocardiography (fECHO) [6], fetal magnetocardiography (fMCG) [7-8], and cardiotocography (CTG) [9], and fetal electrocardiography (fECG) [10]. There are two types of electrocardiographic techniques [11-12]. Direct fetal electrocardiography can be used during delivery after the rupture of membranes [13]. However, this technique is not recommended for prenatal examinations. An indirect measuring method emerged in the 1970s. The mother's abdomen is covered with multi-channel electrodes for the measurement of electrical signals from the fetus' heart [14]. The fetal electrocardiogram (fECG), similar to the maternal (ECG), has both P and T waves, and (QRS) complex. The fetal complex (QRS) is the first feature extracted from the abdominal signal (ECG). The (fECG) is a superposition of the (mECG) and (fECG) and other artifacts [15]. The complexity of (fECG) analysis is related to the low amplitude of the fetal signal compared to the maternal signal, the non-stationary nature of the recorded signals, and the relatively low signal-to-noise ratio of (fECG) [16-17]. The (fECG) can be used to diagnose cardiac abnormalities such as acidosis [18], premature ventricular contractions (PVCs) [19], and arrhythmias [20], as well as to assess the effectiveness of treatment and analyze cardiac parameters [21]. However, the abdominal signal contains various interfering signals such as the maternal electrocardiogram (mECG) [22-23], ambulatory artifact [24], maternal electromyogram (EMG) signal [25], electrical line, and random electronic noise [26]. Therefore, to monitor the (fECG) effectively, it is necessary to develop signal processing algorithms that can extract the (fECG) from the (mECG). Filtering and wavelet processing methods have been developed [27-28-29-30-31-32]. Parsaei et al. [33] propose an algorithm to extract the fetal (fECG) from an (aECG) recorded on the mother's abdomen. The original signal is extracted using a two-level wavelet transform. They used the

Daubechie wavelet transform, which has a shape similar to that of heart waves. To reduce the effect of noise, the resulting signal is then low-pass filtered using the Savitzky-Golay filter. The results show that the proposed algorithm has a promising performance using synthetic and real (ECG) signals. Kamalakar et al [34] developed a feature extraction system (fECG) based on multiscale discrete wavelet transform (DWT). The (QRS) complex is accurately detected. Two-channel perfect reconstruction (PR) filters are used to implement the discrete wavelet transform method. The developed maternal-fetal (ECG) monitor was tested in a local hospital on 35 pregnant women at different intervals during pregnancy. This reliable system detects all (fECG) beats with an accuracy of better than 99.5%. Krupa et al. [35] describe an algorithm based on time-frequency analysis, using the fractional Fourier transform. The abdominal signals (mECG) obtained from pregnant women are pre-processed and subjected to wavelet analysis. The residual wavelet decomposition process is used to obtain a (fECG) and calculate the fetal heart rate (FRC). Al-Sheikh et al [36] propose an adaptive filtering algorithm based on the discrete inverse recursive wavelet transform (DWT-RI) to extract the fetal electrocardiogram from maternal abdominal signals. The algorithm uses the maternal thoracic electrocardiogram (mECG) as a reference and extracts the components of the abdominal signal (aECG) after removing the projections from the (mECG). The algorithm outperforms other adaptive filtering methods regarding accuracy and positive predictivity. Darsana et al [37] also proposed a hybrid technique for (fECG) extraction using an adaptive filtering algorithm based on recursive least squares (RLS) and a stationary wavelet transform (SWT). They improve the accuracy of fetal heartbeat detection using a spatial selective noise filtering (ISSNF) algorithm. The results show that this hybrid method offers better performance than traditional adaptive filtering methods. Thus, these approaches to fetal (ECG) extraction show promise for producing a high-quality signal with low distortion. Karvounis et al. [38] present a new automated method for the detection of (QRS)s complexes of fetal heart activity using multi-channel maternal (ECG) recordings. No additional pre-processing steps for noise filtering are required. The approach is based on the complex continuous wavelet transform and the theory of modulus maxima. Real signals recorded at different times have been used to validate the method. All fetal beats are detected (accuracy: 99.5%). Para et al. [39] present an algorithm that uses wavelet analysis to extract the fetal heart rate from an ECG signal measured in the mother's abdomen. The algorithm consists of three steps: first, the abdominal ECG signal is recorded and decomposed using the wavelet transform to estimate the characteristics of the non-stationary signal. Next, the maternal ECG signal is extracted from the abdominal signal by subtraction. Finally, the fetal ECG signal is obtained by identifying the R peaks in the extracted signal, enabling the fetal heart rate to be calculated. The algorithm is tested using MATLAB on 15 signals recorded in Physionet, demonstrating the reliability of the proposed approach. Abuhantash et al. [40] propose an approach using swarm decomposition (SWD) to isolate fetal components from the abdomen. Using higher-order statistics (HOS) to detect R-peaks, they obtained a high sensitivity of 99.8% and a positive predictivity of 99.8% for the detection of fetal R-peaks. These results demonstrate the effectiveness of (SWD) in extracting fetal (ECGs) of high morphological quality. Ramachandran et al. [41] proposed an algorithm for extracting the fetal (fECG) from the abdominal signal using a single channel. The abdominal (ECG) was pretreated to eliminate signal noise. Maternal R-peaks were detected by thresholding, first-order Gaussian differentiation, and crossed-zero detection on the pre-processed signal. To reduce noise, polynomial approximation and total variation (PATV) improves the signal-to-noise ratio. The algorithm was tested on three databases to assess its performance (DB_{III} abdominal and direct fetal ECG database). The accuracy and the sensitivity were 92.41% and 93.8% respectively. Lima-Herrera et al. [28] introduce a novel method for extracting fetal electrocardiogram (fECG) using wavelet decomposition and an adaptive noise reduction filter with the least mean squares (LMS) algorithm. The method first removes spurious signals through the application of an (FIR) filter and wavelet analysis. The (LMS) algorithm is then used to process the detailed coefficients of the thoracic and abdominal signals, which have similar shapes. Additionally, the stationary wavelet transform (SWT) is applied as a filter. The algorithm was tested on 10 non-invasive recordings from two databases, DaISy and MIT/PhysioNet, featuring signals from different pregnant women at gestational ages between 35 and 40 weeks. The method achieved a 96% accuracy in identifying the (fECG) R-wave, making it a promising approach for future research. The algorithm was used to analyze fetal heart rate (FHR) and fetal heart rate variability (FHRV). In this study, a simple and effective algorithm is proposed for the extraction of the (fECG) from the abdominal (aECG). The paper is organized as follows: Section II, describes the proposed approach. Section III: methodology, the database, and the algorithm. Section IV presents the results. Section V: Discussion and section VI concludes the paper.

II. PROPOSED APPROACH

To extract the fetal electrocardiogram (fECG) from the mother's abdomen, we used a filtering method, and the wavelet transform. The wavelet transform is the most popular and effective method for detecting the characteristic points of an (ECG). We applied (bior2.4) wavelet to our signal to extract the fetal heart rate using MATLAB software.

a. Wavelet transform

Wavelet transform (WT) is a mathematical model, a widely used method for detecting features in (ECG) signals. [42-43]. It is particularly useful for analyzing non-stationary signals and can be used for noise reduction and fetal heart rate detection [44-45]. The wavelet transform replaces the sinusoid of the Fourier transform with a family of translations and dilations of a base function called the mother wavelet. $\boldsymbol{\Psi}$, Wavelet families can be characterized by four main properties: the existence of associated filters, orthogonality or biorthogonality, compact or non-compact support, and real or complex wavelets. Overall, the wavelet transform can be represented by a mathematical equation:

$$F(a,b) = \int_{-\infty}^{+\infty} f(x)\psi^{*}_{(a,b)}(x)dx \quad (1)$$

Where $\psi_{(a,b)}$ is the mother wavelet.

Many studies have used the wavelet transform (WT) due to its advantages in time-frequency representation for (fECG) extraction [46-47-48-49-50-51-52-53].

b. Biorthogonal wavelet

A biorthogonal wavelet is used for signal or image reconstruction, the ideal is to use two wavelets, one for decomposition and the other for reconstruction, to solve the phase distortion problem.

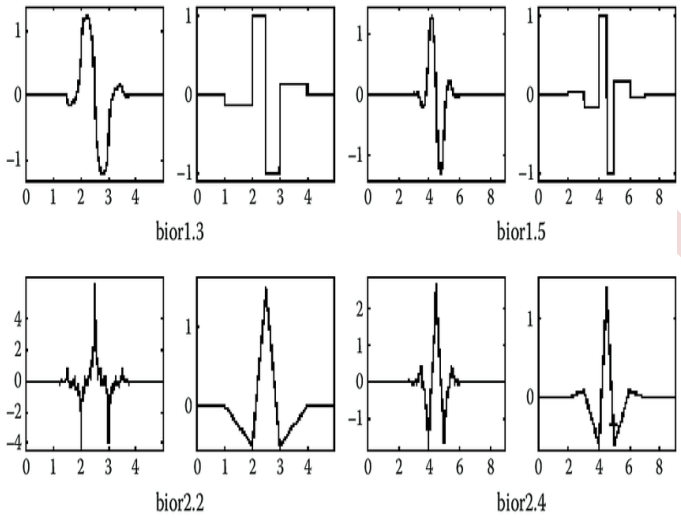


Figure 1. Biorthogonal wavelet

III. METHODOLOGY

The process of extracting fetal (fECG) involves the following steps:

- Import raw data from Physionet.
- Pre-processing with a bandpass filter.
- Application of the Biorthogonal 2.4 wavelet transform.
- Detection of R peaks and calculation of (MRC).
- Extraction of (fECG) and calculation of (FRC).

a. Database definition

The signals processed are extracted from the (adfecgdb) " Abdominal and Direct Fetal ECG Database " of Physiobank. The database contains multi-channel fetal electrocardiogram recordings obtained from five (5) different women between 38 and 41 weeks gestation during labor. Each recording consists of four differential signals recorded from the mother's abdomen and the reference direct fetal electrocardiogram recorded from the fetal head [54]. They are sampled at 1 KHz with a resolution of 16 bits and a recording duration of 10 seconds. The records were obtained at the Department of Obstetrics, Silesian Medical University, using the KOMPOREL system for the acquisition and analysis of fetal electrocardiograms.

b. Pre-processing

Signal filtering is a crucial step in the fetal (fECG) extraction process. The raw signal from the Physionet is noisy. Different noise sources exist such as power line interface, baseline drift, maternal (EMG), and motion artifacts. We use a bandpass filter, which is designed to reduce noise while preserving important signal characteristics. It separates the components of the ECG signal, including QRS complexes, P waves, and T waves. The bandpass [3-30Hz] filter selects a specific frequency range in which the fetal (fECG) signal is found.

c. Algorithm of fetal (ECG) extraction

This section presents our algorithm (shown in Figure 2), for extracting the fetal electrocardiogram (fECG) signal from the abdominal signal (aECG). The algorithm consists of several steps including data collection, signal processing, band-pass filtering, R-peak detection, normalization, and calculation of maternal and fetal heart rates. The data is collected from a database using the MATLAB data import function (Figure 3). Then, signal pre-processing of the raw waveforms by applying filters to remove noise, baseline deviation, and power line interference for both direct and abdominal (ECG) signals. A band-pass filter is used to characterize the frequency content of the signals within the 3-30 Hz frequency (Figures 4 and 5). The biorthogonal 2.4 wavelet is chosen for decomposition and reconstruction, it offers better performance and a lower error compared to other wavelets. An 8-level wavelet decomposition is used to extract the (mECG) (Figures 6 and 7). The reconstruction is based on level 6 as it contains the maternal (QRS)s band (Figure 8). For our signal, which has a sampling frequency of 1 kHz, the first level of decomposition is equivalent to filtering at 500 Hz, and the second at 250 Hz, so the 5th level is 31.25 Hz. After reconstruction, the mother's (mECG) became more visible (Figure 9). The signal is further processed by envelope detection (Figure 10). Maternal R-peaks are localized using The (findpeak function) (Figure 10). Maternal heart rate (MRC) is calculated from the time interval between two R-R peaks. Adaptive thresholding is then applied to the detected envelope peaks. This allows each pulse to be covered by a specific window that locates only the maternal (mECG) (Figure 11). Multiplication of the abdominal signals by these windows directly produces the (fECG) signals (Figure 12). The fetal (QRS), R-peaks, and R-R intervals were obtained to calculate the (FRC).

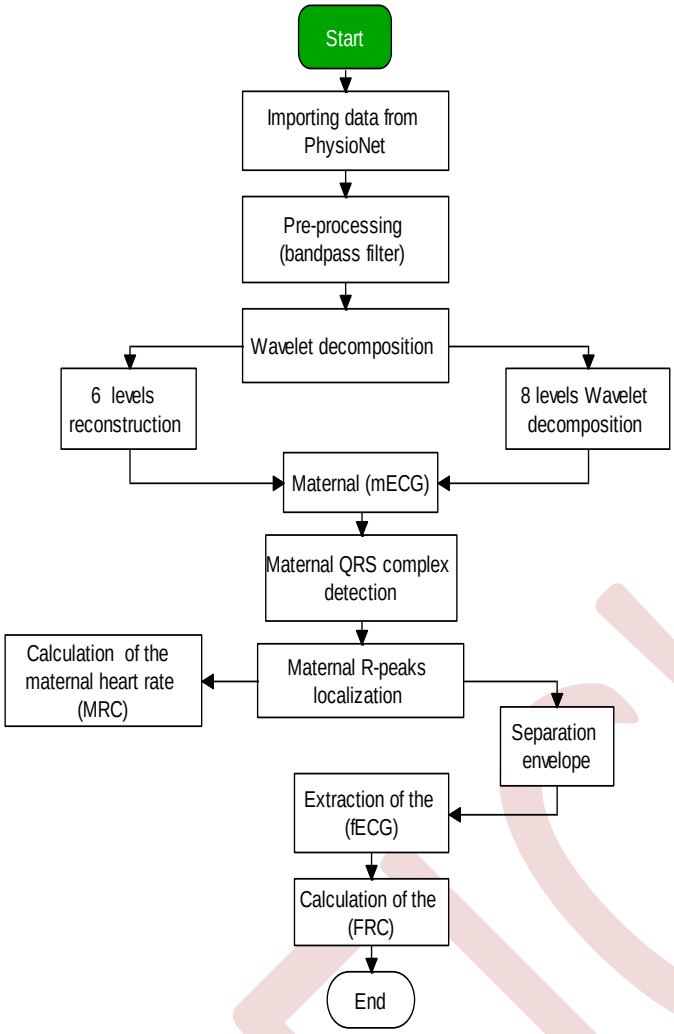


Figure 2. Diagram of fetal (fECG) extraction algorithm

IV. RESULTS AND DISCUSSION

The figures illustrate the various stages of extracting the (fECG) signal from the raw abdominal (aECG) signal. Signal processing, including filtering, noise extraction and reduction, and the application of thresholding, Wavelet decomposition, and reconstruction of abdominal (ECG) signals are used to analyze the different frequency components of the signal and to understand, its temporal structure. The thresholding technique defined peaks in the maternal (mECG). A peak is detected when the amplitude of the signal (ECG) exceeds the threshold.

a. Display of (ECG) signals (direct/abdominal)

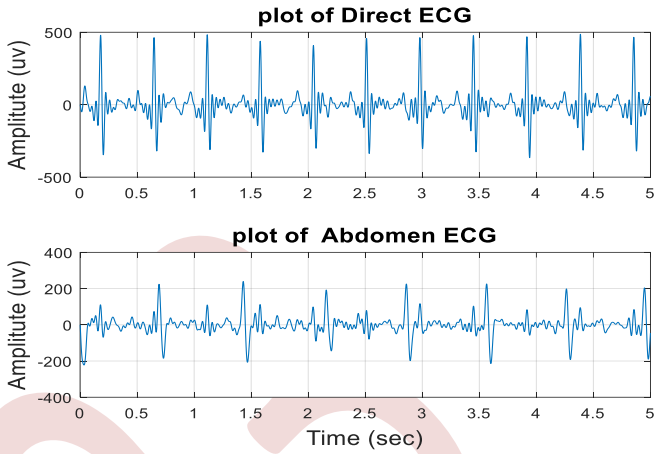


Figure 3. ECG signal display (direct/abdomen)

Figure 3 shows the raw Direct and abdominal (ECG) signals as recorded. It contains artifacts.

b. Band-pass filter

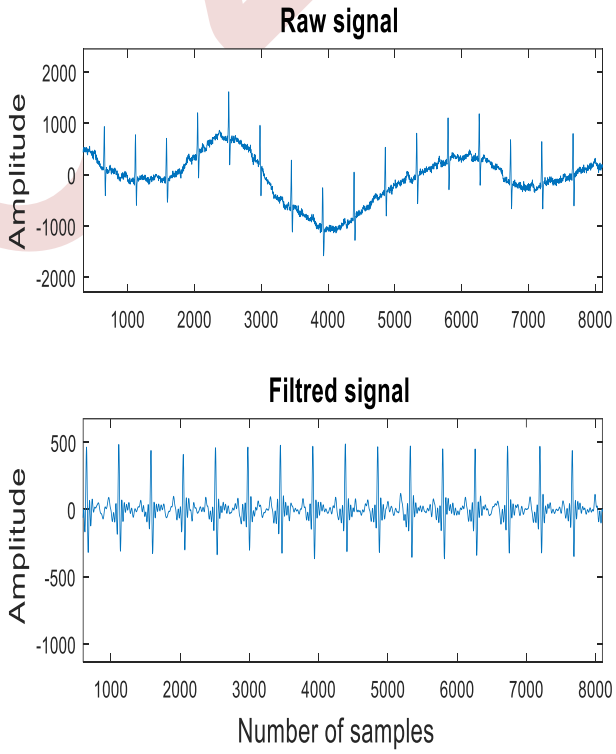


Figure 4. Direct (ECG) after band-pass filtering [3-30 Hz]

In Figure 4, the Direct (ECG) signal has been filtered to reduce noise and artifacts with a band-pass filter. This operation improves the signal clarity.

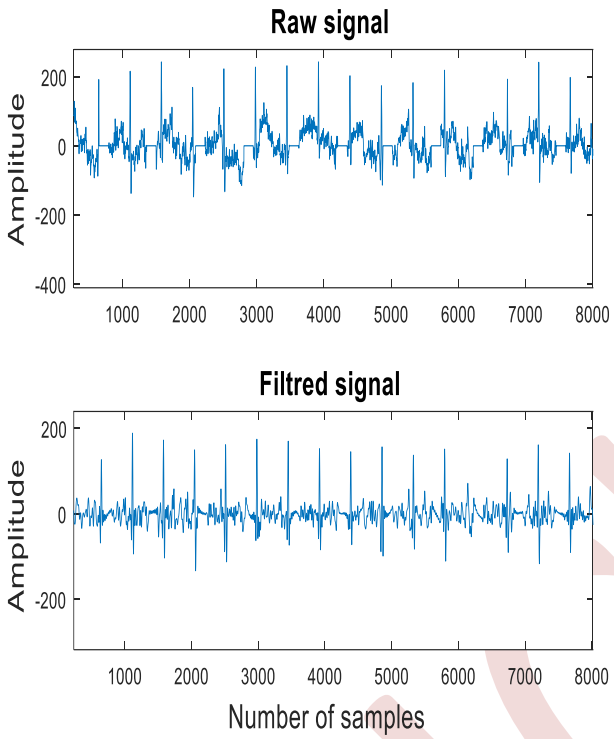


Figure 5 Abdominal (ECG) after band-pass filtering [3-30Hz]

The abdominal (aECG) has been filtered with band-pass filtering [3-30 Hz] to remove unwanted interference (Figure 5). It improves signal quality and simplifies subsequent extraction of the (fECG) signal.

c. Wavelet decomposition

Wavelet decomposition displays show several superimposed plots (Figure 6), representing the different sub-bands of the (ECG) signal. It is used to display signal variations at different frequencies.

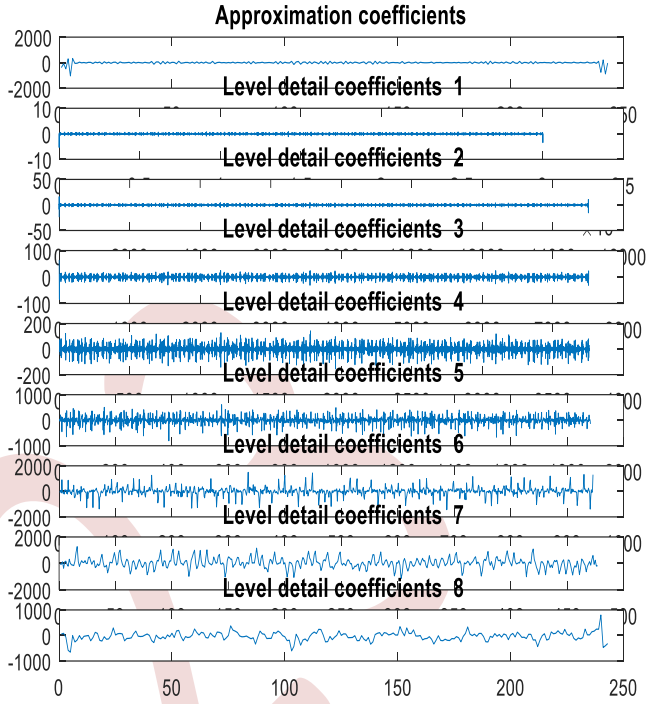


Figure 6. Level 8 decomposition detail coefficients

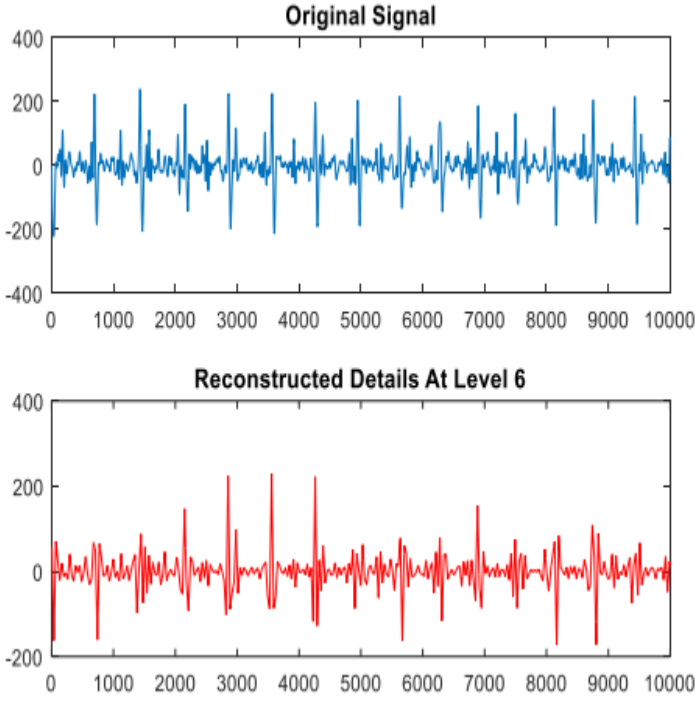


Figure 7. Level 6 Reconstruction of decompositions

The wavelet reconstruction (Figure 7) shows the (ECG) signal reconstructed from the sub-bands, highlighting the information recovered from each scale.

d. Maternal (ECG)

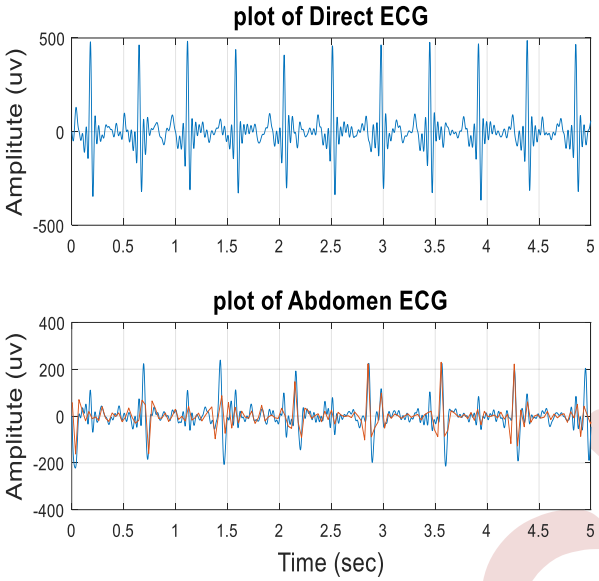


Figure 8. Obtain the maternal (ECG)

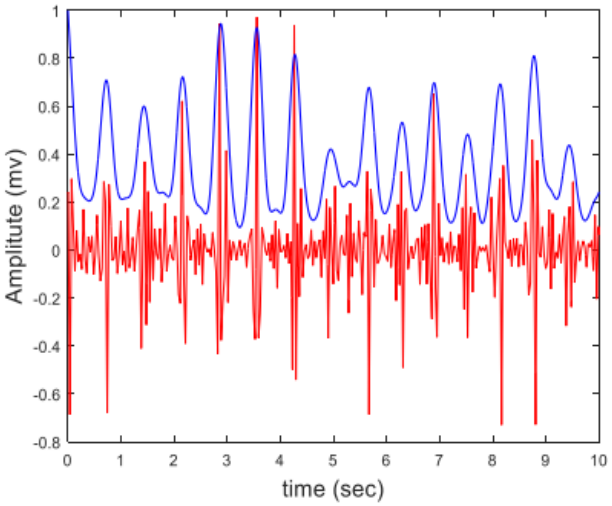


Figure 9. Maternal (ECG) signal with envelope

The maternal (mECG) envelope is a curve that follows the maximum variations in the (ECG) signal (Figure 9). It is obtained by extracting the maximum amplitudes of each R-wave from the (ECG) and combining them to form an envelope curve.

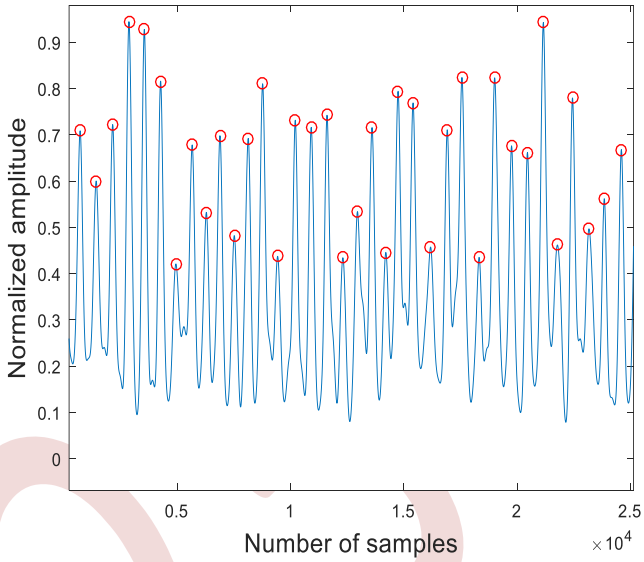


Figure 10. Detection and localization of the maternal R-peaks

R-waves correspond to the characteristic peaks of the cardiac cycle. Once the maternal (mECG) peaks have been detected (Figure 10), the maternal heart rate (MRC) is calculated by measuring the time interval between these peaks. The inverse of this interval is the heart rate.

e. Calculation of the maternal heart rate (MRC)

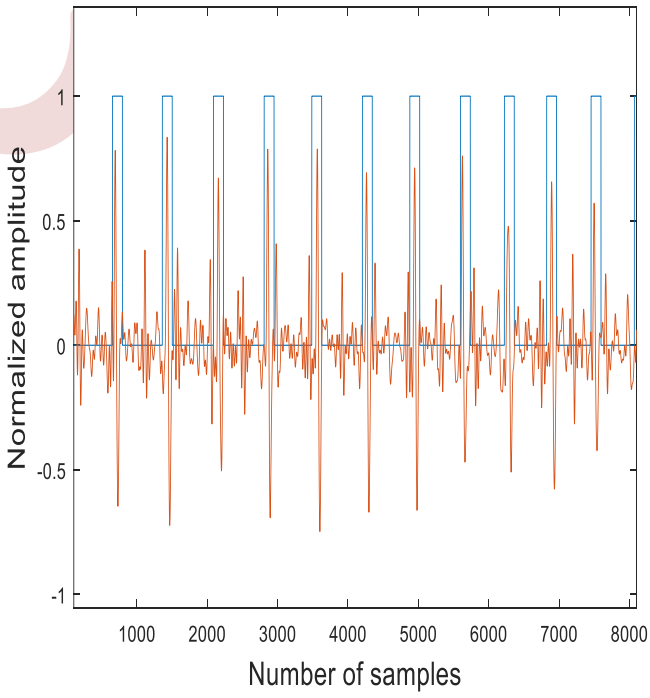


Figure 11. Separation envelope

In Figure 11, thresholding has been applied to the (aECG) signal. The signal values outside the threshold are eliminated, removing additional noise and retaining only the relevant parts of the signal.

f. Extractions of the fetal (ECG)

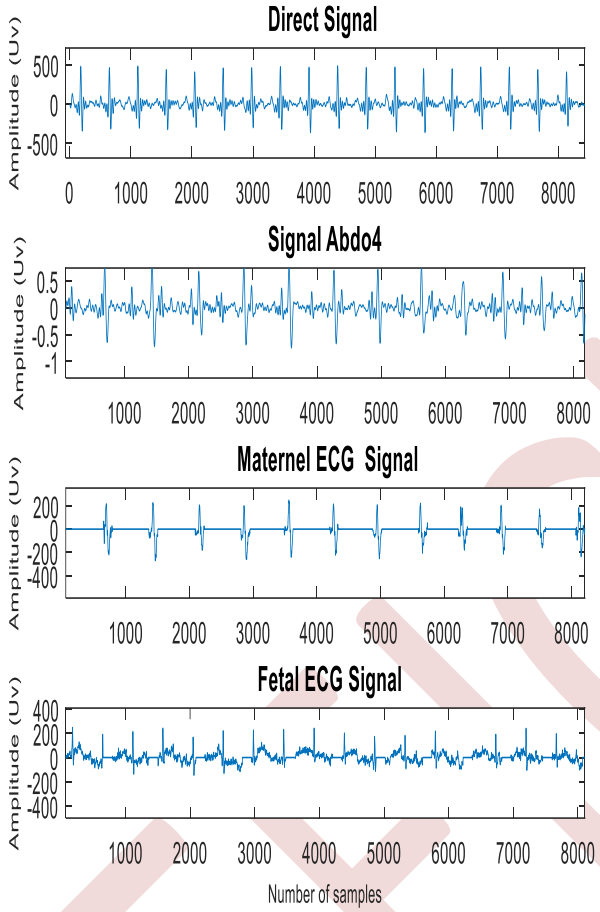


Figure 12. Separating results

Figure 12, shows the (fECG) signal extracted from the (aECG) signal. The algorithm used takes account of the specific characteristics of the (fECG) signal, such as its frequency and waveform, to isolate and separate it from the rest of the signal.

g. Algorithm sensitivity (SEN) and accuracy(ACC)

TABLE I. R-WAVE DETECTION RESULTS

	Number of beats	**TP**	**FP**	**FN**	**SEN (%)**	**ACC (%)**
Maternal ECG	83	82	1	1	98.8	97.6
Fetal ECG	116	110	2	06	94.9	93.2

The sensitivity and specificity are given by the equations:

$$SEN = TP/(TP + FN) \times 100\% \quad (2)$$

$$ACC = TP/(TP + FN + FP) \times 100\% \quad (3)$$

With: TP: number of correct detections, FP: number of false detections, FN: number of missed detections, ACC: accuracy, SEN: sensitivity.

The previous table (TABLE 1) shows the sensitivity and accuracy values of the algorithm of R-wave detection. The total number of beats recorded on the signals was 199, and the average sensitivity and accuracy of the maternal (mECG) were (98.8%) and (97.6) respectively, with a correct detection number of 83 out of 83 beats. The average sensitivity and accuracy of the fetal (fECG) were (94.9%) and (93.2%) respectively, with a correct detection number of 110 out of 116 beats. The results obtained show satisfactory performance. It should be noted that only correct detections are used in this study.

V. DISCUSSION

The study compared the algorithm outputs with previously published results from studies with the same database [39-40]. Results showed that the algorithm had significant advantages over other existing methods. The algorithm's simplicity, high sensitivity, and accuracy in detecting maternal and fetal (ECG)s, R-peaks, and a reduction in false detections. The algorithm successfully detected P, T waves, and (QRS)s complex in the fetal (ECG)s, ensuring a better assessment of fetal health and identification of cardiac events. Effectively handling artifacts leads to an overall improvement in the quality of fetal (ECG) extraction.

VI. CONCLUSION

In this study, we propose a new algorithm for fetal (ECG) extraction from signals recorded on the mother's abdomen (aECG). The (ECG)s signals are obtained from the open-access Abdominal and Direct Fetal ECG Database. This algorithm combines pre-processing and biorthogonal 2.4 wavelet analysis. We evaluated the algorithm's performance by assessing the accuracy and sensitivity of R-wave detection. The results are promising in terms of sensitivity and accuracy. Extraction of twin fetal (ECG) is an area in which this work can be extended for future studies.

CONFLICT OF INTERESTS

The authors declare that they have no conflict of interest.

REFERENCES

[1] *ALNUAIMI, Saeed Abdulrahman, JIMAA, Shihab, et KHANDOKER, Ahsan H. Fetal cardiac Doppler signal processing techniques: challenges and future research directions. Frontiers in bioengineering and biotechnology, 2017, vol. 5, p. 82.*

[2] MARTINEK, R.; KAHANKOVA, R.; JEZEWSKI, J.; JAROS, R.; MOHYLOVA, J.; FAJKUS, M.; NEDOMA, J.; JANKU, P.; NAZERAN, H. Comparative Effectiveness of ICA and PCA in

Extraction of Fetal ECG From Abdominal Signals: Toward Non-invasive Fetal Monitoring. Front. Physiol. 2018, 9.

[3] CREMER M. ¨Uber die Direkte Ableitung der Aktionstrome des Menschlichen Herzens vom Oesophagus und ¨Uber das Elektrokardiogramm des Fetus. M¨unchener Medizinische Wochenschrift. April.1906 53 :811–813.

[4] KOVÁCS, F.; HORVÁTH, C.; BALOGH, Á.T.; HOSSZÚ, G. Fetal phonocardiography—Past and future possibilities. Comput. Methods Progr. Biomed. 2011, 104, 19–25.

[5] KAHANKOVA, Radana, MIKOLASOVA, Martina, JAROS, Rene, et al. A review of recent advances and future developments in fetal phonocardiography. IEEE Reviews in Biomedical Engineering, 2022, vol. 16, p. 653-671.

[6] ROSENBERG, Katherine B., MONK, Catherine, GLICKSTEIN, Julie S., et al. Referral for fetal echocardiography is associated with increased maternal anxiety. Journal of Psychosomatic Obstetrics & Gynecology, 2010, vol. 31, no 2,

[7] KARINIEMI, V., AHOPELTO, J., KARP, Pekka Juhani, et al. The fetal magnetocardiogram. 1974.

[8] GRIMM, Barbara, HAUEISEN, Jens, HUOTILAINEN, Minna, et al. Recommended standards for fetal magnetocardiography. Pacing and clinical electrophysiology, 2003, vol. 26, no 11, p. 2121-2126.

[9] ALFIREVIC, Zarko, GYTE, Gillian ML, CUTHBERT, Anna, et al. Continuous cardiotocography (CTG) is a form of electronic fetal monitoring (EFM) for fetal assessment during labor. Cochrane Database of Systematic Reviews, 2017, no 2.

[10] ZHANG, Yuwei, GU, Aihua, XIAO, Zhijun, et al. Wearable fetal ECG monitoring system from abdominal electrocardiography recording. Biosensors, 2022, vol. 12, no 7, p. 475.

[11] AGOSTINELLI, Angela, GRILLO, Marla, BIAGINI, Alessandra, et al. Noninvasive fetal electrocardiography: An overview of the signal electrophysiological meaning, recording procedures, and processing techniques. Annals of Noninvasive Electrocardiology, 2015, vol. 20, no 4, p. 303-313.

[12] MATONIA, Adam, JEZEWSKI, Janusz, KUPKA, Tomasz, et al. Fetal electrocardiograms, direct and abdominal with reference heartbeat annotations. Scientific data, 2020, vol. 7, no 1, p. 200.

[13] JEZEWSKI, Janusz, MATONIA, Adam, KUPKA, Tomasz, et al. Determination of fetal heart rate from abdominal signals: evaluation of beat-to-beat accuracy about the direct fetal electrocardiogram. Biomedizinische Technik/Biomedical Engineering, 2012, vol. 57, no 5, p. 383-394.

[14] SAMENI, Reza et CLIFFORD, Gari D. A review of fetal ECG signal processing; issues and promising directions. The open pacing, electrophysiology & therapy journal, 2010, vol. 3, p. 4.

[15] HASAN, Muhammad Asfarul, REAZ, M. B. I., IBRAHIMY, M. I., et al. Detection and processing techniques of FECG signal for fetal monitoring. Biological Procedures Online, 2009, vol. 11, p. 263-295.

[16] KAHANKOVA, Radana, MARTINEK, Radek, JAROS, Rene, et al. A review of signal processing techniques for non-invasive fetal electrocardiography. IEEE Reviews in Biomedical Engineering, 2019, vol. 13, p. 51-73.

[17] SAMENI, Reza. Extraction of fetal cardiac signals from an array of maternal abdominal recordings. 2008. Thèse de doctorat. Institut National Polytechnique de Grenoble-INPG; Sharif University of Technology (SUT).

[18] ANISHA, M., KUMAR, S. S., NITHILA, Ezhil E., et al. Detection of fetal cardiac anomaly from composite abdominal electrocardiogram. Biomedical Signal Processing and Control, 2021, vol. 65, p. 102308.

[19] ABBOUD, Shimon, BARKAI, Gad, MASHIACH, Shlomo, et al. Quantification of the fetal electrocardiogram using averaging technique. Computers in biology and medicine, 1990, vol. 20, no 3, p. 147-155.

[20] BEHAR, Joachim A., BONNEMAINS, Laurent, SHULGIN, Vyacheslav, et al. Noninvasive fetal electrocardiography for the detection of fetal arrhythmias. Prenatal diagnosis, 2019, vol. 39, no 3, p. 178-187.

[21] CLIFFORD, Gari D., SILVA, Ikaro, BEHAR, Joachim, et al. Non-invasive fetal ECG analysis. Physiological measurement, 2014, vol. 35, no 8, p. 1521.

[22] JAGANNATH, D. J. et SELVAKUMAR, A. Immanuel. Issues and research on fetal electrocardiogram signal elicitation. Biomedical signal processing and control, 2014, vol. 10, p. 224-244.

[23] MIRZA, Sarfaraj, BHOLE, Kalyani, et SINGH, Prateek. Fetal ECG extraction and QRS detection using independent component analysis. In: 2020 16th IEEE International Colloquium on Signal Processing & Its Applications (CSPA). IEEE, 2020. p. 157-161.

[24] LUO, Yurong, HARGRAVES, Rosalyn H., BELLE, Ashwin, et al. A hierarchical method for removal of baseline drift from biomedical signals: application in ECG analysis. The Scientific World Journal, 2013, vol. 2013.

[25] JAROS, Rene, MARTINEK, Radek, et KAHANKOVA, Radana. Non-adaptive methods for fetal ECG signal processing: A review and appraisal. Sensors, 2018, vol. 18, no 11, p. 3648.

[26] PANIGRAHY, D., RAKSHIT, M., et SAHU, P. K. An efficient method for fetal ECG extraction from single channel abdominal ECG. In: 2015 international conference on industrial instrumentation and control (ICIC). IEEE, 2015. p. 1083-1088.

[27] DESAI, Kamalakar D. et SANKHE, Manoj S. A real-time fetal ECG feature extraction using multiscale discrete wavelet transform. In: 2012 5th international conference on biomedical engineering and informatics. IEEE, 2012. p. 407-412.

[28] LIMA-HERRERA, Sara Lilia, ALVARADO-SERRANO, Carlos, et HERNANDEZ-RODRIGUEZ, Pablo Rogelio. Fetal ECG extraction based on adaptive filters and Wavelet Transform: Validation and application in fetal heart rate variability analysis. In: 2016 13th International Conference on Electrical Engineering, Computing Science and Automatic Control (CCE). IEEE, 2016. p. 1-6.

[29] ALSHEBLY, Y. S. et NAFEA, Marwan. Isolation of fetal ECG signals from abdominal ECG using wavelet analysis. Irbm, 2020, vol. 41, no 5, p. 252-260.

[30] KHAMENE, Ali et NEGAHDARIPOUR, Shahriar. A new method for the extraction of fetal ECG from the composite abdominal signal. IEEE Transactions on Biomedical Engineering, 2000, vol. 47, no 4, p. 507-516.

[31] WU, Shuicai, SHEN, Yanni, ZHOU, Zhuhuang, et al. Research of fetal ECG extraction using wavelet analysis and adaptive filtering. Computers in biology and medicine, 2013, vol. 43, no 10, p. 1622-1627.

[32] SUTHA, P. et JAYANTHI, V. E. Fetal electrocardiogram extraction and analysis using adaptive noise cancellation and wavelet transformation techniques. Journal of Medical Systems, 2018, vol. 42, p. 1-18.

[33] HASSANPOUR, Hamid et PARSAEI, Amin. Fetal ECG extraction using wavelet transform. In: 2006 International Conference on Computational Intelligence for Modelling Control and Automation and International Conference on Intelligent Agents Web Technologies and International Commerce (CIMCA'06). IEEE, 2006. p. 179-179.

[34] DESAI, Kamalakar D. et SANKHE, Manoj S. A real-time fetal ECG feature extraction using multiscale discrete wavelet transform. In: 2012 5th international conference on biomedical engineering and informatics. IEEE, 2012. p. 407-412.

[35] KRUPA, Abel Jaba Deva, DHANALAKSHMI, Samiappan, SANJANA, N. L., et al. Fetal heart rate estimation using fractional Fourier transform and wavelet analysis. Biocybernetics and Biomedical Engineering, 2021, vol. 41, no 4, p. 1533-1547.

[36] AL-SHEIKH, Bahaa, SALMAN, Mohammad Shukri, ELEYAN, Alaa, et al. Non-invasive fetal ECG extraction using discrete wavelet transform recursive inverse adaptive algorithm. Technology and Health Care, 2020, vol. 28, no 5, p. 507-520.

[37] DARSANA, P. et KUMAR, Vaegae Naveen. A Quantitative and Qualitative Research on Fetal ECG extraction using Wavelet-based Adaptive Filtering. In: 2022 International Conference on Computing, Communication, Security and Intelligent Systems (IC3SIS). IEEE, 2022. p. 1-5.

[38] KARVOUNIS, E. C., PAPALOUKAS, Costas, FOTIADIS, D. I., et al. Fetal heart rate extraction from composite maternal ECG using complex

continuous wavelet transform. In: Computers in Cardiology, 2004. IEEE, 2004. p. 737-740.

[39] PARA, Neha et WADHWANI, S. Fetal ECG Extraction using Wavelet Transform. International Journal of Engineering and Technology, 2018, vol. 5, no 7, p. 2577-2581.

[40] ABUHANTASH, Ferial, KHANDOKER, Ahsan H., APOSTOLIDIS, Georgios K., et al. Swarm Decomposition of Abdominal Signals for Non-invasive Fetal ECG Extraction. In: 2021 43rd Annual International Conference of the IEEE Engineering in Medicine & Biology Society (EMBC). IEEE, 2021. p. 775-778.

[41] JOHN, Rolant Gini et RAMACHANDRAN, K. I. Extraction of fetal ECG from abdominal ECG by nonlinear transformation and estimations. Computer Methods and Programs in Biomedicine, 2019, vol. 175, p. 193-204.

[42] KHAMENE, Ali et NEGAHDARIPOUR, Shahriar. A new method for the extraction of fetal ECG from the composite abdominal signal. IEEE Transactions on Biomedical Engineering, 2000, vol. 47, no 4, p. 507-516.

[43] JAFARI, Maria G. et CHAMBERS, Jonathon A. Fetal electrocardiogram extraction by sequential source separation in the wavelet domain. IEEE Transactions on Biomedical Engineering, 2005, vol. 52, no 3, p. 390-400.

[44] ALFAOURI, Mikhled et DAQROUQ, Khaled. ECG signal denoising by wavelet transform thresholding. American Journal of Applied Sciences, 2008, vol. 5, no 3, p. 276-281.

[45] SAHOO, Santanu, KANUNGO, Bhupen, BEHERA, Suresh, et al. Multiresolution wavelet transform-based feature extraction and ECG classification to detect cardiac abnormalities. Measurement, 2017, vol. 108, p. 55-66.

[46] SADOWSKY, John. Investigation of signal characteristics using the continuous wavelet transform. Johns Hopkins apl Technical Digest, 1996, vol. 17, no 3, p. 258-269.

[47] AZZERBONI, Bruno, LA FORESTA, Fabio, MAMMONE, Nadia, et al. A new approach based on wavelet-ICA algorithms for fetal electrocardiogram extraction. In: ESANN. 2005. p. 193-198.

[48] WU, Shuicai, SHEN, Yanni, ZHOU, Zhuhuang, *et al.* Research of fetal ECG extraction using wavelet analysis and adaptive filtering. *Computers in biology and medicine*, 2013, vol. 43, no 10, p. 1622-1627.

[49] MARTINEK, Radek, KAHANKOVA, Radana, NEDOMA, Jan, *et al.* Fetal ECG preprocessing using wavelet transform. In: *Proceedings of the 10th International Conference on Computer Modeling and Simulation*. 2018. p. 39-43.

[50] BALDAZZI, Giulia, SULAS, Eleonora, URRU, Monica, et al. Wavelet denoising as a post-processing enhancement method for non-invasive fetal electrocardiography. Computer Methods and Programs in Biomedicine, 2020, vol. 195, p. 105558.

[51] ALSHEBLY, Y. S. et NAFEA, Marwan. Isolation of fetal ECG signals from abdominal ECG using wavelet analysis. Irbm, 2020, vol. 41, no 5, p. 252-260.

[52] MOCHIMARU, F., FUJIMOTO, Y., et ISHIKAWA, Y. Detecting the fetal electrocardiogram by wavelet theory-based methods. *Progress in Biomedical Research*, 2002, vol. 7, p. 185-193.

[53] SARITHA, C., SUKANYA, V., et MURTHY, Y. Narasimha. ECG signal analysis using wavelet transforms. *Bulg. J. Phys*, 2008, vol. 35, no 1, p. 68-77.

[54] Abdominal and Direct FECG Database. Available online: https://physionet.org/physiobank/database/adfecgdb/ (accessed on 10 January 2023).

A Comparative Study of Local Binary Pattern and Local Ternary Pattern for Fault Detection in Induction Motors

Behloul fatiha, Tafinine farid

fatiha.behloul@univ-bejaia.dz.

farid.tafinine@univ-bejaia.dz.

***Abstract*—Since the induction machine is used in many different sectors, an engine failure would be extremely expensive. Diagnostic methods using numerous signal-processing approaches have been used to solve this issue. To discover flaws in induction motors, this work offered a comparison of two techniques named GLBP and GLTP using the Grey Level Co-occurrence Matrix (GLCM) combined with LBP and LTP, Local Binary Pattern, and Local Ternary Pattern, respectively. The use of an acoustic dataset with various motor problems (bearing faults and broken bars) is made. For defect identification, the multiclass MCSVM (Support Vector Machine One Versus All), K-NN (K-nearest neighborhood), and ANN artificial neural network classifiers are used**.

Keywords: **Faults diagnosis, induction motor, Local Ternary Pattern, local binary pattern, Grey Co-occurrence Matrix.**

I. INTRODUCTION

Devices powered by induction motors are essential to modern industry, and sudden failure would be costly. Bearing, stator, rotor, and other defects are listed as the most prevalent faults in the literature, respectively [1]. It's critical to locate these issues as soon as possible in order to guarantee equipment safety and prevent production halts. A large number of studies have recently been carried out in this field to resolve these problems. Many studies have been based on signal analysis techniques such as Fourier transform (FT) analysis, spectral flattening and envelope spectrum analysis. Subsequently, other methods such as wavelet transform (WT) and empirical mode decomposition (EMD) were used [2]. Recently, two-dimensional (2D) signal processing has been applied in diverse researches on fault diagnosis. One of them is the local binary pattern which is a powerful texture analysis. Shahriar et al. used a fault diagnosis of induction motors utilizing local binary pattern-based texture analysis [3]. O Yaman presented an automated faults classification method based on binary pattern and neighbourhood component analysis using an induction motor [4].

Our approach is to apply new two-dimensional techniques called GLBP grey local binary pattern and GLTP grey local ternary pattern, using acoustic emission signal analysis to detect rotor and bearing faults. Those techniques are combined with the GLCM matrix. The ternary local pattern LTP is an extension of the LBP operator [5]. The features are extracted by the GLCM matrix; these are energy, correlation, homogeneity, mean, and entropy. Following that, the features vector is fed into artificial intelligence techniques such as the multiclass MCSVM, K-NN, and ANN algorithms.

II. LOCAL BINARY PATTERN

This method was first used on a grey-level image by Ojala et al. in 1996 [6]. As shown in (1), a binary pattern is produced by thresholding nearby pixels based on the grey-level value of a centre pixel. Fig. 1 represents the process.

$$s(x) = \begin{cases} 1 & \text{si} \quad x \geq 0 \\ 0 & \text{si} \quad x < 0 \end{cases} \tag{1}$$

Where g_c is the grey-level value of the central pixel, In the 3x3 neighbourhood, g_p represents the grey-level values of the centre pixel's neighbours. P the number of pixels in the neighbourhood, and function s(.) the threshold operation. Equation (2) represents the LBP code [7]:

$$\mathrm{LBP}_{P,R} = \sum_{p=0}^{P-1} s(g_p - g_c) \cdot 2^p \tag{2}$$

Where R is the radius between the central pixel and its neighbours.

Some local binary patterns have important textural characteristics that constitute the majority of the patterns present in the texture and high noise tolerance [8]. These patterns are called 'uniform'. An LBP code is referred to as uniform if the binary code has a maximum of two bitwise transitions from 0 to 1 or from 1 to 0. The operator is designed as (5) and (6).

$$\mathrm{LBP}_{P,R}^{riu2} = \begin{cases} \sum_{p=0}^{P-1} s(g_p - g_c) & \text{if} \quad U(\mathrm{LBP}_{P,R}) \leq 2 \\ P+1 & \text{otherwise} \end{cases} \tag{5}$$

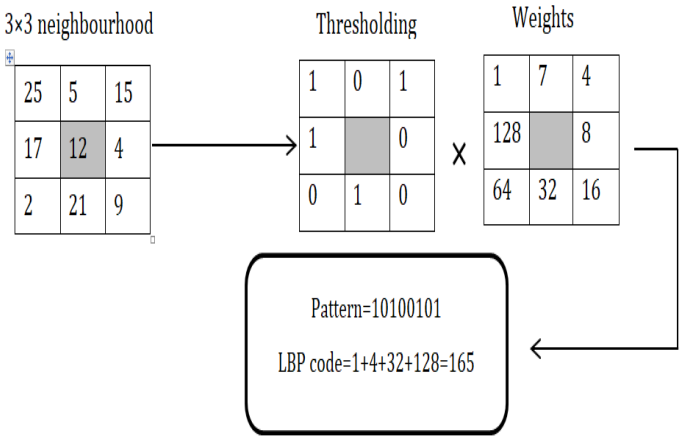


Figure 1. Generating the LBP code

With:

$$U(LBP_{P,R}) = s(g_{P-1} - g_c) - s(g_0 - g_c) + \sum_{p=1}^{P-1} s(g_p - g_c) - s(g_{p-1} - g_c) \quad (6)$$

For a circular neighbourhood of P neighbours, P+1 uniform binary patterns can appear, and each of them has a unique operator $LBP_{P,R}^{riu2}$ that takes values from 0 to P [8].

Local ternary pattern

The LBP code was modified by Tan and Triggs to produce a three-valued code known as the LTP, where the grey values in the t width zone around g_c are scaled to zero, those more than (g_c+t) are scaled to +1, and those less than (g_c-t) are scaled to -1 [6]. The expression of $LTP_{P,R}$ is defined as follows:

$$LTP_{P,R} = \sum_{p=0}^{P-1} s1(g_p - g_c) \cdot 2^p \quad (7)$$

$$s1(x) = \begin{cases} +1 & \text{if} \quad x \geq g_c + t \\ 0 & \text{if} \quad -t < x < t \\ -1 & \text{if} \quad x \leq g_c - t \end{cases} \quad (8)$$

Where g_c, g_p, *R*, and P are defined before in (2) and t=5. After thresholding step which is calculating the s1(.) function, as shown in Fig. 2, the top pattern and the lower pattern are created and coded as such. Separate calculations are performed and the two feature vectors produced are recombined [6].

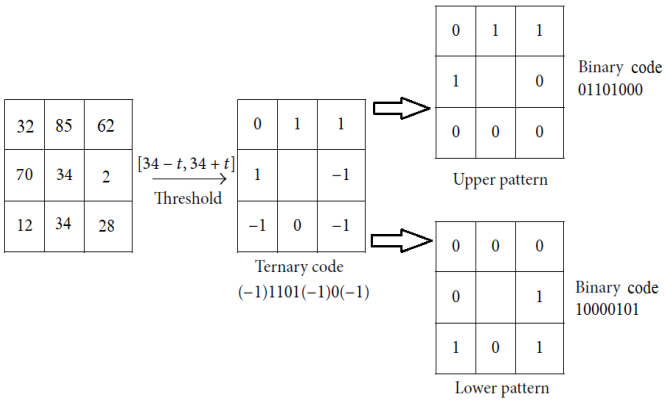


Figure 2. Illustration of calculation of LTP operator

III. GREY CO-OCCURRENCE MATRIX

The GLCM designates the probability of the pair of pixels i and j being separated by a distance d and an orientation θ, labelled $P_{d,\theta}(i,j)$ shown in (7).
In the image I of size M×N the GLCM is a square matrix of size $N_g \times N_g$ where N_g is the number of the grey-levels in the image [9].

$$P_{d,\theta}(i,j) = \#\left\{ \begin{matrix} (r,s): I(r,s) = i, \\ I(r+dx, s+dy) = j \end{matrix} \right\} \quad (7)$$

With # the cardinal functions. The GLCM can be normalised by dividing each element by the total number of possible pairs. Fourteen features can be calculated from the co-occurrence matrix [10.11]. Some features with their formulas are given in TABLE I.

TABLE I. The Texture Features Computed From glcm

Characteristics	Formula
Energy	$\sum_{i,j} P_{d,\theta}{}^2(i,j)$
Correlation	$\frac{\sum_{i,j}(i,j)P_{d,\theta}(i,j) - \mu_x\mu_y}{\sigma_x\sigma_y}$
Means	$\mu_x = \sum_{i,j} i\, P_{d,\theta}(i,j)$ $\mu_y = \sum_{i,j} j\, P_{d,\theta}(i,j)$
Variances	$\sigma_x^2 = \sum_{i,j} (i-\mu)^2\, P_{d,\theta}(i,j)$ $\sigma_y^2 = \sum_{i,j} (j-\mu)^2\, P_{d,\theta}(i,j)$
Standard deviations	$\sigma_x = \sqrt{\sum_{i,j}(i-\mu)^2\, P_{d,\theta}(i,j)}$ $\sigma_y = \sqrt{\sum_{i,j}(j-\mu)^2\, P_{d,\theta}(i,j)}$
Homogeneity	$\sum_{i,j} \frac{P_{d,\theta}(i,j)}{1+i-j}$
Entropy	$\sum_{i,j} P_{d,\theta}(i,j) \log_2(P_{d,\theta}(i,j))$

IV. PROPOSED METHODOLOGY

In this work we proposed a comparative study of different approaches $GLBP_{P,R}$, $GLBP_{1,8}^{riu2}$, and $GLTP_{P,R}$ used for fault detection with an acoustic dataset of five squirrel cage type three-phase induction motors. TABLE II provides a description of the induction machines' specifications utilised for the experimental study. The acoustic data were acquired in the working area where induction motors were running. Four types of faults, namely one broken rotor bar, two broken rotor bars, three broken rotor bars and bearing defects, were examined as part of the study [4].

We have 20000 samples collected in 330 seconds, and Fig.3 shows the acoustic signal. The acoustic data is converted into a 2D image.

The acoustic signal is partitioned into N equal fragments, and each fragment is arranged as the column of a 2D M×N matrix. The amplitude of a sample of each fragment is normalized in a range of 0 to 255 to become the grey-level value of this sample. Then, the $LBP_{P,R}$, $LBP_{1,8}^{riu2}$, and $LTP_{P,R}$ methods are computed from the 2D images with a size of 150×133, resulting from the conversion of the different fault types. This process is shown in Fig. 3. After that, the GLCM method is used to extract the texture features, which are energy, correlation, homogeneity, mean, and entropy. Thus, a vector of characteristics is built with five features, and using 60 samples of each fault, we get a matrix with 300×5. The classification is performed using a multiclass MCSVM classifier, one against all OAA, K-NN, and ANN artificial neural networks. The steps of our method are illustrated in the Fig.4.

TABLE II. INDUCTION MOTOR CHARACTERISTICS OF THE STUDY

Description	Value
Active power	0.75 [kW]
Nominal voltage	380 [V]
Speed	1380 [rpm]
Nominal Current	2.2 [A]
Number of poles	4
Number of rotor bars	22
Nominal frequency	50 [Hz]

V. EXPERIMENTAL RESULT AND DISCUSSION

The 2D images produced by the conversion exhibit texture changes and the additional noise appears as a variation in illumination, which justifies the use of the LBP approach, as this method is capable of illumination invariance and has a powerful greyscale texture analysis capability with low computational difficulty [12]. Most of those advantages are carried over to the LTP method [5]. The $LBP_{1,8}$, $LBP_{1,8}^{riu2}$ EXPE

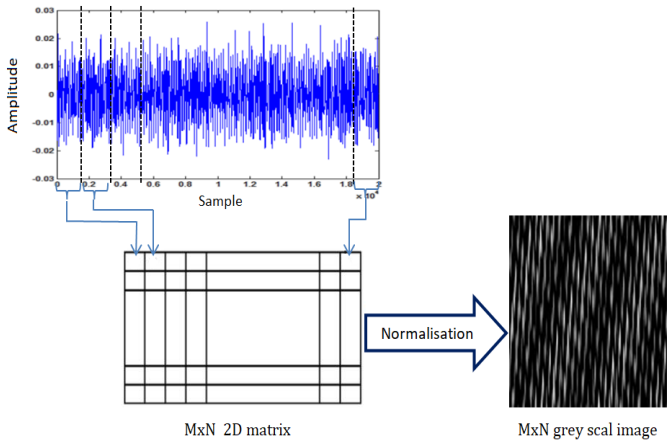


Figure 3. Conversion process from 1D acoustic signal to 2D grey scale image

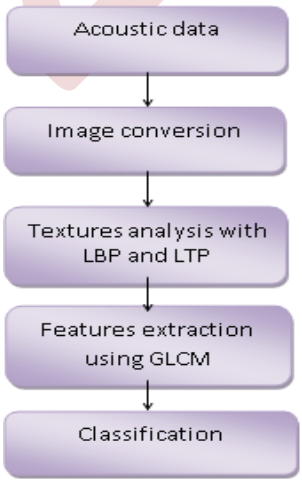


Figure 4. Proposed faults diagnostic methodology

and $LTP_{P,R}$ are used for texture analysis. The grey-level co-occurrence matrix (GLCM) has proven to be a useful statistical approach for extracting textural characteristics from images. Therefore, our approach is to extract five statistical discriminant features sited, from the $LBP_{1,8}$, $LBP_{1,8}^{riu2}$ and $LTP_{P,R}$ matrixes obtained in the texture analysis process. The feature vector acquired from this operation, of size 300, is used as input for the MCSVM and K-NN and ANN classifiers. The dataset is divided into 75% for the training set, i.e. 225 samples, and 25% for testing, i.e. 75 test samples. The results of the classification are given in TABLE III.

TABLE III. CLASSIFICATION RESULTS (%)

operators	MCSVM	K-NN	ANN
$GLBP_{1,8}$	100	97,33	100
$GLBP_{1,8}^{riu2}$	98,33	86,66	97,8
$GLTP_{1,8}$	94,66	92	98,3

The result obtained in this work shows a perfect success rate of 100% with the $GLBP_{1,8}$ using MSVM and ANN classifiers and 97,3% with the K-NN classifier. The $GLBP_{1,8}$ show better accuracy than $GLTP_{1,8}$ and $GLBP_{1,8}^{riu2}$ with all classifiers. It's clear that $GLBP_{1,8}$ is the optimal choice for discriminating fault induction motors because of its simplicity and because it contains some discriminative information.

VI. CONCLUSION

The LBP is a powerful tool for texture analysis, and combined with the GLCM method to become GLTP, it has proved to be a good tool for fault diagnostic in induction motors using 2D images that characterise each single fault created in five different motors. However, the extension LTP, which is used in the literature with a real image database, and also combined with GLCM as GLTP, shows satisfying accuracy but is not good enough as well as GLBP. The GLBP approach has proven an optimal success rate in identifying and diagnosing rotor and bearing faults in induction motors, even in environments of noise and without feature selection.

ACKNOWLEDGMENTS

The authors are grateful to Dr Orhan Yaman Ph.D. Department of Digital Forensics Engineering Technology Faculty Firat University Turkey, for his help and allowing us to use his experimental setup.

REFERENCES

[1] S. Bindu, V.V. Thomas, ''Diagnoses of internal faults of three phase squirrel cage induction motor —A review,''. International Conference on Advances in Energy Conversion Technologies (ICAECT), Manipal, India, 2014, pp. 48-54, doi:10.1109/ICAECT.2014.6757060.

[2] R.K. Jha, P.D. Swami, ''Intelligent fault diagnosis of rolling bearing and gear system under fluctuating load conditions using image processing technique,'' J Mech Sci Technol, 2020; 34, 4107–4115. https://doi.org/10.1007/s12206-020-0903-z.

[3] M.R. Shahriar, T. Ahsan, and U. Chong, '' Fault diagnosis of induction motors utilizing local binary pattern-based texture analysis,'' EURASIP Journal on Image and Video Processing,2013,2013:29.https://doi.org/10.1186/1687-5281-2013-29.

[4] O. Yaman, ''An automated faults classification method based on binary pattern and neighborhood component analysis using induction motor,'' Measurement, 2021, Vol. 168, 108323, ISSN 0263-2241, https://doi.org/10.1016/j.measurement.2020.108323

[5] X. Shu, Z. Song, J. Shi, S. Huang, and X.J. Wu , ''Multiple channels local binary pattern for color texture representation and classification, Signal Processing,'' Image Communication, 2021, Vol. 98, 116392, ISSN 0923-5965, https://doi.org/10.1016/j.image.2021.116392.

[6] T. Ojala, M. Pietikäinen, and D. Harwood, ''A comparative study of texture measures with classification based on featured distributions, '' Pattern Recognition, 1996, Vol. 29, Issue 1, Pages 51-59, ISSN 0031-3203, https://doi.org/10.1016/0031-3203(95)00067-4.

[7] T. Ojala, M. Pietikainen, and T. Maenpa, ''Multiresolution gray-scale and rotation invariant texture classification with local binary patterns,'' in IEEE Transactions on Pattern Analysis and Machine Intelligence, July 2002; vol. 24, no. 7, pp. 971-987, https://doi: 10.1109/TPAMI.2002.1017623.

[8] M. Pietikäinen, A. Hadid, G. Zhao, and T. Ahonen, ''Computer Vision Using Local Binary Patterns,'' Computational Imaging and Vision, Springer,2011, London.

[9] A. Shahbahrami, T.A. Pham, and K. Bertels, ''Parallel implementation of Gray Level Co-occurrence Matrices and Haralick texture features on cell architecture,'' J Supercomput, 2012,59,14551477.https://doi.org/10.1007/s11227-011-0556-x.

[10] R. Haralick, K. Shanmugam, and I.h. Dinstein, ''Textural Features for Image Classification,'' IEEE Trans Syst Man Cybern, 1973, SMC-3. 610-621.

[11] R. Haralick, ''Statistical and Structural Approaches to Texture,'' Proceedings of the IEEE, 1979, 67, 786-804. https://doi.org/10.1109/PROC.1979.11328.

[12] G. Wu, T. Yan, G. Yang, H. Chai, and C. Cao, ''A Review on Rolling Bearing Fault Signal Detection Methods Based on Different Sensors,'' Sensors, 2022, 22(21)ubui_!ç:8330. https://doi.org/10.3390/s22218330

Speech Denoising Based on Empirical Wavelet Transform and Adaptive Threshold

M. KEMIHA [1], A. KACHA [2], L. CHOUIKHI [3]

[1] *Laboratoire de Physique de Rayonnement et Applications. Automatic department. Jijel University*
Jijel. Algeria
mina.kemiha@univ-jijel.dz

[2]*Laboratoire de Physique de Rayonnement et Applications. Electronic department. Jijel University*
Jijel. Algeria
kacha_a@yahoo.com

[3]*Laboratoire Électrotechnique et d'électronique industrielle. Electrotechnic department. Jijel University*
Jijel, Algeria
chouikhi_lotfi@yahoo.fr

***Abstract*—In this paper, the empirical wavelet transform (EWT) is proposed to solve the problem of speech signal denoising. Since the noise is randomly distributed, an adaptive threshold is necessary. The proposed method combines the EWT and the adaptive threshold based on the signal energy. The performance of the proposed approach is tested on real speech sounds chosen from available databases. The proposed method's performances are evaluated via the output signal to noise ratio (SNR) and the correlation coefficient between the original signal and denoised signal. The performances of the proposed method are compared to those of reference methods .**

***Keywords:* speech denoising, empirical wavelet transform, adaptive threshold.**

I. INTRODUCTION

Speech denoising is the task of removing noise from noised speech signal. Speech denoising algorithms are important components in many systems, where speech plays a fundamental role, especially in telephony, in hearing aid systems, voice over IP (internet protocol) and automatic recognition systems. The removing of noise must be performed while the perceptual quality and intelligibility of the signals are preserved.

In the literature, several methods have been proposed for signal denoising, such as spectral subtraction [1], Wiener filtering [2] and neural networks [3]. The signal denoising problem can be solved in the time domain, frequency domain or time-frequency domain [4 , 5]. The wavelet transform has been widely used as a denoising technique [6, 7, 8]. It requires a priori given basis functions making this approach non-optimal. The empirical mode decomposition (EMD) [9] is a local self-adaptive decomposition method that allows analyzing data from non-stationary and/or non-linear processes. The EMD method has been proposed as an alternative to solve the denoising problem [10]. However, the EMD exhibits too much modes, which are sometime really difficult to interpret [11]. Moreover, the EMD is not supported by a strong mathematical background. In [12] the variational mode decomposition (VDM) has been introduced. The limitation of the VDM method is the determination of the number of modes which must be known a priori. In the VMD-based applications, the determination of an accurate number of modes has an essential effect on denoising performance [13].

Recently, a new method for signal analysis called empirical wavelet transform (EWT) has been introduced. The EWT aims to decompose a time series into different modes, and adaptively builds the scaling function and wavelet banks without prior information [11]. The EWT has been proposed to solve many problems of signal processing applications. In [13], it has been used for ECG signal denoising. The method is performed for powerline interference reduction and baseline wander removal, where the EWT is applied on the noisy signal, the estimate of powerline interference is provided by the last mode whereas the baseline is estimated by the first mode. Thus, separating these modes from the noisy ECG signal provides the noise- free ECG. To attenuate the strong noise in seismic data [14], the EWT has been combined with a clustering guided thresholding method which uses an unsupervised clustering algorithm

In this paper, the EWT is proposed to solve the problem of speech signal denoising. First, the noisy speech signal is dividing into non ovelopping frames. Then, the EWT is used to decompose adaptively the frame into several empirical components according to the frequency contents in the data. An adaptive threshold based on the signal energy is used to evaluate the noise [15]. The threshold is modified adaptively by the noise content of each frequency band to get a better denoising performance. The adaptive threshold is applied on each mode obtained via the EWT decomposition to obtain the denoised modes. Finally, the denoised speech signal is built

via the denoised modes. To evaluate the performances of the proposed method, simulations are performed. The proposed method is tested on speech dataset randomly selected and constructed from TIMIT database [16] and NOIZEUS database [17] (available online), and compared to the results obtained via the VDM-based denoising method [18], the EMD-based denoising method [19] and the wavelet-based denoising method [20]. The comparison is performed in terms of the signal to noise ratio (SNR), and the correlation coefficient between original and denoised signal.

The remainder of the paper is organized as follows. Empirical wavelet transform is presented in Section 2. Adaptive threshold is introduced in Section 3. Simulation results are presented in Section 4. Finally, conclusions are given in Section 5.

II. EMPIRICAL WAVELET TRANSFORM

The EWT is a new approach which aims to decompose a time series into different modes. The EWT consists to design an adaptive wavelet filter bank [11] that provides a more consistent decomposition.

Let $y(t)$ be a discrete-time signal, where $t = \{t_i\}$ is a discrete time and $i = 1,..,M$ with M being the number of samples. The Fourier transform of the signal $y(t)$ is denoted $Y(\omega)$. P denotes de set of maxima in $Y(\omega)$ where $P = \{p_i\}$, $i = 1,..,N$ where N represents the number of maxima, and also, the number of filter banks. $\Omega = \{\Omega_i\}$ for $i = 1,..,N-1$denotes a set of boundaries. The EWT decomposition is given by the following steps:

1. Compute the spectrum $Y(\omega)$ using the FFT, then find the set of maxima P in Fourier spectrum, and reduce their corresponding $\omega = \{\omega_i\}, i = 1,..N$
2. Obtain the proper segmentation of the spectrum and the set of boundaries. then, define the boundaries of each segment denoted Ω_i, considered as the center of two consecutive maxima given as follow

$$\Omega_i = \frac{\omega_i + \omega_{i+1}}{2} \tag{1}$$

where ω_i and ω_{i+1} are two consecutive frequencies

3. Based on the boundaries, using a low-pass filter and $N-1$ band pass filters, a bank of N wavelet filters can be composed. The expressions for the Fourier transform of scaling function $\emptyset_1(\omega)$ and the empirical wavelets $\psi_i(\omega)$ are given as follows respectively

$$\emptyset_1 = \begin{cases} 1 & |\omega| \le (1-\gamma)\Omega_1 \\ cos\left(\frac{\pi}{2}\,\alpha(\gamma,\Omega_1)\right) & (1-\gamma)\Omega_1 < |\omega| < (1+\gamma)\Omega_1 \\ 0 & otherwise \end{cases} \tag{2}$$

and

$$\psi_i = \begin{cases} 1 & (1+\gamma)\Omega_i < |\omega| < (1+\gamma)\Omega_{i+1} \\ cos\left(\frac{\pi}{2}\,\alpha(\gamma,\Omega_{i+1})\right).(1-\gamma)\Omega_{i+1} \le |\omega| \le (1+\gamma)\Omega_{i+1} \\ sin\left(\frac{\pi}{2}\,\alpha(\gamma,\Omega_i)\right) & (1-\gamma)\Omega_{i+1} \le |\omega| \le (1+\gamma)\Omega_{i+1} \\ 0 & otherwise \end{cases} \tag{3}$$

To ensure that no overlap between the two consecutive transitions, the parameter γ is introduced. β(x) denotes an arbitrary function given as follows as

$$\beta(\upsilon) = \begin{cases} 0 & \upsilon \le 0 \\ 1 & \upsilon \ge 1 \\ \beta(\upsilon) + \beta(1-\upsilon) = 1 & \upsilon \in [0,1] \end{cases} \tag{4}$$

The detail coefficients $W_y^{\varepsilon}(n,t)$ are given by the inner products with the empirical wavelets:

$$W_y^{\varepsilon}(t,n) = \int y(\tau)\,\psi_n(\tau - t)d\tau \tag{5}$$

and the approximation coefficients $W_y^{\varepsilon}(0,t)$ (we adopt the convention to denote them) by the inner product with the scaling function:

$$W_y^{\varepsilon}(t,0) = \int f(\tau)\,\phi_1(\tau - t)d\tau \tag{6}$$

The signal reconstruction is expressed as follows

$$y(t) = W_y^{\varepsilon}(t,0) * \phi_1(t) + \sum_{n=1}^{N} W_y^{\varepsilon}(t,n) * \psi_n \tag{7}$$

. where $*$ denotes de covolution

III. ADAPTIVE THRESHOLD

The classical thresholding is performed by applying the same quantization on each mode. However, the noise is randomly distributed. So, the excessive noise removal in some frequency bands and insufficient noise removal in other frequency bands will occur. In [15] an adaptive threshold is proposed, where the signal energy is used to quantify the noise. The adaptive threshold is used to modify the threshold adaptively by the noise content of each frequency band and get a better denoising performance. The adaptive threshold is described as

$$\begin{cases} En_j = \sum_{k=1}^{n_j} |w_{j,k}|^2 \\ \sigma = \frac{median(|w_{j,k}|)}{0.675} \end{cases} \tag{8}$$

where En_j denotes the mode energy for each frequency band, n_j is the length of the mode frequency band j. The adaptive threshold function is given by

$$\bar{w}_{j,k} = \begin{cases} w_{j,k} - \dfrac{T_j}{\left(1 + e^{\frac{(w_{j,k}-t)^2}{a}}\right)} - \dfrac{T_j}{\left(2e^{\frac{1}{a}}\right)}. & w_{j,k} \geq T_j \\ 0 & |w_{j,k}| < T_j \\ w_{j,k} + \dfrac{T_j}{\left(1 + e^{\frac{(-w_{j,k}-t)^2}{a}}\right)} + \dfrac{T_j}{\left(2e^{\frac{1}{a}}\right)}. & w_{j,k} \leq -T_j \end{cases} \quad (9)$$

$$T_j = \frac{\sigma\sqrt{2\log N}}{\exp(\frac{En_j}{\sqrt{n_j}})}$$

Where T_j denotes the threshold of modes j, $\bar{w}_{j,k}$ denotes the estimated mode, and $w_{j,k}$ represents the original modes, N is the signal length, and a is the normal number which verify the condition : when $a \to 0$, the function is transformed into a hard threshold function, and when $a \to \infty$, the function is converted to a soft threshold function.

IV. RESULTS AND DISSCUSION

To show the effectiveness of the proposed method, numerical simulations have been performed. The speech dataset has been built from The TIMIT database [16] and NOIZEUS database [17] available online. The sampling rate for the voice signals is $f_s = 16\,kHz$. The speakers might be either female or male. The speech signal $x(t)$ is corrupted by a white gaussian noise $b(t)$ as expressed by the following equation

$$y(t) = x(t) + b(t) \quad (10)$$

where $y(t)$ is the noised signal.

The two parameters used to evaluate the performances of the proposed speech denoising method are the output signal to noise ratio (SNR) and the correlation coefficient (corr coeff) between the original clean signal and the denoised signal expressed, respectively, as :

$$\text{SNR} = 10\log_{10}\frac{\frac{1}{N}\sum_{n=0}^{N-1}|x(t)|^2}{\frac{1}{N}\sum_{n=0}^{N-1}|x(t) - \tilde{x}(t)|^2} \quad (11)$$

and

$$\text{Corr coeff} = \frac{E[[x - \mu_x][\tilde{x} - \mu_{\tilde{x}}]}{\sigma_x\,\sigma_{\tilde{x}}} \quad (12)$$

where E denotes the expectation operator, μ_x and μ_y are the mean values of the original signal $x(t)$ and the denoised signal $\tilde{x}(t)$ and σ_x and $\sigma_{\tilde{x}}$ denote the standard deviations of $x(t)$ and $\tilde{x}(t)$, respectively.

thereafter, we present an illustration of the speech signal denoising using the proposed method applied to speech signal corrupted by a white gaussian noise.

The speech signal waveform is shown in figure 1, the speech signal corrupted by a white gaussian noise with SNR=15 dB is shown by figure 2. A noisy speech frame is shown by figure 3. The decomposition of the noisy speech frame using the EWT method results in 23 modes shown in figure 4

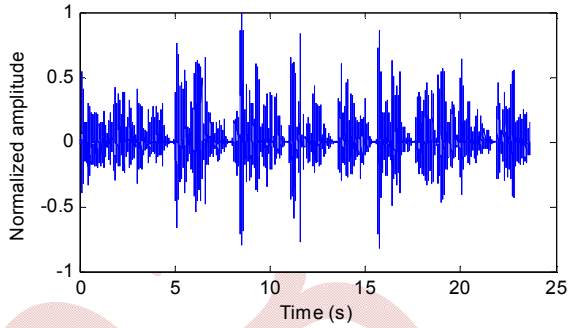


Figure 1. Clean speech signal

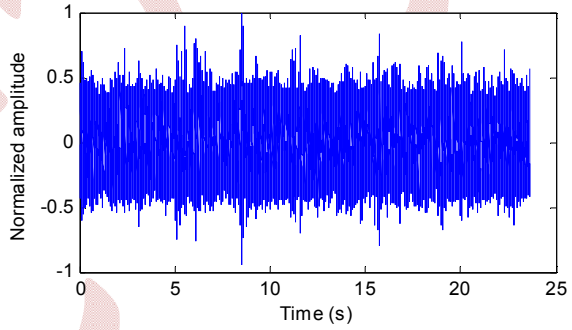


Figure 2. Speech signal corrupted by white gaussian noise with SNR=15dB

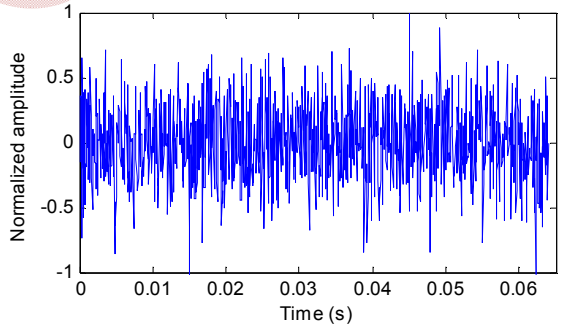


Figure 3. Noised speech frame

The noise is randomly distributed for the modes. The threshold is built adaptively, for each mode the threshold is modified by the noise content of each mode to get a better denoising performance. The adaptive threshold is applied to each mode; the denoised modes are used to reconstruct the denoised signal shown by figure 5 using equation (6).

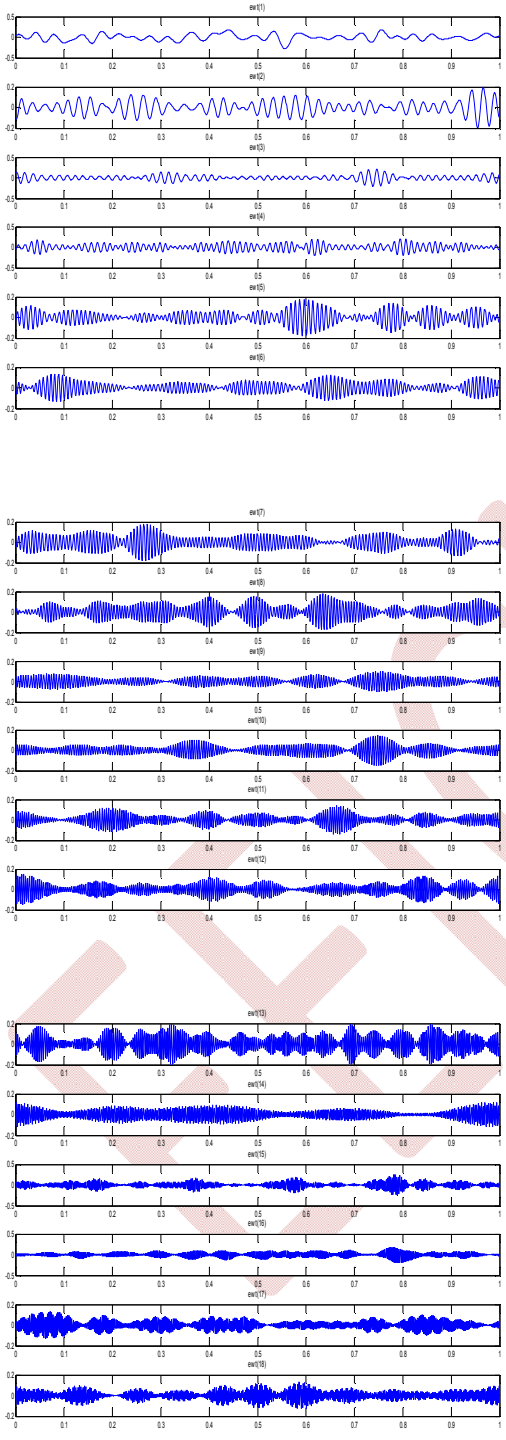


Figure 4. The obtained 32 modes via EWT method application on the noisy speech frame.

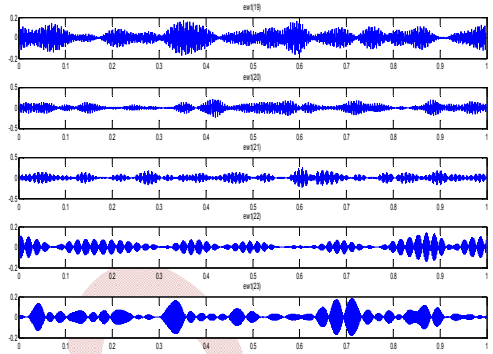


Figure 4. Continued

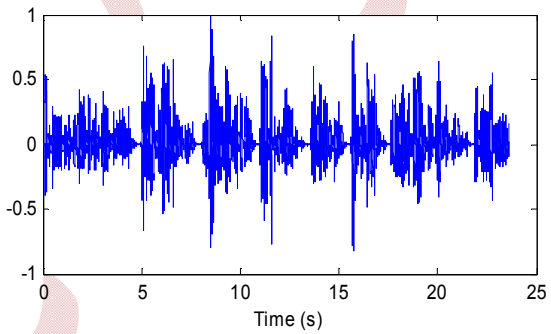


Figure 5. Denoised speech signal (estimated signal)

TABLE I. COMPARISON BETWEEN OUTPUT SNR OBTAINED VIA THE PROPOSED METHOD AND REFERENCE METHODS

input SNR (dB)	Output SNR (dB)			
	EMD-based denoising	***Wavelet-based denoising***	***VDM-based denoising***	***Proposed method***
-5	4.47	4.23	4.58	**4.97**
0	6.88	6.78	7.11	**7.81**
5	10.5	9.83	11.2	**11.4**
10	14.2	13.9	14.3	**14.83**
15	21.2	20.7	21.4	**21.7**

TABLE II. COMPARISON BETWEEN CORRELATION COEFFICIENT OBTAINED VIA THE PROPOSED METHOD AND REFERENCE METHODS

input SNR (dB)	Correlation coefficient			
	EMD-based denoising	***Wavelet-based denoising***	***VDM-based denoising***	***Proposed method***
-5	0.958	0.956	0.968	**0.982**
0	0.977	0.968	0.975	**0.986**
5	0.981	0.978	0.980	**0.989**
10	0.983	0.981	0.986	**0.991**
15	0.988	0.978	0.983	**0.994**

Noisy speech signals database is built using speech signls available onlie. The speech signals are corrupted by white gaussian noise with input SNR varying from -5 dB to 15 dB with a step of 5 dB. The obtained results in terms of ouput SNR and correlation coeficient. The values of the output SNR and correlation coefficient are given in Table I and Table II , respectively.

An improvement in the results in terms of the output SNR as well as the correlation coefficient is noticed. The proposed method provides a better output SNR and correlation coefficient in comparison to reference methods. A comparison between the mean square error (MSE) obtained via the proposed method and reference methods for various values of the input SNR is shown in figure 6.

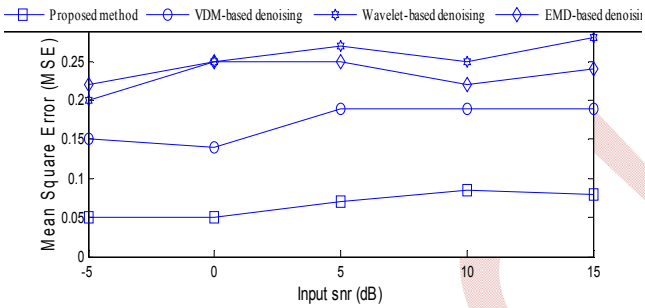


Figure 6. Comparison between the MSE obtained via the proposed method and reference methods for various values of input snr

As can be seen, the EWT method with adaptive threshold provides a better estimate of the original signal and better denoising performances compared to reference methods.

V. CONCLUSION

Speech denoising based on EWT and adaptive threshold is proposed. The EWT advantage has been exploited. The decomposition is completely automatic without a priori information. The adaptive threshold is based on the signal energy and it changes for each mode proportionally to noise concentration. Simulation results show that the proposed method provides a better estimate of the original signal and better denoising performances in term of ouput SNR and correlation coefficient compared to reference methods.

REFERENCES

[1] Lei Hao, Shuai Cao, Pengfei Zhou, Lei Chen , Yi Zhang , Kai Li,Dongdong Xie,and Yijun Geng , Denoising Method Based on Spectral Subtraction in Time-Frequency Domain, Advances in Civil Engineering

[2] Jae Soo Lim and Alan V Oppenheim, "Enhancement and bandwidth compression of noisy speech," Proceedings of the IEEE, 67(12) pp. 1586–1604 (1979).

[3] Shahla Parveen and Phil Green, "Speech enhancement with missing data techniques using recurrent neural networks," in ICASSP, 2004.

[4] Aaron Nicolson and Kuldip K Paliwal, "Deep learning for minimum mean-square error approaches to speech enhancement," Speech Communication, 2019.

[5] Yong Xu et al., "A regression approach to speech enhancement based on deep neural networks," IEEE/ACM Transactions on Audio, Speech, and Language Processing, 2014.

[6] Krishnaveni, V.; Jayaraman, S.; Aravind, S.; Hariharasudhan, V.; Ramadoss, K. Automatic identification and removal of ocular artifacts from EEG using wavelet transform. Meas. Sci. Rev., 6, 45–57. (2006)

[7] Islam, M.K.; Rastegarnia, A.; Yang, Z. A wavelet-based artifact reduction from scalp EEG for epileptic seizure detection. IEEE J. Biomed. Health Inform., 20, 1321–1332 (2015).

[8] Phadikar, S.; Sinha, N.; Ghosh, R. Automatic eyeblink artifact removal from EEG signal using wavelet transform with heuristically.

[9] Huang N.E. et al., "The empirical mode decomposition and the Hilbert spectrum for nonlinear and nonstationary time series analysis," *Proc. R. Soc. London Ser. A* 454 pp. 903-995, 1998.

[10] marcsarossy, jonathancrowston, dineshkumar, zhichaowu empirical mode decomposition denoising of the electroretinogram to enhance measurement of the photopic negative response. 71 part a, 103-164(2022)

[11] J. Gilles, "Empirical wavelet transform," IEEE Trans. Signal Process., 61(16) pp. 3999–4010, Aug. 2013.

[12] K. Dragomiretskiy and D. Zosso, ''Variational mode decomposition,'' IEEE Trans. Signal Process., 62(3) pp. 531–544 (2014).

[13] Omkar Singh, Ramesh Kumar Sunkaria ; ECG signal denoising via empirical wavelet transform; Australas Phys Eng Sci Med (2017) 40:219–229.

[14] WeiChen· HuiSong· Automatic noise attenuation based on clustering and empirical wavelet transform, Journal of Applied Geophysics Volume 159, December 2018, Pages 649-665

[15] Yunpeng Gao, Yunfeng Li , Yanqing Zhu , Cong Wu , Dexi Gu, Power quality disturbance classification under noisy conditions using adaptive wavelet threshold and DBN-ELM hybrid model, Electric Power Systems Research 204 (2022) 107682

[16] TIMIT database. https://catalog.ldc.upenn.edu/Ldc93s1

[17] NOIZEUS database http://ecs.utdallas.edu/loizou/speech/noizeus/

[18] Pratik Singh, Gayadhar Pradhan. Variational mode decomposition based ECG denoising using non-local means and wavelet domain filtering. Australasian Physical & Engineering Sciences in Medicine 41:891–904 (2018)

[19] Yannis Kopsinis, Stephen McLaughlin, Development of EMD-Based Denoising Methods Inspired by Wavelet Thresholding. IEEE transactions on signal processing, 57(4) 1351-1362 (2009)

[20] Md. Abdul Awal, Sheikh Shanawaz Mostafa , Mohiuddin Ahmad, Mohd Abdur Rashid. An adaptive level dependent wavelet thresholding for ECG denoising. Biocybernetics and Biomedical Engineering. 34(4) 238-249 (2014).

Efficient ECG Signal Denoising Technique based on the Empirical Mode Decomposition Method and the Discrete Wavelet Transform

Yaaqoub Kahlessenane [1,2], Fatiha Bouaziz [1,2], Patrick Siarry [3], Hamouche Oulhadj[3]
[1]*Electronic Department, Jijel University, BP98 OuledAissa Jijel 18000, Algeria*
yaqoub.kahlessenane@univ-jijel.dz
[2] *Mechatronic Laboratory (LMT), Jijel University, Jijel, Algeria*
bouhali.fatiha@yahoo.fr
[3] *Laboratory of Images, Signals and Intelligent Systems (LISSI), Paris- East Creteil University, France*
siarry@u-pec.fr (P. Siarry), oulhadj@u-pec.fr (H. Oulhadj).

***Abstract*— This paper describes the denoising of ECG signals obtained from the Physionet database using several signal processing techniques. Baseline wandering noise is removed using Empirical Mode Decomposition (EMD) and Ensemble Empirical Mode Decomposition (EEMD) to decompose the noisy ECG signal into different Intrinsic Mode Functions (IMFs). These IMFs are then filtered using low pass filtering to extract the low frequency baseline component. The reconstructed signal still contains high frequency noises, which are reduced based on the discrete wavelet transform using the 'db4' wavelet function. Finally, a threshold method is used to identify and eliminate noise from the wavelet coefficients. The obtained results show that this method effectively removes noise from ECG signals.**

***Keywords:* ECG signals, EMD, EEMD, Wavelet Transform.**

I. INTRODUCTION

An Electrocardiogram (ECG) represents a visual representation that depicts the electrical activity of the human heart. This is obtained by placing electrodes on different parts of the body such as the chest, arms, and legs. Because it provides crucial medical data, the ECG serves as a diagnostic tool for identifying various heart conditions [1]. The ECG signals obtained are susceptible to interference from external sources such as muscle movements or low-quality sensor performance, leading to signal corruption [2]. Among the various types of noise that can disrupt ECG signal analysis, the baseline wander (BW) is of primary concern.

The baseline wander (BW) typically occurs at frequencies lower than 1 Hz, which is comparable to the frequency range of ST segments in the ECG signal. The wandering of low-frequency ST segments can significantly influence the accuracy of diagnosis, resulting in false positives or false negatives. Therefore, to ensure reliable analysis of ECG features such as the timing and duration of ST segments, it is imperative to eliminate BW artifacts. Failure to do so can seriously hinder the usefulness of recorded ECGs in clinical evaluations, highlighting the need for proper removal of BW [3].

The ECG signal is characterized as a non-stationary signal with overlapping noise and signal spectra, making it challenging to analyze. To overcome this difficulty, a nonlinear approach such as the Empirical Mode Decomposition (EMD) algorithm can be used. This algorithm is well suited for analyzing non-stationary signals like ECG by decomposing the signal into intrinsic mode functions (IMF) that capture the underlying signal characteristics [4].

The current paper presents a new ECG denoising technique using the empirical mode decomposition method (EMD) to eliminate baseline drift from the corrupted ECG signal. After applying the low pass filter to all the resulting IMF, the reconstruction of the signal by the inverse transform is done. Therefore, the baseline wandering that may have disrupted the signal is effectively removed, resulting in a more accurate representation of the ECG signal. We have also utilized Wavelet Transform-based techniques like DWT in our approach. This method involves decomposing the ECG signal into multiple frequency bands of approximation and detail coefficients [5]. Subsequently, we apply a filtering approach using the threshold method to remove unwanted noise and artifacts from the signal.

The paper consists of several sections that delve into different aspects of the proposed approach. Section II and III provide an in-depth explanation of EMD and EEMD techniques, respectively, while Section IV focuses on the use of the DWT method. Section V outlines the methodology employed to extract the baseline component and remove high-frequency noise, using low-pass filtering and soft threshold functions. The obtained results and discussions are shown in Section VI, and the conclusions are summarized in Section VII.

II. EMPIRICAL MODE DECOMPOSITION (EMD)

Empirical Mode Decomposition (EMD) is a signal processing technique that focuses on decomposing a complex signal into a series of initial Intrinsic Mode Functions (IMFs) [6]. The basic concept of EMD involves obtaining the extrema points of the signal and creating an envelope of minima and maxima through interpolation. The mean of the envelope is then obtained, and the difference with the mean is one of the IMFs. The EMD algorithm's basic functions are directly derived from the signal being tested. A function is considered to be an IMF if it satisfies two conditions: first, in the whole data set, the number of local extrema and that of zero crossings [7].
The essential steps of the EMD algorithm are as follow:

- Identify all peaks (local maxima and local minima) in the actual signal.
- Use any feasible interpolation method to calculate upper and lower envelopes from the identified maxima and minima.
- Calculate the mean value of the calculated envelopes.
- Generate the first proto-IMF by calculating the difference between the calculated mean and the actual signal.
- Repeat steps 1-4 on the proto-IMF until a function satisfying the IMF conditions is obtained.
- Terminate the sifting process using a stopping criterion, such as sum of difference (SD).
- Determine the residue function by subtracting the obtained IMF from the actual signal.
- Use the obtained residue as the next data signal and repeat the process until the residue function becomes constant or contains only one extremum.

The EMD of the actual signal is thus written as [8]:

$$Y(t) = \sum_{n=1}^{N} m_n(t) + r_n(t) \qquad (1)$$

With $m_n(t)$ being the n^{th} order *IMF* while $r_n(t)$ being the final residue.

III. ENSEMBLE EMPIRICAL MODE DECOMPOSITION (EEMD)

Empirical mode decomposition (EMD) is a multiresolution technique used to decompose non-linear and non-stationary signals into meaningful components. However, the EMD method [9, 10] has a limitation known as "mode mixing," where two different Intrinsic Mode Functions (IMFs) can represent the oscillations from a certain time scale, leading to a loss of information. To overcome this problem, one can employ Ensemble mode decomposition, which involves repeating the decomposition process on the original signal multiple times and then averaging the resulting IMFs to obtain more accurate and reliable IMFs that do not suffer from mode mixing [11].

Ensemble mode decomposition can be implemented by repeating the EMD process several times, each time adding white noise to the original signal, and then averaging the resulting IMFs over all the realizations. This approach helps to eliminate the problem of mode mixing, and it has been shown to improve the accuracy and stability of the decomposition results [11, 12].

$$c_j = \frac{1}{N}\sum_{i=1}^{N} c_{ij}(t) \qquad (2)$$

Where $\boldsymbol{c_{ij}}$ is the extracted IMFs obtained during each iteration.

IV. DISCREET WAVELET TRANSFORM

Wavelet analysis is a mathematical technique that can be used to break down a signal into a collection of orthogonal waveforms that are both time and frequency localized. This method is comparable to Fourier series analysis, which employs sinusoids as the basis function, but wavelets are more effective for studying transient signals such as ECG signals. The wavelet transform is the product of the subject signal $x(t)$ and the family of wavelet functions,$\psi_{m,n}(t)$, represented as a convolution operation in mathematical terms[13].

$$\boldsymbol{T_{m,n}} = \int_{-\infty}^{+\infty} x(t)\, \psi^{*}_{mn}(\boldsymbol{t})\boldsymbol{dt} \qquad (3)$$

Where $\psi_{m,n}(t) = (1/\sqrt{m})\,\psi(t - n/m)$ m and n are scale and location factors, respectively. The approximation coefficient of the signal *x(t)* is represented as:

$$A_{m,n} = \int_{-\infty}^{+\infty} x(t)\, \phi_{m,n}(t)dt \qquad (4)$$

The DWT (Discrete Wavelet Transform) consists of two filters, a low-pass filter (LPF) and a high-pass filter (HPF), applied on the scaling function $\phi(t)$. These filters modify the resolution of the signal and down sampling or up sampling changes its scale. Using the DWT, a signal is analyzed at various frequency bands with different resolutions by dividing it into approximation and detail information. The approximation coefficients are the output coefficients of the LPF, while the detail coefficients are the output coefficients of the HPF [14].

V. NEW DENOISING METHOD

The ECG signal is decomposed into Intrinsic Mode Functions (IMFs) using EMD and EEMD methods. Each IMF includes both the noise and essential components of the signal. To extract the low-frequency noise components, a bank of low

pass filters is applied to the higher-order IMFs starting from the last IMF. The essential part of the signal is retained in the higher-order modes, making their elimination undesirable. Finally, the baseline wander is extracted from the filtered signals [12]. For removing high-frequency noise, the reconstructed ECG signal is denoised using Discrete Wavelet Transform (DWT).

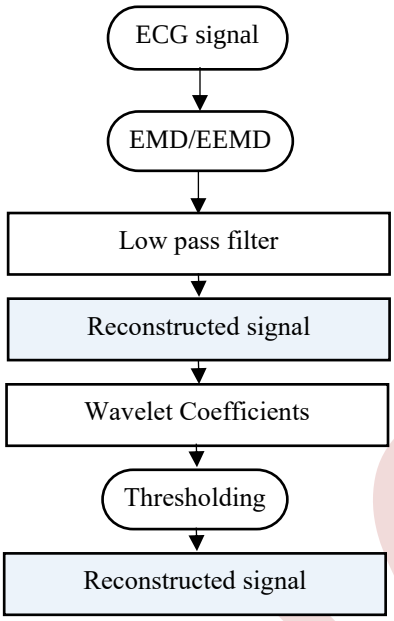


Figure 1. Diagram of the denoising method

The wavelets from Daubechies family have a shape closer to that of QRS complexes of ECG signal. Furthermore, their energy is concentrated around the low frequencies [15].
The choice of db4 wavelet is done by testing our algorithm with use of several types of Daubechies wavelet functions (db4, db6, db10 …). The better results of Denoising are observed with the use of db4. So, this wavelet is selected as it provides a good balance of smoothness, vanishing moments, and support length needed for ECG denoising. A 5 level of DWT decomposition is chosen to balance noise reduction with computational complexity.

The threshold for wavelet coefficient shrinkage is calculated using a signal-dependent approach rather than a fixed universal threshold [16]. Specifically, the threshold T is calculated as:

$$T = \sigma * \sqrt{(2 * \log(N))} \quad (5)$$

Where σ is the noise level estimated from the median absolute deviation of the wavelet coefficients, and N is the signal length.

The noise level σ is estimated as:

$$\sigma = \frac{\text{median}(|c_j[n]|)}{0.6745} \quad (6)$$

Where:

- Median($|c_j[n]|$) is the median absolute deviation of the wavelet coefficients at level *j*.
- 0.6745 is a constant scale factor

This adaptive threshold varies for different levels of detail, with lower thresholds for higher frequency subbands and higher thresholds for lower frequencies. This prevents over-smoothing of signal components at different scales. The noise estimation from median absolute deviation of wavelet coefficients makes the threshold signal-dependent.

VI. RESULTS AND DISCUSSIONS

In Figure. 2, the original ECG signal '222.mat' is presented, which was collected from the MIT-BIH arrhythmia database at a sampling frequency of 360 Hz [17]. This signal is noisy and contains baseline drift, which is eliminated through qualitative analysis in [18]. To extract the baseline component, the signal is decomposed into intrinsic mode functions (IMFs) using EMD and EEMD methods, as shown in Figures 3 and 4. Low pass filtering is then applied to each IMF, and the reconstructed signal is obtained by removing the baseline from the corrupted ECG, as shown in Figure 5 and 6. This reconstructed signal contains high frequency noise which is reduced using wavelet coefficients calculated with 'db4' wavelet function for five levels of decomposition. Afterwards, we have used a thresholding method to identify and remove the noise from the wavelet coefficients. One of the most common thresholding methods is the soft thresholding method, which sets all wavelet coefficients below a certain threshold to zero. To determine the threshold, we can used the variable threshold that depends on the level of detail. After, we have reconstructed the signal using the free-noise wavelet coefficients (Figure 5 and 6).

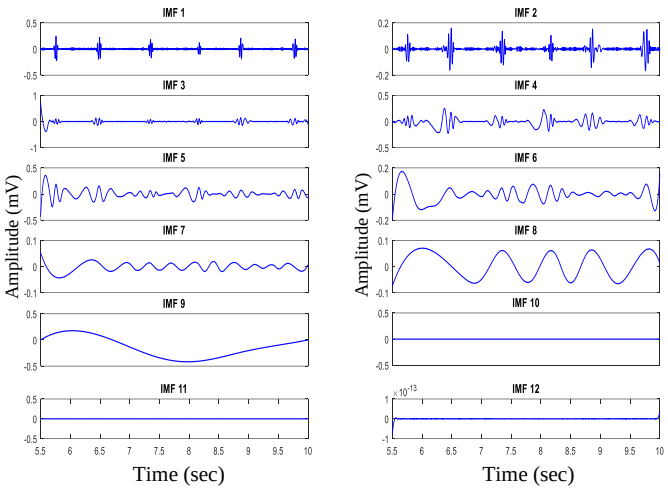


Figure 2. Original ECG signal: record 222 from MIT-BIH database

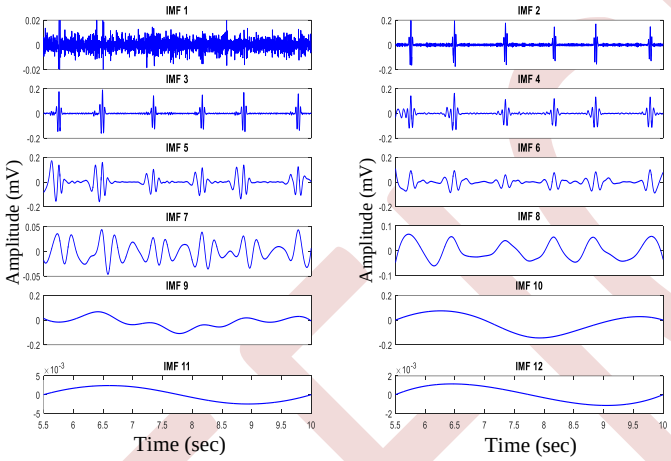


Figure 3. Decomposition of the ECG signal by the EMD method

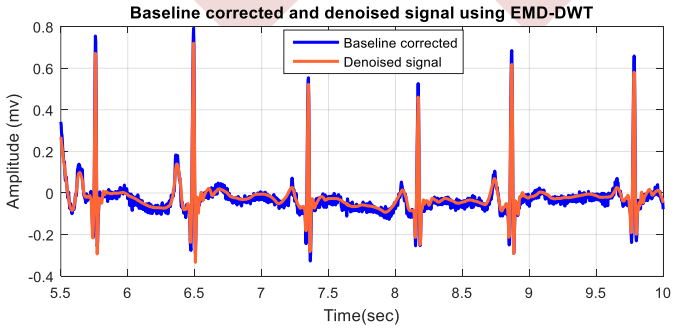


Figure 4. Decomposition of the ECG signal by the EEMD method

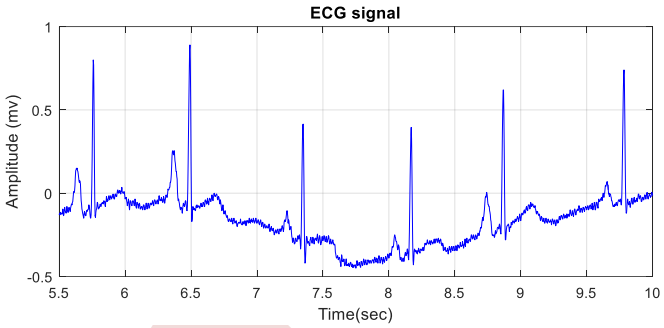


Figure 5. Baseline corrected and denoised signals using EMD-DWT technique

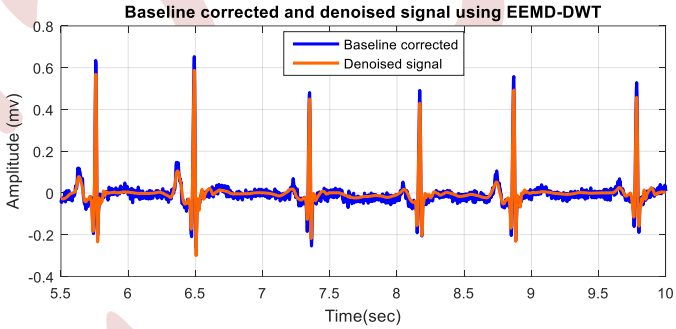


Figure 6. Baseline corrected and denoised signals using EEMD-DWT technique

In TABLE I, we have selected a set of ECG signals with a very turbulent baseline. Then, we have calculated some statistical parameters, such as: Crest factor, Kurtosis, Skewness and RMS value.

TABLE I. Comparison of statistical parameters of reconstructed signal obtained using EMD-DWT and EEMD-DWT

ECG	Method	Crest factor	Kurtosis	Skewness	RMS value
222	***EMD-DWT***	8.1057	28.5365	3.9692	0.0792
	EEMD-DWT	8.9053	34.4211	4.3383	0.0625
101	***EMD-DWT***	8.9945	30.9755	4.0238	0.1426
	EEMD-DWT	9.1173	32.5359	4.1104	0.1051
103	***EMD-DWT***	11.5512	40.0181	4.7993	0.2423
	EEMD-DWT	10.6443	45.0362	5.0404	0.15325
115	***EMD-DWT***	7.5308	24.6681	2.0466	0.24225
	EEMD-DWT	7.6621	27.0204	2.0648	0.16329

The comparaison of the calculated parameters in our denoising technique with another one [12], show the effectiveness of our method (TABLE II).

TABLE II. Comparison of statistical parameters of our method and another one

Method		Crest factor	Kurtosis	Skewness	RMS value
K.TEJA et al [12]	***EMD***	6.2344	17.1023	3.2414	0.1500
	EEMD	6.9824	18.9856	3.3594	0.1700
Proposed method	***EMD-DWT***	9.04555	31.0495	3.7097	0.1765
	EEMD-DWT	9.08225	34.7534	3.8884	0.1221

VII. CONCLUSION

In this paper, we have presented a new ECG denoising technique based on the conjoint use of the empirical mode decomposition method (EMD) and the discrete wavelet transform (DWT). We have obtained a significant enhancement of the original signal quality by eliminating the baseline wander and the high frequency noise. So, this technique can be employed as a powerful pretreatment tool in modern system of segmentation and classification systems.

REFERENCES

[1] Y. Weiting and Z. Runjing, "An improved self-adaptive filter based on LMS algorithm for filtering 50Hz interference in ECG signals," in 2007 8th International Conference on Electronic Measurement and Instruments, 2007, pp. 3–874–3–878.

[2] G. Lenis, N. Pilia, A. D'Ancona, S. Min, H. Han, and K. H. Chon, "Comparison of baseline wander removal techniques considering the preservation of ST changes in the ischemic ECG: A simulation study," Computational and Mathematical Methods in Medicine, vol. 2017, 2017.

[3] S. Boda and M. Mahadevappa, "A hybrid method for removal of power line interference and baseline wander in ECG signals using EMD and EWT," Biomedical Signal Processing and Control, vol. 67, p. 102466, 2021.

[4] A. Zeiler, D. Box, G. Lawrence, C. Gardner, and S. Chintalapudi, "Empirical mode decomposition—An introduction," in The 2010 International Joint Conference on Neural Networks (IJCNN), 2010, pp. 1–8.

[5] M. A. Kabir and C. Shahnaz, "Denoising of ECG signals based on noise reduction algorithms in EMD and wavelet domains," Biomedical Signal Processing and Control, vol. 7, no. 5, pp. 481–489, 2012.

[6] M. Blanco-Velasco, B. Weng, and K. E. Barner, "ECG signal denoising and baseline wander correction based on the empirical mode decomposition," Computers in Biology and Medicine, vol. 38, no. 1, pp. 1–13, 2008.

[7] H. Li, J. Li, L. Zheng, and C. Liu, "Denoising and R-peak detection of electrocardiogram signal based on EMD and improved approximate envelope," Circuits, Systems, and Signal Processing, vol. 33, pp. 1261–1276, 2014.

[8] S. A. Malik, S. A. Parah, and G. M. Bhat, "Electrocardiogram (ECG) denoising method utilizing Empirical Mode Decomposition (EMD) with SWT and a Mean based filter," in 2021 2nd International Conference on Intelligent Engineering and Management (ICIEM), 2021, pp. 322–326.

[9] Z. Wu and N. E. Huang, "Ensemble empirical mode decomposition: A noise-assisted data analysis method," Advances in Adaptive Data Analysis, vol. 1, no. 01, pp. 1–41, 2009.

[10] K.M. Chang, "Arrhythmia ECG noise reduction by ensemble empirical mode decomposition," Sensors, vol. 10, no. 6, pp. 6063–6080, 2010.

[11] S. Maheshwari and A. Kumar, "Empirical mode decomposition: Theory & applications," International Journal of Electronic Engineering, pp. 873-878, 2014.

[12] K. Teja, R. Tiwari, and S. Mohanty, "Adaptive denoising of ECG using EMD, EEMD and CEEMDAN signal processing techniques," Journal of Physics: Conference Series, vol. 012077, IOP Publishing, 2020.

[13] R. Polikar, "The wavelet tutorial. Part IV. Multiresolution analysis: The discrete wavelet transform," Rowan University, 2008.

[14] F. Bouaziz, D. Boutana, and M. Benidir, "Multiresolution wavelet-based QRS complex detection algorithm suited to several abnormal morphologies," IET Signal Processing, vol. 8, no. 7, pp. 774-782, 2014.

[15] S. Z. Mahmoodabadi, A. Ahmadian, and M. D. Abolhasani, "ECG Feature Extraction using Daubechies Wavelets," in Proceedings of the fifth IASTED International conference on Visualization, Imaging and Image Processing, 2005, pp. 343-348.

[16] A.M. Atto, D. Pastor, and G. Mercier, "Wavelet shrinkage: unification of basic thresholding functions and thresholds," Signal, Image and Video Processing, vol. 5, pp. 11-28, 2011.

[17] MIT-BIH. "MIT-BIH Arrhythmia Database." [Online]. Available: http://www.physionet.org/mitdb. [Accessed: 20/10/2023].

[18] P. Bansod and R. Lambhate, "A new approach for removal of baseline wande in ECG signal using Empirical Mode Decomposition & Hurst Exponent," in 2016 International Conference on Recent Advances and Innovations in Engineering (ICRAIE), 2016, pp. 1-6.

Efficient Gear Fault Detection in Rotating Machines through Envelope-Derivative Operator Analysis

Bouhafs Lina [1], Salah Tamalouzt [1], Bouzida Ahcen [2]

[1]Laboratoire de Technologie Industrielle et de l'Information (LTII), Faculté de Technologie, Université de Bejaia, 06000 Bejaia, Algérie
lina.bouhafs@univ-bejaia.dz, salah.tamalouzt@univ-bejaia.dz

[2]Département de Génie Electrique, Faculté des sciences et des sciences appliquées, Université de Bouira, 10000, Algérie
a.bouzida@univ-bouira.dz

Abstract— ***Feature extraction from rotating machine condition monitoring signals is a difficult task and is important to maintenance planning and preventing equipment breakdown. In some applications, such as wind turbines, a gear fault can potentially result in a life-threatening situation. The vibration signals emanating from gear contain not only multiple constituents but also a great deal of background noise. In this paper, the envelope-derivative operator (EDO) is proposed for matching amplitude and frequency in the signal energy. The EDO evaluates the signal's energy content in time and frequency domains, which has been shown to be effective in detecting the impulse-like behaviour associated with gear faults. The procedure brings up accurate results from complicated signals by separating the fault-associated signal components. The results indicate that the proposed operator performs efficiently on gear fault diagnosis in various experimental conditions, requires minimal data fitting and has low computational cost.***

I. INTRODUCTION

Gears are crucial components in many industrial systems [1]. These components are subject to various stresses, which can lead to malfunctions. Early detection of these faults is essential to ensuring service continuity and gear life extension [2]. Several methods exist for detecting gear faults, including frequency-domain signal processing. In [3], the authors proposed how to use empirical modal decomposition (EMD) to improve the demodulation of acoustic signals by using the Hilbert transform to detect gear faults in the envelope spectrum. However, EMD suffers from a major problem related to the mixing of modes, so it is difficult to reconstruct the original signal.

Another method is proposed in [4], which uses a convolutional neural network (CNN) to fuse vibration signals to detect gear faults. However, this method can produce complex models that are difficult to interpret, and it requires a lot of training data to work effectively. This makes the evaluation of this model very expensive in terms of computing resources and time. As stated in [5], the high-frequency resonance technique (HFRT) is also commonly used in industry since it makes it possible to extract information about faults in operating machinery. This method enables the extraction of data on the components indicating the flaws and the assessment of their severity. It is sensitive to noise and random variations in rotational frequencies. However, choosing the proper centre frequency and bandwidth is principal implementation challenge of this technique. [6] The suggested method is used to analyse simulated vibration data generated by a dynamic model of a bevel gearbox. The instantaneous energy of the signal is evaluated using the Teager-Kaiser Energy Operator (TKEO). Then, using shock detector (SD), the shock contents of the TKEO signal, which represent the impact of the defect, are examined and quantified, and in [7], a gearbox with a chipped tooth is monitored utilising experimental data and the Hilbert transform (HT). The modulated signal associated with the gear fault is highlighted after applying HT to each product function (PF) to obtain the envelope for each decomposed component. However, in the presence of considerable noise and vibration interferences, conventional techniques such as HT and TKEO are unable to determine the fault characteristic frequency.

This paper deals with and reviews the performance of the Envelope Derived Operator (ODE) for diagnosing gear teeth defects on a system driven by an electrical motor, which is then experimentally tested on a real gearbox with no data fitting necessary and a minimal computational footprint.

II. THEORETICAL BASIS

A modulated signal x(t), is typically employed as the analytical signal, which is determined by [8]:

$$X(t) = x(t) + jH[x(t)] = A(t)e^{j\varphi(t)} \quad (1)$$

where H[x(t)] is the Hilbert transform of x(t), A(t) and φ(t) are respectively the instantaneous amplitude (envelope, magnitude) and instantaneous phase.

In the event that the Fourier transform of $x(t)$ is $X(\omega)$. Utilising the harmony feature that $\dot{x}(t) = j\omega X(\omega)$, the derivative function is selected as the weighting filter.

The definition of the Envelope Derivative Operator (EDO) is [9]:

$$\Gamma(t) = \left|\dot{x}(t) + jH[\dot{x}(t)]\right|^2 = \dot{x}^2(t) + H[\dot{x}(t)]^2 \quad (2)$$

The EDO is written as follows for the discrete signal x(n) [10]:

$$\Gamma[x(n)] = \frac{1}{4}\left[x^2(n+1) + x^2(n-1) + h^2(n+1) + h^2(n-1)\right] + \frac{1}{2}\left[x(n+1) + x(n-1) + h(n+1) + h(n-1)\right] \quad (3)$$

where h(n) is the discrete Hilbert transform and defined as:

$$h(n) = \left[x(n)\right] \quad (4)$$

III. APPLICATION TO EXPERIMENTAL SIGNALS

A. Experimental study

Fig. 1 describes the experimental test carried out by the University of New Wales, Kensington, Australia, and LASPI, Senlis [11] to investigate the impact of gear profile errors on gearbox error. The proposed method is applied to gearbox vibration signals obtained from an experimental test previously conducted by Sawalhi. The rig features a single stage gearbox with a spur gear set containing 32 teeth on each gear, and a 1:1
gear ratio. The focus is on the first set of tests, with a defective tooth on the driven wheel. Various sensors were
employed to record data signals on the gear reducer; consisting of 7 accelerometers and 1 tachymeter.

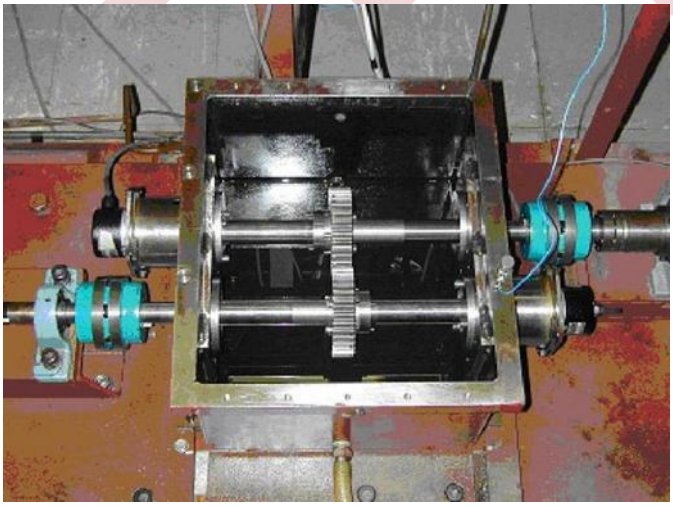


Figure 1. Experimental test of Sawalhi [11]

B. Results and discussion

In this study, a MATLAB simulation was performed to study the behaviour of healthy and defective states of a wheel tooth based on vibration signals obtained from experimental tests performed by Sawalhi. The signals obtained were demodulated using the envelope and ODE transformations to analyse the frequency-amplitude characteristics and identify the defect.

The study's goal is to apply the EDO approach to detecting problems in gearboxes used in wind turbines with background noise by comparing them with the envelope transform. This comparative analysis aims to discern the most suitable approach for reliably identifying defects, even when dealing with noisy environments. Thus, the faulty spectra are compared to the healthy ones, and the recorded vibration signal of the gearbox in both healthy and faulty situations is addressed in the frequency domain. The values given for the driven wheel rotation frequency and the drive wheel rotation frequency are the rotation frequencies of the wheels in the gearbox. These numbers can be used to determine the condition of the gearbox and potentially detect any defects. The meshing frequency is around 960 Hz. The sampling frequency is 97656 hertz.

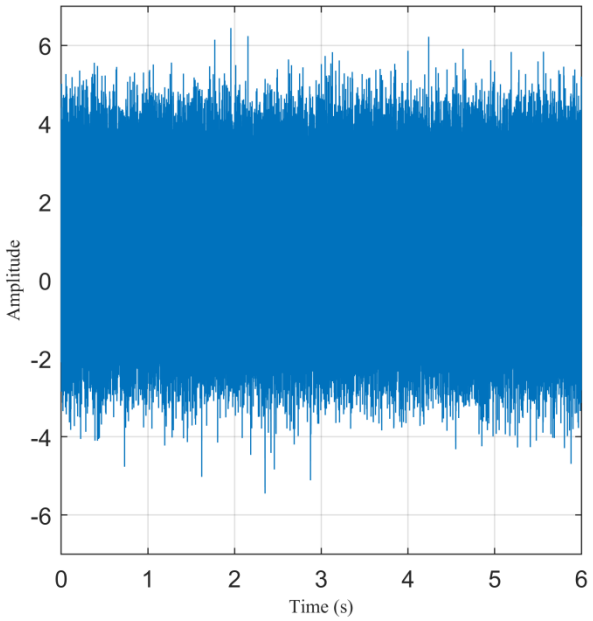


Figure 2. The healthy measured signal

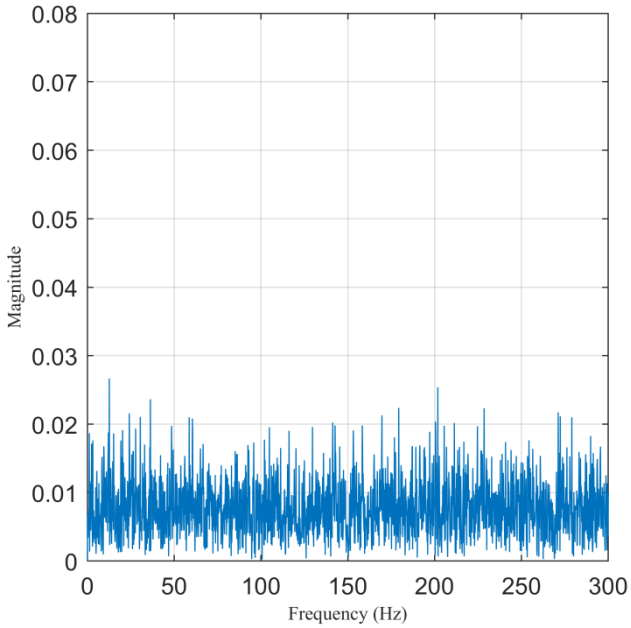


Figure 3. The envelope of the healthy signal

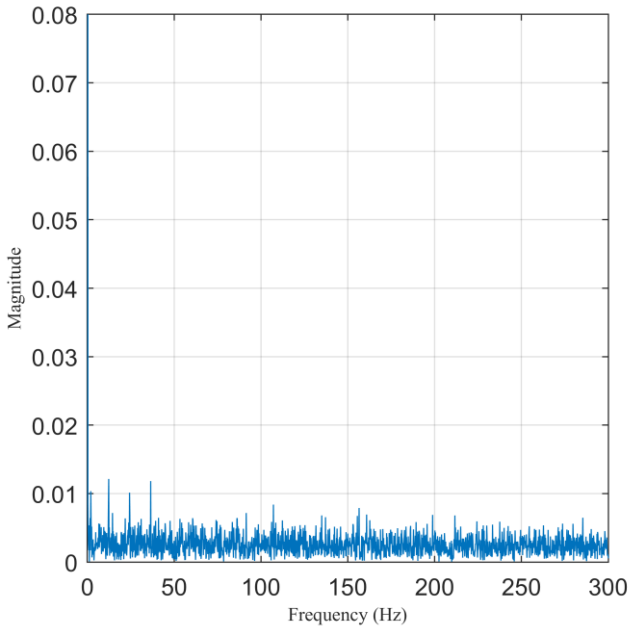


Figure 4. Spectrum of EDO results of the healthy signal

Signal analysis results are presented in Figs. 2, 3 and 4 for the healthy signal and in Figs. 5, 6 and 7 for the faulty signal, using the envelope and ODE transformations.

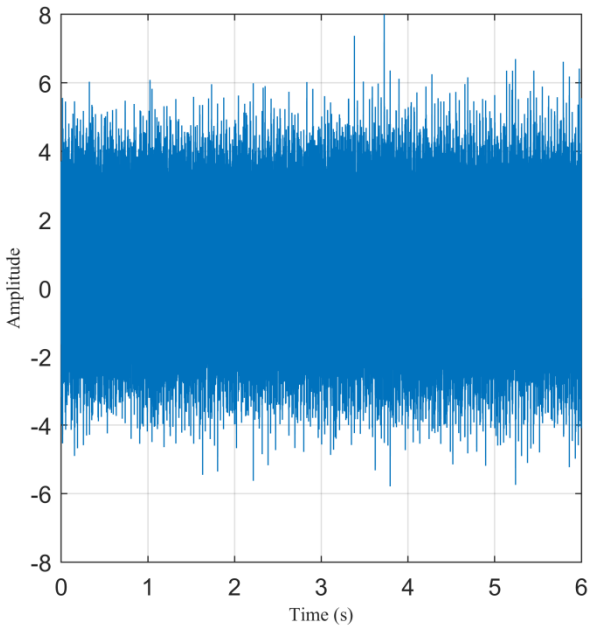


Figure 5. The faulty measured signal

Figs. 2 and 5 depict the temporal vibration signal, while Figs. 3 and 6 depict envelope of healthy and faulty signals.

Figs. 4 and 7, respectively, show the modified spectra for the two signals, one healthy and the other faulty. The location of the degraded tooth is made possible by the obvious determination of

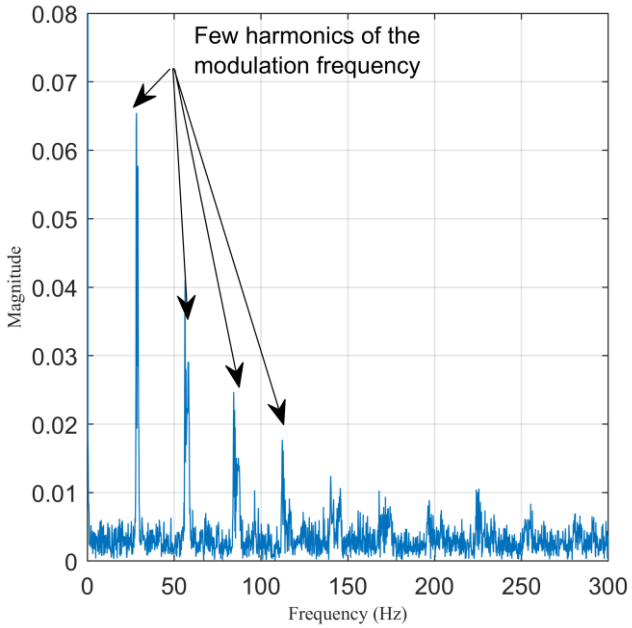


Figure 5. The envelope of the faulty signal

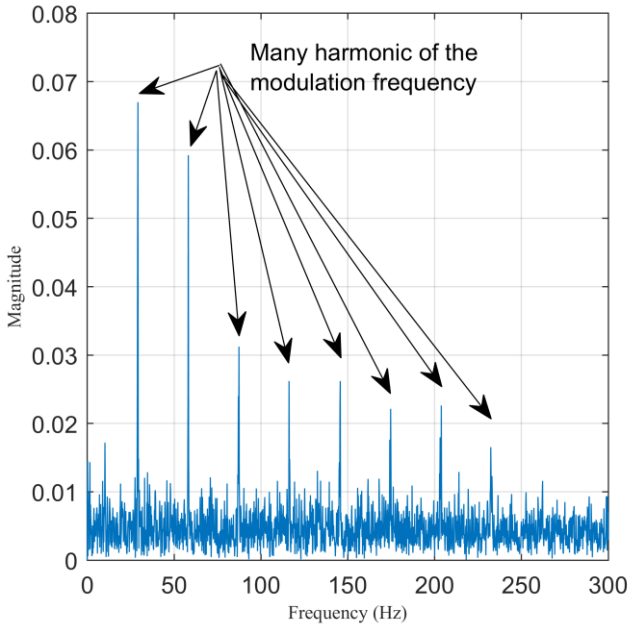


Figure 6. Spectrum of EDO results of the faulty signal

many harmonics of the typical defect frequency (30, 60, 90, 120, and 150, 180, 210, 240 and 270 Hz), Whenever the detoriorated tooth grows, there will be a repetitive shock. This repetitive shock will therefore manifest itself in the harmonics of the affected pinion's rotational frequency."unlike Fig. 6, which shows few harmonics. In contrast, Fig. 4 demonstrates that no appreciable peak is found for healthy gear. It is obvious that the EDO can successfully improve the accuracy of fault identification.

The envelope method cannot match the fault frequency because due to the domination of the interference frequencies. It is important to note that the ODE transformation clarifies the harmonics of the characteristic fault frequency in the signal, as can be seen by comparing Figs. 4 and 7 with Figs. 3 and 6, respectively. This shows that the ODE method is effective in suppressing background noise and improving the accuracy of fault detection at the same time.

IV. CONCLUSION

In this paper, a new approach is proposed to gear fault detection and identification. The application of the envelope derivative operator (ODE) in the analysis of gear monitoring signals has shown an effective ability to suppress background noise and improve fault detection accuracy without using pre-filtering. In summary, ODE is a powerful and valuable tool for ensuring reliable operation and avoiding costly failures. Future prospects could include applying this method to real industrial application data to evaluate its performance, as well as optimising the method for more effective use with other specific fault types.

V. REFERENCE

[1] K. Feng, Q. Ni, M. Beer, H. Du, and C. Li, "A novel similarity-based status characterization methodology for gear surface wear propagation monitoring", Tribology International, 174, 107765, 2022.

[2] J. Hare, X. Shi, S. Gupta, and A. Bazzi, "Fault diagnostics in smart micro-grids: A survey", Renewable and Sustainable Energy Reviews, 60, 1114-1124, 2016.4

[3] F. Leaman, C. M. Clausen, E. Clausen, " Empirical mode decomposition potential for Hilbert demodulation of acoustic emission signals in gearbox diagnostics", Vibration Engieering and Technologies, V. 10, P. 621-637, 2022.

[4] X. Zhu, X. Ye, R. Wang, W. Zhao, X. Luo, J. Zhao, X. Gao , " Investigation and experimental study of the method for diagnosing gearbox vibration faults based on the convolutional learning network of fusion functionalities, experimental techniques ", P. 1- 12, 2022.

[5] Y. Wu and P. Zhang, "Online monitoring for power cables in DFIG-based wind farms using high-frequency resonance analysis ", IEEE Transactions on Sustainable Energy, 13(1), 378-390, 2021.

[6] R. Ziani, A. Hammami, F. Chaari, A. Felkaoui, and M. Haddar, " Gear fault diagnosis under non-stationary operating mode based on EMD, TKEO, and Shock Detector", Comptes Rendus Mécanique, 347(9), 663-675, 2021.

[7] A. Afia, C. Rahmoune, and D. Benazzouz, "An early gear fault diagnosis method based on RLMD, Hilbert transform and cepstrum analysis", Mech Syst Control, 2020.

[8] Y. Imaouchen, M. Khedadouche and M. Thomas, "A frequency-weighted energy operator and complementary ensemble empirical mode decomposition for bearing fault detection", Mechanical system and signal processing, 82, 103-116, 2017.

[9] J.M.O. Toole, A. Temko and N. Stevenson, "Assessing instantaneous energy in the EEG: a non-negative, frequency-weighted energy operator", Proceedings of IEEE conference, 3288–3291, 2014.

[10] P. D. McFadden, , " Detecting fatigue cracks in gears by amplitude and phase demodulation of the meshing vibration", Vibration, Acoustics, Stress and Reliability in Design, 108, 165-170, 1986.

[11] N. Sawalhi, N, Diagnostics, "prognostics and fault simulation for rolling element bearings", The University of New South Wales, School of Mechanical and Manufacturing Engineering, Australia, 2007.

Comparative Evaluation of YOLOv5 and YOLOv8 Across Diverse Datasets

1st SID AHMED Soumia[1], 2nd Belaalia Asma[2], 3rd Namoune Khaoula[3]

[1] *Electrical Engineering, Bordj Bou Arreridj, Algeria*
soumia.sidahmed@univ-bba.dz

[2] *Industrial Electronics, Souk-Ahras, Algeria*
asmabelaalia535@gmail.com

[3] *Industrial Electronics, Mila, Algeria*
khaoulanamoune@gmail.com

***Abstract*— This paper presents a comparative study of object detection models, including YOLOv5, and YOLOv8. It covers the architecture and training process of these models, highlighting their strengths and limitations throughout a comparative analysis of the results. Our primary focus is on retraining YOLOv5 and YOLOv8 on our custom datasets, we aim to determine whether employing algorithms with a high number of parameters is truly necessary for our specific datasets, or if it would be more advantageous to propose a new model architecture. This comparison holds significant importance when considering implementation in embedded systems.**

Keywords: Object Detection, CNN, YOLOV5, YOLOV8.

I. INTRODUCTION

Object detection is a crucial but difficult vision task. It is an essential component of many applications, including object tracking, scene understanding, image auto-annotation, and image search (1). In general, there are two types of object detection algorithms: single stage and two stage (2).

Object detection in images and videos is performed using single-stage object detection algorithms, also referred to as one-stage detectors. In a single forward pass, these algorithms use a single neural network to forecast the bounding boxes and class probabilities for every object in the input image (3).

You Only Look Once (YOLO) and SSD (Single Shot Detector) represent two prominent single-stage object detection methods (4). While these algorithms offer the advantage of speed, enabling real-time performance on low-power devices, they may sacrifice some degree of accuracy. Numerous applications, including robotics, surveillance, and automated driving, where real-time performance is essential, make extensive use of single-stage object detection algorithms.

In contrast, two-stage object detection algorithms adopt a different approach, breaking the detection process into two distinct stages. Initially, a region proposal network (RPN) generates potential object locations as region proposals, each assigned a likelihood score (5). Subsequently, in the second stage, these region proposals undergo refinement and classification into distinct object categories. This second stage employs a separate network that takes each region proposal as input and delivers the final bounding box coordinates and class probabilities for each detected object.

The choice between single-stage and two-stage detectors depends on the specific requirements of the application, weighing the need for real-time performance against the precision of object detection. Fast R-CNN (Region-based Convolutional Neural Network) and Faster R-CNN (Faster Region-based Convolutional Neural Network) are the most widely used two-stage object detection algorithms (6) (7). Two-stage detectors are typically characterized by higher accuracy compared to their single-stage counterparts, albeit at the expense of speed and increased computational demands. They find their niche in high-precision applications such as medical image analysis, satellite image processing, and object recognition within complex natural environments.

In this work, we will shift our focus towards the implementation of the highly regarded algorithm known as YOLO. Specifically, we will explore the latest versions, namely YOLOv5 and YOLOv8, which was launched on January 10th, 2023.

The rest of this paper is structured as outlined below: Section 2 provides an analysis of the distinctions between YOLOv5 and YOLOv8. Section 3 details the data employed in our experiments. Our experimental findings are presented in Section 4, while Section 5 displays the results of our experiments. Finally, Section 6 delves into the discussion, and Section 7 discusses future avenues of research.

II. THE DIFFERENCE BETWEEN YOLOV5 AND YOLOV8

When it comes to object detection, there are numerous models to choose from. Among them, YOLOv8 and YOLOv5 stand out as two highly popular and state-of-the-art models developed by Ultralytics. In our paper, we will concentrate on the nano variants of these two versions, which can be effectively deployed on embedded systems. YOLOv8, the latest addition to the YOLO family, builds upon the success of previous versions and introduces new features and enhancements to improve performance and flexibility. On the other hand, YOLOv5 is celebrated for its speed, simplicity, and accuracy.

When selecting the optimal object detection model, several factors come into play. These factors encompass speed, accuracy and ease of use. In terms of speed, both YOLOv8 and YOLOv5 exhibit fast processing capabilities, with YOLOv8 being notably faster (as shown in Table 1), making it suitable for real-time object detection applications. In terms of accuracy, YOLOv8 outperforms YOLOv5 due to architectural enhancements. As for ease of use, both models are easy to use, but YOLOv5, built on the PyTorch framework, offers the easiest integration and deployment for developers (8).

TABLE I. TOTAL PARAMETERS OF YOLOV5N AND YOLOV8N MODELS.

Models	Params (Million)	Accuracy (mAP)	CPU Time(ms)	GPU Time(ms)
YOLOv5n	1.9	45.7	45	6.3
YOLOv8n	3.2	37.3	8.4	0.99

III. TRAINING DATA

We have chosen datasets from six different categories, including malaria, drone, lung cancer, aircraft, breast cancer, and brain tumor. These diverse categories offer us a wide range of options for our experiments.

The dataset does not have bounding boxes around the objects, we need to add them ourselves. This is often one of the hardest and most costly parts of a Deep Learning project. It is a good idea to spend time looking for the right tools.

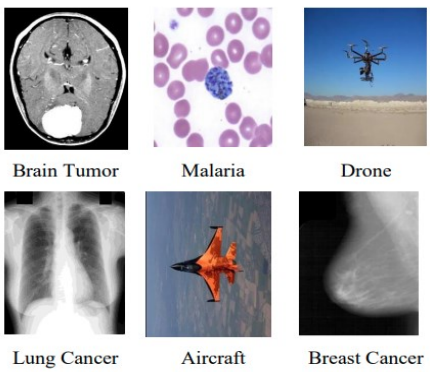


Figure 1. Dataset.

Regarding the Brain Tumor dataset, we employed the LabelImg tool to annotate the images. Nevertheless, this tool produced annotations in XML format, requiring the incorporation of a code snippet to facilitate their conversion into CSV format.

Both the Malaria and Aircraft Datasets were acquired from Roboflow. In the case of the Malaria images, they contained black frames, prompting us to proactively address this concern by cropping out these unwanted black frames from the images. Following dataset collection, the subsequent step involved annotation, where we meticulously labeled the objects of interest within each image by delineating bounding boxes around them. To ensure efficiency and precision in this annotation process, we made the deliberate choice to leverage Roboflow as our annotation tool.

The third dataset, "Drone," was sourced from Roboflow, along with its accompanying CSV file. This dataset was used in its original, unaltered state, without any modifications.

The Lung Cancer dataset was sourced from Kaggle, and subsequently, Roboflow was employed for the annotation process, it is important to note that the dataset is not extensive, comprising only 100 images. In table II below we represent all the data used in this thesis, it shows the number of samples in each dataset that were used for both training and testing

TABLE II. TABLE TYPE STYLES

Dataset	Number of images		Total
	Train	*Test*	
Lung Cancer	80	20	100
Breast Cancer	100	66	166
Brain tumor	120	92	212
Malaria	150	62	213
Aircraft	200	80	280
Drone	400	100	500

After the labeling process as shown in Figure2, we got the information about the object desired which is typically represented by four values: the coordinates of the top-left corner $(Xmin, Ymin)$ and the coordinates of the bottom-right corner $(Xmax, Ymax)$. These details were then stored within a CSV (comma-separated values) file, Figure 3 displays a segment from the CSV file.



Figure 2. Annotated datasets.

.

	A	B	C	D	E	F	G	H
1	filename	width	height	class	xmin	ymin	xmax	ymax
2	JPCLN003_pr	300	300	cancer	117	55	220	184
3	JPCLN082_pr	300	300	cancer	128	59	232	245
4	JPCLN050_pr	300	300	cancer	133	64	227	208
5	JPCLN017_pr	300	300	cancer	128	64	241	217
6	JPCLN105_pr	300	300	cancer	124	78	218	223
7	JPCLN021_pr	300	300	cancer	137	68	219	229
8	JPCLN063_pr	300	300	cancer	109	81	209	254
9	JPCLN130_pr	300	300	cancer	129	83	239	237

Figure 3. A snippet from the CSV file.

IV. EXPERIMENTAL RESULTS

A. YOLOv5 results

In our project we use Google Colab as software tool as it offers the ability of using free GPU.

We utilized TensorBoard to generate graphical representations of training loss, Recall, precision, and MAP metrics. TensorBoard is a web-based visualization tool offered by TensorFlow, a widely adopted Deep Learning framework. It serves as a valuable resource for visualizing and analyzing diverse aspects of the performance of Machine Learning models.

Figure 4 illustrates the application of YOLOv5 for malaria detection.

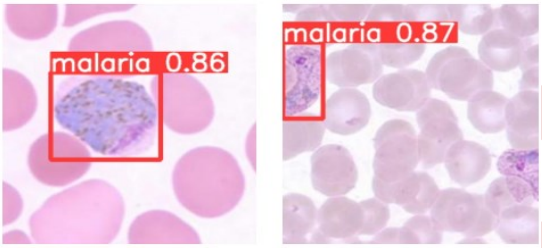


Figure 4. Malaria detection using YOLOv5.

Figure 5 represents the plots of the loss and MAP metrics during training of YOLOv5 on Malaria Dataset.

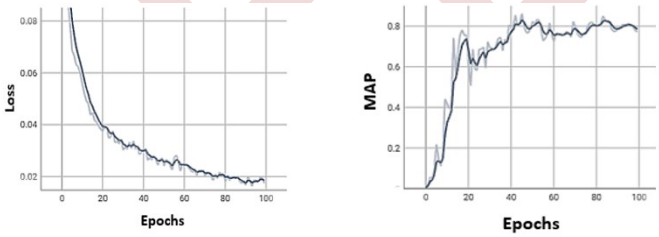


Figure 5. MAP and loss plots after training the YOLOv5 Nano on the Malaria detection Dataset.

Figure 6 below shows the precision and Recall graphs during the training of Malaria Dataset using YOLOv5.

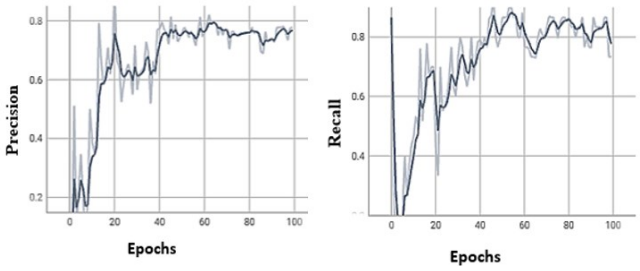


Figure 6. Precision and Recall plots after training the YOLOv5 Nano on the Malaria detection Dataset.

Figure 7 illustrates the application of YOLOv5 for the Drone dataset.

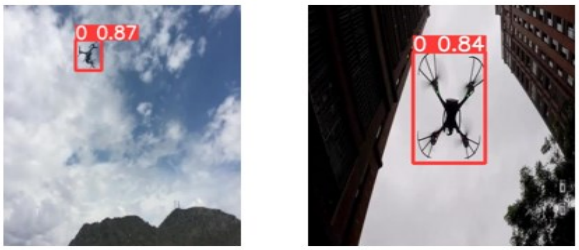


Figure 7. Drone detection using YOLOv5.

Figure 8 displays the training results of YOLOv5 on the Drone Dataset, specifically depicting the loss and MAP metrics. Similarly, Figure 9 provides insights into the Recall and precision metrics for the same training.

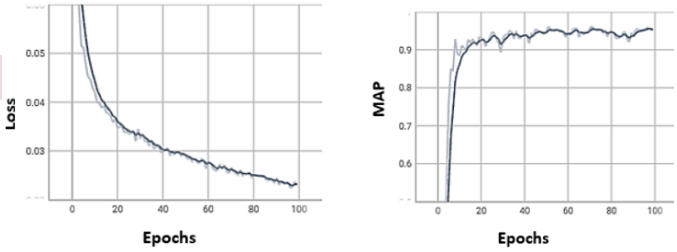


Figure 8. MAP and loss plots after training the YOLOv5 Nano on the Drone detection Dataset.

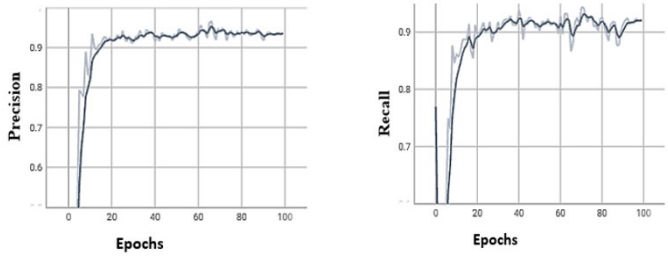


Figure 9. Precision and l Recall plots after training the YOLOv5 Nano on the Drone detection Dataset.

Figure 10 illustrates the application of YOLOv5 for Lung Cancer detection.

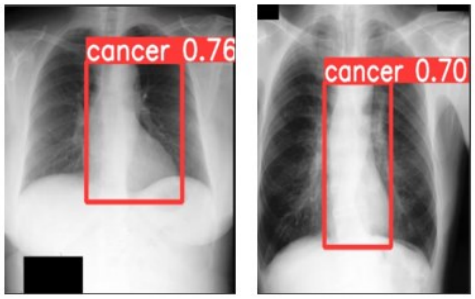


Figure 10. Lung Cancer detection using YOLOv5n.

Figure 11 shows the training outcomes of YOLOv5 concerning the Lung Cancer Dataset, with a particular focus on the loss and MAP metrics. Similarly, Figure 12 provides an overview of the Recall and precision metrics for the identical training scenario.

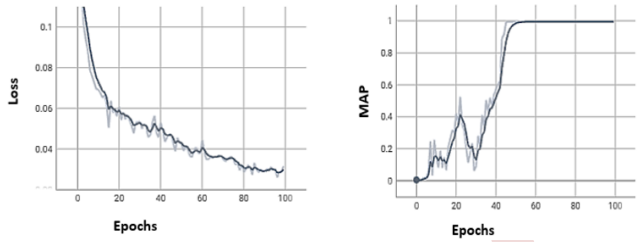


Figure 11. MAP and loss plots after training the YOLOv5 Nano on the Lung Cancer detection Dataset.

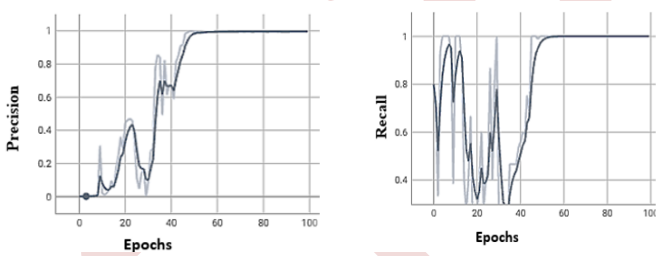


Figure 12. Precision and l Recall plots after training the YOLOv5 Nano on the Lung Cancer detection Dataset.

B. YOLOv8 results

Now we move to the results of the YOLOv8 implementation on our customized Datasets.

Figure 13 illustrates the application of YOLOv8 for malaria detection.

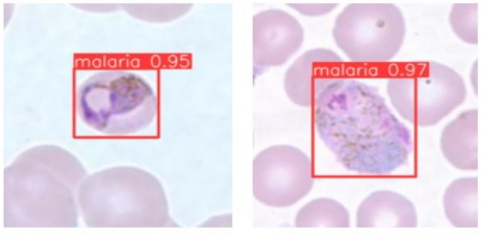


Figure 13. Malaria detection using YOLOv8.

The following figures illustrate the outcomes of the YOLOv8 implementation on Malaria Dataset

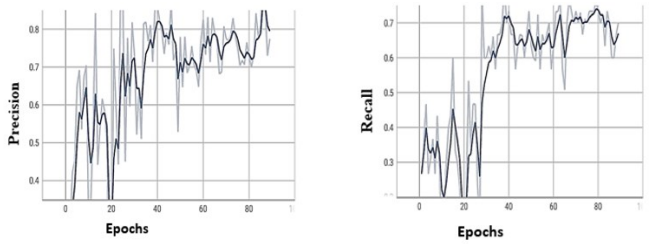


Figure 14. Precision and Recall plots after training the YOLOv8 Nano on the Malaria detection Dataset.

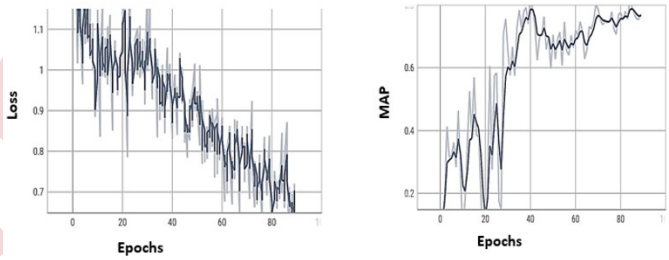


Figure 15. MAP and loss plots after training the YOLOv8 Nano on the Malaria detection Dataset.

Figure 16 illustrates the application of YOLOv8 for the Drone dataset.



Figure 16. Drone detection using YOLOv8.

Figure 17 displays the training results of YOLOv8 on the Drone Dataset, specifically depicting the loss and MAP metrics. Similarly, Figure 18 provides insights into the Recall and precision metrics for the same training.

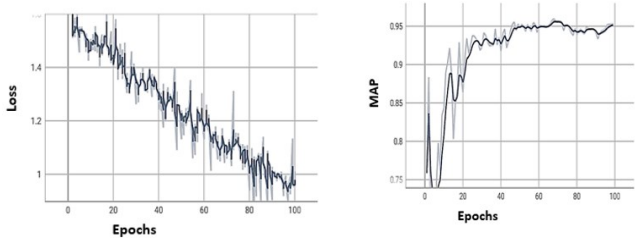


Figure 17. MAP and loss plots after training the YOLOv8 Nano on the Drone detection Dataset.

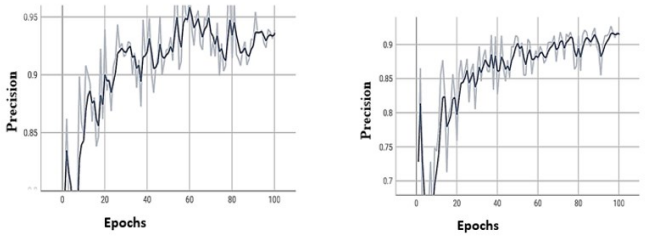


Figure 18. Precision and l Recall plots after training the YOLOv8 Nano on the Drone detection Dataset.

Figure 19 illustrates the application of YOLOv8 for Lung Cancer detection.

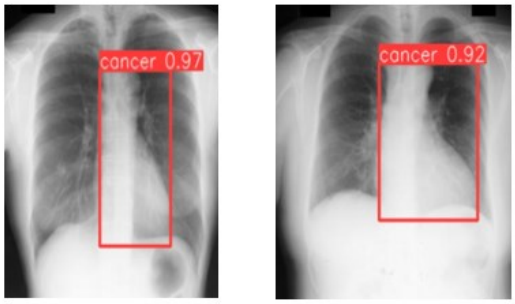


Figure 19. Lung Cancer detection using YOLOv8n.

The performance metrics for loss, Mean Average Precision (MAP), recall, and precision of YOLOv8 training on the Lung Cancer Dataset are depicted in figures 20 and 21.

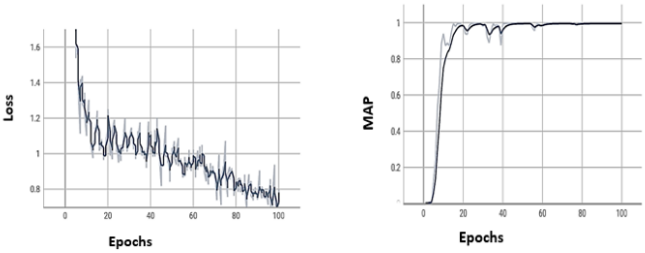


Figure 20. MAP and loss plots after training the YOLOv8 Nano on the Lung Cancer detection Dataset.

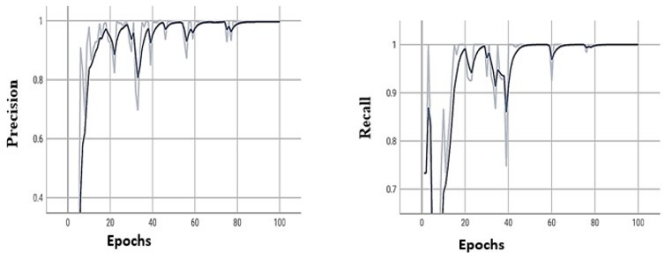


Figure 21. Precision and Recall plots after training the YOLOv8 Nano on the Lung Cancer detection Dataset.

V. YOLOv5 AND YOLOv8 RESULTS INTERPRETATION

With only 1.9 million and 3.2 million parameters, the YOLOv5n and YOLOv8n models proved to be effective. They showed low loss values, high MAP scores, and accurate object detection performance with impressive recall and Precision values.

Our comparison involved utilizing identical datasets, hyper-parameters, and training settings for both YOLOv5n and YOLOv8n. We trained these models for 100 epochs with images resized to a dimension of 300 x 300, as they were previously rescaled.

The loss metric serves as a measure of the model's ability to effectively reduce the disparity between the predicted bounding boxes and the ground truth annotations throughout the training process. As we monitored the model's progress, in both YOLOv5n and YOLOv8n we observed a gradual decline in the loss values. This decline indicates that the model became increasingly adept at accurately predicting the bounding boxes, aligning more closely with the ground truth annotations over time. The diminishing loss values signify the model's improved capability to minimize the deviation between predicted and actual object locations, ultimately leading to enhanced object detection performance.

MAP (Mean Average Precision) serves as a widely adopted metric in object detection, providing an assessment of the precision and recall trade-off across various object categories. Throughout the training of YOLOv5n and YOLOv8n, we closely monitored the progress and noticed a consistent increase in MAP scores. This upward trend in MAP values signifies notable improvements in detection performance across the complete.
Spectrum of object classes. Higher MAP scores indicate that the models achieved a more balanced combination of precision and recall, resulting in enhanced accuracy and reliability in identifying objects of diverse categories. This overall advancement in MAP highlights the effectiveness of YOLOv5n and YOLOv8n in capturing a wide range of objects with increased precision and recall compared to earlier stages of training.

VI. CONCLUSION AND PERSPECTIVE

In conclusion, our paper centered on evaluating the performance of two prominent object detection algorithms, namely YOLOv5n and YOLOv8n, through a comprehensive comparative analysis. The primary objective was to identify the optimal object detection model that balances speed and accuracy.

Our findings indicate that YOLOv8n emerged as the most suitable choice for object detection tasks, offering a remarkable blend of precision and efficiency. In summary, our research underscores the significance of selecting the right object detection model, with YOLOv8n standing out as a highly efficient and accurate option for real-world applications. These insights can significantly contribute to enhancing the performance and efficacy of object detection systems across various domains.

Using the latest Yolo version in our current work has inspired us to apply this algorithm in our forthcoming work,

particularly in the field of medical imaging, encompassing conditions like lung cancer and breast cancer. Our aim is to assist healthcare professionals in the early detection of abnormalities, potentially leading to life-saving interventions.

It's important to highlight that we encountered specific hardware challenges, despite utilizing Google Colab for efficiently managing large datasets. Additionally, we had limited images available, especially for the lung cancer dataset. However, we successfully implemented both algorithms and achieved excellent results when calculating different object detection metrics.

REFERENCES

[1] Chai, Junyi, et al. "Deep learning in computer vision: A critical review of emerging techniques and application scenarios." Machine Learning with Applications 6 (2021): 100134.

[2] Redmon, Joseph, et al. "You only look once: Unified, real-time object detection." Proceedings of the IEEE conference on computer vision and pattern recognition. 2016.

[3] Johnson, A. (2021). "Understanding Single-Stage Object Detection Algorithms: A Comprehensive Review". Journal of Computer Vision and Image Analysis, 10(2), 75-88.

[4] Shafiee, Mohammad Javad, et al. "Fast YOLO: A fast you only look once system for real-time embedded object detection in video." arXiv preprint arXiv:1709.05943 (2017).

[5] Du, Lixuan, Rongyu Zhang, and Xiaotian Wang. "Overview of two-stage object detection algorithms." Journal of Physics: Conference Series. Vol. 1544. No. 1. IOP Publishing, 2020.

[6] Girshick, Ross. "Fast r-cnn." Proceedings of the IEEE international conference on computer vision. 2015.

[7] Jiang, Huaizu, and Erik Learned-Miller. "Face detection with the faster R-CNN." 2017 12th IEEE international conference on automatic face & gesture recognition (FG 2017). IEEE, 2017.

[8] Terven, Juan, and Diana Cordova-Esparza. "A comprehensive review of YOLO: From YOLOv1 to YOLOv8 and beyond." arXiv preprint arXiv:2304.00501 (2023).

EEIC'23

XI

TELECOMMUNICATION SYSTEMS AND NETWORKS (TSN)

Sommaire

XI.1 Analytical study on energy optimization via dynamic transmission power adjustment for task offloading in edge computing **602**
XI.2 Performance analysis of spatially modulated MIMO systems **608**
XI.3 Inter-numerology interference analysis and mitigation techniques for 5G networks **614**
XI.4 Enhacing the performances of 5G communication systems with rate splitting multiple access. **620**
XI.5 Enhancing the performance of wireless communication systems through the use of beamforming antenna and massive MIMO technology **626**
XI.6 Terahertz for wireless communication and radio frequency **632**
XI.7 Cellular-connected UAVs : coverage analysis using SWIPT and up-tilted antenna **638**
XI.8 Improved gain for T-Shaped slot antenna using new EBG/AMC reflector for IOT applications **643**
XI.9 Design and simulation of rectangular microstrip patch antenna for WLAN applications **649**

Analytical Study on Energy Optimization via Dynamic Transmission Power Adjustment for Task Offloading in Edge Computing

Messaoud Babaghayou [1], Noureddine Chaib [1], Nabila Labraoui [2]
[1] *LIM Laboratory. Laghouat University, Laghouat, Algeria*
{messaoud.babaghayou , n.chaib}@lagh-univ.dz
[2] *LRI Laboratory, Tlemcen University, Tlemcen, Algeria*
nabila.labraoui@univ-tlemcen.dz

***Abstract*— This paper presents a novel approach for energy preservation in edge computing environments through dynamic transmission power changing techniques based on the proximity to the closest access point. The proposed technique incorporates four distinct transmission power levels, enabling efficient energy management. We conducted simulations in an edge-enabled environment to evaluate the energy consumption and compared our scheme against a baseline scheme. Analytical results demonstrate that our approach achieved substantial energy savings for mobile devices by leveraging transmission power adjustments. By dynamically adapting the transmission power based on access point proximity, our method demonstrates its effectiveness in optimizing energy consumption in edge computing scenarios, thus contributing to the overall sustainability and efficiency of decentralized networks.**

***Keywords:* Dynamic Transmission Power Changing, Energy Efficiency, Mobile Devices, Task Offloading.**

I. INTRODUCTION

Within the realm of distributed computing, cloud computing (EC) has emerged as a significant and revolutionary concept, distinguishing itself from conventional service-oriented and grid computing paradigms. This novel approach opens doors to synergistic collaborations, presenting a multitude of possibilities. However, despite its vast potential, cloud computing faces various challenges that require thoughtful consideration [1].

Within the computing domain, edge computing (EC), as shown in its architecture illustrated in Fig. 1, emerges as a groundbreaking technology, providing compelling solutions to overcome the limitations encountered by smart devices. Through the offloading of computationally intensive tasks to cloud servers, EC significantly reduces overall energy consumption [2] while extending the battery life of these devices, ensuring seamless operation, even in energy-constrained scenarios. Additionally, the integration of Mobile Edge Computing (MEC) [3] servers in close proximity to end devices minimizes transmission latency, leading to heightened realtime responsiveness [4].

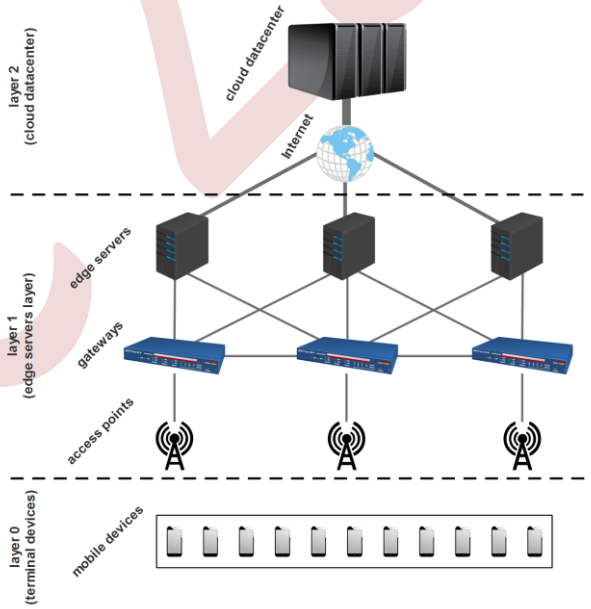


Figure 1. The general satellite edge computing architecture.

EC unlocks a multitude of applications across various domains, such as the Internet of Things (IoT), industrial systems, surveillance, autonomous vehicles [5], XR technologies (Virtual Reality and Augmented Reality), unmanned aerial vehicles (UAVs), smart cities [6], and more. These diverse utilization cases highlight the versatility and potential of edge computing. Moreover, edge computing brings about the convergence of energy-efficient computation and wireless power transfer, paving the way for seamless integration of smart devices into autonomous environments. Despite a number of challenges [7] and the impact of resources geo-location emplacement [8], this convergence holds

immense promise for the future, propelling the advancement of smart devices and their efficient integration into various autonomous systems [4].

In the context of dynamic environments featuring wireless fading channels, effective decision-making between local and remote computation becomes a paramount task. Adapting to the challenges presented by dense networks and time-varying wireless channel conditions [9], the need for optimal offloading actions arises. To determine the most suitable offloading strategy, techniques like reinforcement methods are employed. Addressing this challenge has spurred the research community to explore various solutions by harnessing the capabilities of Artificial Intelligence (AI) and its branch, Machine Learning (ML) [10] (including advanced systems like federated learning [11]). These advanced AI and ML techniques play a pivotal role in tackling the intricacies associated with decision-making in wireless environments.

This paper, we present the following two contributions:

- Proposal of a dynamic transmission power adjustment technique with four transmission power levels to reduce energy consumption by mobile devices in edge computing.
- Analytical evaluation of the proposed technique, demonstrating its effectiveness in optimizing energy consumption within the edge-enabled environment.

These contributions lay the groundwork for improved energy efficiency, extended device lifespan, and optimized task offloading within edge computing environments.

The paper's organization is as follows: Section 2 provides an overview of related works in the domain of edge computing, highlighting the scientific community's advancements and research contributions. In Section 3, our system model is presented, detailing the key components and their interactions within the edge computing environment. Section 4 explores the transmission power technique used in this study, explaining its underlying principles and how it effectively addresses the challenge of rapid battery drain in mobile devices. Moving on to Section 5, the simulations conducted to rigorously evaluate our proposed approach (analytically) are presented. Detailed analysis of the results and comprehensive discussions demonstrate the significant benefits and efficacy achieved through transmission power adjustment. Finally, Section 6 concludes this work by succinctly summarizing key findings, emphasizing the utmost significance of our contributions, and outlining promising future research directions in edge computing and energy-efficient mobile devices.

II. RELATED WORK

The realm of edge computing has witnessed remarkable progress, particularly in the realms of task offloading decision making and resource optimization. Pioneering research endeavors have been devoted to exploring novel approaches and techniques, culminating in heightened efficiency and efficacy of edge computing systems. These advancements have yielded seamless resource allocation and well-informed task offloading decisions, establishing a strong foundation for improved performance, reduced latency, and enhanced resource utilization in edge computing environments. Such strides empower organizations to fully harness the potential of edge computing, unlocking unprecedented levels of efficiency and responsiveness. This collective accomplishment continues to drive the evolution of edge computing, shaping the future landscape of computing paradigms [12].

Cisco's introduction of edge computing in 2012 marked a transformative extension of cloud computing, bringing it closer to the network edge. This paradigm emphasizes distributed processing, real-time analytics, seamless cloud integration, and efficient network management. By leveraging these features, edge computing enables organizations to harness computing resources at the network edge, resulting in faster data processing, improved responsiveness, and seamless collaboration with cloud services [13]. The recognition of edge computing alongside cloud computing expands the technological landscape, offering a wider range of options to meet diverse computing requirements and adapt to dynamic network infrastructures.

The relationship between edge computing and 5G is highly symbiotic, with each reinforcing the other. The convergence of edge computing and 5G is pivotal, as edge computing plays a crucial role in unlocking the full potential of 5G networks. By leveraging edge computing capabilities, 5G networks can leverage low-latency and high-bandwidth features, enabling innovative applications and services across sectors like healthcare [14]. The powerful combination of edge computing and 5G has the potential to revolutionize industries, enhance user experiences, and drive connectivity and digital transformation.

Pioneering studies in the 1990s, such as [15] and [16], focused on enhancing mobile application performance while conserving energy. Collaborative computing with nearby remote servers within reach of the devices [17] was explored in these studies. Their efforts led to the development of Odyssey, a prototype demonstrating the feasibility of adaptive execution for mobile applications. This application-aware adaptation allowed for dynamic adjustments in application behavior based on available resources such as CPU cycles, bandwidth, and battery power. These innovative works laid the foundation for optimizing mobile application performance and energy efficiency through intelligent resource management and adaptive execution techniques.

Dynamic task offloading for IoT devices addresses limitations faced by IoT devices by integrating energy harvesting technology and promoting a hybrid energy supply model. In [18], the authors introduced DTOME, a dynamic task offloading algorithm aimed at minimizing system cost. DTOME optimizes local computing, offloading duration, and edge computing decisions by considering both system cost and queue stability. The algorithm achieves lower system cost compared to conventional strategies, emphasizing the importance of energy efficiency and cost optimization in driving the progress of IoT applications.

These notable research contributions significantly advance the field of edge computing, fostering improved performance, energy efficiency, and scalability.

III. SYSTEM MODEL

Within this section, we introduce a comprehensive system model, meticulously crafted to serve as the fundamental framework for our research study. This model encompasses essential elements and factors crucial to our investigation, as visually depicted in Fig. 2. The construction of this robust system model enables us to gain a comprehensive understanding of the key entities that hold significant roles within the edgeenabled environment. The entities within the edge computing framework are precisely defined as follows:

- Mobile edge devices: As illustrated in Fig. 2, mobile edge devices refer to wireless devices equipped with computational capabilities situated at the network edge. These devices, including smartphones, sensors, and laptops, serve as endpoints for executing computational tasks and offloading them to edge servers. This arrangement enables efficient processing, reduces latency, and optimizes overall system performance.
- Access points: Access points are wireless networking devices that act as gateways, establishing connections between mobile devices and edge servers. Their role is to facilitate communication and connectivity between mobile devices and the edge servers in the network.
- Routers: Routers play a crucial role in networking by forwarding data packets between different networks. These integral devices are responsible for directing traffic and establishing efficient communication paths within the mobile edge computing architecture. Their primary function is to ensure seamless and optimized data transmission within the network infrastructure.
- Edge servers: Edge servers are computing nodes strategically positioned at the network edge to provide computational resources and services to mobile devices. These nodes play a crucial role in enabling accelerated data processing, reducing latency, and improving response times. By bringing computing resources closer to mobile devices, edge nodes contribute to the overall efficiency and performance of the system.
- Brokers: Brokers function as central entities within the edge computing infrastructure, playing a vital role in managing and coordinating resource allocation, task distribution, and service provisioning. This key component efficiently organizes and optimizes resource utilization, ensuring smooth task execution and effective service delivery within the edge computing environment.
- Cloud datacenter: The cloud datacenter is a centralized facility specifically designed to accommodate multiple servers and abundant computing resources. It serves as a hub for storing data, providing substantial processing power, and offering a wide array of services required to handle data-intensive tasks. Cloud datacenters play a pivotal role in supporting the scalability, storage, and computational needs of various applications and services, acting as a backbone for cloud computing infrastructure.
- Radio Medium: The radio medium represents the communication medium through which wireless communication takes place. It encompasses the transmission and reception of radio signals between wireless nodes in a network, along with other physical characteristics of the wireless medium.

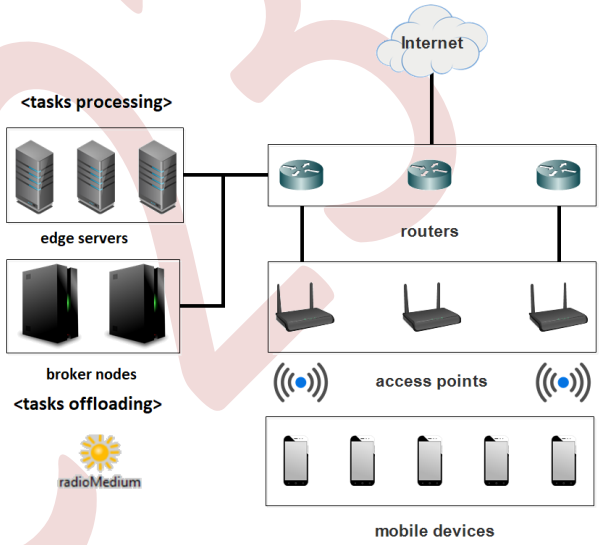


Figure 2. The architecture of our system model.

IV. METHODOLOGY

Our approach focuses on reducing energy consumption and extending mobile device battery lifespan in edge-enabled environments. We employ dynamic transmission power adjustment, optimizing energy usage based on distance to access points. Validation is performed through extensive simulations and analytical analysis to quantify energy savings and confirm the efficacy of our technique. This methodology provides a comprehensive assessment of improved energy efficiency in mobile devices within the edge computing framework. Table I shows the transmission powers and their corresponding ranges and trigger ranges respectively.

TABLE I
THE ESTIMATED TRANSMISSION POWER AND ITS CORRESPONDING RANGE

t.power (mW)	0.9	1.8	2.7	3.6
range (m)	170	230	285	330
trigger range (m)	[0, 150]	]150, 210]	]210, 265]	]265, +∞]
c.percentage (%)	25	50	75	100

In our study, we have simplified the transmission power range, recognizing that the actual range can vary due to wireless technology and regulatory constraints. For example, Wi-Fi networks typically have a transmission power range between 1 mW and 100 mW. However, it is important to acknowledge that regulatory limitations may affect the actual range to optimize signal propagation, mitigate interference, and comply with standards.

In our research, we assume continuous task offloading by mobile devices, resulting in gradual energy depletion over time. This energy loss is influenced by various device operations during usage. By considering the ongoing task offloading process and accounting for the impact of mobile device operations, we aim to capture realistic energy dynamics and gain insights into energy consumption patterns within our experimental setup.

V. SIMULATION

In this section, we performed a simulation in a dense edge-enabled environment, incorporating 100 mobile devices within a 400 x 400 (m) map region and for a duration of 300s, as depicted in Fig. 3. The simulation entailed the manipulation of various parameters and settings to establish a comprehensive evaluation framework, encompassing the following elements:

- **Task Offloading Frequency:** Tasks were offloaded at a frequency of one packet per second.
- **Transmission Power Levels:** We considered four dynamic levels of transmission power: 0.9 mW, 1.8 mW, 2.7 mW, and the default value of 3.6 mW.
- **Mobility Model:** To simulate realistic movement patterns, we utilized the Linear Mobility model, where the mobile devices had a speed of 1 meter per second and a randomly assigned angle of movement.

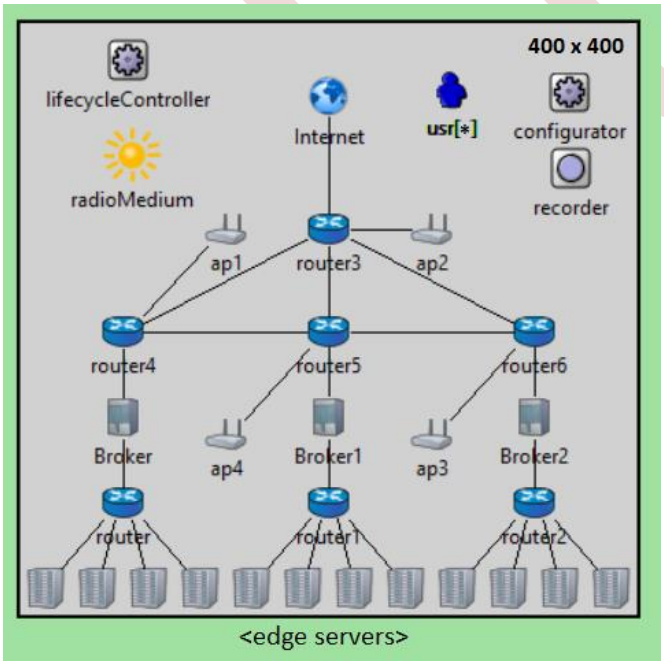


Figure 3. simulation snapshot of the conducted simulation and the existing components.

Lastly, we assume we use the protocol of MQTT (Message Queuing Telemetry Transport) which is a lightweight and efficient messaging protocol commonly used in various Internet of Things (IoT) and machine-to-machine (M2M) applications for communication between devices and servers. It is specifically designed for scenarios where low bandwidth, high latency, and unreliable network connections are common.

The equation for consumed energy for an MQTT packet in a wireless communication scenario can be given as:

$$C.Energy(E) = T.Power(P) \times Time(t) + D.Size(D) \times E.per.bit$$

Where:

T.Power (P) is the power used to transmit the packet wirelessly. **Time (t)** is the time taken to transmit the packet. **D.Size (D)** is the data size of the MQTT packet in bits. **E.per.bit** is the energy consumed per transmitted bit, representing the energy efficiency of the wireless transmission.

For the sake of simplicity, as in Table I, we assume as well that 3.6mW, 2.7mW, 1.8mW and 0.9mW are equivalent to 100%, 75%, 50% and 25% of consumed energy percentage respectively.

To facilitate our research and experimentation, we harness a combination of simulation tools, namely xFogSim [19] and OMNeTPP [20]. These tools offer robust platforms that effectively model and analyze fog computing environments, enabling us to accomplish our research objectives.

xFogSim is a specialized simulation framework designed for fog computing, providing comprehensive capabilities to model and analyze various aspects of fog-based systems, including resource allocation, task scheduling, energy consumption, and system performance. Leveraging xFogSim allows us to simulate and evaluate the behavior and performance of our proposed methodologies in realistic fog computing scenarios.

Additionally, we employ the versatility of OMNeTPP, an open-source and modular simulation framework renowned for its ability to simulate network protocols, communication systems, and distributed systems. With its discrete-event simulation environment, OMNeTPP empowers us to accurately model and analyze complex systems. Through OMNeTPP, we gain valuable insights into the behavior and performance of our proposed methodologies in a controlled and reproducible manner.

Furthermore, we extend the functionality of the xFogSim framework by incorporating our custom "Recorder" module as in Fig. 3. This module enables us to monitor and record the global energy consumption of the system, as well as the operational status of individual mobile devices. Integrating this Recorder module into the xFogSim framework provides us with valuable insights into the energy utilization patterns and performance of mobile devices in our simulations.

The simulation results reveal the count of transmitted packets for each category, as illustrated in Fig. 4.

To estimate the consumed energy in both the base-line scheme and our proposed scheme, we conduct an analytical evaluation based on the simulation results presented in Fig. 4. The obtained results are depicted in Fig. 5.

The analysis of the results reveals that our proposed scheme achieved a significantly lower percentage of analytical energy consumption compared to the base-line scheme. This outcome is evident as the majority of packet transmissions by mobile devices were conducted using the lowest transmission power level, particularly in the context of a dense edge-enabled scenario.

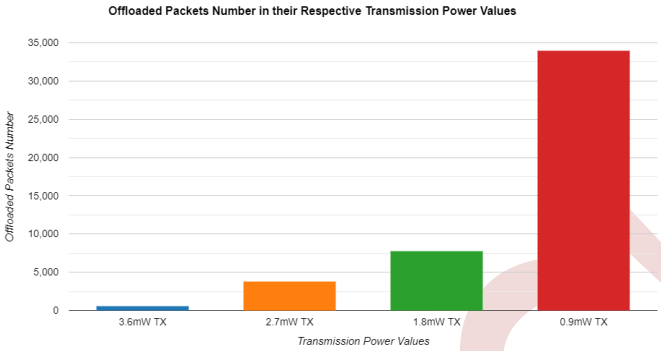


Figure 4. The offloaded packets number and the corresponding transmission power (TX) values in the proposed scheme.

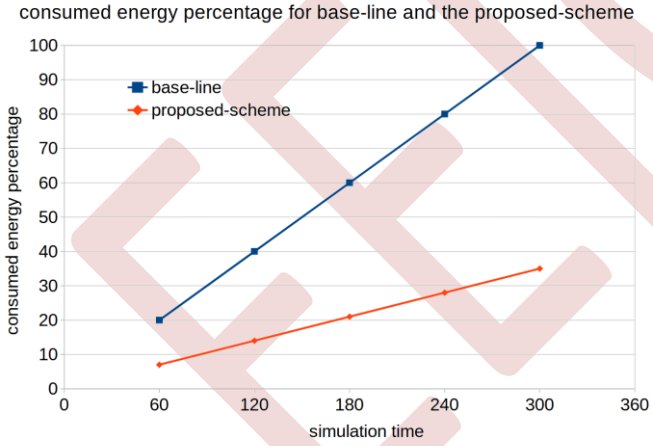


Figure 5. The analytical results of the consumed energy for the base-line scheme and the proposed scheme.

VI. CONCLUSION

In this conference paper, we addressed the critical challenge of energy optimization in edge computing environments through dynamic transmission power adjustment. Our proposed technique aimed to reduce rapid energy consumption and extend the battery lifespan of mobile devices in fogenabled scenarios. By leveraging four dynamic transmission power levels, we sought to optimize energy usage based on the distance between mobile devices and access points.

Through extensive simulations using xFogSim and OMNeTPP, we evaluated the performance of our proposed scheme. The results demonstrated that our approach achieved significantly lower analytical energy consumption compared to the base-line scheme. This substantial reduction in energy usage can be attributed to the prevalent use of the lowest transmission power level by mobile devices in the dense edge-enabled environment.

Our contributions pave the way for enhanced energy efficiency, prolonged device lifespan, and optimized task offloading in fog computing environments. By validating our scheme analytically, we ensured the credibility and effectiveness of our approach. The combination of simulation-based evaluations and analytical analysis provided comprehensive insights into the benefits and efficacy of our proposed technique.

Overall, our research highlights the significance of dynamic transmission power adjustment in mitigating energy draining issues and improving the performance of mobile devices within the edge computing framework. The findings presented herein contribute to the continuous evolution of edge computing, shaping the future of computing paradigms and advancing the field of energy-efficient mobile devices in fog-enabled environments.

In conclusion, our work demonstrates the potential of transmission power optimization as a promising strategy for energy efficiency in edge computing, opening avenues for further research and innovation in this domain. As edge computing continues to play a crucial role in diverse applications, our contributions contribute to the sustainable development of energy-aware solutions and pave the way for a more resourceefficient and eco-friendly technological landscape.

REFERENCES

[1] T. Dillon, C. Wu, and E. Chang, "Cloud computing: issues and challenges," in 2010 24th IEEE International Conference on Advanced Information Networking and Applications, IEEE, 2010, pp. 27–33.

[2] A. Al-Shuwaili and O. Simeone, "Energy-efficient resource allocation for mobile edge computing-based augmented reality applications," IEEE Wireless Communications Letters, vol. 6, no. 3, pp. 398–401, 2017.

[3] M. Babaghayou, N. Chaib, N. Lagraa, M. A. Ferrag, and L. Maglaras, "A safety-aware location privacy-preserving iov scheme with road congestion-estimation in mobile edge computing," Sensors, vol. 23, no. 1, p. 531, 2023.

[4] E. Mustafa, J. Shuja, S. K. u. Zaman, A. I. Jehangiri, S. Din, F. Rehman, S. Mustafa, T. Maqsood, and A. N. Khan, "Joint wireless power transfer and task offloading in mobile edge computing: a survey," Cluster Computing, vol. 25, no. 4, pp. 2429–2448, 2022.

[5] M. A. Al-Shareeda and S. Manickam, "A systematic literature review on security of vehicular ad-hoc network (vanet) based on veins framework," IEEE Access, 2023.

[6] Q. V. Khanh, V.-H. Nguyen, Q. N. Minh, A. D. Van, N. L. Anh, and A. Chehri, "An efficient edge computing management mechanism for sustainable smart cities," Sustainable Computing: Informatics and Systems, vol. 38, p. 100867, 2023.

[7] X. Wang, J. Li, Z. Ning, Q. Song, L. Guo, S. Guo, and M. S. Obaidat, "Wireless powered mobile edge computing networks: A survey," ACM Computing Surveys, 2023.

[8] M. Babaghayou, N. Labraoui, A. A. Abba Ari, M. A. Ferrag, and L. Maglaras, "The impact of the adversary's eavesdropping stations on the location privacy level in the Internet of Vehicles," in 2020 5th South-East Europe Design Automation, Computer Engineering, Computer Networks and Social Media Conference (SEEDA-CECNSM), IEEE, 2020, pp. 1–6.

[9] E. Mustafa, J. Shuja, K. Bilal, S. Mustafa, T. Maqsood, F. Rehman, and A. u. R. Khan, "Reinforcement learning for intelligent online computation offloading in wireless powered edge networks," Cluster Computing, vol. 26, no. 2, pp. 1053–1062, 2023.

[10] S. Zhou, W. Jadoon, and J. Shuja, "Machine learning-based offloading strategy for lightweight user mobile edge computing tasks," Complexity, 2021, pp. 1–11.

[11] Y. Guo, R. Zhao, S. Lai, L. Fan, X. Lei, and G. K. Karagiannidis, "Distributed machine learning for multiuser mobile edge computing systems," IEEE Journal of Selected Topics in Signal Processing, vol. 16, no. 3, pp. 460–473, 2022.

[12] L. Lin, X. Liao, H. Jin, and P. Li, "Computation offloading toward edge computing," Proceedings of the IEEE, vol. 107, no. 8, pp. 1584–1607, 2019.

[13] F. Bonomi, R. Milito, J. Zhu, and S. Addepalli, "Fog computing and its role in the Internet of Things," in Proceedings of the first edition of the MCC workshop on Mobile cloud computing, 2012, pp. 13–16.

[14] J. Li, X. Yang, G. Chu, W. Feng, X. Ding, X. Yin, L. Zhang, W. Lv, L. Ma, L. Sun, et al., "Application of improved robot-assisted laparoscopic telesurgery with 5G technology in urology," European Urology, vol. 83, no. 1, pp. 41–44, 2023.

[15] B. D. Noble, M. Satyanarayanan, D. Narayanan, J. E. Tilton, J. Flinn, and K. R. Walker, "Agile application-aware adaptation for mobility," ACM SIGOPS Operating Systems Review, vol. 31, no. 5, pp. 276–287, 1997.

[16] J. Flinn and M. Satyanarayanan, "Energy-aware adaptation for mobile applications," ACM SIGOPS Operating Systems Review, vol. 33, no. 5, pp. 48–63, 1999.

[17] M. Babaghayou, N. Labraoui, A. A. Abba Ari, and A. M. Gueroui, "Transmission range changing effects on location privacy-preserving schemes in the Internet of Vehicles," International Journal of Strategic Information Technology and Applications (IJSITA), vol. 10, no. 4, pp. 33–54, 2019.

[18] Y. Chen, F. Zhao, Y. Lu, and X. Chen, "Dynamic task offloading for mobile edge computing with hybrid energy supply," Tsinghua Science and Technology, vol. 28, no. 3, pp. 421–432, 2022.

[19] A. W. Malik, T. Qayyum, A. U. Rahman, M. A. Khan, O. Khalid, and S. U. Khan, "XFogSim: A distributed fog resource management framework for sustainable IoT services," IEEE Transactions on Sustainable Computing, vol. 6, no. 4, pp. 691–702, 2020.

[20] A. Varga and R. Hornig, "An overview of the OMNeT++ simulation environment," in 1st International ICST Conference on Simulation Tools and Techniques for Communications, Networks, and Systems, 2010.

Performance analysis of Spatially Modulated MIMO Systems

Beknadj Dalil [1], Tounsi Mohamed [2], Tayakout Hakim[3], Hamadi Yasmine [4]

[1] *LIMed Laboratory University of,Bejaia, Algeria*

dalil.beknadj@univ-bejaia.dz

[2] *LAMOS Research Unit, University of Bejaia, Algerie*

mohamed.tounsi@univ-bejaia.dz

[3]*Telecom Division, Center for Development of Advanced Technologies (CDTA), Algiers, Algeria*

htayakout@cdta.dz

***Abstract*— In modern wireless communication systems, the MIMO (multiple-input multiple-output) technology is increasigly used since it offers significant improvements in data throughput, spectral efficiency and link diversity (reduced fading by using multiple transmit and receive antennas). To improve the energy efficiency and spectral efficiency of MIMO systems, a new transmission concept has been associated. It is spatial modulation (SM) which has induced new, more compact and reconfigurable antenna structures while retaining only a single radio transmission chain (RF) to ensure low complexity. This paper provides a brief insight into the performance analysis of spatially modulated (SM) MIMO systems employing various modulation schemes over Rayleigh fading channels.**

Keywords: **Spatial Modulation, MIMO Systems, PSK, QAM,**

I. INTRODUCTION

Improvements in spatial modulation technologies, once confined to research laboratories, are currently making waves in the wireless communications industry with undeniable power [1]. This revolutionary technological leap transcends the limitations of wireless network speed and capacity by exploiting a spatial three-dimensional encoding. Among the pioneers of this revolution are Nobel laureates Eric A. Cornell, Wolfgang Ketterle, and Carl E. Wieman, whose work on Bose-Einstein condensation laid the foundation for the use of spatial modulation in the field of communications. Their innovative experiments paved the way for faster and more efficient wireless transmission systems [2].

Imagine a world where constraints on wireless connection speed are a thing of the past, where virtual reality achieves an unmatched level of clarity, and where autonomous vehicles exchange real-time data for safer driving. All of this becomes a reality thanks to spatial modulation, an innovative technology that revolutionizes our approach to wireless data transmission. At the heart of this revolution lies MIMO (Multiple Input Multiple Output), a technique that intelligently exploits multiple antennas to enhance transmission capacity. The pioneering work of Gerard J. Foschini and Michael J. Gans in the 1990s laid the groundwork for MIMO, thereby paving the way for more powerful wireless communication systems [3].

However, the revolution does not stop there. Researchers like T. L. Marzetta have also made significant contributions by exploring the boundaries of wireless communications with multiple antennas, opening up exciting new possibilities [4]. The implications of these advancements extend far beyond the academic realm, transforming the way we live and work in an increasingly connected world.

In this communication, we introduce the captivating area of spatial modulation and MIMO, exploring how these technologies are revolutionizing wireless connectivity. We will discover how they have evolved from fundamental research into indispensable technologies in our daily lives, ushering in an era where communication is faster, more reliable, and more versatile than ever before. Throughout this article, we will also shed light on the technological ~~and societal~~ implications of this revolution, while examining how it redefines the standards of modern connectivity, along with a proposal for combining spatial modulation and MIMO for optimal performance.

II. SYSTEM MODEL

Conventional MIMO technologies use continuously all available antennas at the transmitter, limiting energy efficiency optimization. Recently, a promising alternative has emerged in the field of wireless networks, inducing significant research interest: Spatial Modulation (SM). This technique, belonging to the MIMO family, aims to reduce the number of costly Radio Frequency (RF) chains while improving MIMO system performance, energy efficiency and spectral efficiency. Research in spatial modulation has reached a sufficient level of maturity to justify its application in emerging wireless communication systems.

A classical MIMO system model with M_t transmit antennas and Nr receive antennas is depicted in figure 1.

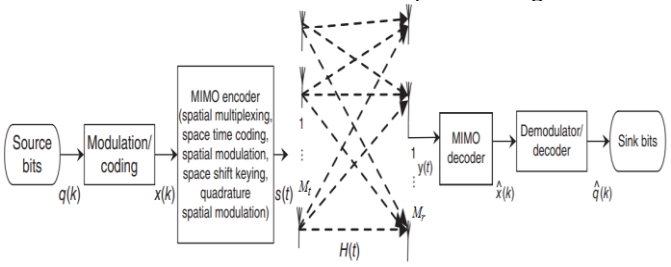


Figure 1. General MIMO system model with (M_t x M_r) antennas[8].

This system can be represented by the following discrete time model.

$$\begin{bmatrix} y_1 \\ y_2 \\ \vdots \\ y_{M_r} \end{bmatrix} = \begin{bmatrix} h_{11} & h_{12} & \cdots & h_{1M_t} \\ h_{21} & h_{22} & \cdots & h_{2M_t} \\ \vdots & \vdots & \ddots & \vdots \\ h_{M_r1} & h_{M_r2} & \cdots & h_{M_rM_t} \end{bmatrix} \cdot \begin{bmatrix} x_t^1 \\ x_t^2 \\ \vdots \\ x_t^{N_t} \end{bmatrix} + \begin{bmatrix} n_1 \\ n_2 \\ \vdots \\ n_{M_r} \end{bmatrix} \quad (1)$$

The simplified form is given by:

$$y = H.x_t + n \quad (2)$$

where:

- x_t is the M_t -length transmitted vector, created from the source data bit using a MIMO encoder with a modulation technique such as QAM, PSK or others.
- n is an M_r -length additive white Gaussian noise (AWGN) at the receiver input, with zero mean and a covariance matrix of $\sigma_n^2 I_{N_r}$, where $\sigma_n^2 = N_0 B$(N_0 is the noise power spectral density and B is the channel bandwidth);
- H is an $M_r \times M_t$ MIMO channel matrix of path gains $h_{n_r n_t}$ between transmit antenna n_t and receive antenna n_r,
- and *y* is the N_r -length vector received signal.

It is assumed that the total transmit power from any number of transmit antennas is the same and unitary. The average SNR at each receive antenna, under unity channel gain assumptions, is given by $SNR = 1/\sigma_n^2$.

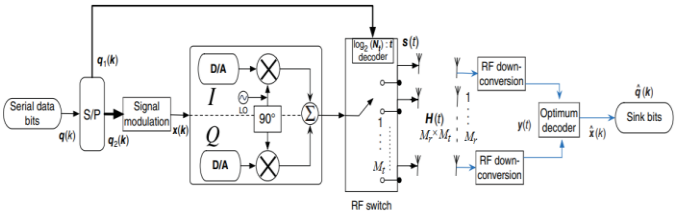


Figure 2. SM-MIMO system model with single RF-chain and (M_t x M_r) transmit and receive antennas [8].

The above figure illustrates an SM-MIMO system model with a single RF emitting chain. The information symbols are modulated onto two information carrying units: i) one PSK/QAM symbol; ii) a single active TA (tranmit antenna) via an information-driven antenna-switching mechanism. For the transmission of a set of data bits q at a specific time, it is possible to transmit simultaneously $\log_2(M_t)+\log_2(M)$ data bits. The data bits, converted into parallel data bits using a shift register, are grouped into two distinct categories:

- The first group of $\log_2(M_t)$ bits, is used to activate one of the M_t antennas using the RF switch;
- The second group of $\log_2(M)$ bits, is used to modulate a symbol from an M-QAM/PSK constellation diagram.

The SM-MIMO encoding mechanism and the SM constellation diagram are illustrated for $M_r = M_t = 4$ in figure 3. The encoder processes the information bits in blocks of $\log_2(M_t) + \log_2(M) = 4$ bits. The block of bits considered to be encoded is ''1110'', the first $\log_2(M_t)=2$ bits, "11" determine the single active TA *(*TX3), while the second $\log_2(M)=2$ bits, "10" determine the transmitted PSK/QAM symbol.

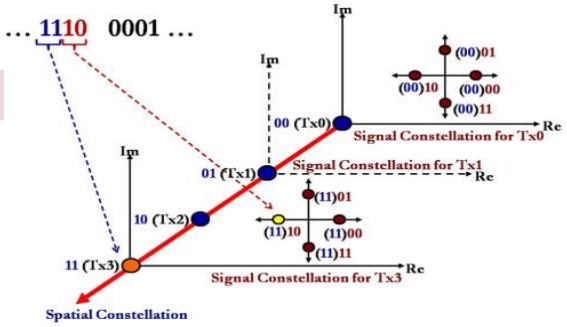


Figure 3. Illustration of the 3-D encoding of SM-MIMO model [1].

At the receiver, a Minimum Mean Square Error (MMSE) detector is used to decode the transmitted messages. The MMSE approach tries to find a matrix W which minimizes the mean square error between the estimated symbols to the transmitted symbols. This criterion leads a equalizing matrix:

$$W_{MMSE} = (H^* H + \sigma_n^2 I_{N_r})^{-1}.H^*$$

This matrix is known as the pseudo inverse for the $M_r \times M_t$ matrix H (W_{MMSE} H = I).

III. Performance Evaluation

We evaluate the performance of SM-MIMO through three fundamental parameters: Bit Error Rate (BER), capacity, and spectral efficiency (SE). We investigate these parameters using two common modulation schemes, namely Quadrature Amplitude Modulation (QAM) and Phase Shift Keying (PSK).

Our analysis unfolds in two distinct stages. Firstly, in the initial stage, we vary the modulation order (M) while keeping the number of transmitting and receiving antennas constant. In the second stage, we fix the modulation order and alter the number of transmitting (Mt) and receiving antennas (Mr). For our study, we have selected a range of modulation orders θ, including 2-PSK, 4-PSK, 8-PSK, 16-PSK, 32-PSK, 4-QAM, 16-QAM, 64-QAM, 128-QAM, and 256-QAM.

For our reception operations, we employed a Minimum Mean Square Error (MMSE) detector. The results of these simulations are presented in a detailed and illustrative manner in the subsequent sections of this document. We adopted this comprehensive approach to assess the performance of SM-

MIMO under various conditions, and we will share the results clearly and explicitly in the following sections.

The design of wireless communication systems requires prior technical planning and practical performance evaluation. This sectionr is dedicated to evaluating the performance of the previously presented SM-MIMO systems, with a focus on computer simulations.

The choice of the programming environment plays a crucial role in the development of any project. For our study, we opted for the MATLAB software due to its powerful compilation capabilities and advanced features.

The evaluation of SM-MIMO system performance relies on three essential metrics: Bit Error Rate (BER), capacity, and spectral efficiency. These three metrics serve as critical quantification criteria for digital transmissions, particularly in selecting the signal modulation type and configuring antennas both at the transmitter and receiver ends.

A. *The Channel MIMO Capacity:*

$$C=B\cdot\log_2(1+\text{SNR}) \quad (3)$$

- B is the bandwidth of the channel in hertz.
- SNR is the Signal-to-Noise Ratio in decibels.

B. *The Signal-to-Noise Ratio:*

$$S/B=P_S/P_B \quad (3)$$

- P_S represents the signal power.
- P_B represents the noise power in watts.

C. *The spectral efficiency:*

$$SE = C/B \quad (4)$$

- Where C is channel capacity
- B is the bandwidth.

IV. SIMULATION

The design of advanced wireless communication systems requires preliminary technical study followed by a comprehensive practical performance evaluation. This section is entirely dedicated to this evaluation, utilizing computer simulations to explore the previously introduced SM-MIMO systems. These simulations enable us to quantify crucial parameters such as Bit Error Rate (BER), capacity, and spectral efficiency, while examining the impact of various factors, including the number of antennas and the signal-to-noise ratio. Thus, this section illustrates how the combination of theoretical knowledge and practical analysis, supported by simulations, contributes to the improvement of SM-MIMO systems in the field of wireless communications.

In the context of our evaluation, we employed the Rayleigh channel, which is commonly used to model propagation channels in wireless communication systems. This channel takes into account factors such as scattering and reflection effects, making it particularly suitable for our simulations, which are described by the following equation:

$$f(r) = r/\alpha^2 \; e^{-r^2/2\alpha^2} \quad (7)$$

- f(r) is the power spectral density of the signal envelope.
- r is the complex amplitude of the signal envelope.
- α is the standard deviation of the signal envelope.

Our evaluation is based on a total of 5000 simulations. We conducted a total of 500 Monte Carlo simulations for each modulation type within θ. Each of these simulations was performed on a dataset consisting of L = 1024 spatial symbols. The simulations also covered a range of signal-to-noise ratio (SNR) values from -15 dB to 25 dB, with a 5 dB interval.

A. *Modulation PSK $M_t=M_r=8$.*

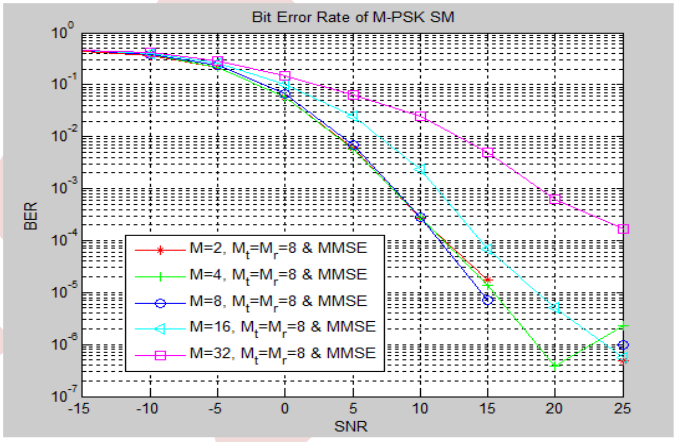


Figure 4. Comparison of BER achieved with different PSK modulation Orders

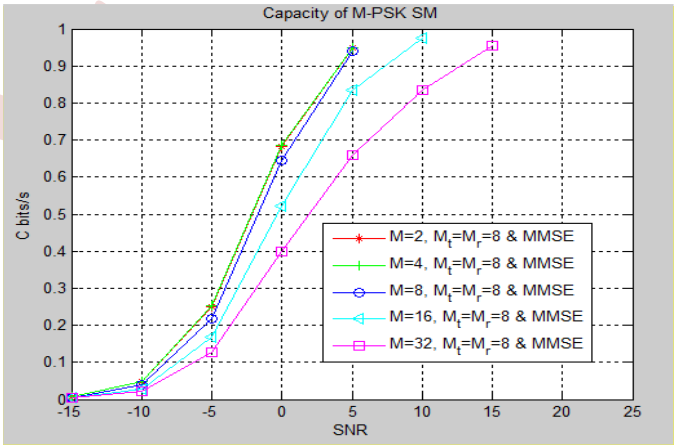


Figure 5. Comparison of capacities achieved with different PSK modulation orders

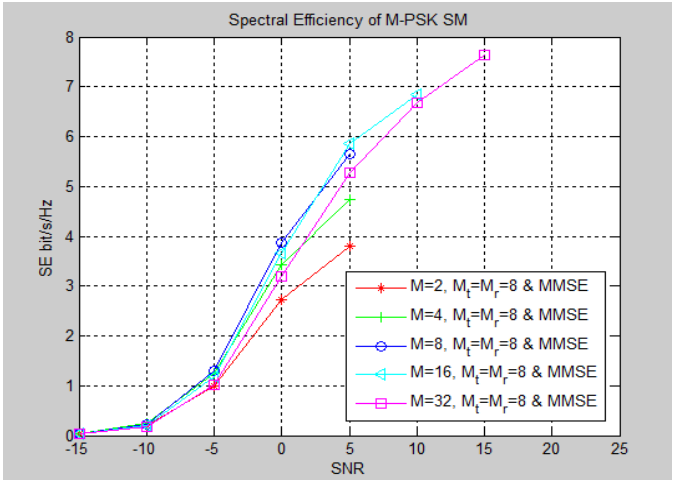


Figure 6. Comparison of Spectral Efficiencies Achieved with Different PSK Modulation Orders

In the signal-to-noise ratio (SNR) range of -15 to 20, it is observed that increasing the size of the constellation, represented by the modulation order (M), leads to an increase in the bit error rate (BER), which degrades performance. This is explained by the reduction in the distance between adjacent symbols on the constellation as M increases, naturally compromising the quality of transmission. However, it is possible to increase the size of the constellation to achieve maximum throughput while keeping the research problem, objectives, and work plan unchanged. Analyzing the results, it is evident that the system's capacity decreases as the number of states increases, as an increase in the modulation order allows for occupying a progressively narrower bandwidth, thereby weakening the system's capacity. Regarding spectral efficiency (SE), there is a gradual increase as M increases, reaching 3.9 bit/s/Hz at an SNR of 5 dB for M = 2, and 4.9 bit/s/Hz for M = 4. When M = 8, SE reaches 5.9 bit/s/Hz at an SNR of 10 dB, and it significantly improves for M = 16. Finally, for M = 32, spectral efficiency reaches 7.9 bit/s/Hz. In summary, spectral efficiency increases with the number of states, allowing for the occupation of a narrower bandwidth, although this is accompanied by a decrease in noise resilience in proportion.

B. Modulation QAM Mt=Mr=8.

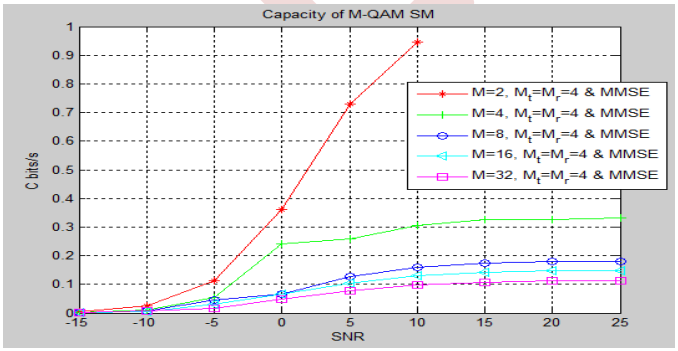


Figure 7. Comparison of Capacities Achieved with Different QAM Modulation Orders

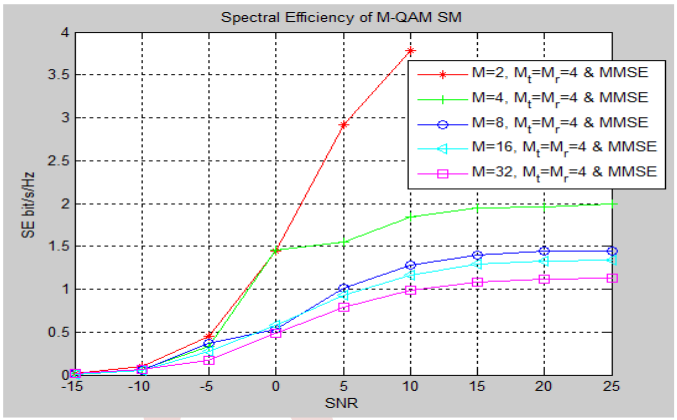


Figure 8. Comparison of Spectral Efficiencies with Different QAM Modulation Orders.

A series of graphs depict various QAM modulation orders with adjustments made to the system's capacity (C) based on the signal-to-noise ratio (SNR). Similar observations to those seen in PSK modulation are applicable, indicating a reduction in capacity as the number of states increases, thereby emphasizing the substantial influence of the constellation size on the system's capacity.

Furthermore, the results highlight that by increasing the number of points in the constellation, there is a noticeable improvement in spectral efficiency. This implies that elevating the modulation order leads to a corresponding increase in data throughput, actively contributing to the overall enhancement of spectral efficiency.

C. Modulation PSK Mt=Mr=8.

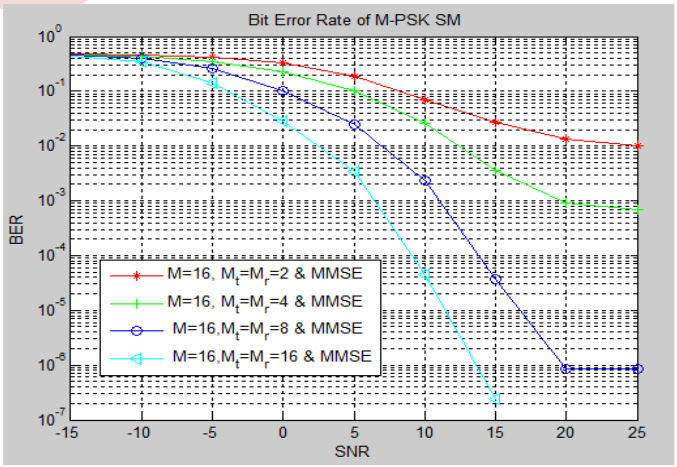


Figure 9. Comparison of BER as a Function of the Number of Transmit/Receive Antennas

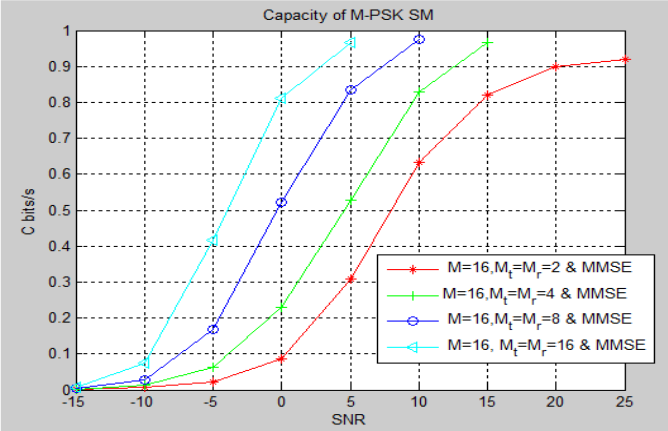


Figure 10. Comparison of Capacity as a Function of the Number of Transmit/Receive Antennas

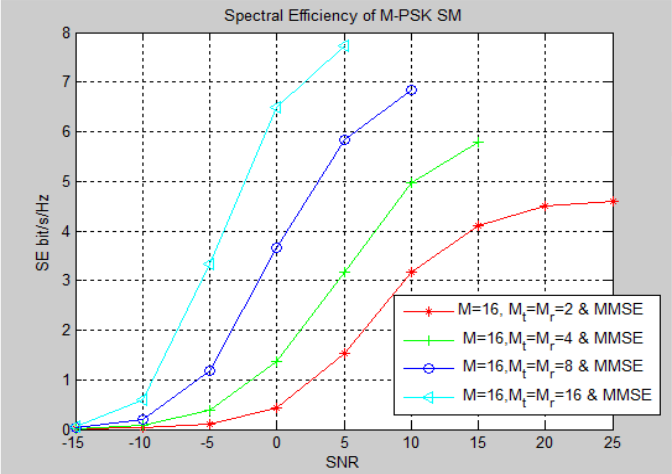


Figure 11. Comparison of Spectral Efficiency as a Function of the Number of Transmit/Receive Antennas.

We observe curves of bit error rate (BER) as a function of signal-to-noise ratio (SNR). Analyzing these data reveals a significant decrease in BER when the number of transmit and receive antennas is increased to 16 compared to only 2, underscoring the clear significance of spatial diversity in enhancing transmission quality and robustness.

As for the capacity curves (in bits per second) in relation to SNR, they illustrate a linear relationship between the number of antennas and capacity, with a proportional increase. Conversely, a reduction in the number of antennas, as seen when Mt=2 Mr=2, results in a performance deterioration.

Finally, we display spectral efficiency (SE) curves against SNR, showcasing a linear progression of spectral efficiency as the number of antennas increases.

D. Modulation PSK Mt=*Mr=8.*

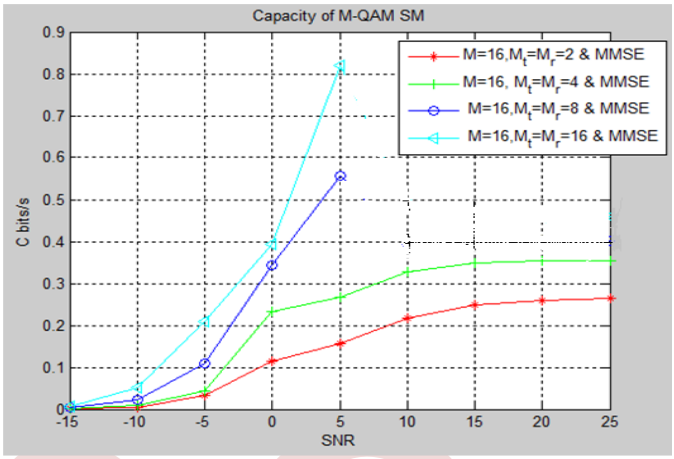


Figure 12. Comparison of Capacities as a Function of the Number of Transmit/Receive Antennas.

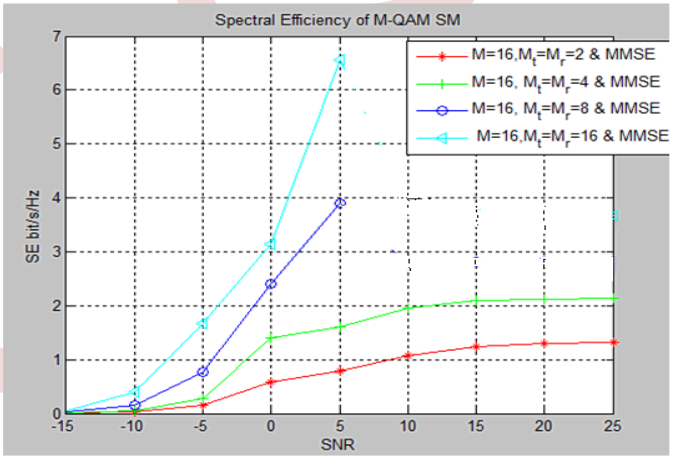


Figure 13. Comparison of Spectral Efficiency as a Function of the Number of Transmit/Receive Antennas.

These curves clearly demonstrate that capacity (C) proportionally grows at high signal-to-noise ratio (SNR) values and significantly improves with an increase in the number of transmitting and receiving antennas.

Likewise, these curves clearly highlight that spectral efficiency proportionally increases with the number of transmitting and receiving antennas, reaching high values.

In conclusion PSK's more performance QAM as depicted by three crucial aspects. Firstly, in terms of Bit Error Rate BER, PSK proves to be more robust because it encodes information solely in the signal phase, mitigating the impact of phase errors, especially in noisy environments. Secondly, concerning the communication channel's capacity, PSK offers distinct advantages. Its resilience to phase errors enables it to operate effectively even in the presence of high noise, fully exploiting

the channel's capacity. Each PSK symbol transmits a single binary information, optimizing bandwidth use. In contrast, QAM requires greater constellation point separation to minimize BER, potentially resulting in less efficient bandwidth utilization. Finally, in terms of spectral efficiency, PSK excels because each symbol conveys a single bit of information, making it more efficient compared to QAM. In summary, PSK is favored due to its phase error robustness, enhanced channel capacity utilization, and increased spectral efficiency. However, the choice between PSK and QAM depends on specific application requirements and communication channel characteristics, as indicated by the simulation results.

CONCLUSION

In this comprehensive letter, we have undertaken an in-depth analysis and rigorous evaluation of the performance of a Spatial Modulation Multiple-Input Multiple-Output (MIMO) system, employing an MMSE-type equalizer at the receiver. We have also examined the influence of several key parameters on the system's performance, including modulation order and the number of antennas at both the transmission and reception ends.

The results obtained have shed crucial light on how we assess the effectiveness of a transmission system. Indeed, a system's ability to maintain a low Bit Error Rate (BER) while maximizing the transmission of useful information, optimizing both its capacity and spectral efficiency, forms the foundation upon which its overall performance rests.

A significant finding lies in the undeniable advantages of PSK modulation over QAM in terms of BER, capacity, and spectral efficiency. This observation underscores the importance of carefully selecting the modulation type based on the specific requirements of a given application.

Simultaneously, we conducted an in-depth study on the impact of the number of antennas both at the transmission and reception ends on system performance. It is worth noting that spatial diversity plays a crucial role in maintaining high-quality transmission, enhancing the system's resilience in the face of disturbances.

In summary, this letter reveals that the combination of an MMSE equalizer, judicious choices in modulation, and effective management of the number of antennas is essential for designing high-performance and resilient wireless transmission systems, capable of ensuring reliable and efficient communication, even in demanding conditions.

REFERENCES

[1] Dalil BEKNADJ, HAMADI Yasmine "Automatic Modulation Type Recognition for SM-MIMO Systems", university of Bejaia, 2020

[2] E. A. Cornell, W. Ketterle, and C. E. Wieman, "Bose-Einstein Condensation in a Dilute Gas, The First 70 Years and Some Recent Experiments," Reviews of Modern Physics, vol. 74, no. 3, pp. 875-893, July 2002.

[3] G. J. Foschini and M. J. Gans, "On Limits of Wireless Communications in a Fading Environment when Using Multiple Antennas," Wireless Personal Communications, vol. 6, no. 3, pp. 311-335, March 1998

[4] T. L. Marzetta, "Noncooperative Cellular Wireless with Unlimited Numbers of Base Station Antennas," IEEE Transactions on Wireless Communications, vol. 9, no. 11, pp. 3590-3600, November 2010

[5] Hakim TAYAKOUT, « Détection itérative par Turbo codage combinant différentes techniques à base de systèmes MIMO », Thèse de doctorat en Electronique, Ecole Nationale Polytechnique, 2019

[6] 3GPP TS 38.101-1 V15.0.0 (2017-12) Spécification technique du réseau d'accès radio-électrique NR ; Transmission et réception radio des équipements utilisateur (UE), 2017

[7] R.Kamath, « Spectrum sensing in cognitive radio networks,» International Conference on Control, Communication and Copmuting, 2010.

[8] Raed Mesleh German Jordanian University, Amman, Jordan Abdelhamid Alhassi University of Benghazi, Benghazi, Libya" Space Modulation Techniques", This edition first published 2018

Inter-Numerology Interference Analysis and Mitigation Techniques for 5G Networks

Yacine Ouazziz [1], Mohamed Azni [1], Tounsi Mohamed [2]

[1] *LIMED, Bejaia, Algeria*

Yacine.ouazziz@univ-bejaia.dz

Mohamed.azni@univ-bejaia.dz

[2]*LaMOS, Bejaia, Algeria*

Mohamed.tounsi@univ-bejaia.dz

***Abstract*— One of the defining characteristics of 5G networks is the flexibility they offer for supporting different services and communication scenarios. However, employing multiple numerologies in a 5G network introduces non-orthogonality into the system, causing interference between users belonging to different numerologies. This interference, also called inter-numerology interference (INI), has garnered increasingly more attention in recent times. In this paper, we present an INI model that describes INI as a function of the frequency response of the system. We then perform a mathematical analysis of INI, specifically how the distance between numerologies and the subcarriers can affect the amount of interference. We also list the mitigation techniques already applied by researchers so far and suggest future research areas. Our study is imperative as it would enable the development of efficient interference cancellation techniques for multi-numerology systems in 5G and beyond.**

***Keywords:* 5G, Mixed Numerologies, OFDM, SCS, INI.**

I. INTRODUCTION

The advent of 5G networks has brought about significant advancements in wireless communication systems, enabling the support of diverse services and user requirements [1]. One of the defining characteristics of 5G is the flexibility it offers in supporting different numerologies, which refers to the subcarrier spacing and symbol duration of the orthogonal frequency-division multiplexing (OFDM) waveform [2]. This flexibility allows for the efficient allocation of resources and the coexistence of multiple services within the same network [3]. However, the introduction of multiple numerologies also introduces a novel challenge known as Inter-Numerology Interference (INI) [4].

In this paper, we present an in-depth analysis of INI in multi-numerology OFDM systems and propose mitigation techniques to address this interference. We begin by introducing the concept of multi-numerology and its significance in 5G networks. We then provide a mathematical modeling of INI, defining its characteristics and impact on system performance. Next, we describe the spectrum of a multi-numerology OFDM system and analyze the presence of INI within this spectrum.

Furthermore, we discuss various INI mitigation techniques that have been proposed in the literature. These techniques aim to minimize the impact of INI and improve the overall system performance. They include interference cancellation algorithms, adaptive guards, precoding techniques, and windowing methods [5].

Finally, we highlight the importance of further research in this area and suggest future research directions. As 5G networks continue to evolve and new technologies such as 6G emerge, it is crucial to develop advanced INI mitigation techniques that can adapt to the changing network requirements and support the diverse set of use cases envisioned for these networks [6]. By addressing the challenges posed by INI, we can unlock the full potential of 5G networks and enable the seamless delivery of emerging services.

II. CONCEPT OF MULTI-NUMEROLOGY

The concept of multi-numerology in a 5G network refers to the ability to support different subcarrier spacings and symbol durations within the same network. This flexibility allows for the efficient allocation of resources and the coexistence of multiple services with varying requirements [1]. In a multi-numerology system, different numerologies, which define the subcarrier spacing and symbol duration of the orthogonal frequency-division multiplexing (OFDM) waveform, can overlap in the frequency domain [2]

The Subcarrier spacing (SCS) refers to the distance between adjacent subcarriers in a given frequency band [7]. In contrast to LTE, which has a single subcarrier spacing of 15 kHz, 5G NR supports multiple numerologies with different SCS values [8]. Depending on the Frequency Range (FR), the most commonly used SCS values in 5G NR are 15, 30, 60, and 120 kHz [8]. However, as of Release 17, there is ongoing research on the possibility of increasing the SCS up to 960 kHz [8].

TABLE I. Numerologies in a 5G network

FR	μ	SCS (kHz)	T_{CP} (μs)	Ts (μs)	Slot duration (ms)
FR-1	0	15	4.76	71	1
	1	30	2.38	35	0.5
	2	60	1.19| 4.17	17	0.25
FR-2	2	60	1.19| 4.17	8.8	0.125
	3	120	0.60	4.4	0.0625

As depicted in TABLE I., a wider SCS enables the reduction of the Cyclic Prefix and symbol duration (TCP and TS), thereby leading to a decrease in latency (Figure 1). It is worth mentioning that when using an SCS of 60 kHz, it is advisable to employ an extended cyclic prefix to mitigate the potential occurrence of Inter-Symbol Interference (ISI) and Inter-Carrier Interference (ICI). This extended cyclic prefix necessitates a reduction in the number of symbols per slot from 14 to 12,

In summary, multi-numerology is a key feature of 5G networks that provides greater flexibility in meeting the diverse requirements of different services and users. However, the use of multiple numerologies also introduces new challenges, such as inter-numerology interference, which is caused by the loss of orthogonality between subcarriers of different numerologies. To address this issue, different techniques can be used, and new research opportunities are emerging to enhance the overall reliability of multi-numerology systems.

III. INI MODELIZATION AND SIMULATION

A Multi-Numerology OFDM system can be represented as in figure 1.

Let us consider a Multi-Numerology OFDM system with a given SCS $\Delta f^{(i)}$ and symbol duration $T^{(i)}$ for numerology i, where $i = \{1,2\}$, As per 3GPP, the two numerologies are related to each other via a scaling factor v, i.e.,

$$\frac{\Delta f^{(1)}}{\Delta f^{(2)}} = \frac{T^{(2)}}{T^{(1)}} = v \qquad (1)$$

For Simpler calculus, we study the case where $v = 2$, assuming $\Delta f^{(1)} = 2\Delta f^{(2)}$ and thus $T^{(2)} = 2\,T^{(1)}$. Figure 2. Illustrates that the symbol k associated with numerology 2 overlaps with twos symbols from numerology 1 (let us index them 2k and 2k +1).

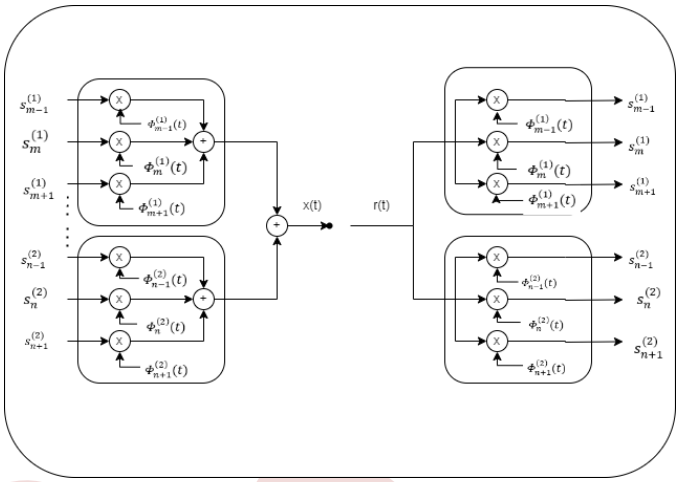


Figure 1. MN-OFDM system

A complex group of symbols $s^{(i)}$ is modulated via a Single Numerology-OFDM (SN-OFDM) system for numerology i. The complex symbol transmitted in instant k on the subcarrier m associated with numerology i is $s_{k,m}^{(i)}$. The transmitted signal for numerology i can be expressed as follows:

$$x^{(i)}(t) = \sum_{k=-\infty}^{\infty} x_k^{(i)}(t) \qquad (2)$$

Where:

$$x_k^{(i)}(t) = \sum_{k=-\infty}^{\infty} \sum_{m=0}^{N^{(i)}-1} s_{k,m}^{(i)}\, \Phi_m^{(i)}(t - kT^{(i)}) \qquad (3)$$

Is the corresponding transmitted signal at the instance k. $N^{(i)} = \frac{B}{\Delta f^{(i)}}$ is the number of subcarriers associated with numerology i with B representing the system bandwidth. $\Phi_m^{(i)}$ is a normalized, frequency-shifted rectangular pulse defined as:

$$\Phi_m^{(i)} = \begin{cases} \frac{1}{\sqrt{T^{(i)}}} \exp\left(j2\pi \frac{m}{T^{(i)}} t\right) & 0 \le t \le T^{(i)} \\ 0 & otherwise \end{cases} \qquad (4)$$

The transmitted signal x(t) is obtained by multiplexing the single-numerology signals associated with both the numerologies. Depending on the perspective, x(t) can take different forms, on the time duration $[kT^{(1)}, (k+1)T^{(1)}]$, it can be expressed as:

$$x_k(t) = x_k^{(1)}(t) + x_{\lfloor \frac{k}{v} \rfloor}^{(2)}(t) \qquad (5)$$

Where $\lfloor . \rfloor$ represents the floor function. On the time duration $[kT^{(2)}, (k+1)T^{(2)}]$, x(t) can be written as:

$$x_k(t) = \sum_{q=0}^{v-1} x_{vk+q}^{(1)}(t) + x_k^{(2)}(t) \qquad (6)$$

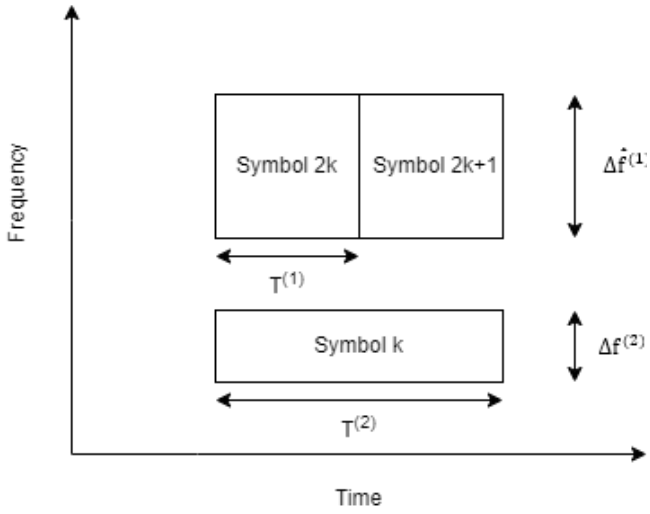


Figure 2. Symbol time overlapping in MN OFDM system

Eq (5) and (6) mathematically describe what Figure 2. illustrates, i.e, how signals on different symbol duration multiplex in the time domain. In particular the k-th symbol associated with numerology 1 overlaps with a truncated portion of the $\left\lfloor \frac{k}{v} \right\rfloor$ -th symbol associated with numerology 2, and the kth symbol of numerology 2, coincides with a block of v consecutive symbols starting from the (vk)-th symbol associated with numerology 1.

Now that we know that symbols from different numerologies interfere with each other, let us prove that two subcarriers with different SCS are not orthogonal.

A. Time Domain

Let $\Phi_m^{(1)}(t)$ and $\Phi_n^{(2)}(t)$be the subcarrier m associated with numerology 1 and subcarrier n associated with numerology 2, respectively. If they were orthogonal to each other (as it is the case for subcarriers from the same numerology) their inner product would be equal to zero, otherwise, they would be correlated, and interfere with each other. So, the interference between two MN subcarriers can be characterized by their inner product, the latter's magnitude being an indicator of the level of correlation.

The inner product between the two subcarriers can be obtained as:

$$p_{m,n}^{(1\leftarrow 2)} = \langle \Phi_m^{(1)}(t), \Phi_n^{(2)}(t) \rangle = \int_{-\infty}^{\infty} \Phi_n^{(1)}(t) * \Phi_n^{(2)}(t)\, dt \quad (7)$$

$$p_{m,n}^{(1\leftarrow 2)} = \frac{1}{\sqrt{T^{(1)}T^{(2)}}} \int_0^{T^{(1)}} \exp\left(-j2\pi\left(\frac{m}{T^{(1)}} - \frac{n}{T^{(2)}}\right)t\right) dt \quad (8)$$

With a simple variable change, it is possible to bring the limits of the integral from [0 $T^{(1)}$] to $\left[\frac{-T^{(1)}}{2} \quad \frac{T^{(1)}}{2}\right]$

Equation (8) becomes:

$$p_{m,n}^{(1\leftarrow 2)} = \frac{1}{\sqrt{T^{(1)}T^{(2)}}} \int_{\frac{-T^{(1)}}{2}}^{\frac{T^{(1)}}{2}} \exp\left(-j2\pi\left(\frac{m}{T^{(1)}} - \frac{n}{T^{(2)}}\right)t\right) dt \quad (9)$$

From (1), we can replace

$$T^{(1)} = \frac{T^{(2)}}{v} \quad (10)$$

The result of the inner product is as follows:

$$p_{m,n}^{(1\leftarrow 2)} = \frac{1}{\sqrt{v}} sinc(d) \quad (11)$$

Where, $sinc(x) = \frac{\sin(\pi x)}{\pi x}$ and d refers to the relative distance between subcarrier m and subcarrier n expressed as

$$d = \left(\frac{m}{T^{(1)}} - \frac{n}{T^2}\right) T^{(1)} = \frac{m\Delta f^{(1)} - n\Delta f^{(2)}}{\Delta f^{(1)}} = m - \frac{n}{v} \quad (12)$$

Which is the actual distance between two subcarrier center-normalized by $\Delta f^{(1)}$. Swapping the order of two subcarriers turns the corresponding inner product into the complex conjugate of eq (11)

$$p_{m,n}^{(1\leftarrow 2)} = p_{m,n}^{(2\leftarrow 1)*} \quad (13)$$

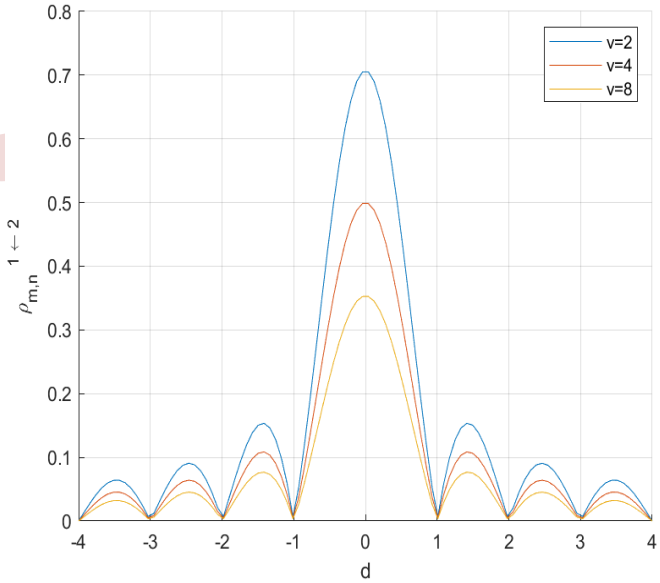


Figure 3. Correlation between subcarriers with different numerologies

And their common magnitude is written as

$$\left|p_{m,n}^{(1\leftarrow 2)}\right| = \left|p_{m,n}^{(2\leftarrow 1)}\right| = \frac{1}{\sqrt{v}} |sinc(d)| \quad (14)$$

Where $|.|$ is the absolute operator. This suggests that the interference between any two subcarriers associated with different numerologies is mutual and equal in magnitude.

In accordance with the preceding mathematical formulations, it is evident that the magnitude of the inner product is contingent upon the relative distance d, a parameter determined by the subcarrier indices m and n as well as the scaling factor denoted as v within the numerology (Figure 3.). It is reasonable to anticipate that as the relative distance increases, the magnitude of the inner product will diminish. Moreover, a larger scaling factor results in a diminished magnitude. As illustrated in Figure 3, the depicted graph portrays the magnitude of the inner product of subcarriers linked to distinct numerologies, each associated with the scaling factor v taking values from the set $\{2, 4, 8\}$. The figure clearly demonstrates an inverse relationship between the magnitude and v suggesting that greater scaling factors correspond to less correlated subcarriers. Consequently, numerologies linked to larger Subcarrier Spacing (SCS) exhibit greater resilience to Inter-Numerology Interference (INI). Furthermore, the figure also illustrates a decline in magnitude as the relative distance increases, indicating that interference originating from nearby subcarriers surpasses that stemming from comparatively distant ones.

B. Frequency Domain

An Orthogonal Frequency Division Multiplexing (OFDM) symbol can be represented as a sum of closely spaced orthogonal subcarriers with overlapping spectra that are transmitted in parallel. Each subcarrier is modulated with a conventional modulation scheme, such as quadrature amplitude modulation or phase-shift keying, at a low symbol rate. The total symbol duration is:

$$T_t = T_g + T_s \quad (15)$$

where T_g is the guard interval and T_s is the useful symbol duration. The complex signals ss(t) can be represented as:

$$ss(t) = \sum_{k=0}^{+\infty} s_k(t) e^{j2\pi f_k t} \quad (16)$$

Where $s_k(t)$ is the complex envelope of the k-th subcarrier, and f_k is its subcarrier.

In OFDM, the subcarriers are closely spaced and overlap in frequency domain. The frequency response of each subcarrier is a sinc function, which is the Fourier transform of a rectangular pulse. The sinc function is used to represent the frequency response of each subcarrier because it has a null at the center frequency of each subcarrier, which helps to minimize inter-carrier interference.

In a Single Numerology (SN-OFDM) system, these subcarriers are orthogonal to each other, meaning that they do not interfere with each other [11]. However, when different numerologies are used, the orthogonality between the subcarriers is compromised, leading to inter-numerology interference (INI) [4]

The orthogonality of OFDM symbols within the same numerology is achieved through the use of a cyclic prefix (CP). The CP is a guard interval inserted at the beginning of each OFDM symbol, which is a copy of the last part of the symbol. This guard interval allows for the elimination of inter-symbol interference (ISI) caused by multipath propagation. It also ensures that the subcarriers within the same OFDM symbol remain orthogonal to each other [12].

s

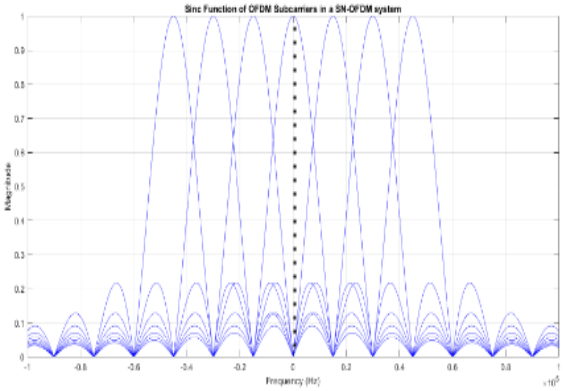


Figure 4. SN-OFDM symbols spectrum

As shown in Figure 4. The spectrum of an OFDM symbol is a sinc function, with a peak at the desired frequency (this is when the desired signal is transmitted), and infinite sidelobes. When the OFDM symbols are aligned and have the same SCS, when the power of a subcarrier is at its peak, all the other symbols are equal to zero, thus, are not causing any interference.

However, when different numerologies are used, the subcarriers from different numerologies do not have the same subcarrier spacing and cyclic prefix length. As a result, the orthogonality between the subcarriers is compromised, leading to INI. This interference can degrade the performance of the system and affect the quality of service for different users or services [13]. Therefore, it is important to carefully manage the allocation of numerologies and guard bands to minimize INI and ensure efficient and interference-free communication in 5G networks [14]. (figure 5.)

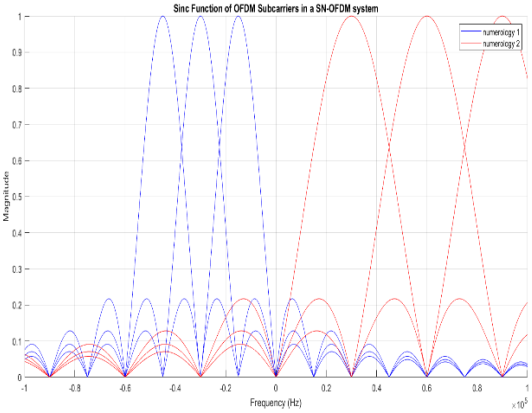


Figure 5. MN-OFDM Symbols spectrum

IV. INI MITIGATION TECHNIQUES AND FUTURE RESEARCH

A. INI mitigation techniques

INI has shown to impact the system in several ways, mainly affecting the spectral efficiency (SE) and Bit Error Rate (BER) of the system, and the problem is starting to raise more and more awareness within researchers, here are some of the latest works published on the topic:

- [5] and [8] tried to tackle the SE issue, the first mentioned Developed a cross-layer approach for INI management while the latter Developed a deep reinforcement learning algorithm for spectrum allocation. While both methods showed promising results, the one applied in [5] Depends on many implementation-dependent factors, such as the application type, operational frequency, bandwidth of the signal and the complexity of the device, whereas the one in [8] was evaluated only through simulations, and it is unclear how well it would perform in real-world scenarios. Additionally, the paper did not address other sources of interference in OFDM systems, such as inter-symbol interference (ISI) and co-channel interference (CCI).
- In order to improve the BER performance of the system, [13] and [15] used of a frequency-domain equalizer to estimate the interference and subtract it from the received signal, [14] Proposed a method for INI analysis and cancellation in massive MIMO-OFDM downlink systems while [16] Proposed a framework for mixed-numerology signals transmission and interference cancellation in Radio Access Network (RAN) slicing and Developed a joint optimization algorithm for subcarrier allocation and power allocation. [17] Proposed a method for INI analysis and cancellation in massive MIMO-OFDM UL systems.

While all these methods have shown promising results, they were evaluated only through simulations, and it is unclear how well they would perform in real-world scenarios. Additionally, the papers did not address other sources of interference in OFDM systems, such as inter-symbol interference (ISI) and co-channel interference (CCI).

In summary, research on the INI topic is just starting and it is a very promising area of interest, further research is necessary in order to fully understand it.

B. Future researh

Future research for 5G INI mitigation can focus on several areas. Firstly, there is a need for further investigation into advanced interference cancellation techniques specifically designed for inter-numerology interference (INI) [15]. Techniques such as adaptive filtering, advanced signal processing algorithms, and machine learning-based approaches can be explored to effectively mitigate INI.

Secondly, the development of efficient resource allocation algorithms and scheduling schemes can help optimize the allocation of numerologies and guard bands to minimize INI [15]. These algorithms should consider factors such as user requirements, traffic patterns, and channel conditions to dynamically allocate resources and mitigate interference.

Thirdly, the design and optimization of waveform and frame structures can play a crucial role in reducing INI [19]. Research can focus on developing new waveform designs that are inherently resistant to INI, such as alternative modulation schemes or novel precoding techniques.

Furthermore, the investigation of cross-layer approaches that integrate physical layer techniques with higher-layer protocols and network management can provide comprehensive solutions for INI mitigation [15]. This can involve joint optimization of numerology selection, power control, and interference management strategies across different layers of the network.

Additionally, the impact of INI on specific applications and services, such as IoT, vehicular networks, and tactile internet, can be studied to understand the specific requirements and challenges in mitigating INI in these scenarios [20] [21] [22]

Moreover, the development of standardized frameworks and protocols for INI mitigation can facilitate interoperability and seamless integration of different 5G systems and technologies [23] [24]. Standardization efforts should focus on defining common interfaces, protocols, and mechanisms for INI management.

Lastly, the evaluation and benchmarking of INI mitigation techniques through extensive simulations and field trials can provide valuable insights into their performance and effectiveness in real-world scenarios [15] [19]. Comparative studies can be conducted to assess the trade-offs between different techniques and identify the most suitable approaches for different deployment scenarios.

In conclusion, future research for 5G INI mitigation should focus on advanced interference cancellation techniques, resource allocation algorithms, waveform and frame structure optimization, cross-layer approaches, application-specific studies, standardization efforts, and performance evaluation through simulations and field trials.

V. CONCLUSION

In conclusion, the introduction of multiple numerologies in 5G networks has brought about the challenge of Inter-Numerology Interference (INI). This interference occurs when different numerologies overlap in the frequency domain, leading to degradation in system performance. In this paper, we have provided a comprehensive analysis of INI in multi-numerology OFDM systems and proposed mitigation techniques to address it.

Through mathematical modeling and simulations, we have demonstrated the cause of INI mentioned various INI mitigation techniques. These techniques, such as interference cancellation algorithms, adaptive guards, precoding techniques, and windowing methods, have shown promising results in reducing the impact of INI and improving system performance.

However, there is still a need for further research in this area. As 5G networks continue to evolve and new technologies such as 6G emerge, it is crucial to develop advanced INI mitigation techniques that can adapt to the changing network requirements and support the diverse set of use cases envisioned for these networks. Future research should focus on developing more efficient and robust INI mitigation techniques, considering factors such as dynamic network conditions, varying traffic patterns, and the coexistence of different services.

By addressing the challenges posed by INI, we can ensure the reliable and efficient operation of 5G networks, enabling the seamless delivery of emerging services and supporting the diverse needs of users. The findings and insights presented in this paper contribute to the body of knowledge in the field of INI analysis and mitigation, providing a foundation for further research and development in this area.

REFERENCES

[1] Yazar, A. and Arslan, H. (2018). Flexible multi-numerology systems for 5g new radio. Journal of Mobile Multimedia, 14(4), 367-394. https://doi.org/10.13052/jmm1550-4646.1442

[2] Kihero, A., Solaija, M., Yazar, A., & Arslan, H. (2018). Inter-numerology interference analysis for 5g and beyond.. https://doi.org/10.1109/glocomw.2018.8644394

[3] Liu, X., Zhang, L., Xiong, J., Zhang, X., Zhou, L., & Wei, J. (2020). Peak-to-average power ratio analysis for ofdm-based mixed-numerology transmissions. Ieee Transactions on Vehicular Technology, 69(2), 1802-1812. https://doi.org/10.1109/tvt.2019.2960801

[4] Mafra, S., Czekailo, G., Chang, B., & Brante, G. (2022). On the use of generalized dft-s-ofdm to reduce inter-numerology interference in 5g-nr networks.. https://doi.org/10.14209/sbrt.2022.1570813087

[5] Demir, A. F. and Arslan, H. (2020). Inter-numerology interference management with adaptive guards: a cross-layer approach. IEEE Access, 8, 30378-30386. https://doi.org/10.1109/access.2020.2972287

[6] Savaux, V. (2023). Ocdm-based multi-numerology communications for 6g.. https://doi.org/10.36227/techrxiv.22140092

[7] Dahlman, E. and Sköld, J. (2018). 5g nr: the next generation wireless access technology.. https://doi.org/10.1016/c2017-0-01347-2

[8] Rinaldi, F., Raschellà, A., & Pizzi, S. (2021). 5g nr system design: a concise survey of key features and capabilities. Wireless Networks, 27(8), 5173-5188. https://doi.org/10.1007/s11276-021-02811-y

[9] Kihero, A. B., Solaija, M. S. J., & Arslan, H. (2019). Multi-numerology multiplexing and inter-numerology interference analysis for 5g.. https://doi.org/10.48550/arxiv.1905.12748

[10] Demmer, D., Gerzaguet, R., Doré, J., & Ruyet, D. L. (2018). Analytical study of 5g nr embb co-existence. 2018 25th International Conference on Telecommunications (ICT). https://doi.org/10.1109/ict.2018.8464938

[11] Mao, J., Farhang, A., Zhang, L., Chu, Z., Xiao, P., & Gu, S. (2021). Interference analysis in multi-numerology ofdm systems: a continuous-time approach. 2021 IEEE International Conference on Communications Workshops (ICC Workshops). https://doi.org/10.1109/iccworkshops50388.2021.9473482

[12] Barhumi, I., Leus, G., & Moonen, M. (2003). Optimal training design for mimo ofdm systems in mobile wireless channels. IEEE Transactions on Signal Processing, 51(6), 1615-1624. https://doi.org/10.1109/tsp.2003.811243

[13] Zhang, X., Zhang, L., Xiao, P., Ma, D., Wei, J., & Yu, X. (2018). Mixed numerologies interference analysis and inter-numerology interference cancellation for windowed ofdm systems. IEEE Transactions on Vehicular Technology, 67(8), 7047-7061. https://doi.org/10.1109/tvt.2018.2826047

[14] Cheng, X., Zayani, R., Shaïek, H., & Roviras, D. (2019). Inter-numerology interference analysis and cancellation for massive mimo-ofdm downlink systems. IEEE Access, 7, 177164-177176. https://doi.org/10.1109/access.2019.2957194

[15] Doğan-Tusha, S., Tusha, A., Başar, E., Althunibat, S., Qaraqe, K., & Arslan, H. (2021). Inter-numerology interference in ofdm-im systems. IET Communications, 15(15), 1941-1949. https://doi.org/10.1049/cmu2.12206

[16] Yang, B., Zhang, L., Onireti, O., Xiao, P., Imran, M. A., & Tafazolli, R. (2020). Mixed-numerology signals transmission and interference cancellation for radio access network slicing. IEEE Transactions on Wireless Communications, 19(8), 5132-5147. https://doi.org/10.1109/twc.2020.2989399

[17] Cheng, X., Zayani, R., Shaïek, H., & Roviras, D. (2020). Analysis and cancellation of mixed-numerologies interference for massive mimo-ofdm ul. IEEE Wireless Communications Letters, 9(4), 470-474. https://doi.org/10.1109/lwc.2019.2959526

[18] Zambianco, M. and Verticale, G. (2020). Spectrum allocation for network slices with inter-numerology interference using deep reinforcement learning. 2020 IEEE 31st Annual International Symposium on Personal, Indoor and Mobile Radio Communications. https://doi.org/10.1109/pimrc48278.2020.9217107

[19] Gökçeli, S., Levanen, T., Yli-Kaakinen, J., Riihonen, T., Renfors, M., & Valkama, M. (2020). Papr reduction with mixed-numerology ofdm. IEEE Wireless Communications Letters, 9(1), 21-25. https://doi.org/10.1109/lwc.2019.2939521

[20] Mrabet, H., Belguith, S., Alhomoud, A., & Jemai, A. (2020). A survey of iot security based on a layered architecture of sensing and data analysis. Sensors, 20(13), 3625. https://doi.org/10.3390/s20133625

[21] Yang, Y. and Hua, K. (2019). Emerging technologies for 5g-enabled vehicular networks. IEEE Access, 7, 181117-181141. https://doi.org/10.1109/access.2019.2954466

[22] Gupta, R., Tanwar, S., Tyagi, S., & Kumar, N. (2019). Tactile internet and its applications in 5g era: a comprehensive review. International Journal of Communication Systems, 32(14). https://doi.org/10.1002/dac.3981

[23] Andrews, J. G., Buzzi, S., Choi, W., Hanly, S. V., Lozano, A., Soong, A. C. K., … & Zhang, J. C. (2014). What will 5g be?. IEEE Journal on Selected Areas in Communications, 32(6), 1065-1082. https://doi.org/10.1109/jsac.2014.2328098

[24] Khan, R., Kumar, P., Jayakody, D. N. K., & Liyanage, M. (2020). A survey on security and privacy of 5g technologies: potential solutions, recent advancements, and future directions. IEEE Communications Surveys &Amp; Tutorials, 22(1), 196-248. https://doi.org/10.1109/comst.2019.2933899

Enhacing the performances of 5G communication systems with Rate Splitting Multiple Access

Hocine BELLAHSENE [1], Sounia KHAROUNI [2]

[1] *Labortory of Electrical Engineering (LGEB), University A.Mira of Bejaia, Algeria*

hocine.bellahsene@univ-bejaia.dz

[2] *Departement of ATE, university A.Mira of Bejaia, Algeria*

sonia.kharouni@univ-bejaia.dz

Abstract— Rate Splitting Multiple Access (RSMA) has emerged as a powerful framework for optimizing 5G communication systems and beyond. In the context of 5G, RSMA addresses the challenges posed by diverse quality of service requirements and the need for massive connectivity. It ensures a smooth transition between interference management strategies by balancing the treatment of interference as noise and decoding interference completely. This is achieved by partially decoding the interference and treating the remaining as noise. The transmission framework employed by RSMA is more general and flexible than the one used by NOMA and SDMA.

RSMA not only reduces the complexity in transceiver design but also enhances system robustness in the presence of varying Channel State Information at the Transmitter (CSIT) quality, consequently improving overall system performance.

In this paper, we aim to demonstrate the ability of the RSMA to meet the massive demands on 5G communication systems with varying parameters (Quality of CSIT, SNR) in different deployment scenarios, and its superiority over both NOMA and SDMA. By providing a comprehensive exploration of the transmission frameworks, alongside a detailed analysis of the results obtained, this study underscores the remarkable potential of RSMA to fit into expectations from 5G networks and beyond.

Keywords: RSMA, NOMA, SDMA, CSIT, SNR, rate region.

I. INTRODUCTION

Multiple access refers to the ability for multiple users to access the same communication channel simultaneously. Multiple access is a key component of cellular communication systems [1].

The early cellular networks implemented orthogonal multiple access techniques (OMA) such as Time Division Multiple Access (TDMA), Frequency Division Multiple Access (FDMA), or Code Division Multiple Access (CDMA) [2].

In TDMA, information's for each user are sent in interference-free time slots, making precise synchronization necessary, which can be challenging, especially in the uplink. In FDMA implementations, such as OFDMA, information for each user is allocated to a subset of orthogonal subcarriers. However, with the advancement of cellular network technologies, these orthogonal techniques can no longer meet the high requirements of future radio access systems [2].

For 5G, several multiple access schemes are under investigation to select the most optimal technique. Each of these schemes has its advantages and disadvantages, so it is unlikely that a single technique can meet all requirements. The goal is to adopt the most optimal techniques to ensure the efficiency and performance of the 5G system [1].

The first access techniques to generate significant interest in the context of 5G were Non-Orthogonal Multiple Access (NOMA), and Space Division Multiple Access (SDMA).

However, 5G goes even further by introducing a new approach called Rate-Splitting Multiple Access (RSMA). This approach divides a message into two parts (common and private) and transmits them in a non-orthogonal manner. By combining linear precoding (LP) and successive interference cancellation (SIC).

To assess the effectiveness of an access technique and understand its impact on the performance of a 5G system, it is essential to consider certain key system parameters and measure its performance. We study in this paper the performances of RSMA and compare it with the performances of NOMA and SDMA

In this work, we focus on identifying the limitations of NOMA and SDMA and the ability to overcome these limitations by RSMA. Throw a study and a simulation of the three access techniques in 5G systems.

The rest of this paper is organized as follows. The transmission framework differences between NOMA, SDMA and RSMA are explained in Section II.

In Section III, we described the system model and defined the parameters and metrics to measure the performances of access techniques. Numerical results are illustrated in Section IV. Section V concludes the paper.

II. ACCESS TECHNIQUES FOR 5G SYSTEMS : TRANSMISSION FRAMEWORK

A. Non-Orthogonal Multiple Access (NOMA)

Unlike Orthogonal Multiple Access (OMA), NOMA allows the superposition of users in the same time-frequency resource [3]. This is achieved through one of the following methods

Power Domain NOMA

In this approach, different power levels are assigned to users based on their distance from the Base Station (BS). Users farther away receive higher power, while those closer to the BS receive lower power [2].

Code domain NOMA

This method employs unique spreading sequences specific to each user to enable superposition [4].

NOMA relies on the concept of SC-SIC: which is superposition coding at the transmitter, consists of a linear combination of the user signals multiplied by their respective coefficients to generate a composite signal received by all the users [4]. Then comes successive interference cancellation at the receiver in which each user first decodes the strongest signal first. It then subtracts the decoded signal from the received signal.

The SIC receiver repeats this iterative subtraction operation until it obtains its own signal [2].

In Multi-antenna Systems: the two main strategies in multi-antenna NOMA are the SC–SIC and SC–SIC per group. SC–SIC can be treated as a special case of SC–SIC per group where there is only one group of users [3].

The SC-SIC per group strategy involves grouping the K users into G groups. Within each group, users are served using SC-SIC to improve interference management [3].

B. Space-Division Multiple Access (SDMA)

In today's wireless networks, access points are often equipped with more than one antenna. This spatial dimension paves the way for another well-known type of multiple access, namely SDMA. SDMA superposes users on the same time-frequency resource and separates them by making appropriate use of spatial dimensions [3].

The most commonly used precoding technique for multi-antenna broadcast systems, such as MIMO and MISO BC, is Multi-User Linear Precoding (MU-LP). This technique is based on creating separate beams, with each beam receiving a fraction of the total transmission power. It allows for user superposition in the power domain, much like NOMA.

However, unlike NOMA, SDMA uses the beamforming technique at the transmitter to separate users, rather than using the SIC technique at the receivers [3].

C. Rate Splitting Multiple Access

This concept is not particularly new. Its roots date back to the early works on the two-user interference channel (IC) by Carleial in [5], as well as the work done by Han and Kobayashi in [6].

Those authors developed transmission strategies based on RS to achieve new rate regions. In the Han-Kobayashi scheme, which achieves the best-known inner bound to date, each source divides its message into a "private" part and a "common" part (sometimes referred to as a "public" part). The two parts are encoded using superposition coding and simultaneously transmitted. In addition to decoding its own message consisting of two parts, each receiver also decodes part of the interference, specifically the other receiver's common part [7].

Rate-Splitting Multiple Access (RSMA) is a multiple access scheme based on the concept of Rate-Splitting (RS) and linear precoding for multi-antenna multi-user communications. it splits user messages into common and private parts, and encodes the common parts into one or several common streams while encoding the private parts into separate streams. The streams are precoded using the available (perfect or imperfect) Channel State Information at the Transmitter (CSIT), superposed and transmitted via the Multi-Input Multi-Output (MIMO) or Multi-Input Single-Output (MISO) channel. All the receivers then decode the common stream(s), perform Successive Interference Cancellation (SIC) and then decode their respective private streams. Each receiver reconstructs its original message from the part of its message embedded in the common stream(s) and its intended private stream [8].

Various RSMA schemes exist, such as 1-layer RS, 2-layer hierarchical RS (HRS), generalized RS, RS and common message decoding (RS-CMD) [9]. Each one of these strategies have its advantages in terms of complexity, and quality of service.

III. SYSTEM MODEL

We Consider the same system as in [3], where a base station (BS) equipped with 4 transmit antennas serves K single-antenna users. The users are indexed by the set $\mathcal{K} = \{1, \dots, K\}$. Let $\boldsymbol{x} \in \mathbb{C}^{N_t \times 1}$ denotes the signal vector transmitted in a given channel use. It is subject to the power constraint $E\{\|\boldsymbol{x}\|^2\} \leq P_t$.

The signal received at user-k is

$$y_k = h_k^H \boldsymbol{x} + n_k \; \forall k \in \mathcal{K} \qquad (1)$$

Where $h_k \in \mathbb{C}^{N_t \times 1}$ is the channel between the BS and user-k. n_k is the additive white Gaussian noise (AWGN) at the receiver. We assume the noise variances are equal to one for all users. The transmit SNR is equal to the total power consumption Pt.

We assume CSI of users is perfectly known at the BS in the following model. The imperfect CSIT scenario will be discussed in the proposed algorithm and the numerical results. Channel state information at the receivers (CSIR) is assumed to be perfect.

A. System's Key Parameters

The Accuracy of Channel State Information (CSI)

Channel State Information (CSI) is a key concept in wireless communications, representing the known properties of a radio link's channel. It characterizes how signals behave as they travel from a transmitter to a receiver, considering factors like signal attenuation, scattering, fading, etc. CSI is crucial for assessing the quality of a radio link [10].

In practical terms, CSI influences the configuration of the physical layer in communication systems. It determines modulation schemes and impacts resource allocation and interference management. Precise CSI is essential for efficient communication [10].

It is evident that obtaining CSI takes a considerable amount of time. Therefore, acquiring CSI cannot meet the CSI refreshment requirement at the pace demanded by a 5G wireless communication system [10]. This is why adopting multiple access techniques that depends less on the quality of CSI in 5G communication systems proves advantageous.

Signal-to-noise ratio

SNR (Signal-to-Noise Ratio), often written as S/N, is the ratio of the received signal power to the noise floor. The SNR is an indicator used to assess the quality of the received signal. Its value is expressed in decibels (dB) and can be calculated using the following formula [11]:

$$SNR(dB) = 10log_{10}\left(\frac{P_{signal-recu}}{P_{bruit}}\right) \qquad (2)$$

The positive SNR means that the signal power is greater than the noise power, i.e. the receiver will be able to demodulate the signal. The negative SNR means that the signal power is less than the noise power [11].

B. Performance matrics

The Rate region:

Consider a Massive MIMO system where a base station (BS) equipped with M antennas serves two users [12]. The achievable data rates for users 1 and 2 can be expressed in:

$$R_1 = log_2\left(1 + \frac{\propto_1 \mu_1}{\mu_{1,1}\eta_1 + \mu_{1,2}\eta_2 + 1}\right) \qquad (3)$$

$$R_2 = log_2\left(1 + \frac{\propto_2 \mu_2}{\mu_{2,1}\eta_1 + \mu_{2,2}\eta_2 + 1}\right) \qquad (4)$$

Where:

$-\ \eta_k$ is the power control coefficient and $\propto_k \geq 0$ is the effective channel gain for user-k, where k = 1, 2. The noise power is normalized to 1.

- $\mu_{1,1} \geq 0\ and\ \mu_{2,2} \geq 0$ are self-interference coefficients caused by imperfect CSI.
- $\mu_{1,2} \geq 0\ and\ \mu_{2,1} \geq 0$ are inter-user interference coefficients.

It should be noted that η_1 and η_2 are design variables.

In DL (DownLink) the power constraint at the BS is:

$0 \leq \eta_1 + \eta_2 \leq 1$. In UL (UpLink), the power constraints for both users are: $0 \leq \eta_1 \leq 1$ and $0 \leq \eta_2 \leq 1$ [12].

The rate region is described by finding the maximum possible data rates achievable when each user is subject to a maximum transmit power constraint [13].

The Weighted Sum Rate (WSR):

In a multi-user system, the rate region is no longer a sufficiently informative metric, which led to the introduction of the WSR. In this case, the performance of each user depends on a new parameter, its assigned weight, denoted μ. The weight assigned to each user is a coefficient that characterizes it within the system [14].

The weights of the user set satisfy the constraint:

$$\sum_{i=1}^{K} \mu_i = 1$$

- K: number of users, the users set $\mathcal{K} = \{1, \dots, K\}$.
- $i \in \mathcal{K} = \{1, \dots, K\}$.

The Weighted Sum Rate (WSR) considers the achievable rate for each user and its weight [14]. It is defined by the following formula:

$$WSR = \sum_{i=1}^{K} \mu_i R_i \qquad (5)$$

IV. Numerical results:

In this section, we evaluate the performance of RSMA by illustrating the achievable rate region of different strategies.

In all the following results:

- SC-SIC refers to NOMA.
- MU-LP refers to SDMA.
- RS refers to RSMA.

A. Achievable rate region:

When K = 2, the rate region of all strategies can be explicitly compared in a two-dimensional figure. As mentioned earlier, the rate region is the set of all achievable points. Its boundary is calculated by varying the weights assigned to users [3].

In this work, the weight of user-1 is fixed to $\mu_1 = 1$.

The weight of user-2 is varied as $\mu_2 = 10^{[-3,-1,-0.95,\cdots,0.95,1,3]}$

The user channels are realized as follows:

$$h_1 = [1,1,1,1]^H, h_2 = \gamma \times \left[1, e^{j\theta}, e^{j2\theta}, e^{j3\theta}\right]^H \qquad (5)$$

In the channel realizations above, the parameters, γ and θ are control variables. The additional path loss experienced by the he channel strength of user-2 is controlled by γ. When γ = 1 the channel strength of user-1 is equal to that of user-2. all the following results are achieved for γ = 1 [3].

The parameter θ is used to adjust the angle formed between the channels used by the two users [3].

- **Underloaded two-user deployment with perfect CSIT:**

In the perfect CSIT (Channel State Information at the Transmitter) scenario, the capacity region is achieved by Dirty Paper Coding (DPC). Therefore, to evaluate the performance of different techniques, we compare the achievable throughput region with the DPC region [14]. The DPC region is generated using the algorithm described in [15].

In the following we study the Effect of Signal-to-Noise Ratio (SNR) on the achievable rate region for various strategies in a underloaded 2-users deployment and perfect CSIT.

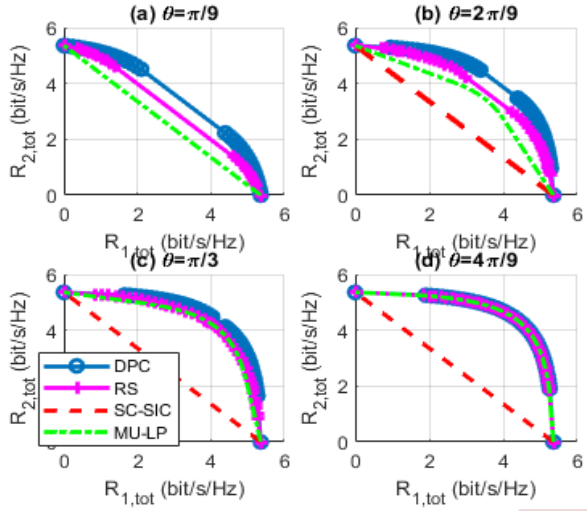


Figure 1. Achievable rate region comparaison with under-loaded two-user deployment with perfect CSIT, SNR=10 dB.

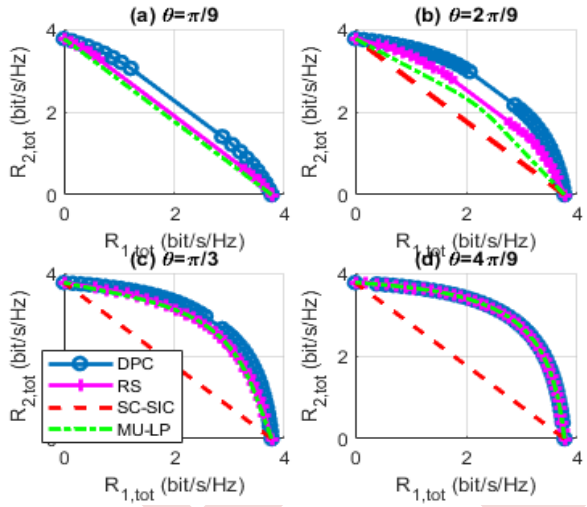


Figure 2. Achievable rate region comparaison with under-loaded two-user deployment with perfect CSIT, SNR=5 dB.

In all subfigures from figure 1 and 2, the rate region achieved by RS is equal to or larger than that of SC–SIC and MU–LP.
We observe that the decrease in SNR leads to a narrowing of the capacity region as well as the achievable rate regions for all three strategies. This decrease is primarily due to an increase in noise power.
The SC-SIC strategy exhibits a constant region that is the smallest among the visualized regions, indicating its limitations in terms of achievable rates. Conversely, the RS and MU-LP regions improve as the value of θ increases. Among the two, the RS region consistently remains the widest, thus demonstrating its superiority over the other strategies.

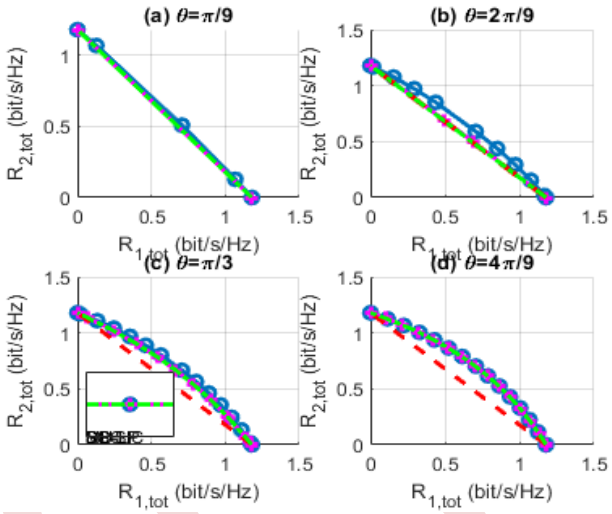


Figure 3. Achievable rate region comparaison with under-loaded two-user deployment with perfect CSIT, SNR=-5 dB.

At an SNR value of -5 dB, significant losses are observed in all regions. This implies that the useful signal is drowned in noise. Under this condition of low SNR, the achievable rate regions for all strategies are severely limited. The performance of the RS strategy remains relatively better than that of the SC-SIC strategy and similar to that of MU-LP, but the achievable rate region for all strategies is significantly reduced.

- **Underloaded two-user deployment with imperfect CSIT:**

In the scenario of imperfect CSIT (Channel State Information at the Transmitter), we assume that both users have perfect channel estimation, while the instantaneous channel estimation at the base station is imperfect [MCL18c].

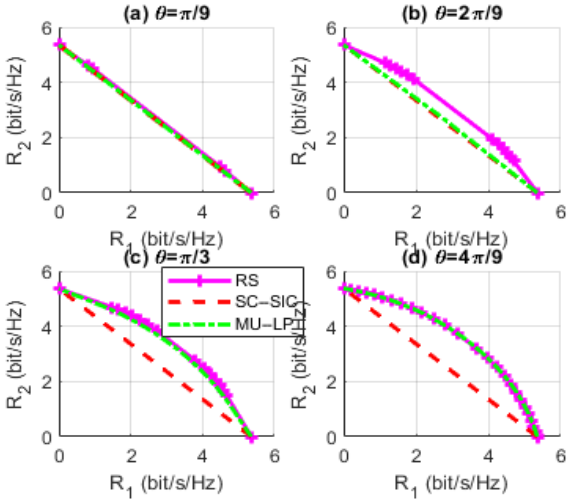


Figure 4. Achievable rate region comparaison with under-loaded two-user deployment with imperfect CSIT, SNR=10 dB.

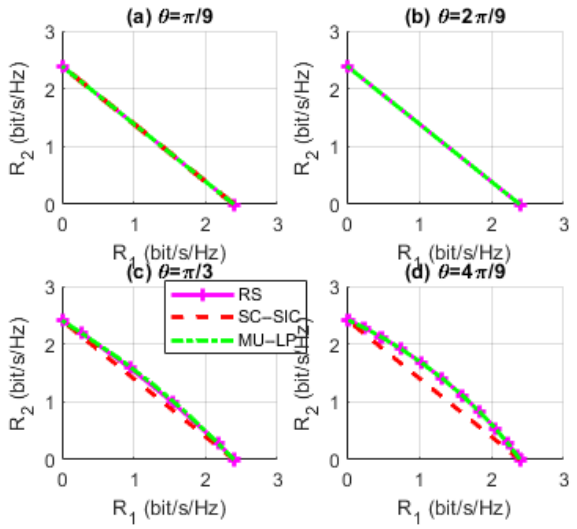


Figure 5. Achievable rate region comparaison with under-loaded two-user deployment with imperfect CSIT, SNR= 5dB.

We observe in figures 4,5 and 6 that the decrease in SNR results in a reduction of the achievable rate region, as well as the capacity region, just like in the case of perfect CSIT.

We can also see that the RS strategy has the most extensive region. The region of MU-LP approaches that of RS when the channels of the two users tend towards orthogonality. On the other hand, the SC-SIC technique reaches its when the channels are aligned.

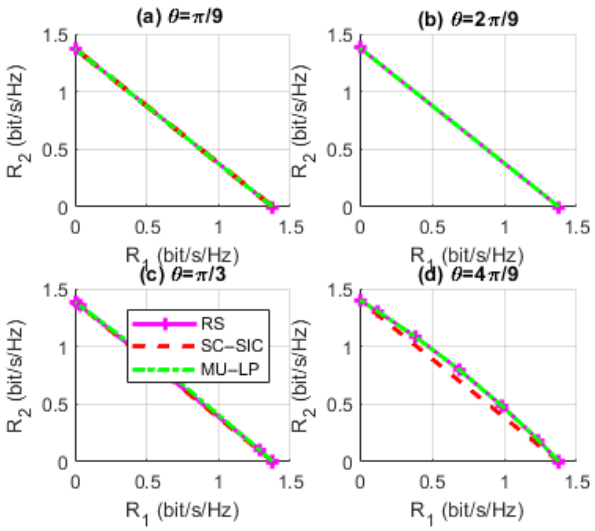


Figure 6. Achievable rate region comparaison with under-loaded two-user deployment with imperfect CSIT, SNR= -5dB.

It is noticed that the gap region between RS and MU-LP, as seen in Figure 4 with imperfect CSIT, is wider than the one seen in Figure 1 with perfect CSIT. Therefore, RS is the most effective technique in the scenario of imperfect CSIT, which is closer to reality.

This compromises the achievable rate. This observation is attributed to the introduction of residual interference. The elimination of interference using MU-LP is disrupted, leading to residual interference at the receiver. This compromises the achievable throughput.

V. CONCLUSION

Finding an access technique that improves the performance of 5G systems with all the massive demands placed on them has been a subject of research for the last few years.

The RSMA technique, with its generality and flexibility, comes closest to meeting these demands. RSMA has stood out as the most effective technique, demonstrating greater robustness to the quality of CSIT. This means that RSMA can maximize the performance measures of a 5G communication system while efficiently utilizing its resources.

Simulation results confirm that the RSMA technique is a generalization of NOMA and SDMA techniques, highlighting its flexibility in interference management.

REFERENCES

[1] Electronics Notes. 5G Multiple Access Scheme. 2023. url : https : / / www . electronics - notes . com / articles / connectivity / 5g - mobile- wireless-cellular/multiple- access- scheme.php (visité le 28/04/2023).

[2] Refik Caglar Kizilirmak et Hossein Khaleghi Bizaki. « Non-orthogonal mu ltiple access (NOMA) for 5G networks ». In : Towards 5G Wireless Networks-A Physical Layer Perspective 83 (2016), p. 83-98.

[3] Yijie Mao, Bruno Clerckx et Victor OK Li. « Rate-splitting multiple access for downlink communication systems : bridging, generalizing, and outperforming SDMA and NOMA ». In : EURASIP journal on wireless communications and networking 2018 (2018), p. 1-54.

[4] Linglong Dai et al. « A survey of non-orthogonal multiple access for 5G».In:IEEE communications surveys & tutorials 20.3 (2018), p. 22942323.

[5] Aydano Carleial. « Interference channels ». In : IEEE Transactions on Information Theory 24.1 (1978), p. 60-70.

[6] Te Han et Kingo Kobayashi. « A new achievable rate region for the interference channel ». In : IEEE transactions on information theory 27.1 (1981), p. 49-60.

[7] runo Clerckx et al. « Rate splitting for MIMO wireless networks : A promising PHY-layer strategy for LTE evolution ». In : IEEE Communications Magazine 54.5 (2016), p. 98-105.

[8] . Onur Dizdar et al. « Rate-splitting multiple access : A new frontier for the PHY layer of 6G ». In : 2020 IEEE 92nd vehicular technology conference (VTC2020-Fall). IEEE. 2020, p. 1-7.

[9] Anup Mishra et al. « Rate-Splitting Multiple Access for 6G—Part I : Principles, Applications and Future Works ». In : IEEE Communications Letters 26.10 (2022), p. 2232-2236.

[10] Changqing Luo et al. « Channel state information prediction for 5G wireless communications : A deep learning approach ». In : IEEE Transactions on Network Science and Engineering 7.1 (2018), p. 227-236.

[11] THE THINGS NETWORK. RSSI and SNR. url : https : / / www . thethingsnetwork . org / docs / lorawan / rssi - and - snr/ (viewed 06/17/2023)

[12] Zheng Chen, Emil Björnson et Erik G Larsson. « When is the achievable rate region convex in two-user massive MIMO systems? » In : IEEE Wireless Communications Letters 7.5 (2018), p. 796-799.

[13] Mohamad Awad Charafeddine et al. « Achievable and crystallized rate regions of the interference channel with interference as noise ». In : IEEE Transactions on Wireless Communications 11.3 (2012), p. 11001111.

[MCL14] Yijie Mao, Bruno Clerckx et Victor OK Li. « Energy efficiency of rate-splitting multiple access, and performance benefits over SDMA and NOMA ». In : 2018 15th International Symposium on Wireless Communication Systems (ISWCS). IEEE. 2018, p. 1-5.

[15] Harish Viswanathan, Sivarama Venkatesan et Howard Huang. « Downlink capacity evaluation of cellular networks with known-interference cancellation ». In : IEEE Journal on Selected Areas in Communications 21.5 (2003), p. 802-811.

EEIC'23

Enhancing the performance of wireless communication systems through the use of beamforming antenna and Massive MIMO technology

Nour El Houda ZAREB [1], Hocine BELLAHSENE [2], Nesrine MERABET[3]

[1] *Laboratory of Medical Informatics (LIMED), Bejaia, Algeria*

nourelhouda.zareb@univ-bejaia.dz

[2]*Labortory of Electrical Engineering (LGE), Bejaia, Algeria*

hocine.bellahsene@univ-bejaia.dz

[3]*Master II student*

Abstract—This paper presents a study on utilizing novel technologies to improve wireless communication performance. We focus on beamforming antenna arrays and Massive MIMO systems, two key areas with significant potential for enhancing system capacity and transmission speed. We investigate the application of beamforming antenna arrays to address technical challenges in implementing Massive MIMO systems. Our objective is to deliver high-quality service, increased data rates, and reduced errors to ensure customer satisfaction. Through simulations, we demonstrate the improved spectral efficiency achievable with beamforming technology. The findings highlight the effectiveness of beamforming antenna arrays and Massive MIMO in optimizing performance, contributing to the development of wireless communication systems.

I. INTRODUCTION

The rapid development of wireless communication technology has led to an explosive growth of the number of mobile users. As a result, new technologies have emerged. However, due to the increasing prevalence of connecting objects with different uses, an overloaded spectrum network will no longer be able to meet the various requirements.

In response to this technological explosion, a revolution has formed a standard for mobile telecommunications systems called IMT 2020. The goal of 5G is not only to address the gaps related to increased speed or bandwidth but also to reduce energy consumption through ubiquitous high-quality services and achieve ultra-low latency. To meet these requirements, this technique must combine several technologies to have a mobile network that can meet expectations [1]. Among these technologies, we can mention Massive MIMO technology and Beamforming. A system that utilizes a large-scale antenna array to serve multiple users is called a Massive Multiple-Input Multiple-Output (MIMO) communication system. Massive MIMO technology is an important and current topic, primarily driven by the demand for fifth-generation (5G) or future wireless communications. This technique is primarily used to enhance system efficiency, with millimeter-wave spectral resources being utilized to expand the system's bandwidth. They are capable of combating signal attenuation. Beamforming is a technique that can be used to steer transmitter beams and increase the receiver's Signal-to-Interference-plus-Noise Ratio (SINR) by mitigating interference. This enables an increase in the capacity of wireless communication systems by employing multiple antennas for transmission and reception, thereby reducing power consumption and achieving spatial diversity enhancement. There are several beamforming techniques, with the most commonly used ones being analog, digital, and hybrid beamforming.

In this paper, we focus on how to leverage more advanced technologies to enhance the transmission performance of wireless mobile networks.

The paper is organized as follows. Section II introduce the study of Massive MIMO technology, the estimation of the channel. Section III defines the Beamforming and its system model, as well as its channel model. Section IV will present the numerical results, and finally, Section V will conclude the paper.

II. LARGE ANTENNA SYSTEMS IN THE 5G CONTEXT

A. Massive MIMO in the 5G

5G base stations can support up to hundreds of ports, which means that more antennas can be accommodated on a single array. This technique is called Massive MIMO, which is a multi-user MIMO technology where each base station (BS) is equipped with an array of M active antenna elements and utilizes them to communicate with K single-antenna terminals

at the same time and frequency band. This allows for increased throughput through spatio-temporal multiplexing and enables energy focusing on a terminal to improve the link budget [2]. As many terminals are allowed to access the same time-frequency resource, MU-MIMO offers superior system efficiency compared to SU-MIMO. We consider single-cell MU-MIMO systems, where the base station serves K user terminals (UTs), with each terminal equipped with a single antenna. On the uplink, the received signal from a MU-MIMO system is represented by [3]:

$$Y = \sum_{k=1}^{K} \sqrt{Pu}\, h_k s_k + W \qquad (1)$$

where Y is the received signal matrix. $\sqrt{Pu}$ is the normalization factor that ensures the transmitted power over the channel remains unchanged by precoding, regardless of M .

$h_k \in H$, where $H = [h_1 ... h_k ... h_K]$, represents the channel vector between the BS antennas and the k^{th} UT.

$s_k \in S$, where $S^T = [s_1 \ ... \ s_k \ ... \ s_K]$ represents the symbol transmitted by the k^{th} UT.

W represents the additive white Gaussian noise (AWGN).

Single User – Multiple Input Multiple Output (SU-MIMO) This single-user technology aims to increase the capacity (primarily throughput) between the transmitter and receiver by introducing multiple antennas on each side. As the name suggests, multiple antenna transmission involves sending data from multiple antennas to multiple antennas located on a single device at the receiving end.

Multi User – Multiple Input Multiple Output (MU-MIMO) MU-MIMO is an enhanced form of MIMO technology that has gained significant interest. A multi-user MIMO system consists of a base station equipped with multiple antennas to communicate with multiple users, each one is equipped with one or more antennas. It improves the communication capacity of each individual terminal, similar to SU-MIMO, where a transmitting antenna communicates with multiple users.

B. Channel Estimation

The transmission channel is considered a key aspect of digital communication, as it can significantly enhance the overall exchange. In Massive MIMO, this information is crucial as it enables the process known as precoding, which involves forming a beam that focuses energy towards or around the user within the cell. As a result, poor channel estimation will lead to a significant decrease in the system's ability to effectively focus the energy [3].

The concept of coherence time (Tc) allows us to determine the duration during which the channel response does not significantly vary. Therefore, it is necessary to estimate the channel with a frequency of at least 1 Tc. In other words, the more mobile elements the channel contains, the more frequent the channel estimation needs to be performed. To perform such estimation quickly, the number of orthogonal pilot sequences that allow the Massive MIMO Base Station (Mass_BS) to estimate all user channels simultaneously is kept low, and they are reused in each channel of adjacent cells [4]. This results in the following consequences:

— Capacity is reduced due to the reduced time for transmitting useful data. Indeed, as the number of users increases, the time (Testimation) allocated for channel estimation also increases. Subsequently, the total cell capacity is then weighted by a factor of (1 - Testimation/Tslot), which can quickly become penalizing for channels with high mobility (low Tc). Tslot refers to the time slot during which the channel is expected to remain static.

— Strong inter-cell interference is a result of the phenomenon known as pilot contamination, which arises from the need to reuse the same pilot sequences in adjacent cells [5].

C. Massive MIMO Technique

Uplink transmission

The partial coherence interval is used for data transmission on the uplink. In the uplink, K users transmit data to the base station on the same time-frequency resource. Then, the base station utilizes channel estimation and linear combining techniques to detect the signals sent by all users.

Downlink transmission

In the downlink, the base station sends signals to all K users on the same time-frequency resource. More specifically, the base station utilizes its channel estimates in combination with the symbols intended for K users to detect the signals transmitted by all users. The symbols enable K users to create M precoded signals, which are then transmitted to M antennas.

III. BEAMFORMING

Beamforming, also known as spatial filtering or beam steering, is a technique that assists base stations in finding an appropriate path to route data to a user. It focuses the signals from multiple antennas into a powerful beam, thus minimizing the energy of the transmitter's sidelobes. Beamforming helps improve signal strength, enhance coverage, and mitigate interference, enabling more efficient and reliable communication in wireless networks. At the receiver level, beamforming is a spatial multiplexing technique that combines the received signals in a way that they add up in a specific direction and reject signals from other directions, treating them as interference. Through beamforming, smart antennas enable increased spectrum efficiency, and in the case of millimeter waves, they can boost data throughput. By focusing the transmitted signals towards the intended user and minimizing interference from other directions, beamforming improves the overall quality and capacity of wireless communication systems [6]. Various beamforming techniques have been studied [7], including analog beamforming [8], digital beamforming [9], and hybrid beamforming as shown in figure 1.

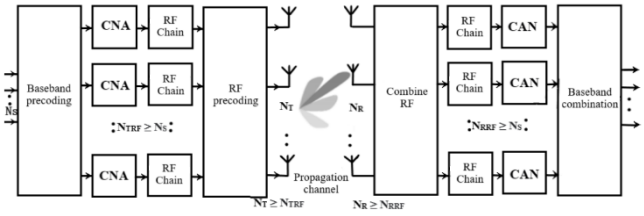


Figure 1. Hybrid beamforming architecture

Hybrid precoding is typically based on two structures: fully connected and sub-connected. The characteristics of the sub-connected structure allow for a better balance between performance and cost. Unlike the one-to-one mapping between the RF chain and antenna in the fully connected structure, each RF chain in the sub-connected structure is only connected to a portion of the antenna. In this paper, we present a model of the millimeter-wave system and the considered channel [11].

A. System model

We primarily focus on the hybrid precoding of large-scale MIMO systems in millimeter-wave based on the sub-connected structure, which can avoid the use of a large number of phase shifters, as illustrated in Figure 2.

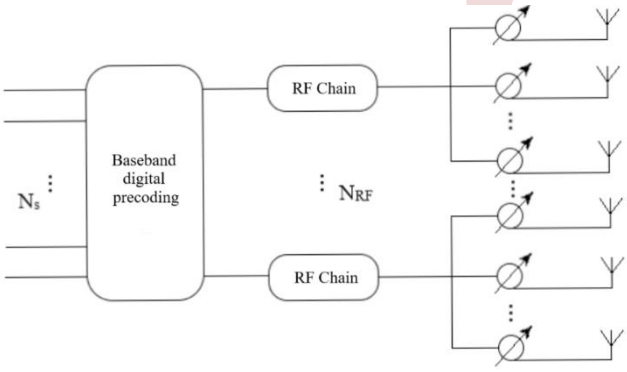


Figure 2. Sub-connected Architecture

Let's consider a single-user massive MIMO system in millimeter-wave, as illustrated in Figure 3, where a transmitter equipped with N_t antennas transmit N_s data streams to the receiver equipped with N_r antennas. The baseband data streams are first precoded by a digital precoder D and then further precoded by an analog precoder A after passing through the corresponding RF chains. Then, each data stream is transmitted through a sub-antenna array, where only M antennas are associated with the corresponding RF chain. The number of RF chains at the transmitter and receiver is respectively N_{RF}^t and N_{RF}^r. To enable multi-stream communication, the following constraints must be satisfied [12]:

$$N_s \leq N_{RF}^t \leq N_t \; and \; N_s \leq N_{RF}^t \leq N_s \qquad (2)$$

The hybrid precoder consists of a baseband digital precoder D and an analog precoder A, with their dimensions as $N_{RF}^t \times N_s$ using N_{RF}^t transmit chains, followed by an $N_t \times N_{RF}^t$ precoder using analog circuits. Assuming the initial signal is s, the emitted signal is then given by [11]: x = ADs, where s is the N_s × 1 symbol vector and satisfies E $[ss^T] = 1/N_s I_{Ns}$

$||AD||_F^2 = N_s$ is the normalized power constraint of the system [11]. To simplify, we consider a narrowband block fading propagation channel, which gives the received signal vector of the system $y = [y_1, y_2, \dots, y_k]^T$ can be expressed as follows:

$$y = \sqrt{\rho}\, H\, x + n = \sqrt{\rho}\, H\, A\, D\, s + n \qquad (3)$$

Where ρ represents the received average power, H is the N_r x $N_t$channel matrix such that $E[||H||_F^2] = N_t\, N_r$, the baseband transmission signal vector can be represented as $s = [s_1, s_2, s_3, \dots, s_N]^T$, and A and D represent the analog precoding matrix and digital precoding matrix, respectively. n denotes the noise vector with i.i.d. complex Gaussian entries $C\, N(0, \sigma^2)$ that are independently and identically distributed. If $F = A\, D$, it denotes the hybrid precoding matrix of size N_t x N_s, which satisfies the condition $||F|| \leq N_s$ to fulfill the total transmit power constraint [12].

In the sub-connected architecture, each RF chain is connected to M $(M = N_t / N_{RF})$ antennas through M phase shifters [13]. Therefore, the digital precoding matrix D for this architecture is a diagonal matrix $D = diag\,[d_1, d_2, \dots, d_N]$, where $d_N \in \Re, n = 1, 2, \dots, N$. The corresponding analog precoding matrix is a block diagonal matrix, expressed in the form [11]:

$$A = \begin{bmatrix} a_1 & \cdots & 0 \\ \vdots & \ddots & \vdots \\ 0 & \cdots & a_n \end{bmatrix} : NM\ x\ N \qquad (4)$$

$a_n \in \mathbb{C}^{M\ x\ 1}$can be considere as an analog weight vector. Due to the constant magnitude constraint, each element of a_n had the same amplitude and different phases [13].

B. Channel Model

Unlike traditional low-frequency channels, the propagation of millimeter-wave channels characteristics is no longer affected by Rayleigh fading due to the strong attenuation in free space path loss. Millimeter waves cause selective or limited spatial scattering of propagation. Similarly, the large antenna arrays that characterize millimeter-wave transceivers can lead to a high degree of correlation between antennas. Therefore, the traditional channel model is not suitable for millimeter-wave channels in massive MIMO systems. That is why there is a need for a model that takes into account the reception of delayed signals in narrowband clusters based on the extended Saleh-Valenzuela model, which accurately captures the mathematical structure present in millimeter-wave channels [12]. Using the clustered channel model, the channel matrix is assumed to be a sum of contributions from N_{cl} scattering clusters, each contributing to the channel matrix H with N_{ray} propagation paths. Therefore, the narrowband channel H is given by [11]:

$$H = \sqrt{\frac{N_t N_r}{N_{cl} N_{ray}}} \sum_{i=1}^{N_{cl}} \sum_{k=1}^{N_{ray}} \alpha_{ik} a_r(\phi_{ik}^r, \theta_{ik}^r)\, a_t\, (\phi_{ik}^t, \theta_{ik}^t)^H \quad (5)$$

	Number of Antennas	***nRx***	8	8	16	16	8	32	16	32	32
		nTx	8	16	8	16	32	8	32	16	32
$M=4$	**Without Beamf-ormin g**	*BER*	0.0955	0.2243	0.0955	0.2243	0.3282	0.0955	0.32 82	0.2243	0.3282
		SNR	9	4	9	4	1	9	1	4	1
	With beamf-ormin g	*BER* (10^{-6})	2	1	2	1	1	2	1	1	1

Where $\alpha_{ik}$is the complex gain of the k^{th} ray in the i^{th} scattering cluster, and it is subject to i.i.d. complex Gaussian distribution $C\ N\ (0, \theta_{ik}^2)$, where θ_{ik}^2 represents the power of the i^{th} cluster [14]. $a_r(\phi_{ik}^r, \theta_{ik}^r)$ and $a_t(\phi_{ik}^t, \theta_{ik}^t)$ represent the normalized response vectors of the receiving and transmitting antenna arrays at an azimuth (elevation) angle of $(\phi_{ik}^r, \theta_{ik}^r)$ and $(\phi_{ik}^t, \theta_{ik}^t)$ respectively, for the k^{th} ray in the i^{th} scattering cluster. The average group angles $(\phi_{ik}^r, \theta_{ik}^r)$ and $(\phi_{ik}^t, \theta_{ik}^t)$ are randomly distributed within the interval $[0, 2\pi]$ [15].

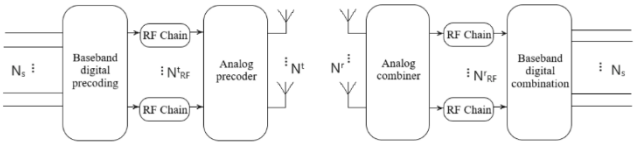


Figure 3. Massive, single-user millimeter-wave MIMO system.

The fundamental objective of the hybrid precoding algorithm is to maximize the spectral efficiency R by designing the optimal hybrid precoder. The system's spectral efficiency is expressed as follows [12]:

$$R = log_2\left(\left|I_{Ns} + \frac{\rho}{N_s\,\sigma^2}\, H\, F\, F^H\, H^H\right|\right) \qquad (6)$$

Where I_{Ns}denotes an N_sxN_s identify matrix and F represents the hybrid precoding matrix in block diagonal form.

IV. Simulation Results

This is dedicated to the simulated interpretation of the results. Firstly, we will evaluate the variation of the bit error rate (BER) as a function of the signal-to-noise ratio (SNR) in wireless transmissions with and without beamforming. Then, we will introduce the basic concepts of hybrid and digital beamforming for millimeter-wave 5G systems.

A. Wireless transmission with and without beamforming

The objective of a wireless communication system is to serve as many users as possible with the highest possible data rate. For this purpose, we increased the number of antennas from 8 to 32 at both the transmitter and receiver, using 106 transmitted symbols with M-QAM modulation in a Rayleigh fading channel. We varied the modulation order from 4 to 256, and the results were evaluated in the SNR range [0:30].

The simulation results are summarized in the tables below, along with their corresponding figures. For $M = 4$, we varied the number of antennas at the transmission and reception for both beamforming and non-beamforming transmissions.

TABLE I BER AND SNR RESULTS IN WIRELESS TRANSMISSION WITH AND WITHOUT BEAMFORMING FOR M=4

The table above shows the variation of the Bit Error Rate (BER) for M-QAM modulation with $M = 4$, while varying the number of antennas. It is evident that the BER is lower when using beamforming compared to the case without beamforming.

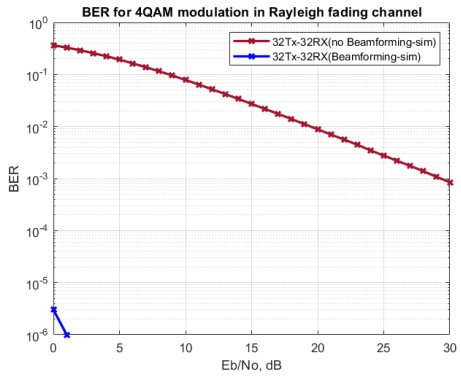


Figure 4. BER and SNR results in wireless transmission with and without beamforming for M=4

Figure 4 shows that at SNR ≈ 1dB, the transmission using beamforming achieves a BER value of 10^{-6}, while the transmission without beamforming achieves a BER value of 0.3282.

TABLE II BER AND SNR RESULTS IN WIRELESS TRANSMISSION WITH AND WITHOUT BEAMFORMING FOR M=64

	Number of Antennas	***nRx***	8	8	16	16	8	32	16	32	32
		nTx	8	16	8	16	32	8	32	16	32
$M=64$	**Without Beamf-ormin g**	*BER*	0.0997	0.2315	0.0997	0.2315	0.3362	0.0997	0.33 62	0.2315	0.3362
		SNR	22	17	22	17	14	22	14	17	14
	With beamf-ormin g	*BER* (10^{-6})	2	2	2	2	1	2	1	2	1

In the present table, we can observe that by increasing the number of levels to 64, there is an increase in the signal to noise ratio, reaching a significantly higher level.

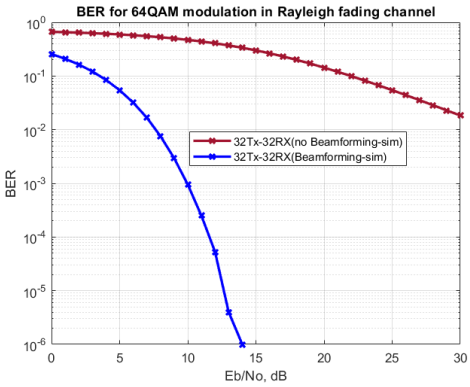


Figure 5. BER and SNR results in wireless transmission with and without beamforming for M=64

Figure 5 shows that for SNR ≈ 14dB, transmission using beamforming achieves a BER value of 10^{-6}, while transmission without beamforming achieves a BER value of 0.3362.

TABLE III BER AND SNR RESULTS IN WIRELESS TRANSMISSION WITH AND WITHOUT BEAMFORMING FOR M=256

	Number of Antennas	nRx	8	8	16	16	8	32	16	32	32
		nTx	8	16	8	16	32	8	32	16	32
$M=256$	**Without Beamforming**	BER	0.0831	0.2339	0.0831	0.2339	0.3388	0.0831	0.3388	0.2339	0.3388
		SNR	29	23	29	23	20	29	20	23	20
	With beamforming	BER (10^{-6})	1	2	1	2	1	1	1	2	1

Table III illustrates the variation of the Bit Error Rate (BER) for 256-QAM modulation while varying the number of antennas. It consistently shows a low BER with beamforming, which is superior to that without beamforming, accompanied by an extremely high Signal-to-Noise Ratio (SNR).

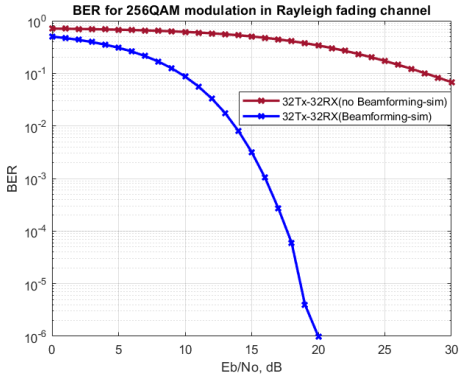


Figure 6. BER and SNR results in wireless transmission with and without beamforming for M=256

Figure 6 shows that for SNR ≈ 20dB, transmission using beamforming achieves a BER value of 10^{-6} while transmission without beamforming achieves a BER value of 0.3388.

We notice that the BER is lower in the transmissions using beamforming, for more details see Appendix D in my project [16].

B. Hybrid beamforming for millimetre-wave 5G systems

To achieve the required data rate, MIMO beamforming implements precoding at the transmitter side and combining at the receiver side to increase the signal-to-noise ratio and separate spatial channels. This allows for improved spectral efficiency, higher data rates, and enhanced overall performance in wireless communication systems.

This section focuses on the simulation of a hybrid MIMO beamforming system with a 64x16 configuration, consisting of a 64-element array with 4 RF chains on the transmitter side and a 16-element array with 4 RF chains on the receiver side. However, each antenna is connected to all the RF chains, allowing for flexible and efficient beamforming in both the transmission and reception processes.

We compare the efficiency achieved using the optimal weights with that obtained using hybrid weights. We observe that the hybrid weights can be successfully utilized to transmit data streams through these beams. The results show that the hybrid beamforming technique is effective in achieving high performance and reliable data transmission in the MIMO system.

Spectral efficiency is a key performance metric for measuring the performance of 5G systems. The next step involves comparing the spectral efficiency achieved using optimal weights with that obtained using hybrid beamforming weights. The simulation is conducted with 1, 2, 3, or 4 data streams. The frequency used in the different simulations is approximately 28GHz ($f_c = 28$GHz). By comparing the spectral efficiency for different scenarios, we can assess the effectiveness of the hybrid beamforming technique in

maximizing system capacity and data rates in 5G networks operating at millimeter-wave frequencies.

To achieve a hybrid curve that closely resembles the optimal case, the number of RF chains on the transmitter and receiver sides should satisfy the following constraints:

$$N_s \leq N_{RF}^t \leq N_t \text{ and } N_s \leq N_{RF}^r \leq N_r$$

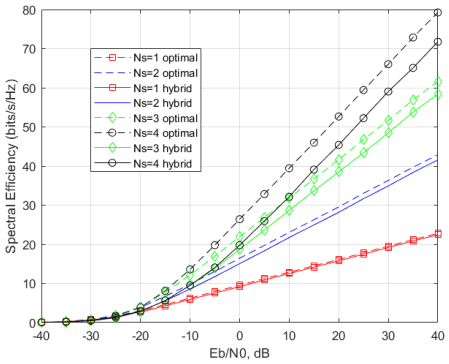


Figure 7. Efficiency as a function of SNR with a number of data streams up to 4, for a number of RF channels 4 on the transmitter side and 4 on the receiver side.

In the following Figure 7, we have attempted to increase the number of data streams up to 4 in order to improve spectral efficiency, with $N_{RF}^t = N_{RF}^r = 4$. We observe that as the number of data streams is increased, the spectral efficiency improves. This indicates that by utilizing more data streams, the system can achieve higher data rates and improve overall performance in terms of spectral efficiency.

V. CONCLUSION

In this paper, over the past few decades, the demand for wireless communications has significantly increased, requiring higher transmission rates, improved reliability, and lower energy consumption. In the first part, we observed that beamforming offers advantages by reducing the bit error rate (BER) through higher modulation orders (M) and increased transmitting and receiving antennas. By enhancing the link budget in 5G, modulation schemes like 256-QAM (8 bits of information) achieve excellent spectral efficiency. The second part introduces the fundamental concepts of optimal hybrid and digital beamforming. Through carefully chosen precoding and combining parameters, hybrid beamforming can achieve comparable performance to fully digital beamforming.

REFERENCES

[1] Nordrum, Amy, and Kristen Clark. "Everything you need to know about 5G." *IEEE Spectrum* 27 (2017): 1.

[2] Björnson, Emil, Erik G. Larsson, and Thomas L. Marzetta. "Massive MIMO: Ten myths and one critical question." *IEEE Communications Magazine* 54, no. 2 (2016): 114-123.

[3] Chouk, Marwa. "Annulation des interférences inter-cellulaires pour les systèmes MIMO massif dans les réseaux hétérogènes 5G." PhD diss., Université Laval, 2019.

[4] Marzetta, Thomas L. "Noncooperative cellular wireless with unlimited numbers of base station antennas." *IEEE transactions on wireless communications* 9, no. 11 (2010): 3590-3600.

[5] Jose, Jubin, Alexei Ashikhmin, Thomas L. Marzetta, and Sriram Vishwanath. "Pilot contamination and precoding in multi-cell TDD systems." *IEEE Transactions on Wireless Communications* 10, no. 8 (2011): 2640-2651.

[6] Chataut, Robin, and Robert Akl. "Massive MIMO systems for 5G and beyond networks—overview, recent trends, challenges, and future research direction." *Sensors* 20, no. 10 (2020): 2753.

[7] Kumar, V. Muthu, V. Karthick, and A. Suban. "Design of Analog and Digital Beamformer for 60GHz MIMO Frequency Selective Channel through Second Order Cone Programming."

[8] Shehata, Mohamed. " Study of precoding techniques for millimetre-wave "wide MIMO" multi-user systems for future 5G networks." PhD diss., INSA de Rennes, 2019.

[9] Challita, Frédéric. "Massive MIMO channel characterization and propagation-based antenna selection strategies: application to 5G and industry 4.0." PhD diss., Université de Lille, 2019.

[10] Shevada, Laxmikant, Hema D. Raut, Rajeshwari Malekar, and Sumit Kumar. "Comparative Study of different beamforming techniques for 5G: A Review." *Inventive Communication and Computational Technologies: Proceedings of ICICCT 2020* (2021): 589-595.

[11] Zhang, Xue, and Feng Zhao. "Hybrid precoding algorithm for millimeter-wave massive MIMO systems with subconnection structures." *Wireless Communications and Mobile Computing* 2021 (2021): 1-9.

[12] El Ayach, Omar, Sridhar Rajagopal, Shadi Abu-Surra, Zhouyue Pi, and Robert W. Heath. "Spatially sparse precoding in millimeter wave MIMO systems." *IEEE transactions on wireless communications* 13, no. 3 (2014): 1499-1513.

[13] Hur, Sooyoung, Taejoon Kim, David J. Love, James V. Krogmeier, Timothy A. Thomas, and Amitava Ghosh. "Millimeter wave beamforming for wireless backhaul and access in small cell networks." *IEEE transactions on communications* 61, no. 10 (2013): 4391-4403.

[14] Fan, Dian, Feifei Gao, Yuanwei Liu, Yansha Deng, Gongpu Wang, Zhangdui Zhong, and Arumugam Nallanathan. "Angle domain channel estimation in hybrid millimeter wave massive MIMO systems." *IEEE Transactions on Wireless Communications* 17, no. 12 (2018): 8165-8179.

[15] Zhao, Jianwei, Feifei Gao, Weimin Jia, Shun Zhang, Shi Jin, and Hai Lin. "Angle domain hybrid precoding and channel tracking for millimeter wave massive MIMO systems." *IEEE Transactions on Wireless Communications* 16, no. 10 (2017): 6868-6880.

[16] Nour El Houda Zareb, Nesrine Merabet, and Hocine Bellahsene. "Study and simulation of beamforming techniques in 5G." University of Bejaia, 2021. URL: https://theses-algerie.com/1966510455038246/memoire-de-master/universite-abderrahmane-mira---bejaia/etude-et-simulation-des-techniques-du-beamforming-en-5g

Terahertz for Wireless Communication and Radio Frequency

S. Latreche [1], H. Bellahsene [1], A. Taleb-Ahmed [2]

[1] *LGEB Laboratory University of Abderrahmane Mira Bejaia*

sofiane.latreche@univ-bejaia.dz

hocine.bellahsene@univ-bejaia.dz

[2] *IEMN DOAE Laboratory Valenciennes University*

abdelmalik.taleb-ahmed@uphf.fr

***Abstract*—Technological development, in terms of electronic and optical material design, gives the possibility of using the last free Radio Frequency band. Communications in this band are considered a key technology for next-generation wireless systems, which promise to integrate a wide range of data-intensive and delay-sensitive applications. This band is the Terahertz (THz) band. In this article, we present the Terahertz band and examples of their uses. Then we take the case of wireless communications and localization. We first detail the particularities of each of these applications in the THz band. We then study several effects and parameters respectively in the two applications. The interpretation of the results obtained will be given at the end of this study.**

***Keywords:* Wireless Communications, 5G, 6G, THz, SNR.**

I. INTRODUCTION

Mobile networks, whether in the radio part or the core part, are evolving very fast. Starting with a generation dedicated to telephony until the arrival of applications that are unimaginable for most people. Those applications need high speed and low latency. To meet these requirements, the terahertz band is considered as the only key technology until now. Terahertz (THz) waves, or sub-millimeter/far-infrared waves, refer to electromagnetic radiation with inside the frequency interval from 0.1 to ten THz. They occupy a large part of the electromagnetic spectrum [1].

A potential capacity in the order of Terabits per second is possible due to the THz frequency guaranteeing extensive bandwidth, which theoretically reaches as much as numerous THz [2]. Hence, the bandwidth provided is one order of magnitude above millimeter-wave (mmW) systems. THz signals additionally permit better hyperlink directionality and provide lower eavesdropping probabilities as compared to their millimeter counterparts [3]. Analysis of the Terahertz band suggests that those frequencies additionally own fixed benefits in comparison to optical frequencies. In uplink, THz waves are a serious candidate for radio transmission. They allow non-line-of-sight (NLoS) propagation [4] and act as good substitutes for inconvenient weather situations such as fog, dust, and turbulence [5]. In addition, the Terahertz frequency band isn't always impacted with the aid of using ambient noise arising from optical sources, nor is it related to any health restrictions or safety limits [6]. Table 1 presents a comparison between the THz frequency band and different current technologies.

In particular, the harsh propagation environment features a high path loss inversely proportional to the square of the wavelength, and thus to the size of a single antenna element, and, in addition, a high molecular absorption in certain frequency bands [7]. the smallest wavelength at terahertz allows many antenna elements to be packed in a small surface, thus enabling Ultra-massive Multiple Input, Multiple Output (UM-MIMO) techniques [7]. The focus of several studies has been on increasing the communication range in macro scenarios [8], as well as on signal generation and modulation. Directional antennas are used to mitigate the increased path loss, as they can focus the power in narrow beams, which increases the link budget, and enhances the security of wireless links [9].

In this paper, terahertz frequencies will be detailed, before studying their usefulness for mobile networks. Then, their applications to detection radars will be studied and the results found will be discussed. A conclusion will be given at the end of this article.

II. THE THZ FREQUENCIES

THz-band communications are predicted to play a pivotal position in the imminent 6th generation (6G) of wireless mobile communications, allowing ultra-high-bandwidth communication paradigms. To this end, many research groups have received significant financial funding to conduct THz research. The objective is to boost the standardization efforts

TABLE I. COMPARISON OF DIFFERENT WIRELESS COMMUNICATION TECHNOLOGIES

Technology	**mmWave**	**THz Band**	**Infrared**	**Visible Light Communication (VLC)**	**Ultra-Violet**
Frequency Range	30 GHz - 300 GHz	100 GHz - 10 THz	Short/Long range	430 THz - 790 THz	790 THz - 30 PHz
Range	Short range	Short/Medium range	Short/Long range	Short range	Short rang
Power Consumption	Medium	Medium	Relatively low	Relatively low	Expected to be low
Network Topology	Point to Multi-point	Point to Multi-point	Point to Point	Point to Point	Point to Multi-point
Noise Source	Thermal noise	Thermal noise	Sun/Ambient Light	Point to Point	Sun/Ambient Light
Weather Conditions	Robust	Robust	Sensitive	-	Sensitive
Security	Medium	High	High	High	To be determined

and to reduce the time allocated to these procedures to a minimum [10]. The last untapped band in the radio frequency (RF) spectrum is the terahertz (THz) band. The deployment of technologies from the neighboring microwave and optical bands has enabled the design of future THz communication techniques [10]. Figure 1 represents the frequency range from 0.1 to 10 Terahertz called the THz band. The evolution in transceivers allows the use of THz bands in wireless communications. Electronics and photonics are the main areas of this evolution. Electronic platforms are superior in their ability to generate higher power, even though photonic technologies have an advantage in data rate [10].

Currently, different technologies are considered to be used in THz transceivers. Like Silicon Germanium (SiGe) technol ogy, compound semiconductor technologies such as Gallium Nitride (GaN) and Indium Phosphide (InP), Photonic devices, such as Quantum Cascade Lasers (QCLs) and bolometric detectors [2]. Plasmonic solutions in particular graphene [11]. Recently, graphene-based solutions have emerged as strong candidates that enable communications at the THz band. The particular electric properties of graphene, which include high electron mobility, electrical tunability, and configurability, permit supporting high-frequency signals [12]. The THz band is guaranteed to lead to higher user density, greater reliability, significantly less latency, greater energy efficiency, higher positioning accuracy, better spectrum utilization, and enhanced adaptability to propagation scenarios [10]. During the beyond decade, diverse Terahertz technology has been present process fast improvement and feature enabled us to use THz sensing and imaging for chemical, biological, biomedical and different interdisciplinary studies [13]. In current years, THz technology have confirmed to be promising method for defense and security applications [1]. Also paving the manner for applications with inside the Terahertz band, ranging from indoor wireless communications to automobile and drone communications, to device-to-device communications and nano-communications. In addition, THz signals have the capability for use in lots of non-communications-based applications, such as spectroscopy of small biomolecules and quality control of pharmaceuticals [11] (Figure 1).

III. THZ AND WIRELESS COMMUNICATIONS

THz-band communications will be important to the future 6G and beyond [14]. Particularly, the large available bandwidths, which range from tens to as much as a hundred gigahertz, and extremely short wavelengths provide an enormous amount of potential to alleviate spectrum scarcity and break the capacity limitation of 5G networks., thereby permitting emerging applications that call for an explosive quantity of data [15]. In addition, ultra-broadband antennas are needed for THz Band communication. Moreover, very large antenna arrays will be necessary to overcome the very high path loss in the THz Band [2]. Below we present simulations of SNR and SNR coverage probability for different antenna configurations and frequencies.

Figure 2 compares the Signal to Noise ratio at totally different distances (5, 50 and 150 m) for THz and mmWave links.

To analyze the impact of the upper carrier frequency on the propagation loss. The SNR is an indicator of the quality of transmission of information. It's given by the proportion of the received signal power and also the noise power, without the beamforming gain, Ptx = 0.5 W, and noise figure F = 10 dB. 400 megahertz is the bandwidth for mmWaves (The maximum bandwidth allowed per carrier of 3GPP NR), and 50 gigahertz for Thz (conforms to IEEE 802.15.3d).

The SNR is computed mistreatment of the 3GPP model in an urban canyon situation within the frequency range considered for 3GPP NR [16], and [17] for THz links in the 300 GHz-1 THz spectrum. We observe the difference between the THz and mmWve carriers. For example, the SNR gap for a distance of 5 m, is 39 dB between a carrier at 41 GHz and at 700 GHz. This difference can be compensated for by increasing the number of antenna elements in each node.

In Figure 3, we consider simulations during which macro base stations are randomly deployed outdoors according to a Poisson point process, with the coverage probability computed as the probability of getting a Signal to Noise ratio higher than a threshold of zero decibels between a test user, and at least

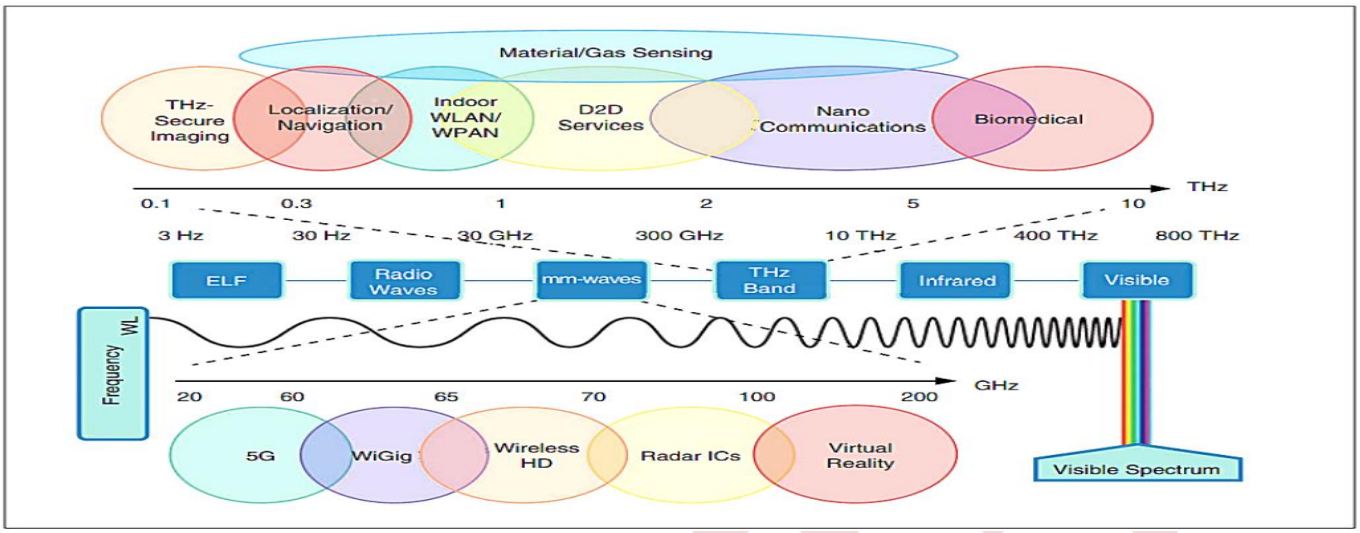


Figure 1. Evolution of mobile wireless systems.

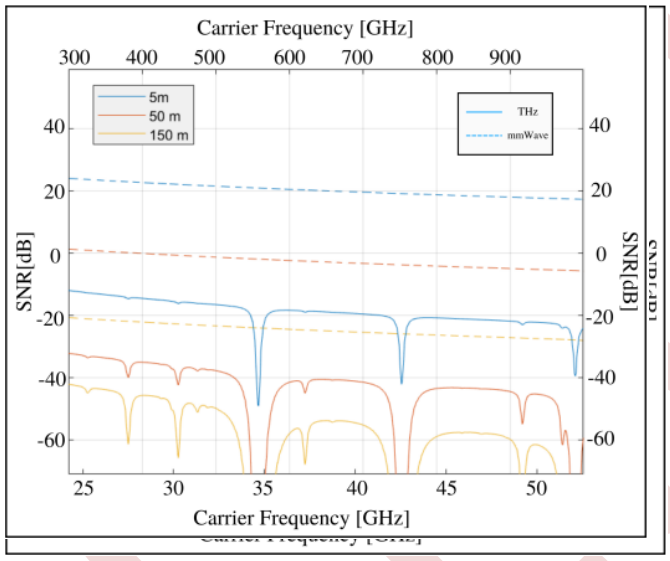


Figure 2. Millimeter waves and terahertz links.

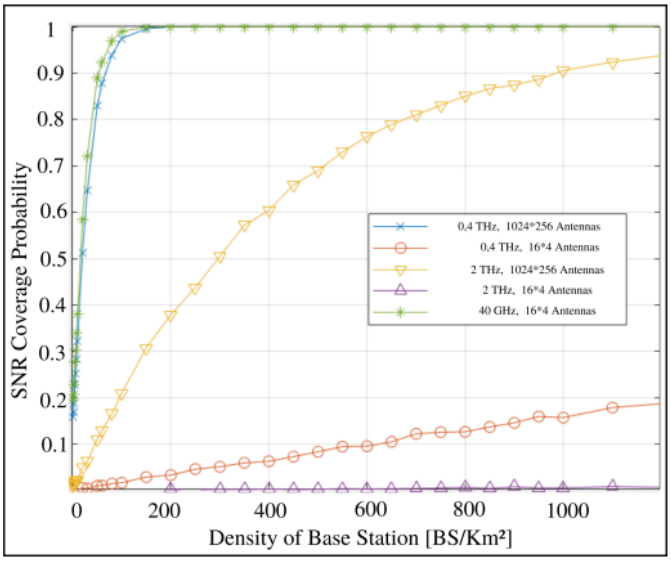


Figure 3. Probability of getting an SNR higher than 0 dB for various deployment configurations.

one base station. The path loss and beamforming gain are modeled as in Figure 2.

This figure illustrates the differences in deployment density that will be expected for mmWave and THz systems. It can be seen that with 16 antenna elements at the BS and 4 at the mobile device, the 40 GHz network has a coverage probability greater than 0.95 with 80 BS/km². The same antenna configuration does not guarantee an adequate performance at the terahertz band, since a similar coverage probability requires much more than 1000 base stations/km² at 0.40 THz. But with 1024 antenna elements for base stations and 256 for mobile devices, it is possible to achieve this coverage probability with 100 BS/km² at 0.40 THz and 1100 BS/km² at 2 THz. So, as we saw in the previous section, antenna arrays with a larger array of antenna elements (small high-density cells) will be needed to remedy the higher path loss at terahertz frequency spectrum.

IV. THZ LOCALIZATION

Localization is the method used to estimate the position and orientation of a target., that is significant for a range of applications, as well as location-aware communications [18], Industrial Internet of Things (IoT) [19], the tactile internet [20], and autonomous driving [21]. Over the years, a plethora of localization techniques are proposed. These techniques use differing types of signals or measurements that embody ultrasound, visible light, radio frequency (RF) [22]. Due to their omnipresence in current wireless communication systems, RF signals are widely used among these modalities.

The process of determining a target's position and orientation is known as localization, that is significant for a

range of applications, as well as location-aware communications [18], the industrial internet of Things (IoT) [19], the tactile internet [20], and autonomous driving [21]. Over the years, a plethora of localization techniques are proposed. These techniques use differing types of signals or measurements that embody ultrasound, visible light, radio frequency (RF) [22].

However, within the fifth generation of wireless communication systems, location is being reshaped from location-based services to location-aware communications. As a result, location information will reduce latency and improve the scalability and robustness of 5G communication systems [18]. This trend continues with future sixth-generation (6G) systems, wherever location and communication should be integrated to attain ubiquitous connectivity, high data rates, and low latency over three-dimensional (3D) network coverage [23]. a variety of applications that are incompatible with present communication methods because they require high data speeds and great localization accuracy, however, will be satisfied by the interaction between localization and communication, particularly within the thz band.

In terahertz (THz) communications, an array of subarrays (AoSA) is a desirable architecture because low-cost phase shifters enable analog beamformers on the subarrays to give beam gain to mitigate severe propagation loss. But the conventional AoSA beamforming approach, in which each subarray serves a single user, is unable to handle the impact of beam split in THz wideband communications [24]. The sub-array network (AoSA) is engaging for terahertz communications as a result of the narrow beam will be complete by low-cost sub-array phase shifters [25]. This structure uses the standard beamforming scheme, i.e., every sub-array serves an single user, will solely transmit narrowband signals, and doesn't afford broadband communications [24]. This is often because the phase shifters are frequency-independent and can't handle broadband signals.

From a localization perspective, we tend to are most interested in the accuracy of a UE's location and orientation. Positioning accuracy is typically measured in terms of error. For orientation estimation, the rotation error is defined as the angular distinction between the estimate and therefore the actual angle. The position and rotation errors are affected by the noise level. each errors are delimited by the position error bound (PEB) and the orientation error bound (OEB). they're typically employed by geometry-based localization methods as effective tools for performance evaluation.

In this section, we offer many simulations to judge the impact of system parameters on localization performance. A 0.5 thz system and a 50 GHz mmWave system in an uplink scenario are considered with the following parameters: Transmission Power P=10 dBm, Noise Figure =13 dBm, bandwidth W=100 MHz. These parameters are the default parameters for the rest of the simulations. In figure 4 and 5 a comparison between millimeter wave and THz systems is shown. We compare the PEB and OEB between 2 systems with totally different network configurations to evaluate the fundamental limit of the localization systems.

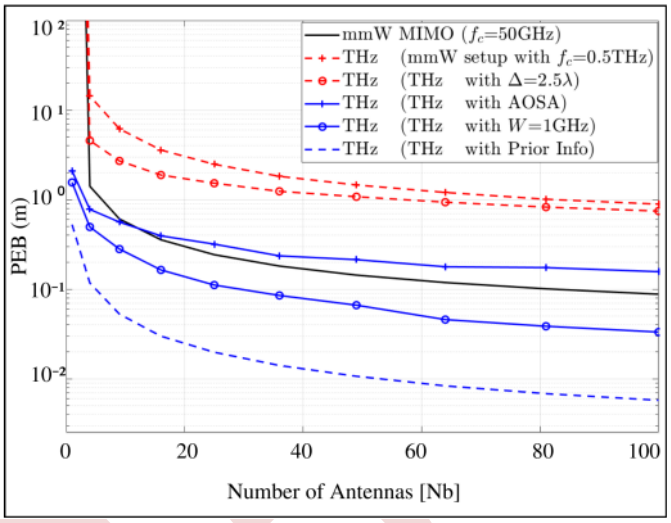


Figure 4. PEB depending on the number of antennas of the base station for 0.5 THz

In figure 4. PEB as a function of base station antenna count. By moving the carrier frequency from 50 ghz to 0.5 THz, the error limit will increase because of high path losses. In addition, increasing the antenna spacing from 0.5λ to 2.5λ (keeping a similar configuration as the mmWW array) reduces the errors. The adoption of an AOSA structure introduces a beamforming gain, and also the error limits are nearly the same with the millimeter-wave reference system's performance. the limits can be even lower with a bigger bandwidth (1 GHz instead of 100 MHz) and within the case of prior information (e.g., by setting the base station beamforming angle to the direction of a UE).

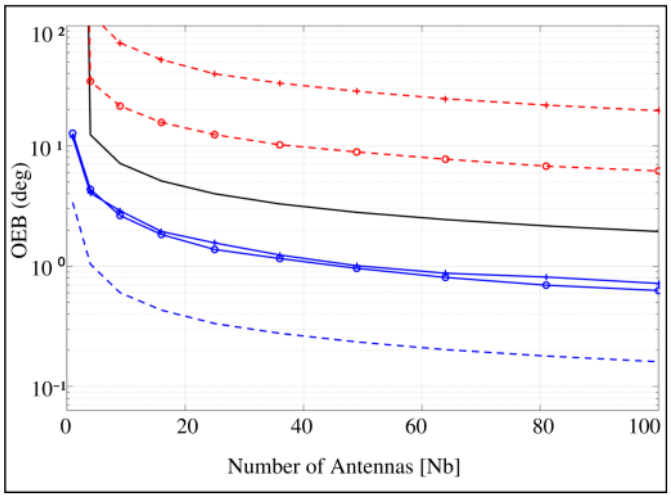


Figure 5. OEB depending on the number of antennas of the base station for 0.5 THz

In Figure 5. OEB as a function of base station antenna count. By moving the carrier frequency from 50 ghz to 0.5 THz, the error limit will increase due to high path losses. In addition, increasing the antenna spacing from 0.5λ to 2.5λ (keeping an equivalent configuration as the mmWW array) reduces the errors. The adoption of an AOSA structure

introduces beamforming gain, and also the error limits exceed the performance of the millimeter-wave reference system. The limits can be even lower with a larger bandwidth (1 GHz instead of 100 MHz) and in the case of prior information (e.g., by setting the bs beamforming angle to the direction of a UE).

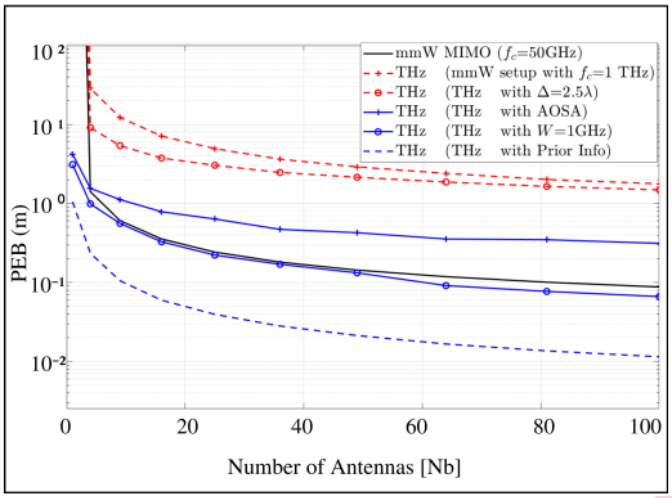


Figure 6. PEB depending on the number of antennas of the base station for 1 THz

In figure 6 and 7. An analysis of PEB/OEB as a function of base station antenna count. By moving the carrier frequency from 0.5 Thz to 1 THz, the error limit will increase because of high path losses. So antenna arrays with a larger number of antenna elements (small high-density cells) will be needed to remedy the higher path loss in the terahertz frequency spectrum. So in addition, increasing the antenna spacing from 0.5λ to 2.5λ (keeping a similar configuration as the mmWW array) reduces the errors. The adoption of an AOSA structure introduces a beamforming gain, and the error limits are reduced.the limits can be even lower with a bigger bandwidth (1 GHz instead of 100 MHz). in the case of prior information (e.g., by setting the base station beamforming angle to the direction of a UE) the error limits exceed the performance of the millimeter-wave reference system.

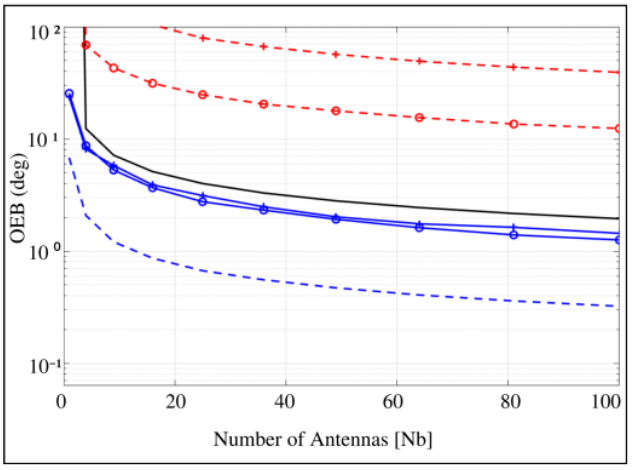


Figure 7. PEB depending on the number of antennas of the base station for 1 THz

V. CONCLUSION

Given the potential of THz communication systems to deliver high data rates in over short distances, they are currently considered the next research frontier in wireless communications.

This paper presents terahertz frequencies. Their use in mobile networks through simulations, by calculating the SNR as a function of different frequency ranges, different distances, and different antenna deployments. Their use, in the case of radars, by modeling several effects of radio frequency propagation. Their use, in the case of localization, by calculating the PEB and OEB for different configurations.

Therefore, it is concluded that for the use of the THz frequency range in mobile networks, antenna arrays with a larger number of antenna elements (UM-MIMO) will be needed to cope with the higher propagation loss in this spectrum. THz frequencies are also proven to be robust to weather conditions.

ACKNOWLEDGMENT

The authors would like to thank the director of the Cerist Béjaia section Pr. A. Belaid and his team for their welcome in their infrastructure, their technical support, and their critical discussions.

REFERENCES

[1] Liu, H. B., Zhong, H., Karpowicz, N., Chen, Y., and Zhang, X. C. (2007). "Terahertz spectroscopy and imaging for defense and security applications". Proceedings of the IEEE, 95(8), 1514-1527.

[2] Akyildiz, I. F., Jornet, J. M., and Han, C.(2014). "TeraNets: Ultra-broadband communication networks in the terahertz band" IEEE Wireless Communications, 21(4), 130-135.

[3] C John Federici and Lothar Moeller, "Review of terahertz and sub-terahertz wireless communications", Journal of Applied Physics 107, 111101 (2010) https://doi.org/10.1063/1.3386413

[4] Moldovan, A., Ruder, M. A., Akyildiz, I. F., and Gerstacker, W. H.(2014, December)."LOS and NLOS channel modeling for terahertz wireless communication with scattered rays". In 2014 IEEE Globecom Workshops (GC Wkshps) (pp. 388-392). IEEE.

[5] Elayan H, Amin O, Shubair RM, Alouini M-S,(2018, April). "Terahertz communication: The opportunities of wireless technology beyond 5G". 2018 International Conference on Advanced Communication Technologies and Networking (CommNet). Available: http://dx.doi.org/10.1109/commnet.2018.8360286.

[6] Siegel, P. H.(2004). "Terahertz technology in biology and medicine". IEEE transactions on microwave theory and techniques, 52(10), 2438-2447.

[7] Akyildiz, I. F., and Jornet, J. M, (2016). "Realizing ultra-massive MIMO (1024× 1024) communication in the (0.06–10) terahertz band". Nano Communication Networks, 8, 46-54.

[8] Akyildiz, I. F., Han, C., and Nie, S, (2018). "Combating the distance problem in the millimeter wave and terahertz frequency bands". IEEE Communications Magazine, 56(6), 102-108.

[9] Yan, L., Han, C., and Yuan, J, (2020). "A dynamic array-of-subarrays architecture and hybrid precoding algorithms for terahertz wireless communications". IEEE Journal on Selected Areas in Communications, 38(9), 2041-2056.

[10] Sarieddeen, H., Saeed, N., Al-Naffouri, T. Y., and Alouini, M. S, (2020). "Next generation terahertz communications: A rendezvous of sensing, imaging, and localization". IEEE Communications Magazine, 58(5), 69- 75

[11] Faisal, A., Sarieddeen, H., Dahrouj, H., Al-Naffouri, T. Y., and Alouini, M. S, (2020). "Ultramassive MIMO systems at terahertz bands: Prospects and challenges". IEEE Vehicular Technology Magazine, 15(4), 33-42

[12] Ju, L., Geng, B., Horng, J., Girit, C., Martin, M., Hao, Z., ... and Wang, F, (2011). "Graphene plasmonics for tunable terahertz metamaterials". Nature nanotechnology, 6(10), 630-634.

[13] Rappaport, T. S., Xing, Y., Kanhere, O., Ju, S., Madanayake, A., Mandal, S., ... and Trichopoulos, G. C,(2019). "Wireless communications and applications above 100 GHz: Opportunities and challenges for 6G and beyond". IEEE access, 7, 78729-78757.

[14] Sarieddeen, H., Alouini, M. S., and Al-Naffouri, T. Y, (2021). "An overview of signal processing techniques for terahertz communications". Proceedings of the IEEE

[15] Shafie, A., Yang, G. N., Han, C., Jornet, J. M., Juntti, M., and Kurner, T. (2022). "Terahertz communications for 6G and beyond wireless networks: Challenges, key advancements, and opportunities". IEEE Network.

[16] 3GPP, "TR 38.901, Study on channel model for frequencies from 0.5 to 100 GHz, V16.1.0," 2020.

[17] J. M. Jornet and I. F. Akyildiz,(Oct.2011). "Channel Modeling and Capacity Analysis for Electromagnetic Wireless Nanonetworks in the Terahertz Band," IEEE Trans. Wireless Commun., vol. 10, no. 10, pp. 3211–3221.

[18] Di Taranto, R., Muppirisetty, S., Raulefs, R., Slock, D., Svensson, T., and Wymeersch, H. (2014), "Location-aware communications for 5G networks: How location information can improve scalability, latency, and robustness of 5G". IEEE Signal Processing Magazine, 31(6), 102-112

[19] ohan, E. S., Koivisto, M., Galinina, O., Andreev, S., Tolli, A., Des tino, G., ... and Valkama, M. (2018), "Benefits of positioning-aided communication technology in high-frequency industrial IoT". IEEE Communications Magazine, 56(12), 142-148.

[20] Antonakoglou, K., Xu, X., Steinbach, E., Mahmoodi, T., and Dohler, M. (2018), "Toward haptic communications over the 5G tactile Internet". IEEE Communications Surveys and Tutorials, 20(4), 3034-3059.

[21] Antonakoglou, K., Xu, X., Steinbach, E., Mahmoodi, T., and Dohler, M. (2018), "Toward haptic communications over the 5G tactile Internet". IEEE Communications Surveys and Tutorials, 20(4), 3034-3059.

[22] Laoudias, C., Moreira, A., Kim, S., Lee, S., Wirola, L., and Fischione, C. (2018), "A survey of enabling technologies for network localization, tracking, and navigation". IEEE Communications Surveys and Tutorials, 20(4), 3607-3644.

[23] Xiao, Z., and Zeng, Y. (2022), " An overview on integrated localization and communication towards 6G". Science China Information Sciences, 65(3), 1-46.

[24] Ning, Boyu. (2022), "Wideband Terahertz Communications with AoSA: Beam Split Aggregation and Multiplexing"

[25] Lin, C., and Li, G. Y. L. (2016), "Terahertz communications: An array of-subarrays solution". IEEE Communications Magazine, 54(12), 124-131.

Cellular-Connected UAVs : Coverage Analysis using SWIPT and Up-Tilted Antenna

Dina Alkama [1], Mohamed Amine Ouamri [1], Lynda Alkama [2], Mohamed Azni [1]

[1] *Laboratoire d'Informatique Medicale (LIMED), Faculté de Technologie, Université de Bejaia, 06000 Bejaia, Algeria*

dina.alkama@univ-bejaia.dz

ouamrimouhamedamine@gmail.com

[2] *Laboratoire LITAN, École supérieure en Sciences et Technologies de l'Informatique et du Numérique, RN 75, Amizour 06300, Bejaia, Algérie*

alkama@estin.dz

mohamed.azni@univ-bejaia.dz

***Abstract*— Unmanned Aerial Vehicles (UAVs) can perform a variety of missions and tasks through wireless connectivity. However, they are prone to low power consumption issues. In this paper, we consider the simultaneous energy and information transfer in cellular-connected UAVs adopting the simultaneous wireless information and power transfer (SWIPT) technology. Specifically, the base stations (BSs) are equipped with up-tilted antennas to provide 3D coverage for aerial users (AUe). Using stochastic geometry, the distribution of BSs follows the homogeneous Poisson Point Process (HPPP). We investigate the energy coverage probability (ECP) and the signal-to-interference-and-noise ratio coverage probability (SCP) for a typical AUe located at a fixed altitude h_u and assumed to be connected to the nearest BS. Simulation results show that increasing BS density enhances ECP while reducing SCP. In addition, ECP and SCP can be improved by carefully adjusting the AUe altitude and tilt angle.**

***Keywords:* Cellular-connected UAV, Energy coverage, Poisson point process (PPP), SINR coverage, SWIPT.**

I. INTRODUCTION

Unmanned Aerial Vehicles (UAVs) have become extremely attractive for a variety of applications due to their autonomy and mobility, making them a fundamental element of the Internet of Things (IoT). For instance, a UAV can perform data collection, deliver packages, remote monitoring, and conduct search and rescue missions [1]. In such applications, wireless connectivity is mandatory for the UAV to effectively perform tasks and operate successfully, thus qualifying it as an aerial user (AUes). Integrating AUes into a traditional cellular network creates what we call a cellular-connected UAV network. Despite the advantages offered by UAVs, their battery capacity remains limited, and the problem of energy constraints persists [2]. On the other hand, harnessing energy through radio frequency (RF) is considered as an appealing and promising power source for energy-limited networks. Typically, within a slot-based system simultaneous wireless information and power transfer (SWIPT) is the most adopted technology to overcome UAV power constraints. The central concept of SWIPT is to simultaneously supply wireless information and energy on demand in the downlink direction [3].

Research on cellular-connected UAVs has drawn growing attention. However, there is a significant lack of literature regarding energy harvesting in cellular-connected UAVs. UAV-enabled SWIPT network was studied in [4], [5] where both of power splitting (PS) and time switching (TS) are employed at the ground users (GUes). The authors were evaluated joint the energy coverage and the information coverage with linear nonlinear energy harvesting. In [6], the coverage and maximum throughput are studied in an energy harvesting network using SWIPT. Some studies have investigated the coexistence of aerial and terrestrial users within a cellular network [7]−[9]. Nevertheless, the authors have neglected the energy limitation, which presents a particular challenge for AUes. The authors in [10] considered a base station (BS) cooperation to deal with the line-of-sight (LoS) interference in downlink cellular-connected UAV and have assumed that the AUes are served by the side lobes of BS antennas. In [11], a slot-based system is adopted where SWIPT was used in cellular-connected UAV served by a terrestrial BSs with down-tilted antennas. However, this antenna model is principally conceived for land-based users and does not provide effective, even coverage of the AUes. In [9], a model featuring up-tilted antennas was proposed and applied in terrestrial BSs to evaluate the three dimensional (3D) coverage probability in cellular-connected UAV for both AUe an GUe. A coexistence of the traditional down-tilted antennas and up-tilted antennas was investigated in [12], [13]. However, the harvesting energy was neglecting in these researches. To the best of our knowledge, harvesting energy in cellular-connected UAV with up-tilted antennas was not being investigated.

In this paper, based on the above motivations, we adopt SWIPT in cellular-connected UAVs, where the AUes are at a fixed altitude and are served by the up-tilted BS antennas.

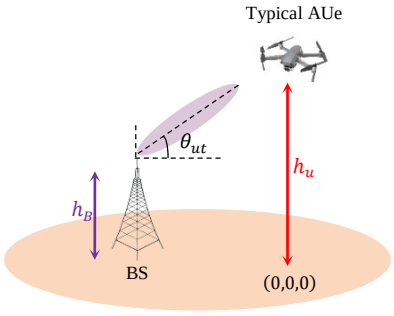


Figure 1. Illustartion of the network model.

Specifically, we consider the power splitting architecture (PS) and determine the energy coverage probability (ECP) and the signal-to-interference-and-noise ratio (SINR) coverage probability (SCP) considering the effect of LoS and non-line-of-sight (NLoS) connection and Nakagami-*m* fading.

II. System Model

A. Network Topology

We consider a downlink cellular-connected UAV network, where the aerial users (AUes) are randomly distributed and located at fixed altitude h_u and are served by an up-tilted ground BSs antennas using SWIPT. The location of the BSs denoted by Ω_i is modeled as a homogeneous Poisson point process (HPPP) $\psi \equiv \{\Omega_i, i \in \mathbb{N}\}$ with density and height respectively denoted by λ and h_B ($h_B < h_u$). All BSs have a same transmit power P_B. Each BS is equipped with horizontal omnidirectional antennas and vertical directional antennas with an up-tilt angle denoted by θ_{ut}. As depicted in Figure. 1, a typical AUe is selected to perform our analysis and assumed to be located at the origin $(0,0,h_u)$ for tractability i.e., the projection of the typical AUe in the ground is (0,0,0). The nearest BS to the typical AUe is assumed to be the serving BS.

B. Cellular to Air Channel

1) LoS and NLoS probabilities : The channel propagation between the BS and AUe cannot be the same as the air-to-ground (A2G) channel adopted in [14] which is intended for GUes at heights of 1.5 meters. On the other hand, the channel model recommended by the International Telecommunication Union (ITU) [15] renders the analysis unmanageable, because the proposed LoS probability is not a continuous function of the distance between the transceivers, therefore following [16] the probability of LoS and NLoS communication can be simplified and given as

$$P^L(z_i) = -a \exp\left(-b \tan^{-1}\left(\frac{h_u - h_B}{z_i}\right)\right) + \delta, \quad (1)$$

$$P^N(z_i) = 1 - P^L(z_i), \quad (2)$$

where a, b and δ are coefficients related to the environment and the height of BS and AUe. z_i denotes the horizontal distance between the typical AUe and BS Ω_i.

2) Path Loss : The path loss model adopted is given as [17]

$$L^s_{\Omega_i}(z_i) = \eta^s({z_i}^2 + (h_u - h_B)^2)^{\frac{\alpha^s}{2}}, \quad (3)$$

where η^s is the path loss at a reference distance $({z_i}^2 + (h_u - h_B)^2)^{1/2} = 1km$, α^s is the path loss exponent with $s \in \{L, N\}$.

3) Small-scale fading : For a better description of small-scale fading channel, we assume that links between AUs and BSs are subject to Nakagami-*m* fading. The fading gain, $h^s_{z_i}$ follows a Gamma distribution $h^s_{z_i} \sim \Gamma(N^s, 1/N^s)$, and its probability density function (PDF) can be given as [17]

$$f_{h^s_{\Omega_i}}(v) = \frac{{N^s}^{N^s} v^{N^s-1}}{\Gamma(N^s)} \exp(-N^s v), \quad (4)$$

where $s \in \{L, N\}$, N^s is a positive-integer fading parameter and $\Gamma(N^s) = \int_0^\infty q^{N^s-1} e^{-q} dq = (N^s - 1)!$.

4) Antenna Gain : We assume that the BSs are equipped with up-tilted antennas. Each BS is equipped with a uniform linear array of M vertically-placed elements for each antenna. Similar to [9] the antenna gain is given as

$$G_{\Omega_i}(z_i) = \frac{1}{M} \frac{\sin^2\frac{M\pi}{2}(\sin(\varphi(z_i)) - \sin(\theta_{ut}))}{\sin^2\frac{\pi}{2}(\sin(\varphi(z_i)) - \sin(\theta_{ut}))} \times 10^{min\left(-1.2\left(\frac{\varphi(z_i)}{\theta_h}\right)^2, \frac{G_{th}}{10}\right)}, \quad (5)$$

where $\varphi(z_i) \triangleq \tan^{-1}\left(\frac{h_B - h_u}{z_i}\right)$, θ_{ut} and θ_h are the up-tilt angle and half power beam width respectively, $G_{th}$is the threshold for antenna nulls.

The received power at the typical AUe can be written as follows

$$P^s_{\Omega_i} = P_B h^s_{\Omega_i} G_{\Omega_i}(z_i) L^s_{\Omega_i}(z_i)^{-1}, \quad (6)$$

III. Coverage Performance

In this section, we formulate the expression of received interference, energy and SINR, in order to derive the energy coverage probability (ECP) and SINR coverage probability (SCP) expressions.

A. Interference

The majority of existing researches on cellular-connected UAV considered that the AUEs received signals from down-tilted antenna side lobes. For tractability analysis we consider that the side lobe gain is very low, therefore, we ignore the interference received from down-tilted BS antennas and consider only those providing from up-tilted BS antennas. Since the typical AUe is connected to the nearest BS. All other BSs deliver interference signals, hence the aggregate interference is given as

$$I = \sum_{\Omega_i \in \psi / \Omega_0} P_B h^s_{\Omega_i} G_{\Omega_i}(z_i) L^s_{\Omega_i}(z_i)^{-1}, \quad (7)$$

where $s \in \{L, N\}$, Ω_0 and z_0 are location of the serving BS and the distance between the serving BS and typical AUe, respectively.

B. Energy Coverage Probability

The harvest energy architecture employed at the AUes is assumed to be a splitting power (SP) architecture. This technique allows to the AUes to receive information and harvest energy simultaneously by using the power fraction $\tau \in (0,1)$ for information and $1-\tau$ for the harvest energy. The received signal is thus divided into two streams. Let denote by T the transmission time. Neglecting the energy harvested from the noise, the energy harvested by the typical AUe can be written as

$$\xi = T(1-\tau)\mathbb{E}\left[P^s_{\Omega_0} + I\right], \quad (8)$$

where $P^s_{\Omega_0} = P_B h^s_{\Omega_0} G_{\Omega_0}(z_0) L^s_{\Omega_0}(z_0)^{-1}$ is the received power from the serving BS located at Ω_0.

We define ξ_{th} as the energy threshold beyond which energy harvesting can be reliably achieved. Therefore, ECP can be formulated as

$$\begin{aligned} ECP(\tau, \xi_{th}) &= \mathbb{P}(\xi > \xi_{th}) \\ &= \sum_s \sum_{n=0}^{N^s} (-1)^n \binom{N^s}{n} \int_0^\infty A^s(\beta) \mathcal{L}_I(\beta)\, P^s(z_0) \\ &\quad \times f_{Z_0}(z_0) dz_0, \end{aligned} \quad (9)$$

where $s \in \{L, N\}$, $\beta = N^s (N^s!)^{\frac{1}{N^s}} T(1-\tau)\xi_{th}^{-1}$, $A^s(\beta) = \frac{1}{\left(1+\beta P_B G_{\Omega_0}(z_0) L^s_{\Omega_0}(z_0)^{-1} N^{s-1}\right)^{N^s}}$.

$f_{Z_0}(z_0)$ and $\mathcal{L}_I(\beta)$ are the PDF of z_0 and the Laplace transform of interference, respectively, given by

$$f_{Z_0}(z_0) = 2\lambda\pi z_0 e^{-\pi\lambda z_0^2}, \quad (10)$$

$$\mathcal{L}_I(\beta) = e^{-2\pi\lambda \int_{z_0}^\infty 1 - \sum_s \frac{1}{\left(1+\beta P_B G_{\Omega_i}(z) L^s_{\Omega_i}(z)^{-1} N^{s-1}\right)^{N^s}} P^s(z) z dz}, \quad (11)$$

C. SINR Coverage Probability

The received SINR at the typical AUe can be written as

$$\gamma = \frac{P_B h^s_{z_0} G_{\Omega_0}(z_0) L^s_{\Omega_0}(z_0)^{-1}}{I + \sigma_n^2}, \quad (12)$$

where σ_n^2 denotes the variance of the Gaussian thermal noise component.

SCP is defined as the probability that the received SINR is above an SINR threshold γ_{th}. SCP can be formulated as follows

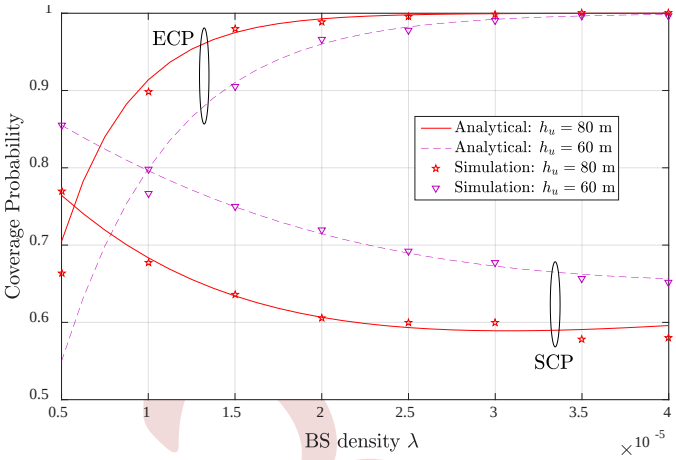


Figure 2. Coverage probability vs. BS density.

$$\begin{aligned} SCP(\tau, \gamma_{th}) &= \mathbb{P}(\gamma > \gamma_{th}) \\ &= \sum_s \sum_{k=1}^{N^s} (-1)^{k+1} \binom{N^s}{n} \int_0^\infty e^{\frac{-\mu\, \sigma_n^2}{\tau}} \mathcal{L}_I(\mu) P^s(z_0) \\ &\quad \times f_{Z_0}(z_0)\, dz_0, \end{aligned} \quad (13)$$

where $\mu = \frac{k N^s (N^s!)^{\frac{1}{N^s}} \gamma_{th} L^s_{\Omega_0}(z_0)}{P_B G_{\Omega_0}(z_0)}$, $\mathcal{L}_I(\mu)$ is the Laplace transform of interference given by

$$\mathcal{L}_I(\mu) = e^{2\pi\lambda \int_{z_0}^\infty \sum_s 1 - \frac{1}{\left(1+\mu P_B G_{\Omega_i}(Z) L^s_{\Omega_i}(Z)^{-1} N^{s-1}\right)^{N^s}} z P^s(z)\, z\, dz}, \quad (14)$$

IV. Simulation Results

In this section, we analyze the system coverage performance and validate the analytical results through Monte Carlo simulations in wide simulation area. We consider a dense urban environment, according to [16] we set $a = 1$, $b = 0.106$, $\delta = 1$, and $h_B = 25$ m. Since we have considered an up-tilted antenna model, the AUe altitude must be higher than that of the BS, in this case $h_u > 25$ m. The transmit power $P_B = 20$W, and $\lambda = 10^{-5}$. The path loss and fading parameters are given as follows $\eta^L = -41.1$dB, $\eta^N = -32.9$dB, $\alpha^L = 2.2$, $\alpha^N = 3.75$, $N^L = 2$, $N^N = 1$. Similar to [9], we set $\theta_h = 60°$ and $G_{th} = 60$dBm. $T = 1$s, $\tau = 0.5$, $\xi_{th} = -35$dB, $\gamma_{th} = -35$dB.

Figure 2 shows the impact of BS density λ and AUe altitude h_u, on the ECP and SCP. We can see that ECP increases with higher λ and h_u, while SCP decreases. Because when there are several BSs and h_u is high, the received SINR decreases as the typical AUe is confronted with an amplified level of interference, mainly from BSs with a LoS communication link while increasing the BS density increases the energy harvested by the typical AUe. Additionally, the simulation results align exactly with the analytical results confirming the correctness of our coverage analysis.

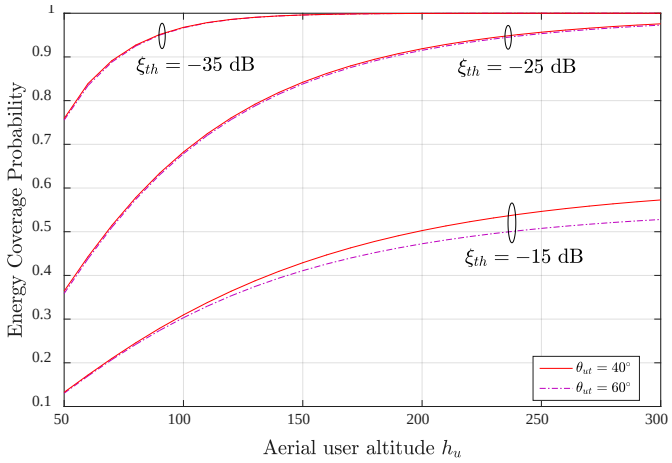


Figure 3. Energy Coverage probability vs. Aerial user altitude h_u.

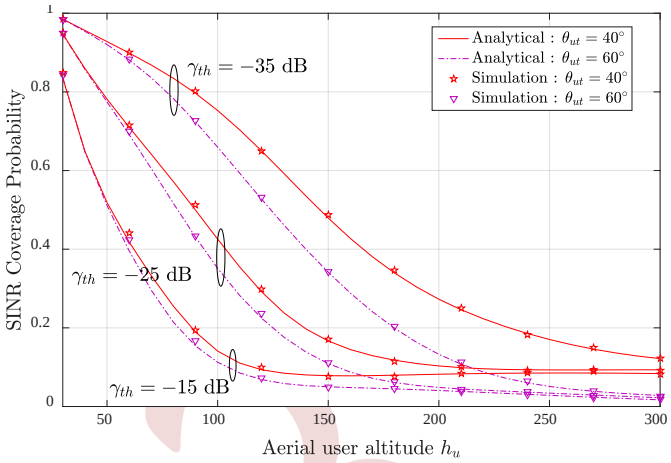


Figure 4. SINR Coverage probability vs. Aerial user altitude h_u.

Figure 3, presents the ECP versus the AUe altitude h_u with different tilt angle θ_{ut} and different threshold ξ_{th}. It is obvious that increasing AUe altitude h_u improves the ECP for different ξ_{th}. Because the communication link between the typical AUe and BS becomes more free of obstructions resulting in improved energy harvesting from the BS. Furthermore, it can be observed that increasing the threshold ξ_{th} diminishes the ECP since more energy is required to guarantee seamless 3D coverage. It is worth noting that the tilt value doesn't really affect the ECP, mainly at low threshold. However, at high threshold and high altitude, increasing the tilt angle from $\theta_{ut} = 40°$ to $\theta_{ut} = 60°$ deteriorates the ECP.

To show the impact of the AUe altitude h_u on the SCP, we plotted in Figure 4 the SCP as a function of the AUe altitude h_u with different tilt angle θ_{ut} and SINR threshold γ_{th}. It is obvious that the SCP deteriorates as both the altitude h_u and the SINR threshold increases. This can be explained by the fact that at high altitude h_u, the communication link between the typical AUe and most BSs remains LoS, as there are no physical obstacles that are likely to disrupt the connection. This causes significant interference to the AUe from LoS BSs, resulting in an extremely low SINR, leading to a limited coverage. On the other hand, as ECP, increasing the tilt angle deteriorates PCS, especially at high altitudes, because the BS's antenna lacks the necessary range.

V. CONCLUSION

This paper investigated joint the energy and SINR coverage probability in cellular-connected UAVs. The SWIPT was adopted to simultaneously harvest energy and transmit information. We considered an up-tilted antenna model in BSs to serve the AUes instead of the down-tilted antenna. We derived both the ECP and SCP expressions considering that the typical AUe is connected to the nearest BS. The analytical results validated by Monte Carlo simulations showed that ECP can be improved with a high density of BS. In addition, both of ECP and SCP can be improved by carefully adjusting the AUe altitude and the tilt angle.

REFERENCES

[1] Y. Qin, M. A. Kishk, and M.-S. Alouini, "Stochastic geometry-based analysis of multipurpose UAVs for package and data delivery," IEEE Internet of Things Journal, vol. 10, no. 5, pp. 4664–4676, 2023.

[2] P. K. Chittoor, B. Chokkalingam, and L. Mihet-Popa, "A review on UAV wireless charging: Fundamentals, applications, charging techniques and standards," IEEE Access, vol. 9, pp. 69 235–69 266, May 2021.

[3] S. Özyurt, A. F. Co¸skun, S. Büyükçorak, G. Karabulut Kurt, and O. Kucur, "A survey on multiuser SWIPT communications for 5G+," IEEE Access, vol. 10, pp. 109 814–109 849, 2022.

[4] R. Jiang, K. Xiong, H.-C. Yang, J. Cao, Z. Zhong, and B. Ai, ''Coverage performance of UAV-assisted SWIPT networks with directional antennas,'' IEEE Internet Things J., vol. 9, no. 13, pp. 10600–10609, Jul. 2022.

[5] R. Jiang, K. Xiong, H.-C. Yang, P. Fan, Z. Zhong, and K. B. Letaief, ''On the coverage of UAV-assisted SWIPT networks with nonlinear EH model,'' IEEE Trans. Wireless Commun., vol. 21, no. 6, pp. 4464–4481, Jun. 2022.

[6] R. Jiang, K. Xiong, T. Liu, D. Wang, and Z. Zhong, ''Coverage probability-constrained maximum throughput in UAV-aided SWIPT networks,'' in Proc. IEEE Int. Conf. Commun. Workshops (ICC Workshops), Dublin, Ireland, pp. 1–6, Jun. 2020.

[7] M. M. Azari, F. Rosas, and S. Pollin, "Cellular connectivity for UAVs: Network modeling, performance analysis, and design guidelines," IEEE Transactions on Wireless Communications, vol. 18, no. 7, pp. 3366–3381, July 2019.

[8] S. Kang, M. Mezzavilla, A. Lozano, G. Geraci, S. Rangan, V. Semkin, W. Xia, G. Loianno, "Coexistence of UAVs and terrestrial users in millimeter-wave urban networks," in Proc. IEEE Globecom Workshops, pp. 1158–1163, 2022.

[9] Y. Du, H. Zhang, and J. Peng, "Modeling and Coverage Analysis for Cellular-Connected UAVs With Up-Tilted Antenna," IEEE Communications Letters, vol. 26, no. 11, pp. 2572–2575, 2022.

[10] Z. Wang and J. Zheng, "Performance modeling and analysis of base station cooperation for cellular-connected UAV networks," IEEE Trans. Veh. Technol., vol. 71, no. 2, pp. 1807–1819, Feb. 2022.

[11] X. Li, X. Zhou, and S. Durrani, "SWIPT-Enabled Cellular-Connected UAV : Energy Harvesting and Data Transmission," in 2022 IEEE International Conference on Com- munications Workshops (ICC Workshops), pp. 1107–1112, IEEE, 2022.

[12] M. M. U. Chowdhury, I. Guvenc, W. Saad, and A. Bhuyan, "Ensuring reliable connectivity to cellular-connected UAVs with uptilted antennas and interference coordination," ITU J. Future Evolving Technol., vol. 2, no. 2, pp. 165–185, Dec. 2021.

[13] S. J. Maeng, M. M. U. Chowdhury, I. Güvenç, A. Bhuyan, and H. Dai, "Base station antenna uptilt optimization for cellular-connected drone corridors," IEEE Trans. Aerosp. Electron. Syst., early access, Jan. 19, 2023.

[14] A. Al-Hourani, S. Kandeepan, and S. Lardner, "Optimal LAP altitude for maximum coverage," IEEE Wireless Commun. Lett., vol. 3, no. 6, pp. 569–572, Dec. 2014.

[15] Propagation Data and Prediction Methods Required for the Design of Terrestrial Broadband Radio Access Systems Operating in a Frequency Range From 3 to 60 GHz, document Recommendation ITU-R, 1410-1415., Tech. Rep. 2012.

[16] N. Cherif, M. Alzenad, H. Yanikomeroglu, and A. Yongacoglu, "Downlink coverage and rate analysis of an aerial user in vertical heterogeneous networks (VHetNets)," IEEE Transactions on Wireless Communications, vol. 20, no. 3, pp. 1501–1516, 2020.

[17] R. Amer,W. Saad, and N.Marchetti, "Mobility in the sky: Performance and mobility analysis for cellular-connected UAVs," IEEE Trans. Commun., vol. 68, no. 5, pp. 3229–3246, May 2020.

EEIC'23

Improved Gain for T-Shaped Slot Antenna Using New EBG/AMC Reflector for IOT Applications

Merabet Imen[1], Rouabah Khaled[2], Belazzoug Massinissa[3]

[1]*LIST Laboratory, University M'hamed Bougara of Boumerdes, Boumerdes, Algeria.*

i.merabet@univ-boumerdes.dz

[2]*Electronics Department, University Mohamed BOUDIAF of M'Sila, M'sila, Algeria.*

khaled.rouabah@univ-msila.dz

[3]*Laboratory of Electronics and Advanced Telecommunications, University of Bordj Bou Arreridj, Bordj Bou Arreridj, Algeria.*

m.belazzoug@univ-bba.dz

***Abstract*— In this paper, we propose a novel EBG/AMC uniplanar reflector, integrated with a low-profile T-shaped slot antenna, for Internet of Things (IOT) applications in wireless communications. The last antenna structure, which has an optimized overall dimension of 80×80×0.51 mm3, is designed in two phases in order to operate at 5.8 GHz. Initially, the performances of the T-shaped slot, etched at the top of the substrate, are investigated using Computer Simulation Technology (CST) Microwave Studio. The obtained results show an operating impedance bandwidth of 11.89 % and a reflection coefficient less than -57 dB at 5.8 GHz frequency. Next, in order to realize gain enhancement, side lobes reduction, and surface waves suppression, the proposed T-shaped slot antenna is backed by a 5×5 uniplanar EBG/AMC structure placed at a distance equal to 13 mm from the antenna. The final proposed combination is also designed and optimized. The simulated results show a maximum gain improvement of 5.25 dBi.**

***Keywords:* uniplanar EBG/AMC reflector, T-shaped slot antenna, gain improvement, IOT.**

I. INTRODUCTION

In wireless communications systems, one of the most revolutionary and impactful advances of our times is the IOT technology which has profoundly transformed our modern society and changed the human environment interaction [1]. The latter one refers to a vast network consisting of interconnected physical devices, sensors, actuators and additional items integrated with software, connections for the purpose of connecting and exchanging data over the internet.

This networked environment enables seamless connectivity and interoperability, transparency, and advancements in communication and data sharing [2].The IOT applications are vast and can potentially affect a wide range of industries and sectors.

Some of the key areas, where IOT has a huge impact on our daily lives, include smart home automation [3], healthcare, wearable devices [4], precision agriculture [5], smart cities and other applications in other sectors [6]. Although IOT is not a wireless standard, it relies on wireless communications protocols such as WLAN, WiMAX, ZigBee and LTE to support connectivity and data exchange between devices. These wireless standards, which differ in coverage, data transfer speed, power consumption and range, allow IOT devices to successfully interoperate based on each application's needs and communication mode [7]. Planar antennas play a crucial role in IOT deployment applications while ensuring reliable and easy wireless connections of IOT devices in a network or infrastructure. Due to their compact size, ease of integration, and ability to provide stable wireless connectivity, this type of antennas actually allows IOT devices to communicate, depending on the design and requirements, over short to medium distances [8]. Some of the prominent IoT applications, such as off-body ones at 5.8 GHz (corresponding to the ISM band), require the use of high-gain antennas with a directed radiation pattern [9]. These antennas are designed to allow the signal strength to be focused in a certain direction, which is essential to ensure optimal connectivity and performance in circumstances where the devices are not physically attached to the body. Recently, various techniques have been proposed to improve antenna gain while reducing its front-to-back ratio. This is achieved by controlling unwanted radiation and minimizing signal interference from undesired directions. These advancements include the application of metamaterials such as Artificial Magnetic Conductor (AMC) and Electromagnetic Band Gap (EBG) [10]. For example, in [11], a microstrip antenna based on the use of an optimized mushroom-like EBG structure is proposed to operate at 5.8 GHz. The proposed design has the ability to increase the gain without affecting the antenna geometric parameters. However, the high number of metallic vias, used in this structure, have increased the design complexity and the manufacturing cost of this antenna

structure. To overcome this problem, the authors in [12] have proposed the use of uniplanar EBG without metallic via to permit offering simplicity of fabrication, planar integration and lower losses. Additionally, to decrease the overall size of these antennas, the use of resonant cavity Fabry-Perot structures, based on AMC, has proven to be a favorable option [13-14-15]. The reduction of this size can also be achieved by the combination of Partially Reflective Surface (PRS) with AMC [16].

In this paper, a novel EBG/AMC uniplanar reflector, integrated with a low-profile T-shaped slot antenna, is proposed for IOT applications including off-body ones.

The first aim of this study is to enhance the gain of T-shaped slot antenna operating at 5.8 GHz to achieve directive radiation characteristics which is suitable for off-body IOT devices. Its second objective, is to reduce the antenna profile and improve its gain by reducing the levels of the side lobes of its radiation pattern. This is realized by the combination of this antennal structure with a novel uniplanar EBG/AMC reflector.

This paper is organized as follows: Section II describes the geometry and the design of EBG/AMC unit cell in the first place and T-shaped slot antenna integrated with EBG/AMC reflector in the second place. In the third section are reported the simulation results and discussions. Finally, we end up by a conclusion.

II. ANTENNAS FOR ON/OFF AND IN-BODY COMMUNICATIONS

When designing antennas suitable for On/Off body communication, several challenges must be taken into account. The latter ones include impedance matching, radiation pattern, size, cost, weight, and performances. For example: On-body antenna requires omnidirectional radiation characteristics and low frequencies. These lasts have a greater ability to mitigate the effects of shadow fading due to their longer wavelength and increased diffraction strength. On the other hand, the higher frequencies are employed for Off-body communication sidelobes level reduction and gain enhancement [17]. Off-body IoT applications involve wearable or implantable devices that interact with the environment and communicate data wirelessly. This makes the choice of antenna materials a vital consideration. Indeed, the materials used in these antennas must meet specific requirements to guarantee optimal performance directly related to the connection between portable wireless devices and the human body. This association comes from the fact that the human body has a distinct electrical conductivity, consisting of multiple layers with varying thicknesses and dielectric properties. This interaction has a negative impact on both gain and efficiency of on-body antennas. Moreover, body reflections can completely disrupt the frequency spectrum [18-19]. Another factor of this type of antennas is the gain which needs to be enhanced especially for off-body applications in order to create a directional radiation pattern allowing to effectively communicate information from the patient to the physician [20].

III. DESIGN OF T-SHAPED SLOT ANTENNA INTEGRATED WITH AN EBG/AMC REFLECTOR

A. EBG/AMC unit cell

The proposed uniplanar EBG/AMC unit cell is presented in figure 1 (a).

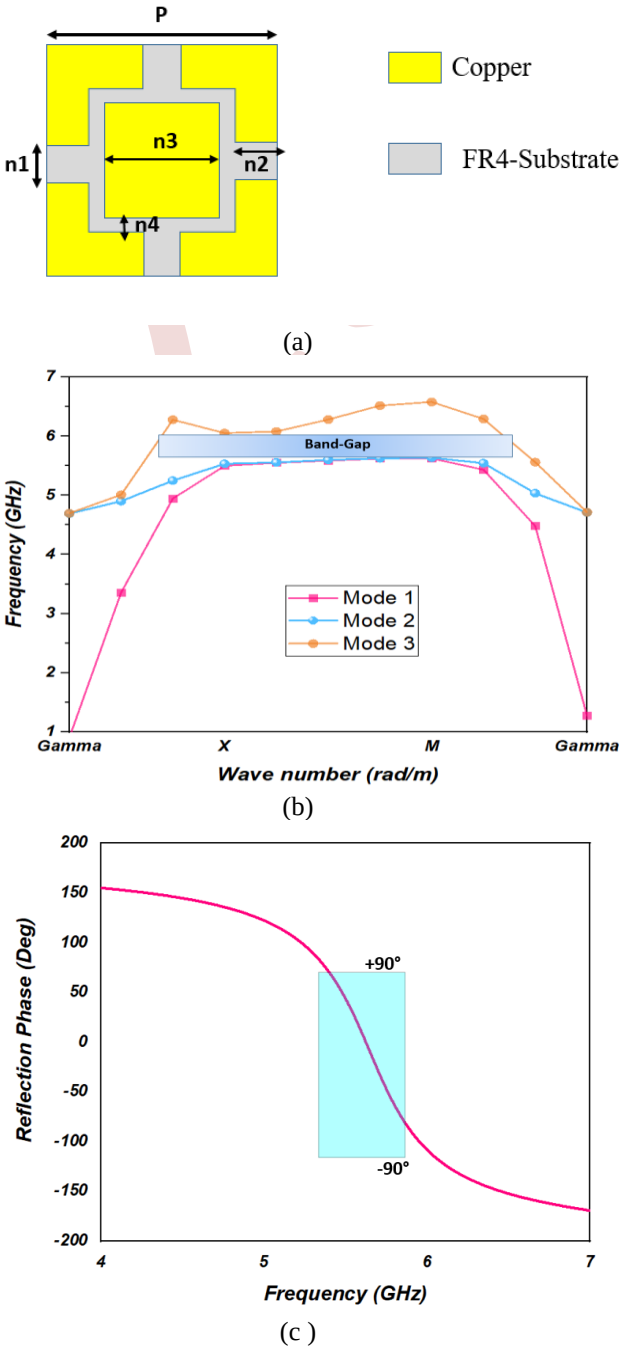


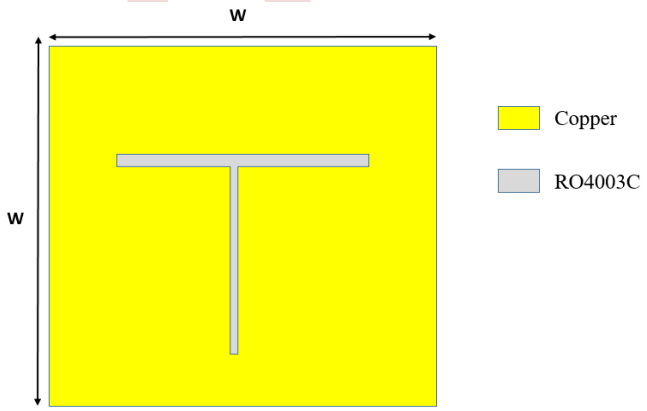
Figure 1. Configuration of EBG/AMC unit cell (a). Geometry of the proposed EBG/AMC unit cell (b). Dispersion diagram (c). Reflection phase.

As illustrated in this figure, this unit cell is designed using FR4 substrate having a permittivity of 4.3 and thickness of 1.6 mm, with metallic patch in the center and square slot at the edge of unit cell. Here, the shape of the metal patch and the four-square slot control, according to their dimensions, the band gap and reflection phase of the unit cell. This is due to the variation in the current path within the uniplanar EBG/AMC unit cell. The latter one exhibits thus LC behavior at a frequency of 5.8 GHz. In addition, the surface exhibits high impedance characteristics. It is worth noting that the uniplanar EBG cell, proposed in this study, has the same characteristics as the AMC cell, which does not require a metal via which reduces the complexity of the proposed structure to provide a flexible design for off-body applications. The optimized parameters of uniplanar EBG/AMC unit cell are given as follows: P=16 mm, n1= n2 =2.5 mm, n3= 6.5 mm, n4= 1mm.

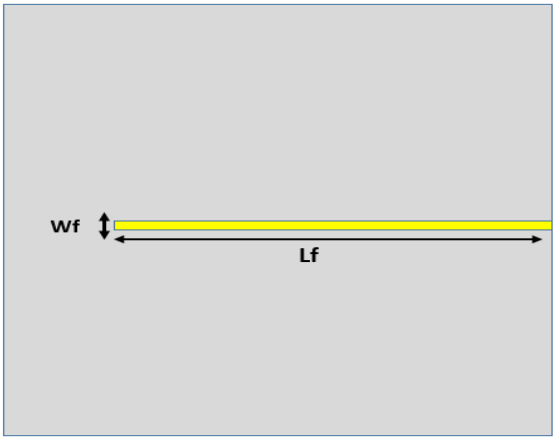
The variation, in the dimensions of the metallic and dielectric parts (corresponding respectively to the inductive and capacitive effects) affects the operating band of the proposed EBG/AMC unit cell. Indeed, when the inductive effect increases, following the reduction in the dimensions of the square slots, there will be a shift in the bandgap towards the lower frequencies. To calculate both band gap and reflection phase, presented respectively in figure 1. (b) and (c), numerical simulations are performed using CST Microwave studio. Indeed, the dispersion diagram is extracted by applying periodic boundary conditions in both x- and y-directions. In addition, the reflection phase is extracted using the boundary conditions, in the x and y directions, of the unit-cell excited by a plane wave along z-direction.

B. Design of T-shaped slot antenna integrated with EBG/AMC reflector

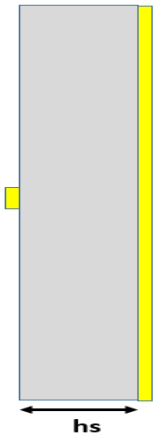
In order to realize the gain improvement of the T-shaped slot antenna, the uniplanar EBG/AMC reflector is integrated within the latter to obtain a combined structure. The T-shaped slot antenna, presented in figure 2, is printed on RO4003C substrate having permittivity of 3.55, loss tangent of 0.0027 and thickness of 0.51 mm. It is excited by a simple micro-strip feedline printed on the bottom of substrate while the T-shaped is etched on its top layer. The optimized dimensions of the proposed T-shaped slot antenna are given as follows: w=80 mm, Lf= 56.43 mm, wf= 2 mm.



(a)



(b)



(c)

Figure 2. The proposed T-shaped slot antenna: (a) Top view; (b) Bottom view; (c) Side view.

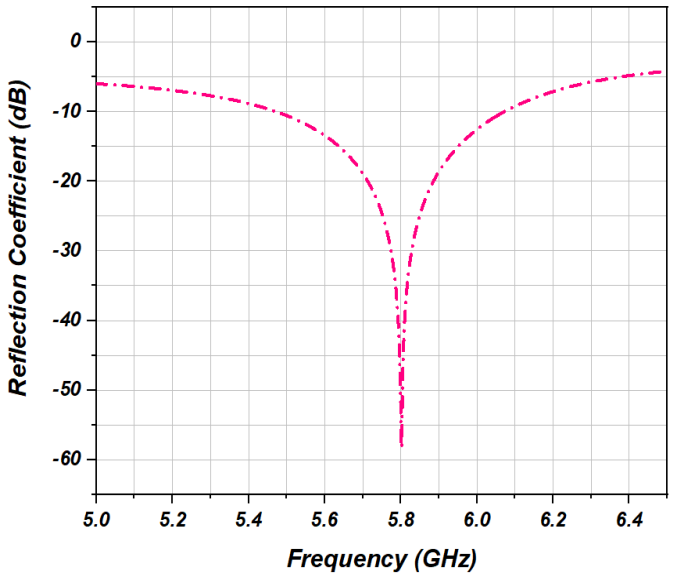


Figure 3. Reflection coefficient of the proposed T-shaped slot antenna.

Figure 3 shows the reflection coefficient of the proposed T-shaped slot antenna that has a loss of -58 dB at 5.8 GHz and impedance bandwidth of 10.53% (from 5.49 GHz to 6.18 GHz).

The dimensions of the proposed antenna, designed together with the feedline, are likewise optimized using the CST microwave studio to allow the optimization of the resonance at the 5.8 GHz frequency, with an impedance bandwidth of 11 .83% (from 5.49 GHz to 6.18 GHz). This is due to the fact that the antenna feed line had an impact on the resonating frequency. Indeed, the variation in the current path through the structure (meaning variation of inductive and capacitive effect), similar to the variation of the dimensions of the T-shaped slot, increases the frequency shifts towards the lower frequencies.

In order to achieve high performances, in terms of gain enhancement, side lobes reduction and surface wave suppression, the proposed T-shaped slot antenna is integrated with the proposed 5x5 uniplanar EBG/AMC reflector, as shown in Figure 4. The overall size of the resulting antenna structure is 80x80x0.51 mm3. As shown in Figure 5, we reached a gain improvement of 5.25 dBi.

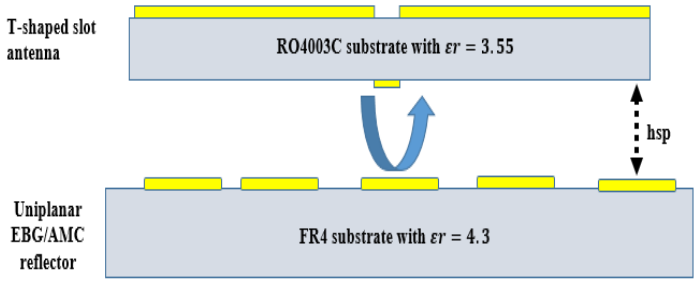


Figure 4. The proposed T-shaped slot antenna backed by the proposed uniplanar EBG/AMC reflector.

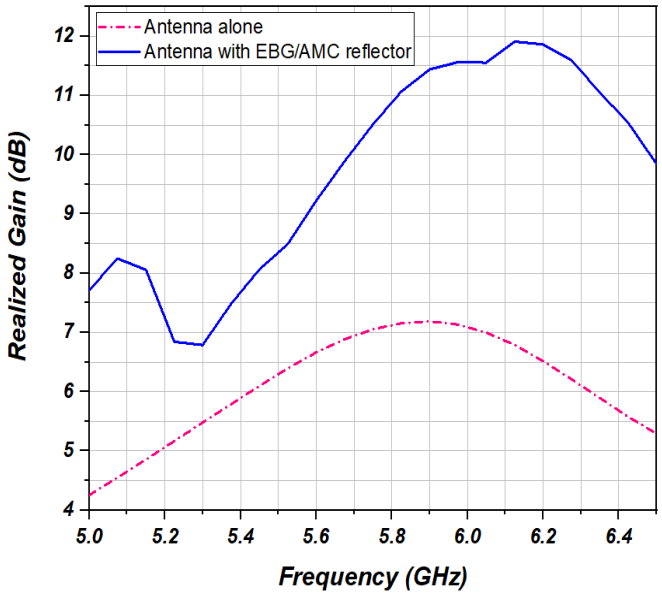
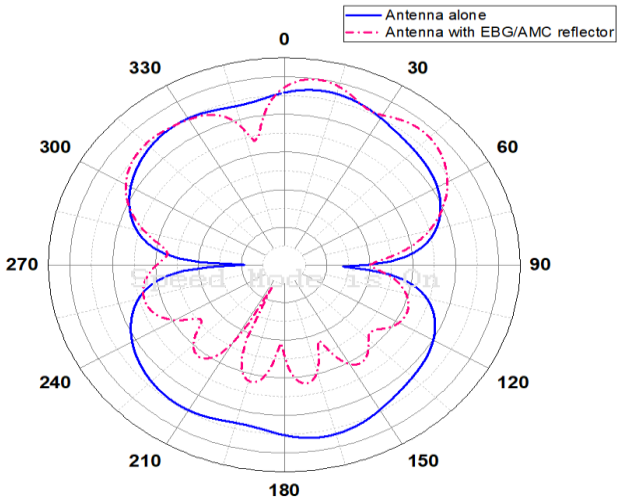


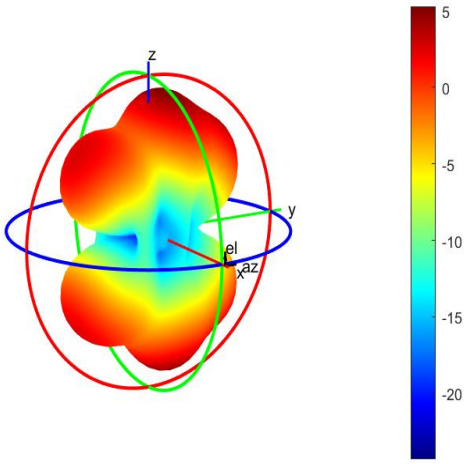
Figure 5. Realized gain of the proposed T-shaped slot antenna integrated with the proposed uniplanar EBG/AMC reflector.

IV. RESULTS AND DISCUSSIONS

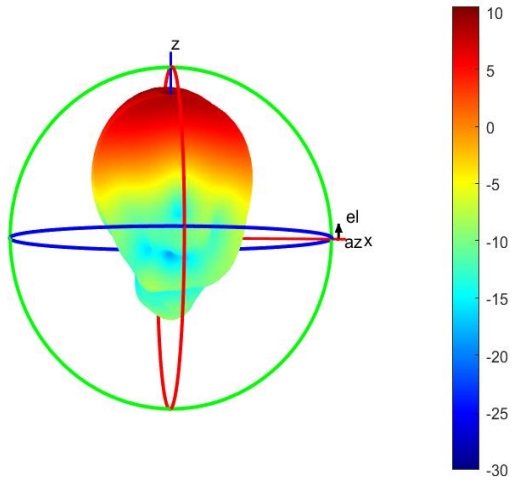
The proposed structure was simulated, using CST microwave studio, in order to test its performance. At this point, the T-shaped slot antenna and the proposed uniplanar EBG/AMC reflector were simulated and optimized separately and then combined to form the proposed antenna backed by EBG/AMC reflector. The simulation results are shown in Figure 6. This figure shows the 2-D radiation patterns of both proposed antenna-alone and the structure resulting from its combination with the proposed uniplanar EBG/AMC reflector. At this time, the beam is tilted towards the desired angle (0°). As shown in this figure, the results show that by integrating the proposed uniplanar EBG/AMC reflector with T-shaped slot antenna, the back lobes are completely reduced. The gain presents consequently a maximum improvement of 5.25 dBi.



(a)



(b)



(c)

Figure 6. Simulated Radiation patterns of the antenna with and without EBG/AMC reflector:(a) 2-D radiation pattern of the antenna with and without EBG/AMC reflector;(b) 3-D radiation pattern of reference antenna;(c) 3-D radiation pattern of the proposed antenna backed by uniplanar EBG/AMC reflector.

The proposed uniplanar EBG/AMC reflector based-structure is compared to the most relevant of those reported in the scientific literature. The results are summarized in Table 1. As shown in this table, the proposed structure presents better performances, in terms of gain improvement and bandwidth, compared to those presented in references [11], [13],[14],[15] and [16]. In addition, it has an optimized overall dimension compared to those of the references mentioned above. Finally, the proposed antenna meets the needs of off-body IOT applications, as it has important characteristics such as high gain, wide bandwidth, directional radiation pattern, and simple complexity. All these features make this structure easy to implement on the human body without affecting the overall antenna performances.

TABLE I. THE PROPOSED ANTENNA VERSUS OTHER RELATED WORKS

Reference	Operating frequency (GHz)	Antenna size (mm^3)	Gain improvement (dBi)	BW(%)	Reflector type
[11]	5.8	1.21λ×1.21λ×0.05λ	2.7	7.20	EBG
[13]	5.2	1.53λ×1.53λ×0.26λ	4.5	9.30	AMC
[16]	5.8	1.54λ×1.93λ	3.5	5.23	AMC+FSS
[14]	5.8	0.85λ×0.85λ×0.03λ	1.5	5.22	AMC
[15]	2.4	0.43λ×0.43λ×0.03λ	5.16	2.76	AMC
This work	5.8	1.54λ×1.54λ×0.23λ	5.25	11.89	EBG/AMC

V. CONCLUSION

In this paper, a T-shaped slot antenna with a low-profile integrated with novel reflector, for IOT applications, is

proposed. The latter antenna, having impedance bandwidth of 11.89% and reflection coefficient less than -57 dB at 5.8 GHz, is backed by a novel 5×5 uniplanar EBG/AMC unit cell

which exhibit simultaneous bandgap proprieties and zero phase reflection at 5.8 GHz.

The resulting gain enhancement is 5.25 dBi, showing that the uniplanar EBG/AMC has a substantial impact on reducing both surface waves and antenna back lobes. The obtained results have shown that the proposed antenna is able to offer good performances for off-body IOT applications.

REFERENCES

[1] S. Kumar, P. Tiwari, and M. Zymbler, "Internet of Things is a revolutionary approach for future technology enhancement : a review," *J. Big Data*, 2019.

[2] A. Sadeghi-niaraki, "Internet of Thing (IoT) review of review : Bibliometric overview since its foundation," Futur. Gener. Comput. Syst., vol. 143, pp. 361–377, 2023

[3] M. Alaa,A.A.Zaidan,B.B.Zaidan,M.Talal,and M.L.M.Kiah., "Author ' s Accepted Manuscript A Review of Smart Home Applications based on Internet of Things Reference :," *J. Netw. Comput. Appl.*, 2017

[4] M. N. Bhuiyan and I. Technology, "Internet of Things (IoT): A review of its enabling technologies in healthcare applications , standards protocols , security and market opportunities," vol. 4662, no. c, 2021

[5] W. Kim, "A Review of the Applications of the Internet of Things (IoT) for Agricultural Automation," no. Borgia 2014, 2020.

[6] A. Zanella *et al.*, "Internet of Things for Smart Cities," vol. 1, no. 1, pp. 22–32, 2014.

[7] H. Kashif, "Selection of Network Protocols for Internet of Things Applications : A Review," *2020 IEEE 14th Int. Conf. Semant. Comput.*, pp. 359–362, 2020

[8] D. Tyagi, "Multifunctional Antenna Design for Internet of Things Applications," pp. 557–560, 2021.

[9] K. A. Malar and R. S. Ganesh, "Measurement : Sensors Novel aperture coupled fractal antenna for Internet of wearable things (IoWT)," *Meas. Sensors*, vol. 24, no. October, p. 100533, 2022,

[10] A. Y. I. Ashyap and Z. Z. Abidin, "Highly Efficient Wearable CPW Antenna Enabled by EBG-FSS Structure for Medical Body Area Network Applications," *IEEE Access*, vol. 6, pp. 77529–77541, 2018,

[11] N. Melouki, A. Hocini, and T. A. Denidni, "Performance enhancement of a compact patch antenna using an optimized EBG structure," *Chinese J. Phys.*, vol. 69, no. December 2020, pp. 219–229, 2021

[12] C. S. Antonopoulos, "Design and Optimization of Uniplanar EBG Structures for Coupling Reduction," vol. 60, no. 10, pp. 4944–4949, 2012.

[13] V. Rajavel, "AMC-Based Low-Profile Dual-Band Slotted Patch Antenna for IoT Devices in the Healthcare System," *Iran. J. Sci. Technol. Trans. Electr. Eng.*, vol. 47, no. 2, pp. 437–450, 2023,

[14] S. Ahmad, S. Member, K. N. Paracha, and S. Member, "A Metasurface-Based Single-Layered Compact AMC-Backed Dual-Band Antenna for Off-Body IoT Devices," IEEE Access, vol. 9, pp. 159598–159615, 2021

[15] A. Y. I. Ashyap *et al.*, "C-shaped antenna based artificial magnetic conductor structure for wearable IoT healthcare devices," *Wirel. Networks*, vol. 27, no. 7, pp. 4967–4985, 2021

[16] D. Boukern, A. Bouacha, D. Aissaoui, and T. A. Denidni, "High-gain cavity antenna combining AMC-reflector and FSS superstrate technique," no. March, pp. 1–8, 2021,

[17] X. Y. Zhang, S. Member, H. Wong, S. Member, T. Mo, and Y. F. Cao, "Dual-Band Dual-Mode Button Antenna for On-Body and Off-Body Communications," pp. 1–9, 2017.

[18] A. Di Serio, J. Buckley, J. Barton, R. Newberry, G. Dunlop, and B. O. Flynn, "Potential of Sub-GHz Wireless for Future IoT Wearables and Design of Compact 915 MHz Antenna," vol. c, pp. 1–25, 2018

[19] T. T. Le and T. Yun, "Wearable Dual-Band High-Gain Low-SAR Antenna for Off-Body Communication," vol. 1225, no. c, 2021

[20] C. Zhao, "Design of a dual band dual mode antenna for on / off body communications," no. May, pp. 1–7, 2019,

Design and Simulation of Rectangular Microstrip Patch Antenna for WLAN Applications

Riadh Degachi [1], Said Ghendir [2]

University of El-Oued, El-Oued, Algeria

degachi-riadh@univ-eloued.dz

University of El-Oued, El-Oued, Algeria

said-ghendir@univ-eloued.dz

***Abstract*— The aim of this paper is to presents a design and simulation of Rectangular Microstrip Patch Antenna for WLAN applications. The proposed antenna is operated at frequency of 2.4 GHZ with -63.5dB return loss and 0.01 VSWR values. The results are obtained by HFSS simulation software tool and the graphs of antenna parameters are analyzed and plotted such as the gain, bandwidth, return loss and VSWR. The design of the proposed antenna is mainly focused on WLAN (802.11b/g/n) applications.**

The proposed antenna is designed using FR4 Epoxy material characterized by relative permittivity of 4.4 as a substrate, height of 1.6 mm from the ground plane, input impedance of 50 ohms and microstrip-line fed is used as a feeding method

Keywords: **Rectangular Microstrip Patch Antenna, WLAN, Return Loss, HFSS.**

I. INTRODUCTION

An antenna is an essential element of any wireless communication system to transmit or receive electromagnetic waves in the free space representing the transmitted or received information. [1]. Antenna is an electromagnetic transducer, used to convert, in the transmitting mode, guided waves within transmission lines to radiated free-space waves, or to convert, in the receiving mode, free-space waves to guided waves [2]. There are several types of antennas such as: Wire antenna, Aperture antenna, Microstrip antenna, Array Antenna, Reflector antenna, Lens antenna [3]. Among all types of antennas, the microstrip antenna is one of the most variation designs in term of architectures, shapes and feeding methods.

The microstrip antenna was first proposed by Deschamps in year 1953, but the first time to came into existence is around the 1970's [4], is a simple antenna mainly used at microwave frequency (above 1 GHz), is consisting of a dielectric substrate containing at the top a radiated patch and at the bottom a ground plane. Usually, the radiated patch and the ground plane is a thin layer fabricated from copper or gold which is a good conductor. The microstrip patch antennas have several advantages, they are electrically thin, lightweight, low-cost fabrication, conformable and so on [2]. In the recent years, because of their good characteristics the microstrip patch antennas is widely used in large number of applications such as global positioning system (GPS), ZigBee, Bluetooth, WiMAX, Wi-Fi applications, 802.11a,b,g, and others [5].

The limitation of this antenna is narrow Bandwidth, lower Gain and weak radiating pattern. The improvement in the limitations is the challenging task for the researchers, because the good design of the antenna can relax system requirements and improve overall system performance [2].

II. ANTENNA DESIGN

The proposed antenna is operating at frequency of 2.4GHZ and was designed using FR4 Epoxy material with relative permittivity of 4.4 and substrate height of 1.6 mm. The dimensions of the antenna can be obtained as follows:

A. *Width of the patch*

$$Wp = \frac{c}{2*F_r}\sqrt{\frac{\epsilon_r}{2}} \quad \ldots\ldots (1)$$

Where c is speed of the light, F_r is resonant frequency and ε_r is the dielectric constant.

B. *Length of the patch*

$$L_{eff} = \frac{c}{2*F_r*\sqrt{\varepsilon_{eff}}} \quad \ldots\ldots (2)$$

The effective dielectric constant ϵ_{reff} is given by

$$\varepsilon_{eff} = \left(\frac{\varepsilon_r+1}{2}\right) + \left(\frac{\varepsilon_r-1}{2}\right)\left(\sqrt{1+\frac{12h}{W_p}}\right) \quad \ldots\ldots (3)$$

Where h is substrate height and W_p is the patch width.

C. *Dimensions of the ground plane*

$$W_g = w_p + 6h \quad \ldots\ldots (4)$$

$$L_g = L_p + 6h \quad \ldots\ldots (5)$$

D. Feed Technique

There are four fundamental techniques to feed or excite a microstrip patch antenna, namely microstrip-line fed, probe-fed, aperture-coupled and proximity-coupled [6]. The microstrip line fed technique is used as feeding method in the proposed antenna. Among all other feeding techniques, the edge-feeding of microstrip patch have several advantages, the features of this technology are its ease of fabrication, when the feed network and radiating patches can be built on some board [6].

III. SIMULATION

The dimensions of the antenna can have obtained using the above equations, we can now design it on HFSS software tools.

The first step in the design is defining the ground plane on the XY Plane and then building the substrate over it with assigning the materiel as FR4 Epoxy with dielectric constant of 4.4 and thickness height of 1.6 mm, then the rectangular patch and the feed line is modeled on the top face of the substrate, also a radiation box surrounds the antenna and a source port are defined on the XZ Plane. The next step is Assigning Boundaries and Excitations, PerfectE boundary for the ground plane, the patch, and the feed line. Radiation boundary for the radiation box, Also Lumped port excitation is assigned to the source port with input impedance of 50 ohms. The final step is adjusting the solution setup.

The proposed antenna geometry is shown in Figure.1.

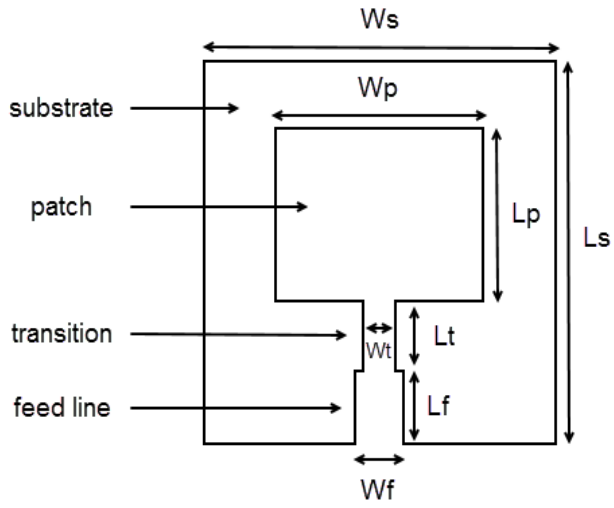


Figure 1: Geometry of the proposed antenna.

The parameters used in the design are illustrated in Table-1.

Table 1: Dimensions of the proposed antenna.

Parameters	Description	Values [mm]
Wp	Patch width	37.29
Lp	Patch length	28.22
H	Substrate height	1.6
Wf width	Feed line	2.98
Lf	Feed line length	15
Wt	Feed line width	1.01
Lt	Feed line length	17.45

The designed antenna in HFSS is shown in Figure. 2.

Where the pink rectangle and line represents the patch and the feed line respectively, the purple box represents the substrate, the transparent box represents the radiation box and the green rectangle shows the source port.

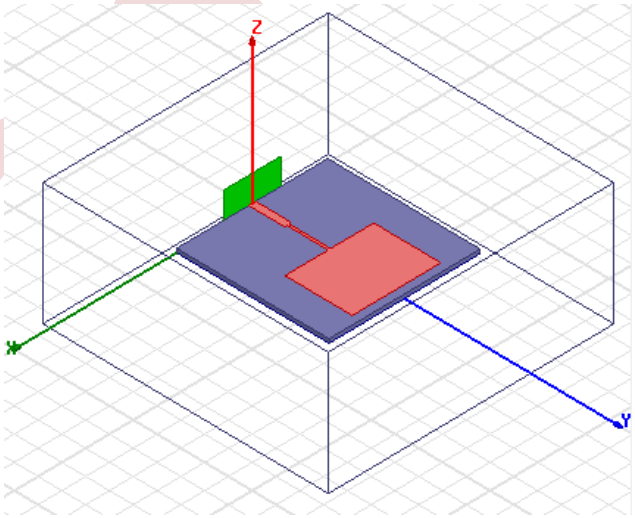


Figure 2: Side view.

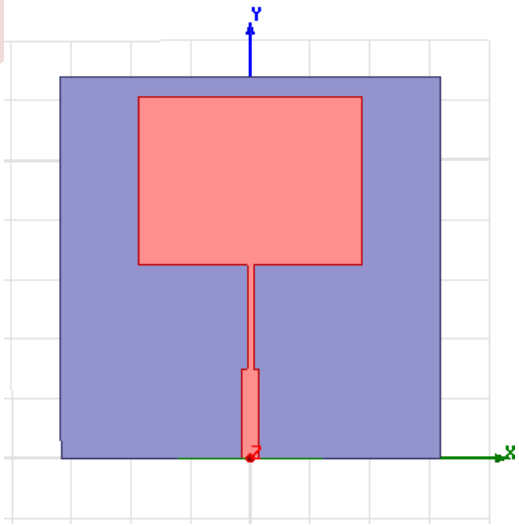


Figure 3: Top view.

IV. RESULTS

After completing the proposed antenna design, we got to the simulated results of the antenna which includes return loss (S11 parameter), VSWR, 2D radiation pattern as well as 3D radiation pattern, following waveforms shows the simulated results of the antenna.

A. Gain

The gain is one of the fundamental antenna parameters, is describes how much power is transmitted in the direction of peak radiation to that of an isotropic source. The gain of the proposed antenna is shown in figure 4.

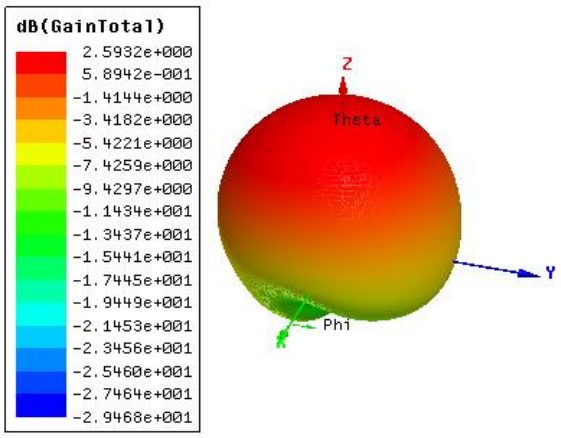


Figure 4: Gain total.

B. Return Loss

Figure 5 displays Simulated return loss Vs. frequency plot of proposed microstrip patch antenna obtained by HFSS software. We could observe that the designed antenna is providing -63.50dB return loss value at frequency of 2.43GHz.

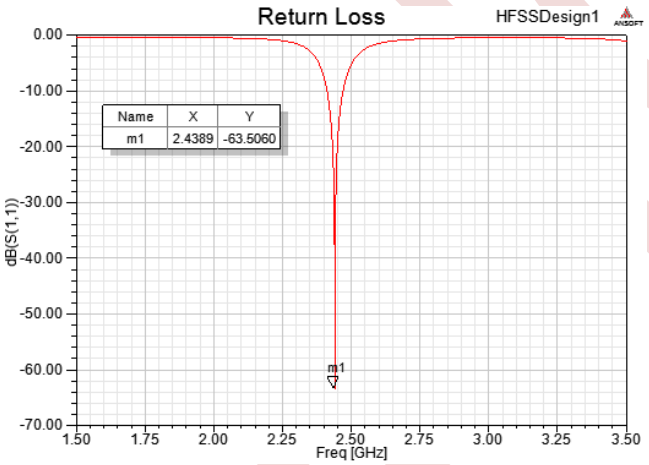


Figure 5: Return Loss.

C. Voltage Standing Wave Ratio

The VSWR is an important parameter for the communication device. It tells as how perfectly the antenna is

matched to the cable impedance without any reflection. In figure 6 we got voltage standing wave ratio with minimum value of 0.01 at 2.43GHz frequency.

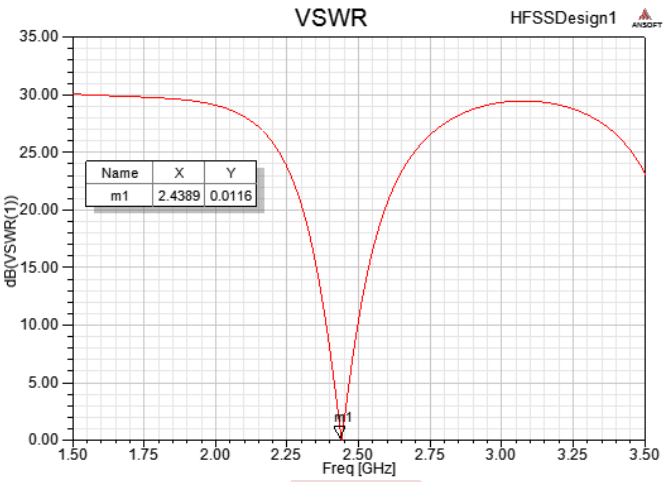


Figure 6: VSWR.

D. Radiation pattern

A radiation pattern defines the variation of the power radiated by an antenna as a function of the direction away from the antenna. Figures 7, 8 shows the 2D radiation pattern and 3D radiation pattern.

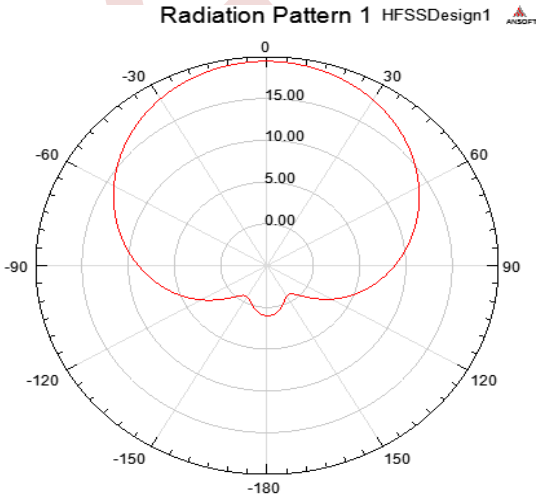


Figure 7: 2D radiation pattern.

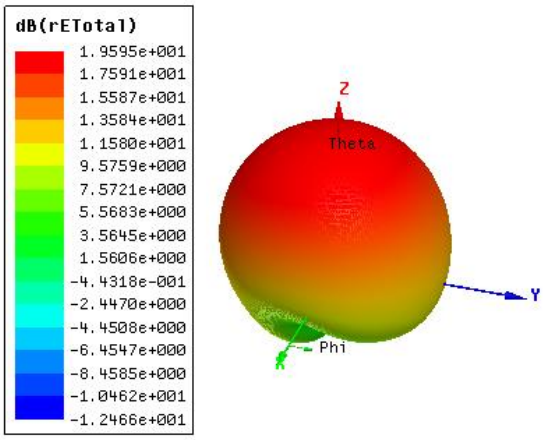


Figure 8: 3D radiation pattern.

V. CONCLUSION

This paper presents a design of a rectangular microstrip patch antenna operate at 2.4GHz frequency with microstrip line feed. The patch is made on a dielectric substrate by FR4 Epoxy materiel with a thickness of 1.6 mm and a relative permittivity of 4.4. Length and width of the patch are calculated as 37.29mm and 28.22mm respectively. Loss tangent for the dielectric is 0.02. Minimum value of S11 is –63.5dB at 2.43GHz. At the same frequency VSWR is 0.01dB

REFERENCES

[1] D.-G. Fang, *Antenna theory and microstrip antennas*. CRC Press, 2017.

[2] C. A. Balanis, *Antenna theory: analysis and design*. John wiley & sons, 2016.

[3] S. S. Holland, "Miniaturization of microstrip patch antennas for GPS applications," *Masters Theses*, p. 120, 2008.

[4] R. Bancroft, *Microstrip and printed antenna design*. The Institution of Engineering and Technology, 2009.

[5] R. Waterhouse, *Microstrip patch antennas: a designer's guide*. Springer Science & Business Media, 2013.

Author Index

Abad Lahlou, 408, 419
Abbas Sadia, 119
Abdellaoui Hassina, 66
Abdelli Radia, 79, 207, 413, 429
Achour Abdelyazid, 115
Adjati Arezki, 162, 381
Aidel Sofiane, 230
Ainouche Toufik, 191
Aissou Massinissa, 294, 325
Ait Said Hakim, 270, 325
Alkama Dina, 638
Alkama Lynda, 638
Alouache Sara, 314
Amimeur Hocine, 30, 369
Amrane Fayssal, 399, 490
Amrouche Bessam, 119, 393, 506
Amrouche Karim, 413
Amroune Mohammed, 152
Aouabed Fatiha, 308
Aouzellag Djamal, 36, 85, 91, 375, 387, 451, 458
Aouzellag Haroune, 393, 506
Aouzellag Narimen, 496
Aroua Fatima, 128
Arzag Kaddour, 218
Asnoun Mustapha, 185
Assem Houria, 447
Atroune Salah, 264, 289
Azni Mohamed, 614, 638
Azzouz Zin-eddine, 218
Babaghayou Messaoud, 602
Babes Badreddine, 464
Bacha Seddik, 3
Baghdadi Hamidouche, 7
Bayadi Abdelhafid, 308
Becherif Mohamed, 2
Bechkoura Hana, 298
Bechouche Ali, 66
Behloul Fatiha, 577
Beknadj Dalil, 608
Belaalia Asma, 595
Belazzoug Massinissa, 643
Belguet Oussama, 226
Belhaddad Abdelah, 53
Belhaouas Nasreddine, 447
Belhaouchet Nouri, 441
Belkhiri Mohammed, 525
Belkhiri Yamina, 191
Bellahsene Hocine, 620, 626, 632
Belmouhoub Amina, 549
Belounis Abdallah, 226
Ben Messaoud Safinaz, 525
Benamara Katia, 30, 369
Benatia Djamel, 243
Benazzouz Younes, 337
Bendahmane Boukhalfa, 278
Benhabsa Imadeddine, 134, 140
Benhacine Nasr-Eddine, 413
Benhadda Yamina, 349, 355, 361
Benidir Mohamed, 213

Benkhoris Mohamed-Fouad, 119
Benlatreche Mohamed Salah, 568
Benouarab Saliha, 73
Bentouhami Larafi, 23
Benyounes Fahima, 519
Berabez Kahina, 435, 469
Berboucha Ali, 375
Beroual Abderrahman, 254
Bouafassa Amar, 343
Bouaziz Fatiha, 586
Boubakeur Ahmed, 302
Bouchabane Abdeslem, 53
Bouchareb Ilhem, 19
Bouchebbah Badis, 248
Bouchelga Fatma, 283, 318
Bouchelkha Abdelhafid, 298
Boudissa Rabah, 308
Boudjelthia El Amin Kouadri, 447
Boudjema Fares, 561
Boudries Zoubir, 399, 490
Bouhafs Lina, 591
Bouheraoua Mustapha, 96
Bousbia Larbi, 480
Bouzid Yasser, 513, 549, 561
Bouzida Ahcene, 79, 429, 591
Bouzidi Athmane, 123, 179, 202
Brahami Sofiane, 115
Brahimi Brahim, 185
Brakna Ikram, 294

Chaib Noureddine, 602
Chekkal Samira, 85, 91, 387, 496
Chenna Amina, 458
Cherif Ahmed El-amine Tayeb, 568
Cherif Tahar Otmane, 506
Chouali Sabrina, 264
Chouikhi Lotfi, 581

Dascalescu Lucian, 264, 278
Deboucha Houssam, 146
Deffaf Brahim, 42, 404, 501
Degachi Riadh, 649
Dendouga Abdelhakim, 451
Derkaoui Mokhtaria, 349, 355, 361
Derrouaoui Saddam Hocine, 549, 561
Djermouni Kamel, 375, 408, 419, 501
Djoudi Oualid, 423
Doumbia Mamadou Lamine, 156

Essounbouli Najib, 7

Fares Belynda, 79
Ferroudj Nour el islem, 152
Ferroudj Yanis, 123
Fredj Siham, 543

Ghedamsi Kaci, 5, 36, 66, 115, 119, 375, 458, 506
Ghendir Said, 649
Gherbi Ahmed, 196
Guedida Sifelislam, 60
Gueguen Hervé, 543
Guendouz Djilalia, 337
Guerroudj Cherif, 108
Guesmi Kamel, 7
Guiatni Mohamed, 513, 549, 561

Habchi Lynda, 73
Hacini Ismail, 435, 469
Haddad Salah, 73
Hadjrioua Farid, 447
Hafdaoui Hichem, 243, 447
Halledj Salah Eddine, 343
Hamadi Yasmine, 608
Hamimid Mourad, 230
Hamitouche Kamel, 387
Hamouche Oulhadj, 586
Hamoudi Farid, 42, 207, 435
Hamoudi Yanis, 30, 85, 369
Hamour Khaled, 318
Hassaini Faycal, 30, 85, 91
Hebbar Nihed, 325
Herzine Mohand Seghir, 270
Hidra Lahlou, 179
Houari Azeddine, 119

Idir Abdelhakim, 60
Idir Badea, 234
Idirene Dimya, 168
Idjdarene Kassa, 435, 469

Idri Souad, 207
Iffouzar Koussaila, 119, 393, 506
Imaouchen Yacine, 91
Issaadi Idris, 490
Itouchene Hichem, 399, 490

Kacha Abdellah, 581
Kachenoura Rahma, 185
Kachi Miloud, 298
Kacimi Mohand Akli, 53
Kahlessenane Yaaqoub, 586
Kasdi Ahmed, 239, 264
Kedjouti Seddik, 19
Kemiha Mina, 581
Kennouche Samir, 496
Kenza Ydjedd, 179
Kerrouche Farid, 13, 47
Khaldi Rabah, 96
Kharouni Sounia, 620
Khemliche Mabrouk, 464, 537
Kornhuber Stefan, 318
Kouadri Ramzi, 134, 140

Labed Mohamed Amir, 213
Labraoui Nabila, 602
Ladgi Khaoula, 568
Lagoune Meryem, 464
Lahacani Narimen, 174
Laib Farah, 202
Laifaoui Abdelkrim, 270, 294
Lalouni Belaid Sofia, 404, 423, 469, 474, 501
Larabi Zina, 36
Latreche Samia, 464
Latreche Sofiane, 632
Latri Fatiha, 196
Latréche Samia, 537
Layachi Djedoui, 23
Lehouche Hocine, 543
Lounnas Fatma, 73

Madi Yazid, 451
Madjoudj Nadira, 447
Maouche Bachir, 234, 239, 248
Mebarki Youcef, 484
Mechnane Amel, 243
Medjahed Sakina, 239
Medjdoub Abdellah, 168, 314
Medjmadj Slimane, 549
Mehasni Rabia, 226
Mekhaldi Abdelouahab, 258, 302
Mekhilef Saad, 146
Mendil Boubekeur, 531, 543
Merabet Imen, 643
Merabet Nesrine, 626
Messaoudène Akila, 278
Meziani Madjid, 258
Mohamed Benbouzid, 60
Mohand Akli Ouakli, 179
Mouassa Souhil, 140
Mouhoub Sarra, 298
Moulai Hocine, 191, 254, 302
Mousli Wafia, 102

Nabab Alam Mahamad, 196
Nacef Sabrina, 506
Nacer Azzeddine, 254
Nacereddine Kamal, 302
Nafa Fares, 36
Naimi Djemai, 128
Namoune Khaoula, 595
Nemra Abdelkrim, 519
Nounou Kamal, 60

Omari Tahar, 568
Ouali Fateh, 174
Ouamri Mohamed Amine, 638
Ouaret Ahmed, 543
Ouazziz Yacine, 614
Ouchenir Nouredine, 283
Oukaour Amrane, 108

Radjef Lilia, 568
Rahman Md Jahidur, 156
Rahmani Allaoua, 278
Rahoui Adel, 185
Reboul Jean-Michel, 270, 294
Redouane Abderrahmane, 108
Rekioua Djamila, 162, 381
Rekioua Toufik, 13, 162, 381
Remache Saadi, 283
Rouabah Khaled, 643

Rouha Nacera, 283, 318
Rreffas Abderrahim, 23

Sahli Zahir, 330
Sahri Younes, 404
Sait Belkacem, 537
Sait Oussama, 537
Salhi Ahmed, 128
Salhi Souheil, 128
Salmi Abdenour, 561
Saou Rachid, 108
Sayah Samir, 441
Sayeh Karim Fathi, 42, 404, 408, 419, 501
Sekhane Hocine, 213
Siarry Patrick, 586
Sid Ahmed Soumia, 595
Slimani Linda, 134, 152
Soufi Youcef, 4
Souici Oussama, 140

Tabbache Bekheira, 60
Tafinine Farid, 577
Tafticht Tahar, 156
Taib Nabil, 13, 47, 289
Takorabet Nourddine, 123
Taleb-Ahmed Abdelmalik, 632
Tamalouzt Salah, 42, 375, 404, 408, 419, 423, 501, 591
Tayakout Hakim, 608
Tazerart Farid, 13, 47
Tchakala Mouctar, 156
Teguar Madjid, 258, 302
Tenniche Nesrine, 531
Tighzert Lyes, 531
Toufouti Riad, 480
Touitou Ikram, 556
Tounsi Mohamed, 608, 614

Yousfi Nabil, 191

Zaidi Elyazid, 23
Zaine Djamel, 404, 501
Zamoum Housseyn, 513
Zareb Nour El Houda, 626
Zerguini Sakina, 234
Ziane Ahmed, 218
Ziani Salim, 556
Zidane Nourredine, 474
Zouache Rafik, 23
Zoughab Samir, 441

EEIC′23

ISBN 978-9969-9732-0-4



EEIC'23

The second Electrical Engineering International Conference (EEIC'23) will provide a forum for researchers and students to present and share recent research results and ideas in the fields of Electrical Engineering and related topics. EEIC'23 will be held in the University Abderrahmane MIRA of Bejaia (Algeria), and will be organized by the Electrical Engineering Department, Faculty of Technology. The opportunity will also be offered to the various actors of the socio-economic sectors to express their concerns to the scientific community and to study together the possibilities of exchange and cooperation on current research topics carrying new and innovative ideas.

The scientific program of EEIC'23 contains the presentation of 121 accepted communications (69 in oral form and 52 in poster) as well as four plenary conferences led by eminent researchers.

REBOBINAGE INDUSTRIEL
Etablissement BOUKARI Boualem
Adresse:TIZI VLG IGHIL OUAZZOUG BEJAIA
TEL/FAX:034 11 61 64 Mob: 0550 90 88 25
e-mail: boukari.rebobinage@yahoo.fr

Electrical Engineering Department, Faculty of Technology,
University A. Mira of Bejaia, Road of Targa Ouzemmour, 06000, Bejaia, Algeria
Tel: +213 (0) 5 54 21 40 61 Fax: +213 (0) 34 81 37 13
Email: eeic23@univ-bejaia.dz https://eeic23.sciencesconf.org

ISBN : 978-9969-9732-0-4